



*cells*

Special Issue Reprint

---

# Molecular and Cellular Mechanisms of Cancers

## Glioblastoma

---

Edited by  
Javier S. Castresana and Bárbara Meléndez

[mdpi.com/journal/cells](https://mdpi.com/journal/cells)



# **Molecular and Cellular Mechanisms of Cancers: Glioblastoma**



# **Molecular and Cellular Mechanisms of Cancers: Glioblastoma**

Guest Editors

**Javier S. Castresana**  
**Bárbara Meléndez**



Basel • Beijing • Wuhan • Barcelona • Belgrade • Novi Sad • Cluj • Manchester

*Guest Editors*

Javier S. Castresana  
Department of Biochemistry  
and Genetics  
University of Navarra  
Pamplona  
Spain

Bárbara Meléndez  
Department of Pathology  
Virgen de la Salud Hospital  
Toledo  
Spain

*Editorial Office*

MDPI AG  
Grosspeteranlage 5  
4052 Basel, Switzerland

This is a reprint of the Special Issue, published open access by the journal *Cells* (ISSN 2073-4409), freely accessible at: [www.mdpi.com/journal/cells/special\\_issues/cells\\_glioblastoma](http://www.mdpi.com/journal/cells/special_issues/cells_glioblastoma).

For citation purposes, cite each article independently as indicated on the article page online and using the guide below:

Lastname, A.A.; Lastname, B.B. Article Title. <i>Journal Name</i> <b>Year</b> , <i>Volume Number</i> , Page Range.
--

**ISBN 978-3-7258-2934-7 (Hbk)**

**ISBN 978-3-7258-2933-0 (PDF)**

**<https://doi.org/10.3390/books978-3-7258-2933-0>**

© 2024 by the authors. Articles in this book are Open Access and distributed under the Creative Commons Attribution (CC BY) license. The book as a whole is distributed by MDPI under the terms and conditions of the Creative Commons Attribution-NonCommercial-NoDerivs (CC BY-NC-ND) license (<https://creativecommons.org/licenses/by-nc-nd/4.0/>).

# Contents

<b>About the Editors</b> . . . . .	<b>vii</b>
<b>Preface</b> . . . . .	<b>ix</b>
<b>Javier S. Castresana and Bárbara Meléndez</b> Molecular and Cellular Mechanisms of Glioblastoma Reprinted from: <i>Cells</i> <b>2021</b> , <i>10</i> , 1456, <a href="https://doi.org/10.3390/cells10061456">https://doi.org/10.3390/cells10061456</a> . . . . .	<b>1</b>
<b>Cornelis J.F. van Noorden, Vashendriya V.V. Hira, Amber J. van Dijck, Metka Novak, Barbara Breznik and Remco J. Molenaar</b> Energy Metabolism in <i>IDH1</i> Wild-Type and <i>IDH1</i> -Mutated Glioblastoma Stem Cells: A Novel Target for Therapy? Reprinted from: <i>Cells</i> <b>2021</b> , <i>10</i> , 705, <a href="https://doi.org/10.3390/cells10030705">https://doi.org/10.3390/cells10030705</a> . . . . .	<b>5</b>
<b>Bernarda Majc, Metka Novak, Nataša Kopitar-Jerala, Anahid Jewett and Barbara Breznik</b> Immunotherapy of Glioblastoma: Current Strategies and Challenges in Tumor Model Development Reprinted from: <i>Cells</i> <b>2021</b> , <i>10</i> , 265, <a href="https://doi.org/10.3390/cells10020265">https://doi.org/10.3390/cells10020265</a> . . . . .	<b>20</b>
<b>Tomás Duraj, Noemí García-Romero, Josefa Carrión-Navarro, Rodrigo Madurga, Ana Ortiz de Mendivil and Ricardo Prat-Acin et al.</b> Beyond the Warburg Effect: Oxidative and Glycolytic Phenotypes Coexist within the Metabolic Heterogeneity of Glioblastoma Reprinted from: <i>Cells</i> <b>2021</b> , <i>10</i> , 202, <a href="https://doi.org/10.3390/cells10020202">https://doi.org/10.3390/cells10020202</a> . . . . .	<b>42</b>
<b>Konstantin Masliantsev, Lucie Karayan-Tapon and Pierre-Olivier Guichet</b> Hippo Signaling Pathway in Gliomas Reprinted from: <i>Cells</i> <b>2021</b> , <i>10</i> , 184, <a href="https://doi.org/10.3390/cells10010184">https://doi.org/10.3390/cells10010184</a> . . . . .	<b>65</b>
<b>Issan Zhang, Paula Lépine, Chanshuai Han, María Lacalle-Aurioles, Carol X.-Q. Chen and Rainer Haag et al.</b> Nanotherapeutic Modulation of Human Neural Cells and Glioblastoma in Organoids and Monocultures Reprinted from: <i>Cells</i> <b>2020</b> , <i>9</i> , 2434, <a href="https://doi.org/10.3390/cells9112434">https://doi.org/10.3390/cells9112434</a> . . . . .	<b>79</b>
<b>Lara Navarro, Teresa San-Miguel, Javier Megías, Nuria Santonja, Silvia Calabuig and Lisandra Muñoz-Hidalgo et al.</b> Identification of New Genetic Clusters in Glioblastoma Multiforme: <i>EGFR</i> Status and <i>ADD3</i> Losses Influence Prognosis Reprinted from: <i>Cells</i> <b>2020</b> , <i>9</i> , 2429, <a href="https://doi.org/10.3390/cells9112429">https://doi.org/10.3390/cells9112429</a> . . . . .	<b>96</b>
<b>Olena Karatsai, Pavel Shliaha, Ole N. Jensen, Oleh Stasyk and Maria Jolanta Redowicz</b> Combinatory Treatment of Canavanine and Arginine Deprivation Efficiently Targets Human Glioblastoma Cells via Pleiotropic Mechanisms Reprinted from: <i>Cells</i> <b>2020</b> , <i>9</i> , 2217, <a href="https://doi.org/10.3390/cells9102217">https://doi.org/10.3390/cells9102217</a> . . . . .	<b>115</b>
<b>Ana M. Hernández-Vega, Aylin Del Moral-Morales, Carmen J. Zamora-Sánchez, Ana G. Piña-Medina, Aliesha González-Arenas and Ignacio Camacho-Arroyo</b> Estradiol Induces Epithelial to Mesenchymal Transition of Human Glioblastoma Cells Reprinted from: <i>Cells</i> <b>2020</b> , <i>9</i> , 1930, <a href="https://doi.org/10.3390/cells9091930">https://doi.org/10.3390/cells9091930</a> . . . . .	<b>141</b>

<b>Yu-Kai Su, Jia Wei Lin, Jing-Wen Shih, Hao-Yu Chuang, Iat-Hang Fong and Chi-Tai Yeh et al.</b> Targeting BC200/miR218-5p Signaling Axis for Overcoming Temozolomide Resistance and Suppressing Glioma Stemness Reprinted from: <i>Cells</i> <b>2020</b> , <i>9</i> , 1859, <a href="https://doi.org/10.3390/cells9081859">https://doi.org/10.3390/cells9081859</a> . . . . .	<b>164</b>
<b>Helena Fellinger, Stefan Stangl, Alicia Hernandez Schnelzer, Melissa Schwab, Tommaso Di Genio and Marija Pieper et al.</b> Time- and Dose-Dependent Effects of Ionizing Irradiation on the Membrane Expression of Hsp70 on Glioma Cells Reprinted from: <i>Cells</i> <b>2020</b> , <i>9</i> , 912, <a href="https://doi.org/10.3390/cells9040912">https://doi.org/10.3390/cells9040912</a> . . . . .	<b>185</b>
<b>Ilaria Cristofaro, Francesco Alessandrini, Zaira Spinello, Claudia Guerriero, Mario Fiore and Elisa Caffarelli et al.</b> Cross Interaction between M2 Muscarinic Receptor and Notch1/EGFR Pathway in Human Glioblastoma Cancer Stem Cells: Effects on Cell Cycle Progression and Survival Reprinted from: <i>Cells</i> <b>2020</b> , <i>9</i> , 657, <a href="https://doi.org/10.3390/cells9030657">https://doi.org/10.3390/cells9030657</a> . . . . .	<b>206</b>
<b>Ana Laura Vieira Alves, Angela Margarida Costa, Olga Martinho, Vinicius Duval da Silva, Peter Jordan and Viviane Aline Oliveira Silva et al.</b> WNK2 Inhibits Autophagic Flux in Human Glioblastoma Cell Line Reprinted from: <i>Cells</i> <b>2020</b> , <i>9</i> , 485, <a href="https://doi.org/10.3390/cells9020485">https://doi.org/10.3390/cells9020485</a> . . . . .	<b>223</b>
<b>Weder Pereira de Menezes, Viviane Aline Oliveira Silva, Izabela Natália Faria Gomes, Marcela Nunes Rosa, Maria Luisa Corcoll Spina and Adriana Cruvinel Carloni et al.</b> Loss of 5'-Methylthioadenosine Phosphorylase (MTAP) is Frequent in High-Grade Gliomas; Nevertheless, it is Not Associated with Higher Tumor Aggressiveness Reprinted from: <i>Cells</i> <b>2020</b> , <i>9</i> , 492, <a href="https://doi.org/10.3390/cells9020492">https://doi.org/10.3390/cells9020492</a> . . . . .	<b>235</b>
<b>Jason Adhikaree, Julia Moreno-Vicente, Aanchal Preet Kaur, Andrew Mark Jackson and Poulam M. Patel</b> Resistance Mechanisms and Barriers to Successful Immunotherapy for Treating Glioblastoma Reprinted from: <i>Cells</i> <b>2020</b> , <i>9</i> , 263, <a href="https://doi.org/10.3390/cells9020263">https://doi.org/10.3390/cells9020263</a> . . . . .	<b>259</b>
<b>Rochelle C. J. D'Souza, Carolin Offenhäuser, Jasmin Straube, Ulrich Baumgartner, Anja Kordowski and Yuchen Li et al.</b> Q-Cell Glioblastoma Resource: Proteomics Analysis Reveals Unique Cell-States Are Maintained in 3D Culture Reprinted from: <i>Cells</i> <b>2020</b> , <i>9</i> , 267, <a href="https://doi.org/10.3390/cells9020267">https://doi.org/10.3390/cells9020267</a> . . . . .	<b>280</b>
<b>Esperanza R. Matarredona and Angel M. Pastor</b> Extracellular Vesicle-Mediated Communication between the Glioblastoma and Its Microenvironment Reprinted from: <i>Cells</i> <b>2019</b> , <i>9</i> , 96, <a href="https://doi.org/10.3390/cells9010096">https://doi.org/10.3390/cells9010096</a> . . . . .	<b>295</b>
<b>Sihana Ziberi, Mariachiara Zuccarini, Marzia Carluccio, Patricia Giuliani, Lucia Ricci-Vitiani and Roberto Pallini et al.</b> Upregulation of Epithelial-To-Mesenchymal Transition Markers and P2X7 Receptors Is Associated to Increased Invasiveness Caused by P2X7 Receptor Stimulation in Human Glioblastoma Stem Cells Reprinted from: <i>Cells</i> <b>2019</b> , <i>9</i> , 85, <a href="https://doi.org/10.3390/cells9010085">https://doi.org/10.3390/cells9010085</a> . . . . .	<b>308</b>
<b>Paulina Vaitkiene, Ruta Urbanaviciute, Povilas Grigas, Giedrius Steponaitis, Arimantas Tamasauskas and Daina Skiriutė</b> Identification of Astrocytoma Blood Serum Protein Profile Reprinted from: <i>Cells</i> <b>2019</b> , <i>9</i> , 16, <a href="https://doi.org/10.3390/cells9010016">https://doi.org/10.3390/cells9010016</a> . . . . .	<b>332</b>

**Digregorio Marina, Lombard Arnaud, Lumapat Paul Noel, Scholtes Felix, Rogister Bernard and Coppieters Natacha**  
Relevance of Translation Initiation in Diffuse Glioma Biology and its Therapeutic Potential  
Reprinted from: *Cells* **2019**, *8*, 1542, <https://doi.org/10.3390/cells8121542> . . . . . **341**

**Alessia Lo Dico, Daniela Salvatore, Cristina Martelli, Dario Ronchi, Cecilia Diceglie and Giovanni Lucignani et al.**  
Intracellular Redox-Balance Involvement in Temozolomide Resistance-Related Molecular Mechanisms in Glioblastoma  
Reprinted from: *Cells* **2019**, *8*, 1315, <https://doi.org/10.3390/cells8111315> . . . . . **370**





# About the Editors

## **Javier S. Castresana**

Javier S. Castresana is a Professor of Genetics at the University of Navarra, Pamplona, Spain. He previously worked for three years at Karolinska Institute as a predoctoral student; for two years at Harvard Medical School as postdoctoral student; and for five years at the Spanish Scientific Research Council as a senior researcher. He is interested in glioblastoma genetics and epigenetics, with a special focus on brain tumor stem cell characterization.

## **Bárbara Meléndez**

Bárbara Meléndez is a researcher at the Molecular Pathology Research Unit, Department of Pathology, Virgen de la Salud Hospital, Toledo, Spain. She is interested in brain tumor genetics and epigenetics.



# Preface

Glioblastoma is the most malignant brain tumor. It has a survival of 12 to 15 months, despite all the therapeutic attempts that have been made in recent years. It is important to better understand the genetics and epigenetics of this tumor, which is highly heterogeneous at the cellular and molecular levels, highlighting four molecular types (proneural, classic, neural, and mesenchymal). Glioblastoma is also divided into those that have IDH mutations and those that do not, with the former having a better prognosis and generally corresponding to what has been called secondary glioblastomas in previous WHO classifications. Resistance to chemotherapy and radiotherapy, brain tumor stem cells, energy metabolism, epithelial-to-mesenchymal transition, immunotherapy, and reactive oxygen species phenotypes are discussed, referring to this deadly tumor.

Furthermore, in the near future, we must better characterize the brain tumor stem cells that initiate and maintain the tumor since they are resistant to chemotherapy and radiotherapy. New advances in glioblastoma can also elucidate oncolytic viruses, mesenchymal stem cells that carry and deliver genes and molecules to tumor cells, experiments with organoids, and even artificial intelligence that could have a great impact on clinical specialties such as pathology and radiology.

**Javier S. Castresana and Bárbara Meléndez**

*Guest Editors*



# Molecular and Cellular Mechanisms of Glioblastoma

Javier S. Castresana <sup>1,\*</sup>  and Bárbara Meléndez <sup>2</sup><sup>1</sup> Department of Biochemistry and Genetics, University of Navarra School of Sciences, 31008 Pamplona, Spain<sup>2</sup> Molecular Pathology Research Unit, Virgen de la Salud Hospital, 45005 Toledo, Spain; [bmelendez@sescam.jccm.es](mailto:bmelendez@sescam.jccm.es)\* Correspondence: [jscastresana@unav.es](mailto:jscastresana@unav.es)

Glioblastoma is the most malignant primary brain tumor. The therapeutic approach consisting of temozolomide, surgery and radiotherapy has not achieved any sufficient therapeutic improvement in recent years. Hence, it is urgent that we find cell therapies and/or molecular targets that, together with improvements in radiotherapy and chemotherapy, may benefit patients suffering from this devastating tumor. In this Special Issue of *Cells*, entitled “Molecular and Cellular Mechanisms of Cancers: Glioblastoma”, 20 articles on glioblastoma have been published (14 original articles and 6 reviews). Here, we will present a summary of the most relevant results presented in this issue, which undoubtedly have an impact at the level of a better understanding of the cellular and molecular biology of glioblastoma, as well as of possible new therapeutic targets to combat it.

The six reviews touch on interesting topics, such as immunotherapy [1,2], extracellular vesicles [3], energy metabolism [4], translational machinery [5] and the Hippo signaling pathway [6] in glioblastoma.

Immunotherapy is a growing field for the treatment of cancer and, in particular, for glioblastoma patients [1,2]. However, the identification of the patients that can benefit from immunotherapy treatments, as well as the type of immunotherapeutic approach to be used, still need to be improved for successful and effective treatments. Majc et al. [2] point to the possible causes of resistance to immunotherapy: intracranial location, inter- and intra-tumor heterogeneity or the immunosuppressive tumor microenvironment, among others. Adhikaree et al. [1] also point to PD-L1 expression levels, tumor mutations and T-cell immunosuppression as additional causes. The variety of immunotherapeutic strategies that have been applied in glioblastoma treatment are nicely described, together with advanced in vitro (cancer stem cells, organotypic tissue slices, organoids) and animal tumor models [2].

Adhikaree et al. [1] focus their review on the immune checkpoint PD-1/PD-L1 pathway. The use of PD-1/PD-L1 blockade antibodies in combination with chemotherapy and radiotherapy, or as a monotherapy, has been shown to be inefficient in glioblastoma. A better understanding of the barriers to immunotherapy and the mechanisms of immune resistance may help us to design future strategies for immune-related therapies.

Matarredona et al. [3] have reviewed the influence of extracellular vesicles derived from glioblastoma cells on the tumor microenvironment, as well as the possibility that such vesicles may serve as diagnostic markers of glioblastoma, and may also help the stratification of molecular subtypes of this tumor and the study of resistance to chemotherapy and radiotherapy. The extracellular vesicles are not only produced by the tumor, but also by the peritumoral cells that launch the vesicles at the tumor itself, possibly increasing its tumorigenicity.

Van Noorden et al. [4] review the production of energy and reactive oxygen species (ROS) in glioblastoma cells, making a clear difference between how the most differentiated tumor cells and cancer stem cells obtain energy. Differentiated glioblastoma cells mainly use aerobic glycolysis for ATP production without ROS production, whereas glioblastoma stem cells use oxidative phosphorylation for ATP and modest ROS production, due to the



**Citation:** Castresana, J.S.; Meléndez, B. Molecular and Cellular Mechanisms of Glioblastoma. *Cells* **2021**, *10*, 1456. <https://doi.org/10.3390/cells10061456>

Received: 3 June 2021

Accepted: 8 June 2021

Published: 10 June 2021

**Publisher's Note:** MDPI stays neutral with regard to jurisdictional claims in published maps and institutional affiliations.



**Copyright:** © 2021 by the authors. Licensee MDPI, Basel, Switzerland. This article is an open access article distributed under the terms and conditions of the Creative Commons Attribution (CC BY) license (<https://creativecommons.org/licenses/by/4.0/>).

hypoxia and quiescence of cancer stem cells. However, in IDH1-mutated glioblastomas, all cells of the tumor use oxidative phosphorylation for ATP and ROS production. Among the possibilities to treat these tumors, we might have a systemic therapeutic inhibition of oxidative phosphorylation, but the anti-cancer effects of ROS production in healthy cells would be inhibited as well. The authors finally suggest removing cancer stem cells out of their hypoxic niches to enable their differentiation and thus increase their sensitivity to radiotherapy and chemotherapy.

Targeting the translational machinery is becoming a new field of research in cancer biology. Digregorio et al. [5] describe cap-dependent and cap-independent translation initiation mechanisms, and indicate some of the targets, e.g., members of the eIF3 family or 4E-BP1, that, if knocked down, could favor the inhibition of the two forms of translation control.

Finally, Masliantsev et al. [6] review the Hippo pathway in glioblastoma. This control pathway prevents the passage to the nucleus of some gene transcription factors that participate in the control of cell proliferation, survival and maintenance of the stem phenotype. Therefore, Hippo, as a whole, behaves as a tumor suppression pathway. Hippo knockdown would make it possible for cells to dedifferentiate to pluripotent cells, and would induce cell death inhibition, therefore creating the tumor-prone subpopulations of cells.

Among the 14 articles, different important issues related to glioblastomas are studied, such as resistance to treatment [7–10], cancer stem cells [7,8,11], metabolism [8,12], epithelial-to-mesenchymal transition (EMT) [11,13] and ROS [9,12,14].

Cristofaro et al. [7] demonstrated the possibility of inhibiting cell cycle progression and survival in glioma stem cells via the activation of M2 muscarinic receptors, which leads to the inhibition of Notch1 and EGFR expression.

Glioblastoma is a heterogeneous tumor, not only at the cellular and molecular levels, but also at the metabolic level. The possibility of treating this tumor based on phenotypic metabolic differences is increasingly being considered [8], with the hope that by inhibiting metabolic pathways, not only can tumor cells be killed, but they can also be made vulnerable to chemotherapy clinical treatments.

Lo Dico et al. [9] investigated the possible relationship between fluctuations in mitochondrial ROS release to cytoplasm, chaperone-mediated autophagy (CMA) and cytotoxic effects in temozolomide-sensitive and temozolomide-resistant glioblastoma cells.

Su et al. [10] presented the interrelation between an lncRNA (BC200) and an miRNA (miR-218-5p) in glioblastoma, as two molecular agents linked to tumor malignancy and to temozolomide resistance. Thus, the lncRNA is over-expressed, while the miRNA shows a decreased expression in glioblastoma, which means that BC200 would act as an oncogenic factor, while miR-218-5p would behave as a tumor suppressor miRNA. Additionally, BC200 would act as a sponge for miR-218-5p.

Glioblastoma stem cells express high levels of ATP/P2X7 receptors (P2X7R). Ziberi et al. [11] reported that agonists of P2X7R would induce an oncogenic response to cells, with the upregulation of EMT marker expression, and increased cell migration and invasiveness.

Karatsai et al. [12] treated arginine-deprived glioblastoma cells with the arginine analogue canavanine, and detected increased apoptotic cell death only in tumor cells, opening the door to metabolic therapy against glioblastoma.

Hernández-Vega et al. [13] determined that 17 $\beta$ -estradiol, through ER- $\alpha$ , induces EMT by the upregulation of vimentin and N-cadherin expression, and increases migration and invasion in glioblastoma cells.

It is important to have glioblastoma models that allow us to perform reproducible and high-quality studies on glioblastoma biology and treatment. The open access Q-Cell glioblastoma claims to do so. D'Souza et al. [14] made a proteomic analysis of the QCell model and found that the molecular status of the cell lines studied associates with the previously determined transcriptome analysis. This makes it possible to clearly divide cells such as mesenchymal-like or neuronal-like glioblastoma cells, which is undoubtedly

important for choosing optimal models of glioblastoma prior to any in vitro research in this tumor.

Vaitkiene et al. [15] made a proteomic analysis of 10 proteins in blood serum from preoperative glioblastoma patients, revealing that the low levels of two of them, osteopontin and IP10, were associated with increased glioblastoma patient survival.

In the present era of biomedical research, experiments using co-cultures and organoid models are very interesting for the evaluation of nanotherapeutics at the experimental level. By combining reconstituted 3D models of glioblastoma (tumoroids) with cerebral organoids and by modulating the activity of microglia with dendritic polyglycerol sulfate (dPGS), Zhang et al. [16] demonstrated that dPGS-treated microglia reduced tumoroid invasiveness. This study proposes the evaluation of well-defined nanostructures in well-characterized human organoids and co-cultures.

Deletions on the 5'-methylthioadenosine phosphorylase (MTAP) gene have been detected in several tumors, although the role of this gene in carcinogenesis is not clear yet. Menezes et al. [17] demonstrated MTAP loss of expression as a frequent genetic event in glioblastoma, but MTAP expression was not associated with survival, which downplays this gene as a potential tumor suppressor gene candidate.

Navarro et al. [18] showed that EGFRvIII mutation and ADD3 loss were bad prognostic markers in a series of glioblastomas studied by multiplex ligation-dependent probe amplification. From this result, we might understand the absence of effect of the inhibitors of receptor tyrosine kinases in those glioblastomas that do not present EGFR mutations.

Alves et al. [19] demonstrated that the WNK2 gene, a known glioma suppressor gene, negatively regulates the migration and invasion of glioblastoma cells and inhibits their autophagic flux.

Lastly, Fellingner et al. [20] presented results on the accumulation of Hsp70 in the membrane of glioblastoma cells after high irradiation doses. Hsp70 can be found overexpressed in the plasma membrane or in the cytosol of tumor cells, including glioblastoma. Depending on its location in the cell, Hsp70 can promote cell growth (cytosolic location) or serve as a target for NK cells (tumor cell membrane location). The localization of this protein in tumor cell membranes and the consequent activation of NK cells suggests the combination of high-dose radiotherapy with immunotherapy treatments.

In summary, this Special Issue presents 20 articles that help us to better understand the biology of glioblastoma and some possible ways to improve its treatment. Resistance to chemotherapy and radiotherapy, cancer stem cells, energy metabolism, EMT, immunotherapy and ROS are discussed, referring to this deadly tumor.

**Funding:** This project was funded by a grant from the Fundación Universidad de Navarra, Pamplona, Spain.

**Conflicts of Interest:** The author declares no conflict of interest.

## References

1. Adhikaree, J.; Moreno-Vicente, J.; Kaur, A.P.; Jackson, A.M.; Patel, P.M. Resistance Mechanisms and Barriers to Successful Immunotherapy for Treating Glioblastoma. *Cells* **2020**, *9*, 263. [CrossRef] [PubMed]
2. Majc, B.; Novak, M.; Jerala, N.K.; Jewett, A.; Breznik, B. Immunotherapy of Glioblastoma: Current Strategies and Challenges in Tumor Model Development. *Cells* **2021**, *10*, 265. [CrossRef] [PubMed]
3. Matarredona, E.R.; Pastor, A.M. Extracellular Vesicle-Mediated Communication between the Glioblastoma and Its Microenvironment. *Cells* **2019**, *9*, 96. [CrossRef] [PubMed]
4. van Noorden, C.J.F.; Hira, V.V.V.; van Dijck, A.J.; Novak, M.; Breznik, B.; Molenaar, R.J. Energy Metabolism in IDH1 Wild-Type and IDH1-Mutated Glioblastoma Stem Cells: A Novel Target for Therapy? *Cells* **2021**, *10*, 705. [CrossRef] [PubMed]
5. Digregorio, M.; Lombard, A.; Lumapat, P.N.; Scholtes, F.; Rogister, B.; Coppieters, N. Relevance of Translation Initiation in Diffuse Glioma Biology and its Therapeutic Potential. *Cells* **2019**, *8*, 1542. [CrossRef]
6. Masliantsev, K.; Karayan-Tapon, L.; Guichet, P.O. Hippo Signaling Pathway in Gliomas. *Cells* **2021**, *10*, 184. [CrossRef] [PubMed]
7. Cristofaro, I.; Alessandrini, F.; Spinello, Z.; Guerriero, C.; Fiore, M.; Caffarelli, E.; Laneve, P.; Dini, L.; Conti, L.; Tata, A.M. Cross Interaction between M2 Muscarinic Receptor and Notch1/EGFR Pathway in Human Glioblastoma Cancer Stem Cells: Effects on Cell Cycle Progression and Survival. *Cells* **2020**, *9*, 657. [CrossRef] [PubMed]



8. Duraj, T.; García-Romero, N.; Carrión-Navarro, J.; Madurga, R.; Mendivil, A.O.; Prat-Acin, R.; Garcia-Cañamaque, L.; Ayuso-Sacido, A. Beyond the Warburg Effect: Oxidative and Glycolytic Phenotypes Coexist within the Metabolic Heterogeneity of Glioblastoma. *Cells* **2021**, *10*, 202. [CrossRef] [PubMed]
9. Lo Dico, A.; Salvatore, D.; Martelli, C.; Ronchi, D.; Diceglie, C.; Lucignani, G.; Ottobrini, L. Intracellular Redox-Balance Involvement in Temozolomide Resistance-Related Molecular Mechanisms in Glioblastoma. *Cells* **2019**, *8*, 1315. [CrossRef] [PubMed]
10. Su, Y.K.; Lin, J.W.; Shih, J.W.; Chuang, H.Y.; Fong, I.H.; Yeh, C.T.; Lin, C.M. Targeting BC200/miR218-5p Signaling Axis for Overcoming Temozolomide Resistance and Suppressing Glioma Stemness. *Cells* **2020**, *9*, 1859. [CrossRef] [PubMed]
11. Ziberi, S.; Zuccarini, M.; Carluccio, M.; Giuliani, P.; Ricci-Vitiani, L.; Pallini, R.; Caciagli, F.; Di Iorio, P.; Ciccarelli, R. Upregulation of Epithelial-To-Mesenchymal Transition Markers and P2X7 Receptors Is Associated to Increased Invasiveness Caused by P2X7 Receptor Stimulation in Human Glioblastoma Stem Cells. *Cells* **2019**, *9*, 85. [CrossRef] [PubMed]
12. Karatsai, O.; Shliaha, P.; Jensen, O.N.; Stasyk, O.; Redowicz, M.J. Combinatory Treatment of Canavanine and Arginine Deprivation Efficiently Targets Human Glioblastoma Cells via Pleiotropic Mechanisms. *Cells* **2020**, *9*, 2217. [CrossRef] [PubMed]
13. Hernandez-Vega, A.M.; Del Moral-Morales, A.; Zamora-Sanchez, C.J.; Pina-Medina, A.G.; Gonzalez-Arenas, A.; Camacho-Arroyo, I. Estradiol Induces Epithelial to Mesenchymal Transition of Human Glioblastoma Cells. *Cells* **2020**, *9*, 1930. [CrossRef] [PubMed]
14. D'Souza, R.C.J.; Offenhauser, C.; Straube, J.; Baumgartner, U.; Kordowski, A.; Li, Y.; Stringer, B.W.; Alexander, H.; Lwin, Z.; Inglis, P.L.; et al. Q-Cell Glioblastoma Resource: Proteomics Analysis Reveals Unique Cell-States are Maintained in 3D Culture. *Cells* **2020**, *9*, 267. [CrossRef] [PubMed]
15. Vaitkiene, P.; Urbanaviciute, R.; Grigas, P.; Steponaitis, G.; Tamasauskas, A.; Skiriute, D. Identification of Astrocytoma Blood Serum Protein Profile. *Cells* **2019**, *9*, 16. [CrossRef] [PubMed]
16. Zhang, I.; Lepine, P.; Han, C.; Lacalle-Aurioles, M.; Chen, C.X.; Haag, R.; Durcan, T.M.; Maysinger, D. Nanotherapeutic Modulation of Human Neural Cells and Glioblastoma in Organoids and Monocultures. *Cells* **2020**, *9*, 2434. [CrossRef] [PubMed]
17. Menezes, W.P.; Silva, V.A.O.; Gomes, I.N.F.; Rosa, M.N.; Spina, M.L.C.; Carloni, A.C.; Alves, A.L.V.; Melendez, M.; Almeida, G.C.; Silva, L.S.D.; et al. Loss of 5'-Methylthioadenosine Phosphorylase (MTAP) is Frequent in High-Grade Gliomas; Nevertheless, it is Not Associated with Higher Tumor Aggressiveness. *Cells* **2020**, *9*, 492. [CrossRef] [PubMed]
18. Navarro, L.; San-Miguel, T.; Megias, J.; Santonja, N.; Calabuig, S.; Munoz-Hidalgo, L.; Roldan, P.; Cerda-Nicolas, M.; Lopez-Gines, C. Identification of New Genetic Clusters in Glioblastoma Multiforme: EGFR Status and ADD3 Losses Influence Prognosis. *Cells* **2020**, *9*, 2429. [CrossRef] [PubMed]
19. Alves, A.L.V.; Costa, A.M.; Martinho, O.; da Silva, V.D.; Jordan, P.; Silva, V.A.O.; Reis, R.M. WNK2 Inhibits Autophagic Flux in Human Glioblastoma Cell Line. *Cells* **2020**, *9*, 485. [CrossRef] [PubMed]
20. Fellingner, H.; Stangl, S.; Hernandez Schnelzer, A.; Schwab, M.; Di Genio, T.; Pieper, M.; Werner, C.; Shevtsov, M.; Haller, B.; Multhoff, G. Time- and Dose-Dependent Effects of Ionizing Irradiation on the Membrane Expression of Hsp70 on Glioma Cells. *Cells* **2020**, *9*, 912. [CrossRef] [PubMed]

Review

# Energy Metabolism in *IDH1* Wild-Type and *IDH1*-Mutated Glioblastoma Stem Cells: A Novel Target for Therapy?

Cornelis J.F. van Noorden <sup>1,2,\*</sup>, Vashendriya V.V. Hira <sup>1</sup>, Amber J. van Dijck <sup>2</sup> , Metka Novak <sup>1</sup>, Barbara Breznik <sup>1</sup>  and Remco J. Molenaar <sup>1,3</sup> 

<sup>1</sup> Department of Genetic Toxicology and Cancer Biology, National Institute of Biology, Večna Pot 111, 1000 Ljubljana, Slovenia; vashendriyavvhira@gmail.com (V.V.V.H.); metka.novak@nib.si (M.N.); barbara.breznik@nib.si (B.B.); r.j.molenaar@amsterdamumc.nl (R.J.M.)

<sup>2</sup> Department of Medical Biology, Amsterdam UMC Location Academic Medical Center, University of Amsterdam, 1105 AZ Amsterdam, The Netherlands; a.j.vandijck@amsterdamumc.nl

<sup>3</sup> Department of Medical Oncology, Amsterdam UMC Location Academic Medical Center, University of Amsterdam, 1105 AZ Amsterdam, The Netherlands

\* Correspondence: c.j.vannoorden@nib.si; Tel.: +31-638-639-561

**Abstract:** Cancer is a redox disease. Low levels of reactive oxygen species (ROS) are beneficial for cells and have anti-cancer effects. ROS are produced in the mitochondria during ATP production by oxidative phosphorylation (OXPHOS). In the present review, we describe ATP production in primary brain tumors, glioblastoma, in relation to ROS production. Differentiated glioblastoma cells mainly use glycolysis for ATP production (aerobic glycolysis) without ROS production, whereas glioblastoma stem cells (GSCs) in hypoxic perivascular niches use OXPHOS for ATP and ROS production, which is modest because of the hypoxia and quiescence of GSCs. In a significant proportion of glioblastoma, isocitrate dehydrogenase 1 (*IDH1*) is mutated, causing metabolic rewiring, and all cancer cells use OXPHOS for ATP and ROS production. Systemic therapeutic inhibition of glycolysis is not an option as clinical trials have shown ineffectiveness or unwanted side effects. We argue that systemic therapeutic inhibition of OXPHOS is not an option either because the anti-cancer effects of ROS production in healthy cells is inhibited as well. Therefore, we advocate to remove GSCs out of their hypoxic niches by the inhibition of their binding to niches to enable their differentiation and thus increase their sensitivity to radiotherapy and/or chemotherapy.

**Keywords:** glioblastoma stem cells; *IDH1*-mutation; energy metabolism



**Citation:** van Noorden, C.J.F.; Hira, V.V.V.; van Dijck, A.J.; Novak, M.; Breznik, B.; Molenaar, R.J. Energy Metabolism in *IDH1* Wild-Type and *IDH1*-Mutated Glioblastoma Stem Cells: A Novel Target for Therapy? *Cells* **2021**, *10*, 705. <https://doi.org/10.3390/cells10030705>

Academic Editors: Javier S. Castresana and Ritva Tikkanen

Received: 7 February 2021

Accepted: 14 March 2021

Published: 22 March 2021

**Publisher's Note:** MDPI stays neutral with regard to jurisdictional claims in published maps and institutional affiliations.



**Copyright:** © 2021 by the authors. Licensee MDPI, Basel, Switzerland. This article is an open access article distributed under the terms and conditions of the Creative Commons Attribution (CC BY) license (<https://creativecommons.org/licenses/by/4.0/>).

## 1. Introduction

James Watson postulated in 2014 that physical activity prevents diseases such as diabetes, dementia, cardiovascular disease, and some types of cancer [1]. Generation of low levels of reactive oxygen species (ROS) during physical activity induce redox potentials that are needed to correctly fold proteins in the endoplasmic reticulum. Therefore, Watson named these diseases redox diseases [1]. We took this hypothesis further with respect to cancer by postulating that this mechanism explains the considerable evidence that physical activity may not only reduce the risk of cancer [2,3], but also prolong the survival of cancer patients, delay the recurrence of cancer [2,4] and improve the quality of life of cancer patients [5].

Proliferating differentiated cancer cells predominantly use glucose in cytoplasmic glycolysis instead of mitochondrial respiration for ATP production, independently of the presence of oxygen (the so-called Warburg effect, Figure 1) [6]. In the past, it was assumed that the Warburg effect occurred because of defective mitochondria in cancer cells, but this is not the case. Proliferating cancer cells preferentially use aerobic glycolysis because besides ATP production, glycolysis enables the synthesis of two elements that are needed by proliferating cells: carbohydrate building blocks and a reduction in the

power required for biosynthetic reactions, i.e., NADPH [6–8]. ROS shortages may be caused by several mechanisms in proliferating cells. First, the Warburg effect has a negative impact on ROS production, resulting in ROS shortages. ROS are mainly produced during oxidative phosphorylation (OXPHOS) in mitochondria from 0.1–2% of the electrons that escape from the electron transport chain (Figure 1) [9], whereas ATP is mainly generated in the cytoplasmic glycolysis in proliferating cancer cells. Second, NADPH is produced in excess and is not only used for reductive biosynthetic reactions, but also facilitates the antioxidant activity of reduced glutathione [6,7] and detoxifying enzymes [10]. ROS production is elevated during physical activity and that may compensate, resulting in anti-cancer effects. The nuclear factor erythroid 2-related factor 2 (Nrf2) is an important regulator of ROS levels in cells [11]. Nrf2 is activated by ROS and it is degraded by proteasomes after ubiquitination when ROS levels are low. When Nrf2 is activated, it induces the expression of antioxidant defense systems, including those in the endoplasmic reticulum and in stem cells, such as hematopoietic stem cells in the bone marrow [11].

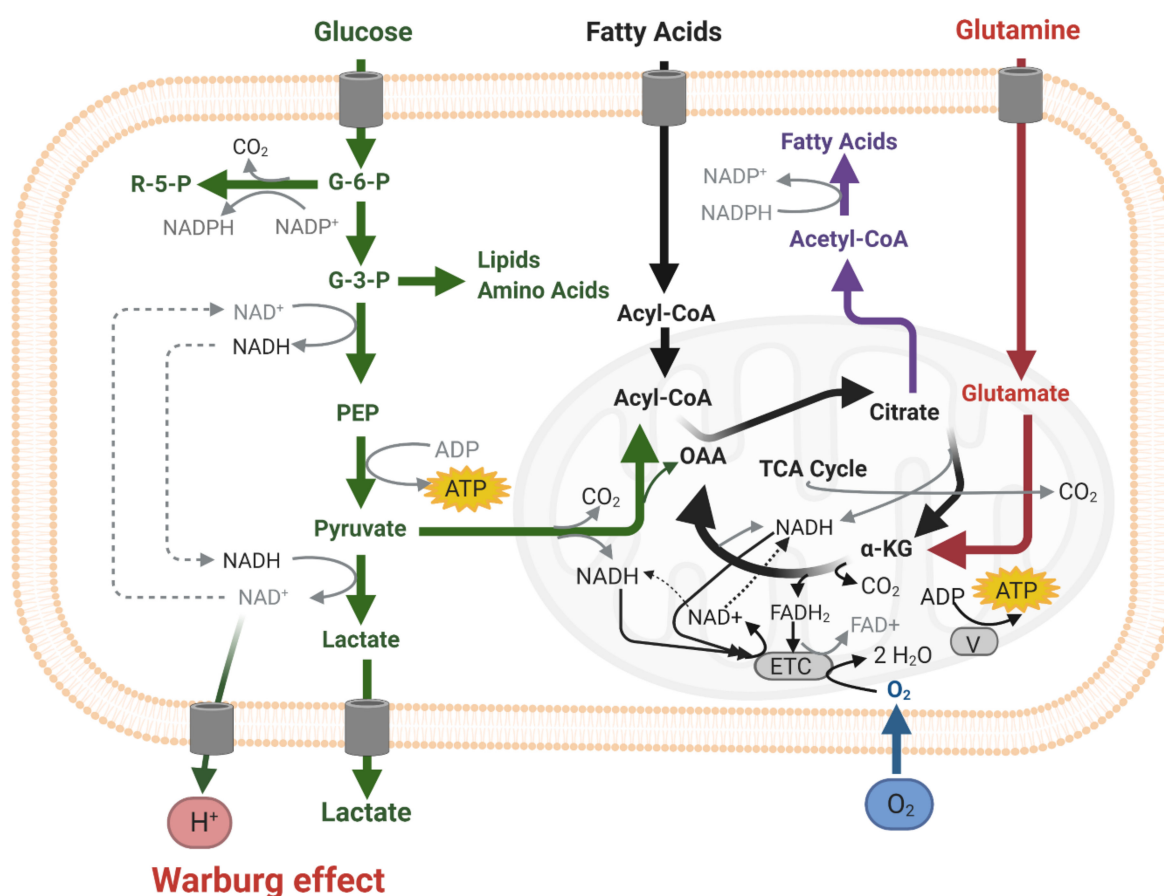


**Figure 1.** Scheme of cellular energy metabolism (ATP production) in the cytoplasm (glycolysis, green) and in mitochondria oxidative phosphorylation (OXPHOS) via the electron transport chain (ETC, grey) with the use of oxygen (blue). Substrate for glycolysis is (extracellular) glucose and for OXPHOS pyruvate (from the cytoplasm, green), or (extracellular) fatty acids (black), or (extracellular) glutamine and/or glutamate (red).

Besides the rapidly proliferating differentiated cancer cells, tumors also contain a small fraction of undifferentiated cancer stem cells (CSCs) with tumor-initiating and self-renewal properties. CSCs reside in specific hypoxic microenvironments, or niches, where CSCs are maintained in a slowly dividing quiescent state. Quiescence of CSCs protects them from the cytotoxic effects of chemotherapy and radiotherapy, as these therapeutic strategies only target proliferating cells. CSC protection in niches results in tumor recurrence in cancer patients [12–16].

It has become generally accepted that more differentiated (i.e., non-CSC) proliferating cancer cells preferentially use aerobic glycolysis for their ATP production, whereas CSCs preferentially use OXPHOS [12–22]. Similar to healthy cells, CSCs benefit from low levels of ROS, but not excess levels of ROS, which are toxic [23,24]. This is corroborated by the fact that CSCs need hypoxic conditions to control their stem cell fate [15], and the low oxygen levels in the hypoxic niches limit, but certainly do not eliminate, the production of ATP and ROS [14,19]. A similar phenomenon occurs in hematopoietic stem cells in their bone marrow niches [25,26].

On the basis of these facts, a ROS-related riddle becomes apparent. On the one hand, the low levels of ROS that are generated in the context of physical exercise facilitate healthy cells to correctly fold proteins in the endoplasmic reticulum, and thus low ROS levels are beneficial to the human body. On the other hand, it has been postulated that CSCs use mitochondrial respiration for ATP production because low levels of ROS aid CSCs in maintaining their stem cell state [23,24]. How can we solve this riddle from a therapeutical point of view and eradicate CSCs in their protective niches and at the same time allow healthy cells in the bodies of patients to produce low levels of ROS? In the present review, we aim to solve this riddle for glioblastoma patients.

In glioblastoma brain tumors, glioblastoma stem cells (GSCs) are protected in their hypoxic peri-arteriolar GSC niches (Figure 2) in a similar way to how healthy HSCs and leukemic stem cells (LSCs) are protected in hypoxic peri-arteriolar niches in the bone marrow [25–28]. In addition, there are similarities between GSCs in hypoxic peri-arteriolar GSC niches and neural stem cells (NSCs) in the hypoxic subventricular zone (SVZ) and subgranular zone (SGZ) [16,29,30]. GSCs are non-dividing or slowly dividing and, in that quiescent state, have a modest metabolism. GSCs are held responsible for the recurrence of glioblastoma after treatment (surgery, radiotherapy, and temozolomide chemotherapy). Survival of glioblastoma patients is on average 15 months, but recently it was reported that survival of the fittest patient population can be prolonged to 20 months by the application of magnetic tumor-treating fields (TTF) [31]. The canonical molecular anti-cancer mechanism of TTF is that this novel modality disrupts mitosis by interference with heterotrimer septin complexes and  $\alpha/\beta$ -tubulin at the metaphase–anaphase transition in the cell cycle causing mitotic catastrophe [32,33]. In addition, interference with energy metabolism seems plausible because the production of pyruvate, the end-product of glycolysis and a critical fuel for mitochondrial respiration, is reduced when TTF are applied [34].

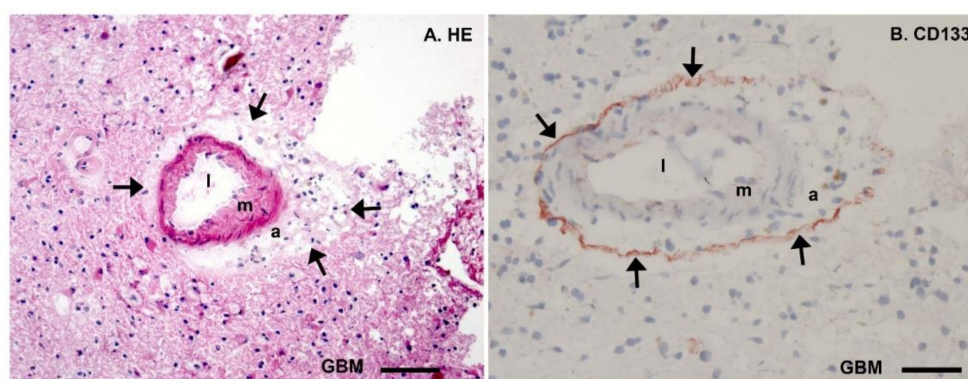


**Figure 2.** Microscopic images of cryostat sections (8  $\mu\text{m}$  thick) of patient glioblastoma tumor tissue stained with hematoxylin-eosin (HE, (A)) and Giemsa combined with immunohistochemical detection of the stem cell biomarker CD133 (arrows, red) showing glioblastoma stem cells (GSCs) in their protective hypoxic peri-arteriolar niche (B). Both in (A) and (B), a cross section of an arteriole is shown with the lumen (l), the tunica media containing smooth muscle (m), the tunica adventitia containing stroma (a) and surrounded by a thin layer of GSCs adjacent to the tunica adventitia in (B) and then differentiated glioblastoma cells (GBM). Bars: (A), 100  $\mu\text{m}$  and (B), 50  $\mu\text{m}$ . Reprinted with permission [24].

In order to solve the ROS-related riddle for glioblastoma patients, we compare the energy metabolism in differentiated glioblastoma cells versus that in GSCs, in the presence

or absence of the canonical heterozygous isocitrate dehydrogenase 1 mutation (*IDH1mt*). First, we review the present state of affairs with respect to energy metabolism in differentiated glioblastoma cells that are *IDH1* wild-type (*IDH1wt*) or *IDH1mt*. Second, we discuss possibilities to differentially target therapeutically the energy metabolism of *IDH1wt* and *IDH1mt* GSCs in primary and secondary glioblastoma, respectively.

*IDH1* is a metabolic enzyme in the cytoplasm, endoplasmic reticulum, and peroxisomes and the mutation causes a neo-enzymatic activity [10,35,36]. The consequences of this altered activity in differentiated glioblastoma cells are relatively well understood [10], but the consequences of the *IDH1mt* for GSCs are unknown, despite the fact that GSCs are considered to be the prime target for therapy to prevent the recurrence of glioblastoma after therapy [10,16,25,26] and energy metabolism is considered to be an attractive therapeutic target in cancer [37]. Therefore, it is crucial to determine whether quiescent GSCs can be effectively and specifically treated therapeutically with metabolic stressors or inhibitors affecting the energy metabolism in mitochondria. Inhibitors of mitochondrial metabolism for the therapeutic targeting of CSCs have been reviewed recently [12,13,17,18,20,38,39]. It has to be stressed here that the inhibition of aerobic glycolysis, which is a hallmark of cancer [37], in differentiated proliferating glioblastoma cells is not an option for treating glioblastoma patients because clinical trials have thus far shown that potential drugs targeting glycolysis are either not well tolerated or had no clinical efficacy [18,38,40,41].

## 2. Energy Metabolism of *IDH1wt* versus *IDH1mt* Differentiated Glioblastoma Cells

A striking example of metabolic flexibility in gliomagenesis is the metabolic rewiring in *IDH1mt* glioblastoma compared to *IDH1wt* glioblastoma [42]. The *IDH1* mutation occurs at a hot spot of the *IDH1* gene and is the main driver of *IDH1mt* glioblastoma that make up 5% of all glioblastoma tumors [10]. *IDH1wt* converts isocitrate and  $\text{NADP}^+$  into  $\alpha$ -ketoglutarate ( $\alpha$ -KG) and NADPH, whereas *IDH1mt* converts  $\alpha$ -KG and NADPH into the oncometabolite D-2-hydroxyglutarate (D-2-HG) and  $\text{NADP}^+$  (Figure 3). The *IDH1* enzyme functions as a dimer of two *IDH1* proteins and only one of the two proteins is mutated, since a dimer of two mutated proteins is nearly completely inactive and may not confer a survival advantage to the glioma cell [43]. Thus, the *IDH1wt* protein of the dimer produces  $\alpha$ -KG and NADPH which are subsequently consumed by the *IDH1mt* protein of the dimer (Figure 3) [10].

Because the capacity to metabolize D-2-HG is low, mainly by D-2-HG dehydrogenase, D-2-HG accumulates in the cells and intracellular concentrations up to 30 mM have been reported [10,44]. The accumulation of D-2-HG and concomitant depletion of  $\alpha$ -KG and NADPH cause a plethora of alterations in cells, affecting metabolism, DNA repair, redox state, epigenetics, phospholipid composition, and epigenetics, ultimately leading to gliomagenesis and the development of glioblastoma [10,45]. Moreover, it was reported recently that *IDH1mt* increases the stiffness of the cytoskeleton which reduces the invasive behavior of *IDH1mt* glioblastoma cells [46] which may well be associated with their reduced glycolytic activity (see below). This finding is in line with the mechanical regulation of glycolysis by the cytoskeleton as a response to the composition of the extracellular environment, whereas cancer cells shut down this mechanical regulation and keep glycolytic activity high [47]. A tenascin-c-enriched extracellular matrix in *IDH1mt* glioblastoma enhances its stiffness, thus reducing glioblastoma aggression [48]. However, it should be stressed here that *IDH1mt* glioblastoma cells are extremely difficult to grow *in vitro*, and thus cells overexpressing *IDH1mt* are used that do not reflect the activity of naturally occurring *IDH1mt* cancer cells, especially because the 1:1 stoichiometry of heterodimers of wild-type and mutated *IDH1* enzymes cannot be reliably replicated with overexpression systems.

For the synthesis of ATP, a thorough metabolic rewiring occurs in *IDH1mt* cells, leading to a vast increase in the number of mitochondria as was shown in oligodendroglioma cells [49]. *IDH1wt* glioblastoma cells mainly use glycolysis as a classical Warburg phenotype that produces lactate [50,51], whereas *IDH1mt* secondary glioblastoma use OXPHOS

for the generation of ATP using pyruvate and glutamate, which has been determined at the gene expression, protein, and metabolite levels [42,45,52–55].

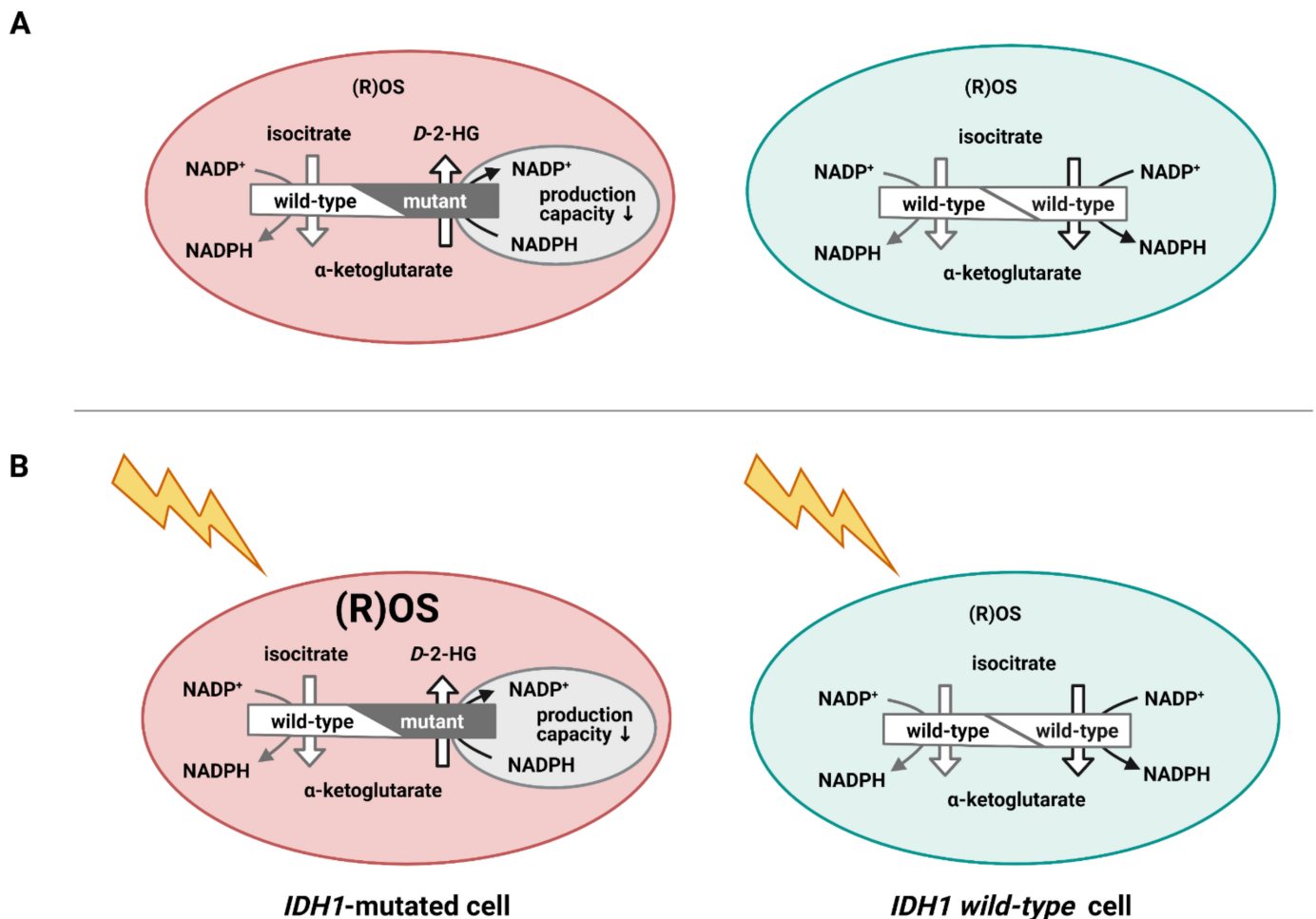


**Figure 3.** Cartoon of isocitrate dehydrogenase 1 (*IDH1*) wild-type cells (blue) and *IDH1*-mutated cells (pink) showing the functional *IDH1* dimer of 2 wild-type alleles and of one wild-type allele and one mutated allele. The wild-type dimer produces  $\alpha$ -ketoglutarate and NADPH and the heterozygous mutated dimer produces d-2-hydroxyglutarate (D-2-HG) and NADP<sup>+</sup>. Reactive oxygen species (ROS) levels are in a steady state more or less similar in both cancer cells (A), whereas ROS levels accumulate in the *IDH1*-mutated cell due to irradiation because of reduced NADPH production, unlike in the wild-type cancer cell (B).

Metabolic rewiring as occurs in *IDH1*mt glioblastoma has also been described as occurring in 3% of glioblastoma patients with fibroblast growth factor receptor 3 (FGFR3)–transforming acidic coiled-coil-containing protein 3 (TACC3) gene fusions [56].

*IDH1*mt is associated with a prolonged survival of glioblastoma patients of approx. 2 years compared to primary glioblastoma [35,36,46]. This is at least partially caused by the increased oxidation of NADPH via *IDH1*mt which renders the affected glioblastoma cells more vulnerable to ROS induced by irradiation and chemotherapy (Figure 3) [46]. NADPH is the major intracellular reducing power to reduce glutathione, thioredoxin, catalase tetramers, and cytochrome P450, all of which are involved in detoxification processes, including those of ROS [7,10] which glioblastoma cells need to survive irradiation and chemotherapy.

In human brain tissue and glioblastoma tumors, *IDH1* is the major provider of NADPH [36]. This is not the case in rodents (Figure 4), and *IDH1*mt does not increase the survival of acute myeloid leukemia patients because glucose-6-phosphate dehydrogenase (G6PD) is the major provider of NADPH in white blood cells rather than *IDH1* [57,58].

However, prolonged survival of *IDH1*mt glioblastoma patients may not only depend on the insufficient availability of NADPH to detoxify ROS during radiotherapy and chemotherapy because *IDH1*mt-transduced astrocytes and glioma cells have been found to retain stable NADPH levels by replenishing NADP<sup>+</sup> and NADPH levels via the synthesis of NADP<sup>+</sup> from NAD<sup>+</sup> by NAD kinase, thus suggesting additional mechanisms of *IDH1*mt-associated vulnerability to therapy [59]. Gelman et al. reported that in *IDH1*mt-transduced human fetal astrocytes, NADPH production by G6PD is increased for D-2-HG synthesis [60]. However, we did not find elevated G6PD activity in *IDH1*mt versus *IDH1*wt glioblastoma tumor samples of patients [36].

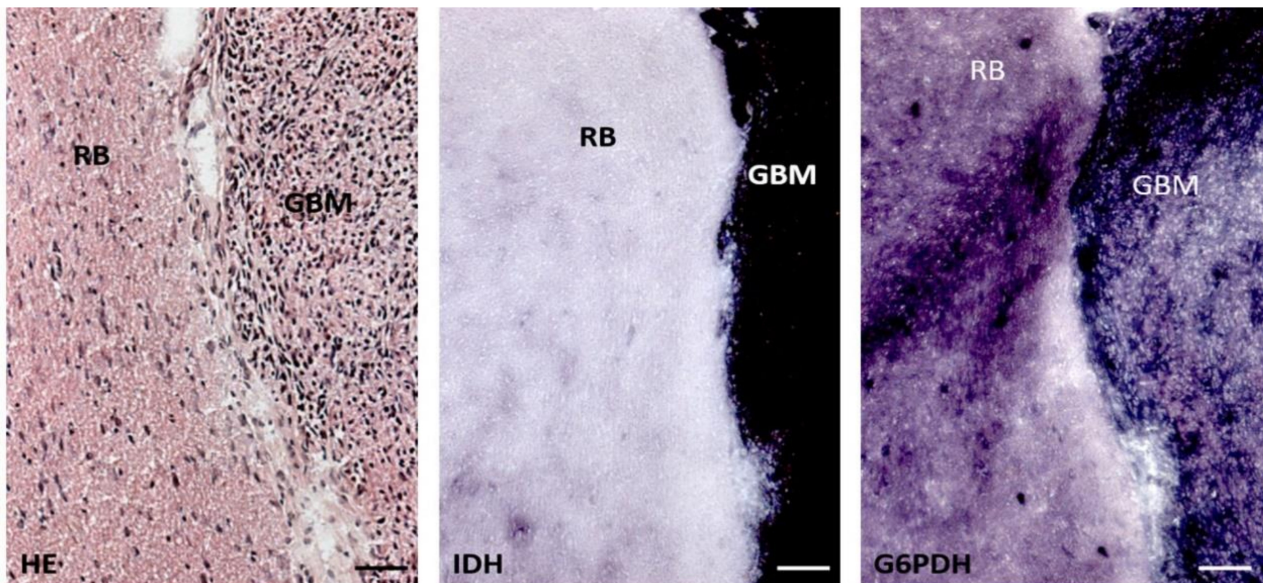


**Figure 4.** Serial cryostat sections (8  $\mu\text{m}$  thick) of rat brain (RB) containing a patient-derived glioblastoma tumor (GBM) stained with hematoxylin–eosin (HE), and stained with metabolic mapping for isocitrate dehydrogenase (IDH) activity and glucose-6-phosphate dehydrogenase (G6PDH) activity. G6PDH activity is more or less similar in rat brain and human tumor tissue, whereas IDH activity is manifold stronger in human glioblastoma tissue than in rat brain. Bars, 100  $\mu\text{m}$ . Reprinted with permission [50].

Phase 1B/II clinical trials are ongoing at present to investigate whether the treatment of *IDH1*mt glioblastoma and other cancer types with the *IDH1*mt gene can be optimized by interfering with the mitochondrial ATP production. For this purpose, patients are treated with the anti-diabetic and FDA-approved drug metformin in combination with the anti-malaria and FDA-approved drug chloroquine [61]. Metformin and its lipophilic analogue phenformin, which may reach higher concentrations in the mitochondria of cancer cells, inhibit complex I of the electron transport chain of OXPHOS, whereas  $\alpha$ -KG production from glutamine and glutamate by glutamate dehydrogenase is inhibited by metformin, phenformin, and chloroquine (Figure 5) [10,61].

In conclusion, differentiated *IDH1*wt glioblastoma cells depend on aerobic glycolysis for ATP production, whereas differentiated *IDH1*mt glioblastoma cells import pyruvate and glutamate into mitochondria [42] to fuel OXPHOS for ATP production.

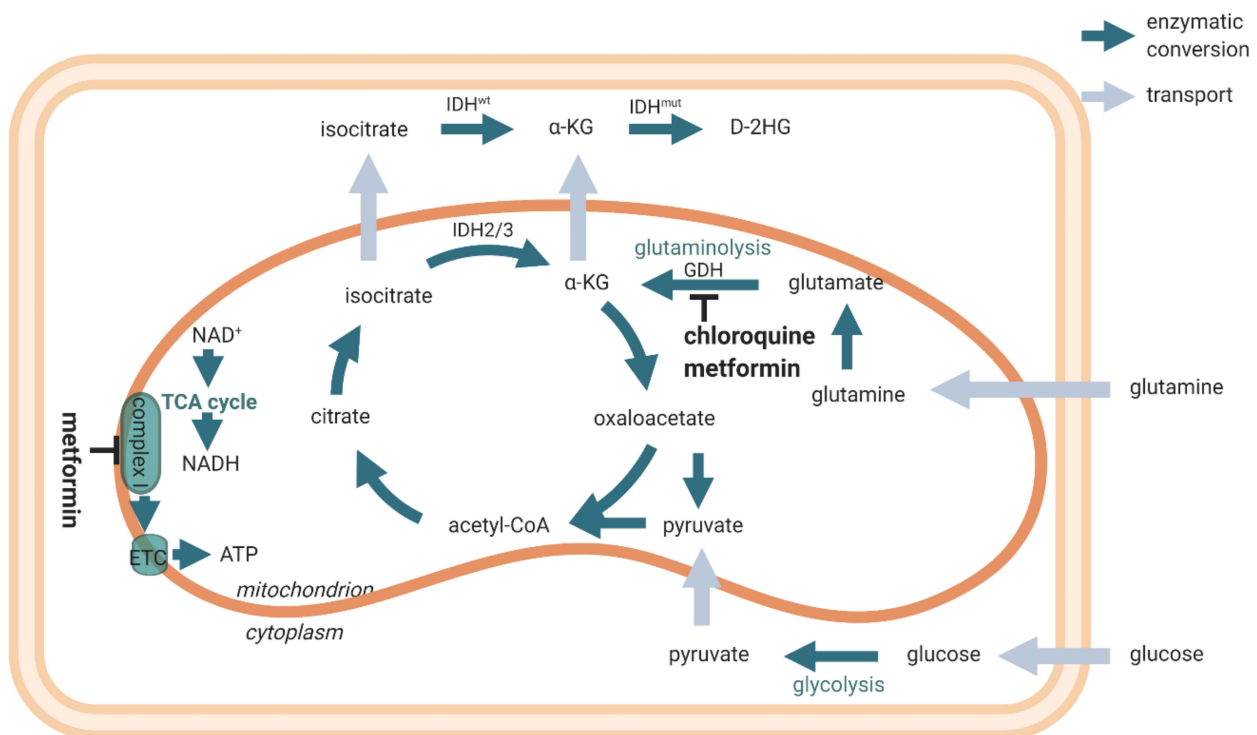


**Figure 5.** Scheme of cellular energy metabolism (ATP production) and the inhibitory actions of metformin and chloroquine. Reprinted with permission [54].

### 3. Energy Metabolism in *IDH1wt* GSCs

The energy metabolism of *IDH1wt* GSCs has not yet been very well studied. However, the general consensus is that GSCs are metabolically flexible but mainly use OXPHOS for the generation of ATP, whereas differentiated *IDH1wt* glioblastoma cells use aerobic glycolysis [51,62,63].

In recent years, a number of proteins has been described that regulate OXPHOS activity in GSCs and may become alternative targets for therapy to shut down OXPHOS in *IDH1wt* GSCs (Table 1). When interpreting these results, it is important to note that Duraj et al. recently reported that GSCs cultured in the absence of serum show heterogeneous energy metabolism and variable responses to inhibitors of cellular metabolism [64].

First, translocator protein (TSPO) is involved in OXPHOS in GSCs. TSPO is a transmembrane protein in the outer mitochondrial membrane and facilitates cholesterol transport across the mitochondrial intermembrane space [65]. In the brain, it is mainly expressed in glial cells [65]. It is also highly expressed in glioma [66]. In human GSCs, the loss of TSPO resulted in a shift from OXPHOS towards glycolysis with an increased glucose uptake and lactate production. Moreover, mitochondria were found to be fragmented after the loss of TSPO, whereas tumor growth intracranially in mice was increased [66]. Therefore, TSPO seems essential for the maintenance of GSCs and thus a promising protein to be targeted therapeutically.

Second, insulin-like growth factor 2 mRNA-binding protein 2 (IGF2BP2 or IMP2) is functional during embryonal development, it is linked with susceptibility to type 2 diabetes and participates in the maintenance of CSCs [67]. Janiszewska et al. [68] reported that OXPHOS is maintained in GSCs by IGF2BP2 that delivers electron transport chain subunit-encoding mRNAs to mitochondria and contributes to complex I and IV assembly. Therefore, IGF2BP2 is another interesting protein to be targeted therapeutically.

Third, glycerol-3-phosphate is a substrate for glycerol synthesis. Glycerol-3-phosphate dehydrogenase I (GPD1) is expressed upon osmotic stress. It is expressed by GSCs but not by NSCs and may well be linked with edema formation in glioblastoma [69]. GSCs express



GPDI in relation to their quiescence. An interesting association was made between GSC quiescence and elevated glycerol levels in dormant insects during their development, and in hibernating mammals [69]. It is suggested that GPDI is an attractive therapeutic target to treat glioblastoma as GSC quiescence is inhibited, resulting in increased therapy sensitivity.

Fourth, oncostatin M is a cytokine of the interleukin-6 (IL-6) subfamily and is expressed in the brain by various cell types (neurons, astrocytes, and microglia). It is involved in immunosurveillance in the brain [70]. Its receptor is expressed by GSCs in mitochondria and interacts with complex I to promote OXPHOS. Deletion of the oncostatin M receptor reduces OXPHOS, increases ROS levels, and sensitizes GSCs to irradiation [71]. IL-6 itself induces CD133 expression via the transfer of STAT3 into the nucleus in hypoxic conditions [72].

**Table 1.** Proteins that are involved in oxidative phosphorylation (OXPHOS) in glioblastoma stem cells (GSCs) as potential selective therapeutic targets.

Protein	Function	Reference
Translocator protein (TSPO)	Mitochondrial transmembrane cholesterol transporter	[66]
Insulin-like growth factor 2 mRNA-binding protein 2 (IGF2BP2)	Delivering of mRNAs to mitochondria	[68]
Glycerol-3-phosphate dehydrogenase I (GPDI)	Prevention of osmotic stress	[69]
Oncostatin M	Cytokine in immunosurveillance	[71]

Various inhibitors of OXPHOS activity of GSCs have been described as well [12,13,17,18,20,63,73] (Table 2).

First, metformin and phenformin are inhibitors of OXPHOS as described above and in Figure 5, and metformin is being tested in clinical trials in patients with cancers with *IDH1mt* [61]. Nuclear magnetic resonance-based metabolomic analysis showed anti-cancer effects of metformin treatment [74].

**Table 2.** Inhibitors of oxidative phosphorylation (OXPHOS) to selectively target glioblastoma stem cells (GSCs).

Inhibitor	FDA-Approved?	Indication	Reference
Atovaquone	Approved	<i>Pneumocystis jirovecii</i> pneumonia treatment, malaria prophylaxis	[75]
Mito-Lonidamine (Mito-LND)	Not approved	N/A	[41]
Metformin	Approved	Type 2 diabetes mellitus	[61]
Phenformin	Not approved	N/A	[61]
Verteporfin	Approved	Macular degeneration	[76]

Second, Mudassar et al. [75] reviewed the role of hypoxia in combination with OXPHOS and resistance of GSCs to irradiation. Their focus was to inhibit OXPHOS to increase the low oxygen levels in hypoxic GSC niches to sensitize GSCs to irradiation. Repurposing of the anti-parasitic drugs atovaquone, ivermectin, proguanil, mefloquine, and quinacrine that inhibit OXPHOS in various ways was their approach to reduce hypoxia in GSC niches and render GSCs more vulnerable to radiotherapy and chemotherapy.

Third, lonidamine (LND) is an anti-glycolytic drug with limited clinical effects in cancer patients [13,38,40,41]. However, LND in a mitochondria-targeting form (Mito-LND) appears to be a selective OXPHOS inhibitor with very low toxicity in mice [41]. These characteristics of Mito-LND makes it an attractive candidate to target CSCs in general and GSCs and *IDH1mt* glioblastoma in particular, as they primarily depend on OXPHOS.

Fourth, verteporfin inhibits OXPHOS at complexes III and IV of the electron transport chain very efficiently ( $IC_{50} = 200$  nM) [76]. It is specifically cytotoxic against GSCs and not to differentiated glioblastoma cells or normal cells.

Fifth, the effects of a ketogenic diet on patient-derived GSCs were studied in vitro by incubation of GSCs in media containing  $\beta$ -hydroxybutyrate and restricted glucose levels that mimic the clinical effects of such a diet. It was found that ROS levels were increased in GSCs and apoptosis was induced, whereas ROS scavengers annihilated these effects [77]. However, an unrestricted ketogenic diet did not reduce tumor growth in vivo in various glioblastoma mouse models, whereas the inhibition of fatty acid oxidation by etomoxir reduced glioblastoma growth in the same mouse models [50]. It appeared that etomoxir prolonged the survival of mice whereas the ketogenic diet did not affect survival or even reduce the survival of the mice. *IDH1*wt and *IDH1*mt glioblastoma cells were not differently affected by etomoxir [50]. We conclude that the long-standing conviction that a ketogenic diet is beneficial for glioblastoma patients has no scientific grounds. It should not be considered for glioblastoma patients because a ketogenic diet may even have adverse effects on glioblastoma tumor growth. Kant et al. demonstrated that fatty acid oxidation provides  $\beta$ -hydroxybutyrate for ketogenesis that stimulates glioblastoma cell proliferation in vitro and that finding was recapitulated in glioblastoma tumors [51]. Furthermore, a ketogenic diet is hard to maintain and thus has unnecessary negative effects on quality of life of glioblastoma patients.

In conclusion, a number of proteins that are involved in OXPHOS activity have been described recently as potential targets for anti-OXPHOS therapy as well as selective inhibitors of OXPHOS activity in GSCs. These developments certainly deserve follow-up studies to establish whether or not one or more can be developed into an opportunity to therapeutically target *IDH1*wt GSCs in patients.

#### 4. Energy Metabolism in *IDH1*mt GSCs

The energy metabolism of GSCs has not been studied in relationship with *IDH1*mt, as far as we know. Therefore, we have to extrapolate from the data that are available regarding energy metabolism in *IDH1*mt and *IDH1*wt glioblastoma tumors in combination with our understanding of the energy metabolism in stem cells in general and in CSCs in particular. In this way, strategies can possibly be formulated for testing in future studies for the rational design of therapies targeting energy metabolism in *IDH1*mt GSCs.

The energy metabolism of *IDH1*mt glioblastoma is forced to be dependent on OXPHOS instead of aerobic glycolysis because of the drain of  $\alpha$ KG and NADPH by the *IDH1*mt enzyme that converts  $\alpha$ KG into D-2-HG with concomitant oxidation of NADPH into NADP<sup>+</sup> [42,45,52–55]. This altered metabolism causes metabolic stress, and it has been hypothesized by us and others that the increased metabolic stress induced by the therapeutic targeting of the mitochondrial energy metabolism prolongs the survival of *IDH1*mt glioblastoma patients [10,50,61]. Candidate compounds in this respect are metformin or phenformin, chloroquine, and epigallocatechin-3-gallate (EGCG) to inhibit the production of  $\alpha$ KG by glutamate dehydrogenase. As explained above, metformin and phenformin inhibit complex I of the electron transport chain of OXPHOS and glutamate dehydrogenase, whereas chloroquine inhibits glutamate dehydrogenase (Figure 5) [10,61]. EGCG, a major polyphenol flavonoid in green tea [78], reduces D-2-HG production and the proliferation of *IDH1*mt glioblastoma cells [79]. In glioblastoma patients, EGCG seems effective only when used in large quantities as an adjuvant during radiotherapy and temozolomide chemotherapy [78]. It is worthwhile to investigate whether this adjuvant effect of EGCG is more profound in *IDH1*mt glioblastoma patients than in *IDH1*wt patients.

Glutamate is present extracellularly in high concentrations in brain tissue and can be imported into the mitochondria by glioblastoma cells [80,81]. Moreover, glutamate has been determined as a necessary metabolite for *IDH1*mt glioblastoma [42,45,52–59]. Reduced levels of glutamate in *IDH1*mt-transduced cells [82] confirm the potential of glutamate dehydrogenase inhibition to increase the metabolic stress of *IDH1*mt glioblastoma cells.

Inhibition of the conversion of glutamine into glutamate by glutaminase has also been investigated to increase metabolic stress in CSCs. The small-molecular inhibitor CB839 of glutaminase activity eradicates GSCs in neurospheres [40]. Moreover, the glu-

tamine analogue (6-diazo-5-oxo-L-norleucine (DON))-containing prodrug JHU083 inhibits glutamine-metabolizing glutaminase in cancer cells. The prodrug is cleaved by cathepsins that are abundantly present in glioblastoma cells and extracellularly in the microenvironment of tumors (Figure 6) [83–85] to release locally the active glutamine analogue DON to inhibit glutamine conversion selectively in cancer cells. This is most relevant because other glutamine-using cells such as T cells are not affected and can still perform their immune anti-cancer function [86].

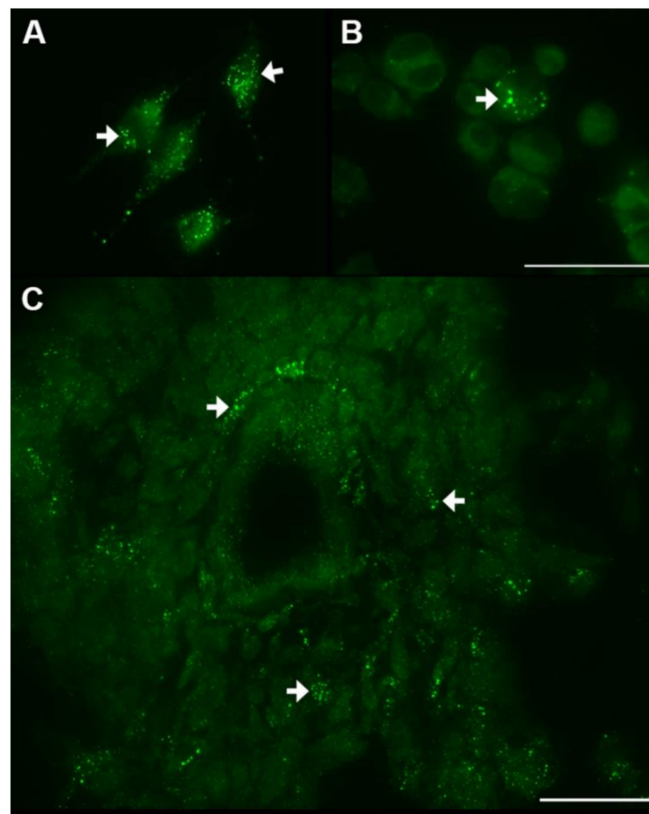


**Figure 6.** Intracellular activity of cathepsin B in lysosomal-like organelles (strongly green fluorescent dots, white arrows) in cultured differentiated glioblastoma cells (U373) (A) and GSCs (B) and in GSCs around an arteriole in a cryostat section of a patient-derived glioblastoma tumor (C). Localization of cathepsin B activity was performed as described in [83]. Bars, 50  $\mu$ m.

Moreover, D-2-HG strongly inhibits the transaminases branched-chain aminotransferase 1 (BCAT1) and BCAT2, thus lowering glutamate levels in *IDH1*mt glioblastoma cells. It explains their sensitivity to glutaminase inhibitors because the inhibitors increase metabolic stress in *IDH1*mt cancer cells [87].

It has also been suggested to treat patients with *IDH1*mt glioblastoma with inhibitors of the mutated protein of *IDH1* [88]. However, we want to emphasize that this has to be done with caution because as a consequence of *IDH1*mt inhibition, metabolic stress is reduced and NADPH production capacity is increased, and thus the more effective radiotherapy and chemotherapy in *IDH1*mt glioblastoma patients is lost. Therefore, inhibitors of the *IDH1*mt protein should not be administered to patients during radiotherapy and chemotherapy [89].

In conclusion, experimental data are not yet available of the identity of the energy metabolism in *IDH1*mt GSCs, but it is reasonable to assume that the metabolic differences between *IDH1*mt GSCs and *IDH1*mt differentiated glioblastoma cells are smaller than the metabolic differences between *IDH1*wt GSCs and *IDH1*wt differentiated glioblastoma cells. A major rationale that supports this hypothesis is the finding that the metabolic rewiring in *IDH1*mt differentiated glioblastoma cells is associated with the metabolic rewiring that is also associated with the acquisition of stemness. This assumption should be tested in

future studies. If this is the case, there is no need for the specific targeting of the OXPHOS metabolism of *IDH1*mt GSCs because both GSCs and differentiated glioblastoma cells depend on OXPHOS. Furthermore, *IDH1*mt glioblastoma patients should not be treated with inhibitors of the *IDH1*mt protein during radiotherapy or chemotherapy because the inhibitors counteract the vulnerability of *IDH1*mt glioblastoma to therapy.

## 5. Concluding Remarks

Cancer is a redox disease and is closely associated with ATP production in mitochondria (OXPHOS), the source of ROS in cells. In healthy cells in our body, low ROS levels are beneficial and may have an anti-cancer effect because they reduce cancer risk, prolong cancer patient survival, delay cancer recurrence, and improve the quality of life of cancer patients. In glioblastoma, like in many other cancer types, the differentiated glioblastoma cells produce ATP preferentially in cytoplasmic glycolysis, both anaerobic and aerobic. This Warburg effect has been excellently reviewed recently by Vaupel and Multhoff [8]. In this review, the Warburg effect is explained on the basis of current metabolic perspectives as an essential part of a selfish metabolic reprogramming in differentiated cancer cells. Because of the high proliferation rate and sensitivity of differentiated glioblastoma cells to cytotoxic agents, radiotherapy and chemotherapy are effective. Inhibition of glycolysis is not an option in glioblastoma patients because clinical trials of inhibitors of glycolysis have been proven to be either ineffective or causing unwanted side effects.

The small amount of GSCs in glioblastoma tumors and in the SVZ, whether they are *IDH1*wt or *IDH1*mt, preferentially use OXPHOS for ATP production and are well protected against radiotherapy and chemotherapy in their hypoxic niches, mainly because they are slowly proliferating. GSCs have a modest metabolism and produce low levels of ROS. Rapidly increasing numbers of specific therapeutic targets that may cause inhibition of OXPHOS are becoming available in order to attack ATP production in GSCs in particular and in CSCs in general.

However, when the need for OXPHOS in healthy cells in the body of cancer patients is taken into consideration, it must be concluded that systemic treatment of cancer patients with OXPHOS inhibitors is not an option either. It annihilates the benefits of low levels of ROS in healthy cells that can be stimulated by physical exercise.

Therefore, we suggest focusing on a different approach to specifically target GSCs irrespective of their mutational status and irrespective of their energy metabolism, as has been proposed by Hira et al. [25,26]. GSCs are kept in their hypoxic peri-arteriolar niches in glioblastoma tumors and the SVZ [16] by stromal-derived factor-1 $\alpha$  (SDF-1 $\alpha$ )–C-X-C receptor type 4 (CXCR4) interactions in a similar way as HSCs and LSCs are kept in their hypoxic peri-arteriolar niches in bone marrow [25,26]. Inhibition of CXCR4 by the FDA-approved drug plerixafor is used successfully to remove LSCs out of the bone marrow niches to render them more sensitive to chemotherapy and HSCs in healthy donors to be harvested in the peripheral blood for stem cell transplantation [26]. Removal of GSCs from their niches in glioblastoma before radiotherapy or chemotherapy may become similarly successful in this context.

**Author Contributions:** All authors have contributed to this article as follows: conception and design, C.J.F.v.N., literature analyses and writing of the manuscript, C.J.F.v.N., A.J.v.D., V.V.V.H., B.B., M.N., R.J.M., final approval of manuscript, C.J.F.v.N., V.V.V.H., A.J.v.D., M.N., B.B., R.J.M. and supervision of the entire study, C.J.F.v.N., R.J.M. All authors have read and agreed to the published version of the manuscript.

**Funding:** The author(s) disclosed receipt of the following financial support for the research, authorship, and/or publication of this article: This study was financially supported by the Dutch Cancer Society (KWF; UVA 2014-6839 and UVA 2016.1-10460; V.V.V.H., R.J.M., C.J.F.v.N.), the IVY Interreg Fellowship (V.V.V.H.), the Slovenian Research Agency (Project J3-2526 to C.J.F.v.N., M.N. and B.B. and Postdoctoral project Z3-1870 to B.B.) and R.J.M. was supported by the Fondation pour la Recherche Nuovo-Soldati 2019.

**Data Availability Statement:** The data presented in this study are available on request from the corresponding author.

**Acknowledgments:** Figures 1, 3 and 5 were created with BioRender.com (accessed on 21 March 2021).

**Conflicts of Interest:** The authors declare no conflict of interest.

## References

1. Watson, J.D. Type 2 diabetes as a redox disease. *Lancet* **2014**, *383*, 841–843. [CrossRef]
2. Molenaar, R.J.; van Noorden, C.J.F. Type 2 diabetes and cancer as redox diseases? *Lancet* **2014**, *384*, 853. [CrossRef]
3. Warburton, D.E.; Nicol, C.W.; Bredin, S.S. Health benefits of physical activity: The evidence. *Can. Med. Assoc. J.* **2006**, *174*, 801–909. [CrossRef]
4. Irwin, M.L.; Smith, A.W.; McTiernan, A.; Ballard-Barbash, R.; Cronin, K.; Gilliland, F.D.; Baumgartner, R.N.; Baumgartner, K.B.; Bernstein, L. Influence of pre- and postdiagnosis physical activity on mortality in breast cancer survivors: The health, eating, activity, and lifestyle study. *J. Clin. Oncol.* **2008**, *26*, 3958–3964. [CrossRef]
5. Thong, M.S.Y.; van Noorden, C.J.F.; Steindorf, K.; Arndt, V. Cancer-related fatigue: Causes and current treatment options. *Curr. Treat. Options Oncol.* **2020**, *21*, 17. [CrossRef]
6. Ward, P.S.; Thompson, C.B. Metabolic reprogramming: A cancer hallmark even Warburg did not anticipate. *Cancer Cell.* **2012**, *21*, 297–308. [CrossRef] [PubMed]
7. Koehler, A.; Van Noorden, C.J.F. Reduced nicotinamide adenine dinucleotide phosphate and the higher incidence of pollution-induced liver cancer in female flounder. *Environ. Toxicol. Chem.* **2003**, *22*, 2703–2710. [CrossRef] [PubMed]
8. Vaupel, P.; Multhoff, G. Revisiting the Warburg effect: Historical dogma versus current understanding. *J. Physiol.* **2020**. [CrossRef]
9. Zhang, C.C.; Sadek, H.A. Hypoxia and metabolic properties of hematopoietic stem cells. *Antioxid. Redox Signal.* **2014**, *20*, 1891–1901. [CrossRef] [PubMed]
10. Molenaar, R.J.; Maciejewski, J.P.; Wilmlink, J.W.; van Noorden, C.J.F. Wild-type and mutated IDH1/2 enzymes and therapy responses. *Oncogene* **2018**, *37*, 1949–1960. [CrossRef]
11. Ma, Q. Role of nrf2 in oxidative stress and toxicity. *Annu. Rev. Pharmacol. Toxicol.* **2013**, *53*, 401–426. [CrossRef]
12. Sancho, P.; Barneda, D.; Heeschen, C. Hallmarks of cancer stem cell metabolism. *Br. J. Cancer* **2016**, *114*, 1305–1312. [CrossRef]
13. Sica, V.; Bravo-San Pedro, J.M.; Stoll, G.; Kroemer, G. Oxidative phosphorylation as a potential therapeutic target for cancer therapy. *Int. J. Cancer* **2020**, *146*, 10–17. [CrossRef]
14. Leonart, M.E.; Abad, E.; Graifer, D.; Lyakhovich, A. Reactive oxygen species-mediated autophagy defines the fate of cancer stem cells. *Antioxid. Redox Signal.* **2018**, *28*, 1066–1079. [CrossRef] [PubMed]
15. Ito, K.; Ito, K. Metabolism and the control of cell fate decisions and stem cell renewal. *Annu. Rev. Cell Dev. Biol.* **2016**, *32*, 399–409. [CrossRef] [PubMed]
16. Hira, V.V.V.; Molenaar, R.J.; Breznik, B.; Lah, T.; Aronica, E.; van Noorden, C.J.F. Immunohistochemical detection of neural stem cells and glioblastoma stem cells in the subventricular zone of glioblastoma patients. *J. Histochem. Cytochem.* **2021**. [CrossRef] [PubMed]
17. Visweswaran, M.; Arfuso, F.; Warriar, S.; Dharmarajan, A. Aberrant lipid metabolism as an emerging therapeutic strategy to target cancer stem cells. *Stem Cells* **2020**, *38*, 6–14. [CrossRef] [PubMed]
18. Li, H.; Feng, Z.; He, M.L. Lipid metabolism alteration contributes to and maintains the properties of cancer stem cells. *Theranostics* **2020**, *10*, 7053–7069. [CrossRef]
19. Peiris-Pagès, M.; Martínez-Outschoorn, U.E.; Pestell, R.G.; Sotgia, F.; Lisanti, M.P. Cancer stem cell metabolism. *Breast Cancer Res.* **2016**, *18*, 55. [CrossRef]
20. Snyder, V.; Reed-Newman, T.C.; Arnold, L.; Thomas, S.M.; Anant, S. Cancer stem cell metabolism and potential therapeutic targets. *Front. Oncol.* **2018**, *8*, 203. [CrossRef]
21. Fiorillo, M.; Sotgia, F.; Lisanti, M.P. “Energetic” Cancer Stem Cells (e-CSCs): A new hyper-metabolic and proliferative tumor cell phenotype, driven by mitochondrial energy. *Front. Oncol.* **2019**, *8*, 677. [CrossRef]
22. Hoang-Minh, L.B.; Siebzehnrubl, F.A.; Yang, C.; Suzuki-Hatano, S.; Dajac, K.; Loche, T.; Andrews, N.; Schmoll Massari, M.; Patel, J.; Amin, K.; et al. Infiltrative and drug-resistant slow-cycling cells support metabolic heterogeneity in glioblastoma. *EMBO J.* **2018**, *37*, e98772. [CrossRef]
23. Erol, A. Type 2 diabetes and cancer as redox diseases? *Lancet* **2014**, *384*, 853–854. [CrossRef]
24. Erol, A. Systemic DNA damage response and metabolic syndrome as a premalignant state. *Curr. Mol. Med.* **2010**, *10*, 321–334. [CrossRef]
25. Hira, V.V.V.; Breznik, B.; Vittori, M.; Loncq de Jong, A.; Mlakar, J.; Oostra, R.J.; Khurshed, M.; Molenaar, R.J.; Lah, T.; van Noorden, C.J.F. Similarities between stem cell niches in glioblastoma and bone marrow: Rays of hope for novel treatment strategies. *J. Histochem. Cytochem.* **2020**, *68*, 33–57. [CrossRef] [PubMed]
26. Hira, V.V.V.; van Noorden, C.J.F.; Molenaar, R.J. CXCR4 antagonists as stem cell mobilizers and therapy sensitizers for acute myeloid leukemia and glioblastoma? *Biology* **2020**, *9*, 31. [CrossRef] [PubMed]

27. Hira, V.V.V.; Wormer, J.R.; Kakar, H.; Breznik, B.; van der Swaan, B.; Hulsbos, R.; Tigchelaar, W.; Tonar, Z.; Khurshed, M.; Molenaar, R.J.; et al. Periarteriolar glioblastoma stem cell niches express bone marrow hematopoietic stem cell niche proteins. *J. Histochem. Cytochem.* **2018**, *66*, 155–173. [CrossRef]
28. Hira, V.V.V.; van Noorden, C.J.F.; Carraway, H.E.; Maciejewski, J.P.; Molenaar, R.J. Novel therapeutic strategies to target leukemic cells that hijack compartmentalized continuous hematopoietic stem cell niches. *Biochim. Biophys. Acta Rev. Cancer* **2017**, *1868*, 183–198. [CrossRef]
29. Maffezzini, C.; Calvo-Garrido, J.; Wredenberg, A.; Freyer, C. Metabolic regulation of neurodifferentiation in the adult brain. *Cell Mol. Life Sci.* **2020**, *77*, 2483–2496. [CrossRef]
30. Geribaldi-Doldan, N.; Fernandez-Ponce, C.; Navarro Quiroz, R.; Sanchez-Gomar, I.; Gomez-Escorcia, L.; Puentes Velasquez, E.; Navarro Quiroz, E. The role of microglia in glioblastoma. *Front. Oncol.* **2021**, *10*, 603495. [CrossRef] [PubMed]
31. Stupp, R.; Taillibert, S.; Kanner, A.; Read, W.; Steinberg, D.; Lhermitte, B.; Toms, S.; Idbaih, A.; Ahluwalia, M.S.; Fink, K.; et al. Effect of tumor-treating fields plus maintenance temozolomide vs maintenance temozolomide alone on survival in patients with glioblastoma: A randomized clinical trial. *JAMA* **2017**, *318*, 2306–2316. [CrossRef]
32. Mun, E.J.; Babiker, H.M.; Weinberg, U.; Kirson, E.D.; Von Hoff, D.D. Tumor-treating fields: A fourth modality in cancer treatment. *Clin. Cancer Res.* **2018**, *24*, 266–275. [CrossRef]
33. Wong, E.T.; Lok, E.; Swanson, K.D. Alternating electric fields therapy for malignant gliomas: From bench observation to clinical reality. *Prog. Neurol. Surg.* **2018**, *32*, 180–195. [CrossRef] [PubMed]
34. Patel, C.B.; Beinart, C.; Xie, Y.; Chang, E.; Gambhir, S.S. Tumor treating fields (TTFields) impairs aberrant glycolysis in glioblastoma as evaluated by [<sup>18</sup>F]DASA-23, a non-invasive probe of pyruvate kinase M2 (PKM2) expression. *Neoplasia* **2021**, *23*, 58–67. [CrossRef]
35. Parsons, D.W.; Jones, S.; Zhang, X.; Lin, J.C.; Leary, R.J.; Angenendt, P.; Mankoo, P.; Carter, H.; Siu, I.M.; Gallia, G.L.; et al. An integrated genomic analysis of human glioblastoma multiforme. *Science* **2008**, *321*, 1807–1812. [CrossRef] [PubMed]
36. Bleeker, F.E.; Atai, N.A.; Lamba, S.; Jonker, A.; Rijkeboer, D.; Bosch, K.S.; Tigchelaar, W.; Troost, D.; Vandertop, W.P.; Bardelli, A.; et al. The prognostic IDH1 (R132) mutation is associated with reduced NADP<sup>+</sup>-dependent IDH activity in glioblastoma. *Acta Neuropathol.* **2010**, *119*, 487–494. [CrossRef] [PubMed]
37. Dewhurst, M.W.; Lee, C.T.; Ashcraft, K.A. The future of biology in driving the field of hyperthermia. *Int. J. Hyperther.* **2016**, *32*, 4–13. [CrossRef]
38. Jagust, P.; de Luxán-Delgado, B.; Parejo-Alonso, B.; Sancho, P. Metabolism-based therapeutic strategies targeting cancer stem cells. *Front. Pharmacol.* **2019**, *10*, 203. [CrossRef]
39. El Hout, M.; Cosialls, E.; Mehrpour, M.; Hamai, A. Crosstalk between autophagy and metabolic regulation of cancer stem cells. *Mol. Cancer* **2020**, *19*, 27. [CrossRef]
40. Koch, K.; Hartmann, R.; Tsiampali, J.; Uhlmann, C.; Nickel, A.C.; He, X.; Kamp, M.A.; Sabel, M.; Barker, R.A.; Steiger, H.J.; et al. A comparative pharmaco-metabolomic study of glutaminase inhibitors in glioma stem-like cells confirms biological effectiveness but reveals differences in target-specificity. *Cell Death Discov.* **2020**, *6*, 20. [CrossRef]
41. Cheng, G.; Zhang, Q.; Pan, J.; Lee, Y.; Ouari, O.; Hardy, M.; Zielonka, M.; Myers, C.R.; Zielonka, J.; Weh, K.; et al. Targeting lonidamine to mitochondria mitigates lung tumorigenesis and brain metastasis. *Nat. Commun.* **2019**, *10*, 2205. [CrossRef] [PubMed]
42. Khurshed, M.; Molenaar, R.J.; Lenting, K.; Leenders, W.P.; van Noorden, C.J.F. In silico gene expression analysis reveals glycolysis and acetate anaplerosis in IDH1 wild-type glioma and lactate and glutamate anaplerosis in IDH1-mutated glioma. *Oncotarget* **2017**, *8*, 49165–49177. [CrossRef] [PubMed]
43. Zhao, S.; Lin, Y.; Xu, W.; Jiang, W.; Zha, Z.; Wang, P.; Yu, W.; Li, Z.; Gong, L.; Peng, Y.; et al. Glioma-derived mutations in IDH1 dominantly inhibit IDH1 catalytic activity and induce HIF-1 $\alpha$ . *Science* **2009**, *324*, 261–265. [CrossRef]
44. Dang, L.; White, D.W.; Gross, S.; Bennett, B.D.; Bittinger, M.A.; Driggers, E.M.; Fantin, V.R.; Jang, H.G.; Jin, S.; Keenan, M.C.; et al. Cancer-associated IDH1 mutations produce 2-hydroxyglutarate. *Nature* **2009**, *462*, 739–744. [CrossRef]
45. Fack, F.; Tardito, S.; Hochart, G.; Oudin, A.; Zheng, L.; Fritah, S.; Golebiewska, A.; Nazarov, P.V.; Bernard, A.; Hau, A.C.; et al. Altered metabolic landscape in IDH-mutant gliomas affects phospholipid, energy, and oxidative stress pathways. *EMBO Mol. Med.* **2017**, *9*, 1681–1695. [CrossRef]
46. Kessler, J.; Hohmann, T.; Güttler, A.; Petrenko, M.; Ostheimer, C.; Hohmann, U.; Bache, M.; Dehghani, F.; Vordermark, D. Radiosensitization and a less aggressive phenotype of human malignant glioma cells expressing isocitrate dehydrogenase 1 (IDH1) mutant protein: Dissecting the mechanisms. *Cancers* **2019**, *11*, 889. [CrossRef]
47. Park, J.S.; Burckhardt, C.J.; Lazcano, R.; Solis, L.M.; Isogai, T.; Li, L.; Chen, C.S.; Gao, B.; Minna, J.D.; Bachoo, R.; et al. Mechanical regulation of glycolysis via cytoskeleton architecture. *Nature* **2020**, *578*, 621–626. [CrossRef]
48. Miroshnikova, Y.A.; Mouw, J.K.; Barnes, J.M.; Pickup, M.W.; Lakins, J.N.; Kim, Y.; Lobo, K.; Persson, A.I.; Reis, G.F.; McKnight, T.R.; et al. Tissue mechanics promote IDH1-dependent HIF1 $\alpha$ -tenascin C feedback to regulate glioblastoma aggression. *Nat. Cell Biol.* **2016**, *18*, 1336–1345. [CrossRef]
49. Navis, A.C.; Niclou, S.P.; Fack, F.; Stieber, D.; van Lith, S.; Verrijp, K.; Wright, A.; Stauber, J.; Tops, B.; Otte-Holler, I.; et al. Increased mitochondrial activity in a novel IDH1-R132H mutant human oligodendroglioma xenograft model: In situ detection of 2-HG and  $\alpha$ -KG. *Acta Neuropathol. Commun.* **2013**, *1*, 18. [CrossRef]

50. Sperry, J.; Condro, M.C.; Guo, L.; Braas, D.; Vanderveer-Harris, N.; Kim, K.K.O.; Pope, W.B.; Divakaruni, A.S.; Lai, A.; Christofk, H.; et al. Glioblastoma utilizes fatty acids and ketone bodies for growth allowing progression during ketogenic diet therapy. *Science* **2020**, *23*, 101453. [CrossRef]
51. Kant, S.; Kesarwani, P.; Prabhu, A.; Graham, S.F.; Buelow, K.L.; Nakano, I.; Chinnaiyan, P. Enhanced fatty acid oxidation provides glioblastoma cells metabolic plasticity to accommodate to its dynamic nutrient microenvironment. *Cell Death Dis.* **2020**, *11*, 253. [CrossRef]
52. Dekker, L.J.M.; Wu, S.; Jurriëns, C.; Mustafa, D.A.N.; Grevers, F.; Burgers, P.C.; Sillevs Smitt, P.; Kros, J.M.; Luider, T.M. Metabolic changes related to the IDH1 mutation in gliomas preserve TCA-cycle activity: An investigation at the protein level. *FASEB J.* **2020**, *34*, 3646–3657. [CrossRef] [PubMed]
53. Grassian, A.R.; Parker, S.J.; Davidson, S.M.; Divakaruni, A.S.; Green, C.R.; Zhang, X.; Slocum, K.L.; Pu, M.; Lin, F.; Vickers, C.; et al. IDH1 mutations alter citric acid cycle metabolism and increase dependence on oxidative mitochondrial metabolism. *Cancer Res.* **2014**, *74*, 3317–3331. [CrossRef] [PubMed]
54. Mustafa, D.A.; Swagemakers, S.M.; Buise, L.; van der Spek, P.J.; Kros, J.M. Metabolic alterations due to IDH1 mutation in glioma: Opening for therapeutic opportunities? *Acta Neuropathol. Commun.* **2014**, *2*, 6. [CrossRef] [PubMed]
55. Lenting, K.; Khurshed, M.; Peeters, T.H.; van den Heuvel, C.N.A.M.; van Lith, S.A.M.; de Bitter, T.; Hendriks, W.; Span, P.N.; Molenaar, R.J.; Botman, D.; et al. Isocitrate dehydrogenase 1-mutated human gliomas depend on lactate and glutamate to alleviate metabolic stress. *FASEB J.* **2019**, *33*, 557–571. [CrossRef]
56. Frattini, V.; Pagnotta, S.M.; Tala Fan, J.J.; Russo, M.V.; Lee, S.B.; Garofano, L.; Zhang, J.; Shi, P.; Lewis, G.; Sanson, H.; et al. A metabolic function of FGFR3-TACC3 gene fusions in cancer. *Nature* **2018**, *553*, 222–227. [CrossRef]
57. Atai, N.A.; Renkema-Mills, N.A.; Bosman, J.; Schmidt, N.; Rijkeboer, D.; Tigchelaar, W.; Bosch, K.S.; Troost, D.; Jonker, A.; Bleeker, F.E.; et al. Differential activity of NADPH-producing dehydrogenases renders rodents unsuitable models to study IDH1R132 mutation effects in human glioblastoma. *J. Histochem. Cytochem.* **2011**, *59*, 489–503. [CrossRef]
58. Molenaar, R.J.; Radivoyevitch, T.; Nagata, Y.; Khurshed, M.; Przychodzen, B.; Makishima, H.; Xu, M.; Bleeker, F.E.; Wilmink, J.W.; Carraway, H.E.; et al. IDH1/2 mutations sensitize acute myeloid leukemia to PARP inhibition and this is reversed by IDH1/2-mutant inhibitors. *Clin. Cancer Res.* **2018**, *24*, 1705–1715. [CrossRef]
59. Biedermann, J.; Preussler, M.; Conde, M.; Peitzsch, M.; Richter, S.; Wiedemuth, R.; Abou-El-Ardat, K.; Krüger, A.; Meinhardt, M.; Schackert, G.; et al. Mutant IDH1 differently affects redox state and metabolism in glial cells of normal and tumor origin. *Cancers* **2019**, *11*, 2028. [CrossRef]
60. Gelman, S.J.; Naser, F.; Mahieu, N.G.; McKenzie, L.D.; Dunn, G.P.; Chheda, M.G.; Patti, G.J. Consumption of NADPH for 2-HG synthesis increases pentose phosphate pathway flux and sensitizes cells to oxidative stress. *Cell Rep.* **2018**, *22*, 512–522. [CrossRef]
61. Molenaar, R.J.; Coelen, R.J.S.; Khurshed, M.; Roos, E.; Caan, M.W.A.; van Linde, M.E.; Kouwenhoven, M.; Bramer, J.; Bovée, J.; Mathôt, R.A.; et al. Study protocol of a phase IB/II clinical trial of metformin and chloroquine in patients with IDH1-mutated or IDH2-mutated solid tumours. *BMJ Open* **2017**, *7*, e014961. [CrossRef]
62. Vlashi, E.; Lagadec, C.; Vergnes, L.; Matsutani, T.; Masui, K.; Poulou, M.; Popescu, R.; Della Donna, L.; Evers, P.; Dekmezian, C.; et al. Metabolic state of glioma stem cells and nontumorigenic cells. *Proc. Natl. Acad. Sci. USA* **2011**, *108*, 16062–16067. [CrossRef]
63. Badr, C.E.; Silver, D.J.; Siebzehnubel, F.A.; Deleyrolle, L.P. Metabolic heterogeneity and adaptability in brain tumors. *Cell Mol. Life Sci.* **2020**, *77*, 5101–5119. [CrossRef]
64. Duraj, T.; Garcia-Romero, N.; Carrion-Navarro, J.; Madurga, R.; Ortiz de Mendivil, A.; Prat-Acin, R.; Garcia-Cañamaque, L.; Ayuso-Sacido, A. Beyond the Warburg effect: Oxidative and glycolytic phenotypes coexist within the metabolic heterogeneity of glioblastoma. *Cells* **2021**, *10*, 202. [CrossRef]
65. Lee, Y.; Park, Y.; Nam, H.; Lee, J.W.; Yu, S.W. Translocator protein (TSPO): The new story of the old protein in neuroinflammation. *BMB Rep.* **2020**, *53*, 20–27. [CrossRef] [PubMed]
66. Fu, Y.; Wang, D.; Wang, H.; Cai, M.; Li, C.; Zhang, X.; Ying, M.; He, W.; Zhang, J. TSPO deficiency induces mitochondrial dysfunction, leading to hypoxia, angiogenesis, and a growth-promoting metabolic shift toward glycolysis in glioblastoma. *Neuro Oncol.* **2020**, *22*, 240–252. [CrossRef]
67. Cao, J.; Mu, Q.; Huang, H. The roles of insulin-like growth factor 2 mRNA-binding protein 2 in cancer and cancer stem cells. *Stem Cells Int.* **2018**, *2018*, 4217259. [CrossRef] [PubMed]
68. Janiszewska, M.; Suvà, M.L.; Riggi, N.; Houtkooper, R.H.; Auwerx, J.; Clément-Schatlo, V.; Radovanovic, I.; Rheinbay, E.; Provero, P.; Stamenkovic, I. Imp2 controls oxidative phosphorylation and is crucial for preserving glioblastoma cancer stem cells. *Genes Dev.* **2012**, *26*, 1926–1944. [CrossRef] [PubMed]
69. Rusu, P.; Shao, C.; Neuerburg, A.; Acikgöz, A.A.; Wu, Y.; Zou, P.; Phapale, P.; Shankar, T.S.; Döring, K.; Dettling, S.; et al. GPD1 specifically marks dormant glioma stem cells with a distinct metabolic profile. *Cell Stem Cell* **2019**, *25*, 241–257. [CrossRef]
70. Houben, E.; Hellings, N.; Broux, B. Oncostatin M, an underestimated player in the central nervous system. *Front. Immunol.* **2019**, *10*, 1165. [CrossRef] [PubMed]
71. Sharanek, A.; Burbán, A.; Laaper, M.; Heckel, E.; Joyal, J.S.; Soleimani, V.D.; Jahani-Asl, A. OSMR controls glioma stem cell respiration and confers resistance of glioblastoma to ionizing radiation. *Nat. Commun.* **2020**, *11*, 4116. [CrossRef]
72. Wei, X.; Chen, Y.; Jiang, X.; Peng, M.; Liu, Y.; Mo, Y.; Ren, D.; Hua, Y.; Yu, B.; Zhou, Y.; et al. Mechanisms of vasculogenic mimicry in hypoxic tumor microenvironments. *Mol. Cancer* **2021**, *20*, 7. [CrossRef]

73. Libby, C.J.; Tran, A.N.; Scott, S.E.; Griguer, C.; Hjelmeland, A.B. The pro-tumorigenic effects of metabolic alterations in glioblastoma including brain tumor initiating cells. *Biochim. Biophys. Acta Rev. Cancer* **2018**, *1869*, 175–188. [CrossRef]
74. Zhang, J.; Hang, C.; Jiang, T.; Yi, S.; Shao, W.; Li, W.; Lin, D. Nuclear magnetic resonance-based metabolomic analysis of the anticancer effect of metformin treatment on cholangiocarcinoma cells. *Front. Oncol.* **2020**, *10*, 570516. [CrossRef]
75. Mudassar, F.; Shen, H.; O'Neill, G.; Hau, E. Targeting tumor hypoxia and mitochondrial metabolism with anti-parasitic drugs to improve radiation response in high-grade gliomas. *J. Exp. Clin. Cancer Res.* **2020**, *39*, 208. [CrossRef] [PubMed]
76. Kuramoto, K.; Yamamoto, M.; Suzuki, S.; Sanomachi, T.; Togashi, K.; Seino, S.; Kitanaka, C.; Okada, M. Verteporfin inhibits oxidative phosphorylation and induces cell death specifically in glioma stem cells. *FEBS J.* **2020**, *287*, 2023–2036. [CrossRef] [PubMed]
77. Ji, C.C.; Hu, Y.Y.; Cheng, G.; Liang, L.; Gao, B.; Ren, Y.P.; Liu, J.T.; Cao, X.L.; Zheng, M.H.; Li, S.Z.; et al. A ketogenic diet attenuates proliferation and stemness of glioma stem-like cells by altering metabolism resulting in increased ROS production. *Int. J. Oncol.* **2020**, *56*, 606–617. [CrossRef] [PubMed]
78. Le, C.T.; Leenders, W.P.J.; Molenaar, R.J.; van Noorden, C.J.F. Effects of the green tea polyphenol epigallocatechin-3-gallate on Glioma: A critical evaluation of the literature. *Nutr. Cancer* **2018**, *70*, 317–333. [CrossRef] [PubMed]
79. Peeters, T.H.; Lenting, K.; Breukels, V.; van Lith, S.A.M.; van den Heuvel, C.N.A.M.; Molenaar, R.; van Rooij, A.; Wevers, R.; Span, P.N.; Heerschap, A.; et al. *Isocitrate dehydrogenase 1*-mutated cancers are sensitive to the green tea polyphenol epigallocatechin-3-gallate. *Cancer Metab.* **2019**, *7*, 4. [CrossRef] [PubMed]
80. Van Lith, S.A.; Navis, A.C.; Verrijp, K.; Niclou, S.P.; Bjerkvig, R.; Wesseling, P.; Tops, B.; Molenaar, R.; van Noorden, C.J.F.; Leenders, W.P. Glutamate as chemotactic fuel for diffuse glioma cells: Are they glutamate suckers? *Biochim. Biophys. Acta* **2014**, *1846*, 66–74. [CrossRef] [PubMed]
81. Van Lith, S.A.; Molenaar, R.; van Noorden, C.J.F.; Leenders, W.P. Tumor cells in search for glutamate: An alternative explanation for increased invasiveness of IDH1 mutant gliomas. *Neuro Oncol.* **2014**, *16*, 1669–1670. [CrossRef]
82. Vasconcelos Esá, J.; Simão, D.; Terrasso, A.P.; Silva, M.M.; Brito, C.; Isidro, I.A.; Alves, P.M.; Carrondo, M. Unveiling dynamic metabolic signatures in human induced pluripotent and neural stem cells. *PLoS Comput. Biol.* **2020**, *16*, 1007780. [CrossRef]
83. Breznik, B.; Limbaeck Stokin, C.; Kos, J.; Khurshed, M.; Hira, V.V.V.; Bošnjak, R.; Lah, T.T.; van Noorden, C.J.F. Cysteine cathepsins B, X and K expression in peri-arteriolar glioblastoma stem cell niches. *J. Mol. Histol.* **2018**, *49*, 481–497. [CrossRef]
84. Breznik, B.; Limback, C.; Porcnik, A.; Blejec, A.; Krajnc, M.K.; Bosnjak, R.; Kos, J.; van Noorden, C.J.F.; Lah, T.T. Localization patterns of cathepsins K and X and their predictive value in glioblastoma. *Radiol. Oncol.* **2018**, *52*, 433–442. [CrossRef]
85. Verbovšek, U.; van Noorden, C.J.F.; Lah, T.T. Complexity of cancer protease biology: Cathepsin K expression and function in cancer progression. *Semin. Cancer Biol.* **2015**, *35*, 71–84. [CrossRef]
86. DeBerardinis, R.J. Tumor microenvironment, metabolism, and immunotherapy. *N. Engl. J. Med.* **2020**, *382*, 869–871. [CrossRef]
87. McBrayer, S.K.; Mayers, J.R.; DiNatale, G.J.; Shi, D.D.; Khanal, J.; Chakraborty, A.A.; Sarosiek, K.A.; Briggs, K.J.; Robbins, A.K.; Sewastianik, T.; et al. Transaminase Inhibition by 2-hydroxyglutarate impairs glutamate biosynthesis and redox homeostasis in Glioma. *Cell* **2018**, *175*, 101–116. [CrossRef]
88. Huang, J.; Yu, J.; Tu, L.; Huang, N.; Li, H.; Luo, Y. Isocitrate dehydrogenase mutations in glioma: From basic discovery to therapeutics development. *Front. Oncol.* **2019**, *9*, 506. [CrossRef]
89. Molenaar, R.J.; Botman, D.; Smits, M.A.; Hira, V.V.V.; van Lith, S.A.; Stap, J.; Henneman, P.; Khurshed, M.; Lenting, K.; Mul, A.N.; et al. Radioprotection of IDH1-mutated cancer cells by the IDH1-mutant inhibitor AGI-5198. *Cancer Res.* **2015**, *75*, 4790–4802. [CrossRef]



Review

# Immunotherapy of Glioblastoma: Current Strategies and Challenges in Tumor Model Development

Bernarda Majc<sup>1,2</sup>, Metka Novak<sup>1</sup>, Nataša Kopitar-Jerala<sup>3</sup> , Anahid Jewett<sup>4</sup> and Barbara Breznik<sup>1,\*</sup> 

<sup>1</sup> Department of Genetic Toxicology and Cancer Biology, National Institute of Biology, 111 Večna pot, SI-1000 Ljubljana, Slovenia; bernarda.majc@nib.si (B.M.); metka.novak@nib.si (M.N.)

<sup>2</sup> International Postgraduate School Jozef Stefan, 39 Jamova ulica, SI-1000 Ljubljana, Slovenia

<sup>3</sup> Department of Biochemistry, Molecular and Structural Biology, Jozef Stefan Institute, 39 Jamova ulica, SI-1000 Ljubljana, Slovenia; natasa.kopitar@ijs.si

<sup>4</sup> Division of Oral Biology and Medicine, The Jane and Jerry Weintraub Center for Reconstructive Biotechnology, University of California School of Dentistry, 10833 Le Conte Ave, Los Angeles, CA 90095, USA; ajewett@dentistry.ucla.edu

\* Correspondence: barbara.breznik@nib.si; Tel.: +386-59-232-870

**Abstract:** Glioblastoma is the most common brain malignant tumor in the adult population, and immunotherapy is playing an increasingly central role in the treatment of many cancers. Nevertheless, the search for effective immunotherapeutic approaches for glioblastoma patients continues. The goal of immunotherapy is to promote tumor eradication, boost the patient's innate and adaptive immune responses, and overcome tumor immune resistance. A range of new, promising immunotherapeutic strategies has been applied for glioblastoma, including vaccines, oncolytic viruses, immune checkpoint inhibitors, and adoptive cell transfer. However, the main challenges of immunotherapy for glioblastoma are the intracranial location and heterogeneity of the tumor as well as the unique, immunosuppressive tumor microenvironment. Owing to the lack of appropriate tumor models, there are discrepancies in the efficiency of various immunotherapeutic strategies between preclinical studies (with in vitro and animal models) on the one hand and clinical studies (on humans) on the other hand. In this review, we summarize the glioblastoma characteristics that drive tolerance to immunotherapy, the currently used immunotherapeutic approaches against glioblastoma, and the most suitable tumor models to mimic conditions in glioblastoma patients. These models are improving and can more precisely predict patients' responses to immunotherapeutic treatments, either alone or in combination with standard treatment.

**Keywords:** glioblastoma; immunotherapy; tumor model; stem cell; organoid; heterogeneity; immunosuppression; microenvironment



**Citation:** Majc, B.; Novak, M.; Kopitar-Jerala, N.; Jewett, A.; Breznik, B. Immunotherapy of Glioblastoma: Current Strategies and Challenges in Tumor Model Development. *Cells* **2021**, *10*, 265. <https://doi.org/10.3390/cells10020265>

Academic Editor: Javier S. Castresana  
Received: 23 December 2020  
Accepted: 26 January 2021  
Published: 29 January 2021

**Publisher's Note:** MDPI stays neutral with regard to jurisdictional claims in published maps and institutional affiliations.



**Copyright:** © 2021 by the authors. Licensee MDPI, Basel, Switzerland. This article is an open access article distributed under the terms and conditions of the Creative Commons Attribution (CC BY) license (<https://creativecommons.org/licenses/by/4.0/>).

## 1. Introduction: Glioblastoma and Its Heterogeneity

The most aggressive and also most common primary brain tumor in adults is glioblastoma (Glioblastoma WHO grade IV). Glioblastoma is poorly responsive to therapy, which includes maximal surgical removal that is followed by chemotherapy and radiation therapy and has one of the shortest survival rates amongst all cancers [1]. For example, tumor treating fields treatment together with chemotherapy improved median overall survival of glioblastoma patients from 16 to 20.9 months [2]. Despite novel modalities in treatment, which rely on the Stupp protocol from 2005, the 5-year survival rate of patients is less than 5% [3–5]. Glioblastoma has distinct histological characteristics, including a pleomorphic cell composition, increased mitotic and cellular activity, and significant angiogenesis and necrosis [6]. The poor response of glioblastoma to treatment and its poor prognosis are associated with diffused invasion patterns within the central nervous system (CNS) [7]. Furthermore, the blood-brain barrier (BBB) presents both a physical and biochemical barrier to the CNS for large molecules [8,9]. Lymphatic vessels have been found in the meninges of

humans and mice [10–12], causing the notion of the CNS as an immune-privileged system to be reconsidered. Brain-resident macrophages, i.e., microglia, are also now broadly recognized as antigen-presenting cells of the CNS. Although the brain is an immunologically distinct site, the brain microenvironment is capable of generating robust immune responses and offers adequate opportunities for the implementation of brain tumor immunotherapy [13]. In addition, the BBB can be disrupted in brain tumor patients, which increases the infiltration of immune cells into the tumor area. However, most GBM patients have variable regions of disrupted BBB, meaning that tumor regions with disrupted BBB and tumor regions with intact BBB exist [14].

The successful treatment of glioblastoma remains one of the most difficult challenges in brain cancer therapy. This is due to (1) the small population of therapy-resistant glioblastoma stem cells (GSCs) [15–18] and (2) inter- and intra-tumor heterogeneity that consists of a variety of different subtypes of glioblastoma [19] and stromal cells in the tumor microenvironment (TME) [20,21]. Glioblastomas have been genetically categorized by The Cancer Genome Atlas into three subtypes: proneural, classical, and mesenchymal. Each of these subtypes is characterized by mutations causing platelet-derived growth factor receptor alpha activation, epidermal growth factor receptor (EGFR) activation, and neurofibromin 1 deletions, respectively. Glioblastoma subtypes differ in their prognostic value, with mesenchymal and proneural subtypes exhibiting the shortest and longest overall survival rates, respectively [19]. Moreover, the composition of the TME is linked to the molecular subtypes of glioblastoma. Mesenchymal tumors contain abundant gene expression signatures for macrophages, CD4<sup>+</sup> T cells, and neutrophils [22]; this is also associated with a higher glioma grade [19]. An increase in macrophages and microglia cells occurs upon disease recurrence and is associated with shorter relapse time after therapy [22].

GSCs are largely responsible for glioblastoma recurrence and therapy resistance due to their DNA repair and multi-drug resistance mechanisms as well as their ability to evade the immune response [15,23,24]. GSCs are maintained in hypoxic and peri-arteriolar GSC niches [25,26] and are more abundant in more aggressive, high-grade tumors with worse prognoses [27,28]. The glioblastoma TME regulates and determines the cellular state and drives GSC plasticity [29], which leads to the therapeutic resistance of tumors [30].

The predominant immune cells in the brain are macrophages, more specifically, tissue-resident macrophages known as microglia [31]. In brain cancer or other brain inflammatory conditions, additional peripheral monocytes are recruited from bone marrow and are differentiated in the brain into macrophages that are phenotypically distinct from microglia [32,33]. Immune cells are recruited and phenotypically changed by glioblastoma cells; this supports tumor growth and an immunosuppressive TME [34] through the release of cytokines, extracellular vesicles, and connecting nanotubes [35]. Chemoattraction between cells is mediated by members of a large family of chemokines [36,37]. For example, in glioblastoma, the chemokine (C-C motif) ligand 5 (CCL5) and its receptor C-C chemokine receptor type 5 (CCR5) are involved in autocrine and paracrine cross-talk between glioblastoma cells and the TME, contributing to stromal and immune cell tumor infiltration and glioblastoma cell invasion [38,39]. The attraction between endothelial and glioblastoma cells in GSC niches is predominantly maintained by the binding of C-X-C motif chemokine 12 (CXCL12, also known as stromal cell-derived factor 1 $\alpha$  (SDF-1 $\alpha$ )) to the C-X-C chemokine receptor type 4 (CXCR4) in GSCs [26].

## 2. The Immunosuppressive Microenvironment of Glioblastoma

Multi-layered immunosuppression exists in glioblastoma, both at the systemic and local level [40]. Systemic immunosuppression in glioblastoma patients is, to a large extent, induced by standard treatment including radiotherapy, temozolomide, and corticosteroids, which weakens the adaptive and innate immune responses [41]. Moreover, defects in antitumor responses arise from defective T cell mobilization from the periphery due to T cell entrapment in the bone marrow, which is caused by the loss of the surface sphingosine-1-phosphate receptor 1 (S1P1) [42,43] that binds the lipid second messenger sphingosine-1-

phosphate (S1P) [44]. The S1P-S1P1 axis plays a role in governing lymphocyte trafficking. Naïve T cell egress from bone marrow or secondary lymphoid organs cannot occur without functional S1P1 on the cell surface, as S1P1 is essential for lymphocyte recirculation [42,45].

The glioblastoma microenvironment is extremely immunosuppressive due to its low immunogenicity, the immunosuppressive properties of many cells (including cancer cells, cancer stem cells (CSCs), and tumor-infiltrating immunosuppressive immune cells, e.g., myeloid cells and T regulatory cells (Tregs)), and the lack of antigen-presenting potential and costimulatory antigens, leading to tumor resistance to immunotherapy.

Glioblastoma cells and GSCs employ several mechanisms to evade the immune response. These include their intrinsic resistance to the induction of cell death, modulation of tumor antigens and cell surface molecules (which are important for the recognition and destruction of immune effector and antigen-presenting cells), and secretion of extracellular vesicles, cytokines, and growth factors. For example, glioblastoma cells express the programmed cell death receptor 1 ligand (PD-L1) that inhibits the cytotoxicity of cytotoxic T cells and downregulates major histocompatibility complex (MHC) class I, resulting in deficient T cell cytotoxicity [40]. Moreover, glioblastoma cells may increase the expression of natural killer (NK) cell inhibitory ligands and decrease the expression of NK cell-activating NK group 2 member D (NKG2D) ligands, leading to inhibited NK cell-mediated lysis [46].

Glioblastoma is immunologically a cold tumor with low NK and T cell infiltration compared to other solid tumors. In glioblastoma, T and NK cells become dysfunctional. T cells are senescent, tolerant, exhausted, and anergic due to the immunosuppressive glioblastoma TME [40,47]. NK cells are important as immune effectors of the first line of defense against tumor cells and have been shown to control metastasis by eliminating circulating cancer cells [48]. The proposed mechanisms for the functional inactivation of tumor-associated NK cells are the overexpression of Fas ligand, the loss of mRNA for granzyme B [49], and the decrease of CD16 and its associated zeta chain [50–52]. T and NK cell dysfunction is also caused by co-expression of multiple co-inhibitory receptors, including programmed cell death protein 1 (PD-1), T cell immunoglobulin and mucin-domain containing-3 (TIM3), lymphocyte activation gene 3 protein (LAG3), cytotoxic T lymphocyte-associated protein 4 (CTLA-4), and T cell immunoreceptor with immunoglobulin and ITIM domains (TIGIT) [53].

Glioblastoma immunosuppressive TME is driven by tumor-intrinsic factors and brain (host) tissue responses to tumor antigens, such as overexpression of the indoleamine 2,3-dioxygenase (IDO) enzyme [54,55] and oncogene transforming growth factor-beta (TGF- $\beta$ ), respectively. IDO is a tryptophan catabolic enzyme overexpressed in several tumor types that creates an immunosuppressive microenvironment via the suppression of cytotoxic (CD8<sup>+</sup>) T cell proliferation and effector function [56] and the promotion of Treg generation via an aryl hydrocarbon receptor-dependent mechanism [56]. Cytokines, such as IL-10 and TGF- $\beta$ , within the glioblastoma TME cause microglia to lose MHC expression [57,58]. TGF- $\beta$  reduces NK and CD8<sup>+</sup> T cell activation through inhibiting NKG2D expression, which is responsible for inducing lysis of NKG2D ligand-bearing cells that express class I MHC-related proteins, MHC Class I Polypeptide-Related Sequence A (MICA) and B, and the UL16 binding protein (ULB) 1–4 protein family [59].

Glioblastoma cells in the TME hijack many different cells to support tumor growth through the recruitment and suppression of many cells of the innate and adaptive immune responses [20]. For example, Tregs and myeloid-derived suppressive cells that inhibit the proliferation and activation of effector cells (i.e., T cells and NK cells) and antigen-presenting cells are recruited. Increased numbers of forkhead box P3 (FOXP3)<sup>+</sup> Tregs were found in glioblastoma [60,61]; however, their correlation with patient survival was modest [60,62,63]. Microglia and tumor-infiltrating macrophages influence immunosuppression by secreting the cytokine IL-10, TGF- $\beta$ , and extracellular vesicles [64,65]. These complex interactions open new therapeutic windows for glioblastoma treatment. Colony-stimulating factor 1 (CSF-1) is a potent chemoattractant that regulates the differentiation of monocytes into tumor-associated macrophages (TAMs), and its overexpression

correlates with increased TAM infiltration and poor clinical outcomes [66]. Inhibition of the CSF-1 receptor (CSF-1R) enhanced sensitivity to irradiation by altering both the recruitment and the phenotype of myeloid-derived cells recruited to the irradiated glioblastoma [67]. TAMs also express high levels of PD-L1 [41]. Moreover, hypoxic conditions in the glioblastoma TME, through increased hypoxia-inducible factor (HIF) transcription factors and vascular endothelial growth factor (VEGF), increase TAM tumor infiltration [40].

### 3. Immunotherapeutic Strategies for Glioblastoma

The goal of immunotherapy is to stimulate patient antitumor immunity and eliminate glioblastoma cells, specifically the therapy-resistant fraction of glioblastoma cells. Several immunotherapeutic approaches, including vaccines, oncolytic viruses, checkpoint inhibitors, and adoptive cellular transfer (chimeric antigen receptor (CAR) T and NK cells), alone or in combination with standard glioblastoma therapy, have been tested against glioblastoma in preclinical and clinical studies [13,41,68–71].

#### 3.1. Vaccines

The main goal of the vaccine-based approach is to strengthen the adoptive immune response in the brain against glioblastoma cells. Several vaccines with peptides, mimicking neoantigens in glioblastoma cells, have been developed to trigger an antitumor immune response in patients. Vaccination of glioblastoma patients with a peptide mimicking the EGFR variant III (EGFRvIII) in glioblastoma cells, together with standard temozolomide chemotherapy or the anti-angiogenic agent bevacizumab, showed promising anti-glioblastoma effects in clinical trials. As only 25–30% of patients express EGFRvIII, and its expression is heterogeneous in tumors and unstable through the course of the disease, the efficiency of these vaccines is limited [72,73]. Moreover, a randomized, double-blind, and international phase 3 trial, which assessed the efficacy of the vaccine, based on EGFRvIII-specific peptide (CDX-110), with temozolomide did not show a survival benefit for newly diagnosed glioblastoma patients with EGFRvIII mutation [74]. To overcome glioblastoma cell heterogeneity, multi-peptide vaccines based on the administration of a combination of tumor-associated peptides overexpressed in glioblastoma cells were developed; however, the overall survival of glioblastoma patients was not significantly improved [41,75]. The advantages of dendritic cell-based therapies are the induction of antitumor T cell responses and enhancement of tumor immunogenicity due to their antigen-presenting functions and ability to link innate immunity with adoptive immunity. This is extremely important, especially in low immunological tumors such as glioblastoma. Vaccines based on autologous dendritic cells, which can be primed *ex vivo* using patient-derived tumor lysates, CSCs, or glioblastoma-associated antigens, have been tested in several clinical trials together with temozolomide as standard treatment [69,76,77]. Based on those findings, vaccination induces immune responses, even antitumor T cell responses have been observed; however, immune stimulation seems to be insufficient to translate into clinical benefit, and thus the efficacy of vaccine immunotherapy is limited [41,77,78]. Recent clinical studies are utilizing personalized vaccines that target a patient's unique tumor-associated neoantigens [41].

#### 3.2. Oncolytic Viruses

Virus-based anticancer therapies are based on viruses that selectively infect or replicate in tumor cells, leading to the lysis of infected tumor cells (direct effect) and the activation of immunogenic tumor cell death pathways that can stimulate antigen presentation and the adaptive antitumor immune response (indirect effects). Additionally, oncolytic viruses activate the innate immune system through pattern recognition receptors and pathogen-associated molecular patterns [79]. Current oncolytic viral approaches utilize replication-competent viruses, such as retroviruses, adenoviruses, herpes simplex viruses, polioviruses, and measles viruses [13,41]. Such viral approaches also include oncolytic viruses that are armed with immunoregulatory inserts, such as interleukin 12 and

OX40 ligand, further boosting innate and adoptive antitumor immune responses [70,80]. Adenoviruses can be modified to become tumoricidal gene delivery vectors, such as the adenoviral vector AdV-tk. This vector contains the herpes simplex virus thymidine kinase gene, which converts the toxic nucleotide analog, the prodrug ganciclovir or valacyclovir that kill fast-growing tumor cells. Moreover, induced cell death of tumor cells elicits immune effects. In phase II of clinical trials for newly diagnosed malignant gliomas, local delivery of AdV-tk plus valacyclovir together with standard treatment improved progression-free and overall survival by a few months [81]. A non-lytic, replicating retrovirus encoding cytosine deaminase has been used in clinical trials in combination with the prodrug 5-fluorocytosine, which is converted in virus-infected tumor cells into the antimetabolite 5-fluorouracil by exogenous cytosine deaminase, which is not otherwise expressed in human cells. This combined viral treatment prolonged the survival of patients with primary and recurrent high-grade gliomas in phase I clinical trials, increased immunogenicity within the TME, and activated the adoptive immune response [41,82]. Oncolytic viral immunotherapy can sensitize cancer patients to other active immunotherapeutic approaches; however, the marginal increases in overall survival have not yet achieved clinical translation. Namely, viruses and viral vectors show low transfection rates and limited penetration of brain tumors [83]. The combined approach with other immunotherapies, including immune checkpoint inhibitors and adoptive cell therapy, is currently the main focus aiming to prolong oncolytic virus-initiated clinical responses [79,84].

### 3.3. Immune Checkpoint Inhibitors

Immune checkpoint inhibitors are antibodies, which reduce the activity of endogenous negative regulatory pathways that limit T cell activation. Antibodies that block the inhibitory immune checkpoint proteins CTLA-4, PD-1, and its ligand PD-L1 have shown major improvements in the outcome of cancer patients in the past decade and are widely used. CTLA-4 and PD-1 are expressed on T cells, whereas PD-L1 is expressed on certain subsets of immune cells, including TAMs, and is aberrantly expressed on tumor cells. PD-L1 expression has been found in glioblastoma cells; however, not all glioblastomas express PD-L1 and its expression changes during the course of the disease [85]. Although there were several encouraging preclinical data on the use of immune checkpoint inhibitors (anti-PD-1 and anti-CTLA-4 antibodies, alone or in combination) for glioblastoma, clinical trials have been disappointing, with no patient survival improvement [41,85]. Several reasons for the poor efficacy of immune checkpoint inhibitors in glioblastoma have been identified, including the timing of delivery (neoadjuvant or adjuvant therapy), BBB, low infiltration of T cells into the tumor, predominant myeloid infiltrate, and multi-layered immunosuppression in the TME [84–88]. A subgroup of glioblastoma patients have benefited from immune checkpoint inhibitor treatment and have exhibited prolonged survival. The tumors of these patients have enriched alterations in the mitogen-activated protein kinase (MAPK) pathway (mutationally activated protein tyrosine phosphatase non-receptor type 11 (PTP11) and B-raf murine sarcoma (BRAF)) [41]. In the same study, non-responders to immune-checkpoint inhibitors exhibited phosphatase and tensin homolog (PTEN) mutations that were associated with immunosuppressive expression signatures [41]. A recent study by Cloughesy et al. have shown that patients with recurrent glioblastoma received neoadjuvant treatment with pembrolizumab (anti-PD-1), with continued adjuvant therapy following surgery, had significantly improved overall survival compared to that receiving only adjuvant post-surgical treatment with pembrolizumab. Neoadjuvant administration of pembrolizumab enhanced local and systemic immune responses in patients [89]. Currently, clinical trials with combinatorial therapy, in which immune checkpoint inhibition is combined with other immunostimulatory approaches, are in progress [84–88].

### 3.4. Adoptive Cell Therapies: CAR T and NK Therapy

Genetically modified T cells that express CARs consist of an extracellular tumor-specific antigen-recognition domain and a T cell activation domain. A great advantage of

CAR T cells is that they can recognize specific antigens and trigger cell lysis independently of major MHC I presentation. After autologous or allogeneic T cells are engineered in the laboratory, they are adoptively transferred into the patient to activate the antitumor immune response. In the case of brain tumors, CAR T cells can be applied intravenously, intracranially, or into the tumor [90]. CAR T cells can target glioblastoma-specific antigens, including interleukin-13 receptor subunit alpha-2 (IL-13R $\alpha$ 2), EGFR wt, and EGFRvIII, and are thus effective against glioblastoma in preclinical models [13,91,92]. In addition, glioblastoma patients who received IL-13R $\alpha$ 2- and EGFRvIII-targeting CAR T cells showed clinical responses in early clinical studies. CAR T cells can infiltrate the glioblastoma, become activated within the glioblastoma microenvironment, and activate various adoptive cell responses in patients. However, CAR T cells must be combined with other therapies or with CAR T cells targeting multiple different antigens because of glioblastoma heterogeneity, tumor antigen loss during tumor progression, CAR T exhaustion in the TME, activation of compensatory adoptive resistance mechanisms, and upregulation of immunosuppressive factors and cells (e.g., IDO1, PD-L1, and Tregs) in the TME that are triggered after CAR T cell application. Trivalent CAR T cells co-targeting human epidermal growth factor receptor 2 (HER2), IL-13R $\alpha$ 2, and EPH receptor A2 (EphA2) have been demonstrated to be more efficacious in preclinical studies than bivalent or monovalent CAR T cells [13,90,93]. CAR T cells targeting tumor-initiating cells through the surface receptor CD133 in glioblastoma have been developed recently. CD133 (prominin 1) has been identified as a surface biomarker of tumor-initiating and therapy-resistant GSCs [94]. Intracranial injection of CD133-specific CAR T cells reduced tumor burden and prolonged survival of glioblastoma-bearing mice. This treatment is considered safe in mice, as it did not incur acute toxicity in normal hematopoietic stem and progenitor cells that also express CD133 [95].

NK cells are the only immune effectors known to recognize and kill GSCs without requiring approaches that generate immunogenic antigens and enable cell priming with appropriate costimulatory signals, as are required for potential T or dendritic cell-based immunotherapies. NK cells preferentially recognize and lyse GSCs in a non-MHC restricted manner [96]. NK cells are the main mediators of antibody-dependent cellular cytotoxicity [46,68]. The use of allogeneic NK cells is preferred because the inhibitory killer-cell immunoglobulin-like receptors (KIR) receptors on the surface of donor NK cells cannot recognize self-MHC class I molecules on the tumor cells of the patient. Consequently, the absence of inhibitory signals allows NK cell activation [46,96]. As NK cells have been shown to preferentially kill GSCs [97,98] and penetrate the BBB [99] in preclinical in vitro and animal models when administered systematically, patients with glioblastoma and high-grade gliomas are now undergoing allogeneic and autologous NK cell administration in clinical trials or are undergoing recruitment (NCT04489420, NCT04254419: ClinicalTrials.gov). To increase natural NK cytotoxicity and attack towards tumors with a heterogeneous expression of CAR target antigens, NK cells can be genetically engineered to express CARs. CAR NK cells targeting the glioblastoma cell-specific antigens EGFR, EGFRvIII, and HER2 have been generated from NK cells derived from the following: the peripheral blood of healthy donors, umbilical cord blood, induced pluripotent stem cells, and the NK-92 cell line, which all display features of activated primary NK cells. CAR NK cells exhibited GSC and differentiated glioblastoma cell cytotoxicity increased levels of interferon-gamma (IFN- $\gamma$ ), and prolonged survival of glioblastoma-bearing mice in preclinical studies [68,100,101]. Currently, glioblastoma patients are being recruited for clinical trials using HER-2-specific CAR NK cells (NCT03383978: ClinicalTrials.gov).

### 3.5. Resistance to Immunotherapy and Combinatorial Approaches

As single immunotherapeutic approaches have shown some promising results but are not sufficiently successful in prolonging the survival of glioblastoma patients, combinatorial immunotherapeutic approaches that can synergize together are now under investigation. The reasons for the poor response to single immunotherapeutic approaches

are adoptive tumor resistance compensatory mechanisms due to multi-layered immunosuppression, local immune cell dysfunction, and glioblastoma tumor heterogeneity [91]. Specific efforts to facilitate the antitumor immune response are focused on targeting the immunosuppressive myeloid compartment, reducing the activity of immunosuppressive molecules (e.g., IDO and CSF-1R), and activating antitumor functions of other immune cells, NK cells, and dendritic cells [41]. Anti-IDO in combination with anti-PD-1 and anti-CTLA-4 approaches are more potent than monotherapy and decrease the accumulation of Tregs in a glioblastoma murine model [86]. The synergistic effects of combining adenovirus-based therapy and anti-PD-1 result in prolonged survival in experimental models of glioblastoma [13,80]. Although CSF-1R inhibitors showed promising results in preclinical studies, the clinical trials with orally administered CSF-1R inhibitor PLX-3397 were negative, with minimal clinical efficacy in patients with recurrent glioblastoma. Microenvironment-driven resistance to CSF-1R inhibitor is mediated through phosphatidylinositol 3-kinase (PI3K) pathway, which was elevated and driven by insulin-like growth factor-1 (IGF-1) and tumor cell IGF-1 receptor (IGF-1R) [102,103]. The use of anti-CSF-1R agents with anti-PD-1 therapy is now in clinical trials [13]. Moreover, CAR T therapy (anti-HER2, anti-IL-13R $\alpha$ 2, and anti-EGFRvIII) in combination with CTLA-4 or PD-1 inhibition has improved the effects in preclinical models and is now in clinical trials [90].

Current standard-of-care treatment for glioblastoma includes maximal surgical tumor resection, hyperfractionated radiotherapy, and temozolomide, which, in combination with commonly used corticosteroids, systemically weakens the immune system, increases immunosuppression, and hinders the immunotherapeutic strategy [41]. It has also been shown that a standard dose of temozolomide induces immunosuppression and abrogates the effect of anti-PD-1 therapy [104] and oncolytic virus-based immunotherapy [105]. Conversely, localized treatment, which increases the availability of tumor antigens, synergizes with immunotherapy. It has been shown that radiation increases the mutational burden of tumors and triggers tumor necrosis and antigen release, leading to increased antigen presentation and immunogenicity [106]. The high mutational burden is associated with response to immunotherapy in several types of cancer, but not in gliomas. For example, gliomas with a high mutational burden and mismatch repair gene deficiency are less responsive to PD-1 blockage [107]. Low mutation burden in recurrent glioblastoma patients was recently associated with longer survival after immunotherapy, implicating that tumor mutational burden itself may not be a causative driver of response to immunotherapy, but may reflect the immunological status of tumor or some other co-related feature, among them time to recurrence, TP53 mutation and any differences in the clinical care between patients with high vs. low mutational burden [108]. The combination of immunotherapy with hypofractionated stereotactic radiosurgery can probably improve the efficacy of immunotherapy as stereotactic radiosurgery does not trigger systemic immunosuppression [13]. Metronomic dosing of temozolomide or local chemotherapy are preferred when combining temozolomide with immunotherapy [104]. However, additional studies are needed to elucidate the efficiency of these combinatorial approaches.

#### **4. Advanced In Vitro and Animal Tumor Models for Testing Immunotherapeutic Approaches**

Glioblastomas are very heterogeneous in their cellular composition, gene expression, and phenotypic properties [109]. In addition, glioblastoma contains a unique and complex immune TME. Based on studies on preclinical tumor models and clinical stages, we conclude that the currently used glioblastoma tumor models do not sufficiently reflect the conditions in humans, as several immunotherapeutic strategies that were efficient in preclinical studies failed to demonstrate sufficient clinical significance. The ability to comprehensively understand glioblastoma phenotypes and mimic their specific therapeutic responses to enable personalized therapy requires the creation of clinically relevant models that reliably reflect the complexity of the tumor in humans. For example, current patient-derived tumor models lack clinically relevant recapitulation of immune compartments [110]. To address all these challenges, different tumor models have been developed, including CSCs, organoids,

patient-derived xenografts, genetically engineered mice models, and humanized mice. Comparisons of various tumor models to explore immunotherapeutic approaches and their advantages and disadvantages are listed in Table 1.

**Table 1.** A comparison of different glioblastoma tumor models for studying immunotherapy.

Tumor Model	Description	Advantages	Disadvantages	References
<b>In Vitro</b>				
Tumor cell lines	established tumor cell lines, grown as monolayers in serum-containing media	+ rapid expansion + low costs + long tradition + easy genetic manipulation + well-characterized + simple	- clonal selection in cell cultures based on media selection - lack of clonal diversity and heterogeneity - lack of TME and ECM	[111]
Cancer stem cells	patient-derived tumor cells grown in serum-free and growth factor-supplemented media as tumorspheres	+ reflect stem-like features and therapeutic resistance + preserve the tumor's genetic background + phenotypic heterogeneity + 3D model	- lack of TME and ECM - clonal selection	[112]
Cell co-cultures	2D or 3D co-cultures of tumor and non-tumor cells, such as immune cells and stromal cells	+ heterotypic cellular interactions + simple + mechanistic studies of cellular cross-talk in TME	- lack of complex TME and architecture	[113]
Organotypic tissue slice cultures	precision-cut slices of tumor tissue, mounted onto porous membranes for mechanical support, and cultured in a controlled conditions	+ recapitulate TME + preserve inter-intra-tumoral heterogeneity and heterotypic cellular interactions + clinically relevant therapeutic response + platform for studying the tumor immune cell environment + tumor cell invasion model system	- limited by the availability of fresh patient samples - short lifespan - cryopreservation method is not optimized - not adapted for high throughput analysis	[114,115]
Patient-derived organoids	3D in vitro tissue constructs composed of multiple cell types, patient-based from resected tumors	+ preserve inter-intra-tumoral heterogeneity and heterotypic cellular interactions + preserve the tumor's genetic background + recapitulate TME + pre-clinical applications + 3D model + high through-put + clinically relevant therapeutic response + feasibility of co-culture with immune cells	- variable ability to maintain over very long periods - limited by the availability of fresh patient samples - limited immune component - lack of model optimization - do not recapitulate tumor initiation	[116,117]



Table 1. Cont.

Tumor Model	Description	Advantages	Disadvantages	References
<b>In Vitro</b>				
Genetically-engineered cerebral organoids	3D in vitro tissue constructs created by using genetic manipulations to induce tumorigenesis in cerebral organoids	+ 3D model + good reproducibility + clinically relevant therapeutic response + enable to study early phases of tumorigenesis and tumor progression + brain tissue architecture	- poorly recapitulate TME - the tumor's genetic background is not preserved - lack of immune component	[118,119]
<b>In Vivo</b>				
Syngeneic mouse model	derived by transplanting mouse tumor cell lines or CSCs into strain-matched mice	+ immune system and response + present TME + simple with a long tradition + allows genetic modifications + tumor cell heterogeneity and clonal diversity with implanted CSCs	- limited tumor cell heterogeneity and clonal diversity with implanted tumor cell line - high costs - laborious, time-consuming - lack of human tumor-immune cell interactions - TME is of rodent origin	[110,120]
Genetically engineered mouse tumor model	created by introducing genetic modifications that result in spontaneous tumor development	+ allows genetic modifications + tumor cell heterogeneity and clonal diversity + tumor-immune cell interactions if immunocompetent mice are used + present TME	- large number of animals - laborious, time-consuming - poor inter-animal comparability - high costs - TME is of rodent origin	[121]
Patient-derived xenografts	derived by transplanting human tumor explants into immunodeficient mice	+ tumor cell heterogeneity and clonal diversity + present TME + reflect tumors in human + little graft-versus-host rejection for adoptive cell therapy (CART) + preserve the tumor's genetic background	- high costs - fail to develop a functional immune system - lack of human tumor-immune cell interactions - laborious, time-consuming - TME is of rodent origin	[90,122]
Humanized mouse tumor model	generated by the engraftment of human cancer cell lines or human PDX tumors into mice with a reconstituted human immune response	+ tumor heterogeneity and clonal diversity + present TME + human immune cells + mimicking human tumor and immune system interactions + realistic representation of immunotherapy safety and clinical response + preserves the tumor's genetic background	- long-lasting establishment - high costs - laborious, time-consuming - slow tumor growth	[110,123, 124]

CSC: cancer stem cell; ECM: extracellular matrix; PDX: patient-derived xenografts; TME: tumor microenvironment.

#### 4.1. CSCs

Considering the importance of targeting therapy-resistant and tumorigenic CSCs, 3D models of CSCs incorporate the cellular heterogeneity of tumors, improve drug response predictability, and represent better models for discovering new targets for anticancer drugs compared to traditional 2D tumor cell lines [125]. GSC tumorspheres represent models generated by the symmetric and asymmetric division of patient-derived GSCs in a defined medium supplemented with growth factors, i.e., epidermal growth factor (EGF), fibroblast growth factor (FGF)-2, and neuronal viability supplement B27 [112]. These factors and the absence of serum are needed to maintain self-renewal and proliferation and to preserve the genetic characteristics observed in patients' samples. Tumorspheres are characterized by an external proliferating zone, intermediate quiescent zone, and an inner necrotic core [126], observed at a certain distance from the presence of nutrients, metabolites, and oxygen, resembling the necrotic areas of *in vivo* glioblastoma [127]. Tumor cells within tumorspheres closely interact with each other, thus reproducing the physical communication and signaling pathways that affect proliferation, survival, and response to therapy *in vivo* [128] and forming a physical barrier that prevents and limits the transport of drugs into the tumorsphere mass [129]. Although a better model than monolayer cultures, tumorspheres represent random aggregations of cells that do not organize into tissue-like structures and also lack extracellular matrix [130]. The greater limitation of these models is the lack of neighboring non-tumor cells, i.e., stromal cells, including astrocytes, neurons, endothelial cells, mesenchymal stem cells, brain-resident microglia, and infiltrated peripheral immune cells; this altogether prevents studying their interactions with GSCs *in vitro*. Tumorspheres can be optimized by co-culturing cancer and stromal cells in so-called heterotypic spheroids, especially for testing cancer immunotherapeutic agents. For example, GSC tumorspheres were used to evaluate the penetration and cytotoxicity of highly cytotoxic super-charged NK cells (Figure 1, our results), grown in the presence of osteoclasts and probiotic bacteria to stimulate their cytotoxic potential towards CSCs [113]. In the study of Cheema et al. [131], the authors used a murine GSC model in syngeneic immunocompetent mice to test a genetically engineered oncolytic herpes simplex virus that is armed with the cytokine interleukin 12 (G47 $\Delta$ -mIL12). In addition to targeting GSCs, oncolytic virus treatment increased IFN- $\gamma$  release, inhibited angiogenesis, and reduced the number of Tregs in the tumor.

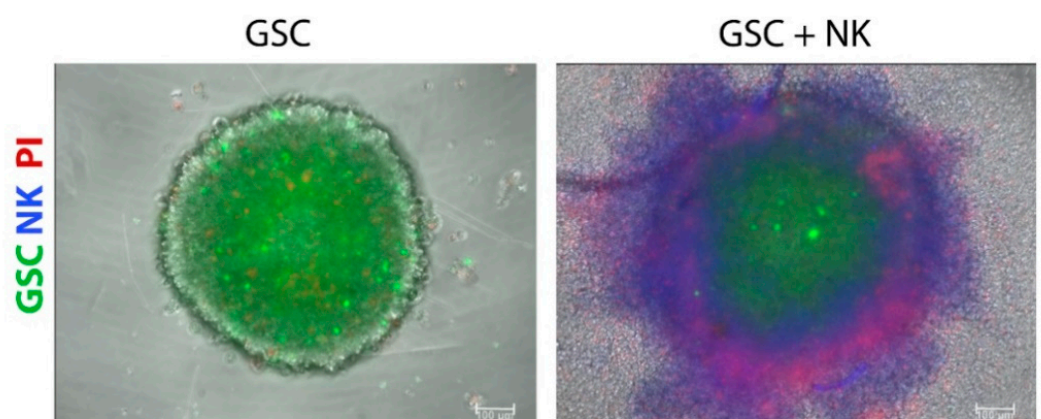


**Figure 1.** Super-charged natural killer (NK; blue) cell treatment decreased the number of glioblastoma stem cells (GSCs; green) and increased the number of dead cells (PI, red) in 3D tumorsphere models. NK cells were added to GSC tumorspheres at a NK:GSC ratio of 10:1, and images were acquired using an inverted fluorescence microscope 4 h later. Propidium Iodide (PI) staining was used to detect dead cells (red). Scale bars: 100  $\mu$ m.

#### 4.2. Organotypic Tissue Slices

Organotypic tissue slice model of glioblastoma represents precision-cut slices of tumor tissue, in which the original inter and intra-tumor heterogeneity and the architecture of the tumor are maintained. Slices of the tumor are prepared with an automated vibratome and transferred onto membrane culture inserts for mechanical support in a specific cultivation medium [114]. This technique is relatively fast, it does not involve selective outgrowth of tumor cells, and therefore can be used for personalized treatment. Organotypic cultures have been used to study the invasive properties of glioblastoma and the patient-specific effect of anti-invasive drugs [115]. Recently an organotypic slice culture technique was developed from fresh pancreatic ductal adenocarcinoma to study the immune response after immunotherapy treatment [132] and can be applied to a variety of solid tumors, including glioblastoma. A disadvantage of this model is its relatively low throughput. The technique is laborious and requires specialized analysis tools.

#### 4.3. Organoids

Organoids are 3D constructs composed of multiple cell types with the ability to self-organize and recapitulate the architecture and functionality of the original organ [110,133]. Different approaches for organoid generation have been applied, including using patient-derived adult stem cells and resected tumor tissues, as first described by Sato et al. [134]. Another approach involves the use of pluripotent stem cells, i.e., pluripotent embryonic stem cells and induced pluripotent stem cells [135]. The term “organotypic tumor spheroid” was initially used at the beginning of organoid development but was later replaced by the term “tumor organoid” [110]. Compared with traditional models, different tumor organoids, including liver [136], pancreatic [137], gastric [138,139], bladder [140], breast [141], and ovarian [142], show a vast potential for basic cancer research, drug screening, and personalized medicine and may bridge the gap between *in vitro* and *in vivo* cancer models. Until recently, it was unclear whether various methods for organoid preparation can be adapted for organoids from non-epithelial tumors. In 2016, Hubert et al. generated patient-derived glioblastoma organoids to study the heterogeneity and hypoxic gradient of tumors using a submerged culture system [116]. In this protocol, finely minced tumor specimens are embedded in a solid gel of extracellular matrix (Matrigel) to form 3–4 mm large organoids in the tissue culture medium, supplemented with EGF, FGF, and B27. These organoids formed in 2 months and could be cultured for over a year. Glioblastoma organoids are characterized by rapidly proliferating cells on the edge of the organoid and highly resistant quiescent CSCs in the hypoxic core with different molecular profiles. Although this is a very promising model of glioblastoma that closely resembles tumor sensitivity *in vitro*, its genetic and molecular features remain unclear. In 2018, Ogawa et al. constructed cerebral organoids using induced pluripotent stem cells and embryonic stem cells and induced glioma carcinogenesis by CRISPR/Cas9 technology to disrupt the TP53 tumor suppressor and express oncogenic HRas<sup>G12V</sup> [110]. Moreover, neoplastic cerebral organoids were established by Bian et al. [118] via recapitulating brain tumorigenesis by introducing oncogenic mutations or amplifications in cerebral organoids using transposon-mediated gene insertion and CRISPR/Cas9 technology. These organoids developed  $CDKN2A^{-/-}/CDKN2B^{-/-}/EGFR^{OE}/EGFR^{III^{OE}}$ ,  $NF1^{-/-}/PTEN^{-/-}/TP53^{-/-}$ , and  $EGFR^{III^{OE}}/CDKN2A^{-/-}/PTEN^{-/-}$  genotypes, which are commonly found in glioblastoma. In contrast to the aforementioned technique, induced pluripotent stem cells and embryonic stem cell organoids represent 3D human tissues generated by directed differentiation, self-morphogenesis, and intrinsically driven self-assembly of cells, recapitulating human organogenesis *in vitro* [143]. This type of organoid can contain multiple tissue cell types, including stroma and vasculature, unlike organoids developed from tissue-specific stem cells [144]. A novel approach using hESC-derived cerebral organoids and patient-derived GSCs to model tumor cell invasion was recently developed, i.e., a glioma cerebral organoid model. This system was shown to recapitulate the cellular behavior of glioblastoma and to maintain genetic aberrations found in the original tumor [145]. In a very recent

study, Jacob et al. [117,146] established patient-derived glioblastoma organoids that accurately recapitulate the molecular, genetic, and cell-type heterogeneity of parental tumors. Compared to other previous protocols of glioblastoma organoids [116,118,119], the authors dissected tumor tissues into approximately 1 mm fragments without the addition of extracellular matrix or EGF and bFGF and cultured them on an orbital shaker for 1–2 weeks to generate 3D structures. These organoids contain heterogeneous populations of cellular subtypes and recapitulate tumor cell phenotypes, as confirmed by histopathology, single-cell RNA sequencing, and molecular profiling analysis. Moreover, glioblastoma organoids develop a hypoxic gradient and retain vasculature and TME composition, which mimics the main features of glioblastoma [117].

Organoids are becoming a very useful platform for cancer research, especially in the field of immuno-oncology; however, organoid establishment and its (pre)clinical applications are still immature. To date, co-cultures of epithelial tumor organoids and additional cellular components have been used to include the interactions between tumor and immune cells and have thus established a better preclinical model for immunotherapy. Immunocompetent organoids can be achieved by adding pre-treated autologous or allogeneic peripheral blood mononuclear cells (PBMCs) or specific immune cell populations, such as TAMs and tumor-infiltrating lymphocytes [110]. For example, in a recent study, Dijkstra et al. [147] enriched tumor-reactive T cells by co-culturing PBMCs and tumor organoids from colorectal and non-small-cell lung cancer and demonstrated that these T cells can be used to assess the efficiency of killing tumor organoids. In another study, gamma delta 2 ( $\gamma\delta 2$ )<sup>+</sup> T cells were co-cultured with organoids from human breast epithelia, and these lymphocytes effectively eliminated triple-negative breast cancer cells [148]. These and other studies demonstrate that T cells can be obtained and activated by organoids for adoptive T cell therapy. Using the air-liquid interface technique, Neal et al. [149] generated patient-derived organoids from different surgically resected primary and metastatic tumors with native embedded immune cells (CD8<sup>+</sup> and CD4<sup>+</sup> T cells, B cells, NK cells, and macrophages). This demonstrated the potential of organoids as tools to predict clinical responses to immune checkpoint therapies. For this method, tumor tissue fragments are embedded in a type I collagen matrix on an inner Transwell insert. Culture medium with different supplements is added to the outer dish to diffuse via the permeable membrane. The collagen layer is exposed to air to ensure oxygen supplies for the long-term preservation of organoids [150]. The latter approach is very promising and can also be applied for future glioblastoma research. In a recent study, the specific oncolytic activity of Zika virus against GSCs in glioblastoma cerebral organoids was demonstrated. The authors showed that SOX2 and integrin  $\alpha_v\beta_5$  represent key markers for Zika virus infection in association with suppression of immune response genes. Thus, Zika virus infection provides the possibility for brain tumor therapy [151]. The organoids established by Jacob et al. [117] are the first that, besides tumor cells, also include the TME. As CAR T cells represent a powerful new approach to treat glioblastoma, these glioblastoma organoids, which preserve the immune microenvironment and other stromal cells, were used as a model. The authors demonstrated that this rapid protocol for organoid generation provides a platform to test and optimize CAR T therapies for tumors of non-epithelial origin and enables a personalized treatment approach. We also showed that organoids established by this protocol after 4 weeks in culture included GSCs, differentiated glioblastoma cells, tumor vasculature, and immune cells, such as macrophages, microglia, and T cells (Figure 2, our results).

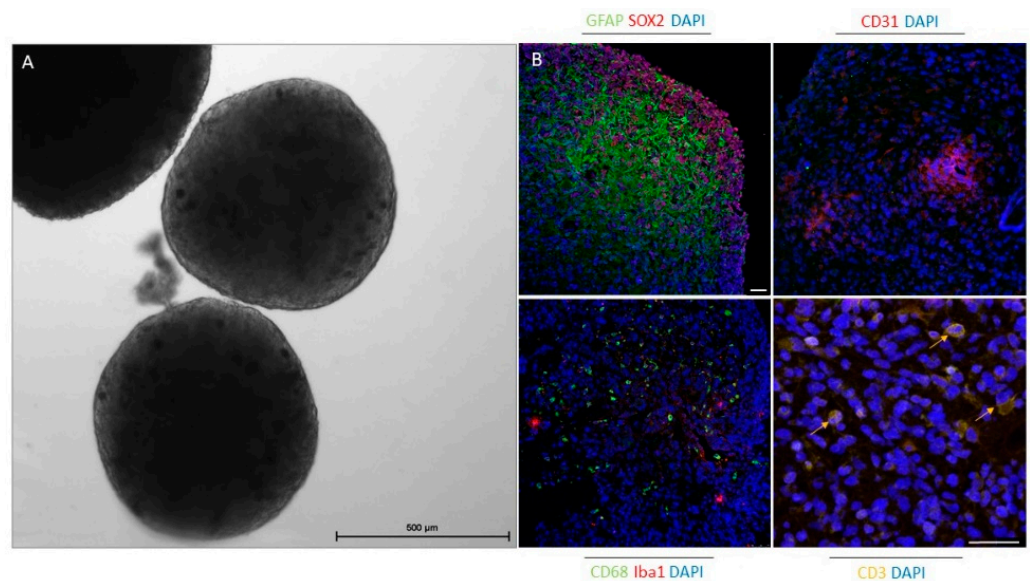


**Figure 2.** Glioblastoma organoids after 4 weeks in culture preserve specific elements of the tumor microenvironment. (A) Phase-contrast image of glioblastoma organoids in culture. Scale bar: 500  $\mu\text{m}$ . (B) Immunofluorescence staining of paraffin-embedded glioblastoma organoids for glioblastoma stem cell marker (SOX2), differentiated glioblastoma cell and astrocyte marker (GFAP), endothelial cell marker (CD31), macrophage marker (CD68), microglia marker (Iba1), and T cell marker (CD3). Cell nuclei were stained with DAPI (blue). Scale bars: 50  $\mu\text{m}$ .

#### 4.4. Animal Models

Syngeneic mouse models represent one of the oldest preclinical models for investigating antitumor therapies, in which spontaneous or chemically/virus-induced tumor cell lines from inbred mice are expanded *in vitro* and then inoculated into the same inbred mouse strain with an intact immune system [152]. The advantages of these models are their ease of use, rapid and reproducible expansion, and the possibility of genetic manipulation [120], especially to evaluate the efficacy of immunotherapeutic agents. However, these models, if implanted with tumor cell lines, lack genomic and microenvironmental heterogeneity due to the limited availability of CSCs that evolve genetic and epigenetic alterations that allow them to differentiate into multiple tumor cell types [153]. The GL261 syngeneic murine model represents one of the best characterized syngeneic, immunocompetent models in glioblastoma immunotherapy preclinical research [152]. Reardon et al. showed that blockade of CTLA-4, PD-1, or PD-L1 alone can eradicate glioblastoma growth in GL261 syngeneic murine models [154]. CAR T cells were shown to inhibit GL261/EGFRvIII tumor growth [155], and the potential of ErbB2-specific CAR-NK (NK-92/5.28) cells was demonstrated for adoptive immunotherapy of glioblastoma [100]. However, further studies are needed to determine whether these murine glioma models faithfully reflect human glioblastoma.

Several syngeneic rat glioma models are currently available for preclinical studies. However, rat glioma models, such as C6, showed immunological instability, since implanted tumor cells that should be syngeneic, triggered allogeneic immune response and lack of tumor growth because C6 glioma cells arose from an outbred strain of Wistar rat. Thus, these models are not useful for evaluating the efficacy of immunotherapy [156].

Genetically engineered mouse tumor models are generated through the introductions of genetic mutations specific to particular human cancers. Genetically engineered mouse tumor models of glioblastoma require gene expression manipulation using Tet regulation, Cre-inducible gene alleles [157], or the replication-competent avian leukosis virus splice-acceptor/avian tumor virus receptor A (RCAS/TVA) system, which uses retroviral or adenoviral vectors to deliver Cre recombinase for somatic cell gene transfers [158]. These models reflect the histology and biology of human glioblastoma; however, the dif-

ferences in the TME and immune system between mice and humans reduce the clinical relevance of such cancer immunotherapy studies [121].

An alternative model system, patient-derived xenografts (PDXs), is also used in cancer research. PDX models of glioblastoma are based on subcutaneous or intracranial transplantation of patient-derived tumor cells, organoids, or tissues into immunodeficient NSG (NOD scid gamma) mice. This model better recapitulates the heterogeneity and complexity of the tumor and represents a valuable tool to investigate the characteristics of glioblastoma [110,122]. Furthermore, PDXs are commonly used to study the CAR T immunotherapeutic response [90] due to the lower chance of graft-versus-host rejection. One of the major limitations of these models is the need to use immunodeficient host strains for tumor engraftment and propagation. Because of the absence of functional elements of the immune system, such as NK cells, macrophages, and Tregs, the current PDX models are also unable to accurately assess the effects of different immunotherapies [90].

Humanized mice tumor models are generated by the engraftment of human tumor cell lines, CSCs, or human PDX tumors into immunodeficient NSG mice with an HLA-matched human immune system, which is initiated by the transplantation of human PBMCs, isolated from human adult blood, or CD34<sup>+</sup> hematopoietic stem cells (HSCs). Transplanted CD34<sup>+</sup> HSCs in immunocompromised mice differentiate into human helper T cells, cytotoxic T cells, B cells, monocytes, NK cells, and dendritic cells [123]; after tumor implantation, these mice can survive several months with a relatively stable percent of human cells in the blood. Human microglia/macrophage-like cells have also been developed in the brain of CD34<sup>+</sup> HSC humanized mice [159]. This model is mostly used to evaluate treatment with anti-PD-1 and anti-CTLA-4 antibodies [160]. For example, in the study by Capasso et al. [161], nivolumab (anti-PD-1 antibody) inhibited MDA-MB-231 triple-negative breast cancer cells and CRC172 colorectal cancer cells in the humanized umbilical cord blood-derived HSC mouse models. Furthermore, the therapeutic antitumor potential of highly cytotoxic allogeneic super-charged NK cells was confirmed using an alternative humanized BLT (bone marrow, liver, thymus) mice model that was implanted with oral CSCs. The BLT model improves the functionality of T and NK cells via co-transplantation of fetal liver and thymus [113,162]. The main difficulty of HSC mouse models is their long-term establishment, and thus PBMCs from adult donors can be used to quickly restore the autologous human immune system [124]. However, the lifespan of PBMCs in mice is very short, i.e., only 3 weeks. As such, the timeframe to evaluate immunotherapies is reduced. These models are also likely to generate stable graft-versus-host reactions [163]. Moreover, the human CD45<sup>+</sup> fraction in peripheral blood is composed mainly of T cells, limiting the investigation of other immune cells, such as monocytes and NK cells [110]. Different studies demonstrated that humanized mice with PBMCs can be successfully used for the evaluation of monoclonal antibodies, cytokine therapy (IL-2), immune checkpoint inhibitors, and dendritic cell-based vaccines [124,164,165]. For example, the efficacy of the anti-PD-1 antibody was evaluated using humanized NOG-dKO mice, in which human PBMCs and the glioblastoma cell line U87 were transplanted [166]. There are both advantages and disadvantages to this model; however, the humanized mouse platform is being improved in a way that the investigation of immunotherapeutics may become more predictive. Currently, the use of humanized mice models in glioblastoma preclinical and clinical studies is limited due to the lack of knowledge and remaining unanswered questions, including whether humanized mice models recapitulate the clinical features of glioblastoma patients.

## 5. Conclusions

We have summarized the recent findings on the progress of glioblastoma immunotherapy, the unique properties of glioblastoma that affect immunotherapy resistance, and tumor models that can facilitate our understanding of the fundamental immunobiology of glioblastoma and test potential novel immunotherapeutic approaches. Immunotherapy to fight glioblastoma holds great promise; however, there are many challenges, including (1) inter-

and intra-tumor heterogeneity, (2) high immunosuppression in the TME, (3) a poor understanding of the mechanisms of immune cell activation in intracranial compartments, (4) the presence of tumor-initiating and therapy-refractory CSCs, and (5) the lack of appropriate tumor models to study combinatorial approaches with standard treatments and to predict treatment responses. Recent improvements in the establishment of glioblastoma organoids that exhibit tumor heterogeneity and include immune compartments as well as immuno-geno(pheno)typing of patient tumors hold great promise to help us resolve the complex immunobiology of brain tumors and to increase the efficiency of immunotherapy.

**Author Contributions:** Conceptualization, B.B., M.N., and B.M.; writing—original draft preparation, B.M., M.N., and B.B.; writing—review and editing, B.M., M.N., N.K.-J., A.J., and B.B.; visualization, B.M.; project administration, B.B., M.N., and A.J.; funding acquisition, B.B. and A.J. All authors have read and agreed to the published version of the manuscript.

**Funding:** This work was supported by the Slovenian Research Agency (Grant program P1-0245, Postdoctoral project Z3-1870, Young researcher grant and Bilateral project BI-US/19-21-021) and by the European Program of Cross-Border Cooperation for Slovenia-Italy Interreg TRANS-GLIOMA.

**Institutional Review Board Statement:** The study was conducted according to the guidelines of the Declaration of Helsinki, and approved by the National Medical Ethics Committee of the Republic of Slovenia (#0120-190/2018/4 and #0120-190/2018/23) and Institutional Review Board of University of California Los Angeles (IRB#11-000781).

**Informed Consent Statement:** Informed consent was obtained from all subjects involved in the study.

**Data Availability Statement:** No datasets were generated during the current study.

**Acknowledgments:** We would like to thank Tamara Lah Turnšek and Eva Lasič for critically reading the manuscript

**Conflicts of Interest:** The authors declare no conflict of interest.

## References

- Louis, D.N.; Perry, A.; Reifenberger, G.; von Deimling, A.; Figarella-Branger, D.; Cavenee, W.K.; Ohgaki, H.; Wiestler, O.D.; Kleihues, P.; Ellison, D.W. The 2016 World Health Organization Classification of Tumors of the Central Nervous System: A summary. *Acta Neuropathol.* **2016**, *131*, 803–820. [CrossRef] [PubMed]
- Stupp, R.; Taillibert, S.; Kanner, A.; Read, W.; Steinberg, D.M.; Lhermitte, B.; Toms, S.; Idbaih, A.; Ahluwalia, M.S.; Fink, K.; et al. Effect of tumor-treating fields plus maintenance temozolomide vs maintenance temozolomide alone on survival in patients with glioblastoma a randomized clinical trial. *JAMA-J. Am. Med. Assoc.* **2017**, *318*, 2306–2316. [CrossRef] [PubMed]
- Noch, E.K.; Ramakrishna, R.; Magge, R. Challenges in the Treatment of Glioblastoma: Multisystem Mechanisms of Therapeutic Resistance. *World Neurosurg.* **2018**, *116*, 505–517. [CrossRef]
- Thomas, A.A.; Brennan, C.W.; DeAngelis, L.M.; Omuro, A.M. Emerging therapies for glioblastoma. *JAMA Neurol.* **2014**, *71*, 1437–1444. [CrossRef]
- Stupp, R.; Mason, W.P.; Van Den Bent, M.J.; Weller, M.; Fisher, B.; Taphoorn, M.J.B.; Belanger, K.; Brandes, A.A.; Marosi, C.; Bogdahn, U.; et al. Radiotherapy plus concomitant and adjuvant temozolomide for glioblastoma. *N. Engl. J. Med.* **2005**, *352*, 987–996. [CrossRef]
- Louis, D.N.; Ohgaki, H.; Wiestler, O.D.; Cavenee, W.K.; Burger, P.C.; Jouvet, A.; Scheithauer, B.W.; Kleihues, P. The 2007 WHO classification of tumours of the central nervous system. *Acta Neuropathol.* **2007**, *114*, 97–109. [CrossRef] [PubMed]
- Omuro, A.; DeAngelis, L.M. Glioblastoma and other malignant gliomas: A clinical review. *JAMA-J. Am. Med. Assoc.* **2013**, *310*, 1842–1850. [CrossRef]
- Theodorakis, P.E.; Müller, E.A.; Craster, R.V.; Matar, O.K. Physical insights into the blood-brain barrier translocation mechanisms. *Phys. Biol.* **2017**, *14*, 041001. [CrossRef]
- Fokas, E.; Steinbach, J.P.; Rödel, C. Biology of brain metastases and novel targeted therapies: Time to translate the research. *Biochim. Biophys. Acta-Rev. Cancer* **2013**, *1835*, 61–75. [CrossRef]
- Herisson, F.; Frodermann, V.; Courties, G.; Rohde, D.; Sun, Y.; Vandoorne, K.; Wojtkiewicz, G.R.; Masson, G.S.; Vinegoni, C.; Kim, J.; et al. Direct vascular channels connect skull bone marrow and the brain surface enabling myeloid cell migration. *Nat. Neurosci.* **2018**, *21*, 1209–1217. [CrossRef]
- Louveau, A.; Smirnov, I.; Keyes, T.J.; Eccles, J.D.; Rouhani, S.J.; Peske, J.D.; Derecki, N.C.; Castle, D.; Mandell, J.W.; Lee, K.S.; et al. Structural and functional features of central nervous system lymphatic vessels. *Nature* **2015**, *523*, 337–341. [CrossRef] [PubMed]
- Aspelund, A.; Antila, S.; Proulx, S.T.; Karlsen, T.V.; Karaman, S.; Detmar, M.; Wiig, H.; Alitalo, K. A dural lymphatic vascular system that drains brain interstitial fluid and macromolecules. *J. Exp. Med.* **2015**, *212*, 991–999. [CrossRef] [PubMed]

13. Medikonda, R.; Dunn, G.; Rahman, M.; Fecci, P.; Lim, M. A review of glioblastoma immunotherapy. *J. Neurooncol.* **2020**. [CrossRef]
14. Oberoi, R.K.; Parrish, K.E.; Sio, T.T.; Mittapalli, R.K.; Elmquist, W.F.; Sarkaria, J.N. Strategies to improve delivery of anticancer drugs across the blood–brain barrier to treat glioblastoma. *Neuro. Oncol.* **2016**, *18*, 27–36. [CrossRef] [PubMed]
15. Lathia, J.D.; Mack, S.C.; Mulkearns-hubert, E.E.; Valentim, C.L.L.; Rich, J.N. Cancer stem cells in glioblastoma. *Genes Dev.* **2015**, *1203–1217*. [CrossRef]
16. Chen, J.; Li, Y.; Yu, T.S.; McKay, R.M.; Burns, D.K.; Kernie, S.G.; Parada, L.F. A restricted cell population propagates glioblastoma growth after chemotherapy. *Nature* **2012**, *488*, 522–526. [CrossRef]
17. Galli, R.; Binda, E.; Orfanelli, U.; Cipelletti, B.; Gritti, A.; De Vitis, S.; Fiocco, R.; Foroni, C.; Dimeco, F.; Vescovi, A. Isolation and characterization of tumorigenic, stem-like neural precursors from human glioblastoma. *Cancer Res.* **2004**, *64*, 7011–7021. [CrossRef]
18. Osuka, S.; Van Meir, E.G. Overcoming therapeutic resistance in glioblastoma: The way forward. *J. Clin. Investig.* **2017**, *127*, 415–426. [CrossRef]
19. Verhaak, R.G.W.; Hoadley, K.A.; Purdom, E.; Wang, V.; Qi, Y.; Wilkerson, M.D.; Miller, C.R.; Ding, L.; Golub, T.; Mesirov, J.P.; et al. Integrated genomic analysis identifies clinically relevant subtypes of glioblastoma characterized by abnormalities in PDGFRA, IDH1, EGFR, and NF1. *Cancer Cell* **2010**, *17*, 98–110. [CrossRef]
20. Broekman, M.L.; Maas, S.L.N.; Abels, E.R.; Mempel, T.R.; Krichevsky, A.M.; Breakefield, X.O. Multidimensional communication in the microenvirons of glioblastoma. *Nat. Rev. Neurol.* **2018**. [CrossRef]
21. Teng, J.; Da Hora, C.C.; Kantar, R.S.; Nakano, I.; Wakimoto, H.; Batchelor, T.T.; Antonio Chiocca, E.; Badr, C.E.; Tannous, B.A. Dissecting inherent intratumor heterogeneity in patient-derived glioblastoma culture models. *Neuro. Oncol.* **2017**, *19*, 820–832. [CrossRef] [PubMed]
22. Wang, Q.; Hu, B.; Hu, X.; Kim, H.; Squatrito, M.; Scarpace, L.; de Carvalho, A.C.; Lyu, S.; Li, P.; Li, Y.; et al. Tumor Evolution of Glioma-Intrinsic Gene Expression Subtypes Associates with Immunological Changes in the Microenvironment. *Cancer Cell* **2017**, *32*, 42–56.e6. [CrossRef] [PubMed]
23. Otvos, B.; Silver, D.J.; Mulkearns-Hubert, E.E.; Alvarado, A.G.; Turaga, S.M.; Sorensen, M.D.; Rayman, P.; Flavahan, W.A.; Hale, J.S.; Stoltz, K.; et al. Cancer Stem Cell-Secreted Macrophage Migration Inhibitory Factor Stimulates Myeloid Derived Suppressor Cell Function and Facilitates Glioblastoma Immune Evasion. *Stem Cells* **2016**. [CrossRef] [PubMed]
24. Alvarado, A.G.; Thiagarajan, P.S.; Mulkearns-Hubert, E.E.; Silver, D.J.; Hale, J.S.; Alban, T.J.; Turaga, S.M.; Jarrar, A.; Reizes, O.; Longworth, M.S.; et al. Glioblastoma Cancer Stem Cells Evade Innate Immune Suppression of Self-Renewal through Reduced TLR4 Expression. *Cell Stem Cell* **2017**. [CrossRef] [PubMed]
25. Hira, V.V.V.; Aderetti, D.A.; van Noorden, C.J.F. Glioma Stem Cell Niches in Human Glioblastoma Are Periarteriolar. *J. Histochem. Cytochem.* **2018**, *66*, 349–358. [CrossRef]
26. Hira, V.V.V.; Breznik, B.; Vittori, M.; Loncq de Jong, A.; Mlakar, J.; Oostra, R.J.; Khurshed, M.; Molenaar, R.J.; Lah, T.; Van Noorden, C.J.F. Similarities Between Stem Cell Niches in Glioblastoma and Bone Marrow: Rays of Hope for Novel Treatment Strategies. *J. Histochem. Cytochem.* **2019**, *68*. [CrossRef]
27. Ardebili, S.; Zajc, I.; Gole, B.; Campos, B.; Herold-Mende, C.; Drmot, S.; Lah, T. CD133/prominin1 is prognostic for GBM patient’s survival, but inversely correlated with cysteine cathepsins’ expression in glioblastoma derived spheroids. *Radiol. Oncol.* **2011**, *45*, 1–13. [CrossRef]
28. Zeppernick, F.; Ahmadi, R.; Campos, B.; Dictus, C.; Helmke, B.M.; Becker, N.; Lichter, P.; Unterberg, A.; Radlwimmer, B.; Herold-Mende, C.C. Stem cell marker CD133 affects clinical outcome in glioma patients. *Clin. Cancer Res.* **2008**, *14*, 123–129. [CrossRef]
29. Dirkse, A.; Golebiewska, A.; Buder, T.; Nazarov, P.V.; Muller, A.; Poovathingal, S.; Brons, N.H.C.; Leite, S.; Sauvageot, N.; Sarkisjan, D.; et al. Stem cell-associated heterogeneity in Glioblastoma results from intrinsic tumor plasticity shaped by the microenvironment. *Nat. Commun.* **2019**, *10*, 1–16. [CrossRef]
30. Perus, L.J.M.; Walsh, L.A. Microenvironmental Heterogeneity in Brain Malignancies. *Front. Immunol.* **2019**, *10*, 2294.
31. Ajami, B.; Bennett, J.L.; Krieger, C.; Tetzlaff, W.; Rossi, F.M.V. Local self-renewal can sustain CNS microglia maintenance and function throughout adult life. *Nat. Neurosci.* **2007**, *10*, 1538–1543. [CrossRef] [PubMed]
32. Lund, H.; Pieber, M.; Parsa, R.; Han, J.; Grommisch, D.; Ewing, E.; Kular, L.; Needhamsen, M.; Espinosa, A.; Nilsson, E.; et al. Competitive repopulation of an empty microglial niche yields functionally distinct subsets of microglia-like cells. *Nat. Commun.* **2018**, *9*, 1–13. [CrossRef] [PubMed]
33. Mildner, A.; Schmidt, H.; Nitsche, M.; Merkler, D.; Hanisch, U.K.; Mack, M.; Heikenwalder, M.; Brück, W.; Priller, J.; Prinz, M. Microglia in the adult brain arise from Ly-6ChiCCR2+ monocytes only under defined host conditions. *Nat. Neurosci.* **2007**, *10*, 1544–1553. [CrossRef]
34. Thorsson, V.; Gibbs, D.L.; Brown, S.D.; Wolf, D.; Bortone, D.S.; Ou Yang, T.H.; Porta-Pardo, E.; Gao, G.F.; Plaisier, C.L.; Eddy, J.A.; et al. The Immune Landscape of Cancer. *Immunity* **2018**, *48*, 812–830.e14. [CrossRef] [PubMed]
35. Matias, D.; Balça-Silva, J.; da Graça, G.C.; Wanjiru, C.M.; Macharia, L.W.; Nascimento, C.P.; Roque, N.R.; Coelho-Aguiar, J.M.; Pereira, C.M.; Dos Santos, M.F.; et al. Microglia/astrocytes–glioblastoma crosstalk: Crucial molecular mechanisms and microenvironmental factors. *Front. Cell. Neurosci.* **2018**, *12*, 235. [CrossRef]
36. Breznik, B.; Motaln, H.; Turnšek, T.L. Proteases and cytokines as mediators of interactions between cancer and stromal cells in tumours. *Biol. Chem.* **2016**, *398*, 709–719. [CrossRef]



37. O'Hayre, M.; Salanga, C.L.; Handel, T.M.; Allen, S.J. Chemokines and cancer: Migration, intracellular signalling and intercellular communication in the microenvironment. *Biochem. J.* **2008**, *409*, 635–649. [CrossRef]
38. Novak, M.; Koprivnikar Krajnc, M.; Hrastar, B.; Breznik, B.; Majc, B.; Mlinar, M.; Rotter, A.; Porčnik, A.; Mlakar, J.; Stare, K.; et al. CCR5-Mediated Signaling Is Involved in Invasion of Glioblastoma Cells in Its Microenvironment. *Int. J. Mol. Sci.* **2020**, *21*, 4199. [CrossRef]
39. Kranjc, M.K.; Novak, M.; Pestell, R.G.; Lah, T.T. Cytokine CCL5 and receptor CCR5 axis in glioblastoma multiforme. *Radiol. Oncol.* **2019**, *53*, 397–406. [CrossRef]
40. Grabowski, M.M.; Sankey, E.W.; Ryan, K.J.; Chongsathidkiet, P.; Lorrey, S.J.; Wilkinson, D.S.; Fecci, P.E. Immune suppression in gliomas. *J. Neurooncol.* **2020**. [CrossRef]
41. Lim, M.; Xia, Y.; Bettgowda, C.; Weller, M. Current state of immunotherapy for glioblastoma. *Nat. Rev. Clin. Oncol.* **2018**, *15*, 422–442. [CrossRef] [PubMed]
42. Chongsathidkiet, P.; Jackson, C.; Koyama, S.; Loebel, F.; Cui, X.; Farber, S.H.; Woroniecka, K.; Elsamadicy, A.A.; Dechant, C.A.; Kemeny, H.R.; et al. Sequestration of T cells in bone marrow in the setting of glioblastoma and other intracranial tumors. *Nat. Med.* **2018**, *24*, 1459–1468. [CrossRef] [PubMed]
43. Antunes, A.R.P.; Scheyltjens, I.; Duerinck, J.; Neyns, B.; Movahedi, K.; Van Ginderachter, J.A. Understanding the glioblastoma immune microenvironment as basis for the development of new immunotherapeutic strategies. *Elife* **2020**, *9*. [CrossRef]
44. Garris, C.S.; Blaho, V.A.; Hla, T.; Han, M.H. Sphingosine-1-phosphate receptor 1 signalling in T cells: Trafficking and beyond. *Immunology* **2014**, *142*, 347–353. [CrossRef]
45. Matloubian, M.; Lo, C.G.; Cinamon, G.; Lesneski, M.J.; Xu, Y.; Brinkmann, V.; Allende, M.L.; Proia, R.L.; Cyster, J.G. Lymphocyte egress from thymus and peripheral lymphoid organs is dependent on S1P receptor 1. *Nature* **2004**, *427*, 355–360. [CrossRef]
46. Golán, I.; De La Fuente, L.R.; Costoya, J.A. NK cell-based glioblastoma immunotherapy. *Cancers* **2018**, *10*, 522. [CrossRef]
47. Adhikaree, J.; Moreno-Vicente, J.; Kaur, A.P.; Jackson, A.M.; Patel, P.M. Resistance Mechanisms and Barriers to Successful Immunotherapy for Treating Glioblastoma. *Cells* **2020**, *9*, 263. [CrossRef]
48. Lo, H.C.; Xu, Z.; Kim, I.S.; Pingel, B.; Aguirre, S.; Kodali, S.; Liu, J.; Zhang, W.; Muscarella, A.M.; Hein, S.M.; et al. Resistance to natural killer cell immunosurveillance confers a selective advantage to polyclonal metastasis. *Nat. Cancer* **2020**, *1*, 709–722. [CrossRef]
49. Mulder, W.M.C.; Bloemena, E.; Stukart, M.J.; Kummer, J.A.; Wagstaff, J.; Scheper, R.J. T cell receptor- $\zeta$  and granzyme B expression in mononuclear cell infiltrates in normal colon mucosa and colon carcinoma. *Gut* **1997**, *40*, 113–119. [CrossRef]
50. Nakagomi, H.; Petersson, M.; Magnusson, I.; Juhlin, C.; Matsuda, M.; Mellstedt, H.; Vivier, J.L.T.; Anderson, P.; Kiessling, R. Decreased Expression of the Signal-transducing  $\zeta$  Chains in Tumor-infiltrating T-Cells and NK Cells of Patients with Colorectal Carcinoma. *Cancer Res.* **1993**, *53*, 5610–5612.
51. Romee, R.; Foley, B.; Lenvik, T.; Wang, Y.; Zhang, B.; Ankarlo, D.; Luo, X.; Cooley, S.; Verneris, M.; Walcheck, B.; et al. NK cell CD16 surface expression and function is regulated by a disintegrin and metalloprotease-17 (ADAM17). *Blood* **2013**, *121*, 3599–3608. [CrossRef] [PubMed]
52. Pellegatta, S.; Eoli, M.; Frigerio, S.; Antozzi, C.; Bruzzone, M.G.; Cantini, G.; Nava, S.; Anghileri, E.; Cuppini, L.; Cuccarini, V.; et al. The natural killer cell response and tumor debulking are associated with prolonged survival in recurrent glioblastoma patients receiving dendritic cells loaded with autologous tumor lysates. *Oncoimmunology* **2013**, *2*. [CrossRef] [PubMed]
53. Wherry, E.J.; Kurachi, M. Molecular and cellular insights into T cell exhaustion. *Nat. Rev. Immunol.* **2015**, *15*, 486–499. [CrossRef] [PubMed]
54. Zhou, W.; Ke, S.Q.; Huang, Z.; Flavahan, W.; Fang, X.; Paul, J.; Wu, L.; Sloan, A.E.; McLendon, R.E.; Li, X.; et al. Periostin secreted by glioblastoma stem cells recruits M2 tumour-associated macrophages and promotes malignant growth. *Nat. Cell Biol.* **2015**, *17*, 170–182. [CrossRef] [PubMed]
55. Komohara, Y.; Jinushi, M.; Takeya, M. Clinical significance of macrophage heterogeneity in human malignant tumors. *Cancer Sci.* **2014**, *105*, 1–8. [CrossRef]
56. Sheridan, C. IDO inhibitors move center stage in immuno-oncology. *Nat. Biotechnol.* **2015**, *33*, 321–322. [CrossRef] [PubMed]
57. Razavi, S.M.; Lee, K.E.; Jin, B.E.; Aujla, P.S.; Gholamin, S.; Li, G. Immune Evasion Strategies of Glioblastoma. *Front. Surg.* **2016**, *3*. [CrossRef]
58. Roy, L.-O.; Poirier, M.-B.; Fortin, D. Transforming growth factor-beta and its implication in the malignancy of gliomas. *Target. Oncol.* **2015**, *10*, 1–14. [CrossRef]
59. Crane, C.A.; Han, S.J.; Barry, J.J.; Ahn, B.J.; Lanier, L.L.; Parsa, A.T. TGF- $\beta$  downregulates the activating receptor NKG2D on NK cells and CD8+ T cells in glioma patients. *Neuro. Oncol.* **2010**, *12*, 7–13. [CrossRef]
60. Jacobs, J.F.M.; Idema, A.J.; Bol, K.F.; Grotenhuis, J.A.; de Vries, I.J.M.; Wesseling, P.; Adema, G.J. Prognostic significance and mechanism of Treg infiltration in human brain tumors. *J. Neuroimmunol.* **2010**, *225*, 195–199. [CrossRef]
61. El Andaloussi, A.; Lesniak, M.S. CD4+CD25+FoxP3+ T-cell infiltration and heme oxygenase-1 expression correlate with tumor grade in human gliomas. *J. Neurooncol.* **2007**, *83*, 145–152. [CrossRef] [PubMed]
62. Thomas, A.A.; Fisher, J.L.; Rahme, G.J.; Hampton, T.H.; Baron, U.; Olek, S.; Schwachula, T.; Rhodes, C.H.; Gui, J.; Tafe, L.J.; et al. Regulatory T cells are not a strong predictor of survival for patients with glioblastoma. *Neuro. Oncol.* **2015**, *17*, 801–809. [CrossRef] [PubMed]

63. Yue, Q.; Zhang, X.; Ye, H.X.; Wang, Y.; Du, Z.G.; Yao, Y.; Mao, Y. The prognostic value of Foxp3+ tumor-infiltrating lymphocytes in patients with glioblastoma. *J. Neurooncol.* **2014**, *116*, 251–259. [CrossRef] [PubMed]
64. Li, W.; Graeber, M.B. The molecular profile of microglia under the influence of glioma. *Neuro. Oncol.* **2012**, *14*, 958–978. [CrossRef] [PubMed]
65. Van Der Vos, K.E.; Abels, E.R.; Zhang, X.; Lai, C.; Carrizosa, E.; Oakley, D.; Prabhakar, S.; Mardini, O.; Crommentuijn, M.H.W.; Skog, J.; et al. Directly visualized glioblastoma-derived extracellular vesicles transfer RNA to microglia/macrophages in the brain. *Neuro. Oncol.* **2016**, *18*, 58–69. [CrossRef]
66. Pollard, J.W. Trophic macrophages in development and disease. *Nat. Rev. Immunol.* **2009**, *9*, 259–270. [CrossRef]
67. Stafford, J.H.; Hirai, T.; Deng, L.; Chernikova, S.B.; Urata, K.; West, B.L.; Brown, J.M. Colony stimulating factor 1 receptor inhibition delays recurrence of glioblastoma after radiation by altering myeloid cell recruitment and polarization. *Neuro. Oncol.* **2016**, *18*, 797–806. [CrossRef]
68. Burger, M.C.; Zhang, C.; Harter, P.N.; Romanski, A.; Strassheimer, F.; Senft, C.; Tonn, T.; Steinbach, J.P.; Wels, W.S. CAR-Engineered NK Cells for the Treatment of Glioblastoma: Turning Innate Effectors Into Precision Tools for Cancer Immunotherapy. *Front. Immunol.* **2019**, *10*, 1–16. [CrossRef]
69. Do, A.S.M.S.; Amano, T.; Edwards, L.A.; Zhang, L.; De Peralta-Venturina, M.; Yu, J.S. CD133 mRNA-Loaded Dendritic Cell Vaccination Abrogates Glioma Stem Cell Propagation in Humanized Glioblastoma Mouse Model. *Mol. Ther. Oncolytics* **2020**, *18*, 295–303. [CrossRef]
70. Martikainen, M.; Essand, M. Virus-based immunotherapy of glioblastoma. *Cancers* **2019**, *11*, 186. [CrossRef]
71. Dunn, G.P.; Cloughesy, T.F.; Maus, M.V.; Prins, R.M.; Reardon, D.A.; Sonabend, A.M. Emerging immunotherapies for malignant glioma: From immunogenomics to cell therapy. *Neuro. Oncol.* **2020**. [CrossRef] [PubMed]
72. Sampson, J.H.; Heimberger, A.B.; Archer, G.E.; Aldape, K.D.; Friedman, A.H.; Friedman, H.S.; Gilbert, M.R.; Herndon, J.E.; McLendon, R.E.; Mitchell, D.A.; et al. Immunologic escape after prolonged progression-free survival with epidermal growth factor receptor variant III peptide vaccination in patients with newly diagnosed glioblastoma. *J. Clin. Oncol.* **2010**, *28*, 4722–4729. [CrossRef]
73. Lynes, J.P.; Nwankwo, A.K.; Sur, H.P.; Sanchez, V.E.; Sarpong, K.A.; Ariyo, O.I.; Dominah, G.A.; Nduom, E.K. Biomarkers for immunotherapy for treatment of glioblastoma. *J. Immunother. Cancer* **2020**, *8*. [CrossRef]
74. Weller, M.; Butowski, N.; Tran, D.D.; Recht, L.D.; Lim, M.; Hirte, H.; Ashby, L.; Mechtler, L.; Goldlust, S.A.; Iwamoto, F.; et al. Rindopepimut with temozolomide for patients with newly diagnosed, EGFRvIII-expressing glioblastoma (ACT IV): A randomised, double-blind, international phase 3 trial. *Lancet Oncol.* **2017**, *18*, 1373–1385. [CrossRef]
75. Rampling, R.; Peoples, S.; Mulholland, P.J.; James, A.; Al-Salihi, O.; Twelves, C.J.; McBain, C.; Jefferies, S.; Jackson, A.; Stewart, W.; et al. A cancer research UK first time in human phase I trial of IMA950 (novel multipeptide therapeutic vaccine) in patients with newly diagnosed glioblastoma. *Clin. Cancer Res.* **2016**, *22*, 4776–4785. [CrossRef] [PubMed]
76. Liao, L.M.; Ashkan, K.; Tran, D.D.; Campian, J.L.; Trusheim, J.E.; Cobbs, C.S.; Heth, J.A.; Salacz, M.; Taylor, S.; D’Andre, S.D.; et al. First results on survival from a large Phase 3 clinical trial of an autologous dendritic cell vaccine in newly diagnosed glioblastoma. *J. Transl. Med.* **2018**, *16*, 1. [CrossRef]
77. Eoli, M.; Corbetta, C.; Anghileri, E.; Di Ianni, N.; Milani, M.; Cuccarini, V.; Musio, S.; Paterra, R.; Frigerio, S.; Nava, S.; et al. Expansion of effector and memory T cells is associated with increased survival in recurrent glioblastomas treated with dendritic cell immunotherapy. *Neuro-Oncol. Adv.* **2019**, *1*, 1–13. [CrossRef]
78. Srivastava, S.; Jackson, C.; Kim, T.; Choi, J.; Lim, M. A characterization of dendritic cells and their role in immunotherapy in glioblastoma: From preclinical studies to clinical trials. *Cancers* **2019**, *11*, 537. [CrossRef]
79. Lichty, B.D.; Breitbach, C.J.; Stojdl, D.F.; Bell, J.C. Going viral with cancer immunotherapy. *Nat. Rev. Cancer* **2014**, *14*, 559–567. [CrossRef]
80. Jiang, H.; Rivera-Molina, Y.; Gomez-Manzano, C.; Clise-Dwyer, K.; Bover, L.; Vence, L.M.; Yuan, Y.; Lang, F.F.; Toniatti, C.; Hossain, M.B.; et al. Oncolytic adenovirus and tumor-targeting immune modulatory therapy improve autologous cancer vaccination. *Cancer Res.* **2017**, *77*, 3894–3907. [CrossRef]
81. Wheeler, L.A.; Manzanera, A.G.; Bell, S.D.; Cavaliere, R.; McGregor, J.M.; Grecula, J.C.; Newton, H.B.; Lo, S.S.; Badie, B.; Portnow, J.; et al. Phase II multicenter study of gene-mediated cytotoxic immunotherapy as adjuvant to surgical resection for newly diagnosed malignant glioma. *Neuro. Oncol.* **2016**, *18*, 1137–1145. [CrossRef]
82. Cloughesy, T.F.; Landolfi, J.; Vogelbaum, M.A.; Ostertag, D.; Elder, J.B.; Bloomfield, S.; Carter, B.; Chen, C.C.; Kalkanis, S.N.; Kesari, S.; et al. Durable complete responses in some recurrent high-grade glioma patients treated with Toca 511 + Toca FC. *Neuro. Oncol.* **2018**, *20*, 1383–1392. [CrossRef]
83. Caffery, B.; Lee, J.S.; Alexander-Bryant, A.A. Vectors for glioblastoma gene therapy: Viral & non-viral delivery strategies. *Nanomaterials* **2019**, *9*, 105. [CrossRef]
84. Passaro, C.; Alayo, Q.; De Laura, I.; McNulty, J.; Grauwet, K.; Ito, H.; Bhaskaran, V.; Mineo, M.; Lawler, S.E.; Shah, K.; et al. Arming an oncolytic herpes simplex virus type 1 with a single-chain fragment variable antibody against PD-1 for experimental glioblastoma therapy. *Clin. Cancer Res.* **2019**, *25*, 290–299. [CrossRef]
85. Sanders, S.; Debinski, W. Challenges to successful implementation of the immune checkpoint inhibitors for treatment of glioblastoma. *Int. J. Mol. Sci.* **2020**, *21*, 2759. [CrossRef]

86. Wainwright, D.A.; Chang, A.L.; Dey, M.; Balyasnikova, I.V.; Kim, C.K.; Tobias, A.; Cheng, Y.; Kim, J.W.; Qiao, J.; Zhang, L.; et al. Durable Therapeutic Efficacy Utilizing Combinatorial Blockade against IDO, CTLA-4, and PD-L1 in Mice with Brain Tumors. *Clin. Cancer Res.* **2014**, *20*. [CrossRef]
87. Schalper, K.A.; Rodriguez-Ruiz, M.E.; Diez-Valle, R.; López-Janeiro, A.; Porciuncula, A.; Idoate, M.A.; Inogés, S.; de Andrea, C.; López-Díaz de Cerio, A.; Tejada, S.; et al. Neoadjuvant nivolumab modifies the tumor immune microenvironment in resectable glioblastoma. *Nat. Med.* **2019**, *25*, 470–476. [CrossRef]
88. Khasraw, M.; Reardon, D.A.; Weller, M.; Sampson, J.H. PD-1 Inhibitors: Do they have a Future in the Treatment of Glioblastoma? *Clin. Cancer Res.* **2020**, *26*, 5287–5296. [CrossRef]
89. Cloughesy, T.F.; Mochizuki, A.Y.; Orpilla, J.R.; Hugo, W.; Lee, A.H.; Davidson, T.B.; Wang, A.C.; Ellingson, B.M.; Rytlewski, J.A.; Sanders, C.M.; et al. Neoadjuvant anti-PD-1 immunotherapy promotes a survival benefit with intratumoral and systemic immune responses in recurrent glioblastoma. *Nat. Med.* **2019**, *25*, 477–486. [CrossRef]
90. Salinas, R.D.; Durgin, J.S. Rourke, Potential of Glioblastoma—Targeted Chimeric Antigen Receptor (CAR) CAR T Therapy. *CNS Drugs.* **2020**, *34*, 127–145. [CrossRef]
91. O'Rourke, D.M.; Nasrallah, M.P.; Desai, A.; Melenhorst, J.J.; Mansfield, K.; Morrisette, J.J.D.; Martinez-Lage, M.; Brem, S.; Maloney, E.; Shen, A.; et al. A single dose of peripherally infused EGFRvIII-directed CAR T cells mediates antigen loss and induces adaptive resistance in patients with recurrent glioblastoma. *Sci. Transl. Med.* **2017**, *9*. [CrossRef]
92. Choi, B.D.; Yu, X.; Castano, A.P.; Bouffard, A.A.; Schmidts, A.; Larson, R.C.; Bailey, S.R.; Boroughs, A.C.; Frigault, M.J.; Leick, M.B.; et al. CAR-T cells secreting BiTEs circumvent antigen escape without detectable toxicity. *Nat. Biotechnol.* **2019**, *37*, 1049–1058. [CrossRef]
93. Bielamowicz, K.; Fousek, K.; Byrd, T.T.; Samaha, H.; Mukherjee, M.; Aware, N.; Wu, M.F.; Orange, J.S.; Sumazin, P.; Man, T.K.; et al. Trivalent CAR T cells overcome interpatient antigenic variability in glioblastoma. *Neuro. Oncol.* **2018**, *20*, 506–518. [CrossRef]
94. Singh, S.K.; Hawkins, C.; Clarke, I.D.; Squire, J.A.; Bayani, J.; Hide, T.; Henkelman, R.M.; Cusimano, M.D.; Dirks, P.B. Identification of human brain tumour initiating cells. *Nature* **2004**, *432*, 396–401. [CrossRef]
95. Vora, P.; Venugopal, C.; Salim, S.K.; Tatari, N.; Bakhshinyan, D.; Singh, M.; Seyfrid, M.; Upreti, D.; Rentas, S.; Wong, N.; et al. The Rational Development of CD133-Targeting Immunotherapies for Glioblastoma. *Cell Stem Cell* **2020**, *26*, 832–844.e6. [CrossRef]
96. Jewett, A.; Kos, J.; Kaur, K.; Turnsek, T.L.; Breznik, B.; Senior, E.; Wong, P.; Nguyen, K.Y.; Ko, M.-W. Multiple defects of Natural Killer cells in cancer patients; Anarchy and dysregulated systemic immunity and immunosuppression in metastatic cancer. *Crit. Rev. Immunol.* **2020**, *40*, 93–133. [CrossRef]
97. Kozłowska, A.K.; Tseng, H.C.; Kaur, K.; Topchyan, P.; Inagaki, A.; Bui, V.T.; Kasahara, N.; Cacalano, N.; Jewett, A. Resistance to cytotoxicity and sustained release of interleukin-6 and interleukin-8 in the presence of decreased interferon- $\gamma$  after differentiation of glioblastoma by human natural killer cells. *Cancer Immunol. Immunother.* **2016**, *65*, 1085–1097. [CrossRef]
98. Guillerey, C.; Huntington, N.D.; Smyth, M.J. Targeting natural killer cells in cancer immunotherapy. *Nat. Immunol.* **2016**, *17*, 1025–1036. [CrossRef]
99. Sharifzad, F.; Mardpour, S.; Mardpour, S.; Fakharian, E.; Taghikhani, A.; Sharifzad, A.; Kiani, S.; Heydarian, Y.; Łos, M.J.; Azizi, Z.; et al. HSP70/IL-2 treated NK cells effectively cross the blood brain barrier and target tumor cells in a rat model of induced glioblastoma multiforme (GBM). *Int. J. Mol. Sci.* **2020**, *21*, 2263. [CrossRef]
100. Zhang, C.; Burger, M.C.; Jennewein, L.; Genßler, S.; Schönfeld, K.; Zeiner, P.; Hattingen, E.; Harter, P.N.; Mittelbronn, M.; Tonn, T.; et al. ErbB2/HER2-Specific NK Cells for Targeted Therapy of Glioblastoma. *J. Natl. Cancer Inst.* **2016**. [CrossRef]
101. Han, J.; Chu, J.; Keung Chan, W.; Zhang, J.; Wang, Y.; Cohen, J.B.; Victor, A.; Meisen, W.H.; Kim, S.H.; Grandi, P.; et al. CAR-engineered NK cells targeting wild-type EGFR and EGFRvIII enhance killing of glioblastoma and patient-derived glioblastoma stem cells. *Sci. Rep.* **2015**. [CrossRef]
102. Quail, D.F.; Bowman, R.L.; Akkari, L.; Quick, M.L.; Schuhmacher, A.J.; Huse, J.T.; Holland, E.C.; Sutton, J.C.; Joyce, J.A. The tumor microenvironment underlies acquired resistance to CSF-1R inhibition in gliomas. *Science* **2016**, *352*, aad3018. [CrossRef]
103. Butowski, N.; Colman, H.; De Groot, J.F.; Omuro, A.M.; Nayak, L.; Wen, P.Y.; Cloughesy, T.F.; Marimuthu, A.; Haidar, S.; Perry, A.; et al. Orally administered colony stimulating factor 1 receptor inhibitor PLX3397 in recurrent glioblastoma: An Ivy Foundation Early Phase Clinical Trials Consortium phase II study. *Neuro. Oncol.* **2016**, *18*, 557–564. [CrossRef]
104. Karachi, A.; Yang, C.; Dastmalchi, F.; Sayour, E.J.; Huang, J.; Azari, H.; Long, Y.; Flores, C.; Mitchell, D.A.; Rahman, M. Neuro-Oncology Modulation of temozolomide dose differentially affects T-cell response to immune checkpoint inhibition. *Neuro Oncol.* **2019**, *21*, 730–741. [CrossRef]
105. Saha, D.; Rabkin, S.D.; Martuza, R.L. Temozolomide antagonizes oncolytic immunovirotherapy in glioblastoma. *J. Immunother. Cancer* **2020**, *8*, 1–8. [CrossRef]
106. Reits, E.A.; Hodge, J.W.; Herberts, C.A.; Groothuis, T.A.; Chakraborty, M.; Wansley, E.K.; Camphausen, K.; Luiten, R.M.; de Ru, A.H.; Neijssen, J.; et al. Radiation modulates the peptide repertoire, enhances MHC class I expression, and induces successful antitumor immunotherapy. *J. Cell Biol.* **2006**. [CrossRef]
107. Touat, M.; Li, Y.Y.; Boynton, A.N.; Spurr, L.F.; Iorgulescu, J.B.; Bohrson, C.L.; Cortes-Ciriano, I.; Birzu, C.; Geduldig, J.E.; Pelton, K.; et al. Mechanisms and therapeutic implications of hypermutation in gliomas. *Nature* **2020**, *580*, 517–523. [CrossRef]
108. Gromeier, M.; Brown, M.C.; Zhang, G.; Lin, X.; Chen, Y.; Wei, Z.; Beaubier, N.; Yan, H.; He, Y.; Desjardins, A.; et al. Very low mutation burden is a feature of inflamed recurrent glioblastomas responsive to cancer immunotherapy. *Nat. Commun.* **2021**, *12*, 352. [CrossRef]

109. Marusyk, A.; Polyak, K. Tumor heterogeneity: Causes and consequences. *Biochim. Biophys. Acta-Rev. Cancer* **2010**, *1805*, 105–117. [CrossRef]
110. Klein, E.; Hau, A.; Oudin, A.; Golebiewska, A. Glioblastoma Organoids: Pre-Clinical Applications and Challenges in the Context of Immunotherapy Glioblastoma Organoids: Pre-Clinical Applications and Challenges in the Context of Immunotherapy. *Front. Oncol.* **2020**. [CrossRef]
111. Goodspeed, A.; Heiser, L.M.; Gray, J.W.; Costello, J.C. Tumor-derived cell lines as molecular models of cancer pharmacogenomics. *Mol. Cancer Res.* **2016**, *14*, 3–13. [CrossRef] [PubMed]
112. Lee, J.; Kotliarova, S.; Kotliarov, Y.; Li, A.; Su, Q.; Donin, N.M.; Pastorino, S.; Purow, B.W.; Christopher, N.; Zhang, W.; et al. Tumor stem cells derived from glioblastomas cultured in bFGF and EGF more closely mirror the phenotype and genotype of primary tumors than do serum-cultured cell lines. *Cancer Cell* **2006**, *9*, 391–403. [CrossRef] [PubMed]
113. Kaur, K.; Topchyan, P.; Kozłowska, A.K.; Ohanian, N.; Chiang, J.; Maung, P.O.; Park, S.H.; Ko, M.W.; Fang, C.; Nishimura, I.; et al. Super-charged NK cells inhibit growth and progression of stem-like/poorly differentiated oral tumors in vivo in humanized BLT mice; effect on tumor differentiation and response to chemotherapeutic drugs. *Oncoimmunology* **2018**, *7*, e1426518. [CrossRef] [PubMed]
114. Merz, F.; Gaunitz, F.; Dehghani, F.; Renner, C.; Meixensberger, J.; Gutenberg, A.; Giese, A.; Schopow, K.; Hellwig, C.; Schäfer, M.; et al. Organotypic slice cultures of human glioblastoma reveal different susceptibilities to treatments. *Neuro. Oncol.* **2013**, *15*, 670–681. [CrossRef]
115. Parker, J.J.; Lizarraga, M.; Waziri, A.; Foshay, K.M. A human glioblastoma organotypic slice culture model for study of tumor cell migration and patient-specific effects of anti-invasive drugs. *J. Vis. Exp.* **2017**, *2017*, 53557. [CrossRef]
116. Hubert, C.G.; Rivera, M.; Spangler, L.C.; Wu, Q.; Mack, S.C.; Prager, B.C.; Couce, M.; McLendon, R.E.; Sloan, A.E.; Rich, J.N. A three-dimensional organoid culture system derived from human glioblastomas recapitulates the hypoxic gradients and cancer stem cell heterogeneity of tumors found in vivo. *Cancer Res.* **2016**, *76*, 2465–2477. [CrossRef] [PubMed]
117. Jacob, F.; Salinas, R.D.; Zhang, D.Y.; Nguyen, P.T.T.; Schnoll, J.G.; Wong, S.Z.H.; Thokala, R.; Sheikh, S.; Saxena, D.; Prokop, S.; et al. A Patient-Derived Glioblastoma Organoid Model and Biobank Recapitulates Inter- and Intra-tumoral Heterogeneity. *Cell* **2020**, *180*, 188–204.e22. [CrossRef]
118. Bian, S.; Repic, M.; Guo, Z.; Kavirayani, A.; Burkard, T.; Bagley, J.A.; Krauditsch, C.; Knoblich, J.A. Genetically engineered cerebral organoids model brain tumor formation. *Nat. Methods* **2018**. [CrossRef]
119. Ogawa, J.; Pao, G.M.; Shokhirev, M.N.; Verma, I.M. Glioblastoma Model Using Human Cerebral Organoids. *Cell Rep.* **2018**, *23*, 1220–1229. [CrossRef]
120. Olson, B.; Li, Y.; Lin, Y.; Liu, E.T.; Patnaik, A. Mouse models for cancer immunotherapy research. *Cancer Discov.* **2018**, *8*, 1358–1365. [CrossRef]
121. Zhao, Y.; Liu, M.; Chan, X.Y.; Tan, S.Y.; Subramaniam, S.; Fan, Y.; Loh, E.; Chang, K.T.E.; Tan, T.C.; Chen, Q. Uncovering the mystery of opposite circadian rhythms between mouse and human leukocytes in humanized mice. *Blood* **2017**, *130*, 1995–2005. [CrossRef] [PubMed]
122. Joo, K.M.; Kim, J.; Jin, J.; Kim, M.; Seol, H.J.; Muradov, J.; Yang, H.; Choi, Y.L.; Park, W.Y.; Kong, D.S.; et al. Patient-Specific Orthotopic Glioblastoma Xenograft Models Recapitulate the Histopathology and Biology of Human Glioblastomas In Situ. *Cell Rep.* **2013**, *3*, 260–273. [CrossRef] [PubMed]
123. Zhao, Y.; Shuen, T.W.H.; Toh, T.B.; Chan, X.Y.; Liu, M.; Tan, S.Y.; Fan, Y.; Yang, H.; Lyer, S.G.; Bonney, G.K.; et al. Development of a new patient-derived xenograft humanised mouse model to study human-specific tumour microenvironment and immunotherapy. *Gut* **2018**, *67*, 1845. [CrossRef] [PubMed]
124. Lin, S.; Huang, G.; Cheng, L.; Li, Z.; Xiao, Y.; Deng, Q.; Jiang, Y.; Li, B.; Lin, S.; Wang, S.; et al. Establishment of peripheral blood mononuclear cell-derived humanized lung cancer mouse models for studying efficacy of PD-L1/PD-1 targeted immunotherapy. *MAbs* **2018**, *10*. [CrossRef]
125. Saygin, C.; Matei, D.; Majeti, R.; Reizes, O.; Lathia, J.D. Targeting Cancer Stemness in the Clinic: From Hype to Hope. *Cell Stem Cell* **2019**, *24*, 25–40. [CrossRef]
126. Mehta, G.; Hsiao, A.Y.; Ingram, M.; Luker, G.D.; Takayama, S. Opportunities and challenges for use of tumor spheroids as models to test drug delivery and efficacy. *J. Control. Release* **2012**, *164*, 192–204. [CrossRef]
127. Louis, D.N. Molecular pathology of malignant gliomas. *Annu. Rev. Pathol.* **2006**, *1*, 97–117. [CrossRef]
128. Hanahan, D.; Coussens, L.M. Accessories to the Crime: Functions of Cells Recruited to the Tumor Microenvironment. *Cancer Cell* **2012**, *21*, 309–322. [CrossRef]
129. Tannock, I.F.; Lee, C.M.; Tunggal, J.K.; Cowan, D.S.M.; Egorin, M.J. Limited penetration of anticancer drugs through tumor tissue: A potential cause of resistance of solid tumors to chemotherapy. *Clin. Cancer Res.* **2002**, *8*, 878–884.
130. Torras, N.; García-Díaz, M.; Fernández-Majada, V.; Martínez, E. Mimicking epithelial tissues in three-dimensional cell culture models. *Front. Bioeng. Biotechnol.* **2018**, *6*, 197. [CrossRef]
131. Cheema, T.A.; Wakimoto, H.; Fecci, P.E.; Ning, J.; Kuroda, T.; Jeyaretna, D.S.; Martuza, R.L.; Rabkin, S.D. Multifaceted oncolytic virus therapy for glioblastoma in an immunocompetent cancer stem cell model. *Proc. Natl. Acad. Sci. USA* **2013**, *110*, 12006–12011. [CrossRef] [PubMed]
132. Jiang, X.; Seo, Y.D.; Sullivan, K.M.; Pillarisetty, V.G. Establishment of slice cultures as a tool to study the cancer immune microenvironment. *Methods Mol. Biol.* **2019**, *1884*, 283–295. [CrossRef] [PubMed]

133. Li, M.; Izipisua Belmonte, J.C. Organoids—Preclinical models of human disease. *N. Engl. J. Med.* **2019**, *380*, 569–579. [CrossRef] [PubMed]
134. Sato, T.; Stange, D.E.; Ferrante, M.; Vries, R.G.J.; Van Es, J.H.; Van Den Brink, S.; Van Houdt, W.J.; Pronk, A.; Van Gorp, J.; Siersema, P.D.; et al. Long-term expansion of epithelial organoids from human colon, adenoma, adenocarcinoma, and Barrett’s epithelium. *Gastroenterology* **2011**, *141*, 1762–1772. [CrossRef]
135. Clevers, H. Modeling Development and Disease with Organoids. *Cell* **2016**, *165*, 1586–1597. [CrossRef]
136. Broutier, L.; Mastrogiovanni, G.; Verstegen, M.M.A.; Francies, H.E.; Gavarró, L.M.; Bradshaw, C.R.; Allen, G.E.; Arnes-Benito, R.; Sidorova, O.; Gaspersz, M.P.; et al. Human primary liver cancer-derived organoid cultures for disease modeling and drug screening. *Nat. Med.* **2017**, *23*, 1424–1435. [CrossRef]
137. Boj, S.F.; Hwang, C.I.; Baker, L.A.; Chio, I.I.C.; Engle, D.D.; Corbo, V.; Jager, M.; Ponz-Sarvisse, M.; Tiriác, H.; Spector, M.S.; et al. Organoid models of human and mouse ductal pancreatic cancer. *Cell* **2015**, *160*, 324–338. [CrossRef]
138. Gao, M.; Lin, M.; Rao, M.; Thompson, H.; Hirai, K.; Choi, M.; Georgakis, G.V.; Sasson, A.R.; Bucobo, J.C.; Tzimas, D.; et al. Development of Patient-Derived Gastric Cancer Organoids from Endoscopic Biopsies and Surgical Tissues. *Ann. Surg. Oncol.* **2018**, *25*, 2767–2775. [CrossRef]
139. Yan, H.H.N.; Siu, H.C.; Law, S.; Ho, S.L.; Yue, S.S.K.; Tsui, W.Y.; Chan, D.; Chan, A.S.; Ma, S.; Lam, K.O.; et al. A Comprehensive Human Gastric Cancer Organoid Biobank Captures Tumor Subtype Heterogeneity and Enables Therapeutic Screening. *Cell Stem Cell* **2018**, *23*, 882–897. [CrossRef]
140. Lee, S.H.; Hu, W.; Matulay, J.T.; Silva, M.V.; Owczarek, T.B.; Kim, K.; Chua, C.W.; Barlow, L.M.J.; Kandath, C.; Williams, A.B.; et al. Tumor Evolution and Drug Response in Patient-Derived Organoid Models of Bladder Cancer. *Cell* **2018**, *173*, 515–528.e17. [CrossRef]
141. Sachs, N.; de Ligt, J.; Kopper, O.; Gogola, E.; Bounova, G.; Weeber, F.; Balgobind, A.V.; Wind, K.; Gracanin, A.; Begthel, H.; et al. A Living Biobank of Breast Cancer Organoids Captures Disease Heterogeneity. *Cell* **2018**, *172*, 373–386. [CrossRef] [PubMed]
142. Kopper, O.; de Witte, C.J.; Löhmußaar, K.; Valle-Inclán, J.E.; Hami, N.; Kester, L.; Balgobind, A.V.; Korving, J.; Proost, N.; Begthel, H.; et al. An organoid platform for ovarian cancer captures intra- and interpatient heterogeneity. *Nat. Med.* **2019**, *25*, 838–849. [CrossRef] [PubMed]
143. Papapetrou, E.P. Patient-derived induced pluripotent stem cells in cancer research and precision oncology. *Nat. Med.* **2016**, *22*, 1392–1401. [CrossRef] [PubMed]
144. Passier, R.; Orlova, V.; Mummery, C. Complex Tissue and Disease Modeling using hiPSCs. *Cell Stem Cell* **2016**, *18*, 309–321. [CrossRef]
145. Linkous, A.; Balamatsias, D.; Snuderl, M.; Edwards, L.; Miyaguchi, K.; Milner, T.; Reich, B.; Cohen-Gould, L.; Storaska, A.; Nakayama, Y.; et al. Modeling Patient-Derived Glioblastoma with Cerebral Organoids. *Cell Rep.* **2019**, *26*, 3203–3211.e5. [CrossRef]
146. Jacob, F.; Ming, G.; Song, H. Generation and biobanking of patient-derived glioblastoma organoids and their application in CAR-T cell testing. *Nat. Protoc.* **2020**, *15*, 4000–4033. [CrossRef]
147. Dijkstra, K.K.; Cattaneo, C.M.; Weeber, F.; Chalabi, M.; van de Haar, J.; Fanchi, L.F.; Slagter, M.; van der Velden, D.L.; Kaing, S.; Kelderman, S.; et al. Generation of Tumor-Reactive T Cells by Co-culture of Peripheral Blood Lymphocytes and Tumor Organoids. *Cell* **2018**, *174*, 1586–1598.e12. [CrossRef]
148. Zumwalde, N.A.; Haag, J.D.; Sharma, D.; Mirrieles, J.A.; Wilke, L.G.; Gould, M.N.; Gumperz, J.E. Analysis of immune cells from human mammary ductal epithelial organoids reveals Vδ2+ T cells that efficiently target breast carcinoma cells in the presence of bisphosphonate. *Cancer Prev. Res.* **2016**, *9*, 305–316. [CrossRef]
149. Neal, J.T.; Li, X.; Zhu, J.; Giangarra, V.; Grzeskowiak, C.L.; Ju, J.; Liu, I.H.; Chiou, S.H.; Salahudeen, A.A.; Smith, A.R.; et al. Organoid Modeling of the Tumor Immune Microenvironment. *Cell* **2018**, *175*, 1972–1988. [CrossRef]
150. Li, X.; Ootani, A.; Kuo, C. An air-liquid interface culture system for 3D organoid culture of diverse primary gastrointestinal tissues. *Methods Mol. Biol.* **2016**. [CrossRef]
151. Zhu, Z.; Mesci, P.; Bernatchez, J.A.; Gimple, R.C.; Wang, X.; Schafer, S.T.; Wettersten, H.I.; Beck, S.; Clark, A.E.; Wu, Q.; et al. Zika Virus Targets Glioblastoma Stem Cells through a SOX2-Integrin  $\alpha v \beta 5$  Axis. *Cell Stem Cell* **2020**, *26*, 187–204.e10. [CrossRef] [PubMed]
152. Oh, T.; Fakurnejad, S.; Sayegh, E.T.; Clark, A.J.; Ivan, M.E.; Sun, M.Z.; Safaee, M.; Bloch, O.; James, C.D.; Parsa, A.T. Immunocompetent murine models for the study of glioblastoma immunotherapy. *J. Transl. Med.* **2014**, *12*, 1–10. [CrossRef] [PubMed]
153. Shackleton, M.; Quintana, E.; Fearon, E.R.; Morrison, S.J. Heterogeneity in Cancer: Cancer Stem Cells versus Clonal Evolution. *Cell* **2009**, *138*, 822–829. [CrossRef]
154. Reardon, D.A.; Gokhale, P.C.; Klein, S.R.; Ligon, K.L.; Rodig, S.J.; Ramkissoon, S.H.; Jones, K.L.; Conway, A.S.; Liao, X.; Zhou, J.; et al. Glioblastoma eradication following immune checkpoint blockade in an orthotopic, immunocompetent model. *Cancer Immunol. Res.* **2016**, *4*, 124–135. [CrossRef]
155. Chen, M.; Sun, R.; Shi, B.; Wang, Y.; Di, S.; Luo, H.; Sun, Y.; Li, Z.; Zhou, M.; Jiang, H. Antitumor efficacy of chimeric antigen receptor T cells against EGFRvIII-expressing glioblastoma in C57BL/6 mice. *Biomed. Pharmacother.* **2019**, *113*, 108734. [CrossRef]
156. Lenting, K.; Verhaak, R.; ter Laan, M.; Wesseling, P.; Leenders, W. Glioma: Experimental models and reality. *Acta Neuropathol.* **2017**, *133*, 263–282. [CrossRef]

157. Huszthy, P.C.; Daphu, I.; Niclou, S.P.; Stieber, D.; Nigro, J.M.; Sakariassen, P.O.; Miletic, H.; Thorsen, F.; Bjerkvig, R. In vivo models of primary brain tumors: Pitfalls and perspectives. *Neuro. Oncol.* **2012**, *14*, 979–993. [CrossRef]
158. Federspiel, M.J.; Bates, P.; Young, J.A.T.; Varmus, H.E.; Hughes, S.H. A system for tissue-specific gene targeting: Transgenic mice susceptible to subgroup A avian leukosis virus-based retroviral vectors. *Proc. Natl. Acad. Sci. USA* **1994**, *91*, 11241–11245. [CrossRef]
159. Mathews, S.; Branch Woods, A.; Katano, I.; Makarov, E.; Thomas, M.B.; Gendelman, H.E.; Poluektova, L.Y.; Ito, M.; Gorantla, S. Human Interleukin-34 facilitates microglia-like cell differentiation and persistent HIV-1 infection in humanized mice. *Mol. Neurodegener.* **2019**, *14*, 1–15. [CrossRef]
160. Wang, M.; Yao, L.C.; Cheng, M.; Cai, D.; Martinek, J.; Pan, C.X.; Shi, W.; Ma, A.H.; De Vere White, R.W.; Airhart, S.; et al. Humanized mice in studying efficacy and mechanisms of PD-1-targeted cancer immunotherapy. *FASEB J.* **2018**. [CrossRef]
161. Capasso, A.; Lang, J.; Pitts, T.M.; Jordan, K.R.; Lieu, C.H.; Davis, S.L.; Diamond, J.R.; Kopetz, S.; Barbee, J.; Peterson, J.; et al. Characterization of immune responses to anti-PD-1 mono and combination immunotherapy in hematopoietic humanized mice implanted with tumor xenografts. *J. Immunother. Cancer* **2019**, *7*, 1–16. [CrossRef] [PubMed]
162. Kaur, K.; Kozłowska, A.K.; Topchyan, P.; Ko, M.W.; Ohanian, N.; Chiang, J.; Cook, J.; Maung, P.O.; Park, S.H.; Cacalano, N.; et al. Probiotic-treated super-charged NK cells efficiently clear poorly differentiated pancreatic tumors in Hu-BLT mice. *Cancers* **2020**, *12*, 63. [CrossRef] [PubMed]
163. Ali, N.; Flutter, B.; Sanchez Rodriguez, R.; Sharif-Paghaleh, E.; Barber, L.D.; Lombardi, G.; Nestle, F.O. Xenogeneic Graft-versus-Host-Disease in NOD-scid IL-2R $\gamma$ null Mice Display a T-Effector Memory Phenotype. *PLoS ONE* **2012**, *7*, e44219. [CrossRef] [PubMed]
164. Spranger, S.; Frankenberger, B.; Schendel, D.J. NOD/scid IL-2Rg nullmice: A preclinical model system to evaluate human dendritic cell-based vaccine strategies in vivo. *J. Transl. Med.* **2012**, *10*, 1–11. [CrossRef] [PubMed]
165. Pandey, V.; Oyer, J.L.; Igarashi, R.Y.; Gitto, S.B.; Copik, A.J.; Altomare, D.A. Anti-ovarian tumor response of donor peripheral blood mononuclear cells is due to infiltrating cytotoxic NK cells. *Oncotarget* **2016**, *7*, 7318. [CrossRef] [PubMed]
166. Ashizawa, T.; Iizuka, A.; Nonomura, C.; Kondou, R.; Maeda, C.; Miyata, H.; Sugino, T.; Mitsuya, K.; Hayashi, N.; Nakasu, Y.; et al. Antitumor effect of Programmed Death-1 (PD-1) blockade in humanized the NOG-MHC double knockout mouse. *Clin. Cancer Res.* **2017**, *23*, 149–158. [CrossRef] [PubMed]

Article

# Beyond the Warburg Effect: Oxidative and Glycolytic Phenotypes Coexist within the Metabolic Heterogeneity of Glioblastoma

Tomás Duraj <sup>1</sup>, Noemí García-Romero <sup>2,3</sup>, Josefa Carrión-Navarro <sup>2,3</sup>, Rodrigo Madurga <sup>2,3</sup>, Ana Ortiz de Mendivil <sup>4</sup>, Ricardo Prat-Acin <sup>5</sup>, Lina Garcia-Cañamaque <sup>6</sup> and Angel Ayuso-Sacido <sup>2,3,\*</sup>

<sup>1</sup> Faculty of Medicine, Institute for Applied Molecular Medicine (IMMA), CEU San Pablo University, 28668 Madrid, Spain; tom.duraj.ce@ceindo.ceu.es

<sup>2</sup> Faculty of Experimental Sciences, Universidad Francisco de Vitoria, 28223 Madrid, Spain; noemi.garcia@ufv.es (N.G.-R.); pepa.carrion@ufv.es (J.C.-N.); rodrigo.madurga@ufv.es (R.M.)

<sup>3</sup> Brain Tumor Laboratory, Fundación Vithas, Grupo Hospitales Vithas, 28043 Madrid, Spain

<sup>4</sup> Fundación de Investigación HM Hospitales, HM Hospitales, 28015 Madrid, Spain; aomendivil@yahoo.es

<sup>5</sup> Neurosurgery Department, Hospital Universitario La Fe, 46026 Valencia, Spain; ricprat@hotmail.com

<sup>6</sup> Departamento de Medicina Nuclear, HM Hospitales, 28015 Madrid, Spain; lgarcianamaque@hmhospitales.com

\* Correspondence: ayusosa@vithas.es; Tel.: +34-686-966-904



**Citation:** Duraj, T.; García-Romero, N.; Carrión-Navarro, J.; Madurga, R.; Ortiz de Mendivil, A.; Prat-Acin, R.; Garcia-Cañamaque, L.; Ayuso-Sacido, A. Beyond the Warburg Effect: Oxidative and Glycolytic Phenotypes Coexist within the Metabolic Heterogeneity of Glioblastoma. *Cells* **2021**, *10*, 202. <https://doi.org/10.3390/cells10020202>

Academic Editor: Javier S. Castresana  
Received: 31 December 2020  
Accepted: 18 January 2021  
Published: 20 January 2021

**Publisher's Note:** MDPI stays neutral with regard to jurisdictional claims in published maps and institutional affiliations.



**Copyright:** © 2021 by the authors. Licensee MDPI, Basel, Switzerland. This article is an open access article distributed under the terms and conditions of the Creative Commons Attribution (CC BY) license (<https://creativecommons.org/licenses/by/4.0/>).

**Abstract:** Glioblastoma (GBM) is the most aggressive primary brain tumor, with a median survival at diagnosis of 16–20 months. Metabolism represents a new attractive therapeutic target; however, due to high intratumoral heterogeneity, the application of metabolic drugs in GBM is challenging. We characterized the basal bioenergetic metabolism and antiproliferative potential of metformin (MF), dichloroacetate (DCA), sodium oxamate (SOD) and diazo-5-oxo-L-norleucine (DON) in three distinct glioma stem cells (GSCs) (GBM18, GBM27, GBM38), as well as U87MG. GBM27, a highly oxidative cell line, was the most resistant to all treatments, except DON. GBM18 and GBM38, Warburg-like GSCs, were sensitive to MF and DCA, respectively. Resistance to DON was not correlated with basal metabolic phenotypes. In combinatory experiments, radiomimetic bleomycin exhibited therapeutically relevant synergistic effects with MF, DCA and DON in GBM27 and DON in all other cell lines. MF and DCA shifted the metabolism of treated cells towards glycolysis or oxidation, respectively. DON consistently decreased total ATP production. Our study highlights the need for a better characterization of GBM from a metabolic perspective. Metabolic therapy should focus on both glycolytic and oxidative subpopulations of GSCs.

**Keywords:** glioblastoma; energy metabolism; glycolysis; oxidative phosphorylation; therapeutics; gene expression profiling

## 1. Introduction

Glioblastoma (GBM) is the most common, heterogeneous and aggressive primary brain tumor in adults (54% of all gliomas) [1–3]. The World Health Organization (WHO, Geneva, Switzerland) classifies GBM based on histopathological findings and molecular features (especially IDH mutation status) [4]. At a gene-expression level, GBM can be classified into four subtypes: mesenchymal, classical, proneural and neural [5,6].

Standard treatment of GBM consists of maximally safe surgical resection, followed by radiotherapy and chemotherapy, usually in the form of temozolomide (TMZ). Despite decades of extensive research and advancements in therapeutics, such as tumor treating fields (TTF), prognosis remains extremely poor, with a median overall survival of 20.9 months [7]. GBM has a low global incidence (less than 10 per 100,000 persons/year), but cumulative survival after five years from diagnosis is less than 10%, making it a critical public health issue [8,9]. Dismal survival is partly owed to GBM's highly invasive,

chemo-resistant and recurrent nature [10]. As standard of care is not a curative option, new therapies are sorely needed, with efforts to characterize GBM from multiple viewpoints, predominantly the omics sciences.

Setting aside the uncertainty behind the origin of cancer [11,12], one of its defining characteristics, at a functional, bioenergetic level, is its ability to exploit glycolytic metabolism even in the presence of oxygen, a phenomenon known as the “Warburg effect” [13]. Among many other solid tumors, this metabolic shift has been extensively documented in gliomas [14,15]. In the mitochondrial theory of cancer, aerobic glycolysis represents a universal feature of transformed cells, allowing the reduction of vast molecular heterogeneity into a smaller number of metabolic categories [16]. Metabolic reprogramming is not merely an *in vitro* artifact, but has wide-ranging clinical applications [11,17,18]. Nowadays, 18F-fluorodeoxyglucose PET (18F-FDG PET) is a common technique for cancer diagnosis and staging, with novel metabolic markers, such as lactate, glutamine, oxygen and even ketone bodies under clinical evaluation [19–21]. Within ample cell diversity, however, the predominance of aerobic glycolysis does not necessarily abrogate ancillary energetic sources: functional oxidative metabolism (glucose, fatty acids, glutamine) and the “reverse Warburg” effect [22,23]. Characteristically, *in vitro*, GBM has shown high variability in mitochondrial respiration, while tissue-derived cell lines revealed glucose dependency and fatty acid oxidation (FAO) [23–26]. Intratumoral heterogeneity makes development of targeted strategies against specific mutations very challenging [27]; therefore, patient stratification based on metabolic pathways should be a key component of improved therapeutic strategies.

The main challenge facing GBM management is the eradication of all malignant cells, including those able to survive drastic changes in the tumor microenvironment and toxic interventions. For this reason, GBM presents as a unique model to study bioenergetic alterations, as both aerobic glycolysis and oxidative phosphorylation (OXPHOS) have been described in high grade gliomas [28–30]. Furthermore, discouraging survival rates are a compelling reason to explore new therapeutic opportunities, either stand-alone or, more likely, in combination with standard of care. To this effect, metabolic inhibitors such as metformin hydrochloride (MF), dichloroacetate (DCA), sodium oxamate (SOD) and 6-diazo-5-oxo-L-norleucine (DON) have a longstanding history in this field, undergoing extensive evaluation in animal models and clinical trials with a variable rate of success [31–34].

To accurately model this disease *in vitro*, it has been proposed that GBM stem cells (GSCs) have a remarkable proliferative ability, sufficient to drive tumor maintenance, recurrence and therapeutic resistance [35–38]. GSCs are a highly heterogeneous and metabolically adaptive cell population: surviving in both perivascular aerobic and hypoxic regions [39,40], seemingly able to shift between glycolytic and oxidative phenotypes [28,29]. Whether these parameters are permanent, stable, independent or complementary, operating on a spectrum, remains to be elucidated [41].

To help us illuminate this question, we performed a Gene Set Variation Analysis (GSVA) [42] for canonical glycolytic/oxidative pathways in The Cancer Genome Atlas (TCGA) GBM datasets. A clustering of highly oxidative signatures was observed in normal tissues, whereas highly glycolytic tumors matched with the mesenchymal subtype; interestingly, mesenchymal signatures are associated with increased inflammation and wound healing pathways, a higher degree of necrosis and the worst survival when restricting for samples with low transcriptional heterogeneity [5,43]. Between these two categories, a high degree of heterogeneity was recognized. Clinically, 18F-FDG PET imaging of GBM can exhibit high or low glucose uptake, but allocation of metabolic substrates is not routine practice.

To verify these observations *in vitro*, we analyzed the basal metabolic phenotype of three tissue-derived and molecularly distinct GSCs (GBM18, GBM27, GBM38), in addition to traditional established cell line U87MG. As metabolic plasticity is being touted as a distinctive feature of GSCs, we wanted to explore antiproliferative responses to metabolic inhibitors and their correlation with basal bioenergetics. High resistance to MF (a mild



mitochondrial inhibitor) and DCA (glycolytic modulator) was detected in GBM27, a distinctively oxidative cell line. GBM38 displayed Warburg-like properties, with higher sensitivity to DCA. Responses to DON (glutaminase inhibitor) varied between cell lines, without a clear correlation with basal metabolic phenotypes. Subsequently, we combined promising drug candidates with bleomycin, a radiomimetic drug that causes single-strand and double-strand DNA breaks [44,45]. Synergism at therapeutically relevant outcomes was detected with all drugs in GBM27, and all cell lines with DON. Lastly, Seahorse XF analysis was performed in surviving, metabolically treated cells to determine vulnerabilities in bioenergetic phenotypes (“metabolic priming”).

Here, we propose that strategic targeting of dysregulated bioenergetic pathways, after an initial assessment of the metabolic phenotypes coexisting within a tumor, could become a valuable stratification and therapeutic tool, improving the efficacy of adjuvant metabolic therapy.

## 2. Materials and Methods

### 2.1. Culture of GSCs from Human GBM Samples, U87MG and Mesenchymal Stem Cells

GSCs were originally isolated from surgical human GBM specimens, as described by our group in [46]. The GSCs used in this study are characterized by distinct molecular and morphological features, differential drug sensitivity profiles and in vivo dissemination patterns that reflect the original tumors. GSCs were cultured under a humidified atmosphere of 5% CO<sub>2</sub> at 37 °C, in a media containing, as a base, DMEM/F-12 (catalog number 11039, Gibco, Grand Island, NY, USA), supplemented with: Non Essential Amino Acids (1% *v/v*; 11140, Gibco), HEPES (38 mM; 15630, Gibco), D-Glucose (0,54% *v/v* or 30 mM; G8769, Sigma-Aldrich, St. Louis, MI, USA), BSA-FV (0,01% *v/v*; 15260037, Invitrogen, Carlsbad, CA, USA), Sodium Pyruvate (1 mM; Invitrogen), L-Glutamine (4 mM; 25030, Gibco), Antibiotic-Antimycotic (0.4% *v/v*; Invitrogen), N1 Supplement (1% *v/v*; Invitrogen), Hydrocortisone (0.3 µg/mL; H0135, Sigma-Aldrich), Tri-iodothyronine (0.03 µg/mL; T5516, Sigma-Aldrich), EGF (10 ng/µL; E9644, Sigma-Aldrich), bFGF (20 ng/mL; F0291, Sigma-Aldrich) and Heparin (2 µg/mL; H3393, Sigma-Aldrich).

U87MG was purchased from ATCC, Rockville, MD, USA and cultured in DMEM/F-12 (11039, Gibco) supplemented with 10% fetal bovine serum (FBS) and 2% penicillin-streptomycin (PS). Cells were maintained at 37 °C in humidified atmosphere air, CO<sub>2</sub> 5%.

Human mesenchymal stem cells (hMSCs) (a gift from Dr. Carmen Escobedo Lucea) were cultured in DMEM, high glucose, GlutaMAX (10566016, Gibco), supplemented with a final concentration of 20% FBS and 1% P/S. All hMSCs experiments were performed in the first five passages from isolation.

### 2.2. Reagents and Metabolic Inhibitors

1,1-Dimethylbiguanide hydrochloride (D150959), sodium oxamate (O2751), sodium dichloroacetate (347795) and 6-Diazo-5-oxo-L-norleucine (D2141) were purchased from Sigma-Aldrich. Bleomycin sulfate (HY-17565) was acquired from MedChemExpress, Monmouth Junction, NJ, USA.

### 2.3. MTS Assays and Drug Combination Studies using the Chou-Talalay Method

The sensitivity to different metabolic drugs was assessed using [3-(4,5-dimethylthiazol-2-yl)-5-(3-carboxymethoxyphenyl)-2-(4-sulfophenyl)-2H-tetrazolium, inner salt (MTS) containing solution from Promega, Madison, WI, USA (CellTiter 96 AQueous One Solution, G3582). Briefly, single-cell suspensions of GSCs were plated in a 96-well plate, 3000 cells/well, and allowed to grow and form spheres for 72 h. U87MG were seeded at 3000 cells/well and allowed to grow for 24 h. Cultures were then treated with their respective culture media (control cells) or increasing concentrations of each drug for 0 h, 24 h, 48 h or 72 h. At each timepoint, MTS reactant was added, incubated at 37 °C for 2 to 4 h and absorbance was measured at 490 nm/630 nm, using a Varioskan Flash (5250030, Thermo Scientific, Waltham, MA, USA) or a Sunrise Absorbance Reader (Tecan

Trading AG, Männedorf, Switzerland). For IC<sub>50</sub> calculations, corrected absorbance was transformed, normalized and extrapolated in GraphPad Prism version 8.0.1, using the logarithmic variable slope equation:

$$Y = 100 / (1 + 10^{((\text{LogIC}_{50} - X) \times \text{HillSlope}))})$$

In specific dose experiments, hMSCs were seeded at 6000 cells/well and allowed to grow for 72 h. Fresh cell culture media was then added to control wells and dissolved treatments to experimental wells. Cells were treated for 72 h before MTS read-out.

Combinatory studies were performed in the same manner as single-drug assays. After seeding and cell-specific recovery/attachment intervals, combined treatments were added in the following final concentrations: IC<sub>50</sub> for drug A alone; IC<sub>50</sub> for drug B alone; full dose IC<sub>50</sub> for drug A + drug B; IC<sub>50</sub>(A + B)/2; IC<sub>50</sub>(A + B)/8. Experimentally, drug “A” was one of the metabolic inhibitors (MF, DCA or DON), whereas drug “B” was the radiomimetic bleomycin. CompuSyn software (version 1.0), based on the Chou-Talalay method, was employed to determine the interaction between the drugs [47,48]. This method utilizes a multiple drug-effect equation derived from enzyme kinetics, generating a “combination index” (CI) for each drug combination, at each fraction of affected cells (Fa) level. CompuSyn software defines synergy as a CI value lower than 1, CI = 1 equals to additive effects and CI values > 1 indicate antagonistic effects. We have determined CI values for each metabolic inhibitor and bleomycin across all tested cell lines using a constant ratio experimental design, as well as other valuable parameters such as the Dose-Reduction Index (DRI), which indicates how many folds of dose-reduction for each drug, at any given effect, would be allowed in synergistic combination.

#### 2.4. Real-Time Quantitative Reverse Transcription PCR (RT-qRT-PCR) Analysis

For RT-qRT-PCR, total RNA was isolated from cell pellets using NZYol (MB18501, NZYTech, Lda.), following the manufacturer’s recommendations. For chronological parity with other experiments, GSCs were seeded in 6-well plates at a density of 90000 cells/well, allowed to grow for 72 h, fresh cell culture media was added (1:1) and pellets were collected after 72 h; the same protocol was applicable to U87MG, but fresh cell culture media was added after 24 h from seeding. Purity of RNA was assessed based on 260/280 and 260/230 ratios using a Thermo Scientific NanoDrop 2000/2000c. RNA was retrotranscribed to cDNA (High-Capacity cDNA Reverse Transcription Kit; Applied BioSystems). Resulting samples were amplified with specific primers (Table 1) in a CFX Connect Real-Time PCR Detection System (Bio-Rad). *β-actin* and *GAPDH* were used as housekeeping genes. For relativization and comparison with a non-tumoral control, we compared our samples with a pool of retrotranscribed RNA from brain tissue obtained from epileptic patients, provided courtesy of Hospital Universitario y Politécnico La Fe (Valencia).

**Table 1.** Forward (FW) and reverse (RV) primers for real-time quantitative reverse transcription PCR (RT-qRT-PCR).

Name	5'-Sequence-3'
<i>β-actin</i> FW	TTCTACAATGAGCTGCGTGTG
<i>β-actin</i> RV	GGGGTGTGTAAGGTCTCAA
<i>GAPDH</i> FW	TCCTCCACCTTTGACGCTG
<i>GAPDH</i> RV	ACCACCCTGTTGCTGTAGCC
<i>GLS1</i> FW	GCCCGCTTTGTGTGACTAAA
<i>GLS1</i> RV	CAGGGGTAATAACGGCACA
<i>GLS2</i> FW	GCACTAAAGGCCACTGGAC
<i>GLS2</i> RV	CCAAGAGGCCACCACTACTG
<i>MTOR</i> FW	CTGACCGCTAGTAGGGAGGT
<i>MTOR</i> RV	AACATCCCAGAACCCTGCTG
<i>PDK1</i> FW	ATCCTCCTGCCTGAGTCTCT
<i>PDK1</i> RV	CAAATGCCAAGGACTGCTGT
<i>PDK2</i> FW	TGCCTACGACATGGCTAAGCTC
<i>PDK2</i> RV	GACGTAGACCATGTGAATCGGC
<i>PDK3</i> FW	TGGAAGGAGTGGGTACTGATGC
<i>PDK3</i> RV	GGATTGCTCCAATCATCGGCTC
<i>PDK4</i> FW	AACTCGGGATGTTGGGGATT
<i>PDK4</i> RV	AGAGAAAAGCCCTTCCTACTGA
<i>PRKAA1</i> FW	GTCCAGGGCTTGTCTATTCA
<i>PRKAA1</i> RV	ATGCTGCACTTAGAGACCCT
<i>PRKAA2</i> FW	TGGAACATTGTTACAGCAGGC
<i>PRKAA2</i> RV	AGCTCTTCTCCCGTGTCTTC

### 2.5. Antibodies

All primary and secondary antibodies were purchased from commercial sources, listed as follows: AMPK $\alpha$  Antibody (2532, Cell Signaling, Danvers, MA, USA), phospho-AMPK $\alpha$  (Thr172) (2535, Cell Signaling), Anti-Pyruvate Dehydrogenase E1-alpha subunit antibody (ab110334, Abcam, Cambridge, UK), Anti-PDHA1 (phospho S293) antibody (ab177461, Abcam),  $\beta$ -Actin (A5441, Sigma-Aldrich),  $\alpha$ -Tubulin (sc-8035, Santa Cruz Biotechnology, Santa Cruz, CA, USA). The secondary antibodies for horseradish peroxidase (HRP) detection were anti-rabbit IgG (sc-2004, Santa Cruz Biotechnology) and anti-mouse IgG (PI-2000, Vector Laboratories, Burlingame, CA, USA).

### 2.6. Protein Isolation/Quantification and Western Blotting

Centrifuged and pelleted U87MG and GSCs were resuspended in 100  $\mu$ L of radioimmunoprecipitation buffer [RIPA; 100 mM Tris-HCl (pH 8.5), 200 mM NaCl, 5 mM EDTA and 0.2% SDS, with phosphatase and a protease inhibitor cocktail and stored at  $-80$   $^{\circ}$ C for a minimum of 24 h. Samples were then centrifuged at 13,200 RPM for 20 min at 4  $^{\circ}$ C; protein-containing supernatant was conserved.

Total protein concentration was determined using Bio-Rad Protein Assay according to the manufacturer instructions; after corresponding incubation, absorbance was read at 595 nm.

In phosphorylation experiments, treatments dissolved at 1:1 concentration in serum-free medium were added 3–4 days after seeding GSCs, and 24 h in the case of U87MG. U87MG cells were washed twice with PBS and serum-deprived for 1 h prior to sample

collection. Protein was subsequently recovered at the indicated timepoints (30 min, 60 min, 2 h, 6 h).

Western blotting experiments were performed adapting the protocol from Mahmood et al. [49]. Briefly, protein extracts were separated by 8%–12% SDS-PAGE and transferred to nitrocellulose membranes. After blocking for 1 h with 5% Bovine Serum Albumin (BSA) in Tween-Tris Buffered Saline 1× [T-TBS; 10 mM Tris-HCl (pH 7.6), 150 mM NaCl and 0.1% Tween-20], membranes were incubated with the corresponding primary antibody O/N at 4 °C. After washing three times for 10 min with T-TBS, membranes were incubated with HRP-linked secondary antibody for 1 h at room temperature (RT). Detection was performed using ECL reagents (GE Healthcare) according to the manufacturer's guidelines and revealed in a BioRad ChemiDoc chemiluminescence system. The same membranes were then incubated with a housekeeping primary antibody O/N at 4 °C, washed the next day and incubated with an HRP-linked secondary antibody for 1 h RT before ECL detection.

### 2.7. Seahorse XFp Protocol for Real-Time Metabolic Evaluation of U87MG Adherent Cells and GSCs Neurospheres

Experiments were performed in an XFp 8-well microplate using the Seahorse XFp Analyzer (Agilent, Santa Clara, CA, USA). Briefly, GSCs were seeded at a density of 10,000 cells/well and allowed to grow for 72 h, in wells previously coated with 20 µL of Collagen Type IV at 20 µg/mL (C6745-1ML, Sigma Aldrich). U87MG cells were seeded at 6000 cells/well and allowed to grow for 24 h. Metabolic drugs were added to the treatment wells and fresh media was added to the control wells. After 72 h, the original media was carefully pipetted out of each well into a centrifuge tube without disturbing the attached cells; then, Seahorse XF DMEM medium, pH 7.4 (103575-100, Agilent) was used to wash, pipetted out and centrifuged with the original media at 1000 rpm for 5 min at 25 °C. After centrifugation, supernatant was aspirated from each tube, conserving only the cell pellet, resuspended in Seahorse medium and added back to respective wells.

We then followed the standard protocol for Standard XF Real-Time ATP Rate Assay, as described in the Seahorse XF Real-Time ATP Rate Assay User Guide (Kit 103592-100, Agilent). Seahorse XF technology measures two key parameters of cellular bioenergetics: oxygen consumption rate (OCR; an estimation of mitochondrial ATP) and extracellular acidification rate (ECAR; quantification of glycolytic activity through changes in pH by lactate production) [50,51]. Results were analyzed in Seahorse Wave software (version 2.6.1), with analysis of OCR and ECAR carried out using the Seahorse XF Real-Time ATP Rate Assay Report Generator (version 4.0.17). For normalization, total protein was quantified using an Invitrogen Qubit 3 Fluorometer (Q33216, Invitrogen).

### 2.8. TCGA Gene-Set Variation Analysis

Affymetrix (HG-U133A) normalized gene expression datasets of GBM and non-tumor tissue samples from TCGA were downloaded from Gliovis repository (gliovis.bioinfo.cnio.es) [52]. As IDH mutation status confers characteristic metabolic rewiring of the TCA cycle, IDH mutant and IDH unknown samples were removed from the analysis [53]. The remaining 498 GBM IDH-wt and 10 non-tumor samples were classified in proneural, classical, mesenchymal and those with a high content in non-tumoral tissue (low cellularity), as proposed elsewhere [54]. Four different canonical gene sets (two oxidative and two glycolytic) were obtained from the Molecular Signatures Database (MSigDB) [55]: KEGG (oxidative phosphorylation and TCA cycle), Hallmark (glycolysis, mTORC1 signaling). Gene set variation analysis (GSVA) was performed on each sample to obtain an enrichment score (ES) using the GSVA R package [42].

### 2.9. Statistical Analysis

Statistical analysis was performed using a 2-tailed Student t test (when comparing two groups) and One-Way ANOVA (three or more groups). Data are presented as means ± standard deviation and calculated using the software package GraphPad Prism version 8.0.1 for Windows, GraphPad Software, San Diego, California USA. RT-qRT-PCR expression data was graphed and analyzed directly in CFX Maestro 1.1 software, version

4.1.2433.1219 (Bio-Rad Laboratories).  $p$  values  $< 0.05$  were considered as statistically significant. For all figures,  $p$  values were expressed according to GraphPad 8 NEJM  $p$ -value style.:  $p > 0.05$  (ns);  $p < 0.05$  (\*);  $p < 0.01$  (\*\*);  $p < 0.001$  (\*\*\*)

### 3. Results

#### 3.1. GBM can be Stratified into Glycolytic and Oxidative Phenotypes

Molecular heterogeneity is a key feature of GBM, with clinical and therapeutic repercussions. To better understand if the vast molecular landscape of GBM could be reduced into a manageable number of metabolic categories, we explored the TCGA expression databases using a GSVA approach. Filtering for canonical gene sets of glycolytic and oxidative pathways, Warburg-like phenotypes were enriched in the mesenchymal subgroup, whereas functional mitochondrial metabolism predominated in healthy tissues (Figure 1a). Between these two extremes, however, we still encountered ample metabolic heterogeneity. Clinically, 18F-FDG PET is valuable for staging and detection of recurrence, but not necessarily to guide treatments. Without further stratification, GBM can be identified as a malignancy with high glucose uptake or low glucose uptake (Figure 1b). Nevertheless, common standardized procedures such as 18F-FDG PET do not allow for differentiation between high glucose uptake due to increased aerobic glycolysis or OXPHOS, or low glucose uptake due to compensatory glutaminolysis, necrosis or quiescent metabolic phenotypes.

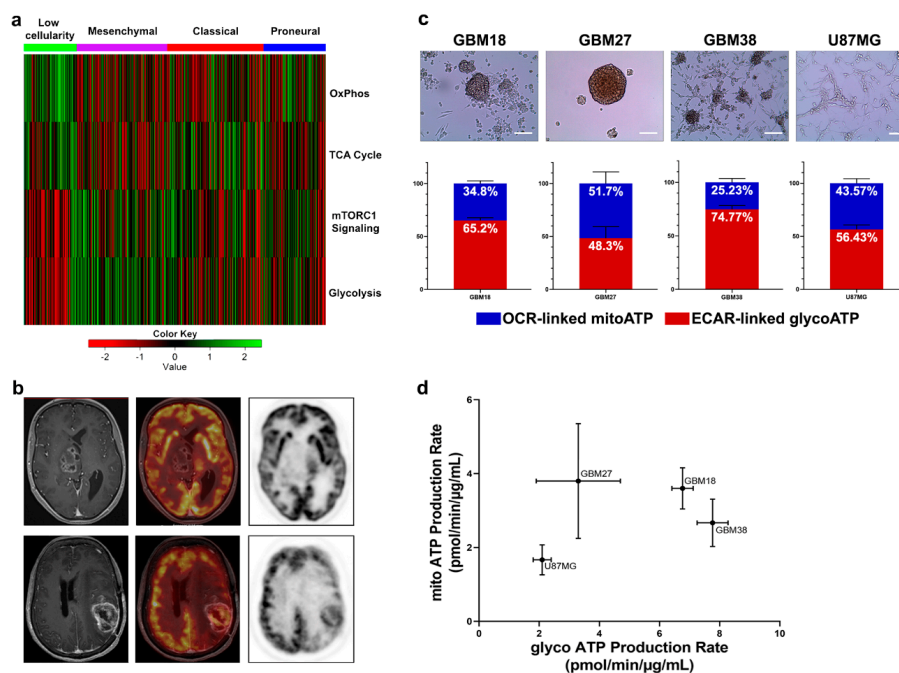


**Figure 1.** (a) Heatmap of the scaled enrichment score (ES) obtained by Gene Set Variation Analysis (GSVA) with the samples grouped by their gene expression subtype (proneural, classical or mesenchymal) including those with high content of non-tumor tissue (low cellularity). (b) Clinically, standard imaging techniques such as 18F-FDG PET-MRI can classify tumors into low glucose uptake (upper) and high glucose uptake (lower). Upper images: Right thalamic glioblastoma shows patchy contrast enhanced areas on 3DT1 (right side) and no uptake of 18F-FDG PET (medium and left side). Lower images: Parietal recurrent glioblastoma in the left hemisphere shows heterogeneous enhancement on axial three-dimensional T1-weighted imaging (3DT1) and extensive uptake of 18F-FDG PET (right and medium side), despite high uptake in surrounding normal brain tissue. (c) Representative optical microscopy images of cellular morphology. Scale bar = 100  $\mu$ m. Under each cell line, average distribution of total ATP production from extracellular acidification rate (ECAR)-linked ATP production and oxygen consumption rate (OCR)-linked ATP production in basal (non-treated) conditions. (d) Seahorse XF Energetic Map. GBM18 and GBM38 clustered together as highly glycolytic-like cells. GBM27 displayed the highest variation in the metabolic profiles, with increased mitochondrial respiration, at a similar level to GBM18, but, in comparison, lower glycolysis. U87MG were not as metabolically active as glioma stem cells (GSCs). Data from three independent experiments, each with  $n = 3$ , normalized to total protein concentration ( $\mu$ g/mL).

Subsequently, to examine the differences in bioenergetic metabolism in phenotypically and molecularly distinct gliomas *in vitro*, we determined OCR and ECAR of our set of GSCs and U87MG (Figure 1c). We can observe that, in basal conditions, GBM27 and U87MG are close to a 1:1 ratio of glycolytic/oxidative metabolism, whereas GBM18 and GBM38 have a strong preference towards a glycolytic phenotype. Furthermore, U87MG, a typically Warburg-like cell line [30], also exhibited a relative elevation in OCR-linked ATP production rate (up to 43.57% of total ATP). As shown in Figure 1d, GBM27 demonstrated high mitochondrial ATP production as well as lower glycolytic ATP production when compared to GSCs GBM18 and GBM38; as much as 50% of its bioenergetic needs were met by OCR-linked ATP production. GBM18 and, especially, GBM38, relied predominantly on glycolytic metabolism (Warburg effect). In GBM27, OCR and ECAR fluctuated slightly between sets of biological experiments, indicating a range of metabolic flexibility: further investigation into metabolite allocation for energy production would be necessary to fully characterize this adaptive capacity. Our data indicate that even under the same cell culture conditions, distinct molecular characteristics of GSCs can in fact produce unique metabolic phenotypes. Interestingly, the global metabolic activity of U87MG is actually lower than GSCs.

Taken together, our data suggest that a high degree of metabolic variability is present between our GSCs, and their ATP production rates are faster than those of U87MG. GSCs and U87MG maintain a stable, basal, metabolic profile, and seem to be able to shift, to some extent, between aerobic glycolysis and OXPHOS to meet their bioenergetic needs.

### 3.2. GSCs Display a Heterogeneous Pattern of Resistance to Metabolic Inhibitors

At the outset, in order to determine the optimal doses to be used in future experiments, we exposed our GSCs (GBM18, GBM27, GBM38) and the U87MG cell line to escalating concentrations of selected metabolic drugs. Inhibitory curves for all time points are presented in Supplementary Figure S1.

After conducting these experiments, we ascertained maximum inhibitory effects and reliable trends in the viability data at 72 h; therefore, for every cell line, IC<sub>50</sub> at 72 h was considered as the optimal inhibitory concentration.

As we can appreciate in Figure 2, GBM27 had the highest resistance to all metabolic treatments except for DON, where, in turn, GBM18 required the highest concentrations to achieve IC<sub>50</sub>. For MF, GBM18 and GBM38 were the most sensitive cell lines ( $10.66 \pm 3.162$  mM and  $21.33 \pm 7.08$  mM, respectively) and GBM27 the most resistant ( $77.41 \pm 34.02$  mM). U87MG revealed an intermediate resistance ( $42.51 \pm 2.742$  mM). For DCA, GBM38 required the lowest concentrations ( $13.52 \pm 5.235$  mM) and GBM27 the highest ( $40.61 \pm 7.400$  mM). In this case, GBM18 ( $29.20 \pm 5.627$  mM) and U87MG ( $27.10 \pm 0.955$  mM) showed no statistically significant differences in IC<sub>50</sub> concentrations. For SOD, all cell lines required relatively high *in vitro* concentrations to reach 50% growth inhibition; no statistical significance was reached between groups. Lastly, regarding glutaminolysis inhibition by DON, U87MG required the lowest IC<sub>50</sub> DON dose ( $99.70 \pm 14.82$   $\mu$ M), followed by GBM27 ( $198.4 \pm 44.13$   $\mu$ M) and GBM38 ( $286.9 \pm 103.2$   $\mu$ M), whereas GBM18 was the most resistant ( $1505 \pm 625.4$   $\mu$ M). It should be noted, however, that a closer look at the growth inhibition curves for DON in GBM18 reveals a cytostatic “threshold” around the IC<sub>50</sub> value regardless of the dose, suggesting a non-linear inhibitory slope (Figure S1). Therefore, the IC<sub>50</sub> provided is a statistical approximation owed to the resistance against the drug, but we should not always assume a linear correlation between dose and effect; this will become especially relevant in subsequent combinatory studies.

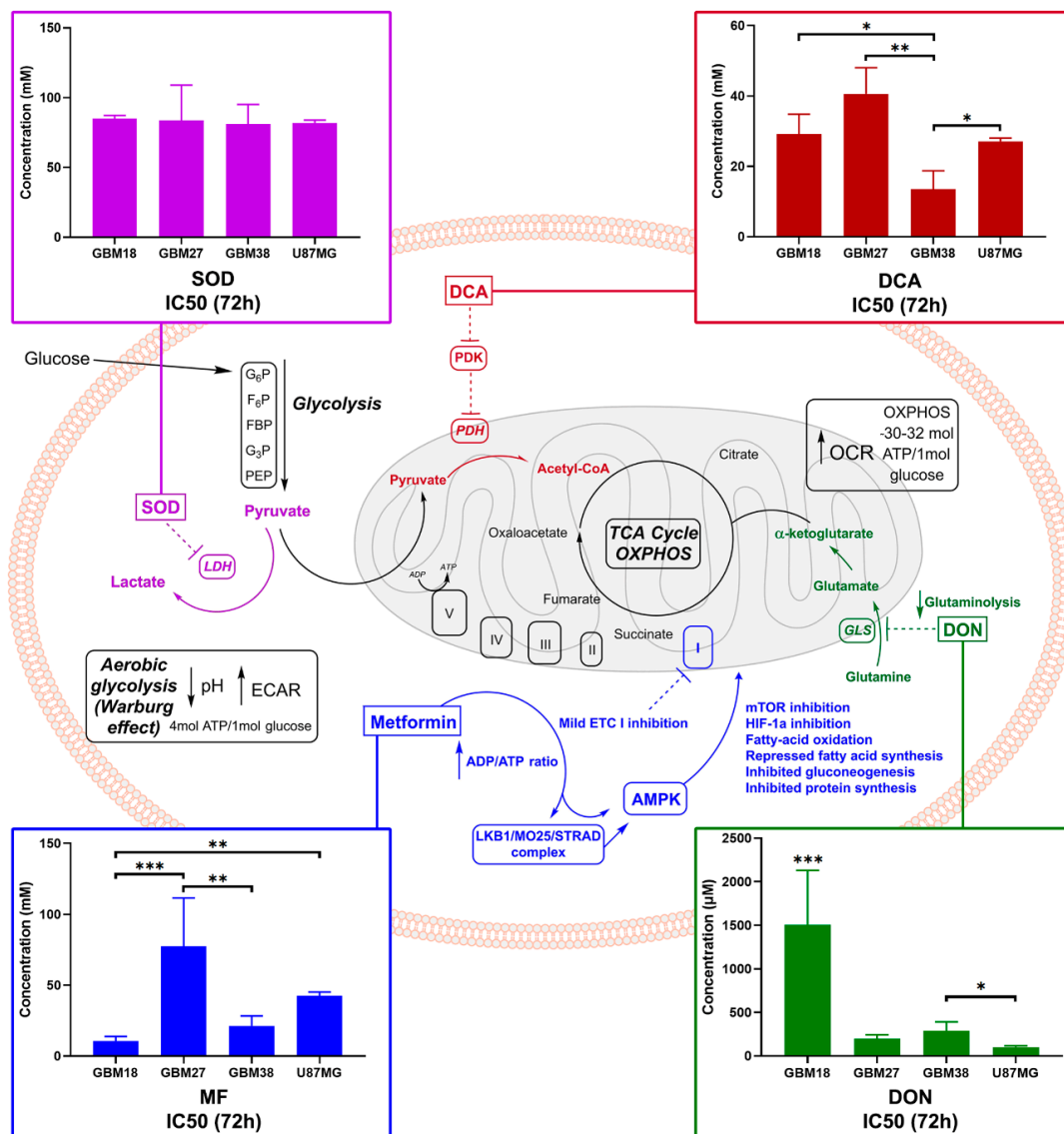


**Figure 2.** Cancer metabolism at a glance, with experimental in vitro IC50 values for selected metabolic inhibitors. Glucose enters cells and undergoes glycolysis, converted into pyruvate. Cancer cells can divert up to 85% of pyruvate to lactate, regardless of the presence of oxygen (Warburg effect, yielding two net ATP); an estimated 10% of pyruvate goes towards biosynthesis and 5% to OXPPOS [56]. In normal, non-tumoral cells, the majority of pyruvate undergoes OXPPOS (30–32 ATP molecules). To decrease the Warburg effect and facilitate oxidative metabolic reprogramming, PDKs can be inhibited by dichloroacetate (DCA), supporting the entry of pyruvate in the mitochondria, and LDH can be targeted via sodium oxamate (SOD). “Glutamine addiction” can be regulated by glutaminase inhibitors such as 6-diazo-5-oxo-L-norleucine (DON) [57]. Lastly, metformin hydrochloride (MF) has pleiotropic effects: ETC complex I inhibition leads to downstream signaling via AMPK and mTOR [58]. In color-matching boxes, we display concentrations required for 50% viability inhibition (IC50) after 72 h of treatment. One-way ANOVA statistical significance of three biological experiments was calculated with normalized raw fluorometric data;  $p < 0.05$  \*;  $p < 0.01$  \*\*;  $p < 0.001$  \*\*\*. Abbreviations: ETC (electron transport chain), mTOR (mammalian target of rapamycin), PDK (pyruvate dehydrogenase kinase), PDH (pyruvate dehydrogenase), GLS (glutaminase), LDH (lactate dehydrogenase), GLS (glutaminase), ECAR (extracellular acidification rate), OCR (oxygen consumption rate).

In summary, GBM18 was the most sensitive to MF, GBM38 to DCA and U87MG to DON; on the other hand, GBM27 was the most resistant to MF and DCA, while GBM18 required the highest doses of DON. A very high resistance towards SOD, as well as low

variability in responses, was observed across all cell lines, so this drug was discarded from further assays.

### 3.3. Differences of Target Enzymes across Cell Lines Predicts Responses to Metabolic Inhibitors

To further investigate the relative sensitivity/resistance profiles of each cell line to our selection of metabolic drugs, we aimed to evaluate their basal genetic expression profiles (Figure 3a).

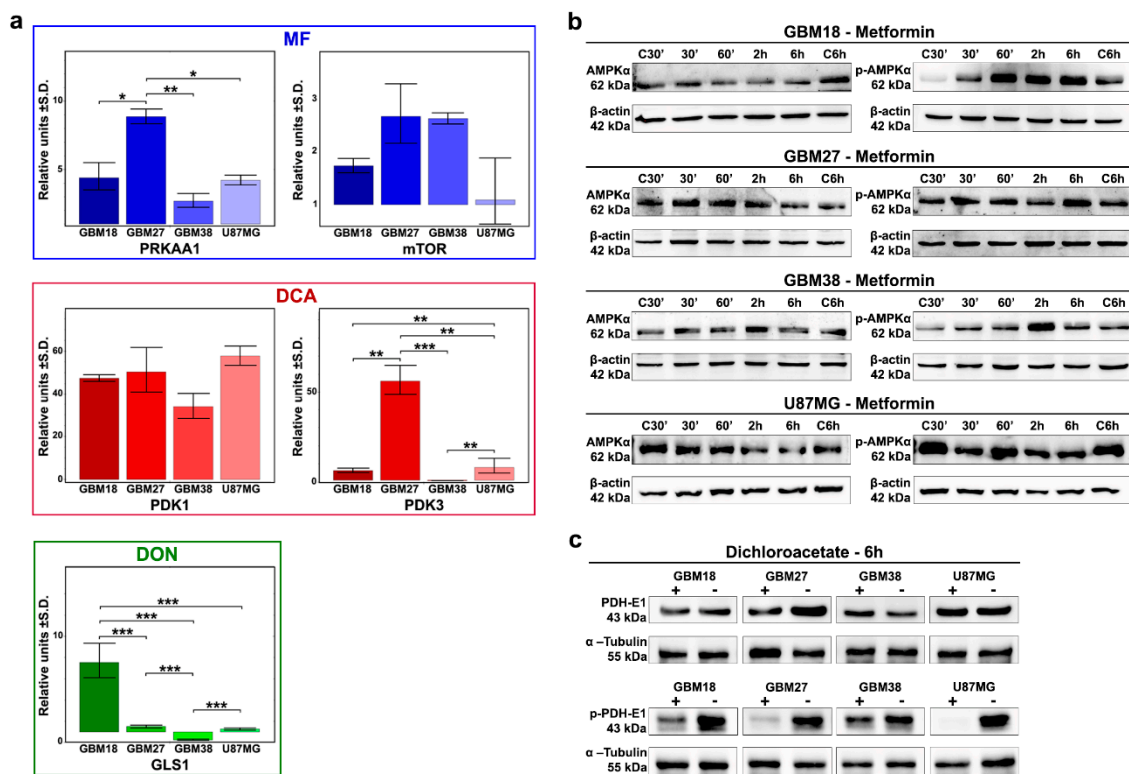


**Figure 3.** (a) Expression profiles of target enzymes for our selection of metabolic drugs under basal conditions determined by RT-qRT-PCR. Representative results from a minimum of two replicates ( $n = 2$ ). One-way ANOVA with Tukey correction.  $p < 0.05$  \*;  $p < 0.01$  \*\*;  $p < 0.001$  \*\*\*. (b) Western Blot analysis at 30 min, 60 min, 2 h, 6 h after MF 72h-IC50 treatment for AMPK $\alpha$  and phospho-Thr172 AMPK $\alpha$ . (c) Western Blot analysis after 6 h of treatment with respective DCA 72h-IC50 doses for phospho-Ser293 PDH-E1 and total PDH-E1.

MF acts through inhibition of the electron transport chain (ETC) complex I, increasing the ADP/ATP ratio, but its primary downstream target is the activation of AMPK (phosphorylation of Thr172 of AMPK $\alpha$ 1), which ultimately leads to mammalian target of rapamycin (mTOR) inhibition. We therefore evaluated expression of PRKAA1 and PRKAA2 (together, catalytic subunits of AMPK) and the mTOR gene. Although PRKAA2 was not expressed in our samples, PRKAA1 was significantly upregulated in GBM27 (9-fold relative to control) and, at similar levels (approximately 3 to 4-fold), in GBM18, GBM38 and U87MG. We also found the highest relative expression levels of mTOR in GBM27 and GBM38, but differences did not reach statistical significance. Additionally, we analyzed the phosphorylation of AMPK $\alpha$  to investigate the biological effects of MF (Figure 3b). We observed strong phosphorylation of Thr172 AMPK $\alpha$  relative to control in GBM18 (60 min, 2 h, 6 h) and GBM38 (2 h). Cell lines GBM27 and U87MG did not phosphorylate AMPK $\alpha$  in the first 6 h, consistent with their need for higher concentrations of MF and slower responses against the drug.

Next, we studied DCA activity in our GBM cell lines. Although we analyzed all PDK subunits, PDK2 and PDK4 were not expressed, with major differences detected primarily



in PDK3 expression, exceptionally upregulated in GBM27, consistent with sensitivity profiles to DCA. At the protein level, the catalytic subunit PDH-E1 $\alpha$  has three major phosphorylation sites, with site 1 (Ser-293) being the most frequent and efficient target, sufficient to fully inhibit PDH activity [59,60]. With inhibition of PDKs by DCA treatment, we detected rapid, visually discernable, de-phosphorylation of Ser-293 in all cell lines after 6 h of treatment with 72h-IC50 concentrations (Figure 3c and Supplementary Figure S2). The expression of PDKs in our dataset could provide a predictive biomarker to explain differential responses to DCA.

When we evaluated GLS genes, our analysis revealed no detectable amplification of GLS2; therefore, we focused on GLS1 as a potential predictor for DON's antiproliferative effects. Relativized to epilepsy control, GLS1 was significantly upregulated in GBM18, neutral in GBM27/U87MG and downregulated in GBM38. Higher GLS1 expression correlated with the relative resistance against DON in GBM18, but comparatively lower expression in GBM38 was not associated with lower doses.

### 3.4. Doses of Metabolic Inhibitors and Radiomimetic Bleomycin Corresponding to Warburg-Like Phenotypes Spare Viability of Non-Tumoral hMSCs

After completing this set of experiments, we questioned whether our cell lines would respond favorably to bleomycin, a radiomimetic/DNA-targeting drug.

The mechanism of action and IC50-72h concentrations for bleomycin are presented in Figure 4a. To substantiate our following combinatory studies, we first performed exploratory MTS assays to determine optimal concentrations of bleomycin for each cell line: we observed relative resistance in GBM18 and GBM27, whereas GBM38 and U87MG were equally sensitive to the drug (Supplementary Figure S3).

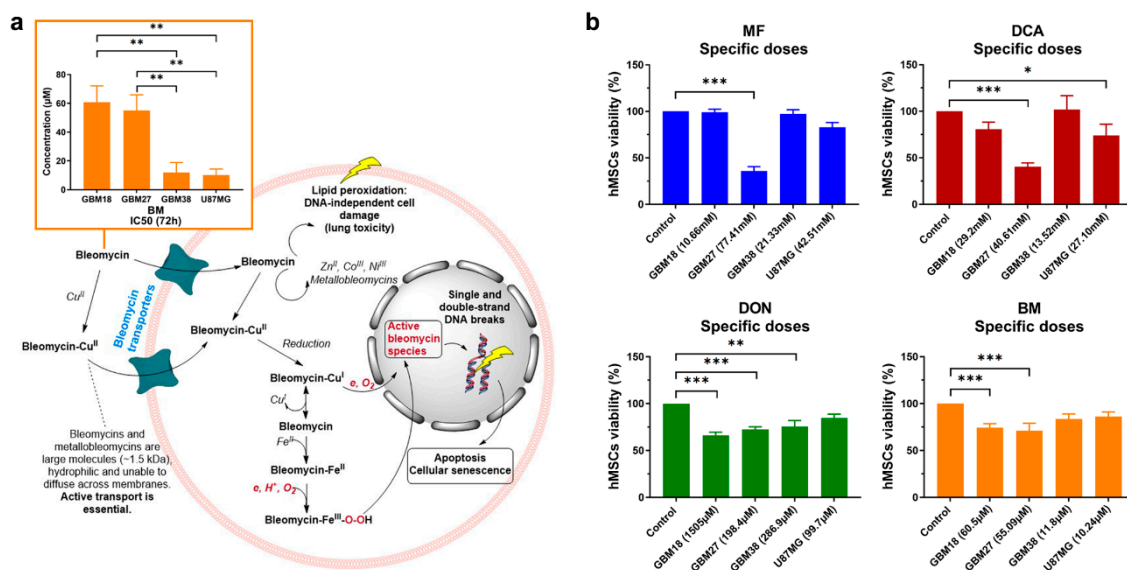


**Figure 4.** (a) IC50 values at 72 h and mechanism of action of radiomimetic drug bleomycin (BM). Bleomycin is a large molecule (~1.5 kDa) and cannot freely diffuse cell membranes; it is transported into cells either alone or as a bleomycin-Cu(II) complex, then reduced to bleomycin-Cu(I), which reacts with oxygen leading to DNA strand breaks. Successful chemotherapy with bleomycin is dependent on active transport; however, there is currently no consensus about the uptake mechanism or the transporters involved. Bleomycin-Cu(I) can also dissociate inside the cell to form bleomycin-Fe(II) complexes, transforming into «activated bleomycin species» resulting in DNA fragmentation and chromosomal aberrations. Complexes with zinc (II), iron (II) and cobalt (III) have also been characterized. Calculated IC50, as per inner salt (MTS) assay, with a minimum of two biological replicates. One-way ANOVA with Tukey correction,  $p < 0.05$  \*;  $p < 0.01$  \*\*;  $p < 0.001$  \*\*\*. (b) Viability profiles relative to control mesenchymal stem cells (hMSCs) treated with all calculated 72h-IC50 doses ( $n = 2$ ). One-way ANOVA with Dunn's correction,  $p < 0.05$  \*;  $p < 0.01$  \*\*;  $p < 0.001$  \*\*\*.

As with any other form of treatment, the success of metabolic therapies could be limited by toxicity to healthy cells. Therefore, we investigated whether all IC50 concentrations determined thus far could be a realistic goal *in vitro*, exploring their effects on non-tumoral hMSCs (Figure 4b). MF/DCA affected more than 60% of cells when using GBM27 IC50s (oxidative-like metabolic phenotype), but all other doses were very well tolerated (toxicity less than 20%). DCA 72h-IC50 from GBM38 actually slightly increased “cell viability” relative to control (as per metabolic activity measured by MTS assay). DON inhibited cell growth up to 35% at the highest dose (1505  $\mu\text{M}$ ), suggesting a saturation point after which increased dosages do not linearly correlate with antiproliferative effects. Bleomycin, in contrast, only affects up to 30% of hMSCs at the highest IC50, correlating well with slower proliferation rates. In summary, cell lines with predominantly Warburg-like phenotypes could be targeted with metabolic inhibitors without affecting normal stem cells, but oxidative-like phenotypes, such as GBM27, will require individualized, unique approaches.

### 3.5. Synergy between Bleomycin and Metabolic Inhibitors Helps to Overcome Dose-Limiting Toxicity in Predominantly Oxidative Metabolic Phenotypes

One way to solve the challenge of non-specific damage to healthy cells is to exploit coexisting weaknesses of tumoral cells in combinatory strategies. Since GBM27 doses of MF/DCA were also affecting the viability of normal cells, we explored the possibility of dose-reduction attributable to synergistic effects with radiomimetic bleomycin. After individually confirming the validity of each calculated 72h-IC50, we performed combinatory studies to determine the existence of synergy, additive or antagonistic effects. Using the Chou-Talalay theorem, the Combination Index (CI) and the Dose Reduction Index (DRI) were calculated for each drug combination.

As shown in Table 2, drug mixtures with  $CI < 1$  and  $DRI > 1$  at a fraction of affected cells ( $F_a$ ) = 0.6 were considered as the optimal cutoff to identify promising therapeutic combinations. Nevertheless, in constant ratio combinatory experiments, close attention needs to be paid to the full range of  $F_a$  and CI/DRI to evaluate synergy for any given combination/antiproliferative effect.

**Table 2.** Summary of synergy/antagonism at an optimal  $F_a$  cutoff of = 0.6. All combinatory experiments were performed in two biological replicates ( $n = 2$ ).

Cell Line	MF + Bleomycin		DCA + Bleomycin		DON + Bleomycin	
	Effect at $F_a = 0.6$	DRI at $F_a = 0.6$	Effect at $F_a = 0.6$	DRI at $F_a = 0.6$	Effect at $F_a = 0.6$	DRI at $F_a = 0.6$
GBM18	Additive	DRI > 1 for both	Antagonism	DRI > 1 for both	Synergism	DRI > 1 for both
GBM27	Synergism	DRI > 1 for both	Synergism	DRI > 1 for both	Synergism	DRI > 1 for both
GBM38	Synergism	DRI > 1 for both	Antagonism	DRI > 1 for bleomycin	Synergism	DRI > 1 for both
U87MG	Synergism	DRI > 1 for both	Antagonism	DRI > 1 for both	Synergism	DRI > 1 for both

All final reports with complete datasets, including Median-Effect Plot, CI Plot, Logarithmic CI Plot, DRI, Isobologram and Sequential Deletion Analysis (SDA; confidence intervals for CI values), are included in Supplementary Material File S1.

Our results describe a wide variety of combinatory effects depending on the cell subtype and  $F_a$  level. Figure 5a describes the combined effects of MF and bleomycin. GBM18 exhibits mostly additive effects (no synergy). GBM27, on the other hand, is a prototypical example of synergistic effects when affecting most tumoral cells (at high  $F_a$  values): in the CI index,  $F_a \geq 0.75$  has a  $CI < 0.4$ , indicative of strong synergism. Consequently, DRI is > 1 for both MF and bleomycin, with significant dose reductions at  $F_a \geq 0.6$ , potentially reducing the toxicity of both agents. GBM38 is synergistic at  $F_a \approx 0.5$  but has a tendency towards antagonism at  $F_a > 0.75$ . GBM38 appears to have a threshold for both MF and bleomycin, where even small doses produce significant anti-proliferative

effects, but further increases provide no additional benefit. Finally, the CI in U87MG is close to synergistic/additive up to  $F_a = 0.75$ , then turning antagonistic.

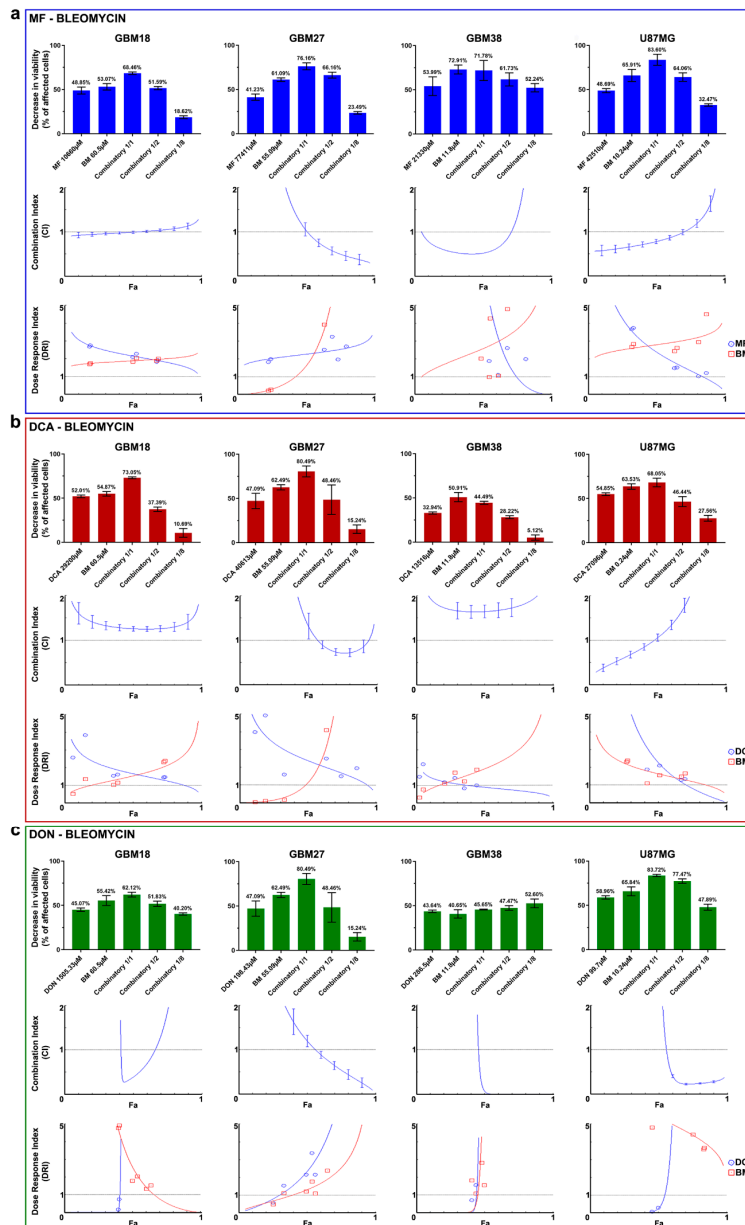


**Figure 5.** (a–c) Combinatory drug studies between metabolic drugs (MF, DCA, DON) and bleomycin (BM). From top to bottom, three graphs for each cell line comprehensively describe synergy/antagonism. First graph: Bar charts of decrease in viability (% of affected cells) relative to control. Second graph: Combination index (CI) is given as a function of the fraction of affected cells ( $F_a$ ) by the drug combination with a continuous line. The central dashed line indicates a  $CI = 1$ . According to the Chou-Talalay’s Combination Index Theorem,  $CI = 0.9$  to  $1.1$  indicates an additive effect.  $CI < 1$  is indicative of synergism, whereas  $CI > 1$  indicates antagonism. The vertical bars indicate 95% confidence intervals for CI values based on Sequential Deletion Analysis (SDA); in some cases, SDA values cannot be graphed in CompuSyn software, but they were always calculated and are available in Supplementary File S1. Third graph: The Dose-Reduction Index (DRI) (also known as the Chou-Martin plot) signifies how many folds of dose-reduction for each drug at any given effect ( $F_a$ ) are allowed in synergistic combination. In blue, metabolic drug DRI index; in red, bleomycin DRI index.  $DRI = 1$  indicates no dose-reduction,  $DRI > 1$  favorable dose-reduction and  $DRI < 1$  no favorable dose-reduction. All experiments were performed in two biological replicates ( $n = 2$ ).

Next, Figure 5b describes the combinatory effects of DCA and bleomycin. For GBM18, the CI is  $> 1$  (antagonistic) at any given  $F_a$ ; despite this,  $DRI > 1$  for bleomycin at high  $F_a$  levels indicates the possibility of dose-reduction. In GBM27, therapeutic effects are determined by  $F_a$  cutoff: close to  $F_a \approx 0.75$ , CI is  $< 1$  (synergistic), with dose reduction predicted at this value. GBM38, on the other hand, represents a clear example of strong antagonism (CI values  $> 1.5$  at any  $F_a$  level); consequently, the combination of drugs does not surpass the effects of bleomycin by itself. Even still, DRI suggests that bleomycin concentrations could be decreased at the expense of DCA. Lastly, up to  $F_a = 0.5$ , U87MG displays synergistic/additive effects, with antagonism prevailing thereafter; this translates to unfavorable dosing at  $F_a > 0.8$  ( $DRI < 1$  for both drugs).

To conclude, Figure 5c details the interaction between DON and bleomycin. For GBM18, combining the compounds presents a strong synergistic relationship at  $F_a$  close to 0.5; however, at higher  $F_a$ , this synergy is lost. Ascending DRI for DON indicates the potential of important dose-reduction. GBM27 benefits from additive effects close to  $F_a \approx 0.5$ , and, as we move closer to  $F_a = 1$ , the combination becomes strongly synergistic; this too would allow for dose reduction. In GBM38, the combined treatment has a similar threshold as in U87MG, as even one eighth of the concentrations significantly decreases proliferation: in these two cell lines, CI is  $< 1$  and  $DRI > 1$  at  $F_a$  levels  $> 0.5$ , making DON and bleomycin a very promising therapeutic combination.

In summary, for GBM27, synergism with radiomimetic bleomycin was observed for all metabolic inhibitors at therapeutically relevant  $F_a = 0.9$ . Combining metabolic inhibitors and bleomycin could be leveraged to reduce dosing requirements of oxidative-like GSC subtypes.

### 3.6. Bioenergetic Profiling after Metabolic Treatment Reveals Opportunities for Metabolic Priming in Surviving Cell Populations

Using Seahorse XF technology, we determined total ATP production and ratios of mitoATP/glycoATP production under metabolically treated conditions.

As shown in Figure 6a,b, normalized total ATP production was decreased in all treated cells, with the exception of DCA-treated GBM27; in this case, rather than a significant drop in total ATP, production shifted from glycolytic to oxidative metabolism, with total ATP rates remaining unaltered. Furthermore, consistent with the proposed biological function for each drug, we observed a reduction in mitoATP production and a shift toward glycolysis using MF. Even though  $IC_{50}$  values should affect all cell lines proportionately, we noticed that the reduction in total ATP production was less pronounced with lower doses; e.g., in GBM18 (lowest MF  $IC_{50}$  of 10.66 mM), mitochondrial ATP was almost completely abolished, but total glycolytic ATP dropped only marginally, indicating a surviving population of almost exclusively glycolytic cells. Mitochondrial ATP production was increased after treatment with DCA, especially in GBM27, a GSC with a clear preference towards oxidative metabolism under both basal and treated conditions. The XF Rate Index for DCA can provide an idea of the oxidative potential of each cell line: highest in GBM27, followed by GBM18 and lowest in GBM38/U87MG. In the case of DON, we can appreciate a notable reduction of total ATP for each calculated  $IC_{50}$  value. As previously stated, DON is a glutamine analog predominantly targeting GLS (inhibition of TCA cycle intermediaries from glutamine would be expected to reduce mitoATP, unless glutamine derived  $\alpha$ -ketoglutarate was diverted towards biosynthesis or mitochondrial substrate-level phosphorylation rather than oxidized). Examining the XF ATP Rate Index, GBM18 and especially GBM27 shifted towards oxidative metabolism, whereas GBM38 and U87MG remained unaltered. In conclusion, DON did not consistently change the metabolic phenotype of surviving cells; interestingly, however, in U87MG, a characteristically glutaminolytic cell line, even small concentrations of DON (99.7  $\mu$ M) were enough to drastically reduce total ATP production.

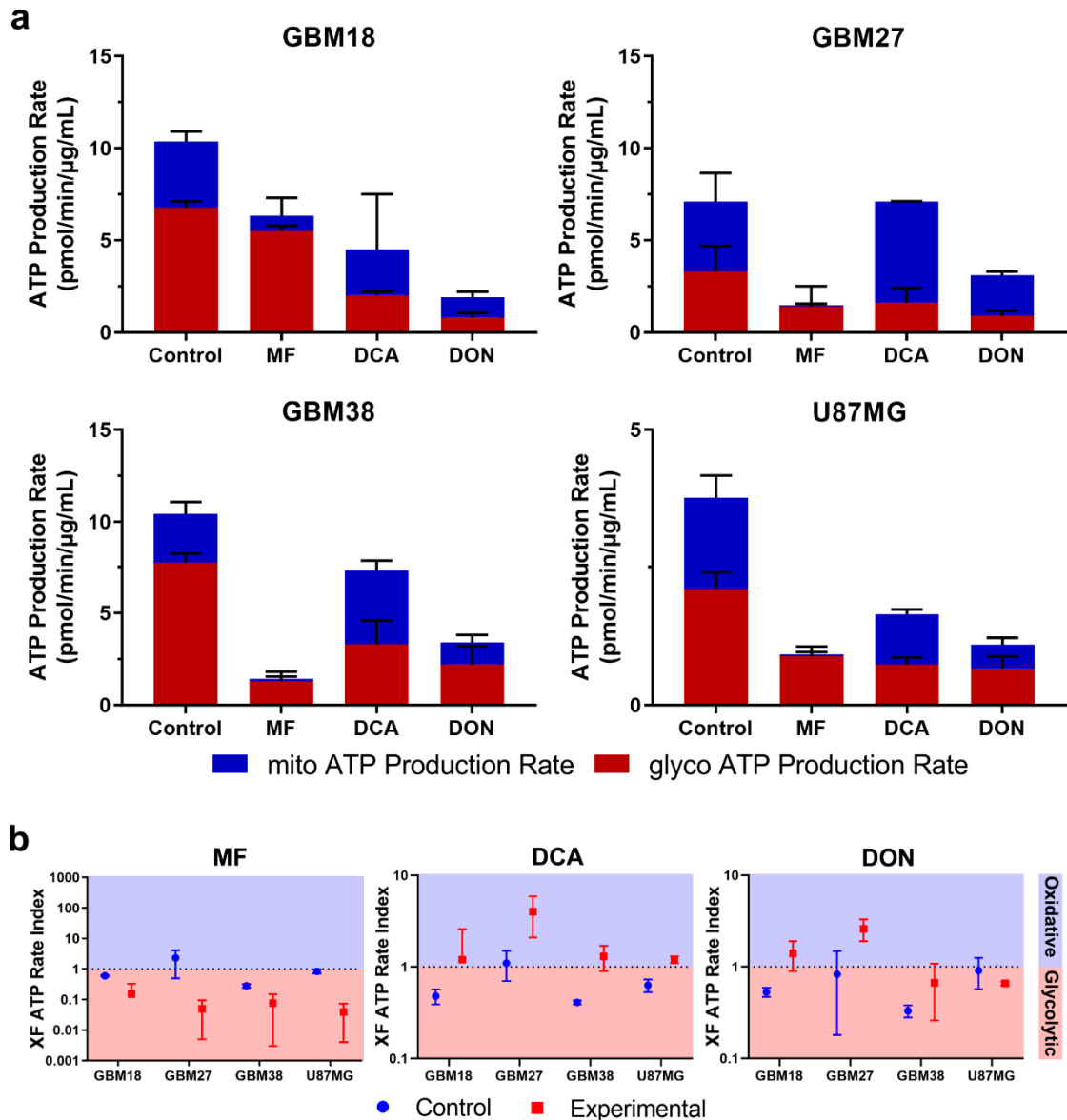


**Figure 6.** (a) Changes in metabolic phenotypes after IC50 treatment for 72 h with metformin (MF), dichloroacetate (DCA) and 6-Diazo-5-oxo-L-norleucine (DON). (b) XF ATP Rate Index for GSCs and U87MG. The ATP Rate Index is the ratio of the mitoATP Production Rate divided by glycoATP Production Rate, indicating higher oxidative or glycolytic bioenergetic profile.

Normalized values of OCR/Proton Efflux Rate (PER) in real-time after each drug injection of the Seahorse XF protocol are provided in Supplementary Figure S4. These kinetic graphs allow us to examine how previous metabolic treatments changed the basal metabolic state and acute responses to mitochondrial inhibitors included in the assay: oligomycin (complex V inhibitor, i.e., mitochondrial ATP synthesis) and rotenone/antimycin A (total inhibition of mitochondrial respiration, complex I and complex III, respectively). Glycolytic upregulation in response to partial and complete mitochondrial inhibition (Warburg phenotype) and residual non-mitochondrial OCR should be highlighted in GBM18 and GBM38.

In conclusion, pre-treatment with metabolic drugs could become a valuable tool to characterize the bioenergetic phenotypes of surviving, resistant fraction of cells, priming them for further treatments. To our knowledge, this is the first time chronic metabolic treatments (>72 h) with DCA and DON have been characterized in GSCs. Despite methodological differences, our results also confirm the bioenergetic changes after low-dose MF in

GSCs [61] and DCA in established glioma cell lines [62,63]. Finally, oxidative GSCs such as GBM27, an abnormality in the predominantly glycolytic phenotypes of solid tumors, need to be fully recognized in order to improve metabolic therapies. Based on our results, sequential drug strategies targeting previously weakened ATP-generating pathways warrant further exploration.

#### 4. Discussion

Cancer metabolism has recently regained interest as a promising therapeutic target, coinciding with the development of standardized techniques for real-time assessment of bioenergetics. Given high intratumoral molecular and metabolic heterogeneity, it is necessary to target glycolytic, glutaminolytic and oxidative phenotypes; for this purpose, primary GSCs cultured from human surgical samples are an excellent model [64].

In this paper, we describe how metabolic modulators (MF, DCA, DON) could be leveraged to inhibit GSCs proliferation, demonstrating that distinct, stable, metabolic phenotypes contrast in their response to these treatments. A comparison between untreated and metabolically treated GSCs populations is presented here for the first time, leading us to hypothesize that inhibiting metabolic pathways might not only kill malignant cells, but also turn them vulnerable to successive targeted treatments (“metabolic priming”).

Consistent with our results, GSCs have been characterized by ample metabolic heterogeneity, exhibiting both glycolytic/oxidative characteristics [29,65,66]. Surprisingly, GBM27 exhibited a highly oxidative phenotype, at odds with Warburg’s central hypothesis of dysfunctional mitochondria; the presence of such metabolic subpopulations will need to be addressed to prevent tumor recurrence after antiglycolytic therapy. Similarly, U87MG had been described numerous times as highly glycolytic (high basal ECAR); however, we and others also described simultaneous elevations in OCR [30,67–70].

Regarding our selection of metabolic inhibitors, GBM27 was the most resistant to all drugs, with the exception of DON. One of the reasons for this might be owed to GBM27’s characteristically oxidative metabolism (up to 50% oxidative) and slower proliferation rates. Metabolic flexibility may grant a survival advantage even if mitochondrial energy production is targeted via MF or glycolysis via DCA. GBM18 and GBM38, on the other hand, were significantly more sensitive to MF; this would be consistent with their Warburg-like metabolic phenotypes. At the protein level, our results are consistent with previous research, where 10 mM MF did not significantly increase phospho-Thr172 at 6 h in U87MG [71]. Next, we hypothesized whether upregulated or downregulated PDK expression could be useful in predicting responses to DCA. While PDK1 was upregulated with respect to non-tumoral controls, expression was similar across all cell lines. PDK3 expression was relatively downregulated in GBM38 and exceptionally upregulated in GBM27. This would be consistent with previous reports where the PDK3 subunit was the most resistant to inhibition by DCA (higher expression of PDK3 would therefore translate into higher doses of DCA) [72,73]. In contrast, PDK2 subunits are the most sensitive to DCA treatment, while PDK1 and PDK4 display intermediate sensitivity ( $K_i$  PDK2 < PDK1  $\simeq$  PDK4 < PDK3). As PDK1 was equally distributed, and PDK2/PDK4 were undetectable in our samples, variances in dose-response profiles were likely related to differences in PDK3. SOD treatment was equally inefficacious in all tested cell lines, but we suspect this was partly related to poor cell membrane permeability of this compound [74–76]. Despite issues with potency, our GSCs appear as highly resistant to SOD, as evidenced by much lower reported IC50s in nasopharyngeal carcinoma and gastric cell lines [77,78]. Concerning DON, glutamine addiction is thought to play an important role in supporting cancer proliferation [79,80]. In our case, GBM18 was the most resistant to DON, while other GSCs and U87MG turned more vulnerable to glutaminase inhibition. Our results confirm the inhibition profile for U87MG/DON at 72 h recounted by Ohba et al., with a similarly flattened inhibitory curve but higher “theoretical” IC50 [81]. With DON, rather than linear, dose-dependent cytotoxicity, we noted a more cytostatic-like effect in GBM18, GBM38 and, to a lesser extent, GBM27. Higher relative mRNA expression of GLS1 was evidenced in

GBM18, accompanied with, indeed, higher doses of DON for the same inhibitory effect; correlations between doses and GLS1 expression was not as clear in other cell lines.

The heterogeneity of cancer could also be managed by combinatorial strategies, focusing on multiple molecular pathways to achieve compounded effects. Even though stand-alone metabolic modulation could become a possibility in the future, a more realistic and approachable goal is to design safe and effective combinations together with well-established chemotherapeutics and radiotherapy. Here, we show that non-tumoral hMSCs are not affected by low/intermediate doses of MF, DCA, DON or bleomycin. Concentrations of MF and DCA corresponding to GBM27, however, decreased viability by more than half in hMSCs, revealing that oxidative cancer cells would require a different management strategy: combinatory therapies could be such an option.

To the extent of our knowledge, ours is the first report of the combinatorial effects in GSCs of the radiomimetic drug bleomycin together with MF, DCA and DON. Bleomycin acts by inducing single and double strand DNA breaks, causing apoptosis and cell cycle arrest in early G2 phase [44]; it is FDA-approved as a clinical prescription against lymphomas, squamous-cell carcinomas and germ-cell tumours, as well as brain cancer [45,82]. IC50 profiles for bleomycin revealed significant disparities among cell lines, with GBM38 and U87MG being more sensitive than GBM18 and GBM27. Direct comparisons with radiotherapy are scarce, however, as we only encounter combined evaluation in traditional glioblastoma cell lines (not GSCs) for MF [61] and DCA [69]. Discussing our results, we want to bring attention to the fact that GBM27, identified as distinctly “oxidative”, was potentially the most benefited by pairing bleomycin and metabolic modulators. Synergistic opportunities in GBM27 would allow for significant dose reduction, as individual IC50 concentrations for MF and DCA are higher than in all other cell lines, thus reducing toxicity in normal cells. One of the strengths of our combinatory approach is the experimental design in a constant drug ratio: this allows for a data-driven, more accurate and comprehensive description of synergy/antagonism using the Chou-Talalay method [83], without relying solely on computer simulations.

As far as we know, sustained metabolic changes in GSCs after extended treatment with DCA and DON had not been properly illustrated until now. In terms of OCR/ECAR, all metabolic modulators exerted biologically coherent responses, especially well-defined for MF and DCA. In the case of MF, as would be expected, surviving cells shifted to a primarily glycolytic behavior, with a very low percentage of mitoATP generation; these results are consistent with Seahorse XF assays in established glioma cell lines and colon cancer CSCs [61]. The metabolic effects of MF were mainly determined by dose-response profiles. Similarly, DCA induced bioenergetic changes consistent with the forced activation of the PDH complex, in congruence with previous reports [69,84]. Interestingly, when comparing total ATP production rates, DCA only reached a maximal attenuation of approximately 50% relative to control. Indeed, DCA is believed to act more as a “metabolic modulator”, not simply reducing cell proliferation, but also “shifting” the glycolytic/OXPHOS ratio via increased mitochondrial uptake of pyruvate [85,86]. Lastly, evaluating the effects of DON, we detected consistent ATP inhibition but heterogeneous metabolic adaptations. In previous reports, no response was observed to low concentrations of DON in U87MG [87]. Preclinical data shows that relatively high *in vitro* doses of DON are required in some cell lines, which might explain the high variability in antiproliferative effects [88–91]. After chronic treatment with DON, we observed either an unchanged (GBM38, U87MG) or increased (GBM18, GBM27) ATP Rate Index. The third alternative, a decrease in ATP Rate Index (enhanced Warburg effect), was not detected; in contrast, this shift was noted with MF in all cell lines. Therefore, after GLS inhibition, we can hypothesize that increased mitoATP cannot be originated from glutamine oxidation: this was apparent in GBM27, where inhibition of glutaminolysis led to preferential oxidation of glucose (indicative of metabolic flexibility). GBM18 displayed a similar trend, albeit less pronounced, whereas GBM38 and U87MG saw their total ATP production diminished without compensatory shifts in mito/glycoATP.

From a translational medicine perspective, avoiding the risk of toxicity associated with high concentrations of MF might be feasible, as even very low doses of this drug revealed antiproliferative effects and radiotherapy enhancement [92,93]. Furthermore, combinatory strategies would allow for meaningful dose reductions, as shown with improved efficacy in radioresistant stem cells [94]. Moreover, DCA could be applied synergistically to prevent MF-induced lactic acidosis [95–97]. Our results agree with previously published data, showing that concentrations of DCA in the range of  $\geq 10$  mM are required for consistent anti-proliferative responses [98–101]. Finally, the prospective of DON for GBM therapy is hindered by a polar structure and reactive moiety that significantly reduces its ability to cross the blood-brain barrier (BBB) [102,103]. Nevertheless, most GBM patients present with a disrupted BBB [104], and, where this might not be applicable, prodrugs and novel glutaminase inhibitors are in active development [31,105].

We believe the origin of cancer is complex, with involvement of both oncogenic signaling and metabolic reprogramming [106,107]. Future directions in this field might entail a more precise molecular classification of tumor biopsies, expanding the comparison between gene expression subtypes and their metabolic milieu, and imaging of patients for improved, tailor-made therapeutics. Stratification and metabolic analysis will be crucial to discover malignancies that could benefit from adjuvant anti-glycolytic therapy [108,109], specific pathway inhibition (e.g., mitochondrial, glutamine and FAO inhibitors [110–112]) and tumors where, due to molecular rewiring, glycolysis inhibition with compensatory fuels might even be contraindicated [25,113,114].

## 5. Conclusions

In summary, we show that molecularly distinct GSCs show a high degree of heterogeneity, both in basal metabolic phenotypes and in response to metabolic inhibitors. Subpopulations of GSCs presented both highly glycolytic and highly oxidative characteristics. Stratification of patients according to coexisting metabolic phenotypes could be advanced into clinical tools for improved metabolic therapies. In highly oxidative GSCs (e.g., GBM27), there is potential for synergistic effects with radiomimetic bleomycin. Inhibition of glutaminolysis (via DON) is also an attractive therapeutic target, as synergy was described regardless of basal metabolism. Application of metabolic drugs produces stable changes in the bioenergetic states of GSCs, which could be leveraged as a form of metabolic priming.

**Supplementary Materials:** The following are available online at <https://www.mdpi.com/2073-4409/10/2/202/s1>. Figure S1: Inhibitory curves for MF, DCA, SOD and DON at 24 h, 48 h, 72 h. Figure S2: Western Blot time-course analysis of phospho-Ser293 PDH-E1 in GBM38. Figure S3: Inhibitory curves for bleomycin at 72 h. Figure S4: Seahorse XF real-time kinetic graphs. File S1: Comprehensive analysis of Chou–Talalay combinatory experiments, as exported from CompuSyn software.

**Author Contributions:** Conceptualization, T.D., N.G.-R. and A.A.-S.; methodology, T.D., J.C.-N., N.G.-R. and A.A.-S.; investigation, T.D. and N.G.-R.; formal analysis, R.M.; resources, A.O.d.M. and L.G.-C. (MRI imaging assistance); data curation, T.D.; writing—original draft preparation, T.D.; writing—review and editing, T.D., J.C.-N., R.P.-A., N.G.-R. and A.A.-S.; project administration, N.G.-R. and A.A.-S.; funding acquisition, A.A.-S. All authors have read and agreed to the published version of the manuscript.

**Funding:** This research was funded by grants from the “Fondo de Investigaciones Sanitarias” (FIS) (PI17-01489), the Miguel Servet Program (CP11/00147) del Instituto de Salud Carlos III (AAS), the Ministerio de Economía y Competitividad-FEDERER (RTC-2016-4990-1). Research funded by Ministerio de Educación, Cultura y Deporte (FPU16/03198).

**Institutional Review Board Statement:** The study was conducted according to the guidelines of the Declaration of Helsinki, and approved by the Ethics Committee 14.06.632-GHM.

**Informed Consent Statement:** Informed consent was obtained from all subjects involved in the study.



**Data Availability Statement:** The data presented in this study is available in the Supplementary Materials of this article. The results shown in the GSVA analysis are in part based upon data generated by the TCGA Research Network: <https://www.cancer.gov/tcga>.

**Acknowledgments:** We thank Irina Palacín-Aliana, Gorjana Rackov and Susana Esteban-Rubio for methodological support and technical help.

**Conflicts of Interest:** The authors declare no conflict of interest.

## References

- Ostrom, Q.T.; Gittleman, H.; Farah, P.; Ondracek, A.; Chen, Y.; Wolinsky, Y.; Stroup, N.E.; Kruchko, C.; Barnholtz-Sloan, J.S. CBTRUS Statistical Report: Primary Brain and Central Nervous System Tumors Diagnosed in the United States in 2006–2010. *Neuro-Oncology* **2013**, *15*, ii1–ii56. [CrossRef] [PubMed]
- Koshy, M.; Villano, J.L.; Dolecek, T.A.; Howard, A.; Mahmood, U.; Chmura, S.J.; Weichselbaum, R.R.; McCarthy, B.J. Improved survival time trends for glioblastoma using the SEER 17 population-based registries. *J. Neuro-Oncol.* **2012**, *107*, 207–212. [CrossRef] [PubMed]
- Tamimi, A.F.; Juweid, M. Epidemiology and Outcome of Glioblastoma. In *Glioblastoma [Internet]*; 201921345W; Codon Publications: Singapore, 2017.
- Louis, D.N.; Perry, A.; Reifenberger, G.; Von Deimling, A.; Figarella-Branger, D.; Cavenee, W.K.; Ohgaki, H.; Wiestler, O.D.; Kleihues, P.; Ellison, D.W. The 2016 World Health Organization Classification of Tumors of the Central Nervous System: A summary. *Acta Neuropathol.* **2016**, *131*, 803–820. [CrossRef] [PubMed]
- Verhaak, R.G.; Hoadley, K.A.; Purdom, E.; Wang, V.; Qi, Y.; Wilkerson, M.D.; Miller, C.R.; Ding, L.; Golub, T.; Mesirov, J.P.; et al. Integrated Genomic Analysis Identifies Clinically Relevant Subtypes of Glioblastoma Characterized by Abnormalities in PDGFRA, IDH1, EGFR, and NF1. *Cancer Cell* **2010**, *17*, 98–110. [CrossRef] [PubMed]
- Teo, W.-Y.; Sekar, K.; Seshachalam, P.; Shen, J.; Chow, W.-Y.; Lau, C.C.; Yang, H.; Park, J.; Kang, S.-G.; Li, X.; et al. Relevance of a TCGA-derived Glioblastoma Subtype Gene-Classifer among Patient Populations. *Sci. Rep.* **2019**, *9*, 7442. [CrossRef] [PubMed]
- Stupp, R.; Taillibert, S.; Kanner, A.; Read, W.; Steinberg, D.M.; Lhermitte, B.; Toms, S.; Idnbaih, A.; Ahluwalia, M.S.; Fink, K.J.J. Effect of tumor-treating fields plus maintenance temozolomide vs maintenance temozolomide alone on survival in patients with glioblastoma: A randomized clinical trial. *JAMA* **2017**, *318*, 2306–2316. [CrossRef]
- Ostrom, Q.T.; Bauchet, L.; Davis, F.G.; Deltour, I.; Fisher, J.L.; Langer, C.E.; Pekmezci, M.; Schwartzbaum, J.A.; Turner, M.C.; Walsh, K.M.; et al. The epidemiology of glioma in adults: A “state of the science” review. *Neuro-Oncology* **2014**, *16*, 896–913. [CrossRef]
- Johnson, D.R.; O’Neill, B.P. Glioblastoma survival in the United States before and during the temozolomide era. *J. Neuro-Oncol.* **2012**, *107*, 359–364. [CrossRef]
- Han, X.; Xue, X.; Zhou, H.; Zhang, G. A molecular view of the radioresistance of gliomas. *Oncotarget* **2017**, *8*, 100931–100941. [CrossRef]
- Seyfried, T.N.; Shelton, L.M. Cancer as a metabolic disease. *Nutr. Metab.* **2010**, *7*, 7. [CrossRef]
- Jose, C.; Bellance, N.; Rossignol, R. Choosing between glycolysis and oxidative phosphorylation: A tumor’s dilemma? *Biochim. Biophys. Acta* **2011**, *1807*, 552–561. [CrossRef] [PubMed]
- Hanahan, D.; Weinberg, R.A. Hallmarks of cancer: The next generation. *Cell* **2011**, *144*, 646–674. [CrossRef] [PubMed]
- Potter, M.; Newport, E.; Morten, K.J. The Warburg effect: 80 years on. *Biochem. Soc. Trans.* **2016**, *44*, 1499–1505. [CrossRef] [PubMed]
- Hsu, P.P.; Sabatini, D.M. Cancer Cell Metabolism: Warburg and Beyond. *Cell* **2008**, *134*, 703–707. [CrossRef] [PubMed]
- Seyfried, T.N.; Flores, R.E.; Poff, A.M.; D’Agostino, D.P. Cancer as a metabolic disease: Implications for novel therapeutics. *Carcinogenesis* **2014**, *35*, 515–527. [CrossRef]
- Ristow, M. Oxidative metabolism in cancer growth. *Curr. Opin. Clin. Nutr. Metab. Care* **2006**, *9*, 339–345. [CrossRef]
- Semenza, G.L.; Artemov, D.; Bedi, A.; Bhujwala, Z.; Chiles, K.; Feldser, D.; Laughner, E.; Ravi, R.; Simons, J.; Taghavi, P.; et al. ‘The Metabolism of Tumours’: 70 Years Later. In Proceedings of the Novartis Foundation Symposium, Singapore, 30 August–1 September 2004; pp. 251–259.
- Timm, K.N.; Kennedy, B.W.; Brindle, K.M. Imaging Tumor Metabolism to Assess Disease Progression and Treatment Response. *Clin. Cancer Res.* **2016**, *22*, 5196–5203. [CrossRef]
- Kim, M.M.; Parolia, A.; Dunphy, M.P.; Venneti, S. Non-invasive metabolic imaging of brain tumours in the era of precision medicine. *Nat. Rev. Clin. Oncol.* **2016**, *13*, 725–739. [CrossRef]
- Paech, D.; Nagel, A.M.; Schultheiss, M.N.; Umathum, R.; Regnery, S.; Scherer, M.; Wick, A.; Platt, T.; Wick, W.; Bendszus, M.; et al. Quantitative Dynamic Oxygen 17 MRI at 7.0 T for the Cerebral Oxygen Metabolism in Glioma. *Radiology* **2020**, *295*, 181–189. [CrossRef]
- Grasso, D.; Zampieri, L.X.; Capelôa, T.; van de Velde, J.A.; Sonveaux, P. Mitochondria in Cancer. *Cell Stress* **2020**, *4*, 114–146. [CrossRef]
- Xu, X.D.; Shao, S.X.; Jiang, H.P.; Cao, Y.W.; Wang, Y.H.; Yang, X.C.; Wang, Y.L.; Wang, X.S.; Niu, H.T. Warburg Effect or Reverse Warburg Effect? A Review of Cancer Metabolism. *Oncol. Res. Treat.* **2015**, *38*, 117–122. [CrossRef]

24. Vidali, S.; Aminzadeh, S.; Lambert, B.; Rutherford, T.; Sperl, W.; Kofler, B.; Feichtinger, R.G. Mitochondria: The ketogenic diet—A metabolism-based therapy. *Int. J. Biochem. Cell Biol.* **2015**, *63*, 55–59. [CrossRef] [PubMed]
25. Lin, H.; Patel, S.; Affleck, V.S.; Wilson, I.; Turnbull, D.M.; Joshi, A.R.; Maxwell, R.; Stoll, E.A. Fatty acid oxidation is required for the respiration and proliferation of malignant glioma cells. *Neuro-Oncology* **2017**, *19*, 43–54. [CrossRef] [PubMed]
26. Chinopoulos, C.; Seyfried, T.N. Mitochondrial substrate-level phosphorylation as energy source for glioblastoma: Review and hypothesis. *ASN Neuro* **2018**, *10*, 1759091418818261. [CrossRef]
27. Hinohara, K.; Polyak, K. Intratumoral heterogeneity: More than just mutations. *Trends Cell Biol.* **2019**, *29*, 569–579. [CrossRef]
28. Saga, I.; Shibao, S.; Okubo, J.; Osuka, S.; Kobayashi, Y.; Yamada, S.; Fujita, S.; Urakami, K.; Kusahara, M.; Yoshida, K.; et al. Integrated analysis identifies different metabolic signatures for tumor-initiating cells in a murine glioblastoma model. *Neuro-Oncology* **2014**, *16*, 1048–1056. [CrossRef]
29. Shibao, S.; Minami, N.; Koike, N.; Fukui, N.; Yoshida, K.; Saya, H.; Sampetean, O. Metabolic heterogeneity and plasticity of glioma stem cells in a mouse glioblastoma model. *Neuro-Oncology* **2018**, *20*, 343–354. [CrossRef]
30. Vlashi, E.; Lagadec, C.; Vergnes, L.; Matsutani, T.; Masui, K.; Poulou, M.; Popescu, R.; Della Donna, L.; Evers, P.; Dekmezian, C.; et al. Metabolic state of glioma stem cells and nontumorigenic cells. *Proc. Natl. Acad. Sci. USA* **2011**, *108*, 16062–16067. [CrossRef]
31. Lemberg, K.M.; Vornov, J.J.; Rais, R.; Slusher, B.S. We're not "DON" yet: Optimal dosing and prodrug delivery of 6-Diazo-5-oxo-L-norleucine. *Mol. Cancer Ther.* **2018**, *17*, 1824–1832. [CrossRef]
32. Tataranni, T.; Piccoli, C. Dichloroacetate (DCA) and Cancer: An Overview towards Clinical Applications. *Oxidative Med. Cell. Longev.* **2019**, *2019*, 8201079. [CrossRef]
33. Kasznicki, J.; Sliwiska, A.; Drzewoski, J. Metformin in cancer prevention and therapy. *Ann. Transl. Med.* **2014**, *2*, 57.
34. Granchi, C.; Paterni, I.; Rani, R.; Minutolo, F. Small-molecule inhibitors of human LDH5. *Future Med. Chem.* **2013**, *5*, 1967–1991. [CrossRef] [PubMed]
35. Al-Hajj, M.; Clarke, M.F. Self-renewal and solid-tumor stem cells. *Oncogene* **2005**, *11*, 14–16. [CrossRef] [PubMed]
36. Pattabiraman, D.R.; Weinberg, R.A. Tackling the cancer stem cells—What challenges do they pose? *Nat. Rev. Drug Discov.* **2014**, *13*, 497–512. [CrossRef] [PubMed]
37. Singh, S.K.; Hawkins, C.; Clarke, I.D.; Squire, J.A.; Bayani, J.; Hide, T.; Henkelman, R.M.; Cusimano, M.D.; Dirks, P.B. Identification of human brain tumour initiating cells. *Nature* **2004**, *432*, 396–401. [CrossRef]
38. Reya, T.; Morrison, S.J.; Clarke, M.F.; Weissman, I.L. Stem cells, cancer, and cancer stem cells. *Nature* **2001**, *414*, 105–111. [CrossRef]
39. Li, Z.; Bao, S.; Wu, Q.; Wang, H.; Eyler, C.; Sathornsumetee, S.; Shi, Q.; Cao, Y.; Lathia, J.; McLendon, R.E.; et al. Hypoxia-Inducible Factors Regulate Tumorigenic Capacity of Glioma Stem Cells. *Cancer Cell* **2009**, *15*, 501–513. [CrossRef]
40. Calabrese, C.; Poppleton, H.; Kocak, M.; Hogg, T.L.; Fuller, C.; Hamner, B.; Oh, E.Y.; Gaber, M.W.; Finklestein, D.; Allen, M.; et al. A Perivascular Niche for Brain Tumor Stem Cells. *Cancer Cell* **2007**, *11*, 69–82. [CrossRef]
41. Peiris-Pagès, M.; Martínez-Outschoorn, U.E.; Pestell, R.G.; Sotgia, F.; Lisanti, M.P. Cancer stem cell metabolism. *Breast Cancer Res.* **2016**, *18*, 1–10. [CrossRef]
42. Hänzelmann, S.; Castelo, R.; Guinney, J. GSEA: Gene set variation analysis for microarray and RNA-Seq data. *BMC Bioinform.* **2013**, *14*, 7. [CrossRef]
43. Behnan, J.; Finocchiaro, G.; Hanna, G. The landscape of the mesenchymal signature in brain tumours. *Brain* **2019**, *142*, 847–866. [CrossRef] [PubMed]
44. Povirk, L.F.; Mutagenesis, M. DNA damage and mutagenesis by radiomimetic DNA-cleaving agents: Bleomycin, neocarzinostatin and other enediynes. *Mutat. Res.* **1996**, *355*, 71–89. [CrossRef]
45. Chen, J.; Stubbe, J. Bleomycins: Towards better therapeutics. *Nat. Rev. Cancer* **2005**, *5*, 102–112. [CrossRef] [PubMed]
46. García-Romero, N.; González-Tejedo, C.; Carrión-Navarro, J.; Esteban-Rubio, S.; Rackov, G.; Rodríguez-Fanjul, V.; Oliver-De La Cruz, J.; Prat-Acín, R.; Peris-Celda, M.; Blesa, D.; et al. Cancer stem cells from human glioblastoma resemble but do not mimic original tumors after in vitro passaging in serum-free media. *Oncotarget* **2016**, *7*, 65888–65901. [CrossRef]
47. Chou, T.-C. Drug Combination Studies and Their Synergy Quantification Using the Chou-Talalay Method. *Cancer Res.* **2010**, *70*, 440–446. [CrossRef]
48. Chou, T.-C. Theoretical Basis, Experimental Design, and Computerized Simulation of Synergism and Antagonism in Drug Combination Studies. *Pharmacol. Rev.* **2006**, *58*, 621–681. [CrossRef]
49. Mahmood, T.; Yang, P.-C. Western blot: Technique, theory, and trouble shooting. *N. Am. J. Med. Sci.* **2012**, *4*, 429–434. [CrossRef]
50. Divakaruni, A.S.; Paradyse, A.; Ferrick, D.A.; Murphy, A.N.; Jastroch, M. Analysis and Interpretation of Microplate-Based Oxygen Consumption and pH Data. In *Methods in Enzymology*; Elsevier: Amsterdam, The Netherlands, 2014; Volume 547, pp. 309–354.
51. Yépez, V.A.; Kremer, L.S.; Iuso, A.; Gusic, M.; Kopajtich, R.; Koňáříková, E.; Nadel, A.; Wachutka, L.; Prokisch, H.; Gagneur, J. OCR-Stats: Robust estimation and statistical testing of mitochondrial respiration activities using Seahorse XF Analyzer. *PLoS ONE* **2018**, *13*, e0199938. [CrossRef]
52. Bowman, R.L.; Wang, Q.; Carro, A.; Verhaak, R.G.; Squatrito, M. GlioVis data portal for visualization and analysis of brain tumor expression datasets. *Neuro-Oncology* **2017**, *19*, 139–141. [CrossRef]
53. Zhou, W.; Wahl, D.R. Metabolic Abnormalities in Glioblastoma and Metabolic Strategies to Overcome Treatment Resistance. *Cancers* **2019**, *11*, 1231. [CrossRef]

54. Madurga, R.; García-Romero, N.; Jiménez, B.; Collazo, A.; Pérez-Rodríguez, F.; Hernández-Laín, A.; Fernández-Carballal, C.; Prat-Acín, R.; Zanin, M.; Menasalvas, E.; et al. Normal tissue content impact on the GBM molecular classification. *Brief. Bioinform.* **2020**, bbaa129. [CrossRef] [PubMed]
55. Subramanian, A.; Tamayo, P.; Mootha, V.K.; Mukherjee, S.; Ebert, B.L.; Gillette, M.A.; Paulovich, A.; Pomeroy, S.L.; Golub, T.R.; Lander, E.S.; et al. Gene set enrichment analysis: A knowledge-based approach for interpreting genome-wide expression profiles. *Proc. Natl. Acad. Sci. USA* **2005**, *102*, 15545–15550. [CrossRef] [PubMed]
56. Fan, T.; Sun, G.; Sun, X.; Zhao, L.; Zhong, R.; Peng, Y. Tumor Energy Metabolism and Potential of 3-Bromopyruvate as an Inhibitor of Aerobic Glycolysis: Implications in Tumor Treatment. *Cancers* **2019**, *11*, 317. [CrossRef] [PubMed]
57. Wise, D.R.; Thompson, C.B. Glutamine addiction: A new therapeutic target in cancer. *Trends Biochem. Sci.* **2010**, *35*, 427–433. [CrossRef] [PubMed]
58. Aljofan, M.; Riethmacher, D. Anticancer activity of metformin: A systematic review of the literature. *Future Sci. OA* **2019**, *5*, FSO410. [CrossRef] [PubMed]
59. Yeaman, S.J.; Hutcheson, E.T.; Roche, T.E.; Pettit, F.H.; Brown, J.R.; Reed, L.J.; Watson, D.C.; Dixon, G.H. Sites of phosphorylation on pyruvate dehydrogenase from bovine kidney and heart. *Biochemistry* **1978**, *17*, 2364–2370. [CrossRef]
60. Korotchkina, L.G.; Patel, M.S. Site specificity of four pyruvate dehydrogenase kinase isoenzymes toward the three phosphorylation sites of human pyruvate dehydrogenase. *J. Biol. Chem.* **2001**, *276*, 37223–37229. [CrossRef]
61. Sesen, J.; Dahan, P.; Scotland, S.J.; Saland, E.; Dang, V.-T.; Lemarié, A.; Tyler, B.M.; Brem, H.; Toulas, C.; Moyal, E.C.-J.; et al. Metformin Inhibits Growth of Human Glioblastoma Cells and Enhances Therapeutic Response. *PLoS ONE* **2015**, *10*, e0123721. [CrossRef] [PubMed]
62. Velpula, K.K.; Guda, M.R.; Sahu, K.; Tuszyński, J.; Asuthkar, S.; Bach, S.E.; Lathia, J.D.; Tsung, A.J. Metabolic targeting of EGFRvIII/PDK1 axis in temozolomide resistant glioblastoma. *Oncotarget* **2017**, *8*, 35639–35655. [CrossRef]
63. Prabhu, A.; Sarcar, B.; Miller, C.R.; Kim, S.-H.; Nakano, I.; Forsyth, P.; Chinnaiyan, P. Ras-mediated modulation of pyruvate dehydrogenase activity regulates mitochondrial reserve capacity and contributes to glioblastoma tumorigenesis. *Neuro-Oncology* **2015**, *17*, 1220–1230. [CrossRef]
64. Brown, D.V.; Stylli, S.S.; Kaye, A.H.; Mantamadiotis, T. Multilayered Heterogeneity of Glioblastoma Stem Cells: Biological and Clinical Significance. In *Cannabinoids and Neuropsychiatric Disorders*; Springer: Berlin/Heidelberg, Germany, 2019; pp. 1–21.
65. Spelhalski, E.I.; Lee, J.A.; Peters, C.; Tofilon, P.; Camphausen, K. The Quiescent Metabolic Phenotype of Glioma Stem Cells. *J. Proteom. Bioinform.* **2019**, *12*, 1–8. [CrossRef] [PubMed]
66. Zhou, Y.; Zhou, Y.; Shingu, T.; Feng, L.; Chen, Z.; Ogasawara, M.; Keating, M.J.; Kondo, S.; Huang, P. Metabolic alterations in highly tumorigenic glioblastoma cells preference for hypoxia and high dependency on glycolysis. *J. Biol. Chem.* **2011**, *286*, 32843–32853. [CrossRef]
67. Massalha, W.; Markovits, M.; Pichinuk, E.; Feinstein-Rotkopf, Y.; Tarshish, M.; Mishra, K.; Llado, V.; Weil, M.; Escriba, P.V.; Kakhlon, O. Minerval (2-hydroxyoleic acid) causes cancer cell selective toxicity by uncoupling oxidative phosphorylation and compromising bioenergetic compensation capacity. *Biosci. Rep.* **2019**, *39*, 39. [CrossRef] [PubMed]
68. Cvrljevic, A.; Akhavan, D.; Wu, M.; Martinello, P.; Furnari, F.B.; Johnston, A.J.; Guo, D.; Pike, L.; Cavenee, W.K.; Scott, A.M.; et al. Activation of Src induces mitochondrial localisation of de2-7EGFR (EGFRvIII) in glioma cells: Implications for glucose metabolism. *J. Cell Sci.* **2011**, *124*, 2938–2950. [CrossRef] [PubMed]
69. Shen, H.; Hau, E.; Joshi, S.; Dilda, P.J.; McDonald, K.L. Sensitization of Glioblastoma Cells to Irradiation by Modulating the Glucose Metabolism. *Mol. Cancer Ther.* **2015**, *14*, 1794–1804. [CrossRef]
70. Kim, J.; Han, J.; Jang, Y.; Kim, S.J.; Lee, M.J.; Ryu, M.J.; Kweon, G.R.; Heo, J.Y. High-capacity glycolytic and mitochondrial oxidative metabolisms mediate the growth ability of glioblastoma. *Int. J. Oncol.* **2015**, *47*, 1009–1016. [CrossRef]
71. Liu, X.; Chhipa, R.R.; Pooya, S.; Wortman, M.; Yachyshin, S.; Chow, L.M.L.; Kumar, A.; Zhou, X.; Sun, Y.; Quinn, B.; et al. Discrete mechanisms of mTOR and cell cycle regulation by AMPK agonists independent of AMPK. *Proc. Natl. Acad. Sci. USA* **2014**, *111*, E435–E444. [CrossRef]
72. Baker, J.C.; Yan, X.; Peng, T.; Kasten, S.; Roche, T.E. Marked Differences between Two Isoforms of Human Pyruvate Dehydrogenase Kinase. *J. Biol. Chem.* **2000**, *275*, 15773–15781. [CrossRef]
73. Bowker-Kinley, M.M.; Davis, I.W.; Wu, P.; Harris, A.R.; Popov, M.K. Evidence for existence of tissue-specific regulation of the mammalian pyruvate dehydrogenase complex. *Biochem. J.* **1998**, *329*, 191–196. [CrossRef]
74. Goldberg, E.B.; Colowick, S.P. The role of glycolysis in the growth of tumor cells. 3. Lactic dehydrogenase as the site of action of oxamate on the growth of cultured cells. *J. Biol. Chem.* **1965**, *240*, 2786–2790. [CrossRef]
75. Elwood, J.C. Effect of oxamate on glycolysis and respiration in sarcoma 37 ascites cells. *Cancer Res.* **1968**, *28*, 2056–2060. [PubMed]
76. Fiume, L.; Manerba, M.; Vettraino, M.; Di Stefano, G. Impairment of Aerobic Glycolysis by Inhibitors of Lactic Dehydrogenase Hinders the Growth of Human Hepatocellular Carcinoma Cell Lines. *Pharmacology* **2010**, *86*, 157–162. [CrossRef] [PubMed]
77. Zhai, X.; Yang, Y.; Wan, J.; Zhu, R.; Wu, Y. Inhibition of LDH-A by oxamate induces G2/M arrest, apoptosis and increases radiosensitivity in nasopharyngeal carcinoma cells. *Oncol. Rep.* **2013**, *30*, 2983–2991. [CrossRef] [PubMed]
78. Liu, X.; Yang, Z.; Chen, Z.; Chen, R.; Zhaofeng, C.; Zhou, Y.; Qiao, L. Effects of the suppression of lactate dehydrogenase A on the growth and invasion of human gastric cancer cells. *Oncol. Rep.* **2014**, *33*, 157–162. [CrossRef] [PubMed]
79. Still, E.R.; Yuneva, M.O. Hopefully devoted to Q: Targeting glutamine addiction in cancer. *Br. J. Cancer* **2017**, *116*, 1375–1381. [CrossRef]

80. DeBerardinis, R.J.; Cheng, T. Q's next: The diverse functions of glutamine in metabolism, cell biology and cancer. *Oncogene* **2010**, *29*, 313–324. [CrossRef] [PubMed]
81. Ohba, S.; Hirose, Y. L-asparaginase and 6-diazo-5-oxo-L-norleucine synergistically inhibit the growth of glioblastoma cells. *J. Neuro-Oncol.* **2020**, *146*, 469–475. [CrossRef]
82. Linnert, M.; Gehl, J. Bleomycin treatment of brain tumors: An evaluation. *Anti-Cancer Drugs* **2009**, *20*, 157–164. [CrossRef]
83. Chou, T.-C.; Talalay, P. Quantitative analysis of dose-effect relationships: The combined effects of multiple drugs or enzyme inhibitors. *Adv. Enzym. Regul.* **1984**, *22*, 27–55. [CrossRef]
84. Shen, H.; Decollogne, S.; Dilda, P.J.; Hau, E.; Chung, S.A.; Luk, P.P.; Hogg, P.J.; McDonald, K.L. Dual-targeting of aberrant glucose metabolism in glioblastoma. *J. Exp. Clin. Cancer Res.* **2015**, *34*, 14. [CrossRef]
85. Park, S.; Jeon, J.-H.; Min, B.-K.; Ha, C.-M.; Thoudam, T.; Park, B.-Y.; Lee, I. Role of the Pyruvate Dehydrogenase Complex in Metabolic Remodeling: Differential Pyruvate Dehydrogenase Complex Functions in Metabolism. *Diabetes Metab. J.* **2018**, *42*, 270–281. [CrossRef] [PubMed]
86. Zhang, W.; Zhang, S.-L.; Hu, X.; Tam, K.Y. Targeting Tumor Metabolism for Cancer Treatment: Is Pyruvate Dehydrogenase Kinases (PDKs) a Viable Anticancer Target? *Int. J. Biol. Sci.* **2015**, *11*, 1390–1400. [CrossRef] [PubMed]
87. Oizel, K.; Chauvin, C.; Oliver, L.; Gratas, C.; Geraldo, F.; Jarry, U.; Scotet, E.; Rabe, M.; Alves-Guerra, M.-C.; Teusan, R.; et al. Efficient Mitochondrial Glutamine Targeting Prevails Over Glioblastoma Metabolic Plasticity. *Clin. Cancer Res.* **2017**, *23*, 6292–6304. [CrossRef] [PubMed]
88. Shelton, L.M.; Huysentruyt, L.C.; Seyfried, T.N. Glutamine targeting inhibits systemic metastasis in the VM-M3 murine tumor model. *Int. J. Cancer* **2010**, *127*, 2478–2485. [CrossRef] [PubMed]
89. Cervantes-Madrid, D.; Romero, Y.; Dueñas-González, A. Reviving Lonidamine and 6-Diazo-5-oxo-L-norleucine to Be Used in Combination for Metabolic Cancer Therapy. *BioMed Res. Int.* **2015**, *2015*, 690492. [CrossRef]
90. Wu, F.; Lukinius, A.; Bergström, M.; Eriksson, B.; Watanabe, Y.; Långström, B. A mechanism behind the antitumour effect of 6-diazo-5-oxo-L-norleucine (DON): Disruption of mitochondria. *Eur. J. Cancer* **1999**, *35*, 1155–1161. [CrossRef]
91. Huber, K.R.; Mayer, E.P.; Mitchell, D.; Roberts, J.W. Cell cycle phase perturbations by 6-diazo-5-oxo-L-norleucine and acivicin in normal and neoplastic human cell lines. *Br. J. Cancer* **1987**, *55*, 653–656. [CrossRef]
92. Wang, G.S.; Hoyte, C. Review of biguanide (metformin) toxicity. *J. Intensive Care Med.* **2019**, *34*, 863–876. [CrossRef]
93. Erices, R.; Bravo, M.L.; Gonzalez, P.; Oliva, B.; Racordon, D.; Garrido, M.; Ibañez, C.; Kato, S.; Brañes, J.; Pizarro, J.; et al. Metformin, at Concentrations Corresponding to the Treatment of Diabetes, Potentiates the Cytotoxic Effects of Carboplatin in Cultures of Ovarian Cancer Cells. *Reprod. Sci.* **2013**, *20*, 1433–1446. [CrossRef]
94. Song, C.W.; Lee, H.; Dings, R.P.M.; Williams, B.; Powers, J.; Dos Santos, T.; Choi, B.-H.; Park, H.J. Metformin kills and radiosensitizes cancer cells and preferentially kills cancer stem cells. *Sci. Rep.* **2012**, *2*, 362. [CrossRef]
95. Stacpoole, P.W.; Kurtz, T.L.; Han, Z.; Langae, T.Y. Role of dichloroacetate in the treatment of genetic mitochondrial diseases. *Adv. Drug Deliv. Rev.* **2008**, *60*, 1478–1487. [CrossRef] [PubMed]
96. Brandsma, D.; Dorlo, T.P.; Haanen, J.H.; Beijnen, J.H.; Boogerd, W. Severe encephalopathy and polyneuropathy induced by dichloroacetate. *J. Neurol.* **2010**, *257*, 2099–2100. [CrossRef] [PubMed]
97. Bonnet, S.; Archer, S.L.; Allalunis-Turner, J.; Haromy, A.; Beaulieu, C.; Thompson, R.B.; Lee, C.T.; Lopaschuk, G.D.; Puttagunta, L.; Bonnet, S.; et al. A Mitochondria-K<sup>+</sup> Channel Axis Is Suppressed in Cancer and Its Normalization Promotes Apoptosis and Inhibits Cancer Growth. *Cancer Cell* **2007**, *11*, 37–51. [CrossRef]
98. Sun, R.C.; Fadia, M.; Dahlstrom, J.E.; Parish, C.R.; Board, P.G.; Blackburn, A.C. Reversal of the glycolytic phenotype by dichloroacetate inhibits metastatic breast cancer cell growth in vitro and in vivo. *Breast Cancer Res. Treat.* **2009**, *120*, 253–260. [CrossRef] [PubMed]
99. Heshe, D.; Hoogstraat, S.; Brauckmann, C.; Karst, U.; Boos, J.; Lanvers-Kaminsky, C. Dichloroacetate metabolically targeted therapy defeats cytotoxicity of standard anticancer drugs. *Cancer Chemother. Pharmacol.* **2010**, *67*, 647–655. [CrossRef] [PubMed]
100. Madhok, B.M.; Yeluri, S.; Perry, S.L.; Hughes, T.A.; Jayne, D.G. Dichloroacetate induces apoptosis and cell-cycle arrest in colorectal cancer cells. *Br. J. Cancer* **2010**, *102*, 1746–1752. [CrossRef] [PubMed]
101. Stockwin, L.H.; Yu, S.X.; Borgel, S.; Hancock, C.; Wolfe, T.L.; Phillips, L.R.; Hollingshead, M.G.; Newton, D.L. Sodium dichloroacetate selectively targets cells with defects in the mitochondrial ETC. *Int. J. Cancer* **2010**, *127*, 2510–2519. [CrossRef]
102. Pinkus, L.M. [45] Glutamine binding sites. In *Methods in Enzymology*; Elsevier: Amsterdam, The Netherlands, 1977; Volume 46, pp. 414–427.
103. Alt, J.; Potter, M.C.; Rojas, C.; Slusher, B.S. Bioanalysis of 6-diazo-5-oxo-L-norleucine in plasma and brain by ultra-performance liquid chromatography mass spectrometry. *Anal. Biochem.* **2015**, *474*, 28–34. [CrossRef]
104. Sarkaria, J.N.; Hu, L.S.; Parney, I.F.; Pafundi, D.H.; Brinkmann, D.H.; Laack, N.N.; Giannini, C.; Burns, T.C.; Kizilbash, S.H.; Laramy, J.K.; et al. Is the blood–brain barrier really disrupted in all glioblastomas? A critical assessment of existing clinical data. *Neuro-Oncology* **2018**, *20*, 184–191. [CrossRef]
105. Song, M.; Kim, S.-H.; Im, C.Y.; Hwang, H.-J. Recent development of small molecule glutaminase inhibitors. *Curr. Top. Med. Chem.* **2018**, *18*, 432–443. [CrossRef]
106. Strickland, M.; Stoll, E.A. Metabolic reprogramming in glioma. *Front. Cell Dev. Biol.* **2017**, *5*, 43. [CrossRef] [PubMed]
107. Woolf, E.C.; Syed, N.; Scheck, A.C. Tumor metabolism, the ketogenic diet and  $\beta$ -hydroxybutyrate: Novel approaches to adjuvant brain tumor therapy. *Front. Mol. Neurosci.* **2016**, *9*, 122. [CrossRef] [PubMed]

108. Akins, N.S.; Nielson, T.C.; Le, H.V. Inhibition of glycolysis and glutaminolysis: An emerging drug discovery approach to combat cancer. *Curr. Top. Med. Chem.* **2018**, *18*, 494–504. [CrossRef] [PubMed]
109. Abdel-Wahab, A.F.; Mahmoud, W.; Al-Harizy, R.M. Targeting glucose metabolism to suppress cancer progression: Prospective of anti-glycolytic cancer therapy. *Pharmacol. Res.* **2019**, *150*, 104511. [CrossRef] [PubMed]
110. Jin, L.; Alesi, G.; Kang, S. Glutaminolysis as a target for cancer therapy. *Oncogene* **2016**, *35*, 3619–3625. [CrossRef]
111. Liu, Y.; Shi, Y. Mitochondria as a target in cancer treatment. *MedComm* **2020**, *1*, 129–139. [CrossRef]
112. Ma, Y.; Temkin, S.M.; Hawkrigde, A.M.; Guo, C.; Wang, W.; Wang, X.-Y.; Fang, X. Fatty acid oxidation: An emerging facet of metabolic transformation in cancer. *Cancer Lett.* **2018**, *435*, 92–100. [CrossRef]
113. Xia, S.; Lin, R.; Jin, L.; Zhao, L.; Kang, H.-B.; Pan, Y.; Liu, S.; Qian, G.; Qian, Z.; Konstantakou, E. Prevention of dietary-fat-fueled ketogenesis attenuates BRAF V600E tumor growth. *Cell Metab.* **2017**, *25*, 358–373. [CrossRef]
114. De Feyter, H.M.; Behar, K.L.; Rao, J.U.; Madden-Hennessey, K.; Ip, K.L.; Hyder, F.; Drewes, L.R.; Geschwind, J.-F.; De Graaf, R.A.; Rothman, D.L. A ketogenic diet increases transport and oxidation of ketone bodies in RG2 and 9L gliomas without affecting tumor growth. *Neuro-Oncology* **2016**, *18*, 1079–1087. [CrossRef]

# Hippo Signaling Pathway in Gliomas

Konstantin Masliantsev<sup>1,2,3</sup>, Lucie Karayan-Tapon<sup>1,2,3</sup> and Pierre-Olivier Guichet<sup>1,2,3,\*</sup>

- <sup>1</sup> Inserm U1084, Laboratoire de Neurosciences Expérimentales et Cliniques, F-86073 Poitiers, France; konstantin.masliantsev@univ-poitiers.fr (K.M.); lucie.karayan-tapon@chu-poitiers.fr (L.K.-T.)  
<sup>2</sup> Université de Poitiers, F-86073 Poitiers, France  
<sup>3</sup> CHU de Poitiers, Laboratoire de Cancérologie Biologique, F-86022 Poitiers, France  
\* Correspondence: pierre-olivier.guichet@inserm.fr

**Abstract:** The Hippo signaling pathway is a highly conserved pathway involved in tissue development and regeneration that controls organ size through the regulation of cell proliferation and apoptosis. The core Hippo pathway is composed of a block of kinases, MST1/2 (Mammalian STE20-like protein kinase 1/2) and LATS1/2 (Large tumor suppressor 1/2), which inhibits nuclear translocation of YAP/TAZ (Yes-Associated Protein 1/Transcriptional co-activator with PDZ-binding motif) and its downstream association with the TEAD (TEA domain) family of transcription factors. This pathway was recently shown to be involved in tumorigenesis and metastasis in several cancers such as lung, breast, or colorectal cancers but is still poorly investigated in brain tumors. Gliomas are the most common and the most lethal primary brain tumors representing about 80% of malignant central nervous system neoplasms. Despite intensive clinical protocol, the prognosis for patients remains very poor due to systematic relapse and treatment failure. Growing evidence demonstrating the role of Hippo signaling in cancer biology and the lack of efficient treatments for malignant gliomas support the idea that this pathway could represent a potential target paving the way for alternative therapeutics. Based on recent advances in the Hippo pathway deciphering, the main goal of this review is to highlight the role of this pathway in gliomas by a state-of-the-art synthesis.

**Keywords:** gliomas; glioblastomas; hippo signaling pathway; MST1/2; LATS1/2; YAP/TAZ; TEADs



**Citation:** Masliantsev, K.; Karayan-Tapon, L.; Guichet, P.-O. Hippo Signaling Pathway in Gliomas. *Cells* **2021**, *10*, 184. <https://doi.org/10.3390/cells10010184>

Received: 16 December 2020  
Accepted: 15 January 2021  
Published: 18 January 2021

**Publisher's Note:** MDPI stays neutral with regard to jurisdictional claims in published maps and institutional affiliations.



**Copyright:** © 2021 by the authors. Licensee MDPI, Basel, Switzerland. This article is an open access article distributed under the terms and conditions of the Creative Commons Attribution (CC BY) license (<https://creativecommons.org/licenses/by/4.0/>).

## 1. Introduction

The Hippo pathway, initially discovered in *Drosophila*, is a well-conserved evolutionary signaling pathway involved in tissue development and regeneration that controls organ size by regulating cell proliferation and apoptosis [1,2]. Physiologically, the Hippo pathway acts as a tumor suppressor, and the mutations found in different pathway actors induce hyperplasia [3]. The core kinases of the Hippo signaling pathway in mammals is composed of MST1/2 (Mammalian STE20-like protein kinase 1/2) and LATS1/2 (Large tumor suppressor 1/2) corresponding to Hpo (Hippo) and Wts (Warts) in *Drosophila* [4] (Figure 1). The role of these kinases is to regulate negatively the transcription cofactors YAP (Yes-Associated Protein 1) and its ortholog TAZ (Transcriptional co-activator with PDZ-binding motif) corresponding to Yki (Yorkie) in the fly. After receiving activating upstream signals, the pathway is initiated by the activation of MST1/2 associated with SAV1 (Salvador). This complex stimulates by phosphorylation LATS1/2 and its cofactor MOB1, which in turn phosphorylates the transcription cofactors YAP/TAZ, leading to inhibition of its nuclear translocation. In fact, phosphorylated YAP/TAZ is sequestered in the cytoplasm by 14-3-3 protein. Furthermore, YAP/TAZ stability can be affected via its phosphorylation by the LATS/CK1( $\epsilon/\delta$ ) (Casein kinase 1  $\epsilon/\delta$ ) complex, inducing its ubiquitination by the recruitment of E3 ubiquitin ligase SCF- $\beta$ -TrCP (Skp1-Cul1-F-box  $\beta$ -transducin repeat-containing protein), leading to YAP/TAZ degradation by the proteasome. On the other hand, when the Hippo pathway is inactivated, the unphosphorylated YAP/TAZ complex is translocated to the nucleus, where it binds the TEAD (TEA domain)

transcription factor family. Indeed, YAP/TAZ association with TEAD transcription factors is essential to the control of several targeted genes such as MYC (MYC proto-oncogene bHLH transcription factor), BIRC5 (baculoviral IAP repeat containing 5), AXL (AXL receptor tyrosine kinase), CTGF (Connective Tissue Growth Factor), or CYR61 (Cysteine Rich Angiogenic Inducer 61) involved in cell proliferation and survival [5].

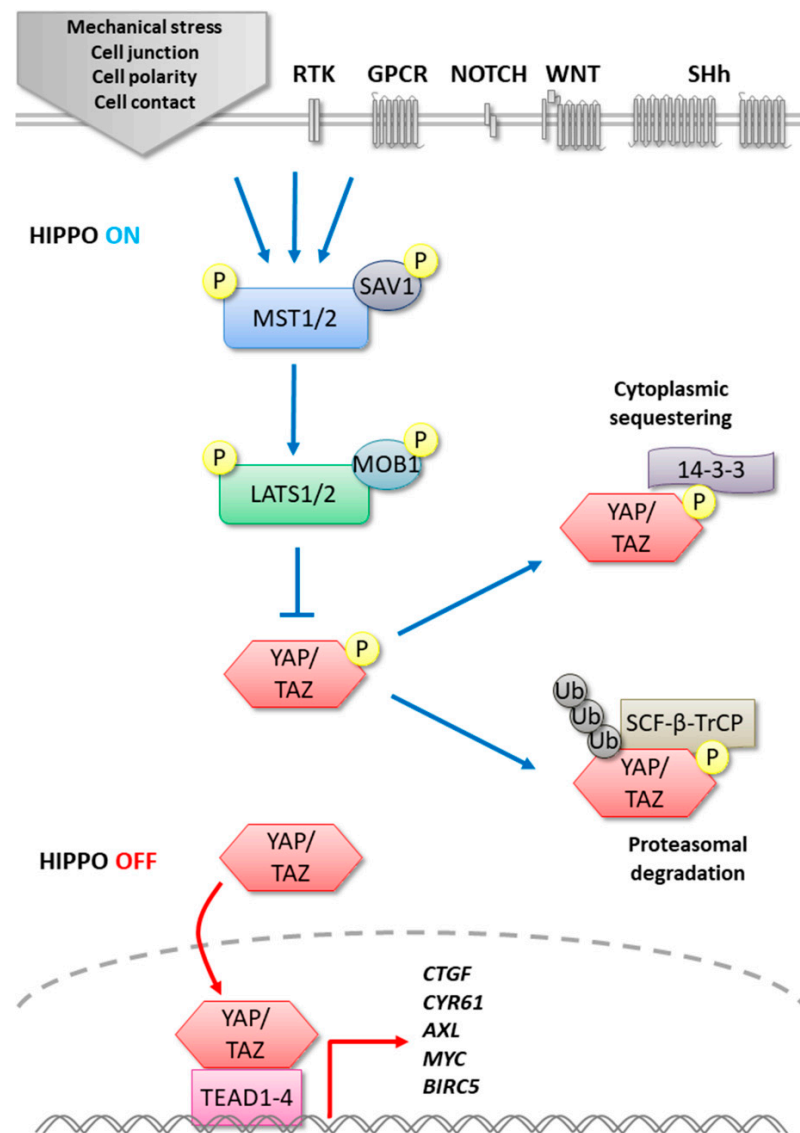


**Figure 1.** Canonical Hippo signaling pathway in mammals.

However, it has also been demonstrated that YAP/TAZ can act in association with other transcription factors, such as RUNX1/2 (RUNT-related transcription factor 1/2) and TBX5 (T-box transcription factor 5) [6,7]. Upstream Hippo pathway activators depend on cellular context. The protein NF2 (Neurofibromine 2), also called MERLIN, represents the most widely described Hippo signaling activator. This cytoskeletal protein is expressed by cell-cell junctions in epithelial cells and stabilizes the interaction between MST1/2 and LATS1/2 [8–10]. Other Hippo signaling modulators include DNA damages, contact inhibition, mechano-transduction, and cross-talks with RTKs (Receptor tyrosine kinases), GPCR (G-coupled receptors), WNT (Wingless-type), NOTCH, and SHh (Sonic hedgehog) signaling pathways [3,10–13].

The first studies investigating the biological role of Hippo signaling were performed using a gain of function approach overexpressing the transcription cofactor YAP. Hippo

pathway inactivation by mimicry approach has shown 3-time mass increasing in mice due to uncontrolled cell proliferation [2]. Interestingly, this effect was reversible after stopping YAP overexpression, suggesting the existence of a negative feedback loop between proliferation and apoptosis in Hippo signaling. Other studies have shown the crucial role of MST1/2 and SAV1 in post-natal hepatic growth restriction by maintaining hepatocytes in a quiescent state through YAP inhibition [11,14–16]. However, the involvement of the Hippo signaling pathway in organ size regulation is not universal. Indeed, YAP overexpression in small intestine cells has induced tissue hyperplasia and loss of terminal cell differentiation, yet without global organ size increasing in mice [17]. Similar results were obtained after inducing SAV1 loss in epithelial mouse cells [18]. These studies suggested the involvement of Hippo signaling in cell cycle regulation. In fact, Reddy et al. have shown that the Hippo pathway could lead to cell cycle arrest and cell differentiation during the development of the optic neuro-epithelium in *Drosophila* [19]. A key role of YAP has also been shown in eye development in several animal models like zebra-fish and mice, where its inhibition induces a strong retina differentiation defect [20]. Moreover, YAP expression is particularly restricted in mice embryos and some adult tissues. YAP is expressed mainly in the stem or progenitor cells in the skin and intestine, suggesting the involvement of Hippo signaling in cell differentiation and/or stem cell pool maintenance [3]. Indeed, it has been shown that Hippo pathway inhibition increases the pool of progenitor cells rather than differentiated cells in epithelial tissue. In the same way, this pathway is known to modulate stem cell proliferation in *Drosophila* intestine epithelium during its regeneration [21]. Cao et al. have shown that YAP overexpression or MST1/2 inhibition in chicken embryo neuro-epithelium increased the neuronal progenitor cell pool of a spinal cord [22]. In mice, Lian et al. have demonstrated that YAP acts in favor of cell pluripotency by inhibiting embryonic stem cell differentiation [23]. Taken together, these results underlined the crucial role of the Hippo signaling pathway during embryo development and adult tissue homeostasis in the balance between stem cells, progenitor cells and differentiated cells, particularly by controlling cell cycle, apoptosis and cell differentiation processes.

Since MST1/2 and LATS1/2 core constitute a regulatory part of the Hippo signaling associated with a tumor suppressor effect, the transcriptional cofactors YAP/TAZ associated with TEAD transcription factors represent the terminal effectors of this pathway and play a pro-oncogenic role. Recent studies have suggested that YAP and TAZ are essential to the initiation and proliferation of several solid tumors. Indeed, YAP/TAZ activation is involved in cell proliferation, mesenchymal transition, invasion, metastasis formation, as well as in cancer stem cell maintenance and chemoresistance. Constitutive activation of YAP/TAZ is currently known to be associated with aberrant cell proliferation by inducing the expression of several proteins involved in DNA synthesis, replication, reparation, and cell cycle control. For example, YAP/TAZ indirectly enforces cell cycle regulation by inducing other pro-oncogenic transcription factors such as c-MYC [24]. YAP/TAZ likewise contributes to cancer cell survival by the induction of anti-apoptotic proteins of the BCL-2 family, escaping not only mitochondrial apoptosis but also to alternative TNF- $\alpha$  and FAS ligands-induced apoptosis [2,7]. Moreover, YAP/TAZ contributes to anoikis resistance induced by the detachment of cells and substrate [25]. Several studies have shown that YAP/TAZ play a functional role in cancer stem cell maintenance and proliferation [26,27]. Indeed, it was shown that TAZ is crucial for tumor initiation, self-renewal, and metastatic capacity [28,29]. Moreover, YAP/TAZ promotes cancer cell population regeneration by maintaining autophagy basal level to avoid senescence and opposing cell death caused by excessive tumor autophagy [30–32]. At the microenvironmental level, YAP/TAZ contributes largely to the interaction between cancer cells and neighboring epithelial cells by inducing the secretion of angiogenic factors such as AREG (an EGF-like growth factor), CYR61, and CTGF. Furthermore, the secretion of chemotactic molecules induced by YAP/TAZ leads to immune tolerance through suppression of myeloid cells by T lymphocytes [33]. In cancer-associated fibroblasts, YAP and TAZ induce the production of pro-inflammatory interleukins and deposition of a rigid extracellular matrix that is a



main upstream inducer of YAP/TAZ, thereby creating positive feedback [34,35]. While all these data support the idea of a large contribution of the Hippo pathway in cancer initiation and progression, the role of the Hippo pathway is still relatively poorly investigated in gliomas.

Gliomas are the most common and the most lethal primary brain tumors and represent about 80% of malignant brain and central nervous system (CNS) tumors [36]. Initially, gliomas were classified according to their histological features, but this classification suffered from high intra/inter-observer variability, which does not sufficiently predict patient outcomes [37,38]. During the past decade, several studies have identified genomic alterations involved in glioma pathogenesis, thereby providing a more accurate stratification than classification based solely on histopathology [39,40]. These key molecular features, including isocitrate dehydrogenase 1 and 2 (IDH1/2) mutations and concurrent loss of both 1p and 19q chromosome arms (1p19q codeletion), have demonstrated their significance in clinical behavior, response to treatment, and patient outcome [41,42]. Indeed, mutations in IDH1/2 and 1p19q codeletion characterize the majority of low-grade gliomas (LGGs) and define a subtype associated with a favorable outcome. On the other hand, glioblastomas (GBMs) (WHO grade IV) are the most common and aggressive form of gliomas [43]. Surgical resection followed by concomitant radiochemotherapy constitutes the gold standard treatment for glioblastoma patients [44]. Despite this intensive clinical protocol, the prognosis for patients remains very poor, with a median survival of 15 months according to tumor invasiveness and radiochemoresistance [45]. Otherwise, treatment failure may also be explained by the persistence of a subpopulation of cancerous cells presenting stem cell capacity termed Glioma Stem Cells (GSCs) [46–48]. Since the last decade, the number of studies focused on the role of the Hippo signaling in gliomas is growing but remains relatively poor compared to other solid tumors. The following part of this review is dedicated to the description of the Hippo pathway core actors and their molecular alterations and deregulations, as well as their role reported in the glioma context.

## 2. MST1/2

MST1 is a serine/threonine kinase that plays an important role in organ size regulation by regulating cell apoptosis and proliferation. In response to apoptotic stimuli, MST1 is activated by dimerization-mediated trans-phosphorylation and caspase-mediated cleavage. Cleaved MST1 translocates to the nucleus and induces chromatin condensation by phosphorylation of different targets, but MST1 apoptotic signaling has yet to be completely defined. In 2014, Tang et al. showed that MST1 was negatively regulated by hMOB3 reported to be upregulated in GBM [49]. Indeed, hMOB3 can physically interact with MST1 and prevent MST1, inducing apoptotic signaling. Likewise, Chao et al. showed that MST1 downregulation in U87 and U251 GBM cultures promoted cell growth and proliferation and inhibited apoptosis [50]. Interestingly, MST1 did not affect YAP phosphorylation but was found to bind to AKT and negatively regulate AKT and mTOR activity. MST1 downregulation in glioma could also be induced through TGF- $\beta$  signaling [51]. Indeed, TGF- $\beta$  increases DNA methyl-transferase DNMT1 expression, which induces MST1 epigenetic repression in U87 and U251 cells, promoting proliferation, migration, and invasiveness. MST1 expression can also be directly repressed by miR-130b, which can target the MST1-adaptor protein SAV1 [52]. Moreover, miR-130b was found to be upregulated in both GBM tissues and cell lines, which is concordant with MST1 downregulation reported by Zhu et al. [53]. Functional MST1 overexpression has been marked by the induction of SIRT6 (Sirtuin 6), reducing glioma cell viability and colony formation and promoting apoptosis through the activation of FOXO3a transcription factor. Recently, Xu et al. demonstrated that CUL7 can be physically associated with MST1, promoting ubiquitin-mediated MST1 protein degradation, leading to the activation of the NF- $\kappa$ B signaling, a pathway known to be involved in glioma proliferation, migration, and invasion [54].

### 3. LATS1/2

LATS1 and LATS2 are serine/threonine kinases that are direct negative regulators of YAP, playing a pivotal role in organ size control and tumor suppression by restricting proliferation and promoting apoptosis. The human LATS1 gene is localized in chromosome 6q24–25, and its overexpression causes G2-M arrest through the inhibition of CDC2 kinase activity in breast cancer cell lines and significantly suppresses tumorigenicity by inducing apoptosis [55–57]. The LATS2 gene is localized on chromosome 13q11–12 and its overexpression has been shown to cause G1-S arrest through the inhibition of cyclin E/CDK2 in vitro and to suppress the tumorigenicity of NIH/v-ras-transformed cells [58–60]. In 2006, Jiang et al. showed that the promoter hypermethylation frequencies of LATS1 and LATS2 were 63.66% and 71.5%, respectively, in 88 astrocytomas compared to 10 non-tumoral brain samples presenting an unmethylated promoter profile [61]. LATS1/2 promoter hypermethylation was also found in U251 and SHS-44 GBM cell lines and was associated with correspondingly decreased mRNA expression in astrocytoma samples. These results were confirmed by Ji et al., who found that LATS1 mRNA and protein were significantly downregulated in glioma compared to non-tumoral brain tissues [62]. Interestingly, reduced LATS1 expression was negatively correlated with tumor grade in glioma patients and was associated with significantly shorter overall survival time. Moreover, forced expression of LATS1 in U251 glioma cells not only significantly suppressed cell growth, migration, and invasion but also retarded cell cycle progression from G2/M to G1 in vitro. LATS1/2 activity can also be downregulated indirectly by reducing the protein level of MOB1, an activator of LATS1/2 kinases. Indeed, Lignitto and Arcella et al. showed that the E3-ubiquitin ligase PRAJA2 was able to interact directly with MOB1, inducing its ubiquitylation and degradation by the proteasome [63]. Proteolysis of MOB1 by PRAJA2 attenuates the Hippo cascade and enhances the proliferation of U87MG glioblastoma cells. LATS1/2 degradation can be mediated by IKBKE (inhibitor of nuclear factor kappa-B kinase subunit epsilon), which was shown to be upregulated in glioma [64]. Liu et al. showed that IKBKE knockdown in U87 and U251 GBM cells dramatically elevated LATS1/2 and YAP phosphorylation on S127, suppressing YAP protein and its downstream targets such as AXL, c-MYC, and CYR61 [65]. Furthermore, the authors demonstrated that IKBKE did not alter mRNA levels of LATS1/2 in glioma cells but was directly bound to LATS1/2, and facilitated its polyubiquitin degradation. Recently, Liu et al. highlighted the mechanism by which Ca<sup>2+</sup> inhibits YAP/TAZ-mediated transcriptional program through the activation of LATS1/2 in the LN229 glioblastoma cell line [66]. The authors showed that the induced elevation of cytosolic Ca<sup>2+</sup> provoked actin cytoskeleton remodeling mediated by INF2, leading to new actin-filament assembly. Ca<sup>2+</sup> also induced PKC beta II translocation to the newly formed F-actin compartment, where activated, PKC beta II induced MST1/2 and LATS1/2 phosphorylation, silencing YAP/TAZ transcriptional program. LATS1 can be downregulated by miRNA in glioma. Indeed, bioinformatic analysis has predicted that LATS1 might be a potential target for miR-4262, which has been shown to be upregulated in glioma patient samples compared to normal tissue [67]. In vitro results have suggested that miR-4262 directly and negatively regulates LATS1 expression in U251 cells. Moreover, the authors suggested that overexpression of LATS1 could reverse the effects of miR-4262 suppressing cell proliferation and migration, as well as the production of MMP-2 and MMP-13. Recently, Ji et al. showed that PMEPA1a (prostate transmembrane protein, androgen-induced 1 a isoform) is strongly expressed in human glioma samples and that overexpression increases GBM cell lines growth. Indeed, PMEPA1 promotes LATS1 ubiquitination and degradation by the E3 ligase NEDD4 leading to the inhibition of Hippo pathway and activation of YAP target genes [68]. PMEPA1a was found to be highly expressed in human gliomas, and overexpression of the protein enhanced growth characteristics of glioma cell lines in vitro and in vivo. Although LATS1/2 are considered as tumor suppressors, RASSF1/LATS2-coupled promoter hypermethylation was found to be associated with better overall survival in glioma patients [69]. Hypermethylated promoter profiles were related to IDH mutation, yet not randomly in IDH-mutated gliomas,

because LATS2 promoter hypermethylation was more frequent in oligodendroglioma than in astrocytoma.

#### 4. YAP/TAZ

Although the role of Hippo signaling pathway in solid tumors is now well established, few studies have investigated its involvement in glioma. It has been shown that TAZ overexpression in GBM is associated with poorer patient prognosis [70–72]. Moreover, TAZ inhibition by shRNA in GSC lines reduces its tumorigenicity in SCID (Severe Combined Immunodeficiency) mice. On the other hand, TAZ overexpression in normal central nervous system stem cells and proneural GSCs was sufficient to induce its aberrant osteoblastic and chondrocyte differentiation by inducing mesenchymal transition in association with TEAD2 transcription factor. More recently, Yee et al. confirmed that GBM cell lines expressing a constitutively active form of TAZ induce tumors with mesenchymal features and extensive necrosis [73]. Moreover, the authors showed that necrosis involved neutrophil-triggered ferroptosis in hyperactivated TAZ GBM mouse model. TAZ could also be involved in GBM chemoresistance, as its overexpression in U87 and U251 cell lines was shown to reduce TMZ (Temolozomide) cytotoxicity by induction of MCL-1, leading to apoptosis resistance. Conversely, TAZ inhibition is able to potentialize TMZ effects in GBM lines [71]. Yang et al. have shown that TAZ promotes cell proliferation and tumor formation in U87 and LN229 cells by activating EGFR (Epidermal growth factor receptor) and its downstream AKT and ERK pathways through c-MYC [72]. TAZ can also be involved in radioresistance in GBM. Zhang et al. investigated long-term cellular responses of human GBM cells to ionizing radiation and showed that later response was associated with increased cellular senescence and TAZ inhibition [74]. Mechanistically, TAZ inhibition depends more on increased degradation mediated by the  $\beta$ -catenin destruction complex in the WNT pathway rather than on the canonical Hippo pathway. The authors also showed that TAZ silencing promoted radiation-induced senescence and growth arrest and concluded that TAZ inhibition is implicated in radiation-induced senescence and might improve GBM radiotherapy. TAZ overexpression can be explained by the upregulation of Histone deacetylase 9 (HDAC9) in glioblastoma patients as its knockdown decreases TAZ expression [75]. On the other hand, overexpressed TAZ or TAZ overexpression in HDAC9-knockdown cells abrogated the effects induced by HDAC9 silencing both in vitro and in vivo. Nawaz et al. identified a member of Polycomb Repressive Complex 1 (PRC1) called Chromobox homolog 7 (CBX7) that is downregulated in GBM due to its promoter hypermethylation [76]. Gene set enrichment analysis (GSEA) of CBX7 regulated genes identified CBX7 as a repressor of transcription co-activators YAP/TAZ. Moreover, exogenous expression of CBX7 repressed the YAP/TAZ-dependent transcription and downregulated CTGF, inducing cell death, cell proliferation inhibition, colony formation, migration, and invasion of the glioma cells. Recently, Escoll et al. showed that NRF2 (Nuclear factor (erythroid-derived 2)-like 2) transcription factor related to cellular defense against oxidative stress was involved in tumor progression by providing metabolic adaptation to tumorigenic demands and resistance to chemotherapeutics and that it induces TAZ expression promoting tumorigenesis in GBM [77]. Indeed, expression of the genes encoding NRF2 (NFE2L2) and TAZ (WWTR1) showed a positive correlation in 721 gliomas from TCGA database, which was confirmed by immunohistochemical tissue array analysis at the protein level. Moreover, overexpression and chemical activation or genetic knockdown of NRF2 showed an increase or a decrease of TAZ at both the transcript and protein level in GSC culture. In the same way, studies concerning YAP function have highlighted its involvement in GBM cell line proliferation in vitro and its association with tumor aggressivity [78,79]. Similarly to its ortholog TAZ, YAP in association with TEAD2 favors mesenchymal transition in U87 cells [80]. Moreover, YAP is able to induce WNT signaling transactivation, which plays a major role in GSC maintenance by modulating  $\beta$ -catenin activity through GSK3 $\beta$  regulation [81]. YAP also seems to closely interact with the PI3K/AKT/mTOR (Phosphatidylinositol 3-kinase/AKT serine/threonine kinase/Mechanistic target of rapamycin kinase) signaling pathway in

glioma. Liu et al. have shown a positive correlation between the phosphorylated form of mTOR and unphosphorylated YAP protein expression [78]. Moreover, the combination of p-mTOR and YAP expression was negatively related to the overall survival of patients and associated with a high grade of glioma. In the same way, Artinian et al. reported that YAP activation in glioma cell lines could be supported via mTOR through the inhibition of AMOTL2 (angiomotin-like 2) [82]. The angiomotin family members directly interact with YAP and the actin cytoskeleton, promoting YAP inactivation by cytoplasmic retention and leading to YAP phosphorylation by Hippo signaling [83]. Moreover, the authors showed the capacity of mTORC2 to inhibit AMOTL2 activity post-translationally by phosphorylation leading to increased YAP function. Indeed, this regulatory phosphorylation prevents AMOTL2 binding to YAP and stimulates YAP transcriptional program associated with enhanced growth and invasiveness in glioma cell lines. Liu et al. demonstrated that YAP1 expression participates to intratumoral heterogeneity in GBM [84]. Indeed, strong expression of YAP1 promotes tumorigenesis and clonal dominance accompanied by growth enhancement. Moreover, the authors suggested that cellular interaction during clonal dominance induces tumorigenic gene expression contributing to tumor growth. YAP/TAZ can be stabilized by actin-like 6A (ACTL6A), which has been shown to be up-regulated in glioma and associated with patient survival [85]. Ji et al. have shown by co-immunoprecipitation assays that ACTL6A can physically associate with YAP/TAZ and disrupts the interaction between YAP and SCF- $\beta$ -TrCP E3 ubiquitin ligase, preventing YAP protein degradation. Strong YAP expression was found to be associated with aggressive glioma molecular subtypes, i.e., IDHwt gliomas, as well as overall patient survival and progression-free survival [86]. More interestingly, YAP could be considered as an independent prognostic factor in lower-grade gliomas. Otherwise, at a cellular level, YAP could play a role in GSC proliferation and phenotype maintenance, notably by repressing the OLIG2 (Oligodendrocyte transcription factor 2) proneural factor. Vigneswaran et al. also showed that YAP/TAZ transcription cofactors regulate the expression of SOX2 (SRF-box transcription factor 2), C-MYC, and EGFR to create a feedforward loop to maintain the proliferation and survival of EGFR-amplified/mutant human GBM cells [87]. Another recent study demonstrated that YAP/TAZ are required for the oncogene-dependent transformation of primary neural cells, maintain GSC phenotype, prevent GSC differentiation, and control GBM cell plasticity showing the pivotal role of these transcriptional cofactors in glioma pathogenesis [88].

## 5. TEADs

Little is currently known concerning the role of the TEAD transcription factor family in glioma. In 2011, Bhat et al. showed that TEAD2 was involved mainly in glioblastoma mesenchymal transition [70]. Using chromatin immunoprecipitation, the authors showed that TEAD2, associated with TAZ, binds to a majority of mesenchymal gene promoters. In a murine model of glioma, the coexpression of TAZ, but not a mutated form of TAZ that lacks the TEAD binding site, with platelet-derived growth factor-B (PDGF-B) induced high-grade tumors with mesenchymal traits. The result was confirmed by Lu et al., showing that TEAD2 in association with YAP favored mesenchymal transition in U87 cells [80]. TEAD1 was found to contribute to EGFR effect amplification by inducing c-MYC expression, which fixes and activates EGFR promoter in U87 cells [89]. TEAD4 was shown to interact directly with TAZ and could be involved in cell proliferation, migration, and invasion as well as in mesenchymal transition in glioma cells [90]. In 2018, Tome-Garcia et al. performed a comparative analysis of chromatin accessibility using an assay for transposase accessible chromatin with sequencing (ATAC-seq) to highlight the differences between neural stem/progenitors and GSCs [91]. The authors identified the transcriptionally accessible regions that are specifically related to GSC migration and enriched for TEAD1/4 motifs. TEAD1 knockout by the CRISPR-Cas9 gene-editing technique showed a decrease of mesenchymal transition genes and cell migration *in vitro* and *in vivo*. Moreover, the authors

showed that TEAD1 directly regulates Aquaporin 4 (AQP4) and that the overexpression of both TEAD1 and AQP4 is sufficient to restore migratory defects in TEAD1-KO cells.

## 6. Hippo Signaling Pathway Signatures

Recently, Wang et al. deciphered the molecular alterations and regulations of 19 Hippo core genes in 9125 tumor samples, using multidimensional omic data from the TCGA [92]. The authors developed a YAP/TAZ transcriptional target signature of 22 genes, which has shown strong prognostic significance through several cancer types. More particularly, the expression of YAP and TAZ at the mRNA and protein level and the expression of YAP/TAZ target genes showed a significant association with worse survival in lower-grade gliomas. Furthermore, the YAP/TAZ target signature was positively correlated with tumor-infiltrating immune cell abundance: Macrophages, CD4 T-cells, neutrophil, and dendritic cells. Finally, the combined analyses of mutations, somatic copy number alterations, methylation, and expression data in lower-grade gliomas showed that the main alterations of Hippo core genes affected YAP/TAZ and TEAD3-4 principally at the expression level. More recently, Kim et al. evaluated the clinical significance of Hippo signaling in glioblastoma by generating a core gene expression signature from four different previously established silences of Hippo pathway (SOH) signatures in the stomach, liver, ovarian, and colorectal cancers [93]. A SOH and active Hippo pathway (AH) from the Hippo core gene expression signature was predicted and validated in glioblastoma samples from The Cancer Genome Atlas (TCGA) and the study of Gravendeel et al. [94]. In both GBM cohorts, the SOH signature was associated with lower overall survival compared to the AH signature. Gene expression and network analysis revealed that SOH subgroup is particularly enriched in genes linked to immune response, mesenchymal transition, and YAP transcriptional targets such as CTGF and CYR61. Interestingly, inhibitory immune checkpoint and M2-polarized macrophages genes were increased in the SOH group suggesting GBM resistance to host immune response. Finally, the SOH signature was strongly correlated with a bad prognosis of GBM patients and may be mediated by pro-tumoral immunosuppression. Taken together, these data show an association between the YAP/TAZ/TEADs Hippo pathway effectors and glioma patient outcome.

## 7. Therapeutic Perspectives

All the data presented above indicate the involvement of Hippo signaling in glioma pathophysiology and support the development of therapeutic avenues targeting this pathway (Figure 2). Despite intensive clinical protocols in the management of glioblastoma, i.e., surgery associated with concomitant radiochemotherapy, no curative treatments exist to date. Indeed, relapse ineluctably occurs, principally due to local invasiveness, therapeutic failure in radiation therapy, and drug response, as well as the existence of cancer stem cell population. In the past, several studies and clinical trials have investigated the potential of signaling-targeted therapy against EGFR, PDGFRA (Platelet derived growth factor receptor alpha), FGFR (Fibroblast growth factor receptor), VEGF (Vascular endothelial growth factor), STAT3 (Signal transducer and activator of transcription 3), and PI3K without significant improvement in overall patient survival. Increased evidence of Hippo pathway involvement in tumor progression and resistance to treatment has led to the recent development of specific inhibitors targeting YAP/TAZ-TEAD signal transduction. Currently, more than 50 drugs have been shown to inhibit YAP/TAZ activity. However, with the exception of verteporfin, none act directly on YAP/TAZ [95]. There are three main approaches to target the Hippo pathway (i) stimulating the LATS1/2-dependent inhibitory phosphorylation of YAP/TAZ (ii) directly inhibiting the TEAD transcription factors or disrupting the formation of the YAP/TAZ-TEAD complex, and (iii) targeting oncogenic proteins that are transcriptionally upregulated by Hippo effectors. Although stimulating the LATS1/2 kinases by upstream signals showed YAP/TAZ inhibition, these drugs are not specific and do not take into account existing signaling cross-talks leading to YAP/TAZ activation independently from the canonical Hippo pathway.

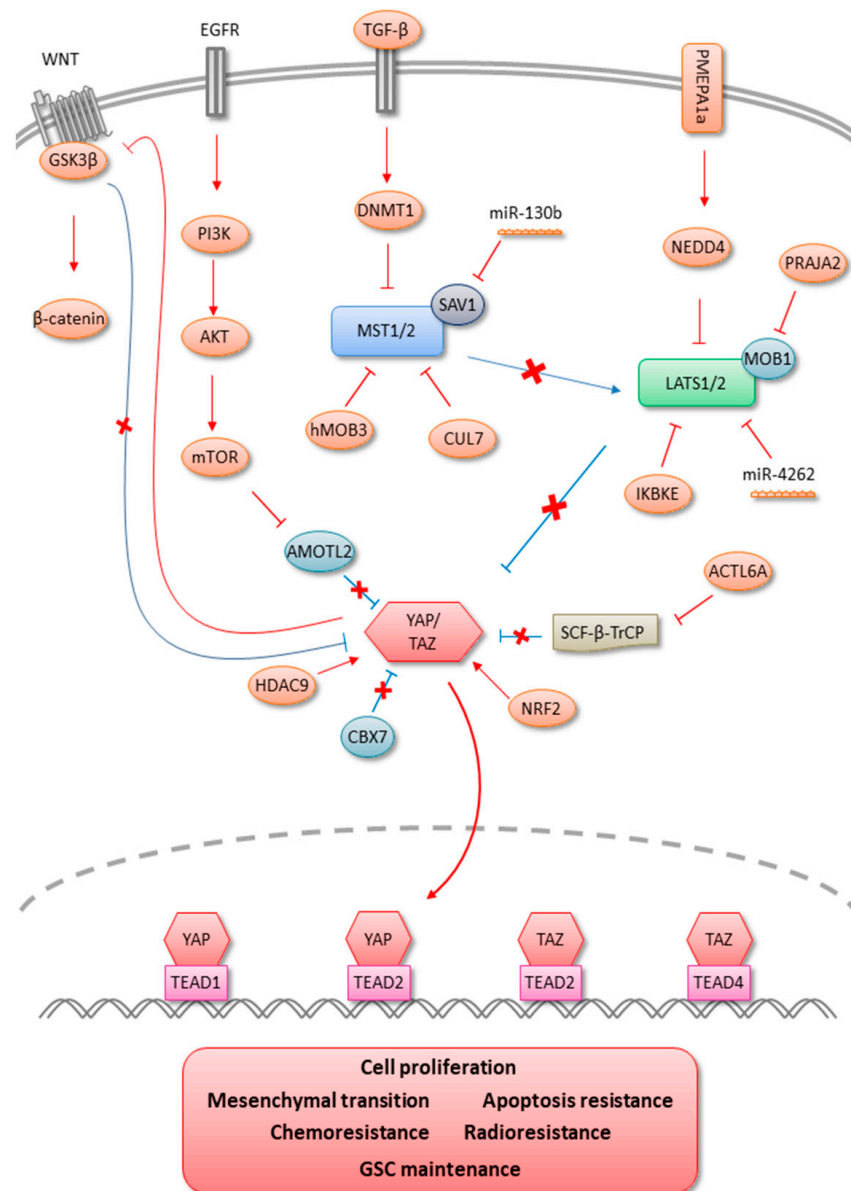


**Figure 2.** Modulations of Hippo signaling in gliomas.

On the other hand, YAP/TAZ-TEAD downstream oncogenic proteins appear difficult to target due to the number of regulated genes and their activation by other pathways [24,92]. Thus, the most efficient strategy to inhibit the hippo signaling pathway effectors seems to directly target YAP/TAZ-TEAD interaction. One of the first and most popular Hippo pathway inhibitors developed is a benzoporphyrin molecule called Verteporfin. This small inhibitor can directly bind YAP, disrupting its interaction with TEAD transcription factors [96]. However, the exact mechanism by which Verteporfin binds to YAP remains poorly understood, and some inhibitory effects appear to be YAP-independent [97,98]. Verteporfin induced apoptosis and suppressed expression of YAP/TAZ transcriptional targets of patient-derived EGFR-amplified/mutant GBM cells leading to better survival in an orthotopic xenograft model [87]. More interestingly, the administration of Visudyne, an FDA-approved form of Verteporfin, in patients with suspected or known recurrent GBM showed its absorption in GBM tumor cells, suggesting the use of Verteporfin as a promising therapeutic agent for EGFR-amplified/mutant GBM. Recently, a VGLL4-mimicking peptide, also known as Super-TDU, showed disruption of YAP-TEAD interaction and may represent a promising new therapeutic strategy against YAP-driven human cancers [99].

The VGLL family represents another TEAD co-regulator protein, which acts as a competitor of YAP and TAZ [5,100]. More recently, a fused tricyclic compound called CA3, and new molecules targeting hydrophobic pocket of TEADs identified by virtual screening approach were shown to inhibit YAP/TEADs transcriptional activity [101,102]. Growing evidence demonstrating the role of Hippo signaling in cancer biology and the lack of efficient treatments for glioblastoma support the idea that Hippo effectors YAP/TAZ-TEADs could represent potential targets paving the way for alternative therapeutics. Thus, it seems essential that the use of vectorized targeted drugs against the Hippo pathway alone or in combination with conventional GBM therapies, i.e., radiotherapy and Temozolomide, to assess their potentiation or synergistic effects should be proposed in the near future.

**Author Contributions:** Conceptualization, K.M., P.-O.G.; Writing—Original draft preparation, K.M.; Writing—Review and editing, K.M., L.K.-T., P.-O.G.; supervision, L.K.-T., P.-O.G. All authors have read and agreed to the published version of the manuscript.

**Funding:** The authors gratefully acknowledge the funding and support from “Ligue contre le cancer”.

**Institutional Review Board Statement:** Not applicable.

**Informed Consent Statement:** Not applicable.

**Acknowledgments:** The authors would like to thank Jeffrey Arsham, an American medical translator, for having reread and reviewed the original English-language text.

**Conflicts of Interest:** The authors declare no conflict of interest.

## References

- Huang, J.; Wu, S.; Barrera, J.; Matthews, K.; Pan, D. The Hippo signaling pathway coordinately regulates cell proliferation and apoptosis by inactivating Yorkie, the Drosophila Homolog of YAP. *Cell* **2005**, *122*, 421–434. [CrossRef] [PubMed]
- Dong, J.; Feldmann, G.; Huang, J.; Wu, S.; Zhang, N.; Comerford, S.A.; Gayyed, M.F.; Anders, R.A.; Maitra, A.; Pan, D. Elucidation of a universal size-control mechanism in Drosophila and mammals. *Cell* **2007**, *130*, 1120–1133. [CrossRef] [PubMed]
- Halder, G.; Johnson, R.L. Hippo signaling: Growth control and beyond. *Development* **2011**, *138*, 9–22. [CrossRef]
- Bae, S.J.; Luo, X. Activation mechanisms of the Hippo kinase signaling cascade. *Biosci. Rep.* **2018**, *38*. [CrossRef] [PubMed]
- Pobbati, A.V.; Hong, W. Emerging roles of TEAD transcription factors and its coactivators in cancers. *Cancer Biol. Ther.* **2013**, *14*, 390–398. [CrossRef] [PubMed]
- Murakami, M.; Nakagawa, M.; Olson, E.N.; Nakagawa, O. A WW domain protein TAZ is a critical coactivator for TBX5, a transcription factor implicated in Holt-Oram syndrome. *Proc. Natl. Acad. Sci. USA* **2005**, *102*, 18034–18039. [CrossRef] [PubMed]
- Rosenbluh, J.; Nijhawan, D.; Cox, A.G.; Li, X.; Neal, J.T.; Schafer, E.J.; Zack, T.I.; Wang, X.; Tsherniak, A.; Schinzel, A.C.; et al. beta-Catenin-driven cancers require a YAP1 transcriptional complex for survival and tumorigenesis. *Cell* **2012**, *151*, 1457–1473. [CrossRef]
- Lallemand, D.; Curto, M.; Saotome, I.; Giovannini, M.; McClatchey, A.I. NF2 deficiency promotes tumorigenesis and metastasis by destabilizing adherens junctions. *Genes Dev.* **2003**, *17*, 1090–1100. [CrossRef]
- Yin, F.; Yu, J.; Zheng, Y.; Chen, Q.; Zhang, N.; Pan, D. Spatial organization of Hippo signaling at the plasma membrane mediated by the tumor suppressor Merlin/NF2. *Cell* **2013**, *154*, 1342–1355. [CrossRef]
- Yu, F.X.; Guan, K.L. The Hippo pathway: Regulators and regulations. *Genes Dev.* **2013**, *27*, 355–371. [CrossRef]
- Lee, K.P.; Lee, J.H.; Kim, T.S.; Kim, T.H.; Park, H.D.; Byun, J.S.; Kim, M.C.; Jeong, W.I.; Calvisi, D.F.; Kim, J.M.; et al. The Hippo-Salvador pathway restrains hepatic oval cell proliferation, liver size, and liver tumorigenesis. *Proc. Natl. Acad. Sci. USA* **2010**, *107*, 8248–8253. [CrossRef] [PubMed]
- Meng, Z.; Moroishi, T.; Guan, K.L. Mechanisms of Hippo pathway regulation. *Genes Dev.* **2016**, *30*, 1–17. [CrossRef] [PubMed]
- Ouyang, T.; Meng, W.; Li, M.; Hong, T.; Zhang, N. Recent Advances of the Hippo/YAP Signaling Pathway in Brain Development and Glioma. *Cell. Mol. Neurobiol.* **2020**, *40*, 495–510. [CrossRef] [PubMed]
- Lu, L.; Li, Y.; Kim, S.M.; Bossuyt, W.; Liu, P.; Qiu, Q.; Wang, Y.; Halder, G.; Finegold, M.J.; Lee, J.S.; et al. Hippo signaling is a potent in vivo growth and tumor suppressor pathway in the mammalian liver. *Proc. Natl. Acad. Sci. USA* **2010**, *107*, 1437–1442. [CrossRef]
- Song, H.; Mak, K.K.; Topol, L.; Yun, K.; Hu, J.; Garrett, L.; Chen, Y.; Park, O.; Chang, J.; Simpson, R.M.; et al. Mammalian Mst1 and Mst2 kinases play essential roles in organ size control and tumor suppression. *Proc. Natl. Acad. Sci. USA* **2010**, *107*, 1431–1436. [CrossRef]
- Zhou, D.; Conrad, C.; Xia, F.; Park, J.S.; Payer, B.; Yin, Y.; Lauwers, G.Y.; Thasler, W.; Lee, J.T.; Avruch, J.; et al. Mst1 and Mst2 maintain hepatocyte quiescence and suppress hepatocellular carcinoma development through inactivation of the Yap1 oncogene. *Cancer Cell* **2009**, *16*, 425–438. [CrossRef]

17. Camargo, F.D.; Gokhale, S.; Johnnidis, J.B.; Fu, D.; Bell, G.W.; Jaenisch, R.; Brummelkamp, T.R. YAP1 increases organ size and expands undifferentiated progenitor cells. *Curr. Biol. CB* **2007**, *17*, 2054–2060. [CrossRef]
18. Lee, J.H.; Kim, T.S.; Yang, T.H.; Koo, B.K.; Oh, S.P.; Lee, K.P.; Oh, H.J.; Lee, S.H.; Kong, Y.Y.; Kim, J.M.; et al. A crucial role of WW45 in developing epithelial tissues in the mouse. *EMBO J.* **2008**, *27*, 1231–1242. [CrossRef]
19. Reddy, B.V.; Rauskolb, C.; Irvine, K.D. Influence of fat-hippo and notch signaling on the proliferation and differentiation of *Drosophila* optic neuroepithelia. *Development* **2010**, *137*, 2397–2408. [CrossRef]
20. Zhu, J.Y.; Lin, S.; Ye, J. YAP and TAZ, the conductors that orchestrate eye development, homeostasis, and disease. *J. Cell. physiol.* **2018**, 10.1002/jcp.26870. [CrossRef]
21. Staley, B.K.; Irvine, K.D. Warts and Yorkie mediate intestinal regeneration by influencing stem cell proliferation. *Curr. Biol. CB* **2010**, *20*, 1580–1587. [CrossRef] [PubMed]
22. Cao, X.; Pfaff, S.L.; Gage, F.H. YAP regulates neural progenitor cell number via the TEA domain transcription factor. *Genes Dev.* **2008**, *22*, 3320–3334. [CrossRef] [PubMed]
23. Lian, I.; Kim, J.; Okazawa, H.; Zhao, J.; Zhao, B.; Yu, J.; Chinnaiyan, A.; Israel, M.A.; Goldstein, L.S.; Abujarour, R.; et al. The role of YAP transcription coactivator in regulating stem cell self-renewal and differentiation. *Genes Dev.* **2010**, *24*, 1106–1118. [CrossRef] [PubMed]
24. Zanconato, F.; Cordenonsi, M.; Piccolo, S. YAP/TAZ at the Roots of Cancer. *Cancer Cell* **2016**, *29*, 783–803. [CrossRef]
25. Zhao, B.; Li, L.; Wang, L.; Wang, C.Y.; Yu, J.; Guan, K.L. Cell detachment activates the Hippo pathway via cytoskeleton reorganization to induce anoikis. *Genes Dev.* **2012**, *26*, 54–68. [CrossRef]
26. Barry, E.R.; Camargo, F.D. The Hippo superhighway: Signaling crossroads converging on the Hippo/Yap pathway in stem cells and development. *Curr. Opin. Cell Biol.* **2013**, *25*, 247–253. [CrossRef]
27. Barron, D.A.; Kagey, J.D. The role of the Hippo pathway in human disease and tumorigenesis. *Clin. Transl. Med.* **2014**, *3*, 25. [CrossRef]
28. Bartucci, M.; Dattilo, R.; Moriconi, C.; Pagliuca, A.; Mottolose, M.; Federici, G.; Benedetto, A.D.; Todaro, M.; Stassi, G.; Sperati, F.; et al. TAZ is required for metastatic activity and chemoresistance of breast cancer stem cells. *Oncogene* **2015**, *34*, 681–690. [CrossRef]
29. Cordenonsi, M.; Zanconato, F.; Azzolin, L.; Forcato, M.; Rosato, A.; Frasson, C.; Inui, M.; Montagner, M.; Parenti, A.R.; Poletti, A.; et al. The Hippo transducer TAZ confers cancer stem cell-related traits on breast cancer cells. *Cell* **2011**, *147*, 759–772. [CrossRef]
30. Garcia-Prat, L.; Martinez-Vicente, M.; Perdiguero, E.; Ortet, L.; Rodriguez-Ubreva, J.; Rebollo, E.; Ruiz-Bonilla, V.; Gutarra, S.; Ballestar, E.; Serrano, A.L.; et al. Autophagy maintains stemness by preventing senescence. *Nature* **2016**, *529*, 37–42. [CrossRef]
31. Liang, N.; Zhang, C.; Dill, P.; Panasyuk, G.; Pion, D.; Koka, V.; Gallazzini, M.; Olson, E.N.; Lam, H.; Henske, E.P.; et al. Regulation of YAP by mTOR and autophagy reveals a therapeutic target of tuberous sclerosis complex. *J. Exp. Med.* **2014**, *211*, 2249–2263. [CrossRef] [PubMed]
32. Song, Q.; Mao, B.; Cheng, J.; Gao, Y.; Jiang, K.; Chen, J.; Yuan, Z.; Meng, S. YAP enhances autophagic flux to promote breast cancer cell survival in response to nutrient deprivation. *PLoS ONE* **2015**, *10*, e0120790. [CrossRef] [PubMed]
33. Wang, G.; Lu, X.; Dey, P.; Deng, P.; Wu, C.C.; Jiang, S.; Fang, Z.; Zhao, K.; Konaparthi, R.; Hua, S.; et al. Targeting YAP-Dependent MDSC Infiltration Impairs Tumor Progression. *Cancer Discov.* **2016**, *6*, 80–95. [CrossRef]
34. Calvo, F.; Ege, N.; Grande-Garcia, A.; Hooper, S.; Jenkins, R.P.; Chaudhry, S.I.; Harrington, K.; Williamson, P.; Moeendarbary, E.; Charras, G.; et al. Mechanotransduction and YAP-dependent matrix remodelling is required for the generation and maintenance of cancer-associated fibroblasts. *Nat. Cell Biol.* **2013**, *15*, 637–646. [CrossRef] [PubMed]
35. Halder, G.; Dupont, S.; Piccolo, S. Transduction of mechanical and cytoskeletal cues by YAP and TAZ. *Nature reviews. Mol. Cell Biol.* **2012**, *13*, 591–600. [CrossRef]
36. Ostrom, Q.T.; Gittleman, H.; Stetson, L.; Virk, S.M.; Barnholtz-Sloan, J.S. Epidemiology of gliomas. *Cancer Treat. Res.* **2015**, *163*, 1–14. [CrossRef] [PubMed]
37. Coons, S.W.; Johnson, P.C.; Scheithauer, B.W.; Yates, A.J.; Pearl, D.K. Improving diagnostic accuracy and interobserver concordance in the classification and grading of primary gliomas. *Cancer* **1997**, *79*, 1381–1393. [CrossRef]
38. Cancer Genome Atlas Research, N.; Brat, D.J.; Verhaak, R.G.; Aldape, K.D.; Yung, W.K.; Salama, S.R.; Cooper, L.A.; Rheinbay, E.; Miller, C.R.; Vitucci, M.; et al. Comprehensive, Integrative Genomic Analysis of Diffuse Lower-Grade Gliomas. *N. Engl. J. Med.* **2015**, *372*, 2481–2498. [CrossRef]
39. Yan, H.; Parsons, D.W.; Jin, G.; McLendon, R.; Rasheed, B.A.; Yuan, W.; Kos, I.; Batinic-Haberle, I.; Jones, S.; Riggins, G.J.; et al. IDH1 and IDH2 mutations in gliomas. *N. Engl. J. Med.* **2009**, *360*, 765–773. [CrossRef]
40. Eckel-Passow, J.E.; Lachance, D.H.; Molinaro, A.M.; Walsh, K.M.; Decker, P.A.; Sicotte, H.; Pekmezci, M.; Rice, T.; Kosel, M.L.; Smirnov, I.V.; et al. Glioma Groups Based on 1p/19q, IDH, and TERT Promoter Mutations in Tumors. *N. Engl. J. Med.* **2015**, *372*, 2499–2508. [CrossRef]
41. van den Bent, M.J.; Mellinghoff, I.K.; Bindra, R.S. Gray Areas in the Gray Matter: IDH1/2 Mutations in Glioma. *American Society of Clinical Oncology educational book. Am. Soc. Clin. Oncol. Annu. Meet.* **2020**, *40*, 1–8. [CrossRef]
42. Venneti, S.; Huse, J.T. The evolving molecular genetics of low-grade glioma. *Adv. Anat. Pathol.* **2015**, *22*, 94–101. [CrossRef] [PubMed]






43. Louis, D.N.; Perry, A.; Reifenberger, G.; von Deimling, A.; Figarella-Branger, D.; Cavenee, W.K.; Ohgaki, H.; Wiestler, O.D.; Kleihues, P.; Ellison, D.W. The 2016 World Health Organization Classification of Tumors of the Central Nervous System: A summary. *Acta Neuropathol.* **2016**, *131*, 803–820. [CrossRef] [PubMed]
44. Stupp, R.; Mason, W.P.; van den Bent, M.J.; Weller, M.; Fisher, B.; Taphoorn, M.J.; Belanger, K.; Brandes, A.A.; Marosi, C.; Bogdahn, U.; et al. Radiotherapy plus concomitant and adjuvant temozolomide for glioblastoma. *N. Engl. J. Med.* **2005**, *352*, 987–996. [CrossRef]
45. Ostrom, Q.T.; Bauchet, L.; Davis, F.G.; Deltour, I.; Fisher, J.L.; Langer, C.E.; Pekmezci, M.; Schwartzbaum, J.A.; Turner, M.C.; Walsh, K.M.; et al. The epidemiology of glioma in adults: A “state of the science” review. *J. Pediatr. Oncol. Nurs.* **2014**, *16*, 896–913. [CrossRef]
46. Galli, R.; Binda, E.; Orfanelli, U.; Cipelletti, B.; Gritti, A.; De Vitis, S.; Fiocco, R.; Foroni, C.; Dimeco, F.; Vescovi, A. Isolation and characterization of tumorigenic, stem-like neural precursors from human glioblastoma. *Cancer Res.* **2004**, *64*, 7011–7021. [CrossRef]
47. Singh, S.K.; Hawkins, C.; Clarke, I.D.; Squire, J.A.; Bayani, J.; Hide, T.; Henkelman, R.M.; Cusimano, M.D.; Dirks, P.B. Identification of human brain tumour initiating cells. *Nature* **2004**, *432*, 396–401. [CrossRef]
48. Yuan, X.; Curtin, J.; Xiong, Y.; Liu, G.; Waschmann-Hogiu, S.; Farkas, D.L.; Black, K.L.; Yu, J.S. Isolation of cancer stem cells from adult glioblastoma multiforme. *Oncogene* **2004**, *23*, 9392–9400. [CrossRef]
49. Tang, F.; Zhang, L.; Xue, G.; Hynx, D.; Wang, Y.; Cron, P.D.; Hundsrucker, C.; Hergovich, A.; Frank, S.; Hemmings, B.A.; et al. hMOB3 modulates MST1 apoptotic signaling and supports tumor growth in glioblastoma multiforme. *Cancer Res.* **2014**, *74*, 3779–3789. [CrossRef]
50. Chao, Y.; Wang, Y.; Liu, X.; Ma, P.; Shi, Y.; Gao, J.; Shi, Q.; Hu, J.; Yu, R.; Zhou, X. Mst1 regulates glioma cell proliferation via the AKT/mTOR signaling pathway. *J. Neuro-Oncol.* **2015**, *121*, 279–288. [CrossRef]
51. Guo, Z.; Li, G.; Bian, E.; Ma, C.C.; Wan, J.; Zhao, B. TGF-beta-mediated repression of MST1 by DNMT1 promotes glioma malignancy. *Biomed. Pharmacother.* **2017**, *94*, 774–780. [CrossRef] [PubMed]
52. Zhu, G.; Wang, Y.; Mijiti, M.; Wang, Z.; Wu, P.F.; Jiafu, D. Upregulation of miR-130b enhances stem cell-like phenotype in glioblastoma by inactivating the Hippo signaling pathway. *Biochem. Biophys. Res. Commun.* **2015**, *465*, 194–199. [CrossRef] [PubMed]
53. Zhu, D.; Sun, C.; Qian, X. MST1 suppresses viability and promotes apoptosis of glioma cells via upregulating SIRT6 expression. *J. Integr. Neurosci.* **2019**, *18*, 117–126. [CrossRef] [PubMed]
54. Xu, J.; Zhang, Z.; Qian, M.; Wang, S.; Qiu, W.; Chen, Z.; Sun, Z.; Xiong, Y.; Wang, C.; Sun, X.; et al. Cullin-7 (CUL7) is overexpressed in glioma cells and promotes tumorigenesis via NF-kappaB activation. *J. Exp. Clin. Cancer Res.* **2020**, *39*, 59. [CrossRef] [PubMed]
55. Nishiyama, Y.; Hirota, T.; Morisaki, T.; Hara, T.; Marumoto, T.; Iida, S.; Makino, K.; Yamamoto, H.; Hiraoka, T.; Kitamura, N.; et al. A human homolog of Drosophila warts tumor suppressor, h-warts, localized to mitotic apparatus and specifically phosphorylated during mitosis. *FEBS Lett.* **1999**, *459*, 159–165. [CrossRef]
56. Yang, X.; Li, D.M.; Chen, W.; Xu, T. Human homologue of Drosophila lats, LATS1, negatively regulate growth by inducing G(2)/M arrest or apoptosis. *Oncogene* **2001**, *20*, 6516–6523. [CrossRef]
57. Xia, H.; Qi, H.; Li, Y.; Pei, J.; Barton, J.; Blackstad, M.; Xu, T.; Tao, W. LATS1 tumor suppressor regulates G2/M transition and apoptosis. *Oncogene* **2002**, *21*, 1233–1241. [CrossRef]
58. Yabuta, N.; Fujii, T.; Copeland, N.G.; Gilbert, D.J.; Jenkins, N.A.; Nishiguchi, H.; Endo, Y.; Toji, S.; Tanaka, H.; Nishimune, Y.; et al. Structure, expression, and chromosome mapping of LATS2, a mammalian homologue of the Drosophila tumor suppressor gene lats/warts. *Genomics* **2000**, *63*, 263–270. [CrossRef]
59. Hori, T.; Takaori-Kondo, A.; Kamikubo, Y.; Uchiyama, T. Molecular cloning of a novel human protein kinase, kpm, that is homologous to warts/lats, a Drosophila tumor suppressor. *Oncogene* **2000**, *19*, 3101–3109. [CrossRef]
60. Li, Y.; Pei, J.; Xia, H.; Ke, H.; Wang, H.; Tao, W. Lats2, a putative tumor suppressor, inhibits G1/S transition. *Oncogene* **2003**, *22*, 4398–4405. [CrossRef]
61. Jiang, Z.; Li, X.; Hu, J.; Zhou, W.; Jiang, Y.; Li, G.; Lu, D. Promoter hypermethylation-mediated down-regulation of LATS1 and LATS2 in human astrocytoma. *Neurosci. Res.* **2006**, *56*, 450–458. [CrossRef] [PubMed]
62. Ji, T.; Liu, D.; Shao, W.; Yang, W.; Wu, H.; Bian, X. Decreased expression of LATS1 is correlated with the progression and prognosis of glioma. *J. Exp. Clin. Cancer Res.* **2012**, *31*, 67. [CrossRef] [PubMed]
63. Lignitto, L.; Arcella, A.; Sepe, M.; Rinaldi, L.; Delle Donne, R.; Gallo, A.; Stefan, E.; Bachmann, V.A.; Oliva, M.A.; Tiziana Storlazzi, C.; et al. Proteolysis of MOB1 by the ubiquitin ligase praja2 attenuates Hippo signalling and supports glioblastoma growth. *Nat. Commun.* **2013**, *4*, 1822. [CrossRef] [PubMed]
64. Guan, H.; Zhang, H.; Cai, J.; Wu, J.; Yuan, J.; Li, J.; Huang, Z.; Li, M. IKBKE is over-expressed in glioma and contributes to resistance of glioma cells to apoptosis via activating NF-kappaB. *J. Pathol.* **2011**, *223*, 436–445. [CrossRef]
65. Liu, Y.; Lu, J.; Zhang, Z.; Zhu, L.; Dong, S.; Guo, G.; Li, R.; Nan, Y.; Yu, K.; Zhong, Y.; et al. Amlexanox, a selective inhibitor of IKBKE, generates anti-tumoral effects by disrupting the Hippo pathway in human glioblastoma cell lines. *Cell Death Dis.* **2017**, *8*, e3022. [CrossRef]
66. Liu, Z.; Wei, Y.; Zhang, L.; Yee, P.P.; Johnson, M.; Zhang, X.; Gulley, M.; Atkinson, J.M.; Trebak, M.; Wang, H.G.; et al. Induction of store-operated calcium entry (SOCE) suppresses glioblastoma growth by inhibiting the Hippo pathway transcriptional coactivators YAP/TAZ. *Oncogene* **2019**, *38*, 120–139. [CrossRef]

67. Liu, C.; Ma, T.; Jiang, T.; Jia, G.; Yang, C.; Peng, Y.; Qian, Y.; Wang, R.; Wang, S. Abnormal increase of miR-4262 promotes cell proliferation and migration by targeting large tumor suppressor 1 in gliomas. *Pathol. Res. Pract.* **2020**, *216*, 152778. [CrossRef]
68. Ji, J.; Ding, K.; Luo, T.; Xu, R.; Zhang, X.; Huang, B.; Chen, A.; Zhang, D.; Miletic, H.; Bjerkvig, R.; et al. PMEPA1 isoform a drives progression of glioblastoma by promoting protein degradation of the Hippo pathway kinase LATS1. *Oncogene* **2020**, *39*, 1125–1139. [CrossRef]
69. Levallet, G.; Creveuil, C.; Bekaert, L.; Peres, E.; Planchard, G.; Lecot-Cotigny, S.; Guillamo, J.S.; Emery, E.; Zalzman, G.; Lechapt-Zalzman, E. Promoter Hypermethylation of Genes Encoding for RASSF/Hippo Pathway Members Reveals Specific Alteration Pattern in Diffuse Gliomas. *JMD* **2019**, *21*, 695–704. [CrossRef]
70. Bhat, K.P.; Salazar, K.L.; Balasubramanian, V.; Wani, K.; Heathcock, L.; Hollingsworth, F.; James, J.D.; Gumin, J.; Diefes, K.L.; Kim, S.H.; et al. The transcriptional coactivator TAZ regulates mesenchymal differentiation in malignant glioma. *Genes Dev.* **2011**, *25*, 2594–2609. [CrossRef]
71. Tian, T.; Li, A.; Lu, H.; Luo, R.; Zhang, M.; Li, Z. TAZ promotes temozolomide resistance by upregulating MCL-1 in human glioma cells. *Biochem. Biophys. Res. Commun.* **2015**, *463*, 638–643. [CrossRef]
72. Yang, R.; Wu, Y.; Zou, J.; Zhou, J.; Wang, M.; Hao, X.; Cui, H. The Hippo transducer TAZ promotes cell proliferation and tumor formation of glioblastoma cells through EGFR pathway. *Oncotarget* **2016**, *7*, 36255–36265. [CrossRef]
73. Yee, P.P.; Wei, Y.; Kim, S.Y.; Lu, T.; Chih, S.Y.; Lawson, C.; Tang, M.; Liu, Z.; Anderson, B.; Thamburaj, K.; et al. Neutrophil-induced ferroptosis promotes tumor necrosis in glioblastoma progression. *Nat. Commun.* **2020**, *11*, 5424. [CrossRef]
74. Zhang, L.; Cheng, F.; Wei, Y.; Zhang, L.; Guo, D.; Wang, B.; Li, W. Inhibition of TAZ contributes radiation-induced senescence and growth arrest in glioma cells. *Oncogene* **2019**, *38*, 2788–2799. [CrossRef]
75. Yang, R.; Wu, Y.; Wang, M.; Sun, Z.; Zou, J.; Zhang, Y.; Cui, H. HDAC9 promotes glioblastoma growth via TAZ-mediated EGFR pathway activation. *Oncotarget* **2015**, *6*, 7644–7656. [CrossRef]
76. Nawaz, Z.; Patil, V.; Arora, A.; Hegde, A.S.; Arivazhagan, A.; Santosh, V.; Somasundaram, K. Cbx7 is epigenetically silenced in glioblastoma and inhibits cell migration by targeting YAP/TAZ-dependent transcription. *Sci. Rep.* **2016**, *6*, 27753. [CrossRef]
77. Escoll, M.; Lastra, D.; Pajares, M.; Robledinos-Anton, N.; Rojo, A.I.; Fernandez-Gines, R.; Mendiola, M.; Martinez-Marin, V.; Esteban, I.; Lopez-Larrubia, P.; et al. Transcription factor NRF2 uses the Hippo pathway effector TAZ to induce tumorigenesis in glioblastomas. *Redox Biol.* **2020**, *30*, 101425. [CrossRef]
78. Liu, M.; Lin, Y.; Zhang, X.C.; Tan, Y.H.; Yao, Y.L.; Tan, J.; Zhang, X.; Cui, Y.H.; Liu, X.; Wang, Y.; et al. Phosphorylated mTOR and YAP serve as prognostic markers and therapeutic targets in gliomas. *Lab. Investig.* **2017**, *97*, 1354–1363. [CrossRef]
79. Orr, B.A.; Bai, H.; Oda, Y.; Jain, D.; Anders, R.A.; Eberhart, C.G. Yes-associated protein 1 is widely expressed in human brain tumors and promotes glioblastoma growth. *J. Neuropathol. Exp. Neurol.* **2011**, *70*, 568–577. [CrossRef] [PubMed]
80. Lu, J.; Yang, Y.; Guo, G.; Liu, Y.; Zhang, Z.; Dong, S.; Nan, Y.; Zhao, Z.; Zhong, Y.; Huang, Q. IKBKE regulates cell proliferation and epithelial-mesenchymal transition of human malignant glioma via the Hippo pathway. *Oncotarget* **2017**, *8*, 49502–49514. [CrossRef] [PubMed]
81. Wang, Y.; Pan, P.; Wang, Z.; Zhang, Y.; Xie, P.; Geng, D.; Jiang, Y.; Yu, R.; Zhou, X. beta-catenin-mediated YAP signaling promotes human glioma growth. *J. Exp. Clin. Cancer Res. Cr* **2017**, *36*, 136. [CrossRef] [PubMed]
82. Artinian, N.; Cloninger, C.; Holmes, B.; Benavides-Serrato, A.; Bashir, T.; Gera, J. Phosphorylation of the Hippo Pathway Component AMOTL2 by the mTORC2 Kinase Promotes YAP Signaling, Resulting in Enhanced Glioblastoma Growth and Invasiveness. *J. Biol. Chem.* **2015**, *290*, 19387–19401. [CrossRef] [PubMed]
83. Zhao, B.; Li, L.; Lu, Q.; Wang, L.H.; Liu, C.Y.; Lei, Q.; Guan, K.L. Angiomotin is a novel Hippo pathway component that inhibits YAP oncoprotein. *Genes Dev.* **2011**, *25*, 51–63. [CrossRef]
84. Liu, Z.; Yee, P.P.; Wei, Y.; Liu, Z.; Kawasawa, Y.I.; Li, W. Differential YAP expression in glioma cells induces cell competition and promotes tumorigenesis. *J. Cell Sci.* **2019**, *132*. [CrossRef]
85. Ji, J.; Xu, R.; Zhang, X.; Han, M.; Xu, Y.; Wei, Y.; Ding, K.; Wang, S.; Bin, H.; Chen, A.; et al. Actin like-6A promotes glioma progression through stabilization of transcriptional regulators YAP/TAZ. *Cell Death Dis.* **2018**, *9*, 517. [CrossRef]
86. Guichet, P.O.; Masliantsev, K.; Tachon, G.; Petropoulos, C.; Godet, J.; Larrieu, D.; Milin, S.; Wager, M.; Karayan-Tapon, L. Fatal correlation between YAP1 expression and glioma aggressiveness: Clinical and molecular evidence. *J. Pathol.* **2018**, *246*, 205–216. [CrossRef]
87. Vigneswaran, K.; Boyd, N.H.; Oh, S.Y.; Lallani, S.; Boucher, A.; Neill, S.G.; Olson, J.J.; Read, R.D. YAP/TAZ transcriptional co-activators create therapeutic vulnerability to verteporfin in EGFR mutant glioblastoma. *Clin. Cancer Res.* **2020**. [CrossRef]
88. Castellan, M.; Guarnieri, A.; Fujimura, A.; Zanconato, F.; Battilana, G.; Panciera, T.; Sladitschek, H.L.; Contessotto, P.; Citron, A.; Grilli, A.; et al. Single-cell analyses reveal YAP/TAZ as regulators of stemness and cell plasticity in glioblastoma. *Nat. Cancer* **2020**. [CrossRef]
89. Zhao, K.; Wang, Q.; Wang, Y.; Huang, K.; Yang, C.; Li, Y.; Yi, K.; Kang, C. EGFR/c-myc axis regulates TGFbeta/Hippo/Notch pathway via epigenetic silencing miR-524 in gliomas. *Cancer Lett.* **2017**, *406*, 12–21. [CrossRef]
90. Li, W.; Dong, S.; Wei, W.; Wang, G.; Zhang, A.; Pu, P.; Jia, Z. The role of transcriptional coactivator TAZ in gliomas. *Oncotarget* **2016**, *7*, 82686–82699. [CrossRef]
91. Tome-Garcia, J.; Erfani, P.; Nudelman, G.; Tsankov, A.M.; Katsyov, I.; Tejero, R.; Bin, Z.; Walsh, M.; Friedel, R.H.; Zaslavsky, E.; et al. Analysis of chromatin accessibility uncovers TEAD1 as a regulator of migration in human glioblastoma. *Nat. Commun.* **2018**, *9*, 4020. [CrossRef]

92. Wang, Y.; Xu, X.; Maglic, D.; Dill, M.T.; Mojumdar, K.; Ng, P.K.; Jeong, K.J.; Tsang, Y.H.; Moreno, D.; Bhavana, V.H.; et al. Comprehensive Molecular Characterization of the Hippo Signaling Pathway in Cancer. *Cell Rep.* **2018**, *25*, 1304–1317 e1305. [CrossRef]
93. Kim, E.H.; Sohn, B.H.; Eun, Y.G.; Lee, D.J.; Yim, S.Y.; Kang, S.G.; Lee, J.S. Silence of Hippo Pathway Associates with Pro-Tumoral Immunosuppression: Potential Therapeutic Target of Glioblastomas. *Cells* **2020**, *9*, 1761. [CrossRef]
94. Gravendeel, L.A.; Kouwenhoven, M.C.; Gevaert, O.; de Rooij, J.J.; Stubbs, A.P.; Duijm, J.E.; Daemen, A.; Bleeker, F.E.; Bralten, L.B.; Kloosterhof, N.K.; et al. Intrinsic gene expression profiles of gliomas are a better predictor of survival than histology. *Cancer Res.* **2009**, *69*, 9065–9072. [CrossRef]
95. Pobbati, A.V.; Hong, W. A combat with the YAP/TAZ-TEAD oncoproteins for cancer therapy. *Theranostics* **2020**, *10*, 3622–3635. [CrossRef]
96. Liu-Chittenden, Y.; Huang, B.; Shim, J.S.; Chen, Q.; Lee, S.J.; Anders, R.A.; Liu, J.O.; Pan, D. Genetic and pharmacological disruption of the TEAD-YAP complex suppresses the oncogenic activity of YAP. *Genes Dev.* **2012**, *26*, 1300–1305. [CrossRef]
97. Dasari, V.R.; Mazack, V.; Feng, W.; Nash, J.; Carey, D.J.; Gogoi, R. Verteporfin exhibits YAP-independent anti-proliferative and cytotoxic effects in endometrial cancer cells. *Oncotarget* **2017**, *8*, 28628–28640. [CrossRef]
98. Zhang, H.; Ramakrishnan, S.K.; Triner, D.; Centofanti, B.; Maitra, D.; Gyorffy, B.; Sebolt-Leopold, J.S.; Dame, M.K.; Varani, J.; Brenner, D.E.; et al. Tumor-selective proteotoxicity of verteporfin inhibits colon cancer progression independently of YAP1. *Sci. Signal.* **2015**, *8*, ra98. [CrossRef]
99. Jiao, S.; Wang, H.; Shi, Z.; Dong, A.; Zhang, W.; Song, X.; He, F.; Wang, Y.; Zhang, Z.; Wang, W.; et al. A peptide mimicking VGLL4 function acts as a YAP antagonist therapy against gastric cancer. *Cancer Cell* **2014**, *25*, 166–180. [CrossRef]
100. Pobbati, A.V.; Chan, S.W.; Lee, I.; Song, H.; Hong, W. Structural and functional similarity between the Vgll1-TEAD and the YAP-TEAD complexes. *Structure* **2012**, *20*, 1135–1140. [CrossRef]
101. Gibault, F.; Coevoet, M.; Sturbaut, M.; Farce, A.; Renault, N.; Allemand, F.; Guichou, J.F.; Drucbert, A.S.; Foulon, C.; Magnez, R.; et al. Toward the Discovery of a Novel Class of YAP(-)TEAD Interaction Inhibitors by Virtual Screening Approach Targeting YAP(-)TEAD Protein(-)Protein Interface. *Cancers* **2018**, *10*, 140. [CrossRef]
102. Song, S.; Xie, M.; Scott, A.W.; Jin, J.; Ma, L.; Dong, X.; Skinner, H.D.; Johnson, R.L.; Ding, S.; Ajani, J.A. A Novel YAP1 Inhibitor Targets CSC-Enriched Radiation-Resistant Cells and Exerts Strong Antitumor Activity in Esophageal Adenocarcinoma. *Mol. Cancer Ther.* **2018**, *17*, 443–454. [CrossRef]

Article

# Nanotherapeutic Modulation of Human Neural Cells and Glioblastoma in Organoids and Monocultures

Issan Zhang <sup>1</sup>, Paula Lépine <sup>2</sup>, Chanshuai Han <sup>2</sup>, María Lacalle-Aurioles <sup>2</sup> , Carol X.-Q. Chen <sup>2</sup>, Rainer Haag <sup>3</sup> , Thomas M. Durcan <sup>2</sup> and Dusica Maysinger <sup>1,\*</sup> 

<sup>1</sup> Department of Pharmacology and Therapeutics, McGill University, 3655 Promenade Sir-William-Osler, Montreal, QC H3G 1Y6, Canada; issan.zhang@mail.mcgill.ca

<sup>2</sup> The Neuro's Early Drug Discovery Unit (EDDU), McGill University, 3801 University Street, Montreal, QC H3A 2B4, Canada; paula.lepine@mcgill.ca (P.L.); chanshuai.han2@mcgill.ca (C.H.); maria.lacalleaurioles@mcgill.ca (M.L.-A.); xiuqing.chen@mcgill.ca (C.X.-Q.C.); thomas.durcan@mcgill.ca (T.M.D.)

<sup>3</sup> Institute of Chemistry and Biochemistry, Freie Universität Berlin, Takustraße 3, 14195 Berlin, Germany; haag@chemie.fu-berlin.de

\* Correspondence: dusica.maysinger@mcgill.ca; Tel.: +1-514-398-1264

Received: 23 August 2020; Accepted: 5 November 2020; Published: 7 November 2020



**Abstract:** Inflammatory processes in the brain are orchestrated by microglia and astrocytes in response to activators such as pathogen-associated molecular patterns, danger-associated molecular patterns and some nanostructures. Microglia are the primary immune responders in the brain and initiate responses amplified by astrocytes through intercellular signaling. Intercellular communication between neural cells can be studied in cerebral organoids, co-cultures or in vivo. We used human cerebral organoids and glioblastoma co-cultures to study glia modulation by dendritic polyglycerol sulfate (dPGS). dPGS is an extensively studied nanostructure with inherent anti-inflammatory properties. Under inflammatory conditions, lipocalin-2 levels in astrocytes are markedly increased and indirectly enhanced by soluble factors released from hyperactive microglia. dPGS is an effective anti-inflammatory modulator of these markers. Our results show that dPGS can enter neural cells in cerebral organoids and glial cells in monocultures in a time-dependent manner. dPGS markedly reduces lipocalin-2 abundance in the neural cells. Glioblastoma tumoroids of astrocytic origin respond to activated microglia with enhanced invasiveness, whereas conditioned media from dPGS-treated microglia reduce tumoroid invasiveness. Considering that many nanostructures have only been tested in cancer cells and rodent models, experiments in human 3D cerebral organoids and co-cultures are complementary in vitro models to evaluate nanotherapeutics in the pre-clinical setting. Thoroughly characterized organoids and standardized procedures for their preparation are prerequisites to gain information of translational value in nanomedicine. This study provides data for a well-characterized dendrimer (dPGS) that modulates the activation state of human microglia implicated in brain tumor invasiveness.

**Keywords:** cerebral organoids; nanomedicines; astrocytes; microglia; glioblastoma; lipocalin-2; inflammation

## 1. Introduction

The brain is particularly challenging to model because of its complex structure and functions. Neural cells constantly interact with each other through signaling molecules as well as cell–cell contacts [1–3]. Monocultures are useful to answer cell type-specific questions, but processes involving multiple cell types benefit from the use of co-cultures and organoid models [4–6].

Although primary dissociated and organotypic slice cultures are attractive models to investigate molecular mechanisms and functions, particularly for genetic knock-ins and knock-outs, key differences between human and mouse brains can impact the translational potential of experimental results [7,8]. Primary human neural cells are valuable resources, but their use is often restrained by access or methodological limitations. Advances in stem cell research have led to the development of organoids as *in vitro* models resembling human tissues in structure and complexity [4–6]. Cerebral organoids differentiated from induced pluripotent stem cells (iPSCs) show organized neurons and astrocytes in three-dimensions (3D) [9,10].

Nanostructures have been extensively studied in different cell lines and rodents [11], but a limited amount of data are available in human primary cells and organoids. Rodent models were valuable for the assessment of absorption, distribution, elimination and metabolism of nanomedicines. They clearly showed problems related to the entry of some nanostructures into the cerebral parenchyma due to the blood–brain barrier [12,13]. Studies in rodents also provided information on how nanostructures can be tuned in terms of size, shape and surface properties to facilitate brain entry. Similar studies are clearly not possible in humans and are rare in non-human primate models (e.g., Onpattro, Abraxane, BIND-014) [14–16]. Organoids therefore offer a valuable platform for the testing of organic and metallic nanostructures.

Among the nanostructures that have been studied in rodents, which showed pronounced intrinsic anti-inflammatory properties, is dendritic polyglycerol sulfate (dPGS) [17–21]. Their structures with terminal sulfate groups resemble that of heparan sulfate, which exerts anti-coagulant effects [17,22–24]. In contrast to heparan sulfate, dPGS shows primarily anti-inflammatory activity with relatively weak anti-coagulant effects that are size- and charge-dependent. Earlier studies indicated that dPGS can effectively reduce hyperactivity of microglia stimulated by danger-associated molecular patterns and lipopolysaccharide (LPS) in mice [18,19,25]. Microglia are the resident immune cells of the central nervous system and constantly survey their surroundings under physiological conditions [26–28]. Their morphology is altered and their phagocytic functions are elevated under many pathological conditions, making them attractive targets for nanotherapeutic interventions. Our previous studies showed that dPGS can modulate microglial activation in response to pathogen-associated molecular patterns and misfolded proteins (e.g., amyloid beta), thereby reducing losses in dendritic spine density of excitatory hippocampal neurons in mouse organotypic slice cultures [18,19,25]. These studies also showed that hyperactive microglia generate reactive astrocytes through the release of acute-phase cytokines such as interleukin-6, tumor necrosis factor alpha and lipocalin-2 (LCN2). However, the abundance and release of LCN2 in human neural cells has not yet been reported. We tested if dPGS can modulate LCN2 in a human cerebral organoid model.

Aside from establishing human cerebral organoids, we also used glioblastoma tumoroids to investigate the effectiveness of nanotherapeutics in the brain tumor microenvironment. Glioblastomas are mainly astrocytomas characterized by their infiltrative nature [29]. Microglia and normal astrocytes in the glioblastoma environment promote disease progression by secreting soluble factors (e.g., cytokines and growth factors) [30–32]. By combining reconstituted 3D models of glioblastoma (tumoroids) with organoids and modulating the activity of microglia with dPGS, we demonstrate that dPGS could be a powerful therapeutic agent that can reduce inflammatory markers and glioblastoma invasiveness.

## 2. Materials and Methods

### 2.1. Generation of Cerebral Organoids from Human iPSC

Procedures for culturing human iPSCs, embedding organoids in optimal cutting temperature (OCT) blocks, cryosectioning and immunostaining were all described previously [10]. The cell-line used was the NCRM1 iPSC line obtained from the National Institutes of Health. The method used to generate the 3D cerebral organoids was adapted from the protocol published by Lancaster and Knoblich [9]. Compositions of the different media are the same and reagents used are similar,

except for: DMEM-F12 (Gibco, Ottawa, ON, Canada), human embryonic stem cell (hESC) quality fetal bovine serum (FBS) (Wisent, St-Bruno, QC, Canada), MEM Non-Essential Amino Acids Solution (MEM-NEAA) (Multicell, Montreal, QC, Canada), 2-mercaptoethanol (Millipore Sigma, Oakville, ON, Canada), Y27632 Rho-associated protein kinase (ROCK) inhibitor (Selleckchem, Burlington, ON, Canada), N2 supplement (Gibco) and Penicillin-Streptomycin (Multicell).

For the generation and maintenance of embryoid bodies (EBs, days 0–11), we started from a 100 mm dish with iPSCs at 70% confluence with high quality (less than 10% differentiated cells). Cells were washed with DMEM-F12 and dissociated with Accutase to generate a suspension of single cells. Cells were gently resuspended in hESC media containing ROCK inhibitor [9], basic fibroblast growth factor (FGF-b) and plated at a density of 10,000 cells/well in a 96-well ultra-low attachment U-bottomed plate (Corning, Burlington, ON, Canada). Plates were centrifuged at 1200 rpm for 10 min and incubated at 37 °C, 5% CO<sub>2</sub> for 48 h. During day 2, a half media change was made, followed by a media change every other day up to day 11. Images of EBs were recorded with Evos XL Core Microscope (Thermo Fisher Scientific, Ottawa, ON, Canada) every 2 days during media changes to measure their diameter using the Image J software (U. S. National Institutes of Health, Bethesda, Maryland, USA). Once EBs had reached  $\geq 350 \mu\text{m}$  in diameter, hESC media was switched to be without ROCK inhibitor and FGF-b [9]. When EBs were about 500–600  $\mu\text{m}$  in diameter with smooth and bright edges, the media was switched to neuronal induction media (NIM). EBs were maintained in NIM for 4–5 days until the outer surface was optically translucent and ready to be embedded in Matrigel<sup>®</sup> (Corning) containing reduced growth factor droplets.

Matrigel<sup>®</sup> was thawed on ice. After media removal from each well containing the EBs, 30  $\mu\text{L}$  of Matrigel<sup>®</sup> was added per well and incubated for 30 min at 37 °C. Next, 200  $\mu\text{L}$  of final differentiation media without vitamin A [9] was added per well. Using a 1000  $\mu\text{L}$  cut tip, the Matrigel<sup>®</sup>-embedded organoids were transferred into an uncoated 6-well ultra-low attachment plate (Corning) with 4 mL of final differentiation media without vitamin A per well. A maximum of five organoids were added and maintained per well to avoid fusion. Following transfer, plates were left for 48 h in stationary culture. After 48 h, media was changed to fresh final differentiation media without vitamin A, followed by a second 48 h incubation. Following the second media change, plates were transferred onto an orbital shaker set at 70 rpm (Scientific Industries Inc., Bohemia, NY, USA) housed in a 37 °C incubator. Media was changed every 3 days with fresh final differentiation media with vitamin A until the organoids were ready for analysis.

## 2.2. Immunofluorescence (IF) Staining in Organoids

Cerebral organoids were fixed with 4% paraformaldehyde (overnight at 4 °C), washed in phosphate-buffered saline (PBS, Multicell), dehydrated in 20% sucrose (1–3 days) and embedded in OCT Compound (Thermo Fisher Scientific). Blocks were kept at  $-80 \text{ }^{\circ}\text{C}$  until needed. For IF, samples were sectioned (20  $\mu\text{m}$ ) in a cryostat (Cryostar NX70, Thermo Fisher Scientific), air dried at room temperature (RT) and kept at  $-20 \text{ }^{\circ}\text{C}$  before IF staining. Cryosections were rehydrated in PBS (15 min) and permeabilized/blocked in blocking solution (1 h at room temperature, RT) containing: 0.2% Triton X-100 (Millipore Sigma), 0.05% bovine serum albumin and 5% normal donkey serum in PBS, before incubation (overnight at 4 °C) with primary antibodies. Antibodies used were as follows: mouse anti-Nestin (1:250, Developmental Studies Hybridoma Bank, Iowa City, IA, USA, rat-401), rabbit anti-SOX2 (1:500, Millipore, Oakville, ON, Canada, AB5603), chicken anti-MAP2 (1:1000, EnCor Biotechnology, Gainesville, FL, USA, CPCA-MAP2), rat anti-CTIP2 (1:500, Abcam, Toronto, ON, Canada, ab18465), rabbit anti-GFAP (1:250 Millipore, MAB144P), chicken anti-Beta III Tubulin (1:400, Millipore, AB9354), rabbit anti-Nestin (1:200, Abcam, ab92391) and rat anti-lipocalin-2 (1:500, R&D Systems, Toronto, ON, Canada, MAB1757). Sections were then washed in PBS (45 min) and incubated (1 h at RT) with secondary antibodies in blocking solution: goat anti-rat Dylight 488 (1:300, Abcam, ab96887), donkey anti-rabbit Dylight 594 (1:400, Abcam, ab96877), donkey anti-chicken Alexa 647 (1:500, Invitrogen, Ottawa, ON, Canada, A21447), donkey anti-mouse Dylight 550 (1:200, Abcam,

ab96876), goat anti-chicken Dylight 650 (1:200, Abcam, ab96950), donkey anti-rabbit Dylight 550 (1:200, Abcam, ab96892) and goat anti-rat Alexa Fluor 647 (1:500, Thermo Fisher Scientific, A21247). Sections were washed (45 min) with PBS and incubated (10 min at RT) with Hoechst 33342 (1:5000, Thermo Fisher Scientific) in PBS, washed in PBS (10 min) and mounted using Aqua-Poly/Mount (Polysciences Inc., Warrington, PA, USA). Samples were imaged on a Leica TCS SP8 confocal microscope (Leica, Richmond Hill, ON, Canada) at a 20× magnification.

### 2.3. Cell Culture

U251N human glioblastoma cells and HMC3 human microglia were originally obtained from the American Type Culture Collection. Unless otherwise indicated, cells were maintained in Dulbecco's Modified Eagle Medium (DMEM, Thermo Fisher Scientific) supplemented with 5% fetal bovine serum (FBS, Wisent) and 1% Penicillin-Streptomycin (Thermo Fisher Scientific). Primary human astrocytes were obtained from Dr. Jack Antel's lab and maintained in DMEM supplemented with 5% FBS and 1% Penicillin-Streptomycin. Primary astrocytes were kept at passages below five. Conditioned media was obtained from cell cultures maintained in the exponential growth phase and used fresh at 50% (*v/v*) in fresh media following centrifugation (3,000 rpm, 5 min) to remove cell debris. When used for the treatment of cerebral organoids, conditioned media was prepared using organoid media.

### 2.4. Time-Dependent dPG/dPGS Internalization in Organoids and Tumoroids

Human cerebral organoids were treated with dPG-Cy5 (1 μM) or dPGS-Cy5 (1 μM) for 1 h, 4 h or 24 h, then used for IF staining or direct imaging. For direct imaging, organoids were fixed in 4% paraformaldehyde overnight and nuclei were labeled with Hoechst 33342 (10 μM, overnight). Organoids were washed in PBS and imaged using a fluorescence microscope. Fluorescence was analyzed in ImageJ. Glioblastoma tumoroids were treated with dPG-Cy5 (1 μM) or dPGS-Cy5 (1 μM) for 24 h, then washed twice with PBS before imaging using a fluorescence microscope.

### 2.5. Western Blot

Western blot analysis followed published procedures [33]. In brief, organoids were washed twice in cold PBS, then were cut into small pieces using a razor blade and incubated in RIPA lysis buffer for 30 min on ice. Monolayer cells were washed twice with cold PBS, then incubated in RIPA lysis buffer for 30 min on ice. Lysates were vortexed for 10 sec every 10 min and lastly centrifuged for 30 min at 4 °C and 13,000 rpm. Lysates and media samples were separated by SDS-PAGE and blotted onto PVDF membranes (Bio-Rad, Mississauga, ON, Canada). Blocked membranes were probed with primary antibodies: rat anti-lipocalin-2 (1:500, R&D Systems, MAB1757), rabbit anti-NFκB p65 (1:1000, Abcam, ab16502), mouse anti-STAT3 (1:1000, Abcam, ab119352), mouse anti-β-actin (1:5000, Millipore Sigma, A5316) or mouse anti-alpha-tubulin (1:5000, Abcam, ab7291) overnight at 4 °C. Membranes were washed and incubated with secondary antibodies (goat anti-rat HRP, 1:1000, Thermo Fisher Scientific, 31470, goat anti-rabbit HRP, 1:1000, Bio-Rad, 1706515 and horse anti-mouse HRP, 1:5000, Cell Signaling, Burlington, ON, Canada, 7076S) for 1 h at RT. Membranes were washed and incubated with enhanced chemiluminescence substrate (Bio-Rad) for 5 min, signals were acquired with an Amersham 6000 imager (Amersham, Oakville, ON, Canada) or on film, and quantified in ImageJ.

### 2.6. Collagen Invasion Assay

U251N tumoroids and human astrocyte spheroids were prepared using the hanging drop method [34]. Briefly, drops of 5,000 cells in 30 μL medium were pipetted onto the inner side of a 100 mm Petri dish (Thermo Fisher Scientific) lid. The lid was quickly flipped to cover the Petri dish filled with 20 mL PBS. Hanging drops were cultured at 37 °C for 48 h to allow tumoroids and spheroids to form. Tumoroids and spheroids were then gently scooped into a medium-filled Petri dish coated with 2% agarose (dissolved in PBS) and cultured for 48 h. Tumoroids and spheroids were implanted in collagen gel (Advanced BioMatrix, San Diego, CA, USA), in the presence or absence of primary human

astrocytes (7,000 cells) and human HMC3 microglia (3,000 cells) dispersed in 200  $\mu$ L gel. Gels were covered with 200  $\mu$ L DMEM with or without treatment. Tumoroids and spheroids were imaged using light microscopy immediately after implantation (time = 0 day) and after 6 days. The average distance of cell outgrowth into the surrounding collagen was measured in ImageJ. For invasion assays of tumoroids into organoids, fluorescently-labeled tumoroids were prepared using U251N cells incubated with CellTracker Red (Thermo Fisher Scientific) following recommendations from the manufacturer. Tumoroids were placed in culture with organoids and observed to adhere after 24 h. Cultures were imaged using a fluorescence microscope over 6 days.

### 2.7. Immunocytochemistry

Cells were seeded at 5,000 cells/coverslip on glass coverslips (Merlan Scientific, Mississauga, ON, Canada) coated with poly-D-lysine (Millipore Sigma). Cells were cultured for 24 h (U251N and HMC3) or 48 h (primary human astrocytes) before treatment. Following treatment, cells were fixed in 4% paraformaldehyde (10 min), permeabilized with 0.1% Triton X-100 (10 min), blocked in 10% goat serum in PBS (Gibco) for 1 h and incubated with primary antibodies overnight at 4 °C: rabbit anti-GFAP (1:500, Abcam, ab7260), mouse anti-Lamp1 (1:500, Developmental Studies Hybridoma Bank, H4A3-c), rat anti-lipocalin-2 (1:500, R&D Systems, MAB1757), rabbit anti-NF $\kappa$ B p65 (1:500, Abcam, ab16502) or rabbit anti-phospho-STAT3 Y705 (1:500, Abcam, ab76315). Cells were washed in PBS three times and incubated with secondary antibodies for 1 h at RT: goat anti-rabbit Alexa Fluor 488 (1:1000, Thermo Fisher, Mississauga, ON, Canada, A27034), goat anti-rat Alexa Fluor 647 (1:500, Thermo Fisher, A21247) or goat anti-mouse Alexa Fluor 488 (1:1000, Thermo Fisher, A28175). Cells were washed with PBS and nuclei were labeled with Hoechst 33342 (10  $\mu$ M, 10 min). After three more washings with PBS, coverslips were mounted on microscope slides (Diamed, Mississauga, ON, Canada) using Aqua-Poly/Mount. Samples were imaged using a fluorescence microscope (Leica DMI4000B, Leica) and intracellular fluorescence was analyzed in ImageJ. The nuclear and/or cytoplasmic fluorescence of NF $\kappa$ B, LCN2 and phospho-STAT3 for each cell was measured and normalized to the nuclear or cytoplasmic area. The background fluorescence was subtracted.

### 2.8. Immunohistochemistry

Immunohistochemistry was performed as previously published [33]. In brief, human brain sections were dewaxed in xylene and rehydrated in ethanol. Antigen retrieval was performed in citrate buffer. Following blocking, samples were incubated with primary antibodies: rat anti-lipocalin-2 (1:500, R&D Systems, MAB1757), mouse anti-IBA1 (1:300, Invitrogen, MA5-27726) or rabbit anti-GFAP (1:250 Millipore, MAB144P) overnight at 4 °C. Samples were washed and incubated with secondary antibodies: goat anti-rat Alexa Fluor 647 (1:500, Thermo Fisher Scientific, A21247), goat anti-mouse Alexa Fluor 647 (1:300, Thermo Fisher Scientific, A28181) or goat anti-rabbit Alexa Fluor 488 (1:500, Thermo Fisher, A27034) for 1 h at RT. Nuclei were labeled with DAPI (1  $\mu$ g/mL, 5 min, Molecular Probes, Ottawa, ON, Canada) and samples were mounted on microscope slides using Dako mounting medium (Dako, Burlington, ON, Canada). Samples were imaged using a fluorescence microscope. The samples were harvested under a protocol approved by the Montreal Neurological Hospital's research ethics board (NEU-10-066). Consent was given by all patients and controls (aged 55–76). Tissues were from the cerebral cortex.

### 2.9. Lipid Droplet Imaging

Cells seeded on glass coverslips at 5,000 cells/coverslip were cultured for 24 h before treatment. Following treatment, cells were washed twice with PBS and fixed in 4% paraformaldehyde (10 min). Cells were washed with PBS and incubated with BODIPY 493/503 (10  $\mu$ M, Thermo Fisher) and Hoechst 33342 (10  $\mu$ M) for 10 min. Cells were washed with PBS four times, then mounted on microscope slides using EverBrite (Biotium, Burlington, ON, Canada). Samples were imaged using a fluorescence microscope.



### 2.10. MTT Assay

Following treatment, organoids were washed in PBS twice and incubated in fresh media in the presence of 3-(4,5-dimethylthiazol-2-yl)-2,5-diphenyltetrazolium bromide (MTT) (0.5 mg/mL, Millipore Sigma) for 1 h at 37 °C. The media was removed, and cells were lysed in 500  $\mu$ L dimethyl sulfoxide (Santa Cruz, Dallas, TX, USA). Samples were measured at 595 nm in triplicate using a microplate reader (Spark 10M, Tecan, Männedorf, Switzerland). Measurements were normalized to the organoid weight.

### 2.11. Statistics

Statistical significance was determined using one-way ANOVA followed by the Student's *t*-test. *p*-values lesser than 0.05 were deemed significant. The Bonferroni correction was applied for multiple comparisons.

## 3. Results

### 3.1. dPGS Are Internalized in 3D Cerebral Organoids

Human cerebral organoids were generated from human iPSCs according to an established protocol [9]. A timeline of organoid formation and biomarkers used to delineate dynamic lineage progression is illustrated in Figure S1. We used these organoids after a 100-day maturation to test dendritic polyglycerol sulfate (dPGS) as a model nanostructure with anti-inflammatory properties in human neural cells, as well as other types of emerging nanostructures with biomedical applications, such as metallic gold nanoclusters [35–39]. Gold nanoclusters have been shown to affect cellular stress and organellar function thanks to their unique physicochemical properties, but little work has been done in human neural cells. The nanostructures were screened for cytotoxic effects (Figure 1a and Figure S2) and results showed that they can be studied in human neural cells without jeopardizing the viability of the organoid cultures. This provides the basis for further investigations on nanomedical applications in a translationally-relevant model. The first step was to show if dPGS was internalized by neural cells within the organoids themselves. To this end, we treated organoids with fluorescently (Cy5)-labeled dPGS (Figure 1). Time-course experiments showed that dPGS-Cy5 was internalized within 1 h ( $12.8 \pm 2.2$  SEM fold increase over baseline fluorescence), then progressively more over 24 h ( $64.5 \pm 11.4$  SEM fold increase) (Figure 1b,c). Compared to dPGS, internalization of the non-sulfated dendritic polyglycerol (dPG) was low ( $8.7 \pm 2.1$  SEM fold increase after 24 h) (Figure 1b,c), underlining the important role of the terminal sulfate groups for cell internalization. In the current study, we showed that GFAP-labeled astrocytes within the outermost layer (200–300  $\mu$ m) of the cerebral organoids contain abundant amounts of dPGS (Figure 1d).

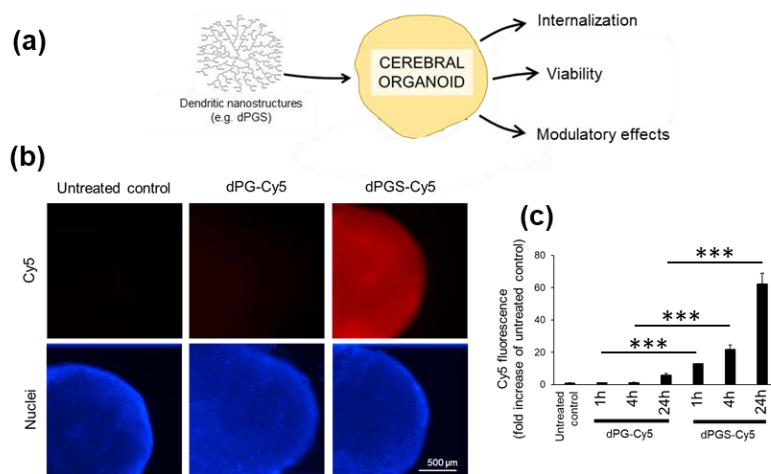
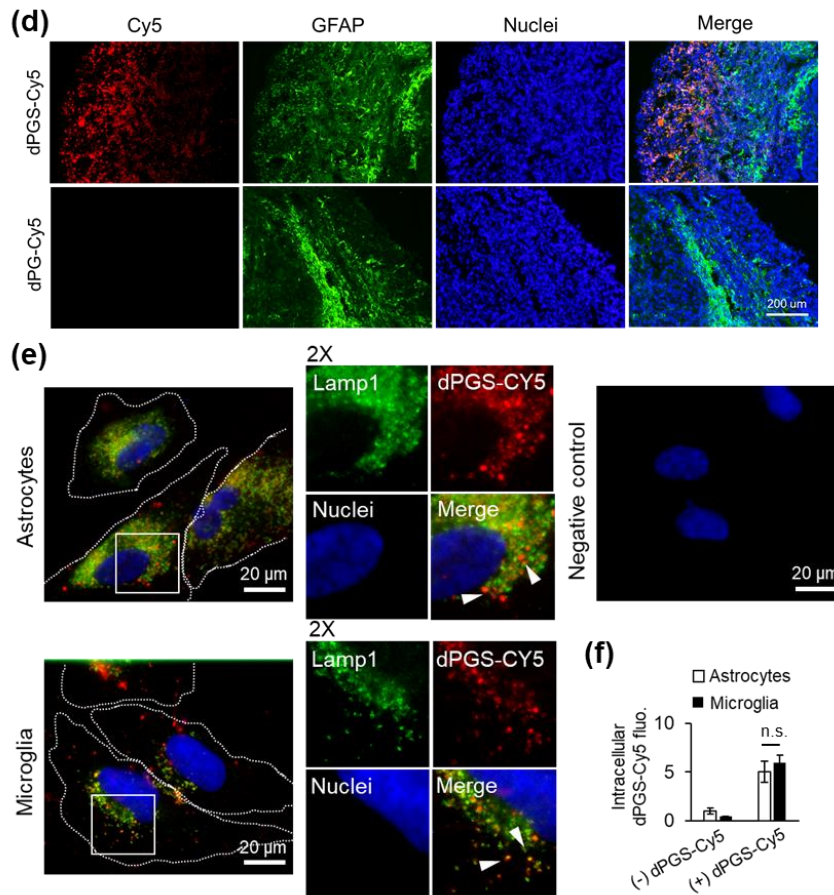


Figure 1. Cont.



**Figure 1.** (a) Schematic representation of cerebral organoid usage for nanostructure screening. (b) Human cerebral organoids were treated with dendritic polyglycerol (dPG)-Cy5 (1  $\mu$ M) or dendritic polyglycerol sulfate (dPGS)-Cy5 (1  $\mu$ M) for 1 h, 4 h or 24 h. Nuclei were labeled with Hoechst 33342. Organoids were imaged using a fluorescence microscope. (c) Cy5 fluorescence in organoids was analyzed in ImageJ. Shown are the average fluorescence per condition  $\pm$  SEM. At least 90 organoids were analyzed from three independent experiments. \*\*\*  $p < 0.001$  (d) Fluorescence micrographs of human cerebral organoids treated with dPG-Cy5 (1  $\mu$ M) or dPGS-Cy5 (1  $\mu$ M) for 24 h and labeled for glial fibrillary acidic protein (GFAP). Nuclei were labeled with Hoechst 33342. (e) Primary human astrocytes and human HMC3 microglia internalization of dPGS-Cy5 (1  $\mu$ M) after 24 h. dPGS-Cy5 (red) is partially co-localized with Lamp1-labeled lysosomal compartments (green). The negative control was prepared in the absence of dPGS-Cy5 and primary antibody to account for background fluorescence. Nuclei were labeled with Hoechst 33342 (blue). Cells were imaged using a fluorescence microscope. (f) Shown are the average intracellular Cy5 fluorescence per cell expressed as fold change from untreated cells  $\pm$  SD. At least 90 cells were analyzed in two independent experiments. n.s. Non-significant.

### 3.2. dPGS Internalization in Human Microglia and Normal Astrocytes

Given the importance of glial cells in regulating inflammatory processes in the brain, we further studied the intracellular effects of dPGS in astrocytes and particularly microglia, which are absent from the cerebral organoids. We established in cell monolayer cultures that human microglia and astrocytes internalized comparable amounts of dPGS within 24 h of treatment (Figure 1e,f). Fluorescence imaging at the single cell level showed that dPGS-Cy5 accumulated in the perinuclear area (Figure 1e), and was partially co-localized with lysosomal compartments labeled with Lamp1 [40]. Given that microglia activated by pro-inflammagens (e.g., LPS) are associated with increased sequestration of neutral lipids into lipid droplets (LDs) [41,42] (Figure S3b), we investigated if dPGS could have modulatory effects on lysosomes, which interact with LDs through lipophagy and other processes [43,44]. This was

suggested by changes in lysosomal positioning, with an increase in perinuclear lysosomes (Figure S3a). In turn, treatment with dPGS prevented LPS-induced lipid droplet accumulation (Figure S3b).

### 3.3. dPGS Reduced Microglia-Stimulated Lipocalin-2 in Cerebral Organoid Models

Considering the importance of microglia-astrocyte crosstalk in rodent [19] and human neural cells [1,3], we measured LCN2 abundance in human neural cells in response to LPS, a prototypical pro-inflammagen whose levels are exacerbated in endotoxemia and sepsis. The presence of microglia is required to stimulate the synthesis of LCN2 in the neural cells, as levels in response to LPS remained comparable to that of the untreated control in the absence of microglia from the organoids (Figure 2a,b and Figure S4). In turn, conditioned media from LPS-stimulated microglia induced a significant increase in intracellular and extracellular LCN2 in the cerebral organoid cultures (Figure 2c–e), confirming that this upregulation is microglia-dependent in human neural cells. Given that astrocytes play a significant role in inflammatory processes in the brain, we investigated if there was increased LCN2 abundance in these cells in response to microglia activation. Similarly to the results from cerebral organoids, direct stimulation of astrocytes with LPS did not have a significant effect (Figure 2f). In contrast, treatment with conditioned media from LPS-activated microglia increased LCN2 abundance, whereas the presence of dPGS returned LCN2 abundance to control levels (Figure 2f). dPGS alone and conditioned media from resting microglia did not have significant effects (Figure 2d–f). Finally, to show that dPGS is not cytotoxic to human neural cells, we measured mitochondrial metabolic activity using the MTT assay. Results from these studies showed that neither dPGS nor dPG affected mitochondrial metabolic activity in 3D organoids for up to 72 h (Figure S2). Our earlier studies indicated that in rodent cells, concentrations of dPGS up to 100  $\mu$ M did not cause any notable cytotoxicity [18]. These results encouraged us to investigate dPGS as a microglia modulator and indirect suppressor of glioblastoma invasiveness.

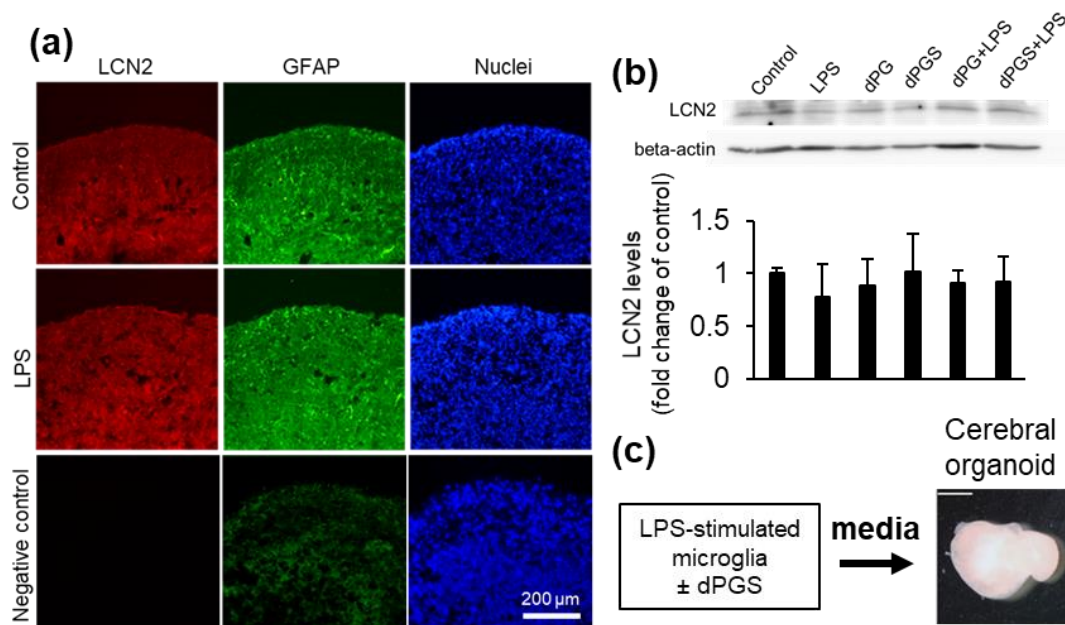
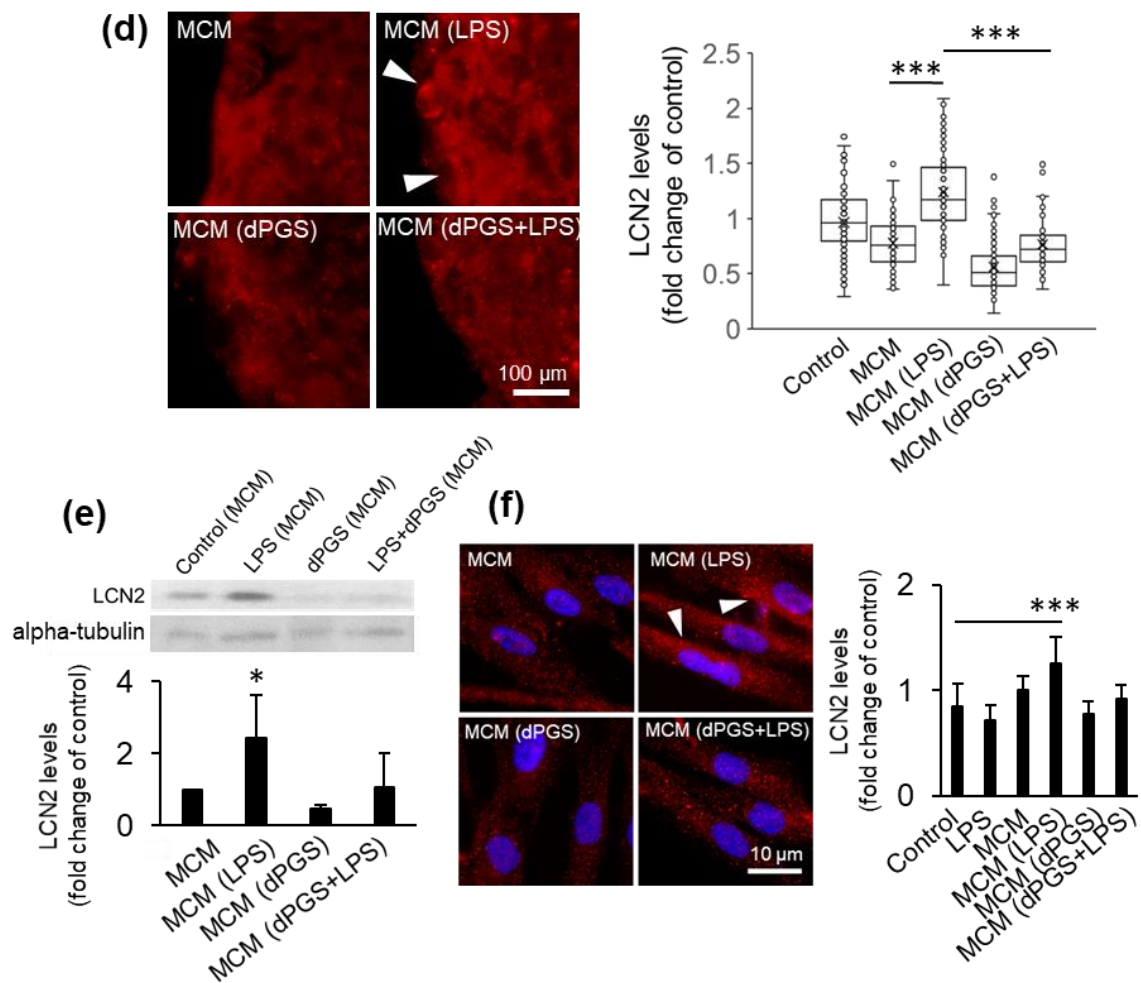


Figure 2. Cont.



**Figure 2.** Lipocalin-2 levels in human cerebral organoids. (a) Micrographs of lipocalin-2 (LCN2) detected by immunofluorescence in organoid cryosections following treatment with LPS (10 ng/mL) for 24 h. Astrocytes were labeled with GFAP and nuclei with Hoechst 33342. The negative control was prepared in the absence of primary antibodies to account for background fluorescence. Samples were imaged using a fluorescence microscope. (b) LCN2 levels in organoids treated with lipopolysaccharide (LPS) (10 ng/mL) with or without dPG (1 μM) and dPGS (1 μM) for 24 h and measured by Western blot, with beta-actin as loading control. Quantification shown are the average intracellular LCN2 levels ±SD in organoids based on immunofluorescence images shown in (a). A total of 27 samples were analyzed from three independent experiments. (c) Schematic representation of media conditioning from microglia used for cerebral organoid treatment. (d) Representative fluorescence micrographs of intracellular LCN2 levels in organoids treated with conditioned media from microglia (MCM) treated with LPS (10 ng/mL), dPGS (1 μM) for 24 h. Quantifications show the average and single-cell levels of LCN2 fluorescence in cryosections. A total of 1017 cells were analyzed from independent experiments. \*\*\*  $p < 0.001$  (e) LCN2 levels from organoids treated as in (d) and measured by Western blot, with alpha-tubulin as loading control. Shown are the average LCN2 levels from two independent experiments. \*  $p < 0.05$  (f) Fluorescence micrographs of LCN2 abundance in primary human astrocytes treated as in (d) and measured using immunocytochemistry. Shown are the average intracellular LCN2 levels in astrocytes as fold increase of the untreated control. A total of 477 cells from two independent experiments were analyzed. \*\*\*  $p < 0.001$ .

### 3.4. Microglia and dPGS Modulate Glioblastoma Invasiveness

Glioblastoma multiforme is an aggressive brain tumor of astrocytic origin for which complete resection is often impossible due to its invasive nature [29,45]. To model the impact of microglia and astrocytes on glioblastoma invasiveness, we designed a 3D invasion assay examining the propensity

of the cancer cells to migrate into the surrounding collagen matrix. Human microglia and primary human astrocytes were embedded into the collagen matrix, wherein a tumoroid was then implanted (Figure 3a). Over time, the normal neural cells extend processes while cancer cells migrate radially from the tumoroid. Glioblastoma outgrowth from the tumoroid into the surrounding collagen was facilitated by the presence of microglia and astrocytes (Figure 3a,b), an effect replicated using microglia-conditioned media and inhibited by dPGS (Figure 3c,d). This indicates that neural cells secrete factors (extracellular matrix degradation enzymes, cytokines, growth factors) that can stimulate tumor invasiveness [46–48]. In contrast, tumoroids grown in isolation or within cerebral organoids in the absence of microglia had comparatively less outgrowth over time (Figure 3a,b and Figure S5), and normal human astrocytes migrated in a scattered pattern without radial outgrowth (Figure S6).

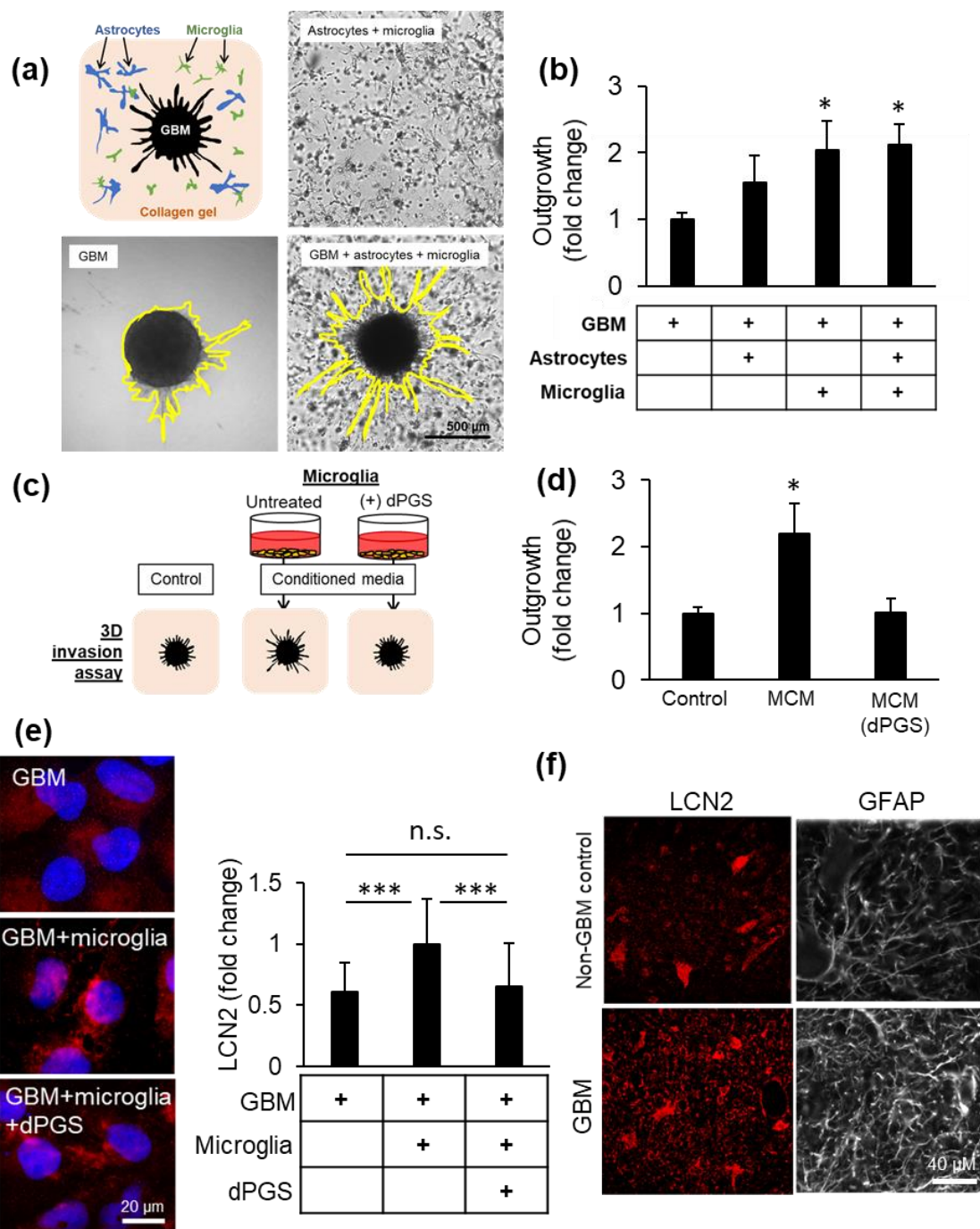
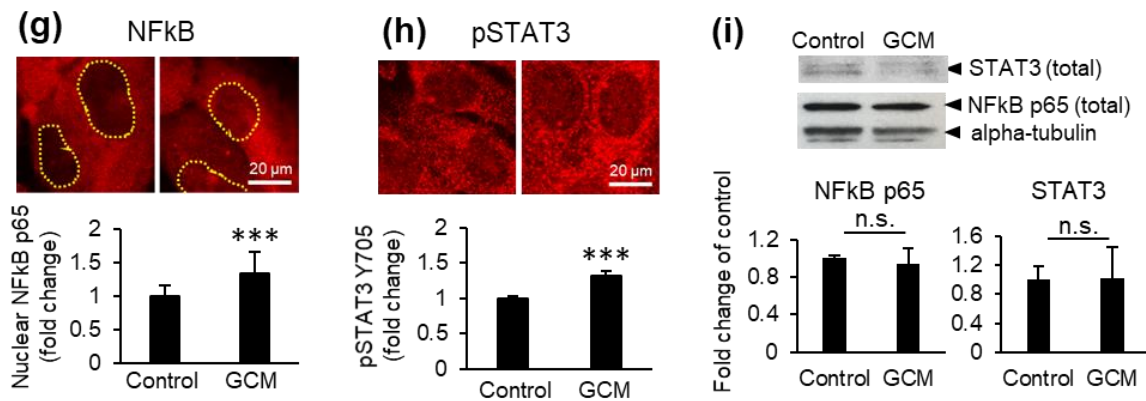


Figure 3. Cont.



**Figure 3.** Glioblastoma (GBM) invasiveness in 3D co-cultures. (a) Collagen gels were seeded with human primary astrocytes and human HMC3 microglia in the presence or absence of a glioblastoma tumoroid. (b) Glioblastoma invasiveness in the presence or absence of microglia and astrocytes in 3D co-cultures after 6 days. Shown are the average distance of outgrowth from the tumoroid as a fold change of the tumoroid monoculture  $\pm$  SEM. A total of 32 tumoroids were tested from at least three independent experiments. \*  $p < 0.05$  (c) Schematic representation of microglial conditioned media (MCM) used to treat collagen-embedded tumoroids. (d) Glioblastoma tumoroid outgrowth in the presence of conditioned media from microglia treated or not with dPGS (1  $\mu$ M) after 6 days  $\pm$  SEM. A total of 29 tumoroids were tested from at least four independent experiments. \*  $p < 0.05$  (e) Representative fluorescence micrographs showing intracellular LCN2 (red) in glioblastoma cells in the presence or absence of microglia cells in direct co-culture and dPGS (1  $\mu$ M) for 24 h. LCN2 was fluorescently immunolabeled and cells were imaged using a fluorescence microscope. Quantifications show the average intracellular LCN2 levels  $\pm$  SD per cell. At least 500 cells were analyzed from five independent experiments. \*\*\*  $p < 0.001$ ; n.s. Non-significant. (f) Fluorescence micrographs of LCN2 (red) and GFAP (white) in human brain sections from non-cancerous brain or glioblastoma tumor tissues. LCN2 and GFAP were fluorescently labeled by immunohistochemistry and imaged using a fluorescence microscope. (g,h) Activation of transcription factors NF $\kappa$ B and STAT3 in microglia in response to glioblastoma secreted factors. Human HMC3 microglia were treated with glioblastoma conditioned media (GCM) for 24 h, after which NF $\kappa$ B p65 and phosphorylated STAT3 Tyr705 were fluorescently immunolabeled (red) and cells were imaged using a fluorescence microscope. Shown are (g) the average nuclear NF $\kappa$ B p65 level per cell  $\pm$  SEM (237 cells from three independent experiments) and (h) the average pSTAT3 Y705 level per cell  $\pm$  SEM (317 cells from three independent experiments) \*\*\*  $p < 0.001$ . (i) Total NF $\kappa$ B p65 and STAT3 protein abundance in microglia treated as in (g,h). Protein levels were determined by measurements of immunopositive bands in Western blots. Alpha-tubulin was used as loading control. Shown are the average protein abundance of NF $\kappa$ B p65 and STAT3 from three independent experiments. n.s. Non-significant.

To characterize the effects of glioblastoma on its surrounding immune cells, glioblastoma cells were directly co-cultured with microglia cells and showed significantly higher LCN2 levels compared to glioblastoma cells in monoculture (Figure 3e). High LCN2 and GFAP levels were also observed in tumor tissues from glioblastoma patients as compared to control brain tissues (Figure 3f). To investigate the mechanism behind LCN2 upregulation, microglia were stimulated with glioblastoma-conditioned media. This resulted in increased nuclear NF $\kappa$ B and STAT3 phosphorylation, two key transcription factors for immune activation (Figure 3g,h) that are also hyperactivated in glioblastoma. The protein levels of total NF $\kappa$ B and STAT3 in the cells remained comparable to the control (Figure 3i).

On the other hand, dPGS was internalized into glioblastoma tumoroids (Figure S7) and decreased LCN2 levels in glioblastoma cells in vitro (Figure 3e). This demonstrates proof of concept for using dPGS as a modulator of the tumor microenvironment (Figure 4).

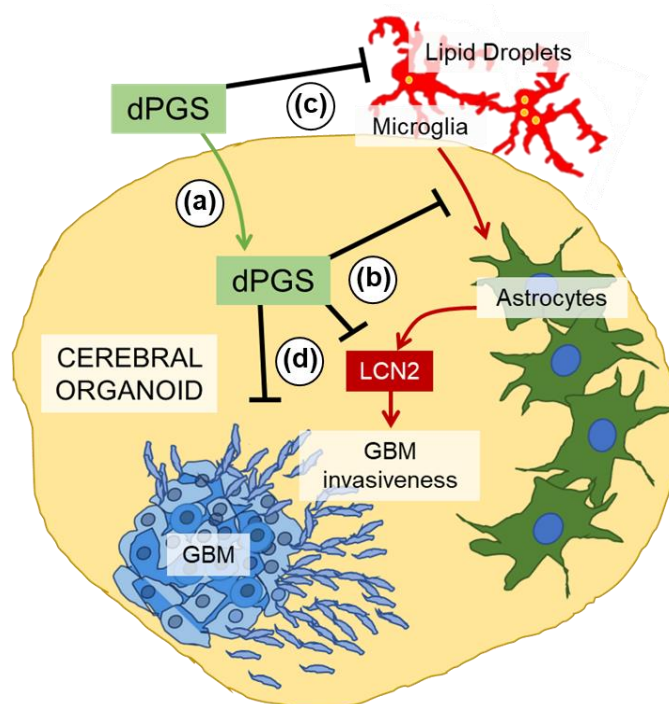


**Figure 4.** Schematic representation of the proposed modulatory effects of dPGS on microglia, astrocyte and glioblastoma crosstalk. (a) dPGS is internalized in cerebral organoids, and (b) downregulates LCN2 produced by microglia-induced astrocytes, thereby (c) reducing markers of inflammation (e.g., lipid droplets) and (d) glioblastoma invasiveness.

#### 4. Discussion

The key question addressed in this study is: can dendritic polyglycerol sulfates with intrinsic anti-inflammatory properties reduce inflammatory markers in cerebral organoids and glioblastoma invasiveness by modulating microglia activity? Mechanistic studies in 3D human neural cultures with new drugs or nanostructures are sparse due to the limited availability of neural tissues. To overcome such a problem, several protocols have been developed for the generation of 3D cerebral organoids and other types of organoids [4,5,7,9]. Human cerebral organoids derived from iPSCs showing properties of different neural cell types are valuable models to study the interactions and effects of nanostructures in 3D. One of the most advanced organoids containing vasculature resembling that of the brain was recently proposed to investigate physiology and pathological changes in neurological disorders [49]. Although our organoids are not as complex as Cakir's, we took advantage of cerebral organoids to reveal how microglia exposed to the pro-inflammatory LPS and the dendritic nanostructure dPGS affect astrocyte reactivity. We show clear anti-inflammatory effects from dPGS and provide the first evidence for this in human brain cells. There are still several limitations to overcome: (1) the integration of resident and peripheral immune cells recruited chemotactically and (2) the contribution of endothelial cells in vasculature as part of the blood–brain barrier.

Our results in organoid cultures showed that the presence of sulfate groups on dPGS was critical for the internalization of nanostructures, as it allowed binding to selectin receptors [17,19,22]. Intracellular changes associated with dPGS included an increase in perinuclear lysosomes, which typically have lower luminal pH and increased degradation activity [44,50], functions often impaired in aging and neurodegenerative diseases. This is interesting given the role of lysosomes in processing LDs, which are upregulated in inflammation and cancer [41,42]. LDs are promiscuous organelles: depending on the cell type, cellular context and their intracellular location, they can play a protective role or become damaging to neural and other cells if peroxidized lipids are released. In aggressive tumors (e.g., glioblastoma and breast), they provide energy for cancer cells to thrive and can sequester lipophilic anticancer

agents, reducing the rate at which they reach their desirable targets [51–53]. Their numbers are highly upregulated in glioblastoma compared to normal astrocytes (Figure S3c,d), and their inhibition was shown to enhance the effectiveness of pharmacological agents [51].

As now shown in human neural cells, LCN2 can be produced by microglia-stimulated astrocytes. Microglia themselves are not significant contributors to LCN2 upregulation due to the LCN2 gene being suppressed by SRSF3 [54]. Instead, they secrete other cytokines (e.g., IL-6, TNF $\alpha$ ) and alarmins under pro-inflammatory conditions that can activate astrocytes and other neural cells [54,55]. Several of these were shown to bind heparan sulfate [23,56], suggesting that dPGS prevented microglia-mediated LCN2 production by blocking some soluble factors and preventing downstream signaling (Figure 2d,e). One of the candidate cytokines is interleukin-6 released from microglia, to which dPGS was shown to bind in our earlier studies using surface plasmon resonance [19].

Cytokines and alarmins play key roles in the tumor microenvironment [57–61]. The cancer cells secrete factors that actively recruit microglia and peripheral macrophages to the tumor site. In turn, these immune cells produce cytokine and growth factors that can promote cancer progression [32]. In this context, microglia-astrocyte crosstalk forms a positive feedback loop that maintains an unfavorable tumor microenvironment [30,62]. LCN2 is an acute-phase protein with emerging roles in the brain and in cancer. It was shown to complex with and enhance the activity of metalloproteinase-9, a protease secreted by cancer cells that breaks down the extracellular matrix and promotes invasiveness [63,64]. This is significant given that dPGS can downregulate LCN2 in neural cells and decrease glioblastoma invasiveness. dPGS can bind P-selectin, which is expressed in the tumor endothelium and in glioblastoma cells [65]. As dPGS can also serve as a nanocarrier, it has the potential to deliver anti-cancer agents [65,66]. Nanocarriers such as functionalized dendrimers for siRNA and drug delivery [67–69] merit testing in human organoid models to reveal how combination therapy could affect interplay between cancer cells and the tumor microenvironment. The modulatory effect of dPGS on organelles could impact glioblastoma cells in several ways: (1) the increase in perinuclear lysosomes could decrease lysosomal exocytosis and the release of extracellular matrix-degrading enzymes (e.g., cathepsins) [70,71], (2) a reduction in lipid droplet size and number [72] is an indicator of reduced microglia hyperactivity, thus fewer cytokines and trophic factors contributing to glioblastoma invasiveness and (3) a decrease in lipid droplets prevents the sequestration of lipophilic anti-cancer agents, allowing them to reach their intracellular targets (e.g., curcumin) [51].

## 5. Conclusions

Our results show that dPGS is an attractive candidate as an anti-inflammatory polyglycerol dendrimer able to modulate human microglia-astrocyte crosstalk. This dendrimer regulated lipocalin 2 abundance in human neural organoids. In the context of inflammation associated with glioblastoma multiforme, dPGS limited glioblastoma invasiveness by modulating microglial activation. Overall, these studies propose the evaluation of well-defined nanostructures in well-characterized human organoids and co-cultures. Cerebral organoids merit further studies as complementary 3D models in nanoscience, but they require rigorous characterization and application of standardized procedures to be widely used [73]. Such three-dimensional systems together with co-cultures and in vivo experiments will provide a valuable evaluation platform for the internalization, cytotoxicity and modulatory effects of nanotherapeutics in human neural cells.

**Supplementary Materials:** The following are available online at <http://www.mdpi.com/2073-4409/9/11/2434/s1>, Figure S1: Maturation and characterization of cerebral organoids, Figure S2: Mitochondrial metabolic activity in cerebral organoids following treatment with nanostructures, Figure S3: Changes in lysosomes and lipid droplets in activated microglia, Figure S4: Absence of microglia in the cerebral organoids, Figure S5: Glioblastoma tumoroid invasiveness in cerebral organoids, Figure S6: Movement of normal human astrocytes in 3D culture, Figure S7: Internalization of fluorescent dPGS-Cy5 in glioblastoma tumoroids.



**Author Contributions:** Conceptualization, D.M. and T.M.D.; investigation, I.Z., P.L., C.H., M.L.-A. and C.X.-Q.C.; writing—original draft preparation, I.Z.; writing—review and editing, I.Z., D.M., T.M.D., R.H., P.L., C.H., M.L.-A. and C.X.-Q.C.; supervision, D.M. and T.M.D.; funding acquisition, D.M. and T.M.D. All authors have read and agreed to the published version of the manuscript.

**Funding:** This research was funded by Canadian Institutes of Health Research, grant number MOP-119425, and Natural Sciences and Engineering Research Council of Canada, grant number RGPIN 2020-07011.

**Acknowledgments:** The authors would like to thank Nadine Rades for kindly providing dPG and dPGS nanostructures, Jack Antel for primary human astrocytes, Kevin Petrecca for human brain sections and Rodolphe Antoine for gold nanoclusters. T.M. Durcan and the EDDU acknowledge that funding for the generation of 3D cerebral organoids is through the Sebastian and Ghislaine Van Berkomp Foundation, the Alain and Sandra Bouchard Foundation and the McGill Healthy Brains for Healthy Lives.

**Conflicts of Interest:** The authors declare no conflict of interest. The funders had no role in the design of the study; in the collection, analyses or interpretation of data; in the writing of the manuscript, or in the decision to publish the results.

## References

1. Paolicelli, R.C.; Bergamini, G.; Rajendran, L. Cell-to-cell Communication by Extracellular Vesicles: Focus on Microglia. *Neuroscience* **2019**, *405*, 148–157. [CrossRef]
2. Simon, E.; Obst, J.; Gomez-Nicola, D. The Evolving Dialogue of Microglia and Neurons in Alzheimer’s Disease: Microglia as Necessary Transducers of Pathology. *Neuroscience* **2019**, *405*, 24–34. [CrossRef]
3. Pósfai, B.; Cserép, C.; Orsolits, B.; Dénes, Á. New Insights into Microglia–Neuron Interactions: A Neuron’s Perspective. *Neuroscience* **2019**, *405*, 103–117. [CrossRef]
4. Rossi, G.; Manfrin, A.; Lutolf, M.P. Progress and potential in organoid research. *Nat. Rev. Genet.* **2018**, *19*, 671–687. [CrossRef]
5. Li, M.; Izpisua Belmonte, J.C. Organoids—Preclinical Models of Human Disease. *N. Engl. J. Med.* **2019**, *380*, 569–579. [CrossRef] [PubMed]
6. Takebe, T.; Wells, J.M. Organoids by design. *Science* **2019**, *364*, 956–959. [CrossRef] [PubMed]
7. Marshall, J.J.; Mason, J.O. Mouse vs man: Organoid models of brain development & disease. *Brain Res.* **2019**, *1724*, 146427. [CrossRef] [PubMed]
8. Breschi, A.; Gingeras, T.R.; Guigó, R. Comparative transcriptomics in human and mouse. *Nat. Rev. Genet.* **2017**, *18*, 425–440. [CrossRef]
9. Lancaster, M.A.; Knoblich, J.A. Generation of cerebral organoids from human pluripotent stem cells. *Nat. Protoc.* **2014**, *9*, 2329–2340. [CrossRef] [PubMed]
10. Chen, X.; Rocha, C.; Rao, T.; Durcan, T.M. NeuroEDDU protocols\_iPSC culture. *Zenodo* **2019**. [CrossRef]
11. Ioannidis, J.P.A.; Kim, B.Y.S.; Trounson, A. How to design preclinical studies in nanomedicine and cell therapy to maximize the prospects of clinical translation. *Nat. Biomed. Eng.* **2018**, *2*, 797–809. [CrossRef]
12. Aparicio-Blanco, J.; Martín-Sabroso, C.; Torres-Suárez, A.-I. In vitro screening of nanomedicines through the blood brain barrier: A critical review. *Biomaterials* **2016**, *103*, 229–255. [CrossRef]
13. Jackson, S.; Meeks, C.; Vézina, A.; Robey, R.W.; Tanner, K.; Gottesman, M.M. Model systems for studying the blood-brain barrier: Applications and challenges. *Biomaterials* **2019**, *214*, 119217. [CrossRef]
14. Akinc, A.; Maier, M.A.; Manoharan, M.; Fitzgerald, K.; Jayaraman, M.; Barros, S.; Ansell, S.; Du, X.; Hope, M.J.; Madden, T.D.; et al. The Onpattro story and the clinical translation of nanomedicines containing nucleic acid-based drugs. *Nat. Nanotechnol.* **2019**, *14*, 1084–1087. [CrossRef] [PubMed]
15. Havel, H.; Finch, G.; Strode, P.; Wolfgang, M.; Zale, S.; Bobe, I.; Youssoufian, H.; Peterson, M.; Liu, M. Nanomedicines: From Bench to Bedside and Beyond. *AAPS J.* **2016**, *18*, 1373–1378. [CrossRef]
16. Hrkach, J.; Hoff, D.V.; Ali, M.M.; Andrianova, E.; Auer, J.; Campbell, T.; Witt, D.D.; Figa, M.; Figueiredo, M.; Horhota, A.; et al. Preclinical Development and Clinical Translation of a PSMA-Targeted Docetaxel Nanoparticle with a Differentiated Pharmacological Profile. *Sci. Transl. Med.* **2012**, *4*, 128ra39. [CrossRef]
17. Rades, N.; Licha, K.; Haag, R. Dendritic Polyglycerol Sulfate for Therapy and Diagnostics. *Polymers (Basel)* **2018**, *10*, 595. [CrossRef]
18. Maysinger, D.; Groger, D.; Lake, A.; Licha, K.; Weinhart, M.; Chang, P.K.-Y.; Mulvey, R.; Haag, R.; McKinney, R.A. Dendritic Polyglycerol Sulfate Inhibits Microglial Activation and Reduces Hippocampal CA1 Dendritic Spine Morphology Deficits. *Biomacromolecules* **2015**, *16*, 3073–3082. [CrossRef]

19. Maysinger, D.; Lalancette-Hébert, M.; Ji, J.; Jabbour, K.; Dervedde, J.; Silberreis, K.; Haag, R.; Kriz, J. Dendritic polyglycerols are modulators of microglia-astrocyte crosstalk. *Future Neurol.* **2019**, *14*, FNL31. [CrossRef]
20. Budde, H.; Sorns, M.-S.; Welker, P.; Licha, K.; Wolff, H.; Riggert, J.; Wulf, G.; Legler, T.J. Dendritic polyglycerol sulfate attenuates murine graft-versus-host disease. *Ann. Hematol.* **2016**, *95*, 465–472. [CrossRef]
21. Xu, X.; Ballauff, M. Interaction of Lysozyme with a Dendritic Polyelectrolyte: Quantitative Analysis of the Free Energy of Binding and Comparison to Molecular Dynamics Simulations. *J. Phys. Chem. B* **2019**, *123*, 8222–8231. [CrossRef]
22. Dervedde, J.; Rausch, A.; Weinhart, M.; Enders, S.; Tauber, R.; Licha, K.; Schirner, M.; Zügel, U.; von Bonin, A.; Haag, R. Dendritic polyglycerol sulfates as multivalent inhibitors of inflammation. *PNAS* **2010**, *107*, 19679–19684. [CrossRef]
23. Parish, C.R. The role of heparan sulphate in inflammation. *Nat. Rev. Immunol.* **2006**, *6*, 633–643. [CrossRef]
24. Türk, H.; Haag, R.; Alban, S. Dendritic Polyglycerol Sulfates as New Heparin Analogues and Potent Inhibitors of the Complement System. *Bioconjugate Chem.* **2004**, *15*, 162–167. [CrossRef] [PubMed]
25. Maysinger, D.; Ji, J.; Moquin, A.; Hossain, S.; Hancock, M.A.; Zhang, I.; Chang, P.K.Y.; Rigby, M.; Anthonisen, M.; Grutter, P.; et al. Dendritic Polyglycerol Sulfates in the Prevention of Synaptic Loss and Mechanism of Action on Glia. *ACS Chem. Neurosci.* **2018**, *9*, 260–271. [CrossRef]
26. Prinz, M.; Jung, S.; Priller, J. Microglia Biology: One Century of Evolving Concepts. *Cell* **2019**, *179*, 292–311. [CrossRef] [PubMed]
27. Masuda, T.; Sankowski, R.; Staszewski, O.; Prinz, M. Microglia Heterogeneity in the Single-Cell Era. *Cell Rep.* **2020**, *30*, 1271–1281. [CrossRef]
28. Rodríguez-Gómez, J.A.; Kavanagh, E.; Engskog-Vlachos, P.; Engskog, M.K.R.; Herrera, A.J.; Espinosa-Oliva, A.M.; Joseph, B.; Hajji, N.; Venero, J.L.; Burguillos, M.A. Microglia: Agents of the CNS Pro-Inflammatory Response. *Cells* **2020**, *9*, 1717. [CrossRef] [PubMed]
29. Li, C.; Wang, S.; Yan, J.-L.; Piper, R.J.; Liu, H.; Torheim, T.; Kim, H.; Zou, J.; Boonzaier, N.R.; Sinha, R.; et al. Intratumoral Heterogeneity of Glioblastoma Infiltration Revealed by Joint Histogram Analysis of Diffusion Tensor Imaging. *Neurosurgery* **2019**, *85*, 524–534. [CrossRef]
30. Broekman, M.L.; Maas, S.L.N.; Abels, E.R.; Mempel, T.R.; Krichevsky, A.M.; Breakefield, X.O. Multidimensional communication in the microenvirons of glioblastoma. *Nat. Rev. Neurol.* **2018**, *14*, 482–495. [CrossRef]
31. Chen, Z.; Hambardzumyan, D. Immune Microenvironment in Glioblastoma Subtypes. *Front. Immunol.* **2018**, *9*, 1004. [CrossRef]
32. Anfray, C.; Ummarino, A.; Andón, F.T.; Allavena, P. Current Strategies to Target Tumor-Associated-Macrophages to Improve Anti-Tumor Immune Responses. *Cells* **2020**, *9*, 46. [CrossRef]
33. Zhang, I.; Beus, M.; Stochaj, U.; Le, P.U.; Zorc, B.; Rajic, Z.; Petrecca, K.; Maysinger, D. Inhibition of glioblastoma cell proliferation, invasion, and mechanism of action of a novel hydroxamic acid hybrid molecule. *Cell Death Discov.* **2018**, *4*, 41. [CrossRef]
34. Del Duca, D.; Werbowetski, T.; Del Maestro, R.F. Spheroid preparation from hanging drops: Characterization of a model of brain tumor invasion. *J. Neurooncol.* **2004**, *67*, 295–303. [CrossRef]
35. Ji, J.; Moquin, A.; Bertorelle, F.; Ky Chang, P.; Antoine, R.; Luo, J.; McKinney, R.A.; Maysinger, D. Organotypic and primary neural cultures as models to assess effects of different gold nanostructures on glia and neurons. *Nanotoxicology* **2019**, *13*, 285–304. [CrossRef]
36. Bonačić-Koutecký, V.; Antoine, R. Enhanced two-photon absorption of ligated silver and gold nanoclusters: Theoretical and experimental assessments. *Nanoscale* **2019**, *11*, 12436–12448. [CrossRef]
37. Maysinger, D.; Gran, E.R.; Bertorelle, F.; Fakhouri, H.; Antoine, R.; Kaul, E.S.; Samhadaneh, D.A.; Stochaj, U. Gold nanoclusters elicit homeostatic perturbations in glioblastoma cells and adaptive changes of lysosomes. *Theranostics* **2019**. [CrossRef]
38. Hakkinen, H. Atomic and electronic structure of gold clusters: Understanding flakes, cages and superatoms from simple concepts. *Chem. Soc. Rev.* **2008**, *37*, 1847–1859. [CrossRef]
39. Jin, R.; Zeng, C.; Zhou, M.; Chen, Y. Atomically Precise Colloidal Metal Nanoclusters and Nanoparticles: Fundamentals and Opportunities. *Chem. Rev.* **2016**, *116*, 10346–10413. [CrossRef] [PubMed]

40. Macairan, J.-R.; Zhang, I.; Clermont-Paquette, A.; Naccache, R.; Maysinger, D. Optical Sensing: Ratiometric pH Sensing in Living Cells Using Carbon Dots (Part. Part. Syst. Charact. 1/2020). *Part. Part. Syst. Charact.* **2020**, *37*, 2070002. [CrossRef]
41. Olzmann, J.A.; Carvalho, P. Dynamics and functions of lipid droplets. *Nat. Rev. Mol. Cell Biol.* **2019**, *20*, 137–155. [CrossRef]
42. Marschallinger, J.; Iram, T.; Zardeneta, M.; Lee, S.E.; Lehallier, B.; Haney, M.S.; Pluvinaige, J.V.; Mathur, V.; Hahn, O.; Morgens, D.W.; et al. Lipid-droplet-accumulating microglia represent a dysfunctional and proinflammatory state in the aging brain. *Nat. Neurosci.* **2020**, *23*, 194–208. [CrossRef]
43. Schulze, R.J.; Sathyanarayan, A.; Mashek, D.G. Breaking fat: The regulation and mechanisms of lipophagy. *Biochim. Biophys. Acta* **2017**, *1862*, 1178–1187. [CrossRef] [PubMed]
44. Pu, J.; Guardia, C.M.; Keren-Kaplan, T.; Bonifacino, J.S. Mechanisms and functions of lysosome positioning. *J. Cell Sci.* **2016**, *129*, 4329–4339. [CrossRef]
45. Davis, M.E. Glioblastoma: Overview of Disease and Treatment. *Clin. J. Oncol. Nurs.* **2016**, *20*, S2–S8. [CrossRef]
46. Ramachandran, R.K.; Sørensen, M.D.; Aaberg-Jessen, C.; Hermansen, S.K.; Kristensen, B.W. Expression and prognostic impact of matrix metalloproteinase-2 (MMP-2) in astrocytomas. *PLoS ONE* **2017**, *12*, e0172234. [CrossRef]
47. Vollmann-Zwerenz, A.; Leidgens, V.; Feliciello, G.; Klein, C.A.; Hau, P. Tumor Cell Invasion in Glioblastoma. *Int. J. Mol. Sci.* **2020**, *21*, 1932. [CrossRef]
48. Medema, J.P. Cancer stem cells: The challenges ahead. *Nat. Cell Biol.* **2013**, *15*, 338–344. [CrossRef]
49. Cakir, B.; Xiang, Y.; Tanaka, Y.; Kural, M.H.; Parent, M.; Kang, Y.-J.; Chapeton, K.; Patterson, B.; Yuan, Y.; He, C.-S.; et al. Engineering of human brain organoids with a functional vascular-like system. *Nat. Methods* **2019**, *16*, 1169–1175. [CrossRef] [PubMed]
50. Johnson, D.E.; Ostrowski, P.; Jaumouillé, V.; Grinstein, S. The position of lysosomes within the cell determines their luminal pH. *J. Cell Biol.* **2016**, *212*, 677–692. [CrossRef]
51. Zhang, I.; Cui, Y.; Amiri, A.; Ding, Y.; Campbell, R.E.; Maysinger, D. Pharmacological inhibition of lipid droplet formation enhances the effectiveness of curcumin in glioblastoma. *Eur. J. Pharm. Biopharm.* **2016**, *100*, 66–76. [CrossRef]
52. Dubey, R.; Stivala, C.E.; Nguyen, H.Q.; Goo, Y.-H.; Paul, A.; Carette, J.E.; Trost, B.M.; Rohatgi, R. Lipid droplets can promote drug accumulation and activation. *Nat. Chem. Biol.* **2020**, *16*, 206–213. [CrossRef] [PubMed]
53. Treyer, A.; Mateus, A.; Wiśniewski, J.R.; Boriss, H.; Matsson, P.; Artursson, P. Intracellular Drug Bioavailability: Effect of Neutral Lipids and Phospholipids. *Mol. Pharm.* **2018**, *15*, 2224–2233. [CrossRef]
54. Boutej, H.; Rahimian, R.; Thammisetty, S.S.; Béland, L.-C.; Lalancette-Hébert, M.; Kriz, J. Diverging mRNA and Protein Networks in Activated Microglia Reveal SRSF3 Suppresses Translation of Highly Upregulated Innate Immune Transcripts. *Cell Rep.* **2017**, *21*, 3220–3233. [CrossRef]
55. Liddelow, S.A.; Guttenplan, K.A.; Clarke, L.E.; Bennett, F.C.; Bohlen, C.J.; Schirmer, L.; Bennett, M.L.; Münch, A.E.; Chung, W.-S.; Peterson, T.C.; et al. Neurotoxic reactive astrocytes are induced by activated microglia. *Nature* **2017**, *541*, 481–487. [CrossRef]
56. Mummery, R.S.; Rider, C.C. Characterization of the heparin-binding properties of IL-6. *J. Immunol.* **2000**, *165*, 5671–5679. [CrossRef]
57. Roesch, S.; Rapp, C.; Dettling, S.; Herold-Mende, C. When Immune Cells Turn Bad—Tumor-Associated Microglia/Macrophages in Glioma. *Int. J. Mol. Sci.* **2018**, *19*, 436. [CrossRef] [PubMed]
58. Sims, G.P.; Rowe, D.C.; Rietdijk, S.T.; Herbst, R.; Coyle, A.J. HMGB1 and RAGE in Inflammation and Cancer. *Annu. Rev. Immunol.* **2010**, *28*, 367–388. [CrossRef]
59. Rapoport, B.L.; Steel, H.C.; Theron, A.J.; Heyman, L.; Smit, T.; Ramdas, Y.; Anderson, R. High Mobility Group Box 1 in Human Cancer. *Cells* **2020**, *9*, 1664. [CrossRef]
60. Matarredona, E.R.; Pastor, A.M. Extracellular Vesicle-Mediated Communication between the Glioblastoma and Its Microenvironment. *Cells* **2020**, *9*, 96. [CrossRef]
61. Conti, I.; Varano, G.; Simioni, C.; Laface, I.; Milani, D.; Rimondi, E.; Neri, L.M. miRNAs as Influencers of Cell–Cell Communication in Tumor Microenvironment. *Cells* **2020**, *9*, 220. [CrossRef] [PubMed]
62. Gieryng, A.; Pszczolkowska, D.; Walentynowicz, K.A.; Rajan, W.D.; Kaminska, B. Immune microenvironment of gliomas. *Lab. Invest.* **2017**, *97*, 498–518. [CrossRef]

63. Kobara, H.; Miyamoto, T.; Suzuki, A.; Asaka, R.; Yamada, Y.; Ishikawa, K.; Kikuchi, N.; Ohira, S.; Shiozawa, T. Lipocalin2 enhances the matrix metalloproteinase-9 activity and invasion of extravillous trophoblasts under hypoxia. *Placenta* **2013**, *34*, 1036–1043. [CrossRef]
64. Lin, Y.; Ren, J.; Qu, X. Catalytically active nanomaterials: A promising candidate for artificial enzymes. *Acc. Chem. Res.* **2014**, *47*, 1097–1105. [CrossRef]
65. Ferber, S.; Tiram, G.; Sousa-Herves, A.; Eldar-Boock, A.; Krivitsky, A.; Scomparin, A.; Yeini, E.; Ofek, P.; Ben-Shushan, D.; Vossen, L.I.; et al. Co-targeting the tumor endothelium and P-selectin-expressing glioblastoma cells leads to a remarkable therapeutic outcome. *Elife* **2017**, *6*. [CrossRef]
66. Sousa-Herves, A.; Würfel, P.; Wegner, N.; Khandare, J.; Licha, K.; Haag, R.; Welker, P.; Calderón, M. Dendritic polyglycerol sulfate as a novel platform for paclitaxel delivery: Pitfalls of ester linkage. *Nanoscale* **2015**, *7*, 3923–3932. [CrossRef]
67. Mendes, L.P.; Sarisozen, C.; Luther, E.; Pan, J.; Torchilin, V.P. Surface-engineered polyethyleneimine-modified liposomes as novel carrier of siRNA and chemotherapeutics for combination treatment of drug-resistant cancers. *Drug Deliv.* **2019**, *26*, 443–458. [CrossRef]
68. Subhan, M.A.; Torchilin, V.P. Efficient nanocarriers of siRNA therapeutics for cancer treatment. *Transl. Res.* **2019**, *214*, 62–91. [CrossRef]
69. Gerecke, C.; Edlich, A.; Giubudagian, M.; Schumacher, F.; Zhang, N.; Said, A.; Yealland, G.; Lohan, S.B.; Neumann, F.; Meinke, M.C.; et al. Biocompatibility and characterization of polyglycerol-based thermoresponsive nanogels designed as novel drug-delivery systems and their intracellular localization in keratinocytes. *Nanotoxicology* **2017**, *11*, 267–277. [CrossRef] [PubMed]
70. Machado, E.; White-Gilbertson, S.; van de Vlekkert, D.; Janke, L.; Moshiah, S.; Campos, Y.; Finkelstein, D.; Gomero, E.; Mosca, R.; Qiu, X.; et al. Regulated lysosomal exocytosis mediates cancer progression. *Sci. Adv.* **2015**, *1*, e1500603. [CrossRef]
71. Sundler, R. Lysosomal and cytosolic pH as regulators of exocytosis in mouse macrophages. *Acta Physiol. Scand.* **1997**, *161*, 553–556. [CrossRef]
72. Kepstutlu, B.; Wycisk, V.; Achazi, K.; Kapishnikov, S.; Pérez-Berná, A.J.; Guttmann, P.; Cossmer, A.; Pereira, E.; Ewers, H.; Ballauff, M.; et al. Cells Undergo Major Changes in the Quantity of Cytoplasmic Organelles after Uptake of Gold Nanoparticles with Biologically Relevant Surface Coatings. *ACS Nano* **2020**, *14*, 2248–2264. [CrossRef]
73. Marx, V. Reality check for organoids in neuroscience. *Nat. Methods* **2020**, *17*, 961–964. [CrossRef]





**Publisher's Note:** MDPI stays neutral with regard to jurisdictional claims in published maps and institutional affiliations.



© 2020 by the authors. Licensee MDPI, Basel, Switzerland. This article is an open access article distributed under the terms and conditions of the Creative Commons Attribution (CC BY) license (<http://creativecommons.org/licenses/by/4.0/>).

Article

# Identification of New Genetic Clusters in Glioblastoma Multiforme: *EGFR* Status and *ADD3* Losses Influence Prognosis

Lara Navarro <sup>1,2,†</sup>, Teresa San-Miguel <sup>1,3,\*,†</sup>, Javier Megías <sup>1,3</sup>, Nuria Santonja <sup>2</sup>, Silvia Calabuig <sup>1,4,5</sup>, Lisandra Muñoz-Hidalgo <sup>1</sup>, Pedro Roldán <sup>6</sup>, Miguel Cerdá-Nicolás <sup>1,3,7</sup> and Concha López-Ginés <sup>1,3</sup>

<sup>1</sup> Department of Pathology, University of Valencia, 46010 Valencia, Spain; Lara.navarro@uv.es (L.N.); Javier.megias@uv.es (J.M.); Silvia.calabuig@uv.es (S.C.); lisandramh@gmail.com (L.M.-H.); Jose.m.cerda@uv.es (M.C.-N.); Concha.lopez@uv.es (C.L.-G.)

<sup>2</sup> Department of Pathology, Hospital General Universitario Valencia, 46014 Valencia, Spain; nuriasantonja3@hotmail.com

<sup>3</sup> INCLIVA Foundation, 46010 Valencia, Spain

<sup>4</sup> Molecular Oncology Laboratory, Fundación para la Investigación Hospital General Valencia, 46014 Valencia, Spain

<sup>5</sup> Centro de Investigación Biomédica en Red de Cáncer, 28029 Madrid, Spain

<sup>6</sup> Department of Neurosurgery, Hospital Clínico Universitario Valencia, 46010 Valencia, Spain; Pedro.roldan@uv.es

<sup>7</sup> Department of Pathology, Hospital Clínico Universitario Valencia, 46010 Valencia, Spain

\* Correspondence: Teresa.miguel@uv.es; Tel.: +34-963-983-946

† Both first authors have contributed equally to this work.

Received: 5 October 2020; Accepted: 3 November 2020; Published: 6 November 2020



**Abstract:** Glioblastoma multiforme (GB) is one of the most aggressive tumors. Despite continuous efforts to improve its clinical management, there is still no strategy to avoid a rapid and fatal outcome. *EGFR* amplification is the most characteristic alteration of these tumors. Although effective therapy against it has not yet been found in GB, it may be central to classifying patients. We investigated somatic-copy number alterations (SCNA) by multiplex ligation-dependent probe amplification in a series of 137 GB, together with the detection of *EGFRvIII* and FISH analysis for *EGFR* amplification. Publicly available data from 604 patients were used as a validation cohort. We found statistical associations between *EGFR* amplification and/or *EGFRvIII*, and SCNA in *CDKN2A*, *MSH6*, *MTAP* and *ADD3*. Interestingly, we found that both *EGFRvIII* and losses on *ADD3* were independent markers of bad prognosis ( $p = 0.028$  and  $0.014$ , respectively). Finally, we got an unsupervised hierarchical classification that differentiated three clusters of patients based on their genetic alterations. It offered a landscape of *EGFR* co-alterations that may improve the comprehension of the mechanisms underlying GB aggressiveness. Our findings can help in defining different genetic profiles, which is necessary to develop new and different approaches in the management of our patients.

**Keywords:** glioblastoma; *IDH*; *ADD3*; *EGFR*; survival; high throughout techniques; precision

## 1. Introduction

Glioblastoma multiforme, *IDH* wild-type (GB-*IDHwt*), is the most frequent malignant brain tumor in adults and the most aggressive in nature, with an average survival of around 15–18 months [1,2]. GB displays, in addition to morphological heterogeneity, a wide genetic heterogeneity [3,4]. This fact is, despite constant efforts, one of the main causes of the absence of effective treatment and thus,

of the extremely poor prognosis this disease offers [5,6]. The last World Health Organization (WHO) classification tackles GB genetic heterogeneity, putting *IDH* status in the spotlight and associating it to prognosis [1,7]. The mutations that GB-*IDH*wt acquires during clonal evolution do not follow a linear development [4,8]. Many efforts have been made since The Pan Cancer project of TCGA deepened on the high frequency of alterations in the receptor tyrosine kinase/PI3K/PTEN/AKT/mTOR-signaling pathway (present in 88% of GB cases), along with the p53/MDM2/p14ARF molecular pathway (87%) and the CDKN2A/CDK4/6/retinoblastoma signaling pathway (78%) [1,9–12]. Those alterations seem to be a core requirement for GB pathogenesis and they are associated with a poor prognosis [13,14]. Identifying genetic changes in shared nodes of convergence may improve our understanding of diseases [4]. In addition, the identification of differential targets among GB *IDH*-wt genetic subgroups could lead to reach better approaches to GB management. *EGFR* amplification is a hallmark of glioma pathogenesis [4,15,16]. In the last decade, many molecules have shown promising results on pre-clinical or phase 1/2 trials targeting *EGFR*. However, they tend to fail, as recently happened with ABT-414 conjugated with ABBV-321 [16,17]. It is also disappointing that while TKI therapies have been successfully expanded to multiple types of cancer, none of them have improved the lifespan of GB patients [18]. Nevertheless, the interest of assessing *EGFR* copy number status [19–24] along with variants that have been related to cell proliferation, angiogenesis and invasion, and thus, with shortened survival, such as the *EGFR* variant III (*EGFRvIII*) [25–27], is undeniable.

Huge efforts have been made using high-throughput techniques for the genomic analysis of GB [4,28,29]. However, the complexity of the data they provide makes it difficult to draw a targetable GB portrait [1,28]. There is still a long way to progressively introduce objective biomarkers towards precision medicine adapted to the molecular profile of the tumor. High-throughput user-friendly techniques such as multiplex ligation-dependent probe amplification (MLPA) could be optimal for the development of new personalized therapies [24,30].

The main goal of this work was to characterize the frequent alteration of *EGFR* via its amplification or the presence of *EGFRvIII* in a series of 137 primary GBs and to assess concomitant somatic copy number alterations (SCNA). We focused on primary, *de novo*, *IDH*wt GBs, and we delved deeper into the potential use of MLPA to study formalin-fixed paraffin-embedded (FFPE) GB. We aimed to define networks of genetic alterations from a simplified point of view, compared to high-throughput techniques, using such a common kind of material as paraffin embedded tumor tissue samples are. Our results highlight the existence of three groups of tumors according to different complex genetic profiles, where *EGFR* plays a crucial role. We also present the importance of *ADD3* and *EGFRvIII* as genetic biomarkers that may determine a more accurate prognostic for GB patients. Taken together, our results improve the comprehension of the mechanisms underlying GB aggressiveness and establish a new genetic classification that could enhance the clinical management of GB patients.

## 2. Materials and Methods

### 2.1. Patients, Samples and Clinical Study

GB samples were obtained from 137 patients surgically treated at the Clinic Hospital of Valencia between 1995 and 2010, with known follow-up. The study was reviewed and approved by Institutional Ethics Committee of the University of Valencia and Clinic Hospital of Valencia. Tumor specimens were fixed in neutral buffered formalin, embedded in paraffin, sectioned, and stained with hematoxylin and eosin (H&E). Samples were categorized according to the WHO classification [1]. Glioblastoma, *IDH*-mutant (n = 9), including those that progressed from lower-grade gliomas, were not included in the different statistical analyses. All patients underwent treatment consisting of maximum safe tumor resection and none of them received chemotherapy or radiotherapy before surgery. Similar schemes of first-line treatment, encompassing radiotherapy (50–65 Gray) with concomitant and adjuvant temozolomide-based chemotherapy were applied after surgery in all the cases. A retrospective

survival analysis was performed. Overall survival (OS) was calculated as time from surgery to death. Event times were censored if the patient was alive at the time of last follow-up.

## 2.2. DNA Extraction, Molecular Analysis of IDH1/2, TP53 and MLPA

Genomic DNA was extracted from FFPE tissue samples using a QIAamp DNA FFPE Tissue Kit (Qiagen, Inc., Valencia, CA, USA) according to the manufacturer's instructions. We analyzed by direct sequencing the genomic regions spanning wild-type R132 of *IDH1* and wild-type R172 of *IDH2*. Exons 5–8 of TP53 were also sequenced. PCRs were performed using standard buffer conditions, 200 ng of DNA and an AmpliTaq Gold Master Mix (Thermo Fisher Scientific, Waltham, MA, USA). PCR products were purified with Centricon columns (Amicon, Beverly, MA, USA) and analyzed on an ABI 310 Sequencer (Applied Biosystems, Foster City, CA, USA). Primer sequences forward (fw) and reverse (rv) were as follow: *IDH1* fw 5'-ACCAAATGGCACCATACGAA and rv 5'-TCACATTATTGCCAACATGACTT, *IDH2* fw 5'-CCAATGGAACCTATCCGGAAC and rv 5'-CCTCTCCACCCTGGCCTAC, TP53 (exon 5) fw 5'-CAGCCCTGTCGTCTCTCCAG and rv 5'-TTCAACTCTGTCTCCTTCCT, TP53 (exon 6) fw 5'-GTCTGGCCCCCTCCTC AGCAT and rv 5'-GTCTGGCCCCCTCCTCAGCAT, TP53 (exon 7) fw 5'-CTCATCTTGGGCCTGTGTTA and rv, 5'-AGTGTGCAGGGTGGCAAGTG, TP53 (exon 8) fw 5'-ACCTGATTTC TACTGCCTCTTGC and rv 5'-GTCCTGCTTGCTTACCTC GCTTAGT.

Multiplex Ligation-dependent Probe Amplification (MLPA) using the MLPA KIT P105 (version C1-C2) and ME024 (version A1-B1) was performed in accordance with the manufacturer's protocol (MRC Holland, Amsterdam, Netherland) [30,31]. Amplification products were separated on an ABI 310 Sequencer (Applied Biosystems, Inc, Foster City, CA, USA) and data analysis was made with Coffalyser excel-based software (MRC-Holland) [32], where relative probe values of probe-amplified products are compared with normal controls. These kits included multiple glioma and cancer related genes that were evaluated depending on their probes based on previous reports [30,31,33,34], as explained below. Both kits are approved for investigational-use only.

## 2.3. Status of EGFR: EGFRvIII, Copy Number Alterations and Interphase Fluorescence In Situ Hybridization

*EGFR* was studied by MLPA using the P105 kit (MRC-Holland). It includes 11 probes for exons 1–8, 13, 18 and 24 of *EGFR*. This design allowed us to determine on one hand, the presence of the variant III and on the other hand, somatic copy number alterations (SCNAs) of *EGFR* in the samples analyzed. Following previously published descriptions, to identify *EGFR*vIII we determined the average value for exons 2–7 probes and established the ratio with the average value of probes for exons 1, 8, 13, 18 and 24. Patients with ratios below 0.8 were considered to harbor the *EGFR*vIII [31,35]. SCNAs of *EGFR* were determined based on the average value of exons 1, 8, 13, 18 and 24 in order to exclude the ones that are frequently involved in *EGFR* variants. The thresholds applied classified the samples as no amplified ( $0.7 < x < 1.3$ ) or gained ( $x \geq 1.3$ ) for downstream statistical analysis. We also analyzed the *EGFR* gene status in interphase cells by dual-color FISH probes using interphase Fluorescence in situ hybridization (iFISH). For that purpose, we used tissue microarrays (TMAs) and the probe LSI *EGFR* SpectrumOrange/CEP-7 SpectrumGreen Probe from Vysis (Abbott Laboratories, IL, USA). Hybridizations were performed according to the manufacturer's instructions, and signals were counted in two different regions of 200 non-overlapping nuclei. We calculated the ratio between the average signal count of *EGFR* and the control probe CEP-7 (*EGFR*/CEP7 ratio). *EGFR* was considered to be amplified when the *EGFR*/CEP-7 signal ratio was  $>2$  [36]. Cases were subclassified according to previous descriptions as GBs with high level of amplification (H-amp) when more than 20% of the cells showed more than 20 copies of *EGFR*. GBs with low levels of amplification (L-amp) included cases with 5–20% of cells with 4–12 copies of *EGFR*. Cases without amplification (N-amp) showed two copies of *EGFR*. The exact ratio was not calculated in cases with high amplification levels [19,36]. The aim of this validation study was to determine the concordance rates of these techniques. Concordance between both techniques was assessed by the Cohen's Kappa statistic. It has a range of 0–1.0 and  $\kappa$

values  $< 0.2$  means a poor agreement,  $0.21 < \kappa < 0.4$  means a weak agreement,  $0.41 < \kappa < 0.6$  means a moderate agreement,  $0.61 < \kappa < 0.8$  means a good agreement and  $0.81 < \kappa < 1$  means a very good agreement between techniques.

#### 2.4. Analysis of Locus 9p21 and Other Glioma and Cancer-Related Genes

SALSA MLPA P105 and ME024 included a collection of probes to determine *PTEN* status and genes located on 9p21. Many probes in order to characterize *CDKN2A-CDKN2B* (p15INK4B-p14ARF-p16INK4A) were included. These kits also comprised probes for other genes located up and downstream on 9p21.3 (*KLHL9*, *MIR31*, *MLLT3* and *MTAP*) and for genes located near on 9p (*DOCK8* 9p24.3 and *GLDC* on 9p24.1, and *PAX5* on 9p13.2). In addition, a wide collection of probes addressed to many different genes were assayed, including: *DYSF* (2p13), *MSH6* (2p16), *SIX3* (2p21), *SPAST* (2q22.3), *EDAR* (2q12.3), *CTNNB1* (3p22), *ATR* (3q23), *TGFBR2* (3p24), *CFI* (4q25), *WDR36* (5q22.1), *IL4* (5q31), *CDH7* (8q12), *ADD3* (10q25.2), *MEN1* (11q13.1), *SMPD1* (11p15.4), *COL2A1* (12q13.11), *HNFB1A* (12q24), *PCCA* (13q32.3), *ING1* (13q34), *ATL1* (14q22.1), *SNRPN-HB2-85* (15q11.2), *SPG11* (15q21.1), *IQGAP1* (15q26.1), *MVP* (16p11.2), *TRAF4* (17q11.2), *ERBB2* (17q12), *NPC1* (18q11.2), *CACNA1A* (19p13.2), *SMARCA4* (19p13.2), *JAG1* (20p12.2), *ADAMTS5* (21q21.3), and *TIMP3* (22q12.3). The variety of loci explored offered a detailed landscape of GB SCNAs.

To categorize MLPA call to SCNA value, we established deletions as  $x < 0.7$ , normal as  $0.7 < x < 1.3$  and gain as  $x > 1.3$ . When probe values within the different exons of one locus were heterogeneously distributed across some categories such as heterozygous and homozygous deletions, we defined the category in which more than 70% of probe values belonged. For convenience, homozygous and/or heterozygous deletions collectively were referred to as deletion, while amplification and/or gain as gain/amp. Non-canonical SCNAs such as gain/amp in *CDKN2A*, *PTEN* or *TP53* and deletion in *EGFR* or *CDK4* were not considered in the data analysis.

#### 2.5. Statistical Analysis

The statistical analysis of the data was carried out according to the type of variable. Quantitative variables were evaluated using the Kolmogorov-Smirnov and Levene tests; depending on their results and their characteristics, Student's t-test, ANOVA, Mann-Whitney-Wilcoxon test or Kruskal-Wallis test were performed. For comparisons among categorical variables, Fisher's exact, Pearson's chi-squared, and Kruskal-Wallis test were used depending on the number of rows/columns and the expected frequencies. A survival analysis using the Kaplan-Meier method was also done. The statistical significance of these curves was calculated using the log-rank (Mantel-Cox) test. Significance was accepted at least at  $p < 0.050$  level. Data were analyzed with SPSS (version 26) software (IBM, Madrid, Spain). To perform the clusters, the average-linkage method was used. Therefore, distance between clusters was obtained as the average distance between all possible pairs of cases from both clusters, providing robust groups. Euclidean distance was used because of the binary scale of the genetic variables. The choice of three clusters was decided from the hierarchical tree, according to the level of heterogeneity at which the clusters were combined. Cluster combination stopped when this level was roughly 70% of the total amount.

#### 2.6. TCGA Analysis and Functional Protein Associations

We accessed data for GB samples from The Cancer Genome Atlas (TCGA) by using cBioPortal for Cancer Genomics ([www.cbioportal.org](http://www.cbioportal.org)) [12,37,38] to validate whether the SCNAs detected in our cohort were associated with EGFR amplification there. We studied the Genomic Profile "Putative copy-number alterations from GISTIC" for the latest dataset available in cBioportal for GB (TCGA, Provisional 604 samples). Copy number alteration data from 577 cases were obtained and further analyzed. A "User-Defined List", including *EGFR*, *CDKN2A*, *MTAP*, *TRAF4*, *JAG1* and *MSH6*, was entered into the "Enter Gene" box. Samples were classified for each gene according to their putative copy number variation calculated by GISTIC with default cBioportal thresholds 33. The groups were



Diploid (0), Shallow Deletion (−1), Deep deletion (−2), Gain (1) and Amplification (2). The associations between EGFR amplification and the copy number profile were analyzed using the “Plots” tool and retrieving the raw data. Outlier values ( $n < 10$  from 577 cases) were negligible. Statistical significance for amplification vs. diploid and deletion (shallow or deep) vs. diploid for each gene was assessed using Fisher’s exact test.

We also used the Search Tool for the Retrieval of Interacting Genes/Proteins (STRING) database of known and predicted protein-protein interactions (<https://string-db.org>) to establish associations among the proteins encoded by the genes affected by SCNAs in this series. This database contains information from numerous sources, including KEGG, Reactome or Pubmed, among others [37]. To make a restrictive analysis, we explored both evidence and confidence meaning of network edges and we increased the minimum required interaction score to ‘high confidence (0.700)’ to reach a greater reliability.

### 3. Results

#### 3.1. Clinical and Histopathological Data

Our study included 137 patients. Clinical data, including age, sex, tumor location, size, initial symptom and Karnofsky performance status scale (KPS), are summarized in Table 1. Mean age at diagnosis was 57.7 years and male/female ratio was 1.17. OS was 210 days and did not reflected statistical differences depending on sex nor age. Histologically, all tumors showed features of GB with pleomorphic astrocytic tumor cells, prominent microvascular proliferation and necrosis (Figure 1). From confirmed primary GB ( $n = 135$ ), the majority were IDHwt ( $n = 128$ ) but a little subgroup of tumors displayed IDH mutations ( $n = 7$ ) despite being primary GB (GB-IDHmut). In agreement with the WHO 2016 classification, these GB-IDHmut-affected patients were significantly younger (40.9 years in IDHmut vs. 59 years in IDHwt,  $p < 0.001$  \*\*). OS was also significantly higher in IDHmut than in IDHwt patients (3300 days vs. 180 days,  $p < 0.001$  \*\*). From the 128 cases, 63.9% of patients were >55 years old at diagnosis, the 56.3% were male and 76.9% had a KPS  $\leq 85$  preoperatively. Interestingly, tumor Pearson correlation test demonstrated an association between tumor size and OS ( $p = 0.020$  \*).

#### 3.2. EGFR Status Assessment by iFISH and MLPA

iFISH analysis showed a distribution of cases among N-amp, L-amp and H-amp of 35.6%, 12.7% and 51.7%, respectively (Figure 1). Similarly, MLPA analysis, which only separates two categories, showed that 29.7% of cases had no EGFR gains, whereas 70.3% of the cases displayed gain of EGFR copies. Comparing FISH H-amp and L-amp with MLPA “gain”, and FISH N-amp with MLPA “no gain”, concordance between both techniques was good, with a coincident result in 83.05% of the samples (Cohen’s kappa index: 0.610). Agreement was 93.4% for L-amp and H-amp GBs assessed by iFISH that were detected as gains by MLPA. Regarding N-amp tumors, the concordance dropped to 64.3% (Supplementary Table S1 shows the result from both techniques for each case). The visual determination of EGFR made iFISH more suitable to categorizing the cases according to their amplification status. Thus, the following analyses regarding EGFR amplification status were established according to the iFISH data. Among the 128 GB patients, we found no significant associations between EGFR amplification and survival ( $p = 0.387$ ). Clinical data did not reveal any strong association to the amplification status either: 50.8% of men and 49.2% of women displayed H-amp EGFR, reflecting no differences depending on the basis of sex. We did not find significant associations between EGFR amplification and patient age.

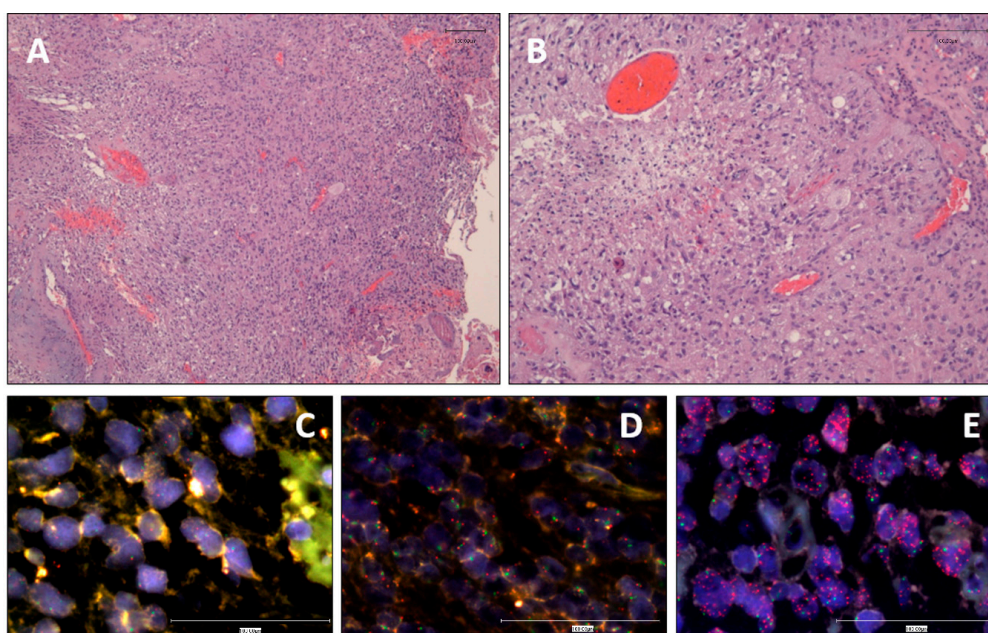


**Figure 1.** Representative microphotographs of GB, *IDH*-wt. (A) High cellularity and poor differentiation with prominent microvascular proliferation and necrosis (Hematoxylin and Eosin, 10×). (B) Highly anaplastic, heterogeneous cells and microvascular proliferation (Hematoxylin and Eosin, 20×). (C–E) iFISH microphotographs showing the status of *EGFR* by an orange LSI-*EGFR* probe and the centromere of chromosome 7 as a reference, stained by CEP-7 green probe in cases representing the tree levels of amplification. (C) No *EGFR* amplification (40×). (D) Low level of *EGFR* amplification (40×). (E) High *EGFR* amplification (40×).

### 3.3. *EGFR* Variant III Is More Frequent in Women and Is Associated with Shortened Survival

MLPA allowed us to determine the presence of *EGFR*vIII. *IDH*wt GBs ( $n = 128$ ) exhibited *EGFR*vIII in 35.2% of the cases ( $n = 45$ ). Clinical data revealed no differences between both groups regarding age, tumor location nor size. Nevertheless, there was a significant increase in the presence of this variant in women (55.6% *EGFR*vIII vs. 37.3% *EGFR*wt,  $p = 0.047$  \*). Interestingly, Kaplan–Meier analysis revealed statistical differences in OS (Figure 2,  $p = 0.014$  \*), accounting 150 days in *EGFR*wt vs. 90 days in *EGFR*vIII (Student *t*-test  $p = 0.027$  \*). In addition, *EGFR*vIII was significantly more frequent in GBs with *EGFR* amplification. We found it in 10 cases of N-amp GBs (23.8%), 2 cases of L-amp GBs (13.3%) and 31 cases of H-amp GBs (50.8%,  $p = 0.003$  \*\*).

**Table 1.** Clinical data and baseline molecular characteristics of 137 glioblastoma patients.

Parameter	Specification	Outcome	Wild-Type <i>IDH1/2</i> ( $n = 128$ )	Mutated <i>IDH1</i> ( $n = 9$ )	<i>p</i> -Value
Age	Mean (range), in years	57.7 (24–81)	59 (24–81)	40.9 (32–52)	*** <0.001 <sup>mw</sup>
	≤55	40.6%	36.1%	100%	*** <0.001 $\chi^2$
	>55	59.4%	63.9%		
Sex	Male	54.0%	56.3%	22.2%	0.080 <sup>ft</sup>
	Female	46.0%	43.7%	77.8%	
Tumor location	Parietal	35.0%	33.9%	50.0%	0.282 <sup>kw</sup>
	Frontal	20.3%	19.1%	37.5%	
	Temporal	36.6%	38.3%	12.5%	
	Occipital	4.9%	5.2%		
	Intraventricular	0.8%	0.9%		
	Corpus Callosum	2.4%	2.6%		

Table 1. Cont.

Parameter	Specification	Outcome	Wild-Type IDH1/2 (n = 128)	Mutated IDH1 (n = 9)	p-Value		
Size (cm <sup>3</sup> )	Mean (range)	5.2 cm (2–11)	5.1 cm (2–11)	6.0 cm (5–7)	0.210 <sup>mw</sup>		
Initial symptom	Neurological deficit	30.0%	32.1%	0%	0.146 <sup>kw</sup>		
	Epileptic seizure	21.7%	21.4%	25.0%			
	Intracranial hypertension	48.3%	46.5%	75.0%			
KPS	≤85	76.9%	77.0%	75.0%	1.000 <sup>ft</sup>		
	>85	23.1%	23.0%	25.0%			
Overall survival	Median (95 CI)	210 days	180 days	3300 days	*** <0.001 <sup>lr</sup>		
TP53	Mutation	20.2%	17.3%	50.0%	* 0.028 <sup>χ<sup>2</sup></sup>		
EGFR FISH	Alteration	61.4%	64.4%	22.2%	* 0.012 <sup>χ<sup>2</sup></sup>		
	N-amp	38.6%	35.6%	77.8%	* 0.011 <sup>χ<sup>2</sup></sup>		
	L-amp	13.4%	12.7%	22.2%			
	H-amp	48.0%	51.7%	0.0%			
EGFRvIII	No	65.9%					
	Yes	34.1%					
SCNA	EGFR	Gain	65.4%	70.1%	0.0%	*** <0.001 <sup>χ<sup>2</sup></sup>	
		Normal	34.6%	29.9%	100%	*** <0.001 <sup>kw</sup>	
	CDKN2A	Alteration	63.5%	65.6%	33.3%	0.052 <sup>χ<sup>2</sup></sup>	
		Loss	53.3%				
	CDKN2B	Gain	10.2%				
		Alteration	54.0%	56.3%	22.2%		
		Loss	48.9%			0.080 <sup>ft</sup>	
	PTEN	Gain	5.1%				
		Alteration	65.9%	65.9%	66.7%	0.961 <sup>χ<sup>2</sup></sup>	
		Loss	55.6%				
		Gain	10.4%				
		MTAP	Alteration	52.9%	53.5%	44.4%	0.734 <sup>ft</sup>
		TIMP3	Alteration	65.0%	64.1%	77.8%	0.404 <sup>χ<sup>2</sup></sup>
		ERBB2	Alteration	26.5%			
MVP	Alteration	59.5%	56.3%	100%	* 0.020 <sup>ft</sup>		
MEN1	Alteration	60.6%	57.8%	100%	* 0.012 <sup>χ<sup>2</sup></sup>		
ADD3	Alteration	45.3%	46.9%	22.2%	0.183 <sup>ft</sup>		
PCCA	Alteration	44.1%	46.6%	12.5%	0.075 <sup>ft</sup>		

Prevalence of genetic alterations and cross tabulation of IDH1 mutation status versus clinical characteristics and genetic alterations are depicted. For genetic alteration, only significant findings are shown (\* means  $0.05 > p > 0.01$ , \*\* means  $0.01 > p > 0.001$ , \*\*\* means  $p < 0.001$ ). Data are mean (range), number (%), or median (95%CI). Abbreviations: CNA, copy number alteration; ft, Fisher's exact test; KFS, Karnofsky Performance Status; kw, Kruskal–Wallis test; lr, long-rank test; mw, Mann–Whitney–Wilcoxon test and  $\chi^2$ , Pearson's chi-squared test.

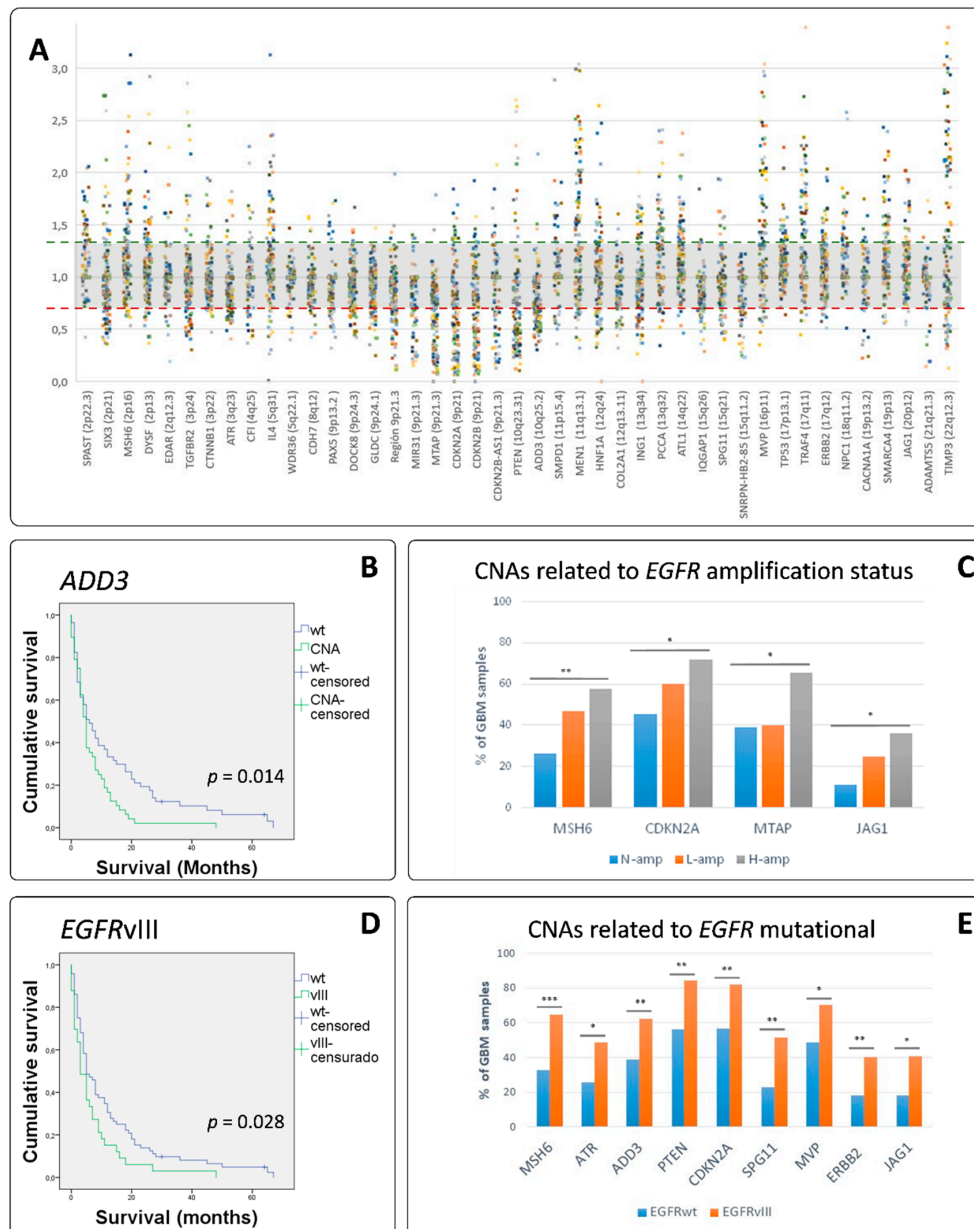


**Figure 2.** GB somatic copy number alterations (SCNA). **(A)** Distribution of MLPA calls from each case on the targeted genes assayed showing the heterogeneity of GB. **(B)** Association between ADD3 SCNA and overall survival (OS). The Y-axis represents the cumulative survival time in terms of probability: it oscillates between 0 (0% of cases) and 1 (100% of cases). The X-axis shows the survival period, expressed in months. The blue line represents survival on patients with wild-type ADD3 (mean = 13.46 months). The green line represents survival in patients which tumors showed SCNA on ADD3 (mean = 6.98 months). Long Rank (Mantel–Cox) analysis demonstrate statistical significance. **(C)** Concomitant SCNA with the EGFR amplification status. MSH6  $p = 0.007$ , CDKN2A  $p = 0.023$ , MTAP  $p = 0.017$  and JAG1  $p = 0.029$ . **(D)** Association between EGFRvIII and OS. The blue line represents survival on patients with EGFRwt (mean= 180 days). The green line represents survival in patients which tumors showed EGFRvIII (mean= 150 days). Long Rank (Mantel–Cox) analysis demonstrate statistical significance. **(E)** Concomitant SCNA with the presence of EGFRvIII. MSH6  $p = 0.001$ , ATR  $p = 0.019$ , ADD3  $p = 0.010$ , PTEN  $p = 0.002$ , CDKN2A  $p = 0.004$ , SPG11  $p = 0.003$ , MVP  $p = 0.032$ , ERBB2  $p = 0.008$ , and JAG1  $p = 0.013$ . \* was used for  $0.050 > p > 0.010$ , \*\* for  $0.010 > p > 0.001$  and \*\*\* for  $p \leq 0.001$ .

### 3.4. MLPA Analysis Showed a Great Heterogeneity in GB

We identified that 100% of the tumor cases showed SCNA in at least two of the genes analyzed. In addition, from all the loci explored, we found SCNA in all of them in at least seven cases. An overview of the prevalence of genetic alterations identified in 128 GB-IDHwt patients is shown in Table 1. A summary of all the SCNAs detected among the studied genes can be seen in Figure 2A which offers a landscape of the high genetic heterogeneity found. We detected alterations affecting more than 45% of the cases on EGFR (70.1% of the cases), CDKN2A (65.6%), TIMP3 (64.1%), MEN1 (57.8%), CDKN2B (56.3%), MVP (56.3%), PTEN (54.8%), MTAP (53.5%), ADD3 (46.9%) and PCCA (46.6%). From those loci, only ADD3 tend to be more altered in women (55.4% of the cases) than in men (40.3% of the cases). However, ADD3 demonstrated to be associated with OS, as patients with SCNAs on ADD3 showed an OS of  $6.98 \pm 1.17$  months while patients with no-SCNA on ADD3 showed an OS of  $13.46 \pm 2.24$  months ( $p = 0.012$  \*). Long Rank (Mantel–Cox) analysis demonstrate a statistic association ( $p = 0.014$  \*, Figure 2B).

### 3.5. EGFR Amplified GBs Displayed Different SCNAs to Non-EGFR Amplified Cases

In this series, four genes revealed statistical differences on their affectation, depending on the amplification status of EGFR: losses/gains of MSH6 on 2p16.3, losses of CDKN2A and MTAP, both on 9p21 and gains of JAG1 on 20p12.2 (Figure 2C). TCGA analysis through cBioportal supported our data, as it showed strong associations between both CDKN2A and MTAP losses and EGFR gain/amp ( $p < 0.0001$  \*\*\*). Of note is that both genes are located in 9p21. TCGA data also showed statistical association between JAG1 gain/amp and EGFR gain/amp ( $p < 0.0001$  \*\*\*). MSH6 showed alterations in a little number of GBs and did not reach a significant result (Table 2). STRING analysis provided a PPI enrichment  $p$ -value of 0.000987 and association to NOTCH3 activation and to a negative regulation of cell–matrix adhesion. Based on previous reports [7], we looked for GB with triple SCNA (EGFR, CDKN2A and PTEN); in our series, this appeared in 25.0% of the cases and they showed an OS of  $7.64 \pm 1.97$  months, which was lower than the  $11.25 \pm 1.71$  months in cases with no triple SCNA.

Looking for differences depending on EGFR status, we found in our series that EGFRvIII cases displayed statistically different SCNAs than their EGFRwt counterparts: MSH6 (2p16.3), ATR (3q23), ADD3 (10q25.1), PTEN (10q23.31), CDKN2A (9p21), SPG11 (15q21), MVP (16p11.2), ERBB2 (17q12), JAG1 (20p12.2) (Figure 2E). STRING functional analysis of these genes revealed a PPI enrichment  $p$ -value of  $9.2 \times 10^{-6}$  and a non-random association with negative regulation of cell–matrix adhesion processes (false discovery rate –FDR- of 0.00100).

**Table 2.** Data from TCGA analysis performed using cBioportal.

		<i>EGFR</i>			
		Shallow Deletion	Diploid	Gain	Amplification
<i>CDKN2A</i>	Deep deletion	2	20	131	178
	Shallow deletion	3	19	48	38
	Diploid	1	22	61	35
	Gain	0	2	14	3
	Amplification	0	1	0	0
*** n = 577; $p < 0.00001$ ; Chi-square 461.258					
<i>JAG1</i>	Shallow deletion	1	3	13	1
	Diploid	3	52	153	126
	Gain	2	9	88	125
	Amplification	0	0	0	1
*** n = 576; $p < 0.00001$ ; Chi-square 41.9092					

Table 2. Cont.

		<i>EGFR</i>			
		Shallow Deletion	Diploid	Gain	Amplification
<i>MSH6</i>	Shallow deletion	0	8	15	14
	Diploid	4	55	220	225
	Gain	2	1	19	14
n = 571; $p > 0.05$ ; Chi-square 7.2998					
<i>MTAP</i>	Deep deletion	2	18	114	169
	Shallow deletion	3	21	61	46
	Diploid	1	22	65	35
	Gain	0	2	14	3
	Amplification	0	1	0	0
*** n = 570; $p < 0.00001$ ; Chi-square 46.413					

Annotated CNAs depending on *EGFR* amplification status. \* was used for  $0.050 > p > 0.010$ , \*\* for  $0.010 > p > 0.001$  and \*\*\* for  $p \leq 0.001$ .

### 3.6. Clustering Analysis Revealed Different Genetic Glioblastoma Groups

Hierarchical cluster classification distinguished three groups (C1, C2 and C3) depending on the frequencies of alteration within the different loci explored (Table 3). In this analysis we excluded 37 patients because some markers were not available. From the 91 patients to classify, 18 were unclassifiable subjects due to the diversity of the SCNAs found and 73 were distributed among the three different groups performed. The clusters showed partially overlapped changes and others completely differentiated among them (Figure 3). The Chi-squared test was used to assess the dependence between the normal/altered presence of a gene and the membership cluster in order to identify which genes have a higher power of discrimination. When the expected frequency in cells of the cross-table was too small ( $n < 5$ ) in more than 33% of cells, the Kruskal–Wallis test was used as an alternative to Chi-squared. Regarding clinical data, size was similar in the different clusters, showing an average of 5.7 cm in C1, and 5.3 cm in C2 and 4.9 in C3. Age at diagnosis also showed similar averages (59, 57 and 61 years, respectively). Overall survival was 7.2 months for C1, 5.9 for C2 and 10.7 months for C3. Genetically, the analysis showed that C1 was the least affected, C2 showed alterations of near half of the loci explored in more than 50% of the cases, and C3, displayed an intermediate situation, with near 30% of the genes included affected in more than 50% of the cases. When we analyzed the *EGFR* amplification status by iFISH in relation to these clusters, we found statistically significant differences ( $p = 0.007$  \*\*): most cases from C1 were N-amp (63.0%), compared to 28.0% and 19.0% in C2 and C3, respectively. Most cases from C2 and C3 were H-amp (64.0% and 61.9%, respectively), compared to 22.2% in C1. This distribution of the cases for the L-amp group was more homogeneous, accounting 14.8%, 8.0% and 19.0% in C1, C2 and C3, respectively.

**Table 3.** Clustering analysis of GBM IDHwt.

Genes Studied	Cluster 1	Cluster 2	Cluster 3	p-Value
<i>CTNNB1</i>	11.1	8.0	28.6	0.120 (KW)
<i>CDH7</i>	0.0	12.0	4.8	0.166 (KW)
<i>IQGAP1</i>	18.5	12.0	23.8	0.581 (KW)
<i>GLDC</i>	7.4	12.0	23.8	0.254 (KW)
<i>TP53</i>	11.1	12.0	42.9	<b>0.011 * (Chi)</b>
<i>TGFBR2</i>	11.1	16.0	9.5	0.781 (KW)
<i>ING1</i>	18.5	24.0	33.3	0.495 (Chi)
<i>SIX3</i>	14.8	24.0	52.4	<b>0.014 * (Chi)</b>
<i>IL4</i>	14.8	24.0	66.7	<b>&lt;0.001 *** (Chi)</b>
<i>PCCA</i>	44.4	24.0	85.7	<b>&lt;0.001 *** (Chi)</b>
<i>DYSF</i>	18.5	28.0	42.9	0.180 (Chi)
<i>HNFA1</i>	37.0	28.0	57.1	0.124 (Chi)
<i>DOCK8</i>	7.4	32.0	9.5	<b>0.036 * (KW)</b>
<i>ERBB2</i>	14.8	36.0	19.0	0.169 (Chi)
<i>ATL1</i>	22.2	36.0	52.4	0.096 (Chi)
<i>ATR</i>	25.9	48.0	19.0	0.080 (Chi)
<i>TRAF4</i>	44.4	52.0	28.6	0.268 (Chi)
<i>JAG1</i>	3.7	56.0	9.5	<b>&lt;0.001 *** (Chi)</b>
<i>SPG11</i>	14.8	56.0	9.5	<b>&lt;0.001 *** (Chi)</b>
<i>EGFRvIII</i>	14.8	56.0	23.8	<b>&lt;0.001 *** (Chi)</b>
<i>MSH6</i>	11.1	60.0	66.7	<b>&lt;0.001 *** (Chi)</b>
<i>ADD3</i>	40.7	72.0	42.9	<b>0.048 * (Chi)</b>
<i>SMARCA4</i>	33.3	84.0	4.8	<b>&lt;0.001 *** (Chi)</b>
<i>MVP</i>	51.9	84.0	14.3	<b>&lt;0.001 *** (Chi)</b>
<i>MTAP</i>	22.2	84.0	76.2	<b>&lt;0.001 *** (Chi)</b>
<i>PTEN</i>	44.4	88.0	38.1	<b>&lt;0.001 *** (Chi)</b>
<i>TIMP3</i>	44.4	92.0	57.1	<b>0.001 ** (Chi)</b>
<i>EGFR</i>	40.7	92.0	85.7	<b>&lt;0.001 *** (Chi)</b>
<i>MEN1</i>	44.4	96.0	23.8	<b>&lt;0.001 *** (Chi)</b>
<i>CDKN2A</i>	7.4	100.0	100.0	<b>&lt;0.001 *** (Chi)</b>

p-values were calculated by the (Chi), Pearson's chi-squared test  $\chi^2$  and (KW), Kruskal–Wallis test. To highlight statistical significance \* was used for  $0.050 > p > 0.010$ , \*\* for  $0.010 > p > 0.001$  and \*\*\* for  $p \leq 0.001$ .

### 3.7. Genetic Changes According to Clustering Analysis Point to Differentially Altered Pathways

EGFRvIII and losses in ADD3, associated with survival, were concentrated in cluster 2. In concordance, C2 displayed as aforementioned, the shortest OS. In addition, it showed the highest frequency of SCNAs in CDKN2A, MEN1, EGFR, TIMP3, PTEN, MTAP, MVP, SMARCA4, ADD3, MSH6, JAG1, SPG11 and DOCK8. The gene function and pathway annotation analysis by the STRING software showed a PPI enrichment p-value of 0.000522 and an association to the biological processes 'regulation of cell-substrate adhesion' (FDR =  $8.36 \times 10^{-5}$ , by JAG1, CDKN2A, PTEN and MEN1) and 'cell-matrix adhesion' (FDR = 0.000522, by JAG1, CDKN2A and PTEN). Moreover, the Cellular Component analysis showed a significant association to the presence of the proteins encoded in different parts of the cell. They were detected both in the plasma membrane region (count in gene

set: 5/1061), in organelle lumen (count in gene set: 10/5162) and in the nuclear part (count in gene set: 9/4359), all with FDR = 0.0364, suggesting an intense trafficking of these proteins through the cell (Figure 4).

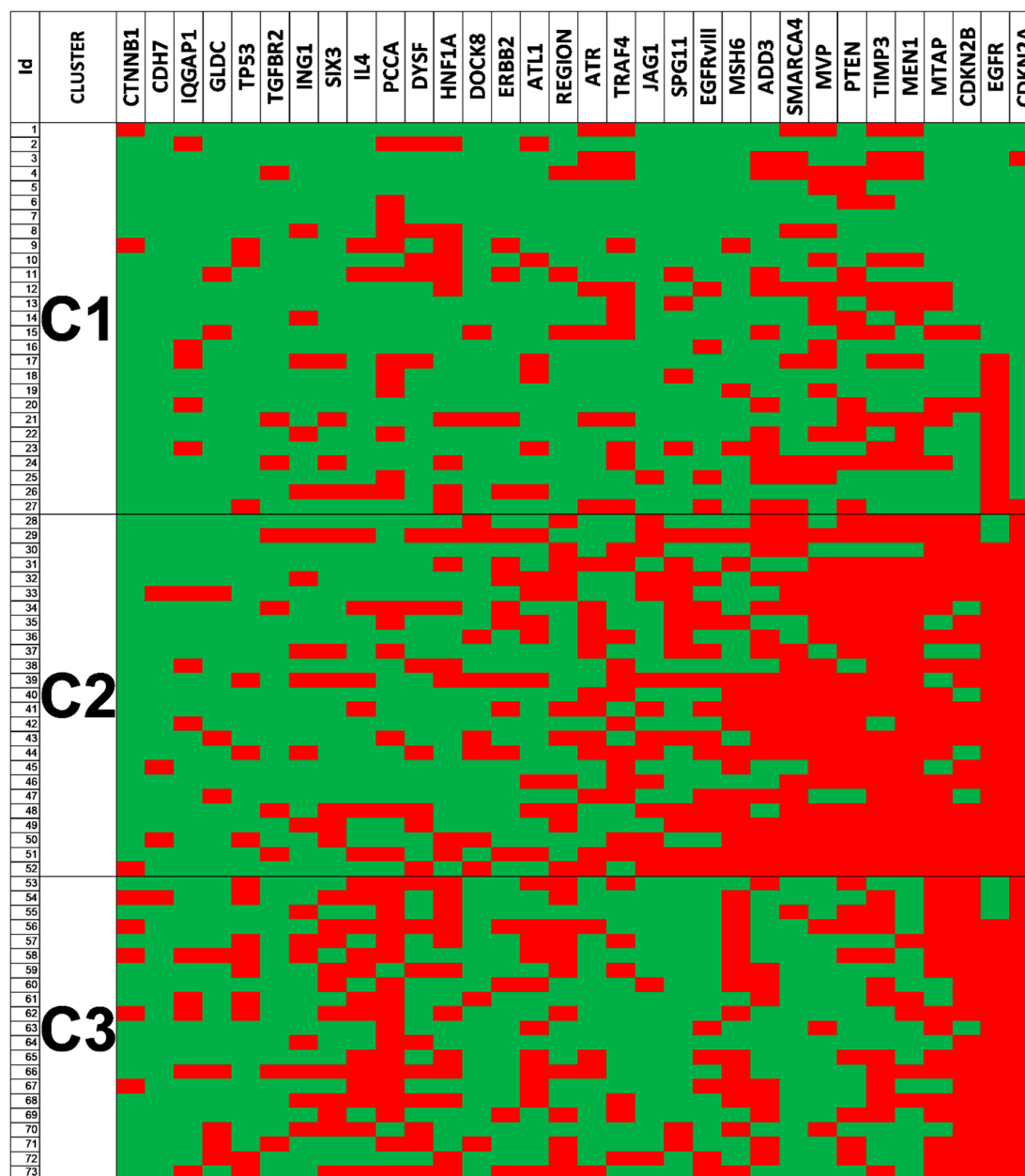


**Figure 3.** Clustering analysis. Heatmap from the hierarchical cluster classification. The patients included are represented on the Y-axis and the genes that contributed to the model on the X. Green squares show no SCNA, red squares show SCNA. C1, C2 and C3 are shown separately, and the distribution of SCNAs among offers a landscape where C1 is the one with less genetic alterations while C2 is the most affected one.

Cluster 3, in common with C2, showed losses in CDKN2A in 100% of the cases, a high frequency of EGFR amplification and SCNA in MTAP and MSH6. Additionally, this C3 displayed frequent SCNAs in TP53, IL4, PCCA and SIX3. STRING analysis showed a PPI enrichment *p*-value of 0.0019 and an association to the biological processes ‘regulation of cell cycle phase transition’ with an FDR of 0.0060. However, no specific cellular component was revealed. Finally, C1 was the less altered cluster.



It showed a statistically significant lower level of CDKN2A, MSH6, MTAP and EGFR alterations compared with its counterparts.

Overall, GB-IDHwt displayed a wide genetic heterogeneity. However, cluster analysis allowed a separation based on the frequency of alterations detected by MLPA into three groups. From them, the two that displayed EGFR amplification offered completely different outcomes, depending on the presence of additional alterations, as SCNA on ADD3 and the variant III of EGFR. These two changes were shown to be independent biomarkers for bad prognosis, and their statistical association to C2 highlights the interest of exploring the aggregation of genetic alterations in it.

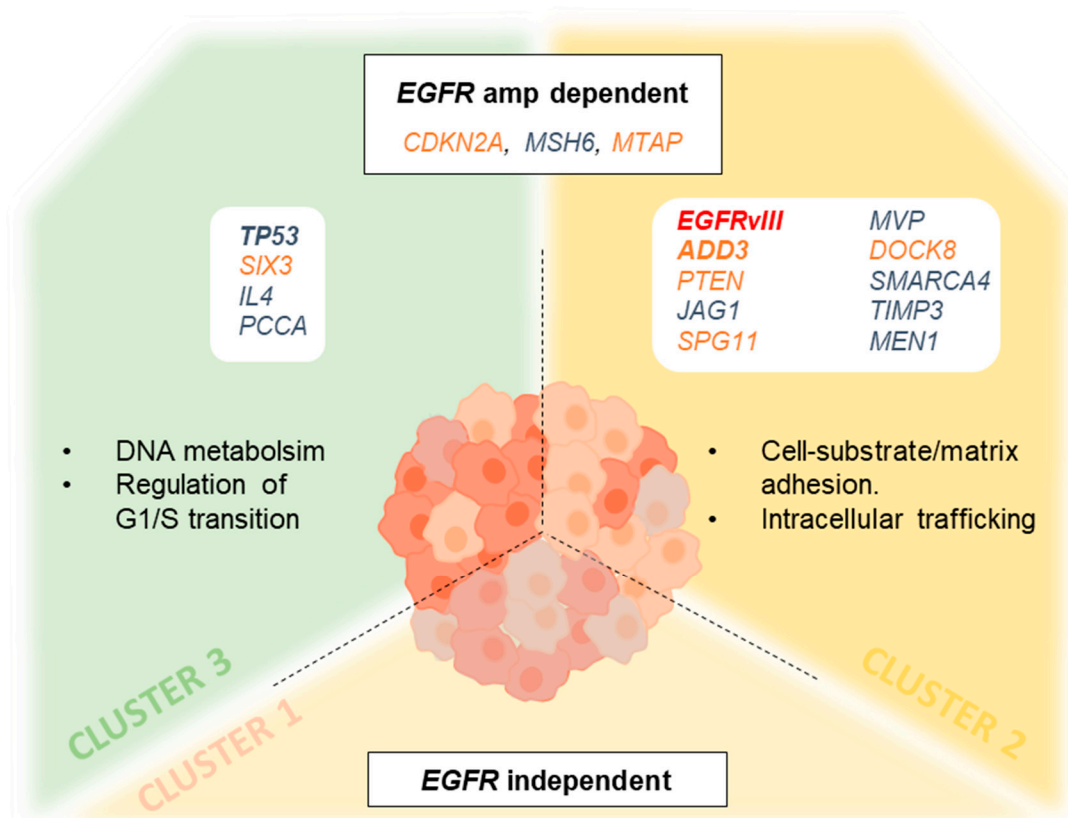


**Figure 4.** Pathways outlined by clustering analysis. The introduction of genes that differentially contributed to the clusters on the STRING database analysis platform offered a variety of genetic pathways and processes that were especially damaged in C2 and C3. Genes in blue displayed gains, genes in orange displayed losses, *EGFRvIII* includes loss from exons 2–7. Genes in bold were the most distinctive among the clusters. It needs to be mentioned that MSH6, in addition to gains, showed losses in <10% of the cases. The main difference between C2/C3 and C1 is that on C1, *EGFR* alterations were found only in half of the cases. Despite C2 and C3 share some alterations, the downstream connections lead to a subtly quicker disease on C2 compared to the slowest situation on C3.

#### 4. Discussion

*EGFR* genetic alteration is an essential component of the portrait of most GBs occurring in 57% of tumors [4,38]. This frequency is similar to what we find for *EGFR* amplification and *EGFR* mutation in this work. This fact, along with the devastating outcome of GB, justifies the continuous search for associations in relation to *EGFR* changes and the therapeutic responses of patients. In light of the TCGA project, RTK alterations and their downstream effectors are of potential interest as targetable driver mutations [39]. However, it could be especially interesting to be able to classify our patients depending on specific common changes or even better, different pathways affected, to understand what makes them undergo a quicker or slower disease.

The use of iFISH to precisely determine the *EGFR* amplification status is the current gold-standard in GB [19,40]. Previous works of our and others groups, demonstrated that this method allows the detection of intermediate levels of amplification [19,24]. Lassman and his colleagues deepened the potential of different new techniques in comparison to iFISH with positive results [40]. In the present work, we compared the potential of MLPA to that aim because it is a user-friendly and cost-effective technique, and the Cohen agreement we got was also good. The point of iFISH remains the possibility of separating that intermediately amplified group, for which it is not entirely clear whether it represents a progression via the amplification status or a separate path for tumor progression in GB. In any case, MLPA proves to be an easy and fast technique, with the additional advantage of being able to determine mutant variants such it is *EGFRvIII*, in agreement with previous works [21,24,31,35].

The wide heterogeneity of cancer cells is a common challenge in terms of learning how to stop tumor growth. The clonal evolution of GB *IDHwt* and the acquisition of new mutations represent a major problem for finding effective therapies [1,4,8,23]. This heterogeneity is patent in our work; from all the loci explored, we found SCNA in all of them in at least one case. The genetics of H-amp GB and GB displaying *EGFRvIII* offers landscapes that are statistically different from their N-amp/L-amp or *EGFRwt* counterparts, respectively. STRING analysis correlates the SCNA statistically associated with amplified-*EGFR* GBs with *NOTCH3* activation and negative regulation of cell–matrix adhesion. Crespo et al., using high-density (500K) single-nucleotide polymorphism arrays, achieved similar relevance for the axis established with *MTAP* [16]. In concordance with that work, our group of patients that displayed *EGFRvIII*, which is the one with the worst outcome, also showed the impairment of cell–matrix adhesion processes. Despite the alteration of different sets of genes, we found a higher frequency of *EGFRvIII* among the *EGFR* amplified GBs, in concordance with previous works [9,24], and interestingly, we found a significant association between *EGFRvIII* and a shortening in survival, supporting previous descriptions [22,27,41].

An outstanding finding when analyzing the genes whose alterations were associated with *EGFRvIII* is that *ADD3* SCNAs is associated with bad prognosis, with a marked reduction in OS. *ADD3* codifies the  $\gamma$ -adducin, which build heterotetramers with its counterparts  $\alpha$ - and  $\beta$ -adducin, and has been widely studied in red-cell membranes [42]. Different works put a spotlight on adducin's controversial role as either oncogene or tumor suppressor in cancer [42–45]. Our findings support a recent report of Kiang KM et al. that points to the downregulation of *ADD3* in GB, but not in less malignant gliomas, as a critical event during malignant progression [46]. While most cell-based studies suggest an oncogenic behavior, different papers on glioma tumor specimens, in agreement with our data, relate *ADD3* downregulation to progression [43,44] and to migration [45]. Other cancer that shows *EGFR* amplification, such as non-small cell lung cancer, shares this *ADD3* infraexpression associated with cell migration [47]. We suggest that the use of such easy techniques as MLPA to assess *ADD3* SCNA could be considered for diagnostic routines to better tailor clinical decisions as an independent prognostic factor and to delve deeper into the GB classification of patients.

The frequency of *ADD3* SCNAs and its co-occurrence with *EGFRvIII* led us to look for genetic clustering. Thus, according to the genetic probes analyzed by MLPA, clustering analysis causes GBs to separate into three different groups. The first cluster (C1) offers a low rate of SCNAs compared with the rest. Cluster 2 (C2) and cluster 3 (C3) share a high rate of SCNAs in *MTAP*, *CDKN2A*, *MSH6* and *EGFR*, in agreement with previous descriptions [16], and suggesting that GBs from both clusters display alterations in DNA metabolic processes (by STRING). However, the second cluster (C2) concentrates the co-existence of *EGFR* alterations through *EGFRvIII* or *EGFR* amplification and the highest rate of SCNAs. Of these, it is worth mentioning that *JAG1*, which is involved in angiogenesis [48], *MVP*, was recently implicated in vesicle trafficking [21] or the aforementioned *ADD3*. Coherent with these data, this cluster displayed the shortest OS. It is curious that *MSH6*, in addition to showing gains as was previously reported in association with resistance to chemotherapy [49], displays losses in a short set of cases in this series. These cases with losses do not show an increase on the tumor genetic burden consequence of the defect on DNA repair, but interestingly, they show a really subtle increase in

survival. It is not significant, but it deserves to be further studied, as it resembles the protective effect of the promoter methylation of *MGMT*, which improves responsiveness to temozolomide treatment [1,50]. Regarding *MTAP*, its deficiency is usually seen as a collateral effect of *CDKN2A* deletion, because of its location next to this gene [51,52]. Nevertheless, it is necessary to improve our understanding of the consequences of this loss because it could offer different insights into therapy. It is known that the loss of *MTAP* influences the metabolism of ATP: both adenine and adenosine are disturbed as a consequence of the disruption of the polyamine salvage pathway [53,54]. This fact could be related to the metabolic reprogramming strategy to actively modulate the immune landscape of GB [55]. Contrary to what was expected, it was shown that adenosine did not significantly accumulate in GB [55]. This fact would be in line with previous descriptions of N6-isopentenyladenosine and other modified nucleosides, with important anti-proliferative and pro-apoptotic effects in GB cases that display amplification on *EGFR* [56,57]. Interestingly, in our study, cluster 2 and 3 showed amplifications on *EGFR* and losses on *CDKN2A* in all cases, along with a high proportion of cases displaying *MTAP* losses. It would be desirable to further study whether the efficacy of those molecules could represent a therapeutic benefit for these specific patients with adenosine metabolism disturbances.

A noteworthy fact is that *ADD3* and *EGFRvIII*, both previously reported as alterations associated with shortened survival in GB [27,46] and confirmed here, are a signature in this C2. On the other hand, C3 involves *TP53* alterations in addition to the shared ones. This fact completely makes sense considering that *TP53* mutations are, according to the WHO, more frequent in the group of GB with *IDH* mutations, characterized by a higher survival than *IDHwt* GBs [1]. Moreover, *EGFRvIII* has been broadly associated with a poorer outcome [22,27]. These findings reflect that, not only the amplification status of *EGFR* could be decisive in the comprehension of GB progression, but also the interconnection established with parallel genetic pathways.

A comparison between the main findings in the clusters defined here and the previously reported TCGA expression subtypes [10,38] is worthy of some comments: the small set of GB, *IDH*-mutant cases we studied may fit in the proneural TCGA group, with mutations in *TP53* in half of the samples and loss of *PTEN* in 2/3 of the cases. Similarly, lifespan is higher, as we expected for being *IDH1*-mutant [1]. Cluster 2 fits quite well in the “Classical” subtype [10,38]. *EGFR* amplification is the main characteristic accompanied by losses on *CDKN2A* in all the cases and losses on *PTEN* in a high proportion (88%). However, cluster 3 seems to be a variant of this classical subtype. It is also characterized by *EGFR* amplification and losses on *CDKN2A*, but losses on *PTEN* drop down to a half. However, other alterations define it better than *PTEN* status, such as gains on *TP53* or losses on *SIX3*. It is worth mentioning that *TP53* stands out, but it does so because of *SCNA*, and not mutations, as would be more characteristic of the mesenchymal TCGA subtype [10,38]. Thus, between these two clusters, a better genetic definition of the patients is offered. It is of note that C1 seems to have little to do with *EGFR*, in contrast to C2 and C3. C1 agrees with the mesenchymal subtype, being the only set of patients that are not characterized by *EGFR* amplification. It displays a complex mix of genetic changes without dominance of any specific feature, all them in lower proportions than its counterparts cluster 2 and 3, and in a similar way as happens in the mesenchymal TCGA subtype [10,38]. On both sides, *EGFR* status-dependent subgroups of GBs, genetically and clinically different, can be separated. The identification of alterations in shared nodes of convergence downstream of RTKs has been an interesting approach in cancer [4,8,58].

The present work sets out MLPA as an advantageous methodology, simple and useful for FFPE specimens. In addition, it may provide new insights into the molecular underpinnings of GB pathogenesis in a comprehensive manner. Clustering the genetic alterations of GB highlights the importance of *EGFR* in this very aggressive tumor type and could represent a strong step towards precision medicine: the aggregation of changes depending on the presence of the amplification of *EGFR*, the mutation variant III or both simultaneously, lead to different pathways to analyze. Our results underline the importance of *EGFRvIII* and *ADD3* SCNAs as markers of poor prognosis that need further consideration in GB. The presence of a group of GB-*IDHwt* without alterations in *EGFR* may

explain part of the absence of effect of RTK inhibitors in this type of tumor. Furthermore, the clear separation of *EGFR*-amplified related GBs, showing sets of genes that are differentially altered, points to the need to rethink the possibilities of personalized therapy in future clinical settings. The differential groups that can be established could be used for a more accurate therapy.

**Supplementary Materials:** The following are available online at <http://www.mdpi.com/2073-4409/9/11/2429/s1>, Table S1: Amplification status of *EGFR* determined by interphase Fluorescence in situ hybridization and MLPA analysis.

**Author Contributions:** Conceptualization, T.S.-M., S.C., P.R., M.C.-N. and C.L.-G.; data curation, L.N., T.S.-M., J.M., L.M.-H. and C.L.-G.; formal analysis, L.N., T.S.-M., J.M. and L.M.-H.; funding, T.S.-M. and M.C.-N.; investigation, L.N., N.S. and J.M.; methodology L.N., T.S.-M., N.S., L.M.-H. and C.L.-G.; project administration, T.S.-M., M.C.-N. and C.L.-G.; resources, J.M., P.R. and M.C.-N.; software, L.N., T.S.-M., J.M. and N.S.; supervision, J.M., P.R., M.C.-N. and C.L.-G.; validation, T.S.-M., S.C., M.C.-N. and C.L.-G.; visualization, L.N. and N.S.; writing—original draft—L.N. and T.S.-M.; writing—review & editing, L.N., T.S.-M., J.M., N.S., S.C., M.C.-N. and C.L.-G. All the authors have approved the submitted version, they have agreed both to be personally accountable for their own contributions and to ensure that questions related to the accuracy or integrity of any part of the work, even ones in which they were not personally involved, were appropriately investigated, resolved, and the resolution documented in the literature. All authors have read and agreed to the published version of the manuscript.

**Funding:** This research was funded by Ministerio de Economía y Competitividad-Instituto de Salud Carlos III, grant number “PI14/01669” and by Conselleria d’Educació, Investigació, Cultura i Esport from Generalitat Valenciana grant number “PROMETEO/2011/83” and grant number “GV/2020/048”. The APC was funded by the University of Valencia and the Generalitat Valenciana.

**Acknowledgments:** The authors want to thank ISCIII-Ministerio de Economía y Competitividad and the Conselleria d’Educació, Investigació, Cultura i Esport from Generalitat Valenciana for the funds received. Thanks to A.M. Clari, R. Gil-Benso and to R. Navarro-Lucas for their continuous support.

**Conflicts of Interest:** The authors declare no conflict of interest. The funders had no role in the design of the study; in the collection, analyses, or interpretation of data; in the writing of the manuscript, or in the decision to publish the results.

## References

1. Louis, D.N.; Perry, A.; Reifenberger, G.; von Deimling, A.; Figarella-Branger, D.; Cavenee, W.K.; Ohgaki, H.; Wiestler, O.D.; Kleihues, P.; Ellison, D.W. The 2016 World Health Organization Classification of Tumors of the Central Nervous System: A summary. *Acta Neuropathol.* **2016**, *131*, 803–820. [CrossRef] [PubMed]
2. Ostrom, Q.T.; Gittleman, H.; Liao, P.; Vecchione-Koval, T.; Wolinsky, Y.; Kruchko, C.; Barnholtz-Sloan, J.S. CBTRUS Statistical Report: Primary brain and other central nervous system tumors diagnosed in the United States in 2010–2014. *Neuro Oncol.* **2017**, *19*, v1–v88. [CrossRef] [PubMed]
3. Lawrence, M.S.; Stojanov, P.; Mermel, C.H.; Robinson, J.T.; Garraway, L.A.; Golub, T.R.; Meyerson, M.; Gabriel, S.B.; Lander, E.S.; Getz, G. Discovery and saturation analysis of cancer genes across 21 tumour types. *Nature* **2014**, *505*, 495–501. [CrossRef] [PubMed]
4. Furnari, F.B.; Cloughesy, T.F.; Cavenee, W.K.; Mischel, P.S. Heterogeneity of epidermal growth factor receptor signalling networks in glioblastoma. *Nat. Rev. Cancer* **2015**, *15*, 302–310. [CrossRef] [PubMed]
5. Karsy, M.; Gelbman, M.; Shah, P.; Balumbu, O.; Moy, F.; Arslan, E. Established and emerging variants of glioblastoma multiforme: Review of morphological and molecular features. *Folia Neuropathol.* **2012**, *50*, 301–321. [CrossRef]
6. Lu, J.; Cowperthwaite, M.C.; Burnett, M.G.; Shpak, M. Molecular predictors of long-term survival in glioblastoma multiforme patients. *PLoS ONE* **2016**, *11*, e0154313. [CrossRef]
7. Umehara, T.; Arita, H.; Yoshioka, E.; Shofuda, T.; Kanematsu, D.; Kinoshita, M.; Kodama, Y.; Mano, M.; Kagawa, N.; Fujimoto, Y.; et al. Distribution differences in prognostic copy number alteration profiles in IDH-wild-type glioblastoma cause survival discrepancies across cohorts. *Acta Neuropathol. Commun.* **2019**, *7*, 99. [CrossRef]
8. Gerlinger, M.; Rowan, A.J.; Horswell, S.; Math, M.; Larkin, J.; Endesfelder, D.; Gronroos, E.; Martinez, P.; Matthews, N.; Stewart, A.; et al. Intratumor heterogeneity and branched evolution revealed by multiregion sequencing. *N. Engl. J. Med.* **2012**, *366*, 883–892. [CrossRef]

9. Hochberg, F.H.; Atai, N.A.; Gonda, D.; Hughes, M.S.; Mawejje, B.; Balaj, L.; Carter, R.S. Glioma diagnostics and biomarkers: An ongoing challenge in the field of medicine and science. *Expert Rev. Mol. Diagn.* **2014**, *14*, 439–452. [CrossRef]
10. Verhaak, R.G.W.; Hoadley, K.A.; Purdom, E.; Wang, V.; Qi, Y.; Wilkerson, M.D.; Miller, C.R.; Ding, L.; Golub, T.; Mesirov, J.P.; et al. An integrated genomic analysis identifies clinically relevant subtypes of glioblastoma characterized by abnormalities in PDGFRA, IDH1, EGFR and NF1. *Cancer Cell* **2010**, *17*, 98. [CrossRef]
11. Ohgaki, H.; Kleihues, P. Genetic alterations and signaling pathways in the evolution of gliomas. *Cancer Sci.* **2009**, *100*, 2235–2241. [CrossRef] [PubMed]
12. Cancer Genome Atlas Research Network. The Cancer Genome Atlas Research Network Comprehensive genomic characterization defines human glioblastoma genes and core pathways. *Nature* **2008**, *455*, 1061–1068. [CrossRef]
13. Huse, J.T. Elucidating the oncogenic role of ATRX deficiency in glioma. *Neuro Oncol.* **2014**, *16*, iii45. [CrossRef]
14. Ohgaki, H.; Kleihues, P. Genetic pathways to primary and secondary glioblastoma. *Am. J. Pathol.* **2007**, *170*, 1445–1453. [CrossRef]
15. Sahm, F.; Reuss, D.E.; Giannini, C. WHO 2016 classification: Changes and advancements in the diagnosis of miscellaneous primary CNS tumours. *Neuropathol. Appl. Neurobiol.* **2018**, *44*, 163–171. [CrossRef]
16. Lassman, A.B.; Roberts-Rapp, L.; Sokolova, I.; Song, M.; Pestova, E.; Kular, R.; Mullen, C.; Zha, Z.; Lu, X.; Gomez, E.; et al. Comparison of biomarker assays for EGFR: Implications for precision medicine in patients with glioblastoma. *Clin. Cancer Res.* **2019**, *25*, 3259–3265. [CrossRef]
17. Anderson, M.G.; Falls, H.D.; Mitten, M.J.; Oleksijew, A.; Vaidya, K.S.; Boghaert, E.R.; Gao, W.; Palma, J.P.; Cao, D.; Chia, P.-L.; et al. Targeting Multiple EGFR-expressing Tumors with a Highly Potent Tumor-selective Antibody-Drug Conjugate. *Mol. Cancer Ther.* **2020**, *19*, 2117–2125. [CrossRef]
18. Kim, G.; Ko, Y.T. Small molecule tyrosine kinase inhibitors in glioblastoma. *Arch. Pharm. Res.* **2020**, *43*, 385–394. [CrossRef]
19. Lopez-Gines, C.; Gil-Benso, R.; Ferrer-Luna, R.; Benito, R.; Serna, E.; Gonzalez-Darder, J.; Quilis, V.; Monleon, D.; Celda, B.; Cerdá-Nicolas, M. New pattern of EGFR amplification in glioblastoma and the relationship of gene copy number with gene expression profile. *Modern Pathol.* **2010**, *23*, 856–865. [CrossRef]
20. Stichel, D.; Ebrahimi, A.; Reuss, D.; Schrimpf, D.; Ono, T.; Shirahata, M.; Reifenberger, G.; Weller, M.; Hänggi, D.; Wick, W.; et al. Distribution of EGFR amplification, combined chromosome 7 gain and chromosome 10 loss, and TERT promoter mutation in brain tumors and their potential for the reclassification of IDHwt astrocytoma to glioblastoma. *Acta Neuropathol.* **2018**, *136*, 793–803. [CrossRef]
21. Navarro, L.; Gil-Benso, R.; Megías, J.; Muñoz-Hidalgo, L.; San-Miguel, T.; Callaghan, R.C.; González-Darder, J.M.; López-Ginés, C.; Cerdá-Nicolás, M.J. Alteration of major vault protein in human glioblastoma and its relation with EGFR and PTEN status. *Neuroscience* **2015**, *297*, 243–251. [CrossRef]
22. An, Z.; Aksoy, O.; Zheng, T.; Fan, Q.-W.; Weiss, W.A. Epidermal growth factor receptor (EGFR) and EGFRvIII in glioblastoma (GBM): Signaling pathways and targeted therapies. *Oncogene* **2018**, *37*, 1561–1575. [CrossRef]
23. Parker, J.J.; Canoll, P.; Niswander, L.; Kleinschmidt-DeMasters, B.K.; Foshay, K.; Waziri, A. Intratumoral heterogeneity of endogenous tumor cell invasive behavior in human glioblastoma. *Sci. Rep.* **2018**, *8*, 18002. [CrossRef]
24. Muñoz-Hidalgo, L.; San-Miguel, T.; Megías, J.; Monleón, D.; Navarro, L.; Roldán, P.; Cerdá-Nicolás, M.; López-Ginés, C. Somatic copy number alterations are associated with EGFR amplification and shortened survival in patients with primary glioblastoma. *Neoplasia* **2020**, *22*, 10–21. [CrossRef]
25. Pedersen, M.W.; Tkach, V.; Pedersen, N.; Berezin, V.; Poulsen, H.S. Expression of a naturally occurring constitutively active variant of the epidermal growth factor receptor in mouse fibroblasts increases motility. *Int. J. Cancer* **2004**, *108*, 643–653. [CrossRef]
26. Feng, H.; Hu, B.; Vuori, K.; Sarkaria, J.N.; Furnari, F.B.; Cavenee, W.K.; Cheng, S.-Y. EGFRvIII stimulates glioma growth and invasion through PKA-dependent serine phosphorylation of Dock180. *Oncogene* **2014**, *33*, 2504–2512. [CrossRef] [PubMed]
27. Keller, S.; Schmidt, M.H.H. EGFR and EGFRvIII promote angiogenesis and cell invasion in glioblastoma: Combination therapies for an effective treatment. *Int. J. Mol. Sci.* **2017**, *18*, 1295. [CrossRef]
28. Boisselier, B.; Dugay, F.; Belaud-Rotureau, M.-A.; Coutolleau, A.; Garcion, E.; Menei, P.; Guardiolo, P.; Rousseau, A. Whole genome duplication is an early event leading to aneuploidy in IDH-wild type glioblastoma. *Oncotarget* **2018**, *9*, 36017–36028. [CrossRef]

29. Mao, X.; Hamoudi, R.A. Molecular and cytogenetic analysis of glioblastoma multiforme. *Cancer Genet. Cytogenet.* **2000**, *122*, 87–92. [CrossRef]
30. Jeuken, J.; Cornelissen, S.; Boots-Sprenger, S.; Gijzen, S.; Wesseling, P. Multiplex Ligation-Dependent Probe Amplification. *J. Mol. Diagn.* **2006**, *8*, 433–443. [CrossRef] [PubMed]
31. Jeuken, J.; Sijben, A.; Alenda, C.; Rijntjes, J.; Dekkers, M.; Boots-Sprenger, S.; McLendon, R.; Wesseling, P. Robust Detection of EGFR Copy Number Changes and EGFR Variant III: Technical Aspects and Relevance for Glioma Diagnostics. *Brain Pathol.* **2009**, *19*, 661–671. [CrossRef]
32. González, J.R.; Carrasco, J.L.; Armengol, L.; Villatoro, S.; Jover, L.; Yasui, Y.; Estivill, X. Probe-specific mixed-model approach to detect copy number differences using multiplex ligation-dependent probe amplification (MLPA). *BMC Bioinform.* **2008**, *9*, 261. [CrossRef]
33. Gessi, M.; Hammes, J.; Lauriola, L.; Dörner, E.; Kirfel, J.; Kristiansen, G.; zur Muehlen, A.; Denkhaus, D.; Waha, A.; Pietsch, T. GNA11 and N-RAS mutations: Alternatives for MAPK pathway activating GNAQ mutations in primary melanocytic tumours of the central nervous system. *Neuropathol. Appl. Neurobiol.* **2013**, *39*, 417–425. [CrossRef]
34. Gessi, M.; Gielen, G.H.; Denkhaus, D.; Antonelli, M.; Giangaspero, F.; zur Mühlen, A.; Japp, A.S.; Pietsch, T. Molecular heterogeneity characterizes glioblastoma with lipoblast/adipocyte-like cytology. *Virchows Arch.* **2015**, *467*, 105–109. [CrossRef]
35. Gan, H.K.; Kaye, A.H.; Luwor, R.B. The EGFRvIII variant in glioblastoma multiforme. *J. Clin. Neurosci.* **2009**, *16*, 748–754. [CrossRef]
36. Layfield, L.; Willmore, C.; Tripp, S.; Jones, C.; Jensen, R. Epidermal growth factor receptor gene amplification and protein expression in glioblastoma multiforme. *Appl. Immunohistochem. Mol. Morphol.* **2006**, *14*, 91–96. [CrossRef]
37. Cerami, E.; Gao, J.; Dogrusoz, U.; Gross, B.E.; Sumer, S.O.; Aksoy, B.A.; Jacobsen, A.; Byrne, C.J.; Heuer, M.L.; Larsson, E.; et al. The cBio Cancer Genomics Portal: An open platform for exploring multidimensional cancer genomics data. *Cancer Discov.* **2012**, *2*, 401–404. [CrossRef]
38. Brennan, C.W.; Verhaak, R.G.W.; McKenna, A.; Campos, B.; Nounshmehr, H.; Salama, S.R.; Zheng, S.; Chakravarty, D.; Sanborn, J.Z.; Berman, S.H.; et al. The Somatic Genomic Landscape of Glioblastoma. *Cell* **2013**, *155*, 462–477. [CrossRef]
39. Szklarczyk, D.; Gable, A.L.; Lyon, D.; Junge, A.; Wyder, S.; Huerta-Cepas, J.; Simonovic, M.; Doncheva, N.T.; Morris, J.H.; Bork, P.; et al. STRING v11: Protein–protein association networks with increased coverage, supporting functional discovery in genome-wide experimental datasets. *Nucleic Acids Res.* **2019**, *47*, D607–D613. [CrossRef] [PubMed]
40. Ciriello, G.; Sinha, R.; Hoadley, K.A.; Jacobsen, A.S.; Reva, B.; Perou, C.M.; Sander, C.; Schultz, N. The molecular diversity of Luminal A breast tumors. *Breast Cancer Res. Treat.* **2013**, *141*, 409–420. [CrossRef]
41. Crespo, I.; Vital, A.L.; Nieto, A.B.; Rebelo, O.; Tão, H.; Lopes, M.C.; Oliveira, C.R.; French, P.J.; Orfao, A.; Taberner, M.D. Detailed characterization of alterations of chromosomes 7, 9, and 10 in glioblastomas as assessed by single-nucleotide polymorphism arrays. *J. Mol. Diagn.* **2011**, *13*, 634–647. [CrossRef] [PubMed]
42. Sahin, A.; Sanchez, C.; Bullain, S.; Waterman, P.; Weissleder, R.; Carter, B.S. Development of third generation anti-EGFRvIII chimeric T cells and EGFRvIII-expressing artificial antigen presenting cells for adoptive cell therapy for glioma. *PLoS ONE* **2018**, *13*, e0199414. [CrossRef]
43. Kiang, K.M.-Y.; Leung, G.K.-K. A review on Adducin from functional to pathological mechanisms: Future direction in cancer. *BioMed Res. Int.* **2018**, 1–14. [CrossRef]
44. van den Boom, J.; Wolter, M.; Kuick, R.; Misek, D.E.; Youkilis, A.S.; Wechsler, D.S.; Sommer, C.; Reifemberger, G.; Hanash, S.M. Characterization of gene expression profiles associated with glioma progression using oligonucleotide-based microarray analysis and real-time reverse transcription-polymerase chain reaction. *Am. J. Pathol.* **2003**, *163*, 1033–1043. [CrossRef]
45. Huang, H.; Colella, S.; Kurrer, M.; Yonekawa, Y.; Kleihues, P.; Ohgaki, H. Gene expression profiling of low-grade diffuse astrocytomas by cDNA arrays. *Cancer Res.* **2000**, *60*, 6868–6874.
46. Mariani, L.; Beaudry, C.; McDonough, W.S.; Hoelzinger, D.B.; Demuth, T.; Ross, K.R.; Berens, T.; Coons, S.W.; Watts, G.; Trent, J.M.; et al. Glioma cell motility is associated with reduced transcription of proapoptotic and proliferation genes: A cDNA microarray analysis. *J. Neurooncol.* **2001**, *53*, 161–176. [CrossRef]
47. Kiang, K.M.-Y.; Zhang, P.; Li, N.; Zhu, Z.; Jin, L.; Leung, G.K.-K. Loss of cytoskeleton protein ADD3 promotes tumor growth and angiogenesis in glioblastoma multiforme. *Cancer Lett.* **2020**, *474*, 118–126. [CrossRef]

48. Lechuga, S.; Amin, P.H.; Wolen, A.R.; Ivanov, A.I. Adducins inhibit lung cancer cell migration through mechanisms involving regulation of cell-matrix adhesion and cadherin-11 expression. *Biochim. Biophys. Acta Mol. Cell Res.* **2019**, *1866*, 395–408. [CrossRef]
49. Sun, Q.; Pei, C.; Li, Q.; Dong, T.; Dong, Y.; Xing, W.; Zhou, P.; Gong, Y.; Zhen, Z.; Gao, Y.; et al. Up-regulation of MSH6 is associated with temozolomide resistance in human glioblastoma. *Biochem. Biophys. Res. Commun.* **2018**, *496*, 1040–1046. [CrossRef]
50. Skiriute, D.; Vaitkiene, P.; Saferis, V.; Asmoniene, V.; Skauminas, K.; Deltuva, V.P.; Tamasauskas, A. MGMT, GATA6, CD81, DR4, and CASP8 gene promoter methylation in glioblastoma. *BMC Cancer* **2012**, *12*, 218. [CrossRef]
51. Hansen, L.J.; Sun, R.; Yang, R.; Singh, S.X.; Chen, L.H.; Pirozzi, C.J.; Moure, C.J.; Hemphill, C.; Carpenter, A.B.; Healy, P.; et al. MTAP Loss Promotes Stemness in Glioblastoma and Confers Unique Susceptibility to Purine Starvation. *Cancer Res.* **2019**, *79*, 3383–3394. [CrossRef]
52. Lubin, M.; Lubin, A. Selective killing of tumors deficient in methylthioadenosine phosphorylase: A novel strategy. *PLoS ONE* **2009**, *4*, e5735. [CrossRef]
53. Marjon, K.; Cameron, M.J.; Quang, P.; Clasquin, M.F.; Mandley, E.; Kunii, K.; McVay, M.; Choe, S.; Kernytsky, A.; Gross, S.; et al. MTAP Deletions in Cancer Create Vulnerability to Targeting of the MAT2A/PRMT5/RIOK1 Axis. *Cell Rep.* **2016**, *15*, 574–587. [CrossRef]
54. Tang, B.; Lee, H.-O.; An, S.S.; Cai, K.Q.; Kruger, W.D. Specific Targeting of MTAP-Deleted Tumors with a Combination of 2'-Fluoroadenine and 5'-Methylthioadenosine. *Cancer Res.* **2018**, *78*, 4386–4395. [CrossRef]
55. Kesarwani, P.; Prabhu, A.; Kant, S.; Chinnaiyan, P. Metabolic Remodeling Contributes Towards an Immune Suppressive Phenotype in Glioblastoma. *Cancer Immunol. Immunother.* **2019**, *68*, 1107–1120. [CrossRef]
56. Ciaglia, E.; Abate, M.; Laezza, C.; Pisanti, S.; Vitale, M.; Seneca, V.; Torelli, G.; Franceschelli, S.; Catapano, G.; Gazzero, P.; et al. Antiglioma effects of N6-isopentenyladenosine, an endogenous isoprenoid end product, through the downregulation of epidermal growth factor receptor. *Int. J. Cancer* **2017**, *140*, 959–972. [CrossRef]
57. Ciaglia, E.; Grimaldi, M.; Abate, M.; Scrima, M.; Rodriguez, M.; Laezza, C.; Ranieri, R.; Pisanti, S.; Ciuffreda, P.; Manera, C.; et al. The isoprenoid derivative N6-benzyladenosine CM223 exerts antitumor effects in glioma patient-derived primary cells through the mevalonate pathway. *Br. J. Pharmacol.* **2017**, *174*, 2287–2301. [CrossRef]
58. Qiu, X.-X.; Chen, L.; Wang, C.-H.; Lin, Z.-X.; Chen, B.-J.; You, N.; Chen, Y.; Wang, X.-F. The Vascular Notch Ligands Delta-Like Ligand 4 (DLL4) and Jagged1 (JAG1) Have Opposing Correlations with Microvascularization but a Uniform Prognostic Effect in Primary Glioblastoma: A Preliminary Study. *World Neurosurg.* **2016**, *88*, 447–458. [CrossRef]




**Publisher's Note:** MDPI stays neutral with regard to jurisdictional claims in published maps and institutional affiliations.



© 2020 by the authors. Licensee MDPI, Basel, Switzerland. This article is an open access article distributed under the terms and conditions of the Creative Commons Attribution (CC BY) license (<http://creativecommons.org/licenses/by/4.0/>).

Article

# Combinatory Treatment of Canavanine and Arginine Deprivation Efficiently Targets Human Glioblastoma Cells via Pleiotropic Mechanisms

Olena Karatsai <sup>1</sup>, Pavel Shliaha <sup>2</sup>, Ole N. Jensen <sup>2</sup>, Oleh Stasyk <sup>3</sup> and Maria Jolanta Rędownicz <sup>1,\*</sup>

<sup>1</sup> Nencki Institute of Experimental Biology, Polish Academy of Sciences, 3 Pasteur St., 02-093 Warsaw, Poland; o.karatsai@nencki.edu.pl

<sup>2</sup> Department of Biochemistry and Molecular Biology and VILLUM Center for Bioanalytical Sciences, University of Southern Denmark, DK-5230 Odense M, Denmark; shliahap@mskcc.org (P.S.); jenseno@bmb.sdu.dk (O.N.J.)

<sup>3</sup> Department of Cell Signaling, Institute of Cell Biology, National Academy of Sciences of Ukraine, 14/16 Drahomanov St., 79005 Lviv, Ukraine; oleh11@gmail.com

\* Correspondence: j.redowicz@nencki.edu.pl; Tel.: +48-225892456

Received: 28 August 2020; Accepted: 24 September 2020; Published: 30 September 2020



**Abstract:** Glioblastomas are the most frequent and aggressive form of primary brain tumors with no efficient cure. However, they often exhibit specific metabolic shifts that include deficiency in the biosynthesis of and dependence on certain exogenous amino acids. Here, we evaluated, *in vitro*, a novel combinatory antiglioblastoma approach based on arginine deprivation and canavanine, an arginine analogue of plant origin, using two human glioblastoma cell models, U251MG and U87MG. The combinatory treatment profoundly affected cell viability, morphology, motility and adhesion, destabilizing the cytoskeleton and mitochondrial network, and induced apoptotic cell death. Importantly, the effects were selective toward glioblastoma cells, as they were not pronounced for primary rat glial cells. At the molecular level, canavanine inhibited prosurvival kinases such as FAK, Akt and AMPK. Its effects on protein synthesis and stress response pathways were more complex and dependent on exposure time. We directly observed canavanine incorporation into nascent proteins by using quantitative proteomics. Although canavanine in the absence of arginine readily incorporated into polypeptides, no motif preference for such incorporation was observed. Our findings provide a strong rationale for further developing the proposed modality based on canavanine and arginine deprivation as a potential antiglioblastoma metabolic therapy independent of the blood–brain barrier.

**Keywords:** adhesion; apoptosis; arginine deprivation; canavanine; cancer; cytoskeleton; ER stress; glioblastoma; migration; unfolded protein response

## 1. Introduction

It has been described in a number reports that numerous cancers are defective in arginine biosynthesis, and some of them become hypersensitive to the deprivation of this amino acid [1]. Arginine is a semi-essential amino acid in humans, and its exogenous requirement is dependent on the stage of the organism's development and its health status [2,3]. Arginine plays an important role in various molecular pathways regulating cell division, wound healing, neurological and immune functions, and hormone synthesis [1,4,5]. It is also a key precursor in the synthesis of cancer-associated compounds such as nitric oxide (NO) and polyamines [3,6,7].

In the normal condition, intracellular arginine homeostasis depends on dietary uptake, the degradation of intracellular proteins, efficiency of transport through cell membranes by cationic



amino acid transporters (CATs), and de novo synthesis from aspartate and citrulline in the urea cycle [7–9]. There are two closely coupled enzymes, which are crucial in arginine biosynthesis: argininosuccinate synthetase 1 (ASS1) and argininosuccinate lyase (ASL) [4]. The auxotrophy for arginine, in vivo, of several tumors, such as melanoma, hepatocellular carcinoma, some mesotheliomas, some renal cell cancers, and glioblastomas, is mainly related to the epigenetic silencing of ASS1 [9–11]. In contrast to cancer cells with elevated nutrient requirements, the majority of normal non-transformed cells are able to synthesize arginine by conversion from circulating exogenous citrulline mediated by ASS and ASL under conditions of nutrient stress [12].

Arginine deprivation with recombinant arginine-degrading enzymes is considered as nontoxic and selective since it decreases viability and allows the control of the growth of malignant tumors that lack ASS1 expression [4,5,13–15]. Such a strategy is now under Phase I/II clinical trials for combating malignant melanomas, hepatocellular and pancreatic carcinomas, pleural mesotheliomas, thoracic cancers and other malignancies, and is well tolerated by the organism [16–22].

Due to specific metabolic shifts in subsets of glioblastomas, the strategy of arginine deprivation could also be a promising approach for the treatment of these devastating cancers [7,9,23,24]. It was observed by several groups, including ours, that arginine deprivation affects glioblastoma cell viability, morphology and invasiveness [1,25]. However, the effects of arginine deprivation on glioblastoma cells were reversible after arginine resupplementation. Three-hour culture in arginine-enriched conditions leads to the restoration of cancer cell morphology and growth [25]. In the majority of tumors, arginine deprivation affects only cell growth and does not promote cell death, therefore bringing the danger of cancer recurrence after stopping the treatment. To overcome this problem, we propose combining arginine deprivation-based treatment with an arginine antimetabolite, L-canavanine.

L-canavanine, a non-proteinogenic amino acid found in certain leguminous plants, is a naturally occurring structural analog of L-arginine. The sole structural difference between arginine and canavanine is the replacement of carbon with oxygen in the terminal methylene group (Figure 1) [26]. There are several reports that consider canavanine as a possible proteomimetic amino acid that could be incorporated instead of arginine into newly synthesized proteins [13,27]. Importantly, in the case of gliomas as targets, the effect of the combination of enzymatic arginine deprivation with canavanine does not depend on the permeability of the brain–blood barrier, as canavanine is transported by the same carriers as arginine, thus increasing the feasibility of a potential prospective therapy [27].

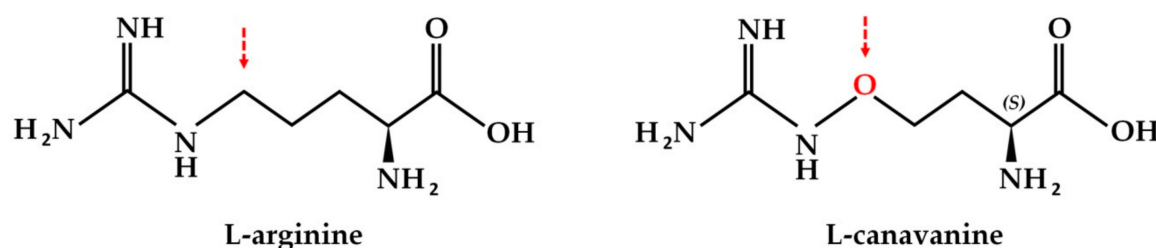


**Figure 1.** Chemical structures of L-arginine and L-canavanine.

In the current study, we examined, in detail, the combined effects of canavanine in arginine-free conditions on the proliferation, morphology, motility and adhesion of two human glioblastoma cell lines. Primary rat glial cells served as control non-transformed cells. We observed that under arginine deprivation, canavanine stimulated pleiotropic mechanisms leading to apoptotic cell death only in cancer but not in normal cells. These data support the notion that canavanine is a good potential candidate in the development of combination metabolic antiglioblastoma therapy.

## 2. Materials and Methods

### 2.1. Materials

L-canavanine (Sigma-Aldrich C9758, St. Louis, MO, USA) was dissolved in water to a 50 mM concentration and stored at 4 °C. The MTS reagent (CellTiter 96<sup>®</sup> AQueous Non-Radioactive Cell Proliferation Assay, G5421) was from Promega Corporation (Madison, WI, USA). <sup>13</sup>C<sub>6</sub>, <sup>15</sup>N<sub>4</sub>-arginine was obtained from ThermoFisher Scientific (89990, Waltham, MA, USA). ER-Tracker™ Blue-White DPX was obtained from ThermoFisher Scientific (E12353). Alexa Fluor 488- and 546-conjugated phalloidin were obtained from Invitrogen (A12379 and A22283, respectively; Waltham, MA, USA). Vectashield anti-fade reagent with or without DAPI was obtained from Vector Laboratories (H-1200 and H-1000, respectively; Burlingame, CA, USA). The following antibodies were used: those against c-PARP (Cell Signaling Technologies #9546, Danvers, MA, USA, and Enzo Life Sciences BML-SA249-0100, Farmingdale, NY, USA), caspase 3 (#9662) and caspase 9 (#9502), FAK (#3285) and p-FAK (#8556), eIF2 $\alpha$  (#2103) and p-eIF2 $\alpha$  (#9721), SAPK/JNK (#9252) and p-SAPK/JNK (#4668), AMPK $\alpha$  (#2532) and p-AMPK $\alpha$  (#2535), p38 (#9212) and p-p38 (#9211), S6 (#2217) and p-S6 (#4858), 4EBP1 (#9452), ATF-4 (#11815), CHOP (#2895), lamin A/C (#4777), tensin 2 (#11990), LC3A/B (#4108) (Cell Signaling Technologies), talin (sc-7534), HSP60 (sc-59567), HSP70 (sc-32239) (Santa Cruz Biotechnology, Heidelberg, Germany), vinculin and  $\beta$ -tubulin (V4505 and T0198, respectively; Sigma-Aldrich), GRP78 BiP (ab21685), GFAP (ab7260), GRP75/MOT (ab2799), lamin B1 (ab16048) and lamin B2 (ab151735) (Abcam, Cambridge, UK), and GAPDH (Millipore MAB374, St. Louis, MO, USA). The following secondary antibodies were used: HRP-conjugated anti-mouse and anti-rabbit IgG (AP308P and AP307P, respectively; Millipore), HRP-conjugated anti-goat IgG (Santa Cruz Biotechnology sc-2020), Alexa Fluor 546-conjugated anti-mouse, Alexa Fluor 488-conjugated anti-rabbit (A11003 and A11008, respectively; Millipore) and Alexa Fluor 488-conjugated anti-mouse (Abcam ab150113). The protein bands were visualized using ECL reagent (Millipore P90720).

### 2.2. Cell Lines and Culture Conditions

Human glioblastoma U251MG and U87MG cell lines were obtained from the Cell Lines Service (Eppelheim, Germany). Cells were cultivated at 37 °C with 5% CO<sub>2</sub> in Dulbecco's Modified Eagle Medium (DMEM; Gibco 31966021, Waltham, MA, USA) supplemented with GlutaMAX-1, 10% heat inactivated fetal bovine serum (FBS; Gibco 10500064) and antibiotics, 1% penicillin/streptomycin (Gibco 15140122). For all experiments, we formulated DMEM (Sigma-Aldrich D9443) with or without 0.4 mmol/L arginine (complete medium (CM) and arginine-free medium (AFM), respectively), supplemented with 5% dialyzed serum (Sigma-Aldrich F0392).

### 2.3. Primary Rat Glial Cell Culture

The primary culture of rat glial cells, used here as the control non-modified normal cells, was isolated from one-day-old Wistar rat pups as described by [28] with the following modifications. The forebrains were isolated, washed with ice-cold DMEM GlutaMAX-1 supplemented with 1% penicillin/streptomycin, and transferred to 0.25% trypsin-EDTA (Gibco 25200056) for 25 min at 37 °C with 5% CO<sub>2</sub>. Next, DMEM, supplemented with 10% FBS and antibiotics, was added to the tissue suspension, followed by mechanical dissociation by pipetting, and the suspension was passed through a 70  $\mu$ m cell strainer (Falcon<sup>®</sup> 352350, Glendale, AZ, USA). The single cells were plated into poly-L-lysine-coated (100  $\mu$ g/mL; Sigma-Aldrich P4707) flasks and maintained in complete DMEM. After 3 days, 2/3 of the medium was refreshed. On Day 7, the flasks with primary glial cultures were transferred to an orbital shaker at 100 rpm for 30 min to remove microglia. After that, the entire medium with detached cells was removed. The homogeneity of the cell population was maintained for at least four passages. More than 80% of the cells were astrocytes as confirmed by immunofluorescence staining for glial fibrillary acidic protein (GFAP). Afterwards, cells were seeded and cultured under experimental conditions.

#### 2.4. MTS Cell Viability Assay

The cell viability MTS assay was performed according to the manufacturer's instructions. Briefly, cells were seeded in a regular DMEM medium in 96-well plates ( $8 \times 10^3$  cells/well) and allowed to adhere for 18 h, and then, the medium was removed. Next, the cells were washed twice with phosphate buffered saline (PBS) and finally treated with different canavanine concentrations (10–250  $\mu$ M) in complete medium or arginine-free medium for 24, 48 and 72 h. MTS solution was added to each well, and the cells were further incubated for 1 h. The absorbance was measured using a Tecan SUNRISE XFluor4 plate reader at a wavelength of 490 nm. The percentage of viable cells after treatment was calculated by assuming 100% viability for the absorbance recorded for the control conditions (i.e., in the absence of canavanine).

#### 2.5. Western Blot Analysis

The cells were washed three times in ice-cold PBS and lysed in RIPA Buffer (50 mM Tris-HCl pH 7.5, 150 mM NaCl, 0.5% sodium deoxycholate, 0.1% SDS, 1% IGEPAL (nonionic, non-denaturing detergent), 50 mM NaF, 2 mM  $\text{Na}_3\text{VO}_4$ , 1 mM PMSF, and protease and phosphatase inhibitor cocktails (04693116001 and 04906837001, respectively; Roche, Mannheim, Germany) at 4 °C for 20 min. Cell extracts were obtained after centrifugation at  $13,500 \times g$  at 4 °C for 20 min, and the supernatants were used for the study. Protein concentrations were quantified according to the Bradford method. Then, the supernatants were incubated with the Laemmli buffer for 5 min at 98 °C. Equal amounts of protein were separated in 10, 12 or 15% SDS–polyacrylamide gels (SDS-PAGE) and transferred onto nitrocellulose membranes (Amersham 10600002, Freiburg, Germany). The membranes were blocked with 3–5% fat-free milk or 5% BSA (Bioshop ALB001, Burlington, Canada) in TBS containing 0.2% Triton X-100 and then probed with the appropriate primary and secondary antibodies.  $\beta$ -Tubulin and GAPDH were used as protein loading controls. After 2 h, one-minute-UV-irradiated Jurkat cells were lysed and were subjected to analysis as an apoptotic cell death positive control. The protein bands were visualized using ECL reagent. Band densitometry quantification was performed using the Fiji distribution of the ImageJ 1.52a software (National Institutes of Health and the University of Wisconsin, Madison, WI, USA).

#### 2.6. Immunocytochemical Staining and Microscopy Analysis

Cells were seeded on glass coverslips (VWR 631-0153, Gdańsk, Poland), cultured in respective conditions and then washed twice with PBS, fixed with 4% paraformaldehyde solution (PFA) for 20 min, washed twice with PBS, quenched for 30 min with 50 mM  $\text{NH}_4\text{Cl}$ , permeabilized with 0.2% Triton X-100 in PBS for 10 min and finally incubated for 1.5 h in a blocking solution (2% horse serum in PBS/0.02% Triton X-100). To visualize actin filaments, cells were stained for 20 min with Alexa Fluor 488- or 546-conjugated phalloidin (diluted 1:40 in PBS) and then washed three times with PBS/0.02% Triton X-100. Next, cells were incubated overnight at 4 °C with primary antibodies and for 1.5 h at room temperature with Alexa Fluor 546- or 488-conjugated anti-mouse or Alexa Fluor 488-conjugated anti-rabbit antibodies diluted to 1:1000. Coverslips were extensively washed in PBS/0.02% Triton X-100 and mounted using Vectashield anti-fade reagent supplemented with DAPI to stain nuclei. Images were taken with the Zeiss LSM780, Inverted Axio Observer Z.1 with Plan Apochromat 40 $\times$ /1.4 and 63 $\times$ /1.4 Oil DIC objectives. The images were processed using the Zen Blue 2.1 software (Carl Zeiss Microscopy, Jena, Germany).

#### 2.7. Confocal Endoplasmic Reticulum Localization

The endoplasmic reticulum was visualized by staining with the endoplasmic reticulum (ER)-specific dye, ER Tracker™ Blue/White DPX, which is retained within the ER lumen, thus labeling the ER tubular network. The assay was performed according to the manufacturer's instructions. Briefly, cells were seeded on the glass coverslips and cultured under respective conditions. After that,

the cells were incubated for 30 min at 37 °C and 5% CO<sub>2</sub> with 1 μM ER Tracker diluted in experimental conditions. Then, the stained cells were fixed with 4% formaldehyde for 10 min, washed and mounted using the Vectashield anti-fade reagent. Images were taken with the Zeiss LSM780, Inverted Axio Observer Z.1 with Plan Aplanachromat 63×/1.4 Oil DIC objectives. The images were processed using the Zen Blue 2.1 software (Carl Zeiss Microscopy).

### 2.8. Transwell Migration Assay

Cell migration was assayed using 24-well Transwell™ chambers with 6.5 mm-diameter polycarbonate filters with 8 μm-pore-size Transwell™ migration inserts according to the manufacturer's instructions with the following modifications (Corning CLS3422-48EA, Glendale, AZ, USA). The assay was based on chemotactic directional migration. Cells were treated under experimental conditions for 48 h, as were the control cells. Then, the cells were trypsinized, washed twice with serum-free medium and counted. The same numbers of living cells were seeded ( $2.5\text{--}3 \times 10^4$  cells/well depending on the cell line) on the upper chamber and allowed to migrate through the filter to the lower chamber containing DMEM with 10% FBS. After 8–18 h (for U251MG and U87MG cells, respectively), the cells were fixed with 4% PFA for 15 min and stained with 0.5% crystal violet (Sigma-Aldrich) for 7–10 min. Cells that did not migrate through the filter were removed from the upper chamber by using a cotton swab. Migrated cells were photographed using a Nikon Eclipse Ti-U fluorescent microscope equipped with a 20× objective and DS-Qi2 digital camera and then counted with the Fiji distribution of the ImageJ 1.52a software (National Institutes of Health and the University of Wisconsin). The percentage of migrated cells was calculated by assuming 100% for the control conditions.

### 2.9. Cell Adhesion Assay

The cell adhesion assay was performed with the CytoSelect™ 48-well cell adhesion assay according to the instructions provided by the manufacturer (Cell Biolabs, Inc. CBA-070, San Diego, CA, USA). Briefly, cells were cultured under the indicated experimental conditions for 48 h as were the control cells, trypsinized, washed once with medium with serum and twice with serum-free medium, and then seeded ( $10^5$  living cells/well) onto the collagen I-coated wells. After 2.5 h, unbound cells were washed away with PBS, and the adherent cells were stained. Finally, the stain was extracted and the OD560 measured with a Tecan SUNRISE XFluor4 plate reader.

### 2.10. Stable Isotope Labeling by Amino Acids in Cell Culture (SILAC)

Amino acid labeling was performed as described by Ong and Mann [29]. We performed the experiments on U251MG cells, for which the effects of both arginine deprivation and canavanine co-treatment were more visible. The cells were grown to 80–90% confluency in standard DMEM medium formulated with heavy <sup>13</sup>C<sub>6</sub>, <sup>15</sup>N<sub>4</sub>-arginine (0.1 mM) in culture dishes. The medium was changed every 2–3 days in the cases when the cells were not ready for passaging.

### 2.11. Protein Extraction and Digestion

After SILAC labeling, cells were subjected to differential treatment: (1) complete medium with heavy arginine; (2) complete medium with light arginine; (3) arginine-free medium with 50 μM canavanine for 24 h; (4) AFM with 50 μM canavanine for 48 h. The treatments yielded different numbers of cells, due to differences in cell proliferation and survival rates ( $1\text{--}1.7 \times 10^6$  cells). Cells were washed with ice-cold PBS three times and scraped off the plates in RIPA Buffer (250 μL per  $10^6$  cells; see RIPA buffer composition above). The lysate was frozen on dry ice without preclearing. After thawing, the lysate was sonicated using a QSonica, Q125 sonicator probe homogenizer at 50% energy (1 min cycle; 15 s on and 15 s off). Protein from 320 μL (i.e., from around  $1.2 \times 10^6$  cells) was precipitated by the addition of 1280 μL of ice-cold acetone, incubated at –20 °C for 2 h and pelleted by centrifugation at 20,000× g for 30 min. The protein pellet was resuspended in 60 μL of 8 M urea and quantified with BCA (Pierce™ BCA Protein Assay Kit, ThermoFisher Scientific 23225). All samples had concentrations

between 1.6–2 g/L. The samples were diluted 4-fold and digested at a 1:20 ratio of protein/Wako LysC (the protease was added at 1:40 twice with a 4 h interval). The peptides were desalted on an Oasis HLB 1 cc Vac Cartridge with 30 mg of sorbent as suggested by the manufacturer and speedvac-ed, and 1 µg of material was injected on the column.

### 2.12. LC-MS/MS Analysis

Samples were analyzed using a nanoAcquity UPLC system (Waters, Milford, MA, USA) coupled to an Orbitrap Fusion Lumos (ThermoFisher Scientific). Peptides were trapped on a Symmetry C18 5 µm, 180 µM × 20 mm precolumn (Waters, MA, USA) and desalted at 10 µL/min flow for 2 min with 0.1% TFA (trifluoroacetic acid). The separation was performed on a nanoACQUITY CSH130 C18 1.7 µm, 75 µm × 250 mm at a 300 nL/min flow rate with 0.1% formic acid as Buffer A and 0.1% formic acid in acetonitrile as Buffer B. The gradient was 6–40% B over 75 min, 40–60% over 10 min and 60–100% over 15 min.

Eluted peptides were electrosprayed through an etched emitter [30] and analyzed using the Universal Method with a 60 s exclusion time (see the supplementary information S1 Experimental procedures: MS/MS method settings section). MS1 was performed in an orbitrap at a 120K resolution, and MS2, in ion trap rapid mode.

### 2.13. Proteomics Data Analysis

Data were analyzed in Proteome Discoverer in 2.4.035. A database search was performed with Sequest using the human UniProt database (retrieved on 06 June 2019). Methionine oxidation, <sup>13</sup>C<sub>6</sub>, <sup>15</sup>N<sub>4</sub>-arginine and canavanine (user defined) were set as variable modifications; Cys carbamidomethylation was set as a fixed modification. The precursor and fragment mass tolerances were 3 ppm and 0.6 Da, respectively (we observed a large number of false positive canavanine identifications in samples where no canavanine labeling was performed at higher precursor mass tolerance). Peptides were validated with Percolator with a 0.01 posterior error probability (PEP) threshold. Peptide intensities were calculated with the Minora Feature Detector node. Top3 quantitation was performed only on samples with 48 h canavanine treatment in R using the dplyr package [31] as described previously [32]; only proteins with at least 2 proteotypic peptides were considered. GO (Gene Ontology) analysis was performed using the clusterProfiler R package [33]. The mass spectrometry proteomics data have been deposited to the ProteomeXchange Consortium via the PRIDE [34] partner repository with the dataset identifier PXD019044.

### 2.14. Theoretical Calculation of Necessary Mass Spectrometer Resolution

Calculations were performed essentially as described in [35] using the canavanine-containing peptides identified in this study. The atomic masses for <sup>1</sup>H, <sup>12</sup>C, <sup>13</sup>C and <sup>16</sup>O were taken as equal to 1.0078, 12, 13.0033 and 15.9949, respectively, from the CIAAW atomic weights of the elements (2019) [36]. The mass difference between the 3rd isotope of the unmodified peptide and 1st isotope of the canavanine-containing peptide is  $(13.0033 - 12) \times 2 - (15.9949 - 12 - 1.0078 \times 2) = 0.0273$  or 27.3 mDa. The theoretical full width at 10% maximum (FWTM) peak height was computed for each identified peptide at the measured m/z and charge containing canavanine at 100 different resolutions (starting with  $1 \times 10^4$  and incrementing by  $1 \times 10^4$  until  $1 \times 10^6$ ) using Equation (1).

$$FWTM = 1.822 \times \frac{m/z}{R \times \sqrt{\frac{200}{m/z}}} \quad (1)$$

The FWTM was then compared to the expected distance between the 3rd and the 1st isotope of the unmodified peptide, which was calculated as 27.3 mDa divided by the peptide charge.

### 2.15. Statistical Analysis

All experiments were run in triplicate and repeated at least three times. The results are expressed as means  $\pm$  SD. Statistical analyses were performed using one way-ANOVA tests in the GraphPad Prism 8.4.3 software (San Diego, CA, USA). Statistical significance was defined as  $p < 0.05$ .

## 3. Results

### 3.1. Canavanine Treatment Decreases the Viability and Proliferative Potential of Human Glioblastoma Cells under Arginine Deprivation

First, we addressed the question whether the effects of canavanine on two human glioblastoma cell lines, U251MG and U87MG, which are known to differ in their proliferation, migration and invasiveness [37]. It was observed that canavanine strongly inhibited the viability of both cell lines in concentration- and time-dependent manners specifically under arginine deprivation (Figure 2a).

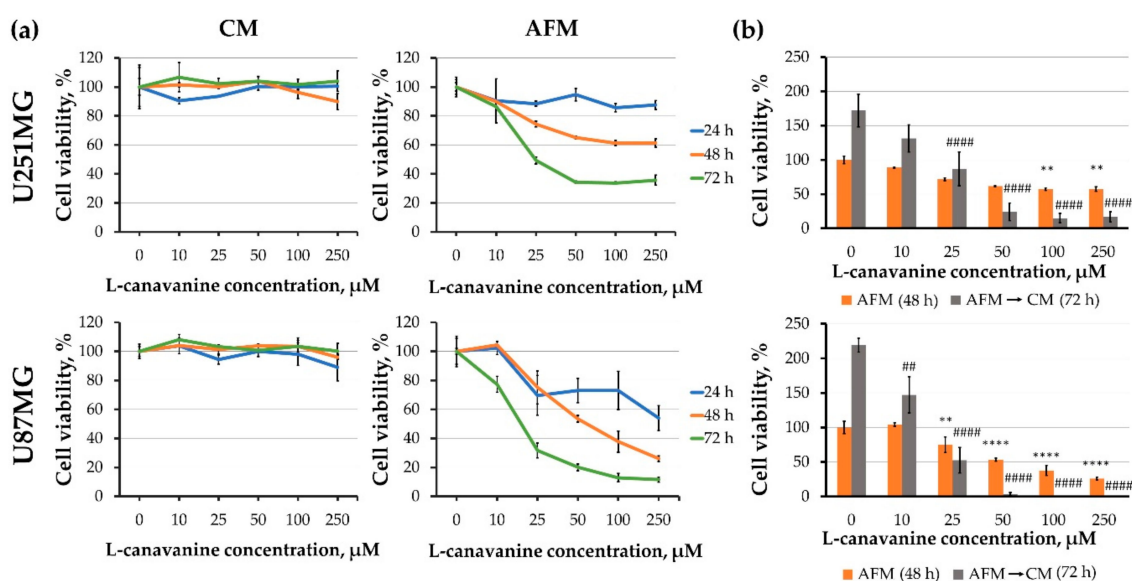


**Figure 2.** Effect of canavanine on glioblastoma cell viability and ability to restore growth upon arginine resupplementation. (a) MTS assay for U251MG and U87MG human glioblastoma cells treated for up to 72 h with increasing concentrations of canavanine (CAV) in the complete (CM) or arginine-free (AFM) media. (b) After 48 h of treatment, the medium was changed for arginine-containing complete medium (CM), and the cells were cultured for an additional 72 h. Then, growth restoration was assessed using the MTS test. Graphs represent mean values  $\pm$  SD from three independent experiments. \*\*  $p < 0.01$ , \*\*\*\*  $p < 0.0001$  relative to arginine-free medium (AFM) (control, 100%); ##  $p < 0.01$ , ####  $p < 0.0001$  relative to control cells after resupplementation.

Although after 48 h of incubation in arginine-deficient medium, both cell lines could readily restore their proliferation when arginine was resupplemented. It was observed that preincubation with canavanine at concentrations above 50  $\mu$ M essentially blocked such growth restoration (Figure 2b). Furthermore, the number of dead cells was noticeably increased after 48 h of treatment with 100  $\mu$ M canavanine, which coincided with a progressive accumulation of the cleaved forms of PARP1 and caspase 3 after 48 h of treatment in both glioblastoma cell lines (Figure 3). Additionally, under canavanine co-treatment, a decreased level of the proapoptotic protein Bcl-2 was observed in U251MG cells (Figure S1). No significant differences in the level of the active cleaved form of caspase 9 in either cell line under all the examined conditions were detected (Figure S1).

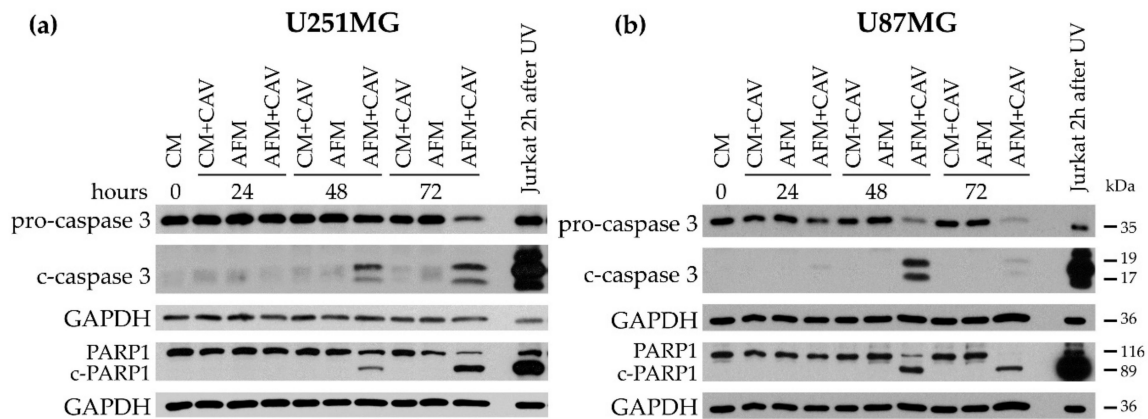


**Figure 3.** Assessment of the levels of the markers of apoptotic cell death in U251MG (a) and U87MG (b) cells under 100  $\mu$ M canavanine treatment in complete or arginine-free medium. GAPDH was used as a protein loading control. UV-irradiated Jurkat cells were used as a positive control.

These observations indicate that canavanine co-treatment, contrarily to arginine deprivation alone, induces caspase-dependent apoptotic cell death in the human U251MG and U87MG glioblastoma cell lines. Of note, we did not detect apoptotic markers in primary cultured rat glial cells under canavanine co-treatment (Figure S2).

### 3.2. Canavanine Profoundly Affects Morphology of U251MG and U87MG Cells under Arginine Deprivation

Many biological processes essential for both untransformed and cancer cells such as cell migration, morphogenesis, cytokinesis and endocytosis rely on the dynamics of the actin cytoskeleton [38,39]. Previously, we have also shown that arginine deprivation itself selectively destabilizes the actin cytoskeleton in glioma cells but not in primary rat glial cells [25]. Therefore, our next step was to examine the organization of actin filaments in the presence of 50  $\mu$ M canavanine, a concentration near the IC<sub>50</sub> for both examined cell lines. We noted that after 48 h of treatment in the absence of arginine, canavanine significantly affected the morphology of the examined U251MG and U87MG cells, especially the organization of the actin-rich structures of the leading edge such as lamellipodia and filopodia (Figure 4, solid arrows). This was accompanied by a decrease in the presence of filamentous actin as well as the appearance of bleb-like structures and actin-containing aggregates, which are indicative of progressing cell death. Both glioblastoma cell lines exhibited similar alterations. Importantly, there were no apparent changes either in the morphology or in the actin cytoskeleton organization in the glioblastoma cells treated with canavanine in CM or in the control rat glial cells subjected to combined treatment with canavanine and arginine deprivation (Figure 4).

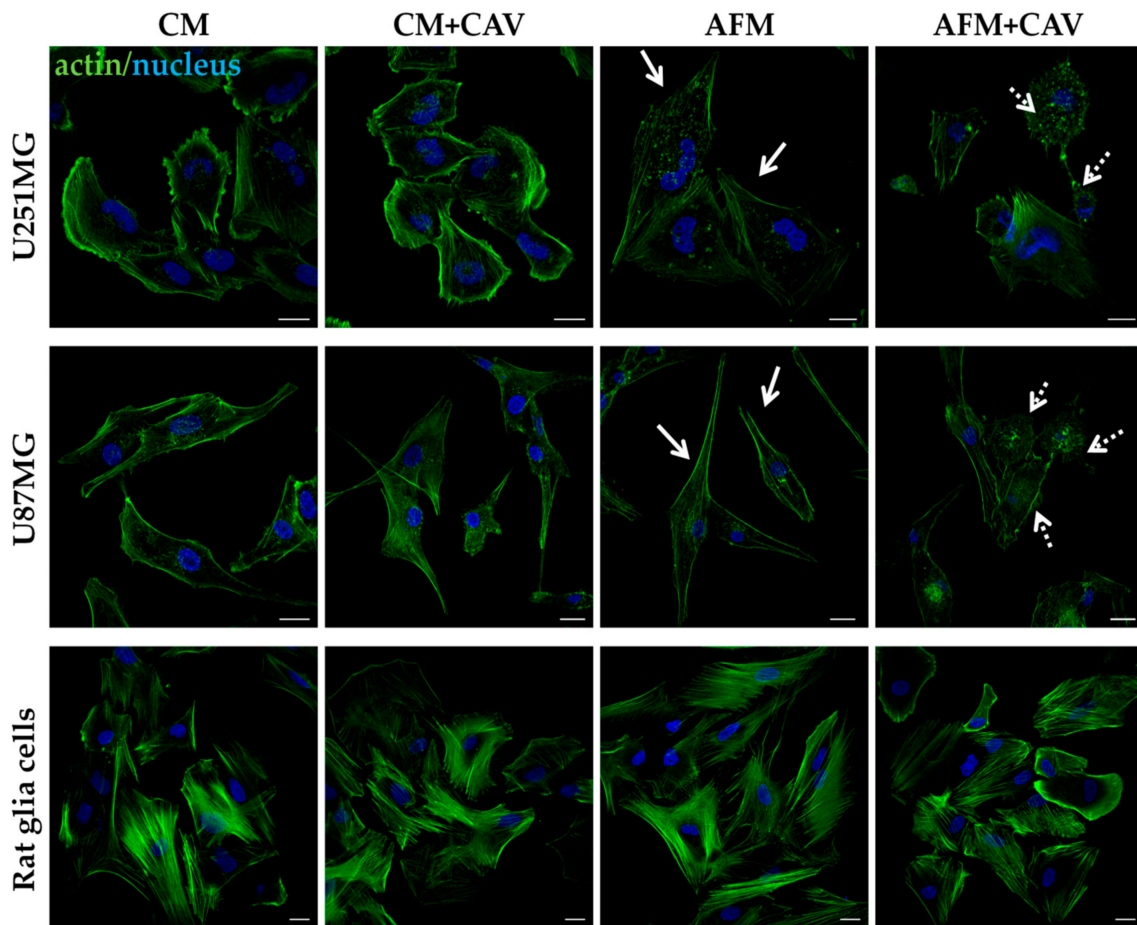


**Figure 4.** Organization of the actin cytoskeleton, probed with Alexa Fluor 488-conjugated phalloidin, of U251MG and U87MG human glioblastoma cells as well as normal rat glial cells. Cells were cultured for 48 h under experimental conditions with or without 50  $\mu$ M canavanine. Untreated cells (CM) served as a control. Nuclei were labeled with DAPI. Solid arrows indicate altered leading-edge morphology in cancer cells starved for arginine, and dotted arrows indicate actin-rich aggregates and blebs elicited by canavanine. Bars, 20  $\mu$ m.

It is known that actin filaments play an essential role in the control of both cellular and nuclear shape, and the geometry of the nucleus, in turn, affects cell proliferation, gene expression and protein synthesis [40–42]. A/C- and B-type lamins are major components of the nuclear lamina [43] that play an important role in the nucleo-cytoskeletal connection, and this interaction is essential for cell polarization, cell migration and cancer progression [41].

Staining for lamin B1 revealed abnormally shaped cell nuclei after 48 h of the culturing of U251MG cells, but not of U87MG ones, under arginine deprivation (Figure 5a, solid arrows). More pronounced changes in both glioblastoma cell lines were observed under canavanine co-treatment (Figure 5a, dotted arrows). Western blotting of the levels of nuclear lamins showed a decrease in lamin B1 in both glioblastoma cell lines and lamin B2 in U251MG cells under arginine deprivation in combination with canavanine treatment (Figure 5b).

We also observed fragmentation of lamins A/C and B1 in both U251MG and U87MG cells under prolonged co-treatment that could be also considered as one of the hallmarks of apoptosis (Figure 5b) [43]. Again, no substantial changes in the nuclear lamina pattern in analogously treated normal rat glial cells were observed (Figure S3).

Thus, our data show that combined treatment with arginine deprivation and canavanine evokes pronounced detrimental alterations in cytoskeleton and nuclear organization specifically in glioblastoma cells.



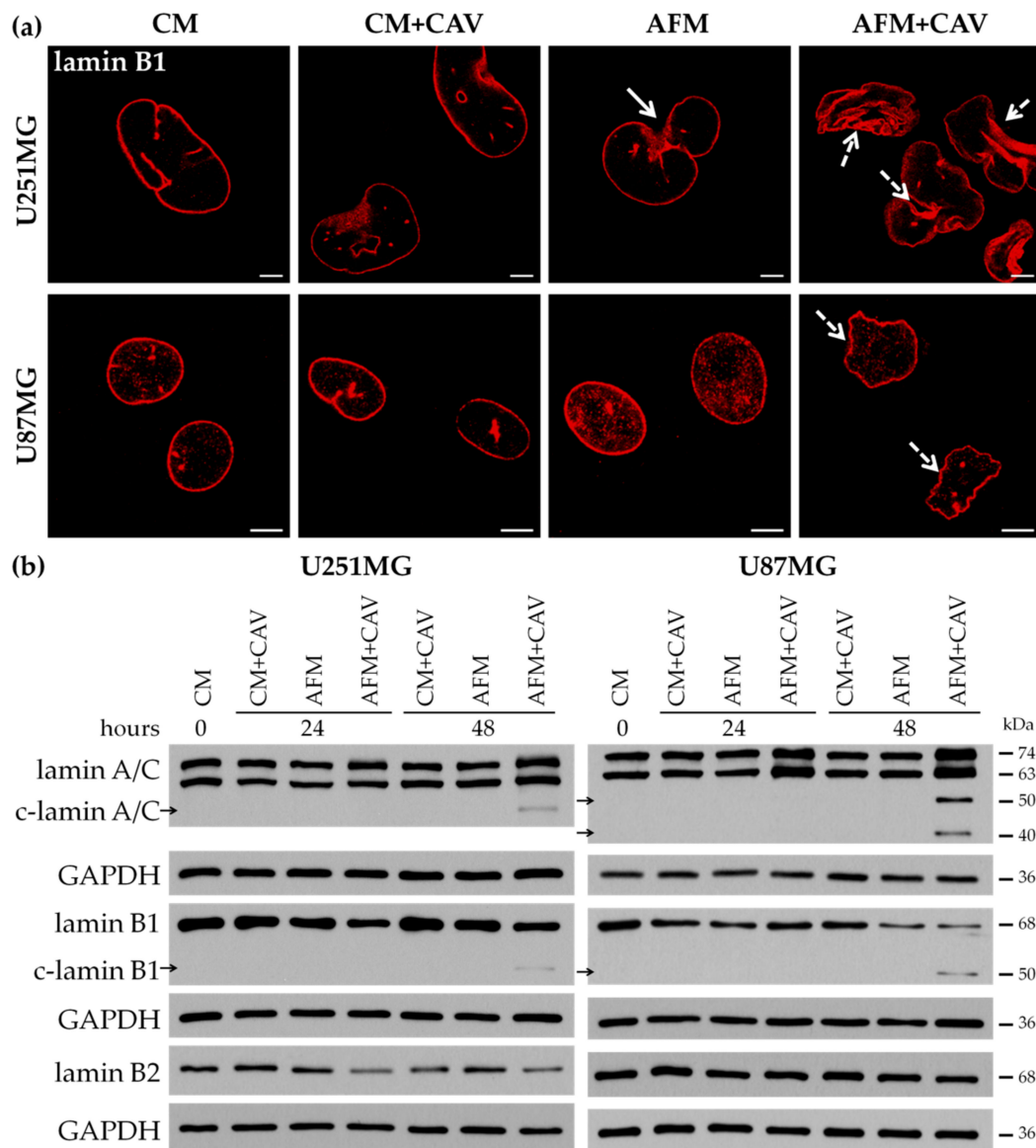


**Figure 5.** Analysis of nuclear lamina in U251MG and U87MG cells undergoing combined treatment of arginine deprivation with 50  $\mu$ M canavanine. (a) Immunofluorescence analysis of lamin B1. Solid arrows indicate abnormal nuclei under arginine deprivation; dotted arrows point to misshaped cell nuclei under co-treatment. Bars, 5  $\mu$ m. (b) Western blots of nuclear envelope proteins lamin A/C and lamin B1 and their cleaved forms (c-lamin A/C and c-lamin B1) and lamin B2. GAPDH was used as a protein loading control.

### 3.3. Lack of Arginine in Combination with Canavanine Profoundly Impairs Migration and Adhesion of Human Glioblastoma Cell Lines

Cell migration and invasion play a key role in cancer metastasis [44]. We previously demonstrated that arginine deficiency specifically impaired the motility and adhesive interactions of human glioblastoma and melanoma cells [25,45]. The above-described exacerbated alterations of cell morphology observed under canavanine co-treatment could be associated with changes in cell adhesion and motility. Therefore, we analyzed the cell migration of U251MG and U87MG glioblastoma cells treated with canavanine under arginine deprivation using the Transwell™ system [46]. While arginine deprivation itself profoundly decreased migration by ~50%, almost complete inhibition of cell penetration through the porous membrane after 48 h of canavanine co-treatment was observed for both glioblastoma cell lines (Figure 6).

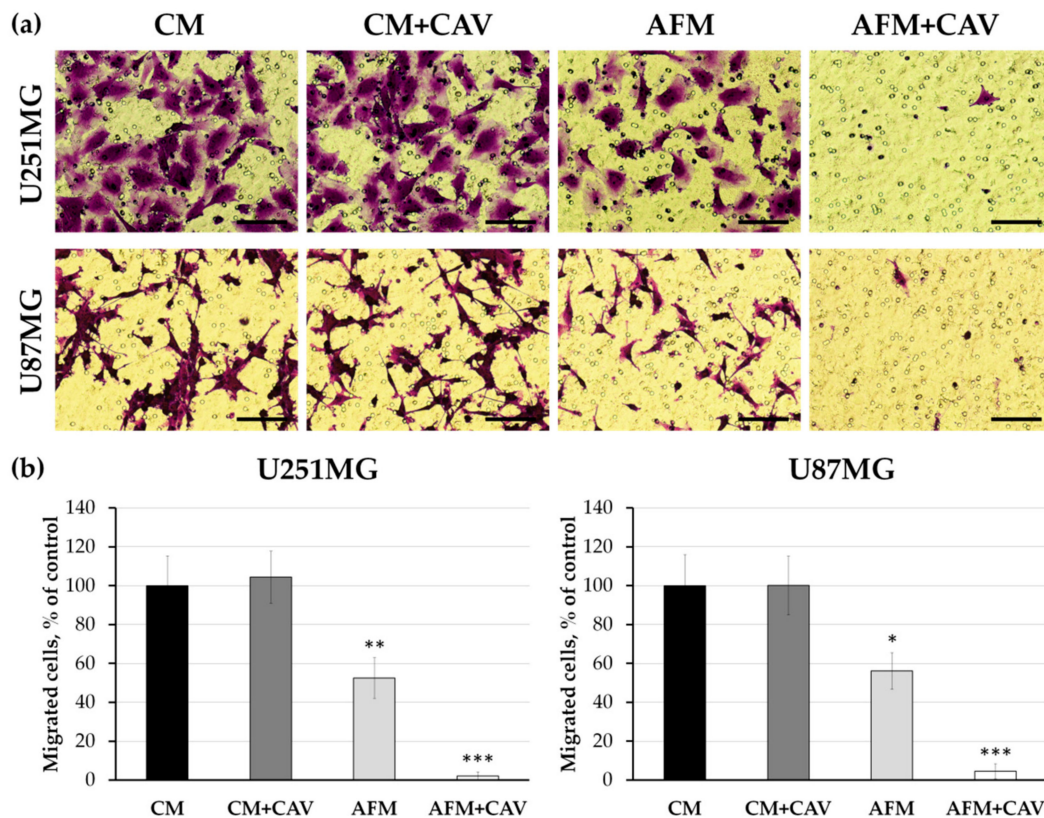


**Figure 6.** Effect of canavanine on human glioblastoma cell migration. (a) Representative images of migrated cells after the 48 h of co-treatment with 50  $\mu$ M canavanine under CM and AFM conditions. Bars, 100  $\mu$ m. (b) Quantification of migrated cells. Graphs represent mean values  $\pm$  SD from three independent experiments. \*  $p < 0.05$ , \*\*  $p < 0.01$ , \*\*\*  $p < 0.001$  relative to CM (control, 100%).

Cell adhesion to the extracellular matrix is a highly dynamic process that plays a crucial role in the regulation of cell proliferation and growth, cell motility and gene expression [47–49]. We analyzed the focal adhesion structures in glioblastoma cells using immunostaining for an integrin-associated linker protein, vinculin. We observed that canavanine augmented alterations in the focal contact morphology evoked by arginine deprivation in both studied cancer cell lines (Figure 7a). This was more pronounced for U251MG cells, where vinculin-stained adhesive structures were smaller and more dispersed. Additionally, changes in focal contact structures were also noticeable in a control primary rat glial cell under canavanine co-treatment, although they were not as pronounced as in both cancer cell lines (Figure S4a).

Next, we analyzed cell adhesion by the assessment of the cell-matrix interactions of glioblastoma cells with a surface covered with collagen I, one of the main components of the extracellular matrix. We observed that under arginine deprivation, canavanine caused a dramatic decrease (by ~75%) in cell adherence to the surface of both glioblastoma cell lines (Figure 7b). Of note, arginine deprivation itself practically did not evoke a negative effect on adhesion to collagen I.

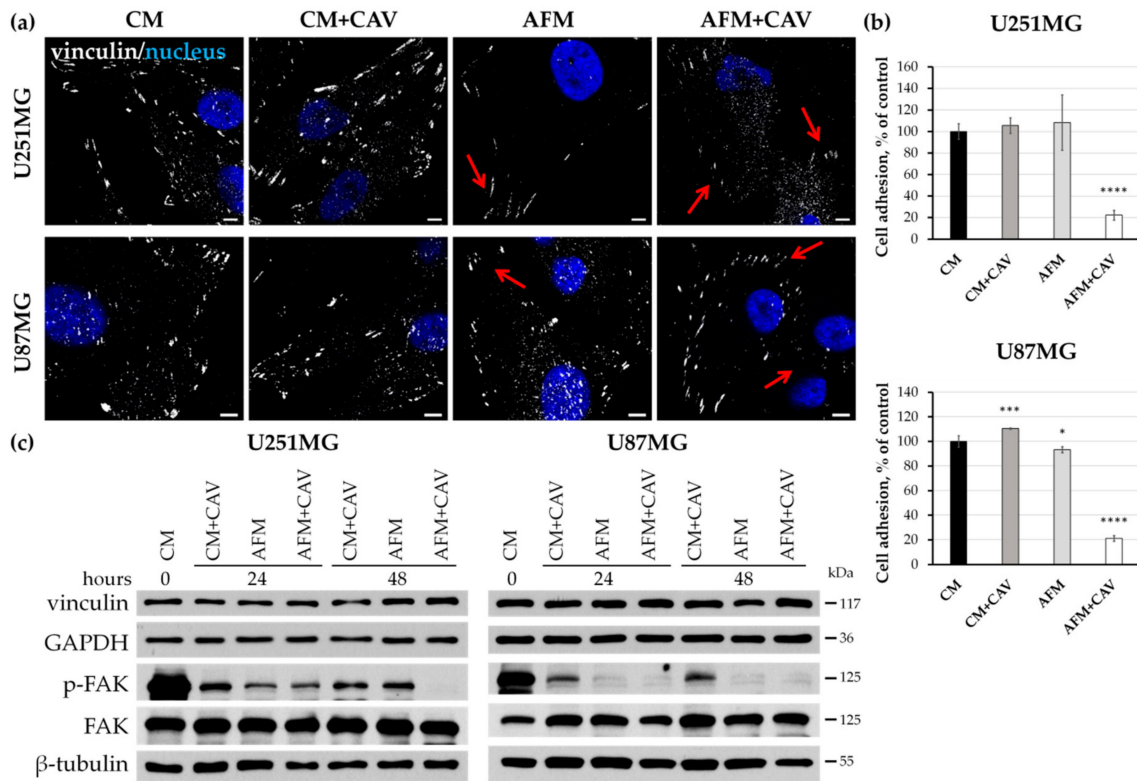


**Figure 7.** Effects of canavanine on adhesion of human glioblastoma cells. **(a)** Immunocytochemical staining for vinculin. Nuclei were labeled with DAPI. Cells were treated for 48 h under indicated experimental conditions under CM and AFM, with or without 50 μM canavanine. Bars, 10 μm. Arrows point to altered focal adhesion contacts. **(b)** Cancer cell adhesion to collagen I after the 48 h of treatment in CM and AFM with or without CAV. Graphs represent mean values ± SD from three independent experiments. \*  $p < 0.05$ , \*\*\*  $p < 0.001$ , \*\*\*\*  $p < 0.0001$  relative to CM (control, 100%). **(c)** Immunoblotting of proteins involved in cell adhesion and migration. GAPDH and β-tubulin were used as protein loading controls.

Despite such evident changes in adhesive structures and cell-surface adhesion, the levels of proteins involved in cell adhesion such as vinculin, talin and tensin 2 did not change substantially with respect to those in control cells (Figure 7c and Figure S5). Since focal adhesion kinase (FAK) is a key regulator of adhesive structure organization, we next assessed its levels as well as the level of its phosphorylated (active) form (p-FAK, Tyr397) in the examined conditions. We observed a substantial reduction of the p-FAK level under arginine deprivation in the absence of canavanine (Figure 7c). Combined treatment with canavanine for 48 h augmented the decrease only in U251MG cells. Interestingly, the presence of canavanine in the complete medium also led to a decrease in FAK activity (Figure 7c). Similar, but less dramatic, effects were observed in primary rat glial cells (Figure S4b).

It is known that actin-cytoskeleton organization, cell morphology and survival as well as cell adhesion are under the control of Akt kinase [50–53]. Therefore, we examined the activation level of this kinase by analysis of its phosphorylation at S473. As shown in Figure S6, 48 h of incubation in arginine-free conditions with canavanine treatment led to a ~50% decrease in Akt activation (phosphorylation at Ser473) in both glioblastoma cell lines. Moreover, 48 h of canavanine treatment led to a decrease in total Akt protein in U251MG cells.

Overall, our data suggest that canavanine effectively augments the negative effects of arginine deprivation on glioblastoma cells' heterotypic adhesion.

### 3.4. Proteomics Analysis of Canavanine Incorporation into Proteins in U251MG Glioblastoma Cells

While previous reports have suggested that canavanine gets incorporated into polypeptides during translation [13,27], the direct observation of canavanine in proteins by mass spectrometry and the extent of its incorporation or whether it is more likely to get incorporated as part of a motif have not been reported. The challenge is that Arg-to-canavanine substitution would result in a 1.9793 shift ( $16\text{O}-12\text{C}-1\text{H} \times 2$ ), which is very close to the mass difference of +2.0066 Da between the third and the first isotopes of an unmodified peptide,  $2 \times (13\text{C}-12\text{C})$ . Resolving this difference of 27.3 mDa on an Orbitrap LUMOS in MS1 would require operating at a 240K resolution for half of the peptides and 540K for 95% of the peptides (Figure 8a, see Materials and Methods for a description of the calculation). Such a high resolution is currently not attainable on this platform but would also be impractical for operation, due to the very long scan times on the majority of Orbitrap platforms [54]. Moreover, even if the unmodified and canavanine-containing peptides were resolved at the MS1 level, it would be impossible to generate their separate MS2 spectra due to quadrupole co-isolation. Hence, we labeled arginine (Arg) with  $^{13}\text{C}_6^{15}\text{N}_4$  to shift the masses of Arg-containing peptides by +10 Da to avoid the overlap with canavanine-containing peptides. Unlabeled arginine was termed as light Arg, and the labeled one was termed as heavy Arg. We also used endoproteinase LysC as the only protease, since the efficiency of trypsin for canavanine is currently unclear. Treatment with LysC generates longer and hence more hydrophobic peptides, and we also optimized the LC gradient for a higher final concentration of ACN.

To demonstrate canavanine incorporation into the proteins, we labelled U251MG cells with heavy Arg for seven passages and then transferred them to one of the following media: (i) AFM with 0.1 mM light Arg, (ii) AFM with 0.1 mM heavy Arg, and (iii) AFM with 50  $\mu\text{M}$  canavanine. Cells were harvested, and their proteome was analyzed after 48 h. An additional time point at 24 h was added for the AFM with 50  $\mu\text{M}$  canavanine. Each sample was analyzed in biological triplicate, and we calculated the incorporation of light Arg, heavy Arg and canavanine as proportions of identifications and signals (Table 1, only Arg-containing peptides were considered). Assuming that canavanine incorporation does not significantly affect ionization efficiency, the proportion of the signal can be interpreted as the proportion of canavanine at all residues normally occupied by arginine. We observed that ~12.6% of all Arg sites were occupied by canavanine after culturing cells in media with 50  $\mu\text{M}$  canavanine for 48 h. In comparison, culturing with 100  $\mu\text{M}$  light Arg for the same period of time resulted in 68.3% incorporation.

In total, we identified 1589 peptide sequences containing canavanine (see Table S1a) corresponding to 1980 canavanine sites. We investigated whether canavanine incorporation was more or less likely in the context of other amino acids using the motif-x software [55]. We used the sequences of canavanine-containing peptides as the foreground set and used all the identified Arg (or canavanine)-containing sequences as the background set (i.e., we compared the sequences of canavanine-containing peptides and all Arg/canavanine peptides). We looked at five amino acids at both sides of each heavy Arg (or canavanine) site. We identified no enriched motifs at the  $p$ -value of  $1 \times 10^{-6}$  (recommended settings in the motif-x software) (Table S1a).

We also tested whether specific functional categories were enriched among the proteins labeled with canavanine (using all the identified proteins as a background) in samples treated with canavanine for 48 h using the clusterProfiler R package [33]. While there was a significant enrichment of many GO terms, especially those related to cell adhesion and the unfolded protein response (see Table S2a for the list of proteins used in the GO analysis, and Table S2b and Figure S7 for the set of enriched categories), the implications of this enrichment are unclear. This could be interpreted as canavanine being preferentially incorporated into these proteins or these proteins being preferentially synthesized under canavanine treatment. At the same time, the group of canavanine-labeled proteins was also significantly more abundant (Figure S7d), and canavanine-labeled peptides were generally less intense than their heavy-Arg counterparts (see below). This could mean that peptides containing canavanine

fall below the limit of detection in less-abundant proteins, resulting in the high abundance of proteins enriched in the canavanine-labeled set.

The sequences of 1081 peptides had two variants identified within a single run: a variant with a single incorporated canavanine and a variant with all heavy Arg (Table S1b). We used this peptide set to investigate the effect of canavanine incorporation on the peptide charge and retention time, since a significant change in these properties would allow the analysis of canavanine-containing peptides in label-free proteomics data. Interestingly, we did not find a significant effect of canavanine on either of these properties (see Figure 8b,c), validating the necessity of heavy-Arg labeling. The median ratio of the intensities for heavy-Arg to canavanine-containing peptides was 7.5 (see Figure 8d).

As a final illustration of our strategy, we observed a small subset of peptides that had all three variants (i.e., heavy Arg, light Arg and canavanine) present at a certain Arg position, due to the incomplete heavy-Arg labeling prior to canavanine treatment. Figure S8 demonstrates the elution profiles and spectra for the three variants for one such peptide. As expected, the canavanine and light-Arg peptide variants were not resolved at the MS1 level at a 120 K resolution.

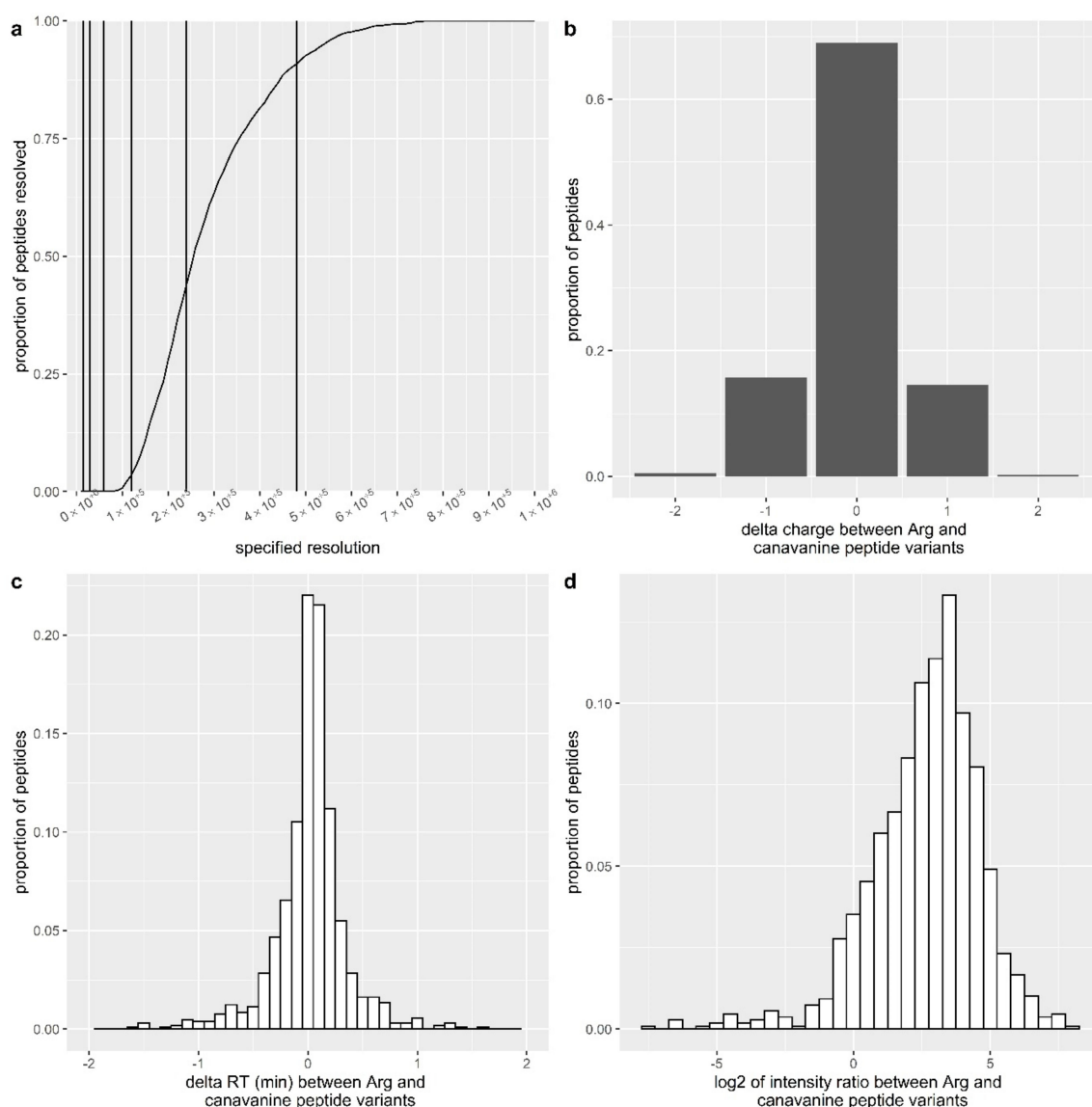


**Figure 8.** Proteomics of canavanine-bearing peptides. (a) Proportion of peptide variants with light Arg and canavanine resolved at different instrument resolutions (vertical lines indicate resolution settings available on Orbitrap Lumos). (b–d) Effect of canavanine incorporation on peptide charge state, retention time and intensity.

**Table 1.** Incorporation of arginine (Arg) and canavanine (CAV) into proteins of U251MG cells under examined conditions.

	ArgH, 48 h	ArgL, 48 h	CAV, 24 h	CAV, 48 h
	% of identifications			
ArgH	97.16 ± 0.19	33.85 ± 0.86	83.59 ± 0.47	76.91 ± 0.26
ArgL	2.78 ± 0.2	65.94 ± 0.83	6.48 ± 0.44	6.3 ± 0.23
CAV	0.06 ± 0.03	0.22 ± 0.04	9.93 ± 0.28	16.79 ± 0.46
	% of total intensity			
ArgH	98.72 ± 0.07	31.59 ± 0.95	90.09 ± 0.39	83.48 ± 0.38
ArgL	1.24 ± 0.06	68.34 ± 0.95	4.08 ± 0.38	3.88 ± 0.63
CAV	0.04 ± 0	0.06 ± 0.01	5.83 ± 0.11	12.63 ± 0.39

Incorporation presented as proportions of identifications (top part of the table) and proportions of intensity (bottom part of the table) ± SD. Three replicates were recorded per condition. ArgH, heavy arginine; ArgL, light arginine.

### 3.5. Canavanine Enhances ER Stress Evoked by Arginine Deprivation

Since arginine deficiency has been shown to induce endoplasmic reticulum (ER) stress in many cancer cell lines [56] and our mass spec data showed a significant enrichment of GO terms related to the unfolded protein response, our next goal was to analyze the effect of canavanine on this process in human glioblastoma cells. We performed immunofluorescence staining for a marker of ER stress, namely, the ER chaperone 78-kDa glucose-regulated protein (GRP78) [57,58]. We noticed an accumulation of GRP78 within the ER of both analyzed glioblastoma cell lines after 48 h of incubation under arginine deprivation in the presence of canavanine (Figure 9a, see arrows). These observations were confirmed by Western Blot analysis, which showed a significant increase in the level of GRP78 in cell lysates (Figure 9b). On the other hand, canavanine co-treatment only slightly increased the level of GRP78 in primary rat glial cells under analogous conditions (Figure S9).

In order to visualize the ER tubular network, we performed staining with the ER-specific dye, ER Tracker Blue/White DPX, which is retained within the ER lumen. As shown in Figure S10, the organization of the ER was changed in both arginine-deprived glioblastoma cell lines, and numerous ER tracker-stained vesicles (possibly autophagosomes) became visible. Additionally, 48 h of co-treatment with canavanine caused a complete disintegration of the ER network (Figure S10).

It is known that the accumulation of unfolded or misfolded proteins within the ER lumen activates unfolded protein response pathways implicated in protective/adaptive responses and in the promotion of apoptosis [59,60]. We examined the activation status of several proteins involved in the regulation of protein synthesis in our experimental conditions. As shown in Figure S11, already 4 h of culture with 50 µM canavanine in arginine-free medium evoked pronounced changes in the phosphorylation status of proteins involved in protein synthesis such as 4EBP1 (mTOR pathway) and eIF2α (GCN2 pathway) in both glioblastoma cell lines. Prolonged arginine deprivation or combined treatment further promoted the hyperphosphorylation of eIF2α and dephosphorylation of ribosomal protein S6 and 4EBP1, and canavanine only partially affected the processes leading to the inhibition of global protein translation (Figure 10a). Of note, canavanine also upregulated the dephosphorylation of 4EBP1, even in complete medium, in U87MG cells, a cell line that is slightly more sensitive to this toxic arginine analogue (Figure 1).

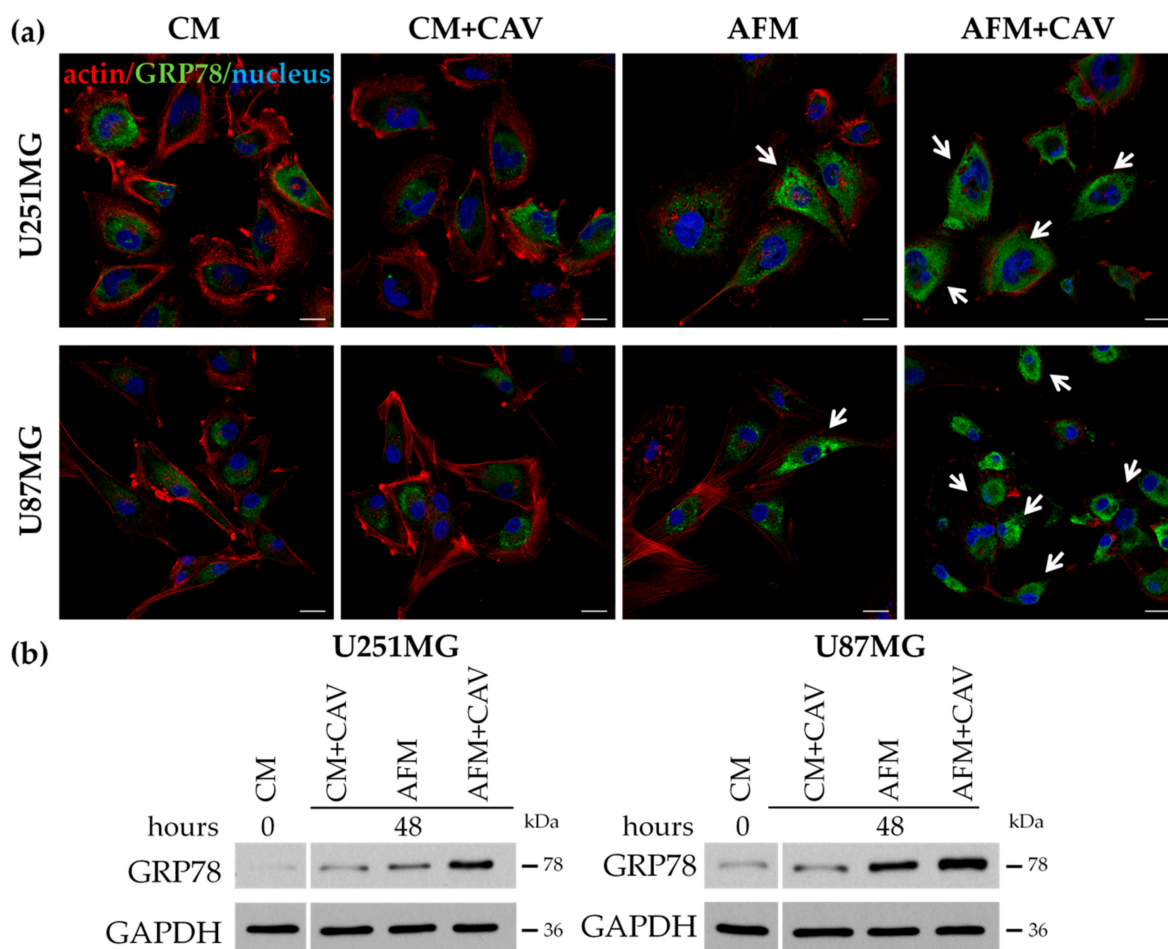


**Figure 9.** Canavanine (50  $\mu$ M) enhances endoplasmic reticulum (ER) stress during arginine deprivation in U251MG and U87MG human glioblastoma cells. (a) Immunostaining for GRP78 and actin filaments of the cells subjected to 48 h of canavanine co-treatment under arginine starvation. Nuclei were stained with DAPI. Bars, 20  $\mu$ m. Arrows point to cells with increased GRP78 fluorescence. (b) Western blot analysis of GRP78 protein level. GAPDH was used as a protein loading control.

Additionally, the level of a cAMP-dependent transcription factor, ATF4, a marker of ER stress-induced apoptosis, was dramatically increased under co-treatment with canavanine, in comparison to that with single arginine deprivation as a monotreatment (Figure 10b). Interestingly, canavanine under arginine-free conditions induced the formation of an additional ~38 kDa band, probably ATF4 isoform CRA\_a, which has been described in the literature [61].

Canavanine also evidently augmented the proapoptotic signaling pathway activated by arginine deprivation as evidenced by the increased phosphorylation of stress-activated protein kinase SAPK/JNK and mitogen-activated protein kinase p38 in glioblastoma cells (Figure 10b). Interestingly, the increase in the level of the proapoptotic transcription factor CHOP observed under arginine deprivation was not further elevated by the presence of canavanine in either glioblastoma cell line (Figure 10b).

Analysis of the rat glial cells' response to canavanine under arginine deprivation revealed the dephosphorylation of the S6 protein and a weak activation of proapoptotic markers such as ATF-4, p-SAPK/JNK and p-p38 after 48 h of co-treatment (Figure S12).

These data indicate that canavanine significantly enhances ER stress and profoundly promotes proapoptotic responses selectively in malignant U251MG and U87MG glioblastoma cells.

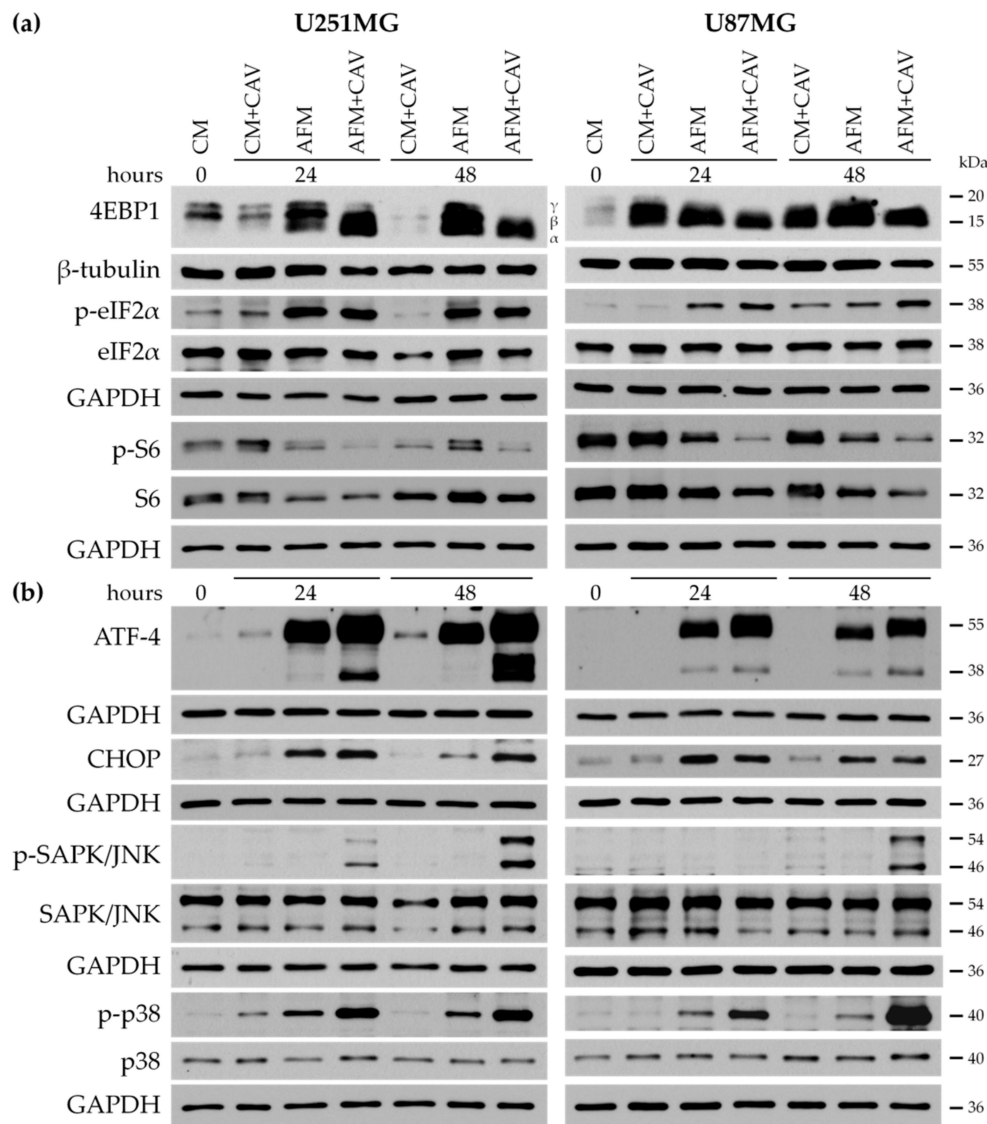


**Figure 10.** Western blot analysis of selected molecular markers of ER stress and cells' adaptive responses. (a) Proteins involved in protein synthesis. (b) Proapoptotic markers. Cells were incubated for up to 48 h under experimental conditions with or without 50  $\mu$ M canavanine. GAPDH was used as a protein loading control.

### 3.6. Canavanine Affects Mitochondria under Arginine Deficiency

It is known that mitochondrial dynamics can be significantly disturbed under stress conditions, and their adaptations are crucial for many cellular processes [62,63]. Additionally, the accumulation of misfolded or damaged proteins in mitochondria under metabolic stress can lead to organelle dysfunction. In order to examine whether canavanine in arginine-deprived conditions could also affect mitochondria, we performed immunocytochemical staining for heat shock protein glucose-regulated protein 75 (GRP75/mortalin), essential for maintaining the ER–mitochondrial contacts (Figure 11a) [64,65]. Under arginine deprivation, we observed a long, apparently hyperfused mitochondrial network, which was especially visible in U251MG cells (Figure 11a, solid arrows). Additionally, canavanine evoked dramatic changes, as the mitochondrial network became disrupted and aggregate-like structures were visible in both cell lines (Figure 11a, dotted arrows). Western blot analysis showed a decrease in mortalin levels in both cell types treated with canavanine in the absence of arginine for 48 h, but statistical significance was only found for U251MG cells (Figure 11b,c). Moreover, a concomitant



significant increase in the heat shock proteins HSP70 and HSP60 involved in mitochondrial stress was observed in glioblastoma cells under canavanine co-treatment (Figure S13).

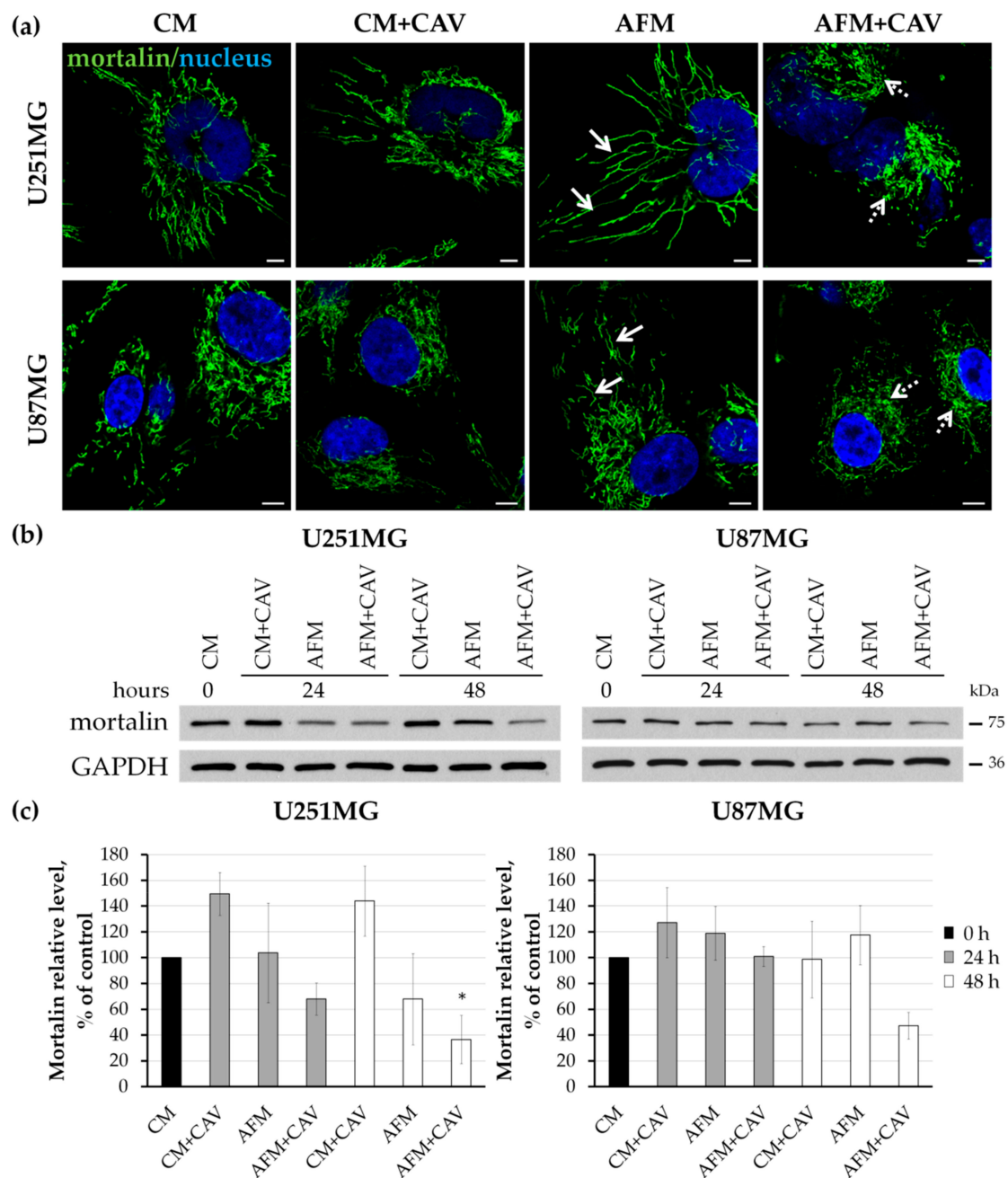


**Figure 11.** Assessment of mitochondrial organization in human U251MG and U87MG glioblastoma cells treated with 50  $\mu$ M canavanine under CM and AFM conditions. (a) Immunostaining for mortalin. Nuclei were labeled with DAPI. Cells were treated for 48 h under experimental conditions. Bars, 5  $\mu$ m. Arrows indicate hyperconnected mitochondria, and dotted arrows point to aggregate-like mitochondria. (b) Western blot analysis of mortalin levels. GAPDH was used as a protein loading control. (c) Densitometry of mortalin protein levels. Graphs represent mean values  $\pm$  SD from three independent experiments. \*  $p < 0.05$  relative to CM (control, 100%).

It should be also emphasized that canavanine under arginine deprivation caused a decrease in the phosphorylation of a catalytic  $\alpha$  subunit of AMP-dependent kinase, AMPK, a known cellular energy sensor, indicative of the inhibition of the kinase's activity (Figure 12).

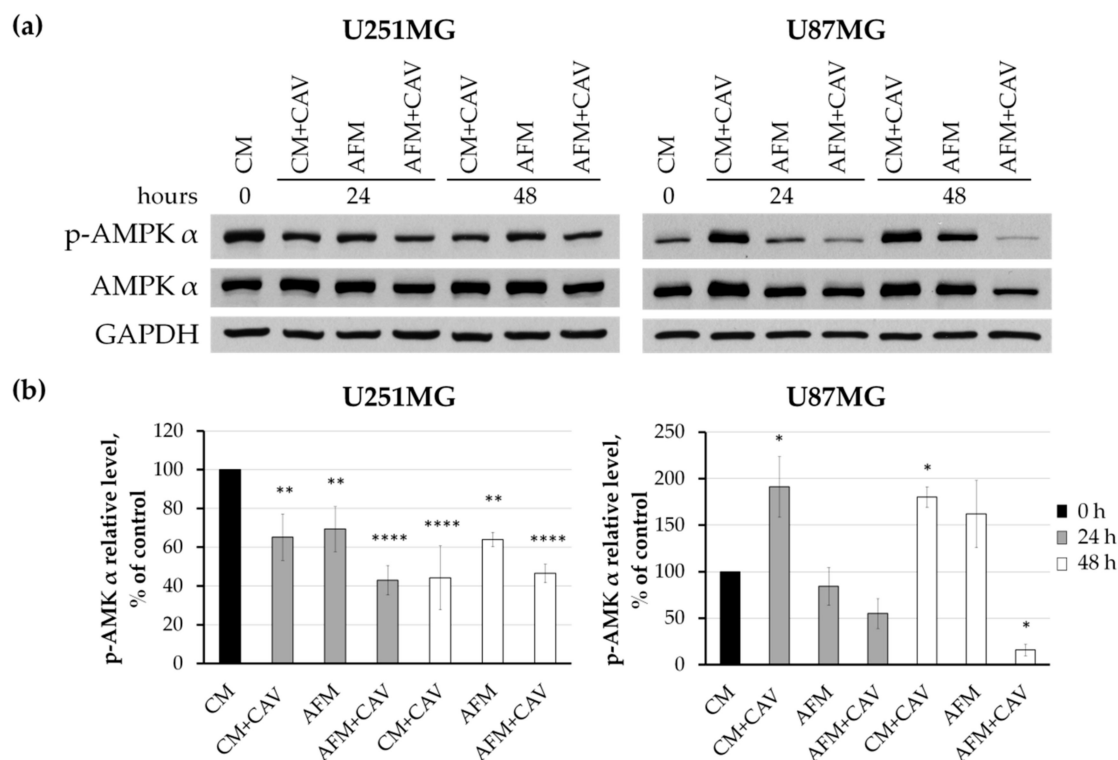


**Figure 12.** Analysis of the level of 5'-AMP-activated protein kinase AMPK  $\alpha$  subunit. (a) Western blotting of AMPK  $\alpha$  subunit and its phosphorylated form (p-AMPK  $\alpha$ ). GAPDH served as the internal loading control. (b) Densitometry of AMPK level. Graphs represent mean values  $\pm$  SD from three independent experiments. \*  $p < 0.05$ , \*\*  $p < 0.01$ , \*\*\*\*  $p < 0.0001$  relative to CM (control, 100%).

These data show that the arginine analogue canavanine, under arginine deprivation, induces the unfolded protein response in mitochondria and inhibits the activation of AMPK, responsible for energy homeostasis.

#### 4. Discussion

Glioblastoma is one of the most frequent and aggressive forms of primary brain tumors that develops from glial cells such as astrocytes and oligodendrocytes [66]. Glioblastomas are difficult to eliminate surgically and to treat in general due to their highly infiltrative and invasive nature [66]. Moreover, the blood–brain barrier prevents the delivery of many medications from the bloodstream to glioblastoma sites. The average survival time for glioblastoma patients after diagnosis is only 15–18 months, and the 5-year survival rate is only 10% [67]. Today, clinical trials are exploring new, potentially more efficient antiglioblastoma approaches in chemotherapy, radiation therapy, immunotherapy or their combinations [67]. We and others proposed that anticancer therapy based on single-amino-acid arginine deprivation that utilizes recombinant arginine-degrading enzymes could be applied as an antiglioblastoma treatment [1,24,25]. This metabolic approach has already achieved significant progress in cell culture and animal studies, and in clinical trials aimed at a growing number of cancer types [68]. Although the feasibility of this approach for the treatment of various cancers, primarily those with defects in arginine anabolism, has been demonstrated [67,68], we have found that the strong antitumor effect of arginine starvation observed in standard in vitro monolayer cell cultures does not fully translate into 3D cultures [69]. We and others proposed, therefore, that rationally designed combinational modalities are needed for the approach to successfully proceed into clinical use [1,15].

As we previously reported, arginine deprivation selectively and profoundly affected human glioblastoma cell morphology and migration, but these effects did not lead to glioma cell death and

were fully reversible after arginine resupplementation [25]. In this study, we aimed to examine whether a proteomimetic plant arginine analogue, canavanine, could augment the effect of arginine deprivation on two human glioblastoma cell lines, U251MG and U87MG. Additionally, we addressed the molecular mechanisms behind canavanine's effects on human glioblastoma cells.

We revealed that the combination treatment with canavanine had the strong time- and concentration-dependent cytotoxic effects on both examined human glioblastoma cell lines. The effects were irreversible after 48 h of co-treatment with 50  $\mu$ M canavanine, in contrast to in the arginine-deprivation-only condition, in which resupplementation with arginine fully restored cell growth. These observations support our notion that the combination of arginine starvation with canavanine could be considered as a promising new modality for antiglioblastoma treatment independent of the blood–brain barrier.

It is known that tumor invasiveness and aggressiveness are highly dependent on malignant cell motility. A negative impact of arginine deprivation as a monotreatment on the motility of glioblastoma, melanoma and colon carcinoma cells was observed [25,45,70]. This phenomenon in glioblastoma cells was most probably evoked by the decrease in the content of the positively charged arginylated form of  $\beta$ -actin and polymerized F-actin [25]. Herein, using several independent techniques, we showed that canavanine significantly augmented the effects of arginine deprivation on the morphology and migration of glioblastoma cells. Dramatic changes in the actin cytoskeleton organization, as well as changes in cell polarity and adhesion, such as the substantial loss of lamellipodia and defects in adhesive structures, essentially abrogated cancer cell migration after 48 h of co-treatment. The co-treatment significantly affected the FAK/Akt/Bcl-2 signaling pathway by the deactivation of FAK and Akt kinases, the main players in the regulation of cell migration and survival [71]. At the same time, canavanine did not evoke significant effects on the morphology and adhesion of normal rat glial cells deprived of arginine.

Alterations in the actin cytoskeleton's organization are also known to affect the nuclear architecture [72]. The nuclear lamina, a key structural element of the nucleus, is a complex protein network that provides structural support to the nuclear envelope and serves as the structural link between the nucleo- and cytoskeleton [42,73,74]. Upon canavanine co-treatment, we observed specific disturbances in the nuclear lamina, which could affect the mechanical stability of the nucleus, genome organization and signal transduction. Furthermore, based on numerous reports, it is plausible that the here-observed fragmentation of lamins A/C and B1 is associated with the initiation of apoptotic cell death [75,76].

In order to reveal the mechanism(s) behind the observed effects, we examined whether they could result from canavanine incorporation into polypeptide chains under arginine deprivation. Previously, it was shown with the use of cycloheximide, an inhibitor of protein biosynthesis, that canavanine incorporation into nascent proteins could be a cause its observed cytotoxic effects on several cancer cell lines such as keratinocytic carcinoma A431, lung adenocarcinoma A549, hepatocellular carcinoma HepG2, and pancreatic carcinoma MIA PaCa-2 [13]. Of note, we have also demonstrated that canavanine is much more cytotoxic towards malignant cells of different organ origin than towards pseudonormal cells [6,13]. Moreover, we showed that, *in vitro*, it is a rather weak substrate for recombinant human arginase [13,77]. Of note, canavanine's proteomimetic capability has been suggested as a main contributing factor in toxicologic diseases, for which data are already available in proteomics repositories [34]. We were first to observe and directly quantify canavanine incorporation into polypeptide chains in the examined U251MG cells with the use of LC-MS/MS analysis. Importantly, we observed that the analysis of label-free data from proteomics repositories for canavanine incorporation is not feasible since the MS1 signals for unmodified and canavanine-containing peptides would overlap. To address this challenge, we successfully employed the method of SILAC arginine labeling [29] for our model of aggressive and chemotherapy-resistant glioblastoma U251MG cells. Our analysis revealed that canavanine in the absence of arginine was indeed readily incorporated into the polypeptide chains at rates of up to ~13%. Of note, we did

not observe a motif preference for canavanine incorporation, and while certain GO categories were enriched among the proteins labeled with canavanine, the biological implications of this are not clear at the moment.

It is well established that amino acid starvation, in general, triggers the transcriptional amino acid response pathway and inhibits mTOR signaling [78]. It was also demonstrated that single-amino-acid arginine deprivation halts global protein synthesis but activates the machinery of a stress response [56,79]. Therefore, it was interesting—knowing that in, the examined conditions, canavanine is indeed built into the proteins—to address the effects of canavanine on these mechanisms. We observed that canavanine co-treatment had complex activating effects on the ER stress response, with the involvement of several signal transduction pathways. We observed both the suppression of mTOR activity and activation of the PERK signaling cascade of the stress response, causing an arrest of protein synthesis. Moreover, it is known that the hyperphosphorylation of eIF2 $\alpha$  significantly promotes the synthesis of the activating transcription factor 4 (ATF4), and this alters the pattern of gene expression, for example, of CHOP, a protein involved in the induction of apoptosis [80]. Furthermore, we observed that canavanine under arginine deficiency stimulated the mitogen-activated protein kinase (MAPK) pathway by the dramatic activation of the SAPK/JNK and p38 kinases, which play important roles in inflammatory gene expression and apoptosis [80,81].

The ER compartment is known to be associated with mitochondria, which play an essential role in the cell's energetic metabolism and calcium storage, and in the control of cell death [82,83]. We demonstrated that canavanine under arginine deprivation affected mitochondrial morphology and AMPK signaling, thus pointing at possible defects in energy metabolism.

Summarizing, our data indicate that under arginine deprivation, the arginine analogue canavanine has multifaceted effects on glioblastoma cells that, in the end, promote cell death. Moreover, these effects predominantly concerned transformed glioblastoma cells but not normal glial cells. We are aware, however, that this type of treatment, like many other types of anticancer therapy, could be somewhat stressful for healthy cells/tissues. The selective cytotoxic effect of canavanine on cancer cells is due to its more efficient uptake by these cells, which unlike normal cells, have defects in arginine metabolism.

Our findings thus provide strong mechanistic grounds for considering the co-treatment as a possible novel strategy for the development of a specific and effective antiglioblastoma metabolic therapy independent of the blood–brain barrier. To our knowledge, no similar approaches, in particular, against glioblastoma, are considered in clinics. However, numerous clinical studies on arginine-degrading enzymes, or their combination with certain chemotherapy drugs, are in progress for several tumor entities [7,10,84].

**Supplementary Materials:** The following are available online at <http://www.mdpi.com/2073-4409/9/10/2217/s1>. Supplementary Information S1: Experimental procedures: MS/MS method settings, Figure S1: Western blot analysis of the apoptotic markers in U251MG and U87MG glioblastoma cells, Figure S2: Western blot analysis of markers of apoptotic cell death in rat glial cells, Figure S3: Western blot analysis of nuclear lamina proteins (lamins A/C and B1) in rat glial cells, Figure S4: Analysis of the focal adhesions in rat glial cells after 48 h of treatment with 50  $\mu$ M canavanine under CM and AFM conditions, Figure S5: Western blot analysis of proteins involved in cell adhesion in U251MG and U87MG cell lines, Figure S6: The level of Akt kinase in U251MG and U87MG cells, Figure S7: Gene ontology analysis of proteins with canavanine incorporation against the set of all identified proteins, Figure S8: Illustration of spectrum cohesion for QLEDGRTLSDYNIQK peptide, Figure S9: Analysis of the ER stress marker, GRP78, in rat glial cells after 48 h of treatment with 50  $\mu$ M canavanine under CM and AFM conditions, Figure S10: Effect of 50  $\mu$ M canavanine on the ER in U251MG and U87MG glioblastoma cell lines, Figure S11: Canavanine (50  $\mu$ M) evokes early glioblastoma cell stress response after as little as 4 h of treatment under arginine deprivation, Figure S12: Western blot analysis of the markers of ER stress in rat glial cells treated with 50  $\mu$ M canavanine under CM and AFM conditions, Figure S13: The level of the heat shock proteins HSP70 and HSP60, markers of mitochondrial stress, Table S1a: Arginine and canavanine sites, Table S1b: Peptides with arginine and canavanine variants, Table S2a: Proteins used in GO analysis, Table S2b: GO analysis.

**Author Contributions:** Conceptualization, O.K., O.S. and M.J.R.; experimental work, O.K. and P.S.; data analysis, O.K., P.S., O.S. and M.J.R.; writing—original draft preparation, O.K.; writing—review and editing, O.K., P.S., O.S., O.N.J. and M.J.R.; visualization, O.K.; supervision, M.J.R.; project administration, M.J.R.; funding acquisition, M.J.R. All authors have read and agreed to the published version of the manuscript.

**Funding:** This research was funded by the European Union’s Horizon 2020 research and innovation program under the Marie Skłodowska-Curie grant, agreement number 665735, granted to the Nencki Institute and statutory funds from the Ministry of Science and Higher Education to the Nencki Institute.

**Acknowledgments:** The authors thank Yana Yushkevich and Damian Matyśniak from the Nencki Institute for their invaluable help in glial cell isolation.

**Conflicts of Interest:** The authors declare no conflict of interest.

## References

1. Hinrichs, C.N.; Ingargiola, M.; Käubler, T.; Löck, S.; Temme, A.; Köhn-Luque, A.; Deutsch, A.; Vovk, O.; Stasyk, O.; Kunz-Schughart, L.A. Arginine Deprivation Therapy: Putative Strategy to Eradicate Glioblastoma Cells by Radiosensitization. *Mol. Cancer Ther.* **2018**, *17*, 393–406. [CrossRef] [PubMed]
2. Tapiero, H.; Mathé, G.; Couvreur, P.; Tew, K.D.I. Arginine. *Biomed. Pharmacother.* **2002**, *56*, 439–445. [CrossRef]
3. Tabe, Y.; Lorenzi, P.L.; Konopleva, M. Amino acid metabolism in hematologic malignancies and the era of targeted therapy. *Blood* **2019**, *134*, 1014–1023. [CrossRef] [PubMed]
4. Riess, C.; Shokraie, F.; Classen, C.F.; Kreikemeyer, B.; Fiedler, T.; Junghanss, C.; Maletzki, C. Arginine-Depleting Enzymes—An Increasingly Recognized Treatment Strategy for Therapy-Refractory Malignancies. *Cell. Physiol. Biochem.* **2018**, *51*, 854–870. [CrossRef]
5. Patil, M.D.; Bhaumik, J.; Babykutty, S.; Banerjee, U.C.; Fukumura, D. Arginine dependence of tumor cells: Targeting a chink in cancer’s armor. *Oncogene* **2016**, *35*, 4957–4972. [CrossRef]
6. Vynnytska-Myronovska, B.; Bobak, Y.; Garbe, Y.; Dittfeld, C.; Stasyk, O.; Kunz-Schughart, L.A. Single amino acid arginine starvation efficiently sensitizes cancer cells to canavanine treatment and irradiation. *Int. J. Cancer* **2012**, *130*, 2164–2175. [CrossRef]
7. Karatsai, O.; Stasyk, O.; Redowicz, M.J. Effects of Arginine and Its Deprivation on Human Glioblastoma Physiology and Signaling. *Adv. Exp. Med. Biol.* **2020**, *1202*, 243–258. [CrossRef]
8. Szeffel, J.; Danielak, A.; Kruszewski, W.J. Metabolic pathways of L-arginine and therapeutic consequences in tumors. *Adv. Med. Sci.* **2019**, *64*, 104–110. [CrossRef]
9. Mören, L.; Perryman, R.; Crook, T.; Langer, J.K.; Oneill, K.; Syed, N.; Antti, H. Metabolomic profiling identifies distinct phenotypes for ASS1 positive and negative GBM. *BMC Cancer* **2018**, *18*, 167. [CrossRef]
10. Feun, L.; You, M.; Wu, C.J.; Kuo, M.T.; Wangpaichitr, M.; Spector, S.; Savaraj, N. Arginine Deprivation as a Targeted Therapy for Cancer. *Curr. Pharm. Des.* **2008**, *14*, 1049–1057. [CrossRef]
11. Syed, N.; Langer, J.; Janczar, K.; Singh, P.; Nigro, C.L.; Lattanzio, L.; Coley, H.M.; Hatzimichael, E.; Bomalaski, J.; Szlosarek, P.; et al. Epigenetic status of argininosuccinate synthetase and argininosuccinate lyase modulates autophagy and cell death in glioblastoma. *Cell Death Dis.* **2013**, *4*, e458. [CrossRef] [PubMed]
12. Cheng, C.-T.; Qi, Y.; Wang, Y.-C.; Chi, K.K.; Chung, Y.; Ouyang, C.; Chen, Y.-R.; Oh, M.E.; Sheng, X.; Tang, Y.; et al. Arginine starvation kills tumor cells through aspartate exhaustion and mitochondrial dysfunction. *Commun. Biol.* **2018**, *1*. [CrossRef] [PubMed]
13. Vynnytska, B.; Mayevska, O.; Kurlishchuk, Y.; Bobak, Y.; Stasyk, O. Canavanine augments proapoptotic effects of arginine deprivation in cultured human cancer cells. *Anti-Cancer Drugs* **2011**, *22*, 148–157. [CrossRef]
14. Phillips, M.M.; Sheaff, M.T.; Szlosarek, P.W. Targeting arginine-dependent cancers with arginine-degrading enzymes: Opportunities and challenges. *Cancer Res. Treat.* **2013**, *45*, 251–262. [CrossRef]
15. Stasyk, O.V.; Boretsky, Y.R.; Gonchar, M.V.; Sibirny, A.A. Recombinant arginine-degrading enzymes in metabolic anticancer therapy and bioanalytics. *Cell Biol. Int.* **2015**, *39*, 246–252. [CrossRef] [PubMed]
16. Glazer, E.S.; Piccirillo, M.; Albino, V.; Di Giacomo, R.; Palaia, R.; Mastro, A.A.; Beneduce, G.; Castello, G.; De Rosa, V.; Petrillo, A.; et al. Phase II Study of Pegylated Arginine Deiminase for Nonresectable and Metastatic Hepatocellular Carcinoma. *J. Clin. Oncol.* **2010**, *28*, 2220–2226. [CrossRef]
17. Ott, P.A.; Carvajal, R.D.; Pandit-Taskar, N.; Jungbluth, A.A.; Hoffman, E.W.; Wu, B.-W.; Bomalaski, J.S.; Venhaus, R.; Pan, L.; Old, L.J.; et al. Phase I/II study of pegylated arginine deiminase (ADI-PEG 20) in patients with advanced melanoma. *Investig. New Drugs* **2013**, *31*, 425–434. [CrossRef]
18. Szlosarek, P.W.; Steele, J.P.; Nolan, L.; Gilligan, D.; Taylor, P.; Spicer, J.; Lind, M.; Mitra, S.; Shamash, J.; Phillips, M.M.; et al. Arginine Deprivation With Pegylated Arginine Deiminase in Patients With Argininosuccinate Synthetase 1–Deficient Malignant Pleural Mesothelioma: A Randomized Clinical Trial. *JAMA Oncol.* **2017**, *3*, 58–66. [CrossRef]

19. Beddowes, E.; Spicer, J.; Chan, P.Y.; Khadeir, R.; Corbacho, J.G.; Repana, D.; Steele, J.P.; Schmid, P.; Szyszko, T.; Cook, G.; et al. Phase 1 Dose-Escalation Study of Pegylated Arginine Deiminase, Cisplatin, and Pemetrexed in Patients With Argininosuccinate Synthetase 1-Deficient Thoracic Cancers. *J. Clin. Oncol.* **2017**, *35*, 1778–1785. [CrossRef]
20. Lowery, M.A.; Yu, K.H.; Kelsen, D.P.; Harding, J.J.; Bomalaski, J.S.; Glassman, D.C.; Covington, C.M.; Brenner, R.; Hollywood, E.; Barba, A.; et al. A phase 1/B trial of ADI-PEG 20 plus nab-paclitaxel and gemcitabine in patients with advanced pancreatic adenocarcinoma. *Cancer* **2017**, *123*, 4556–4565. [CrossRef]
21. Harding, J.J.; Do, R.K.; Dika, I.E.; Hollywood, E.; Uhlitskykh, K.; Valentino, E.; Wan, P.; Hamilton, C.; Feng, X.; Johnston, A.; et al. A phase 1 study of ADI-PEG 20 and modified FOLFOX6 in patients with advanced hepatocellular carcinoma and other gastrointestinal malignancies. *Cancer Chemother. Pharmacol.* **2018**, *82*, 429–440. [CrossRef] [PubMed]
22. Abou-Alfa, G.K.; Qin, S.; Ryoo, B.-Y.; Lu, S.-N.; Yen, C.-J.; Feng, Y.-H.; Lim, H.Y.; Izzo, F.; Colombo, M.; Sarker, D.; et al. Phase III randomized study of second line ADI-PEG 20 plus best supportive care versus placebo plus best supportive care in patients with advanced hepatocellular carcinoma. *Ann. Oncol.* **2018**, *29*, 1402–1408. [CrossRef] [PubMed]
23. Houry, O.; Ghazale, N.; Stone, E.; El-Sibai, M.; Frankel, A.E.; Abi-Habib, R.J. Human recombinant arginase I (Co)-PEG5000 [HuArgI (Co)-PEG5000]-induced arginine depletion is selectively cytotoxic to human glioblastoma cells. *J. Neurooncol.* **2015**, *122*, 75–85. [CrossRef] [PubMed]
24. Fiedler, T.; Strauss, M.; Hering, S.; Redanz, U.; William, D.; Rosche, Y.; Classen, C.F.; Kreikemeyer, B.; Linnebacher, M.; Maletzki, C. Arginine deprivation by arginine deiminase of *Streptococcus pyogenes* controls primary glioblastoma growth in vitro and in vivo. *Cancer Biol. Ther.* **2015**, *16*, 1047–1055. [CrossRef]
25. Pavlyk, I.; Rzhpetskyy, Y.; Jagielski, A.K.; Drozak, J.; Wasik, A.; Pereverzieva, G.; Olchowik, M.; Kunz-Schugart, L.A.; Stasyk, O.; Redowicz, M.J. Arginine deprivation affects glioblastoma cell adhesion, invasiveness and actin cytoskeleton organization by impairment of  $\beta$ -actin arginylation. *Amino Acids* **2015**, *47*, 199–212. [CrossRef]
26. Rosenthal, G.A. L-Canavanine: A higher plant insecticidal allelochemical. *Amino Acids* **2001**, *21*, 319–330. [CrossRef]
27. D’Mello, J.P.F. (Ed.) *Amino Acids in Human Nutrition and Health*; CAB International: Wallingford, UK, 2012. [CrossRef]
28. Zawadzka, M.; Kaminska, B. Immunosuppressant FK506 affects multiple signaling pathways and modulates gene expression in astrocytes. *Mol. Cell. Neurosci.* **2003**, *22*, 202–209. [CrossRef]
29. Ong, S.-E.; Mann, M. A practical recipe for stable isotope labeling by amino acids in cell culture (SILAC). *Nat. Protoc.* **2006**, *1*, 2650–2660. [CrossRef]
30. Kelly, R.T.; Page, J.S.; Luo, Q.; Moore, R.J.; Orton, D.J.; Tang, K.; Smith, R.D. Chemically etched open tubular and monolithic emitters for nanoelectrospray ionization mass spectrometry. *Anal. Chem.* **2006**, *78*, 7796–7801. [CrossRef]
31. Wickham, H.; François, R.; Henry, L.; Müller, K.; RStudio. Dplyr: A Grammar of Data Manipulation. 2020. Available online: <https://cran.r-project.org/web/packages/dplyr/index.html> (accessed on 3 July 2020).
32. Silva, J.C.; Gorenstein, M.V.; Li, G.-Z.; Vissers, J.P.C.; Geromanos, S.J. Absolute quantification of proteins by LCMSE: A virtue of parallel MS acquisition. *Mol. Cell. Proteom.* **2006**, *5*, 144–156. [CrossRef]
33. Yu, G.; Wang, L.-G.; Han, Y.; He, Q.-Y. ClusterProfiler: An R package for comparing biological themes among gene clusters. *OMICS* **2012**, *16*, 284–287. [CrossRef] [PubMed]
34. Perez-Riverol, Y.; Csordas, A.; Bai, J.; Bernal-Llinares, M.; Hewapathirana, S.; Kundu, D.J.; Inuganti, A.; Griss, J.; Mayer, G.; Eisenacher, M.; et al. The PRIDE database and related tools and resources in 2019: Improving support for quantification data. *Nucleic Acids Res.* **2019**, *47*, D442–D450. [CrossRef] [PubMed]
35. Merrill, A.E.; Hebert, A.S.; MacGilvray, M.E.; Rose, C.M.; Bailey, D.J.; Bradley, J.C.; Wood, W.W.; El Masri, M.; Westphall, M.S.; Gasch, A.P.; et al. NeuCode labels for relative protein quantification. *Mol. Cell Proteom.* **2014**, *13*, 2503–2512. [CrossRef]
36. CIAAW Commission on Isotopic Abundances and Atomic Weights. Available online: <https://ciaaw.org/atomic-masses.htm> (accessed on 3 July 2020).
37. Li, H.; Lei, B.; Xiang, W.; Wang, H.; Feng, W.; Liu, Y.; Qi, S. Differences in Protein Expression between the U251 and U87 Cell Lines. *Turk. Neurosurg.* **2017**, *27*, 894–903. [CrossRef] [PubMed]

38. Lee, S.H.; Dominguez, R. Regulation of actin cytoskeleton dynamics in cells. *Mol. Cells* **2010**, *29*, 311–325. [CrossRef]
39. Yasar, D.; Waterman-Storer, C.M.; Schmid, S.L. A dynamic actin cytoskeleton functions at multiple stages of clathrin-mediated endocytosis. *Mol. Biol. Cell* **2005**, *16*, 964–975. [CrossRef]
40. Capell, B.C.; Collins, F.S. Human laminopathies: Nuclei gone genetically awry. *Nat. Rev. Genet.* **2006**, *7*, 940–952. [CrossRef]
41. Ho, C.Y.; Lammerding, J. Lamins at a glance. *J. Cell Sci.* **2012**, *125*, 2087–2093. [CrossRef]
42. Dechat, T.; Adam, S.A.; Taimen, P.; Shimi, T.; Goldman, R.D. Nuclear Lamins. *Cold Spring Harb. Perspect. Biol.* **2010**, *2*. [CrossRef]
43. Burke, B. Lamins and Apoptosis: A Two-Way Street? *J. Cell Biol.* **2001**, *153*, F5–F7. [CrossRef]
44. Bravo-Cordero, J.J.; Hodgson, L.; Condeelis, J. Directed Cell Invasion and Migration During Metastasis. *Curr. Opin. Cell Biol.* **2012**, *24*, 277–283. [CrossRef] [PubMed]
45. Mayevska, O.; Chen, O.; Karatsai, O.; Bobak, Y.; Barska, M.; Lyniv, L.; Pavlyk, I.; Rzhpetsky, Y.; Igmentseva, N.; Redowicz, M.J.; et al. Nitric oxide donor augments antineoplastic effects of arginine deprivation in human melanoma cells. *Exp. Cell Res.* **2017**, *355*, 162–171. [CrossRef]
46. Pijuan, J.; Barceló, C.; Moreno, D.F.; Maiques, O.; Sisó, P.; Martí, R.M.; Macià, A.; Panosa, A. In vitro Cell Migration, Invasion, and Adhesion Assays: From Cell Imaging to Data Analysis. *Front. Cell Dev. Biol.* **2019**, *7*. [CrossRef] [PubMed]
47. Lodish, H.; Berk, A.; Zipursky, S.L.; Matsudaira, P.; Baltimore, D.; Darnell, J. Cell-Matrix Adhesion. In *Molecular Cell Biology*, 4th ed.; W.H. Freeman: New York, NY, USA, 2000. Available online: <https://www.ncbi.nlm.nih.gov/books/NBK21539/> (accessed on 23 October 2019).
48. Matsunaga, T.; Iyoda, T.; Fukai, F. Chapter 12—Adhesion-dependent cell Regulation via Adhesion molecule, integrin: Therapeutic application of integrin activation-modulating factors. In *Colloid and Interface Science in Pharmaceutical Research and Development*; Ohshima, H., Makino, K., Eds.; Elsevier: Amsterdam, The Netherlands, 2014; pp. 243–260. [CrossRef]
49. Goodman, S.R. (Ed.) Chapter 6—Cell Adhesion and the Extracellular Matrix. In *Medical Cell Biology*, 3rd ed.; Academic Press: Cambridge, MA, USA, 2008; pp. 191–225. [CrossRef]
50. Chin, Y.R.; Toker, A. Function of Akt/PKB signaling to cell motility, invasion and the tumor stroma in cancer. *Cell. Signal.* **2009**, *21*, 470–476. [CrossRef] [PubMed]
51. Boccafoschi, F.; Bosetti, M.; Sandra, P.M.; Leigh, M.; Cannas, M. Effects of mechanical stress on cell adhesion: A possible mechanism for morphological changes. *Cell Adhes. Migr.* **2010**, *4*, 19–25. [CrossRef]
52. Fayard, E.; Tintignac, L.A.; Baudry, A.; Hemmings, B.A. Protein kinase B/Akt at a glance. *J. Cell Sci.* **2005**, *118*, 5675–5678. [CrossRef]
53. Hart, J.R.; Vogt, P.K. Phosphorylation of AKT: A Mutational Analysis. *Oncotarget* **2011**, *2*, 467–476. [CrossRef]
54. Kelstrup, C.D.; Jersie-Christensen, R.R.; Batth, T.S.; Arrey, T.N.; Kuehn, A.; Kellmann, M.; Olsen, J.V. Rapid and deep proteomes by faster sequencing on a benchtop quadrupole ultra-high-field Orbitrap mass spectrometer. *J. Proteome Res.* **2014**, *13*, 6187–6195. [CrossRef]
55. Chou, M.F.; Schwartz, D. Using the scan-x Web site to predict protein post-translational modifications. *Curr. Protoc. Bioinform.* **2011**. [CrossRef]
56. Bobak, Y.; Kurlishchuk, Y.; Vynnytska-Myronovska, B.; Grydzuk, O.; Shuvayeva, G.; Redowicz, M.J.; Kunz-Schughart, L.A.; Stasyk, O. Arginine deprivation induces endoplasmic reticulum stress in human solid cancer cells. *Int. J. Biochem. Cell Biol.* **2016**, *70*, 29–38. [CrossRef]
57. Wang, M.; Wey, S.; Zhang, Y.; Ye, R.; Lee, A.S. Role of the unfolded protein response regulator GRP78/BiP in development, cancer, and neurological disorders. *Antioxid. Redox Signal.* **2009**, *11*, 2307–2316. [CrossRef] [PubMed]
58. Bernales, S.; Soto, M.M.; McCullagh, E. Unfolded protein stress in the endoplasmic reticulum and mitochondria: A role in neurodegeneration. *Front. Aging Neurosci.* **2012**, *4*, 5. [CrossRef] [PubMed]
59. Van Vliet, A.; Sassano, M.; Agostinis, P. The Unfolded Protein Response and Membrane Contact Sites: Tethering as a Matter of Life and Death? *Contact* **2018**, *1*. [CrossRef]
60. Nguyen, L.; Lucke-Wold, B.P.; Mookerjee, S.A.; Cavendish, J.Z.; Robson, M.J.; Scandinaro, A.L.; Matsumoto, R.R. Role of sigma-1 receptors in neurodegenerative diseases. *J. Pharmacol. Sci.* **2015**, *127*, 17–29. [CrossRef]

61. Tissue Expression of ATF4—Summary—The Human Protein Atlas. Available online: <https://v18.proteinatlas.org/ENSG00000128272-ATF4/tissue> (accessed on 15 January 2020).
62. Tilokani, L.; Nagashima, S.; Paupe, V.; Prudent, J. Mitochondrial dynamics: Overview of molecular mechanisms. *Essays Biochem.* **2018**, *62*, 341–360. [CrossRef]
63. Kühlbrandt, W. Structure and function of mitochondrial membrane protein complexes. *BMC Biol.* **2015**, *13*, 89. [CrossRef]
64. Honrath, B.; Culmsee, C.; Dolga, A.M. One protein, different cell fate: The differential outcome of depleting GRP75 during oxidative stress in neurons. *Cell Death Dis.* **2018**, *9*, 32. [CrossRef]
65. Liu, Y.; Zhu, X. Endoplasmic reticulum-mitochondria tethering in neurodegenerative diseases. *Transl. Neurodegener.* **2017**, *6*, 21. [CrossRef]
66. Obacz, J.; Avril, T.; Le Reste, P.-J.; Urra, H.; Quillien, V.; Hetz, C.; Chevet, E. Endoplasmic reticulum proteostasis in glioblastoma—From molecular mechanisms to therapeutic perspectives. *Sci. Signal.* **2017**, *10*. [CrossRef]
67. Glioblastoma Multiforme—Symptoms, Diagnosis and Treatment Options. Available online: <https://www.aans.org/en/Patients/Neurosurgical-Conditions-and-Treatments/Glioblastoma-Multiforme> (accessed on 2 January 2020).
68. Thongkum, A.; Wu, C.; Li, Y.-Y.; Wangpaichitr, M.; Navasumrit, P.; Parnlob, V.; Sricharunrat, T.; Bhudhisawasdi, V.; Ruchirawat, M.; Savaraj, N. The Combination of Arginine Deprivation and 5-Fluorouracil Improves Therapeutic Efficacy in Argininosuccinate Synthetase Negative Hepatocellular Carcinoma. *Int. J. Mol. Sci.* **2017**, *18*, 1175. [CrossRef]
69. Vynnytska-Myronovska, B.; Kurlishchuk, Y.; Bobak, Y.; Dittfeld, C.; Kunz-Schughart, L.A.; Stasyk, O. Three-dimensional environment renders cancer cells profoundly less susceptible to a single amino acid starvation. *Amino Acids.* **2013**, *45*, 1221–1230. [CrossRef] [PubMed]
70. Al-Koussa, H.; Al-Haddad, M.; Abi-Habib, R.; El-Sibai, M. Human Recombinant Arginase I [HuArgI (Co)-PEG5000]-Induced Arginine Depletion Inhibits Colorectal Cancer Cell Migration and Invasion. *Int. J. Mol. Sci.* **2019**, *20*, 6018. [CrossRef] [PubMed]
71. Zhao, X.; Guan, J.-L. Focal adhesion kinase and its signaling pathways in cell migration and angiogenesis. *Adv. Drug Deliv. Rev.* **2011**, *63*, 610–615. [CrossRef] [PubMed]
72. Méjat, A.; Misteli, T. LINC complexes in health and disease. *Nucleus* **2010**, *1*, 40–52. [CrossRef]
73. Shimi, T.; Kittisopikul, M.; Tran, J.; Goldman, A.E.; Adam, S.A.; Zheng, Y.; Jaqaman, K.; Goldman, R.D. Structural organization of nuclear lamins A, C, B1, and B2 revealed by superresolution microscopy. *Mol. Biol. Cell.* **2015**, *26*, 4075–4086. [CrossRef]
74. Lammerding, J.; Fong, L.G.; Ji, J.Y.; Reue, K.; Stewart, C.L.; Young, S.G.; Lee, R.T. Lamins A and C but Not Lamin B1 Regulate Nuclear Mechanics. *J. Biol. Chem.* **2006**, *281*, 25768–25780. [CrossRef]
75. He, B.; Lu, N.; Zhou, Z. Cellular and Nuclear Degradation during Apoptosis. *Curr. Opin. Cell Biol.* **2009**, *21*, 900–912. [CrossRef]
76. Neamati, N.; Fernandez, A.; Wright, S.; Kiefer, J.; McConkey, D.J. Degradation of lamin B1 precedes oligonucleosomal DNA fragmentation in apoptotic thymocytes and isolated thymocyte nuclei. *J. Immunol.* **1995**, *154*, 3788–3795.
77. Vovk, O.; Chen, O.; Igumentseva, N.; Senchuk, O.; Barska, M.; Sybirna, N.; Stasyk, O. Effects of the combined arginase and canavanine treatment on leukemic cells in vitro and in vivo. *Ukr. Biochem. J.* **2016**, *88*, 45–55. [CrossRef]
78. Tang, X.; Keenan, M.M.; Wu, J.; Lin, C.-A.; Dubois, L.; Thompson, J.W.; Freedland, S.J.; Murphy, S.K.; Chi, J.-T. Comprehensive Profiling of Amino Acid Response Uncovers Unique Methionine-Deprived Response Dependent on Intact Creatine Biosynthesis. *PLoS Genet.* **2015**, *11*. [CrossRef]
79. Caso, G.; Mcnurlan, M.A.; Mcmillan, N.D.; Eremin, O.; Garlick, P.J. Tumour cell growth in culture: Dependence on arginine. *Clin. Sci.* **2004**, *107*, 371–379. [CrossRef] [PubMed]
80. Zhang, S.X.; Ma, J.H.; Bhatta, M.; Fliesler, S.J.; Wang, J.J. The Unfolded Protein Response in Retinal Vascular Diseases: Implications and Therapeutic Potential Beyond Protein Folding. *Prog. Retin. Eye Res.* **2015**, 111–131. [CrossRef] [PubMed]
81. Barnes, P.J. Corticosteroid effects on cell signalling. *Eur. Respir. J.* **2006**, *27*, 413–426. [CrossRef] [PubMed]



82. Zhu, Y.; Chen, G.; Chen, L.; Zhang, W.; Feng, D.; Liu, L.; Chen, Q. Chapter Three—Monitoring Mitophagy in Mammalian Cells. In *Methods in Enzymology*; Murphy, A.N., Chan, D.C., Eds.; Mitochondrial Function; Academic Press: Cambridge, MA, USA, 2014; Volume 547, pp. 39–55. [CrossRef]
83. Mijaljica, D.; Prescott, M.; Devenish, R.J. Mitophagy: An overview. In *Autophagy—Cancer, Other Pathologies, Inflammation, Immunity, Infection and Aging*; Academic Press: Cambridge, MA, USA, 2014; Volume 4, pp. 103–116. [CrossRef]
84. Zou, S.; Wang, X.; Liu, P.; Ke, C.; Xu, S. Arginine metabolism and deprivation in cancer therapy. *Biomed. Pharmacother.* **2019**, *118*, 109210. [CrossRef] [PubMed]



© 2020 by the authors. Licensee MDPI, Basel, Switzerland. This article is an open access article distributed under the terms and conditions of the Creative Commons Attribution (CC BY) license (<http://creativecommons.org/licenses/by/4.0/>).

Article

# Estradiol Induces Epithelial to Mesenchymal Transition of Human Glioblastoma Cells

Ana M. Hernández-Vega <sup>1</sup>, Aylin Del Moral-Morales <sup>1</sup>, Carmen J. Zamora-Sánchez <sup>1</sup>,  
Ana G. Piña-Medina <sup>2</sup>, Aliesha González-Arenas <sup>3</sup> and Ignacio Camacho-Arroyo <sup>1,\*</sup>

<sup>1</sup> Unidad de Investigación en Reproducción Humana, Instituto Nacional de Perinatología-Facultad de Química, Universidad Nacional Autónoma de México, México City CP 11000, Mexico; anahdzvg@gmail.com (A.M.H.-V.); aybindmm@gmail.com (A.D.M.-M.); carmenjaninzamora@comunidad.unam.mx (C.J.Z.-S.)

<sup>2</sup> Departamento de Biología, Facultad de Química, Universidad Nacional Autónoma de México, México City CP 04510, Mexico; a.gabriela.pime@gmail.com

<sup>3</sup> Departamento de Medicina Genómica y Toxicología Ambiental, Instituto de Investigaciones Biomédicas, Universidad Nacional Autónoma de México, México City CP 04510, Mexico; alieshag@iibiomedicas.unam.mx

\* Correspondence: camachoarroyo@gmail.com; Tel.: +52-55-5622-3732

Received: 4 July 2020; Accepted: 11 August 2020; Published: 21 August 2020



**Abstract:** The mesenchymal phenotype of glioblastoma multiforme (GBM), the most frequent and malignant brain tumor, is associated with the worst prognosis. The epithelial–mesenchymal transition (EMT) is a cell plasticity mechanism involved in GBM malignancy. In this study, we determined 17 $\beta$ -estradiol (E2)-induced EMT by changes in cell morphology, expression of EMT markers, and cell migration and invasion assays in human GBM-derived cell lines. E2 (10 nM) modified the shape and size of GBM cells due to a reorganization of actin filaments. We evaluated EMT markers expression by RT-qPCR, Western blot, and immunofluorescence. We found that E2 upregulated the expression of the mesenchymal markers, vimentin, and N-cadherin. Scratch and transwell assays showed that E2 increased migration and invasion of GBM cells. The estrogen receptor- $\alpha$  (ER- $\alpha$ )-selective agonist 4,4',4''-(4-propyl-[1H]-pyrazole-1,3,5-triyl)trisphenol (PPT, 10 nM) affected similarly to E2 in terms of the expression of EMT markers and cell migration, and the treatment with the ER- $\alpha$  antagonist methyl-piperidino-pyrazole (MPP, 1  $\mu$ M) blocked E2 and PPT effects. ER- $\beta$ -selective agonist diarylpropionitrile (DNP, 10 nM) and antagonist 4-[2-phenyl-5,7-bis(trifluoromethyl)pyrazole[1,5-a]pyrimidin-3-yl]phenol (PHTPP, 1  $\mu$ M) showed no effects on EMT marker expression. These data suggest that E2 induces EMT activation through ER- $\alpha$  in human GBM-derived cells.

**Keywords:** epithelial–mesenchymal transition (EMT); glioblastoma multiforme (GBM); 17 $\beta$ -estradiol (E2); estrogen receptors (ERs)

## 1. Introduction

Malignant tumors of the central nervous system (CNS) are among the cancers with the worst prognosis. Glioblastoma multiforme (GBM) comprises approximately half of the malignant primary brain tumors and causes 3–4% of cancer-related deaths [1]. The World Health Organization defines GBM as a grade IV astrocytoma tumor characterized by uncontrolled proliferation, necrosis propensity, angiogenesis, deep infiltration, apoptosis resistance, genomic instability, and extensive heterogeneity at the cellular and molecular levels [2,3]. The Cancer Genome Atlas (TCGA) network identified four molecular subtypes of GBM on the basis of the gene expression profile of neural progenitor cells (proneural, PN), neurons (neural, N), proliferative cells with activation of the tyrosine kinase receptor

(classical, CL), and mesenchymal tissue (mesenchymal, MES) [4]. The mesenchymal phenotype of GBM tends to have the worst survival rates compared to the other subtypes, and it is associated with a highly invasive behavior [5–7].

Epithelial-to-mesenchymal transition (EMT) is a mechanism of cellular plasticity that regulates a set of transient states between the epithelial and mesenchymal phenotype. During EMT, epithelial cells lose their junctions with other cells and the apicobasal polarity while they acquire a mesenchymal phenotype with migratory and invasive properties [8]. EMT is a highly dynamic and transient mechanism induced by diverse signals and orchestrated by EMT-inducing transcription factors (EMT-TFs), which act in close association with the epigenetic machinery by repressing epithelial genes and activating mesenchymal genes [9]. The reverse process is the mesenchymal–epithelial transition (MET) [10]. EMT is essential in diverse physiological and pathological processes [11]. This mechanism is associated with embryogenesis [12–14], heart regeneration [15], wound healing, fibrosis, and organ repair [16]. In tumor cells, the activation of EMT-TFs promotes the mechanisms of migration, invasion, metastasis, apoptosis inhibition, resistance to radio- and chemotherapy, as well as maintenance of the plasticity of cancer stem cells [17].

Although EMT is typical in epithelial tumors, evidence suggests that EMT-TFs also lead to a gain in mesenchymal properties and the promotion of malignancy of non-epithelial tumors, including brain tumors, hematopoietic malignancies, and sarcomas [18,19]. Currently, the classic description of EMT as a process of change between two alternative states (epithelial and mesenchymal) has been replaced by a new concept of cellular plasticity and transient states, which proposes that cells move through a spectrum of various intermediate phases, which means that cells can carry out partial EMT programs [20]. Several studies have shown the role of EMT in GBM progression. Large-scale expression analysis of 85 highly diffuse glioma tumors revealed a set of genes associated with mesenchymal tissue overexpressed in GBM biopsies [21]. Tso et al. showed that a subset of primary GBM tumors expresses cellular and molecular markers associated with mesenchymal stem cells [22]. Then, the definition of the GBM mesenchymal subtype convincingly showed the clinical importance of the EMT program in tumor diagnosis and treatment [4,5]. Molecular profile analysis of the four GBM subtypes demonstrated that the mesenchymal subtype, unlike the other subtypes, presents the molecular characteristics of EMT [23].

Determination of the complete molecular network of the EMT program, as well as the fundamental mechanisms necessary to activate it, could provide new therapeutic approaches for GBM treatment. Autocrine and paracrine interactions within the GBM microenvironment induce EMT through intracellular signaling pathways that activate EMT-TFs. Although different studies have described several signaling pathways that induce EMT in GBM, the role of the different factors within the tumor microenvironment, as well as all the interactions that coordinate this cellular program, is still not understood.

Sex steroid hormones such as estrogens participate in a wide variety of functions throughout the nervous system. These hormones are mainly synthesized in the gonads and the adrenal glands, but they can also be produced *de novo* within the brain [24,25]. Estrogens include estrone (E1), 17 $\beta$ -estradiol (E2), and estriol (E3). E2 is involved in many brain functions, such as brain development during sexual differentiation [26], differentiation of neurons and glial cells [27,28], and regulation of neurite growth and synaptic patterns [29,30], and it interacts with the glutamatergic, dopaminergic, and serotonergic neurotransmission pathways that influence the generation of memory, learning, and emotional state [31–33]. Estrogens act by binding specific intracellular and membrane receptors. There are two estrogen-specific intracellular receptor subtypes, estrogen receptors  $\alpha$  and  $\beta$  (ER $\alpha$  and ER $\beta$ ), which are ligand-activated transcription factors that directly regulate gene expression. Moreover, these receptors are associated with the plasma membrane, where they activate intracellular signaling pathways [34].

E2 concentrations, as well as ERs expression and activity, are determinant in the malignant progression of tumors growing in estrogen-sensitive tissues [35–38]. On the basis of these studies,

ER- $\alpha$  promotes cell proliferation, whereas ER- $\beta$  has anti-proliferative effects [39]. ER expression status in GBM is controversial. Some studies have reported the absence of ER in GBM [40,41], while other researchers have determined that ER expression varies according to malignancy degree, suggesting that these receptors are involved in GBM malignant progression [42–50]. ER subtypes have shown different effects in GBMs. E2 and 4,4',4''-(4-propyl-[1H]-pyrazole-1,3,5-triyl)trisphenol (PPT), a selective agonist of ER- $\alpha$ , increased the number of cells derived from human GBM [45], while ER- $\beta$ -specific agonists decreased GBM cell proliferation [44]. However, the molecular mechanisms of E2 related to GBM malignant progression are still unclear.

E2-promoted signaling is known to be related to EMT induction in estrogen-responsive tissues. In ovarian and prostate cancer, E2 treatment induces ER- $\alpha$ -dependent EMT, while receptor silencing inhibits EMT [51–53]. Nevertheless, loss of ER- $\alpha$  expression in breast and endometrial cancer promotes morphological changes, motility, and improved invasion, as well as increased expression of EMT markers [54–58]. These investigations demonstrate the importance of specific cell context in the E2-induced EMT. However, E2 involvement in the EMT program in GBM is unknown.

To increase the knowledge regarding the EMT program of GBM, in this study, we investigated the participation of E2 on EMT induction in human GBM-derived cells expressing both ER subtypes. Our results showed that the treatment with E2 (10 nM) promoted: (1) changes in cell morphology and the structure of the actin cytoskeleton, (2) increased expression of mesenchymal markers such as vimentin and N-cadherin, and (3) increased migratory and invasive capacity of GBM cells. These effects were dependent on ER- $\alpha$ , since the treatment with its agonist, PPT (10 nM), produced similar results to E2, while the treatment with its antagonist methyl-piperidino-pyrazole (MPP, 1  $\mu$ M), blocked the effects of E2 and PPT.

## 2. Materials and Methods

### 2.1. TCGA Data Analysis

Ribonucleic acid sequencing (RNA-Seq) counts were obtained from low-grade gliomas (LGG,  $n = 167$ ) and glioblastoma (GBM,  $n = 155$ ) projects of The Cancer Genome Atlas (TCGA) repository (<https://portal.gdc.cancer.gov/>). The data were downloaded and processed using TCGAbiolinks package version 2.12.6 for R [59]. Additionally, expression profiles were obtained from healthy brain cortex samples ( $n = 249$ ) in the GTEx database (<https://gtexportal.org/home/>). Data were normalized by DESeq2 version 1.22.2 [60] and plotted. TCGA\_analyse\_survival utility from the TCGAbiolinks package for R performed survival analysis.

### 2.2. Cell Cultures

Human GBM-derived cell lines U87, U251, T98, and LN229 (American Type Culture Collection, ATCC, Manassas, VA, USA) were cultivated in Dulbecco's modified Eagle's medium (DMEM, L0107-500) high glucose supplemented with 10% fetal bovine serum (FBS; S1650), 1.0 mM pyruvate (L0642-100), 1.0 mM antibiotic (streptomycin 10 g/L; penicillin G 6.028 g/L; and amphotericin B 0.025 g/L, L0010), and 0.1 mM non-essential amino acids (X0557-100, Biowest, Nuaille, PDL, France). Cell cultures were maintained at 37 °C in a humidified atmosphere with 5% CO<sub>2</sub>. At 60% confluence (24 h before treatments), cells were culture in DMEM no phenol red (ME-019 Thermo Fisher Scientific, Waltham, MA, USA) supplemented with 10% charcoal/dextran-treated FBS (SH30068.03, Thermo Fisher Scientific), 1.0 mM pyruvate, 1.0 mM antibiotics, and 0.1 mM non-essential amino acids. When indicated, cells were treated with E2 (10 nM, E4389, Sigma-Aldrich, St. Louis, MO, USA), ER- $\alpha$ -selective agonist PPT (10 nM, 1426, Tocris, Bristol, UK, England), ER- $\beta$ -selective agonist diarylpropionitrile (DNP, 10 nM, 1494, Tocris), ER- $\alpha$ -selective antagonist MPP (1  $\mu$ M, 1991, Tocris), and ER- $\beta$ -selective antagonist 4-[2-phenyl-5,7-bis(trifluoromethyl)pyrazole[1,5-a]pyrimidin-3-yl]phenol (PHTPP, 1  $\mu$ M, 2662, Tocris). In combined treatments, antagonists MPP and PHTPP were added 2 h before the addition of agonist.

### 2.3. Cell Morphology Analysis

The epithelial phenotype is characterized by a polygonal shape, while the mesenchymal phenotype is spindle-shaped. Therefore, the geometric characteristics of both phenotypes differ from each other. Geometric characteristics can be quantified using high-performance software for the analysis of cell images [61–64]. The morphological changes of the U251, U87, T98G, and LN229 cells treated with vehicle and E2 at 0, 48, and 72 h were determined by phase contrast microscopy (IX71, inverted microscope Olympus, Shinjuku, TY, Japan), digitally capturing six arbitrary fields with a 400X magnification for each of the treatments. Adobe Photoshop CS6 software (Adobe Systems Inc., San Jose, CA, USA) was used to process the background correction and illumination of the captured images. Subsequently, the orientation, shape, and position of each of the cells in each image was determined to segment them with the Image-Pro software 10.0.6 (Media Cybernetics Inc., Rockville, MD, USA), which has automated algorithms to identify, separate, and quantify each of the cells that appear in the image. This quantification allows the extraction of various geometric characteristics that determine morphological parameters of the cells segmented in the two-dimensional plane.

### 2.4. RT-qPCR

Total RNA was extracted from cells by guanidine–thiocyanate–phenol–chloroform method with TRIzol LS Reagent (10296028, Thermo Fisher Scientific, Waltham, MA, USA), following the supplier’s protocol, and was measured by spectrophotometry (Nanodrop 2000 spectrophotometer, Thermo Fisher Scientific). RNA integrity was checked by electrophoresis with 1.5% agarose gel in Tris-Borate-ethylenediaminetetraacetic acid (EDTA) buffer (TBE: 89 mM Tris, 89 mM boric acid, 2.0 mM EDTA (pH 8.3)) detected by fluorescence with GreenSafe (MB13201, NZYTech, Lisboa, PT, Portugal). Human astrocyte RNA was purchased from ScienCell Research Laboratories (1805, Carlsbad, CA, USA). Moloney Murine Leukemia Virus Reverse Transcriptase (M-MLV RT, 28025013, Thermo Fisher Scientific) was used to obtain the complementary DNA (cDNA) from one microgram of extracted RNA following the protocol recommended by the provider. Gene expression relative to the 18S ribosomal RNA (rRNA) gene was quantified through the quantitative polymerase chain reaction (qPCR) using standardized primers for each gene: ESR1 (estrogen receptor 1/ $\alpha$ ) (FW-5'-agcaccctgaagtctctgga-3', RV-5'-gatgtgggagaggatgagga-3'); ESR2 (estrogen receptor 2/ $\beta$ ) (FW-5'-aagaagattcccgcttgg-3', RV-5'-tctacgcatttcccctcatc-3'); VIM (vimentin) (FW-5'-ggaccagtaaccaacgaca-3', RV-5'-aaggtcaagacgtgccagag-3'); CDH2 (cadherin-2/N-cadherin) (FW-5'-ctggagacattggggacttc-3', RV-5'-gagcactgccttcatagt-3'); TJP1 (tight junction protein 1/zonula occludens 1 (ZO-1)) (FW-5'-gccattcccgaaggagtga-3', RV-5'-atcacagtgtggaagcg-3'); rRNA18S (FW-5'-agtgaaactgcgaa tggctc-3', RV-5'-ctgaccgggtggtttgat-3'). FastStart DNA Master SYBR Green I kit (12239264001, Roche, Basel, Switzerland) was used to perform gene amplification in a LightCycler 2.0 instrument (03531414001, Roche). Relative expression was quantified by the comparative  $2^{-\Delta\Delta C_t}$  method [65,66].

### 2.5. Western Blot

U251, U87, T98G, and LN229 cells were detached from culture plates using cold phosphate-buffered saline (PBS: 137 mM NaCl, 2.7 mM KCl, 10.0 mM Na<sub>2</sub>HPO<sub>4</sub>, 1.8 mM KH<sub>2</sub>PO<sub>4</sub> (pH 7.4)) and cell scraper. The pellet obtained from the centrifuged cells at 45 × g for 3 min were lysed with radioimmunoprecipitation assay buffer (RIPA: 50 mM Tris-HCl, 150 mM NaCl, 1% Triton X-100, 0.1% sodium dodecyl sulfate (SDS) (pH 8.0)) supplemented with protease inhibitor cocktail (P8340, Sigma-Aldrich, St. Louis, MO, USA). Total proteins were extracted by centrifugation at 20,817 × g at 4 °C for 15 min and quantified by spectrophotometry (NanoDrop 2000 spectrophotometer, Thermo Fisher Scientific, Waltham, MA, USA) using the Pierce 660 nm protein assay reagent (22660, Thermo Fisher Scientific). Thirty µg of total protein was separated on 10% SDS-polyacrylamide gel electrophoresis (PAGE) at 80 V for 4 h and then transferred to a polyvinylidene fluoride (PVDF) membrane (IPVH00010, Merck, Kenilworth, NY, USA) at 20 V in semidry conditions at room temperature for 45 min. Membranes were blocked with 5% bovine serum albumin (BSA, A9418, Sigma-Aldrich) in Tris-buffered saline-Tween

(TBST: 150 mM NaCl, 50 mM Tris-HCl, 0.1% Tween (pH 7.6)) with constant agitation at 37 °C for 2 h, and then incubated with primary antibodies: anti-ER $\alpha$  (2  $\mu$ g/mL, rabbit polyclonal, ab3575, Abcam, Cambridge, UK, England), anti-ER $\beta$  (0.4  $\mu$ g/mL, mouse monoclonal 1531: sc-53494), anti-ZO-1 (0.6  $\mu$ g/mL, rat monoclonal R40.76: sc-33725), anti-N-cadherin (0.8  $\mu$ g/mL, mouse monoclonal D-4: sc-8424), anti-vimentin (0.4  $\mu$ g/mL, mouse monoclonal V9: sc-6260), and  $\alpha$ -tubulin (0.4  $\mu$ g/mL, mouse monoclonal A-6: sc-398103) (Santa Cruz Biotechnology, Dallas, TX, USA), diluted with 5% BSA in TBST at 4 °C for 48 h. Subsequently, the membranes were washed with TBST three times every 5 min and incubated with secondary antibodies conjugated to horseradish peroxidase (HRP): anti-rabbit (0.06  $\mu$ g/mL, goat polyclonal Immunoglobulin G (IgG) containing two heavy chains (H) and two light chains (L) (H+L), 65-6120; Thermo Fisher Scientific), anti-mouse (0.013  $\mu$ g/mL, purified recombinant mouse IgG $\kappa$  light chain: sc-516102; Santa Cruz Biotechnology), and anti-rat (0.06  $\mu$ g/mL, goat polyclonal IgG (H+L), ab97057, Abcam) at room temperature and constant agitation for 45 min, and again washed with TBST three times every 5 min. Finally, Super Signal West Femto Maximum Sensitivity Substrate reagent (34096, Thermo Fisher Scientific) was incubated in the membranes, and immunoreactive bands were detected by chemiluminescence exposing blots to Kodak Biomax Light Film (Z370371, Sigma-Aldrich) captured by a digital camera of 14.1 megapixels (SD1400IS, Canon Inc., Ota, TY, Japan). ImageJ software (1.52u, National Institutes of Health, NIH, Bethesda, MD, USA) performed the densitometric analysis of blot images.

## 2.6. Immunofluorescence

U251 and U87 cells were fixed with 4% paraformaldehyde (4% PFA) at room temperature for 20 min, washed with PBS, and then incubated in permeabilizing blocking solution (1% BSA, 1% glycine, 0.2% Triton X-100, diluted in PBS) at room temperature for 90 min. Subsequently, cells were incubated with primary antibodies: anti-Actin (4  $\mu$ g/mL, goat polyclonal C-11, sc-1615), anti-ZO-1 (8  $\mu$ g/mL, rat monoclonal R40.76: sc-33725), anti-N-cadherin (8  $\mu$ g/mL, mouse monoclonal D-4: sc-8424), and anti-vimentin (4  $\mu$ g/mL, mouse monoclonal V9: sc-6260) (Santa Cruz Biotechnology, Dallas, TX, USA) at 4 °C overnight, and then rinsed three times every 5 min with PBST (PBS with 0.05% Tween). Later, cells were incubated with secondary antibodies: anti-mouse (4  $\mu$ g/mL, goat polyclonal IgG (H+L) Alexa Fluor 488: A11001, Thermo Fisher Scientific, Waltham, MA, USA), anti-rat (4  $\mu$ g/mL, goat polyclonal IgG (H+L) Alexa Fluor 488: ab150157, Abcam, Cambridge, UK, England), and anti-goat (8  $\mu$ g/mL, donkey IgG-FITC: sc-2024, Santa Cruz Biotechnology) at room temperature for 90 min, and again rinsed with PBST three times every 5 min. Nuclei were stained with Hoechst 33,342 (1 mg/mL, 62249, Thermo Fisher Scientific) at room temperature for 7 min and rinsed three times every 5 min with PBST. Finally, cells were coverslipped with mounting medium (18606-20, Polysciences, Warrington, PA, USA) and visualized by fluorescence microscopy (Bx43, light microscope, Olympus, Shinjuku, TY, Japan), digitally capturing six arbitrary fields with a 400 $\times$  magnification. Fluorescence density was measured as integrated density from the *Analyze* menu of ImageJ software.

## 2.7. Migration Assay

Wound healing assays were performed to determine the migratory capacity of cells. U251 and U87 cells grew in DMEM high glucose supplemented until reaching 70% confluence. Then, the medium was changed to DMEM no phenol red supplemented 10% charcoal/dextran-treated FBS, 1.0 mM pyruvate, 1.0 mM antibiotics, and 0.1 mM non-essential amino acids, and incubated at 37 °C in a humidified atmosphere with 5% CO<sub>2</sub>. Upon 90% confluence, a scratch was made using a 200  $\mu$ L pipette tip. Cells floating were rinsed with PBS and DMEM no phenol red-supplemented 10% charcoal/dextran treated-FBS, 1.0 mM pyruvate, 1.0 mM antibiotics, and 0.1 mM non-essential amino acids were added again. One hour before adding the experimental treatments, we incubated the cells with cytosine  $\beta$ -D-arabinofuranoside hydrochloride (10  $\mu$ M, Ara-C, C1768, Sigma-Aldrich, St. Louis, MO, USA), a selective inhibitor of DNA synthesis. Images of the wound area captured at 100 $\times$  magnification with an Infinity 1-2C camera (Lumenera, Ottawa, ON, Canada) connected to an inverted microscope (CKX41,

Olympus, Shinjuku, TY, Japan) at 0, 12, and 24 h of treatment were analyzed using the MRI Wound Healing Tool plugins of Image J software.

### 2.8. Invasion Assay

Transwell assay determined the invasion potential of cells. Transwell inserts with 10  $\mu\text{m}$  membrane thickness and 8  $\mu\text{m}$  pore size (3422, Corning, Corning, NY, USA) were placed in 24-well plates, and each well was covered with 50  $\mu\text{L}$  of ECM Gel from Engelbreth-Holm-Swarm murine sarcoma (2 mg/mL, matrigel E1270, Sigma-Aldrich, St. Louis, MO, USA) diluted in DMEM no phenol red without supplement, and immediately incubated at 37  $^{\circ}\text{C}$  for 2 hours. Then, 15,000 U87 cells or 10,000 U251 cells suspended in 150  $\mu\text{L}$  DMEM no phenol red and without supplement with 10  $\mu\text{M}$  Ara-C and treatments (vehicle or E2 10 nM) were added to the upper insert, while the lower wells were filled with 500  $\mu\text{L}$  DMEM supplemented with 10% FBS as a chemoattractant were incubated in a humidified atmosphere with 5%  $\text{CO}_2$  at 37  $^{\circ}\text{C}$  for 24 h. Transwell inserts were rinsed with PBS, fixed with 4% PFA for 20 min, and stained with 0.1% crystal violet dye for an additional 20 min. Inserts were washed three times with PBS for each 15 min in order to remove excess dye. Finally, images of invasive cells captured at 100 $\times$  magnification with an Infinity 1-2C camera (Lumenera, Ottawa, ON, Canada) connected to an inverted microscope (CKX41, Olympus, Shinjuku, TY, Japan) were analyzed using the Cell Counter plugin in the ImageJ software.

### 2.9. Statistical Analysis

Data were analyzed and plotted with the GraphPad Prism 5.0 software (GraphPad, San Diego, CA, USA). Statistical analysis between comparable groups was performed using a one-way ANOVA with a Tukey post hoc-test. Time course analysis was performed using a two-way ANOVA test followed by Bonferroni post-test to compare replicate means by row. Values of  $p < 0.05$  were considered statistically significant. Plotted data are representative of three independent experiments for each treatment.

## 3. Results

### 3.1. Differential Expression of ER $\alpha$ and ER $\beta$ Subtypes in Human GBM-Derived Cells

We evaluated the mRNA expression levels of ESR1 (ER- $\alpha$ ) and ESR2 (ER- $\beta$ ) genes in astrocytoma samples with different histological grades from the data obtained of the low-grade gliomas (LGG) and glioblastoma (GBM) projects from the TCGA repository, as well as samples of healthy cerebral cortex in the GTEx database. Low ESR1 expression levels were observed in GBM and LGG when compared to healthy tissue. A slight but significant increase was found in ESR1 expression in GBM as compared with LGG. These data highlight two critical points: (1) ESR1 expression was lower in gliomas compared to healthy tissue, (2) but also was higher in GBM compared to LGG, suggesting an important oncogenic role of ER- $\alpha$  in development of low- and high-grade gliomas. In contrast, ESR2 expression levels were higher in GBM as compared with LGG and healthy tissue (Figure 1A). Next, we compared ESR1 and ESR2 expression among the four GBM subtypes defined by Verhaak et al. [4]. The mesenchymal subtype showed higher levels of ESR1 mRNA expression compared to the classical and neural subtypes, without significant differences when compared with the proneural subtype. ESR2 expression in the mesenchymal subtype showed a tendency to be the highest, although it was only significantly higher when compared with the neural subtype ( $p < 0.05$ ) (Figure 1B). It is interesting to highlight that our results showed that expression of both ER subtypes was enriched in the mesenchymal subtype. Analysis of expression in cell lines showed a similar trend to the TCGA data: the expression of both ESR1 and ESR2 in four cell lines derived from human GBM (U251, U87, T98G, and LN229) was found to be lower compared to the expression of normal human astrocytes (NHA). Among GBM cells, the ESR1 gene was expressed in a higher proportion in U251 cells, while ESR2 had a higher expression in U87 cells (Figure 1C). We evaluated the expression of both ERs subtypes at the protein level in GBM cells, and a higher content of ER- $\alpha$  than that of ER- $\beta$  was observed in all cell lines. Moreover, we found two

isoforms of ER- $\beta$  (ER- $\beta$ 1 and ER- $\beta$ 5) expressed in GBM cells; ER- $\beta$ 1 was more abundant than ER- $\beta$ 5 (Figure 1D). An analysis of the clinical outcome of ER expression in GBM patients showed that the higher expression of ER- $\alpha$  and ER- $\beta$  was correlated with a poor prognosis. Therefore, patients with a low expression of both ER subtypes live longer than those with higher levels of expression (Figure 1E). Importantly, although lower ER- $\alpha$  expression was observed in GBM TCGA data compared to healthy tissue, survival analysis showed that high ER- $\alpha$  expression is a poor prognostic factor for the patients, which suggests that ER- $\alpha$  expression levels in GBM may not always be proportional to its oncogenic activity. These results suggest that ER- $\alpha$  and ER- $\beta$  expression differentially changes among healthy tissue, LGG, and GBM, both in vivo and in vitro, and it also varies among GBM subtypes.

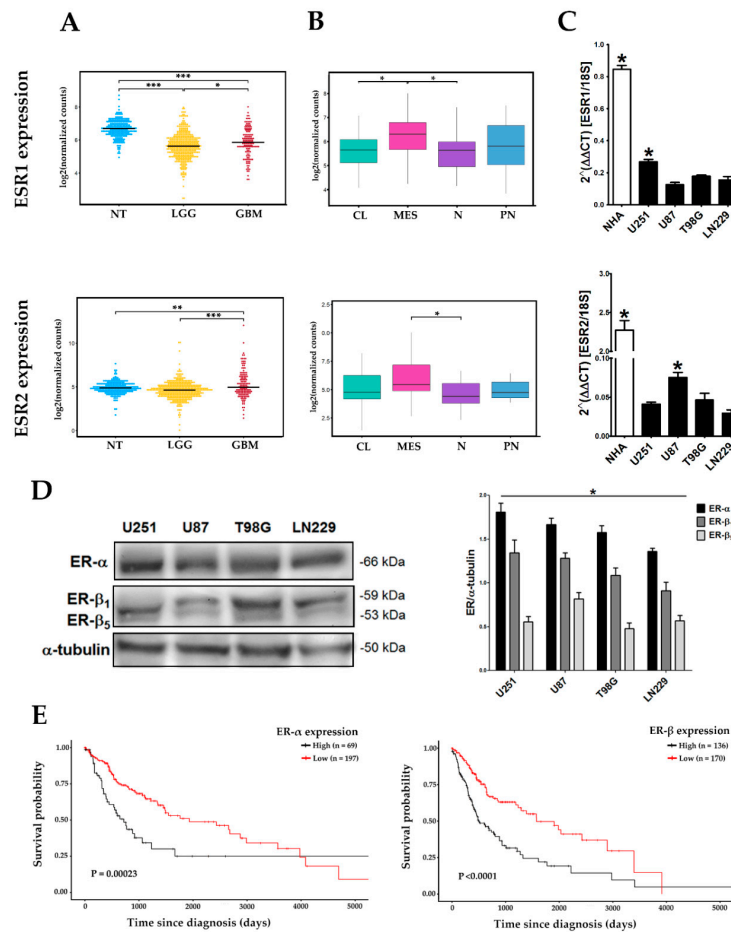
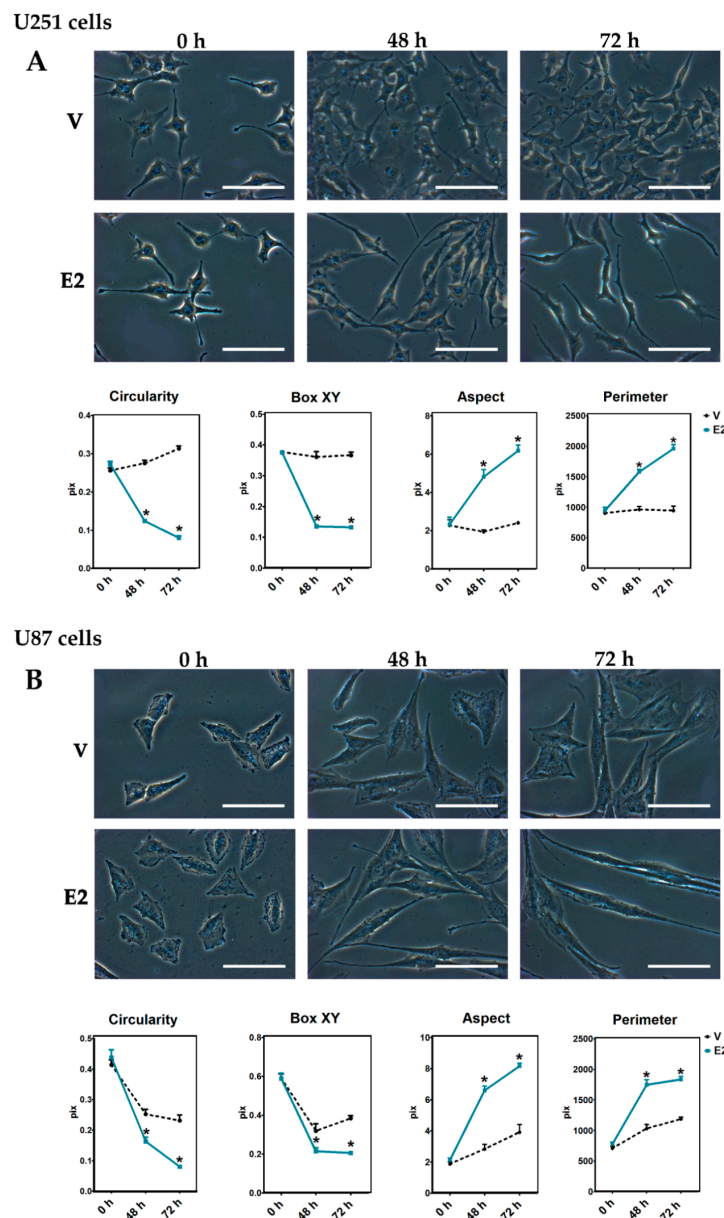


**Figure 1.** The estrogen receptor- $\alpha$  (ER- $\alpha$ ) and estrogen receptor- $\beta$  (ER- $\beta$ ) subtype gene expressions in human glioblastoma multiforme (GBM). **(A)** Ribonucleic acid sequencing (RNA-Seq) counts obtained from low-grade gliomas (LGG,  $n = 167$ ) and GBM ( $n = 155$ ) projects from The Cancer Genome Atlas (TCGA) and expression profiles obtained from healthy brain cortex samples (normal tissue, NT;  $n = 249$ ) in the GTEx database. LGG includes grade I, II, and III gliomas. \*  $p < 0.05$ ; \*\*  $p < 0.01$ ; \*\*\*  $p < 0.001$ . **(B)** RNA-Seq counts from GBM subtypes: classical (CL), mesenchymal (MES), neural (N), and proneural (PN) obtained from TCGA. \*  $p < 0.05$ . **(C)** RT-qPCR quantified gene expression of estrogen receptor 1/ $\alpha$  (ESR1) and estrogen receptor 2/ $\beta$  (ESR2) relative to the reference gene 18S ribosomal RNA (rRNA) using the comparative  $2^{-\Delta\Delta C_t}$  method in total RNA from normal human astrocyte (NHA) and U251, U87, T98G, and LN229 human GBM-derived cells. Both receptor subtypes were less expressed in GBM cells than in NHAs. \*  $p < 0.05$  vs. all other groups; mean  $\pm$  standard error of the mean (SEM),  $n = 3$ . **(D)** ER- $\alpha$  and ER- $\beta$  content analyzed by Western blot using  $\alpha$ -tubulin as load control. The two main isoforms of ER- $\beta$  expressed in GBM are shown: ER- $\beta$ 1 and ER- $\beta$ 5. Representative blot image and the corresponding densitometric analysis for ER $\alpha$  and ER $\beta$  expression in human GBM-derived cells. \*  $p < 0.05$  ER- $\alpha$  vs. ER- $\beta$  and ER- $\beta$ 1 vs. ER- $\beta$ 5; mean  $\pm$  SEM,  $n = 3$ . **(E)** Survival analysis for ER- $\alpha$  and ER- $\beta$  expression in GBM using TCGA data.












### 3.2. Changes in Cell Morphology During E2-Induced EMT

Morphological changes associated with EMT in U251 and U87 cells were evaluated after E2 (10 nM) treatment. At the beginning of the treatments, U251 cells presented a typical star-like morphology, and U87 cells a polygonal shape. Interestingly, the cells treated with E2 showed a spindle-shape and the typical features of mesenchymal cells at 48 and 72 h (Figure 2). Table 1 details the geometric parameters quantified in this work. Values close to the unity of the circularity and box XY (width/height) measurements are characteristic of a polygonal shape, while a high aspect (major/minor axis) and perimeter denote a fusiform shape. Plots show that E2 decreased circularity and box XY, while increased aspect and perimeter (Figure 2). This effect on the cellular morphology was consistent in T98G and LN229 cells (Figures S1 and S2). These results show that E2 promotes morphological changes associated with EMT.



**Figure 2.** 17 $\beta$ -Estradiol (E2)-induced morphological changes in human GBM-derived cells. (A) U251 and (B) U87 cells observed by phase-contrast microscopy with a magnification of 400 $\times$  at 0, 48, and 72 h after adding 17 $\beta$ -estradiol (E2, 10 nM) and the vehicle (V, 0.01% cyclodextrin). Magnification white bar = 100  $\mu$ m. Plots represent the quantification of the geometric parameters (circularity, box XY, aspect, perimeter) in this study. Results are expressed as the mean  $\pm$  standard error of the mean (SEM);  $n = 3$ ; \*  $p < 0.05$  vs. V.

**Table 1.** Geometric parameters of Image-Pro software.

Parameter	Description	Image
Area	The area included in the polygon that defines the figure contour	
Axis major	Major axis length of an imaginary ellipse surrounding figure	
Axis minor	Minor axis length of an imaginary ellipse surrounding figure	
Aspect	The ratio between the major and minor axis of an ellipse	
Bound box height	Bounding box height of the figure	
Bound box width	Bounding box width of the figure	
Box XY	The ratio of width to height of bounding box	
Circularity	The ratio of figure area to the diameter of a circle around it	
Perimeter	Length of the region surrounding the figure	

### 3.3. E2-Induced Reorganization of Actin Filaments

To determine whether the morphological changes observed above were related to changes in the arrangement of actin filaments, we performed immunofluorescence assays in U251 and U87 cells. In U251 cells treated with vehicle, the actin filaments were predominantly organized into bundles of dense reticulated mesh, characteristic of cortical actin. In contrast, in cells treated with E2 (10 nM), the actin filaments assembled in parallel along the ventral surface of the cell, forming long projections towards the leading edge, which in the extreme showed focal sites with a high concentration of actin (Figure 3). In U87 cells, we observed a higher proportion of concentrated actin focal points, both in vehicle and E2 treated cells. However, cells incubated with E2 showed long parallel filament projections with a high concentration of actin around the edge (Figure 3). Thereby, the morphological changes induced by E2 in GBM cells were related to a reorganization of the actin filaments.

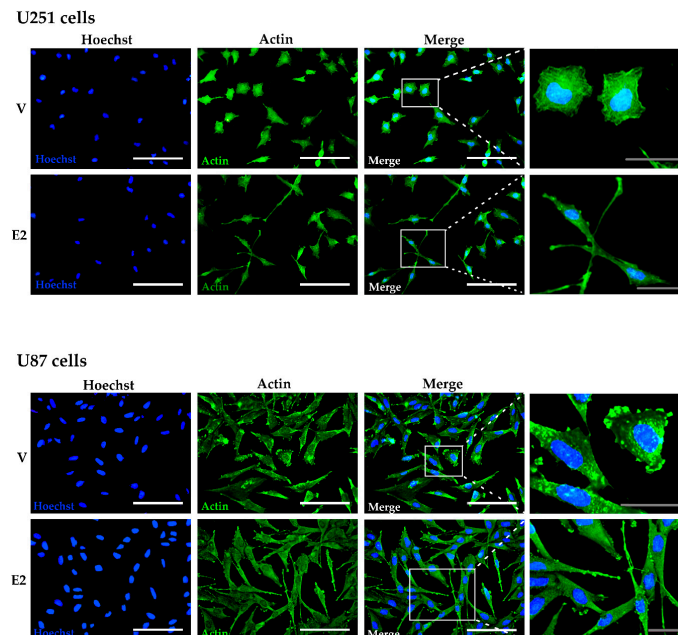


**Figure 3.** E2 rearranged the actin cytoskeleton of human GBM-derived cells. Actin immunostaining in U251 and U87 cells treated with 17 $\beta$ -estradiol (E2, 10 nM) and vehicle (V, 0.01% cyclodextrin) for 48 h. Representative images captured under a fluorescence microscope at a magnification of 400 $\times$ . Magnification white bar = 100  $\mu$ m and gray bar = 30  $\mu$ m.

### 3.4. E2 Regulated EMT Marker Expression

We analyzed the effects of E2 on EMT marker expression and distribution in GBM cells by RT-qPCR, Western blot, and immunofluorescence. We evaluated the peripheral membrane protein zonula occludens 1 (ZO-1, encoded by the TJP1 gene) as an epithelial marker, and the evaluated mesenchymal phenotype markers were N-cadherin (encoded by the CDH2 gene) and vimentin (encoded by the VIM gene). In U251 cells, E2 increased TJP1 expression only at 48 h, CDH2 expression from 24 to 72 h, and VIM expression from 48 h (Figure 4A). Importantly, ZO-1 protein content showed no changes due to E2 treatment, while the hormone increased the content of N-cadherin and vimentin proteins at 72 h (Figure 4B). E2 effects on U87 cells were like those of U251 cells. E2 upregulated TJP1 and ZO-1 expression from 48 h, CDH2 expression from 24 h, and N-cadherin expression from 48 h; VIM expression increased at 24 h, and decreased at 72 h, while the vimentin protein content increased at 72 h (Figure 4C,D).

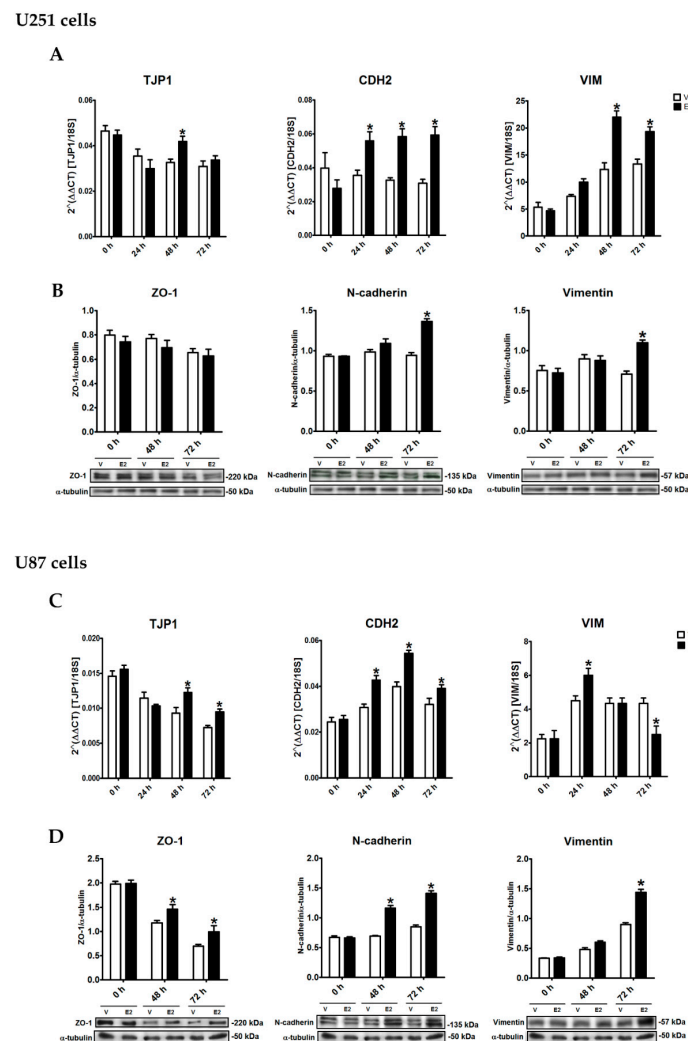


**Figure 4.** E2-regulated epithelial-to-mesenchymal transition (EMT) marker expression of human GBM-derived cells. (A,B) U251 and (C,D) U87 cells were treated with 17β-estradiol (E2, 10 nM) and vehicle (V, 0.01% cyclodextrin) for 24, 48, and 72 h. (A,C) Epithelial gene (tight junction protein 1 (TJP1)) and mesenchymal genes (vimentin (VIM) and cadherin-2/N-cadherin (CDH2)) expression was quantified by RT-qPCR using the comparative method 2<sup>-ΔΔCt</sup> concerning the reference gene 18S rRNA. (B,D) Zonula occludens 1 (ZO-1), N-cadherin, and vimentin content was determined by Western blot. Densitometric analysis of EMT marker expression with their respective representative bands using α-tubulin as a load control showed that E2 increased EMT marker expression with different temporal dynamics. Results are expressed as the mean ± standard error of the mean (SEM); n = 3; \* p < 0.05 vs. V.

The analysis of EMT markers by immunofluorescence showed that in U251 and U87 cells treated with the vehicle, ZO-1, and N-cadherin proteins were expressed in localized regions of the plasmatic membrane, particularly at cell-binding sites. In contrast, in E2-treated cells, these proteins were shown along the entire cell surface, especially in long projections at the cell ends (Figure 5A,B). Vimentin filaments formed a network within the cytoplasm in cells without E2, whereas in E2-incubated cells, vimentin filaments were arranged in parallel along the ventral surface of the cell, particularly at the borders, similar to actin filaments (Figure 5A,B). Overall, the fluorescence intensity of EMT markers significantly increased in E2-treated U251 and U87 cells (Figure 5C). These results show that E2 induces EMT marker expression and its redistribution in GBM cells.

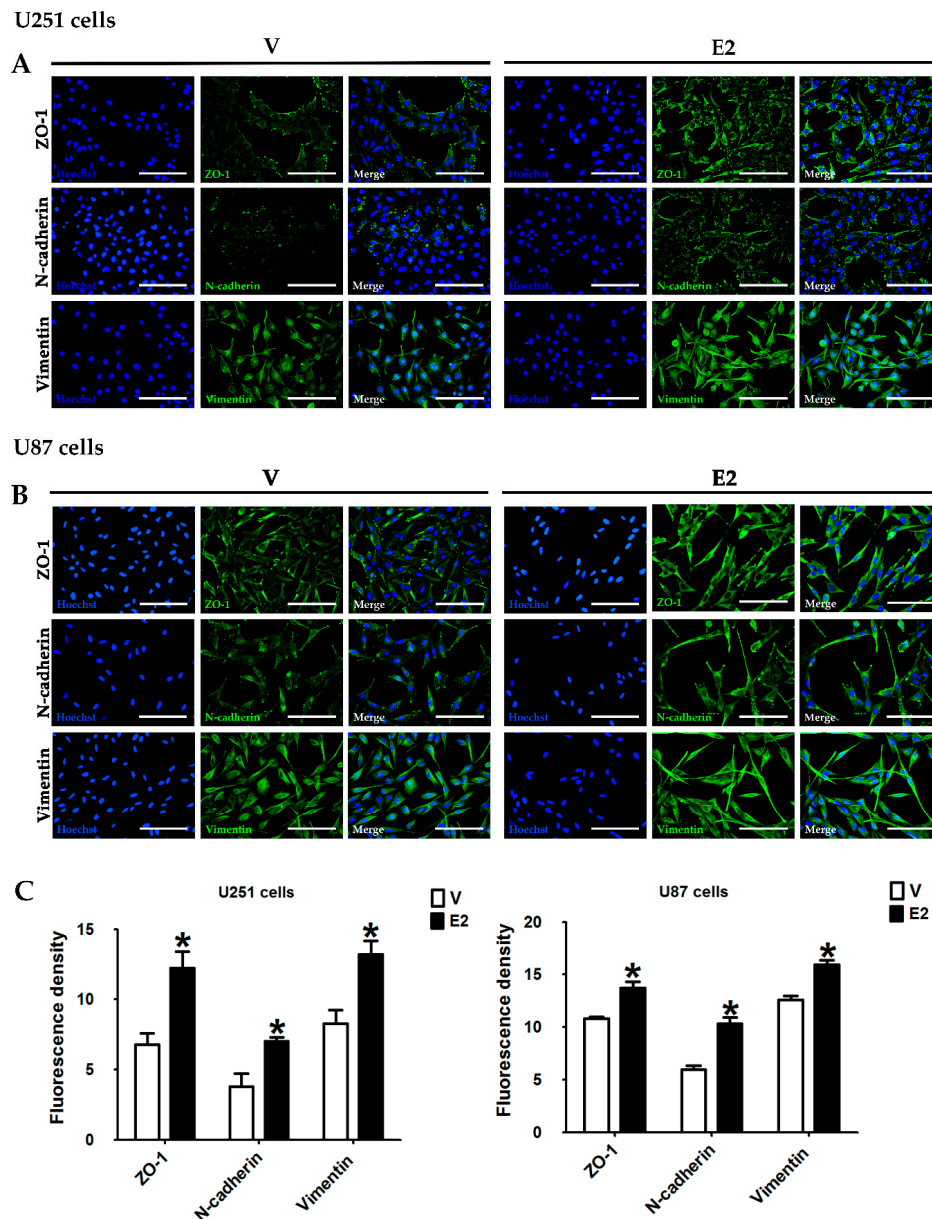


**Figure 5.** E2 modified EMT marker distribution and immunoreactivity in human GBM-derived cells. ZO-1, N-cadherin, and vimentin immunostaining in (A) U251 and (B) U87 cells treated with 17 $\beta$ -estradiol (E2, 10 nM) and vehicle (V, 0.01% cyclodextrin) for 48 h. Representative images were captured under a fluorescence microscope at a magnification of 400 $\times$ . (C) EMT marker expression measured as a fluorescence density. Results are expressed as the mean  $\pm$  standard error of the mean (SEM);  $n = 3$ ; \*  $p < 0.05$  vs. V.

Furthermore, the increase in both epithelial and mesenchymal markers suggests that E2 promotes the induction of a partial EMT, which expresses both phenotypes. Nevertheless, the increase in ZO-1 in U251 cells was not as evident as in U87 cells, and thus these results are not sufficient to determine the status of E2-induced EMT. However, these results showed that E2 significantly induced the expression of mesenchymal markers, promoting the mesenchymal phenotype of cells derived from GBM.

### 3.5. E2 Promoted Migration and Invasion of Human GBM-Derived Cells

We evaluated cell migration by wound healing assay, and we observed that E2-treated U251 and U87 cells showed a higher migratory capacity by rapidly closing the wound compared to cells without E2 (Figure 6A,B). We also evaluated invasive capacity through transwell assay. E2 increased the number of invading U251 and U87 cells as compared with the vehicle (Figure 6C,D). These data show that E2, in addition to changing cell morphology and regulating EMT marker expression, also increased the migratory and invasive capacity of GBM-derived cells.

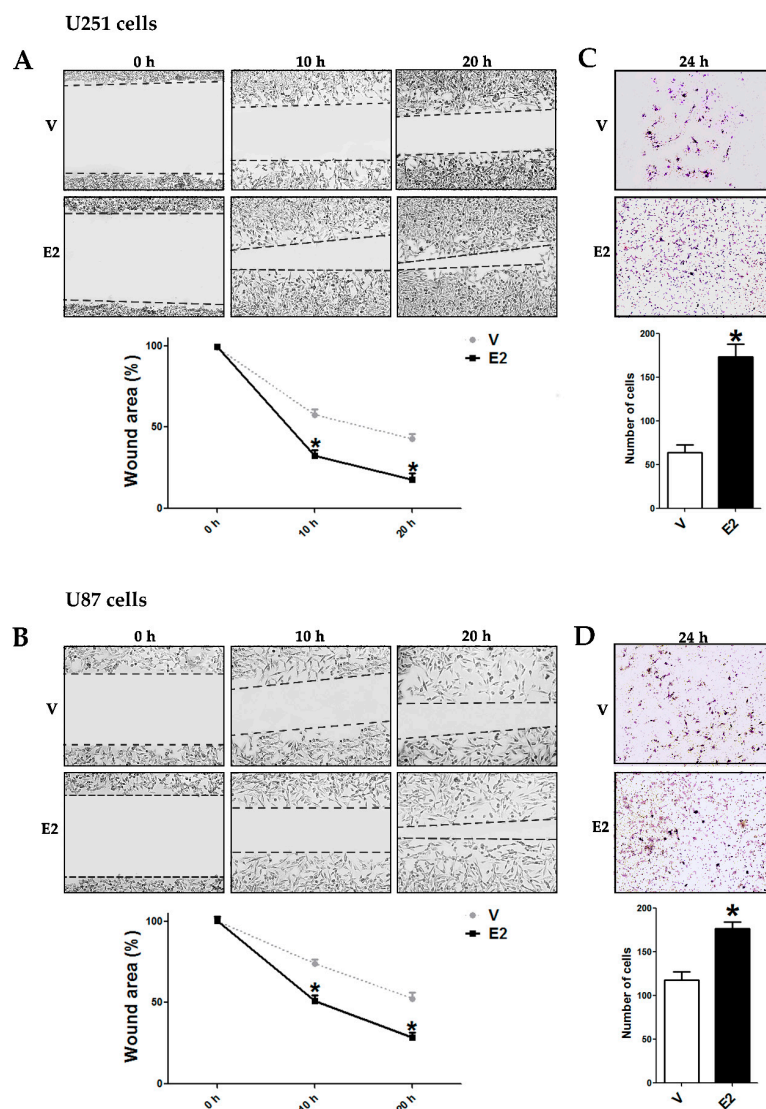


**Figure 6.** E2 increased migration and invasion of human GBM-derived cells. (A,B) Wound healing assays were performed in U251 and U87 cells treated with 17 $\beta$ -estradiol (E2, 10 nM) and vehicle (V, cyclodextrin 0.01%). Representative images of wound closure at 0, 10, and 20 h and quantification of the wound area are shown. (C,D) Transwell assays were carried out in both cell lines. Quantification of cells staining with 0.1% crystal violet dye shows the number of invasive cells. Results are expressed as the mean  $\pm$  standard error of the mean (SEM);  $n = 3$ ; \*  $p < 0.05$  vs. V.

3.6. ER- $\alpha$  Mediated E2 Effects on EMT

To determine the intracellular receptor subtype involved in E2 effects, we used specific agonists and antagonists' ER subtypes and assessed the expression of EMT markers. PPT, a selective ER- $\alpha$  agonist, increased TJP1, CDH2, and VIM gene expression in a similar way to E2 in U251 and U87 cells, and ER- $\alpha$  antagonist MPP blocked E2 effects in both cell types (Figure 7A,B). Treatment with antagonist alone did not show a significant effect on the expression of EMT markers, consistent with characterization of the effects of MPP in vitro, which showed that the antagonist does not behave as a partial or inverse agonist when administered in absence of an agonist. Treatments with the ER- $\beta$ -selective agonist DPN and the antagonist PHTPP did not show any significant statistical effect on the regulation of EMT marker expression in either U251 or U87 cells (Figure 7A,B). These data suggest that E2 regulates EMT marker expression through the ER- $\alpha$  subtype. To functionally assess the role of ER- $\alpha$  in the EMT process, we performed wound healing assays using PPT and MPP. PPT-treated U251 cells rapidly closed the wound compared to cells treated with the vehicle, while the antagonist MPP blocked the PPT effect. Similarly, PPT increased the wound closure rate of U87 cells, and MPP blocked the agonist effect (Figure 8).

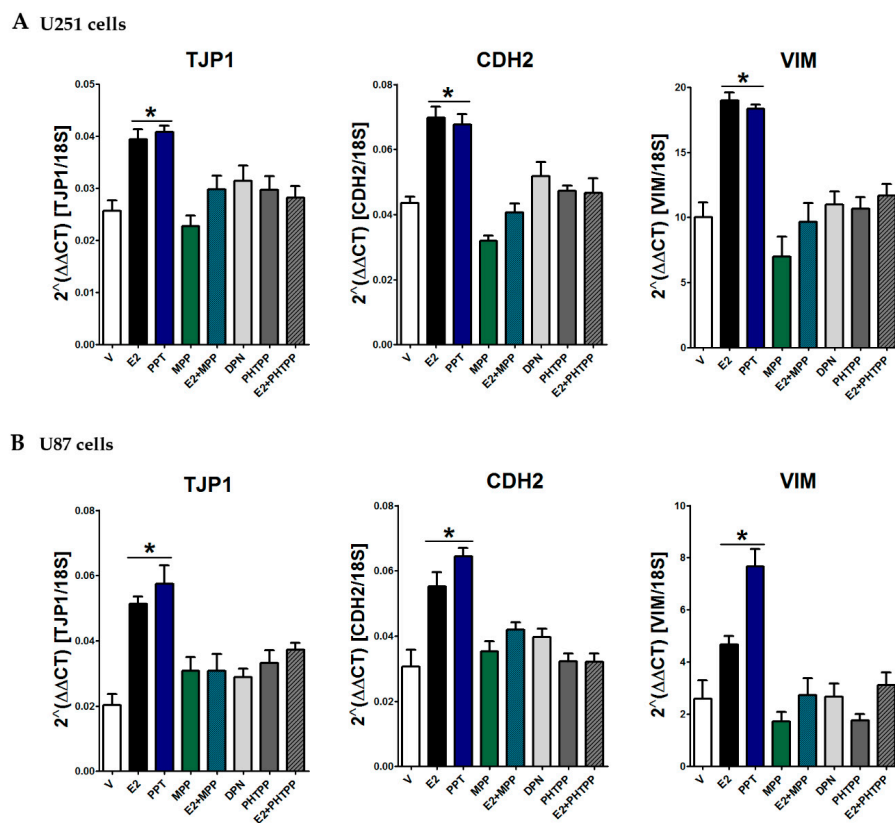


**Figure 7.** Effect of selective ER- $\alpha$  and ER- $\beta$  agonists and antagonists on the EMT marker expression in GBM cells. U251 (A) and U87 (B) cells were treated with vehicle (V, 0.01% cyclodextrin + 0.01% DMSO), 17 $\beta$ -estradiol (E2, 10 nM), 4,4',4''-(4-propyl-[1H]-pyrazole-1,3,5-triyl)trisphenol (PPT, 10 nM, selective ER- $\alpha$  agonist), methyl-piperidino-pyrazole (MPP, 1  $\mu$ M, selective ER- $\alpha$  antagonist), E2 + MPP, diarylpropionitrile (DPN, 10 nM, selective ER- $\beta$  agonist), 4-[2-phenyl-5,7-bis(trifluoromethyl)pyrazole[1,5-a]pyrimidin-3-yl]phenol (PHTPP, 1  $\mu$ M, selective ER- $\beta$  antagonist), and E2 + PHTPP for 48 h. Epithelial gene (TJP1) and mesenchymal gene (VIM and CDH2) expression were quantified by RT-qPCR using the comparative method  $2^{-\Delta\Delta C_t}$  concerning the reference gene 18S rRNA. Results are expressed as the mean  $\pm$  standard error of the mean (SEM);  $n = 3$ ; \*  $p < 0.05$  vs. all other groups.

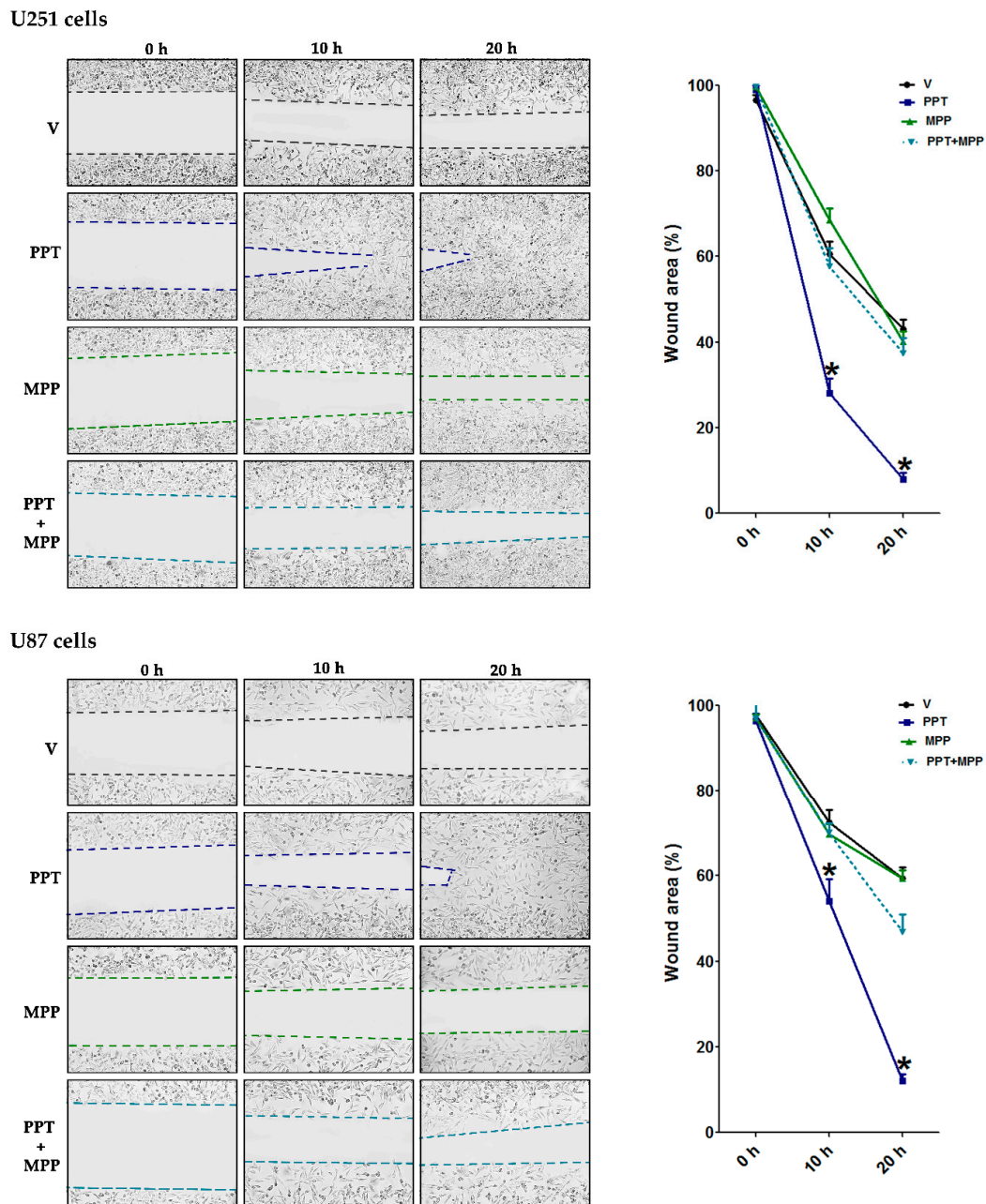


**Figure 8.** Effect of the selective ER- $\alpha$  agonist and antagonist on the migration of GBM cells. (A) U251 and (B) U87 cells that were treated for 20 h, with PPT (10 nM, selective ER- $\alpha$  agonist), MPP (1  $\mu$ M, selective ER- $\alpha$  antagonist), PPT + MPP, and vehicle (V, DMSO 0.01%). Wound healing assays determined the migratory capacity of the U251 and U87 cells. Representative images show wound closure at 0, 10, and 20 h and quantification of the wound area. Results are expressed as the mean  $\pm$  standard error of the mean (SEM);  $n = 3$ ; \*  $p < 0.05$  vs. all other groups.

#### 4. Discussion

The present study provides evidence of E2 effects on EMT-related molecular and cellular processes in human GBM-derived cells. EMT comprises a set of states between the epithelial and mesenchymal phenotypes, and its activation could be closely related to the high degree of phenotypic heterogeneity of GBM.

GBM is a highly heterogeneous tumor at both the molecular and cellular levels. The TCGA determined the existence of four main subtypes with different molecular expression profiles [4],

and some studies have shown the simultaneous presence of these subtypes within the same tumor [67,68]. GBM cells with proneural and mesenchymal expression are the most consistent subtypes in the literature. The proneural subtype is related to a more favorable prognosis, and the mesenchymal subtype tends to have the worst survival rate [5,69,70]. It has been shown that recurring GBM tumors that initially showed proneural expression presented mesenchymal expression profile after radiotherapy and chemotherapy [6,71,72], which has led to the proposal of a proneural–mesenchymal transition (PMT), whose molecular events are equivalent to those of EMT [7,73]. The transition between the two molecular subtypes is closely related to an enrichment of cells of the immune system within the GBM tumor microenvironment, which activate various signaling pathways that promote PMT/EMT [74–76]. The data shown in these studies highlight the importance of the factors found within the tumor microenvironment that promote phenotypic transitions between GBM subtypes. Immune system cells produce chemokines, cytokines, growth and angiogenic factors, immunosuppressive molecules, and extracellular matrix-modifying enzymes, which make the surroundings favorable for tumor progression [77]. Among the many factors found within the GBM tumor microenvironment, in this work, we focused on E2, which is produced by microglial cells, astrocytes, and GBM cells [78–81]. In this study, we evaluated E2 effects on the mesenchymal transition of human GBM-derived cells.

Both ER subtypes are predominantly expressed through healthy CNS; however, in human astrocytomas, both ER- $\alpha$  [45,47–49] and ER- $\beta$  [44] expression decreases as the grade of tumor malignancy increases. Therefore, different researchers have proposed that ER expression may be reduced or lost during tumor development, although it is not clear if this represents a cause or consequence of tumor development. Much remains to be investigated on this topic, since determining the mechanisms underlying ER decrease during the development of gliomas could better understand the malignant tumor progression. Our results regarding the decrease of ER- $\alpha$  expression in gliomas compared with healthy tissue show agreement with that observed in other investigations. Likewise, we showed that ER- $\alpha$  subtype expression is higher in GBM than LGG (Figure 1A), which suggests an important oncogenic role of such receptor in the development of low- and high-grade gliomas. Among gliomas, a higher expression of ER- $\alpha$  could be involved in developing a high-grade glioma (GBM), while lower ER- $\alpha$  expression is associated with LGG development. The decrease or loss of ER expression during tumor development supposes the homeostatic imbalance of the normal functions of ERs in cells. Although this topic is not yet well studied in GBM, in breast cancer, it has been determined in more detail that in the most malignant tumors with multiple metastases, the nuclear factor kappa-light-chain-enhancer of activated B cells (NF- $\kappa$ B) represses ER- $\alpha$  transcription through the enhancer of zeste homolog2 (EZH2), which negatively regulates ER- $\alpha$  transcription [82]. However, NF- $\kappa$ B also improves the recruitment of ER- $\alpha$  to estrogen response elements (EREs) of its target promoters and increases its transcriptional activity [83,84]. The change in ER- $\alpha$  functions may also be due to other factors, such as altered structural conformations that increase interaction with transcriptional coactivators, point mutations that promote active forms of the receptor in the absence of an agonist, or variations by alternative splicing that change receptor transactivation mechanisms [85–87]. These data suggest that ER- $\alpha$  expression levels may not always be proportional to its activity. The positive correlation of ER- $\beta$  expression concerning the GBM malignancy grade observed in this work does not correspond to other studies that find the opposite. However, we must consider that these studies do not specify the brain region of the used healthy tissue. We used expression data from the cerebral cortex, but there are other regions with a higher abundance of ESR2, such as the pons, cerebellum, thalamus, basal ganglia, and hypothalamus. Nevertheless, ESR1 and ESR2 expression on human GBM-derived cell lines were lower compared to healthy astrocytes, reinforcing the hypothesis of the studies above, which establish that the expression of both ER subtypes is inversely proportional to the tumor evolution degree. Different actions have been observed between ER subtypes in GBM. E2 (10 nM) and PPT (1 nM), the selective ER- $\alpha$  agonist, increased the number of cells derived from GBM [45], while treatment with different ER- $\beta$ -specific agonists decreased GBM cell proliferation [44]. Within the cancer context, a positive correlation has been determined between EMT activation and



increased cell proliferation [88–91]. Previously, our group determined in GBM-derived cells that E2 induces cell growth and the expression of vascular endothelial growth factor (VEGF), epidermal growth factor receptor (EGFR), and cyclin D1 genes, which are involved in cell proliferation. These effects depended on ER- $\alpha$  activation [45]. This previous study represents the primary antecedent of our work. Once we demonstrated that E2 induces cell growth in GBM cells, we decided to investigate the relationship between E2 and canonical cellular processes of EMT activation, such as morphological and actin cytoskeleton organization changes, EMT marker expression, as well as cellular migration and invasion, which represent the main functional consequences of cells that undergo EMT. Additionally, it is worth mentioning that recently Castruccio et al. demonstrated that E2 significantly increases cell proliferation in U87 cells [92], which is consistent with our previously published results [45]. Still, our survival analysis showed that both ER- $\alpha$  and ER- $\beta$  expression was positively correlated with a poor prognosis. It is interesting to highlight that our results showed that expression of both ER subtypes was enriched in the mesenchymal subtype concerning the other subtypes since this data led us to investigate the role of ERs on the induction of the mesenchymal phenotype.

EMT is a transition process between cellular phenotypes; therefore, it involves cellular morphological changes. To characterize the effects of E2 on EMT-related processes, in this study, we first evaluated changes in the morphology of cells treated with E2. Our results showed that E2 significantly changed the morphology of the four GBM-derived cells, towards an elongated mesenchymal phenotype. Moreover, these changes were correlated with an actin filament rearrangement. E2 regulates the reorganization of actin filaments through phosphorylation of actin-binding proteins such as cofilin and moesin in neurons, fibroblasts, and breast and endometrial cancer cells [93–96]. During EMT, actin filaments progressively reorganize from thin cortical bundles to thick contractile filaments that withstand stress fibers. The mesenchymal phenotype presents distribution of actin filaments in a front–rear polarization, with a network of short actin filaments branched at the leading edge, and long filaments arranged in different types of fibers behind the leading edge, which are associated with adhesion structures. This arrangement of the mesenchymal actin network allows cells to carry out migratory and invasive processes [97–99]. Thus, in this study, we demonstrated that E2 promotes a morphology change in GBM cells towards a mesenchymal phenotype due to the rearrangement of actin filaments, which were assembled in parallel along the ventral surface with long projections toward the leading edge. These changes in cellular morphology and reorganization of actin filaments suggest that E2 provides GBM-derived cells migratory and invasive capabilities.

All molecular events that occur during EMT are spatially and temporally coordinated during the transition. Therefore, the reorganization of the actin filaments is coupled with the expression changes that modify the cellular phenotype. Previously, the EMT definition described a complete transition between two different states, the epithelial and mesenchymal phenotype. Therefore, the primary experimental model for EMT evaluated the decrease in epithelial markers and the increase in mesenchymal markers. However, this perspective has generated extensive debate about the presence of EMT in certain circumstances, such as in cancer progression, which tends to create hybrid epithelial/mesenchymal (E/M) phenotypes that exhibit both epithelial and mesenchymal characteristics in a process known as partial EMT. Hybrid E/M phenotypes in cancer cells present better migratory and invasive capacities, as well as higher resistance to therapy [100–102].

We showed that E2 increased the expression of the epithelial marker ZO-1 and the mesenchymal markers N-cadherin and vimentin in U251 and U87 cells. However, the ZO-1 expression regulation was variable between cell lines, since in U251 cells, it only was increased by E2 at the mRNA level at 48 h, while in U87 cells, the expression increased both at the mRNA and protein levels at 48 and 72 h. ZO-1 marker is an adapter protein that binds to multiple components, such as integral proteins of the plasma membrane [103,104], and its presence is essential for assembly of tight and adherent junctions of epithelial cells [105,106]. Therefore, tumor cells from epithelial tissues decrease ZO-1 expression by activating EMT. The implications that ZO-1 expression may have on GBM have not yet been studied. Furthermore, our results showed that the regulation of E2 on ZO-1 expression varies

between different human GBM-derived cell lines, possibly due to the different expression profiles among these cells [107,108].

N-cadherin is a transmembrane protein that belongs to the calcium-dependent cell adhesion molecule (CAMs) family that is characteristic of mesenchymal tissue. Increased N-cadherin expression promotes cells to form elongated multicellular chains that migrate faster and more persistently, with a higher proportion of actin stress fibers that provide contractile forces during cell migration [109–111]. EMT activation in GBM cells leads to increased expression of N-cadherin, which is associated with increased migratory and invasive capacities. Vimentin is a type III intermediate filament protein that has an essential role in integrity maintaining of mesenchymal cells by providing support and anchorage to organelles, in addition to offering flexibility to cells by stabilizing dynamic interactions of the cytoskeleton during cell migration [112–114]. During EMT, there is an extensive change in the composition of intermediate filaments of epithelial cells, which generally express cytokeratin and initiates the expression of vimentin when they differentiate towards the mesenchymal phenotype. Our results showed that E2 promotes the mesenchymal phenotype by increasing the expression of N-cadherin and vimentin both at the mRNA and protein levels in two different human GBM cell lines. Although it was observed that E2 increased the expression of both epithelial and mesenchymal markers, we cannot affirm the induction of a partial EMT, since doing so requires the analysis of more epithelial and mesenchymal markers. However, our results open new perspectives regarding the determination of the status of E2-induced EMT in cells derived from GBM, since estradiol may promote partial EMT. Regardless of the status of EMT induced by E2, our results convincingly showed the acquisition of mesenchymal characteristics in GBM cells by E2 effect, since the changes in the expression of N-cadherin and vimentin are sufficiently forceful in the two cell lines studied.

Taken together, the effects promoted by E2 on GBM cells, such as reorganization of actin filaments as well as increased expression of N-cadherin and vimentin, are related to increased migratory and invasive capacities of U251 and U87 cells. These effects, associated with EMT activation, were replicated with PPT, a selective ER- $\alpha$  agonist that has a 410-fold relative binding affinity for ER- $\alpha$  over ER- $\beta$  [115], suggesting that the E2 effects on EMT are regulated through ER- $\alpha$ . The latter was verified when using a highly selective ER- $\alpha$  antagonist (MPP,  $K_i = 2.7$ ) [116], which blocked effects produced by E2 on EMT marker expression, as well as the increase of the migratory capacity provided by PPT. Furthermore, neither agonist DNP nor antagonist PHTPP, both selective for ER- $\beta$  [117], showed significant effects on the expression of EMT markers. Therefore, we conclude that E2 effects observed on the expression of EMT markers are mainly produced by ER- $\alpha$  activation. Much remains to be known about the actions of both ER subtypes during the GBM's malignant progression. A more in-depth study of the molecular mechanisms of E2 signaling on GBM and its interaction with other signaling factors in specific cellular contexts is necessary for understanding E2 effects on this tumor, which could provide new strategies in GBM treatment.

In this work, we characterized E2-induced EMT in human GBM-derived cells. We found that E2 induces changes in cell morphology through actin filament reorganization and by increased expression of mesenchymal markers. These effects are related to the increased migratory and invasive capacities of GBM cells. Furthermore, E2 effects were mediated by ER- $\alpha$ , since the treatment with its agonist PPT produced similar results to E2, while the treatment with its antagonist MPP blocked these effects. Thus, E2 induces a mesenchymal phenotype through ER- $\alpha$  in cells derived from human GBM.

**Supplementary Materials:** The following are available online at <http://www.mdpi.com/2073-4409/9/9/1930/s1>, Figure S1: E2-induced morphological changes in human GBM-derived T98G cells. Figure S2: E2-induced morphological changes in human GBM-derived LN229 cells.

**Author Contributions:** A.M.H.-V., A.D.M.-M., C.J.Z.-S., and A.G.P.-M. contributed to carrying out the experiments and data analysis. A.M.H.-V., A.G.-A., and I.C.-A. conceived and managed experiments. A.M.H.-V. and I.C.-A. contributed to writing the manuscript. All authors have read and agreed to the published version of the manuscript.

**Funding:** This work was financially supported by *Programa de Apoyo a Proyectos de Investigación e Innovación Tecnológica (PAPIIT)*, project IN217120, DGAPA-UNAM, Mexico.

**Acknowledgments:** We would like to thank Marisol De La Fuente-Granada (Departamento de Medicina Genómica y Toxicología Ambiental, Instituto de Investigaciones Biomédicas, UNAM, Mexico) for the facilitation of cell culture during morphology analysis.

**Conflicts of Interest:** The authors declare no conflict of interest.

## References

1. Ostrom, Q.T.; Cioffi, G.; Gittleman, H.; Patil, N.; Waite, K.; Kruchko, C.; Barnholtz-Sloan, J.S. CBTRUS Statistical Report: Primary Brain and Other Central Nervous System Tumors Diagnosed in the United States in 2012–2016. *Neuro Oncol.* **2019**, *21*, v1–v100. [CrossRef] [PubMed]
2. Furnari, F.B.; Fenton, T.; Bachoo, R.M.; Mukasa, A.; Stommel, J.M.; Stegh, A.; Hahn, W.C.; Ligon, K.L.; Louis, D.N.; Brennan, C.; et al. Malignant astrocytic glioma: Genetics, biology, and paths to treatment. *Genes Dev.* **2007**, *21*, 2683–2710. [CrossRef] [PubMed]
3. Louis, D.N.; Perry, A.; Reifenberger, G.; von Deimling, A.; Figarella-Branger, D.; Cavenee, W.K.; Ohgaki, H.; Wiestler, O.D.; Kleihues, P.; Ellison, D.W. The 2016 World Health Organization Classification of Tumors of the Central Nervous System: A summary. *Acta Neuropathol.* **2016**, *131*, 803–820. [CrossRef] [PubMed]
4. Verhaak, R.G.W.; Hoadley, K.A.; Purdom, E.; Wang, V.; Qi, Y.; Wilkerson, M.D.; Miller, C.R.; Ding, L.; Golub, T.; Mesirov, J.P.; et al. Integrated Genomic Analysis Identifies Clinically Relevant Subtypes of Glioblastoma Characterized. *Cancer Cell* **2010**, *17*, 98–110. [CrossRef] [PubMed]
5. Phillips, H.S.; Kharbanda, S.; Chen, R.; Forrester, W.F.; Soriano, R.H.; Wu, T.D.; Misra, A.; Nigro, J.M.; Colman, H.; Soroceanu, L.; et al. Molecular subclasses of high-grade glioma predict prognosis, delineate a pattern of disease progression, and resemble stages in neurogenesis. *Cancer Cell* **2006**, *9*, 157–173. [CrossRef]
6. Bhat, K.P.L.; Balasubramanian, V.; Vaillant, B.; Ezhilarasan, R.; Hummelink, K.; Hollingsworth, F.; Wani, K.; Heathcock, L.; James, J.D.; Goodman, L.D.; et al. Mesenchymal Differentiation Mediated by NF- $\kappa$ B Promotes Radiation Resistance in Glioblastoma. *Cancer Cell* **2013**, *24*, 331–346. [CrossRef]
7. Behnan, J.; Finocchiaro, G.; Hanna, G. The landscape of the mesenchymal signature in brain tumours. *Brain* **2019**, *142*, 847–866. [CrossRef]
8. Nieto, M.A.; Huang, R.Y.J.; Jackson, R.A.; Thiery, J.P. EMT: 2016. *Cell* **2016**, *166*, 21–45. [CrossRef]
9. Skrypek, N.; Goossens, S.; De Smedt, E.; Vandamme, N.; Berx, G. Epithelial-to-Mesenchymal Transition: Epigenetic Reprogramming Driving Cellular Plasticity. *Trends Genet.* **2017**, *33*, 943–959. [CrossRef]
10. Lamouille, S.; Xu, J.; Derynck, R. Molecular mechanisms of epithelial–mesenchymal transition. *Nat. Rev. Mol. Cell Biol.* **2014**, *15*, 178–196. [CrossRef]
11. Thiery, J.P.; Huang, R.Y.J.; Nieto, M.A. Epithelial-Mesenchymal Transitions in Development and Disease. *Cell* **2009**, *139*, 1–13. [CrossRef] [PubMed]
12. Trelstad, R.L.; Hay, E.D.; Revel, J.D. Cell contact during early morphogenesis in the chick embryo. *Dev. Biol.* **1967**, *16*, 78–106. [CrossRef]
13. Nieto, M.A.; Sargent, M.; Wilkinson, D.; Cooke, J. Control of cell behavior during vertebrate development by Slug, a zinc finger gene. *Science* **1994**, *6*, 835–839. [CrossRef] [PubMed]
14. Lim, J.; Thiery, J.P. Epithelial-mesenchymal transitions: Insights from development. *Development* **2012**, *139*, 3471–3486. [CrossRef] [PubMed]
15. Lepilina, A.; Coon, A.N.; Kikuchi, K.; Holdway, J.E.; Roberts, R.W.; Burns, C.G.; Poss, K.D. A Dynamic Epicardial Injury Response Supports Progenitor Cell Activity during Zebrafish Heart Regeneration. *Cell* **2006**, *127*, 607–619. [CrossRef] [PubMed]
16. Stone, R.C.; Pastar, I.; Ojeh, N.; Chen, V.; Liu, S.; Garzon, K.I.; Tomic-Canic, M. Epithelial-mesenchymal transition in tissue repair and fibrosis. *Cell Tissue Res.* **2016**, *365*, 495–506. [CrossRef]
17. Dongre, A.; Weinberg, R.A. New insights into the mechanisms of epithelial–mesenchymal transition and implications for cancer. *Nat. Rev. Mol. Cell Biol.* **2019**, *20*, 69–84. [CrossRef]
18. Kahlert, U.D.; Joseph, J.V.; Kruyt, F.A.E. EMT- and MET-related processes in non-epithelial tumors: Importance for disease progression, prognosis, and therapeutic opportunities. *Mol. Oncol.* **2017**, *11*, 860–877. [CrossRef]
19. Kahlert, U.D.; Nikkhah, G.; Maciaczyk, J. Epithelial-to-mesenchymal (-like) transition as a relevant molecular event in malignant gliomas. *Cancer Lett.* **2013**, *331*, 131–138. [CrossRef]

20. Brabletz, T.; Kalluri, R.; Nieto, M.A.; Weinberg, R.A. EMT in cancer. *Nat. Rev. Cancer* **2018**, *18*, 128–134. [CrossRef]
21. Freije, W.A.; Castro-Vargas, F.E.; Fang, Z.; Horvath, S.; Cloughesy, T.; Liao, L.M.; Mischel, P.S.; Nelson, S.F. Gene Expression Profiling of Gliomas Strongly Predicts Survival. *Cancer Res.* **2004**, *15*, 6503–6510. [CrossRef] [PubMed]
22. Tso, C.L.; Shintaku, P.; Chen, J.; Liu, Q.; Liu, J.; Chen, Z.; Yoshimoto, K.; Mischel, P.S.; Cloughesy, T.F.; Liao, L.M.; et al. Primary Glioblastomas Express Mesenchymal Stem-Like Properties. *Mol. Cancer Res.* **2006**, *4*, 607–619. [CrossRef] [PubMed]
23. Zarkoob, H.; Taube, J.H.; Singh, S.K.; Mani, S.A.; Kohandel, M. Investigating the Link between Molecular Subtypes of Glioblastoma, Epithelial-Mesenchymal Transition, and CD133 Cell Surface Protein. *PLoS ONE* **2013**, *8*, e64169. [CrossRef] [PubMed]
24. Azcoitia, I.; Yague, J.G.; Garcia-Segura, L.M. Estradiol synthesis within the human brain. *Neuroscience* **2011**, *191*, 139–147. [CrossRef]
25. Barakat, R.; Oakley, O.; Kim, H.; Jin, J.; Ko, C.M.J. Extra-gonadal sites of estrogen biosynthesis and function. *BMB Rep.* **2016**, *49*, 488–496. [CrossRef]
26. Toran-allerand, C.D. Sex steroids and the development of the newborn mouse hypothalamus and preoptic area In Vitro: Implications for sexual differentiation. *Brain Res.* **1976**, *106*, 407–412. [CrossRef]
27. Díaz, N.F.; Guerra-Arraiza, C.; Díaz-Martínez, N.E.; Salazar, P.; Molina-Hernández, A.; Camacho-Arroyo, I.; Velasco, I. Changes in the content of estrogen  $\alpha$  and progesterone receptors during differentiation of mouse embryonic stem cells to dopamine neurons. *Brain Res. Bull.* **2007**, *73*, 75–80. [CrossRef]
28. Denley, M.C.S.; Gattford, N.J.F.; Sellers, K.J.; Srivastava, D.P. Estradiol and the development of the cerebral cortex: An unexpected role? *Front. Neurosci.* **2018**, *12*, 245. [CrossRef]
29. Díaz, H.; Lorenzo, A.; Carrer, H.F.; Cáceres, A. Time lapse study of neurite growth in hypothalamic dissociated neurons in culture: Sex differences and estrogen effects. *J. Neurosci. Res.* **1992**, *33*, 266–281. [CrossRef]
30. Pérez, J.; Naftolin, F.; García-Segura, L.M. Sexual differentiation of synaptic connectivity and neuronal plasma membrane in the arcuate nucleus of the rat hypothalamus. *Brain Res.* **1990**, *527*, 116–122. [CrossRef]
31. Sugiyama, N.; Andersson, S.; Lathe, R.; Fan, X.; Schwend, T.; Nalvarte, I. Spatiotemporal dynamics of the expression of estrogen receptors in the postnatal mouse brain. *Mol. Psychiatry* **2009**, *14*, 223–232. [CrossRef] [PubMed]
32. Barth, C.; Villringer, A.; Sacher, J. Sex hormones affect neurotransmitters and shape the adult female brain during hormonal transition periods. *Front. Neurosci.* **2015**, *9*, 37. [CrossRef] [PubMed]
33. Hansberg-Pastor, V.; González-Arenas, A.; Piña-Medina, A.G.; Camacho-Arroyo, I. Sex hormones regulate cytoskeletal proteins involved in brain plasticity. *Front. Psychiatry* **2015**, *6*, 165. [CrossRef] [PubMed]
34. Kuiper, G.G.; Carlsson, B.; Grandien, K.; Enmark, E.; Häggblad, J.; Nilsson, S.; Gustafsson, J.A. Comparison of the Ligand Binding Specificity and Transcript Tissue Distribution of Estrogen Receptors  $\alpha$  and  $\beta$ . *Endocrinology* **1997**, *138*, 863–870. [CrossRef]
35. Russo, J.; Russo, I.H. The role of estrogen in the initiation of breast cancer. *J. Steroid Biochem. Mol. Biol.* **2006**, *102*, 89–96. [CrossRef]
36. Cuna, S.; Hoffmann, P.; Pujol, P. Estrogens and epithelial ovarian cancer. *Gynecol. Oncol.* **2004**, *94*, 25–32. [CrossRef]
37. Kumar, M.M.; Davuluri, S.; Poojar, S.; Mukherjee, G.; Bajpai, A.K.; Bafna, U.D.; Devi, U.K.; Kallur, P.P.R.; Kshitish, A.K.; Jayshree, R.S. Role of estrogen receptor alpha in human cervical cancer-associated fibroblasts: A transcriptomic study. *Tumor Biol.* **2016**, *37*, 4409–4420. [CrossRef]
38. Di Zazzo, E.; Galasso, G.; Giovannelli, P.; Di-Donato, M.; Castoria, G. Estrogens and Their Receptors in Prostate Cancer: Therapeutic Implications. *Front. Oncol.* **2018**, *8*, 1–7. [CrossRef]
39. Pearce, S.T.; Jordan, V.C. The biological role of estrogen receptors  $\alpha$  and  $\beta$  in cancer. *Crit. Rev. Oncol. Hematol.* **2004**, *50*, 3–22. [CrossRef]
40. Vaquero, J.; Marcos, M.L.; Martínez, R.; Bravo, G. Estrogen- and progesterone-receptor proteins in intracranial tumors. *Surg. Neurol.* **1983**, *19*, 11–13. [CrossRef]
41. Carroll, R.S.; Zhang, J.; Dashner, K.; Sar, M.; Black, P.M. Steroid Hormone Receptors in Astrocytic Neoplasms. *Neurosurgery* **1995**, *37*, 496–504. [CrossRef] [PubMed]
42. Khalid, H.; Yasunaga, A.; Kishikawa, M.; Shibata, S. Immunohistochemical expression of the estrogen receptor-related antigen (ER-D5) in human intracranial tumors. *Cancer* **1995**, *75*, 2571–2578. [CrossRef]

43. Batistatou, A.; Stefanou, D.; Goussia, A.; Arkoumani, E.; Papavassiliou, A.; Agnantis, N. Estrogen receptor beta (ER $\beta$ ) is expressed in brain astrocytic tumors and declines with dedifferentiation of the neoplasm. *J. Cancer Res. Clin. Oncol.* **2004**, *130*, 405–410. [CrossRef] [PubMed]
44. Sareddy, G.R.; Nair, B.C.; Gonugunta, V.K.; Zhang, Q.g.; Brenner, A.; Brann, D.W.; Tekmal, R.R.; Vadlamudi, R.K. Therapeutic Significance of Estrogen Receptor Agonists in Gliomas. *Mol. Cancer* **2012**, *11*, 1174–1182. [CrossRef] [PubMed]
45. González-Arenas, A.; Hansberg-Pastor, V.; Hernández-Hernández, O.T.; González-García, T.K.; Henderson-Villalpando, J.; Lemus-Hernández, D.; Cruz-Barrios, A.; Rivas-Suárez, M.; Camacho-Arroyo, I. Estradiol increases cell growth in human astrocytoma cell lines through ER $\alpha$  activation and its interaction with SRC-1 and SRC-3 coactivators. *Biochim. Biophys. Acta* **2012**, *1823*, 379–386. [CrossRef] [PubMed]
46. Li, W.; Winters, A.; Poteet, E.; Ryou, M.G.; Lin, S.; Hao, S.; Wu, Z.; Yuan, F.; Hatanpaa, K.J.; Simpkins, J.W.; et al. Involvement of estrogen receptor  $\beta$ 5 in the progression of glioma. *Brain Res.* **2013**, *1503*, 97–107. [CrossRef]
47. Dueñas, J.M.; Candanedo, A.; Santerre, A.; Orozco, S.; Sandoval, H.; Feria, I.; López-Elizalde, R.; Venegas, M.A.; Netel, B.; de la Torre-Valdovinos, B.; et al. Aromatase and estrogen receptor alpha mRNA expression as prognostic biomarkers in patients with astrocytomas. *J. Neurooncol.* **2014**, *119*, 275–284. [CrossRef]
48. Liu, C.; Zhang, Y.; Zhang, K.; Bian, C.; Zhao, Y.; Zhang, J. Expression of estrogen receptors, androgen receptor and steroid receptor coactivator-3 is negatively correlated to the differentiation of astrocytic tumors. *Cancer Epidemiol.* **2014**, *38*, 291–297. [CrossRef]
49. Tavares, C.B.; Gomes-Braga, F.; Sousa, E.B.; Borges, U.S.; Escórcio-Dourado, C.S.; Da Silva-Sampaio, J.P.; Borges da Silva, B. Evaluation of estrogen receptor expression in low-grade and high-grade astrocytomas. *Rev. Assoc. Med. Bras.* **2018**, *64*, 1129–1133. [CrossRef]
50. Wan, S.; Jiang, J.; Zheng, C.; Wang, N.; Zhai, X.; Fei, X.; Wu, R.; Jiang, X. Estrogen nuclear receptors affect cell migration by altering sublocalization of AQP2 in glioma cell lines. *Cell Death Discov.* **2018**, *4*, 49. [CrossRef]
51. Park, S.H.; Cheung, L.W.T.; Wong, A.S.T.; Leung, P.C.K. Estrogen Regulates Snail and Slug in the Down-Regulation of E-Cadherin and Induces Metastatic Potential of Ovarian Cancer Cells through Estrogen Receptor  $\alpha$ . *Mol. Endocrinol.* **2008**, *22*, 2085–2098. [CrossRef] [PubMed]
52. Mishra, S.; Tai, Q.; Gu, X.; Schmitz, J.; Poullard, A.; Fajardo, R.J.; Mahalingam, D.; Chen, X.; Zhu, X.; Sun, L.Z. Estrogen and Estrogen Receptor Alpha Promotes Malignancy and Osteoblastic Tumorigenesis in Prostate Cancer. *Oncotarget* **2015**, *6*, 44388–44402. [CrossRef] [PubMed]
53. Shi, X.; Peng, Y.; Du, X.; Liu, H.; Klocker, H.; Lin, Q.; Shi, J.; Zhang, J. Estradiol promotes epithelial-to-mesenchymal transition in human benign prostatic epithelial cells. *Prostate* **2017**, *77*, 1424–1437. [CrossRef] [PubMed]
54. Dhasarathy, A.; Kajita, M.; Wade, P.A. The Transcription Factor Snail Mediates Epithelial to Mesenchymal Transitions by Repression of Estrogen Receptor- $\alpha$ . *Mol. Endocrinol.* **2007**, *21*, 2907–2918. [CrossRef]
55. Al Saleh, S.; Al Mulla, F.; Luqmani, Y.A. Estrogen receptor silencing induces epithelial to mesenchymal transition in human breast cancer cells. *PLoS ONE* **2011**, *6*, e20610. [CrossRef]
56. Bouris, P.; Skandalis, S.S.; Piperigkou, Z.; Afratis, N.; Karamanou, K.; Aletras, A.J.; Moustakas, A.; Theocharis, A.D.; Karamanos, N.K. Estrogen receptor alpha mediates epithelial to mesenchymal transition, expression of specific matrix effectors and functional properties of breast cancer cells. *Matrix Biol.* **2015**, *43*, 42–60. [CrossRef]
57. Scherbakov, A.M.; Andreeva, O.E.; Shatskaya, V.A.; Krasil’nikov, M.A. The relationships between snail1 and estrogen receptor signaling in breast cancer cells. *J. Cell Biochem.* **2012**, *113*, 2147–2155. [CrossRef]
58. Wik, E.; Ræder, M.B.; Krakstad, C.; Trovik, J.; Birkeland, E.; Hoivik, E.A.; Mjos, S.; Werner, H.M.J.; Mannelqvist, M.; Stefansson, I.M.; et al. Lack of estrogen receptor- $\alpha$  is associated with epithelial-mesenchymal transition and PI3K alterations in endometrial carcinoma. *Clin. Cancer Res.* **2013**, *19*, 1094–1105. [CrossRef]
59. Colaprico, A.; Silva, T.C.; Olsen, C.; Garofano, L.; Cava, C.; Garolini, D.; Sabedot, T.S.; Malta, T.M.; Pagnotta, S.M.; Castiglioni, I.; et al. TCGAAbiolinks: An R/Bioconductor package for integrative analysis of TCGA data. *Nucleic Acids Res.* **2016**, *44*, e71. [CrossRef]
60. Costa-Silva, J.; Domingues, D.; Lopes, F.M. RNA-Seq differential expression analysis: An extended review and a software tool. *PLoS ONE* **2017**, *12*, e0190152. [CrossRef]
61. Bakal, C.; Church, G.; Perrimon, N. Quantitative Morphological Signatures Define Local Signaling Networks Regulating Cell Morphology. *Science* **2007**, *316*, 1753–1756. [CrossRef] [PubMed]

62. Carpenter, A.E.; Jones, T.R.; Lamprecht, M.R.; Clarke, C.; Kang, I.; Friman, O.; Guertin, D.A.; Chang, J.H.; Lindquist, R.A.; Moffat, J.; et al. CellProfiler: Image analysis software for identifying and quantifying cell phenotypes. *Genome Biol.* **2006**, *7*, R100. [CrossRef] [PubMed]
63. Chen, S.; Zhao, M.; Wu, G.; Yao, C.; Zhang, J. Recent Advances in Morphological Cell Image Analysis. *Comput. Math. Methods Med.* **2012**, *2012*, 101536. [CrossRef] [PubMed]
64. Ren, Z.X.; Yu, H.B.; Li, J.S.; Shen, J.L.; Du, W.S. Suitable parameter choice on quantitative morphology of A549 cell in epithelial—mesenchymal transition. *Biosci. Rep.* **2015**, *35*, e00202. [CrossRef]
65. Schmittgen, T.D.; Livak, K.J. Analyzing real-time PCR data by the comparative CT method. *Nat. Protoc.* **2008**, *3*, 1101–1108. [CrossRef]
66. Pfaffl, M.W. A new mathematical model for relative quantification in real-time RT-PCR. *Nucleic Acids Res.* **2001**, *29*, e45. [CrossRef]
67. Sottoriva, A.; Spiteri, I.; Piccirillo, S.G.M.; Touloumis, A.; Collins, V.P.; Marioni, J.C.; Curtis, C.; Watts, C.; Tavaré, S. Intratumor heterogeneity in human glioblastoma reflects cancer evolutionary dynamics. *Proc. Natl. Acad. Sci. USA* **2013**, *110*, 4009–4014. [CrossRef]
68. Patel, A.P.; Tirosh, I.; Trombetta, J.J.; Shalek, A.K.; Gillespie, S.M.; Wakimoto, H.; Cahill, D.P.; Nahed, B.V.; Curry, W.T.; Martuza, R.L.; et al. Single-cell RNA-seq highlights intratumoral heterogeneity in primary glioblastoma. *Science* **2014**, *344*, 1396–1401. [CrossRef]
69. Lin, N.; Yan, W.; Gao, K.; Wang, Y.; Zhang, J.; You, Y. Prevalence and clinicopathologic characteristics of the molecular subtypes in malignant glioma: A multi-institutional analysis of 941 cases. *PLoS ONE* **2014**, *9*, e94871. [CrossRef]
70. Olar, A.; Aldape, K.D. Using the molecular classification of glioblastoma to inform personalized treatment. *J. Pathol.* **2014**, *232*, 165–177. [CrossRef]
71. Ozawa, T.; Riester, M.; Cheng, Y.; Huse, J.T.; Squatrito, M.; Helmy, K.; Charles, N.; Michor, F.; Holland, E.C. Most Human Non-GCIMP Glioblastoma Subtypes Evolve from a Common Proneural-like Precursor Glioma. *Cancer Cell* **2014**, *26*, 288–300. [CrossRef] [PubMed]
72. Segerman, A.; Niklasson, M.; Haglund, C.; Bergström, T.; Jarvius, M.; Xie, Y.; Westermark, A.; Sönmez, D.; Hermansson, A.; Kastemar, M.; et al. Clonal Variation in Drug and Radiation Response among Glioma-Initiating Cells Is Linked to Proneural-Mesenchymal Transition. *Cell Rep.* **2016**, *17*, 2994–3009. [CrossRef] [PubMed]
73. Fedele, M.; Cerchia, L.; Pegoraro, S.; Sgarra, R.; Manfioletti, G. Proneural-mesenchymal transition: Phenotypic plasticity to acquire multitherapy resistance in glioblastoma. *Int. J. Mol. Sci.* **2019**, *20*, 2746. [CrossRef] [PubMed]
74. Wang, Q.; Hu, B.; Hu, X.; Kim, H.; Squatrito, M.; Scarpace, L.; deCarvalho, A.C.; Lyu, S.; Li, P.; Li, Y.; et al. Tumor Evolution of Glioma-Intrinsic Gene Expression Subtypes Associates with Immunological Changes in the Microenvironment. *Cancer Cell* **2017**, *32*, 42–56. [CrossRef]
75. Stanzani, E.; Martínez-Soler, F.; Mateos, T.M.; Vidal, N.; Villanueva, A.; Pujana, M.A.; Serra-Musach, J.; Iglesia, N.; Giménez-Bonafé, P.; Tortosa, A. Radioresistance of mesenchymal glioblastoma initiating cells correlates with patient outcome and is associated with activation of inflammatory program. *Oncotarget* **2017**, *8*, 73640–73653. [CrossRef]
76. Kaffes, I.; Szulzewsky, F.; Chen, Z.; Herting, C.J.; Gabanic, B.; Velazquez, J.E.; Shelton, J.; Switchenko, J.M.; Ross, J.L.; McSwain, L.F.; et al. Human Mesenchymal glioblastomas are characterized by an increased immune cell presence compared to Proneural and Classical tumors presence compared to Proneural and Classical tumors. *Oncoimmunology* **2019**, *8*, e1655360. [CrossRef]
77. Quail, D.F.; Joyce, J.A. The Microenvironmental Landscape of Brain Tumors. *Cancer Cell* **2017**, *31*, 326–341. [CrossRef]
78. Bruce-Keller, A.J.; Keeling, J.L.; Keller, J.N.; Huang, F.F.; Camondola, S.; Mattson, M.P. Antiinflammatory effects of estrogen on microglial activation. *Endocrinology* **2000**, *141*, 3646–3656. [CrossRef]
79. Baker, A.E.; Brautigam, V.M.; Watters, J.J. Estrogen modulates microglial inflammatory mediator production via interactions with estrogen receptor  $\beta$ . *Endocrinology* **2004**, *145*, 5021–5032. [CrossRef]
80. Acaz-Fonseca, E.; Sanchez-Gonzalez, R.; Azcoitia, I.; Arevalo, M.A.; Garcia-Segura, L.M. Role of Astrocytes in the Neuroprotective Actions of  $17\beta$ -estradiol and Selective Estrogen Receptor Modulators. *Mol. Cell Endocrinol.* **2014**, *389*, 48–57. [CrossRef]

81. Pinacho-Garcia, L.M.; Valdez, R.A.; Navarrete, A.; Cabeza, M.; Segovia, J.; Romano, M.C. The Effect of Finasteride and Dutasteride on the Synthesis of Neurosteroids by Glioblastoma Cells. *Steroids* **2020**, *155*, 108556. [CrossRef] [PubMed]
82. Reijm, E.; Jansen, M.; Ruigrok-Ritstier, K.; van Staveren, I.L.; Look, M.; van Gelder, M.E.M.; Sieuwerts, A.M.; Sleijfer, S.; Foekens, J.A.; Berns, E.M.J.J. Decreased expression of EZH2 is associated with upregulation of ER and favorable outcome to tamoxifen in advanced breast cancer. *Breast Cancer Res Treat* **2011**, *125*, 387–394. [CrossRef] [PubMed]
83. Frasor, J.; Weaver, A.; Pradhan, M.; Dai, Y.; Miller, L.D.; Lin, C.Y.; Stanculescu, A. Positive cross-talk between estrogen receptor and NF- $\kappa$ B in breast cancer. *Cancer Res.* **2009**, *14*, 8918–8925. [CrossRef] [PubMed]
84. Frasor, J.; El-Shennawy, L.; Stender, J.; Kastrati, I. NF $\kappa$ B affects estrogen receptor expression and activity in breast cancer through multiple mechanisms. *Mol. Cell Endocrinol.* **2015**, *418*, 235–239. [CrossRef] [PubMed]
85. Hui, H.; Hongying, Z.; Qingbin, K.; Yangfu, J. Mechanisms for estrogen receptor expression in human cancer. *Exp. Hematol. Oncol.* **2018**, *7*, 24. [CrossRef]
86. Katzenellenbogen, J.; Mayne, C.; Katzenellenbogen, B.; Greene, G.; Chandralapaty, S. Structural Underpinnings of Estrogen Receptor Mutations in Endocrine Therapy Resistance. *Nat. Rev. Cancer* **2018**, *18*, 377–388. [CrossRef]
87. Christoforos, T.; Gustafsson, J. Estrogen receptor mutations and functional consequences for breast cancer. *Trends Endocrinol Metab* **2015**, *26*, 467–476. [CrossRef]
88. Thompson, S.; Petti, F.; Sujka-Kwok, I.; Mercado, P.; Bean, J.; Monaghan, M.; Seymour, S.L.; Argast, G.M.; Epstein, D.M.; Haley, J.D. A systems view of epithelial-mesenchymal transition signaling states. *Clin Exp Metastasis* **2011**, *28*, 137–155. [CrossRef]
89. D’Souza, R.; Knitte, A.; Nagaraj, N.; van Dinther, M.; Choudhary, C.; Dijke, P.; Mann, M.; Sharma, K. Time-resolved dissection of early phosphoproteome and ensuing proteome changes in response to TGF- $\beta$ . *Sci Signal* **2014**, *7*, 5. [CrossRef]
90. Rojas-Puente, L.; Cardona, A.; Carranza, H.; Vargas, C.; Jaramillo, L.; Zea, D.; Cetina, L.; Wills, B.; Ruiz-Garcia, E.; Arrieta, O. Epithelial-mesenchymal transition, proliferation, and angiogenesis in locally advanced cervical cancer treated with chemoradiotherapy. *Cancer Med.* **2016**, *5*, 1989–1999. [CrossRef]
91. Qun-Ying, L.; Zhang, H.; Zhao, B.; Zheng-Yu, Z.; Bai, F.; Xin-Hai, P.; Zhao, S.; Xiong, Y.; Kun-Liang, G. TAZ promotes cell proliferation and epithelial-mesenchymal transition and is inhibited by the hippo pathway. *Mol. Cell Biol.* **2008**, *28*, 2426–2436. [CrossRef]
92. Castruccio, C.; Longhitano, L.; Distefano, A.; Anfusio, D.; Kalampoka, S.; Spina, E.L.; Astuto, M.; Avola, R.; Caruso, M.; Nicolosi, D.; et al. Role of 17 $\beta$ -Estradiol on Cell Proliferation and Mitochondrial Fitness in Glioblastoma Cells. *J. Oncol.* **2020**, *2020*, 2314693. [CrossRef]
93. DePasquale, J.A. Rearrangement of the F-actin cytoskeleton in estradiol-treated MCF-7 breast carcinoma cells. *Histochem. Cell Biol.* **1999**, *112*, 341–350. [CrossRef] [PubMed]
94. Briz, V.; Baudry, M. Estrogen regulates protein synthesis and actin polymerization in hippocampal neurons through different molecular mechanisms. *Front. Endocrinol* **2014**, *5*, 22. [CrossRef] [PubMed]
95. Carnesecchi, J.; Malbouyres, M.; De Mets, R.; Bolland, M.; Beauchef, G.; Vié, K.; Chamot, C.; Lionnet, C.; Ruggiero, F.; Vanacker, J.M. Estrogens Induce Rapid Cytoskeleton Re-Organization in Human Dermal Fibroblasts via the Non-Classical Receptor GPR30. *PLoS ONE* **2015**, *10*, e0120672. [CrossRef]
96. Flamini, M.I.; Sanchez, A.M.; Goglia, L.; Tosi, V.; Genazzani, A.R.; Simoncini, T. Differential actions of estrogen and SERMs in regulation of the actin cytoskeleton of endometrial cells. *Mol. Hum. Reprod.* **2009**, *15*, 675–685. [CrossRef]
97. O’Neill, G.M. The coordination between actin filaments and adhesion in mesenchymal migration. *Cell Adhes. Migr.* **2009**, *3*, 355–357. [CrossRef]
98. Hotulainen, P.; Lappalainen, P. Stress fibers are generated by two distinct actin assembly mechanisms in motile cells. *J. Cell Biol.* **2006**, *173*, 383–394. [CrossRef]
99. Zaidel-Bar, R.; Ballestrem, C.; Kam, Z.; Geiger, B. Early molecular events in the assembly of matrix adhesions at the leading edge of migrating cells. *J. Cell Sci.* **2003**, *116*, 4605–4613. [CrossRef]
100. Saitoh, M. Involvement of partial EMT in cancer progression. *J. Biochem.* **2018**, *164*, 257–264. [CrossRef]
101. Aiello, N.M.; Maddipati, R.; Norgard, R.J.; Balli, D.; Li, J.; Yuan, S.; Yamazoe, T.; Black, T.; Sahnoud, A.; Furth, E.E.; et al. EMT Subtype Influences Epithelial Plasticity and Mode of Cell Migration. *Dev. Cell* **2018**, *45*, 681–695.e4. [CrossRef] [PubMed]

102. Yang, J.; Antin, P.; Berx, G.; Blanpain, C.; Brabletz, T.; Bronner, M.; Campbell, K.; Cano, A.; Casanova, J.; Christofori, G.; et al. Guidelines and definitions for research on epithelial–mesenchymal transition. *Nat. Rev. Mol. Cell Biol.* **2020**, *21*, 341–352. [CrossRef] [PubMed]
103. Bazzoni, G.; Martínez-Estrada, O.M.; Orsenigo, F.; Cordenonsi, M.; Citi, S.; Dejana, E. Interaction of junctional adhesion molecule with the tight junction components ZO-1, cingulin, and occludin. *J. Biol. Chem.* **2000**, *275*, 20520–20526. [CrossRef]
104. Ebnet, K.; Schulz, C.U.; Meyer Zu Brickwedde, M.K.; Pendl, G.G.; Vestweber, D. Junctional adhesion molecule interacts with the PDZ domain-containing proteins AF-6 and ZO-1. *J. Biol. Chem.* **2000**, *275*, 27979–27988. [CrossRef]
105. McNeil, E.; Capaldo, C.T.; Macara, I.G. Zonula Occludens-1 Function in the Assembly of Tight Junctions in Madin-Darby Canine Kidney Epithelial Cells. *Mol. Biol. Cell* **2006**, *17*, 1922–1932. [CrossRef] [PubMed]
106. Fanning, A.S.; Anderson, J.M. Zonula Occludens-1 and -2 Are Cytosolic Scaffolds That Regulate the Assembly of Cellular Junctions. *Ann. N. Y. Acad. Sci.* **2009**, *1165*, 113–120. [CrossRef]
107. Patil, V.; Pal, J.; Somasundaram, K. Elucidating the cancer-specific genetic alteration spectrum of glioblastoma derived cell lines from whole exome and RNA sequencing. *Oncotarget* **2015**, *6*, 43452–43471. [CrossRef]
108. Li, H.; Lei, B.; Xiang, W.; Wang, H.; Feng, W.; Liu, Y.; Qi, S. Differences in protein expression between the U251 and U87 cell lines. *Turk. Neurosurg.* **2017**, *27*, 894–903. [CrossRef]
109. Derycke, L.D.M.; Bracke, M.E. N-cadherin in the spotlight of cell-cell adhesion, differentiation, embryogenesis, invasion and signalling. *Int. J. Dev. Biol.* **2004**, *48*, 463–476. [CrossRef]
110. Shih, W.; Yamada, S. N-cadherin-mediated cell-cell adhesion promotes cell migration in a three-dimensional matrix. *J. Cell Sci.* **2012**, *125*, 3661–3670. [CrossRef]
111. Shih, W.; Yamada, S. N-cadherin as a key regulator of collective cell migration in a 3D environment. *Cell Adhes. Migr.* **2012**, *6*, 513–517. [CrossRef] [PubMed]
112. Katsumoto, T.; Mitsushima, A.; Kurimura, T. The role of the vimentin intermediate filaments in rat 3Y1 cells elucidated by immunoelectron microscopy and computer-graphic reconstruction. *Biol. Cell* **1990**, *68*, 139–146. [CrossRef]
113. Chang, L.; Goldman, R.D. Intermediate filaments mediate cytoskeletal crosstalk. *Nat. Rev. Mol. Cell Biol.* **2004**, *5*, 601–613. [CrossRef]
114. Goldman, R.D.; Khuon, S.; Chou, Y.H.; Opal, P.; Steinert, P.M. The function of intermediate filaments in cell shape and cytoskeletal integrity. *J. Cell Biol.* **1996**, *134*, 971–983. [CrossRef] [PubMed]
115. Stauffer, S.R.; Coletta, C.J.; Tedesco, R.; Nishiguchi, G.; Carlson, K.; Sun, J.; Katzenellenbogen, B.S.; Katzenellenbogen, J.A. Pyrazole ligands: Structure-Affinity/activity relationships and estrogen receptor- $\alpha$ -selective agonists. *J. Med. Chem.* **2000**, *43*, 4934–4947. [CrossRef] [PubMed]
116. Sun, J.; Huang, Y.R.; Harrington, W.R.; Sheng, S.; Katzenellenbogen, J.A.; Katzenellenbogen, B.S. Antagonists selective for estrogen receptor  $\alpha$ . *Endocrinology* **2002**, *143*, 941–947. [CrossRef]
117. Meyers, M.J.; Sun, J.; Carlson, K.E.; Marriner, G.A.; Katzenellenbogen, B.S.; Katzenellenbogen, J.A. Estrogen receptor- $\beta$  potency-selective ligands: Structure-activity relationship studies of diarylpropionitriles and their acetylene and polar analogues. *J. Med. Chem.* **2001**, *44*, 4230–4251. [CrossRef]



© 2020 by the authors. Licensee MDPI, Basel, Switzerland. This article is an open access article distributed under the terms and conditions of the Creative Commons Attribution (CC BY) license (<http://creativecommons.org/licenses/by/4.0/>).



Article

# Targeting BC200/miR218-5p Signaling Axis for Overcoming Temozolomide Resistance and Suppressing Glioma Stemness

Yu-Kai Su <sup>1,2,3,4,†</sup>, Jia Wei Lin <sup>1,2,3,4,†</sup>, Jing-Wen Shih <sup>5,6</sup> , Hao-Yu Chuang <sup>7</sup>, Iat-Hang Fong <sup>2,3,4</sup>, Chi-Tai Yeh <sup>1,8,9</sup>  and Chien-Min Lin <sup>1,2,3,4,\*</sup> 

<sup>1</sup> Graduate Institute of Clinical Medicine, College of Medicine, Taipei Medical University, Taipei City 11031, Taiwan; yukai.su@gmail.com (Y.-K.S.); ns246@tmu.edu.tw (J.W.L.); ctyeh@s.tmu.edu.tw (C.-T.Y.)

<sup>2</sup> Department of Neurology, School of Medicine, College of Medicine, Taipei Medical University, Taipei City 11031, Taiwan; impossiblewasnothing@hotmail.com

<sup>3</sup> Division of Neurosurgery, Department of Surgery, Taipei Medical University-Shuang Ho Hospital, New Taipei City 23561, Taiwan

<sup>4</sup> Taipei Neuroscience Institute, Taipei Medical University, Taipei City 11031, Taiwan

<sup>5</sup> Graduate Institute of Cancer Biology and Drug Discovery, College of Medical Science and Technology, Taipei Medical University, Taipei 11031, Taiwan; shihjw@tmu.edu.tw

<sup>6</sup> Ph.D. Program for Cancer Biology and Drug Discovery, College of Medical Science and Technology, Taipei Medical University, Taipei 11031, Taiwan

<sup>7</sup> Department of Neurosurgery, An Nan Hospital, China Medical University, Tainan 70965, Taiwan; greeberg1975@gmail.com

<sup>8</sup> Department of Medical Research & Education, Taipei Medical University-Shuang Ho Hospital, New Taipei City 23561, Taiwan

<sup>9</sup> Department of Medical Laboratory Science and Biotechnology, Yuanpei University of Medical Technology, Hsinchu 300, Taiwan

\* Correspondence: m513092004@tmu.edu.tw; Tel.: +886-2-2490088 (ext. 8881)

† These authors contributed equally to this work.

Received: 15 May 2020; Accepted: 4 August 2020; Published: 8 August 2020



**Abstract:** *Background:* Glioblastoma (GB) is one of the most common (~30%) and lethal cancers of the central nervous system. Although new therapies are emerging, chemoresistance to treatment is one of the major challenges in cancer treatment. Brain cytoplasmic 200 (BC200) RNA, also known as BCYRN1, is a long noncoding RNA (lncRNA) that has recently emerged as one of the crucial members of the lncRNA family. BC200 atypical expression is observed in many human cancers. BC200 expression is higher in invasive cancers than in benign tumors. However, the clinical significance of BC200 and its effect on GB multiforme is still unexplored and remains unclear. *Methods:* BC200 expression in GB patients and cell lines were investigated through RT-qPCR, immunoblotting, and immunohistochemistry analysis. The biological importance of BC200 was investigated in vitro and in vivo through knockdown and overexpression. Bioinformatic analysis was performed to determine miRNAs associated with BC200 RNA. *Results:* Our findings revealed that in GB patients, BC200 RNA expression was higher in blood and tumor tissues than in normal tissues. BC200 RNA expression have a statistically significant difference between the IDH1 and P53 status. Moreover, the BC200 RNA expression was higher than both p53, a prognostic marker of glioma, and Ki-67, a reliable indicator of tumor cell proliferation activity. Overexpression and silencing of BC200 RNA both in vitro and in vivo significantly modulated the proliferation, self-renewal, pluripotency, and temozolomide (TMZ) chemo-resistance of GB cells. It was found that the expressions of BC200 were up-regulated and that of miR-218-5p were down-regulated in GB tissues and cells. miR-218-5p inhibited the expression of BC200. *Conclusions:* This study is the first to show that the molecular mechanism of BC200 promotes GB oncogenicity and TMZ resistance through miR-218-5p expression

modulation. Thus, the noncoding RNA BC200/miR-218-5p signaling circuit is a potential clinical biomarker or therapeutic target for GB.

**Keywords:** non-coding RNA; noncoding RNA BC200/miR-218-5p signaling circuit; glioblastoma stem cells; temozolomide resistance

---

## 1. Background

Glioblastoma (GB) is one of the most common (~30%) and lethal cancers of the central nervous system [1]. The World Health Organization classifies glioma into grades I to IV based on its histopathologically determined malignancy level [2]. GB, a grade IV astrocytoma, is highly aggressive, malignant and invasive [3]. Despite improved therapeutic interventions, the treatment of high-grade glioma is challenging, even after combining radiation therapy with surgical resection [4]. Therefore, the molecular mechanism of GB pathogenesis and treatment resistance must be explored. With the advances in sequencing technologies, evidence indicates a regulatory role of long noncoding RNA (lncRNA) [5]. Recent studies have shown that lncRNAs play a role in the development, progression, and metastasis [6] of many cancers, including GB [7]. These lncRNAs consist of >200 nucleotides and cannot translate proteins. Furthermore, studies have reported dysregulated lncRNA expressions, which determine the temozolomide (TMZ)-drug sensitivity or TMZ-drug resistance of GB [8]. This lncRNA exerts its functions through lncRNA–miRNA interactions and mRNA silencing [9].

BCYRN1, also known as brain cytoplasmic 200 (BC200) RNA, is a lncRNA highly expressed in the brain (neuron-specific transcript) in the presence of neurodegenerative diseases [10]. Sometimes, BC200 RNA expression is atypically elevated in the presence of various human cancers [11] and its expression is higher in invasive cancer cells than in benign tumors [12]. BC200 RNA was also found in blood specimens such as breast cancer and hepatocellular carcinoma [13,14]. These data suggest the BC200 RNA has potential value as a diagnostic and prognostic marker for human cancers. However, information regarding BC200 RNA as a clinical biomarker or therapeutic target for GB is still lacking. The exact underlying molecular mechanism of BC200 RNA in glioma development and progression is still under investigation.

In this study, the role of BC200 RNA in GB was evaluated to understand the molecular mechanism of chemoresistance and disease progression. The expression level of BC200 RNA in the tissue of GB patients and GB cell lines was evaluated. The sulforhodamine B (SRB) assay was used to determine the effect of TMZ treatment on GB cells. Furthermore, the stem cell population was evaluated through flow cytometric analysis of GB cell lines. Overexpression and silencing of BC200 RNA showed its role in survival and GB tumorigenesis reduction both *in vitro* and *in vivo*. Ours is the first study to show the molecular mechanism of BC200 RNA in the promotion of TMZ resistance in GB through miR-218-5p expression modulation. Thus, BC200 RNA is suggested as a potential clinical biomarker or therapeutic target for GB.

## 2. Materials and Methods

### 2.1. Patients and Tumor Samples

The study was approved by the Joint Institutional Review Board (JIRB) of the Taipei Medical University—Shuang Ho Hospital. Written informed consents were obtained from all participants (Approval number: N201903047). Tissue samples from patients with primary and recurrent GB were obtained from the Taipei Medical University–Shuang Ho Hospital GB cohort. Surgically resected tissues samples were immediately frozen in RNALater (QIAGEN, Hilden, Germany) and subsequently stored at –80 °C until use.

## 2.2. Cell Lines and Cell Culture

Human GB cell line T98G (ATCC<sup>®</sup> CRL-1690<sup>™</sup>) (ATCC, Manassas, VA, USA) and U87MG (ATCC<sup>®</sup> HTB-14<sup>™</sup>) (ATCC) were cultured in DMEM; DBTRG-05MG (ATCC<sup>®</sup> CRL-2020<sup>™</sup>) (ATCC) and GBM8901 (Bioresource Collection and Research Center, Hsinchu, Taiwan) were cultured in RPMI. In order to demonstrate the association between BC200 and MGMT, the U87MG cells were transfected to overexpress MGMT. The human MGMT open reading frame (ORF) plasmid was purchased from OriGene (Cat# MGMT (RC229131, Taipei, Taiwan) and the cells transfected according to vendor's instructions; MGMT-overexpressing U87MG cells were then allowed to grow at 37 °C in 5% CO<sub>2</sub> humidified atmosphere in Dulbecco's modified Eagle's medium (DMEM). Media was supplemented with 10% fetal bovine serum, and streptomycin (100 µg/mL), penicillin (100 IU/mL), and at 80% confluency the cells were sub-cultured every 2–3 days. The expression of MGMT was verified by western blots.

## 2.3. Sulforhodamine B (SRB) Viability Assay

T98G, U87MG, DBTRG-05MG and GBM8901 cells were seeded in 96-well plates in triplicates at a concentration of 3000 cells per well. After 24 h incubation in a 5% CO<sub>2</sub> humidified incubator at 37 °C, the cells were treated with varying concentrations of 0–1000 µM TMZ as indicated for 24 h. Thereafter, cells were washed in PBS twice, fixed in cold 10% trichloroacetic acid (TCA) for 1h, washed with distilled water, and then incubated in 0.4 SRB (*w/v*) in 1% acetic acid at room temperature for 1 h. After washing of unbound SRB dye with 1% acetic acid thrice, the plates were air-dried. Attached dye was dissolved in 20 mM trizma base, and absorbance was read in a microplate reader at a wavelength of 570 nm. (Molecular Devices, Sunnyvale, CA, USA).

## 2.4. Cell Proliferation Assay

Cell Counting Kit-8 (CCK-8, Dojindo Laboratories, Rockville, MD, USA) was applied for detecting the cell proliferation. T98G, U87MG, DBTRG-05MG and GBM8901 cells were seeded in 96-well plates in triplicates, incubated for 24, 48, 72 or 96 hrs. For each time point, 10 µL CCK-8 solution was added per well and the cells were incubated at 37 °C for 2 h and absorbance was read in a microplate reader at a wavelength of 450 nm. (Molecular Devices).

## 2.5. Vector Construction and Infection

Lentivirus containing BC200 short hairpin (shBC200) RNA and BC200 overexpression (OEBC200) vectors were purchased from ThermoFisher Scientific (Waltham, MA, USA) and were used according to the manufacturer's instructions. Two clones of shRNA were used to effectively knockdown (shBC200) and overexpress (OEBC200) BC200; the complete procedure of shRNA lentivirus infection and construction was conducted according to the practice guidelines at a certified BSL-2 laboratory, The Integrated Laboratories for Translational Medicine, Taipei Medical University. Human GB cells were transfected with miR-218-5p (mimic), miR-negative control (miR-NC), and miR-218-5p (inhibitor) were purchased from Qiagen and used as per the manufacturer's protocol.

## 2.6. Immunohistochemistry

For immunohistochemical (IHC) staining, GB tissue ( $n = 48$ ) and non-tumor brain tissue ( $n = 15$ ) sections (5-µm thick) were obtained from formalin-fixed and paraffin-embedded tissue blocks. Then, the samples were incubated overnight in primary antibodies against mut-p53, Ki-67, MGMT, SOX2, OCT4, BCRP1, MDR1, and MRP1 at 4 °C. The anti-human primary antibodies were shown in Supplementary Table S1. After the primary antibodies were washed off, the sections were incubated with goat anti-mouse biotin-conjugated secondary antibodies (1:1000 dilution; Ventana, Oro Valley, AZ, USA) for 20 min at 37 °C. Then, the tissue sections were incubated with streptavidin horseradish peroxidase for 20 min at 37 °C. A 3,3'-diaminobenzidine substrate was applied to the section for

10 min before counterstaining with hematoxylin. The sections in which the primary antibodies were eliminated were used as negative controls.

### 2.7. Western Blot and RT-qPCR

GB cells were washed with PBS and then lysed in RIPA lysis buffer. Cellular protein lysates were isolated using Protein Extraction Kit (Qiagen, Germantown, MD, USA) and quantified using Bradford Protein Assay Kit (Qiagen). In total, 20 µg of samples from different experiments were loaded and subjected to SDS-PAGE using the Mini-Protean III system (Bio-Rad, Taipei City, Taiwan). Separated proteins were transferred onto polyvinylidene fluoride (PVDF) membranes using Trans-Blot Turbo Transfer System (Bio-Rad) followed by blocking with Tris-buffered saline plus skim milk. Then, these PVDF membranes were probed with respective primary antibodies followed by a secondary antibody. The primary antibodies for CD133, KLF4, and SOX2 are shown in Supplementary Table S1. ECL detection kit was used for detecting proteins of interest. Images were captured and analyzed using an UVP BioDoc-It system (Analytik Jena, Thuringia, Germany). RT-qPCR was performed using isolated total RNA according to the TRIzol-based protocol (Life Technologies, Carlsbad, CA, USA) provided by the manufacturer. One microgram of total RNA was reverse transcribed using a Qiagen OneStep RT-PCR Kit (Qiagen), and the PCR reaction was performed using a Rotor-Gene SYBR Green PCR Kit (400, Qiagen).

### 2.8. Colony Formation Assay

The colony-forming assay was performed through modification of a previously explained protocol [15]. Briefly, 500 GB cells (BC200, suppressed and overexpressed) were seeded in six-well plates. These cells were allowed to grow for a week and then harvested, fixed, and counted.

### 2.9. Wound Healing Migration Assay

GB cells were seeded in six-well plates (Corning, Corning, NY, USA) with RPMI 1640 medium containing 10% FBS and cultured to 95–100% confluence. Then, a scratch was made along the median axis with a sterile yellow pipette tip across the cells. Cell migration pictures were captured at 0 and 48 h after the medium scratch under a microscope and analyzed with NIH Image J software (<https://imagej.nih.gov/ij/download.html>).

### 2.10. Matrigel Invasion Assay

GB cells ( $2 \times 10^5$ ) were seeded in 24-transwell chambers with an 8-µm pore membrane coated with Matrigel in the upper chamber of the transwell system containing serum-free RPMI 1640 medium. The lower chamber of the transwell contained a medium with 20% FBS. After incubation of the cells at 37 °C for 6 h, noninvaded GB cells on the upper side of the membrane were carefully removed with a cotton swab, whereas the invaded cells were stained with crystal violet dye, air-dried, and photographed under a microscope. Images were analyzed using NIH Image J software. (<https://imagej.nih.gov/ij/download.html>).

### 2.11. Sphere Formation Assay

GB cells ( $5 \times 10^3$  per well) were plated in ultra-low-attachment six-well plates (Corning) containing stem-cell medium consisting of serum-free RPMI 1640 medium supplemented with 10 ng/mL human basic fibroblast growth factor (Invitrogen, Grand Island, NY, USA),  $1 \times B27$  supplement (Thermo Fisher Scientific, Carlsbad, CA, USA), and 20 ng/mL epidermal growth factor (Invitrogen). The medium was changed every 72 h. After incubation for 7–14 days, the spheres formed were counted and photographed.

### 2.12. Flow Cytometry

One of the characteristics of cancer stem cells (CSCs) is an increased aldehyde dehydrogenase (ALDH) activity compared with non-CSCs counterparts. In this study, Aldefluor assay kit (StemCell

Technologies, Kent, WA, USA) was used to determine the ALDH activity of GB cell lines following the standard protocol. GB cells were removed from the culture dishes with Trypsin-EDTA (Invitrogen), suspended in a buffer containing an ALDH substrate, and incubated at 37 °C for 1.5 h. Flow cytometry was performed using BD LSRFortessa (BD Biosciences, East Rutherford, NJ, USA), and results were analyzed using BD software. Annexin-V was used to detect the drug-induced apoptosis [16]. PE Annexin V and its binding buffer were purchased from Becton-Dickinson. During apoptosis, the phospholipid phosphatidylserine (PS) is translocated from the inner to the outer leaflet of the plasma membrane, thus exposing PS to the external cellular environment. Annexin V has a high affinity for PS, and staining with PE Annexin V serves as a sensitive probe for flow cytometric analysis of cells that are undergoing apoptosis.

### 2.13. *In Vivo* Studies

An animal study was conducted according to the protocols approved by the Taipei Medical University (Laboratory Animal Center, Affidavit of Approval of Animal Use Protocol, Taipei Medical University, protocol no. LAC-2017-0512). NOD/SCID mice (6–8 weeks old) were purchased from Bio-LASCO Taiwan Co., Ltd. A subcutaneous GB xenograft mouse model was established using tumor spheres grown from GBM8901 cells ( $1 \times 10^6$  cells/20  $\mu$ L/injection). All treatments started when the tumor became palpable. Mice were then randomly subdivided into four groups: vehicle control (sham injection), TMZ (0.9 mg/kg, p.o., five times/week), shBC200 (where BC200-silenced GBM8901 tumor spheres were injected), and combination of shBC200 with TMZ treatment (0.9 mg/kg, p.o., five times/week). The tumor size was measured using a standard caliper once a week and expressed in cubic centimeters using the formula tumor volume = (length  $\times$  width<sup>2</sup>)/2, where length represents the longest tumor diameter, and width represents the perpendicular tumor diameter. After the experimental period, mice were sacrificed humanely and tumor samples were collected for further analysis.

### 2.14. Statistical Analysis

All experiments were executed in triplicates. The comparison between two groups was done using the 2-sided Student's t-test, while one-way analysis of variance (ANOVA) was used to compare  $\geq 3$  groups. A *p*-value < 0.05 was considered statistically significant. The Chi-square test were used to evaluate the correlation between BC200 expression and clinicopathological features of primary glioblastoma (GB) patients.

## 3. Results

### 3.1. Upregulation of BC200 RNA Expression in GB Patients

We examined the association of BC200 expression with clinicopathological features of patients with primary GB (*n* = 48). All related data collected are summarized in Table 1.

Our results showed that BC200 RNA expression have a statistically significant difference between the IDH1 and P53 status. No significant correlation was observed between age and gender. For evaluate the role of BC200 RNA in GB, we initially detected the expression level of BC200 RNA in the blood (whole blood and peripheral blood) of GB and normal patients. Results revealed elevated levels (~2 folds) of BC200 RNA expression in GB patients compared with healthy participants (Figure 1A). Furthermore, the results of IHC analysis of tissue sections obtained from GB patients showed concordance with those of RT-qPCR. Quantitative analysis shows that BC200 RNA expression was higher in 48 GB tissues than in 15 normal adjacent tissues (Figure 1B). The widely used markers to determine the prognostic behavior of brain tumors and survival of GB patients are Ki-67 and p53 [17,18]. Figure 1C,D indicates that high BC200 RNA expression was positively correlated with Ki-67 (*p* < 0.001) and p53-mut expression (*p* < 0.01), suggesting that BC200 RNA is strongly associated with unfavorable prognoses in GB patients.

**Table 1.** Analysis of the association of BC200 expression with clinicopathological features of patients with primary GB ( $n = 48$ ).

	High BC200 n=25 (52%)	Low BC200 n=23 (48%)	<i>p</i> -Value
Age			
<65	15 (60%)	8 (35%)	0.0806
≥65	10 (40%)	15 (65%)	
Gender			
male	14 (56%)	13 (57%)	0.971
female	11 (44%)	10 (43%)	
IDH1 status			
wildtype	24 (96%)	17 (74%)	0.0303
mutation	1 (4%)	6 (26%)	
P53 status			
wildtype	9 (36%)	15 (65%)	0.0431
mutation	16 (64%)	8 (35%)	

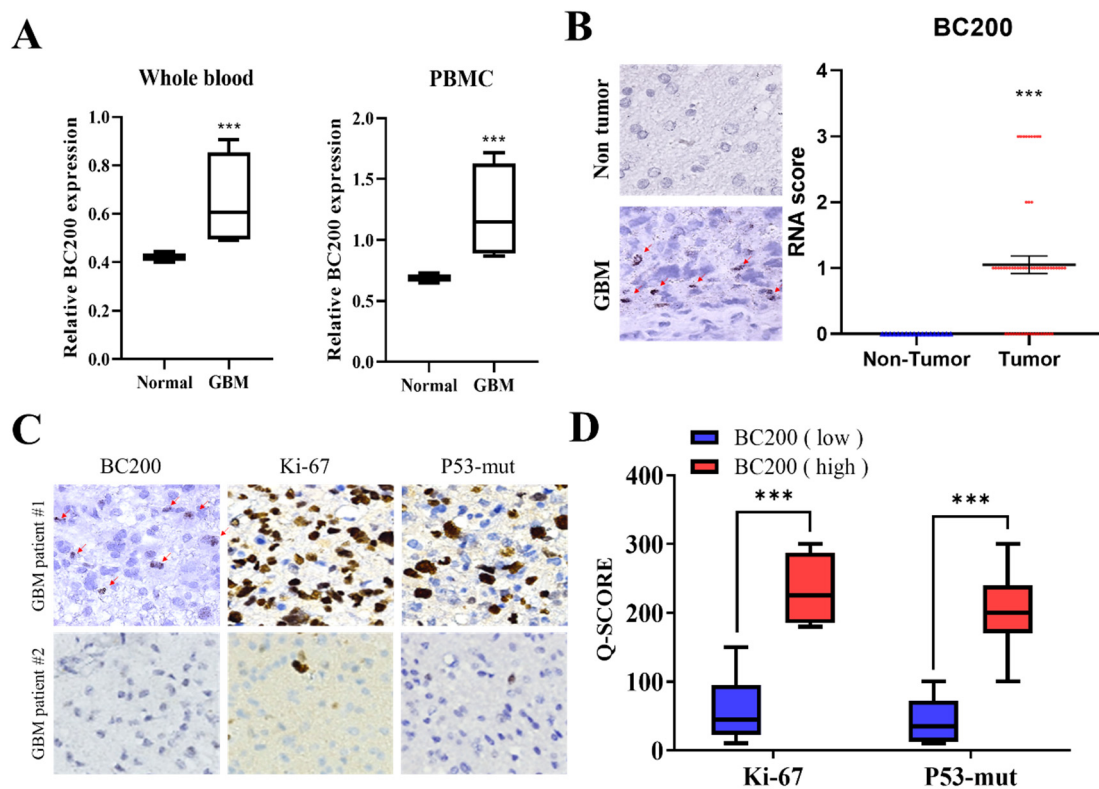


**Figure 1.** Expression level of full-length BC200 RNA in the blood and tissue. (A) Whole blood or PBMC from healthy participants and GB patients were assessed using RT-qPCR. GAPDH was used as the endogenous control. (B) The differential expression of BC200 in GB samples ( $n = 48$ ) and adjacent normal tissues ( $n = 15$ ) is shown. (C, D) The differential expression of Ki-67 and p53-mut in GB patients ( $n = 48$ ) with a high or low expression of BC200 RNA. \*\*\*  $p < 0.001$ .

### 3.2. High BC200 RNA Expression Associated with TMZ Resistance of Stem-Cell-Like Population in GB Cells

We attempted to confirm the role of BC200 RNA expression in chemo-resistance through upregulation of the stem-cell-like population in GB. We first evaluated the differential expression of BC200 RNA in GB (U87MG, DBTRG-05MG, T98G, and GBM8901) and normal human astrocytes (NHA)

cells. BC200 RNA expression was significantly higher in GB cell lines than in NHA cells (Figure 2A). The evaluation of cell viability after TMZ treatment revealed that more invasive glioblastoma cells GB cells (GBM8901, T98G) showed higher chemo-resistance (TMZ) than the likely GB cells DBTRG05MG and U87MG cancer cell (Figure 2B). Previous studies have suggested that the increased expression of ALDH+ and CD133+ cells was associated with mesenchymal phenotype and chemoresistance [19], cancer recurrence, and poor prognosis [20]. Furthermore, the role of BC200 RNA in TMZ resistance was assessed through flow cytometric analysis, revealing a significantly higher number of ALDH+/CD133+ cells in cancer cells than in normal human astrocytes (Figure 2C). The expression levels of key markers associated with drug resistance [21–23], proliferation, migration, and invasion, such as BCRP1, MDR1, MRP1 and MGMT along with BC200 RNA, were significantly highly expressed in GB cells (Figure 2D).

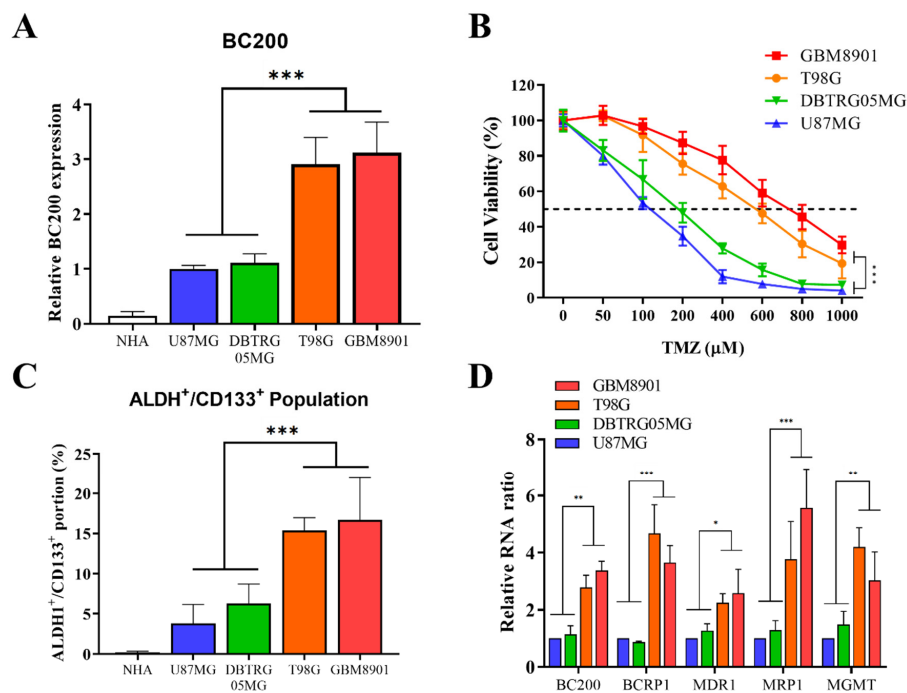


**Figure 2.** Differential expression of BC200 RNA in GB cell lines. (A) The differential expression of BC200 RNA in GB cell lines and normal human astrocytes are shown. (B) The viability of GB cells was analyzed through SRB assay 48 h after TMZ (0–1000 μM) treatment. (C) Flow cytometry analysis of the ALDH1<sup>+</sup>/CD133<sup>+</sup> portion in GB cell lines and normal human astrocytes. (D) The level of BC200, BCRP1, MDR1, MRP1 and MGMT in GB cell lines was analyzed using RT-qPCR. \*  $p < 0.05$ , \*\*  $p < 0.01$ , and \*\*\*  $p < 0.001$ .

### 3.3. BC200 RNA Silencing Inhibits the Proliferation, Migration, Invasion, and Self-Renewal Ability of GB Cells

To definitively understand the role of BC200 in GB, we knocked down BC200 RNA and examined its effect on cell migration, motility, and invasion. An analysis using RT-qPCR revealed the transfection efficiency of BC200 shRNA (shBC200 and OEBC200) in GB cells (Figure 3A). All GB cells tested demonstrated a significant reduction in cell migration (Figure 3B), wound healing (Figure 3B), and invasiveness (Figure 3C). Silencing the BC200 RNA significantly inhibited the expression of EMT-associated markers, such as N-cadherin, vimentin, and Slug (Figure 3D). Moreover, the self-renewal capacity was suppressed because of BC200 RNA inhibition, indicated through significant reduction in colony-forming ability (Figure 3E), but no effect on cell proliferation (Figure 3F) and neurosphere generation (Figure 3G) in comparison with mock-transfected control groups. Furthermore, the effect of BC200 RNA inhibition was evaluated on marker expression associated with the self-renewal and pluripotency of GB cells (Figure 3H), such as Oct4, SOX2,

and KLF4 [24], which were observed to be downregulated in BC200-suppressed cells in comparison with control mock-transfected cells.

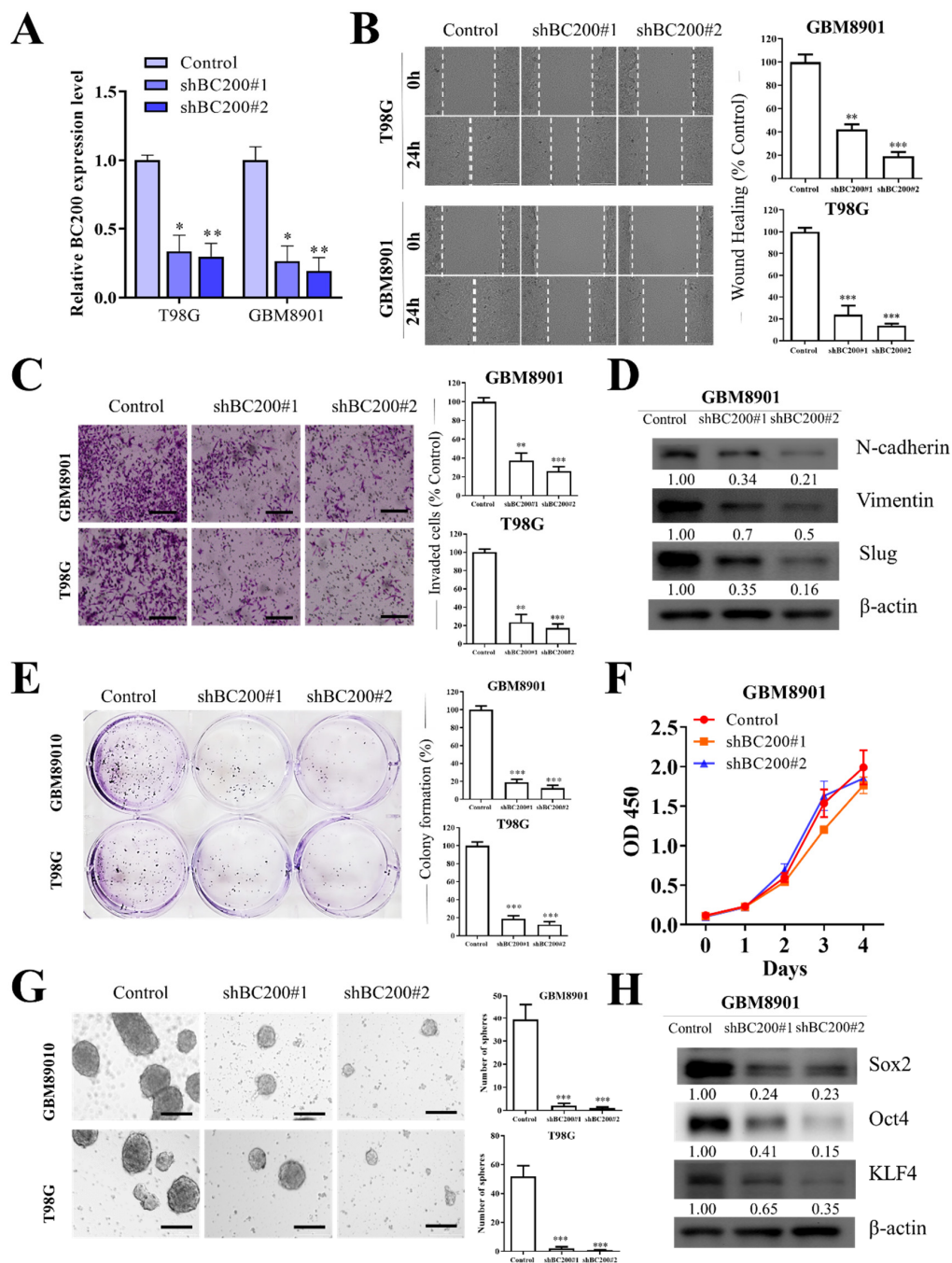


**Figure 3.** BC200 knockdown inhibited cell migration, invasion, colony formation, and sphere formation in GB cells in vitro. (A) The level of BC200 transfection with shBC200 was analyzed using RT-qPCR. (B) Wound-healing assay or migration assay showed that shBC200 resulted in delayed healing of the scratch wound. (C) Transwell invasion assay was used and results were expressed as the number of invaded cells per field. (D) The levels of N-cadherin, vimentin, and slug following shBC200 in GB cells were determined through western blot. (E) Colony formation assays showed that BC200 knockdown inhibited GB cell survival. (F) CCK-8 assay showed that BC200 knockdown had no effect on GB cell proliferation. (G) Neurosphere formation assays showed that BC200 knockdown inhibited GB cell stemness. (H) The levels of SOX2, Oct4, and KLF4 following shBC200 transfection in GB cells were determined through western blot analysis. \*  $p < 0.05$ , \*\*  $p < 0.01$ , and \*\*\*  $p < 0.001$ .



### 3.4. BC200 RNA Overexpression Enhances Aggressiveness Behavior and Self-Renewal Ability of GB Cells

To further understand the role of BC200 in GB cells, we increased BC200 expression through transfection of a BC200 expression vector OEBC200 in GB cells and used an empty vector as a negative control. Analysis with RT-qPCR showed the transfection efficiency of OEBC200 in GB cells (Figure 4A). BC200 expression was higher in the OEBC200 group than in the control group. Next, BC200 overexpression in GB cell lines demonstrated significantly increased cell wound healing migration (Figure 4B), invasiveness (Figure 4C), and colony-forming ability (Figure 4E) but no effect on GB cell proliferation (Figure 4F) compared with the negative control group. Because of BC200 RNA overexpression, the expression of EMT-associated genes N-cadherin, vimentin, and Slug (Figure 4D) was significantly upregulated. Furthermore, the self-renewal potential of overexpressed BC200 RNA in GB cells compared with mock-transfected cells showed significantly high neurosphere generation (Figure 4G). Moreover, the self-renewal and pluripotency properties of overexpressed BC200 RNA in GB cells (Figure 4H) showed that markers for self-renewal and pluripotency, such as Oct4, SOX2, and KLF4, were upregulated in OEBC200 cells compared with control mock-transfected cells.

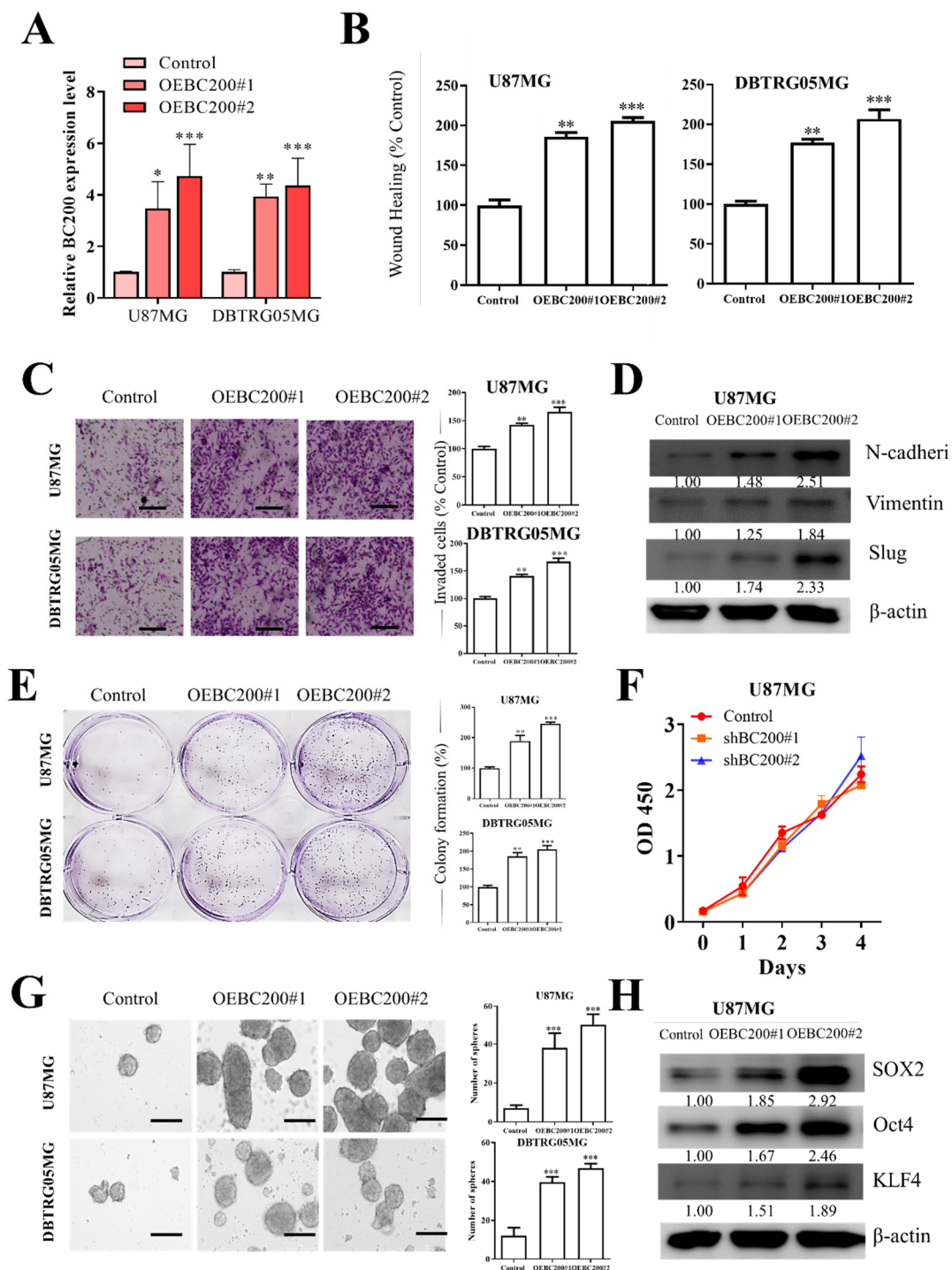


**Figure 4.** BC200 RNA overexpression promotes cell migration, invasion, colony formation, and sphere formation on GB cells in vitro. (A) The level of BC200 transfection with OEBC200, an expression vector, was analyzed using RT-qPCR. (B) Migration assay showed that OEBC200 resulted in fast scratch wound healing. (C) Transwell invasion assay was performed, and the results were expressed as the number of invaded cells per field. (D) Following OEBC200 treatment, the levels of N-cadherin, vimentin, and slug in GB cells were determined through western blot. (E) Colony formation assays showed that BC200 RNA overexpression enhances GB cell survival. (F) CCK-8 assay showed that OEBC200 had no effect on GB cell proliferation. (G) Neurosphere formation assays showed that a high expression of BC200 promotes GB cell stemness. (H) Following OEBC200 treatment, the levels of SOX2, Oct4, and KLF4 in GB cells were determined through western blot. \*  $p < 0.05$ , \*\*  $p < 0.01$ , and \*\*\*  $p < 0.001$ .

### 3.5. BC200 RNA Expression Associated with TMZ Resistance and miR-218-5p Expression

We demonstrated that BC200 RNA expression plays a crucial role in TMZ resistance. To further understand the underlying mechanism of BC200 RNA in GB chemosensitivity, cell viability assay was performed on GB cells with silenced and overexpressed BC200 RNA. The results revealed that the silenced BC200 (shBC200) cells showed decreased TMZ resistance compared with the control group, and OEBC200 cells showed increased TMZ resistance (Figure 5A). Furthermore, we evaluated the expression level of markers associated with drug resistance, proliferation, migration, and invasion in GB cells. Western blot analysis results showed that the levels of O-6-methylguanine-DNA methyltransferase (MGMT), ABCG2 human, ABC transporter (BCRP1), multidrug resistance protein (MDR1), and MRP1 proteins were significantly higher in OEBC200 cells than in BC200-silenced cells (Figure 5B). To further correlate the effect of BC200 RNA on miRNA expression, we applied bioinformatic analysis and observed that miR expression was inversely correlated with BC200 RNA expression. As shown in the heatmap of shBC200 and OEBC200 groups, the level of miR-218-5p was negatively associated with BC200 RNA expression (Figure 5C). The binding prediction of these miRNAs (miR-218-5p) from DIANA and PITA database [25] shows that BC200 RNA is targeted by miR-218-5p (Figure 5D,E). This indicates that a key interaction exists between BC200 RNA and miR-218-5p.

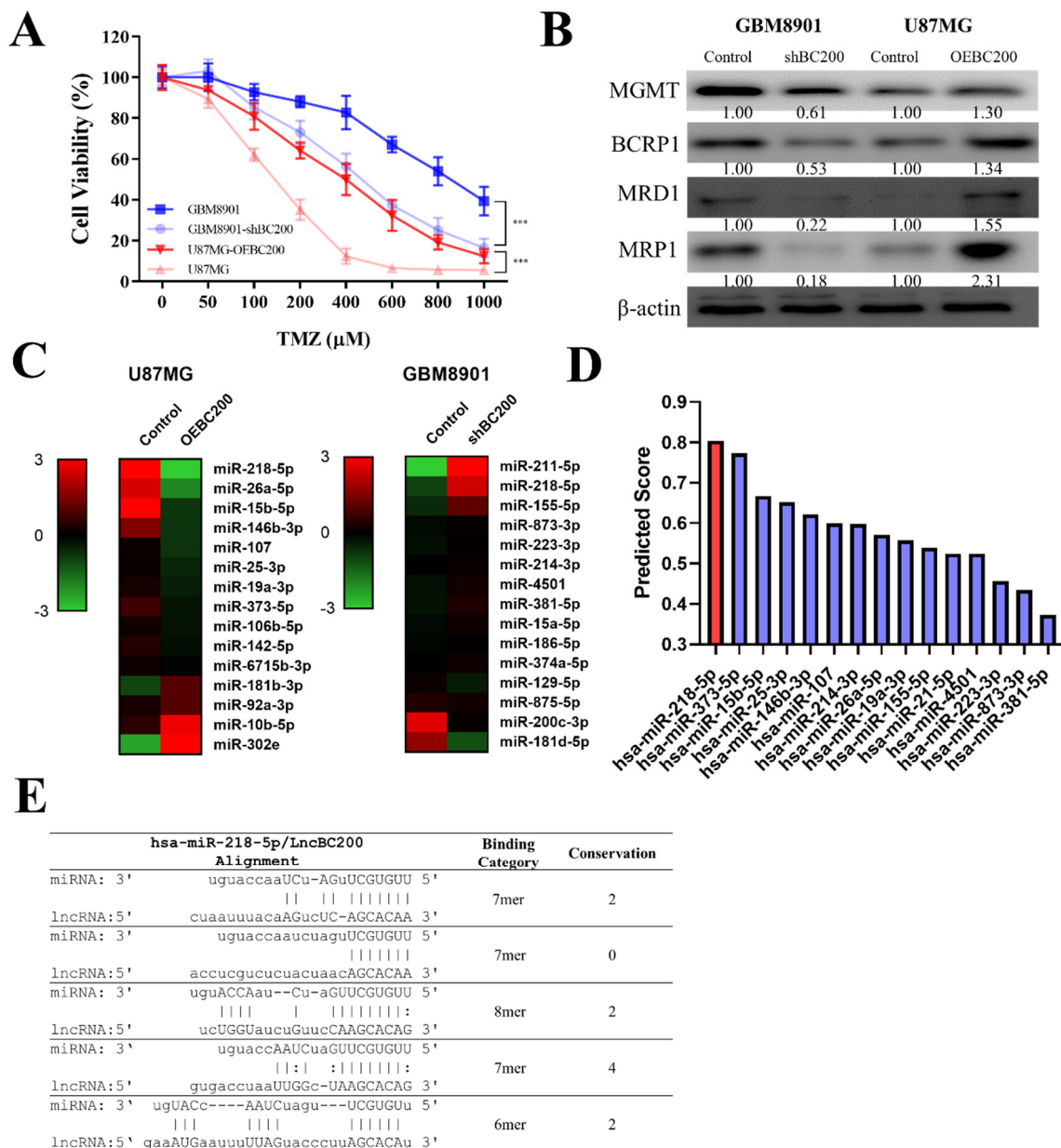


**Figure 5.** BC200 RNA promotes TMZ resistance in GB through sponge miR-218-5p. (A) The viability of shBC200 and OEBC200 GB cell lines was analyzed through SRB assay 48 h after TMZ (0–1000 μM) treatment. (B) The levels of MGMT, BCRP1, MDR1, and MRP1 following shBC200 and OEBC200 in GB cells were determined through western blot. (C) MicroRNA profiling analyses showed that shBC200 and OEBC200 contained high and low levels of miR-218-5p, respectively. (D) LncBase Predicted v.2 predicted that a high binding score of miR-218-5p with BC200. (E) BC200 directly interacts with multiple binding sites to hsa-miR-218-5p. \*\*\*  $p < 0.001$ .

### 3.6. miR-218-5p Modulates Stem Cell Characteristics and TMZ Resistance

Prediction binding of miRNAs (miR-218-5p) from DIANA and PITA database shows it targets BC200 RNA [25]. Thus, we wanted to investigate the relevance of miR-218-5p in controlling the self-renewal potential and TMZ resistance of GB cells. We first verified the expression of miR-218-5p by using RT-qPCR in GB and control cells (Figure 6A). The expression of miR-218-5p was lower in GB cells than in normal human astrocytes. Furthermore, the relative expression of miR-218-5p was observed to be negatively correlated with BC200 RNA expression (Figure 6B) in GB tissues.

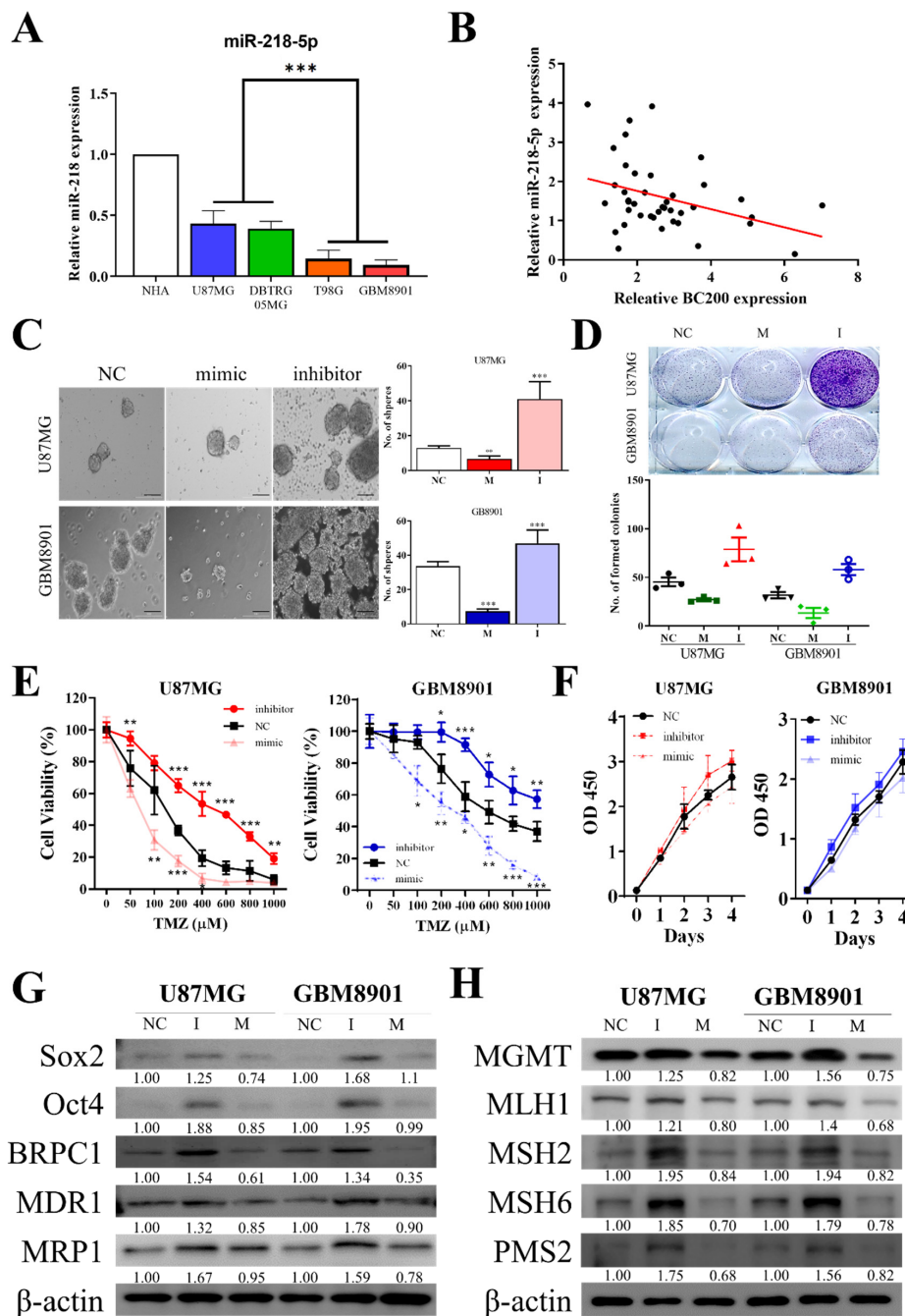


**Figure 6.** miR-218-5p regulated cell sphere formation, colony formation, and TMZ resistance in GB cells in vitro. (A) The differential expression of miR-218-5p in GB cell lines and normal human astrocytes. (B) Pearson’s correlation curve identified a negative correlation between BC200 and miR-218-5p in GB tissues. (C) Sphere formation assays showed that inhibition or mock transfection of miR-218-5p regulated GB cell stemness. (D) Colony formation assays showed that inhibition or mock transfection of miR-218-5p regulated GB cell survival. (E) The viability of GB cells with inhibition or mock transfection of miR-218-5p was analyzed through SRB assay 48 h after TMZ (0–1000  $\mu$ M) treatment. (F) CCK-8 assay showed that inhibition or mock transfection of miR-218-5p had no effect on GB cell proliferation. (G) The protein levels of SOX2, Oct4, BRPC1, MRP1 and MDR1 with inhibition or mock transfection of miR-218-5p. (H) The protein levels of MGMT, MLH1, MSH2, MSH6 and PMS2 following inhibition or mock transfection of miR-218-5p in GB cells were determined through western blot. \*  $p < 0.05$ , \*\*  $p < 0.01$  and \*\*\*  $p < 0.001$ .

The self-renewal and pluripotency properties of GB cells were analyzed by targeting miR-218-5p. The inhibition of miR-218-5p showed a significantly higher tumorsphere and colony-forming abilities (Figure 6C,D) in GB cells than in the control (NC) mock-transfected groups. Furthermore, the effect of miR-218-5p inhibition was noted on TMZ resistance; miR-218-5p-inhibited cells show higher TMZ resistance than the control mock-transfected groups (Figure 6E) but no significant effect on cell proliferation (Figure 6F). Moreover, markers for self-renewal and ABC Transporters in miR-218-5p-inhibited GB cells (Figure 6G) were evaluated. Markers such as Oct4, SOX2, KLF4, BCRP1, MDR1, and MRP1 were observed to be upregulated in miR-218-5p-inhibited cells compared with control NC and mock-transfected cells. Results revealed that the protein levels of genes associated with Drug resistance, such as MGMT, MLH1, MSH2, MSH6 and PMS2, were significantly higher in the miR-218-5p-inhibited group than in the control NC mock-transfected groups (Figure 6H).

### 3.7. BC200 RNA Inactivity Sensitized GB Cells to TMZ Combined Therapy *In Vivo*

We evaluated the potential of BC200 RNA knockdown together with TMZ combination treatment in inhibiting the tumor-initiating ability in xenograft models. Tumor was induced in NOD/SCID mice, which were then treated with shBC200, TMZ, control (Vehicle), and combination (shBC200/TMZ) treatments. Tumor volume, body weight, and survival were analyzed for 28 days after cell implantation. At 28 days, mice were sacrificed for immunohistochemistry and gene expression analysis (RT-qPCR). The combination treatment with shBC200 and TMZ led to a significant reduction in tumor size (Figure 7A). Mice treated with shBC200 and the shBC200/TMZ combination showed increased bodyweight but no sign of toxicity and negative treatment effects (Figure 7B). Moreover, the overall survival time was higher in mice treated with the shBC200/TMZ combination compared with that in mice treated with shBC200 and TMZ individually (Figure 7C). Moreover, comparative real-time PCR analyses showed an increased level of miR-218-5p expression in the shBC200/TMZ combination group in comparison with vehicle, TMZ, and shBC200 groups (Figure 7D), suggesting the role of miR-218-5p in GB progression. Furthermore, IHC analysis results of tissue sections in GB patients were consistent with the results of RT-qPCR. IHC results showed that shBC200 and shBC200/TMZ combination groups showed significantly suppressed tumor proliferation, oncogenicity, and tumorigenesis-associated markers (Figure 7E) in tissue samples.

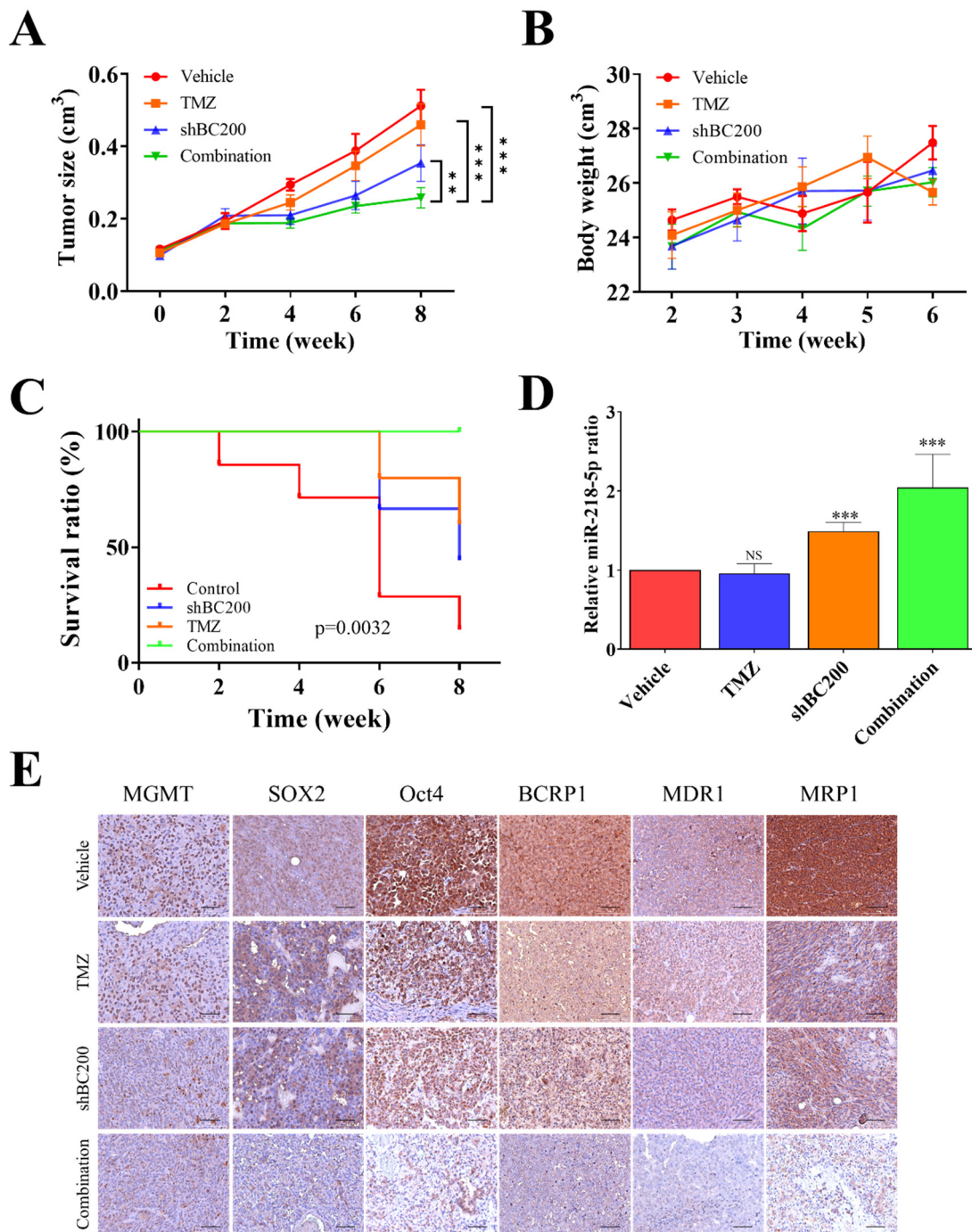


**Figure 7.** Combination of shBC200 and TMZ inhibits tumor growth in GB mice models. (A) Tumor size over time curve indicates that the most significantly delayed tumor growth was observed in the shBC200 and TMZ combination group, followed by shBC200 group, whereas TMZ and control groups did not differ significantly. (B) Bodyweight curves over time suggest no clear cytotoxic effects in all mice because no significant decrease in weight was observed. (C) Kaplan–Meier survival curve showed increased median overall survival in TMZ, shBC200, and shBC200/TMZ combination, whereas the combination group showed the best survival ratio. (D) Comparative real-time PCR analyses showed a significantly increased mRNA level of miR-218-5p expression in both shBC200 and shBC200/TMZ combination groups as compared with vehicle and TMZ counterparts. (E) IHC staining showed that treatment in the shBC200 group and shBC200/TMZ combination group suppressed tumorigenesis and TMZ resistance. \*\*  $p < 0.01$  and \*\*\*  $p < 0.001$ .

#### 4. Discussion

Despite major developments in therapeutic interventions, GB is one of the most lethal and invasive malignancies of the central nervous system and is the leading cause of overall cancer-associated mortality. Patients with GB exhibit poor prognosis [26] and the current therapy mostly fails because these patients develop multidrug resistance and do not respond to the treatment [27–29]. Studies have shown that lncRNAs are widely accepted and play a crucial role in the development, progression, and metastasis of cancer as well as in drug resistance of GB. The expression of BC200, a lncRNA, is high in the neuron-specific transcript in the brain [11]. The increased expression of BC200 RNA was atypically found in various human cancers, and its expression was higher in invasive cancers than in benign tumors [13,14]. However, BC200 RNA as a clinical therapeutic target or biomarker for GB is still understudied. In this study, the molecular mechanism of BC200 RNA in glioma development and progression was explored.

In vitro results have suggested that expression of lncRNAs is involved in multiple cellular processes of neurological tumor disease. Regulatory BC200 RNA is highly expressed in the peripheral blood of patients with breast cancer, suggesting that it can be an important molecular tumor biomarker for indicating human malignancies [30]. In our results, BC200 expression have a statistically significant difference in IDH1 and P53 status of GB patients. The overexpression of IDH1 is required to tumor growth in glioblastoma, it could catalyze the conversion of isocitrate and NADP<sup>+</sup> to 2-oxoglutarate and NADPH. The most of IDH1/2-mutant brain gliomas affected adults, there is evidence that IDH1/2 mutations are possibly involved with the progression of brain gliomas from grade II to grade III [31]. The different IDH1 mutational status may participate in the development of GBM, IDH1 mutations have been identified an important prognostic marker for GB patients [32–34]. In our study, we demonstrated that BC200, both at protein and mRNA level, was significantly upregulated in blood and tissue samples of GB patients (Figure 1). The expression of Ki-67 and p53-mut markers are indicative of prognosis and survival of GB patients [17,18], indicating a positive and significant correlation of BC200 RNA expression with Ki-67 and p53. Thus, BC200 RNA is strongly related to poor prognosis of GB patients.

CSCs are now increasingly being recognized as a critical target in cancer treatment because these stem cells are often correlated with the resistance against conventional chemo- and radiotherapy. Overcoming their treatment resistance is the key issue in cancer therapeutics [35,36]. Moreover, studies have reported that dysregulated lncRNA expression remains associated with the TMZ drug resistance of GB. In this study, we observed that the expression of BC200 increased in GB cells compared with normal brain cells (Figure 2). Furthermore, this study showed that GB cells exhibited high expression of ALDH<sup>+</sup>/CD133<sup>+</sup> cells, and key markers associated with drug resistance, proliferation, invasions and metastasis. TMZ resistance is a main reason for treatment fails. The causes of TMZ resistance are mainly DNA repair system, MMR is critical for inducing appropriate cellular responses to DNA damage, previous research suggests that GB cells are TMZ sensitive when MMR is expressed and active [37]. Much of resistance to TMZ observed clinically is due to high expression of MGMT or loss of MMR [38,39]. TMZ treatment induces DNA lesions and the MMR system causing apoptosis in GB [40]. The combination of BC200 inhibition and TMZ treatment may lead to a new therapeutic strategy to improve the efficacy of TMZ in glioblastoma multiforme patients. ABC transporter such as BCRP1, MDR1, and MRP1, were associated with chemoresistance [9]. Moreover, we found that in GB cells, the expression of these markers together with BC200 RNA expression is significantly higher, suggesting their role in TMZ chemoresistance.

To further understand the role of BC200 RNA in GB progression, we used the gain and loss of function of BC200 RNA through gene silencing and overexpression experiments. BC200 knockdown significantly reduced the proliferation, migration, and invasion of GB cells and the expression of markers associated with the self-renewal and pluripotent ability by reducing the colony-forming and neurosphere generation (Figure 3). Meanwhile, BC200 overexpression significantly reduced the BC200 knockdown effect (Figure 4). Therefore, our result indicates that BC200 RNA plays a key role in GB.



This result is consistent with those of previous reports indicating the role of BC200 RNA as an oncogene in other cancers, such as breast, cervical, and colon cancers [41,42].

Additionally, to understand the underlying molecular mechanism of BC200 in GB chemosensitivity, a cell viability assay was performed. BC200-silenced cells showed decreased resistance to TMZ compared with the control group (Figure 5A), whereas OEBC200 showed the reverse effect (Figure 5). Western blot analysis showed a reduction in the expression of markers associated with drug resistance in BC200-knockdown cells, and the results were reverse in OEBC200 cells. A previous study indicated that miR in correlation with lncRNA (BC200) expression attenuated the viability, migration, and invasiveness of cancer cells [43]. Subsequently, bioinformatic analysis was performed to evaluate the potential miRNA expression in BC200-inhibited and -overexpressed GB cells. Results from heatmap and binding prediction show that the expression of miR-218-5p is negatively associated with BC200 RNA expression, indicating that miR-218-5p targets BC200 RNA (Figure 5). Studies have shown that an increased expression of miR-218-5p affects cell viability in GB cells [44], but the role of miR-218-5p in conferring chemosensitivity is still not studied. Our result confirms that miR-218-5p is an effective tumor suppressor miRNA that targets BC200 RNA, with high expression in normal cells than in GB cells (Figure 6).

In our model, miR-218 inhibits MGMT expression, i.e., high BC200 results in low miR-218 and this results in high MGMT and, concomitantly, low toxicity driven by O6-methylguanine adducts that are repaired by MGMT. Additionally, the miR-218-5p plays a key role in preventing the invasiveness of glioma cells. Zhixiao et al. noticed that miR-218-5p can specifically bind to LHFPL3 mRNA and inhibit epithelial-mesenchymal transitions [45]. This is another possible reason to support these results. Furthermore, the relative expression of miR-218-5p was negatively correlated with BC200 RNA expression in GB tissues. In vitro results showed that targeted inhibition of miR-218-5p significantly increased tumorsphere and colony-forming abilities in GB cells compared with the control (NC) mock-transfected groups, confirming TMZ resistance. Again, we observed that markers associated with multidrug resistance, self-renewal, and pluripotency were upregulated in the miR-218-5p-inhibited group, (Figure 6) compared with the control mock-transfected groups, suggesting the role of miR-218-5p in GB cell chemosensitivity, inhibit the expression of the MGMT and MMR system induces resensitization to TMZ. Although the relative expression of ABC-transport protein has regulated by BC200/miR-218-5p axis, but ABC-transport protein as inducers of the TMZ resistant phenotype in GB is still controversial [46]. Finally, we demonstrated that the combination of BC200 inhibition and TMZ treatment increased GB sensitivity. It greatly inhibited the tumor growth in the xenograft mouse model with no negative impact on body weight and survival (Figure 7). The results of IHC analysis are concordant with those of RT-qPCR; the shBC200/TMZ combination group shows significant suppression of tumor proliferation, oncogenicity, and tumorigenesis-associated markers. Moreover, the miR-218-5p level expressed was significantly high in the combination treatment group. Collectively, we provided a strong preclinical evidence in support of using shBC200/TMZ combination for treating malignant glioma cancer. In addition, miR-218-5p could be used as a biomarker for monitoring therapeutic responses.

## 5. Conclusions

TMZ resistance is one of the critical causes of treatment failure in GB patients. The molecular mechanisms of TMZ resistance are still unclear. Hence, we used GB cell lines exposed to TMZ treatment to analyze the relevance of MGMT and MMR system between BC200/miR-218-5p axis in the TMZ resistance phenomenon. In summary, as shown in schema abstract of Figure 8, our results suggested that BC200 RNA, a lncRNA, is highly expressed both in vitro and in vivo and significantly modulates GB oncogenicity and enhances TMZ chemoresistance through concomitantly enhancing self-renewal and pluripotency of GB cells by modulating the expression of tumor-suppressor miR-218-5p. MiR-218-5p effectively targets and inhibits self-renewal and ABC Transporters markers such as Oct4, SOX2, BCRP1,

MDR1, MRP1, and MGMT. Resultant in the reduction of TMZ-resistance. Our findings highlight the therapeutic efficacy of BC200 RNA as a clinical biomarker or therapeutic target for GB.

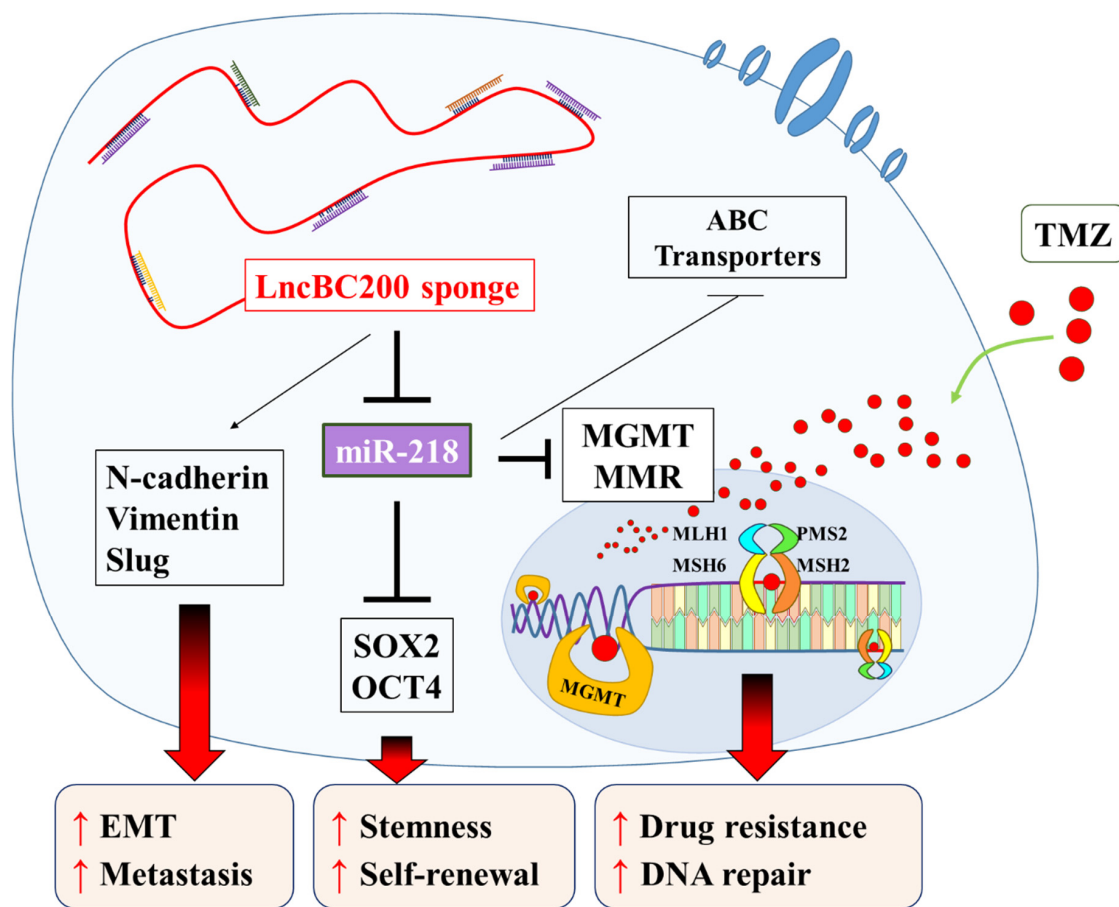


**Figure 8.** The lncRNA BC200 RNA sponges miR-218-5p regulated MGMT and MMR system enhancing self-renewal and TMZ resistance of GBM cells.

**Supplementary Materials:** The following are available online at <http://www.mdpi.com/2073-4409/9/8/1859/s1>. Table S1: Western blot antibodies sheet used in this study, Figure S1: Full-size blots of Figure 3D,H, Figure S2: Full-size blots of Figure 4D,H, Figure S3: Full-size blots of Figure 5B, Figure S4: Full-size blots of Figure 6G, Figure S5: Full-size blots of Figure 6H.

**Author Contributions:** Study conception and experimental design, Y.-K.S.; Performed the experiments, J.W.L., I.-H.F.; Data collation and analysis, Y.-K.S. and J.-W.S.; Manuscript writing, Y.-K.S. and H.-Y.C.; Provided reagents, materials, and experimental infrastructure, C.-T.Y. and C.-M.L. All authors read and approved the final submitted version of the manuscript.

**Funding:** This work was supported by National Science Council of Taiwan: Chien-Min Lin (MOST 107-2314-B-038-056-MY3) and grants to Yu-Kai Su (MOST 107-2314-B-038-022-). This study was also supported by grants from Taipei Medical University, Taiwan (106FRP-03) to Chien-Min Lin.

**Acknowledgments:** The authors thank Ting-Yi Huang and all research assistants of the Translational Research Laboratory and Core Facility Center, Taipei Medical University—Shuang Ho Hospital for their assistance with the flow cytometry, molecular and cell-based assays. The author also thanks the CRISPR Gene Targeting Core Lab at Taipei Medical University in Taiwan for providing technical support.

**Conflicts of Interest:** The authors declare no conflicts of interest.

### Abbreviations

GB: Glioblastoma; TMZ: temozolomide; SRB: Sulforhodamine B; MGMT: O-6-methylguanine-DNA methyltransferase; MMR: DNA mismatch repair; lncRNAs: long non-coding RNAs; BC200: Brain cytoplasmic 200

**Ethics approval and consent to participate:** The study was approved by the Joint Institutional Review Board (JIRB) of the Taipei Medical University–Shuang Ho Hospital (Approval number: N201903047). Tissue samples from patients with primary and recurrent GB were obtained from the Taipei Medical University–Shuang Ho Hospital GB cohort.

**Availability of data and materials:** The datasets used and analyzed in the current study are publicly-accessible as indicated in the manuscript.

## References

1. Hanif, F.; Muzaffar, K.; Perveen, K.; Malhi, S.M.; Simjee, S.U. Glioblastoma Multiforme: A Review of its Epidemiology and Pathogenesis through Clinical Presentation and Treatment. *Asian Pac. J. Cancer Prev.* **2017**, *18*, 3–9.
2. Louis, D.N.; Ohgaki, H.; Wiestler, O.D.; Cavenee, W.K.; Burger, P.C.; Jouvet, A.; Scheithauer, B.W.; Kleihues, P. The 2007 WHO classification of tumours of the central nervous system. *Acta Neuropathol.* **2007**, *114*, 97–109. [CrossRef]
3. Jovcevska, I.; Kocevar, N.; Komel, R. Glioma and glioblastoma—how much do we (not) know? *Mol. Clin. Oncol.* **2013**, *1*, 935–941. [CrossRef]
4. Lara-Velazquez, M.; Al-Kharboosh, R.; Jeanneret, S.; Vazquez-Ramos, C.; Mahato, D.; Tavanaiepour, D.; Rahmathulla, G.; Quinones-Hinojosa, A. Advances in Brain Tumor Surgery for Glioblastoma in Adults. *Brain Sci.* **2017**, *7*, 166. [CrossRef]
5. Uszczyńska-Ratajczak, B.; Lagarde, J.; Frankish, A.; Guigó, R.; Johnson, R. Towards a complete map of the human long non-coding RNA transcriptome. *Nat. Rev. Genet.* **2018**, *19*, 535–548. [CrossRef] [PubMed]
6. Huarte, M. The emerging role of lncRNAs in cancer. *Nat. Med.* **2015**, *21*, 1253–1261. [CrossRef] [PubMed]
7. Zhang, X.; Sun, S.; Pu, J.K.S.; Tsang, A.C.O.; Lee, D.; Man, V.O.Y.; Lui, W.M.; Wong, T.S.; Leung, G.K.K. Long non-coding RNA expression profiles predict clinical phenotypes in glioma. *Neurobiol. Dis.* **2012**, *48*, 1–8. [CrossRef] [PubMed]
8. Quinn, J.J.; Zhang, Q.C.; Georgiev, P.; Ilik, I.; Akhtar, A.; Chang, H.Y. Rapid evolutionary turnover underlies conserved lncRNA–genome interactions. *Genes Dev.* **2016**, *30*, 191–207. [CrossRef]
9. Cai, T.; Liu, Y.; Xiao, J. Long noncoding RNA MALAT1 knockdown reverses chemoresistance to temozolomide via promoting microRNA-101 in glioblastoma. *Cancer Med.* **2018**, *7*, 1404–1415. [CrossRef]
10. Kopp, F.; Mendell, J.T. Functional Classification and Experimental Dissection of Long Noncoding RNAs. *Cell* **2018**, *172*, 393–407. [CrossRef]
11. Tiedge, H.; Chen, W.; Brosius, J. Primary structure, neural-specific expression, and dendritic location of human BC200 RNA. *J. Neurosci.* **1993**, *13*, 2382–2390. [CrossRef] [PubMed]
12. Booy, E.P.; McRae, E.K.S.; Howard, R.; Deo, S.R.; Ariyo, E.O.; Dzananovic, E.; Meier, M.; Stetefeld, J.; McKenna, S.A. RNA Helicase Associated with AU-rich Element (RHAU/DHX36) Interacts with the 3′-Tail of the Long Non-coding RNA BC200 (BCYRN1). *J. Boil. Chem.* **2016**, *291*, 5355–5372. [CrossRef] [PubMed]
13. Chen, W.; Bocker, W.; Brosius, J.; Tiedge, H. Expression of neural BC200 RNA in human tumours. *J. Pathol.* **1997**, *183*, 345–351. [CrossRef]
14. Iacoangeli, A.; Lin, Y.; Morley, E.J.; Muslimov, I.A.; Bianchi, R.; Reilly, J.; Weedon, J.; Diallo, R.; Böcker, W.; Tiedge, H. BC200 RNA in invasive and preinvasive breast cancer. *Carcinogenesis* **2004**, *25*, 2125–2133. [CrossRef]
15. Franken, N.A.; Rodermond, H.M.; Stap, J.; Haveman, J.; van Bree, C. Clonogenic assay of cells in vitro. *Nat. Protoc.* **2006**, *1*, 2315–2319. [CrossRef]
16. Vermes, I.; Haanen, C.; Reutelingsperger, C. Flow cytometry of apoptotic cell death. *J. Immunol. Methods* **2000**, *243*, 167–190. [CrossRef]
17. Arshad, H.; Ahmad, Z.; Hasan, S.H. Gliomas: Correlation of Histologic Grade, Ki67 and p53 Expression with Patient Survival. *Asian. Pac. J. Cancer Prev.* **2010**, *11*, 1637–1640.
18. Mu, N.; Gu, J.; Liu, N.; Xue, X.; Shu, Z.; Zhang, K.; Huang, T.; Chu, C.; Zhang, W.; Gong, L.; et al. PRL-3 is a potential glioblastoma prognostic marker and promotes glioblastoma progression by enhancing MMP7 through the ERK and JNK pathways. *Theranostics* **2018**, *8*, 1527–1539. [CrossRef]
19. Butler, S.J.; Richardson, L.; Farias, N.; Morrison, J.; Coomber, B.L. Characterization of cancer stem cell drug resistance in the human colorectal cancer cell lines HCT116 and SW480. *Biochem. Biophys. Res. Commun.* **2017**, *490*, 29–35. [CrossRef]

20. Yasgar, A.; Titus, S.A.; Wang, Y.; Danchik, C.; Yang, S.-M.; Vasiliou, V.; Jadhav, A.; Maloney, D.J.; Simeonov, A.; Martinez, N.J. A High-Content Assay Enables the Automated Screening and Identification of Small Molecules with Specific ALDH1A1-Inhibitory Activity. *PLoS ONE* **2017**, *12*, e0170937. [CrossRef]
21. Zhou, S.; Schuetz, J.D.; Bunting, K.D.; Colapietro, A.M.; Sampath, J.; Morris, J.J.; Lagutina, I.; Grosveld, G.C.; Osawa, M.; Nakauchi, H.; et al. The ABC transporter Bcrp1/ABCG2 is expressed in a wide variety of stem cells and is a molecular determinant of the side-population phenotype. *Nat. Med.* **2001**, *7*, 1028–1034. [CrossRef] [PubMed]
22. Schaich, M.; Kestel, L.; Pfirrmann, M.; Robel, K.; Illmer, T.; Kramer, M.; Dill, C.; Ehniger, G.; Schackert, G.; Krex, D. A MDR1 (ABCB1) gene single nucleotide polymorphism predicts outcome of temozolomide treatment in glioblastoma patients. *Ann. Oncol.* **2009**, *20*, 175–181. [CrossRef] [PubMed]
23. Yan, J.; Yang, R. Dopamine receptor D1 promotes the proliferation, invasion and migration of gliomas by inhibiting cAMP signaling pathway. *Xi bao yu fen zi mian yi xue za zhi = Chin. J. Cell. Mol. Immunolog.* **2018**, *34*, 1116–1121.
24. Xu, N.; Papagiannakopoulos, T.; Pan, G.; Thomson, J.A.; Kosik, K.S. MicroRNA-145 regulates OCT4, SOX2, and KLF4 and represses pluripotency in human embryonic stem cells. *Cell* **2009**, *137*, 647–658. [CrossRef]
25. Kertesz, M.; Iovino, N.; Unnerstall, U.; Gaul, U.; Segal, E. The role of site accessibility in microRNA target recognition. *Nat. Genet.* **2007**, *39*, 1278–1284. [CrossRef]
26. Naydenov, E.; Tzekov, C.; Minkin, K.; Nachev, S.; Romansky, K.; Bussarsky, V. Long-term survival with primary glioblastoma multiforme: A clinical study in bulgarian patients. *Case Rep. Oncol.* **2011**, *4*, 1–11. [CrossRef]
27. Bredel, M. Anticancer drug resistance in primary human brain tumors. *Brain Res. Rev.* **2001**, *35*, 161–204. [CrossRef]
28. Tseng, Y.-Y.; Huang, Y.-C.; Yang, T.-C.; Yang, S.-T.; Liu, S.-C.; Chang, T.-M.; Kau, Y.-C.; Liu, S.-J. Concurrent Chemotherapy of Malignant Glioma in Rats by Using Multidrug-Loaded Biodegradable Nanofibrous Membranes. *Sci. Rep.* **2016**, *6*, 30630. [CrossRef]
29. Tivnan, A.; Zakaria, Z.; O’Leary, C.; Kögel, D.; Pokorny, J.L.; Sarkaria, J.N.; Prehn, J.H.; Kögel, N. Inhibition of multidrug resistance protein 1 (MRP1) improves chemotherapy drug response in primary and recurrent glioblastoma multiforme. *Front. Mol. Neurosci.* **2015**, *9*, 218. [CrossRef]
30. Iacoangeli, A.; Adzovic, L.; Chen, E.Q.; Cattie, R.L.; Soff, G.A.; Tiedge, H. Regulatory BC200 RNA in peripheral blood of patients with invasive breast cancer. *J. Investig. Med.* **2018**, *66*, 1055–1063. [CrossRef]
31. Deng, L.; Xiong, P.; Luo, Y.; Bu, X.; Qian, S.; Zhong, W.; Lv, S. Association between IDH1/2 mutations and brain glioma grade. *Oncol. Lett.* **2018**, *16*, 5405–5409. [CrossRef] [PubMed]
32. Stancheva, G.; Goranova, T.; Laleva, M.; Kamenova, M.; Mitkova, A.; Velinov, N.; Poptodorov, G.; Mitev, V.; Kaneva, R.; Gabrovsky, G. IDH1/IDH2 but not TP53 mutations predict prognosis in Bulgarian glioblastoma patients. *BioMed Res. Int.* **2014**, *2014*, 6547272014. [CrossRef] [PubMed]
33. Hata, N.; Hatae, R.; Yoshimoto, K.; Murata, H.; Kuga, D.; Akagi, Y.; Sangatsuda, Y.; Suzuki, S.O.; Iwaki, T.; Mizoguchi, M.; et al. Insular primary glioblastomas with IDH mutations: Clinical and biological specificities. *Neuropathology* **2017**, *37*, 200–206. [CrossRef] [PubMed]
34. Wang, Q.; Zhang, L.; Cui, Y.; Zhang, C.; Chen, H.; Gu, J.; Qian, J.; Luo, C. Increased RLIP76 expression in IDH1 wild-type glioblastoma multiforme is associated with worse prognosis. *Oncol. Rep.* **2019**, *43*, 188–200. [CrossRef] [PubMed]
35. Yu, Y.; Ramena, G.; Elble, R.C. The role of cancer stem cells in relapse of solid tumors. *Front. Biosci. (Elite Ed)* **2012**, *4*, 1528–1541. [CrossRef] [PubMed]
36. Vescovi, A.; Binda, E. Heterogeneity of cancer-Initiating cells within glioblastoma. *Front. Biosci. (Schol Ed)* **2012**, *4*, 1235–1248. [CrossRef] [PubMed]
37. Sang, Y. Lee. Temozolomide resistance in glioblastoma multiforme. *Gene Funct. Dis.* **2016**, *3*, 198–210.
38. Hegi, M.E.; Liu, L.; Herman, J.G.; Stupp, R.; Wick, W.; Weller, M.; Mehta, M.; Gilbert, M.R. Correlation of O6-Methylguanine Methyltransferase (MGMT) Promoter Methylation With Clinical Outcomes in Glioblastoma and Clinical Strategies to Modulate MGMT Activity. *J. Clin. Oncol.* **2008**, *26*, 4189–4199. [CrossRef]
39. Sarkaria, J.N.; Kitange, G.J.; James, C.D.; Plummer, R.; Calvert, H.; Weller, M.; Wick, W. Mechanisms of chemoresistance to alkylating agents in malignant glioma. *Clin. Cancer Res.* **2008**, *14*, 2900–2908. [CrossRef]


40. Yoshimoto, K.; Mizoguchi, M.; Hata, N.; Murata, H.; Hatae, R.; Amano, T.; Nakamizo, A.; Sasaki, T. Complex DNA repair pathways as possible therapeutic targets to overcome temozolomide resistance in glioblastoma. *Front. Oncol.* **2012**, *2*, 186. [CrossRef]
41. Wu, K.; Xu, K.; Liu, K.; Huang, J.; Chen, J.; Zhang, J.; Zhang, N. Long noncoding RNA BC200 regulates cell growth and invasion in colon cancer. *Int. J. Biochem. Cell Boil.* **2018**, *99*, 219–225. [CrossRef] [PubMed]
42. Peng, J.; Hou, F.; Feng, J.; Xu, S.; Meng, X. Long non-coding RNA BCYRN1 promotes the proliferation and metastasis of cervical cancer via targeting microRNA-138 in vitro and in vivo. *Oncol. Lett.* **2018**, *15*, 5809–5818. [CrossRef] [PubMed]
43. Li, Z.; Xu, C.; Ding, B.; Gao, M.; Wei, X.; Ji, N. Long non-coding RNA MALAT1 promotes proliferation and suppresses apoptosis of glioma cells through derepressing Rap1B by sponging miR-101. *J. Neuro-Oncol.* **2017**, *134*, 19–28. [CrossRef] [PubMed]
44. Xia, H.; Yan, Y.; Hu, M.; Wang, Y.; Wang, Y.; Dai, Y.; Chen, J.; Di, G.; Chen, X.; Jiang, X. MiR-218 sensitizes glioma cells to apoptosis and inhibits tumorigenicity by regulating ECOP-mediated suppression of NF- $\kappa$ B activity. *Neuro-Oncology* **2012**, *15*, 413–422. [CrossRef]
45. Li, Z.; Qian, R.; Zhang, J.; Shi, X. MiR-218-5p targets LHFPL3 to regulate proliferation, migration, and epithelial–mesenchymal transitions of human glioma cells. *Biosci. Rep.* **2019**, *39*, BSR20180879. [CrossRef]
46. Riganti, C.; Salaroglio, I.C.; Caldera, V.; Campia, I.; Kopecka, J.; Mellai, M.; Annovazzi, L.; Bosia, A.; Ghigo, D.; Schiffer, D. Temozolomide downregulates P-glycoprotein expression in glioblastoma stem cells by interfering with the Wnt3a/glycogen synthase-3 kinase/ $\beta$ -catenin pathway. *Neuro-Oncology* **2013**, *15*, 1502–1517. [CrossRef]



© 2020 by the authors. Licensee MDPI, Basel, Switzerland. This article is an open access article distributed under the terms and conditions of the Creative Commons Attribution (CC BY) license (<http://creativecommons.org/licenses/by/4.0/>).

Article

# Time- and Dose-Dependent Effects of Ionizing Irradiation on the Membrane Expression of Hsp70 on Glioma Cells

Helena Fellingner <sup>1</sup> , Stefan Stangl <sup>1</sup>, Alicia Hernandez Schnelzer <sup>1</sup>, Melissa Schwab <sup>1</sup>, Tommaso Di Genio <sup>1</sup>, Marija Pieper <sup>1</sup>, Caroline Werner <sup>1</sup>, Maxim Shevtsov <sup>1,2,3</sup>, Bernhard Haller <sup>4</sup> and Gabriele Multhoff <sup>1,5,\*</sup>

<sup>1</sup> Radiation Immuno-Oncology Group, Center for Translational Cancer Research (TranslaTUM), School of medicine, Technical University of Munich (TUM), 81675 Munich, Germany; skygallery@web.de (H.F.); Stefan.stangl@tum.de (S.S.); Alicia.hernandez@tum.de (A.H.S.); Melissa.schwab@tum.de (M.S.); tommasodigenio@hotmail.it (T.D.G.); Marija.pieper@tum.de (M.P.); c.werner@tum.de (C.W.); Maxim.shevtsov@tum.de (M.S.)

<sup>2</sup> Institute of the Russian Academy of Sciences (RAS), 194064 St. Petersburg, Russia

<sup>3</sup> Department of Biotechnology, Pavlov First Saint Petersburg State Medical University, 197022 St. Petersburg, Russia

<sup>4</sup> Institute of Medical Informatics, Statistics and Epidemiology, Technical University of Munich (TUM), 81675 Munich, Germany; Bernhard.haller@tum.de

<sup>5</sup> Department of Radiation Oncology, School of Medicine, Technical University of Munich (TUM), 81675 Munich, Germany

\* Correspondence: gabriele.multhoff@tum.de; Tel.: +49-89-4140-4514

Received: 24 March 2020; Accepted: 7 April 2020; Published: 8 April 2020



**Abstract:** The major stress-inducible protein Hsp70 (HSPA1A) is overexpressed in the cytosol of many highly aggressive tumor cells including glioblastoma multiforme and presented on their plasma membrane. Depending on its intracellular or membrane localization, Hsp70 either promotes tumor growth or serves as a target for natural killer (NK) cells. The kinetics of the membrane Hsp70 (mHsp70) density on human glioma cells (U87) was studied after different irradiation doses to define the optimal therapeutic window for Hsp70-targeting NK cells. To maintain the cells in the exponential growth phase during a cultivation period of 7 days, different initial cell counts were seeded. Although cytosolic Hsp70 levels remained unchanged on days 4 and 7 after a sublethal irradiation with 2, 4 and 6 Gy, a dose of 2 Gy resulted in an upregulated mHsp70 density in U87 cells which peaked on day 4 and started to decline on day 7. Higher radiation doses (4 Gy, 6 Gy) resulted in an earlier and more rapid onset of the mHsp70 expression on days 2 and 1, respectively, followed by a decline on day 5. Membrane Hsp70 levels were higher on cells in G2/M than in G1; however, an irradiation-induced cell cycle arrest on days 4 and 7 was not associated with an increase in the mHsp70 density. Extracellular Hsp70 concentrations in the supernatant of irradiated cells were significantly higher than sham (0 Gy) irradiated cells on days 4 and 7, but not on day 1. Functionally, elevated mHsp70 densities were associated with a significantly better lysis by Hsp70-targeting NK cells. In summary, the kinetics of changes in the mHsp70 density upon irradiation on tumor cells is time- and dose-dependent.

**Keywords:** radiotherapy; glioblastoma; membrane Hsp70; dose- and time-kinetics; NK cell-based therapy

## 1. Introduction

The therapeutic application of ionizing radiation, either alone or in combination with surgery and chemotherapy, plays a pivotal role in the treatment of solid tumors. Ionizing radiation elicits its

cytotoxic activity against tumor cells by causing DNA single- and double-strand breaks, predominantly mediated and fixed by reactive oxygen species (ROS). Although the major goal of irradiation is to achieve local tumor control and a decreased dissemination by reducing the viable tumor mass, also immunostimulatory effects have been assigned to ionizing radiation [1,2]. However, it remains to be elucidated which dose and radiation regimen is optimal to induce anti-tumor immune effects. Herein, cytosolic, extracellular and plasma membrane-bound heat shock protein 70 (Hsp70) [3,4] was studied in highly aggressive glioblastoma cells as a radiation-inducible target for natural killer (NK) cells.

Besides its intracellular chaperoning functions, which include assisting the correct folding of proteins, the assembly of nascent polypeptides, the prevention of protein aggregation and thereby controlling cellular protein homeostasis, members of the HSP70 family fulfil various cytoprotective tasks under physiological conditions and upon environmental stress [3]. An up-regulated Hsp70 expression enhances the viability of tumor cells by fostering protein damage repair and impairing apoptotic pathways [5]. By stimulating the overexpression of anti-apoptotic proteins (Bcl-2/Bcl-xL), downregulating pro-apoptotic Bax, Bcl-Xs and Bak or blocking tumor necrosis factor (TNF)-related apoptosis-inducing ligand (TRAIL)-induced apoptosis and formation of the death-inducing signaling complex with death receptors DR4 and DR5 [5], cytosolic Hsp70 promotes tumor cell survival, protects against apoptosis and promotes tumor progression [6].

A large variety of stress factors including hypoxia and reoxygenation, heavy metals, glucose deprivation and cytotoxic drugs can induce the Hsp70 expression and stimulate antigen release and danger signal expression [6,7].

In contrast to intracellular Hsp70, extracellular and mHsp70 play a pivotal role in stimulating both adaptive and innate immune responses and thereby initiating protective anti-tumor immunity [8]. By its exclusive expression on the plasma membrane of tumor cells [9], mHsp70 provides a tumor-specific target for Hsp70-specific, activated NK cells [10]. Therefore, increasing the density of mHsp70 on tumor cells by irradiation combined with a mHsp70-targeting NK cell-based immunotherapy might provide a novel strategy to improve clinical outcome and extend overall survival of patients with advanced tumors [11–13]. Herein, we were interested to identify the optimal radiation dose and time point for an up-regulated mHsp70 density as a target for NK cells on highly aggressive glioblastoma cells.

## 2. Materials and Methods

### 2.1. Cell Line and Culture Conditions

The epithelial human glioblastoma cell line U87 MG (ATCC HTB-14, MGMT<sup>-</sup>) and the human hepatocellular carcinoma cell line HepG2 (ATCC HB-8065) were grown in complete growth medium, consisting of Dulbecco's Eagle's Minimum Essential Medium (DMEM) (Sigma-Aldrich, Steinheim Germany) supplemented with 10% *v/v* heat inactivated fetal calf serum (FCS) (Sigma-Aldrich), 1% antibiotics (10,000 IU/mL penicillin, 10 mg/mL streptomycin, Sigma-Aldrich), L-glutamine (Sigma-Aldrich), MEM non-essential amino acid solution 100× (Sigma-Aldrich) and sodium pyruvate (Sigma-Aldrich). The epithelial human cervix carcinoma cell line HeLa (ATCC CCL-2) was grown in complete growth medium, consisting of RPMI-1640 (Sigma-Aldrich, Germany) supplemented with 10% *v/v* heat inactivated FCS (Sigma-Aldrich), 1% antibiotics (10,000 IU/mL penicillin, 10 mg/mL streptomycin, Sigma-Aldrich), L-glutamine (Sigma-Aldrich) and sodium pyruvate (Sigma-Aldrich). After reaching confluency, adherent growing tumor cells were trypsinized for 2 min at 37 °C in trypsin ethylene diamine-tetra-acetic acid (EDTA) (Sigma-Aldrich). Single cell suspensions with different cell counts were seeded in 15 mL supplemented medium in T-75 ventilated culture flasks. Tumor cells were routinely checked for mycoplasma contamination.

## 2.2. Irradiation

Tumor cells were irradiated with a single dose of 0 (sham), 2, 4 and 6 Gy using the Gulmay RS225A irradiation machine (Gulmay Medical Ltd., Camberley, UK) at a dose rate of 0.90 Gy/min (15 mA, 200 keV) or were kept untreated.

## 2.3. Flow Cytometry and Cell Cycle Analysis

Single cell suspensions of sham (0 Gy) irradiated and irradiated cells ( $0.4 \times 10^6$  cells per vial) were collected at different time-points after radiation. After a washing step in phosphate-buffered saline (PBS)/10% *v/v* fetal calf serum (FCS), cells were incubated either with fluorescein-isothiocyanate (FITC)-conjugated mouse monoclonal antibody (mAb) specific for mHsp70 (cmHsp70.1, IgG1, multimmune GmbH, Munich, Germany) or with an isotype-matched FITC-labeled control antibody on ice in the dark for 30 min. Only viable cells (propidium iodide negative cells) were gated, and the proportion of positively stained cells and mean fluorescence intensity (mfi) values were analyzed on a FACSCalibur™ flow cytometer (BD Biosciences, Heidelberg, Germany). The mfi is a relative value of the total fluorescence intensity of cmHsp70.1-FITC antibody stained, viable cells subtracted by the intensity of the signal intensity obtained after staining of the cells with an isotype-matched IgG1-FITC control antibody. Fluorescence data were analyzed and plotted by using CellQuest software (BD Biosciences, Heidelberg, Germany).

For a concomitant analysis of the mHsp70 expression during the cell cycle, viable cells which have been stained with cmHsp70.1 mAb were washed and fixed in 2% *w/v* paraformaldehyde (PFA) and then ice-cold methanol (70% *v/v*). After rehydration, cells were suspended in 500  $\mu$ L propidium iodide/RNase staining solution (Sigma/Aldrich), incubated for 60 min at room temperature and analyzed on a FACSCalibur™ flow cytometer, as described above.

## 2.4. Immunocytochemistry (ICC)

Cells were grown on poly-L-lysine-coated glass slides. On days 4 and 7 after irradiation with 0 (sham) and 4 Gy, cells were stained with FITC-labeled cmHsp70.1 monoclonal antibody (multimmune GmbH, Munich) on ice for 30 min. After antibody incubation, cells were washed in ice-cold PBS and fixed in 3.7% *w/v* PFA in PBS (pH 7.4). Nuclei were counterstained with 4',6-diamidino-2-phenylindole (DAPI). Fluorescence images were taken with an AxioImager M2 microscope, equipped with a 100 $\times$  oil immersion objective (Carl Zeiss Microscope, Jena, Germany) at a resolution of 2048  $\times$  2048 pixels. To avoid potential cross-interferences of the different fluorophores, images for FITC and DAPI were acquired using a sequential image recording mode.

## 2.5. Hsp70 lipELISA

Levels of extracellular Hsp70 in the supernatant of sham irradiated and irradiated U87 cells on days 1, 4 and 7 were determined using the lipHsp70 ELISA, as described elsewhere [14]. The measured values of extracellular Hsp70 were normalized to  $1 \times 10^6$  viable tumor cells.

## 2.6. Europium Assay

The lytic activity of human NK cells cultured in RPMI-1640 medium supplemented with 10% *v/v* heat inactivated fetal calf serum (FCS), 1% antibiotics (10,000 IU/mL penicillin, 10 mg/mL streptomycin), L-glutamine, sodium pyruvate and Hsp70 peptide TKD (2  $\mu$ g/mL) and IL-2 (100 IU/mL) at a cell density of  $5 \times 10^6$  peripheral blood lymphocytes (PBL) for 4 days against sham (0 Gy) and 4 Gy irradiated tumor cells was determined at different effector-to-target (E:T) ratios ranging from 50:1 to 3:1 using a standard 3.5 h Europium assay. The tumor cells were washed twice with fresh medium before the assay



starts to exclude the presence of extracellular Hsp70 during the assay. Mean values of an experiment in triplicates are shown. The specific lysis was calculated according to Equation (1):

$$\text{Specific Lysis} = \frac{\text{Experimental Release} - \text{Spontaneous Release}}{\text{Maximum Release} - \text{Spontaneous Release}} \quad (1)$$

### 2.7. Statistical Analysis

Each sample was measured in at least three independent experiments. Means and standard deviations are presented for quantitative data. Analysis of variance (ANOVA) was used for comparisons of group means. If the global null hypothesis of all group means being equal could be rejected on a significance level of  $\alpha = 5\%$ , pairwise group comparisons were conducted by *t*-tests. For these pairwise comparisons, standard deviations were pooled over all groups, and Bonferroni correction was applied to account for multiple testing. A two-way ANOVA was used to assess the impact of radiation dose on the specific lysis at different E:T ratios by fitting a model including main effects and their interaction term to the data. A significance level of 5% was used.

## 3. Results

### 3.1. Membrane Hsp70 Expression Remains Stable During a Culture Period of 7 Days

To maintain cells in the exponential growth phase during a culture period of 7 days, different tumor cell counts were seeded. For a culture period of 1–4 days  $0.25 \times 10^6$  cells, for 5 days  $0.125 \times 10^6$  cells, for 6 days  $0.06 \times 10^6$  cells and for 7 days  $0.01 \times 10^6$  cells were seeded on day 0. Representative data for mHsp70 expression on U87 cells during a period of 7 days after sham irradiation (0 Gy) are summarized in Figure 1. No significant differences in the percentage of positively stained cells (Figure 1A;  $F(6,14) = 0.526$ ,  $p = 0.780$ ) and mean fluorescence intensity (mfi) (Figure 1B;  $F(6,14) = 2.202$ ,  $p = 0.105$ ) were detected over a 7 day culture period. The slightly lower mHsp70 density on day 0 could be attributed to the very short incubation period of 5 h after trypsin treatment and seeding.

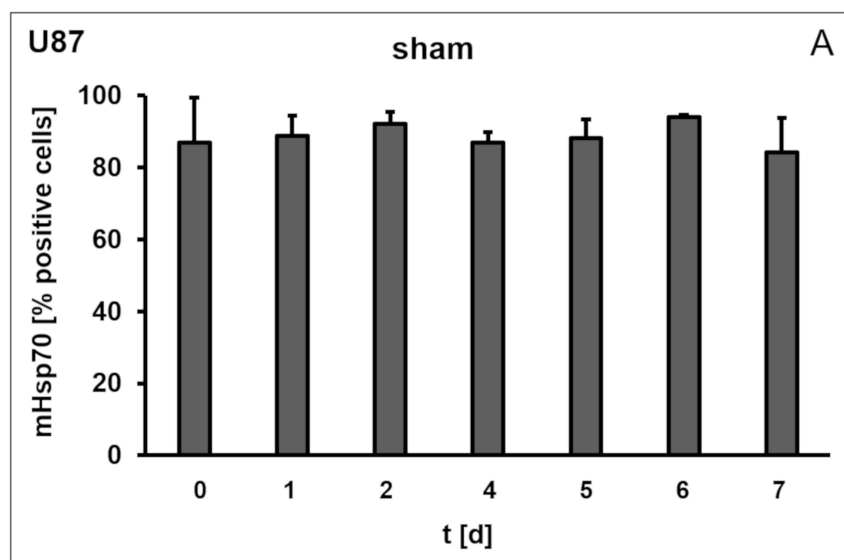
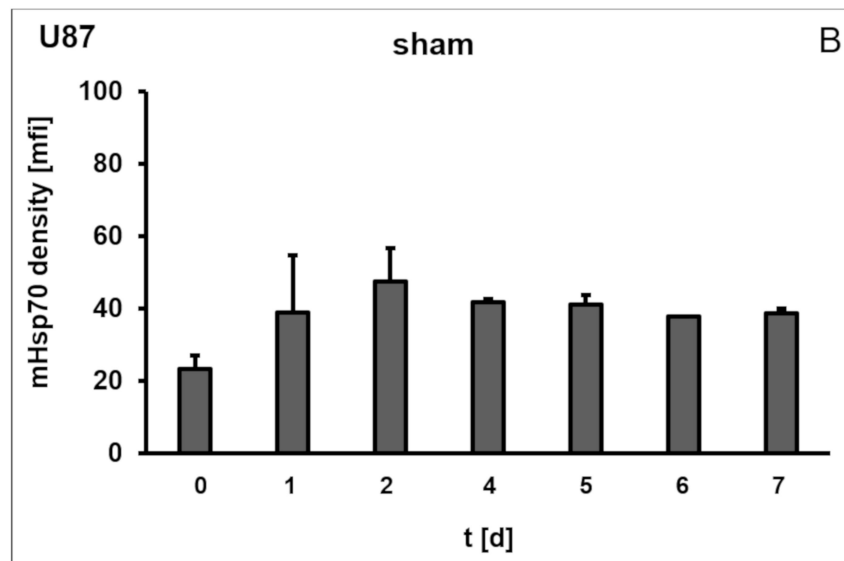


Figure 1. Cont.



**Figure 1.** Percentage (A) and mean fluorescence intensity (mfi) (B) of mHsp70-positive U87 glioblastoma cells after sham irradiation (0 Gy) on days 0, 1, 2, 4, 5, 6 and 7. Bars represent the mean value and the corresponding standard deviation (SD) of  $n = 3$  independent experiments. ANOVA was used to compare data across all days.

### 3.2. Irradiation Induces an Increase in the Mhsp70 Density on Different Tumor Cell Lines

Although the percentage of mHsp70-positive cells remained unaltered on U87 (Figure 2A), HeLa (Figure 2B) and HepG2 (Figure 2C) cells on day 1 after sham (0 Gy), 4 and 6 Gy irradiation, the mHsp70 density differed significantly upon radiation. A radiation dose of 6 Gy nearly doubled the mean fluorescence intensity (mfi) in all three tumor cell lines. In U87 cells the mfi increased from  $38.9 \pm 15.8$  (sham) to  $47.1 \pm 16.0$  after irradiation with 4 Gy and to  $83.5 \pm 14.2$  after irradiation with 6 Gy, on day 1 (Figure 2D;  $F(2,6) = 4.77$ ,  $p = 0.058$ ). In HeLa cells the mfi increased from  $9.2 \pm 1.9$  (sham) to  $15.7 \pm 0.8$  ( $p = 0.04$ ) and  $20.6 \pm 6.8$  ( $p = 0.03$ ) after irradiation with 4 and 6 Gy, respectively (Figure 2E), and in HepG2 the mfi increased from  $13.9 \pm 2.7$  to  $22.0 \pm 2.6$  ( $p = 0.04$ ) after 4 Gy and to  $22.3 \pm 4.6$  (Figure 2F) after 6 Gy, on day 1. The mHsp70 density on sham treated and completely untreated control cells was identical (data not shown). Cell viability of all tumor cell lines was not affected by radiation doses ranging from 2 to 6 Gy.

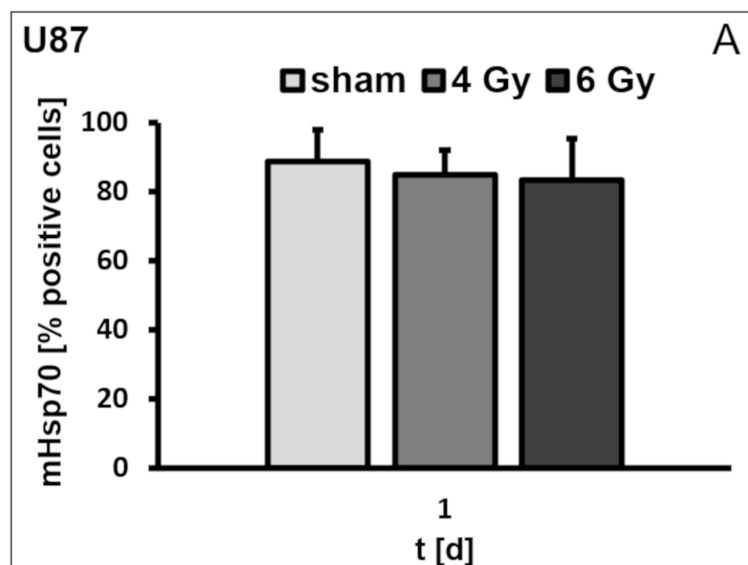


**Figure 2. Cont.**

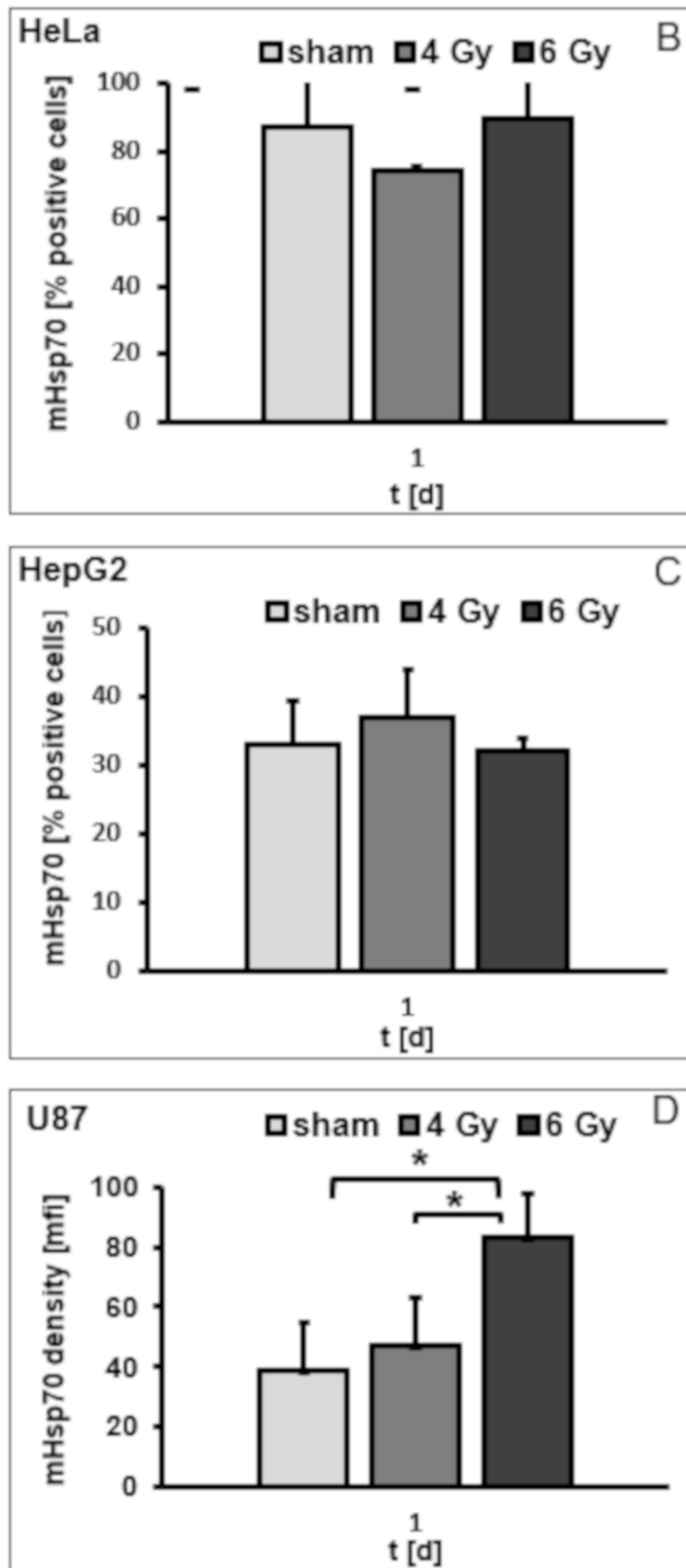
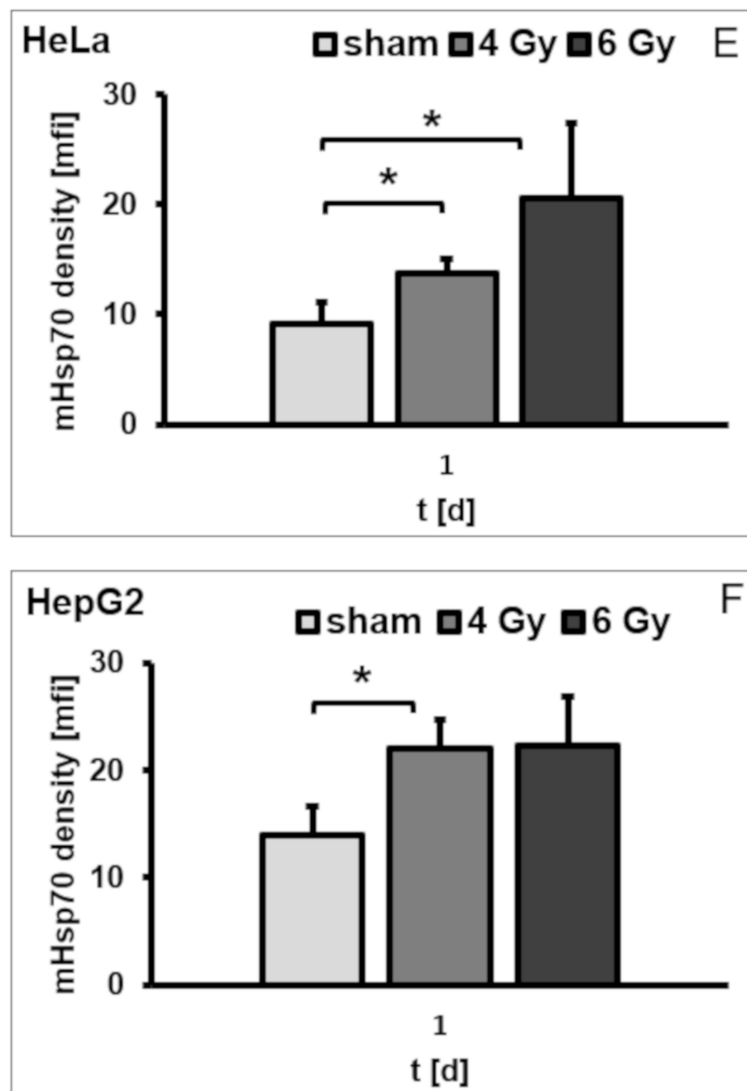


Figure 2. Cont.



**Figure 2.** Percentage of mHsp70-positive U87 (A), HeLa (B) and HepG2 (C) cells on day 1 after irradiation with 0 (sham), 4 and 6 Gy. Mean fluorescence intensity (mfi) of mHsp70 expression on U87 (D), HeLa (E) and HepG2 (F) cells on day 1 after irradiation with 0 (sham), 4 and 6 Gy. Bars represent the mean value and the corresponding standard deviation (SD) of  $n = 3$  (U87),  $n = 4$  (HeLa), and  $n = 3$  (HepG2) independent experiments. For comparison of different irradiation doses, ANOVA has been conducted followed by pairwise *t*-tests (with Bonferroni correction). Significance (sham vs. different irradiation doses on day 1, after Bonferroni correction): \*  $p \leq 0.05$ .

### 3.3. Irradiation-Induced Upregulation of mHsp70 Is Time-Dependent

A comparison of the mHsp70 densities on days 4 and 7 after irradiation with 4 and 6 Gy revealed that mfi values on day 4 remained significantly upregulated, but dropped on day 7 after radiation in HeLa (Figure 3A) and U87 (Figure 3B) cells. The mfi of sham (0 Gy) treated HeLa cells was  $7.9 \pm 1.3$  compared to  $14.8 \pm 3.0$  and  $18.6 \pm 3.1$  after radiation with 4 and 6 Gy on day 4 (Figure 3A;  $p = 0.05$ ). The mfi of sham (0 Gy) treated U87 cells was  $41.9 \pm 0.8$  compared to  $79.3 \pm 12.8$  and  $75.1 \pm 7.7$  after radiation with 4 Gy ( $p = 0.02$ ) and 6 Gy ( $p = 0.03$ ) on day 4 (Figure 3B;  $F(2,6) = 11.24$ ,  $p = 0.009$ ). Significant differences were observed between sham and 4 Gy and between sham and 6 Gy irradiated cells, whereas no statistically significance was observed between 4 and 6 Gy irradiated HeLa (Figure 3A) and U87 cells (Figure 3B). On day 7 after irradiation, the mfi of sham treated HeLa cells remained at  $9.2 \pm 1.4$ , but that of 4 and 6 Gy irradiated cells dropped to  $12.4 \pm 1.0$  and  $17.5 \pm 1.7$ , respectively, on day 7 (Figure 3A). In line with these results, the mfi of sham treated U87 cells

remained at  $38.73 \pm 1.41$ , but that of 4 and 6 Gy irradiated cells dropped to  $37.60 \pm 7.24$  and  $40.02 \pm 5.71$ , respectively, on day 7 (Figure 3B;  $F(2,6) = 0.1003$ ,  $p = 091$ ). No significant differences in the mfi were observed in the differently irradiated U87 cells on day 7 (Figure 3B). The upregulated mHsp70 density on day 4 and the downregulation of mHsp70 on day 7 after irradiation with 4 Gy was confirmed by immunocytochemistry (ICC) (Figure 3C). In contrast to the mHsp70 expression, the cytosolic Hsp70 content in U87 cells remained unaltered upon irradiation with 2, 4 and also 6 Gy, as determined by Western blot (Figure 3D) and intracellular Hsp70 staining on days 4 and 7 (Figure 3E). Similar results were observed with HeLa cells (data not shown).

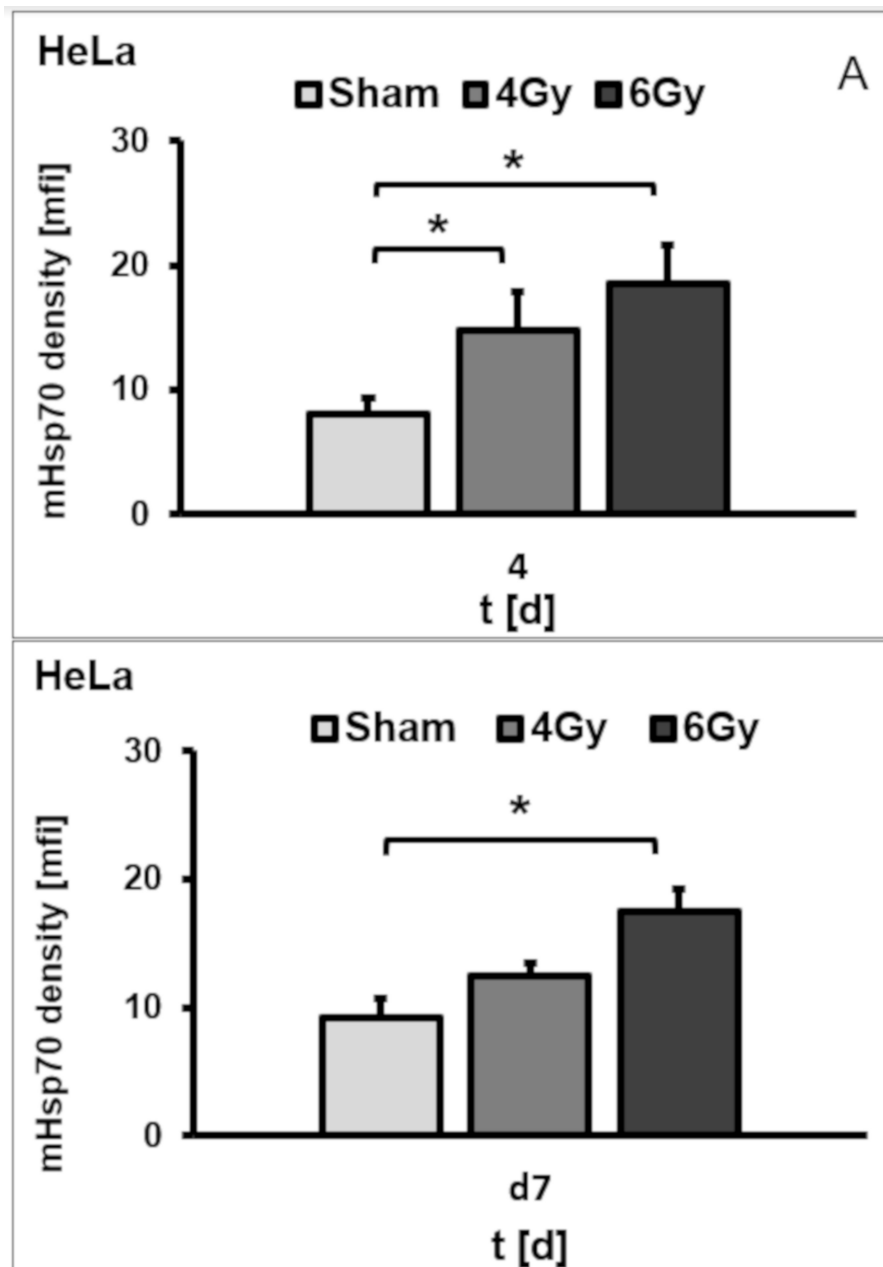


Figure 3. Cont.

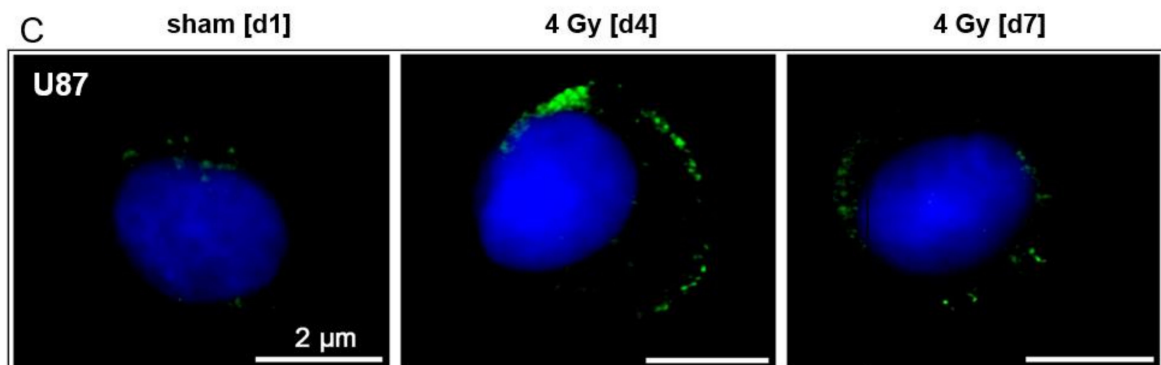
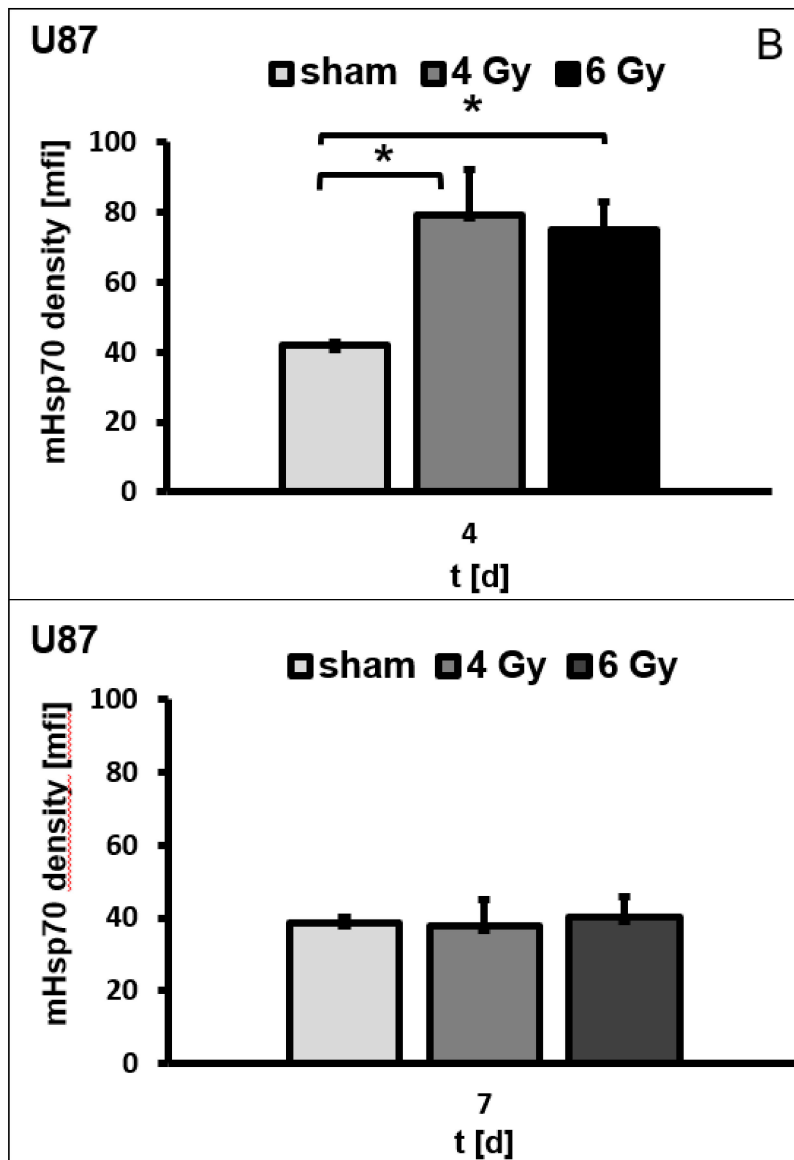
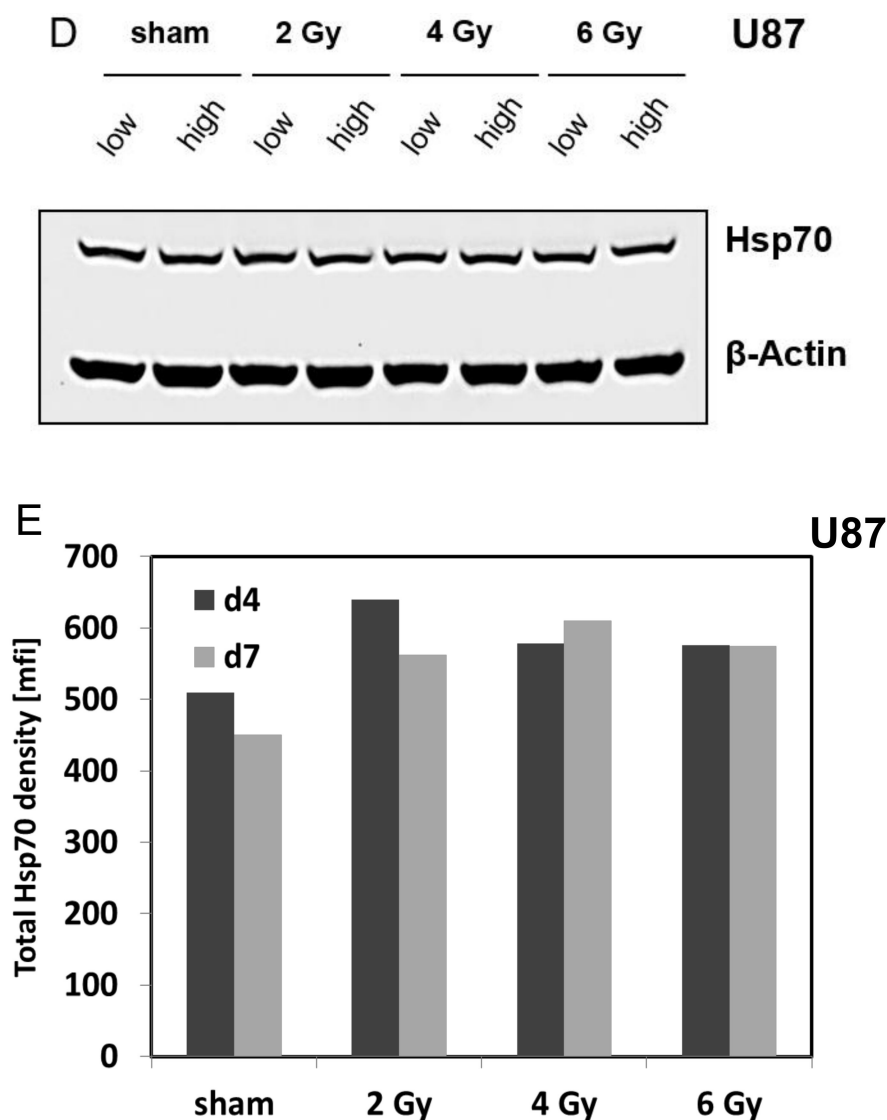


Figure 3. Cont.



**Figure 3.** Mean fluorescence intensity (mfi) of mHsp70 expression in HeLa (A) and U87 (B) cells after sham (0 Gy), 4 and 6 Gy irradiation on days 4 and 7. Bars represent the mean values and the corresponding standard deviation (SD) of  $n = 3$  independent experiments. Significance (sham vs. different irradiation doses on day 4):  $* p \leq 0.05$  (after Bonferroni correction). Comparison of different doses (sham 0, 4, 6 Gy) were performed by pairwise  $t$ -tests with pooled SD and Bonferroni correction for multiple testing. An upregulation of the mHsp70 expression density upon irradiation with 4 Gy on day 4 and a downregulation of the mHsp70 expression on day 7 shown by immunocytochemistry (ICC) in U87 cells (C). Cytosolic Hsp70 expression was determined by Western blot analysis (D) and intracellular Hsp70 staining (E) in U87 cells after sham (0 Gy), 4 and 6 Gy irradiation on days 4 and 7.  $\beta$ -actin staining served as a loading control. Data show one representative experiment out of two independent experiments with similar results.

#### 3.4. Irradiation-Induced Effects on the mHsp70 Density Are Dose- and Time-Dependent

The previous results indicated clear differences in the mHsp70 density on U87 cells that depend on the recovery time after irradiation. Figure 4 summarizes dose- and time-dependent effects on the mHsp70 density. Although mfi values for sham (0 Gy) treated cells did not differ significantly over a period of 7 days when different initial cell counts were seeded (Figure 1B), an exposure to 2 Gy induced a progressive slow increase in mfi values from day 0 up to a maximum value of  $67.4 \pm 16.7$  on day 5 that decreased to  $39.3 \pm 4.3$  on day 7 (Figure 4A;  $F(6,14) = 3.8952$ ,  $p = 0.017$ ). Cells that have been irradiated with a higher dose (4 Gy) reached the maximum mfi value ( $79.3 \pm 12.8$ ;  $p \leq 0.05$ ) by day 4

(Figure 4B;  $F(6,14) = 3.916, p = 0.016$ ); however, the drop in the mfi values thereafter occurred more rapidly than after irradiation with 2 Gy. Following an irradiation with 6 Gy, mHsp70 expression density was significantly increased already on day 1 compared to sham (0 Gy) irradiated cells ( $23.3 \pm 3.7$  versus  $83.6 \pm 14.2; p \leq 0.05$ ), persisted for 3 days and dropped on day 5 (Figure 4C;  $F(6,14) = 10.70, p = 0.0002$ ). In Figure 4A–C, mfi values differing significantly ( $p \leq 0.05$ ) from the value on day 0 at each individual irradiation dose (2, 4, 6 Gy) using a pairwise comparison *t*-test with pooled SD marked with an asterisk. A comparison of all time points (day 0 to day 7) and all radiation doses (0, 2, 4, 6 Gy) reflects the different dose- and time-kinetics of the mHsp70 densities in U87 cells (Figure 4D).

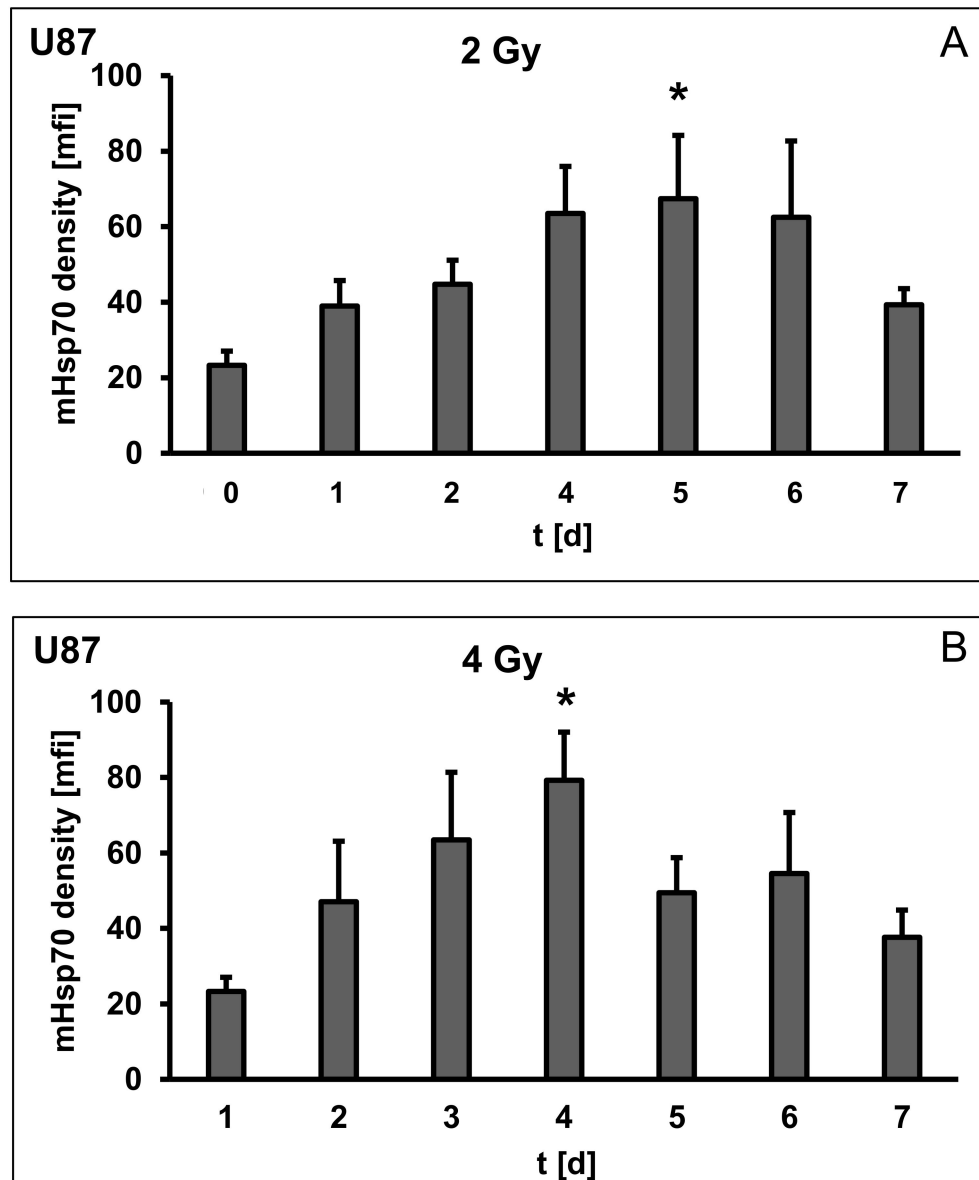
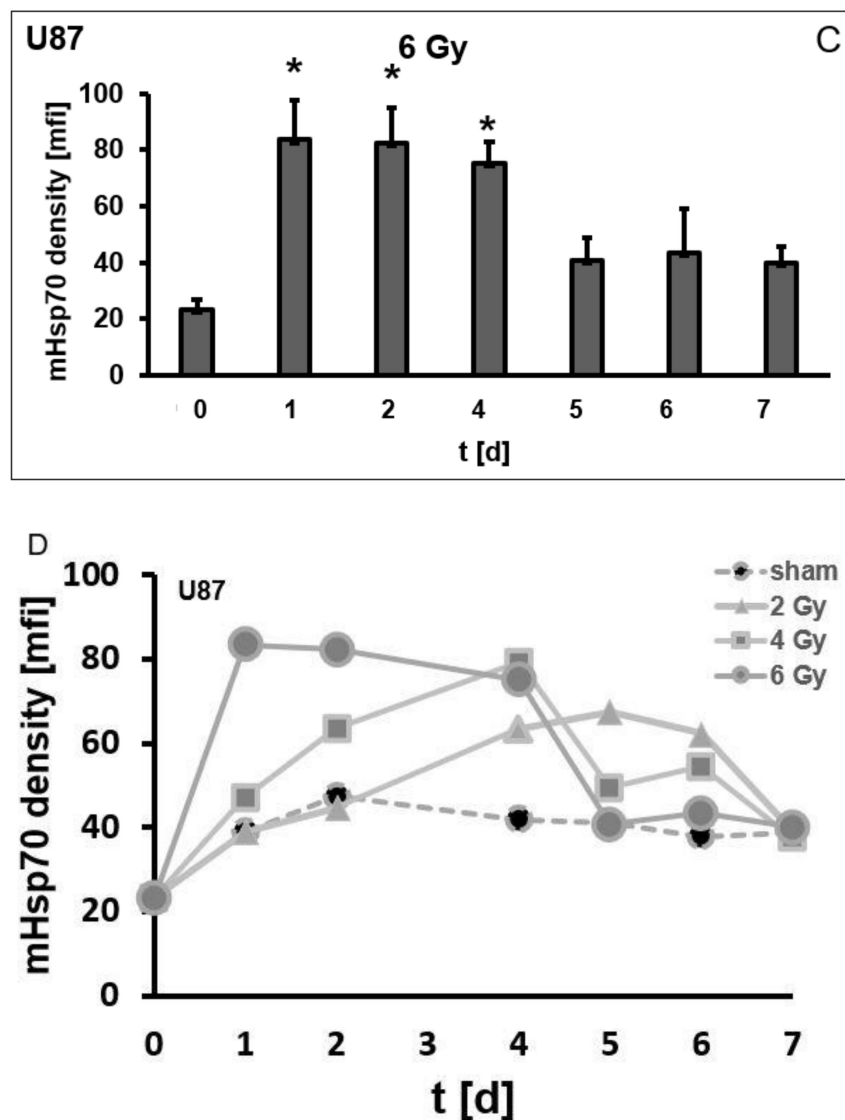


Figure 4. Cont.





**Figure 4.** Dose- and time-dependent radiation effects on the mean fluorescence intensity (mfi) of mHsp70 on U87 human glioblastoma cells over 7 days with different radiation doses (2 Gy (A), 4 Gy (B), 6 Gy (C)). Bars represent the mean values and the corresponding standard deviation (SD) of  $n = 3$  independent experiments. Significance (comparison of one dose on different days):  $* p \leq 0.05$ . For comparison of different days at a single dose ANOVA has been conducted. Comparisons to sham (0 Gy) treated cells were performed by pairwise  $t$ -tests with pooled SD and Bonferroni correction for multiple testing. (D) Summary of the kinetics of the mHsp70 density after sham (0 Gy), 2, 4, 6 Gy over a period of 7 days. For a better clarity, statistical significance was only shown in Figure 4A–C, but not in Figure 4D.

### 3.5. Irradiation-Induced Cell Cycle Arrest and Its Impact on the mHsp70 Density

On day 4 ( $F(3,24) = 64.83, p < 0.001$ ) and on day 7 ( $F(3,24) = 4.232, p = 0.016$ ) after irradiation with 2, 4 and 6 Gy, a dose-dependent cell cycle arrest in G2/M was observed in U87 cells (Figure 5A). A concomitant analysis of the mHsp70 density with the cell cycle revealed higher mHsp70 densities in G2/M compared to G1 in sham (0 Gy) and irradiated (2, 4, 6 Gy) tumor cells (Figure 5B). However, the mHsp70 density appeared not to be associated with the irradiation-induced G2/M arrest since a higher proportion of cells in G2/M on day 7 was not associated with a further increase in the mHsp70 density. An assessment of extracellular Hsp70 concentrations normalized to  $1 \times 10^6$  viable tumor cells showed significantly increased values on days 4 and 7 after an irradiation with 4 and 6 Gy compared

to sham irradiated cells ( $p \leq 0.05$ ), whereas on day 1 no significant increase in extracellular Hsp70 in the cell culture supernatant was detected (Figure 5C).

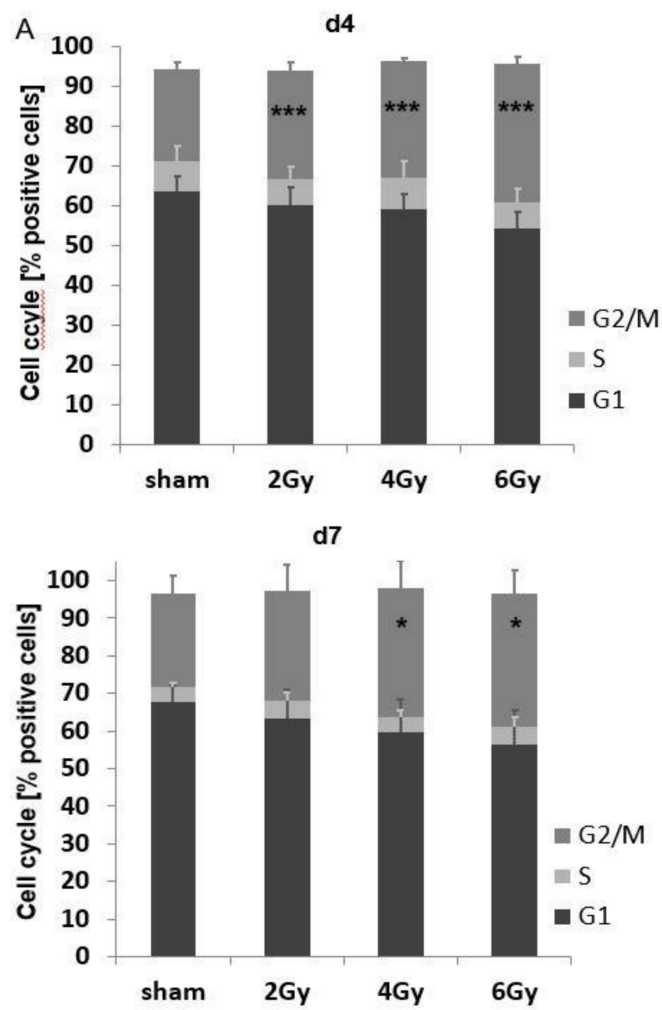


Figure 5. Cont.

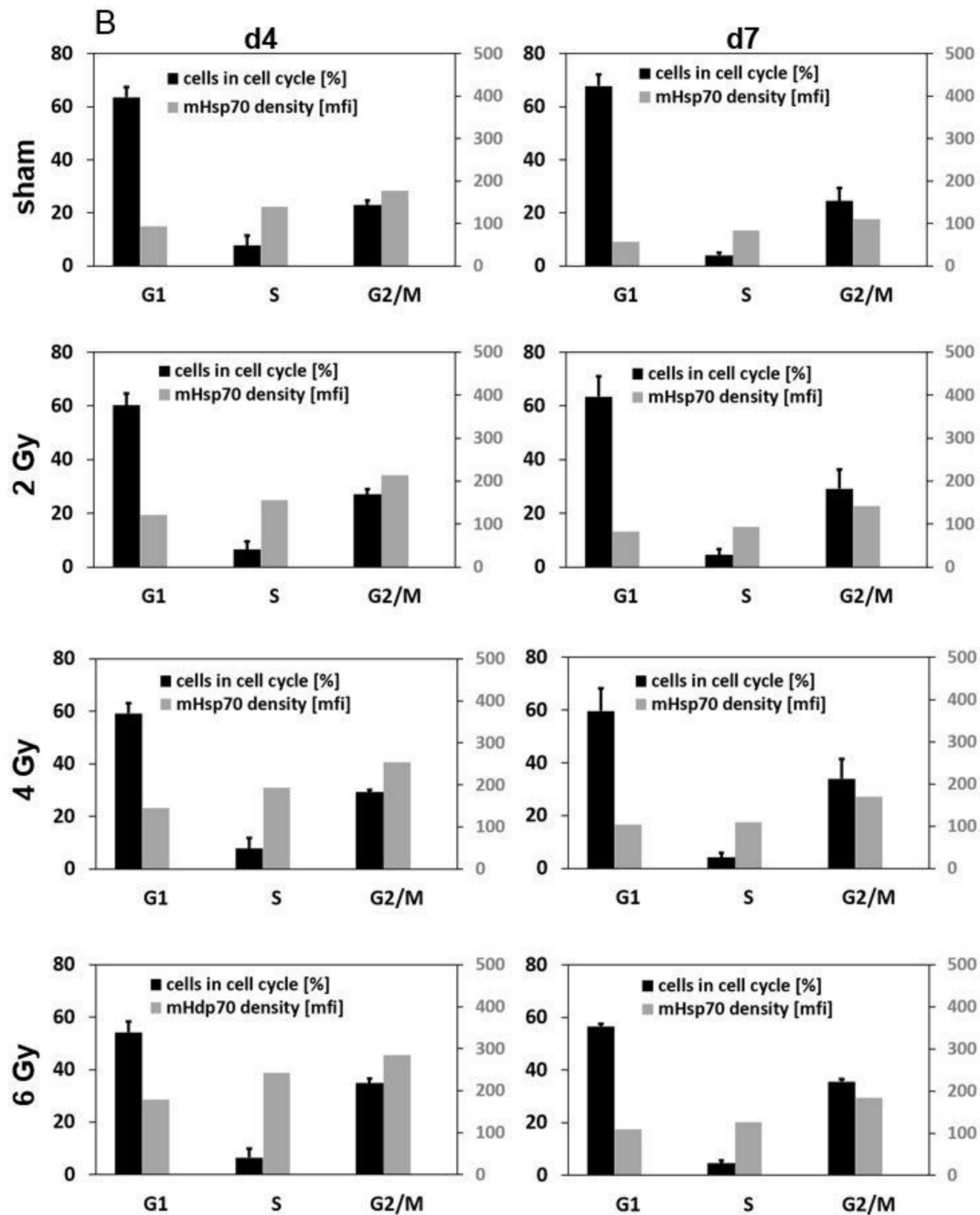
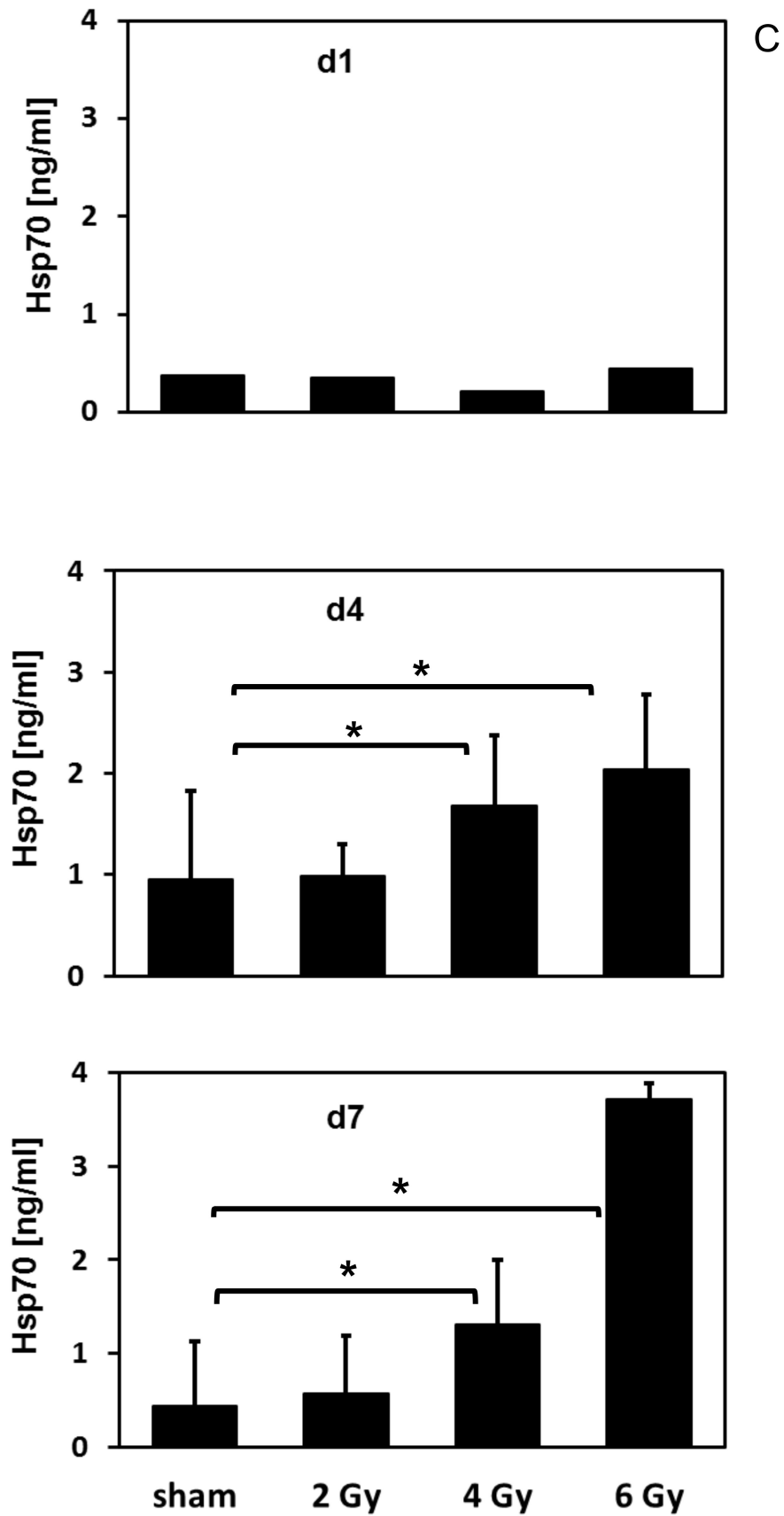


Figure 5. Cont.



**Figure 5.** Comparative analysis of the cell cycle (G0, S, G2/M) in U87 cells after sham (0 Gy), 2, 4 and 6 Gy irradiation on days 4 and 7: \*  $p \leq 0.05$ ; \*\*\*  $p \leq 0.001$  (A). For comparison of different cell cycle phases

ANOVA has been used. Differences in the G2/M phase were analyzed by pairwise t-tests with pooled SD and Bonferroni correction for multiple testing. Comparative analysis of the mHsp70 expression in the different cell cycle phases (G0, S, G2/M) in U87 cells on days 4 and 7 after sham (0 Gy), 2, 4 and 6 Gy irradiation (B). Comparative analysis of extracellular Hsp70 concentrations in the supernatant of U87 cells on days 1, 4 and 7 after sham (0 Gy), 2, 4 and 6 Gy irradiation (C). The data were normalized to a defined number of  $1 \times 10^6$  cells viable cells. Data represent the mean values and the corresponding standard deviation (SD) of  $n = 3$  independent experiments. Significance (sham vs. all different irradiation doses): \*  $p \leq 0.05$ . For comparisons of extracellular Hsp70 levels, pairwise t-tests with pooled SD and Bonferroni correction were performed.

3.6. Increased mHsp70 Expression Density Is Associated with an Increased Sensitivity to Lysis Mediated by TKD/IL-2-Activated NK Cells

The density of mHsp70 expression plays a crucial role in the recognition of tumor cells by Hsp70-peptide TKD/IL-2-activated NK cells, but not by cytotoxic CD8-positive T lymphocytes, as previously demonstrated [15]. Therefore, the cytolytic activity of Hsp70-targeting NK cells against sham (0 Gy) and irradiated (4 Gy) tumor cells was tested. The increase in the mHsp70 density of tumor cells on day 4 after irradiation that were used in the cytotoxicity assay is illustrated in Figure 6A. The lysis of irradiated (4 Gy) tumor cells by TKD/IL-2-activated NK cells is significantly higher than that of sham (0 Gy) irradiated cells at E:T ratios ranging from 50:1 to 3:1 (Figure 6B;  $F(1,4) = 8.11$ ,  $p = 0.00004$ ).

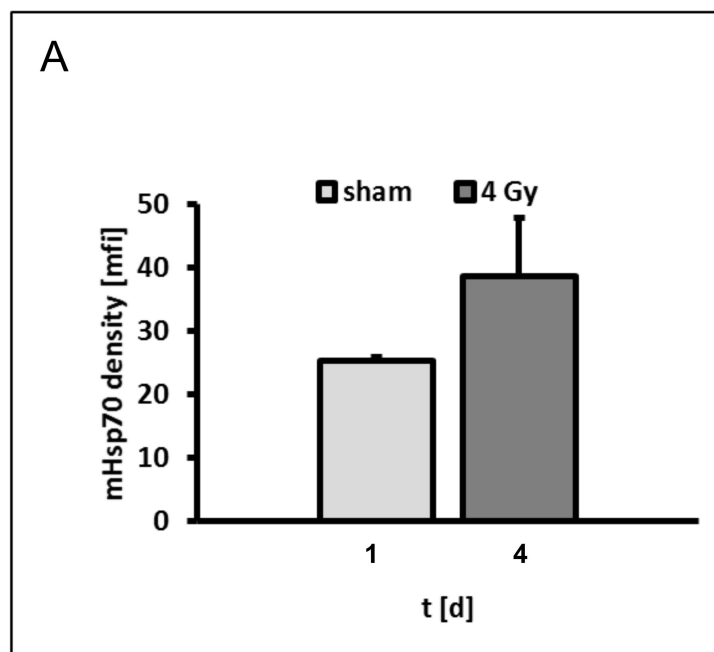
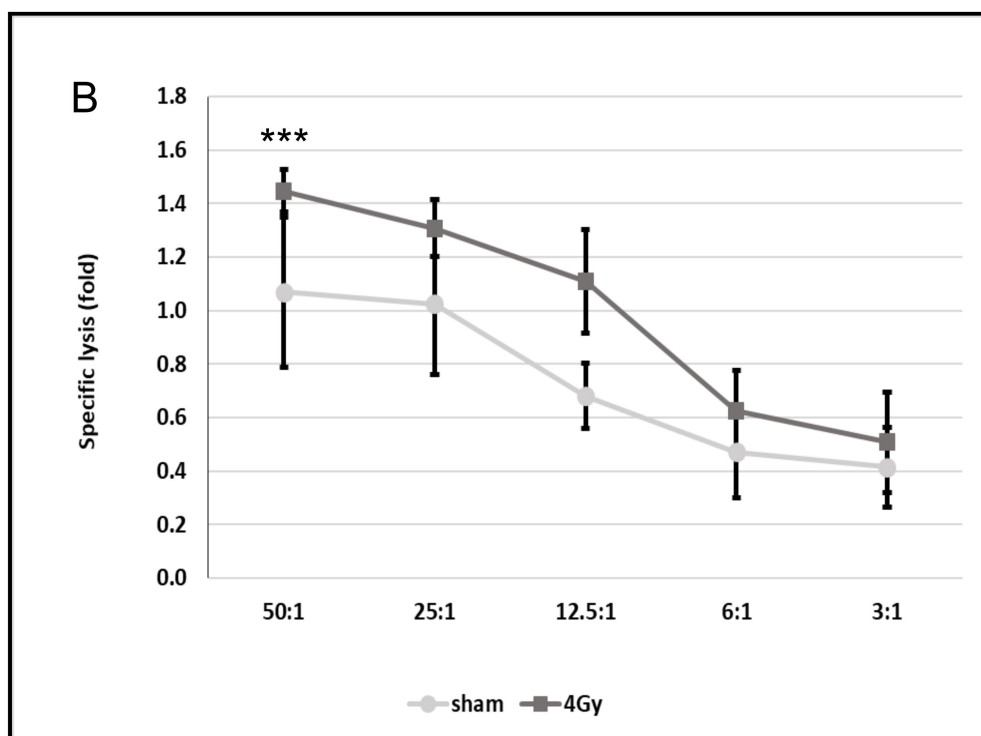


Figure 6. Cont.



**Figure 6.** Comparative analysis of the cytolytic activity of TKD/IL-2-activated natural killer (NK) cells targeting mHsp70-positive tumor cells. Sham (0 Gy) and 4 Gy irradiated tumor cells on day 4 were used as target cells. (A) mHsp70 mean fluorescence intensity (mfi) on sham (0 Gy) and 4 Gy irradiated tumor target cells. The results represent mean values and the corresponding standard deviation (SD) of  $n = 2$  independent experiments. The Welch two sample  $t$ -test was used. (B) Lytic activity of NK cells against sham (0 Gy) and 4 Gy irradiated tumor target cells. The effector to target (E:T) ratios range from 50:1 to 3:1. The results represent mean values and the corresponding standard deviation (SD) of  $n = 2$  independent experiments in triplicate. Significance (lysis of sham vs. 4 Gy irradiated target cells): \*\*\*  $p \leq 0.001$ . Two-way ANOVA were used to compare lysis at different E:T ratios against tumor cells after different irradiation (sham (0 Gy) vs. 4 Gy).

#### 4. Discussion

Compared to normal cells, highly aggressive tumor cells frequently exhibit higher cytosolic Hsp70 levels, which are further upregulated upon a variety of different environmental stress factors [7]. Intracellularly, Hsp70 ensures correct protein folding and transport [3] and interferes with both intrinsic and extrinsic apoptosis pathways to avoid cell death and thereby foster tumor cell survival [5]. Apart from its cytosolic localization, Hsp70 can be actively released in lipid microvesicles, such as exosomes [13,16–18], and Hsp70 is also expressed on the plasma membrane of tumor cells [19]. While cytosolic Hsp70 is mainly responsible for maintaining protein homeostasis and protection against programmed cell death [3,5], mHsp70 mediates dual functions: on the one hand it stabilizes lysosomal and plasma membranes and thereby also can prevent apoptosis [20,21], on the other hand, it provides a tumor-specific target for NK cells that have been pre-activated with Hsp70 plus low-dose IL-2 [8,15]. The specific membrane localization of Hsp70 on tumor cells can be explained by an interaction of Hsp70 with tumor-specific lipid compounds such as globoyltriaosylceramide Gb3 [22]. In vitro lipid copellation assays revealed that recombinant Hsp70 specifically interacts with the tumor-specific lipid raft component globoyltriaosylceramid Gb3 [22] or with the non-raft lipid compound phosphatidylserine (PS), which translocates to the outer plasma membrane leaflet upon environmental stress [23]. Since mHsp70 has been found to serve as a target for Hsp70-peptide TKD/IL-2-activated NK cells in vitro [24] and in vivo [25], time- and dose-dependent effects of irradiation with respect to the mHsp70 density on different human tumor cell lines were studied.

The relevance of mHsp70 as a target for C-type lectin receptor CD94-positive NK cells [14] has previously been demonstrated in isogenic tumor cell systems which express differential levels of mHsp70, but identical cytosolic Hsp70 levels, and by Hsp70 antibody blocking studies [21]. A better understanding of the mHsp70 kinetics following irradiation might help to identify an optimal therapeutic window for combination therapies consisting of ionizing irradiation and Hsp70-targeting NK cell-based immune therapies.

Glioblastoma multiforme (GBM) the most common malignant neoplasia of the brain in adults is associated with a high mortality. Despite multimodal treatment strategies consisting of surgery, radiotherapy and systemic chemotherapy using temozolomide [26], the median survival remains poor (15–18 months) and recurrence rates are high. Its intratumoral heterogeneity, concerning genetic alterations and morphology, as well as the infiltrative growth and diffuse dissemination into the brain parenchyma often limit a successful treatment of GBM. Therefore, there is a high medical need for innovative treatment strategies for GBM. The mHsp70 density as a potential target for NK cells was measured in the highly radiation-resistant human glioblastoma cell line U87 and two other tumor cell lines at different time points after irradiation with doses ranging from 2 to 6 Gy. In a previous study, we demonstrated that a high mHsp70 expression was also found on primary glioblastoma cells without isocitrate-dehydrogenase 1 (IDH-1) mutation, whereas secondary glioblastoma with IDH-1 mutation and low-grade anaplastic gliomas exhibited a lower mHsp70 density. The O6-methylguanine DNA methyltransferase (MGMT) status appeared to be not associated with the mHsp70 expression [27]. Regarding these results, we hypothesize that the MGMT-negative glioblastoma cell line U87 might serve as a model for highly aggressive, mHsp70-positive primary glioblastomas without IDH-1 mutation.

To maintain cells in the exponential growth phase, tumor cells were seeded at different cell densities, which were adapted to the different culture periods. In sham as well as non-treated tumor cells, the proportion of mHsp70-positive cells remained at nearly 100% with a relatively low density over the whole culture period of 7 days. These findings are in line with previous results obtained with other tumor types such as epithelial tumor cells of the head and neck area [28].

Environmental stress, including irradiation, can cause an up-regulation of the mHsp70 density on tumor cells [10,20]. Herein, we have shown for the first time that the kinetics of the mHsp70 expression is dependent on the irradiation dose, but not on the cytosolic Hsp70 levels. While the maximum mHsp70 expression is reached only on day 5 after an irradiation with 2 Gy, the peak mHsp70 expression is detected already on day 1 after irradiation with 6 Gy. This means that low-dose irradiation might be associated with a later onset of the mHsp70 expression compared to high-dose irradiation. These findings are in accordance to results of Diller et al. [29] who showed that the kinetics of the heat shock protein synthesis are transient and proportional to the applied stress.

Synthesis and expression of Hsp70 is often dependent on dose- and time-dependent factors; therefore, cytoprotective repair mechanisms that depend on the anti-apoptotic molecular chaperone Hsp70 in U87 cells are also related to the applied stress [29]. Our findings indicate that a high, but yet non-lethal, irradiation dose of 6 Gy induces an early onset of the mHsp70 expression after 1 day with a sustained overexpression that persists for 3 days, whereas lower irradiation doses induce a slower up-regulation in U87 cells.

In an effort to define the optimal timing for the application of ex vivo stimulated mHsp70-targeting NK cells [24] after radiotherapy, it is important to determine the maximum density of mHsp70 on tumor cells. In the case of U87 cells, an irradiation dose between 4 and 6 Gy might be optimal to achieve a fast and long-lasting upregulation of the mHsp70 expression in vitro. However, future preclinical studies using fractionated irradiation protocols are needed to define the optimal irradiation dose that is suitable for an in vivo application of mHsp70-targeting immune cell-based therapies. Interestingly, in highly radiation-resistant U87 cells [29], none of the applied radiation doses caused an upregulation in intracellular Hsp70 levels. This finding might suggest that anti-apoptotic pathways that are predominantly regulated by cytosolic Hsp70 might not be initiated in U87 cells up to a radiation dose of 6 Gy. Furthermore, these data indicate that the radiation-induced translocation of Hsp70

from the cytosol to the plasma membrane is not dependent on *de novo* Hsp70 synthesis. An ER–Golgi pathway could also be ruled out for the translocation of Hsp70 from the cytosol to the plasma membrane, since inhibitors of classical protein transport pathways like monensin, brefeldin A, tunicamycin and thapsigargin neither affected mHsp70 expression nor exosomal release [30]. It is more likely that non-classical vesicular transport pathways [29] that appear to be inducible by non-lethal irradiation might enable mHsp70 translocation and release, since we observed an increase in extracellular Hsp70 on days 4 and 7 after irradiation with 4 and 6 Gy. Moreover, a radiation-induced cell cycle arrest appeared to be not associated with mHsp70 transport.

There is strong evidence that lethal stress which drastically harms tumor cell survival cannot be compensated by cytoprotective repair mechanisms that include the cytosolic overexpression of Hsp70 [31,32]. After lethal stress, Hsp70 can be externalized by dying tumor cells as a danger-associated molecular pattern (DAMP) with the capacity to initiate anti-tumor immune responses [1,2,33]. Hsp70-chaperoned tumor peptides can induce CD8-positive T cell mediated immune responses after cross-presentation of immunogenic tumor antigens on MHC class I molecules [34], whereas peptide-free Hsp70 in the context of pro-inflammatory cytokines, such as IL-2, can augment the cytolytic and migratory capacity of NK cells that recognize and kill remaining therapy-resistant mHsp70-positive tumor cells [16,21]. Herein, we could show that upon sub-lethal irradiation with 4 and 6 Gy, extracellular Hsp70 concentrations started to increase on days 4 and 7. As to whether elevated extracellular Hsp70 levels are able to further stimulate NK cell mediated immunity *in vivo* remains to be determined in preclinical models.

In summary, the applied radiation dose- and time-kinetics play a critical role in optimizing radiation-induced effects by increasing the density of mHsp70 expression on the surface of surviving residual tumor cells as a target for immune cells. Membrane-bound Hsp70 plays a crucial role in stimulating the innate and adaptive immune system as it is selectively expressed on the cell surface of tumor, but not normal cells [35], and therefore serves as a tumor-specific recognition structure [13]. We could show that Hsp70-targeting NK cells are capable to specifically recognize and kill tumor cells presenting Hsp70 on their plasma membrane most likely via granzyme B mediated apoptosis [36].

## 5. Conclusions

In contrast to intracellular Hsp70, extracellular and mHsp70 play key roles in stimulating both adaptive and innate immune responses and thereby might provide protective anti-tumor immunity [8]. By its exclusive expression on the surface of tumor cells, but not normal cells [9], mHsp70 serves as a tumor-specific target for activated NK cells [10]. In this study we present evidence that the radiation dose plays a pivotal role on the kinetics of the mHsp70 density of human glioblastoma cells. Low-dose irradiation is associated with a later onset of the mHsp70 expression compared to higher irradiation doses. Therefore, hypofractionated irradiation schemes with higher doses might be beneficial for generating an extended therapeutic window for mHsp70-targeting immunotherapies.

**Author Contributions:** Conceptualization, writing reviewing editing, funding acquisition, supervision G.M., Funding acquisition, S.S., methodology, software, data validation B.H., writing original draft, H.F., data acquisition and analyses H.F., S.S., A.H.S., M.S. (Melissa Schwab), T.D.G. M.P., C.W., M.S. (Maxim Shevtsov). All authors have read and agreed to the published version of the manuscript.

**Funding:** This research was funded by the Deutsche Forschungsgemeinschaft DFG (SFB824/3, INST 411/36FUGG, INST 95/980-1FUGG, STA1520/1-1), BMBF (01GU823, 02NUK038A), BMWi (ZF4320102CS7, ZF4320104AJ8), DKTK and Russian Foundation for Basic Research (19-08-0024).

**Acknowledgments:** We thank Anett Lange for excellent editorial assistance.

**Conflicts of Interest:** Gabriele Multhoff declares a conflict of interest with respect to multimmune GmbH. The company did not have a role in the results or the interpretation of the results but provided the antibody cmHsp70.1. All other authors declare no conflicts of interest.



## References

- Formenti, S.C.; Demaria, S. Combining radiotherapy and cancer immunotherapy: A paradigm shift. *J. Natl. Cancer Inst.* **2013**, *105*, 256–265. [CrossRef] [PubMed]
- Pasi, F.; Paolini, A.; Nano, R.; Di Liberto, R.; Capelli, E. Effects of single or combined treatments with radiation and chemotherapy on survival and danger signals expression in glioblastoma cell lines. *Biomed. Res. Int.* **2014**, *2014*, 453497. [CrossRef] [PubMed]
- Radons, J. The human Hsp70 family of chaperones: Where do we stand? *Cell Stress Chaperones* **2016**, *21*, 379–404. [PubMed]
- Multhoff, G.; Hightower, L.E. Distinguishing integral and receptor-bound heat shock protein 70 (Hsp70) on the cell surface by Hsp70-specific antibodies. *Cell Stress Chaperones* **2011**, *16*, 251–255. [CrossRef]
- Beere, H.M.; Wolf, B.B.; Cain, K.; Mosser, D.D.; Mahboubi, A.; Kuwana, T.; Taylor, P.; Morimoto, R.I.; Cohen, G.M.; Green, D.R. Heat-shock protein 70 inhibits apoptosis by preventing recruitment of procaspase-9 to the apaf-1 apoptosome. *Nat. Cell Biol.* **2000**, *2*, 469–475. [CrossRef]
- Kumar, S.; Stokes, J., 3rd; Singh, U.P.; Scissum Gunn, K.; Acharya, A.; Manne, U.; Mishra, M. Targeting Hsp70: A possible therapy for cancer. *Cancer Lett.* **2016**, *374*, 156–166. [CrossRef]
- Craig, E.A. The stress response: Changes in eukaryotic gene expression in response to environmental stress. *Science* **1985**, *230*, 800–801. [CrossRef]
- Shevtsov, M.; Multhoff, G. Heat shock protein-peptide and hsp-based immunotherapies for the treatment of cancer. *Front. Immunol.* **2016**, *7*, 171. [CrossRef]
- Radons, J.; Multhoff, G. Immunostimulatory functions of membrane-bound and exported heat shock protein 70. *Exerc. Immunol. Rev.* **2005**, *11*, 17–33.
- Multhoff, G.; Pockley, A.G.; Schmid, T.E.; Schilling, D. The role of heat shock protein 70 (Hsp70) in radiation-induced immunomodulation. *Cancer Lett.* **2015**, *356*, 179–184. [CrossRef]
- Kokowski, K.; Stangl, S.; Seier, S.; Hildebrandt, M.; Vaupel, P.; Multhoff, G. Radiochemotherapy combined with NK cell transfer followed by second-line PD-1 inhibition in a patient with NSCLC stage IIIb inducing long-term tumor control: A case study. *Strahlenther. Onkol.* **2019**, *195*, 352–361. [CrossRef] [PubMed]
- Schmid, T.E.; Multhoff, G. Radiation-induced stress proteins—The role of heat shock proteins (HSP) in anti-tumor responses. *Curr. Med. Chem.* **2012**, *19*, 1765–1770. [CrossRef] [PubMed]
- Multhoff, G. Heat shock protein 70 (Hsp70): Membrane location, export and immunological relevance. *Methods* **2007**, *43*, 229–237. [CrossRef] [PubMed]
- Breuninger, S.; Ertl, J.; Knape, C.; Gunther, S.; Regel, I.; Rödel, F.; Gaipl, U.S.; Thorsteinsdottir, J.; Giannitrapani, L.; Dickinson, A.M.; et al. Quantitative analysis of liposomal Hsp70 in the blood of tumor patients using a novel lipHsp70 ELISA. *J. Clin. Cell. Immunol.* **2014**, *5*, 515. [CrossRef]
- Multhoff, G.; Mizzen, L.; Winchester, C.C.; Milner, C.M.; Wenk, S.; Eissner, G.; Kampinga, H.H.; Laumbacher, B.; Johnson, J. Heat shock protein 70 (Hsp70) stimulates proliferation and cytolytic activity of natural killer cells. *Exp. Hematol.* **1999**, *27*, 1627–1636. [CrossRef]
- Gastpar, R.; Gehrmann, M.; Bausero, M.A.; Asea, A.; Gross, C.; Schroeder, J.A.; Multhoff, G. Heat shock protein 70 surface-positive tumor exosomes stimulate migratory and cytolytic activity of natural killer cells. *Cancer Res.* **2005**, *65*, 5238–5247. [CrossRef]
- Ireland, H.E.; Leoni, F.; Altaie, O.; Birch, C.S.; Coleman, R.C.; Hunter-Lavin, C.; Williams, J.H. Measuring the secretion of heat shock proteins from cells. *Methods* **2007**, *43*, 176–183. [CrossRef]
- Vega, V.L.; Rodriguez-Silva, M.; Frey, T.; Gehrmann, M.; Diaz, J.C.; Steinem, C.; Multhoff, G.; Arispe, N.; De Maio, A. Hsp70 translocates into the plasma membrane after stress and is released into the extracellular environment in a membrane-associated form that activates macrophages. *J. Immunol.* **2008**, *180*, 4299–4307. [CrossRef]
- Hantschel, M.; Pfister, K.; Jordan, A.; Scholz, R.; Andreesen, R.; Schmitz, G.; Schmetzer, H.; Hiddemann, W.; Multhoff, G. Hsp70 plasma membrane expression on primary tumor biopsy material and bone marrow of leukaemic patients. *Cell Stress Chaperones* **2000**, *5*, 438–442. [CrossRef]
- Murakami, N.; Kühnel, A.; Schmid, T.E.; Ilicic, K.; Stangl, S.; Braun, I.S.; Gehrmann, M.; Molls, M.; Itami, J.; Multhoff, G. Role of membrane Hsp70 in radiation sensitivity of tumor cells. *Radiat. Oncol.* **2015**, *10*, 149. [CrossRef]

21. Gehrmann, M.; Marienhagen, J.; Eichholtz-Wirth, H.; Fritz, E.; Ellwart, J.; Jäättelä, M.; Zilch, T.; Multhoff, G. Dual function of membrane-bound heat shock protein 70 (Hsp70), Bag-4, and Hsp40: Protection against radiation-induced effects and target structure for natural killer cells. *Cell Death Differ.* **2005**, *12*, 38–51. [CrossRef]
22. Gehrmann, M.; Liebisch, G.; Schmitz, G.; Anderson, R.; Steinem, C.; DeMaio, A.; Pockley, A.G.; Multhoff, G. Tumor-specific Hsp70 plasma membrane localization is enabled by the glycosphingolipid Gb3. *PONE.* **2008**, *3*, e1925. [CrossRef] [PubMed]
23. Schilling, D.; Gehrmann, M.; Steinem, C.; De, M.A.; Pockley, A.G.; Abend, M.; Molls, M.; Multhoff, G. Binding of heat shock protein 70 to extracellular phosphatidylserine promotes killing of normoxic and hypoxic tumor cells. *FASEB J.* **2009**, *23*, 2467–2477. [CrossRef] [PubMed]
24. Multhoff, G.; Pfister, K.; Gehrmann, M.; Hantschel, M.; Gross, C.; Hafner, M.; Hiddemann, W. A 14-mer Hsp70 peptide stimulates natural killer (NK) cell activity. *Cell Stress Chaperones* **2001**, *6*, 337–344. [CrossRef]
25. Stangl, S.; Wortmann, A.; Guertler, U.; Multhoff, G. Control of metastasized pancreatic carcinomas in scid/beige mice with human IL-2/TKD-activated NK cells. *J. Immunol.* **2006**, *176*, 6270–6276. [CrossRef]
26. Stupp, R.; Hegi, M.E.; Mason, W.P.; Van Den Bent, M.J.; Taphoorn, M.J.; Janzer, R.C.; Ludwin, S.K.; Allgeier, A.; Fisher, B.; Belanger, K.; et al. Effects of radiotherapy with concomitant and adjuvant temozolomide versus radiotherapy alone on survival in glioblastoma in a randomised phase III study: 5-year analysis of the EORTC-NCIC trial. *Lancet Oncol.* **2009**, *10*, 459–466. [CrossRef]
27. Thorsteinsdottir, J.; Stangl, S.; Fu, P.; Guo, K.; Albrecht, V.; Eigenbrod, S.; Erl, J.; Gehrmann, M.; Tonn, J.-C.; Multhoff, G.; et al. Overexpression of cytosolic, plasma membrane bound and extracellular heat shock protein 70 (Hsp70) in primary glioblastomas. *J. Neurooncol.* **2017**, *135*, 443–452. [CrossRef] [PubMed]
28. Kleinjung, T.; Arndt, O.; Feldmann, H.J.; Bockmühl, U.; Gehrmann, M.; Zilch, T.; Pfister, K.; Schönberger, J.; Marienhagen, J.; Eilles, C.; et al. ; et al. Heat shock protein 70 (Hsp70) membrane expression on head-and-neck cancer biopsy—a target for natural killer (NK) cells. *Int. J. Radiat. Oncol. Biol. Phys.* **2003**, *57*, 820–826. [CrossRef]
29. Diller, K.R. Stress protein expression kinetics. *Annu. Rev. Biomed. Eng* **2006**, *8*, 403–424. [CrossRef]
30. Bausero, M.A.; Gastpar, R.; Multhoff, G.; Asea, A. Alternative mechanism by which IFN- $\gamma$  enhances tumor recognition: Active release of Hsp72. *J. Immunol.* **2005**, *175*, 2900–2912. [CrossRef]
31. Paolini, A.; Pasi, F.; Facoetti, A.; Mazzini, G.; Corbella, F.; Di Liberto, R.; Nano, R. Cell death forms and Hsp70 expression in U87 cells after ionizing radiation and/or chemotherapy. *Anticancer Res.* **2011**, *31*, 3727–3731. [PubMed]
32. Rylander, M.N.; Feng, Y.; Bass, J.; Diller, K.R. Thermally induced injury and heat-shock protein expression in cells and tissues. *Ann. N Y Acad. Sci.* **2005**, *1066*, 222–242. [CrossRef] [PubMed]
33. Pockley, A.G.; Henderson, B. Extracellular cell stress (heat shock) proteins-immune responses and disease: An overview. *Philos. Trans. R. Soc. Lond. B Biol. Sci.* **2018**, *373*, 20160522. [CrossRef] [PubMed]
34. Srivastava, P. Interaction of heat shock proteins with peptides and antigen presenting cells: Chaperoning of the innate and adaptive immune responses. *Annu. Rev. Immunol.* **2002**, *20*, 395–425. [CrossRef]
35. Multhoff, G.; Botzler, C.; Wiesnet, M.; Muller, E.; Meier, T.; Wilmanns, W.; Issels, R.D. A stress-inducible 72-kDa heat-shock protein (Hsp72) is expressed on the surface of human tumor cells, but not on normal cells. *Int. J. Cancer* **1995**, *61*, 272–279. [CrossRef]
36. Gross, C.; Koelch, W.; Arispe, N.; DeMaio, A.; Multhoff, G. Cell surface-bound Hsp70 mediates perforin-independent apoptosis by specific binding and uptake of granzyme B. *J. Biol. Chem.* **2003**, *17*, 41173–41181. [CrossRef]



Article

# Cross Interaction between M2 Muscarinic Receptor and Notch1/EGFR Pathway in Human Glioblastoma Cancer Stem Cells: Effects on Cell Cycle Progression and Survival

Ilaria Cristofaro <sup>1</sup>, Francesco Alessandrini <sup>1,†</sup> , Zaira Spinello <sup>1</sup>, Claudia Guerriero <sup>1</sup>, Mario Fiore <sup>2</sup>, Elisa Caffarelli <sup>2</sup>, Pietro Laneve <sup>2</sup>, Luciana Dini <sup>1</sup>, Luciano Conti <sup>3</sup>  and Ada Maria Tata <sup>1,4,\*</sup> 

<sup>1</sup> Department of Biology and Biotechnologies Charles Darwin, Sapienza, University of Rome, 00185 Rome, Italy; ilaria.cristofaro@uniroma1.it (I.C.); francesco.alessandrini@northwestern.edu (F.A.); zaira.spinello@uniroma1.it (Z.S.); Claudia.Guerriero@uniroma1.it (C.G.); luciana.dini@uniroma1.it (L.D.)

<sup>2</sup> IBPM, Institute of Molecular Biology and Pathology, CNR, 00185 Rome, Italy; mario.fiore@uniroma1.it (M.F.); Elisa.caffarelli@gmail.com (E.C.); Pietro.laneve@uniroma1.it (P.L.)

<sup>3</sup> Department of Cellular, Computational and Integrative Biology-CIBIO, University of Trento, 38123 Trento, Italy; Luciano.Conti@unitn.it

<sup>4</sup> Research center of Neurobiology, Sapienza, University of Rome, 00185 Rome, Italy

\* Correspondence: adamaria.tata@uniroma1.it; Tel.: +39-06-4991-2822

† current address. F. A. Northwestern University, Feinberg School of Medicine, Chicago, IL 60611, USA.

Received: 31 December 2019; Accepted: 5 March 2020; Published: 9 March 2020



**Abstract:** Glioblastomas (GBM) are the most aggressive form of primary brain tumors in humans. A key feature of malignant gliomas is their cellular heterogeneity. In particular, the presence of an undifferentiated cell population of defined Glioblastoma Stem cells (GSCs) was reported. Increased expression of anti-apoptotic and chemo-resistance genes in GSCs subpopulation favors their high resistance to a broad spectrum of drugs. Our previous studies showed the ability of M2 muscarinic receptors to negatively modulate the cell growth in GBM cell lines and in the GSCs. The aim of this study was to better characterize the inhibitory effects of M2 receptors on cell proliferation and survival in GSCs and investigate the molecular mechanisms underlying the M2-mediated cell proliferation arrest and decreased survival. Moreover, we also evaluated the ability of M2 receptors to interfere with Notch1 and EGFR pathways, whose activation promotes GSCs proliferation. Our data demonstrate that M2 receptors activation impairs cell cycle progression and survival in the primary GSC lines analyzed (GB7 and GB8). Moreover, we also demonstrated the ability of M2 receptor to inhibit Notch1 and EGFR expression, highlighting a molecular interaction between M2 receptor and the Notch-1/EGFR pathways also in GSCs.

**Keywords:** cancer stem cells; M2 muscarinic receptors; EGFR; Notch; cell cycle; apoptosis

## 1. Introduction

Malignant gliomas are the most common type of primary malignant brain tumor, with an annual incidence of 5.6 per 100,000 individuals. This pathology is most common in the sixth through eighth decades of life. The World Health organization (WHO) groups gliomas into four histological grades based on degrees of differentiation, anaplasia and aggressiveness: (I) grade I or pilocytic astrocytoma, (II) grade II or low-grade astrocytoma, (III) grade III or anaplastic astrocytoma, and (IV) grade IV or glioblastoma multiforme (GBM) [1].

Among these, GBM is the most frequent and malignant histological type, accounting for 65% of gliomas. The median survival of patients diagnosed with GBM is 12–15 months and the 5 years survival rate for GBM patients is less than 5%.

The standard therapeutic regimen for GBM includes chirurgic resection, followed by concurrent radio- and chemo-therapy, including the treatment with the alkylating agent Temozolomide (TMZ) [2,3]. Unfortunately, these therapeutic treatments do not allow to eradicate completely the tumor and, as a result, are inefficient especially in counteracting the undifferentiated tumor cells growth. In fact, in GBM, such as in other solid tumors, the presence of an undifferentiated tumor cell subpopulation named “Cancer Stem Cells” (CSCs) was shown [4,5]. The properties of CSCs include self-renewal; the capability to induce oncogenesis in immunosuppressed xenografts recipients; the ability to enhance proliferation, invasiveness, migration, metastasis, and resistance to drugs and radiation; and finally the competence to differentiate, giving rise to heterogeneous cell populations establishing the tumor bulk [4–6].

In the Glioblastomas Cancer Stem Cells (GSCs), Notch and Epidermal Growth Factor receptor (EGFR) pathways are among the most frequent components involved in cell proliferation and survival [7]. The EGF pathway is a landmark of classical GBM subtype and one of the most important signaling pathways that regulate growth, proliferation, migration, and cell survival through various inter-acting downstream effectors [8,9].

The Notch pathway is involved in important cellular function such as proliferation, differentiation and maintenance of stem cell properties [10].

Muscarinic receptors belong to the class of the G-protein coupled receptors (GPCRs) [11]. These are expressed in several tumors (e.g., colon, ovary, lung, breast cancer) and are involved in tumor cell proliferation and migration [12–14]. Muscarinic receptors are expressed in astrocytes and low grade astrocytomas, and their activation modulates cell proliferation and migration [15]. In our previous studies, we demonstrated that GBM cells express different muscarinic receptor subtypes, and that the stimulation of M2 receptor subtype by selective M2 agonist *arecaidine propargyl ester* (APE), decreases cell proliferation and survival in GBM cell lines and in primary cell cultures [16,17]. Recently, we also demonstrated that the selective activation of M2 receptors by APE or dualsteric agonist N8-Iperoxo inhibits cell growth in GSCs obtained from two different human tumor biopsies (GB7 and GB8 cells) [18,19]. In order to better understand the mechanisms underlying the decreased cell proliferation and survival, in the present work we described the ability of APE to differently modulate the cell cycle progression in GB7 and GB8 cells. Moreover, the cross-interaction between M2 receptors and Notch1/EGFR pathways has also been investigated, demonstrating that the APE-induced decreased cell proliferation is dependent on the impaired activity of these two signaling pathways.

## 2. Materials and Methods

### 2.1. Cell Cultures

The glioblastoma cancer stem cell lines (GSCs) GB7 and GB8 were obtained from human biopsies [5,20]. The cells were cultured on a laminin-coated plastic (1 µg/mL, Sigma-Aldrich, St. Louis, MO, USA) or as neurospheres (in uncoated plastic) and maintained in Euromed-N medium (EuroClone, Milan, Italy) supplemented with 1% streptomycin, 50 IU/mL penicillin, (Sigma-Aldrich, St. Louis, MO, USA), 1% glutamine (Sigma-Aldrich, St. Louis, MO, USA), 1% N2 supplement (Invitrogen, Monza, Italy), 2% B27 (Invitrogen, Monza, Italy), 20 ng/mL EGF (Recombinant Human Epidermal growth factor, Peprotec, London, UK), and 20 ng/mL FGF (Recombinant Human FGF-basic, Preprotech, London, UK). The cell cultures were maintained at 37 °C in an atmosphere of 5% CO<sub>2</sub>/95% air.

### 2.2. Pharmacological Treatments

M2 agonist arecaidine propargyl ester hydrobromide (APE) was used to selectively stimulate the M2 muscarinic receptor subtype. The ability of this agonist to bind the M2 receptor subtype was

previously demonstrated in GBM established cell lines (U87 and U251) and in GSCs (GB7 and GB8 cells) by pharmacological binding experiments and knockdown of the receptors by siRNA transfection pool [17,18].

Epidermal Growth Factor receptor (EGFR) tyrosine kinase inhibitor (TKI) N-(3-chlorophenyl)-6,7-dimethoxy-4-quinazolinamine), tyrphostin AG1478 (Sigma-Aldrich, St. Louis, MO, USA) was used at final concentration of 1  $\mu$ M, to inhibit the EGFR pathway [21].

### 2.3. Immunocytochemistry

GB7 cells were plated onto 35-mm-diameter dishes in complete medium. Then, the cells were rinsed with phosphate buffer saline (PBS) pH 7.4, fixed with 4% paraformaldehyde for 20 min at room temperature (RT), washed in PBS, and permeabilized by treatment with blocking buffer (0.1% Triton X-100, 10% NGS in PBS) for 1 h at RT. The cells were then incubated overnight at +4 °C with anti-Nestin (1:200, Abcam, Cambridge, UK), anti-CD133 (1:100, Miltenyi Biotec, Teterow, Germany), anti-REST (1:200, Abcam, Cambridge, UK) antibodies diluted in antibody incubation buffer (0.1% Triton X-100, 1% NGS, 1% BSA in PBS). The next day, after three washes with PBS, the cells were incubated for 1 h at RT with a goat anti-mouse-Alexa 594-conjugated (1:2000, Promega, Madison, WI, USA) or goat anti-rabbit-Alexa 488-conjugated (1:2000 Promega, Madison, WI, USA) secondary antibodies diluted in incubation buffer. After washing in PBS, the cells were finally mounted with 30  $\mu$ L of Anti Fade Mounting Medium with DAPI (Immunological Science, Rome, Italy). Negative controls were obtained by omitting the primary antibodies (data not shown).

### 2.4. RNA Extraction and RT-PCR Analysis

Total RNA was extracted by using Cultured Cell Total RNA Extraction Mini Kit (FMB, PA, USA) following the manufacturer's instructions. RNA samples (2  $\mu$ g) were reverse transcribed for 60 min at 37 °C with Random Primers (Promega, Madison, WI, USA) and M-MLV reverse transcriptase (Promega, Madison, WI, USA). Then, PCR reagents, primers, and GoTaq Green Master Mix (Promega, Madison, WI, USA) were added to each reaction tube. The expression of the transcripts was evaluated by semi-quantitative RT-PCR analysis using the following primers:

**M2:** forward, 5'-CCAAGACCCCGTTTCTCCAAG-3';

reverse, 5'- CCTTCTCCTCTCCCCTGAACAC-3'.

**Nestin:** forward, 5'-TGCGGGCTACTGAAAAGTTC-3'

reverse, 5'-TGTAGGCCCTGTTTCTCCTG-3'

**Sox2:** forward, 5'-ACACCAATCCCATCCACACT-3'

reverse, 5'-GCAAACCTTCTTGCAAAGCTC-3'

**CD133:** forward 5'-GCATTGGCATCTTCTATGGTT-3'

reverse, 5'-CGCCTTGTCCTTGGTAGTGT-3'

**REST:** forward 5'-ACTTTGTCCTTACTCAAGTT-3'

reverse 5'-GCATGGCGGGTACTTCAT-3'

**Hes1:** forward, 5'- ATGACAGTGAAGCACCTCCG- 3';

reverse, 5' - AGGTCATGGCATTGATCTGG- 3'

**Notch1:** forward, 5' AGGCATCATGCATGTCAAAC - 3';

reverse, 5' - TGTGTTGCTGGAGCATCTTC - 3'

**Notch2:** forward, 5' TTGTGTGAACAATGGGCAGT - 3';

reverse, 5' - TTCATAGCCATTGGGGTGAT - 3'

**Notch3:** forward, 5'- CATCTGGTTGCTGCTGACAT-3'

reverse, 5'- ATCAGGTCGGAGATGATGCT-3'

**Egfr:** forward, 5'- AGCATGTCAAGATCACAGAT - 3';

reverse, 5' - TGGATCCAAAGGTCATCAA - 3'

**ErbB3:** forward, 5'- GGAGTCTTGCCAGGAGTCT-3'

reverse 5'- AGGAGTCAGCAGACTGTGG-3'

**18S:** forward, 5'-CCAGTAAGTGCGGGTCATAAGC -3';  
reverse, 5'-AACGATCCAATCGGTAGTAGCG -3'

PCR conditions were: initial denaturation at 95 °C for 3 min; 35 cycles with the following profile: 95 °C for 30 s, 60 °C for 30 s and 72 °C for 30 s; and final extension at 72 °C for 5 min. For each PCR reaction, 25 µL samples were run on 3% agarose gel. 18 S transcript level was used as a housekeeping gene.

For miR-34-5p expression, 6 ng of cDNA, synthesized through the miScript II Reverse Transcription kit (cat. n. 218161, Qiagen, Milan, Italy), were used as a template for the qRT-PCR reaction. Amplifications were performed through the miScript-SYBR green PCR kit (cat. n. 218073, Qiagen) on a 7500 Fast Real-Time PCR (Applied Biosystems Italia, Monza, Italy). Commercially available DNA oligonucleotides were used as primers for the detection of miR-34-5p (Hs\_miR-34a\_1, cat. n. MS00003318, Qiagen) and as a control of snRNA U6 (Hs\_RNU6B\_13, cat. n. MS00014000, Qiagen). Relative quantification was performed using the comparative  $\Delta\Delta CT$  method.

### 2.5. Western Blot Analysis

To detect the expression of M2 receptor, Notch1 and EGFR, protein extracts were run on 10% SDS-polyacrilamide gel (PAGE) and transferred to PVDF membranes (Merck Millipore, Darmstadt, Germany) and blocked for 1 h in 5% non-fat milk powder (Sigma-Aldrich, St. Louis, MO, USA) in PBS containing 0.1% Tween-20, and then incubated with monoclonal anti-M2 (1:800 Abcam, Cambridge, UK), anti-Notch (1:200, Santa Cruz Biotechnologies, Dallas, TX, USA), anti-PCNA (1:700, Sigma-Aldrich, St. Louis, MO, USA), anti-p53 (1:100; Santa Cruz, Temecula, CA, USA) and anti-EGFR (1:1000, Merck Millipore, Darmstadt, Germany) primary antibodies, overnight at 4 °C. Then the blots were washed and incubated for 1 h at RT with secondary antibodies horseradish-peroxidase-conjugated (1:20000 Promega, Madison, WI, USA). The reaction was revealed by ECL chemiluminescence reagent (Euroclone, Milan, Italy). The immunoreactive signal was revealed by exposure to Chemidoc (Molecular Imager ChemiDoc XRS+ System with Image Lab Software, Biorad, CA, USA), and band intensities were quantified by optical density using ImageJ software (National Institutes of Health). GAPDH and  $\beta$ -actin were used as reference proteins (loading control).

### 2.6. Flow Cytometry Analysis

The cells were plated onto T25 flask at a density of  $4 \times 10^4$  cells/cm<sup>2</sup>. The day after plating, the cells, excluding control samples, were treated with  $10^{-4}$  M APE agonist for 72, 96 and 120 h. At the end of the treatment, cells were incubated for 90 min with 45 µM bromodeoxyuridine (BrdUrd, Sigma-Aldrich, St. Louis, MO, USA), collected by trypsinization, centrifuged for 3 min at 1500 RPM, washed with PBS for three times, and then fixed in methanol/PBS (1:1; *v/v*).

To identify cells in S phase, DNA content and BrdU incorporation were determined by staining with propidium iodide (PI) and anti-BrdU antibody, respectively. DNA was denaturated by incubating the cells in 3N HCl for 45 min at RT, followed by neutralization with 0.1 M sodium tetraborate. Samples were then incubated with monoclonal anti-BrdU antibody (1:50 *v/v*; Dako, MI, Italy) for 1 h at RT, washed twice with 0.5% Tween-20 in PBS and incubated for 45 min with goat anti-mouse Alexa fluor 488-conjugated antibody (1:1200; Invitrogen Monza, Italy). Samples were washed twice with PBS and stained with propidium iodide (10 µg/mL) for 15 min at RT. Flow cytometry analysis was performed with a flow cytometer Coulter Epics XL with 488 nm wavelength excitation, and  $10^4$  events were collected for each sample. To evaluate the apoptotic cells, Annexin V kit was used following the manufacturer's instructions (Immunological Sciences, Rome, Italy).

To identify the cells with DNA damage, the samples were incubated with monoclonal antibody directed against phospho- $\gamma$ H2AX (Millipore, MI, Italy) for 1 h at RT, washed, and incubated for 45 min with anti-mouse Alexa fluor 488-conjugated antibody (1:1200; Invitrogen Monza, Italy). Monoparametric (DNA histograms) and biparametric (BrdU content vs. DNA content) analyses were obtained using WinMDI 2.9 software (Scripps Research Institute, La Jolla, CA, USA).

### 2.7. Cell Death Analysis

Cell death was evaluated by flow cytometry analysis using propidium iodide (PI) staining. Cells were plated into flask T25 at density of  $4 \times 10^4$  cells/cm<sup>2</sup> and the day after treated with  $10^{-4}$  M APE for 72, 96, and 120 h for GB8 cells and 48, 72, and 96 h for GB7 cells. Then, the cells were collected, suspended in 2 mL of PBS buffer containing 0.1% Triton X-100 (Sigma-Aldrich, St. Louis, MO, USA), incubated for 5 min at RT, and subsequently stained with PI (10 µg/mL) and analysed by using a Coulter Epics XL flow cytometer. For each sample,  $10^4$  events were recorded. Cells with a hypodiploid DNA content and a higher granularity (SSC) at G0-G1 phase (sub-G1) were quantified as dead cells [22,23].

### 2.8. Statistical Analysis

Student's t test and one-way ANOVA test followed by Bonferroni's post test were used to evaluate statistical significance within the different samples. The results were considered statistically significant at  $p < 0.05$  (\*),  $p < 0.01$  (\*\*),  $p < 0.001$  (\*\*\*), and  $p < 0.0001$  (\*\*\*\*).

## 3. Results

### 3.1. Different GSC Lines Exhibit Different M2 Muscarinic Receptor Expression Levels

The presence of M2 muscarinic receptors was investigated in several GSC lines derived from different patients' biopsies. Semi-quantitative RT-PCR analysis showed that all GSCs express the M2 transcript, albeit different levels of expression were evident (Figure 1 upper panels). Western blotting analysis was also performed in the same GSC lines, indicating that only some of these express M2 receptor at the protein level (i.e., GB6, GB7, GB8, GB10, and GB166) (Figure 1 lower panels). For subsequent studies, we selected GB7 and GB8 cells, considering their different levels of M2 receptor expression. In fact, the levels of M2 receptor expression appeared significantly higher in GB7 than in GB8 cells (GB7>GB8) [18]. In particular, the expression of M2 receptor protein in GB7 cells was also evaluated in GB7 grown in adherent or neurosphere conditions, confirming that the expression of M2 receptor was present in both culture conditions (see Supplementary Figure S1).

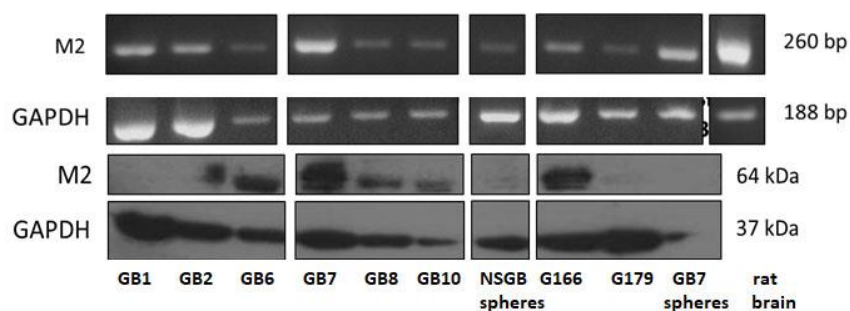


**Figure 1.** M2 protein expression in different GSC lines. Upper panels RT-PCR analysis; Lower panels Western blot analysis. GAPDH was used as an internal reference for transcript and protein analysis.

### 3.2. GB7 and GB8 Cells Express Stemness Markers and Components of Notch/EGFR Molecular Pathways

The expression of stemness markers (i.e., REST, CD133, Nestin and Sox2) in the two cell lines selected for our subsequent experiments was evaluated by semi-quantitative RT-PCR analysis. GSCs were cultured in adherent and as neurospheres in floating conditions (Figure 2A). In Figure 2, only the results obtained for GB7 cells are reported, nevertheless, similar results have been obtained also for the GB8 cell line (see Supplementary Figure S2 and [18]). The presence of REST, CD133 and NESTIN was also investigated at protein level by immunocytochemistry (Figure 2B). The results confirmed that the stem cell markers were expressed in GB7 cells grown both as an adherent and as neurosphere cultures. We also investigated the expression of Notch/ Delta and EGFR family members by RT-PCR analysis. We found that the transcripts for different members of Notch pathway (Notch1, Notch2, Notch3, Delta

like1, Jagged 1, Jagged 2, and Hes1) were expressed both in GB7 and GB8 cells (Figure 2C). Similarly, also EGFR and ErbB3 receptors appeared to be expressed in both GSC lines. Interestingly, the mutated form of EGFR (Variant III), usually expressed in different GBM and breast cancers [24], did not appear to be expressed in either of the two GSC lines considered (Figure 2C).

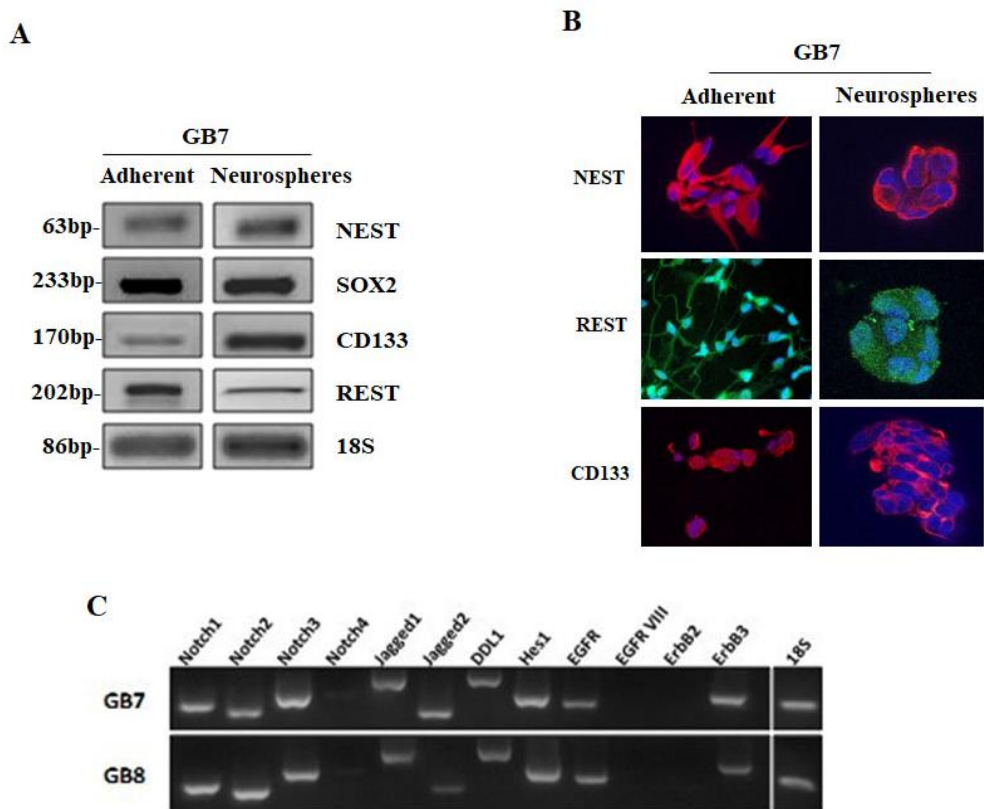


**Figure 2.** GB7 cells grown in adherent and as neurospheres. (A) RT-PCR analysis of stemness markers Nestin (NEST), SOX2, CD133, and REST. 18 S was used as a housekeeping gene. (B) Immunostaining for NESTIN, REST and CD133 in GB7 cells grown as a monolayer and as neurospheres in floating conditions (magnification  $\times 100$ ). (C) RT-PCR analysis for gene expression for different genes involved in Notch and EGFR pathways in GB7 and GB8 cells. 18 S was used as a housekeeping gene.

### 3.3. Activation of M2 Muscarinic Receptor Differently Affects Cell Growth and Survival in GB7 and GB8 Cells

Previous data showed that APE treatment was able to significantly inhibit cell growth in GB7 cells in a time- and dose-dependent manner, while in GB8 cells, only higher doses of APE (100  $\mu$ M) were able to affect cell growth, in a time-dependent manner [18].

To evaluate whether the APE-induced decrease in cell number was dependent on the impaired cell proliferation or survival, we performed a cell cycle analysis on GB7 and GB8 cells treated with 100  $\mu$ M APE for 72, 96 and 120 h. Before collecting the cells, BrdU incorporation was performed for 90 min to monitor the S phase progression. The flow cytometry analysis has been performed selecting specific gates that have allowed to analyze the distribution of the cells in different cell cycle phases (G1-S-G2/M). The bi-parametric analysis of BrdU labeling versus DNA content allowed to evaluate both cell progression through the G1/S/G2-M phases and the identification of cells in S phase. This analysis showed that GB7 cells exhibited a significant decrease in the BrdU labelled cell fraction after APE treatment accompanied by a decrease in the percentage of cells in S phase and accumulation of cells in the G2/M phase (Figure 3A,B).



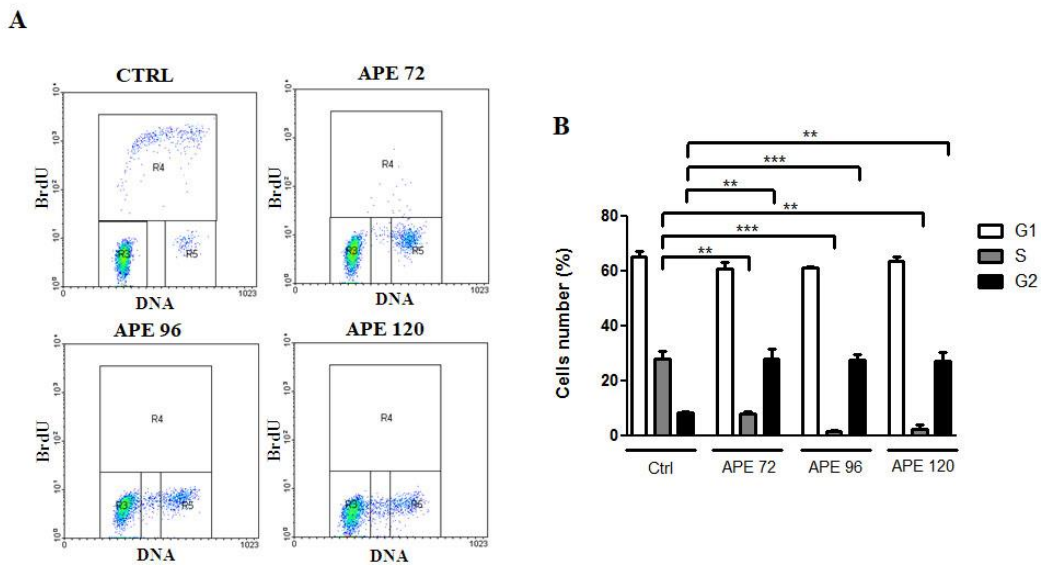


**Figure 3.** (A) Bivariate analysis of BrdU incorporation and DNA content in GB7 cells at 72, 96 and 120 h after 100  $\mu$ M APE treatment. (B) Percentage of GB7 cells in G1, S, and G2/M phases after 100  $\mu$ M APE treatment. (t-test; \*\* $p < 0.01$ ; \*\*\* $p < 0.001$ ). The data are the average  $\pm$ SEM of three independent experiments.

Instead, FACS analysis after BrdU incorporation performed on GB8 cells showed that APE treatment did not modify significantly the percentage of cells in S phase, although a faint reduction of cells in S phase was visible after 96 h of APE treatment accompanied by a progressive increase of cells in G2/M phase (Figure 4A,B). Western blot analysis of the cell cycle-associated protein PCNA has demonstrated an increase of expression that was higher in GB8 cells compared to GB7 cells (Figure 5A,B). Interestingly, the test of recovery performance by maintaining the GSC cells in the presence of APE for 120 h and then, after M2 agonist withdrawal, for an additional 72 h, 96 and 120 h in fresh medium without APE, demonstrated that only GB7 cells were able to rescue their proliferation (Figure 5C,D).

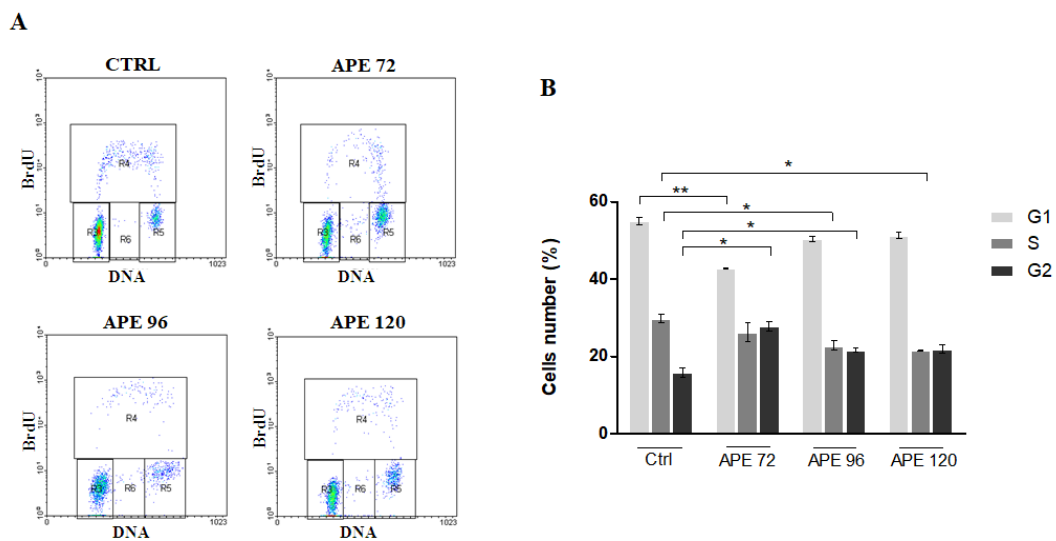


**Figure 4.** (A) Bivariate analysis of BrdU incorporation and DNA content in GB8 cells at 72, 96 and 120 h after 100  $\mu$ M APE treatment. (B) Percentage of GB8 cells in G1, S, G2/M phases after 100  $\mu$ M APE treatment. (t-test; \* $p < 0.05$ ; \*\* $p < 0.01$ ). The data are the average  $\pm$ SEM of three independent experiments.

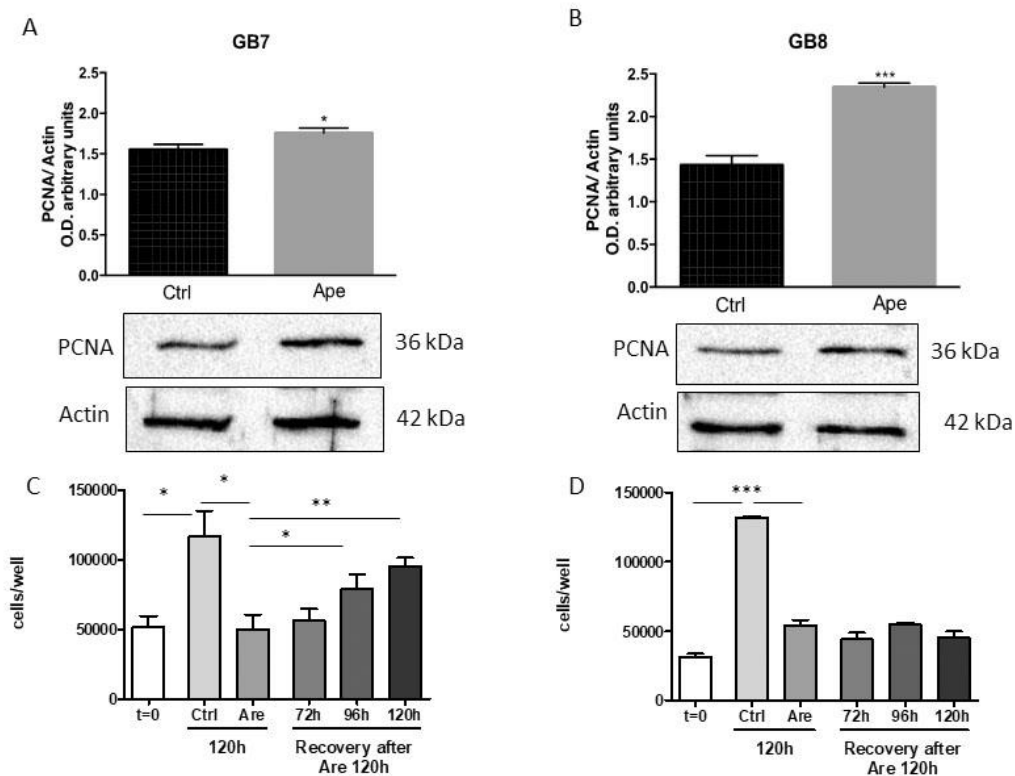


**Figure 5.** Western blot analysis for PCNA expression in GB7 (A) and GB8 (B) cells in absence (ctrl) and presence of 100  $\mu$ M APE (48 h). The diagrams above report the densitometric analysis of the PCNA immunoreactive bands normalized to those of the  $\beta$ -actin reference. The data are the average  $\pm$ SEM of three independent experiments (t-test; \* $p < 0.05$ ; \*\*\* $p < 0.01$ ). (C) and (D) Recovery of cell proliferation after APE withdrawal. The cells were maintained for 120 h in the presence of APE 100  $\mu$ M. Then the APE was removed from the culture media and substituted by fresh medium without APE for an additional 72, 96 and 120 h. Results are reported for GB7 (C) and GB8 (D) cells. (t-test; \* $p < 0.05$ ; \*\* $p < 0.01$ ; \*\*\* $p < 0.001$ ).

To assess whether the decrease in cell number observed after APE treatment in GSCs was also determined by cell death occurrence, we determined by FACS analysis the fraction of cells with hypodiploid DNA content and higher granularity (SSC) (this fraction was assumed to represent dead cells). This analysis showed that APE treatment is able to increase the percentage of hypodiploid cells in GB8 (Figure 6A,B) and somewhat less in GB7 cultures. On the contrary, the analysis of cell death by FACS analysis after propidium iodide staining in GB7 cells demonstrated a lower percentage of cell death upon APE treatment as compared to GB8 (Figure 6C,D). In order to confirm the apoptotic cell death, the annexin V positive cell number has been evaluated by FACS analysis after 72 h treatment. As shown in Figure 7, APE treatment significantly increased the percentage of annexin V positive cells both in GB7 and GB8 cells. However, the GB8 cells exhibited a higher percentage of annexin V positive cells when compared to GB7 (Figure 7).

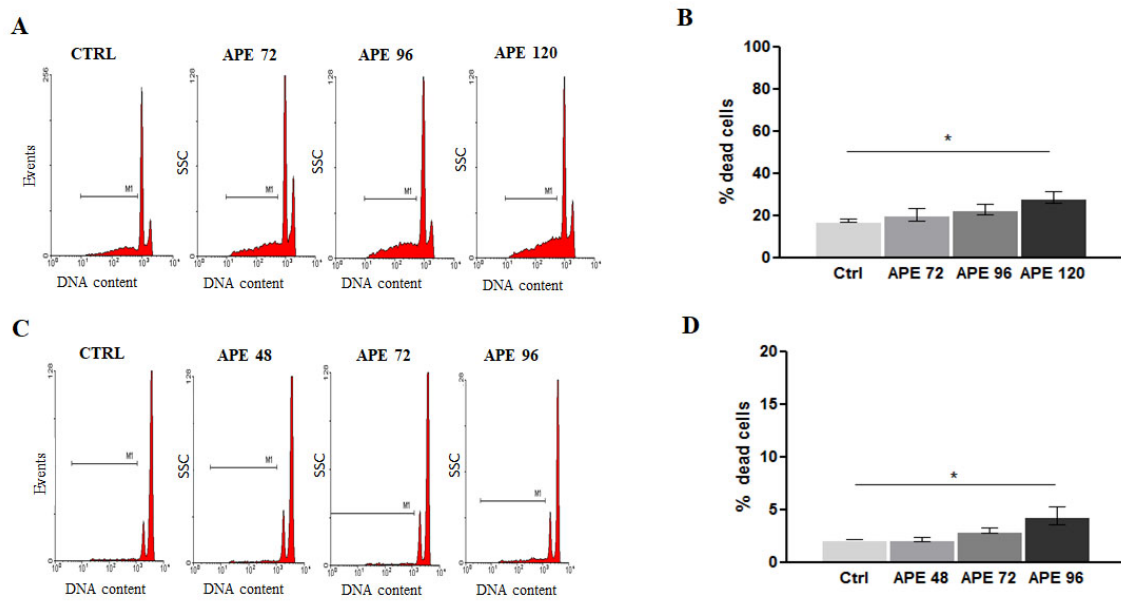


**Figure 6.** (A) Cytometric analysis of dead cells in GB8 cell cultures after 100  $\mu$ M APE treatment. (B) Percentage of apoptotic cells present in GB8 cultures after 100  $\mu$ M APE treatment. (C). Cytometric analysis of apoptosis in GB7 cells after APE treatment. (D) Percentage of apoptotic cells present in GB7 cultures after 100  $\mu$ M APE treatment. (ANOVA test; \*  $p < 0.05$ ). The data are the average  $\pm$ SEM of three independent experiments.

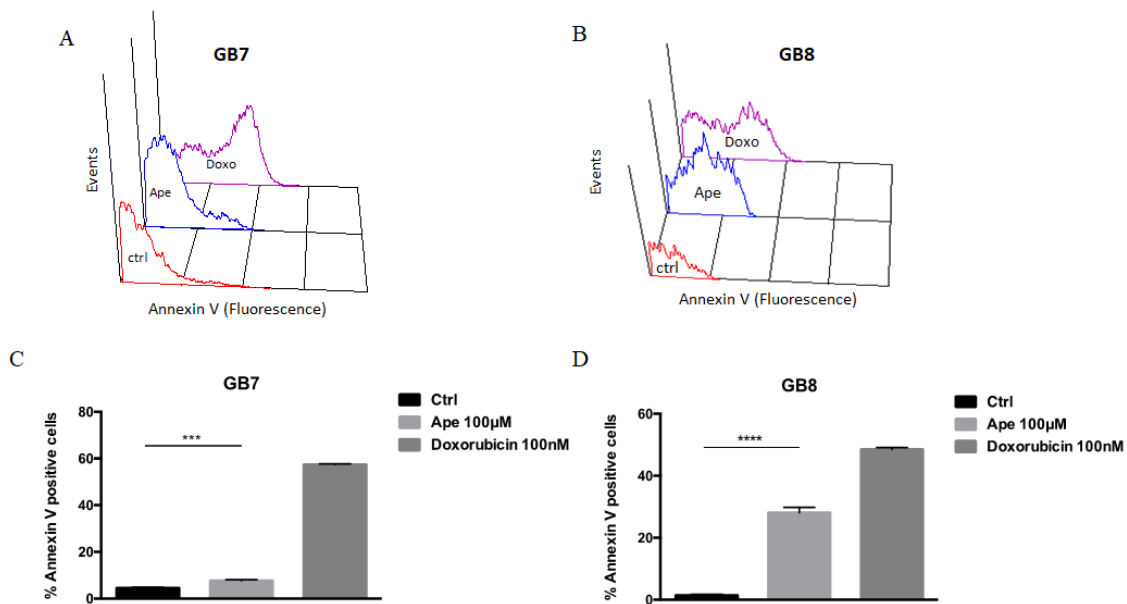


**Figure 7.** Distribution diagram of Annexin V expression in GB7 (A) and GB8 (B) cells. Percentage of Annexin V positive cells in GB7 (C) and GB8 (D) cultures after 100  $\mu$ M APE treatment. Doxorubicin (100 nM) was used as a positive control. (t-test; APE 72 h vs. Ctrl \*\*\*  $p < 0.001$ ; \*\*\*\*  $p < 0.0001$ ). The data are the average  $\pm$ SEM of three independent experiments.

### 3.4. Activation of M2 Muscarinic Receptor Differently Induces DNA Damage Effects in GB7 and GB8 Cells

Since a consistent cell death effect was observed in GB8 cells after APE treatment, we investigated its possible causes. Phosphorylated histone  $\gamma$ -H2AX is a marker of cellular response to Double-Strand DNA Breaks (DSB). We used this marker to identify the presence of genotoxic damage induced by APE treatment. Camptothecin treatment was used as a positive control. Flow cytometry analysis

on GB7 and GB8 cultures treated with 100  $\mu$ M APE for 48 h or with 5  $\mu$ M camptothecin for 24 h, showed that the percentage of the  $\gamma$ -H2AX positive cells increased significantly in GB8 cells after APE treatment, suggesting the occurrence of DNA double-strand breaks induced by M2 agonist treatment (Figure 8A,B). GB7 cells did not exhibit  $\gamma$ -H2AX expression neither in untreated or in APE treated conditions (data not shown).

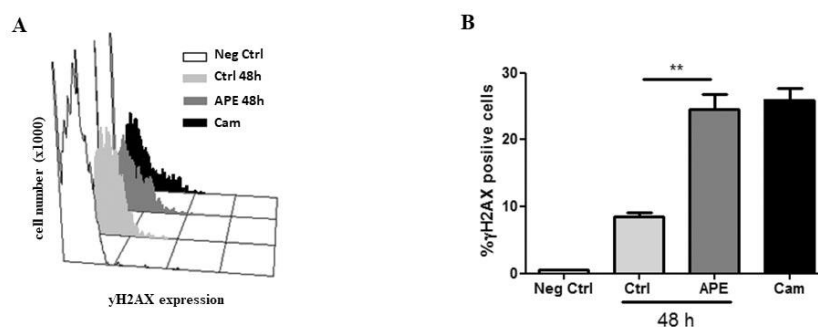


**Figure 8.** (A) Distribution diagram of p- $\gamma$ H2AX expression vs. cell number ( $\times 1000$ ). (B) Percentage of p- $\gamma$ H2AX positive cells in GB8 cells after 100  $\mu$ M APE treatment. Camptothecin (5  $\mu$ M) was used as a positive control. (t-test; APE 48 h vs. Ctrl \*\*  $p < 0.01$ ). The data are the average  $\pm$ SEM of three independent experiments.

### 3.5. M2 Modulation Affects Notch1 and EGFR Expression in GB7 Cells

In order to clarify the mechanisms responsible for the decreased cell proliferation induced by M2 receptor activation observed in particular in GB7 cells, we evaluated Notch-1 transcript and protein expression by RT-PCR and Western blot analyses upon APE treatment (Figure 7). Analysis of Notch genes' expression by RT-PCR indicated that neither Notch1 or Notch2 and Notch3 were modulated by M2 agonist treatment, although the main Notch target gene, Hes gene, appeared to be negatively modulated by APE at least after 24 h of treatment (Figure 9A). Interestingly, Western blot analysis demonstrated that the expression of Notch1 protein was significantly decreased after 48 h of APE treatment (Figure 9B). Our previous work performed in U87 cells demonstrated that Notch1 protein levels are controlled by miR-34a [25] through p53 activity. In order to explain the decreased Notch1 protein levels after APE treatment, we evaluated the levels of miR-34a in both GSC lines. Interestingly, we observed that both GB7 and GB8 cells express miR-34a (Figure 10), and APE treatment significantly reduced the expression levels in GB8 cells only (Figure 10B). Interestingly, also p53 protein that play a relevant role in miR-34a modulation, albeit expressed in both cell lines, was reduced only in GB8 cells after APE treatment (Figure 10D).

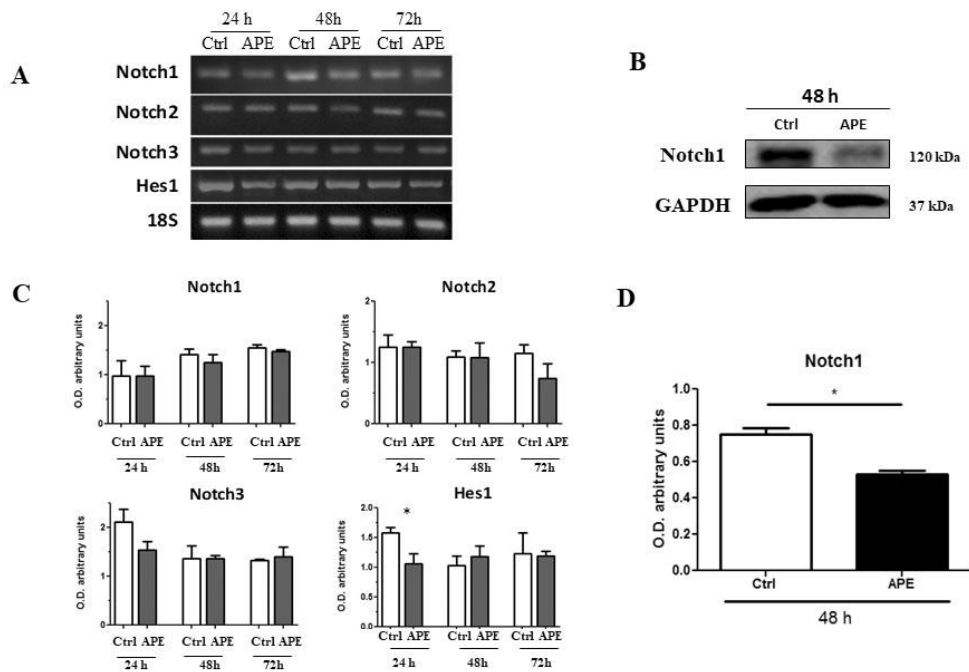


**Figure 9.** (A) RT-PCR analysis for Notch1, Notch2, Notch3, and Hes transcripts in GB7 cells. 18 S was used as a housekeeping gene. (B) Notch1 expression by Western blot analysis in GB7 cells. GAPDH was used as the internal reference protein. (C) Densitometric analysis of the RT-PCR bands indicated in Figure A normalized with the bands of housekeeping gene 18 S. The data are the average  $\pm$ SEM of three independent experiments. (D) Densitometric analysis of Notch1 immunoreactive bands; Western blot normalized with the bands of the reference protein GAPDH. The data are the average  $\pm$ SEM of three independent experiments (\*  $p < 0.05$  t-test).

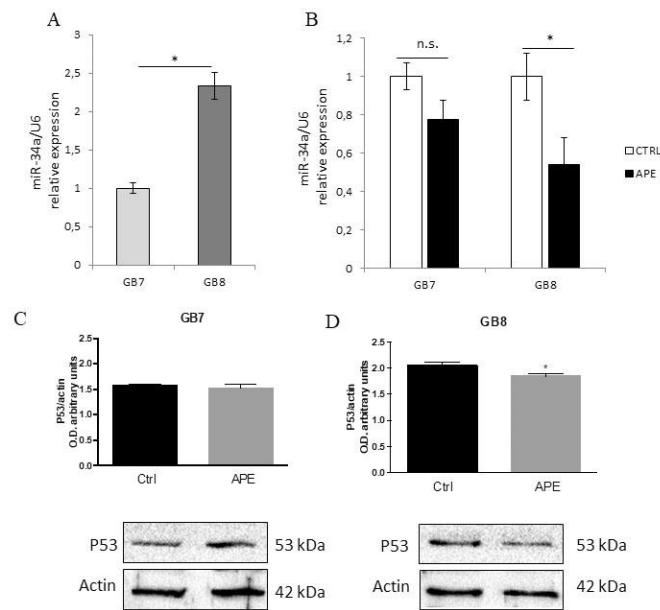


**Figure 10.** qRT-PCR analysis for miR-34a-5p expression in GB7 and GB8 cells. **(A)** miR-34a-5p levels in untreated GB7 or GB8 cultures. MiRNA relative expression in GB7 was set as one and snRNA U6 used as an internal standard. Data are expressed as the average  $\pm$ SEM. (N = 3, \*  $p \leq 0.05$ , t-test). **(B)** miR-34a-5p levels in untreated (CTRL) or APE-treated (100  $\mu$ M for 24 h) GB7 or GB8 cells. For each cell line, miRNA relative expression in CTRL samples was set as one and snRNA U6 used as an internal standard. Data are expressed as the average  $\pm$ SEM. (N = 3, \*  $p \leq 0.05$ , t-test). Western blot analysis of p53 expression in GB7 **(C)** and GB8 **(D)** cells in absence (ctrl) and presence of 100  $\mu$ M APE (48 h). The graphs above report the densitometric analysis of the p53 immunoreactive bands normalized with the bands of the reference protein  $\beta$ -actin. The data are the average  $\pm$ SEM of three independent experiments (t-test; \*  $p < 0.05$ ).

Another pathway involved in GBM growth and survival is EGFR signaling [24]. In order to understand whether this pathway was also affected by M2 receptor activation, we evaluated EGFR and ErbB3 transcripts and protein expression levels in GB7 cells by RT-PCR and Western blot analysis, respectively. RT-PCR analysis showed that the EGFR and ErbB3 receptor expressions were negatively modulated following APE treatment (Figure 11A). This result was also confirmed by Western blot analysis that showed that M2 receptor activation negatively modulated the EGFR receptor expression (Figure 11B).

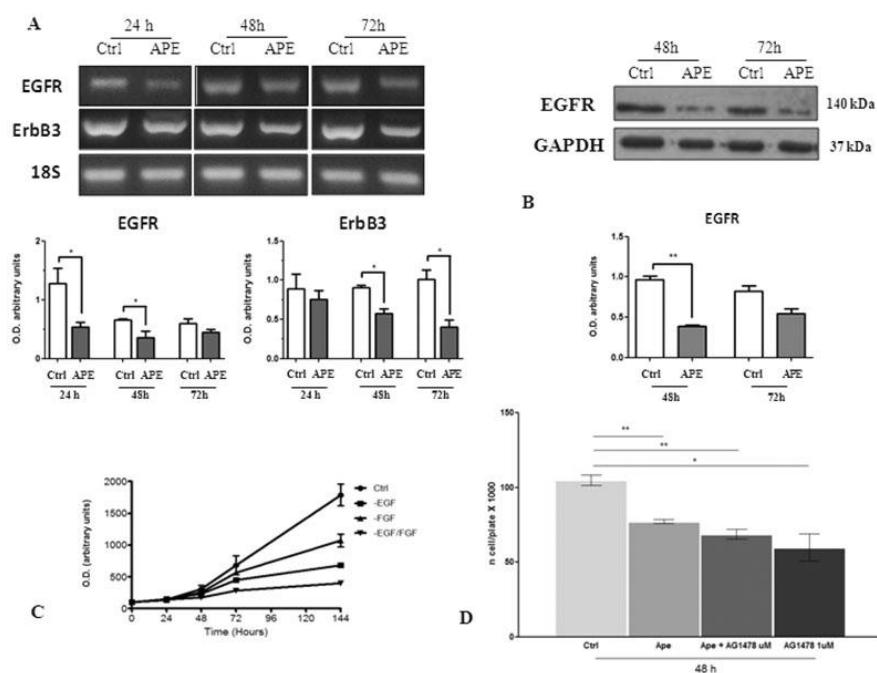


**Figure 11.** (A) RT-PCR analysis of EGFR and ErbB3 receptors in GB7 cells. 18 S was used as a housekeeping gene. The graphs below show the densitometric analysis of the bands of RT-PCR indicated in Fig. A normalized with the bands of housekeeping gene 18 S. The data are the average  $\pm$ SEM of three independent experiments (\*  $p < 0.05$  t-test). (B) EGFR expression by Western blot analysis on GB7 cells. GAPDH was used as an internal reference protein. The graph below shows the densitometric analysis of the bands of Western blot analysis for EGFR normalized with the bands of the reference protein GAPDH. The data are the average  $\pm$ SEM of three independent experiments (\*\*  $p < 0.01$  t-test). (C) MTT assay performed on GB7 cells maintained in complete culture medium containing EGF and FGF (ctrl) either in the absence of FGF, or of EGF, or in absence of both growth factors. (D) MTT assay performed after 48 h of treatment with 100  $\mu$ M APE or 1  $\mu$ M of TKI AG1478 inhibitor (t-test; \*  $p < 0.05$ ; \*\*  $p < 0.01$ ). The data are the average  $\pm$ SEM of three independent experiments performed in triplicate.

To confirm the involvement of EGFR in cell proliferation, we cultured GB7 cells in the presence or absence of EGF. MTT assay resulted in a significant decrease of cell number when GB7 cells were maintained without EGF (Figure 11C). The treatment with (EGFR) tyrosine kinase inhibitor (TKI) tyrphostin AG1478 moreover demonstrated that the GB7 cell proliferation is mainly dependent on EGFR receptor activity. Indeed, the inhibition of EGFR pathway by AG1478 induced a significant reduction of cell growth comparable to APE treatment. Additionally, co-treatment of GB7 cells with APE and AG1478 did not show any synergic effect of the two drugs (Figure 11D).

#### 4. Discussion

Muscarinic receptors are classical G-protein coupled receptors involved in many physiological functions. In the last years, several evidences have described an involvement of these receptors in different pathological conditions, both in neuronal and non-neuronal tissues [26,27]. Moreover, the contribution of muscarinic receptors in tumor progression has also been demonstrated and the use of agonists or antagonists for different cholinergic receptor subtypes is emerging as therapy for different pathologies [11,26–28]. Previously it has been demonstrated the ability of M2 receptor to counteract tumor cell growth and survival both in GBM and in GSCs [16–19], in neuroblastoma [29] and in urothelial bladder cells [30].

Here we have extended these studies by evaluating the mechanisms downstream of the M2 receptor activation by orthosteric agonist APE in the modulation of cell cycle progression and reduced

survival in GSCs. For this purpose, we have selected two GSC lines derived from human biopsies (GB7 and GB8 cells) that expressed different levels of M2 muscarinic receptor, in order to further compare the effects mediated by APE on GSCs expressing different amounts of M2 receptor. Previous analysis of cell viability demonstrated that APE triggered a decrease of the cell growth in a time- and dose-dependent manner in GB7 cells. In GB8 cells, instead, the decrease on the cell number is evident only after treatment with a high dose (100  $\mu$ M) of APE [18]. In order to clarify whether the APE-induced decrease in cell number was dependent on impaired cell proliferation, the cell cycle progression was evaluated by FACS analysis and BrdU incorporation. The results indicated a different behavior of the two GSC lines upon APE treatment. In fact, GB7 cells exhibited a decrease of cells in S phase with their accumulation in G2/M and a non-substantial change in G1 phase, confirming an APE-induced decrease in cell proliferation. Conversely, in GB8 cells, M2 stimulation produced a significant change in percentage of cells in S phase only at longer exposure (96–120 h) of APE treatment, and a cell accumulation in G2/M with a progressive reduction of cells in G1 phase was evident. To better evaluate the proliferative block in the two cell lines, PCNA expression was assessed by Western blot analysis. Unexpectedly, PCNA expression increased after APE treatment in both cell lines. This could be explained as a consequence of the accumulation of cells in G1-G2/M phases rather than an increased proliferation. However, to understand if the proliferative arrest was reversible, we performed a rescue analysis of the cell proliferation after 120 h of treatment with APE. It is evident that GB7 cells are able to recover cell proliferation after removing APE from the culture medium, while GB8 cells are unable to resume proliferation. It is evident that the two cell lines behave differently, and in GB7 cells the activation of the M2 receptor causes reversible arrest while in GB8, proliferative arrest is permanent at least at the doses used. Interestingly, FACS analysis and propidium iodide staining demonstrated that the APE treatment caused an increase of the number of hypodiploid cells overall in GB8 cells. Conversely, in GB7 cells, APE induced a lower percentage of cell death compared with GB8 cells. The apoptotic cell death is also confirmed by the analysis of annexin V. Moreover, similarly, as observed by propidium iodide analysis, GB8 cells present a higher percentage of annexin V positive cells than GB7 cells. These results suggest that the decrease in cell number observed following APE treatment was probably due to reduced cell proliferation in GB7 cells while in GB8 cells it may be dependent on decreased cell survival. The cell death effects observed in GB8 cultures were caused by DNA damage, in fact, we found a significant increase of the number of  $\gamma$ H2AX-positive cell lines. The apoptotic effects observed in GB8 cells and the presence of APE-induced genotoxic effects in these cells may be explained by the occurrence, only in GB8 cells, of a mutation in p53 at the level of Arg342 [18]. The presence of the mutated form of p53 protein may therefore contribute to confer higher susceptibility of GB8 cells to an APE toxic effect. In fact, the cells presenting the genotoxic damage may continue in the mitotic division, and in the presence of mutated p53, failing to resolve the DNA damage, they go into cell death. On the other hand, GB7 cells presenting p53 wild type may be able to resolve possible APE-induced genotoxic effects. However, these results are in agreement with that previously reported for GBM cell lines U87 and U251. Indeed, similar to that observed in GSCs, U251 cells that presented p53 mutated showed APE-induced cytotoxic and genotoxic damage and increased cell death compared to U87 cells that presented wild type p53 genotype [31].

In order to explain the significant decrease of cell proliferation occurring in GB7 cells, we also investigated the ability of APE to impair Notch/EGFR pathways. In fact, our previous studies performed in GBM cell lines have indicated the ability of M2 receptors to negatively regulate Notch and EGFR pathways [25]. Similarly, in the present study we described that APE treatment caused a significant decrease of Notch1 protein levels. This decrease appeared to be caused by post-transcriptional control produced by M2 receptor stimulation on Notch expression, considering that the mRNA levels of Notch did not appear significantly modified by APE treatment. However, the analysis of miR-34a-5p, one of the main miRNA involved in the post-transcriptional regulation of Notch1 [31], revealed its expression in both cell lines, and the activation of the M2 receptor seems to downregulate miR-34a expression preferentially in GB8 than in GB7 cells, indicating that miR-34a-5p is not involved in the



post-transcriptional control of Notch1 in these GSC cell line. The expression of miR-34a is regulated by p53 [25]. For this reason, we have also analyzed the p53 expression in both GSC cell lines, observing that p53 is expressed both in GB7 and GB8 cells and that the APE treatment caused a significant decrease of p53 expression but only in GB8 cells. Therefore, the downregulation of miR-34a after APE treatment may be dependent on the reduced expression of p53, at least in GB8 cells.

Notch1 positively regulates EGFR transcription [10,32]; therefore, the downregulation of EGFR observed in GB7 cells could also be explained through APE-induced Notch-1 downregulation. The role played by Notch and EGFR in GSCs proliferation might be relevant. In fact, the absence of EGF in the culture media or the inhibition of EGFR activity by TKI AG1478 inhibitor, indicated that the absence of EGF or the block of the pathway downstream EGFR, significantly impaired GB7 cell proliferation.

## 5. Conclusions

The reported data confirm that the M2 agonist APE is able to counteract cell proliferation and survival in GSCs. The results indicate that the M2 receptor activation may differently act in GSCs with wild type and mutant p53 genotypes. In GB7 cells bearing the wild type p53 genotype, the M2 receptor activation may activate a molecular circuitry based on the cross-talk between M2 receptor and the Notch-1/EGFR pathways [25].

This circuitry is deregulated in the GB8 cells characterized by p53 mutated and negatively modulated by APE. In these cells, M2 receptor activation may cause a genotoxic effect probably mediated by ROS production that impair GB8 cell survival [31].

In both cases, M2 receptor appears as an interesting therapeutic tool for glioblastoma therapy. Although the level of expression of M2 receptors in GSC obtained by different patients is heterogeneous (see Figure 1) and the therapeutic potential of the M2 receptor may be conditioned by the genetic background (i.e., p53 wild type or mutated) of each patient, the last advances in the treatment of these tumors showed the development of personalized therapies to be the most efficient way to pursue this. In this panorama, our results represent a remarkable step in the perspective of a new possible therapeutic approach for GBM treatment.

**Supplementary Materials:** The following are available online at <http://www.mdpi.com/2073-4409/9/3/657/s1>, Figure S1: Western blot analysis for M2 receptor expression in GB7 cells maintained in adherent and neurosphere conditions. Rat brain was used as positive control. Beta-actin was used as reference protein. Figure S2: Expression of stemness markers in GB8 cell line. (A) Analysis by RT-PCR of Nestin and Sox2 transcripts in GB8 cell line in adherent and sphere conditions. U87 stable cell line was used as negative control. 18s was used as housekeeping gene. (B) Immunocytochemistry analysis of Nestin (green) and Sox2 (red) protein expression in GB8 cells. DAPI was used to counterstain the nuclei ( $\times 100$ ).

**Author Contributions:** A.M.T. conceived and designed the experiments; L.C. provided the GSCs and analysis of stemness markers; I.C., F.A., Z.S., C.G., M.F., P.L. performed the experiments and analyzed the data; A.M.T., L.D., E.C. contributed reagents/materials/analysis tools; A.M.T., I.C., F.A. wrote the paper; All authors have read and agreed to the published version of the manuscript.

**Funding:** This work was supported by Ateneo Sapienza Funds to A.M.T.

**Conflicts of Interest:** The authors declare no conflict of interests.

## References

1. Kleihues, P.; Louis, D.N.; Scheithauer, B.W.; Rorke, L.B.; Reifenberger, G.; Burger, P.C.; Cavenee, W.K. The WHO classification of tumors of the nervous system. *J. Neuropathol. Exp. Neurol.* **2002**, *61*, 215–225. [CrossRef]
2. Kesari, S. Understanding glioblastoma tumor biology: The potential to improve current diagnosis and treatments. *Semin. Oncol.* **2011**, *38*, 2–10. [CrossRef]
3. Ohka, F.; Natsume, A.; Wakabayashi, T. Current trends in targeted therapies for glioblastoma multiforme. *Neurol. Res. Int.* **2012**, *2012*, 878425. [CrossRef]
4. Reya, T.; Morrison, S.J.; Clarke, M.F.; Weissman, I.L. Stem cells, cancer, and cancer stem cells. *Nature* **2001**, *414*, 105–111. [CrossRef]

5. Rispoli, R.; Conti, C.; Celli, P.; Caroli, E.; Carletti, S. Neural stem cells and glioblastoma. *Neuroradiol. J.* **2014**, *27*, 169–174. [CrossRef]
6. Vescovi, A.L.; Galli, R.; Reynolds, B.A. Brain tumour stem cells. *Nat. Rev. Cancer* **2006**, *6*, 425–436. [CrossRef]
7. Mao, H.; Lebrun, D.G.; Yang, J.; Zhu, V.F.; Li, M. Deregulated signaling pathways in glioblastoma multiforme: Molecular mechanisms and therapeutic targets. *Cancer Investig.* **2012**, *30*, 48–56. [CrossRef]
8. Jorissen, R.N.; Walker, F.; Pouliot, N.; Garrett, T.P.J.; Ward, C.W.; Burgess, A.W. Epidermal growth factor receptor: Mechanisms of activation and signalling. *Exp. Cell Res.* **2003**, *284*, 31–53. [CrossRef]
9. Nishikawa, R.; Ji, X.D.; Harmon, R.C.; Lazar, C.S.; Gill, G.N.; Cavenee, W.K.; Huang, H.J. A mutant epidermal growth factor receptor common in human glioma confers enhanced tumorigenicity. *Proc. Natl. Acad. Sci. USA* **1994**, *91*, 7727–7731. [CrossRef]
10. Purow, B.W.; Haque, R.M.; Noel, M.W.; Su, Q.; Burdick, M.J.; Lee, J.; Sundaresan, T.; Pastorino, S.; Park, J.K.; Mikolaenko, I.; et al. Expression of Notch-1 and its ligands, Delta-like-1 and Jagged-1, is critical for glioma cell survival and proliferation. *Cancer Res.* **2005**, *65*, 2353–2363. [CrossRef]
11. Eglen, R.M. Muscarinic receptor subtype pharmacology and physiology. *Prog Med. Chem.* **2005**, *43*, 105–136. [PubMed]
12. Rayford, W.; Noble, M.J.; Austenfeld, M.A.; Weigel, J.; Mebust, W.K.; Shah, G.V. Muscarinic cholinergic receptors promote growth of human prostate cancer cells. *Prostate* **1997**, *30*, 160–166. [CrossRef]
13. Oppitz, M.; Möbus, V.; Brock, S.; Drews, U. Muscarinic receptors in cell lines from ovarian carcinoma: Negative correlation with survival of patients. *Gynecologic. Oncol.* **2002**, *85*, 159–164. [CrossRef] [PubMed]
14. Song, P.; Sekhon, H.S.; Lu, A.; Arredondo, J.; Sauer, D.; Gravett, C.; Mark, G.P.; Grando, S.A.; Spindel, E.R. M3 muscarinic receptor antagonists inhibit small cell lung carcinoma growth and mitogen-activated protein kinase phosphorylation induced by acetylcholine secretion. *Cancer Res.* **2007**, *67*, 3936–3944. [CrossRef] [PubMed]
15. Guizzetti, M.; Costa, P.; Peters, J.; Costa, L.G. Acetylcholine as a mitogen: Muscarinic receptor-mediated proliferation of rat astrocytes and human astrocytoma cells. *Eur. J. Pharmacol.* **1996**, *297*, 265–273. [CrossRef]
16. Ferretti, M.; Fabbiano, C.; Di Bari, M.; Ponti, D.; Calogero, A.; Tata, A.M. M2 muscarinic receptors inhibit cell proliferation in human glioblastoma cell lines. *Life Sci.* **2012**, *91*, 1134–1137. [CrossRef]
17. Ferretti, M.; Fabbiano, C.; Di Bari, M.; Conte, C.; Castigli, E.; Sciacaluga, M.; Ponti, D.; Ruggieri, P.; Raco, A.; Ricordy, R.; et al. M2 receptor activation inhibits cell cycle progression and survival in human glioblastoma cells. *J. Cell. Mol. Med.* **2013**, *17*, 552–566. [CrossRef]
18. Alessandrini, F.; Cristofaro, I.; Di Bari, M.; Zasso, J.; Conti, L.; Tata, A.M. The activation of M2 muscarinic receptor inhibits cell growth and survival in human glioblastoma cancer stem cells. *Int. Immunopharmacol.* **2015**, *29*, 105–109. [CrossRef]
19. Cristofaro, I.; Spinello, Z.; Matera, C.; Fiore, M.; Conti, L.; De Amici, M.; Dallanocce, C.; Tata, A.M. Activation of M2 muscarinic acetylcholine receptors by a hybrid agonist enhances cytotoxic effects in GB7 glioblastoma cancer stem cells. *Neurochem. Int.* **2018**, *118*, 52–60. [CrossRef]
20. Conti, L.; Crisafulli, L.; Caldera, V.; Tortoreto, M.; Brilli, E.; Conforti, P.; Zunino, F.; Magrassi, L.; Schiffer, D.; Cattaneo, E. REST controls self-renewal and tumorigenic competence of human glioblastoma cells. *PLoS ONE* **2012**, *7*, e38486. [CrossRef]
21. Weglicki, W.B.; Kramer, J.H.; Spurney, C.F.; Chmielinska, J.J.; Mak, I.T. The EGFR tyrosine kinase inhibitor tyrphostin AG1478 cause hypomagnesemia and cardiac dysfunction. *Can. J. Physiol. Pharmacol.* **2012**, *90*, 1145–1149. [CrossRef] [PubMed]
22. Ridet, A.; Guillouf, C.; Duchaud, E.; Cundari, E.; Fiore, M.; Moustacchi, E.; Rosselli, F. Deregulated apoptosis is a hallmark of Fanconi anemia syndrome. *Canc Res.* **1997**, *57*, 1722–1730.
23. Darzynkiewicz, Z.; Bruno, S.; Del Bino, G.; Gorczyca, W.; Hotz, M.A.; Lassota, P.; Traganos, F. Features of apoptotic cells measured by flow cytometry. *Cytometry* **1992**, *13*, 795–808. [CrossRef] [PubMed]
24. Felsberg, J.; Hentschel, B.; Kaulich, K.; Gramatzki, D.; Zacher, A.; Malzkorn, B.; Kamp, M.; Sabel, M.; Simon, M.; Westphal, M.; et al. Epidermal Growth Factor Receptor Variant III (EGFRvIII) Positivity in EGFR-Amplified Glioblastomas: Prognostic Role and Comparison between Primary and Recurrent Tumors. *Clin. Cancer Res.* **2017**, *23*, 6846–6855. [CrossRef]
25. Guessous, F.; Zhang, Y.; Kofman, A.; Catania, A.; Li, Y.; Schiff, D.; Purow, B.; Abounader, R. microRNA-34a is tumor suppressive in brain tumors and glioma stem cells. *Cell Cycle Georget. Tex.* **2010**, *9*, 1031–1036. [CrossRef]

26. Matera, C.; Tata, A.M. Pharmacological approaches to targeting muscarinic acetylcholine receptors. *Rec. Pat. CNS Drug Discov.* **2014**, *9*, 85–100. [CrossRef]
27. De Jaco, A.; Bernardini, L.; Rosati, J.; Tata, A.M. Alpha-7 Nicotinic Receptors in Nervous System Disorders: From Function to Therapeutic Perspectives. *Cent. Nerv. Syst. Agents. Med. Chem.* **2017**, *17*, 100–108. [CrossRef]
28. Tata, A.M. Muscarinic acetylcholine receptors: New potential therapeutic targets in antinociception and in cancer therapy. *Rec Pat. CNS Drug Discov.* **2008**, *3*, 94–103. [CrossRef]
29. Lucianò, A.M.; Mattei, F.; Damo, E.; Panzarini, E.; Dini, L.; Tata, A.M. Effects mediated by M2 muscarinic orthosteric agonist on cell growth in human neuroblastoma cell lines. *Pure Appl. Chem.* **2019**. [CrossRef]
30. Pacini, L.; De Falco, E.; Di Bari, M.; Coccia, A.; Siciliano, C.; Ponti, D.; Pastore, A.L.; Petrozza, V.; Carbone, A.; Tata, A.M.; et al. M2 muscarinic receptors inhibit cell proliferation and migration in urothelial bladder cancer cells. *Cancer Biol. Ther.* **2014**, *15*, 1489–1498. [CrossRef]
31. Di Bari, M.; Tombolillo, V.; Conte, C.; Castigli, E.; Sciacaluga, M.; Iorio, E.; Carpinelli, G.; Ricordy, R.; Fiore, M.; Degrassi, F.; et al. Cytotoxic and genotoxic effects mediated by M2 muscarinic receptor activation in human glioblastoma cells. *Neurochem. Int.* **2015**, *90*, 261–270. [CrossRef] [PubMed]
32. Di Bari, M.; Bevilacqua, V.; De Jaco, A.; Laneve, P.; Piovesana, R.; Talora, C.; Caffarelli, E.; Tata, A.M. MiR-34a mediates cross-talk between M2 muscarinic receptors and Notch-1/EGFR pathways in human glioblastoma: Implication in cell proliferation. *Int. J. Mol. Sci.* **2018**, *19*, 1631. [CrossRef] [PubMed]



© 2020 by the authors. Licensee MDPI, Basel, Switzerland. This article is an open access article distributed under the terms and conditions of the Creative Commons Attribution (CC BY) license (<http://creativecommons.org/licenses/by/4.0/>).

Article

# WNK2 Inhibits Autophagic Flux in Human Glioblastoma Cell Line

Ana Laura Vieira Alves <sup>1</sup>, Angela Margarida Costa <sup>2,3</sup>, Olga Martinho <sup>1,2,3</sup>,  
Vinicius Duval da Silva <sup>1</sup>, Peter Jordan <sup>4,5</sup>, Viviane Aline Oliveira Silva <sup>1</sup> and  
Rui Manuel Reis <sup>1,2,3,\*</sup>

<sup>1</sup> Molecular Oncology Research Center, Barretos Cancer Hospital, 14784 400 Barretos, Brazil; alves.anav@gmail.com (A.L.V.A.); olgamartinho@med.uminho.pt (O.M.); vinids@gmail.com (V.D.d.S.); vivianeaos@gmail.com (V.A.O.S.)

<sup>2</sup> Life and Health Sciences Research Institute (ICVS), School of Medicine, University of Minho, 4710-057 Braga, Portugal; angela.amorimcosta@ineb.up.pt

<sup>3</sup> ICVS/3B's—PT—Government Associate Laboratory, 4806-909 Braga, Portugal

<sup>4</sup> Department of Human Genetics, National Health Institute Doutor Ricardo Jorge, 1649-016 Lisbon, Portugal; peter.jordan@insa.min-saude.pt

<sup>5</sup> BioISI—Biosystems & Integrative Sciences Institute, Faculty of Sciences, University of Lisbon, 1749-016 Lisbon, Portugal

\* Correspondence: ruireis.hcb@gmail.com; Tel.: +55-173-321-6600

Received: 29 December 2019; Accepted: 25 January 2020; Published: 20 February 2020;  
Corrected: 19 July 2024



**Abstract:** Autophagy is a cell-survival pathway with dual role in tumorigenesis, promoting either tumor survival or tumor death. *WNK2* gene, a member of the WNK (with no lysine (K)) subfamily, acts as a tumor suppressor gene in gliomas, regulating cell migration and invasion; however, its role in autophagy process is poorly explored. The *WNK2*-methylated human glioblastoma cell line A172 WT (wild type) was compared to transfected clones A172 EV (empty vector), and A172 *WNK2* (*WNK2* overexpression) for the evaluation of autophagy using an inhibitor (bafilomycin A1—baf A1) and an inducer (everolimus) of autophagic flux. Western blot and immunofluorescence approaches were used to monitor autophagic markers, LC3A/B and SQSTM1/p62. A172 *WNK2* cells presented a significant decrease in LC3B and p62 protein levels, and in LC3A/B ratio when compared with control cells, after treatment with baf A1 + everolimus, suggesting that *WNK2* overexpression inhibits the autophagic flux in gliomas. The mTOR pathway was also evaluated under the same conditions, and the observed results suggest that the inhibition of autophagy mediated by *WNK2* occurs through a mTOR-independent pathway. In conclusion, the evaluation of the autophagic process demonstrated that *WNK2* inhibits the autophagic flux in glioblastoma cell line.

**Keywords:** *WNK2*; glioblastoma cell line; autophagy; inhibition; autophagic flux

## 1. Introduction

Gliomas are the most common adult primary brain tumors [1]. Glioblastoma (GBM) is the highest-grade form of glioma (WHO grade IV), as well as one of the most aggressive types of cancer with rapid cellular growth, and highly invasive behavior, with a median overall survival time of 15–18 months [2]. The current therapeutic approach is surgery followed by concomitant radiotherapy and temozolomide-based chemotherapy [3–5]; however, despite significant advances in diagnosis and therapy in recent decades, the outcomes for high grade gliomas (WHO grade III–IV) remains unfavorable [6]. To change this scenario, a deeper understanding of glioma cancer biology is needed.

Autophagy is a catabolic mechanism that maintains cellular homeostasis. In this cellular process proteins or cytoplasmic organelles are sequestered by double-membrane vesicles known

as autophagosomes [7]. Fusion of autophagosomes with lysosomes forms a structure in which intracellular degradation occurs, leading to a state of equilibrium of cellular metabolism, as well as apoptosis [8]. Uncontrolled autophagy is also a cell death mechanism that may occur either in the absence or concomitantly with signs of apoptosis [9]. The autophagy process has been found activated in many tumors and its inhibition can lead to both increased cell death and increased survival, depending on the tissue type, tumor grade, and therapy used [10,11]. Furthermore, it is known that prolonged and progressive autophagy stress can lead to cell death [12]. Thus, induction of autophagic cell death has been proposed as a possible mechanism of tumor suppression [13]. Since autophagy can be viewed as pro- or anti-tumor, depending on the context [14], the dissection of its role in gliomas, as well as the associated molecular mechanisms is of critical importance. This is particularly relevant because glioma cells usually respond to therapeutic agents that induce the autophagic process such as, TMZ and rapamycin in a clinical setting [15].

The serine/threonine kinase WNK2 (with no lysine protein kinase 2) acts as a tumor suppressor in GBM and is associated to carcinogenesis-related pathways [16–18]. WNK2 inhibits cell proliferation, invasion, and migration [19–21]. These effects are lost following epigenetic silencing by hypermethylation of *WNK2* promoter region [16,17]. However, the role of *WNK2* in cell death is still unclear and contradictory data concerning *WNK2* as an autophagic modulator has been reported [22,23]. Therefore, the present study aimed to explore the *in vitro* role of *WNK2* in autophagic process in gliomas.

## 2. Materials and Methods

### 2.1. Cell Lines and Cell Culture

The human glioblastoma cell lines A172 WT (wild-type), A172 EV (empty-vector), and A172 WNK2 (*WNK2* overexpression) (Supplementary Figure S1) were cultured in Dulbecco's modified Eagle's medium (DMEM) supplemented with 10% fetal bovine serum (FBS) (Sigma-Aldrich, St. Louis, MO, USA), 1% p/s (penicillin/streptomycin) (Life Technologies, Carlsbad, CA, USA) at 37 °C under humidified atmosphere containing 5% CO<sub>2</sub>. A172 EV and A172 WNK2 were generated and maintained as previously described [18]. The authentication of the cell lines was performed by a DNA short tandem repeat (STR) profile at the Diagnostic Laboratory at Barretos Cancer Hospital (São Paulo, Brazil), as previously described [24].

### 2.2. Cell Treatment

The A172 WT, A172 EV, and A172 WNK2 cell lines were plated in 6-well plates at a density of  $6 \times 10^5$  cells/well, and allowed to adhere overnight. After this period, the cells were starved for 3 h with DMEM 0.5% FBS. Next, for the control cells, the growth medium was replaced with DMEM 10% FBS. To evaluate the autophagic process, the cells were treated with Earle's Balanced Salt Solution (EBSS) (Thermo Fisher Scientific, Waltham, MA, USA). To evaluate the autophagy process, 20 nM bafilomycin A1 (baf A1) (Sigma-Aldrich) was added to the EBSS. Furthermore, 10 nM everolimus (Sigma-Aldrich) was added, acting on the inhibition of mammalian target of rapamycin (mTOR), resulting in the induction of autophagy. Cells were incubated with the respective treatments for 4 and 6 h.

### 2.3. Immunofluorescence

Cells were plated in a 24-well plate at a density of  $7.5 \times 10^5$  cells/well, and allowed to adhere for at least 24 h. Subsequently, the cells were starved for 3 h with DMEM (0.5% FBS) before treatment, and then treated with 30 μM chloroquine (CQ) (Molecular Probes, Invitrogen, Eugene, OR, USA) for 16 h. Next, the cells were incubated with formaldehyde 3.7% in Dulbecco's phosphate-buffered saline (DPBS 1X) (Sigma-Aldrich) and permeabilized with 0.2% Triton X-100 in DPBS 1X for 15 min at room temperature. The cells were incubated for 2 h with a primary LC3 rabbit polyclonal antibody (Molecular Probes, Invitrogen, Eugene, OR, USA) diluted in DPBS with 5% BSA (Bovine Serum

Albumin), followed by the secondary antibody Alexa Fluor 488 (Life Technologies, Carlsbad, CA, USA) for 1 h at room temperature. Finally, the cells were labeled with HOECHST 33342 (1:2000) (Life Technologies) and phalloidin-rhodamine (1:200) (Molecular Probes, Invitrogen, Eugene, OR, USA). Images were acquired by the High Content In Cell Analyzer 2200 platform (GE Healthcare Life Sciences, Chicago, IL, USA) and quantification was performed in the Image-Pro software (Media Cybernetics, Rockville, MD, USA).

#### 2.4. Transient Transfection

The pDest-mCherry-EGFP-LC3B and pDest-mCherry-GFP-p62 plasmids were kindly provided by Prof. Terje Johansen (Molecular Cancer Research group, Institute of Medical Biology, University of Tromsø, Tromsø, Norway) for transient transfection. Cells were plated in 6-well plates at a density of  $2.5 \times 10^5$  cells/well 24 h before transfection with plasmid using the Lipofectamine 3000 reagent (Invitrogen) according to the manufacturer's recommendations. After 5 h, the transfection medium was replaced by a fresh culture medium, and the cells were incubated for another 24 h. Subsequently, the cells were starved with Hank's Balanced Salt solution (HBSS) (Invitrogen) for 4 h prior to treatment with 200  $\mu$ M baf A1 (Sigma Aldrich) for 24 h. After this period, the cells were labeled with HOECHST (1:2000) (Life Technologies). Images were acquired by the High Content In Cell Analyzer 2200 platform (GE Healthcare Life Sciences) and quantification was performed in the Image-Pro software (Media Cybernetics).

#### 2.5. Western Blotting Analysis

Total protein from cell death and autophagy assays was analyzed by western blot as previously described [25]. The following antibodies were used: Anti-LC3A/B (1:1000), anti-SQSTM1/p62 (1:1000), anti-p-p70<sup>S6K</sup> (Thr389) (1:1000), anti-p-4EBP1 (1:1000), anti-p-mTOR (Ser2448) (1:1000),  $\alpha$ -tubulin (1:2000), and  $\beta$ -actin (1:2000), all purchased from Cell Signaling (Danvers, MA, USA).  $\beta$ -actin and  $\alpha$ -tubulin were used as a loading control. HRP-conjugated goat anti-mouse and goat anti-rabbit (all from Cell Signaling) were used as secondary antibodies. Chemiluminescence using ECL (GE Healthcare Life Sciences) was detected on an Image Quant LAS4000 mini photo documentation system (GE Healthcare Life Sciences). The subsequent quantification was performed by Image J software version 1.52s (National Institutes of Health—<https://imagej.nih.gov/ij/>).

#### 2.6. Statistical Analysis

Data from experiments were expressed as the mean  $\pm$  standard deviation (SD) of three independent experiments. *p*-values were calculated by two-way ANOVA. Symbols indicate statistical comparisons (\* *p* < 0.05, \*\* *p* < 0.01, \*\*\* *p* < 0.001). The aforementioned analysis was performed using GraphPad PRISM version 5 (GraphPad Software, San Diego, CA, USA).

### 3. Results

#### *WNK2 Inhibits Autophagic Flux*

To investigate the potential effect of *WNK2* overexpression on autophagy, the A172-derived cell lines (A172 WT, A172 EV, and A172 *WNK2*) were evaluated for the main markers recommended by the guidelines for the use and interpretation of assays for autophagy monitoring (3rd edition) [26]. The cells were treated with baf A1 as an autophagy flux inhibitor, as well as with starvation (EBSS) and everolimus as autophagy inducers. The western blot analysis demonstrated that *WNK2* overexpression significantly decreased LC3B (microtubule-associated protein 1 light chain 3 beta) protein lipidation, and SQSTM1 (sequestosome 1)/p62 levels after 4 and 6 h of combinatorial treatments (Figure 1A,B) indicating a clear autophagic flux inhibition.

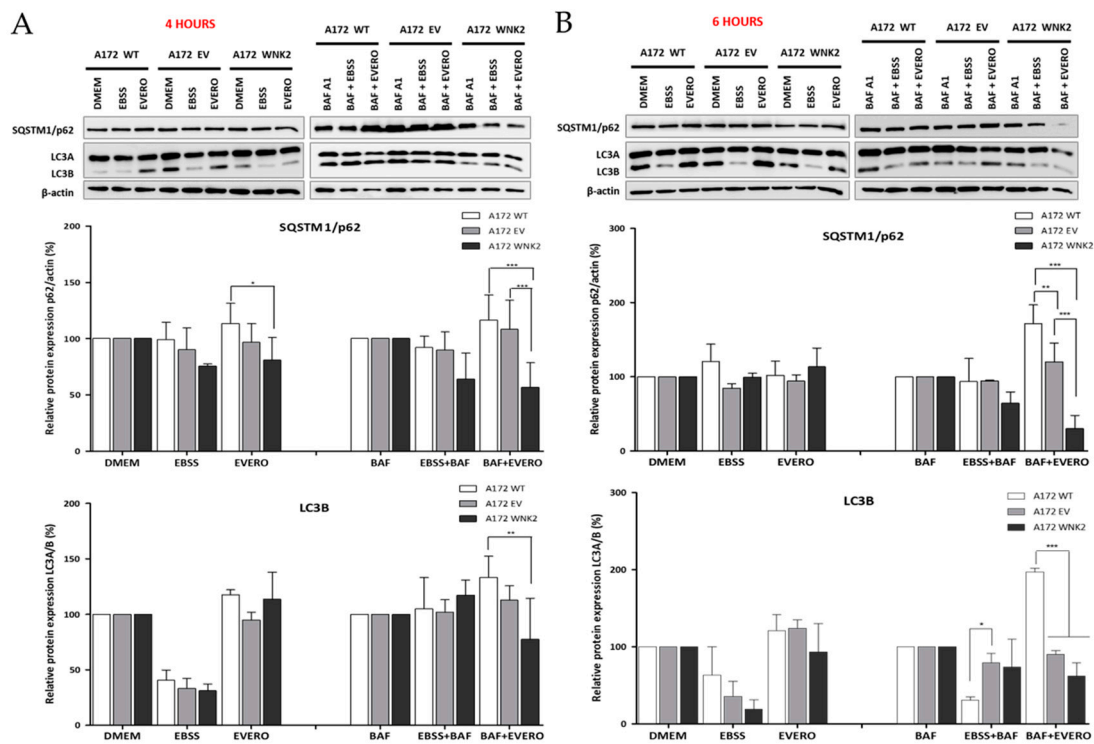


**Figure 1.** Evaluation of LC3B and p62 proteins by western blot. A172 WT, A172 EV, and A172 WNK2 cell lines were treated with bafilomycin A1 (BAF, 20 nM), starvation (EBSS medium), everolimus (EVERO, 10 nM), or the combination BAF+EVERO for 4 (A) or 6 h (B). The graphs are representative of three independent biological experiments.  $\beta$ -actin protein was used as an endogenous loading control. Symbols mean (\*)  $p < 0.05$ ; (\*\*)  $p < 0.01$ ; (\*\*\*)  $p < 0.001$ .

Since everolimus, an mTOR pathway inhibitor, was used in combination with baf A1 treatment, proteins belonging to this pathway were evaluated. Interestingly, under these conditions, the activity of mTOR or the phosphorylation of its substrates EBP1 and p70S6K did not differ between the WNK2-overexpressing cell line compared to the WT and EV controls (Figure 2A,B), suggesting that the observed autophagic flux inhibition in the WNK2 presence is mTOR-independent.

To confirm the autophagy flux inhibition observed in the WNK2 overexpressing cells, we transfected the three A172-derived cell lines with *tandem* conjugated pDest.mCherry-GFP-p62 and pDest.mCherry-GFP-LC3B plasmids [27] and then treated for autophagy induction with HBSS and with the autophagy flux inhibitor baf A1. In this approach, yellow signal indicates the presence of LC3B or p62 in autophagosomes, whereas red signal indicates autophagolysosomes due to loss of green fluorescence in their acidic environment. We found a marked decrease in p62-positive puncta in A172 WNK2 cells in the HBSS + baf A1 treated condition (Figure 3A). On the other hand, these cells showed no change in autophagic flux as evidenced by the number of LC3B-positive puncta when compared to control cells; however, a decrease in red dots representing autophagolysosomes was evidenced between WT and WNK2 cell line (Figure 3B).

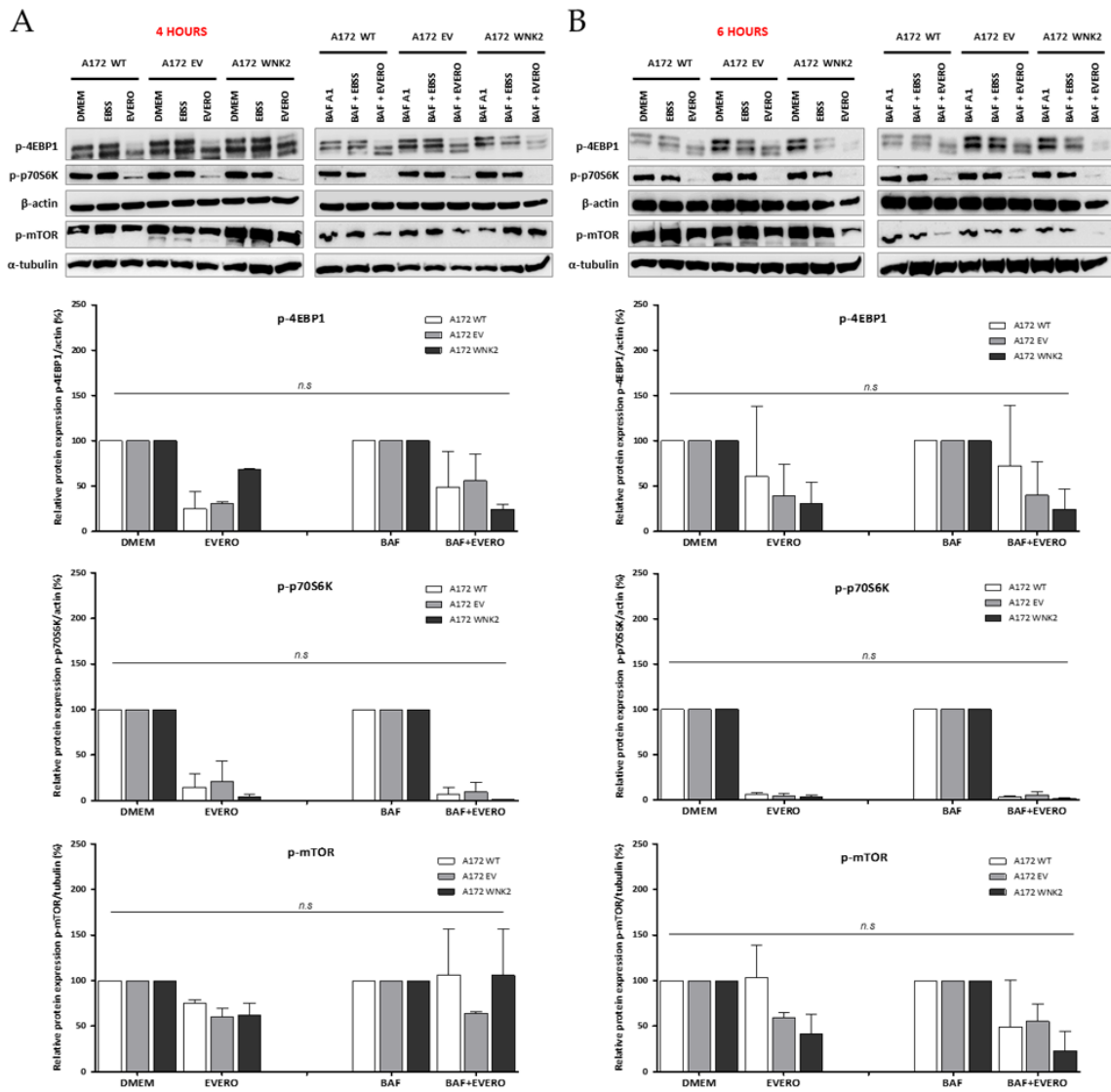


**Figure 2.** Evaluation of proteins involved in the mammalian target of rapamycin (mTOR) pathway by western blot. A172 WT, A172 EV, and A172 WNK2 cell lines were treated with bafilomycin A1 (BAF, 20 nM), starvation (EBSS medium), or everolimus (EVERO, 10 nM) for 4 (A) and 6 h (B). The protein extract was evaluated for phosphorylation of mTOR and its substrates p-p70S6K and p-4EBP1 by western blot. Normalized densitometric band intensities of mTOR activity used  $\alpha$ -tubulin as an endogenous loading control. For the substrates p-p70S6K and p-4EBP1,  $\beta$ -actin was used as an endogenous control. The graphs are representative of two independent biological experiments. n.s.: Not significant.



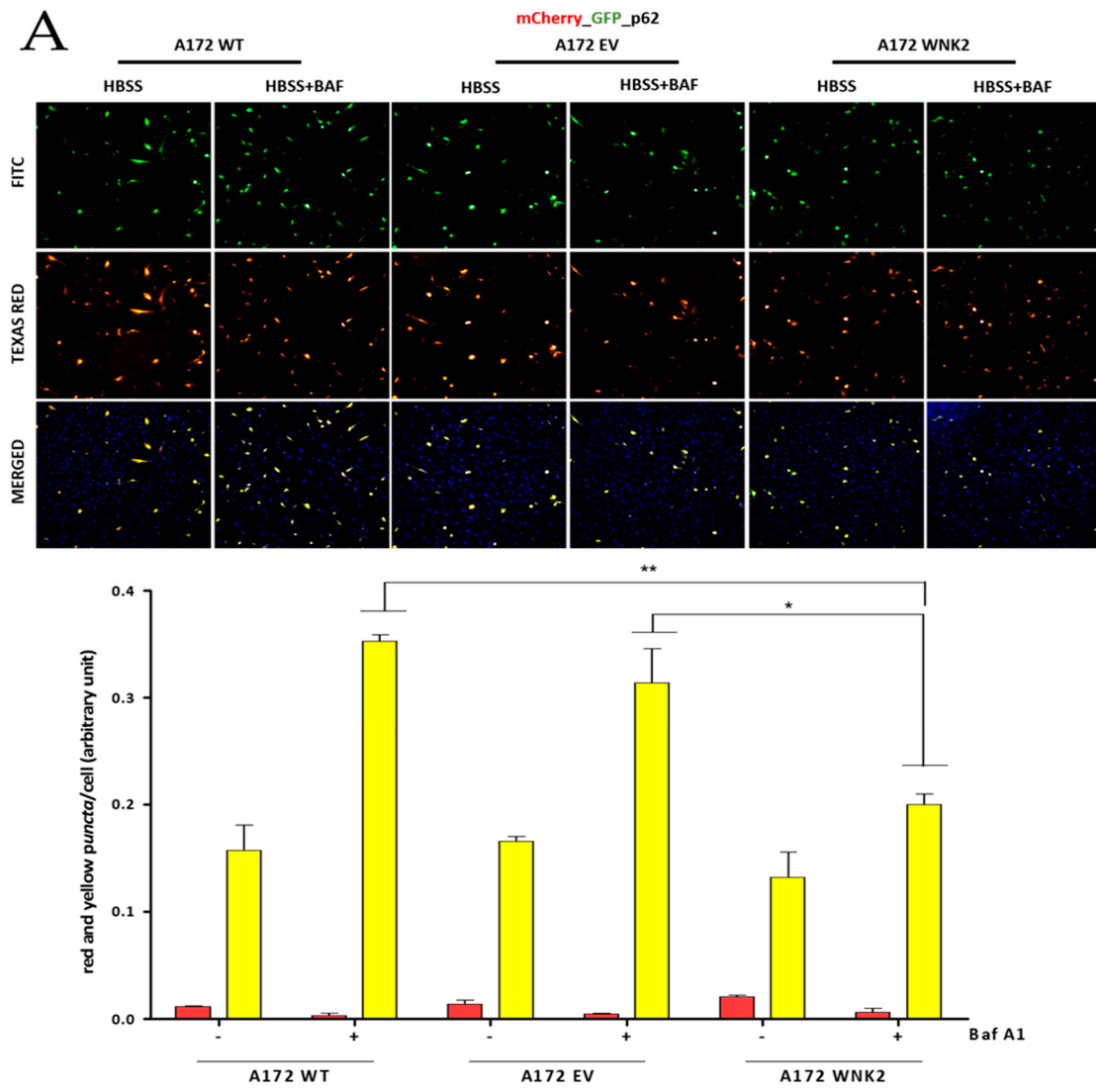
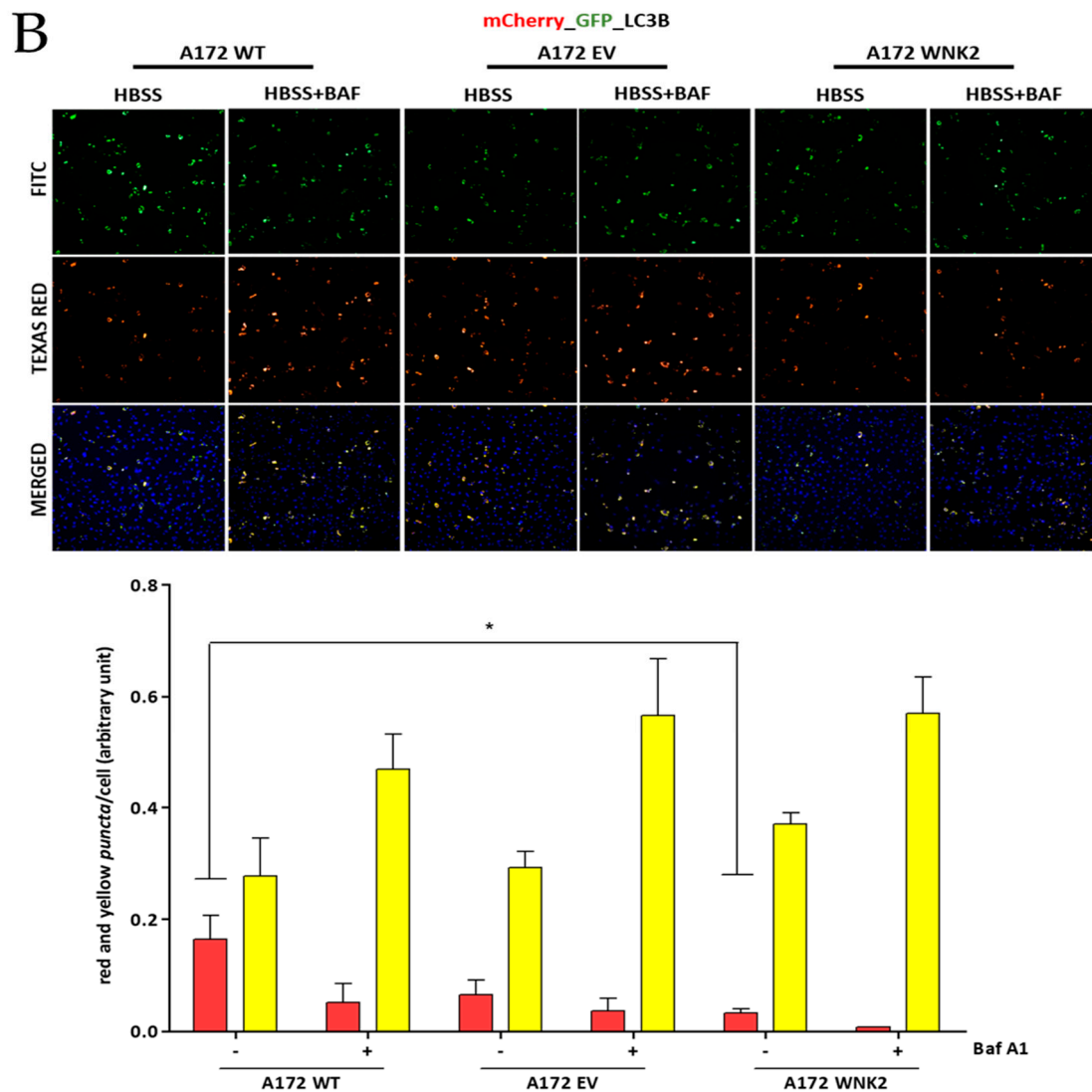
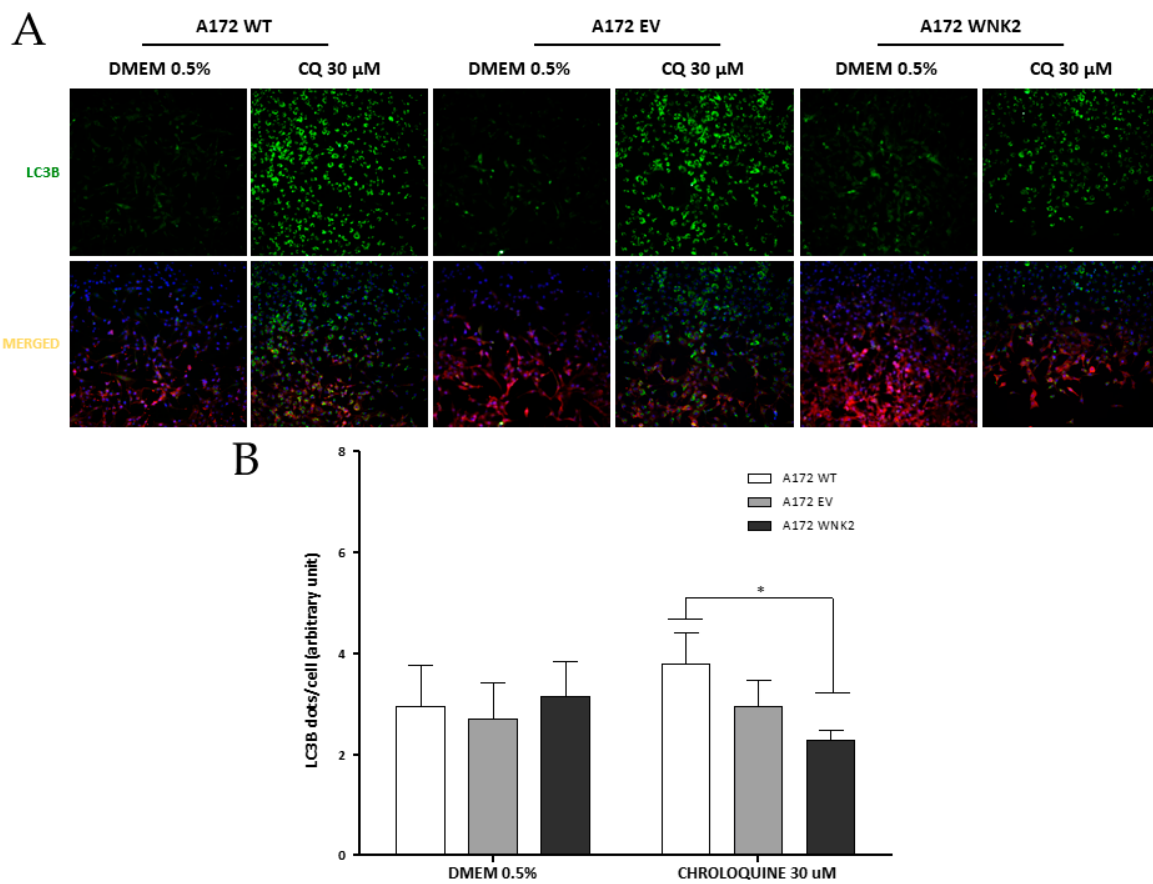


Figure 3. *Cont.*



**Figure 3.** Evaluation of LC3B and p62 proteins by using transient transfection with pDest.mCherry-GFP-LC3B and pDest.mCherry-GFP-p62 plasmids. A172 WT, A172 EV, and A172 WNK2 cell lines were transfected with plasmid pDest.mCherry-GFP-LC3B (A) or pDest.mCherry-GFP-p62 (B) and then treated for 24 h with bafilomycin A1 (baf A1). Hoechst (DAPI) treatment indicates nuclear staining by blue fluorescence. FITC indicates green fluorescence and Texas Red indicates red fluorescence wavelengths by the In Cell Analyzer platform. In the figures, yellow dots indicate the presence of LC3B or p62 in autophagosomes, whereas red dots indicate autophagolysosomes due to loss of green fluorescence in an acidic environment. In the graphics, the yellow and red bars indicate the quantification of autophagosomes and autophagolysosomes, respectively, observed in the merged. The graphs are representative of two independent biological experiments. Images were quantified using Image-Pro software. Symbols mean (\*)  $p < 0.05$ ; (\*\*)  $p < 0.01$ ; (\*\*\*)  $p < 0.001$ . (+) means presence of baf A1; (-) means absence of baf A1.

Additionally, another approach was used for evaluating autophagic flux in the edited cell lines. In these results, *WNK2* overexpression changed LC3B levels after 16 h upon another autophagy inhibitor treatment, chloroquine at 30  $\mu$ M (Figure 4A,B) when compared with WT cell line.



**Figure 4.** Evaluation of the effect of *WNK2* overexpression on the autophagic process after chloroquine (CQ) treatment. **(A)** A172 WT, A172 EV, and A172 WNK2 cell lines were treated with DMEM 0.5% FBS for control conditions and to induce autophagy with the autophagy flux inhibitor chloroquine (CQ, 30 μM) for 16 h after a 3-h starvation period. Images were acquired at DAPI (blue, nuclei), FITC (green, LC3 dots), and CY3 (red, cytoplasm) wavelengths by the In Cell Analyzer platform. **(B)** Graph of the quantification of LC3B vesicles in merged after control condition and treatment with CQ for 16 h. The graphs are representative of three independent biological experiments. The quantification of images was realized in Image-Pro software. Symbols mean (\*)  $p < 0.05$ ; (\*\*)  $p < 0.01$ ; (\*\*\*)  $p < 0.001$ .

#### 4. Discussion

The role of *WNK2* in the autophagic process is still contradictory. In this study, the assessment of the autophagic process using different methodological approaches has suggested that the presence of *WNK2* inhibits the autophagic flux in glioma cell lines and it is independent of the mTOR pathway.

In the autophagic process, some important markers allow to estimate autophagic activity, such as LC3 and p62. Typically, LC3A is converted to LC3B by lipidation and is present in the formation of autophagosomes [26]. p62 protein binds to ubiquitinated proteins, that are labeled for degradation and direct them to the lysosome. Generally, p62 levels correlate inversely with autophagic activity. However, it is unclear whether p62 is degraded only by autophagy or partially by the ubiquitin-proteasome pathway [28]. Thus, p62, as well as LC3, can be transcriptionally regulated during autophagy [29]. Western blot analysis showed a significant decrease in the levels of LC3B and p62 markers after 4 and 6 h of baf A1 treatment and everolimus. In addition, immunofluorescence results demonstrated a decrease in LC3B level after CQ treatment and p62 *puncta* after HBSS + baf A1 treatment and although no statistical difference was found in the LC3B *puncta*, there was a decrease in red dots in the overexpressing *WNK2* cell line when compared to the WT cell line. Previous studies point to *WNK2* acting in the early stages of autophagic flux, however, with contradictory functions. Szyaniarowski et al.

(2011) [23] silenced *WNK2* via siRNA (small interfering RNA) in MCF-7 human breast carcinoma cells and reported p62 accumulation, thus inhibiting autophagic flux [30]. Accumulation of this protein indicates defective maturation of autophagosomes [23], thus *WNK2* would act as a positive regulator of the autophagic process. On the other hand, Guo et al. (2015) silenced *WNK2* through shRNAs (short hairpin RNA) that induced a significant increase in LC3B by immunofluorescence [22] demonstrating that *WNK2* could inhibit autophagy flux. It is noteworthy that according to Yoshii et al. (2017), cells that present a low number of positive puncta in the basal condition, as we reported, and that do not suffer alterations after treatment with baf A1 are suggestive of defects in the autophagy induction process [31].

It is known that one of the major biological changes in glioma is the alteration of the PI3K (phosphatidylinositol 3 kinase)/AKT/mTOR pathway [32]. Inhibition of mTOR may be detected as dephosphorylation of its substrates p70S6K kinase and 4EBP1 (4E binding protein 1) [33] and are correlated with the autophagic process in gliomas [34,35]. To assess the impact of this pathway, we used treatment with the autophagic inducer (everolimus), a rapamycin analog that inhibits mTOR signaling in combination with an autophagic inhibitor (baf A1). The results suggest that *WNK2*-mediated autophagy inhibition occurs independently of the mTOR pathway. Previous studies relating *WNK2* and autophagy have also contradicted the effect of this gene on mTOR activity. While Szyniarowski et al. (2011) did not find any effect on mTORC1 activity in breast cancer cell lines by analyzing the phosphorylation status its p70S6K [23], another study using chronic myeloid leukemia demonstrated suppressed autophagy by activating mTOR [22]. Furthermore, it was recently reported that *mTOR* mutations have essential implication in inducing resistance to the mTOR inhibitors preserving its activity [36], as observed in our study. One hypothesis for our findings would be that *WNK2* could promote defects in the initial autophagy flux or autophagosome maturation [22,23]. During autophagosome formation PI3K activity, an upstream element in the mTOR pathway, is required and when suppressed inhibits autophagic flux. In this sense, the mechanism used by *WNK2* to inhibit autophagic flux would be similar to the 3-methyladenine autophagy inhibitor (3-MA) [36].

TMZ is considered the most effective treatment drug for GBMs and its main mechanism of action is on autophagy [37,38]. However, depending on the cellular context, it has been shown that autophagy could lead to the development of resistance to TMZ treatment rather than cell death [39–41]. Recently, therapeutic molecules that inhibit autophagy such as CQ and hydroxychloroquine have been used in phase I/II clinical trials concomitant with TMZ treatment and radiation and have shown increased survival in patients diagnosed with GBM [15,42]. In this study, assessment of the autophagic process has suggested that the presence of *WNK2* inhibits the autophagic flux in glioblastoma cell line. It will now be interesting to study the role of *WNK2* in autophagic vesicular trafficking in response to therapy.

**Supplementary Materials:** The following are available online at <http://www.mdpi.com/2073-4409/9/2/485/s1>, Figure S1: Validation of *WNK2* overexpression by RT-PCR.

**Author Contributions:** Conception or design of the work, Acquisition, Analysis and interpretation of data, Writing—original draft preparation, Final approval, A.L.V.A.; Writing—Review and Editing, Final approval, A.M.C.; Writing—Review and Editing, Final approval, O.M.; Software Analysis and interpretation of data, Writing—Review and Editing, Final approval, V.D.d.S.; Writing—Review and Editing, Final approval, P.J.; Analysis and interpretation of data, Writing—Review and Editing, Final approval, V.A.O.S.; (Corresponding author)—Conception or design of the work, Interpretation of data, Drafting the work, Supervision of study, Project Administration, Resources, Funding Acquisition, Final approval, R.M.R. All authors have read and agreed to the published version of the manuscript.

**Funding:** This project was supported by the Barretos Cancer Hospital Internal Research Funds (PAIP) to Rui Manuel Reis and by the Public Ministry of Labor Campinas (Research, Prevention, and Education of Occupational Cancer Project), Campinas, Brazil. Ana Laura Vieira Alves is the recipient of a FAPESP master fellowship (2016/18907-0).

**Acknowledgments:** José M Bravo-San Pedro (Centre de Recherche des Cordeliers, Paris, France) for all the scientific and technical support available for this study to be carried out. Terje Johansen (Molecular Cancer Research group, Institute of Medical Biology, University of Tromsø, Norway) for kindly giving the *tandem* plasmids used in this study.

**Conflicts of Interest:** The authors declare no conflict of interest.

**Correction Statement:** This article has been republished with a minor change. The change does not affect the scientific content of the article and further details are available within the backmatter of the website version of this article.

## References

1. Ostrom, Q.T.; Gittleman, H.; Truitt, G.; Boscia, A.; Kruchko, C.; Barnholtz-Sloan, J.S. CBTRUS Statistical Report: Primary Brain and Other Central Nervous System Tumors Diagnosed in the United States in 2011-2015. *Neuro-Oncology* **2018**, *20*, iv1–iv86. [CrossRef] [PubMed]
2. Omuro, A.; DeAngelis, L.M. Glioblastoma and other malignant gliomas: A clinical review. *JAMA* **2013**, *310*, 1842–1850. [CrossRef] [PubMed]
3. Zhu, Y.; Parada, L.F. The molecular and genetic basis of neurological tumours. *Nat. Rev. Cancer* **2002**, *2*, 616–626. [CrossRef] [PubMed]
4. Cruceru, M.L.; Neagu, M.; Demoulin, J.B.; Constantinescu, S.N. Therapy targets in glioblastoma and cancer stem cells: Lessons from haematopoietic neoplasms. *J. Cell. Mol. Med.* **2013**, *17*, 1218–1235. [CrossRef]
5. Lapointe, S.; Perry, A.; Butowski, N.A. Primary brain tumours in adults. *Lancet* **2018**, *392*, 432–446. [CrossRef]
6. Stupp, R.; Mason, W.P.; van den Bent, M.J.; Weller, M.; Fisher, B.; Taphoorn, M.J.; Belanger, K.; Brandes, A.A.; Marosi, C.; Bogdahn, U.; et al. Radiotherapy plus concomitant and adjuvant temozolomide for glioblastoma. *New Engl. J. Med.* **2005**, *352*, 987–996. [CrossRef]
7. Mizushima, N.; Levine, B. Autophagy in mammalian development and differentiation. *Nat. Cell Biol.* **2010**, *12*, 823–830. [CrossRef]
8. Yuanchao, S.; Xunsi, Q.; Hong, C.; Wei, S. Epigenetic control of autophagy. *Yi Chuan Hered.* **2014**, *36*, 447–455.
9. Yan, Y.; Xu, Z.; Dai, S.; Qian, L.; Sun, L.; Gong, Z. Targeting autophagy to sensitive glioma to temozolomide treatment. *J. Exp. Clin. Cancer Res.* **2016**, *35*, 23. [CrossRef]
10. Eskelinen, E.L. The dual role of autophagy in cancer. *Curr. Opin. Pharmacol.* **2011**, *11*, 294–300. [CrossRef]
11. Notte, A.; Leclere, L.; Michiels, C. Autophagy as a mediator of chemotherapy-induced cell death in cancer. *Biochem. Pharmacol.* **2011**, *82*, 427–434. [CrossRef] [PubMed]
12. Mathew, R.; Karantza-Wadsworth, V.; White, E. Role of autophagy in cancer. *Nat. Rev. Cancer* **2007**, *7*, 961–967. [CrossRef] [PubMed]
13. Kroemer, G.; Levine, B. Autophagic cell death: The story of a misnomer. *Nat. Rev. Mol. Cell Biol.* **2008**, *9*, 1004–1010. [CrossRef] [PubMed]
14. Jiang, H.; White, E.J.; Conrad, C.; Gomez-Manzano, C.; Fueyo, J. Autophagy pathways in glioblastoma. *Methods Enzymol.* **2009**, *453*, 273–286. [CrossRef] [PubMed]
15. Golden, E.B.; Cho, H.Y.; Jahanian, A.; Hofman, F.M.; Louie, S.G.; Schonthal, A.H.; Chen, T.C. Chloroquine enhances temozolomide cytotoxicity in malignant gliomas by blocking autophagy. *Neurosurg. Focus* **2014**, *37*, E12. [CrossRef] [PubMed]
16. Hong, C.; Moorefield, K.S.; Jun, P.; Aldape, K.D.; Kharbanda, S.; Phillips, H.S.; Costello, J.F. Epigenome scans and cancer genome sequencing converge on WNK2, a kinase-independent suppressor of cell growth. *Proc. Natl. Acad. Sci. USA* **2007**, *104*, 10974–10979. [CrossRef]
17. Jun, P.; Hong, C.; Lal, A.; Wong, J.M.; McDermott, M.W.; Bollen, A.W.; Plass, C.; Held, W.A.; Smiraglia, D.J.; Costello, J.F. Epigenetic silencing of the kinase tumor suppressor WNK2 is tumor-type and tumor-grade specific. *Neuro-Oncology* **2009**, *11*, 414–422. [CrossRef]
18. Moniz, S.; Martinho, O.; Pinto, F.; Sousa, B.; Loureiro, C.; Oliveira, M.J.; Moita, L.F.; Honavar, M.; Pinheiro, C.; Pires, M.; et al. Loss of WNK2 expression by promoter gene methylation occurs in adult gliomas and triggers Rac1-mediated tumour cell invasiveness. *Hum. Mol. Genet.* **2013**, *22*, 84–95. [CrossRef]
19. Moniz, S.; Verissimo, F.; Matos, P.; Brazao, R.; Silva, E.; Kotelevets, L.; Chastre, E.; Gerspach, C.; Jordan, P. Protein kinase WNK2 inhibits cell proliferation by negatively modulating the activation of MEK1/ERK1/2. *Oncogene* **2007**, *26*, 6071–6081. [CrossRef]
20. Moniz, S.; Matos, P.; Jordan, P. WNK2 modulates MEK1 activity through the Rho GTPase pathway. *Cell. Signal.* **2008**, *20*, 1762–1768. [CrossRef]

21. Costa, A.M.; Pinto, F.; Martinho, O.; Oliveira, M.J.; Jordan, P.; Reis, R.M. Silencing of the tumor suppressor gene WNK2 is associated with upregulation of MMP2 and JNK in gliomas. *Oncotarget* **2015**, *6*, 1422–1434. [CrossRef] [PubMed]
22. Guo, S.; Liang, Y.; Murphy, S.F.; Huang, A.; Shen, H.; Kelly, D.F.; Sobrado, P.; Sheng, Z. A rapid and high content assay that measures cyto-ID-stained autophagic compartments and estimates autophagy flux with potential clinical applications. *Autophagy* **2015**, *11*, 560–572. [CrossRef] [PubMed]
23. Szyniarowski, P.; Corcelle-Termeau, E.; Farkas, T.; Hoyer-Hansen, M.; Nylandsted, J.; Kallunki, T.; Jaattela, M. A comprehensive siRNA screen for kinases that suppress macroautophagy in optimal growth conditions. *Autophagy* **2011**, *7*, 892–903. [CrossRef] [PubMed]
24. Silva-Oliveira, R.J.; Silva, V.A.; Martinho, O.; Cruvinel-Carlioni, A.; Melendez, M.E.; Rosa, M.N.; de Paula, F.E.; de Souza Viana, L.; Carvalho, A.L.; Reis, R.M. Cytotoxicity of allitinib, an irreversible anti-EGFR agent, in a large panel of human cancer-derived cell lines: KRAS mutation status as a predictive biomarker. *Cell. Oncol.* **2016**, *39*, 253–263. [CrossRef] [PubMed]
25. Teixeira, T.L.; Oliveira Silva, V.A.; da Cunha, D.B.; Poletini, F.L.; Thomaz, C.D.; Pianca, A.A.; Zambom, F.L.; da Silva Leitao Mazzi, D.P.; Reis, R.M.; Mazzi, M.V. Isolation, characterization and screening of the in vitro cytotoxic activity of a novel L-amino acid oxidase (LAAOcdt) from *Crotalus durissus terrificus* venom on human cancer cell lines. *Toxicon* **2016**, *119*, 203–217. [CrossRef] [PubMed]
26. Klionsky, D.J.; Abdelmohsen, K.; Abe, A.; Abedin, M.J.; Abeliovich, H.; Acevedo Arozena, A.; Adachi, H.; Adams, C.M.; Adams, P.D.; Adeli, K.; et al. Guidelines for the use and interpretation of assays for monitoring autophagy (3rd edition). *Autophagy* **2016**, *12*, 1–222. [CrossRef]
27. Bravo-San Pedro, J.M.; Niso-Santano, M.; Gomez-Sanchez, R.; Pizarro-Estrella, E.; Aiastui-Pujana, A.; Gorostidi, A.; Climent, V.; Lopez de Maturana, R.; Sanchez-Pernaute, R.; Lopez de Munain, A.; et al. The LRRK2 G2019S mutant exacerbates basal autophagy through activation of the MEK/ERK pathway. *Cell. Mol. Life Sci.* **2013**, *70*, 121–136. [CrossRef]
28. Mizushima, N.; Yoshimori, T.; Levine, B. Methods in mammalian autophagy research. *Cell* **2010**, *140*, 313–326. [CrossRef]
29. He, C.; Klionsky, D.J. Regulation mechanisms and signaling pathways of autophagy. *Annu. Rev. Genet.* **2009**, *43*, 67–93. [CrossRef]
30. Pankiv, S.; Clausen, T.H.; Lamark, T.; Brech, A.; Bruun, J.A.; Outzen, H.; Overvatn, A.; Bjorkoy, G.; Johansen, T. p62/SQSTM1 binds directly to Atg8/LC3 to facilitate degradation of ubiquitinated protein aggregates by autophagy. *J. Biol. Chem.* **2007**, *282*, 24131–24145. [CrossRef]
31. Yoshii, S.R.; Mizushima, N. Monitoring and Measuring Autophagy. *Int. J. Mol. Sci.* **2017**, *18*. [CrossRef] [PubMed]
32. Furnari, F.B.; Fenton, T.; Bachoo, R.M.; Mukasa, A.; Stommel, J.M.; Stegh, A.; Hahn, W.C.; Ligon, K.L.; Louis, D.N.; Brennan, C.; et al. Malignant astrocytic glioma: Genetics, biology, and paths to treatment. *Genes Dev.* **2007**, *21*, 2683–2710. [CrossRef] [PubMed]
33. Saxton, R.A.; Sabatini, D.M. mTOR Signaling in Growth, Metabolism, and Disease. *Cell* **2017**, *168*, 960–976. [CrossRef] [PubMed]
34. Ito, H.; Daido, S.; Kanzawa, T.; Kondo, S.; Kondo, Y. Radiation-induced autophagy is associated with LC3 and its inhibition sensitizes malignant glioma cells. *Int. J. Oncol.* **2005**, *26*, 1401–1410. [CrossRef]
35. Iwamaru, A.; Kondo, Y.; Iwado, E.; Aoki, H.; Fujiwara, K.; Yokoyama, T.; Mills, G.B.; Kondo, S. Silencing mammalian target of rapamycin signaling by small interfering RNA enhances rapamycin-induced autophagy in malignant glioma cells. *Oncogene* **2007**, *26*, 1840–1851. [CrossRef]
36. Murugan, A.K. mTOR: Role in cancer, metastasis and drug resistance. *Semin. Cancer Biol.* **2019**. [CrossRef]
37. Sui, X.; Chen, R.; Wang, Z.; Huang, Z.; Kong, N.; Zhang, M.; Han, W.; Lou, F.; Yang, J.; Zhang, Q.; et al. Autophagy and chemotherapy resistance: A promising therapeutic target for cancer treatment. *Cell Death Dis.* **2013**, *4*, e838. [CrossRef]
38. Li, S.; Jiang, T.; Li, G.; Wang, Z. Impact of p53 status to response of temozolomide in low MGMT expression glioblastomas: Preliminary results. *Neurol. Res.* **2008**, *30*, 567–570. [CrossRef]
39. Carmo, A.; Carvalheiro, H.; Crespo, I.; Nunes, I.; Lopes, M.C. Effect of temozolomide on the U-118 glioma cell line. *Oncol. Lett.* **2011**, *2*, 1165–1170. [CrossRef]
40. Kanzawa, T.; Germano, I.M.; Komata, T.; Ito, H.; Kondo, Y.; Kondo, S. Role of autophagy in temozolomide-induced cytotoxicity for malignant glioma cells. *Cell Death Differ.* **2004**, *11*, 448–457. [CrossRef]










41. Filippi-Chiela, E.C.; Bueno e Silva, M.M.; Thome, M.P.; Lenz, G. Single-cell analysis challenges the connection between autophagy and senescence induced by DNA damage. *Autophagy* **2015**, *11*, 1099–1113. [CrossRef] [PubMed]
42. Rosenfeld, M.R.; Ye, X.; Supko, J.G.; Desideri, S.; Grossman, S.A.; Brem, S.; Mikkelsen, T.; Wang, D.; Chang, Y.C.; Hu, J.; et al. A phase I/II trial of hydroxychloroquine in conjunction with radiation therapy and concurrent and adjuvant temozolomide in patients with newly diagnosed glioblastoma multiforme. *Autophagy* **2014**, *10*, 1359–1368. [CrossRef] [PubMed]



© 2020 by the authors. Licensee MDPI, Basel, Switzerland. This article is an open access article distributed under the terms and conditions of the Creative Commons Attribution (CC BY) license (<http://creativecommons.org/licenses/by/4.0/>).

Article

# Loss of 5'-Methylthioadenosine Phosphorylase (MTAP) is Frequent in High-Grade Gliomas; Nevertheless, it is Not Associated with Higher Tumor Aggressiveness

Weder Pereira de Menezes <sup>1</sup>, Viviane Aline Oliveira Silva <sup>1</sup> , Izabela Natália Faria Gomes <sup>1</sup> ,  
Marcela Nunes Rosa <sup>1</sup> , Maria Luisa Corcoll Spina <sup>1</sup> , Adriana Cruvinel Carloni <sup>1</sup>,  
Ana Laura Vieira Alves <sup>1</sup> , Matias Melendez <sup>1</sup>, Gisele Caravina Almeida <sup>2</sup>,  
Luciane Sussuchi da Silva <sup>1</sup> , Carlos Clara <sup>3</sup>, Isabela Werneck da Cunha <sup>4</sup>,  
Gláucia Noeli Maroso Hajj <sup>4</sup> , Chris Jones <sup>5</sup>, Lucas Tadeu Bidinotto <sup>1,6,7</sup>  and  
Rui Manuel Reis <sup>1,8,9,\*</sup> 

- <sup>1</sup> Molecular Oncology Research Center, Barretos Cancer Hospital, Barretos, São Paulo 14.784-400, Brazil; wedermenezes1@gmail.com (W.P.d.M.); vivianeaos@gmail.com (V.A.O.S.); izabela.faria.tk@hotmail.com (I.N.F.G.); nr.marcela2@gmail.com (M.N.R.); mluisaspina@hotmail.com (M.L.C.S.); drybiomedic@gmail.com (A.C.C.); alves.anav@gmail.com (A.L.V.A.); matiasmelendez@gmail.com (M.M.); lsussuchi@gmail.com (L.S.d.S.); lucasbidinotto@gmail.com (L.T.B.)
- <sup>2</sup> Department of Pathology, Barretos Cancer Hospital, Barretos, São Paulo 14.784-400, Brazil; giselecaravina@gmail.com
- <sup>3</sup> Department of Neurosurgery, Barretos Cancer Hospital, Barretos, São Paulo 14.784-400, Brazil; carlosclara.neuro@gmail.com
- <sup>4</sup> A.C Camargo Cancer Center, São Paulo, São Paulo 015.080-10, Brazil; isabela.werneck@rededor.com.br (I.W.d.C.); ghajj@cipe.accamargo.org.br (G.N.M.H.)
- <sup>5</sup> Institute of Cancer Research, London SW7 3RP, UK; chris.jones@icr.ac.uk
- <sup>6</sup> Barretos School of Health Sciences, Dr. Paulo Prata - FACISB, Barretos, São Paulo 14.785-002, Brazil
- <sup>7</sup> Department of Pathology, Botucatu Medical School, Universidade Estadual Paulista – Unesp, Botucatu, São Paulo 18.618-970, Brazil
- <sup>8</sup> Life and Health Sciences Research Institute (ICVS), School of Medicine, University of Minho, 4710-057 Braga, Portugal
- <sup>9</sup> 3B's - PT Government Associate Laboratory, 4806-909 Braga/Guimarães, Portugal
- \* Correspondence: ruireis.hcb@gmail.com; Tel.: +55-173-3216-600

Received: 27 December 2019; Accepted: 10 February 2020; Published: 20 February 2020



**Abstract:** The 5'-methylthioadenosine phosphorylase (MTAP) gene is located in the chromosomal region 9p21. *MTAP* deletion is a frequent event in a wide variety of human cancers; however, its biological role in tumorigenesis remains unclear. The purpose of this study was to characterize the *MTAP* expression profile in a series of gliomas and to associate it with patients' clinicopathological features. Moreover, we sought to evaluate, through glioma gene-edited cell lines, the biological impact of *MTAP* in gliomas. *MTAP* expression was evaluated in 507 glioma patients by immunohistochemistry (IHC), and the expression levels were associated with patients' clinicopathological features. Furthermore, an *in silico* study was undertaken using genomic databases totalizing 350 samples. In glioma cell lines, *MTAP* was edited, and following *MTAP* overexpression and knockout (KO), a transcriptome analysis was performed by NanoString Pan-Cancer Pathways panel. Moreover, *MTAP*'s role in glioma cell proliferation, migration, and invasion was evaluated. Homozygous deletion of 9p21 locus was associated with a reduction of *MTAP* mRNA expression in the TCGA (The Cancer Genome Atlas) - glioblastoma dataset ( $p < 0.01$ ). In addition, the loss of *MTAP* expression was markedly high in high-grade gliomas (46.6% of cases) determined by IHC and Western blotting (40% of evaluated cell lines). Reduced *MTAP* expression was associated with a better prognostic in the



adult glioblastoma dataset ( $p < 0.001$ ). Nine genes associated with five pathways were differentially expressed in MTAP-knockout (KO) cells, with six upregulated and three downregulated in MTAP. Analysis of cell proliferation, migration, and invasion did not show any significant differences between MTAP gene-edited and control cells. Our results integrating data from patients as well as in silico and in vitro models provide evidence towards the lack of strong biological importance of MTAP in gliomas. Despite the frequent loss of MTAP, it seems not to have a clinical impact in survival and does not act as a canonic tumor suppressor gene in gliomas.

**Keywords:** glioma; glioblastoma; 5'-methylthioadenosine phosphorylase (MTAP); immunohistochemistry; tumor biology; proliferation; migration; invasion

## 1. Introduction

Gliomas represent the most common group of primary central nervous system (CNS) tumors [1]. According to the World Health Organization (WHO), these tumors can be categorized in low-grade gliomas (LGG, WHO grades I and II) and high-grade gliomas (HGG, WHO grades III and IV) according to their histological and molecular features [2,3]. Pilocytic astrocytoma (PA) (WHO grade I) is a good-prognosis childhood tumor, and conversely, glioblastoma (GBM) (WHO grade IV) occurs mainly in adults and has the poorest prognosis [2,4]. GBM has a mean survival of ~14 months after gold-standard therapy—surgery—followed by radiation therapy plus concomitant temozolomide [5–7]. GBM accounts for 70% of gliomas and can be subdivided in GBM *IDH*-wild type (the most frequent, >90%), previously known as primary (de novo) GBM and exhibiting a short clinical history, and GBM *IDH*-mutant, also called secondary GBM, which results from the malignant progression from lower-grade gliomas of diffuse (WHO grade II) or anaplastic (WHO grade III) astrocytomas [6,8] and is related to point mutations in *IDH1/2* genes.

In fact, several efforts have been made to improve the molecular characterization of GBM. In 2014, the International Society of Neuropathology recommended the support of molecular analysis for determining brain tumor entities [9] and, in 2016, the World Health Organization proposed the use of molecular features, including *IDH* mutation to GBM, in addition to histologic features in the tumor entities [3]. Additionally, there are many other biomarkers studied in GBMs as subjects of special attention. *TERT* promoter mutations have been found to be markedly high in primary GBMs (from 54% to 83% of the cases) [10]. Further studies have shown poorer survival of *TERT*-mutated patients in comparison to *TERT*-wild type [11–13]. Finally, studies have found an interaction between *TERT* promoter mutation and *MGMT* methylation. By performing pairwise comparisons, it was identified that *MGMT* methylation improved the survival of *TERT* promoter mutated-patients [14]. On the other hand, *TERT*-mutant and *MGMT* unmethylated patients presented the poorest prognosis, pointing to a possible impact in the use of *IDH*, *TERT*, and *MGMT* in the improvement of diffuse gliomas classification and prognostication [15].

We previously described the most frequent chromosomal alterations in a series of Brazilian astrocytomas [11]. We identified chromosome 7 gain, *EGFR* amplification, and losses in chromosomes 9p, 10, and 13, in accordance with other populations [4,11,16]. We also found 9p- deletion in approximately 50% of GBMs, affecting primarily the 9p21 locus where several tumor suppressor genes are located, including *CDKN2A/B* and *MTAP* [11].

*MTAP* (5'-methylthioadenosine phosphorylase) encodes a key enzyme involved in the metabolism of polyamines and purines [17–19]. This enzyme converts 5'-methylthioadenosine (MTA), a by-product of polyamine biosynthesis, into adenine and MTR-1-P (methylthioribose-1-phosphate), which are recycled into AMP (adenosine monophosphate) and methionine [19,20]. This protein is expressed virtually in all tissues throughout the body, and its homozygous deletion is frequently associated with solid and hematologic tumors such as mesothelioma, lung carcinoma, hepatocellular carcinoma, gastrointestinal

stromal tumors, metastatic melanoma, leukemias, and lymphoma [18,21–25]. Therefore, *MTAP* has been reported as a tumor suppressor gene [24,26–30]; however, many studies have demonstrated the contradictory function of *MTAP*. For instance, the loss of *MTAP* expression has been associated with inhibition of growth and progression of head and neck carcinoma and lung cancer by MTA accumulation [31,32]. Bistulfi et al. [33] showed that knockdown of *MTAP* blocks prostate cancer growth in vitro and *in vivo*. In addition, methionine deprivation acts by inhibiting cell migration, invasion, and metastasis in breast cancer [34]. Metabolic changes in tumors, especially those relating to polyamines metabolism, demonstrate that many mechanisms underlying *MTAP* function need to still be clarified [35,36]. In gliomas, loss of *MTAP* locus is also frequently reported [37–41]. Nevertheless, the clinical and the biological impacts of *MTAP* are poorly explored in gliomas [37,38,42].

Therefore, the aim of this study was to characterize the *MTAP* protein expression profile in a large series of glioma and to associate it with the patients' clinicopathological features. Moreover, by using glioma cell lines, the biological role of *MTAP* was evaluated. By integrating data from patients and in vitro models, this study showed that, despite the frequent loss of *MTAP*, it does not have a clinical impact in survival and does not act as a canonic tumor suppressor gene in gliomas.

## 2. Materials and Methods

### 2.1. Cell Lines and Gene Editing

One cell line derived from normal astrocytes (NHA), seven short-term primary glioma cell lines, and 11 established glioma cell lines were evaluated. The *MTAP* positive U251 cell line was transfected with *MTAP* Clustered Regularly Interspaced Short Palindromic Repeats (CRISPR)/CRISPR-associated protein 9 (Cas9) (*MTAP*-CRISPR/Cas9 KO) or empty vector CRISPR/Cas9 Plasmid (Santa Cruz Biotechnology, Santa Cruz, CA, USA), leading to a U251 *MTAP*<sup>-/-</sup> clone. The *MTAP* negative SW1088 cell line was transduced with the *MTAP* human lentivirus or the blank control lentiviral vector in accordance with the manufacturer's instructions (ABM Inc.<sup>®</sup>, Richmond, BC, Canada), resulting in SW1088 *MTAP*<sup>+/+</sup> clones. Detailed information about the cell lines used and the gene editing are described in the Appendix A material.

### 2.2. Patients

Adult and pediatric glioma tissues were obtained from 507 patients who underwent surgery for glioma at Barretos Cancer Hospital (BCH), Hospital of Clinics of Faculty of Medicine of São Paulo University (HCRP), AC Camargo Cancer Center, and The Institute of Cancer Research between 1980 and 2013. Histologic review of the slides was performed by expert neuropathologists (according to the latest WHO histopathological criteria) [3] to confirm the diagnosis. Overall, patient age ranged from 0.3 to 82.8 years (median: 57 years old). The stratification showed 49 (9.7%) patients in pediatric (0–19 years) and 458 (90.3%) in the adult group (>19 years). Histological subtypes of gliomas were distributed into diffuse astrocytoma (n = 18), anaplastic astrocytoma (n = 24), pediatric glioblastoma (n = 42), and adult glioblastoma (n = 423). This study was approved by the Ethics Committee of Barretos Cancer Hospital under approval number 630/2012, number 1175879 (961/2015), and AC Camargo Cancer Center (number 1485/10).

### 2.3. DNA Isolation

Tissue from a patient's tumor was manually microdissected from 4 µm unstained histological sections. DNA was isolated from each target using the DNeasy Blood and Tissue kit (Qiagen, Valencia, CA, USA) according to the protocols provided by the supplier. The 260/280 and the 260/230 ratios were determined by a NanoDrop 2000C spectrophotometer (Thermo Scientific, Wilmington, DE, USA), and the DNA was quantified using Quant-iT PicoGreen dsDNA (Invitrogen, Eugene, OR, USA) according to the supplier's protocol.

#### 2.4. RNA Extraction and RT-qPCR

RNA from cultured cell lines was isolated using a modified TRIzol<sup>®</sup> reagent protocol (Thermo Scientific, Waltham, MA, USA) [43]. In brief, cultured cells were washed twice with Dulbecco's phosphate-buffered saline (DPBS; Thermo Scientific, Waltham, MA, USA), and 1.5 mL TRIzol<sup>®</sup> was added. Flasks were scraped, and TRIzol/cell mixture was transferred to a 1.5 mL eppendorf tube. Subsequently, 200  $\mu$ L of chloroform was added, homogenized for 30 s, and centrifuged at 17,982 $\times$  g for 15 min. The supernatant was collected, and 750  $\mu$ L isopropanol was added and kept overnight at  $-20$  °C. Samples were then centrifuged at 17,982 $\times$  g for 10 min at 4 °C. The resulting RNA pellet was washed twice with 75% ethanol after removing the supernatant. Finally, the RNA pellet was dried and dissolved in 20  $\mu$ L of ultra-pure water. The integrity of all the RNA preparations was checked by RNA 600 nano assay (Agilent Technologies, Santa Clara, CA, USA), and RNA concentrations were measured with NanoDrop<sup>™</sup> 2000C spectrophotometer (Thermo Scientific, Waltham, MA, USA). Complementary DNA (cDNA) was synthesized using Superscript III reverse transcriptase (Thermo Scientific, Waltham, MA, USA) according to the supplier protocol.

RT-qPCR reactions were carried out in a total volume of 10  $\mu$ L using 2X Fast SYBR<sup>®</sup>Green Master Mix kit (Thermo Scientific, Waltham, MA, USA) containing 100 ng (1  $\mu$ L) of cDNA, 10  $\mu$ M (0.8  $\mu$ L) of each primer, and 7.4  $\mu$ L of ultra-pure water in a final volume of 20  $\mu$ L. Gene amplification was performed with the programmable cyclic reactor StepOne<sup>™</sup> Real-Time PCR System (Applied Biosystems, Grand Island, USA) as follows: 95 °C for 10 min; 40 cycles at 95 °C for 15 s; and 64 °C for 1 min. The primers used for RT-qPCR amplification of *MTAP* were forward primer: 5'-TCTTGTGCCAGAGGAGTGTG-3'; reverse primer: 5'-ACCATTGTCCCCTTTGAGTG-3'. Samples were then normalized using the housekeeping gene *HPRT1* (forward primer: 5'-GACCAGTCAACAGGGGACAT-3'; reverse primer: 5'-CTGCATTGTTTTGCCAGTGT-3'). The normalized expressions of the gene of interest were calculated using the  $2^{-\Delta C_t}$  method. The primers used were synthesized by Sigma-Aldrich, St. Louis, MO, USA, and all reactions were performed in three biological replicates.

#### 2.5. IDH1 Mutation Analysis

The analysis of hotspot mutations of isocitrate dehydrogenase 1 (IDH1-exon 4) was performed by PCR followed by direct sequencing. Briefly, the IDH1 region of interest was amplified by PCR using the following primers: 59-CGGTCTTCAGAGAAGCCATT-39 (forward) and 59-CACATTATTGCCAACATGAC-39 (reverse) [11]. An amplification PCR reaction was performed in a total volume of 15  $\mu$ L comprising: 1  $\mu$ L of DNA, 1X buffer solution, 2 mM MgCl<sub>2</sub>, 200  $\mu$ M of each dNTP, 0.3  $\mu$ M of each primer set, and 0.5 U of *Taq* DNA polymerase (Invitrogen, Eugene, OR, USA), and was performed in a Veriti 96-well Thermal Cycler with an initial denaturation at 95 °C for 10 min, amplification for 40 cycles with denaturation at 95 °C for 45 s, annealing at 58 °C for 45 s, extension at 72 °C for 45 s, and a final extension at 72 °C for 10 min. Amplification of PCR products was confirmed by gel electrophoresis. PCR sequencing was performed using the Big Dye terminator v3.1 cycle sequencing ready reaction kit (Applied Biosystems, Grand Island, NY, USA) and an ABI PRISM 3500 xL Genetic Analyzer (Applied Biosystems, Grand Island, NY, USA).

#### 2.6. TERT Mutation Analysis

The analysis of hotspot mutations in the promoter region of the telomerase reverse transcriptase gene (*TERT*) was performed by PCR followed by direct Sanger sequencing [44]. Briefly, the *TERT* promoter region was amplified by PCR using the following primers: 59-AGTGGATTTCGCGGGCACAGA-39 (forward) and 59-CAGCGCTGCCTGAAACTC-39 (reverse), leading to a 235 bp PCR product containing C228T and C250T mutations. Amplification by PCR was performed with an initial denaturation at 95 °C for 15 min, followed by 40 cycles of denaturation at 95 °C for 30 s, annealing at 64 °C for 90 s, elongation at 72 °C for 30 s, and final elongation at 72 °C for 7 min. Amplification of PCR products was confirmed by gel electrophoresis. PCR sequencing was

performed using the Big Dye terminator v3.1 cycle sequencing ready reaction kit (Applied Biosystems, Grand Island, NY, USA) and an ABI PRISM 3500 xL Genetic Analyzer (Applied Biosystems, Grand Island, NY, USA).

### 2.7. MGMT Promoter Methylation

To evaluate the methylation status of the promoter region of the O<sup>6</sup>-methylguanine-DNA methyltransferase gene (*MGMT*), sodium bisulfite treatment of DNA (300–1500 ng) was performed using the Epiect Kit (Qiagen, Valencia, CA, USA) according to the manufacturer's instructions. Methylation-specific (MS) PCR for the *MGMT* promoter was performed as described previously [45].

### 2.8. Western Blotting Analysis

The Western blot analysis was performed as previously described [42]. In brief, cells were lysed with lysis buffer (50 mM Tris; pH 7.6; 150 mM NaCl; 5 mM EDTA; 1 mM Na<sub>3</sub>VO<sub>4</sub>; 10 mM NaF; 10 mM sodium pyrophosphate; 1% NP-40) containing protease inhibitor cocktail (0.01 M EDTA; 1 mM DTT; 1 mM Leupeptin; 1 mM PMSF; and 1 μM Aprotinin). The cell lysate was placed on ice for 60 min and centrifuged at 17,982× *g* for 15 min. The total protein was quantified using the Bradford method (Quick Start™ Bradford Protein Assay; Bio-Rad, Hercules, CA, USA). Total proteins were separated by 12% polyacrylamide gel and transferred onto Trans-Blot Turbo Midi Nitrocellulose Transfer Packs (Bio-Rad, Hercules, CA, USA). The membrane was incubated with primary followed by secondary antibodies after blocking with 5% non-fat milk. Immunodetection was performed using the ECL KIT (Amersham Biosciences, Uppsala, Uppland, Sweden) in ImageQuant LAS 4000 mini (GE Healthcare Life Sciences, Pittsburgh, PA, USA) and quantified by the platform for scientific image analysis ImageJ (NIH) [46]. The following antibodies were used: polyclonal anti-MTAP antibody (Proteintech, Rosemont, IL, USA) diluted 1:800 and anti-β actin antibody (Cell Signaling Technology, Danvers, MA, USA) diluted at 1:2000.

### 2.9. Immunohistochemistry Analysis

For the immunohistochemistry (IHC) analysis, a tissue microarray (TMA) was constructed with tumors areas obtained from each case and inserted in the recipient paraffin block using the tissue arrayer MTA-1 platform (Beecher Instruments™, Silver Springs, MD, USA). To represent possible heterogeneity of tumors, two 1.0 mm cores from each case were used in TMA blocks. IHC was performed from 4.0 μm sections of the TMA block for MTAP, as previously described [42]. Glass slides were deparaffinized and subjected to antigen retrieval in a Pascal pressure chamber (Dako, Carpinteria, CA, USA). The primary MTAP polyclonal antibody (Proteintech, Rosemont, IL, USA) was diluted 1:300 with the background-reducing medium and kept at 4 °C overnight. The Avidin–Biotin Complex (ABC) method was performed according to the manufacturer's recommendations with staining with DAB (3,3' Diaminobenzidine) and counterstaining with Harris' hematoxylin (Leica Biosystems, Newcastle, UK). The extension of immunoreactions was measured according to the following criteria: 0 = negative; 1 = ≤25% of positive cells; 2 = 25–50% of positive cells; 3 = ≥50% of positive cells. Moreover, the intensity of reaction was defined as: 0 = negative; 1 = weak; 2 = moderate; 3 = strong. Cases presenting the sum of the scores (extension and intensity) between 0 and 3 were considered negative, and those presenting scores between 4 and 6 were considered positive. Non-neoplastic tissue microarray (BN 961-Biomax INC, Rockville, MD, USA) was used as a positive control for IHC reactions.

### 2.10. In Silico Analysis

*MTAP* copy number alterations (CNA) data were downloaded from comparative genomic hybridization/single-nucleotide polymorphism (CGH\_SNP) arrays (n = 350) [47]. Based on normalized *MTAP* values, patients were stratified in normal (n = 150) (>−0.1) and *MTAP* homozygous deletion carriers (n = 200) (≤−1.5). For expression analysis, *MTAP* mRNA G450 array data were downloaded (n = 299) [47]. The median *MTAP* value was calculated considering all samples. Patients with *MTAP*

values at least 20% higher than the median were considered positive ( $n = 138$ ), while those with *MTAP* values at least 20% lower than the median were considered negative ( $n = 161$ ). Finally, for methylation analysis, *MTAP* methylation beta values were downloaded from 283 samples [47]. Patients were stratified as hypermethylated ( $\text{beta} > 0.5$ ) and hypomethylated ( $\text{beta} \leq 0.5$ ). Integrated in silico analyses of *MTAP* CNA expression and methylation status were performed using the TCGA2STAT package implemented in R software downloaded from <https://www.r-project.org/>. Moreover, in silico analysis was conducted to evaluate *MTAP* expression in glioblastoma subtypes in The Cancer Genome Atlas (TCGA) dataset. The median *MTAP* value was calculated considering all samples.

### 2.11. mRNA NanoString™ Data Analysis

Gene expression analysis on *MTAP* gene-edited U251 and SW1088 cell lines was performed using the NanoString nCounter PanCancer Pathways panel (730 gene transcripts distributed in 13 biological pathways) according to the manufacturer's standards (NanoString Technologies, Seattle, WA, USA). Moreover, 24 of 730 genes associated with tumor aggressiveness were selected, and the differential expression was evaluated to better understand the function of *MTAP* gene-edited on migration and invasion ability. Briefly, 100 ng aliquots of RNA were hybridized with probe pools, hybridization buffer, and TagSet reagents in a total volume of 30  $\mu\text{L}$  and incubated at 65 °C for 20 h. After codeset hybridization overnight, the samples were washed and immobilized to a cartridge using the Nanostring nCounter Prep Station (NanoString Technologies, Seattle, WA, USA) for 4 h. Finally, the cartridges containing immobilized and aligned reporter complexes were scanned in the nCounter Digital Analyzer (NanoString Technologies, Seattle, WA, USA), and image data were subsequently generated using the high-resolution setting, which takes 577 images per sample. Quality control assessment of raw NanoString gene expression counts was performed with nSolver Analysis Software version 2.5 and the default settings (NanoString Technologies, Seattle, WA, USA). Normalization with internal positive controls and housekeeping genes was performed in R statistical environment using NanostringNorm package [48]. Normalized  $\log_2$  mRNA expression values were used for subsequent data analysis. Genes with fold change (FC)  $\pm 2$  and  $p < 0.05$  were considered significant.

### 2.12. xCELLigence Proliferation Assay

U251 *MTAP*<sup>-/-</sup> and SW1088 *MTAP*<sup>+/+</sup> cell proliferation was monitored with a real-time cell analyzer using xCELLigence Technology (Roche Applied Science, Indianapolis, IN, USA). This impedance value was measured by the Real Time Cell Analysis Dual purpose (RTCA DP) system and is reported in the dimensionless unit of cell index. Prior to seeding of cells in the 96-well E-plate, 100  $\mu\text{L}$  Dulbecco's modified Eagle's medium (DMEM) was added to wells, and background was recorded. U251 *MTAP*<sup>-/-</sup>; U251 EV; U251 WT and SW1088 *MTAP*<sup>+/+</sup>; SW1088 LB; SW1088 WT were split, and 5–10  $\times 10^3$  cells in 100  $\mu\text{L}$  of media supplemented with fetal bovine serum (FBS; 10%) were added to each well. Real-time monitoring of cell proliferation measured as cell index was recorded every 5 min for up to 72 h. Data represent changes in cell index over time.

### 2.13. Transwell Migration Assay

Boyden chamber type Transwell permeable supports (Corning, Chelmsford St. Lowell, MA, USA) were used to examine the ability of cells to invade the 8  $\mu\text{m}$  pore size membrane ( $1 \times 10^5$  pores/cm<sup>2</sup>) and migrate through the polyethylene terephthalate (PET)-membrane surface. The CRISPR-edited cell line (U251 *MTAP*<sup>-/-</sup>) and the stable expression cell line (SW1088 *MTAP*<sup>+/+</sup>) beside the control cell lines were seeded into the inner chamber at  $5 \times 10^4$  and  $10 \times 10^4$ , respectively, in 500  $\mu\text{L}$  of DMEM without serum and allowed to migrate onto the coated undersurface at 37 °C in a CO<sub>2</sub> incubator for 24 h. At the bottom, 750  $\mu\text{L}$  of DMEM supplemented with 10% FBS was added to the chambers. Migrated cells were fixed and stained with hematoxylin and eosin for three minutes followed by phosphate-buffered saline (PBS) washing of the membranes. The migrated cells in each well were

counted in ten different fields per experiment under the microscope. The mean values were obtained from three replicate experiments and were subjected to t-test.

#### 2.14. Cell Invasion Assay

U251 MTAP<sup>-/-</sup> and SW1088 MTAP<sup>+/+</sup> beside control cells were cultured to near confluence in DMEM+10% FBS. Cells were harvested by trypsinization and washed and suspended in DMEM without serum at  $2 \times 10^5$  and  $4 \times 10^5$  cells/mL. Prior to preparing the cell suspension, the dried layer of matrigel matrix was rehydrated with serum-free DMEM for 1 h at 37 °C. The rehydration solution was carefully removed, 750 µL DMEM containing 10% FBS was added to each well as a chemoattractant, and 500 µL ( $1-2 \times 10^5$  cells) of cell suspension was added into the inner chamber Corning, Chelmsford St. Lowell, MA, USA). The plates were incubated for 24 h at 37 °C. The invasive cells on the bottom surface of the membrane were fixed and stained with hematoxylin and eosin for three minutes followed by 1X PBS washing of the membranes. The migrated cells in each well were counted in ten different fields per experiment under the microscope. The mean values were obtained from three replicate experiments and were subjected to t-test.

#### 2.15. Statistical Analysis

The statistical analysis was performed using SPSS version 24 for Windows™ (IBM, Chicago, Ill, USA) considering statistically significant values of  $p < 0.05$ . Levene and Kolmogorov–Smirnov tests were performed to test the variance and the normality of the data. One-way ANOVA or Kruskal–Wallis tests were performed to compare copy number, expression, and methylation of *MTAP* profiles. ANOVA followed by Tukey post hoc test was performed to evaluate *MTAP* expression in glioblastoma subtypes. The association between clinicopathological categorical variables and *MTAP* was analyzed by Pearson’s chi-square test or Fisher exact test. The overall survival (OS) analysis was done by constructing Kaplan–Meier curves, and the log-rank test was applied for the comparison between the obtained curves. OS was defined as the time between the date of diagnosis and the date of the patient’s last information or death. Cell line experiments were analyzed with Student’s t-test and are expressed as mean values of at least three independent experiments  $\pm$  standard errors. Differences were considered significant at \*  $p < 0.05$ , \*\*  $p < 0.01$ , and \*\*\*  $p < 0.001$ .

### 3. Results

#### 3.1. Loss of *MTAP* Expression is Associated with 9p21 Locus Deletion in Gliomas

Initially, in order to understand the molecular mechanism underlying *MTAP* expression, we investigated the impact of copy number alteration (CNA) of 9p21 locus on *MTAP* mRNA expression levels in a TCGA-GBM dataset ( $n = 350$ ). As shown in Figure 1A, *MTAP* gene expression was significantly ( $p < 0.01$ ) lower in the homozygously deleted group ( $n = 169$ ) than in those with normal ploidy ( $n = 181$ ). Since *MTAP* regulation can also occur by epigenetic mechanisms [27], we then evaluated the association of *MTAP* mRNA expression and the methylation status in 283 samples from the TCGA-GBM dataset (Figure 1B). *MTAP* gene promoter was methylated in 60 of 283 (21.2%) samples. However, no association of methylation status and *MTAP* expression levels in glioblastomas was observed (Figure 1B,  $p = 0.633$ ). Additionally, we evaluated the *MTAP* expression levels in the five molecular subtypes of TCGA-GBM ( $n = 291$ ) (Table 1). We found loss of *MTAP* expression greater than 50% in almost all subtypes analyzed, except for the glioma CpG island methylator phenotype (G-CIMP) (Table 1). The classical subtype presented a higher frequency of loss of *MTAP* gene expression with 65.2% (43/66) against only 7.4% (2/25) for the G-CIMP+ subtype ( $p < 0.001$ ) (Table 1).

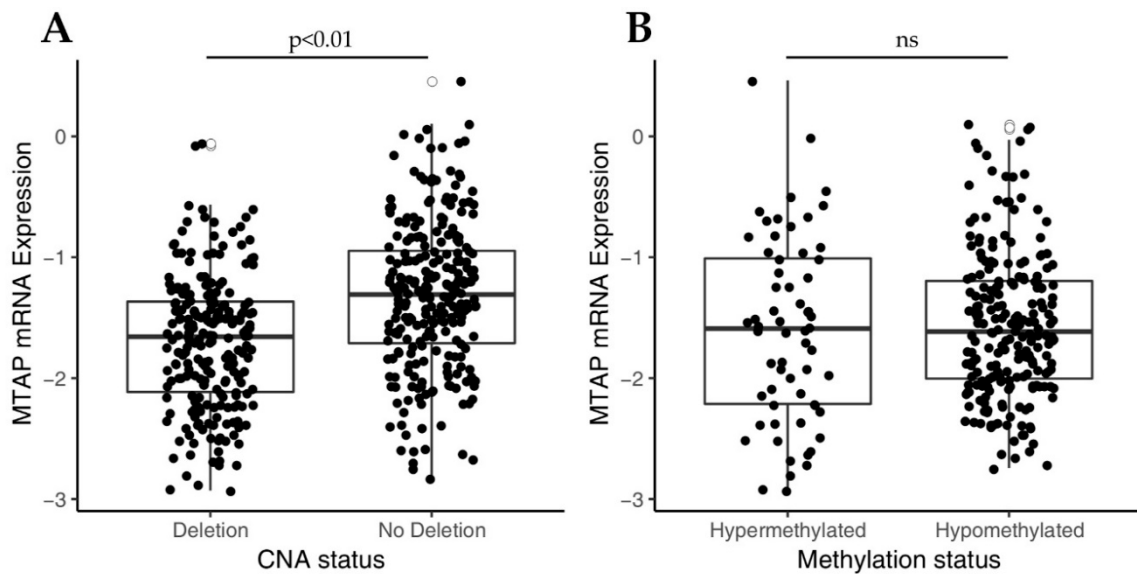


**Figure 1.** Analysis of *MTAP* mRNA expression in The Cancer Genome Atlas glioblastoma (TCGA-GBM) dataset correlates to copy number alterations (CNA) status for 9p21 locus and *MTAP* promoter methylation. (A) Box-plot analysis showing downregulation in *MTAP* expression in 9p21 homozygous deleted samples compared to matched normal samples ( $p$ -value  $< 0.01$ ). (B) Box-plot of *MTAP* expression and promoter methylation in TCGA-GBM dataset. *ns*: not significant  $p$ -value.

**Table 1.** *MTAP* differential expression in subtypes of glioblastoma.

Subtype	<i>MTAP</i> Positive	<i>MTAP</i> Negative	Total	$p$ -Value
Classical	23 (34.8%)	43 (65.2%)	66 (100%)	<math>< 0.001</math>
Mesenchymal	36 (41.9%)	50 (58.1%)	86 (100%)	
Neural	19 (37.3%)	32 (62.7%)	51 (100%)	
Proneural	30 (49.2%)	31 (50.8%)	61 (100%)	
G-CIMP+	25 (92.6%)	2 (7.4%)	27 (100%)	

G-CIMP+: glioma-CpG island methylator phenotype.

Next, in a set of eleven established and seven short-term primary gliomas cells, we compared *MTAP* copy number with *MTAP* mRNA and protein expression by RT-qPCR and Western blot, respectively (Supplementary Table S1). Overall, we found loss of *MTAP* mRNA expression in 33.3% (6/18) of the cell lines evaluated (Figure 2), particularly in 36.3% (4/11) of established cell lines, with 25% (1/4) for pediatric and 42.8% (3/7) for adult glioma cell lines (Figure 2A), and 29% (2/7) of patient-derived glioma cell lines (Figure 2B). A 100% concordance was found between protein and mRNA levels (Figure 2C–F). Of note, 40% (6/15) of high-grade glioma (HGG; WHO grade III–IV) cell lines presented loss of *MTAP* expression, contrasting with 0% in low-grade glioma (LGG; WHO grade I–II) cell lines (0/3) (Figure 2A,B). Considering only the GBM subtype, a lack of *MTAP* mRNA and protein expression was found in 33.3% (4/12) of samples, with 44.4% (4/9) of adult GBM cell lines having no detectable *MTAP* in the cell extracts (Figure 2C,D). These results suggest that *MTAP* loss of expression is associated with higher-grade gliomas.

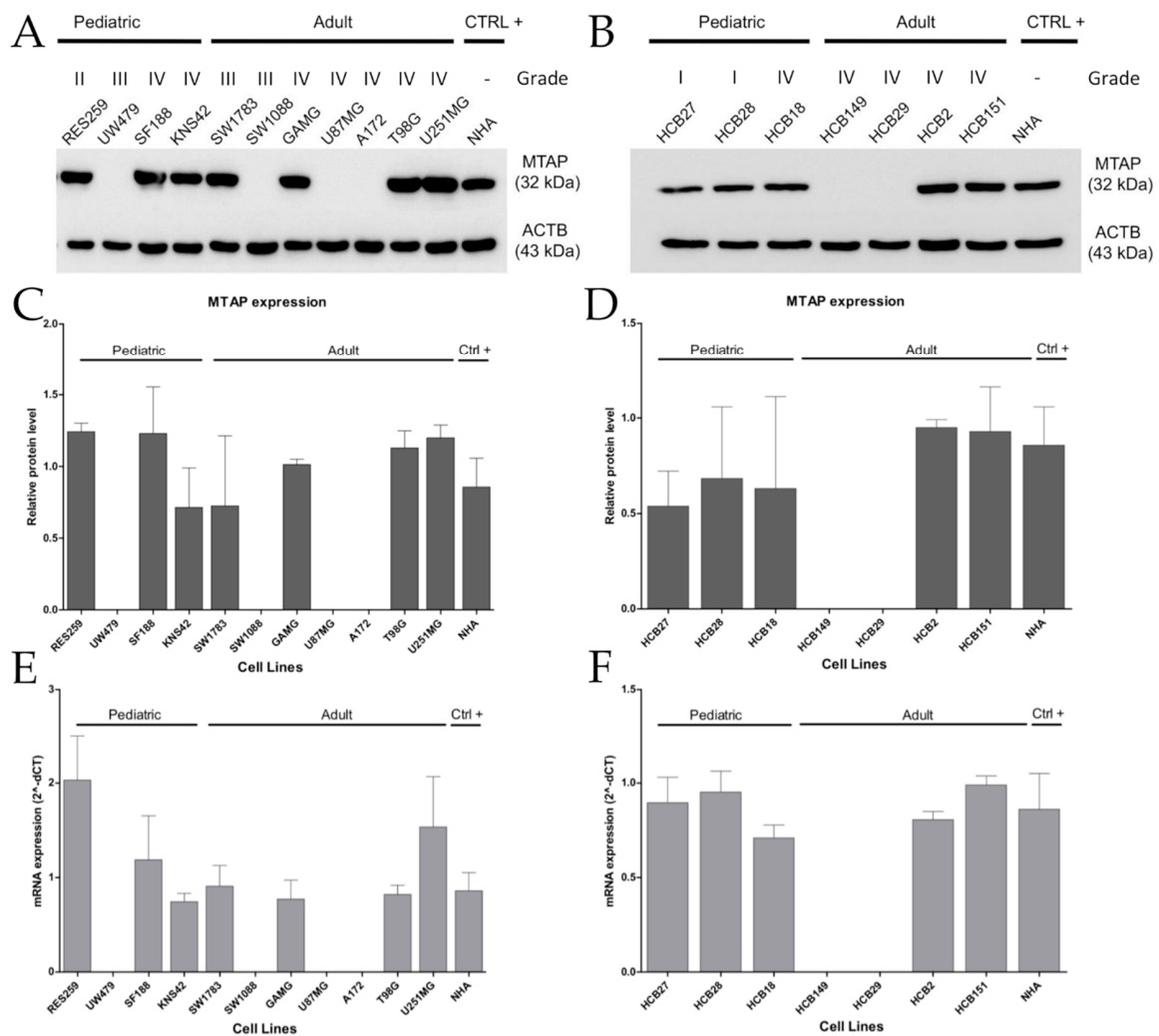


**Figure 2.** Loss of MTAP expression is more present in high-grade glioma (HGG) cell lines. MTAP protein expression analysis of established (A) and short-term primary glioma cells (B) assessed by Western blotting. Plot representative of MTAP protein (C,D) and gene (E,F) expression in glioma cell lines. Samples were normalized to *HPRT-1* (mRNA) and beta-actin (ACTB) (protein) as an endogenous control. Abbreviations: CTRL+: positive control.

### 3.2. MTAP Expression Profile and Clinicopathological Association in Gliomas

We further evaluated MTAP protein expression by immunohistochemistry in a large set of diffuse gliomas (n = 507) (Table 2 and Figure 3). Overall, we found loss of MTAP expression in 45.95% (233/507) of cases, this being observed in 27.8% (5/18) of diffuse astrocytoma, 50.0% (12/24) of anaplastic astrocytoma, 45.6% (193/423) of adult glioblastoma, and 54.8% (23/42) of pediatric glioblastoma (Figure 3A–E). When we stratified the samples by grade, the loss of MTAP expression in the high-grade glioma subgroup was almost two-fold greater (46.6%, 228/489) than in the low-grade glioma subgroup (27.8%; 5/18) (Table 2 and Figure 3E). However, we did not observe a significant association between MTAP expression and other patients' clinicopathological features, such as gender, age, or Karnofsky Performance Status (KPS), except for tumor location (*p* = 0.013) (Table 2).



**Table 2.** Clinicopathological features of glioma patients and association with *MTAP* expression.

	MTAP Expression				<i>p</i> -Value
	Total	(%)	Negative (%)	Positive (%)	
<b>Gender (N = 491)</b>					
Male	300	(61.1)	141 (47.0)	159 (53.0)	0.503
Female	191	(38.9)	83 (43.5)	108 (56.5)	
<b>Age group (N = 504)</b>					
0–19	49	(9.7)	26 (53.1)	23 (46.9)	0.479
20–59	256	(50.8)	112 (43.8)	144 (56.2)	
>59	199	(39.5)	92 (46.2)	107 (53.8)	
<b>Location (N = 210)</b>					
Frontal Lobe	88	(41.9)	24 (27.3)	64 (72.7)	<b>0.013</b>
Parietal Lobe	41	(19.5)	9 (22.0)	32 (78.0)	
Temporal Lobe	66	(31.4)	28 (42.4)	38 (57.6)	
Occipital Lobe	10	(4.8)	5 (50.0)	5 (50.0)	
Cerebellum	5	(2.4)	4 (80.0)	1 (20.0)	
<b>KPS (N = 168)</b>					
<70	75	(44.6)	11 (14.7)	64 (85.3)	0.539
>70	93	(55.4)	18 (19.4)	75 (80.6)	
<b>Grade (N = 507)</b>					
Low Grade	18	(3.6)	5 (27.8)	13 (72.2)	0.149
High Grade	489	(96.4)	228 (46.6)	261 (53.4)	
<b>Histologic Subtype (N = 507)</b>					
DA (WHO Grade II, NOS)	18	(3.6)	5 (27.8)	13 (72.2)	0.272
AA (WHO Grade III, NOS)	24	(4.7)	12 (50.0)	12 (50.0)	
Ped. GBM (WHO Grade IV, NOS)	42	(8.3)	23 (54.8)	19 (45.2)	
Ad. GBM (WHO Grade IV, NOS)	423	(83.4)	193 (45.6)	230 (54.4)	
<b>GBM status mutation (N = 460)</b>					
<b>IDH1 mutation (N = 229)</b>					
No	220	(96.1)	117 (53.2)	103 (46.8)	0.185
Yes	9	(3.9)	7 (77.8)	2 (22.2)	
<b>TERT promoter mutation (N = 45)</b>					
No	11	(24.4)	3 (27.3)	8 (72.7)	0.687
Yes	34	(75.6)	7 (20.6)	27 (79.4)	
<b>MGMT promoter methylation (N = 186)</b>					
No	120	(64.5)	75 (62.5)	45 (37.5)	0.753
Yes	66	(35.5)	39 (59.1)	27 (40.9)	

Abbreviation: DA: diffuse astrocytoma, AA: anaplastic astrocytoma, Ped. GBM: pediatric glioblastoma, Ad. GBM: adult glioblastoma KPS: Karnofsky Performance Status, NOS: not otherwise specified. T-test ( $p < 0.05$ ).

Following the assessment of *TERT*, *IDH1* mutational profile, and *MGMT* methylation status in a subset of cases, the association of these molecular alterations with the loss of *MTAP* protein expression was evaluated. No significant association was observed (Table 2).

Importantly, we evaluated the impact of *MTAP* expression on overall survival (OS) of patients diagnosed with GBMs. In total, 398 adult patients were included in the OS analysis from which 83.1% ( $n = 331$ ) died during total observation time: 76.6% ( $n = 138$ ) in the *MTAP*-negative group and 88.5% ( $n = 193$ ) in the *MTAP*-positive group (Figure 4A). We found that, in adult glioblastoma, patients exhibiting a lack of *MTAP* expression had better survival than those presenting *MTAP* expression (median survival of  $9.8 \pm 0.86$  vs.  $6.23 \pm 0.70$  months, respectively,  $p = 0.00023$  in log-rank test) (Figure 4A). Two-year OS rates were 10.6% for the *MTAP*-negative group and 7.6% for the *MTAP*-positive group. In the pediatric context, 40 pediatric glioblastoma patients included in the analysis—86.3% ( $n = 19$ ) in the *MTAP*-negative group and 77.7% ( $n = 14$ ) in the *MTAP*-positive group—died during the total observational time (Figure 4B). There was no association of *MTAP* loss and patients' OS, with a median OS of  $13.0 \pm 1.71$  months in the *MTAP*-negative group and  $14.0 \pm 4.83$  months for the *MTAP*-positive

group ( $p = 0.499$  in log-rank test) (Figure 4B). The two-year OS rates were 7.2% and 5.56% for MTAP-negative and MTAP-positive groups, respectively.

In order to extend these findings, we performed *in silico* survival analysis considering CNA status in TCGA-GBM datasets ( $n = 246$ ). The analysis did not demonstrate a significant difference between *MTAP* CNA and overall survival (Figure 4C;  $p = 0.942$ ). We further evaluated disease-free survival (DFS) considering relapse and death as endpoints. Similarly, the five-year DFS was not different between *MTAP* groups (Figure 4D;  $p = 0.230$ ).

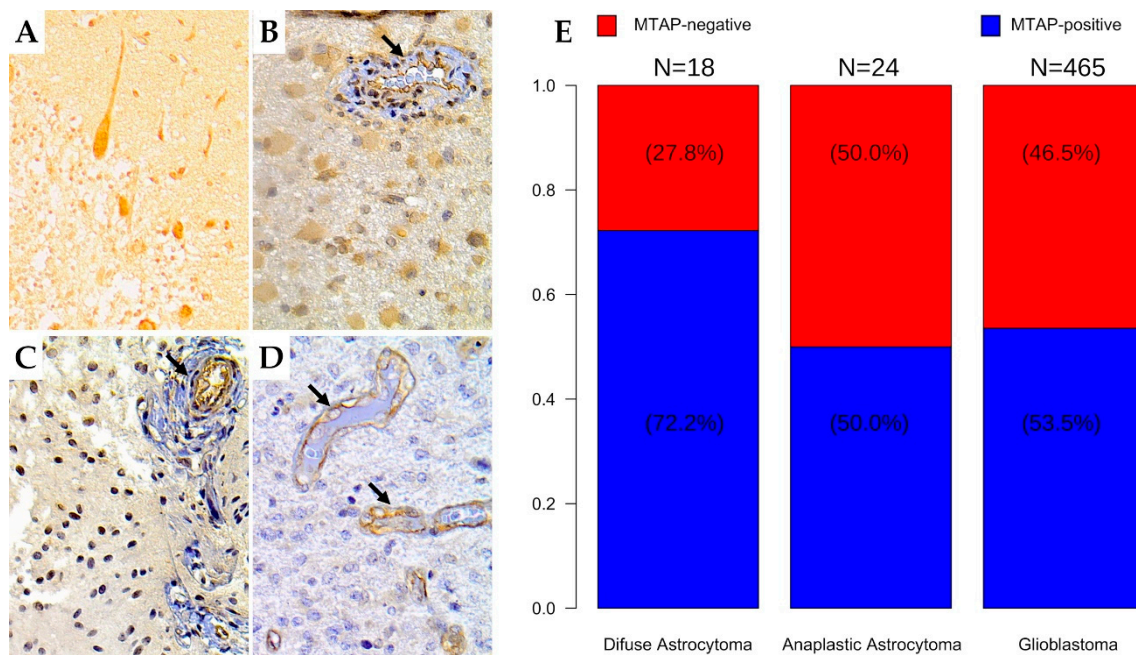


**Figure 3.** Immunohistochemistry staining for *MTAP* in human brain tumor tissues. The human brain tissue slide used for this study contained 507 cases of patients with different grades of gliomas in duplicates. Representative images from (A) normal cerebellum tissue (positive control); (400×) (B) diffuse astrocytoma (grade II); (400×) (C) anaplastic astrocytoma (grade III); 400× (D) glioblastoma (grade IV); 400×. Arrows indicate vessels with endothelial staining for *MTAP* protein (positive internal control). (E) Frequency of loss of *MTAP* protein expression in the glioma dataset according to histologic subtype.

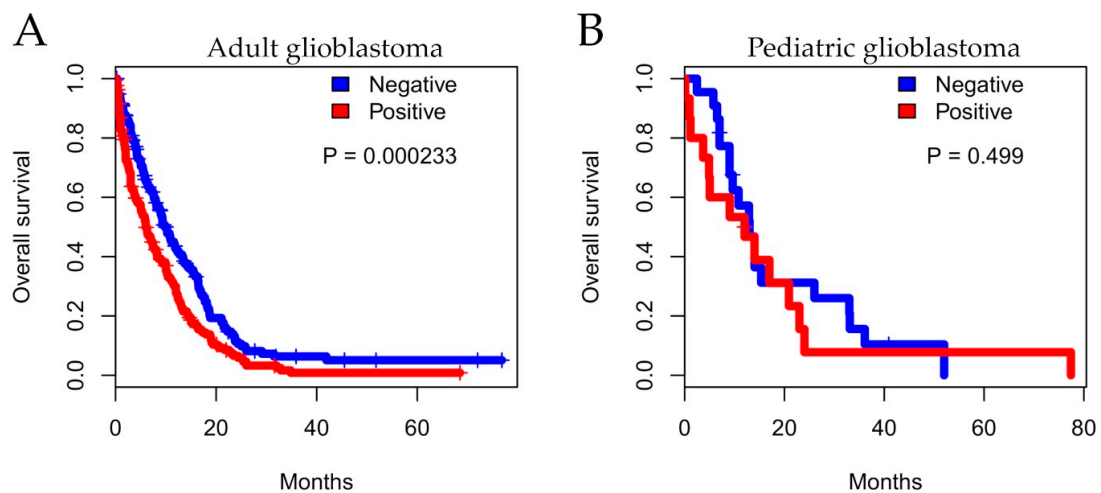


**Figure 4.** *Cont.*

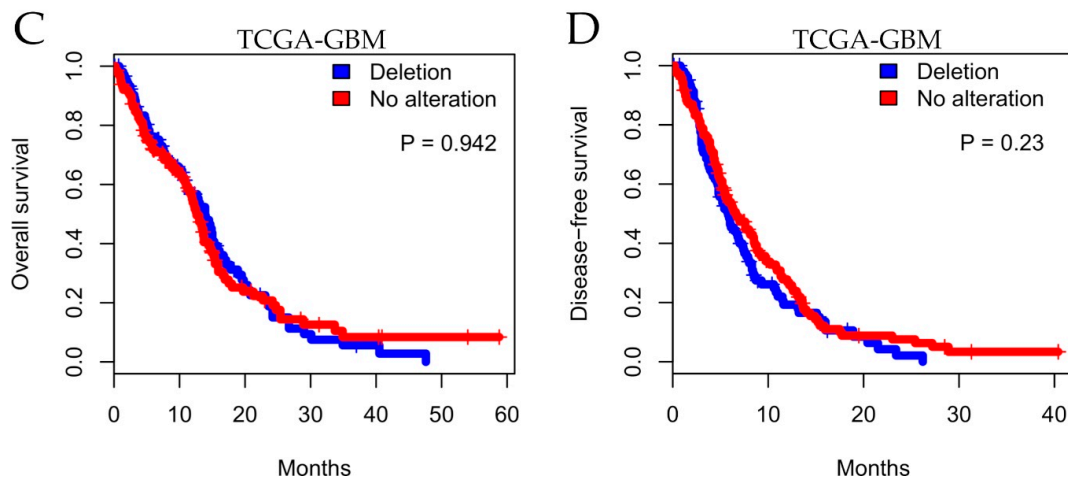


**Figure 4.** Kaplan–Meier analysis for *MTAP* expression associated with patient survival. Overall survival for a series of patients with glioma diagnosis according to histopathological grade. Shown for (A) adult glioblastoma, (B) pediatric glioblastoma, and (C) TCGA-GBM dataset status and (D) five-year disease-free survival (DFS) for TCGA-GBM dataset.

### 3.3. *MTAP* Cell Line Editing and Differential Gene Expression

To further underpin the *MTAP* biological role in gliomas, the U251 cell line, which expressed *MTAP*, was transfected with *MTAP* CRISPR/Cas9 KO to create the stable knockout clones (U251MTAP<sup>-/-</sup>). On the other hand, SW1088 cells that normally do not express *MTAP* were transduced by the *MTAP* human lentivirus to establish *MTAP* expression clones (SW1088MTAP<sup>+/+</sup>). Stable cell lines were confirmed by Western blotting post puromycin selection (Supplementary Figure S1).

After *MTAP* gene editing, the transcriptomic profiles of U251MTAP<sup>-/-</sup> and SW1088MTAP<sup>+/+</sup> cells as well as control cells (U251EV and SW1088LB) and parental cells (U251WT and SW1088WT) were evaluated for the expression of specific genes using the NanoString PanCancer Pathways Panel, which assessed thirteen canonical pathways (Notch, Wnt, Hedgehog, chromatin modification, transcriptional regulation, DNA damage control, transforming growth factor-beta (TGF-beta), mitogen-activated protein kinase (MAPK), The Janus kinase/signal transducers and activators of transcription (JAK/STAT), Phosphoinositide 3-kinase (PI3K), RAS, cell cycle, and apoptosis). In the U251 cells, we found that the U251MTAP<sup>-/-</sup> clone showed 17 differentially expressed genes in comparison with controls, with seven (*ANGPT1*, *NGFR*, *FN1*, *COL11A1*, *SPP1*, *RASGRF1*, and *MAPK10*) being associated with the PI3K/RAS/MAPK pathways, three (*TGFBR2*, *THBS1*, and *BMP5*) with the TGF- $\beta$  pathway, two (*IDH2* and *ERBB2*) belonging to the Driver pathway, and five genes (*TNFSF10*, *SFRP1*, *PLAT*, *NOTCH1*, and *BRIP1*) associated with other pathways (Figure 5A, Supplementary Table S2). When analyzing only differentially expressed genes ( $p$ -adjusted <0.05;  $\log_2FC \geq \pm 2$ ), we found six upregulated (*ANGPT1*, *FN1*, *NGFR*, *RASGRF1*, *THBS1*, and *TNFSF10*) and three downregulated genes (*BMP5*, *COL11A1*, and *MAPK10*) in the *MTAP* KO cells (Figure 5B).

We further performed the same approach in the SW1088 gene-edited cells. In the SW1088MTAP<sup>+/+</sup> clone, we observed significant alterations in six genes (*IL6R*, *GPC4*, *IL13RA2*, *MAP2K6*, *E2F5*, and *ETV1*) belonging to JAK-STAT, PI3K, WNT, MAPK, transcriptional regulation, and apoptosis pathways (Figure 5C, Supplementary Table S3). Following adjustment ( $p$ -adjusted <0.05;  $\log_2FC > \geq 2$ ), only *GPC4* and *IL13RA2* were differentially expressed when compared with control cells (Figure 5D, Supplementary Table S3). Subsequently, an analysis of the functional connections among the proteins encoded by the 17 and the six genes differently expressed by U251MTAP<sup>-/-</sup> and SW1088MTAP<sup>+/+</sup> was performed using STRING software. For U251MTAP<sup>-/-</sup> cell, 11 of 17 genes had at least two connections, as shown in Figure 5E. Notably, these 11 genes were centered on five genes (*NOTCH1*, *ANGPT1*, *ERBB2*, *THBS1*, and *FN1*). On the other hand, for SW1088MTAP<sup>+/+</sup>, only *IL6R* and *MAP2K6* showed the signal connection (Figure 5F).

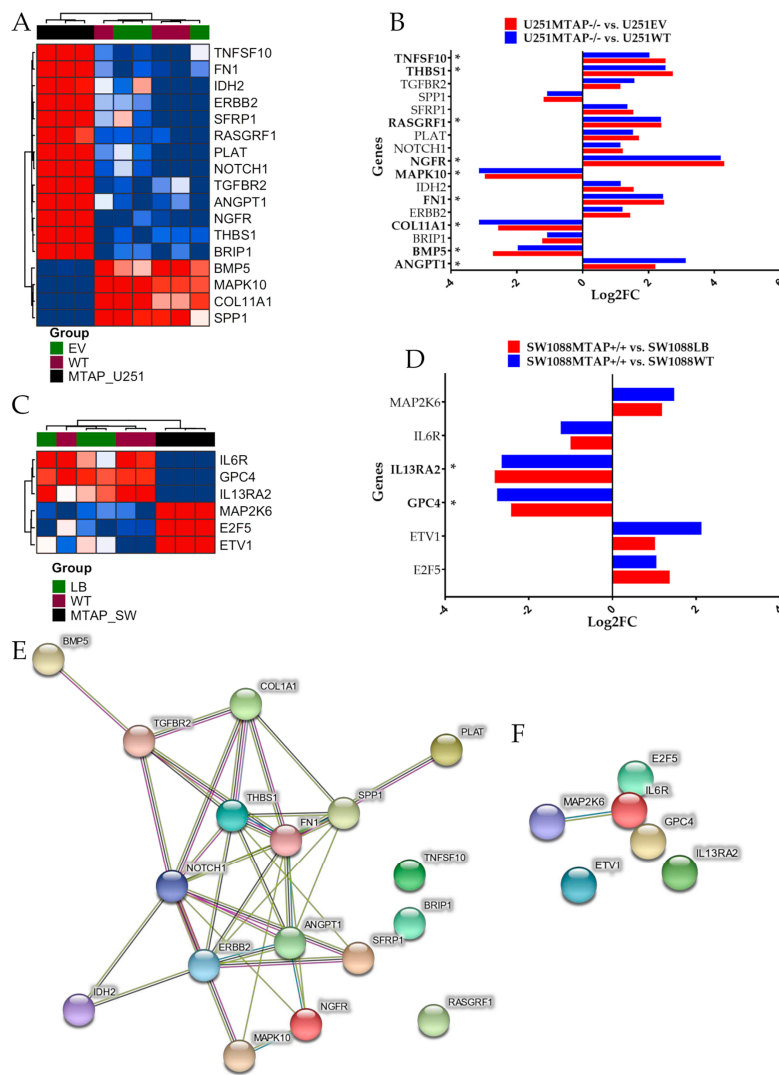


**Figure 5.** Detection of differentially expressed genes affected by *MTAP* gene-edited in glioma cell lines. **(A)** Heatmap representing the expression profile of the most differentially expressed genes for U251MTAP<sup>-/-</sup> cell compared to U251EV and U251WT cells. **(B)** Bar plots showing gene expression as the mean SD of log changes of U251MTAP<sup>-/-</sup> relative to U251EV and U251WT cells. **(C)** Heatmap representing the expression profile of the most differentially expressed genes for SW1088MTAP<sup>+/+</sup> cell compared to SW1088LB and SW1088WT cells. **(D)** Bar plots showing the gene expression as the mean SD of log changes of SW1088MTAP<sup>+/+</sup> relative to SW1088LB and SW1088WT cells. **(E,F)** Isolated networks of protein–protein interaction using STRING (<http://www.string-db.org>). The weight of these lines represents the confidence within which a predicted interaction occurs. Interactions networks for 17 and six proteins differentially regulated in U251MTAP<sup>-/-</sup> and SW1088MTAP<sup>+/+</sup> cells compared to controls U251EV and SW1088LB, respectively. Rows represent genes and columns represent cell lines. Red pixels: upregulated genes; blue pixels: downregulated genes. The intensity of each color denotes the standardized ratio between each value and the average expression of each gene across all samples. Each sphere represents an individual protein, and edges represent protein–protein associations. A red line indicates the presence of fusion evidence; a green line indicates neighborhood evidence; a blue line indicates co-occurrence evidence; a purple line indicates experimental evidence; a yellow line indicates text-mining evidence; a light blue line indicates database evidence; and a black line indicates co-expression evidence. Asterisks (\*) labeling the bar indicates a significant difference ( $p$ -value  $< 0.05$  and  $\log_2FC \geq \pm 2$ ) between the gene expression of respective groups and the control. The network nodes represent proteins. Edges represent protein–protein associations. Student t-test: \*  $p < 0.05$ , \*\*  $p < 0.01$ , \*\*\*  $p < 0.001$ , ns: not significant

### 3.4. MTAP Deletion Does Not Modulate Glioma Cell Proliferation

To address the functional impact on cell proliferation, U251MTAP<sup>-/-</sup>, U251EV, and U251WT ( $1 \times 10^5$  cells) as well as SW1088MTAP<sup>+/+</sup>, SW1088LB, and SW1088WT ( $5 \times 10^3$  cells) were seeded in E-plates, and then the cell index and the doubling time were evaluated (Figure 6). We observed that U251MTAP<sup>-/-</sup> showed analogous kinetic trace characteristics when compared to U251EV after 72 h (Figure 6A). When we analyzed the cell doubling time, within 24 h (cell doubling time  $2.36 \pm 1.51$  vs.  $3.32 \pm 0.88$ ;  $p = 0.400$ ) and persisting up to 72 h (cell doubling time;  $10.36 \pm 1.64$  vs.  $11.64 \pm 1.40$ ,  $p = 0.800$ ), the U251MTAP<sup>-/-</sup> cell showed increased proliferation rates in relation to U251EV, although it did not show a significant difference (Figure 6B, 24 h:  $p > 0.999$ ; 48 h:  $p > 0.999$ ; 72 h:  $p = 0.547$ ). Likewise, the SW1088MTAP<sup>+/+</sup> cells did not exhibit distinct proliferation rates (Figure 6C,  $p > 0.05$ ) and doubling time (Figure 6D, 24 h:  $p = 0.700$ ; 48 h:  $p = 0.885$ ; 72 h:  $p = 0.885$ ) when compared with the control clone (SW1088LB). Together, these results suggest that the *MTAP* gene alone does not modulate cell proliferation.

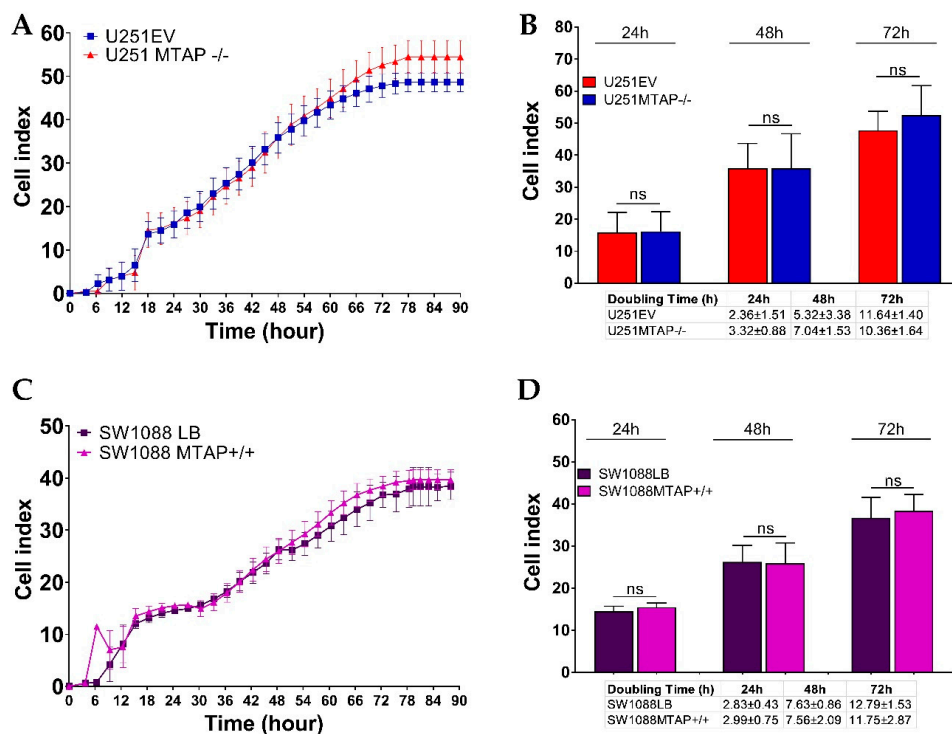


**Figure 6.** Dynamic monitoring of cell proliferation using impedance technology. Cell index values representative for U251MTAP<sup>-/-</sup> vs. U251EV (A) and SW1088MTAP<sup>+/+</sup> vs. SW1088LB (C) measured by the Real Time Cell Analysis (RTCA) assay for 90 h. Plot representative of cell index and doubling time at 24, 48, and 72 h for U251MTAP<sup>-/-</sup> vs. U251EV (B) and SW1088MTAP<sup>+/+</sup> vs. SW1088LB (D). Plot representative of three independent experiments. Student t-test: \*  $p < 0.05$ , \*\*  $p < 0.01$ , \*\*\*  $p < 0.001$ , ns: not significant.

### 3.5. Loss of MTAP Gene is Not Associated with Cell Migration and Invasion

To investigate whether the loss of *MTAP* could affect glioma cell motility and invasiveness, we used the transwell cell migration assay (Figure 7A,B). U251MTAP<sup>-/-</sup> cells promoted decreased ability of migration compared with U251EV by 10% (U251MTAP<sup>-/-</sup>  $552.5 \pm 205.3$  vs. U251EV:  $614.2 \pm 223$ ) (Figure 7A,  $p > 0.999$ ), while the overexpressed clone SW1088MTAP<sup>+/+</sup> showed an increase in migration ability about of 19% (SW1088LB:  $557.8 \pm 40.8$  vs. SW1088MTAP<sup>+/+</sup>:  $687.6 \pm 138.1$ ) (Figure 7B,  $p = 0.400$ ). Regarding the invasive properties of edited cells, as shown in Figure 7C, U251EV cells ( $601.7 \pm 201.6$ ) exhibited an 8% greater invasion compared to U251MTAP<sup>-/-</sup> ( $553.5 \pm 92.1$ ), yet it was not statistically

significant ( $p = 0.857$ ). Likewise, an increase of SW1088MTAP+/+ invasion was observed in ~12% (SW1088MTAP+/+:  $264.3 \pm 50.7$  vs. SW1088LB:  $230.7 \pm 31.9$ ) compared to SW1088LB cell, also not statistically significant (Figure 7D,  $p = 0.628$ ). Moreover, we obtained similar results when comparing U251MTAP-/- and SW1088MTAP+/+ with U251WT and SW1088WT parental controls, respectively (data not shown).

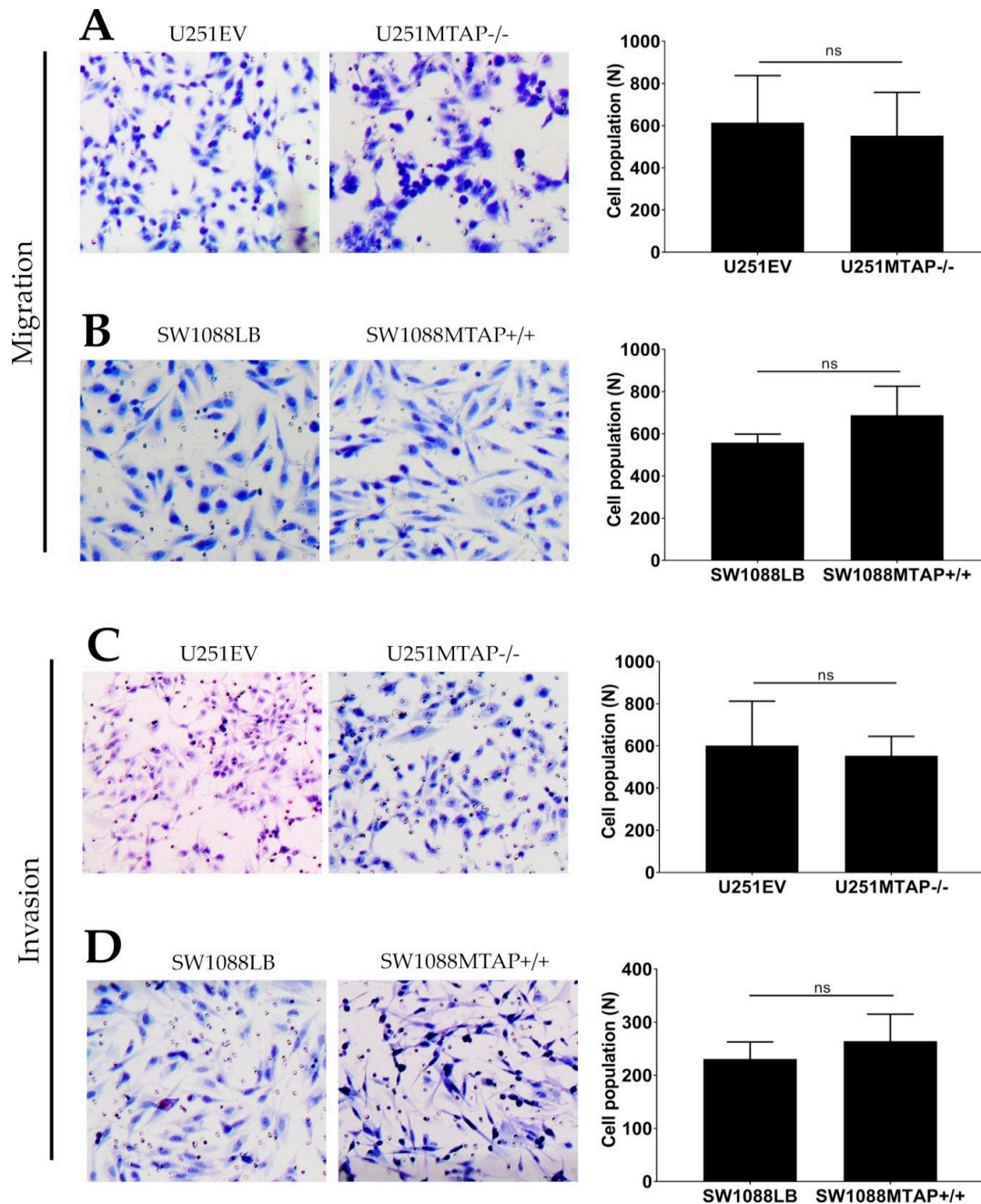


**Figure 7.** MTAP gene does not modulate migration and invasion abilities. Migration potential in both clone cell lines U251MTAP-/- (A) and SW1088MTAP+/+ (B) compared to controls (U251EV and SW1088LB) measured by Transwell assays and expressed as relative cell population. Transmembrane invasion assay of U251MTAP-/- (C) and SW1088MTAP+/+ (D) compared to controls (U251EV and SW1088LB). Quantification of migrated and invaded cells numbers per field. A minimum of 10 fields of two separate wells within each experiment were analyzed. The graphs represent data from three separate experiments. Student t-test: \*  $p < 0.05$ , \*\*  $p < 0.01$ , \*\*\*  $p < 0.001$ , ns: not significant.

Next, to support in vitro results, we evaluated the differential expression of 24 genes associated with invasion and migration processes. Only two of these genes were differently expressed in the U251 MTAP gene-edited cell line compared to U251EV cells (Supplementary Figure S2A). The *FN1* gene was found to be upregulated ( $\log_2FC = 2.26$ ;  $p = 0.0006$ ) and, inversely, *MAPK10* was found downregulated ( $\log_2FC = -3.28$ ;  $p < 0.0001$ ) in U251MTAP<sup>-/-</sup> compared to U251EV (Supplementary Figure S2C). Furthermore, no differential expression was found between SW1088MTAP<sup>+/+</sup> and control (Supplementary Figure S2C).

#### 4. Discussion

In the present study, we evaluated *MTAP* expression in a large series of gliomas. Moreover, by using a genome edition gain- or loss-of *MTAP*-function approach in glioma cell lines, we explored *MTAP* biological impact on gliomas. We observed that, despite the frequent loss of *MTAP* expression in high-grade gliomas, *MTAP* was not associated with a worse outcome, and the in vitro models showed that *MTAP* does not affect cell line proliferation, invasion, and migration.

Initially, using an in silico approach, we showed that 48% (168/350) of gliomas had 9p21 locus deleted, and this deletion was directly associated with reduced *MTAP* expression. In fact, Zhao and Zhao in a tumor suppressor pan-cancer study reported the association between copy number loss (9p21) and reduced *MTAP* mRNA expression [49]. In addition, the homozygous deletion of 9p21 locus was identified to be significantly associated with a decrease of *MTAP* (mRNA and protein) expression levels [50]. This region of the human genome is especially interesting because *MTAP* is located close to a fragile site [51]. The deletion of this region usually causes co-deletion of *MTAP* and some classic and well-known tumor suppressor genes such as *CDKN2A/B* [52]. The cyclin-dependent kinase inhibitor 2A (*CDKN2A*) and the cyclin-dependent kinase inhibitor 2B (*CDKN2B*) genes both encode putative regulators of cyclin-dependent kinases on chromosome 9p21 that could lead to uncontrolled cell proliferation and have been associated with poor prognosis in many cancer types included gliomas [23,53–55]. The 9p21 chromosomal region deletion is rare in grade I but frequent in grade IV glioma [39]. Our findings, in combination with the detection of other biomarkers, show *CDKN2A/B* could be used to predict 9p21 deletion and to stratify patients for stricter surveillance. By analyzing the TCGA-GBM dataset, we also observed that deletion, rather than *MTAP* promoter methylation, is associated with *MTAP* mRNA expression. Our results contrast with a recent study that found a significant association of *MTAP* methylation with gene expression [40]. However, Hansen et al. observed a very low coefficient of determination ( $R^2$ ) (0.19) with a low correlation coefficient ( $R$ ) value (0.44) clearly below the values considered as strong correlation ( $>0.6$ ); therefore, caution should be taken in interpreting the reported correlation between DNA promoter methylation and *MTAP* expression described [40].

We then evaluated *MTAP* expression profile in accordance with the molecular subtype of glioblastomas described by Verhaak et al. [56] and Noushmehr et al. [16]. When using the TCGA-GBM dataset, we observed that *MTAP* loss of expression was more pronounced within the classical subtype (65.2%), corroborating previous reports that patients with classical subtype are characterized by *CDKN2A* gene deletion that is contiguous with the *MTAP* gene [26]. On the other hand, only 7.4% of the G-CIMP glioblastomas showed loss of *MTAP*, which is associated with secondary glioblastoma, tumor-harboring mutation of the *IDH1* gene, and lesions that progressed from LGG [16,57,58].

In glioma cell lines, we observed loss of *MTAP* in high-grade glioma cells, contrasting with low-grade glioma (40% vs. 0%). Interestingly, there was no loss of *MTAP* expression in pediatric GBM cell lines, whereas 50% (4/8) of adult GBM cell lines presented the loss of expression. These findings are in line with the less frequent (10–19%) 9p21 locus deletion event in pediatric HGG cases [8,59].

We further characterized *MTAP* expression by IHC, and we sought to associate it with its prognostic value. We previously reported that *MTAP* loss occurs in less than 15% of pilocytic astrocytomas (WHO grade I) [42]. Herein, we extended the immunohistochemistry analysis to a large set of diffuse infiltrative astrocytomas and observed association between loss of *MTAP* expression and malignancy

grade of gliomas. This result is in line with the report by Suzuki et al. [60] that identified the high frequency of *MTAP* deletion (60%) in glioblastoma series but rare presence in low-grade glioma [39,42]. Differently, in glioma cell lines, the loss of *MTAP* for pediatric glioblastoma (54.8%) was higher than in adult glioblastoma (45.6%) series. This finding was unexpected and may suggest that our series of pediatric GBM harbored histological characteristics such as those described in the receptor tyrosine kinases (RTK) II classic subgroup. These tumors exhibit features of copy number alterations of adult glioblastomas [8,61]. In a recent study, Frazão et al. [39] identified, in a series of pediatric gliomas, rare episodes of deletion in grade I glioma (12.2%) but frequent 9p21 deletion in high-grade glioma (62.5%). These results point to the correlation of *MTAP* deficiency with increased malignancy and histological subtype of gliomas [11,38,42,50,60].

Despite the frequent loss of expression associated with higher-grade lesions, when evaluating its clinical impact in our HGG and adult GBM cases, the loss of *MTAP* was surprisingly correlated with a better prognosis. One hypothesis that may explain this fact is that patients diagnosed with the classical subtype (frequent chromosome 9p deletion) presented better survival after intensive therapy (chemotherapy/radiotherapy) [56]. Our dataset is composed of patients with primary GBM characteristics (median age of 59 years, *IDH1*-mutated in 3.9%) with 79% (287/363) having undergone chemo or radiotherapy treatment, corroborating this result. In addition, through the bioinformatics approach, we did not observe any association of *MTAP* expression/deletion with overall survival ( $p = 0.942$ ) and disease-free survival ( $p = 0.230$ ) from the TCGA-GBM dataset. These results are not in accordance with Hansen et al. [40], which also analyzed the TCGA-GBM dataset and reported that *MTAP*-deleted cases presented worse disease-free survival (DFS) when compared to *MTAP*-normal patients. The lack of accuracy of DFS in GBM prognostic evolution, particularly outside a clinical trial assessment, is already known; therefore, overall survival (OS) is the most used criterion. When analyzing the same TCGA GBM dataset, we observed that *MTAP*-deleted patients did not show a worse OS when compared with *MTAP*-normal patients. Additionally, in agreement with Hansen et al. [40], we performed the DFS analysis of the same GBM dataset, considering the gold standard DFS endpoints (7), namely relapse and death events, different to the study by Hansen that only considered relapse and censored the events of death. The results also showed a lack of association between *MTAP* deletion and GBM patients' prognosis.

Our NanoString Pan-Cancer Panel analysis of *MTAP* gene-edited cell lines showed a significantly altered expression of genes associated with RAS/MAPK/PI3K-AKT and apoptosis pathways after *MTAP* gene knockout. Signaling by these pathways governs fundamental physiological processes, such as cell proliferation, differentiation, metabolism, cell death, and survival [62–64]. Out of nine genes differentially expressed in our study, five are included in the PI3K-AKT pathway, with three of them—*FN1*, *NGFR*, and *THBS1*—being associated with tumor progression [65–68]. Besides, upregulated *ANGPT1* and downregulated *CO11A1* are related to a better prognosis in lung cancer metastasis and proliferation in colorectal cancer [68,69]. Another gene, *TNFSF10*, was identified as upregulated in U251MTAP<sup>-/-</sup>. This gene is frequently associated with the pro-apoptotic process by caspase 8 activation [70,71]. Curiously, only two genes, *GPC4* and *IL13RA2*, showed altered expression for SW1088MTAP<sup>+/+</sup> cell line when compared to the control. These two genes exhibit differential expression and controversial function in various tumors acting as tumor promoters and inhibitors in a cancer type-specific manner [72–75].

Importantly, in U251MTAP<sup>-/-</sup> and SW1088MTAP<sup>+/+</sup> edited glioma cells, we showed that *MTAP* does not regulate glioma cell proliferation, migration, and invasion mechanisms, major cancer biological features of classic tumor suppressor genes. The results are consistent with the ones observed in our mRNA expression analysis obtained by the Pan-Cancer Pathway Panel assay. For these genes, significant differences were observed only for *FN1* and *MAPK10* between U251MTAP<sup>-/-</sup> and U251EV without difference for other genes evaluated. A recent study with prostate cancer cells silenced for *MTAP* also showed similar growth rates to controls [33]. Furthermore, it was observed in hepatocellular carcinoma that the re-expression of *MTAP* did not change the proliferation rates when compared to



mock controls [28]. In gliomas, a recent study showed compelling data that MTAP loss is responsible for epigenetic remodeling and stemness properties [40]. The comparison of the present study with Hansen et al. [40] shows an important limitation related to culture systems. Our findings were obtained from 2D monolayer cultures, a high-serum adherent culture system that failed to maintain glioma stem-like subpopulation of cells and overrepresented only neoplastic cells [76]. We highlight that the process of in vitro culturing of GBM cells is fraught with challenges [77]. Although Hansen and colleagues provided the first evidence for relevance of MTAP loss in stemness-induction in GBM, their study also failed to account for a wide range of factors known to influence tumor growth, migration, invasion, and resistance to therapy. Therefore, for now, despite efforts, there is a lack of satisfactory methods for detailed monitoring of molecular and cellular determinants of tumor growth in patients as well as ideal in vitro systems for modeling of these processes [77]. Thus, additional studies with implementation of new culture models that better recapitulate the complex reality of glioma growing in situ are warranted to address this topic.

MTAP has been reported as an important therapeutic regulator. It may contribute to selective therapy with thiopurines in combination with MTA in MTAP-deleted tumors as a strategy to induce selective cell death [19,40,78]. However, in the context of treatment strategy, MTAP status as a factor of molecular vulnerability to increase the efficacy of treatment in patients with glioma should be further studied with caution. Our data provide arguments towards the lack of strong biological importance of MTAP in gliomagenesis. Clearly, a better understanding of the molecular changes of MTAP-depleted cells is needed to exploit this direct and indirect molecular vulnerability, increasing the efficacy of treatment in patients with glioma.

In summary, the present work showed that loss of MTAP expression is a frequent event in high-grade gliomas. In silico and in vitro models provided evidences towards the lack of strong biological importance of MTAP in gliomas. This study also showed that, despite the frequent loss of MTAP, it does not have a clinical impact in survival and does not act as a canonic tumor suppressor gene in gliomas.

**Supplementary Materials:** The following are available online at <http://www.mdpi.com/2073-4409/9/2/492/s1>. Table S1: Histological diagnosis of established and primary cell lines; Table S2: Genes differentially expressed post-MTAP gene-editing (U251MTAP<sup>-/-</sup>). Table S3: List of genes differentially expressed post-MTAP gene editing (SW1088MTAP<sup>+/+</sup>); Supplementary Figure S1: Generation of MTAP<sup>-/-</sup> (U251) and MTAP<sup>+/+</sup> (SW1088) cells by CRISPR/Cas9 and Lentiviral technology; Supplementary Figure S2: Superimposed box plot demonstrates average of the log<sub>2</sub> gene expression of 24 Pan-Cancer Pathway panel genes across U251MTAP<sup>-/-</sup> (A) and SW1088MTAP<sup>+/+</sup> (B) cell lines. (C) List of the 24 genes differentially expressed in gene-edited cell lines.

**Author Contributions:** W.P.d.M.—Conception or design of the work; acquisition, analysis, and interpretation of data; Drafting the work; Final approval; V.A.O.S.—Critical review; Drafting the work; Final approval. I.N.F.G.—Analysis, and interpretation of data, Final approval; M.N.R.—Analysis, and interpretation of data, Final approval; M.L.C.S.—Acquisition of data, interpretation of data, Final approval; A.C.C.—Acquisition, analysis, and interpretation of data, Final approval; A.L.V.A.—Acquisition of data, Final approval; M.M.—Analysis of data, final approval; G.C.A.—analysis, and interpretation of data; final approval; L.S.d.S.—Acquisition, analysis, and interpretation of data, Final approval; A.P.B.—Sample collection; interpretation of data; final approval. L.N.—Sample collection; Critical review; Final approval. C.C.—Sample collection; Final approval. I.W.d.C.—Sample collection; Final approval. G.N.M.H.—Sample collection; Final approval. C.J.—Sample collection; Critical review; Final approval; L.T.B.—Acquisition, analysis, and interpretation of data; Drafting the work; Final approval. R.M.R. Corresponding author—Conception or design of the work; interpretation of data; Drafting the work; Supervision of study; Final approval. All authors have read and agreed to the published version of the manuscript.

**Funding:** Menezes W.P. and Alves A.L.V. was a recipient of Coordenação de Aperfeiçoamento de Pessoal de Nível Superior (CAPES) fellowship and is recipient of Fundação de Amparo à Pesquisa do Estado de São Paulo (FAPESP) fellowships (2016/06833-2 and 2016/18907-0). Gomes INF was a recipient of Fundação de Amparo à Pesquisa do Estado de São Paulo (FAPESP) fellowship (2017/22305-9). Rosa MN was a recipient of Coordenação de Aperfeiçoamento de Pessoal de Nível Superior (CAPES) fellowship. Spina MLC was a recipient of Conselho Nacional de Desenvolvimento Científico e Tecnológico (CNPq) fellowships (100707/2014-9, 116477/2014-8, 1282245/2014-0). Bidinotto LT was recipient of the Universal/CNPq grant (472447/2013-0). This study was supported by grants from the Barretos Cancer Hospital and by Public Ministry of Labor Campinas (Research, Prevention and Education of Occupational Cancer). Reis RM acknowledges the support of CNPq. Chris Jones acknowledges support from the National Institute for Health Research (NIHR) Biomedical Research

Center at the Royal Marsden and the Institute of Cancer Research in London. The CNPq, FAPESP and NIHR grants were responsible for the purchase of reagents used in data collection, described in manuscript (commercial Tissue Microarray (TMA), reagents utilized for making TMA, Medium reagents, cell lines acquisition, western blot and RT-qPCR reagents) analysis (antibody and immunohistochemistry reagents) and interpretation (fellowships).

**Acknowledgments:** We thank Barretos Cancer Hospital and Public Ministry of Labor (Research, Prevention, and Education of Occupational Cancer Project), Campinas, Brazil, for partially funding the present for Scientific and Technological Development (CNPq, Brazil). We thank the nucleus of support to the researcher for assisting in the analysis of statistical data. We thank the macrovector / Freepik and the New England Journal of Medicine by design the images used in the development of the graphic abstract.

**Conflicts of Interest:** The authors declare no conflict of interest.

## Appendix A

### *Appendix A.1. Cell Lines*

One cell line derived from normal astrocytes (NHA), seven primary glioma cell lines, and 11 human glioma cell lines were evaluated. Human glioma cell lines were as follows: U251 (obtained from Costello Laboratory), GAMG (obtained from DSMZ, German Collection of Microorganisms and Cell Cultures), RES259, SF188, UW479, and KNS42 (obtained from Bax et al. [79] ), A172, U87MG, SW1088, SW1783, and T98G (obtained from ATCC, American Type Culture Collection), NHA (obtained from The European Collection of Authenticated Cell Cultures (ECACC). NHA, pediatric, and adult glioma cell lines (RES259, SF188, UW479, KNS42, U251, GAMG, A172, U87MG, SW1088, SW1783, and T98G) were grown in Dulbecco's modified Eagle's medium (DMEM) (GIBCO®, Paisley, Scotland, UK). Cell culture media were supplemented with 10% fetal bovine serum (FBS) (GIBCO®, Paisley, Scotland, UK) and 1% penicillin-streptomycin (P/S) (GIBCO®, Paisley, Scotland, UK). Primary short-term and immortalized glioma cell lines (HCB27, HCB28, HCB18, HCB149, HCB29, HCB2, and HCB151) established at Hospital de Cancer de Barretos, Brazil [80,81] were cultured in DMEM medium supplemented with 10% FBS and 1% P/S. All cell lines were checked for the absence of mycoplasma infection. Authentication of cell lines was performed and confirmed by short tandem repeat (STR) DNA typing according to the International Reference Standard for Authentication of Human Cell Lines.

### *Appendix A.2. Gene Editing*

#### Appendix A.2.1. CRISPR/Cas9-Mediated MTAP Gene Editing

The U251 cell line was transfected with CRISPR/Cas9 KO (Santa Cruz Biotechnology, Santa Cruz, CA, USA) according to the modified supplier's protocol. Briefly, in a six-well tissue culture plate,  $2.5 \times 10^5$  cells were seeded in 1 mL of DMEM medium supplemented with FBS at 10% per well, at 37 °C and supplemented with 5% CO<sub>2</sub> per 24 h until reaching 70–90% of confluence. Next, DMEM medium was removed, and 200 µL of opti-MEM was added into wells and cultivated at 37 °C and 5% of CO<sub>2</sub> until the transfection solutions were ready. For solution A, 1.5 µg of MTAP CRISPR/Cas9 KO plasmid (h) (sc-406223) and 1.5 µg of MTAP HDR Plasmid (h) (sc-406223-HDR) or 3.0 µg of Control CRISPR/Cas9 Plasmid (sc-418922) were added into opti-MEM medium to bring the final volume to 150 µL. For solution B, 15 µL of UltraCruz Transfection Reagent (sc-395739) was added into the opti-MEM medium to a total of 150 µL. The Plasmid DNA solution (Solution A) was then added dropwise directly to the UltraCruz Transfection Reagent (Solution B), vortexed, and incubated for 20 min at room temperature (Solution C). Then, 300 µL of solution C was added into each well and incubated for 72 h under conditions normally used to culture the cells. At 72 h post-transfection, the medium was aspirated, and DMEM medium containing 10% of FBS and 5 µg/mL of puromycin antibiotic was added (Santa Cruz, Dallas, USA #CAS 58-58-2) for 7 days. Every 3 days, the medium was aspirated, and new freshly selective media were added into well. The success of MTAP CRISPR/Cas9 KO Plasmid and HDR Plasmid was confirmed by the detection of the red fluorescent protein (RFP) via fluorescent microscopy

and Western blotting assay. The stably deleted cell line was designated as U251 MTAP<sup>-/-</sup> and U251 EV for empty vector control as well as the wild type parental control (U251 WT).

#### Appendix A.2.2. Cell Transduction and Generation of MTAP Overexpressing Cell Line

The lentivirus for *MTAP* overexpression (MTAP Lentivirus Human, No. #LVP712487) and the control lentivirus (pLenti-III-CMV-GFP-2A-Puro-Blank Control Lentiviral Vector, No. #LV590) were obtained commercially from Applied Biological Materials (ABM Inc.<sup>®</sup>, Richmond, BC, Canada). Stable cell lines were generated by transducing the MTAP or the Blank control (without insert) and were selected with 25 µg/mL puromycin according to the supplier's protocol. First, to select the multiplicity of infection (MOI), the green fluorescent protein (GFP) control (LV006) was transfected into the SW1088 cell line cultured in a 96-well tissue culture plate (TPP<sup>®</sup>, Lausanne, Vaud, Switzerland) at a MOI of 2, 4, 6, 8, or 10. The success of GFP expression was observed under a fluorescence microscope (Leica, Wetzlar, Hesse, Germany) after 48 h. An MOI=10 was selected for subsequent experiments, which was adequate for sufficient genetic overexpression in the infected cells with minimum damage. After that,  $1 \times 10^4$  cells (SW1088) were seeded in a 96-well tissue culture plate in 100 µL of DMEM medium supplemented with FBS at 10% per well at 37 °C and supplemented with 5% CO<sub>2</sub> overnight until reaching 70–80% of confluence. Next, the DMEM medium was removed from wells and replaced with 150 µL of transduction mixture [Viral Plus transduction enhancer (G968) diluted 1:100 into MTAP Lentiviral vector, #LVP712487 or Puro-Blank Lentivirus; #LV590; ABM Inc.<sup>®</sup>, Richmond, BC, Canada] following incubation of the 96-plate at 37 °C with 5% CO<sub>2</sub> overnight. After 72 h, the DMEM medium was removed and replaced with 100 µL of complete medium. Stably transfected cells were selected by the addition of 25 µg/mL puromycin to the medium, which was changed every 3 days. The selection was terminated after 7 days when the uninfected control cells were completely dead. The stably expressing cell lines were designated as SW1088 MTAP<sup>+/+</sup> and SW1088 LB for lentivirus blank control, beyond the wild type cell line (SW1088 WT). The infected cells were selected using puromycin antibiotic (25 µg/mL) for 10 days, and stable expression was confirmed by Western blot.

#### References

- Ostrom, Q.T.; Gittleman, H.; Truitt, G.; Boscia, A.; Kruchko, C.; Barnholtz-Sloan, J.S. CBTRUS Statistical Report: Primary Brain and Other Central Nervous System Tumors Diagnosed in the United States in 2011–2015. *Neuro Oncol.* **2018**, *20*, 86. [CrossRef] [PubMed]
- Ganau, L.; Paris, M.; Ligarotti, G.K.; Ganau, M. Management of Gliomas: Overview of the Latest Technological Advancements and Related Behavioral Drawbacks. *Behav. Neurol.* **2015**, *2015*, 1–7. [CrossRef] [PubMed]
- Louis, D.N.; Perry, A.; Reifenberger, G.; von Deimling, A.; Figarella-Branger, D.; Cavenee, W.K.; Ohgaki, H.; Wiestler, O.D.; Kleihues, P.; Ellison, D.W. The 2016 World Health Organization Classification of Tumors of the Central Nervous System: A summary. *Acta Neuropathol.* **2016**, *131*, 803–820. [CrossRef] [PubMed]
- Appin, C.L.; Brat, D.J. Molecular genetics of gliomas. *Cancer J.* **2014**, *20*, 66–72. [CrossRef]
- Stupp, R.; Mason, W.P.; van den Bent, M.J.; Weller, M.; Fisher, B.; Taphoorn, M.J.; Belanger, K.; Brandes, A.A.; Marosi, C.; Bogdahn, U.; et al. Radiotherapy plus concomitant and adjuvant temozolomide for glioblastoma. *N. Engl. J. Med.* **2005**, *352*, 987–996. [CrossRef]
- Omuro, A.; DeAngelis, L.M. Glioblastoma and other malignant gliomas: A clinical review. *JAMA* **2013**, *310*, 1842–1850. [CrossRef]
- Knizhnik, A.V.; Roos, W.P.; Nikolova, T.; Quiros, S.; Tomaszowski, K.H.; Christmann, M.; Kaina, B. Survival and death strategies in glioma cells: Autophagy, senescence and apoptosis triggered by a single type of temozolomide-induced DNA damage. *PLoS ONE* **2013**, *8*, e55665. [CrossRef]
- Sturm, D.; Bender, S.; Jones, D.T.; Lichter, P.; Grill, J.; Becher, O.; Hawkins, C.; Majewski, J.; Jones, C.; Costello, J.F.; et al. Paediatric and adult glioblastoma: Multiform (epi)genomic culprits emerge. *Nat. Rev. Cancer* **2014**, *14*, 92–107. [CrossRef]
- Louis, D.N.; Perry, A.; Burger, P.; Ellison, D.W.; Reifenberger, G.; von Deimling, A.; Aldape, K.; Brat, D.; Collins, V.P.; Eberhart, C.; et al. International Society of Neuropathology–Haarlem consensus guidelines for nervous system tumor classification and grading. *Brain Pathol.* **2014**, *24*, 429–435. [CrossRef]

10. Killela, P.J.; Reitman, Z.J.; Jiao, Y.; Bettegowda, C.; Agrawal, N.; Diaz, L.A., Jr.; Friedman, A.H.; Friedman, H.; Gallia, G.L.; Giovannella, B.C.; et al. TERT promoter mutations occur frequently in gliomas and a subset of tumors derived from cells with low rates of self-renewal. *Proc. Natl. Acad. Sci. USA* **2013**, *110*, 6021–6026. [CrossRef]
11. Bidinotto, L.T.; Torrieri, R.; Mackay, A.; Almeida, G.C.; Viana-Pereira, M.; Cruvinel-Carlioni, A.; Spina, M.L.; Campanella, N.C.; Pereira de Menezes, W.; Clara, C.A.; et al. Copy Number Profiling of Brazilian Astrocytomas. *G3* **2016**, *6*, 1867–1878. [CrossRef] [PubMed]
12. Eckel-Passow, J.E.; Lachance, D.H.; Molinaro, A.M.; Walsh, K.M.; Decker, P.A.; Sicotte, H.; Pekmezci, M.; Rice, T.; Kosel, M.L.; Smirnov, I.V.; et al. Glioma Groups Based on 1p/19q, IDH, and TERT Promoter Mutations in Tumors. *N. Engl. J. Med.* **2015**, *372*, 2499–2508. [CrossRef] [PubMed]
13. Foote, M.B.; Papadopoulos, N.; Diaz, L.A., Jr. Genetic Classification of Gliomas: Refining Histopathology. *Cancer Cell* **2015**, *28*, 9–11. [CrossRef] [PubMed]
14. Nguyen, H.N.; Lie, A.; Li, T.; Chowdhury, R.; Liu, F.; Ozer, B.; Wei, B.; Green, R.M.; Ellingson, B.M.; Wang, H.J.; et al. Human TERT promoter mutation enables survival advantage from MGMT promoter methylation in IDH1 wild-type primary glioblastoma treated by standard chemoradiotherapy. *Neuro-Oncol.* **2017**, *19*, 394–404. [CrossRef] [PubMed]
15. Arita, H.; Yamasaki, K.; Matsushita, Y.; Nakamura, T.; Shimokawa, A.; Takami, H.; Tanaka, S.; Mukasa, A.; Shirahata, M.; Shimizu, S.; et al. A combination of TERT promoter mutation and MGMT methylation status predicts clinically relevant subgroups of newly diagnosed glioblastomas. *Acta Neuropathol. Commun.* **2016**, *4*, 79. [CrossRef]
16. Noushmehr, H.; Weisenberger, D.J.; Diefes, K.; Phillips, H.S.; Pujara, K.; Berman, B.P.; Pan, F.; Pelloski, C.E.; Sulman, E.P.; Bhat, K.P.; et al. Identification of a CpG island methylator phenotype that defines a distinct subgroup of glioma. *Cancer Cell* **2010**, *17*, 510–522. [CrossRef]
17. Savarese, T.M.; Crabtree, G.W.; Parks, R.E. 5'-methylthioadenosine phosphorylase—I. *Biochem. Pharmacol.* **1981**, *30*, 189–199. [CrossRef]
18. Traweek, S.T.; Riscoe, M.K.; Ferro, A.J.; Braziel, R.M.; Magenis, R.E.; Fitch, J.H. Methylthioadenosine phosphorylase deficiency in acute leukemia: Pathologic, cytogenetic, and clinical features. *Blood* **1988**, *71*, 1568–1573. [CrossRef]
19. Tang, B.; Lee, H.O.; An, S.S.; Cai, K.Q.; Kruger, W.D. Specific Targeting of MTAP-Deleted Tumors with a Combination of 2'-Fluoroadenine and 5'-Methylthioadenosine. *Cancer Res.* **2018**, *78*, 4386–4395. [CrossRef]
20. Chaturvedi, S.; Hoffman, R.M.; Bertino, J.R. Exploiting methionine restriction for cancer treatment. *Biochem. Pharmacol.* **2018**, *154*, 170–173. [CrossRef]
21. Batova, A.; Diccianni, M.B.; Nobori, T.; Vu, T.; Yu, J.; Bridgeman, L.; Yu, A.L. Frequent deletion in the methylthioadenosine phosphorylase gene in T-cell acute lymphoblastic leukemia: Strategies for enzyme-targeted therapy. *Blood* **1996**, *88*, 3083–3090. [CrossRef] [PubMed]
22. Mirebeau, D.; Acquaviva, C.; Suci, S.; Bertin, R.; Dastugue, N.; Robert, A.; Boutard, P.; Mechinaud, F.; Plouvier, E.; Otten, J.; et al. The prognostic significance of CDKN2A, CDKN2B and MTAP inactivation in B-lineage acute lymphoblastic leukemia of childhood. Results of the EORTC studies 58881 and 58951. *Haematologica* **2006**, *91*, 881–885.
23. Illei, P.B.; Rusch, V.W.; Zakowski, M.F.; Ladanyi, M. Homozygous deletion of CDKN2A and codeletion of the methylthioadenosine phosphorylase gene in the majority of pleural mesotheliomas. *Clin. Cancer Res.* **2003**, *9*, 2108–2113. [PubMed]
24. Huang, H.Y.; Li, S.H.; Yu, S.C.; Chou, F.F.; Tzeng, C.C.; Hu, T.H.; Uen, Y.H.; Tian, Y.F.; Wang, Y.H.; Fang, F.M.; et al. Homozygous deletion of MTAP gene as a poor prognosticator in gastrointestinal stromal tumors. *Clin. Cancer Res.* **2009**, *15*, 6963–6972. [CrossRef] [PubMed]
25. Nobori, T.; Szinai, I.; Amos, D.; Parker, B.; Olopade, O.I.; Buchhagen, D.L.; Carson, D.A. Methylthioadenosine phosphorylase deficiency in human non-small cell lung cancers. *Cancer Res.* **1993**, *53*, 1098–1101. [PubMed]
26. Christopher, S.A.; Diegelman, P.; Porter, C.W.; Kruger, W.D. Methylthioadenosine phosphorylase, a gene frequently codeleted with p16(cdkN2a/ARF), acts as a tumor suppressor in a breast cancer cell line. *Cancer Res.* **2002**, *62*, 6639–6644.
27. Behrmann, I.; Wallner, S.; Komyod, W.; Heinrich, P.C.; Schuierer, M.; Buettner, R.; Bosserhoff, A.K. Characterization of methylthioadenosine phosphorylase (MTAP) expression in malignant melanoma. *Am. J. Pathol.* **2003**, *163*, 683–690. [CrossRef]

28. Hellerbrand, C.; Muhlbauer, M.; Wallner, S.; Schuierer, M.; Behrmann, I.; Bataille, F.; Weiss, T.; Scholmerich, J.; Bosserhoff, A.K. Promoter-hypermethylation is causing functional relevant downregulation of methylthioadenosine phosphorylase (MTAP) expression in hepatocellular carcinoma. *Carcinogenesis* **2006**, *27*, 64–72. [CrossRef]
29. Kirovski, G.; Stevens, A.P.; Czech, B.; Dettmer, K.; Weiss, T.S.; Wild, P.; Hartmann, A.; Bosserhoff, A.K.; Oefner, P.J.; Hellerbrand, C. Down-regulation of methylthioadenosine phosphorylase (MTAP) induces progression of hepatocellular carcinoma via accumulation of 5'-deoxy-5'-methylthioadenosine (MTA). *Am J. Pathol.* **2011**, *178*, 1145–1152. [CrossRef]
30. Tang, B.; Kadariya, Y.; Chen, Y.; Slifker, M.; Kruger, W.D. Expression of MTAP inhibits tumor-related phenotypes in HT1080 cells via a mechanism unrelated to its enzymatic function. *G3* **2014**, *5*, 35–44. [CrossRef]
31. Basu, I.; Cordovano, G.; Das, I.; Belbin, T.J.; Guha, C.; Schramm, V.L. A transition state analogue of 5'-methylthioadenosine phosphorylase induces apoptosis in head and neck cancers. *J. Biol. Chem.* **2007**, *282*, 21477–21486. [CrossRef] [PubMed]
32. Basu, I.; Locker, J.; Cassera, M.B.; Belbin, T.J.; Merino, E.F.; Dong, X.; Hemeon, I.; Evans, G.B.; Guha, C.; Schramm, V.L. Growth and metastases of human lung cancer are inhibited in mouse xenografts by a transition state analogue of 5'-methylthioadenosine phosphorylase. *J. Biol. Chem.* **2011**, *286*, 4902–4911. [CrossRef] [PubMed]
33. Bistulfi, G.; Affronti, H.C.; Foster, B.A.; Karasik, E.; Gillard, B.; Morrison, C.; Mohler, J.; Phillips, J.G.; Smiraglia, D.J. The essential role of methylthioadenosine phosphorylase in prostate cancer. *Oncotarget* **2016**, *7*, 14380–14393. [CrossRef] [PubMed]
34. Jeon, H.; Kim, J.H.; Lee, E.; Jang, Y.J.; Son, J.E.; Kwon, J.Y.; Lim, T.G.; Kim, S.; Park, J.H.; Kim, J.E.; et al. Methionine deprivation suppresses triple-negative breast cancer metastasis in vitro and in vivo. *Oncotarget* **2016**, *7*, 67223–67234. [CrossRef]
35. Casero, R.A., Jr.; Murray Stewart, T.; Pegg, A.E. Polyamine metabolism and cancer: Treatments, challenges and opportunities. *Nat. Rev. Cancer* **2018**, *18*, 681–695. [CrossRef]
36. Zhong, Y.; Lu, K.; Zhu, S.; Li, W.; Sun, S. Characterization of methylthioadenosine phosphorylase (MTAP) expression in colorectal cancer. *Artif. Cellsnanomedicineand Biotechnol.* **2018**, *46*, 2082–2087. [CrossRef]
37. Nobori, T.; Karras, J.G.; Della Ragione, F.; Waltz, T.A.; Chen, P.P.; Carson, D.A. Absence of methylthioadenosine phosphorylase in human gliomas. *Cancer Res.* **1991**, *51*, 3193–3197.
38. Olopade, O.I.; Jenkins, R.B.; Ransom, D.T.; Malik, K.; Pomykala, H.; Nobori, T.; Cowan, J.M.; Rowley, J.D.; Diaz, M.O. Molecular analysis of deletions of the short arm of chromosome 9 in human gliomas. *Cancer Res.* **1992**, *52*, 2523–2529.
39. Frazao, L.; do Carmo Martins, M.; Nunes, V.M.; Pimentel, J.; Faria, C.; Miguens, J.; Sagarribay, A.; Matos, M.; Salgado, D.; Nunes, S.; et al. BRAF V600E mutation and 9p21: CDKN2A/B and MTAP co-deletions—Markers in the clinical stratification of pediatric gliomas. *Bmc Cancer* **2018**, *18*, 1259. [CrossRef]
40. Hansen, L.J.; Sun, R.; Yang, R.; Singh, S.X.; Chen, L.H.; Pirozzi, C.J.; Moure, C.J.; Hemphill, C.; Carpenter, A.B.; Healy, P.; et al. MTAP Loss Promotes Stemness in Glioblastoma and Confers Unique Susceptibility to Purine Starvation. *Cancer Res.* **2019**, *79*, 3383–3394. [CrossRef]
41. Huang, T.; Li, S.; Yang, Z.; Liu, J.; Han, Y. Loss of Heterozygosity of 9p Is Associated with Poorer Survival in Patients with Gliomas. *Mol. Neurobiol.* **2016**, *53*, 6407–6412. [CrossRef] [PubMed]
42. Becker, A.P.; Scapulatempo-Neto, C.; Menezes, W.P.; Clara, C.; Machado, H.R.; Oliveira, R.S.; Neder, L.; Reis, R.M. Expression of Methylthioadenosine Phosphorylase (MTAP) in Pilocytic Astrocytomas. *Pathobiology* **2015**, *82*, 84–89. [CrossRef] [PubMed]
43. Simms, D.; Paul, E.; Cizdziel, P.E.; Piotr, C.N. Trizol: A new reagent for optimal single step of RNA. *Focus* **1993**, *15*, 532–535.
44. Batista, R.; Cruvinel-Carlioni, A.; Vinagre, J.; Peixoto, J.; Catarino, T.A.; Campanella, N.C.; Menezes, W.; Becker, A.P.; de Almeida, G.C.; Matsushita, M.M.; et al. The prognostic impact of TERT promoter mutations in glioblastomas is modified by the rs2853669 single nucleotide polymorphism. *Int. J. Cancer* **2016**, *139*, 414–423. [CrossRef] [PubMed]

45. Gaspar, N.; Marshall, L.; Perryman, L.; Bax, D.A.; Little, S.E.; Viana-Pereira, M.; Sharp, S.Y.; Vassal, G.; Pearson, A.D.; Reis, R.M.; et al. MGMT-independent temozolomide resistance in pediatric glioblastoma cells associated with a PI3-kinase-mediated HOX/stem cell gene signature. *Cancer Res.* **2010**, *70*, 9243–9252. [CrossRef] [PubMed]
46. Schneider, C.A.; Rasband, W.S.; Eliceri, K.W. NIH Image to ImageJ: 25 years of image analysis. *Nat. Methods* **2012**, *9*, 5. [CrossRef]
47. Wan, Y.-W.; Allen, G.I.; Liu, Z. TCGA2STAT: Simple TCGA data access for integrated statistical analysis in R. *Bioinformatics* **2016**, *32*, 952–954. [CrossRef]
48. Waggott, D.; Chu, K.; Yin, S.; Wouters, B.G.; Liu, F.F.; Boutros, P.C. NanoStringNorm: An extensible R package for the pre-processing of NanoString mRNA and miRNA data. *Bioinformatics* **2012**, *28*, 1546–1548. [CrossRef]
49. Zhao, M.; Zhao, Z. Concordance of copy number loss and down-regulation of tumor suppressor genes: A pan-cancer study. *Bmc Genom.* **2016**, *17* (Suppl. 7), 532. [CrossRef]
50. Crespo, I.; Tao, H.; Nieto, A.B.; Rebelo, O.; Domingues, P.; Vital, A.L.; Patino Mdel, C.; Barbosa, M.; Lopes, M.C.; Oliveira, C.R.; et al. Amplified and homozygously deleted genes in glioblastoma: Impact on gene expression levels. *PLoS ONE* **2012**, *7*, e46088. [CrossRef]
51. Zhang, H.; Chen, Z.H.; Savarese, T.M. Codeletion of the genes for p16INK4, methylthioadenosine phosphorylase, interferon-alpha1, interferon-beta1, and other 9p21 markers in human malignant cell lines. *Cancer Genet. Cytogenet.* **1996**, *86*, 22–28. [CrossRef]
52. Su, C.Y.; Chang, Y.C.; Chan, Y.C.; Lin, T.C.; Huang, M.S.; Yang, C.J.; Hsiao, M. MTAP is an independent prognosis marker and the concordant loss of MTAP and p16 expression predicts short survival in non-small cell lung cancer patients. *Eur. J. Surg. Oncol.* **2014**, *40*, 1143–1150. [CrossRef] [PubMed]
53. Ueki, K.; Ono, Y.; Henson, J.W.; Efirid, J.T.; von Deimling, A.; Louis, D.N. CDKN2/p16 or RB alterations occur in the majority of glioblastomas and are inversely correlated. *Cancer Res.* **1996**, *56*, 150–153. [PubMed]
54. Lopez, F.; Sampedro, T.; Llorente, J.L.; Hermsen, M.; Alvarez-Marcos, C. Alterations of p14 (ARF), p15 (INK4b), and p16 (INK4a) Genes in Primary Laryngeal Squamous Cell Carcinoma. *Pathol. Oncol. Res.* **2017**, *23*, 63–71. [CrossRef] [PubMed]
55. Krasinskas, A.M.; Bartlett, D.L.; Cieply, K.; Dacic, S. CDKN2A and MTAP deletions in peritoneal mesotheliomas are correlated with loss of p16 protein expression and poor survival. *Mod Pathol* **2010**, *23*, 531–538. [CrossRef]
56. Verhaak, R.G.; Hoadley, K.A.; Purdom, E.; Wang, V.; Qi, Y.; Wilkerson, M.D.; Miller, C.R.; Ding, L.; Golub, T.; Mesirov, J.P.; et al. Integrated genomic analysis identifies clinically relevant subtypes of glioblastoma characterized by abnormalities in PDGFRA, IDH1, EGFR, and NF1. *Cancer Cell* **2010**, *17*, 98–110. [CrossRef]
57. Malta, T.M.; de Souza, C.F.; Sabedot, T.S.; Silva, T.C.; Mosella, M.S.; Kalkanis, S.N.; Snyder, J.; Castro, A.V.B.; Nounshmehr, H. Glioma CpG island methylator phenotype (G-CIMP): Biological and clinical implications. *Neuro Oncol.* **2018**, *20*, 608–620. [CrossRef]
58. Turcan, S.; Rohle, D.; Goenka, A.; Walsh, L.A.; Fang, F.; Yilmaz, E.; Campos, C.; Fabius, A.W.; Lu, C.; Ward, P.S.; et al. IDH1 mutation is sufficient to establish the glioma hypermethylator phenotype. *Nature* **2012**, *483*, 479–483. [CrossRef]
59. Velázquez Vega, J.E.; Brat, D.J. Molecular-Genetic Classification of Gliomas and Its Practical Application to Diagnostic Neuropathology. In *Diffuse Low-Grade Gliomas in Adults*; Springer: Berlin/Heidelberg, Germany, 2017; pp. 73–100. [CrossRef]
60. Suzuki, T.; Maruno, M.; Wada, K.; Kagawa, N.; Fujimoto, Y.; Hashimoto, N.; Izumoto, S.; Yoshimine, T. Genetic analysis of human glioblastomas using a genomic microarray system. *Brain Tumor Pathol.* **2004**, *21*, 27–34. [CrossRef]
61. Sturm, D.; Witt, H.; Hovestadt, V.; Khuong-Quang, D.A.; Jones, D.T.; Konermann, C.; Pfaff, E.; Tonjes, M.; Sill, M.; Bender, S.; et al. Hotspot mutations in H3F3A and IDH1 define distinct epigenetic and biological subgroups of glioblastoma. *Cancer Cell* **2012**, *22*, 425–437. [CrossRef]
62. Vivanco, I.; Sawyers, C.L. The phosphatidylinositol 3-Kinase–AKT pathway in human cancer. *Nat. Rev. Cancer* **2002**, *2*, 489–501. [CrossRef] [PubMed]
63. Pearson, G.; Robinson, F.; Beers Gibson, T.; Xu, B.E.; Karandikar, M.; Berman, K.; Cobb, M.H. Mitogen-activated protein (MAP) kinase pathways: Regulation and physiological functions. *Endocr. Rev.* **2001**, *22*, 153–183. [CrossRef] [PubMed]

64. Rubinfeld, H.; Seger, R. The ERK Cascade: A Prototype of MAPK Signaling. *Mol. Biotechnol.* **2005**, *31*, 151–174. [CrossRef]
65. Sun, Y.; Zhao, C.; Ye, Y.; Wang, Z.; He, Y.; Li, Y.; Mao, H. High expression of fibronectin 1 indicates poor prognosis in gastric cancer. *Oncol. Lett.* **2019**. [CrossRef] [PubMed]
66. Zhou, X.; Hao, Q.; Liao, P.; Luo, S.; Zhang, M.; Hu, G.; Liu, H.; Zhang, Y.; Cao, B.; Baddoo, M.; et al. Nerve growth factor receptor negates the tumor suppressor p53 as a feedback regulator. *eLife* **2016**, *5*. [CrossRef] [PubMed]
67. Daubon, T.; Leon, C.; Clarke, K.; Andrique, L.; Salabert, L.; Darbo, E.; Pineau, R.; Guerit, S.; Maitre, M.; Dedieu, S.; et al. Deciphering the complex role of thrombospondin-1 in glioblastoma development. *Nat. Commun.* **2019**, *10*, 1146. [CrossRef] [PubMed]
68. Wang, J.; Deng, L.; Huang, J.; Cai, R.; Zhu, X.; Liu, F.; Wang, Q.; Zhang, J.; Zheng, Y. High expression of Fibronectin 1 suppresses apoptosis through the NF- $\kappa$ B pathway and is associated with migration in nasopharyngeal carcinoma. *Am. J. Transl. Res.* **2017**, *9*, 4502–4511.
69. Zhang, Z.; Fang, C.; Wang, Y.; Zhang, J.; Yu, J.; Zhang, Y.; Wang, X.; Zhong, J. COL1A1: A potential therapeutic target for colorectal cancer expressing wild-type or mutant KRAS. *Int. J. Oncol.* **2018**, *53*, 1869–1880. [CrossRef]
70. De Miguel, D.; Lemke, J.; Anel, A.; Walczak, H.; Martinez-Lostao, L. Onto better TRAILs for cancer treatment. *Cell Death Differ.* **2016**, *23*, 733–747. [CrossRef]
71. Knight, M.J.; Riffkin, C.D.; Muscat, A.M.; Ashley, D.M.; Hawkins, C.J. Analysis of FasL and TRAIL induced apoptosis pathways in glioma cells. *Oncogene* **2001**, *20*, 5789–5798. [CrossRef]
72. Kirkpatrick, C.A.; Selleck, S.B. Heparan sulfate proteoglycans at a glance. *J. Cell Sci.* **2007**, *120*, 1829–1832. [CrossRef] [PubMed]
73. Kaur, S.P.; Cummings, B.S. Role of glypicans in regulation of the tumor microenvironment and cancer progression. *Biochem. Pharmacol.* **2019**, *168*, 108–118. [CrossRef] [PubMed]
74. Kawakami, K.; Kawakami, M.; Snoy, P.J.; Husain, S.R.; Puri, R.K. In vivo overexpression of IL-13 receptor alpha2 chain inhibits tumorigenicity of human breast and pancreatic tumors in immunodeficient mice. *J. Exp. Med.* **2001**, *194*, 1743–1754. [CrossRef] [PubMed]
75. Fujisawa, T.; Joshi, B.H.; Puri, R.K. IL-13 regulates cancer invasion and metastasis through IL-13Ralpha2 via ERK/AP-1 pathway in mouse model of human ovarian cancer. *Int. J. Cancer* **2012**, *131*, 344–356. [CrossRef] [PubMed]
76. Lee, J.; Kotliarova, S.; Kotliarov, Y.; Li, A.; Su, Q.; Donin, N.M.; Pastorino, S.; Purow, B.W.; Christopher, N.; Zhang, W.; et al. Tumor stem cells derived from glioblastomas cultured in bFGF and EGF more closely mirror the phenotype and genotype of primary tumors than do serum-cultured cell lines. *Cancer Cell* **2006**, *9*, 391–403. [CrossRef] [PubMed]
77. Caragher, S.; Chalmers, A.J.; Gomez-Roman, N. Glioblastoma’s Next Top Model: Novel Culture Systems for Brain Cancer Radiotherapy Research. *Cancers* **2019**, *11*. [CrossRef]
78. Bertino, J.R.; Waud, W.R.; Parker, W.B.; Lubin, M. Targeting tumors that lack methylthioadenosine phosphorylase (MTAP) activity: Current strategies. *Cancer Biol.* **2011**, *11*, 627–632. [CrossRef]
79. Bax, D.A.; Little, S.E.; Gaspar, N.; Perryman, L.; Marshall, L.; Viana-Pereira, M.; Jones, T.A.; Williams, R.D.; Grigoriadis, A.; Vassal, G.; et al. Molecular and phenotypic characterisation of paediatric glioma cell lines as models for preclinical drug development. *PLoS ONE* **2009**, *4*, e5209. [CrossRef]
80. Martinho, O.O.R.; Miranda-Gonçalves, V.; Clara, C.; Almeida, J.R.; Carvalho, A.L.; Barata, J.T.; Reis, R.M. In Vitro and In Vivo Analysis of RTK Inhibitor Efficacy and Identification of Its Novel Targets in Glioblastomas. *Transl. Oncol.* **2013**, *6*, 187–196. [CrossRef]
81. Cruvinel-Carloni, A.; Silva-Oliveira, R.; Torrieri, R.; Bidinotto, L.T.; Berardinelli, G.N.; Oliveira-Silva, V.A.; Clara, C.A.; de Almeida, G.C.; Martinho, O.; Squire, J.A.; et al. Molecular characterization of short-term primary cultures and comparison with corresponding tumor tissue of Brazilian glioblastoma patients. *Transl. Cancer Res.* **2017**, *6*, 332–345. [CrossRef]



Review

# Resistance Mechanisms and Barriers to Successful Immunotherapy for Treating Glioblastoma

Jason Adhikaree <sup>1,\*</sup>, Julia Moreno-Vicente <sup>2</sup>, Aanchal Preet Kaur <sup>1</sup>, Andrew Mark Jackson <sup>1</sup> and Poulam M. Patel <sup>1</sup>

<sup>1</sup> Host-Tumour Interactions Group, Division of Cancer and Stem Cells, BioDiscovery Institute, University of Nottingham, Nottingham NG7 2RD, UK; Aanchal.Kaur@nottingham.ac.uk (A.P.K.); andrew.jackson@nottingham.ac.uk (A.M.J.); poulam@nottingham.ac.uk (P.M.P.)

<sup>2</sup> Antibody and Vaccine Group, Centre for Cancer Immunology, University of Southampton, Southampton General Hospital, Southampton, Hants SO16 6YD, UK; jmv1e16@soton.ac.uk

\* Correspondence: jason.adhikaree@nottingham.ac.uk

Received: 31 December 2019; Accepted: 16 January 2020; Published: 21 January 2020



**Abstract:** Glioblastoma (GBM) is inevitably refractory to surgery and chemoradiation. The hope for immunotherapy has yet to be realised in the treatment of GBM. Immune checkpoint blockade antibodies, particularly those targeting the Programme death 1 (PD-1)/PD-1 ligand (PD-L1) pathway, have improved the prognosis in a range of cancers. However, its use in combination with chemoradiation or as monotherapy has proved unsuccessful in treating GBM. This review focuses on our current knowledge of barriers to immunotherapy success in treating GBM, such as diminished pre-existing anti-tumour immunity represented by low levels of *PD-L1* expression, low tumour mutational burden and a severely exhausted T-cell tumour infiltrate. Likewise, systemic T-cell immunosuppression is seen driven by tumoural factors and corticosteroid use. Furthermore, unique anatomical differences with primary intracranial tumours such as the blood-brain barrier, the type of antigen-presenting cells and lymphatic drainage contribute to differences in treatment success compared to extracranial tumours. There are, however, shared characteristics with those known in other tumours such as the immunosuppressive tumour microenvironment. We conclude with a summary of ongoing and future immune combination strategies in GBM, which are representative of the next wave in immuno-oncology therapeutics.

**Keywords:** glioblastoma; immunotherapy; resistance mechanisms; programme death-1; immune checkpoint blockade

## 1. Introduction

There is a high clinical need for new approaches to combat glioblastoma (GBM) outside of the traditional approaches such as surgery, radiation and chemotherapy. Immunotherapy, and particularly, the inhibition of the programme death 1 (PD-1)/PD-1 ligand (PD-L1) pathway, has arisen as a successful strategy to treat several cancers types [1–7]. Since the first Food and Drug Agency (FDA) approval in 2014 of Pembrolizumab, a PD-1 inhibitor, to treat metastatic melanoma, there have been a further five drugs developed in this class with almost fifty FDA approvals within the last five years between them. In conjunction with the rapid growth in clinical utility of immune checkpoint inhibitors, there is now increasing knowledge of mechanisms of action, biomarkers, disease response patterns and toxicity in relation to cancer immunotherapy treatment. This has led to a renewed hope that this class of immunotherapies will provide the long-anticipated immunotherapy breakthrough to treat GBM.

Unfortunately in 2019, two-phase III first-line trials recruiting patients with either methylated or unmethylated O6-methylguanine methyltransferase (MGMT) GBM using Nivolumab (a PD-1 inhibitor)



concurrently with standard of care radiotherapy or chemoradiotherapy, failed to meet its primary end-point of improved progression-free or overall survival. Likewise, a completed randomised phase III trial using Nivolumab in relapsed patients with GBM, failed to meet its primary outcome of improved overall survival versus Bevacizumab [8]. A disappointing response rate of 8% was seen in this trial, however, those few who responded had a durable response (median 11.1 months with Nivolumab vs. 5.3 months with Bevacizumab) suggesting a subgroup of patients who could derive benefit from such approaches. However, this highlights the current priority area in the immuno-oncology field of how to treat checkpoint blockade unresponsive tumours. This review aims to evaluate the unique challenges of using PD-1/PD-L1 axis inhibiting drugs and other immunotherapies to treat GBM, and barriers that may restrict their success. It also considers what can be learnt from other tumour types and whether this is the beginning or end of PD-1 targeted immunotherapies in GBM.

## 2. Why is the PD-1/PD-L1 Pathway a Relevant Therapeutic Target to Treat Cancer?

Cytotoxic T-lymphocytes (CTL) can selectively kill cancer and viruses while sparing healthy tissue. However, these tumour-specific T-cells are suppressed in the tumour microenvironment [9]. *PD-1* is an inhibitory transmembrane receptor dynamically expressed upon T-cell receptor (TCR) engagement on activated T-lymphocytes. It favours immune evasion in cancer by down-regulating T-cell activation and effector function [10]. Although absent in naïve T-cells, higher levels of PD-1 are found on infiltrating T-lymphocytes, which are thought to be exhausted due to chronic antigen stimulation [11,12]. On binding to its ligand, PD-L1 and PD-L2, SHP-2 phosphatase is recruited to the cytoplasmic immunoreceptor tyrosine-based switch motif (ITSM) domain of PD-1. This and other phosphatases attenuate the co-stimulatory signal predominately through CD28 [13]. Furthermore, signalling through the co-stimulation B7/CD28 complex is required for PD-1 inhibitors to be effective, illustrating the importance of this signal [13,14].

The ligation of *PD-1* on T-cells, by tumour or tumour-infiltrating immune cells expressing *PD-L1*, results in T-cell dysfunction. This includes, but is not limited to, attenuation of activation, decreased cytokine secretion and impaired production of cytotoxic molecules. There is also reduced anti-apoptotic and increased pro-apoptotic gene expression, thereby decreasing T-cell survival. In addition, metabolic reprogramming within T-cells further contributes to T-cell exhaustion and inhibition [10]. Therefore, immune evasion mediated by PD-1/PD-L1 signalling may explain why endogenous or strong vaccine-induced T-cell responses against tumour antigens fail to translate to tumour regression [15]. The relevance of this axis is further supported by the recent explosion of FDA approvals for drugs that target this axis.

It transpires that there are many such receptors that modulate the T-cell response and, therefore, it is somewhat surprising that a single checkpoint has translated to such clinical success [16].

## 3. Clinical Efficacy of Immune Checkpoint in GBM

The remarkable responses to PD-1 inhibitors seen in lymphoma subtypes, where response rates are high (87% in Hodgkin's lymphoma), are not recapitulated by solid organ cancers where response rates range from 15 to 40% [17]. This means that, despite significant and durable responses in patients that respond, the majority will progress and, furthermore, be at risk of immunotherapy associated side effects.

Recently, phase III, randomised, multicentre trial, checkmate-143, compared Nivolumab to Bevacizumab in 369 relapsed GBM patients, showed no overall survival advantage for the PD-1 inhibitor above Bevacizumab [8]. In both treatment arms, 40% of patients were on steroids at baseline including approximately 15% in both arms taking  $\geq 4$  mg/day. The median overall survival (OS) was 9.8 months with Nivolumab compared to 10.0 months with bevacizumab and the 12-month OS rate was 42% in both treatment arms. The progression-free survival was shorter in the Nivolumab group at 1.5 months, compared to 3.5 months in Bevacizumab group. Likewise, the objective response rate was lower in the Nivolumab group –8% vs. 23%, despite the majority of patients having measurable disease

at baseline (83%). The duration of response was, however, longer with Nivolumab –11.1 months compared to 5.3 months and less grade 3–4 treatment-related adverse events (13% vs. 18%). However, on the basis of this phase III trial Nivolumab could not be recommended in the relapsed setting for GBM.

In May 2019, a Bristol Squibb Myers press release stated that the eagerly awaited front line phase III trial, Checkmate-498, had failed to meet its primary endpoint of overall survival (OS) and both secondary endpoints of progression-free survival (PFS), and OS rate at two years. This trial recruited over 500 treatment-naïve patients to receive either Nivolumab plus radiation or Temozolomide plus radiation. After surgery, patients in the experimental arm received Nivolumab every two weeks concurrent with radiation, followed by maintenance with Nivolumab every four weeks until disease progression or unacceptable toxicity. Eligible patients had centrally confirmed mgMT-unmethylated disease and a Karnofsky performance status  $\geq 70$ . Likewise, the randomised, multicentred phase III frontline trial, Checkmate-548, which recruited mgMT-methylated GBM, had a similar press release in September, stating a failure to meet the primary endpoint of PFS, although OS data is not mature. This trial compared the addition of Nivolumab with Temozolomide and radiation compared to Temozolomide and radiation alone.

There has also been published case series and early phase trials investigating combination therapy approaches. Part of the checkmate-143 trial comprised multiple phase I safety cohorts of Nivolumab or Nivolumab in combination with Ipilimumab. In the former, the monotherapy arm ( $n = 10$ ) produced one partial response and no grade 3–4 toxicities. This contrasts to Nivolumab 1 mg and Ipilimumab 3mg, where 9 of the 10 patients experienced grade 3–4 toxicities and 5 discontinued the drug due to adverse events. This is not unexpected, as the combination of Nivolumab with Ipilimumab is known to have a maximum tolerated dose in both melanoma and non-small cell lung cancer (NSCLC), and in combination is too toxic to use at full monotherapy doses [18,19]. However, in contrast to melanoma, increased toxicity was not accompanied by increased objective response rates. In this cohort, 0/10 patients achieved a partial response [20]. Nivolumab at 3 mg and Ipilimumab at 1 mg produced one partial response ( $n = 20$ ) [21]. The first reports of clinical efficacy using Pembrolizumab in relapsed GBM patients found 1 partial response in the first cohort of 6. The study also extended to combination use with bevacizumab, which was reported as safe [22].

There are also initial reports on multimodal combination strategies. For example, Pembrolizumab at two doses (100 mg and 200 mg every three weeks), combined with hypo-fractionated radiotherapy and bevacizumab was again shown to be safe. The responses of the first three patients treated with 100 mg dose is known and included two stable disease and one complete response at the time of abstract publication [23].

Overall, however, the available data on PD-1 inhibitors in GBM are mainly from published abstracts and case studies, as summarised in Table 1. We can infer that there is a similar safety profile to that known in other solid cancers, but initial response rates are lower (Table 1). More mature trial information will guide objective response rates and, more importantly, survival data. Nevertheless, numerous combination trials are already underway with the aim of improving efficacy.

**Table 1.** Clinical efficacy of programme death 1 (PD-1) therapy in Glioblastoma.

Drug	Patient Cohort	Study Type	Toxicity	Efficacy	Reference
Pembrolizumab	Recurrent GBM ( $n = 9$ ), AA ( $n = 2$ ), BSG ( $n = 1$ ), Paeds ( $n = 5$ )	Retrospective	Safe	No responses	Blumenthal et al. 2015 [24]
Pembrolizumab + Bevacizumab	Recurrent GBM N = 6	Phase I	Safe	1 PD 2 SD 3 PD	Reardon et al. 2016 [22]
Pembrolizumab + hypo-fractionated RT + Bevacizumab	Recurrent GBM or AA N = 3	Phase I	Safe	1 CR 2 SD	Sahebjam et al. 2016 [23]

Table 1. Cont.

Drug	Patient Cohort	Study Type	Toxicity	Efficacy	Reference
Pembrolizumab	Recurrent solid tumours, Glioma (n = 3)	Case series	Safe	1 MR	Leibowitz-amit et al. 2015 [25]
Pembrolizumab	Hypermutated GBM (POLE germline deficiency)	Case study	Safe	1 PR	Johanns et al. 2016 [26]
Nivolumab +/- Ipilimumab	Recurrent GBM Monotherapy (3 mg/kg) (n = 10)	Phase I	0 grade 3–4 AE 1 discontinued due to AE	1 PR 5 SD 3 PD	Reardon et al. 2016 [20]
	Nivolumab 1 mg/Ipilimumab 3 mg (n = 10)	Phase I	9/10 grade 3–4 AE 5 discontinued	0 PR 4 SD 6 PD	
	Nivolumab 3 mg/Ipilimumab 1 mg (n = 20)	Phase I	5/20 grade 3–4 AE 2 discontinued	0 PR 10 SD 9 PD	
Nivolumab	Paediatric GBM with biallelic mismatch repair deficiency (n = 2)	Case study	1 seizure at initiation	2 PR	Bouffet et al. 2016 [27]
Pembrolizumab + Bevacizumab + GMCSF	Recurrent GBM (n = 4)	Case series	Safe	1 PR 3 SD	Brown et al. 2016 [28]
Durvalumab	Recurrent GBM (n = 31)	Phase II, cohort B	Safe 9.7% Grade 3–4 AE	4 PR 14 SD 12mOS –44.4%	Reardon et al. 2017 [29]
PD-1 inhibitors + RT	Recurrent HGG (n = 20)	Case series	Safe	7 PR 5 SD 8PD	Iwamoto et al. 2017 [30]
Nivolumab	Recurrent GBM	Case report	Safe	PR	Roth et al. 2017 [31]
Nivolumab vs. Bevacizumab	Recurrent GBM (n = 369)	Phase III	13% grade 3–4 toxicity Nivolumab	RR 8% vs. 23% (Nivolumab vs. Bevacizumab)	Reardon et al. 2017 [8]
Nivolumab + RT vs. TMZ + RT	1 <sup>st</sup> line (n = 550) unmethylated-MGMT	Phase III	not published	failed to extend OS and PFS	BMS Press release
Nivolumab+TMZ + RT vs. TMZ + RT	1 <sup>st</sup> line (n = 693) methylated mgMT	Phase III	not published	failed to extend PFS	BMS Press release

RT = radiotherapy; TMZ = Temozolomide; PR = partial response; SD = stable disease; MR = mixed response; PD = progressive disease; HGG = high grade glioma; AA = anaplastic astrocytoma; BSG = brain stem glioma; Paeds = paediatric; POLE = DNA polymerase epsilon deficiency; OS = overall survival; PFS = progression-free survival; GMCSF = granulocyte-macrophage colony-stimulating factor.

#### 4. Brain Tumour Immunity and Barrier to Immunotherapy

The brain has historically been seen as an immuno-privileged site, however, it is now clear that this is highly contextual. The lack of traditional lymphatics and known antigen-presenting cells have supported this theory [32]. The challenge of immunotherapy to treat GBM are numerous and includes a limited understanding of basic cellular mechanisms governing anti-tumour responses in the brain, mechanical barriers such as the blood–brain barrier (BBB), in addition to a suppressive tumour microenvironment (TME).

##### 4.1. Antigen Presentation Cell (APC)

Microglia cells are tissue resident macrophages that have entered the CNS in early embryonic life. When activated, microglia express MHC class I and II molecules, as well as adhesion and co-stimulatory molecules, acquiring the ability to act as APCs [33–35]. Microglia express toll-like receptors 1–9 and nucleotide-binding oligomerisation domain-like receptors which contributes to their activation and recognition of a range of pathogen-associated molecular patterns [36]. Macrophage and microglial cells have functional plasticity and polarise their phenotype depending on the cytokine milieu and microbial environment. The M1 phenotype is activated by IFN- $\gamma$  and lipopolysaccharide (LPS) to polarise

a macrophage towards a pro-inflammatory IL-12 secreting cell capable of supporting a Th1 response. The M2 or alternatively activated phenotypes are induced by IL-10, glucocorticoids or IL-4 to induce a Th2 or immunoregulatory response [37]. However, in the context of high-grade gliomas, current data suggest that microglia lose their capacity to present antigens due to the highly immunosuppressive TME and resemble alternatively activated macrophages [36,38]. For example, TGF- $\beta$  inhibits microglial proliferation and when microglial cells are co-cultured with glioma stem cells, they phenotypically revert to an M2 status. These microglial cells have reduced phagocytosis and secrete high levels of IL-10 [39]. The M2 phenotype microglial cells also have lower MHC-class II and surface co-stimulatory molecule expression, reducing antigen-presenting capacity [40,41]. Indeed, microglia have a large regulatory role in the central nervous system (CNS) immunity and plasticity which is utilized by glioma to promote growth. Upwards of 30% of a GBM tumour mass can include these immune cells and higher numbers are seen at higher grades [42]. Microglia release chemoattractants (monocyte chemoattractant protein-1 (MCP-1) and macrophage inflammatory protein-1) when associated with glioma cells promoting further microglial/monocyte recruitment from the peripheral blood and, in combination with the cytokine milieu (IL-10, TGF- $\beta$  and IL-6), promote further immunosuppression [36,41]. Furthermore, glioma-associated microglia can release matrix metalloproteinase-14, which degrades normal brain parenchyma and promotes tumour invasion [43].

Distinct from the role of microglia, T-cell reactivation can occur in several anatomical niches including the choroid plexus, the meninges and the perivascular space within the CNS parenchyma, where co-localisation with distinct antigen-presenting cells and T-cells are seen [44]. For example, classical myeloid dendritic (cDC) type 1 cells have been identified in the CSF space adjacent to subarachnoid vessels and choroid plexus stroma. cDC type 2 have been identified in post-capillary venules of parenchymal tissue in mouse models [44]. These cells are potent antigen-presenting cells capable of re-stimulating a T-cell response. There are also distinct macrophage populations at these sites, with perivascular macrophages sharing embryonic origins with microglia, while choroid plexus macrophages are replenished by blood-derived monocytes [44]. There is also a consensus that lymphatic drainage of the outer lining and subarachnoid space is via dural sinuses and into deep cervical lymph nodes, where MHC class II-expressing cells localize and can present antigen [45,46]. Hence, this route may indeed prove the pivotal source of antigen presentation within the CNS. Interestingly, recent single-cell mass and fluorescence cytometry in parallel with genetic fate mapping systems, have shown key differences in the dendritic cell, microglia and macrophage distribution and abundance in disease and ageing [47]. It is known that microglial cells appear to be the only leukocyte in the brain parenchyma in the steady-state. However, outside the parenchyma, in the choroid plexus, perivascular space and lining the meninges they found 4 distinct subsets of macrophages which they named border associated macrophages (BAM). These subsets may have different roles in disease, for example the CCR2<sup>+</sup> subset was predominately found near the choroid plexus and have a high turnover from bone-marrow. This has implications for disease, for example, in an experimental autoimmune encephalitis (EAE) mouse model, the BAM decreased in frequency, replaced by peripheral monocytes and a homogenous BAM MHCII<sup>+</sup>CD38<sup>+</sup> population was seen [47]. They also found that during EAE, microglia skewed to an inflammatory phenotype, which was also seen in ageing and Alzheimer disease mouse models, suggesting a common activation programme [47]. Additionally, they confirmed that the cDC2, cDC1 and plasmacytoid DC exist intracranially and, consistent with recent descriptions in the periphery, cDC2 are a heterogeneous cell group as defined by surface marker expression. Such studies identifying the heterogeneity of innate cells and dynamic infiltration into the brain and will guide future immunotherapy combinations for targeting GBM.

Clinical support of antigen detection in the CNS and extracranial de-novo T-cell responses are seen from reports of the abscopal effect following CNS radiotherapy [48,49]. In a series of 13 patients whom received CNS radiotherapy for metastatic melanoma and had disease progression in the brain following Ipilimumab, 7 experienced a partial response at extracranial sites including liver, lung, pelvic and cutaneous [49]. This provides support to the theory that the presentation of glioma antigens can

trigger a peripheral immune response, likely via priming and activation in the deep cervical lymph nodes [46].

#### 4.2. Lymphatics

The lack of traditional lymphatics has led to controversies in regard to the CNS communication with peripheral lymph nodes and therefore the site of antigen presentation and T cell priming. However, the cervical lymph nodes seem to be important with in-vivo tracers following CNS antigens draining through CSF, across the cribriform plate and into the nasal mucosa. This subsequently drains into the cervical lymph nodes [50]. Recently, dissection of mouse meninges and immunohistochemistry staining has co-localised endothelial cells, T-cells and *MHC-II* expressing cells with high concentration of immune cells near the dural sinuses. Indeed, intravenous and intracerebral injection of lectin dyes and anti-CD45 fluorescent antibodies have revealed alignment of T-cells and antigen-presenting cells along perisinusoidal vessels [46]. Alternatively, soluble antigens have been shown to travel down a separate pathway in the perivascular spaces within the wall of the cerebral arteries and into the cervical lymph nodes [51].

Further support to the importance of the cervical lymph nodes in T-cell priming comes from a mouse model of MS, EAE. This condition occurs in mice after intracranial injection of purified myelin antigen and is exacerbated by an intracranial cryo-lesion. The removal of the cervical lymph nodes, prior to inflicting the cryo-lesion ameliorates this phenotype [50].

Furthermore, in the perivascular space, circulates T-cells which display a memory phenotype, rather than naive [35]. In support of this, homing of CD8<sup>+</sup> T-cells towards the brain has been found to occur after the presentation of tumour-specific antigens at the cervical lymph nodes [52]. Under physiological circumstances, activated memory CD4<sup>+</sup> T-cells enter the CSF from the bloodstream and monitor perivascular spaces as part of the immunosurveillance machinery in the CNS. Upon encounter of antigen-loaded APCs, CD4<sup>+</sup> T-cells differentiate into effector cells and acquire the competence to invade the parenchyma, thereby triggering local immune responses in the brain [53]. In a similar fashion, many CD8<sup>+</sup> T-cells that are found in the CNS during neuroinflammation display an effector memory phenotype and are thought to be selectively recruited by  $\alpha 4$ -integrin-expressing endothelial cells at the BBB [54]. This data supports the notion that there is a constant interaction between the extracranial and intracranial immune responses and suggests that the priming and expansion of T-cells occurs outside the CNS in the cervical lymph nodes.

#### 4.3. Blood–Brain Barrier (BBB) and Immune Privilege

The blood–brain barrier is not a static barrier, but dynamic. The integrity of the BBB across CNS microvessels relies on endothelial cells and intact tight junctions between them. This close association reduces permeability and prevents solute exchange to occur paracellularly [55–57]. Nevertheless, the endothelial BBB is a dynamic entity that responds to environmental cues. Inflammation and brain pathologies can compromise the integrity of the BBB, thereby increasing its permeability, and thus allowing the infiltration of circulating monocytes and lymphocytes from the periphery [57,58]. As in other tissues, the extravasation of T-cells across the BBB involves the interaction between specific adhesion molecules and chemokines expressed on immune and endothelial cells. However, trafficking into the brain is known to be less efficient than in other organs and may involve transcellular instead of paracellular extravasation, to preserve endothelial tight junctions [57,59]. For example, there is also evidence that inducible metalloproteinases facilitate penetrance of leukocytes migration following perivascular cuffing across the glia limitans and basement membrane, particularly in inflammation such as a diseased pathology of the brain [60]. In the inflamed blood–brain barrier, monocytes, Th1 and Th17 cells migration across the blood–brain barrier is a multistep process involving E- and P-selectin mediated rolling along the surface of the endothelium, followed by chemokine mediated activation and adhesion to the endothelium. This is preceded by intracellular adhesion molecule-1 (ICAM-1) and vascular adhesion molecule-1 (VCAM-1) and activated leukocyte adhesion molecule

(ALCAM) upregulation by pro-inflammatory cytokines. These bind to affiliated T-cell receptors leukocyte function-associated antigen-1 (LFA-1), very late antigen-4 (VLA-4) and CD6. BBB endothelial cells and glial cells are an important source of the pro-inflammatory chemokines such as CCL2/MCP-1, RANTES and CXCL10/IP-10 and thus facilitate immune cell recruitment. CD8<sup>+</sup> T-cells seem to be dependent on  $\alpha$ 4 integrin, distinct to the aforementioned mechanisms [54,57,61,62]. Immunoglobulins can also cross the BBB via the immunoglobulin receptor, FcRn, by carrier-mediated transportation via the cerebral blood vessel and into the brain parenchyma [63–65].

Clinical support of the effective penetration of T-cells into the CNS comes from a phase II trial which included 52 patients with untreated or progressive brain metastases diagnosed with metastatic melanoma or NSCLC. These patients had similar responses intracranially, as to their extracranial disease following treatment with Pembrolizumab, a T-cell immune checkpoint inhibitor, targeting PD-1 [66]. Thus, suggesting that these drugs are effective intracranially if the relevant immune signatures against the tumour are present. This has also been observed in GBM, where a recent case report of two patients with recurrent GBM on a background of paediatric biallelic mismatch deficiency, had a deep and durable response to Nivolumab [27]. These tumours have a high mutational burden, which predicts response to immune checkpoint blockade and is discussed later. Although a rare subtype of GBM, in certain countries, where consanguineous rates are higher, biallelic mismatch repair deficiency is estimated to account for 40% of paediatric GBM cases [67].

#### 4.4. T-cell Dysfunction

GBM patients have been recognised to have severe deficits in cell-mediated immunity, particularly within the lymphocyte population [68,69]. This has been narrowed down to the CD4 compartment. T-regulatory cells (Tregs) are highly diverse and plastic subset of CD4 T-cells and have a universal role in immune tolerance [70]. The thymic derived, natural Tregs (nTregs), characterised by high constitutive expression of *FoxP3*, cause contact-dependent cytokine independent immunosuppression through CTLA-4, PD-L1, granzyme/perforin and Fas/FasL pathways [32]. Inducible Tregs, have transient or absent *FoxP3* expression and induce immunosuppression through IL-10 and TGF- $\beta$  [71]. Fecci et al. described suppressed absolute CD4 counts in 20 patients with GBM, however, they noted the fraction containing CD4<sup>+</sup>CD25<sup>+</sup>FoxP3<sup>+</sup>CD45RO<sup>+</sup> T cells was increased compared to healthy controls [72]. Overall these patients' T-cells showed anergy or secreted Th2 polarising cytokines on stimulation. Removal of the Treg population reversed this cytokine signature. Furthermore, in the murine immunocompetent model using the mouse strain VM/Dk injected with SMA-560 (mouse glioma cell tumour) intracranially, anti-CD25 was shown to deplete Tregs and increase survival [72]. Similarly, the presence of tumour infiltrating lymphocytes has been described as improving prognosis, although the rate of infiltration is low [73]. In support of an important role of Tregs in glioma is an immunohistochemistry study comprising 62 patients, whose tumours were stained for FoxP3 and CD8 and found Treg accumulation at the tumour site was associated with poorer prognosis, while CD8<sup>+</sup> tumour infiltrating lymphocytes (TILs) were not associated with increased survival [74]. Indeed, the nTreg population may predominate in glioma, with high *FoxP3* expression also seen by another group in glioma samples and linked with higher grade and high levels of Helios transcription factor, another nTreg marker [75,76]. This group expanded this theory to a mouse orthotopic model with intracranially injected (i.c.) GL261 mouse cell line of GBM and found thymectomy, prior to i.c., significantly decreased Treg levels [76]. This may be through high expression of *CCL-2* chemokine by glioma. In 19 GBM patients where CD4/CD25<sup>bright</sup> cells were isolated, Tregs migrated preferentially to glioma conditioned media and was reversed by using a *CCL-2* blocking antibody [77].

A more recent study has quantified the CD4 compartment compromise in newly diagnosed GBM as equivalent to that in HIV patients. They found GBM patients had CD4<sup>+</sup> counts of  $\leq 200/\mu\text{L}$  compared to a healthy adult numbers of  $>1000$  [78]. They proposed a mechanism of sequestration of T-cells in the bone marrow of patients causing a relative lymphopenia through loss of sphingosine-1-phosphate (S1P) receptor on the T-cell surface. In health, a S1P ligand gradient directs T-cell chemotaxis to blood

and lymph node areas and maintains circulating lymphocyte frequency [78]. They showed in mice which are S1P1-deficient, T cells accumulated in the bone marrow of glioma-bearing mice. However, S1P1-knockin, glioma-bearing mice did not have T-cell sequestration [78].

It is now clear that evidence of pre-existing anti-tumour immunity predicts response to PD-1 therapy [79]. Immunologically 'hot' tumours, which includes those with high *PD-L1* expression, adjacent CD8 TILs, enriched interferon gene signature and upregulation of other checkpoints have shown stronger predictive value [79]. This is in contrast to 'cold' tumours that have no immune infiltrate. A number of studies have shown that *PD-L1* is expressed on GBM tissue albeit at variable levels. A range between 50–90% positive cells was described in a cohort of 10 primary GBM samples, which was later backed by a larger cohort of 135 samples, of which 86% expressed the marker [80,81]. Contrary to this, another study of 92 IHC samples showed that a median of 2.7% of tumour cells expressed *PD-L1*, despite 61% defined as positive using a threshold of  $\geq 1\%$ . The same study also performed flow cytometry on five primary samples, which was supportive of their IHC analysis [82]. Hence, although a reasonable proportion of samples are positive by the 1% cut-off, these are of low intensity. PD-L1 is often viewed as a signature of pre-existing immunity, where this is a fingerprint of previous IFN- $\gamma$  release by an antigen-specific cytotoxic T-lymphocyte (CTL). However, oncogenic pathways can also lead to constitutive *PD-L1* expression. Mutated/loss of PTEN leads to increased PI3K pathway activation and subsequent *PD-L1* up-regulation [83]. Mutations/inactivation of the *PTEN* gene ranges from 5–40% in GBM [84]. Others have shown that in pre-clinical melanoma models, loss of PTEN in tumour cells inhibits T-cell mediated killing and decreases T-cell trafficking. In patients with melanoma, loss of PTEN correlated with decreased T-cell infiltrate and poorer response to PD-1 therapy [85]. However, in this study loss of PTEN was not associated with increased *PD-L1* expression and hence, at least in melanoma, PTEN causes immunosuppression independent of PD-L1 [85]. Oncogene activation, such as *MYC* and *EGFR*, also up-regulate *PD-L1* expression and attenuates the anti-tumour response [86–88]. Therefore, whether the mechanism of *PD-L1* expression is oncogene-driven intrinsic constitutive expression, or adaptive upregulation via the STAT pathways in response to IFN, is of unknown importance. Ultimately, the clinical response to PD-1 antibody, in the phase III trial of relapsed GBM, had been disappointing [8].

Another important element that differentiates immunologically 'hot' tumours, likely to respond to immunotherapy, from 'cold' inert tumours, is mutational burden [79]. With higher mutational burden, greater neoantigens are created, which leads to a greater potential for T-cell repertoire against tumour specific antigens [89]. This is supported by estimates of neoantigens using exome sequencing of tumours, where melanoma and NSCLC have the greatest numbers of somatic mutations and neoantigens predicted. This is clinically validated, as these tumours are known to be particularly sensitive to checkpoint inhibitors. In contrast, GBM sits in the lower third of neoantigens burden in the 30 tumours reported in this study [90].

One subgroup of patients, that have a high mutational load regardless of cancer site of origin are mismatch repair (MMR) tumours. A phase II study showed that in 41 patients with mainly colorectal cancer, those whom were MMR proficient were unresponsive to PD-1 inhibitor; however, those MMR deficient tumours had objective response rates  $>70\%$  to PD-1 inhibitor [91]. This was also seen in the non-colorectal MMR deficient cancers ( $n = 7$ ) in this study. On average, the MMR tumour had 100-fold greater somatic mutations than the proficient tumours [91]. This has also been observed in GBM, where a recent case report of two patients with recurrent GBM on a background of paediatric biallelic MMR deficiency, had a deep and durable response to Nivolumab [27].

It has also been well described that recurrent GBM has a high frequency of mutations in the *MSH6* MMR gene, which is seen as a consequence to previous Temozolomide treatment and induces a hypermutated phenotype [92].

Interestingly, two recent phase I trials in GBM have shown that it is possible to turn cold tumours hot. Kerstin et al. used a vaccine designed to target neoantigens, personalised to 8 patients, 5 of which had surgical resection following disease progression while on the vaccine treatment. In the two patients,

not taking corticosteroids, TIL infiltrate targeting the neoantigens was seen and had upregulated a number of immune checkpoints, potentially accounting for the disease progression [93]. Likewise, using a similar protocol another group used personalised vaccines based on mutation analyses of the transcriptomes and immunopeptidomes of the individual tumours. Two vaccines were administered in 15 patients against both unmutated and neo-antigens. They were able to elicit CD8<sup>+</sup> T-cell expansion in the unmutated antigen vaccine and CD4 responses against neoantigens. In a patient who had a response, tumour resection showed a favourable CD8<sup>+</sup>:regulatory T (Treg) cell ratio and CD4<sup>+</sup> T-cell reactivity against one immunised peptide [94].

It may be that a particular subtype of GBM is more immunogenic. Using The Cancer Genome Atlas data, the mesenchymal subtype upregulated both proinflammatory and immunosuppressive gene profiles. For example, there was mRNA rich signature suggesting immune checkpoint activation such as PD-L1, CTLA-4 and galectin-3 (ligand to TIM-3), immunosuppressive monocyte and macrophage recruiters (CCL2, CD163 and CD204) and Treg markers [95]. This mixed immune signature suggests combination immune strategies may be successful for this subtype.

A recent publication has revealed that the poor response rates seen to PD-1 inhibitor monotherapy may be due to the upregulation of multiple checkpoints and a more severely exhausted T-cell phenotype [96]. Woroniecka et al. have studied T-cell exhaustion in GBM in more depth. They isolated TIL and peripheral blood lymphocytes (PBL) from 21 GBM patients and assessed for the presence of multiple immune checkpoint markers including PD-1, CTLA-4, TIM-3, LAG-3, CD160, 2B4, TIGIT, CD39, and BTLA [96]. Interestingly, they found PD-1<sup>+</sup>CD8<sup>+</sup> were present in 96% of patient TIL samples. The CD8<sup>+</sup> T-cells were of an effector memory phenotype (CD45RA<sup>-</sup>CD62L<sup>-</sup>), however, noted LAG-3, TIGIT, TIM-3 and CD39 were all upregulated, in addition to PD-1. They also measured post-stimulation levels of intracellular IFN- $\gamma$ , TNF- $\alpha$  and IL-2 by flow cytometry and found cytokines levels were severely suppressed in TIL expressing PD-1, TIM-3 and LAG-3 (triple positive), but not PD-1 single positive. Indeed, the CD8<sup>+</sup>PD-1<sup>+</sup> produced more IL-2 than CD8<sup>+</sup>PD-1<sup>-</sup> which the authors reflected demonstrates that PD-1 alone is an activation marker rather than purely a marker of exhaustion. They modelled T-cell exhaustion in two mouse models of GBM and found the TIL population mirrored those found in mouse models of chronic lymphocytic choriomeningitis virus, with the loss of Tbet<sup>hi</sup>PD-1<sup>int</sup> T cells, and the accumulation Eomes<sup>hi</sup>PD-1<sup>hi</sup> exhausted T cells [97]. Furthermore, the GBM mouse model TILs had more CD8<sup>+</sup>PD-1<sup>+</sup>TIM-3<sup>+</sup>LAG-3<sup>+</sup> than equivalent models in melanoma, breast and lung cancer [96]. Simultaneously, a second group published supportive findings to these showing that CD8<sup>+</sup> TILs isolated from GBM showed a severe exhausted phenotype [98]. This group also compared relapsed and primary GBM patients' TILs and tumour transcriptomic immune signature which they found were similar. However, the relapsed patients had a restricted TCR repertoire clonality and thereby supports the role of boosting antigen presentation and priming through DC targeted immunotherapies [98].

#### 4.5. Immunosuppressive Tumour Microenvironment

GBM has a wide variety of mechanisms of immunosuppression, most of which are also common in non-CNS tumours [32]. Over 4 decades ago impaired cell-mediated immunity was described in brain cancer patients driven by a sera-mediated factor likely to be a cytokine [69]. Indeed, this was likely to be TGF- $\beta$  isoform 2, originally described as glioblastoma-derived T cell suppressor factor, given its discovery in GBM cell lines and patient serum, where it was noted to be immunosuppressive to T-cell proliferation through IL-2 dependent and independent pathways [99,100]. TGF- $\beta$  is pleiotropic and plays a role in both glioma tumorigenicity and immunosuppression. Its receptor is highly expressed on glioma cells and RNA silencing of TGF- $\beta$  reduces glioma proliferation, migration and invasiveness. TGF- $\beta$  also inhibits the transcription factors for the activating immunoreceptor NKG2D and its ligand MHC class I polypeptide-related sequence A (MICA), thus suppressing CD8 T-cell and NK function [101]. MHC class II expression on glioma cells, microglia and macrophages is also reduced following TGF- $\beta$  exposure [102]. Interestingly, TGF- $\beta$ 2 has been measured pre- and post-operatively



in GBM patients, with a favourable prognosis seen in those with a greater reduction in the cytokine, implying an important role of the cytokine in progression [103].

IL-10 is a potent anti-inflammatory cytokine. IL-10 induces immature and tolerogenic DC and hinders cytotoxic T cell effector function through sustaining the FoxP3 transcription factor on Treg [104,105]. IL-10 messenger RNA has been seen in gliomas, with higher levels associated with higher grades [106]. IL-10 production by gliomas seems to polarise the tumour associated macrophages and microglia in the tumour microenvironment [107]. IL-10 also promotes expression of the negative checkpoint molecule *PD-L1* on glioma-associated macrophages and peripheral monocytes [80].

Another important immunomodulatory mechanism of DCs and other immune cells is through indolamine 2,3-dioxygenase 1 (IDO) [32]. This orchestrates response to the cytokine environment, for example, it is upregulated in response to interferons [108]. IDO is a cytosolic enzyme which controls tryptophan degradation particularly kynurenine and in addition to the above, facilitates Treg expansions and inhibits T effector function. Furthermore, it can also attract and activate circulating Tregs in the TME to mediate immunosuppression [77]. Overall it, therefore, downregulates the immune response [109,110]. It is highly expressed by GBM (but not normal brain tissue) and levels of *IDO* expressions by malignant tumours has been correlated to poorer prognosis. Supportive of the above, mice implanted with IDO producing glioma cells (GL261), had increased intra-tumoral Treg accumulation and reduced survival [109]. Furthermore, administration of 1-methyl-tryptophan (an IDO inhibitor) in combination with PD-L1 and CTLA-4 inhibitors resulted in 100% glioma mice survival, improved over PD-L1 and CTLA-4 dual inhibitor therapy [111].

Overall the TME in glioma is profoundly immunosuppressive through a number of cell populations and cytokine factors.

#### 4.6. Corticosteroids

Corticosteroids are universally used to alleviate symptoms of vasogenic oedema in GBM patients. Vasogenic oedema is a major consequence of BBB disruption and increased vascular permeability in GBM, resulting in accumulation of fluid entering the brain extracellular space [112]. Administration of glucocorticoids effectively reduces BBB permeability by reinforcing endothelial tight junctions. In addition, dexamethasone (Dex) can inhibit the effects of tumour-derived VEGF and suppress vascular permeability [113].

This type of oedema is characteristic of brain malignancies that are progressing, but it can also appear after treatment with chemotherapy and radiotherapy due to uncontrolled inflammation of the CNS [114]. Owing to tumour location and volume limitation, cerebral oedema increases intracranial pressure and can compromise neurologic function, causing significant morbidity and mortality [112,115].

Unfortunately, treatment with glucocorticoids also has several negative effects. Of particular relevance is the anti-inflammatory and immunosuppressive action of steroids [116]. Several studies have shown that the use of Dex can lower CD4<sup>+</sup> T lymphocytes, as well as exert global immunosuppression by inhibiting the activity of NF- $\kappa$ B in T-cells [116–118]. More recently, studies in GBM animal models and patients indicate that Dex lowers the efficacy of chemotherapy and radiotherapy, resulting in a decreased overall survival [119,120]. Steroids are known to be immunosuppressive and characteristically exert this effect by directing T-cell apoptosis, both at thymic development and in the periphery during activation-induced cell death [121,122]. Indeed clinically, steroids have direct cytotoxic effects on lymphoid origin cancers such as lymphoma and acute lymphoblastic leukaemia whereas have minimal cytotoxic effect on myeloid leukaemias [123]. A group studied the systemic immune suppression in glioma patients (n = 37) including T-cells, myeloid-derived suppressor cells (MDSC) and monocytes and compared patients on and off Dex, to elicit tumour versus corticosteroid-induced immune changes [124]. They found Dex exacerbated lymphopenia in patients compared to healthy controls particularly to the T-cell compartment. In the patients on steroids, although they had similar numbers of monocytes, there was an increase in CD14<sup>+</sup>HLA-DR<sup>-/lo</sup> monocytes, which inhibited T cell proliferation and failed to differentiate into MoDC. These cells were also negative for CD80 and had reduced CD86

co-stimulatory molecule expression. Furthermore, these immature cells made up to a third of the monocyte population and were distinct from other CD14<sup>+</sup> immune cells such as MDSC [124]. Serum from GBM patients could induce the same changes to healthy monocytes from healthy controls and the authors proposed this to be CCL2 driven. Dex could not induce the loss of *HLA-DR*<sup>+</sup> expression on healthy monocytes, but reduced CCL2 expression in a series of GBM cell lines and, furthermore, inversely correlated with serum CCL2 levels in a dose-dependent manner. Therefore, the authors concluded that tumour induced factors led to the low *HLA-DR* expression in the monocyte phenotype, however, Dex reduced CCL2 secretion by the tumour, reducing tumour recruitment of monocytes and resulting in increased peripheral CD14<sup>+</sup>HLA-DR<sup>-/lo</sup> monocytes [124]. Therefore, these groups suggest the immunosuppressive effects of Dex and tumour-derived factors are additive. Dex is also known to interfere with monocyte differentiation into monocyte-derived DC and production of pro-inflammatory cytokines on maturation [125]. Indeed, measurement of in-vivo circulating DC showed both classical DC and plasmacytoid DC numbers were profoundly suppressed in GBM patients and the numbers were inversely correlated with dexamethasone dose. Furthermore, isolated CD1c<sup>+</sup> DC exposed to Dex both in-vivo and in-vitro, showed impaired cytokine secretion and T-cell stimulatory ability [126]. The effect of Dex was recognised as a limiting factor in the success of monocyte-derived DC vaccine trials to treat GBM, particularly with the production of good-quality DCs and hence restricted inclusion criteria to the absence of Dex [127,128]. The Checkmate trial investigating the use of Nivolumab also limited patients to less than 4mg of Dex for trial inclusion.

## 5. Resistance Mechanisms

Primary resistance to PD-1/PD-L1 blockade has been linked to a transcriptomic signature that was found to be over-represented among non-responding melanoma tumours. This signature was enriched in genes involved in epithelial-to-mesenchymal transition (EMT), angiogenesis, hypoxia and wound healing [129]. These gene signatures were collectively described as signatures of innate anti-PD-1 resistance (IPRES) [129]. There are also higher differentially expressed genes related to immunosuppression (*IL-10*, *VEGFA/C*), monocyte and macrophage chemotaxis in non-responders [129]. In a similar fashion, a strong association between EMT and an inflammatory TME was found in lung cancer, where tumours displaying an EMT-like phenotype showed up-regulation of multiple checkpoint molecules (PD-L1/2, Tim-3, CTLA-4) as well as increased Treg infiltration. This suggested that tumours bearing an EMT-like phenotype could trigger immunosuppression through several mechanisms and promote tumour progression [130].

Despite an initial response to therapy, some patients develop secondary resistance and disease progression. In melanoma, 25% of the patients that had responded to PD-1 blockade relapsed and progressed within the first two years of treatment [131]. Genomic analysis of pre-treatment melanoma biopsies and their respective relapsed counterparts identified that alterations in the  $\beta$ -2 microglobulin and *JAK1/2* genes were the drivers of the adaptive resistance to PD-1 blockade. Because of their role in the interferon receptor pathway, homozygous loss-of-function mutations in *JAK1/2* kinases desensitised cancer cells to IFN signalling, leading to escape from IFN-induced growth inhibition, upregulation of PD-L1 and reduced antigen presentation. On the other hand, the deletion found on the  $\beta$ -2 microglobulin gene prevented the localisation of MHC class I molecules at the cell surface, hence decreasing immunorecognition of cancer cells [132]. Mutations in the *JAK1/2* pathway conferring IFN insensitivity and absence of *PD-L1* expression has been recently confirmed as a mechanism of primary resistance to PD-1 directed therapies in other studies [133]. Alternate means of adaptive resistance to *PD-1* blockade include the expression of alternative checkpoint molecules, such as TIM-3, which appeared to be up-regulated upon tumour progression following an initial response to PD-1 blockade in human and murine samples of lung adenocarcinoma [134]. Indeed, chronic IFN exposure regulates several IFN stimulated genes and T-cell inhibitory receptors, independent of PD-L1 which confers resistance to PD-1 inhibitory agents [135]. For example, epigenetic changes to STAT1 following chronic IFN- $\gamma$  leads to elevated expression of these genes on resistant tumours [135]. The nature and balance

of IFN exposure may regulate when PD-L1-independent adaptive resistance dominates over PD-L1 alone and thus susceptibility to PD-1 therapy (Table 2).

**Table 2.** Restriction to PD-1 inhibitor response.

GBM Specific Barriers	Primary Resistance *	Secondary Resistance *
Low-intermediate <i>PD-L1</i> expression	Enriched genes epithelial-mesenchymal transition	Alterations $\beta$ 2 microglobulin
Low-Intermediate mutational burden	Angiogenesis, wound healing, hypoxia, <i>IL-10</i> , <i>VEGF-A/C</i> gene signature	Alteration <i>JAK1/2</i> genes
Low-intermediate CD8 TIL infiltrate	High monocyte, macrophage chemotaxis genes	Upregulation of alternate checkpoints e.g., TIM-3
Blood–brain barrier		
High corticosteroid use		
Low dendritic cell populations		
High IL-10, TGF- $\beta$ , CCL2 and IDO suppressive humoral factors		

\* in all tumours.

## 6. Future Immune Strategies and Challenges

Despite the disappointing overall results of the phase III Nivolumab trials in GBM, the information derived from these trials should provide important insights such as favourable subgroups to PD-1 inhibitor treatment. Indeed, the limited success of PD-1 inhibitor monotherapy is not unexpected due to the immunosuppressive barriers in GBM. Furthermore, the cancer immunity cycle reveals the complexity and the multiple steps that are vital for the successful eradication of the tumour [136]. These steps include antigen release and detection, successful priming and activation of the T-cell, followed by successful migration to the tumour site. At the tumour site, the T-cells then must recognise and infiltrate the tumour and subsequently initiate cytotoxicity [136]. Blockade of the PD-1/PD-L1 axis, which predominately dampens cancer immunity in the final steps at the tumour site, is, therefore, targeting one arm of this cycle. This cycle also assumes a T-cell focus for effective immunity against cancer, however natural killer cells, MDSC, macrophages, B-cells may be more than just attenuators in the local TME. Figure 1 summarises some of the approaches already undergoing in clinical trials for GBM, matching them with the process of the cancer immunity cycle that they target.

In C57BL/6 mice implanted with murine glioma cell line GL261-luc2, the use of combination treatment such as radiotherapy, anti-PD-1 and anti-TIM3 has been shown to be synergistic and improve survival above dual therapy [137]. Likewise, in GBM mouse model, the use of toll-like receptor agonist PolyI:C to mature DC combined with anti-PD-1 improved survival than either treatment alone. The combination treatment increased rates of T-effector cells and decreased Treg which reinforces the rationale of targeting two components of the cancer immunity cycle [138].

These approaches only represent a few of over a thousand trial combinations involving a checkpoint blockade backbone that is being tested in oncology trials. Although this is the treatment avenue most likely to achieve success in the management of GBM, it also raises economic challenges for pharmaceutical companies and healthcare systems. Furthermore, the optimum combination may be unique to a tumour type depending on the predominant barrier to immunity. For example, in pancreatic cancer, dense in stromal tissue, a mouse model has shown depletion of carcinoma-associated fibroblast expressing fibroblast activation protein (FAP), restores sensitivity to checkpoint blockade [139]. Whereas, in other cancers, such as renal cell carcinoma, Treg may predominate to attenuate the effect of PD-1/L1 axis inhibition, as supported by higher Treg fraction been a biomarker of poor response in an early clinical trial of Atezolizumab in the treatment of this cancer [140].

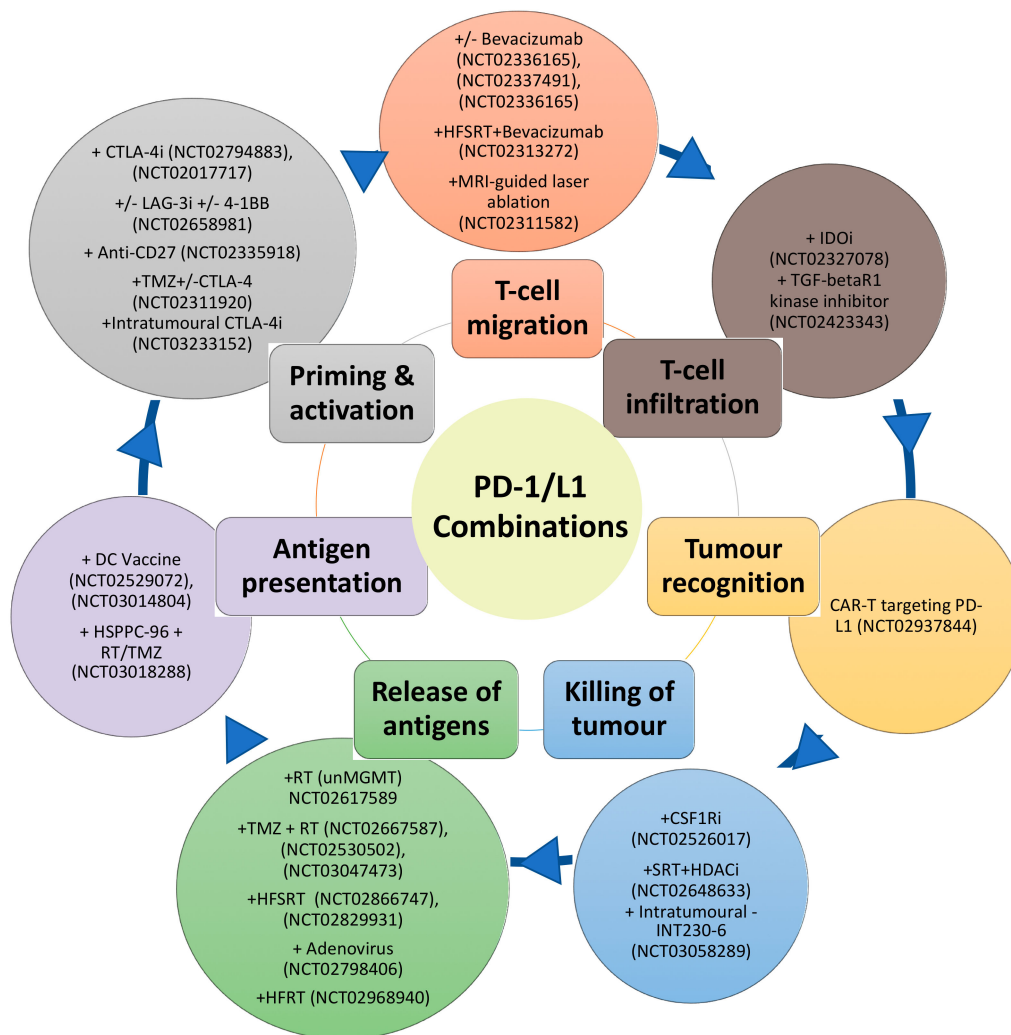


**Figure 1.** Schematic of combination therapies with PD-1/L1 inhibitors (outer circle) targeting different aspects of the cancer-immunity cycle (inner circle).

## 7. Concluding Remarks

PD-1 inhibitors have revolutionised the treatment of cancers such as NSCLC, bladder cancer and metastatic melanoma. These tumours have a high mutational burden and have pre-existing immunity signature on biopsy as represented by high *CD8 TILs*, *PD-L1* expression and *IFN- $\gamma$*  enriched signature. In the tumour immunity continuum spanning from pro-inflammatory to immunologically ignorant tumours, GBM would be in the mid-lower end of this spectrum. In addition to targeting immunosuppressive barriers in the TME, the success in the treatment of GBM will likely depend on developing a rational combination therapy able to induce a long-lasting anti-tumour immunity. These combination strategies are not unique to GBM and are now the forefront of questions for the immuno-oncology field to address, particularly in the PD-1/L1 axis inhibition non-responsive and secondary resistant tumours.

**Author Contributions:** Conceptualization and writing by J.A.; J.M.-V. and P.M.P., supervision by A.M.J. and P.M.P. and review and editing by A.P.K., A.M.J. and P.M.P. All authors have read and agreed to the published version of the manuscript.

**Funding:** This research received no external funding

**Conflicts of Interest:** The authors declare no conflict of interest.

## References

1. Robert, C.; Long, G.V.; Brady, B.; Dutriaux, C.; Maio, M.; Mortier, L.; Hassel, J.C.; Rutkowski, P.; McNeil, C.; Kalinka-Warzocha, E.; et al. Nivolumab in previously untreated melanoma without BRAF mutation. *N. Engl. J. Med.* **2015**, *372*, 320–330. [CrossRef] [PubMed]
2. Ferris, R.L.; Blumenschein, G., Jr.; Fayette, J.; Guigay, J.; Colevas, A.D.; Licitra, L.; Harrington, K.; Kasper, S.; Vokes, E.E.; Even, C.; et al. Nivolumab for recurrent squamous-cell carcinoma of the head and neck. *N. Engl. J. Med.* **2016**, *375*, 1856–1867. [CrossRef] [PubMed]
3. Reck, M.; Rodriguez-Abreu, D.; Robinson, A.G.; Hui, R.; Csoszi, T.; Fulop, A.; Gottfried, M.; Peled, N.; Tafreshi, A.; Cuffe, S.; et al. Pembrolizumab versus chemotherapy for PD-L1-Positive non-small-cell lung cancer. *N. Engl. J. Med.* **2016**, *375*, 1823–1833. [CrossRef] [PubMed]
4. Ansell, S.M.; Lesokhin, A.M.; Borrello, I.; Halwani, A.; Scott, E.C.; Gutierrez, M.; Schuster, S.J.; Millenson, M.M.; Cattray, D.; Freeman, G.J.; et al. PD-1 blockade with nivolumab in relapsed or refractory Hodgkin’s lymphoma. *N. Engl. J. Med.* **2015**, *372*, 311–319. [CrossRef]
5. Rosenberg, J.E.; Hoffman-Censits, J.; Powles, T.; van der Heijden, M.S.; Balar, A.V.; Necchi, A.; Dawson, N.; O’Donnell, P.H.; Balmanoukian, A.; Loriot, Y.; et al. Atezolizumab in patients with locally advanced and metastatic urothelial carcinoma who have progressed following treatment with platinum-based chemotherapy: A single-arm, multicentre, phase 2 trial. *Lancet* **2016**, *387*, 1909–1920. [CrossRef]
6. Nghiem, P.T.; Bhatia, S.; Lipson, E.J.; Kudchadkar, R.R.; Miller, N.J.; Annamalai, L.; Berry, S.; Chartash, E.K.; Daud, A.; Fling, S.P.; et al. PD-1 blockade with pembrolizumab in advanced merkel-cell carcinoma. *N. Engl. J. Med.* **2016**, *374*, 2542–2552. [CrossRef]
7. Motzer, R.J.; Escudier, B.; McDermott, D.F.; George, S.; Hammers, H.J.; Srinivas, S.; Tykodi, S.S.; Sosman, J.A.; Procopio, G.; Plimack, E.R.; et al. Nivolumab versus everolimus in advanced renal-cell carcinoma. *N. Engl. J. Med.* **2015**, *373*, 1803–1813. [CrossRef]
8. Reardon, D.A.; Omuro, A.; Brandes, A.A.; Rieger, J.; Wick, A.; Sepulveda, J.; Phuphanich, S.; de Souza, P.; Ahluwalia, M.S.; Lim, M.; et al. OS10.3 randomized phase 3 study evaluating the efficacy and safety of nivolumab vs. bevacizumab in patients with recurrent glioblastoma: CheckMate 143. *Neuro Oncol.* **2017**, *19*, iii21–iii21. [CrossRef]
9. Joyce, J.A.; Fearon, D.T. T cell exclusion, immune privilege, and the tumor microenvironment. *Science* **2015**, *348*, 74–80. [CrossRef]
10. Baumeister, S.H.; Freeman, G.J.; Dranoff, G.; Sharpe, A.H. Coinhibitory pathways in immunotherapy for cancer. *Annu. Rev. Immunol.* **2016**, *34*, 539–573. [CrossRef]
11. Dong, H.; Zhu, G.; Tamada, K.; Chen, L. B7-H1, a third member of the B7 family, co-stimulates T-cell proliferation and interleukin-10 secretion. *Nat. Med.* **1999**, *5*, 1365–1369. [CrossRef] [PubMed]
12. Freeman, G.J.; Long, A.J.; Iwai, Y.; Bourque, K.; Chernova, T.; Nishimura, H.; Fitz, L.J.; Malenkovich, N.; Okazaki, T.; Byrne, M.C.; et al. Engagement of the Pd-1 immunoinhibitory receptor by a novel B7 family member leads to negative regulation of lymphocyte activation. *J. Exp. Med.* **2000**, *192*, 1027–1034. [CrossRef] [PubMed]
13. Kamphorst, A.O.; Wieland, A.; Nasti, T.; Yang, S.; Zhang, R.; Barber, D.L.; Konieczny, B.T.; Daugherty, C.Z.; Koenig, L.; Yu, K.; et al. Rescue of exhausted CD8 T cells by PD-1-targeted therapies is CD28-dependent. *Science* **2017**, *355*, 1423–1427. [CrossRef] [PubMed]
14. Hui, E.; Cheung, J.; Zhu, J.; Su, X.; Taylor, M.J.; Wallweber, H.A.; Sasmal, D.K.; Huang, J.; Kim, J.M.; Mellman, I.; et al. T cell costimulatory receptor CD28 is a primary target for PD-1-mediated inhibition. *Science* **2017**, *355*, 1428–1433. [CrossRef]
15. Hirano, F.; Kaneko, K.; Tamura, H.; Dong, H.; Wang, S.; Ichikawa, M.; Rietz, C.; Flies, D.B.; Lau, J.S.; Zhu, G.; et al. Blockade of B7-H1 and PD-1 by monoclonal antibodies potentiates cancer therapeutic immunity. *Cancer Res.* **2005**, *65*, 1089.
16. Mahoney, K.M.; Rennert, P.D.; Freeman, G.J. Combination cancer immunotherapy and new immunomodulatory targets. *Nat. Rev. Drug. Discov.* **2015**, *14*, 561–584. [CrossRef]
17. Zou, W.; Wolchok, J.D.; Chen, L. PD-L1 (B7-H1) and PD-1 pathway blockade for cancer therapy: Mechanisms, response biomarkers, and combinations. *Sci. Transl. Med.* **2016**, *8*, 328rv324. [CrossRef]

18. Wolchok, J.D.; Kluger, H.; Callahan, M.K.; Postow, M.A.; Rizvi, N.A.; Lesokhin, A.M.; Segal, N.H.; Ariyan, C.E.; Gordon, R.A.; Reed, K.; et al. Nivolumab plus ipilimumab in advanced melanoma. *N. Engl. J. Med.* **2013**, *369*, 122–133. [CrossRef]
19. Hellmann, M.D.; Rizvi, N.A.; Goldman, J.W.; Gettinger, S.N.; Borghaei, H.; Brahmer, J.R.; Ready, N.E.; Gerber, D.E.; Chow, L.Q.; Juergens, R.A.; et al. Nivolumab plus ipilimumab as first-line treatment for advanced non-small-cell lung cancer (CheckMate 012): Results of an open-label, phase 1, multicohort study. *Lancet Oncol.* **2017**, *18*, 31–41. [CrossRef]
20. Reardon, D.S.J.; Sahebjam, S. Safety and activity of nivolumab monotherapy and nivolumab in combination with ipilimumab in recurrent glioblastoma: Updated results from CheckMate 143. In Proceedings of the 52nd Annual Meeting of the American Society of Clinical Oncology, Chicago, IL, USA, 2–7 June 2016.
21. Omuro, A.; Vlahovic, G.; Lim, M.; Sahebjam, S.; Baehring, J.; Cloughesy, T.; Voloschin, A.; Ramkissoon, S.H.; Ligon, K.L.; Latek, R.; et al. Nivolumab with or without ipilimumab in patients with recurrent glioblastoma: Results from exploratory phase I cohorts of CheckMate 143. *Neuro. Oncol.* **2018**, *20*, 674–686. [CrossRef]
22. Reardon, D.A.; De Groot, J.F.; Colman, H.; Jordan, J.T.; Daras, M.; Clarke, J.L.; Peters, K.B. Safety of pembrolizumab in combination with bevacizumab in recurrent glioblastoma (rGBM). *J. Clin. Oncol.* **2016**, *34*. [CrossRef]
23. Sahebjam, S.J.P.; Forsyth, P.A. Safety and antitumor activity of hypofractionated stereotactic irradiation (HFSRT) with pembrolizumab (Pembro) and bevacizumab (Bev) in patients (pts) with recurrent high grade gliomas: Preliminary results from phase I study. *J. Clin. Oncol.* **2016**, *34*. [CrossRef]
24. Blumenthal, D.T. Pembrolizumab: First experience with recurrent primary central nervous system (CNS) tumours. *Neuro Oncol.* **2015**, *17*, v107. [CrossRef]
25. Leibowitz-Amit, R. Initial clinical experience with pembrolizumab in metastatic heavily pre-treated patients with solid cancers in a single institution. *Eur. J. Cancer* **2015**, *51*, S111. [CrossRef]
26. Johanns, T.M.; Miller, C.A.; Dorward, I.G.; Tsien, C.; Chang, E.; Perry, A.; Uppaluri, R.; Ferguson, C.; Schmidt, R.E.; Dahiya, S.; et al. Immunogenomics of hypermutated glioblastoma: A patient with germline pole deficiency treated with checkpoint blockade immunotherapy. *Cancer Discov.* **2016**, *6*, 1230–1236. [CrossRef]
27. Bouffet, E.; Larouche, V.; Campbell, B.B.; Merico, D.; de Borja, R.; Aronson, M.; Durno, C.; Krueger, J.; Cabric, V.; Ramaswamy, V.; et al. Immune checkpoint inhibition for hypermutant glioblastoma multiforme resulting from germline biallelic mismatch repair deficiency. *J. Clin. Oncol.* **2016**, *34*, 2206–2211. [CrossRef]
28. Brown, N.F.; Carter, T.; Shaw, H.M.; Cohn-Brown, D.; Chester, K.; Mulholland, P.J. Sequential immune checkpoint inhibition with concurrent bevacizumab for relapsed glioblastoma: A single centre experience. *J. Clin. Oncol.* **2016**, *34*, e13514–e13514. [CrossRef]
29. Reardon, D.A.; Kaley, T.J.; Dietrich, J.; Clarke, J.L.; Dunn, G.P.; Lim, M.; Cloughesy, T.F.; Gan, H.K.; Park, A.J.; Schwarzenberger, P.; et al. Phase 2 study to evaluate safety and efficacy of MEDI4736 (durvalumab [DUR]) in glioblastoma (GBM) patients: An update. *J. Clin. Oncol.* **2017**, *35*, 2042–2042. [CrossRef]
30. Iwamoto, F.M.; Donovan, L. OS09.5 synergistic effect of reirradiation and PD-1 inhibitors in recurrent high-grade gliomas. *Neuro Oncol.* **2017**, *19*, iii19–iii19. [CrossRef]
31. Roth, P.; Valavanis, A.; Weller, M. Long-term control and partial remission after initial pseudoprogression of glioblastoma by anti-PD-1 treatment with nivolumab. *Neuro Oncol.* **2017**, *19*, 454–456. [CrossRef]
32. Perng, P.; Lim, M. Immunosuppressive mechanisms of malignant gliomas: Parallels at Non-CNS sites. *Front. Oncol.* **2015**, *5*, 153. [CrossRef] [PubMed]
33. Jarry, U.; Jeannin, P.; Pineau, L.; Donnou, S.; Delneste, Y.; Couez, D. Efficiently stimulated adult microglia cross-prime naive CD8+ T cells injected in the brain. *Eur. J. Immunol.* **2013**, *43*, 1173–1184. [CrossRef] [PubMed]
34. Hambardzumyan, D.; Gutmann, D.H.; Kettenmann, H. The role of microglia and macrophages in glioma maintenance and progression. *Nat. Neurosci.* **2016**, *19*, 20–27. [CrossRef]
35. Ransohoff, R.M.; Engelhardt, B. The anatomical and cellular basis of immune surveillance in the central nervous system. *Nat. Rev. Immunol.* **2012**, *12*, 623–635. [CrossRef]
36. Saijo, K.; Glass, C.K. Microglial cell origin and phenotypes in health and disease. *Nat. Rev. Immunol.* **2011**, *11*, 775–787. [CrossRef] [PubMed]
37. Mantovani, A.; Sica, A.; Sozzani, S.; Allavena, P.; Vecchi, A.; Locati, M. The chemokine system in diverse forms of macrophage activation and polarization. *Trends Immunol.* **2004**, *25*, 677–686. [CrossRef] [PubMed]

38. Wei, J.; Gabrusiewicz, K.; Heimberger, A. The controversial role of microglia in malignant gliomas. *Clin. Dev. Immunol.* **2013**, *2013*, 285246. [CrossRef] [PubMed]
39. Wu, A.; Wei, J.; Kong, L.-Y.; Wang, Y.; Priebe, W.; Qiao, W.; Sawaya, R.; Heimberger, A.B. Glioma cancer stem cells induce immunosuppressive macrophages/microglia. *Neuro Oncol.* **2010**, *12*, 1113–1125. [CrossRef]
40. Zou, J.P.; Morford, L.A.; Chougnet, C.; Dix, A.R.; Brooks, A.G.; Torres, N.; Shuman, J.D.; Coligan, J.E.; Brooks, W.H.; Roszman, T.L.; et al. Human glioma-induced immunosuppression involves soluble factor(s) that alters monocyte cytokine profile and surface markers. *J. Immunol.* **1999**, *162*, 4882–4892.
41. Yang, I.; Han, S.J.; Kaur, G.; Crane, C.; Parsa, A.T. The role of microglia in central nervous system immunity and glioma immunology. *J. Clin. Neurosci.* **2010**, *17*, 6–10. [CrossRef]
42. Glass, R.; Synowitz, M. CNS macrophages and peripheral myeloid cells in brain tumours. *Acta Neuropathol.* **2014**, *128*, 347–362. [CrossRef] [PubMed]
43. Markovic, D.S.; Vinnakota, K.; Chirasani, S.; Synowitz, M.; Raguette, H.; Stock, K.; Sliwa, M.; Lehmann, S.; Kalin, R.; van Rooijen, N.; et al. Gliomas induce and exploit microglial MT1-MMP expression for tumor expansion. *Proc. Natl. Acad. Sci. USA* **2009**, *106*, 12530–12535. [CrossRef] [PubMed]
44. Korn, T.; Kallies, A. T cell responses in the central nervous system. *Nat. Rev. Immunol.* **2017**, *17*, 179–194. [CrossRef] [PubMed]
45. Aspelund, A.; Antila, S.; Proulx, S.T.; Karlsen, T.V.; Karaman, S.; Detmar, M.; Wiig, H.; Alitalo, K. A dural lymphatic vascular system that drains brain interstitial fluid and macromolecules. *J. Exp. Med.* **2015**, *212*, 991–999. [CrossRef]
46. Louveau, A.; Smirnov, I.; Keyes, T.J.; Eccles, J.D.; Rouhani, S.J.; Peske, J.D.; Derecki, N.C.; Castle, D.; Mandell, J.W.; Lee, K.S.; et al. Structural and functional features of central nervous system lymphatic vessels. *Nature* **2015**, *523*, 337–341. [CrossRef]
47. Mrdjen, D.; Pavlovic, A.; Hartmann, F.J.; Schreiner, B.; Utz, S.G.; Leung, B.P.; Lelios, I.; Heppner, F.L.; Kipnis, J.; Merkler, D.; et al. High-dimensional single-cell mapping of central nervous system immune cells reveals distinct myeloid subsets in health, aging, and disease. *Immunity* **2018**, *48*, 380–395. [CrossRef]
48. Postow, M.A.; Callahan, M.K.; Barker, C.A.; Yamada, Y.; Yuan, J.; Kitano, S.; Mu, Z.; Rasalan, T.; Adamow, M.; Ritter, E.; et al. Immunologic correlates of the abscopal effect in a patient with melanoma. *N. Engl. J. Med.* **2012**, *366*, 925–931. [CrossRef]
49. Grimaldi, A.M.; Simeone, E.; Giannarelli, D.; Muto, P.; Falivene, S.; Borzillo, V.; Giugliano, F.M.; Sandomenico, F.; Petrillo, A.; Curvietto, M.; et al. Abscopal effects of radiotherapy on advanced melanoma patients who progressed after ipilimumab immunotherapy. *Oncoimmunology* **2014**, *3*, e28780. [CrossRef]
50. Weller, R.O.; Engelhardt, B.; Phillips, M.J. Lymphocyte targeting of the central nervous system: A review of afferent and efferent CNS-immune pathways. *Brain Pathol.* **1996**, *6*, 275–288. [CrossRef]
51. Laman, J.D.; Weller, R.O. Drainage of cells and soluble antigen from the CNS to regional lymph nodes. *J. Neuroimmune Pharm.* **2013**, *8*, 840–856. [CrossRef]
52. Calzascia, T.; Masson, F.; Di Bernardino-Besson, W.; Contassot, E.; Wilmotte, R.; Aurrand-Lions, M.; Ruegg, C.; Dietrich, P.Y.; Walker, P.R. Homing phenotypes of tumor-specific CD8 T cells are predetermined at the tumor site by crosspresenting APCs. *Immunity* **2005**, *22*, 175–184. [CrossRef] [PubMed]
53. Kivisakk, P.; Mahad, D.J.; Callahan, M.K.; Trebst, C.; Tucky, B.; Wei, T.; Wu, L.; Baekkevold, E.S.; Lassmann, H.; Staugaitis, S.M.; et al. Human cerebrospinal fluid central memory CD4+ T cells: Evidence for trafficking through choroid plexus and meninges via P-selectin. *Proc. Natl. Acad. Sci. USA* **2003**, *100*, 8389–8394. [CrossRef] [PubMed]
54. Ifergan, I.; Kebir, H.; Alvarez, J.I.; Marceau, G.; Bernard, M.; Bourbonniere, L.; Poirier, J.; Duquette, P.; Talbot, P.J.; Arbour, N.; et al. Central nervous system recruitment of effector memory CD8+ T lymphocytes during neuroinflammation is dependent on alpha4 integrin. *Brain* **2011**, *134*, 3560–3577. [CrossRef] [PubMed]
55. Abbott, N.J.; Ronnback, L.; Hansson, E. Astrocyte-endothelial interactions at the blood-brain barrier. *Nat. Rev. Neurosci.* **2006**, *7*, 41–53. [CrossRef]
56. Abbott, N.J.; Patabendige, A.A.; Dolman, D.E.; Yusof, S.R.; Begley, D.J. Structure and function of the blood-brain barrier. *Neurobiol. Dis.* **2010**, *37*, 13–25. [CrossRef]
57. Engelhardt, B.; Ransohoff, R.M. Capture, crawl, cross: The T cell code to breach the blood-brain barriers. *Trends Immunol.* **2012**, *33*, 579–589. [CrossRef]

58. Giunti, D.; Borsellino, G.; Benelli, R.; Marchese, M.; Capello, E.; Valle, M.T.; Pedemonte, E.; Noonan, D.; Albini, A.; Bernardi, G.; et al. Phenotypic and functional analysis of T cells homing into the CSF of subjects with inflammatory diseases of the CNS. *J. Leukoc. Biol.* **2003**, *73*, 584–590. [CrossRef]
59. Lossinsky, A.S.; Shivers, R.R. Structural pathways for macromolecular and cellular transport across the blood-brain barrier during inflammatory conditions. Review. *Histol. Histopathol.* **2004**, *19*, 535–564. [CrossRef]
60. Konnecke, H.; Bechmann, I. The role of microglia and matrix metalloproteinases involvement in neuroinflammation and gliomas. *J. Clin. Dev. Immunol.* **2013**, *2013*, 15. [CrossRef]
61. Greenwood, J.; Wang, Y.; Calder, V.L. Lymphocyte adhesion and transendothelial migration in the central nervous system: The role of LFA-1, ICAM-1, VLA-4 and VCAM-1. *Immunology* **1995**, *86*, 408–415.
62. Cayrol, R.; Wosik, K.; Berard, J.L.; Dodelet-Devillers, A.; Ifergan, I.; Kebir, H.; Haqqani, A.S.; Kreyborg, K.; Krug, S.; Moumdjian, R.; et al. Activated leukocyte cell adhesion molecule promotes leukocyte trafficking into the central nervous system. *Nat. Immunol.* **2008**, *9*, 137–145. [CrossRef] [PubMed]
63. Schlachetzki, F.; Zhu, C.; Pardridge, W.M. Expression of the neonatal Fc receptor (FcRn) at the blood-brain barrier. *J. Neurochem.* **2002**, *81*, 203–206. [CrossRef] [PubMed]
64. Roopenian, D.C.; Akilesh, S. FcRn: The neonatal Fc receptor comes of age. *Nat. Rev. Immunol.* **2007**, *7*, 715–725. [CrossRef] [PubMed]
65. Ohtsuki, S.; Terasaki, T. Contribution of carrier-mediated transport systems to the blood-brain barrier as a supporting and protecting interface for the brain; importance for CNS drug discovery and development. *Pharm. Res.* **2007**, *24*, 1745–1758. [CrossRef] [PubMed]
66. Goldberg, S.B.; Gettinger, S.N.; Mahajan, A.; Chiang, A.C.; Herbst, R.S.; Sznol, M.; Tsiouris, A.J.; Cohen, J.; Vortmeyer, A.; Jilaveanu, L.; et al. Pembrolizumab for patients with melanoma or non-small-cell lung cancer and untreated brain metastases: Early analysis of a non-randomised, open-label, phase 2 trial. *Lancet Oncol.* **2016**, *17*, 976–983. [CrossRef]
67. Amayiri, N.; Tabori, U.; Campbell, B.; Bakry, D.; Aronson, M.; Durno, C.; Rakopoulos, P.; Malkin, D.; Qaddoumi, I.; Musharbash, A.; et al. High frequency of mismatch repair deficiency among pediatric high grade gliomas in Jordan. *Int. J. Cancer* **2016**, *138*, 380–385. [CrossRef]
68. Roszman, T.L.; Brooks, W.H. Immunobiology of primary intracranial tumours. III. Demonstration of a qualitative lymphocyte abnormality in patients with primary brain tumours. *Clin. Exp. Immunol.* **1980**, *39*, 395–402.
69. Brooks, W.H.; Netsky, M.G.; Normansell, D.E.; Horwitz, D.A. Depressed cell-mediated immunity in patients with primary intracranial tumours. *J. Exp. Med.* **1972**, *136*, 1631–1647. [CrossRef]
70. Zou, W. Regulatory T cells, tumour immunity and immunotherapy. *Nat. Rev. Immunol.* **2006**, *6*, 295–307. [CrossRef]
71. Colombo, M.P.; Piconese, S. Regulatory-T-cell inhibition versus depletion: The right choice in cancer immunotherapy. *Nat. Rev. Cancer* **2007**, *7*, 880–887. [CrossRef]
72. Fecci, P.E.; Mitchell, D.A.; Whitesides, J.F.; Xie, W.; Friedman, A.H.; Archer, G.E.; Herndon, J.E., 2nd; Bigner, D.D.; Dranoff, G.; Sampson, J.H. Increased regulatory T-cell fraction amidst a diminished CD4 compartment explains cellular immune defects in patients with malignant glioma. *Cancer Res.* **2006**, *66*, 3294–3302. [CrossRef] [PubMed]
73. Palma, L.; Di Lorenzo, N.; Guidetti, B. Lymphocytic infiltrates in primary glioblastomas and recidivous gliomas. Incidence, fate, and relevance to prognosis in 228 operated cases. *J. Neurosurg.* **1978**, *49*, 854–861. [CrossRef] [PubMed]
74. Yue, Q.; Zhang, X.; Ye, H.X.; Wang, Y.; Du, Z.G.; Yao, Y.; Mao, Y. The prognostic value of Foxp3+ tumor-infiltrating lymphocytes in patients with glioblastoma. *J. Neurooncol.* **2014**, *116*, 251–259. [CrossRef] [PubMed]
75. Wang, L.; Zhang, B.; Xu, X.; Zhang, S.; Yan, X.; Kong, F.; Feng, X.; Wang, J. Clinical significance of FOXP3 expression in human gliomas. *Clin. Transl. Oncol.* **2014**, *16*, 36–43. [CrossRef]
76. Wainwright, D.A.; Sengupta, S.; Han, Y.; Lesniak, M.S. Thymus-derived rather than tumor-induced regulatory T cells predominate in brain tumors. *Neuro Oncol.* **2011**, *13*, 1308–1323. [CrossRef]
77. Vasco, C.; Canazza, A.; Rizzo, A.; Mossa, A.; Corsini, E.; Silvani, A.; Fariselli, L.; Salmaggi, A.; Ciusani, E. Circulating T regulatory cells migration and phenotype in glioblastoma patients: An in vitro study. *J. Neurooncol.* **2013**, *115*, 353–363. [CrossRef]



78. Chongsathidkiet, P.; Jackson, C.; Koyama, S.; Loebel, F.; Cui, X.; Farber, S.H.; Woroniecka, K.; Elsamadicy, A.A.; Dechant, C.A.; Kemeny, H.R.; et al. Sequestration of T cells in bone marrow in the setting of glioblastoma and other intracranial tumors. *Nat. Med.* **2018**, *24*, 1459–1468. [CrossRef]
79. Hegde, P.S.; Karanikas, V.; Evers, S. The Where, the When, and the How of Immune Monitoring for Cancer Immunotherapies in the Era of Checkpoint Inhibition. *Clin. Cancer Res.* **2016**, *22*, 1865–1874. [CrossRef]
80. Wintterle, S.; Schreiner, B.; Mitsdoerffer, M.; Schneider, D.; Chen, L.; Meyermann, R.; Weller, M.; Wiendl, H. Expression of the B7-related molecule B7-H1 by glioma cells: A potential mechanism of immune paralysis. *Cancer Res.* **2003**, *63*, 7462–7467.
81. Berghoff, A.S.; Kiesel, B.; Widhalm, G.; Rajky, O.; Ricken, G.; Wohrer, A.; Dieckmann, K.; Filipits, M.; Brandstetter, A.; Weller, M.; et al. Programmed death ligand 1 expression and tumor-infiltrating lymphocytes in glioblastoma. *Neuro Oncol.* **2015**, *17*, 1064–1075. [CrossRef]
82. Nduom, E.K.; Wei, J.; Yaghi, N.K.; Huang, N.; Kong, L.Y.; Gabrusiewicz, K.; Ling, X.; Zhou, S.; Ivan, C.; Chen, J.Q.; et al. PD-L1 expression and prognostic impact in glioblastoma. *Neuro Oncol.* **2016**, *18*, 195–205. [CrossRef] [PubMed]
83. Parsa, A.T.; Waldron, J.S.; Panner, A.; Crane, C.A.; Parney, I.F.; Barry, J.J.; Cachola, K.E.; Murray, J.C.; Tihan, T.; Jensen, M.C.; et al. Loss of tumor suppressor PTEN function increases B7-H1 expression and immunoresistance in glioma. *Nat. Med.* **2007**, *13*, 84–88. [CrossRef] [PubMed]
84. Srividya, M.R.; Thota, B.; Shailaja, B.C.; Arivazhagan, A.; Thennarasu, K.; Chandramouli, B.A.; Hegde, A.S.; Santosh, V. Homozygous 10q23/PTEN deletion and its impact on outcome in glioblastoma: A prospective translational study on a uniformly treated cohort of adult patients. *Neuropathology* **2011**, *31*, 376–383. [CrossRef] [PubMed]
85. Peng, W.; Chen, J.Q.; Liu, C.; Malu, S.; Creasy, C.; Tetzlaff, M.T.; Xu, C.; McKenzie, J.A.; Zhang, C.; Liang, X.; et al. Loss of PTEN Promotes Resistance to T Cell-Mediated Immunotherapy. *Cancer Discov.* **2016**, *6*, 202–216. [CrossRef]
86. Casey, S.C.; Tong, L.; Li, Y.; Do, R.; Walz, S.; Fitzgerald, K.N.; Gouw, A.M.; Baylot, V.; Gütgemann, I.; Eilers, M.; et al. MYC regulates the antitumor immune response through CD47 and PD-L1. *Science* **2016**, *352*, 227. [CrossRef]
87. Akbay, E.A.; Koyama, S.; Carretero, J.; Altabef, A.; Tchaicha, J.H.; Christensen, C.L.; Mikse, O.R.; Cherniack, A.D.; Beauchamp, E.M.; Pugh, T.J.; et al. Activation of the PD-1 pathway contributes to immune escape in EGFR-driven lung tumors. *Cancer Discov.* **2013**, *3*, 1355. [CrossRef]
88. Casey, S.C.; Baylot, V.; Felsher, D.W. MYC: Master regulator of immune privilege. *Trends Immunol.* **2017**, *38*, 298–305. [CrossRef]
89. Topalian, S.L.; Taube, J.M.; Anders, R.A.; Pardoll, D.M. Mechanism-driven biomarkers to guide immune checkpoint blockade in cancer therapy. *Nat. Rev. Cancer* **2016**, *16*, 275–287. [CrossRef]
90. Schumacher, T.N.; Schreiber, R.D. Neoantigens in cancer immunotherapy. *Science* **2015**, *348*, 69. [CrossRef]
91. Le, D.T.; Uram, J.N.; Wang, H.; Bartlett, B.R.; Kemberling, H.; Eyring, A.D.; Skora, A.D.; Luber, B.S.; Azad, N.S.; Laheru, D.; et al. PD-1 blockade in tumors with mismatch-repair deficiency. *N. Engl. J. Med.* **2015**, *372*, 2509–2520. [CrossRef]
92. Yip, S.; Miao, J.; Cahill, D.P.; Iafrate, A.J.; Aldape, K.; Nutt, C.L.; Louis, D.N. MSH6 mutations arise in glioblastomas during temozolomide therapy and mediate temozolomide resistance. *Clin. Cancer Res.* **2009**, *15*, 4622. [CrossRef] [PubMed]
93. Keskin, D.B.; Anandappa, A.J.; Sun, J.; Tirosh, I.; Mathewson, N.D.; Li, S.; Oliveira, G.; Giobbie-Hurder, A.; Felt, K.; Gjini, E.; et al. Neoantigen vaccine generates intratumoral T cell responses in phase Ib glioblastoma trial. *Nature* **2019**, *565*, 234–239. [CrossRef]
94. Hilf, N.; Kuttruff-Coqui, S.; Frenzel, K.; Bukur, V.; Stevanovic, S.; Gouttefangeas, C.; Platten, M.; Tabatabai, G.; Dutoit, V.; van der Burg, S.H.; et al. Actively personalized vaccination trial for newly diagnosed glioblastoma. *Nature* **2019**, *565*, 240–245. [CrossRef] [PubMed]
95. Doucette, T.; Rao, G.; Rao, A.; Shen, L.; Aldape, K.; Wei, J.; Dziurzynski, K.; Gilbert, M.; Heimberger, A.B. Immune heterogeneity of glioblastoma subtypes: Extrapolation from the cancer genome atlas. *Cancer Immunol. Res.* **2013**, *1*, 112–122. [CrossRef] [PubMed]
96. Woroniecka, K.; Chongsathidkiet, P.; Rhodin, K.; Kemeny, H.; Dechant, C.; Farber, S.H.; Elsamadicy, A.A.; Cui, X.; Koyama, S.; Jackson, C.; et al. T-cell exhaustion signatures vary with tumor type and are severe in glioblastoma. *Clin. Cancer Res.* **2018**, *24*, 4175–4186. [CrossRef]

97. Mohme, M.; Schliffke, S.; Maire, C.L.; Runger, A.; Glau, L.; Mende, K.C.; Matschke, J.; Gehbauer, C.; Akyuz, N.; Zapf, S.; et al. Immunophenotyping of newly diagnosed and recurrent glioblastoma defines distinct immune exhaustion profiles in peripheral and tumor-infiltrating lymphocytes. *Clin. Cancer Res.* **2018**, *24*, 4187–4200. [CrossRef]
98. Paley, M.A.; Kroy, D.C.; Odorizzi, P.M.; Johnnidis, J.B.; Dolfi, D.V.; Barnett, B.E.; Bikoff, E.K.; Robertson, E.J.; Lauer, G.M.; Reiner, S.L.; et al. Progenitor and terminal subsets of CD8+ T cells cooperate to contain chronic viral infection. *Science* **2012**, *338*, 1220–1225. [CrossRef]
99. Fontana, A.; Hengartner, H.; de Tribolet, N.; Weber, E. Glioblastoma cells release interleukin 1 and factors inhibiting interleukin 2-mediated effects. *J. Immunol.* **1984**, *132*, 1837–1844.
100. Siepl, C.; Bodmer, S.; Frei, K.; MacDonald, H.R.; De Martin, R.; Hofer, E.; Fontana, A. The glioblastoma-derived T cell suppressor factor/transforming growth factor-beta 2 inhibits T cell growth without affecting the interaction of interleukin 2 with its receptor. *Eur. J. Immunol.* **1988**, *18*, 593–600. [CrossRef]
101. Friese, M.A.; Wischhusen, J.; Wick, W.; Weiler, M.; Eisele, G.; Steinle, A.; Weller, M. RNA interference targeting transforming growth factor-beta enhances NKG2D-mediated antiglioma immune response, inhibits glioma cell migration and invasiveness, and abrogates tumorigenicity in vivo. *Cancer Res.* **2004**, *64*, 7596–7603. [CrossRef]
102. Zagzag, D.; Salnikow, K.; Chiriboga, L.; Yee, H.; Lan, L.; Ali, M.A.; Garcia, R.; Demaria, S.; Newcomb, E.W. Downregulation of major histocompatibility complex antigens in invading glioma cells: Stealth invasion of the brain. *Lab. Invest.* **2005**, *85*, 328–341. [CrossRef] [PubMed]
103. Schneider, T.; Sailer, M.; Ansorge, S.; Firsching, R.; Reinhold, D. Increased concentrations of transforming growth factor beta1 and beta2 in the plasma of patients with glioblastoma. *J. Neurooncol.* **2006**, *79*, 61–65. [CrossRef] [PubMed]
104. Moore, K.W.; de Waal Malefyt, R.; Coffman, R.L.; O’Garra, A. Interleukin-10 and the interleukin-10 receptor. *Annu. Rev. Immunol.* **2001**, *19*, 683–765. [CrossRef] [PubMed]
105. Murai, M.; Turovskaya, O.; Kim, G.; Madan, R.; Karp, C.L.; Cheroutre, H.; Kronenberg, M. Interleukin 10 acts on regulatory T cells to maintain expression of the transcription factor Foxp3 and suppressive function in mice with colitis. *Nat. Immunol.* **2009**, *10*, 1178–1184. [CrossRef] [PubMed]
106. Huettnner, C.; Paulus, W.; Roggendorf, W. Messenger RNA expression of the immunosuppressive cytokine IL-10 in human gliomas. *Am. J. Pathol.* **1995**, *146*, 317–322. [PubMed]
107. Wagner, S.; Czub, S.; Greif, M.; Vince, G.H.; Suss, N.; Kerkau, S.; Rieckmann, P.; Roggendorf, W.; Roosen, K.; Tonn, J.C. Microglial/macrophage expression of interleukin 10 in human glioblastomas. *Int. J. Cancer* **1999**, *82*, 12–16. [CrossRef]
108. Carlin, J.M.; Borden, E.C.; Sondel, P.M.; Byrne, G.I. Biologic-response-modifier-induced indoleamine 2,3-dioxygenase activity in human peripheral blood mononuclear cell cultures. *J. Immunol.* **1987**, *139*, 2414–2418.
109. Wainwright, D.A.; Balyasnikova, I.V.; Chang, A.L.; Ahmed, A.U.; Moon, K.S.; Auffinger, B.; Tobias, A.L.; Han, Y.; Lesniak, M.S. IDO expression in brain tumors increases the recruitment of regulatory T cells and negatively impacts survival. *Clin. Cancer Res.* **2012**, *18*, 6110–6121. [CrossRef]
110. Hwu, P.; Du, M.X.; Lapointe, R.; Do, M.; Taylor, M.W.; Young, H.A. Indoleamine 2,3-dioxygenase production by human dendritic cells results in the inhibition of T cell proliferation. *J. Immunol.* **2000**, *164*, 3596–3599. [CrossRef]
111. Wainwright, D.A.; Chang, A.L.; Dey, M.; Balyasnikova, I.V.; Kim, C.K.; Tobias, A.; Cheng, Y.; Kim, J.W.; Qiao, J.; Zhang, L.; et al. Durable therapeutic efficacy utilizing combinatorial blockade against IDO, CTLA-4, and PD-L1 in mice with brain tumors. *Clin. Cancer Res.* **2014**, *20*, 5290–5301. [CrossRef]
112. Kotsarini, C.; Griffiths, P.D.; Wilkinson, I.D.; Hoggard, N. A systematic review of the literature on the effects of dexamethasone on the brain from in vivo human-based studies: Implications for physiological brain imaging of patients with intracranial tumors. *Neurosurgery* **2010**, *67*, 1799–1815, discussion 1815. [CrossRef] [PubMed]
113. Heiss, J.D.; Papavassiliou, E.; Merrill, M.J.; Nieman, L.; Knightly, J.J.; Walbridge, S.; Edwards, N.A.; Oldfield, E.H. Mechanism of dexamethasone suppression of brain tumor-associated vascular permeability in rats. Involvement of the glucocorticoid receptor and vascular permeability factor. *J. Clin. Investig.* **1996**, *98*, 1400–1408. [CrossRef] [PubMed]

114. Grossman, S.A.; Ye, X.; Lesser, G.; Sloan, A.; Carraway, H.; Desideri, S.; Piantadosi, S.; Consortium, N.C. Immunosuppression in patients with high-grade gliomas treated with radiation and temozolomide. *Clin. Cancer Res.* **2011**, *17*, 5473–5480. [CrossRef] [PubMed]
115. Papadopoulos, M.C.; Saadoun, S.; Binder, D.K.; Manley, G.T.; Krishna, S.; Verkman, A.S. Molecular mechanisms of brain tumor edema. *Neuroscience* **2004**, *129*, 1011–1020. [CrossRef] [PubMed]
116. Bourke, E.; Moynagh, P.N. Antiinflammatory Effects of Glucocorticoids in Brain Cells, Independent of NF-KB. *J. Immunol.* **1999**, *163*, 2113. [PubMed]
117. Auphan, N.; DiDonato, J.A.; Rosette, C.; Helmborg, A.; Karin, M. Immunosuppression by glucocorticoids: Inhibition of NF-KB activity through induction of IKB synthesis. *Science* **1995**, *270*, 286. [CrossRef]
118. Hughes, M.A.; Parisi, M.; Grossman, S.; Kleinberg, L. Primary brain tumors treated with steroids and radiotherapy: Low CD4 counts and risk of infection. *Int. J. Radiat. Oncol. Biol. Phys.* **2005**, *62*, 1423–1426. [CrossRef]
119. Wong, E.T.; Lok, E.; Gautam, S.; Swanson, K.D. Dexamethasone exerts profound immunologic interference on treatment efficacy for recurrent glioblastoma. *Br. J. Cancer* **2015**, *113*, 232–241. [CrossRef]
120. Pitter, K.L.; Tamagno, I.; Alikhanyan, K.; Hosni-Ahmed, A.; Pattwell, S.S.; Donnola, S.; Dai, C.; Ozawa, T.; Chang, M.; Chan, T.A.; et al. Corticosteroids compromise survival in glioblastoma. *Brain* **2016**, *139*, 1458–1471. [CrossRef]
121. Herold, M.J.; McPherson, K.G.; Reichardt, H.M. Glucocorticoids in T cell apoptosis and function. *Cell Mol. Life Sci.* **2006**, *63*, 60–72. [CrossRef]
122. Dietrich, J.; Rao, K.; Pastorino, S.; Kesari, S. Corticosteroids in brain cancer patients: Benefits and pitfalls. *Expert Rev. Clin. Pharmacol.* **2011**, *4*, 233–242. [CrossRef]
123. Pufall, M.A. Glucocorticoids and cancer. *Adv. Exp. Med. Biol.* **2015**, *872*, 315–333. [CrossRef] [PubMed]
124. Gustafson, M.P.; Lin, Y.; New, K.C.; Bulur, P.A.; O’Neill, B.P.; Gastineau, D.A.; Dietz, A.B. Systemic immune suppression in glioblastoma: The interplay between CD14+HLA-DRlo/neg monocytes, tumor factors, and dexamethasone. *Neuro Oncol.* **2010**, *12*, 631–644. [CrossRef] [PubMed]
125. Piemonti, L.; Monti, P.; Allavena, P.; Sironi, M.; Soldini, L.; Leone, B.E.; Socci, C.; Di Carlo, V. Glucocorticoids Affect Human Dendritic Cell Differentiation and Maturation. *J. Immunol.* **1999**, *162*, 6473.
126. Adhikaree, J.; Franks, H.A.; Televantos, C.; Vaghela, P.; Kaur, A.P.; Walker, D.; Schmitz, M.; Jackson, A.M.; Patel, P.M. Impaired circulating myeloid CD1c+ dendritic cell function in human glioblastoma is restored by p38 inhibition—Implications for the next generation of DC vaccines. *Oncoimmunology* **2019**, *8*, 1593803. [CrossRef] [PubMed]
127. Van Gool, S.; Maes, W.; Ardon, H.; Verschuere, T.; Van Cauter, S.; De Vleeschouwer, S. Dendritic cell therapy of high-grade gliomas. *Brain Pathol.* **2009**, *19*, 694–712. [CrossRef]
128. Rozkova, D.; Horvath, R.; Bartunkova, J.; Spisek, R. Glucocorticoids severely impair differentiation and antigen presenting function of dendritic cells despite upregulation of Toll-like receptors. *Clin. Immunol.* **2006**, *120*, 260–271. [CrossRef]
129. Hugo, W.; Zaretsky, J.M.; Sun, L.; Song, C.; Moreno, B.H.; Hu-Lieskovan, S.; Berent-Maoz, B.; Pang, J.; Chmielowski, B.; Cherry, G.; et al. Genomic and transcriptomic features of response to Anti-PD-1 therapy in metastatic melanoma. *Cell* **2016**, *165*, 35–44. [CrossRef]
130. Lou, Y.; Diao, L.; Cuentas, E.R.; Denning, W.L.; Chen, L.; Fan, Y.H.; Byers, L.A.; Wang, J.; Papadimitrakopoulou, V.A.; Behrens, C.; et al. Epithelial-mesenchymal transition is associated with a distinct tumor microenvironment including elevation of inflammatory signals and multiple immune checkpoints in lung adenocarcinoma. *Clin. Cancer Res.* **2016**, *22*, 3630–3642. [CrossRef]
131. Ribas, A.; Hamid, O.; Daud, A.; Hodi, F.S.; Wolchok, J.D.; Kefford, R.; Joshua, A.M.; Patnaik, A.; Hwu, W.J.; Weber, J.S.; et al. Association of Pembrolizumab with tumor response and survival among patients with advanced melanoma. *JAMA* **2016**, *315*, 1600–1609. [CrossRef]
132. Zaretsky, J.M.; Garcia-Diaz, A.; Shin, D.S.; Escuin-Ordinas, H.; Hugo, W.; Hu-Lieskovan, S.; Torrejon, D.Y.; Abril-Rodriguez, G.; Sandoval, S.; Barthly, L.; et al. Mutations associated with acquired resistance to PD-1 blockade in melanoma. *N. Engl. J. Med.* **2016**, *375*, 819–829. [CrossRef] [PubMed]
133. Shin, D.S.; Zaretsky, J.M.; Escuin-Ordinas, H.; Garcia-Diaz, A.; Hu-Lieskovan, S.; Kalbasi, A.; Grasso, C.S.; Hugo, W.; Sandoval, S.; Torrejon, D.Y.; et al. Primary resistance to PD-1 blockade mediated by JAK1/2 mutations. *Cancer Discov.* **2017**, *7*, 188–201. [CrossRef] [PubMed]







134. Koyama, S.; Akbay, E.A.; Li, Y.Y.; Herter-Sprie, G.S.; Buczkowski, K.A.; Richards, W.G.; Gandhi, L.; Redig, A.J.; Rodig, S.J.; Asahina, H.; et al. Adaptive resistance to therapeutic PD-1 blockade is associated with upregulation of alternative immune checkpoints. *Nat. Commun.* **2016**, *7*, 10501. [CrossRef]
135. Benci, J.L.; Xu, B.; Qiu, Y.; Wu, T.J.; Dada, H.; Twyman-Saint Victor, C.; Cucolo, L.; Lee, D.S.; Pauken, K.E.; Huang, A.C.; et al. Tumor interferon signaling regulates a multigenic resistance program to immune checkpoint blockade. *Cell* **2016**, *167*, 1540–1554. [CrossRef]
136. Chen, D.S.; Mellman, I. Oncology meets immunology: The cancer-immunity cycle. *Immunity* **2013**, *39*, 1–10. [CrossRef]
137. Kim, J.E.; Patel, M.A.; Mangraviti, A.; Kim, E.S.; Theodoros, D.; Velarde, E.; Liu, A.; Sankey, E.W.; Tam, A.; Xu, H.; et al. Combination therapy with Anti-PD-1, Anti-TIM-3, and focal radiation results in regression of murine gliomas. *Clin. Cancer Res.* **2017**, *23*, 124–136. [CrossRef]
138. Garzon-Muvdi, T.; Theodoros, D.; Luksik, A.S.; Maxwell, R.; Kim, E.; Jackson, C.M.; Belcaid, Z.; Ganguly, S.; Tyler, B.; Brem, H.; et al. Dendritic cell activation enhances anti-PD-1 mediated immunotherapy against glioblastoma. *Oncotarget* **2018**, *9*, 20681–20697. [CrossRef]
139. Feig, C.; Jones, J.O.; Kraman, M.; Wells, R.J.B.; Deonarine, A.; Chan, D.S.; Connell, C.M.; Roberts, E.W.; Zhao, Q.; Caballero, O.L.; et al. Targeting CXCL12 from FAP-expressing carcinoma-associated fibroblasts synergizes with anti-PD-L1 immunotherapy in pancreatic cancer. *Proc. Natl. Acad. Sci. USA* **2013**, *110*, 20212–20217. [CrossRef] [PubMed]
140. McDermott, D.F.; Sosman, J.A.; Sznol, M.; Massard, C.; Gordon, M.S.; Hamid, O.; Powderly, J.D.; Infante, J.R.; Fasso, M.; Wang, Y.V.; et al. Atezolizumab, an Anti-programmed death-ligand 1 antibody, in metastatic renal cell carcinoma: Long-term safety, clinical activity, and immune correlates from a phase Ia study. *J. Clin. Oncol.* **2016**, *34*, 833–842. [CrossRef] [PubMed]



© 2020 by the authors. Licensee MDPI, Basel, Switzerland. This article is an open access article distributed under the terms and conditions of the Creative Commons Attribution (CC BY) license (<http://creativecommons.org/licenses/by/4.0/>).

Article

# Q-Cell Glioblastoma Resource: Proteomics Analysis Reveals Unique Cell-States Are Maintained in 3D Culture

Rochelle C. J. D'Souza <sup>1</sup>, Carolin Offenhäuser <sup>1</sup>, Jasmin Straube <sup>2</sup>, Ulrich Baumgartner <sup>1</sup>, Anja Kordowski <sup>1</sup>, Yuchen Li <sup>1</sup>, Brett W. Stringer <sup>1</sup>, Hamish Alexander <sup>1,3</sup>, Zarnie Lwin <sup>1,3</sup>, Po-Ling Inglis <sup>1,3</sup>, Rosalind L. Jeffree <sup>1,3</sup>, Terrance G. Johns <sup>4</sup>, Andrew W. Boyd <sup>1,5</sup> and Bryan W. Day <sup>1,5,6,\*</sup>

<sup>1</sup> Cell and Molecular Biology Department, QIMR Berghofer Medical Research Institute, Sid Faithfull Brain Cancer Laboratory, Brisbane, QLD 4006, Australia; Rochelle.D'Souza@qimrberghofer.edu.au (R.C.J.D.); Carolin.Offenhauser@qimrberghofer.edu.au (C.O.); Ulrich.Baumgartner@qimrberghofer.edu.au (U.B.); Anja.Kordowski@qimrberghofer.edu.au (A.K.); Michelle.Li@qimrberghofer.edu.au (Y.L.); Brett.W.Stringer@gmail.com (B.W.S.); Hamish.Alexander@health.qld.gov.au (H.A.); Zarnie.Lwin@health.qld.gov.au (Z.L.); Po-Ling.Inglis@health.qld.gov.au (P.-L.I.); Lindy.Jeffree@health.qld.gov.au (R.L.J.); Andrew.Boyd@qimrberghofer.edu.au (A.W.B.)

<sup>2</sup> Immunology Department, QIMR Berghofer Medical Research Institute, Gordon and Jessie Gilmour Leukaemia Research Laboratory, Brisbane, QLD 4006, Australia; Jasmin.Straube@qimrberghofer.edu.au

<sup>3</sup> Royal Brisbane and Women's Hospital, Brisbane, QLD 4006, Australia

<sup>4</sup> Telethon Kids Institute, Perth, WA 6009, Australia; Terrance.Johns@telethonkids.org.au

<sup>5</sup> School of Biomedical Sciences, The University of Queensland, Brisbane 4072, Australia

<sup>6</sup> School of Biomedical Sciences, Faculty of Health, Queensland University of Technology, Brisbane 4059, Australia

\* Correspondence: Bryan.Day@qimrberghofer.edu.au; Tel.: +61-7-3845-3885

Received: 30 December 2019; Accepted: 17 January 2020; Published: 21 January 2020



**Abstract:** Glioblastoma (GBM) is a treatment-refractory central nervous system (CNS) tumour, and better therapies to treat this aggressive disease are urgently needed. Primary GBM models that represent the true disease state are essential to better understand disease biology and for accurate preclinical therapy assessment. We have previously presented a comprehensive transcriptome characterisation of a panel (n = 12) of primary GBM models (Q-Cell). We have now generated a systematic, quantitative, and deep proteome abundance atlas of the Q-Cell models grown in 3D culture, representing 6167 human proteins. A recent study has highlighted the degree of functional heterogeneity that coexists within individual GBM tumours, describing four cellular states (MES-like, NPC-like, OPC-like and AC-like). We performed comparative proteomic analysis, confirming a good representation of each of the four cell-states across the 13 models examined. Kyoto Encyclopedia of Genes and Genomes (KEGG) pathway analysis identified upregulation of a number of GBM-associated cancer pathway proteins. Bioinformatics analysis, using the OncoKB database, identified a number of functional actionable targets that were either uniquely or ubiquitously expressed across the panel. This study provides an in-depth proteomic analysis of the GBM Q-Cell resource, which should prove a valuable functional dataset for future biological and preclinical investigations.

**Keywords:** glioblastoma (GBM); proteomics; GBM cell-states; recurrence; tumour heterogeneity; therapeutic targets

## 1. Introduction

Glioblastoma (GBM) is the most common and aggressive form of adult brain cancer, and patients have not experienced significant increases in overall survival for several decades [1–3]. This lack of progress is, in part, attributable to the significant heterogeneity that exists within these tumours [4–8]. Recent seminal studies by Suva and colleagues have discovered that multiple dynamic cell-states (MES-like, NPC-like, OPC-like and AC-like) can reside within a single tumour entity, highlighting the degree of heterogeneity and plasticity present within GBM [9]. Therefore, therapeutic strategies with the ability to target each functional state have the potential to produce more durable clinical responses. Another significant factor preventing successful disease translation has been the lack of faithful models to drive meaningful neuro-oncology discoveries. To address this problem, we embarked upon the generation and characterisation of a panel of clinically relevant primary *in vitro* and *in vivo* GBM models (termed Q-Cell) [10,11]. Our previous Q-Cell characterisation studies have primarily focused on transcriptome expression analysis using microarray and RNA Sequencing (RNA-Seq) approaches. This study sought to expand upon our previous transcriptome findings by better understanding the proteomic profile of these models. Relative protein abundances of 6167 human proteins were quantitated using mass spectrometry (MS) and their expression patterns analysed bioinformatically. Principal component analysis, conducted on independent Q-Cell replicates, revealed consistent protein expression within a given model. These data indicated a high degree of fidelity at the protein level. All Q-Cell GBM models have been generated from IDH1 WT (wild-type) disease specimens. Not surprisingly, given this IDH1 wild-type (WT) status, we observed a high degree of correlation when comparing total protein expression between each model. Correlation at the protein level was most pronounced in a pair-matched pre- and post-treatment GBM specimen (SB2/SB2b). We also sought to analyse the relevance of the recently described GBM cell-states in our Q-Cell resource. Proteomics analysis revealed a good representation of each of the four cell-states across the 13 models examined. We also characterised a number of hybrids ( $n = 5$ ) that displayed significant heterogeneity with elevated protein expression of multiple cell-state markers within a given model. This finding was consistent with the Suva study, where the single-cell RNA-Seq data showed a significant number of tumour cells in transition states [9]. Despite a small sample size, detailed analysis of the single pair-matched model SB2/SB2b highlighted a transition at recurrence to a more MES-like state. This is consistent with the findings of others, indicating an increase in mesenchymal disease when GBM tumours recur post-therapy [4,12]. Furthermore, of the 257 cell-state-characterisation genes assessed, we detected 153 (57%) at the protein level. This finding indicated reasonably high levels of mRNA translation, providing significant scope for future biological and preclinical therapy studies aimed at targeting multiple GBM cell-states.

Unsupervised hierarchical clustering identified that eight of the models tended to express structural proteins associated with a broad mesenchymal-like signature, while the remaining five models expressed proteins associated with a more neuronal-like GBM signature. Kyoto Encyclopedia of Genes and Genomes (KEGG) pathway analysis identified upregulation of a number of GBM-associated cancer pathway proteins across the 13 models, as expected. We also undertook bioinformatics analysis, using the OncoKB database, to identify functional actionable targets that were either uniquely or ubiquitously expressed across the models.

The present effort has sought to provide a detailed proteomics analysis and build upon our previously described transcriptomic analysis of the Q-Cell GBM resource. Findings of this study have increased our understanding of GBM tumour heterogeneity and cell-states at the protein level and further validated our previous mRNA datasets. Given the highly functional nature of proteomics analysis, we hope this freely available GBM resource and combined datasets will provide a highly relevant functional platform to drive meaningful biological and translational neuro-oncology discoveries into the future.

## 2. Materials and Methods

### 2.1. Cell Culture

We have developed a characterised GBM patient-derived cell line resource (Q-Cell) [10–13], in which lines are maintained as glioma neural stem cell (GNS) cultures [14] or as 3D neurosphere cultures [15] using StemPro NSC SFM (Invitrogen, Carlsbad, CA, USA) or KnockOut™ DMEM (Gibco, Thermo Fisher Scientific, Waltham, MA, USA) as per the manufacturer's guidelines. Characterisation data is freely available from <https://www.qimrberghofer.edu.au/q-cell/>. All tissues were collected following ethical approval from the Royal Brisbane Women's Hospital and QIMR Berghofer Human Research Ethics Committees. Ethical approval number: P3420, HREC/17/QRBW/577 Novel Therapies for Brain Cancer. In order to maintain pluripotency, KnockOut™ DMEM (Gibco) media were supplemented with GlutaMAX™ Supplement (Gibco), StemPro™ Neural Supplement (Gibco), Recombinant Human EGF (Gibco), Recombinant Human FGFb (Gibco), and Penicillin/Streptomycin (Gibco). Cells were cultured on flasks coated with Basement Membrane Matrigel® Matrix (Corning, New York, NY, USA). Passaging the cells was done by detaching the cells from the flask surface using Accutase® solution (Sigma-Aldrich, St. Louis, MO, USA). Glioma cells were cultured as glioma neural stem (GNS) cultures as outlined in detail in [14] or as tumourspheres using StemPro® NSC SFM.

### 2.2. Proteome Sample Preparation

GBM cells ( $5 \times 10^6$ ) were seeded in T75 flasks with StemPro® NSC SFM (Thermo Fisher Scientific, Waltham, MA, USA). Cell lysates were collected in biological triplicates 72 hours postseeding. Cells were lysed in buffer containing 2% SDS (Sigma-Aldrich), EDTA-free protease inhibitor (Roche, Basel, Switzerland) and 100 mM tris-HCl (pH 7.6) [16]. The lysates were sonicated and incubated for 5 min at 95 °C, protein concentration was quantified, and samples were processed by an in-solution digest protocol. Briefly, 100 µg of cell lysate was precipitated overnight with 5 volumes of ice-cold acetone. The precipitate was collected by centrifugation and resuspended in 8 M urea (Sigma-Aldrich). The samples were reduced with dithiothreitol (Sigma-Aldrich) for 1 h at room temperature, alkylated with iodoacetamide (Sigma-Aldrich) in the dark, diluted to a final concentration of 2 M urea, 10% acetonitrile (Merck, Kenilworth, NJ, USA) and 1 µg of trypsin (Promega, Madison, WI, USA) and digested to peptides overnight at 37 °C. The peptides were desalted on C18 stage tips as described [17] and resuspended in 0.1% formic acid.

### 2.3. Liquid Chromatography (LC) and Mass Spectrometry (MS) Analysis

Peptides were injected under trapping conditions using a Waters (Milford, MA, USA) NanoAcquity system interfaced to a linear triple quadrupole (LTQ)-Orbitrap elite mass spectrometer (Thermo Fisher Scientific). Acidified digested samples were loaded onto a Waters 2G-V/M C18 Symmetry trap (5 µm particle size, 180 µm × 20 mm) at 5 µL/min in 99% solvent A (0.1% (v/v) aqueous formic acid) and 1% solvent B (100% (v/v) acetonitrile containing 0.1% (v/v) formic acid) for 3 minutes, and the peptides were subsequently separated inline using a pre-equilibrated analytical column (Waters C18 BEH 130 Å, 1.7 µm particle size, 75 µm × 200 µm) at a flow rate of 0.3 µL/min and temperature of 35 °C. The gradient ran at 300 nL/min from 2% B (0.1% formic acid in acetonitrile) to 40% B over 190 min, rose to 95% B to wash the column, then re-equilibrated at 2% B for the next injection. Eluate was delivered into the mass spectrometer via a Nanospray Flex Ion Source (Thermo Fisher Scientific) containing a 10 µm P200P coated silica emitter (New Objective, Woburn, MA, USA). Typical spray voltage was 1.8 kV with no sheath, sweep, or auxiliary gases; the heated capillary temperature was set to 285 °C. The LTQ-Orbitrap Elite mass spectrometer (Thermo Fisher Scientific) was controlled using Xcalibur 2.2 SP1.48 software (Thermo Fisher Scientific) and operated in a data-dependent acquisition mode to automatically switch between Orbitrap-MS and collision induced dissociation (CID)- based ion trap-MS/MS. The survey full scan mass spectra (from m/z 380 to 1700) were acquired in the Orbitrap with a resolving power of 120,000 after accumulating ions to an automatic gain control (AGC) target value of  $1.0 \times 10^6$  charges in

the LTQ. MS/MS spectra were concurrently acquired in the LTQ on the 20 most intense ions from the survey scan, using an AGC target value of  $1.0 \times 10^4$ . Charge state filtering (unassigned precursors and singly charged ions were not selected for fragmentation) and dynamic exclusion (repeat count 1, repeat duration 30 s, exclusion list size 500, exclusion duration 90 s) were used. CID fragmentation conditions in the LTQ were 35% normalized collision energy, activation  $q$  of 0.25, 10 ms activation time, and minimum ion selection intensity of 5000 counts. Maximum ion injection times were 200 ms and 50 ms for survey full scans and MS/MS scans, respectively.

#### 2.4. Data Processing and Analysis

Spectra were analyzed using MaxQuant [18] version 1.5.3.30, and Andromeda [19]. The MS2 spectra were searched against the UniProt FASTA database version 31/01/2013. Enzyme specificity was set to trypsin, allowing for cleavage N-terminal to proline and between aspartic acid and proline. The search included carbamidomethylation of cysteine as a fixed modification and N-acetylation and oxidation of methionine as variable modifications. Up to two missed cleavages were allowed for protease digestion, and enzyme specificity was set to trypsin, defined as C-terminal to arginine and lysine excluding proline. The *identify* module in MaxQuant was used to filter (1% false identification rate (FDR)) identifications at the peptide and protein level. The identity of precursor peptides present in MS1, but not selected for fragmentation and identification by MS2 in a given run, was obtained by transferring peptide identifications based on accurate mass and retention times across liquid chromatography–mass spectrometry (LC–MS) runs where possible using MaxQuant [20]. Protein identifications were collapsed to the minimal number that contained the set of identified peptides. Proteome quantification was performed in MaxQuant using the extracted ion chromatography (XIC)-based label-free quantification (LFQ) algorithm [21]. In MaxQuant, a quantification event was reported only when isotope pattern could be detected and was consistent in terms of charge state of peptide. For quantification, intensities were determined as the intensity maximum over the retention time profile. Intensities of different isotopic peaks in an isotope pattern were summed up for further analysis. All RAW files and protein-based quantification results are available for download from the Q-Cell website at <https://www.qimrberghofer.edu.au/q-cell/>.

#### 2.5. Bioinformatics and Statistical Analysis

Bioinformatics analyses were performed using Perseus in MaxQuant [22]. Proteins identified on the basis of at least one unique peptide were used for all subsequent analyses. We selected the normalized abundances of proteins that were quantified in duplicates from at least one cell line. For comparing differences between all cell lines, biological triplicates were grouped by cell line, and the analysis of variance (ANOVA) was performed. We used the ANOVA method with largest power, permutation-based FDR of 0.05, and at least 250 repetitions for truncation. A two-sided student's  $t$ -test was used to perform the comparison between two cell lines SB2 and SB2b employing a  $p$ -value cutoff of 0.05.

Unsupervised hierarchical clustering was performed on the  $z$ -score-transformed protein intensities or the  $z$ -scored  $\log_2$  normalised mRNA read counts. Proteins were annotated with GO (Gene Ontology) biological process terms [23] and KEGG (Kyoto Encyclopedia of Genes and Genomes) pathway terms [24]. Statistical analysis of the enrichment of proteins with functional annotations was evaluated using a Fisher's exact test ( $p$ -value  $< 0.05$ ). An enrichment score of greater than 1 indicates enrichment, and a score from 0 to 1 indicates negative enrichment. For comparison of mRNA and protein expression of the GBM-associated genes, the normalized protein intensities and normalized mRNA read counts were matched by gene name, and Pearson's coefficient of correlation was calculated.

#### 2.6. Cell-State ssGSEA

NPC1, NPC2, MES1, MES2, APC, and OPC marker genes were extracted from [9]. NPC1 and NPC2 were combined into a single gene set called NP, and MES1 and MES2 were combined into



MES. z-score-scaled protein intensities of the models were assessed for NPC, MES, APC, and OPC enrichment using the R GSVA library (v1.32) with the ssGSEA algorithm as developed by Barbie et al. (2009) [25]. Principal component analysis was performed on scaled and centered ssGSEA enrichment scores. Replicates were summarised using an ellipse with the Euclidean distance from the centre and radius of 1. Heat maps were generated on the average ssGSEA enrichment scores of the cell line replicates. Hierarchical clustering of models and marker gene sets was performed on the 1-Spearman correlation dissimilarity matrix using the ward.D2 algorithm. A similar analysis was performed on the log<sub>2</sub>-normalised mRNA read counts from the previous transcriptomics study.

### 2.7. Cytoscape-Based Data Visualisation

Proteins identified from the list of metamodule genes describing the six different cell-states (MES1-, MES2-, NPC1-, NPC2-, OPC-, and AC-like) were visualised as nodes and grouped by the respective cell-states. z-score-scaled protein intensity values were plotted using continuous colour mapping of the nodes in Cytoscape version 3.7.2 [26]. For enrichment analysis, the top 100 significantly regulated proteins with the highest fold change absolute value were analysed for enrichment of gene ontology (GO) molecular functions, GO biological processes, and Kyoto Encyclopedia of Genes and Genomes (KEGG) pathways using the ClueGO App version 2.5.5 [27] in Cytoscape version 3.7.2 [26]. Analysis parameters were set to include GO terms (level 3 to 8), and KEGG pathways for which at least 5 proteins and 4% of associated proteins per term/pathway were present in the list of regulated proteins. A two-sided hypergeometric test with Benjamini–Hochberg correction was performed to identify significantly enriched/depleted terms ( $p$ -value <0.05) against a custom reference set consisting of all proteins identified in the SB2 and SB2b MS datasets. The kappa score threshold for clustering of related terms was set to 0.4.

## 3. Results

### 3.1. Q-Cell Proteomics Analysis

To accurately quantify proteome expression in the Q-Cell GBM panel, we performed label-free quantitative MS analysis of protein lysates from GBM cells grown in 3D neurosphere suspension cultures [15]. Primary models were initially grown as adherent GNS cultures on matrigel under serum-free conditions [14]. In order to avoid confounding our results with high abundance proteins present in the basement membrane of matrigel, cells were grown in 3D suspension cultures as neurospheres for 72 hours before lysis. We have previously shown that GBM cells either grown as neurospheres or on a substrate of matrigel tend to display equivalent characteristics [28]. Cell lysates were subjected to a defined proteomics workflow (Figure 1A). Peptides were analysed with 4 hour gradients on an LTQ-Orbitrap Elite mass spectrometer with CID fragmentation. Combined analysis of the spectra from all samples resulted in the identification of 6180 proteins at FDR of 1%. Using the label-free quantification algorithm in MaxQuant [21], we measured the abundance of 6167 proteins in at least one pairwise comparison (Table S1). Analysis of triplicate samples showed excellent reproducibility when compared using principal component analysis of all quantified proteins (Figure 1B). Next, we compared the expression of the proteome by calculating the Pearson correlation coefficient ( $r$ ) between each model. As expected, the highest correlation ( $r = 0.97$ ) was observed between the pair-matched primary and recurrent model (SB2 and SB2b), while the least similar model identified was PB1 ( $r = 0.82$ ) (Figure 1C).

We next measured the number of proteins identified in each of the triplicate runs from each Q-Cell model. Proteomics analysis identified an average of 2200 common proteins between each model. PB1 and SJH1 expressed the largest number of unique proteins (145 and 85 respectively) and therefore correlated the least to the remaining 11 models (Figure 1D and Table S1). Some of the uniquely expressed genes include *CD44* (quantified in FPW1), *ERBB2* (quantified in RN1), and *OLIG2* (quantified in PB1) and are genes with key roles in brain cancer. *CDKN1A* and *CDKN2A* were highly

expressed in RKI1 and detected in JK2 and MMK1; these cell lines are the only ones in our panel which do not have deletion of the coding gene at the genome level.

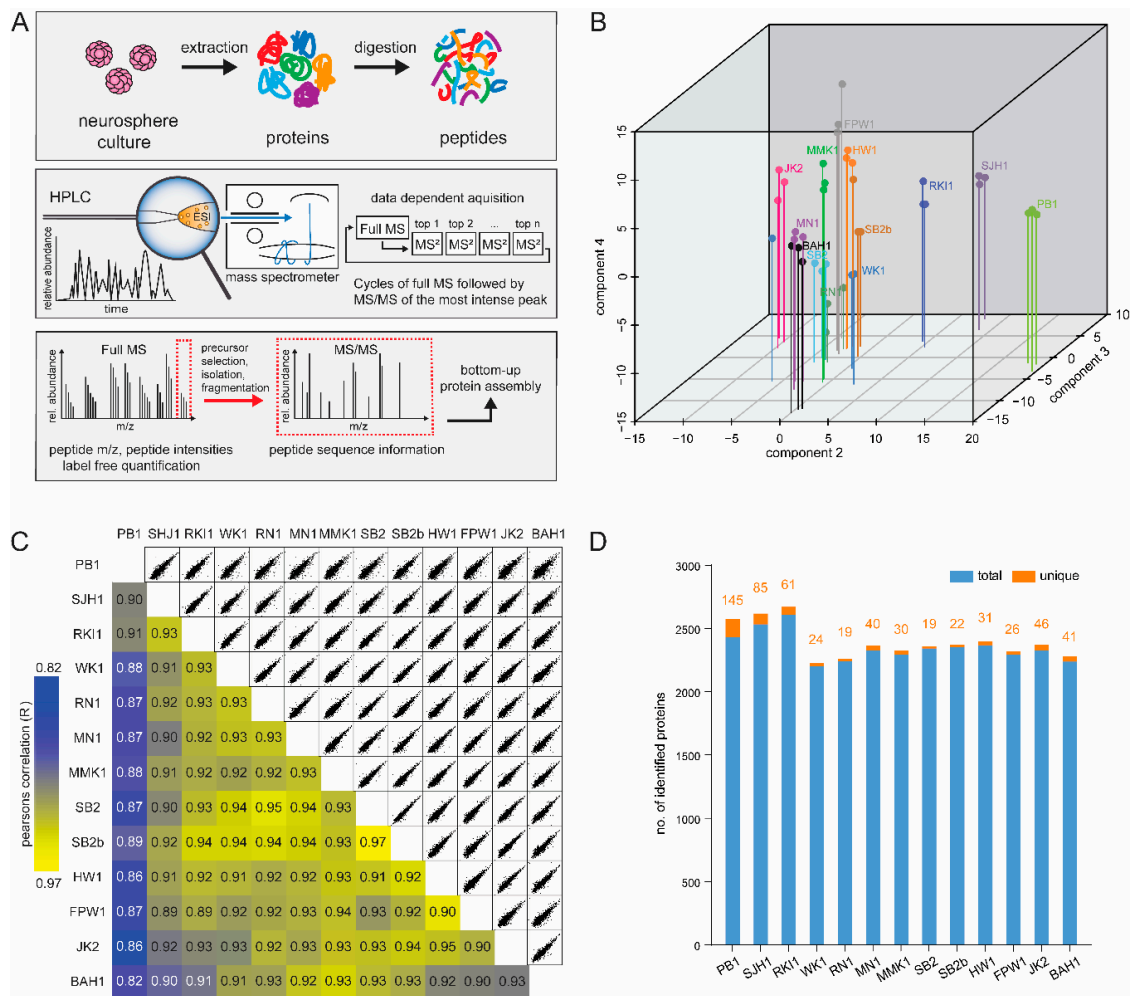


**Figure 1.** Proteome mapping of 13 Q-cell cell lines. **(A)** Graphical illustration of the workflow for glioblastoma (GBM) cell line proteome analysis. GBM primary cell lines were cultured as neurospheres, lysed in SDS-based buffer, trypsin digested by in-solution digestion in biological triplicate. LC–MS/MS with 4 hour runs and CID fragmentation were performed in the LTQ-Orbitrap Elite. **(B)** 3D-PCA plot. The proteome of thirteen cell lines measured in triplicates segregated into major cell types showing well-correlated triplicates within a cell line. **(C)** The matrix of 78 correlation plots revealed very high correlations between protein intensities in triplicates (Pearson correlation coefficient 0.82–0.97 between cell types). The colour code follows the indicated values of the correlation coefficient. **(D)** A bar chart showing the number of total proteins identified in each of the cell lines with false identification rate (FDR) of 1%.

### 3.2. GBM Cell-State Analysis

As outlined above, four dynamic cell-states which functionally drive intratumoural heterogeneity within GBM have recently been described [9]. To better understand the contribution of these GBM cell-states within our Q-Cell resource, we firstly analysed 257 unique genes, separating tumours into six metamodules (MES1-, MES2-, NPC1-, NPC2-, OPC-, and AC-like) as per Suva and colleagues [9] encompassing each of the identified four cell-states. We next matched gene expression to the 6172 identified proteins from our MS analysis. Identified proteins corresponded to 38/50 and 29/50 genes from MES1 and MES2, 24/50 and 28/50 genes from NPC1 and NPC2, 26/39 genes from

OPC and 30/50 genes from AC-like metamodules respectively (Table S1). A total of 153 proteins were identified from the corresponding 257 unique cell-state genes outlined by Suva and colleagues.

To identify the contribution of each cell-state in the Q-Cell panel, z-score-scaled protein intensities were assessed for enrichment of the four states using an ssGSEA algorithm [25]. We thus obtained a cell-state score, which was used to predict the predominant cell-state of each model (Figure 2A and Figure S1). Four of the models showed an MES-like state, while two of each model showed an NPC-like and AC-like profile. Four models showed an enrichment of more than one cell-state, termed hybrids. This finding was consistent with Suva and colleagues, highlighting a significant number of GBM cells present in transition states [9]. Principal component analysis showed an enrichment of the predominant cell-state when compared to the rest (Figure 2B and Figure S2). JK2 and MN1 displayed a clear MES-like phenotype matching a total of 39 proteins from the Suva study, with 25 of these proteins showing very high expression (Figure 3 and Table S1). Similarly, HW1 and FPW1 showed a strong AC-like phenotype with high expression of 15 matched proteins, and RKI1 and WK1 displayed the strongest NPC-like phenotype, while BAH1 showed an OPC-like phenotype (Figure 3). Our analysis identified four of the Q-cell lines, PB1, SHJ1, RN1, and MMK1, to be intermediate hybrids, showing a strong ssGSEA score of more than one cell-state, which is concordant with the results from Suva and colleagues (Figure 3). In addition, we similarly generated cell-state scores for 12 of these cell lines previously analysed by transcriptomics using 252 genes that were identified (Figure 2C and Table S2) [11]. The proteomics-based and transcriptomics-based cell-state phenotypes for our cell lines were remarkably similar, except for FPW1, which switched from being AC-like to OPC-like.

Our panel of 13 primary GBM cell lines consisted of one pair-matched primary and one recurrent tumour, designated SB2 and SB2b; respectively. SB2 showed an OPC-like state, while SB2b was enriched for the MES-like cell-state with increased expression of marker proteins SERPINE1, GSN, NNMT, SOD2, PLP2, and PRDX6 (Figure 4A,B) with an overall increase of the ssGSEA MES score. We performed a student’s t-test (two-sided, *p*-value cut off >0.05) to identify the significantly regulated subset of proteins between the two cell lines (Table S3) and then performed enrichment analysis to look for GO molecular functions and KEGG pathways that are among the top 100 most regulated genes in the recurrent SB2b model. The analysis revealed an enrichment of DNA recombination and replication, ECM organisation and cell–substrate junctions, antigen presentation, morphogenesis and organ development, and calcium homeostasis (Figure 3C and Table S4).

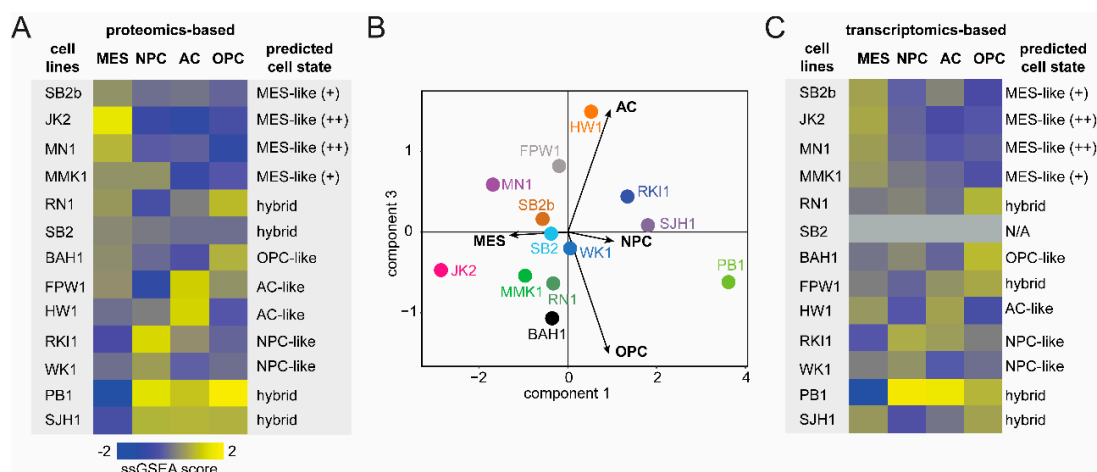


**Figure 2.** ssGSEA based cell-state scores (A) Heatmap of the z-scored ssGSEA scores of the thirteen cell line proteomes with predicted cell-states on the right. (B) PCA plot showing the distribution of the cell lines across the four cell-states. (C) Heatmap of the z-scored ssGSEA scores of the twelve cell line transcriptomes with predicted cell-states on the right. (Note: SB2 was not analysed by transcriptomics). Abbreviations: MES-like, mesenchymal-like; AC-like, astrocyte-like; OPC-like, oligodendrocyte progenitor cell-like; NPC-like, neural progenitor cell-like.

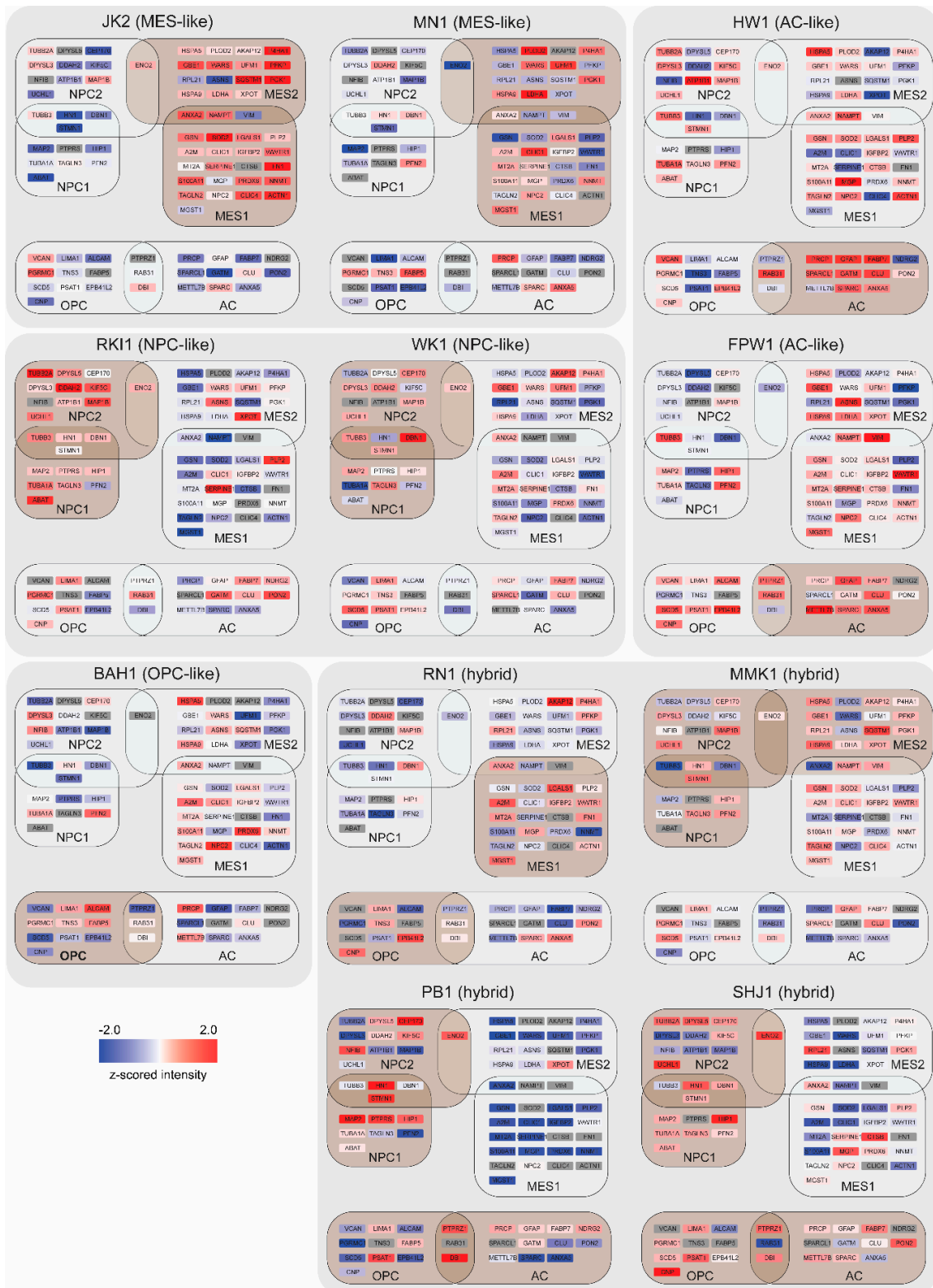


**Figure 3.** Depiction of cell-states in 11 GBM cell lines. z-scored expression values of genes that contribute to MES1-like, MES2-like, NPC1-like, NPC2-like, and AC-like metamodules (gene list from [9]). Brown boxes indicate predominant cell-state(s) in each cell line. Colour key: red, high expression; blue, low expression; grey, not detected.

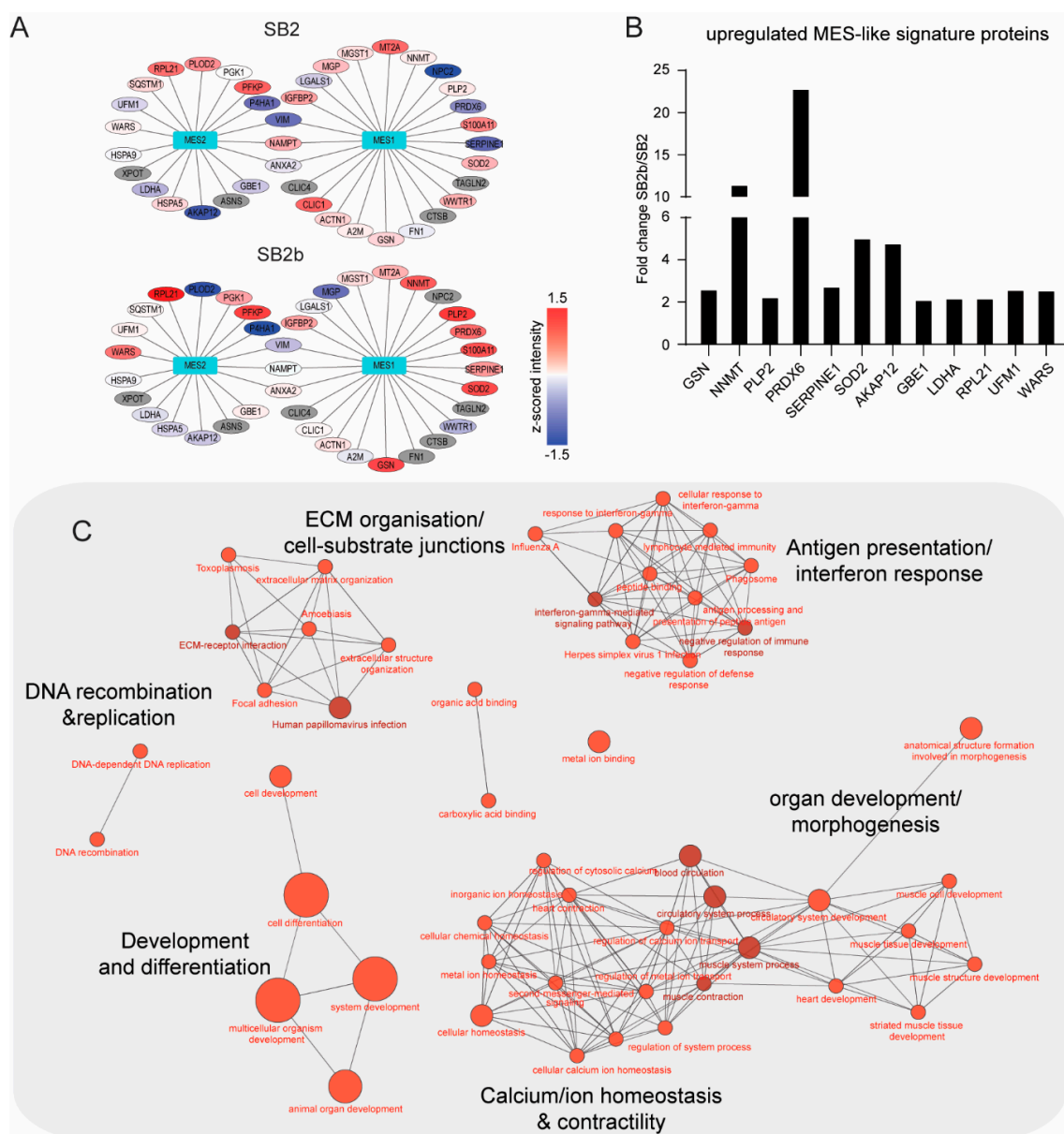


**Figure 4.** Changing cell-states in a pair-matched recurrent model. (A) z-scored expression values of genes that contribute to MES1-like and MES2-like metamodules (gene list from [9]). Colour key: red, high expression; blue, low expression; grey, no expression. (B) A bar graph of MES-1-like and MES-2-like genes with >2-fold increase in expression in the recurrent model (SB2b) when compared with the primary model (SB2). (C) Kyoto Encyclopedia of Genes and Genomes (KEGG) pathways and gene ontology (GO) molecular function terms enriched in the top 100 most regulated proteins in the recurrent SB2b model when compared to the primary SB2B model. Node size reflects the number of regulated proteins associated with a particular term/pathway. Node colour intensity increases with increasing significance of term enrichment.

### 3.3. Bioinformatics and Gene-Ontology-Based Protein Analysis

To gain a broader understanding of the differences in biological processes and signalling pathways between Q-Cell models, we performed an analysis of variance (ANOVA) at a 1% permutation-based FDR cut-off (Table S1). Amongst the top ten regulated proteins were GBM-associated structural and signalling members, including glial fibrillary acidic protein (GFAP), fibronectin (FN1), and Notch1 [29–31]. PB1 protein expression correlated the least with the rest of the Q-Cell models (Figure 1) and displays a

number of unique morphological characteristics, including high growth and small cell morphology in culture (data not shown). The highest exclusively expressed proteins, identified in PB1, were ubiquitin-conjugating enzyme-2 (UBE2) and SKI. Interestingly, the SKI protein has been associated with high cellular tumours and functions to negatively regulate transforming growth factor beta (TGF-beta) by direct interaction with Smads [32,33].

We next performed a Fisher’s exact test to evaluate the enrichment of KEGG pathways in the ANOVA-positive subset of proteins. Analysis revealed an enrichment of the KEGG term “Pathways in Cancer”, that consists of proteins mediating extracellular matrix (ECM), focal adhesion, and other associated pathways (Table S5). We extracted all identified member proteins belonging to this pathway and performed unsupervised hierarchical clustering. Results showed a segregation of eight models with higher expression of EMT/-mesenchymal-related proteins BAH1, MMK1, MN1, RN1, SB2b, SB2, WK1, and JK2, termed mesenchymal protein cluster 1 and cluster 2 (Figure 5).

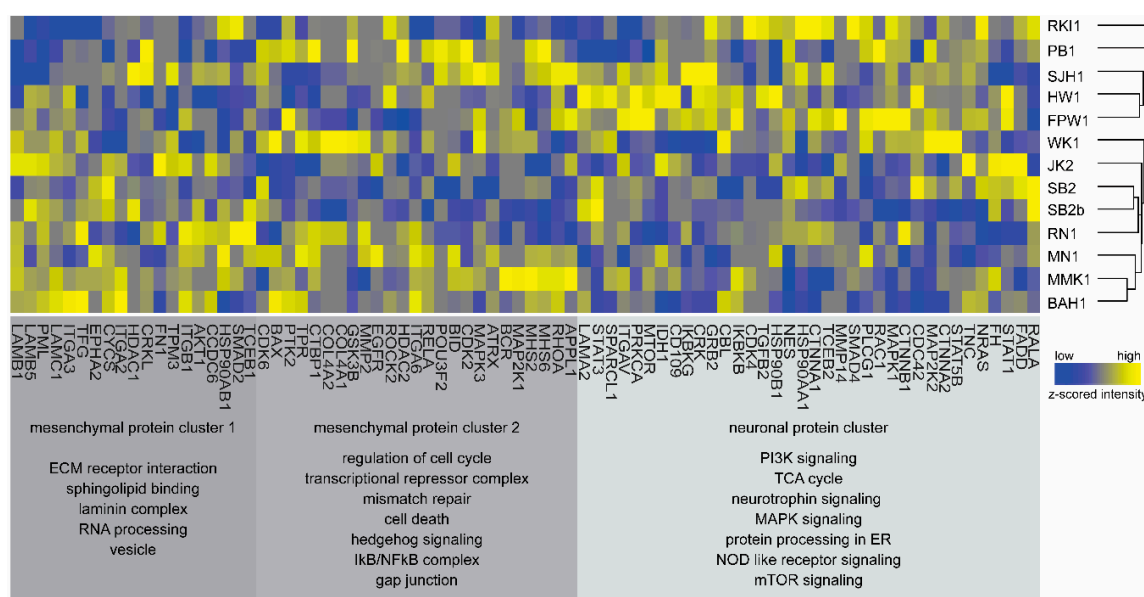


**Figure 5.** Functional analysis of the expressed proteome. Heatmap of proteins (z-scored intensities) belonging to the KEGG cancer pathway. The proteins segregate into three clusters: mesenchymal cluster 1, mesenchymal cluster 2, and neuronal cluster listing the pathways that proteins represent. Dendrogram depicts the similarity in protein profiles among the 13 cell lines. Colour legend: blue, low expression; and yellow, high expression.

Mesenchymal cluster 1 and cluster 2 consist of structural proteins known to be over-expressed in predominantly mesenchymal-like disease, including laminins, integrins, and collagens, as well as proteins involved in GAP junctions and cell cycle [34]. The remaining Q-Cell panel displayed strong expression of proteins correlated with genes identified from the TCGA GBM neuronal signature and was therefore termed neuronal protein cluster. Models in this cluster showed higher expression of proteins associated with PI3K and mTOR signalling pathways, TCA cycle, NFκB, and MAPK signalling. CDKN2A was found expressed only in MMK1 and RKI1, in concordance with the observation that these were the only lines that did not have a homozygous deletion on the gene level in our characterisation data [10,11]. All individual proteins and their z-scored expression values are provided in Table S6. We compared the proteome-based expression of proteins shown in Figure 6 to the transcriptomics-based RNA-Seq expression values from our previous study [11]. The Pearson’s coefficient of correlation was low to moderate between mRNA and protein levels for most cell lines and ranged between 0.18 and 0.56, with the exception of PB1, which showed a high correlation of 0.78 (Figure S3). While genes such as *EGFR*, *CDKN2A*, *PRKCA*, and *HSP90B1* showed good correlation between mRNA and protein; others such as *lamininB1*, *NRAS*, and *tenascin* showed a poor correlation. A caveat to our data was that

some key GBM-associated genes such as *PTEN*, *MYC* and *MET* were not identified in our proteomics analysis. In addition, we also performed hierarchical clustering of mRNA expression values and found that the Q-Cell panel segregated into two major clusters similar to our proteomics data (Figure S4).

To identify potentially actionable targets that could be either uniquely or ubiquitously expressed in the Q-Cell panel, we matched the OncoKB annotated genes to our dataset. OncoKB is a comprehensive precision oncology database that offers evidence-based drug information on FDA-approved therapies and other investigational agents. We identified 298/642 OncoKB annotated genes in our dataset and extracted the list of proteins identified that corresponded to genes that could be targeted with FDA-approved drugs (Figure 6). Previous therapy studies using the Q-Cell resource have validated our proteomic findings. Johns and colleagues showed that BAH1, which expresses high-level EGFR, effectively responded to gefitinib and panitumumab [35].

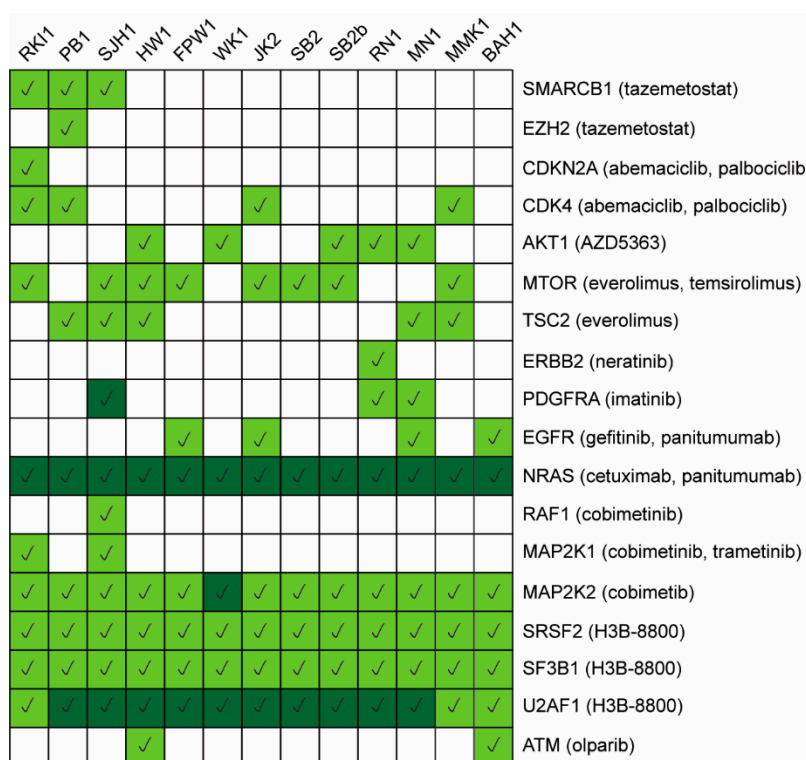


**Figure 6.** Protein expression matrix of targetable proteins. Expression levels (high, dark green; medium to low, light green; white, not detected) of proteins with potential FDA-approved drugs extracted from the OncoKB knowledgebase.

#### 4. Discussion

Here, we built upon our existing body of work to develop a well-described and characterised open-access collection of relevant GBM models for the neuro-oncology research community. Despite significant effort, there is yet to be meaningful increases in survival for GBM sufferers. Our previous Q-Cell resource characterisation study primarily focused on transcriptome-based mRNA expression analysis [11]. mRNA translation is tightly regulated by numerous processes, and gene expression is not always an accurate predictor of protein abundance [36]. We performed MS-based proteomics analysis of the thirteen Q-Cell models, generating a quantitative and deep proteome abundance atlas representing 6167 human proteins. In our analysis, we observed a number of key GBM-associated genes that were not detected at the protein level and may reflect either a lack of translation or limitations of the MS-based approach used. MS-based proteomics has been used effectively by others to measure the proteome, secretome, and glycoproteins in immortalised GBM cell lines [37,38].

Our objective was to further increase the translational significance of the Q-Cell datasets and to provide a platform for researchers to undertake faithful preclinical neuro-oncology studies.

Principal component analysis of Q-Cell replicates grown as 3D neurospheres, showed a high degree of fidelity of protein expression within a given model. All samples in the Q-Cell resource have been generated from IDH1 WT GBM specimens. We found a high degree of common protein expression across the panel, which was expected given the IDH status of the models. Despite this commonality, there were also a number of unique proteins highly expressed in each model.

Elevated expression of common GBM-associated proteins was identified with a trend toward either a broad mesenchymal or neuronal-like signature. An MES-like signature was identified in eight models, while the remaining five models displayed a neuronal-like signature. Given that all models were cultured under the same conditions, this result likely reflects the population of cells captured during the initial cell line generation process. It is worth noting that the majority of Q-Cell models were generated from surgical waste tissue aspirates taken from multiple tumour regions [10]. This was a deliberate attempt to better capture the spectrum of heterogeneous elements within any given tumour, though subclonal elements were likely enriched during the culture generation process.

A major contributing factor to the poor clinical responses observed in GBM patients can be attributed to the significant tumour heterogeneity present within these tumours [8]. Numerous attempts have been made to classify GBM subtypes underlying this heterogeneity [4–6,39]. Suva and colleagues have recently extended current thinking and shown that four functional and dynamic GBM cell-states can exist within a single tumour entity [9]. Given this recent finding, we sought to determine the distribution of these cell-states within the Q-Cell resource. Our initial findings highlighted a good representation of each cell-state across the panel, with a number of models expressing multiple cell-state markers at high levels. These models, termed hybrids, likely contain multiple initiating clones arising from different cell-states or might have arisen from a single clone that has two/more major cell-states. Interestingly, of the 257 cell-state genes described in the Suva study, we detected 153 (57%) at the protein level. MS-based proteomics is not exhaustive, and some key proteins may not have been detected in our analysis. Alternatively, some of the cell-state marker genes may not have been translated to protein. Hence, using gene expression data alone may not be the best approach for accurate biological assessment or translational studies. The NPC-like RKI1 model was derived from a patient with the longest survival from the Q-Cell panel. The NPC-like markers in RKI1 were high, resembling a proneural subtype which is associated with a better prognosis. We also analysed a single pair-matched pre- and post-treatment model (SB2/SB2b). Proteomic results generated from this paired model were intriguing and indicated a number of uniquely overexpressed proteins in the recurrent setting. We also noted a shift to a more mesenchymal phenotype post-treatment, a phenomenon previously reported by others [4,12].

To guide potential future translational studies, we identified a number of unique and common targetable proteins using the OncoKB database. These proteins were targeted with either FDA-approved therapies or other investigational agents and could be used to validate precision oncology or cell-state targeting strategies in the future.

In summary, here we present our detailed proteomics findings of the open-access Q-Cell GBM resource and hope this will accurately guide and inform future studies to improve outcomes for GBM sufferers.

**Supplementary Materials:** The following are available online at <http://www.mdpi.com/2073-4409/9/2/267/s1>, Figure S1: Cell-state scores of thirteen Q-cell lines, Figure S2: PCA plot showing the distribution of the cell lines across the four cell-states from the triplicate experiments, Figure S3: Pearson's co-efficient of correlation comparing mRNA and protein expression, Figure S3: Functional analysis of the expressed transcriptome, Table S1: Proteins identified, Table S2: mRNA expression of Neftel genes, Table S3: t-test SB2b vs SB2, Table S4: ClueGO enrichment, Table S5: ANOVA KEGG terms, Table S6: Heatmap proteins.

**Author Contributions:** Conceptualisation, R.C.J.D., T.G.J., A.W.B., and B.W.D.; methodology, R.C.J.D., B.W.S., and B.W.D.; formal analysis and investigation, R.C.J.D., C.O., J.S., U.B., A.K., Y.L., and B.W.D.; resources, B.W.S., B.W.D., H.A., Z.L., P.-L.I., and R.L.J.; data curation, R.C.J.D., C.O., J.S., U.B., A.K., and B.W.D.; writing—original



draft preparation, R.C.J.D. and B.W.D.; supervision, B.W.D. project administration, B.W.D.; funding acquisition, B.W.D. All authors have read and agreed to the published version of the manuscript.

**Funding:** This research was funded by generous donation support from the Sid Faithfull Group and Cure Brain Cancer Foundation. R.C.J.D. was supported by a priority-driven collaborative cancer research scheme (PdCCRS) early-career grant from Cancer Australia.

**Acknowledgments:** We acknowledge the QIMR Berghofer Proteomics Facility, especially Keyur Dave and Marcus Hastie for their assistance in performing the MS analysis.

**Conflicts of Interest:** Authors declare no conflict of interest.

## References

1. Furnari, F.B.; Fenton, T.; Bachoo, R.M.; Mukasa, A.; Stommel, J.M.; Stegh, A.; Hahn, W.C.; Ligon, K.L.; Louis, D.N.; Brennan, C.; et al. Malignant astrocytic glioma: Genetics, biology, and paths to treatment. *Genes Dev.* **2007**, *21*, 2683–2710. [CrossRef] [PubMed]
2. Stupp, R.; Mason, W.P.; van den Bent, M.J.; Weller, M.; Fisher, B.; Taphoorn, M.J.; Belanger, K.; Brandes, A.A.; Marosi, C.; Bogdahn, U.; et al. Radiotherapy plus concomitant and adjuvant temozolomide for glioblastoma. *N. Engl. J. Med.* **2005**, *352*, 987–996. [CrossRef] [PubMed]
3. Louis, D.N.; Perry, A.; Reifenberger, G.; von Deimling, A.; Figarella-Branger, D.; Cavenee, W.K.; Ohgaki, H.; Wiestler, O.D.; Kleihues, P.; Ellison, D.W. The 2016 World Health Organization Classification of Tumors of the Central Nervous System: A summary. *Acta Neuropathol.* **2016**, *131*, 803–820. [CrossRef] [PubMed]
4. Phillips, H.S.; Kharbanda, S.; Chen, R.; Forrest, W.F.; Soriano, R.H.; Wu, T.D.; Misra, A.; Nigro, J.M.; Colman, H.; Soroceanu, L.; et al. Molecular subclasses of high-grade glioma predict prognosis, delineate a pattern of disease progression, and resemble stages in neurogenesis. *Cancer Cell* **2006**, *9*, 157–173. [CrossRef]
5. Verhaak, R.G.; Hoadley, K.A.; Purdom, E.; Wang, V.; Qi, Y.; Wilkerson, M.D.; Miller, C.R.; Ding, L.; Golub, T.; Mesirov, J.P.; et al. Integrated genomic analysis identifies clinically relevant subtypes of glioblastoma characterized by abnormalities in PDGFRA, IDH1, EGFR, and NF1. *Cancer Cell* **2010**, *17*, 98–110. [CrossRef]
6. Wang, Q.; Hu, B.; Hu, X.; Kim, H.; Squatrito, M.; Scarpace, L.; deCarvalho, A.C.; Lyu, S.; Li, P.; Li, Y.; et al. Tumor Evolution of Glioma-Intrinsic Gene Expression Subtypes Associates with Immunological Changes in the Microenvironment. *Cancer Cell* **2017**, *32*, 42–56.e46. [CrossRef]
7. Akgul, S.; Patch, A.M.; D’Souza, R.C.J.; Mukhopadhyay, P.; Nones, K.; Kempe, S.; Kazakoff, S.H.; Jeffree, R.L.; Stringer, B.W.; Pearson, J.V.; et al. Intratumoral Heterogeneity Underlies Distinct Therapy Responses and Treatment Resistance in Glioblastoma. *Cancers* **2019**, *11*, 190. [CrossRef]
8. Patel, A.P.; Tirosch, I.; Trombetta, J.J.; Shalek, A.K.; Gillespie, S.M.; Wakimoto, H.; Cahill, D.P.; Nahed, B.V.; Curry, W.T.; Martuza, R.L.; et al. Single-cell RNA-seq highlights intratumoral heterogeneity in primary glioblastoma. *Science* **2014**, *344*, 1396–1401. [CrossRef]
9. Neftel, C.; Laffy, J.; Filbin, M.G.; Hara, T.; Shore, M.E.; Rahme, G.J.; Richman, A.R.; Silverbush, D.; Shaw, M.L.; Hebert, C.M.; et al. An Integrative Model of Cellular States, Plasticity, and Genetics for Glioblastoma. *Cell* **2019**, *178*, 835–849.e821. [CrossRef]
10. Day, B.W.; Stringer, B.W.; Wilson, J.; Jeffree, R.L.; Jamieson, P.J.; Ensbey, K.S.; Bruce, Z.C.; Inglis, P.; Allan, S.; Winter, C.; et al. Glioma Surgical Aspirate: A Viable Source of Tumor Tissue for Experimental Research. *Cancers* **2013**, *5*, 357–371. [CrossRef]
11. Stringer, B.W.; Day, B.W.; D’Souza, R.C.J.; Jamieson, P.R.; Ensbey, K.S.; Bruce, Z.C.; Lim, Y.C.; Goasdoue, K.; Offenhauser, C.; Akgul, S.; et al. A reference collection of patient-derived cell line and xenograft models of proneural, classical and mesenchymal glioblastoma. *Sci. Rep.* **2019**, *9*, 4902. [CrossRef] [PubMed]
12. Bhat, K.P.; Balasubramanian, V.; Vaillant, B.; Ezhilarasan, R.; Hummelink, K.; Hollingsworth, F.; Wani, K.; Heathcock, L.; James, J.D.; Goodman, L.D.; et al. Mesenchymal differentiation mediated by NF-kappaB promotes radiation resistance in glioblastoma. *Cancer Cell* **2013**, *24*, 331–346. [CrossRef] [PubMed]
13. Day, B.W.; Stringer, B.W.; Al-Ejeh, F.; Ting, M.J.; Wilson, J.; Ensbey, K.S.; Jamieson, P.R.; Bruce, Z.C.; Lim, Y.C.; Offenhauser, C.; et al. EphA3 maintains tumorigenicity and is a therapeutic target in glioblastoma multiforme. *Cancer Cell* **2013**, *23*, 238–248. [CrossRef]
14. Pollard, S.M.; Yoshikawa, K.; Clarke, I.D.; Danovi, D.; Stricker, S.; Russell, R.; Bayani, J.; Head, R.; Lee, M.; Bernstein, M.; et al. Glioma stem cell lines expanded in adherent culture have tumor-specific phenotypes and are suitable for chemical and genetic screens. *Cell Stem Cell* **2009**, *4*, 568–580. [CrossRef]

15. Reynolds, B.A.; Weiss, S. Generation of neurons and astrocytes from isolated cells of the adult mammalian central nervous system. *Science* **1992**, *255*, 1707–1710. [CrossRef]
16. Wisniewski, J.R.; Zougman, A.; Nagaraj, N.; Mann, M. Universal sample preparation method for proteome analysis. *Nat. Methods* **2009**, *6*, 359–362. [CrossRef]
17. Rappsilber, J.; Ishihama, Y.; Mann, M. Stop and go extraction tips for matrix-assisted laser desorption/ionization, nanoelectrospray, and LC/MS sample pretreatment in proteomics. *Anal. Chem.* **2003**, *75*, 663–670. [CrossRef]
18. Cox, J.; Mann, M. MaxQuant enables high peptide identification rates, individualized p.p.b.-range mass accuracies and proteome-wide protein quantification. *Nat. Biotechnol.* **2008**, *26*, 1367–1372. [CrossRef]
19. Cox, J.; Neuhauser, N.; Michalski, A.; Scheltema, R.A.; Olsen, J.V.; Mann, M. Andromeda: A peptide search engine integrated into the MaxQuant environment. *J. Proteome Res.* **2011**, *10*, 1794–1805. [CrossRef]
20. Geiger, T.; Wehner, A.; Schaab, C.; Cox, J.; Mann, M. Comparative proteomic analysis of eleven common cell lines reveals ubiquitous but varying expression of most proteins. *Mol. Cell. Proteom.* **2012**, *11*, M111.014050. [CrossRef]
21. Cox, J.; Hein, M.Y.; Lubner, C.A.; Paron, I.; Nagaraj, N.; Mann, M. Accurate proteome-wide label-free quantification by delayed normalization and maximal peptide ratio extraction, termed MaxLFQ. *Mol. Cell. Proteom.* **2014**, *13*, 2513–2526. [CrossRef] [PubMed]
22. Tyanova, S.; Temu, T.; Sinitcyn, P.; Carlson, A.; Hein, M.Y.; Geiger, T.; Mann, M.; Cox, J. The Perseus computational platform for comprehensive analysis of (prote)omics data. *Nat. Methods* **2016**, *13*, 731–740. [CrossRef] [PubMed]
23. Ashburner, M.; Ball, C.A.; Blake, J.A.; Botstein, D.; Butler, H.; Cherry, J.M.; Davis, A.P.; Dolinski, K.; Dwight, S.S.; Eppig, J.T.; et al. Gene ontology: Tool for the unification of biology. The Gene Ontology Consortium. *Nat. Genet.* **2000**, *25*, 25–29. [CrossRef] [PubMed]
24. Kanehisa, M.; Goto, S.; Kawashima, S.; Nakaya, A. The KEGG databases at GenomeNet. *Nucleic Acids Res.* **2002**, *30*, 42–46. [CrossRef] [PubMed]
25. Barbie, D.A.; Tamayo, P.; Boehm, J.S.; Kim, S.Y.; Moody, S.E.; Dunn, I.F.; Schinzel, A.C.; Sandy, P.; Meylan, E.; Scholl, C.; et al. Systematic RNA interference reveals that oncogenic KRAS-driven cancers require TBK1. *Nature* **2009**, *462*, 108–112. [CrossRef]
26. Shannon, P.; Markiel, A.; Ozier, O.; Baliga, N.S.; Wang, J.T.; Ramage, D.; Amin, N.; Schwikowski, B.; Ideker, T. Cytoscape: A software environment for integrated models of biomolecular interaction networks. *Genome Res.* **2003**, *13*, 2498–2504. [CrossRef] [PubMed]
27. Bindea, G.; Mlecnik, B.; Hackl, H.; Charoentong, P.; Tosolini, M.; Kirilovsky, A.; Fridman, W.H.; Pages, F.; Trajanoski, Z.; Galon, J. ClueGO: A Cytoscape plug-in to decipher functionally grouped gene ontology and pathway annotation networks. *Bioinformatics* **2009**, *25*, 1091–1093. [CrossRef]
28. Rahman, M.; Reyner, K.; Deleyrolle, L.; Millette, S.; Azari, H.; Day, B.W.; Stringer, B.W.; Boyd, A.W.; Johns, T.G.; Blot, V.; et al. Neurosphere and adherent culture conditions are equivalent for malignant glioma stem cell lines. *Anat. Cell Biol.* **2015**, *48*, 25–35. [CrossRef]
29. Yu, Q.; Xue, Y.; Liu, J.; Xi, Z.; Li, Z.; Liu, Y. Fibronectin Promotes the Malignancy of Glioma Stem-Like Cells Via Modulation of Cell Adhesion, Differentiation, Proliferation and Chemoresistance. *Front. Mol. Neurosci.* **2018**, *11*, 130. [CrossRef]
30. Jung, C.S.; Foerch, C.; Schanzer, A.; Heck, A.; Plate, K.H.; Seifert, V.; Steinmetz, H.; Raabe, A.; Sitzer, M. Serum GFAP is a diagnostic marker for glioblastoma multiforme. *Brain* **2007**, *130*, 3336–3341. [CrossRef]
31. Bazzoni, R.; Bentivegna, A. Role of Notch Signaling Pathway in Glioblastoma Pathogenesis. *Cancers* **2019**, *11*, 292. [CrossRef] [PubMed]
32. Wilson, J.J.; Malakhova, M.; Zhang, R.; Joachimiak, A.; Hegde, R.S. Crystal structure of the dachshund homology domain of human SKI. *Structure* **2004**, *12*, 785–792. [CrossRef] [PubMed]
33. Vignais, M.L. Ski and SnoN: Antagonistic proteins of TGFbeta signaling. *Bull. Cancer* **2000**, *87*, 135–137. [PubMed]
34. Behnan, J.; Finocchiaro, G.; Hanna, G. The landscape of the mesenchymal signature in brain tumours. *Brain* **2019**, *142*, 847–866. [CrossRef] [PubMed]
35. Greenall, S.A.; McKenzie, M.; Seminova, E.; Dolezal, O.; Pearce, L.; Bentley, J.; Kuchibhotla, M.; Chen, S.C.; McDonald, K.L.; Kornblum, H.; et al. Most clinical anti-EGFR antibodies do not neutralize both wtEGFR and EGFRvIII activation in glioma. *Neuro Oncol.* **2019**, *21*, 1016–1027. [CrossRef]



36. Baker, K.E.; Collier, J. The many routes to regulating mRNA translation. *Genome Biol.* **2006**, *7*, 332. [CrossRef]
37. Okawa, S.; Gargica, S.; Blin, C.; Ender, C.; Pollard, S.M.; Krijgsveld, J. Proteome and Secretome Characterization of Glioblastoma-Derived Neural Stem Cells. *Stem Cells* **2017**, *35*, 967–980. [CrossRef]
38. Bock, T.; Moest, H.; Omasits, U.; Dolski, S.; Lundberg, E.; Frei, A.; Hofmann, A.; Bausch-Fluck, D.; Jacobs, A.; Krayenbuehl, N.; et al. Proteomic analysis reveals drug accessible cell surface N-glycoproteins of primary and established glioblastoma cell lines. *J. Proteome Res.* **2012**, *11*, 4885–4893. [CrossRef]
39. Brennan, C.W.; Verhaak, R.G.; McKenna, A.; Campos, B.; Nounshmehr, H.; Salama, S.R.; Zheng, S.; Chakravarty, D.; Sanborn, J.Z.; Berman, S.H.; et al. The somatic genomic landscape of glioblastoma. *Cell* **2013**, *155*, 462–477. [CrossRef]



© 2020 by the authors. Licensee MDPI, Basel, Switzerland. This article is an open access article distributed under the terms and conditions of the Creative Commons Attribution (CC BY) license (<http://creativecommons.org/licenses/by/4.0/>).

Review

# Extracellular Vesicle-Mediated Communication between the Glioblastoma and Its Microenvironment

Esperanza R. Matarredona \*  and Angel M. Pastor 

Departamento de Fisiología, Facultad de Biología, Universidad de Sevilla, 41012 Seville, Spain; ampastor@us.es

\* Correspondence: matarredona@us.es; Tel.: +34-954559549

Received: 15 November 2019; Accepted: 27 December 2019; Published: 30 December 2019



**Abstract:** The glioblastoma is the most malignant form of brain cancer. Glioblastoma cells use multiple ways of communication with the tumor microenvironment in order to tune it for their own benefit. Among these, extracellular vesicles have emerged as a focus of study in the last few years. Extracellular vesicles contain soluble proteins, DNA, mRNA and non-coding RNAs with which they can modulate the phenotypes of recipient cells. In this review we summarize recent findings on the extracellular vesicles-mediated bilateral communication established between glioblastoma cells and their tumor microenvironment, and the impact of this dialogue for tumor progression and recurrence.

**Keywords:** tumor microenvironment; exosomes; microvesicles; glioma stem cells

## 1. Introduction

The glioblastoma is the most aggressive primary adult brain cancer. In accordance with the World Health Organization, this tumor is classified as a grade IV glioblastoma multiforme (GBM), and is associated with very poor prognosis. Despite surgery, radiotherapy and chemotherapy, the median survival is less than 15 months [1]. Considerable research has been carried out to deepen in the understanding of the GBM biology, but still, this cancer remains incurable and lethal.

GBMs are characterized by a strong invasive nature and a high level of cellular heterogeneity, with genetic and epigenetic differences among tumor cells of the same GBM, which makes challenging the characterization and treatment of this disease [2–4]. Among the tumor's cellular heterogeneity, it contains a small population of self-renewing and highly proliferative tumor-initiating cells, called GBM stem cells (GSCs), which are resistant to treatments and are thought to be responsible for tumor progression and tumor recurrence [5–7].

GBMs recruit normal brain cells to promote their growth, invasion and nourishment in the brain. For this purpose, GBMs make use of different communication routes with the environs, which include secreted molecules, gap junctions, tunneling nanotubes and extracellular vesicles (EVs) [8]. EV-mediated communication has unique features compared to the other communication pathways mentioned, since it allows the delivery of the vesicle cargo not only in the tumor environs but also at distant sites [9,10]. In addition, the cargo includes nucleic acids that can alter gene expression in recipient cells [11]. Recent findings have demonstrated that EVs released by GBMs are able to create a tumor-supportive microenvironment through their actions on immune cells, vasculature and glial cells. In turn, cells from the tumor microenvironment also secrete EVs that can modulate GBM behavior. In this article we review recent literature showing EV-mediated bilateral communication between GBM cells and the tumor microenvironment, and we discuss its relevance for tumor progression and recurrence.

## 2. Extracellular Vesicles: Structure, Biogenesis, Secretion and Uptake

EVs are phospholipid-bilayer-enclosed extracellular spherical structures, with a size range between 30 nm and 10  $\mu$ m, which contain a wide variety of proteins, fragments of double-stranded DNA, mRNAs and non-coding RNAs, such as microRNAs (miRNAs), transfer RNAs and long non-coding RNAs [11–13]. EVs are secreted by multiple cell types and have been involved in intercellular communication between neighboring or distant cells through the transfer of genetic, protein or lipid-based messages from the host cell to recipient ones [10,11]. While in some cases, EV release is constitutive by nature, in others it is influenced by pathological situations, such as cancer, immune responses or cardiovascular diseases [14–16]. EVs can be formed at the plasma membrane by direct budding towards the extracellular space [17]. The plasma membrane-derived EVs have been classically called “microvesicles” (100–1000 nm in diameter) (Figure 1); they are released by many cell types during biological events of considerable diversity although the nature, and significance of the underlying process is still not completely understood [18,19]. In addition to “microvesicles,” there are additional plasma membrane-derived EVs, such as apoptotic bodies (50–2000 nm), oncosomes (100–400 nm) and large oncosomes (1–10  $\mu$ m) (Figure 1) [18,20–22]. Apoptotic bodies are released from dying cells by blebbing and fragmentation of cell membranes in a controlled manner. Oncosomes and large oncosomes are secreted by cancer cells and contain abnormal and transforming macromolecules, such as oncogenic proteins that can promote malignant transformation in recipient cells [23,24]. Alternatively, EVs can form by an intracellular endocytic trafficking pathway, involving the fusion of multivesicular endosomes or bodies (MVEs/MVBs) with the plasma membrane. This event leads to the extracellular release of the intraluminal vesicles (ILVs) contained in the MVEs generating a subtype of small EVs (30–100 nm) usually referred to as “exosomes” (Figure 1). The microvesicle/exosome nomenclature has been lately considered controversial, since there are not specific markers to clearly distinguish each EV biogenesis pathway. Therefore, following the recommendations stated by the positional paper of the International Society for Extracellular Vesicles (ISEV) in 2018, EVs should rather be named according for instance to their size: small EVs (<100 nm or <200 nm) and medium/large EVs (>200 nm) [25].

Irrespective of their origin, all EVs are circular membrane vesicles that contain cytosolic components and express surface adhesion molecules characteristic of their cells of origin. Specific differences in EV size and/or in surface molecules may influence their recognition and capture by target cells. EVs can be taken up nonspecifically by two endocytic means, phagocytosis and macropinocytosis (Figure 1). Alternatively, EVs can be captured by other canonical forms of endocytosis through specific receptor-ligand interaction (clathrin or caveolin-mediated) [26]. EV may also deliver their cargo by fusion with the plasma membrane [26]. Once the vesicle is internalized, its content can be degraded or released into the cytoplasm and transported into the nucleus or cellular membranes, leading to functional consequences. Additionally, interaction of EV membrane proteins with receptors of the recipient cell plasma membrane may lead to stimulation of intracellular signaling cascades (Figure 1). All these specific and nonspecific mechanisms of EV capture and interaction open a wide spectrum of possibilities for EV-mediated intercellular communication, such as the transfer of enzymes, receptors, transcription factors, oncogene products, infectious particles, mRNAs and miRNAs (which can induce epigenetic modifications in the recipient cells), and the stimulation of the target cells through interaction with cell surface-expressed receptors [27].

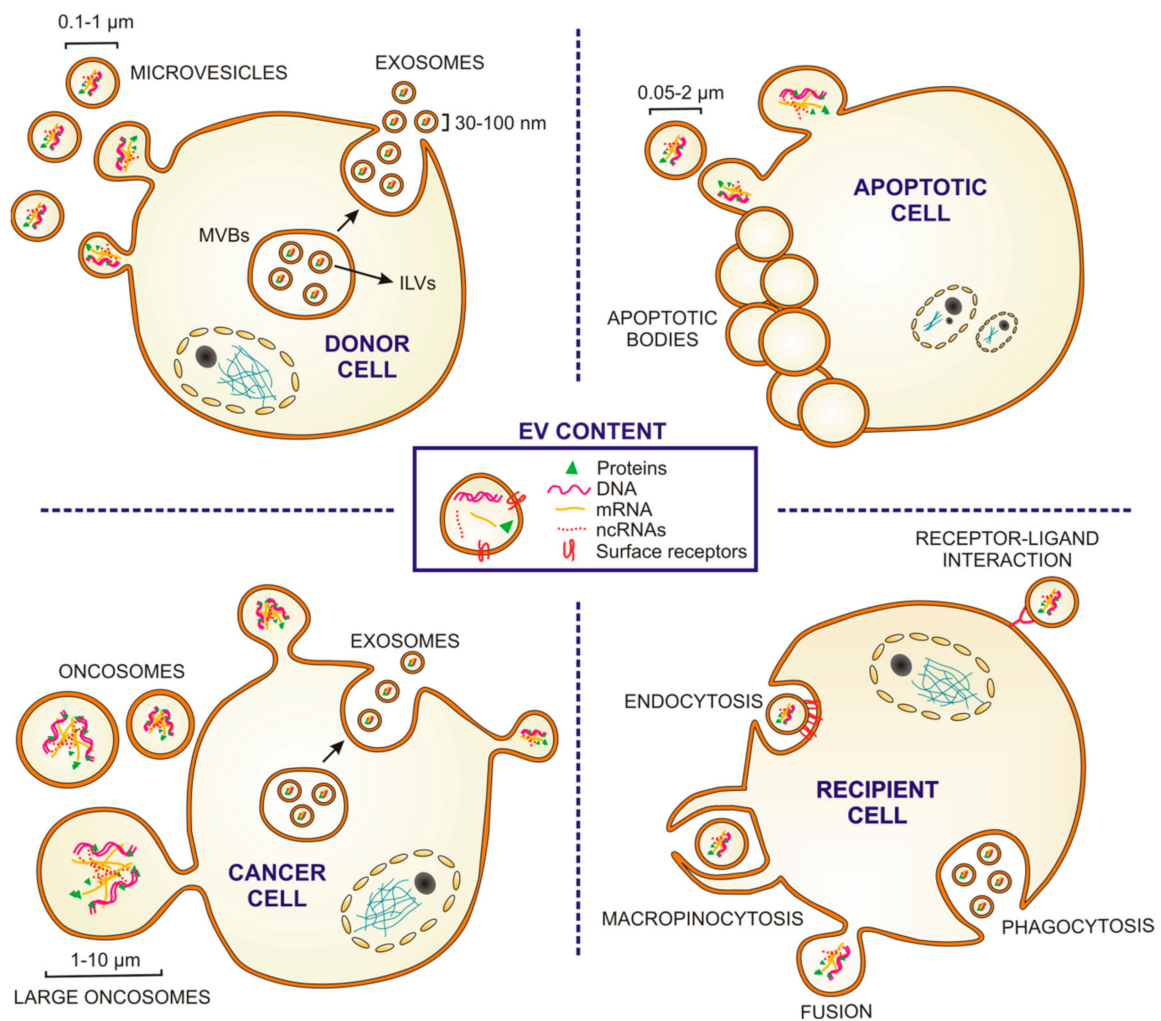


**Figure 1.** Extracellular vesicles: types, sizes, content, biogenesis and uptake. Cartoon depicting the origin and sizes of different types of extracellular vesicles (EVs). Microvesicles are released by outward budding of the plasma membrane, and exosomes from the endosomal system via fusion of multivesicular bodies (MVBs) with the cytoplasmic membrane which releases the intraluminal vesicles (ILVs) (see “DONOR CELL”). Apoptotic bodies are EVs released by membrane budding of cells dying by apoptosis (see “APOPTOTIC CELL”). Some tumor cells release oncosomes and/or large oncosomes (see “CANCER CELL”). EVs can be taken up through different mechanisms: macropinocytosis, phagocytosis, endocytosis or fusion. They can also interact with receptors in the recipient cell membrane (see RECIPIENT CELL). EVs contain cytosolic components (soluble proteins, DNA, mRNA and non-coding RNAs (ncRNAs)) and express surface molecules of their cell of origins.

The fact that EVs are molecularly reflective of their tissue of origin is particularly important in the context of cancer, since cancer cells are known to produce greater numbers of EVs compared to healthy cells and they contain molecules specific of their neoplastic origin. This is relevant in order to use EVs as cancer biomarkers but also to design potential therapeutics to target tumor-derived EVs in order to avoid cancer dissemination or to convert EVs into vehicles for the delivery of therapeutic molecules.

### 3. Extracellular Vesicles Released by Glioblastoma Modulate the Tumor Microenvironment

The GBM microenvironment consists of diverse cellular populations, including tumor cells, endothelial cells and pericytes of blood vessels; innate immune cells (microglia, monocytes,

macrophages, neutrophils and mast cells), T cells, neurons, astrocytes, oligodendrocytes and GSCs; and extracellular matrix components [8].

It is well known that GBMs interact with surrounding non-cancer cells to maintain a microenvironment that favors tumor proliferation, invasion of the brain, angiogenesis and immunosuppression. Multiple modes of communication are involved in this phenomenon, such as soluble factors, gap-junctional communication, connecting nanotubes and EVs (reviewed in [8]). EVs constitute an outstanding communication system in the sense that they can deliver not only soluble proteins, but a wide variety of coding and non-coding RNAs that can alter gene expression in recipient cells [28–30]. EVs have been involved in the mechanisms of tumor progression and invasion in different types of cancers [16]. Their relevance in GBMs is being object of study in the last years, as they might be partially responsible for the high degree of recurrence of this cancer type, as well as for their interest as GBM biomarker.

We will describe below relevant findings showing effects of EVs released by GBMs on different component of the tumor microenvironment, specifically on immune cells, vasculature, astrocytes and GSCs.

### 3.1. *Effects on Monocytes, Macrophages and Microglia*

Infiltrating monocytes, macrophages and microglia are the most prevalent cell types within the GBM microenvironment [31]. They used to be termed together as tumor-associated macrophages (TAMs), although they represent different cell populations [32]. Microglia are the resident innate immune cells in the brain and are important in the defense against pathogens and noxious stimuli [33]. Disruption of the blood brain barrier induced by the GBM leads to infiltration of monocytes that can subsequently differentiate to macrophages [32]. Macrophages can acquire different phenotypes according to cytokines and signaling molecules of the microenvironment [34,35]. Macrophages with the classical M1 phenotype are capable of phagocytosis, cytotoxicity, antigen presentation and the promotion of inflammation. In contrast, in response to GBM-derived soluble factors, macrophages can acquire a so-called M2 phenotype in which they produce chemokines, cytokines, growth factors, angiogenic factors, extracellular matrix-modifying enzymes and immunosuppressive molecules, which make the environment favorable to the tumor progression [36]. Evidence from the last few years show that EVs released by GBM cells intervene in the induction of such tumor-supportive TAMs' phenotype modulation. In an article published in 2015, de Vrij et al. [37] reported that EVs derived from GBMs (U87MG GBM cell line and GBM primary cultures) were able to modify the phenotype of TAMs in vitro, changing it to a M2-like anti-inflammatory phenotype that resembles the tumor-supportive phenotype observed in patients. Phenotypic changes included modified expression of a wide variety of cell surface molecules (e.g., increased CD14 and reduced HLA-DR), and increased secretion of cytokines such as interleukin-6 (IL-6) and vascular endothelial growth factor (VEGF). In addition, GBM EVs induced and increased phagocytic activity of macrophages, which may enhance degradation of extracellular matrix and facilitate the migration of tumor cells.

One year later, van der Vos et al. [38] demonstrated efficient uptake of EVs released by GBM cells (GL261 GBM cell line and primary human GBM cells) by TAMs, both in vitro and in vivo. In addition, they showed that miRNAs contained in these vesicles were transferred to the recipient TAMs, resulting in downregulation of target mRNAs. The same group recently demonstrated functional delivery of miRNA-21 (mi-R21) contained in EVs from the GBM cell line GL261 to surrounding microglia, subsequently leading to downregulation of specific miR-21 mRNA targets [39]. One of these targets is the Btg2 gene, which exerts antiproliferative effects. Consequently, microglial cells might increase their proliferation and their influence on shaping the tumor microenvironment. Related experiments performed by Gabrusiewicz and colleagues [40] showed that exosomes, isolated among the EVs released by the GBM cell line U87 and by GSCs, mainly target monocytes to induce reorganization of the actin cytoskeleton and the immune suppressive M2 phenotype, with the secretion of cytokines such as monocyte-chemotactic protein 3 (MCP-3) and chemokine (C-X-C motif) ligand 1 (CXCL1), and

the expression of the programmed death-ligand 1 (PD-L1). The expression of PD-L1 by monocytes may be responsible for cancer-induced immune evasion, since PD-L1 can bind to programmed cell death protein 1 (PD1) of activated T cells to inhibit T cell function [41] (Figure 2).

In this regard, researchers have tried to modify the tumor-supportive phenotype of TAMs by means of exogenous EVs. This has been performed with EVs released from microglia in inflammatory conditions. The injection of these vesicles in glioma-bearing mice reduced the anti-inflammatory phenotype of TAMs and significantly reduced tumor size and tumor induced neurotoxicity [42]. These results are important in terms of achieving valuable approaches to transfer signals to TAMs to restore the homeostatic microglial phenotype.

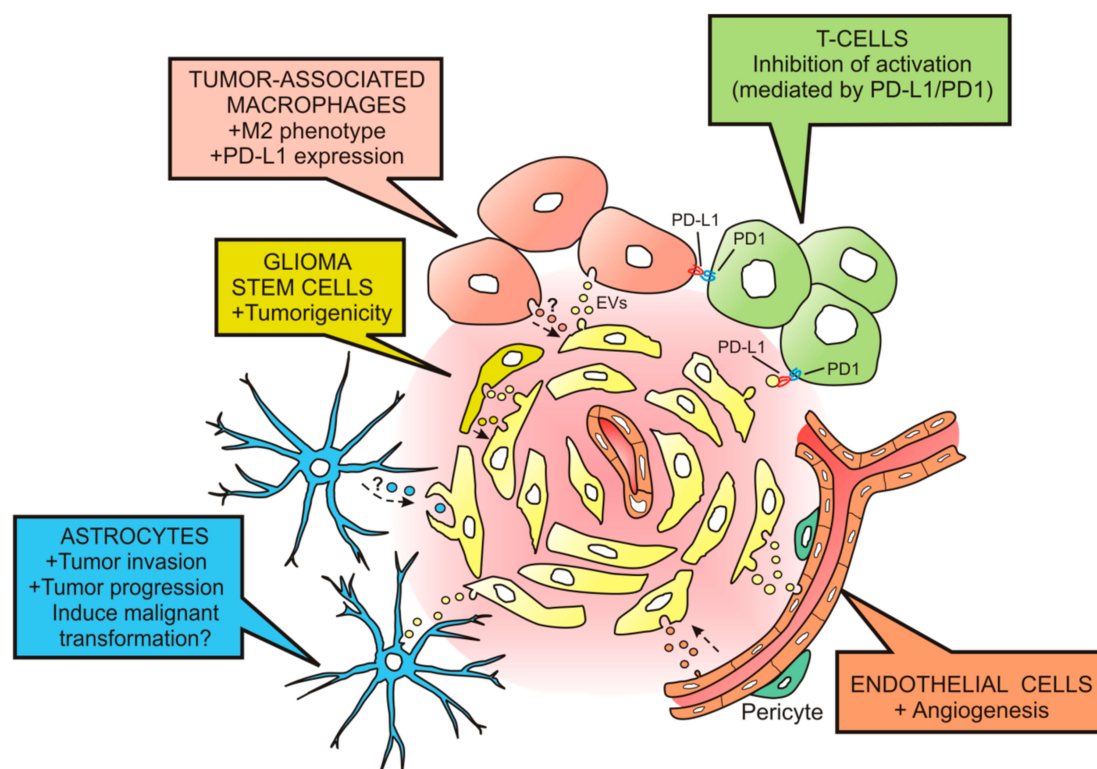


**Figure 2.** Effects of glioblastoma-derived extracellular vesicles on cells from the tumor microenvironment. Extracellular vesicles (EVs) released by glioblastoma (GBM) cells (in pale yellow) can be taken up by tumor-associated macrophages (in flesh color) to induce the M2 phenotype and the expression of PD-L1. By interacting with the ligand PD1 expressed on activated T cells (in green), they inhibit the T cell-associated immune response. Additionally, EVs can target T cells and suppress their activation through PD-L1/PD1 interaction. Endothelial cells (in orange) are also targets for GBM-derived EVs; they activate angiogenic mechanisms. The uptake of GBM EVs by astrocytes (in blue) leads to astrocytic responses favoring tumor invasion and progression. The malignant transformation of astrocytes might also be produced by EVs delivering oncogenic cargo. GBM-derived EVs can also deliver their cargo in glioma stem cells (in dark yellow) producing an increase in their tumorigenicity. Tumor microenvironment components might also release EVs to induce effects on the GBM cell population (see dashed arrows).

### 3.2. Effects on T Cells

T cells can also be the targets of EVs released by primary human GBM cells, and their activation can be blocked as a result of such interaction [42]. This interaction is probably achieved through PD-L1/PD1, since PD-L1 is found in GBM EVs and the EV-induced inhibition of T cell activation is partially reversed by PD1 blockade [43]. These results indicate that PD-L1 expression on EVs may be an additional mechanism for GBM to suppress antitumor immunity (Figure 2).



### 3.3. Effects on Endothelial Cells

GBMs are among the most vascularized tumors, characterized by microvascular proliferation and endothelial hyperplasia. Indeed, these features are used as histological markers to define high-grade gliomas [44]. These regions of angiogenesis are critical for tumor progression and are key locations for GSCs [45,46]. Glioma cells release soluble factors that contribute to the shape of tumor vasculature, such as VEGF-A [47], stromal-derived factor-1 [48] and hepatoma-derived growth factor [49].

The laboratory of Xandra O. Breakfield was the first one to demonstrate that human patient GBMs produce EVs containing mRNA, miRNA and angiogenic proteins that can be taken up and translated by cultured endothelial cells to stimulate angiogenesis [28] (Figure 2). This work pioneered with the assumption of EVs acting as vehicles to deliver genetic information and proteins to recipient cells in the GBM microenvironment. They identified several mRNAs and miRNAs in GBM-derived EVs, among which the epidermal growth factor receptor (EGFR) mRNA is of particular interest since the expression of the EGFR mutant/variant III (EGFRvIII) is characteristic of a clinical subtype of GBM [50]. This raised expectations for the use of EVs as diagnostic markers for GBM.

The ability of GBM-derived EVs to modify the phenotype of endothelial cells has been reported thereafter by other groups. For instance, Li et al. described changes in gene expression in cultured vascular endothelial cells exposed to EVs released from U251 glioma cells [29]. EVs produced by primary GBM cells grown at hypoxic conditions are potent inducers of angiogenesis *ex vivo* and *in vitro*, and through mechanisms derived of EV-induced phenotypic modulation of endothelial cells [51]. Moreover, endothelial cells programmed by GBM-derived hypoxic EVs secrete cytokines and growth factors that stimulate pericyte migration and PI3K/AKT signaling [51]. These findings indicate that EVs are mediators of hypoxia-dependent intercellular communication between GBM and vascular cells.

Molecules delivered by EVs that have been involved in the promotion of angiogenesis are: VEGF-A [47]; miR-21, which in turn upregulates VEGF expression [52]; transforming growth factor  $\beta$  (TGF $\beta$ ); and proteolytic enzymes [53] or long non-coding RNA CCAT2 [54], which induces upregulation of VEGF-A and TGF $\beta$  in cultured endothelial cells. EVs from patient-derived GBM cells can exert additional effects on vasculature, such as an increase in vascular permeability associated to the expression of the pro-permeability factor Semaphorin3A in EV surface [55].

### 3.4. Effects on Astrocytes

Among all the cell types surrounding GBMs, astrocytes are the phenotypically most similar to the bulk of this tumor. Although it is well known that peritumoral astrocytes may contribute to glioma progression, not much has been reported on the effects induced by GBM cells on the modulation of astrocyte function to contribute to tumor support [56,57]. Chen et al. showed that brain metastatic cells can assemble to astrocytes through gap junctions composed of connexin 43. Once engaged with the astrocytic gap-junctional network, cancer cells transfer the second messenger cGAMP to astrocytes. This messenger activates the astrocytic production of inflammatory cytokines such as interferon- $\alpha$  and tumor necrosis factor, which in turn induce the activation of STAT-1 and NF- $\kappa$ B pathways in the brain's metastatic cells, thereby supporting tumor cell invasion and resistance to chemotherapy [58]. More recently, two articles have reported tumor-supportive effects of astrocytes driven by EVs released by GBMs [59,60]. Oushy et al. demonstrated that astrocytes cultured with EVs from patient-derived GBMs display profound modifications of the secretome that results in positive effects on tumor growth [59]. These include increased production of growth factors (EGF, VEGF, colony stimulating factors (CSFs), fibroblast growth factors and hepatocyte growth factor), chemokines (CXCL1, 9, 10 and 11; chemokine C-C motif ligand 3, 5, 7 and 20), matrix metalloproteinase-9; and some cytokines that could induce immune suppression, such as CSF2 and 3, and ILs 4, 10 and 13.

In a later study, Hallal et al. [60] reported increased podosome formation and extracellular matrix degradation in astrocytes cultured with GBM-derived EVs. In addition, they showed that the proteome of astrocytes exposed to GBM-derived EVs presented significant modifications in signaling pathways involved in tumorigenesis, such as decreased TP53 and increased MYC. TP53 is a tumor suppressor

gene that encodes for the sequence-specific DNA-binding protein p53. This protein, p53, is important in the cell response to genotoxic stress, since it induces apoptosis or cell cycle arrest, thereby blocking the transmission of DNA mutations to progeny cells [61]. TP53 mutations leading to p53 loss are frequent in GBM [62]. Results from previous studies suggest that the p53 status of GBM cells may affect the microenvironment to promote tumor progression. For instance, astrocytes grown with GBM cell conditioned media show decreased p53 levels which correlates with a modulation in extracellular matrix composition to favor tumor malignancy [63]. MYC is a proto-oncogene that codes for Myc proteins, which act as transcription factors involved in cell cycle regulation, apoptosis, proliferation and differentiation, with important roles in acquisition and maintenance of stem cell properties, including in GSCs [64,65]. Interestingly, transduction of p53(−/−) astrocytes with Myc induces tumorigenic abilities [66], an effect also observed in astrocytes transformed with a combined transduction of Myc, a dominant negative form of p53, Oct-4 and H-ras [67]. All these findings reported in in vitro experiments suggest that GBM-derived EVs may stimulate astrocytes to promote the invasion and expansion of GBMs also in vivo (Figure 2).

The relevance of these findings is not only that GBM EVs could modify neighboring astrocytes to induce tumor-supportive functions, but, importantly enough, GBM EVs may drive astrocytes to become tumorigenic themselves. GBM EVs' contents include oncogenic proteins and regulators, such as EGFRvIII (mRNA and protein), miR-10b or miR-21 [23,38,68], which could induce the malignant transformation of astrocytes. Indeed, in the above mentioned study by Oushy and colleagues [59], GBM EVs drove significant molecular changes in astrocytes that resemble cancer signaling pathways, and reduced astrocyte dependence on anchorage to a solid matrix, an indicator of cellular transformation. In line with this, it is important to highlight that astrocyte-like stem cells of the neurogenic niche of the subventricular zone have been considered a putative origin of human GBMs [69]. It is therefore feasible that astrocyte-like stem cells of the subventricular zone may acquire GSC features as a result of receiving instructive signals from EVs of variable origin. It is worth mentioning the recent study by Wang and colleagues [70] in which they demonstrate that GBM-derived EVs induce the transformation of human embryonic neural stem cells into tumor-promoting cells.

### 3.5. Effects on Glioma Stem Cells

GBMs harbor stromal cells resembling mesenchymal stem cells [71] that have been involved in GSC tumorigenicity by mechanisms depending on the secretion of IL-6 [72]. A subsequent study revealed that GBM mesenchymal stem cells from surgical specimens also release EVs that increase the proliferation and clonogenicity of GSCs [73] by transfer of miR-1587, which in turn induces a decrease in the expression of the tumor suppressor NCOR1 (nuclear hormone receptor corepressor-1). Therefore, it is important to take into account that GSCs are targets for EVs released within the GBM microenvironment, and, at the same time, GSCs release EVs which can induce protumorigenic effects on GBM cells (Figure 2). For instance, Palumbo et al. [74] have shown that EVs released by GSCs exert a stimulatory effect on cell growth and migration of the adherent GBM cell line U87MG. GSC-derived EVs decorated with the cell adhesion molecule L1CAM are also able to induce motility, proliferation and invasiveness of different types of GBM cell lines [75].

Interestingly, these GSC-GBM exchange of EVs might be involved in the well known intratumoral heterogeneity characteristic of GBMs. Ricklefs et al. demonstrated that EVs released by GSCs retain tumor subtype characteristics and that their transfer between GSC subtypes leads to protumorigenic changes in the target GSC [76].

### 3.6. Effects on Other Cell Populations of the Tumor Microenvironment

To date, no evidence has been published on the effects mediated by EVs released by GBM on neighboring oligodendrocytes or neurons, although such effects can not be discarded.

### 3.7. Technical Considerations

Isolation of EVs from conditioned media or biological fluids can be achieved to various degrees through different techniques such as ultracentrifugation, ultrafiltration, chromatography, polymer-based precipitation, affinity capture on antibody-coupled magnetic beads and microfluidic devices [77]. They all have advantages and disadvantages, and still, an ideal and universal method for EV isolation is lacking. The studies mentioned in this section have used ultracentrifugation-based methods such as differential ultracentrifugation [28,29,40,43,51,52,59,60,73] or density gradient ultracentrifugation [37–39]. These are the most used technical procedures (at least in 2018 [77]), and have been validated by the ISEV2018 position paper [25].

To characterize isolated EVs (size distribution and concentration), most reports showing effects of GBM EVs on tumor microenvironment used nanoparticle tracking analysis, with the exception of de Vrij and colleagues [37] that performed the EV quantification by tunable resistive pulse sensing. Some of these studies also performed transmission electron microscopy to further characterize the EV structure, morphology and size [60,73].

## 4. Extracellular Vesicles Released by Tumor Microenvironment Cells Might Also Modulate Glioblastoma Cells

Although most work has been carried out on the effects of GBM-derived EVs on the tumor microenvironment, the reverse phenomenon is slowly gaining importance. That is, tumor environment cells might in turn release EVs that could be taken up by GBM cells to mediate effects such as proliferation, migration or immunosuppression. Some recent papers support this hypothesis. The close proximity in the perivascular niche of endothelial cells with GSCs suggests that endothelial cell-derived EVs may target GSCs. It has been previously reported that endothelial cells can transfer miRNA to breast cancer cells via exosomes with induced modifications in their proliferative and invasive capacities [78]. Based on this background, Li et al. [79] analyzed the effects of EVs secreted by human endothelial cells on GSC proliferation and self-renewal. They demonstrated that treatment with endothelial cell EVs promotes GSC tumorigenicity through mechanisms derived of the transfer of CD9, a transmembrane protein involved in the regulation of cell fusion, adhesion and motility that is relevant for the maintenance of GSCs [80].

EVs released by reactive astrocytes could also enter GBM cells. In favor of this idea Zhang et al. [81] reported astrocyte-derived EV transfer of microRNAs targeting the tumor suppressor protein PTEN to brain metastatic breast cancer and melanoma cells. The epigenetic PTEN loss induced by this intercellular transfer to brain metastatic cells led to enhanced tumor proliferation and reduced apoptosis. TAMs might also release EVs and target GBM cells. For instance, in gastric cancer cells, there is an EV-mediated transfer of miR-21 from TAMs to tumor cells, which also downregulates PTEN and suppresses apoptosis [82].

Future work will reveal whether EVs released by GBM microenvironment cells, such as endothelial cells, TAMs or astrocytes, have an impact on GBM growth, progression and resistance to therapy, and will evaluate the relevance of these positive feedback loops of cellular communication.

## 5. New Perspectives

The facts that EVs can be released into biological fluids and that their contents are reflective of the cellular origin have enabled their use as cancer biomarkers. Thus, the analysis of the cargo of EVs purified from serum or cerebrospinal fluid is emerging as a powerful tool for GBM diagnosis, subtype identification and assessment of tumor resistance to therapies [83,84]. However, EVs' therapeutic importance in GBMs extends beyond their use as biomarkers, and currently they are beginning to be considered for antitumoral therapy. The therapeutic application takes advantage of the EV ability to cross the blood brain barrier and consists of encapsulating therapeutic cargo in EVs to deliver messages aimed at suppressing oncogenicity of GSCs or inhibiting tumor-supportive actions of microenvironment cells [85]. In addition, knowing the important roles played by EVs in

the maintenance of a tumor-supportive environment, in the tumorigenicity of GSCs or even in the induction of malignant transformation, it is logically sound to think that future strategies will be focused in trying to suppress EV biogenesis or EV release by GBM cells.

## 6. Conclusions

EVs constitute one of the multiple ways through which GBM cells communicate with the tumor microenvironment for their own benefit. GBM-derived EVs can be taken up by different components of the tumor environment, such as TAMs, endothelial cells, astrocytes and GSCs. EV cargo delivery in these cells leads to effects involved in tumor growth, tumor invasion, neo-angiogenesis, oncogenic transformation and modulation of the immune response. In turn, cells from the tumor environs also release EVs that may target GBM cells to increase tumorigenicity.

Future therapeutic strategies for GBM could aim at interrupting this EV-mediated cooperative crosstalk established between GBM cells and their stromal counterparts.

**Author Contributions:** Conceptualization, E.R.M.; writing—original draft preparation, E.R.M.; writing—review and editing, E.R.M. and A.M.P. All authors have read and agreed to the published version of the manuscript.

**Funding:** This research was funded by MINISTERIO DE CIENCIA, INNOVACIÓN Y UNIVERSIDADES (SPAIN), grant number PGC2018-094654-B-100.

**Conflicts of Interest:** The authors declare no conflict of interest. The funders had no role in the design of the study; in the collection, analyses, or interpretation of data; in the writing of the manuscript, or in the decision to publish the results.

## References

1. Stupp, R.; Mason, W.P.; van den Bent, M.J. Radiotherapy plus concomitant and adjuvant temozolomide for glioblastoma. *Oncol. Times* **2005**, *27*, 15–16. [CrossRef]
2. Patel, A.P.; Tirosh, I.; Trombetta, J.J.; Shalek, A.K.; Gillespie, S.M.; Wakimoto, H.; Cahill, D.P.; Nahed, B.V.; Curry, W.T.; Martuza, R.L.; et al. Single-cell RNA-seq highlights intratumoral heterogeneity in primary glioblastoma. *Science* **2014**, *344*, 1396–1401. [CrossRef] [PubMed]
3. Parker, N.R.; Khong, P.; Parkinson, J.F.; Howell, V.M.; Wheeler, H.R. Molecular heterogeneity in glioblastoma: Potential clinical implications. *Front. Oncol.* **2015**, *5*, 55. [CrossRef] [PubMed]
4. Brennan, C.W.; Verhaak, R.G.W.; McKenna, A.; Campos, B.; Nounshmehr, H.; Salama, S.R.; Zheng, S.; Chakravarty, D.; Sanborn, J.Z.; Berman, S.H.; et al. The somatic genomic landscape of glioblastoma. *Cell* **2013**, *157*, 753. [CrossRef]
5. Galli, R.; Binda, E.; Orfanelli, U.; Cipelletti, B.; Gritti, A.; De Vitis, S.; Fiocco, R.; Foroni, C.; Dimeco, F.; Vescovi, A. Isolation and characterization of tumorigenic, stem-like neural precursors from human glioblastoma. *Cancer Res.* **2004**, *64*, 7011–7021. [CrossRef]
6. Singh, S.K.; Hawkins, C.; Clarke, I.D.; Squire, J.A.; Bayani, J.; Hide, T.; Henkelman, R.M.; Cusimano, M.D.; Dirks, P.B. Identification of human brain tumour initiating cells. *Nature* **2004**, *432*, 396–401. [CrossRef]
7. Chen, J.; Li, Y.; Yu, T.S.; McKay, R.M.; Burns, D.K.; Kernie, S.G.; Parada, L.F. A restricted cell population propagates glioblastoma growth after chemotherapy. *Nature* **2012**, *488*, 522–526. [CrossRef]
8. Broekman, M.L.; Maas, S.L.N.; Abels, E.R.; Mempel, T.R.; Krichevsky, A.M.; Breakefield, X.O. Multidimensional communication in the microenvirons of glioblastoma. *Nat. Rev. Neurol.* **2018**, *14*, 482–495. [CrossRef]
9. Mathivanan, S.; Ji, H.; Simpson, R.J. Exosomes: Extracellular organelles important in intercellular communication. *J. Proteomics* **2010**, *70*, 1907–1920. [CrossRef]
10. Van der Pol, E.; Böing, A.N.; Harrison, P.; Sturk, A.; Nieuwland, R. Classification, functions, and clinical relevance of extracellular vesicles. *Pharmacol. Rev.* **2012**, *64*, 676–705. [CrossRef]
11. Yáñez-Mó, M.; Siljander, P.R.M.; Andreu, Z.; Zavec, A.B.; Borràs, F.E.; Buzas, E.I.; Buzas, K.; Casal, E.; Cappello, F.; Carvalho, J.; et al. Biological properties of extracellular vesicles and their physiological functions. *J. Extracell. Vesicles* **2015**, *4*, 27066. [CrossRef] [PubMed]

12. Zappulli, V.; Pagh Friis, K.; Fitzpatrick, Z.; Maguire, C.A.; Breakefield, X.O. Extracellular vesicles and intercellular communication within the nervous system. *J. Clin. Invest.* **2016**, *126*, 1198–1207. [CrossRef] [PubMed]
13. Salido-Guadarrama, I.; Romero-Cordoba, S.; Peralta-Zaragoza, O.; Hidalgo-Miranda, A.; Rodríguez-Dorantes, M. MicroRNAs transported by exosomes in body fluids as mediators of intercellular communication in cancer. *Onco. Targets. Ther.* **2014**, *7*, 1327–1338. [PubMed]
14. D’Asti, E.; Chennakrishnaiah, S.; Lee, T.H.; Rak, J. Extracellular vesicles in brain tumor progression. *Cell. Mol. Neurobiol.* **2016**, *36*, 383–407. [CrossRef]
15. Cossetti, C.; Smith, J.A.; Iraci, N.; Leonardi, T.; Alfaro-Cervello, C.; Pluchino, S. Extracellular membrane vesicles and immune regulation in the brain. *Front. Physiol.* **2012**, *3*, 117. [CrossRef]
16. Jaiswal, R.; Sedger, L.M. Intercellular vesicular transfer by exosomes, microparticles and oncosomes—Implications for cancer biology and treatments. *Front. Oncol.* **2019**, *9*, 125. [CrossRef]
17. Trams, E.G.; Lauter, C.J.; Norman Salem, J.; Heine, U. Exfoliation of membrane ecto-enzymes in the form of micro-vesicles. *BBA Biomembr.* **1981**, *645*, 63–70. [CrossRef]
18. Al-Nedawi, K.; Meehan, B.; Rak, J. Microvesicles: Messengers and mediators of tumor progression. *Cell Cycle* **2009**, *8*, 2014–2018. [CrossRef]
19. Muralidharan-Chari, V.; Clancy, J.W.; Sedgwick, A.; D’Souza-Schorey, C. Microvesicles: Mediators of extracellular communication during cancer progression. *J. Cell Sci.* **2010**, *123*, 1603–1611. [CrossRef]
20. Zaborowski, M.P.; Balaj, L.; Breakefield, X.O.; Lai, C.P. Extracellular vesicles: Composition, biological relevance, and methods of study. *Bioscience* **2015**, *65*, 783–797. [CrossRef]
21. Virgintino, D.; Rizzi, M.; Errede, M.; Strippoli, M.; Girolamo, F.; Bertossi, M.; Roncali, L. Plasma membrane-derived microvesicles released from tip endothelial cells during vascular sprouting. *Angiogenesis* **2012**, *15*, 761–769. [CrossRef] [PubMed]
22. Bertolini, I.; Terrasi, A.; Martelli, C.; Gaudioso, G.; Di Cristofori, A.; Storaci, A.M.; Formica, M.; Braidotti, P.; Todoerti, K.; Ferrero, S.; et al. A GBM-like V-ATPase signature directs cell-cell tumor signaling and reprogramming via large oncosomes. *EBioMedicine* **2019**, *41*, 225–235. [CrossRef] [PubMed]
23. Al-Nedawi, K.; Meehan, B.; Micallef, J.; Lhotak, V.; May, L.; Guha, A.; Rak, J. Intercellular transfer of the oncogenic receptor EGFRvIII by microvesicles derived from tumour cells. *Nat. Cell Biol.* **2008**, *10*, 619–624. [CrossRef] [PubMed]
24. Di Vizio, D.; Morello, M.; Dudley, A.C.; Schow, P.W.; Adam, R.M.; Morley, S.; Mulholland, D.; Rotinen, M.; Hager, M.H.; Insabato, L.; et al. Large oncosomes in human prostate cancer tissues and in the circulation of mice with metastatic disease. *Am. J. Pathol.* **2012**, *185*, 1573–1584. [CrossRef] [PubMed]
25. Théry, C.; Witwer, K.W.; Aikawa, E.; Alcaraz, M.J.; Anderson, A.J.; Andriantsitohaina, R.; Antoniou, A.; Archer, F.; Arkin-Smith, G.K.; Ayre, D.C.; et al. Minimal information for studies of extracellular vesicles 2018 (MISEV2018): A position statement of the International Society for Extracellular Vesicles and update of the MISEV2014 guidelines. *J. Extracell. Vesicles* **2018**, *7*, 1535750. [CrossRef] [PubMed]
26. Mulcahy, L.A.; Pink, R.C.; Carter, D.R.F. Routes and mechanisms of extracellular vesicle uptake. *J. Extracell. Vesicles* **2014**, *4*, 3. [CrossRef]
27. Camussi, G.; C. Deregibus, M.; Tetta, C. Tumor-derived microvesicles and the cancer microenvironment. *Curr. Mol. Med.* **2012**, *13*, 58–67. [CrossRef]
28. Skog, J.; Würdinger, T.; van Rijn, S.; Meijer, D.H.; Gainche, L.; Curry, W.T.; Carter, B.S.; Krichevsky, A.M.; Breakefield, X.O. Glioblastoma microvesicles transport RNA and proteins that promote tumour growth and provide diagnostic biomarkers. *Nat. Cell Biol.* **2008**, *10*, 1470–1476. [CrossRef]
29. Li, C.C.Y.; Eaton, S.A.; Young, P.E.; Lee, M.; Shuttleworth, R.; Humphreys, D.T.; Grau, G.E.; Combes, V.; Bebawy, M.; Gong, J.; et al. Glioma microvesicles carry selectively packaged coding and noncoding RNAs which alter gene expression in recipient cells. *RNA Biol.* **2013**, *10*, 1333–1344. [CrossRef]
30. Wei, Z.; Batagov, A.O.; Schinelli, S.; Wang, J.; Wang, Y.; El Fatimy, R.; Rabinovsky, R.; Balaj, L.; Chen, C.C.; Hochberg, F.; et al. Coding and noncoding landscape of extracellular RNA released by human glioma stem cells. *Nat. Commun.* **2017**, *8*, 1145. [CrossRef]
31. Morantz, R.A.; Wood, G.W.; Foster, M.; Clark, M.; Gollahon, K. Macrophages in experimental and human brain tumors. *J. Neurosurg.* **1979**, *50*, 305–311. [CrossRef] [PubMed]

32. Bowman, R.L.; Klemm, F.; Akkari, L.; Pyonteck, S.M.; Sevenich, L.; Quail, D.F.; Dhara, S.; Simpson, K.; Gardner, E.E.; Iacobuzio-Donahue, C.A.; et al. Macrophage ontogeny underlies differences in tumor-specific education in brain malignancies. *Cell Rep.* **2016**, *17*, 2445–2459. [CrossRef] [PubMed]
33. Li, Q.; Barres, B.A. Microglia and macrophages in brain homeostasis and disease. *Nat. Rev. Immunol.* **2018**, *18*, 225–242. [CrossRef] [PubMed]
34. Sica, A.; Mantovani, A. Macrophage plasticity and polarization: In vivo veritas. *J. Clin. Invest.* **2012**, *122*, 787–795. [CrossRef]
35. Wu, A.; Wei, J.; Kong, L.Y.; Wang, Y.; Priebe, W.; Qiao, W.; Sawaya, R.; Heimberger, A.B. Glioma cancer stem cells induce immunosuppressive macrophages/microglia. *Neuro. Oncol.* **2010**, *12*, 1113–1125. [CrossRef]
36. Hambardzumyan, D.; Gutmann, D.H.; Kettenmann, H. The role of microglia and macrophages in glioma maintenance and progression. *Nat. Neurosci.* **2015**, *19*, 20–27. [CrossRef]
37. De Vrij, J.; Niek Maas, S.L.; Kwappenberg, K.M.C.; Schnoor, R.; Kleijn, A.; Dekker, L.; Luider, T.M.; De Witte, L.D.; Litjens, M.; Van Strien, M.E.; et al. Glioblastoma-derived extracellular vesicles modify the phenotype of monocytic cells. *Int. J. Cancer* **2015**, *137*, 1630–1642. [CrossRef]
38. Van der Vos, K.E.; Abels, E.R.; Zhang, X.; Lai, C.; Carrizosa, E.; Oakley, D.; Prabhakar, S.; Mardini, O.; Crommentuijn, M.H.W.; Skog, J.; et al. Directly visualized glioblastoma-derived extracellular vesicles transfer RNA to microglia/macrophages in the brain. *Neuro. Oncol.* **2016**, *18*, 58–69. [CrossRef]
39. Abels, E.R.; Maas, S.L.N.; Nieland, L.; Wei, Z.; Cheah, P.S.; Tai, E.; Kolsteeg, C.-J.; Dusoswa, S.A.; Ting, D.T.; Hickman, S.; et al. Glioblastoma-associated microglia reprogramming is mediated by functional transfer of extracellular miR-21. *Cell Rep.* **2019**, *28*, 3105–3119. [CrossRef]
40. Gabrusiewicz, K.; Li, X.; Wei, J.; Hashimoto, Y.; Marisetty, A.L.; Ott, M.; Wang, F.; Hawke, D.; Yu, J.; Healy, L.M.; et al. Glioblastoma stem cell-derived exosomes induce M2 macrophages and PD-L1 expression on human monocytes. *Oncoimmunology* **2018**, *7*, e1412909. [CrossRef]
41. Mahoney, K.M.; Rennert, P.D.; Freeman, G.J. Combination cancer immunotherapy and new immunomodulatory targets. *Nat. Rev. Drug Discov.* **2015**, *14*, 561–584. [CrossRef] [PubMed]
42. Grimaldi, A.; Serpe, C.; Chece, G.; Nigro, V.; Sarra, A.; Ruzicka, B.; Relucenti, M.; Familiari, G.; Ruocco, G.; Pascucci, G.R.; et al. Microglia-derived microvesicles affect microglia phenotype in glioma. *Front. Cell. Neurosci.* **2019**, *13*, 1–14. [CrossRef] [PubMed]
43. Ricklefs, F.L.; Alayo, Q.; Krenzlin, H.; Mahmoud, A.B.; Speranza, M.C.; Nakashima, H.; Hayes, J.L.; Lee, K.; Balaj, L.; Passaro, C.; et al. Immune evasion mediated by PD-L1 on glioblastoma-derived extracellular vesicles. *Sci. Adv.* **2018**, *4*, 1–14. [CrossRef] [PubMed]
44. Wen, P.Y.; Kesari, S. Malignant gliomas in adults. *N. Engl. J. Med.* **2008**, *359*, 492–507.
45. Calabrese, C.; Poppleton, H.; Kocak, M.; Hogg, T.L.; Fuller, C.; Hamner, B.; Oh, E.Y.; Gaber, M.W.; Finklestein, D.; Allen, M.; et al. A perivascular niche for brain tumor stem cells. *Cancer Cell* **2007**, *11*, 69–82. [CrossRef]
46. Hadjipanayis, C.G.; Van Meir, E.G. Tumor initiating cells in malignant gliomas: Biology and implications for therapy. *J. Mol. Med.* **2009**, *87*, 363–374. [CrossRef]
47. Treps, L.; Perret, R.; Edmond, S.; Ricard, D.; Gavard, J. Glioblastoma stem-like cells secrete the pro-angiogenic VEGF-A factor in extracellular vesicles. *J. Extracell. Vesicles* **2017**, *6*, 1359479. [CrossRef]
48. Folkens, C.; Shaked, Y.; Man, S.; Tang, T.; Lee, C.R.; Zhu, Z.; Hoffman, R.M.; Kerbel, R.S. Glioma tumor stem-like cells promote tumor angiogenesis and vasculogenesis via vascular endothelial growth factor and stromal-derived factor 1. *Cancer Res.* **2009**, *61*, 7243–7251. [CrossRef]
49. Thirant, C.; Galan-Moya, E.M.; Gustavo Dubois, L.; Pinte, S.; Chafey, P.; Broussard, C.; Varlet, P.; Devaux, B.; Soncin, F.; Gavard, J.; et al. Differential proteomic analysis of human glioblastoma and neural stem cells reveals HDGF as a novel angiogenic secreted factor. *Stem Cells* **2012**, *30*, 845–853. [CrossRef]
50. Pelloski, C.E.; Ballman, K.V.; Furth, A.F.; Zhang, L.; Lin, E.; Sulman, E.P.; Bhat, K.; McDonald, J.M.; Yung, W.K.A.; Colman, H.; et al. Epidermal growth factor receptor variant III status defines clinically distinct subtypes of glioblastoma. *J. Clin. Oncol.* **2007**, *25*, 2288–2294. [CrossRef]
51. Kucharzewska, P.; Christianson, H.C.; Welch, J.E.; Svensson, K.J.; Fredlund, E.; Ringnér, M.; Mörgelin, M.; Bourseau-Guilmain, E.; Bengzon, J.; Belting, M. Exosomes reflect the hypoxic status of glioma cells and mediate hypoxia-dependent activation of vascular cells during tumor development. *Proc. Natl. Acad. Sci. USA* **2013**, *110*, 7312–7317. [CrossRef] [PubMed]

52. Sun, X.; Ma, X.; Wang, J.; Zhao, Y.; Wang, Y.; Bihl, J.C.; Chen, Y.; Jiang, C. Glioma stem cells-derived exosomes promote the angiogenic ability of endothelial cells through miR-21/VEGF signal. *Oncotarget* **2017**, *8*, 36137–36148. [CrossRef] [PubMed]
53. Giusti, I.; Delle Monache, S.; Di Francesco, M.; Sanità, P.; D’Ascenzo, S.; Gravina, G.L.; Festuccia, C.; Dolo, V. From glioblastoma to endothelial cells through extracellular vesicles: Messages for angiogenesis. *Tumor Biol.* **2016**, *37*, 12743–12753. [CrossRef] [PubMed]
54. Lang, H.L.; Hu, G.W.; Zhang, B.; Kuang, W.; Chen, Y.; Wu, L.; Xu, G.H. Glioma cells enhance angiogenesis and inhibit endothelial cell apoptosis through the release of exosomes that contain long non-coding RNA CCAT2. *Oncol. Rep.* **2017**, *38*, 785–798. [CrossRef] [PubMed]
55. Treps, L.; Edmond, S.; Harford-Wright, E.; Galan-Moya, E.M.; Schmitt, A.; Azzi, S.; Citerne, A.; Bidere, N.; Ricard, D.; Gavard, J. Extracellular vesicle-transported Semaphorin3A promotes vascular permeability in glioblastoma. *Oncogene* **2016**, *35*, 2615–2623. [CrossRef] [PubMed]
56. O’Brien, E.; Howarth, C.; Sibson, N.R. The role of astrocytes in CNS tumours: Pre-clinical models and novel imaging approaches. *Front. Cell. Neurosci.* **2013**, *7*, 40. [PubMed]
57. Brandao, M.; Simon, T.; Critchley, G.; Giamas, G. Astrocytes, the rising stars of the glioblastoma microenvironment. *Glia* **2019**, *67*, 779–790. [CrossRef]
58. Chen, Q.; Boire, A.; Jin, X.; Valiente, M.; Er, E.E.; Lopez-Soto, A.; Jacob, L.S.; Patwa, R.; Shah, H.; Xu, K.; et al. Carcinoma-astrocyte gap junctions promote brain metastasis by cGAMP transfer. *Nature* **2016**, *533*, 493–498. [CrossRef]
59. Oushy, S.; Hellwinkel, J.E.; Wang, M.; Nguyen, G.J.; Gunaydin, D.; Harland, T.A.; Anchordoquy, T.J.; Graner, M.W. Glioblastoma multiforme-derived extracellular vesicles drive normal astrocytes towards a tumour-enhancing phenotype. *Philos. Trans. R. Soc. B Biol. Sci.* **2017**, *5*, 373. [CrossRef]
60. Hallal, S.; Mallawaarachy, D.M.; Wei, H.; Ebrahimkhani, S.; Stringer, B.W.; Day, B.W.; Boyd, A.W.; Guillemin, G.J.; Buckland, M.E.; Kaufman, K.L. Extracellular vesicles released by glioblastoma cells stimulate normal astrocytes to acquire a tumor-supportive phenotype via p53 and MYC signaling pathways. *Mol. Neurobiol.* **2018**, *56*, 4566–4581. [CrossRef]
61. Kasthuber, E.R.; Lowe, S.W. Putting p53 in Context. *Cell* **2017**, *170*, 1062–1078. [CrossRef] [PubMed]
62. Ohgaki, H.; Kleihues, P. Genetic pathways to primary and secondary glioblastoma. *Am. J. Pathol.* **2007**, *170*, 1445–1453. [CrossRef] [PubMed]
63. Biasoli, D.; Sobrinho, M.F.; Da Fonseca, A.C.C.; De Matos, D.G.; Romão, L.; De Moraes Maciel, R.; Rehen, S.K.; Moura-Neto, V.; Borges, H.L.; Lima, F.R.S. Glioblastoma cells inhibit astrocytic p53-expression favoring cancer malignancy. *Oncogenesis* **2014**, *3*, e123. [CrossRef] [PubMed]
64. Laurenti, E.; Wilson, A.; Trumpp, A. Myc’s other life: Stem cells and beyond. *Curr. Opin. Cell Biol.* **2009**, *21*, 844–854. [CrossRef]
65. Wang, J.; Wang, H.; Li, Z.; Wu, Q.; Lathia, J.D.; McLendon, R.E.; Hjelmeland, A.B.; Rich, J.N. c-Myc is required for maintenance of glioma cancer stem cells. *PLoS ONE* **2008**, *3*, e3769. [CrossRef]
66. Radke, J.; Bortolussi, G.; Pagenstecher, A. Akt and c-Myc induce stem-cell markers in mature primary p53-/- astrocytes and render these cells gliomagenic in the brain of immunocompetent mice. *PLoS ONE* **2013**, *8*, e56691. [CrossRef]
67. Li, F.; Liu, X.; Sampson, J.H.; Bigner, D.D.; Li, C.Y. Rapid reprogramming of primary human astrocytes into potent tumor-initiating cells with defined genetic factors. *Cancer Res.* **2016**, *76*, 5143–5150. [CrossRef]
68. El Fatimy, R.; Subramanian, S.; Uhlmann, E.J.; Krichevsky, A.M. Genome editing reveals glioblastoma addiction to microRNA-10b. *Mol. Ther.* **2017**, *25*, 368–378. [CrossRef]
69. Lee, J.H.; Lee, J.E.; Kahng, J.Y.; Kim, S.H.; Park, J.S.; Yoon, S.J.; Um, J.Y.; Kim, W.K.; Lee, J.K.; Park, J.; et al. Human glioblastoma arises from subventricular zone cells with low-level driver mutations. *Nature* **2018**, *560*, 243–247. [CrossRef]
70. Wang, J.; Liu, J.; Sun, G.; Meng, H.; Wang, J.; Guan, Y.; Yin, Y.; Zhao, Z.; Dong, X.; Yin, S.; et al. Glioblastoma extracellular vesicles induce the tumour-promoting transformation of neural stem cells. *Cancer Lett.* **2019**, *466*, 1–12. [CrossRef]
71. Behnan, J.; Isakson, P.; Joel, M.; Cilio, C.; Langmoen, I.A.; Vik-Mo, E.O.; Badn, W. Recruited brain tumor-derived mesenchymal stem cells contribute to brain tumor progression. *Stem Cells* **2014**, *32*, 1110–1123. [CrossRef] [PubMed]

72. Hossain, A.; Gumin, J.; Gao, F.; Figueroa, J.; Shinojima, N.; Takezaki, T.; Priebe, W.; Villarreal, D.; Kang, S.G.; Joyce, C.; et al. Mesenchymal stem cells isolated from human gliomas increase proliferation and maintain stemness of glioma stem cells through the IL-6/gp130/STAT3 pathway. *Stem Cells* **2015**, *33*, 2400–2415. [CrossRef] [PubMed]
73. Figueroa, J.; Phillips, L.M.; Shahar, T.; Hossain, A.; Gumin, J.; Kim, H.; Bean, A.J.; Calin, G.A.; Fueyo, J.; Walters, E.T.; et al. Exosomes from glioma-associated mesenchymal stem cells increase the tumorigenicity of glioma stem-like cells via transfer of miR-1587. *Cancer Res.* **2017**, *77*, 5808–5819. [CrossRef] [PubMed]
74. Palumbo, P.; Lombardi, F.; Augello, F.R.; Giusti, I.; Luzzi, S.; Dolo, V.; Cifone, M.G.; Cinque, B. NOS2 inhibitor 1400W induces autophagic flux and influences extracellular vesicle profile in human glioblastoma U87MG cell line. *Int. J. Mol. Sci.* **2019**, *20*, 3010. [CrossRef]
75. Pace, K.R.; Dutt, R.; Galileo, D.S. Exosomal L1CAM stimulates glioblastoma cell motility, proliferation, and invasiveness. *Int. J. Mol. Sci.* **2019**, *20*, 3982. [CrossRef]
76. Ricklefs, F.; Mineo, M.; Rooj, A.K.; Nakano, I.; Charest, A.; Weissleder, R.; Breakefield, X.O.; Chiocca, E.A.; Godlewski, J.; Bronisz, A. Extracellular vesicles from high-grade glioma exchange diverse pro-oncogenic signals that maintain intratumoral heterogeneity. *Cancer Res.* **2016**, *76*, 2876–2881. [CrossRef]
77. Konoshenko, M.Y.; Lekchnov, E.A.; Vlassov, A.V.; Laktionov, P.P. Isolation of extracellular vesicles: General methodologies and latest trends. *BioMed Res. Int.* **2018**, 8545347. [CrossRef]
78. Bovy, N.; Blomme, B.; Frères, P.; Dederen, S.; Nivelles, O.; Lion, M.; Carnet, O.; Martial, J.A.; Noël, A.; Thiry, M.; et al. Endothelial exosomes contribute to the antitumor response during breast cancer neoadjuvant chemotherapy via microRNA transfer. *Oncotarget* **2015**, *6*, 10253–10266. [CrossRef]
79. Li, D.; Tian, Y.; Hu, Y.; Qi, Y.; Tian, N.; Li, S.; Hu, P.; Wu, F.; Wei, Q.; Wei, Z.; et al. Glioma-associated human endothelial cell-derived extracellular vesicles specifically promote the tumorigenicity of glioma stem cells via CD9. *Oncogene* **2019**, *38*, 6898–6912. [CrossRef]
80. Podergajs, N.; Motaln, H.; Rajčević, U.; Verbovšek, U.; Koršič, M.; Obad, N.; Espedal, H.; Vittori, M.; Herold-Mende, C.; Miletic, H.; et al. Transmembrane protein CD9 is glioblastoma biomarker, relevant for maintenance of glioblastoma stem cells. *Oncotarget* **2016**, *7*, 593–609. [CrossRef]
81. Zhang, L.; Zhang, S.; Yao, J.; Lowey, F.J.; Zhang, Q.; Huang, W.-C.; Li, P.; Li, M.; Wang, X.; Zhang, C.; et al. Microenvironment-induced PTEN loss by exosomal microRNA primes brain metastasis outgrowth. *Nature* **2015**, *527*, 100–104. [CrossRef] [PubMed]
82. Zheng, P.; Chen, L.; Yuan, X.; Luo, Q.; Liu, Y.; Xie, G.; Ma, Y.; Shen, L. Exosomal transfer of tumor-associated macrophage-derived miR-21 confers cisplatin resistance in gastric cancer cells. *J. Exp. Clin. Cancer Res.* **2017**, *36*, 53. [CrossRef] [PubMed]
83. Rennert, R.C.; Hochberg, F.H.; Carter, B.S. ExRNA in biofluids as biomarkers for brain tumors. *Cell. Mol. Neurobiol.* **2016**, *36*, 353–360. [CrossRef] [PubMed]
84. Lane, R.; Simon, T.; Vintu, M.; Solkin, B.; Koch, B.; Stewart, N.; Benstead-Hume, G.; Pearl, F.M.G.; Critchley, G.; Stebbing, J.; et al. Cell-derived extracellular vesicles can be used as a biomarker reservoir for glioblastoma tumor subtyping. *Commun. Biol.* **2019**, *2*, 315. [CrossRef] [PubMed]
85. Basu, B.; Ghosh, M.K. Extracellular vesicles in glioma: From diagnosis to therapy. *BioEssays* **2019**, *41*, 1–9. [CrossRef] [PubMed]




© 2019 by the authors. Licensee MDPI, Basel, Switzerland. This article is an open access article distributed under the terms and conditions of the Creative Commons Attribution (CC BY) license (<http://creativecommons.org/licenses/by/4.0/>).



Article

# Upregulation of Epithelial-To-Mesenchymal Transition Markers and P2X7 Receptors Is Associated to Increased Invasiveness Caused by P2X7 Receptor Stimulation in Human Glioblastoma Stem Cells

Sihana Ziberi <sup>1,2,3,†</sup>, Mariachiara Zuccarini <sup>1,2,†</sup>, Marzia Carluccio <sup>1,2,3</sup>, Patricia Giuliani <sup>1,2</sup>, Lucia Ricci-Vitiani <sup>4</sup>, Roberto Pallini <sup>5</sup>, Francesco Caciagli <sup>2</sup>, Patrizia Di Iorio <sup>1,2</sup> and Renata Ciccarelli <sup>1,2,3,\*</sup> 

<sup>1</sup> Department of Medical, Oral and Biotechnological Sciences, University of Chieti-Pescara, Via dei Vestini 29, 66100 Chieti, Italy; sihana.ziberi@unich.it (S.Z.); mariachiara.zuccarini@unich.it (M.Z.); marzia.carluccio@unich.it (M.C.); patricia.giuliani@unich.it (P.G.); patrizia.diiorio@unich.it (P.D.I.)

<sup>2</sup> Center for Advanced Study and Technologies (CAST). University of Chieti-Pescara, Via L. Polacchi, 66100 Chieti, Italy; f.caciagli@unich.it

<sup>3</sup> StemTeCh Group, Via L. Polacchi, 66100 Chieti, Italy

<sup>4</sup> Department of Oncology and Molecular Medicine, Istituto Superiore di Sanità, Via Regina Elena 299, 00161 Rome, Italy; lriccivitiani@yahoo.it

<sup>5</sup> Institute of Neurosurgery, Università Cattolica del Sacro Cuore, Largo Agostino Gemelli 8, 00168 Rome, Italy; roberto.pallini@Unicatt.it

\* Correspondence: renata.ciccarelli@unich.it

† equally contributed.

Received: 25 November 2019; Accepted: 25 December 2019; Published: 29 December 2019



**Abstract:** Glioblastoma (GBM) stem cells (GSCs), which contribute to GBM unfavorable prognosis, show high expression levels of ATP/P2X7 receptors (P2X7R). Here, we reported that cells exposure to 2'(3')-O-(4-benzoylbenzoyl)-ATP (BzATP), a P2X7R agonist, up-regulated the expression of markers associated to epithelial-to-mesenchymal transition (EMT), a process likely contributing to GSC malignancy, and increased GSC migration/invasiveness like the known EMT inducer, Transforming Growth Factor  $\beta$ 1 (TGF $\beta$ 1). These effects were coupled to phosphorylation of SMAD2, a downstream effector in the TGF $\beta$  pathway, suggesting its involvement in P2X7R-mediated activity in GSCs. All BzATP effects, including a decrease in the caspase 3/7 activity in GSC medium, were mostly counteracted by the P2X7R antagonist A438079. Finally, BzATP increased the subunit expression of two main human P2X7R splice variants, the full-length P2X7A and the truncated P2X7B, lacking the carboxylic tail, which have different functional properties depending on their arrangement. Since up-regulation of A/B subunits might favor their assembly into a heterotrimeric P2X7R with great sensitivity towards agonists and cell energy support, this is in line with increased EMT markers expression, cell migration/invasion and GSC survival observed following P2X7R stimulation. As in GBM microenvironment extracellular ATP levels may activate P2X7R, our data suggest a P2X7R role in GBM recurrence/invasiveness.

**Keywords:** glioblastoma stem cells (GSCs); epithelial-to-mesenchymal transition (EMT) markers; GSC invasiveness; transforming growth factor beta; BzATP; P2X7 receptor splice variants A and B

## 1. Introduction

Glioblastoma (GBM) is the most common malignant primary brain tumor in adults, characterized by high invasiveness and recurrence [1]. Unfortunately, the current therapy including maximal safe

surgical resection followed by radio- and chemo-therapy is largely ineffective so that the prognosis is poor and most patients die within the first two years. As in other malignant tumors, GBM aggressiveness seems due to the presence of a restrict population of stem-like cells inside the tumor mass, called GBM stem cells (GSCs), which are characterized by high proliferative potential, long life-span and resistance to antitumor agents [2]. GSCs can be isolated from tumor specimens and cultured in vitro in conditions favoring the growth of neural stem cells, which allow them to mimic the phenotype and genotype of primary tumors more closely than serum-cultured cell lines [3,4]. Moreover, upon injection into immunodeficient mice, they are able to recapitulate human tumor [5], thus representing a useful model to study the efficacy of old and new anti-tumor therapies.

GSC aggressiveness seems to also rely on epithelial-to-mesenchymal transition (EMT), an important biological process usually involved in embryogenesis, tissue repair and wound healing [6]. Although still debated in a neuro-epithelial context like GBM, in primary epithelial tumors EMT favors a more aggressive phenotype in cancer cells, with enhanced migration and invasiveness ability [6,7]. These cells also express a number of mesenchymal features including molecules such as Snails, Twist, Zinc finger E-box-binding homeobox (ZEB), vimentin and N-cadherin, which are considered specific EMT markers. More in detail, Snails, comprising Snail1 and Slug, also called Snail2, are transcriptional factors able to inhibit epithelial-related genes by binding to E-box DNA sequences through their carboxy-terminal zinc-finger domains [8]. Other EMT transcriptional factors are represented by ZEB, i.e., ZEB1 and ZEB2, whose molecular structure contains two zinc-finger domains that bind to E-boxes in DNA regulatory regions, contributing to inhibit epithelial genes while activating mesenchymal genes, including vimentin [9]. ZEB proteins may play a crucial role in tumor development, invasiveness and drug resistance [10]. Further EMT transcription factors are Twist1 and Twist2, which promote or repress several EMT related genes, thus inducing the expression of a mesenchymal phenotype in epithelial cells [11]. Another feature of EMT is the so-called “cadherin switch” in epithelial carcinomas, accounting for a loss in the expression of E-cadherin, a key protein in the formation of cell–cell junctions, and increased N-cadherin expression [7]. Finally, vimentin is a major constituent of the intermediate filament family of proteins, ubiquitously expressed in normal mesenchymal cells, being responsible of the maintenance of cell integrity and resistance against stress. An increased vimentin expression has been reported in various epithelial cancers [12]. The occurrence and activity of EMT markers have been also reported in GBM [7]. Thus, in human GBM cell lines, Snail1 silencing decreases cell proliferation, invasion and migration [13,14]. As well, ZEB1 contributes to GBM progression, acting as a pro-tumor factor, and its expression inversely correlates with survival of GBM patients [15]. Moreover, in GBM cell lines the overexpression of Twist1 enhances their migratory capacity and the cytoskeleton reorganization, two features supporting cell invasiveness once transplanted in mice brain [16]. As for cadherin, some data [17] showed that its switch from E- to N-cadherin is not essential to prove EMT in gliomas. Similarly, it has become a controversial issue also in epithelial tumors. In GBM, the role of N-cadherin is probably not associated with its increased expression, but with its differential distribution in cell membrane, which can alter the tumor cell capacity of adhesion and motility [7]. Finally, an increase in the vimentin expression has been observed also in GBM [18]. Altogether, findings from GBM and related cell lines support the involvement of EMT in GBM malignancy.

Among the factors contributing to the EMT onset and progression, a crucial role might be played by purines. [19]. ATP, adenosine and related compounds are ubiquitous substances present inside and released from virtually all types of cells, including tumor cells, and are involved in multiple physiological and pathological processes [20]. In particular, both ATP and adenosine are implicated in tumor growth and recurrence [21,22]. Noteworthy, in most tumors including GBM, the extracellular concentrations of ATP and adenosine are very high as compared to the microenvironment of normal cells [23]. In line with this evidence, we previously reported [24] that all four metabotropic receptors for adenosine were expressed in GSCs derived from GBM surgical specimens of three different patients, with a prevalence of the subtypes A3 for adenosine, and, among P2 receptors (P2R) for ATP, the ionotropic P2X7 receptor (P2X7R) showed the highest levels. Nine different P2X7R splice variants

(P2X7A–J) of this receptor have been individuated so far, being the human main functional isoforms the canonical full-length monomer A and the truncated isoform B with a shorter amino acid sequence. The receptor resulting from P2X7A subunit assembly (P2X7AR) is equipped with a pore, while that formed by a P2X7B trimer (P2X7BR) is provided only with a functional cationic channel. ATP, the natural agonist of P2R, interacting at millimolar concentrations with the P2X7R, opens the pore—where present—that is permeable to molecules up to 900 Da, inducing plasma membrane permeabilization as well as apoptotic and necrotic events [25]. Accordingly, in the aforementioned paper [24], we observed a dose-dependent growth inhibition of GSCs when they were stimulated for two consecutive days by elevated concentrations of ATP or 2′[3′]-O-[4-benzoylbenzoyl]-ATP (BzATP), a rather selective P2X7R agonist. The same drugs, at the concentration of 500  $\mu$ M, also potentiated the cytotoxicity of temozolomide, an agent currently used in GBM therapy. In contrast, lower ATP concentrations, likely closer to the extracellular ones found in GBM microenvironment, open only P2X7R cationic channels. Indeed, the P2X7BR variant, lacking the pore, is today regarded as a pro-cancerous receptor, able to increase tumor growth and invasiveness [26,27].

Based on these premises, we aimed our study at investigating, in GSCs, the influence of P2X7R activation on: i) EMT process, ii) cell migration/invasion, iii) expression of P2X7R, with a particular interest towards the two main splice variants A and B. To these purposes, we administered BzATP only once to the cultures at concentrations ranging from 50 up to 200  $\mu$ M, which did not result to be cytotoxic to the cells (see the Results section). Of note, we compared BzATP effects with those caused by cell exposure to Transforming Growth Factor  $\beta$ 1 (TGF $\beta$ 1), known EMT inducer. Our findings showed that P2X7R activation upregulated EMT marker expression and increased cell invasiveness in the examined cells, also protecting them from apoptotic events. Interestingly, these effects were coupled to increased expression of the two P2X7R splice variants, the co-assembly of which into a hetero-trimeric receptor would likely support the pro-tumor effect consequent to GSC exposure to relatively low concentrations of the P2X7R agonist, BzATP.

## 2. Materials and Methods

### 2.1. Chemicals

Disposables for tissue culture were from Falcon (Steroglass, Perugia, Italy). Dulbecco's Modified Eagle's Medium/Nutrient Mixture F-12 Ham (DMEM/F-12) was purchased from Sigma-Aldrich S.p.A. (Milan, Italy) as well as penicillin/streptomycin, amphotericin B, 2′[3′]-O-[4-benzoylbenzoyl]adenosine-5′triphosphate tri[triethylammonium] salt (BzATP) and all the other chemicals, unless differently indicated. 3-[[5-[2,3-Dichlorophenyl]-1H-tetrazol-1-yl]methyl]pyridine hydrochloride (A438079) and 3-[6-methyl-2-pyridinyl]-N-phenyl-4-[4-quinolinyl]-1H-pyrazole-1-carbothioamide (A8301) were ordered from Tocris Bioscience (Space Import, Milan, Italy); Transforming Growth Factor  $\beta$  (TGF $\beta$ ) and human Epidermal (EGF) and Fibroblast (FGF) growth factors were purchased from PeproTech (SIAL, Rome, Italy).

### 2.2. Cell Cultures

We used GSCs obtained from three different patients (who provided written informed consent to the study according to research proposals approved by the Institutional Ethics Committee of Fondazione Policlinico Gemelli, UCSC (Prot. 4720/17) with a primary GBM, the molecular profile of which has previously been reported [24]. Here, cells maintained the same numeration used in the aforementioned paper [24], even though they are now officially registered with a number corresponding to the patient from whom the primary GBM was isolated and the GSCs derived. Thus, the nomenclature of GSCs #1 is invariant (deriving from the patient #1), whereas GSCs #2 and #3 correspond to cells #28 and #83 in the new nomenclature [28,29]. It has also to mention that these cells have been previously characterized for some important characteristics. They indeed showed high self-renewal, stemness marker expression and resistance to chemotherapy drugs when cultured in vitro, whereas, when

injected in the brain of immune-compromised mice, they were able to reproduce a tumor identical to the human one as for antigen expression and histological tissue organization [30–32]. In this study, GSCs were grown using a standard protocol previously reported [30]. Briefly, cells isolated from tumor were cultured and expanded in DMEM/F12 medium without serum but supplemented with some mitogens (20 ng/mL of human recombinant EGF and 10 ng/mL of human recombinant FGF-basic). Under these conditions, cells formed classical neurospheres and were expanded. However, the pharmacological treatments were performed on cells grown as monolayer obtained pre-coating culture plates with Matrigel (Corning, SIAL) dissolved in culture medium and then seeding the cells that were fed with the usual culture medium containing also the growth factors above mentioned (dilution 1:200). In this condition, GSCs maintained spherogenic properties [30,31], but their use allowed a more precise quantification of cell survival *in vitro*. GSCs were used from passage 5 to 10 throughout the study. During this period, we found no significant modification in cell morphology or response to applied drugs.

### 2.3. Experimental Protocol

We exposed GSCs to different concentrations of BzATP ranging from 50 to 200  $\mu$ M. We compared BzATP effects with those induced by 5–10 ng/mL TGF $\beta$ 1, a known inducer of the EMT process. Both TGF $\beta$ 1 and BzATP were administered only once to the GSC cultures, whereas the evaluation of different functional/biochemical parameters was carried out at different time points as indicated in the Results section. In some experiments, cells were pre-treated with the antagonist of P2X7R (A438079, 10  $\mu$ M) or TGF $\beta$  type I receptors (A8301, 0.5  $\mu$ M), which were added to the cells 1 or 2h, respectively, prior to BzATP or TGF $\beta$ .

### 2.4. Real Time PCR

RNA was extracted from cells by TRIZOL (Invitrogen, Thermo Fisher Scientific, Milan, Italy). and its amount was measured by spectrophotometry (Nanodrop 2000 spectrophotometer, Thermo Fisher Scientific). Additionally, RNA integrity was tested by 1.5% agarose gel electrophoresis in Tris Borate EDTA (TBE) (89 mM Tris, 89 mM boric acid, 20 mM EDTA, pH 8.0) and subsequent gel analysis by RED analyzer (Cell Biosciences, Santa Clara, CA, USA). All samples were amplified by Turbo DNA-free kit (Invitrogen, Thermo Fisher Scientific). Reverse transcription was performed using 1  $\mu$ g of total RNA/sample and high Capacity cDNA Reverse Transcription kit (Applied Biosystems, Foster City, CA, USA), following the manufacturer's instructions. The reaction mixture was loaded to the Gene Amp PCR system 9700 (Applied Biosystem) undergoing the cycle at 37 °C for 120 min.

Real-Time PCR was carried out with the ABI Prism 7900 Sequence Detection System (Applied Biosystems). Expression of ZEB1, N-cadherin and Snail1 as well as of P2X7 A and B variants was evaluated at 0, 12, 24, and 48 h in GSCs untreated or exposed to drugs. Some forward and reverse primers were purchased from Integrated DNA Technologies (IDT, Leuven, Belgium) and are the following: ZEB1, forward 5'-CAAGGTGGCCATTCTGTTAT-3' and reverse 5'-CTAGGCTGCTCAAGACTGTAG-3'; N-cadherin, forward 5'-CAACTTGCCAGAAACTCC

AGG-3' and reverse 5'-ATGAAACCGGGCTATCAGCTC-3'; Snail1, forward 5'-CGTTTTCCAGACCCTGGTTA-3' and reverse 5'-TGACCTGTCTGCAAATGCTC-3'; GAPDH (glyceraldehyde 3-phosphate dehydrogenase), forward 5'-CATCACTGCCACCCAGAAG-3' and reverse 5'-CAGTGAGCTTCCCGTTCAG-3'. The SYBR<sup>TM</sup> Green PCR Master Mix (Applied Biosystems) was used to perform the assay. The custom TaqMan Gene Expression Assays for P2X7A (forward 5' AGATGCTGGAGAATGGAGTG 3', reverse 5' TTCTCGTGGTGTAGTTGTGG 3') and P2X7B (forward 5'-CCCATCGAGGCAGTGA-3', reverse 5'-TTCTCGTGGTGTAGTTGTGG-3') were designed according to [33], and the TaqMan Universal PCR Master Mix (Applied Biosystems) was used according to standard protocols. Gene expression levels were normalized ( $\Delta$ Ct) by using as endogenous control the house keeping GAPDH for EMT markers and the  $\beta$ 2-microglobulin (B2M, Hs99999907\_m1, Applied Biosystems, Foster City, CA, USA) for P2X7A and P2X7B splice variants.

The results were analyzed for relative quantitation among groups using the comparative  $2^{-\Delta\Delta Ct}$  method [34].

### 2.5. Western Blot Analysis

Cells, harvested at 4 °C in lysis buffer containing a protease inhibitor cocktail (Sigma-Aldrich), were centrifuged at 14,000 rpm (10 min, 4 °C). Protein amount was measured by BioRad protein assay (Bio-Rad Laboratories, Milan, Italy). Samples (usually 60 µg), diluted in sodium dodecyl sulphate (SDS)-bromophenol blue buffer, were boiled (5 min) and separated on 10% SDS polyacrylamide gels. Proteins, once transferred on polyvinylidene fluoride membrane, were blocked with PBS/0.1 % Tween20/5 % nonfat milk (Bio-Rad Laboratories) for 2 h at 4 °C and then overnight incubated at 4 °C with primary antibodies [polyclonal rabbit anti-P2X7R (extracellular), dilution 1:200 (Alomone Labs, Jerusalem, Israel)]; [polyclonal rabbit anti-P2X7R (intracellular, C-terminus) dilution 1:300 (Sigma-Aldrich)], (monoclonal rabbit anti-vimentin (Cell Signaling, Euroclone, Pero, Italy), dilution 1:1000), (polyclonal rabbit anti-N-cadherin (Cell Signaling), dilution 1:1000), (monoclonal rabbit anti-ZEB1 (Cell Signaling), dilution 1:1000), (polyclonal rabbit anti-Twist1 (Cell Signaling), dilution 1:1000), (monoclonal anti-phosphoSMAD2, (Cell Signaling), dilution 1:1000). Subsequently, the membranes were exposed to goat anti-rabbit HRP-conjugated secondary antibody (final dilution 1:5000, incubation for 1h at, room temperature; Bethyl Laboratories Inc., Montgomery, TX, USA). Sample equal loading was determined by stripping and re-probing the blots with an anti-β-actin antibody (dilution 1:1000, incubation overnight at 4 °C; Santa Cruz Biotechnologies, Heidelberg, Germany). Immunocomplexes were visualized by chemiluminescence (ECL) detection system (GE Healthcare Life Sciences, Milan, Italy) and quantified by densitometric analysis (ImageJ software; U.S. National Institutes of Health, Bethesda, MD, USA).

### 2.6. Lactate Dehydrogenase Activity

Lactate dehydrogenase (LDH) levels were assayed in GSC medium as an index of necrotic cell death since LDH is a cytoplasm enzyme that can be released following cell membrane injury. To this aim, cells were seeded ( $3 \times 10^3$  cells/well) in 96-well plates and incubated with drugs following the usual protocol. At the indicated time points, cells were incubated (45 min, 37 °C, 5% CO<sub>2</sub>) with a specific lysis buffer, then the plates were centrifuged (250 g, 4 min). Subsequently, 50 µL of supernatant from each well were transferred to a new 96-well plate, to which 50 µL of substrate buffer (composition: 0.7 mM p-iodonitrotetrazolium violet, 50 mM L-lactic acid, 0.3 mM phenazine methoxysulfate, 0.4 mM NAD, and 0.2 M Tris-HCl pH 8.0) were added. The plate suitably blanket was incubated in the dark (30 min, room temperature). The reaction was blocked adding 50 µL/well of stop solution. The absorbance was spectrophotometrically measured at 490 nm. The results, expressed as a percentage of the total LDH released from positive controls, consisting of cells exposed to 25 µL of 10% Nonidet P-40 (NP-40), were calculated as follows: (supernatant absorbance value—white absorbance value)/(supernatant absorbance + lysate absorbance) × 100. All reagents were purchased from Promega Italia (Milan, Italy).

### 2.7. Caspase 3/7 Activity Assay

Apoptosis of GSCs, exposed or not to P2X7R agonist/antagonist, was evaluated by the Caspase-Glo Assay (Promega Italia), which contains a pro-luminescent peptide DEVD-aminoluciferin that can be cleaved by caspases 3/7 liberating aminoluciferin. A thermostable luciferase, included in the kit, generates a luminescent signal that is proportional to caspase-3/7 activity. Briefly, caspase-3/7 detection reagent was added at 1:1 ratio to the culture medium and cells were incubated at 25 °C for 1 h. The luminescent signal was revealed by a luminometer (Veritas™ Microplate Luminometer Turner Biosystems, Sunnyvale, CA, USA). The background value, measured in a sample containing growth medium and caspase-3/7 detection reagent but no cells, was subtracted from each measurement.

### 2.8. MTS Assay

Cell proliferation was assayed by 3-[4,5-dimethylthiazol-2-yl]-5-[3-carboxymethoxy phenyl]-2-[4-sulfophenyl]-2H-tetrazolium (MTS), using the CellTiter 96<sup>®</sup> AQueous OneSolution Cell Proliferation Assay (Promega Italia). The absorbance was evaluated by a microtiter plate reader (Spectracount<sup>™</sup>, PerkinElmer Life, Waltham, MS, USA) at 490 nm.

### 2.9. Scratch Assay

Drug effects on GSC migration were evaluated by scratch assay. Briefly, cells were seeded in 6-well plates at  $3 \times 10^5$  cells/well and once they reached 80% confluence were pretreated with 5 µg/mL mitomycin-C (Sigma-Aldrich) at 37 °C with 5% CO<sub>2</sub> for 3 h to arrest cell proliferation. Cell monolayer was scratched by a sterile 200-µL pipette tip and then washed, being the edge of the scratch smoothed with PBS. After pharmacological treatments performed according to the experimental protocol, GSCs were observed at a phase contrast microscope (Nikon Eclipse TS100) and images were acquired, using the Zoom Browser EX software for Windows 10 (Canon Italia), prior to (0 h) and at 6 and 24 h after the monolayers were scratched. The migration area was quantified by densitometric analysis (ImageJ software, 64-bit Java 1.8.0\_112) and expressed as percentage of closing  $= [A_0 - A_n]/A_0 \times 100$ ,  $A_0$  and  $A_n$  representing the initial wound area ( $t = 0$  h) and the residual wound area at the time of measurement ( $t = n$  h), respectively.

### 2.10. Transwell Migration Assay

This assay measures cell chemotaxis and invasion through the extracellular matrix. We used filter membranes (EMD Millipore Corporation, Billerica, MA, USA) with 8 µm size pore suitable to test cell migration. Thirty/fifty microliters of Matrigel were plated on the top of the transwell membrane inserts placed in a 24well-plate, which were then transferred into a 37 °C incubator for 15–30 min allowing Matrigel to form a thin gel layer. Approximately  $5 \times 10^4$  cells were plated in the upper chamber and 700 µL of the desired attractant was added into the bottom of the lower chamber. More in detail, in a set of plates GSCs were incubated in the usual culture medium; in another set a high percentage of serum (10%), used as an attractant for cells, was added to the usual medium; further two sets of plates were incubated in the usual culture medium in the presence of TGFβ1 or BzATP. When present, the P2X7R antagonist A438079 or the antagonist of TGFβ receptors, A8301, were added 1 or 2 h prior to the other pharmacological treatments, respectively. After 24 h the inserts were removed from the plate and a cotton-tipped was used to eliminate cells that have not migrated through the membrane. The membranes were fixed using cold methanol, stained with crystal violet 0.2% and then washed as many times as needed to remove dye excess. Subsequently, the cells on the membrane undersurface were counted under a light microscope (at an average of five semirandom non-overlapping fields at 200× magnification).

### 2.11. Statistical Analysis

The results are expressed as means ± standard error of mean (SEM) of at least three replicates. The significance has been calculated using one-way analysis of variance (ANOVA) followed by Dunnett's post hoc test (GraphPad Prism 6.0, San Diego, CA, USA). Difference was considered to be statistically significant at a value of  $p < 0.05$ .

## 3. Results

The experiments in this study, like in a previous one [24], were performed on GSCs isolated from GBM of three different patients obtaining comparable results.

### 3.1. Influence of P2X7R Activation and TGFβ1 on the Expression of Selected EMT Markers in GSCs

We started our study performing pivotal experiments in which we exposed GSC cultures to ATP, the natural ligand for most subtypes of the purinergic P2R family. The selected ATP concentrations (100, 200, and 300 µM) were administered only once to the cultures and were lower than that (500

μM) able to cause a definite cytotoxicity to the cells [24]. In this condition, only the highest ATP concentration was able to increase the expression of some EMT markers, as evaluated by real time PCR (N-cadherin and ZEB1) at 12 and 24 h or by western blot analysis (N-cadherin, ZEB1 and also vimentin and Twist1) within 72 h. In particular, ATP enhanced the protein content of vimentin and N-cadherin up to 72 h, whereas the increase of Twist1 or ZEB1 proteins lasted 48 h or 24h, respectively (Figure 1A,B). Cell pretreatment with the P2X7R antagonist A438079 reduced ATP-induced effects, except that on N-cadherin at 72 h.

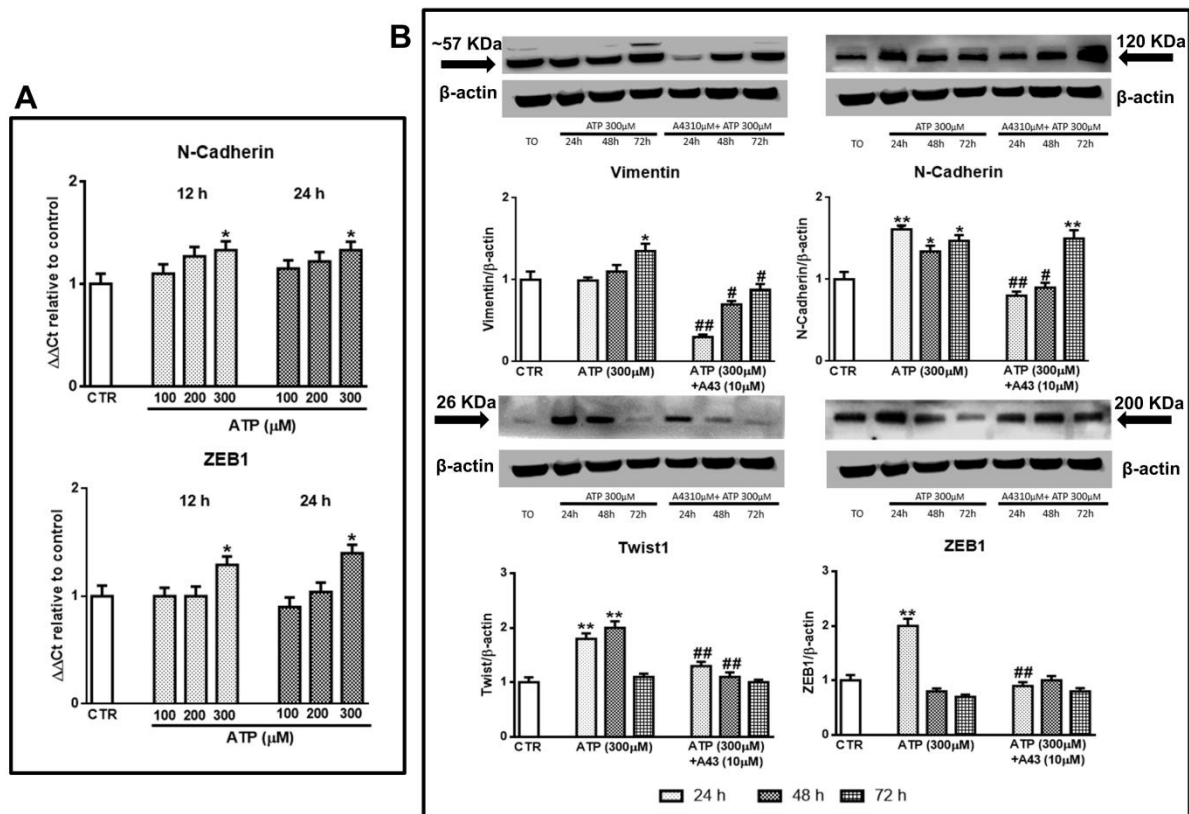


**Figure 1.** Effect of ATP on epithelial-to-mesenchymal transition (EMT) markers evaluated at different times after drug administration to cultured glioblastoma stem cells (GSCs). GSCs, cultured up to their confluence in vitro were exposed to different concentrations (A) or 300 μM of ATP (B), in the presence or not of the P2X7R antagonist, A438079, added to the cultures 1 h prior to ATP. (A) At the indicated time periods cells were collected and mRNA was extracted and analyzed for the gene expression of N-cadherin and ZEB1. mRNA levels were normalized (ΔCt) by using the house keeping GAPDH as endogenous control and the results were obtained by relative quantitation among groups using the comparative 2<sup>ΔΔCt</sup> method. Values, calculated as fold of increase vs. untreated cells assumed as control (CTR) are the mean ± S.E.M. of three independent experiments where each sample was tested in duplicate. (B) cells, harvested at the indicated time periods, were lysed and the protein levels of EMT markers such as vimentin, N-cadherin, Twist1, and ZEB1 were determined by western blot analysis. Immunoblots were re-probed with an antibody against β actin, quantified by densitometric analysis, normalized to β actin used as an internal control, and reported in the histograms assuming the value of control/β-actin = 1. Immunoblots in the figure are representative of independent experiments carried out in GSCs #1 and tested in triplicate. Of note, the band of β-actin is the same for all blots reported in the figures, which were obtained by cutting the same membrane at different heights corresponding to the molecular weights of the selected markers. \*p < 0.05, \*\*p < 0.01: statistical significance vs. untreated GSCs assumed as control (CTR); #p < 0.05, ##p < 0.01: statistical significance vs. cells exposed to ATP (one-way ANOVA plus Dunnett’s test).

Next, we compared the activity of TGFβ1, a known EMT inducer, with that of BzATP, a rather selective P2X7R agonist, on the expression of EMT markers. As for ATP, both drugs were administered only once to the cultures. In GSCs #1 and #3, we observed that TGFβ1, yet at the dose of 5 ng/mL, enhanced mRNA levels of the selected EMT markers after 12–48 h of treatment. Similarly, cell exposure to BzATP caused an increase of all marker expression, although with some differences each other, related to the effect onset/duration (Figures 2 and 3). Indeed, in GSCs #1 BzATP significantly enhanced mRNA levels of N-cadherin at 12 h, of ZEB1 at 12 and 24 h and of Snail1 mainly at 24 h, whereas GSCs #3 showed a greater responsiveness to BzATP, the effect of which was evident at 24 h for N-cadherin and up to 48 h for ZEB1 and Snail1.

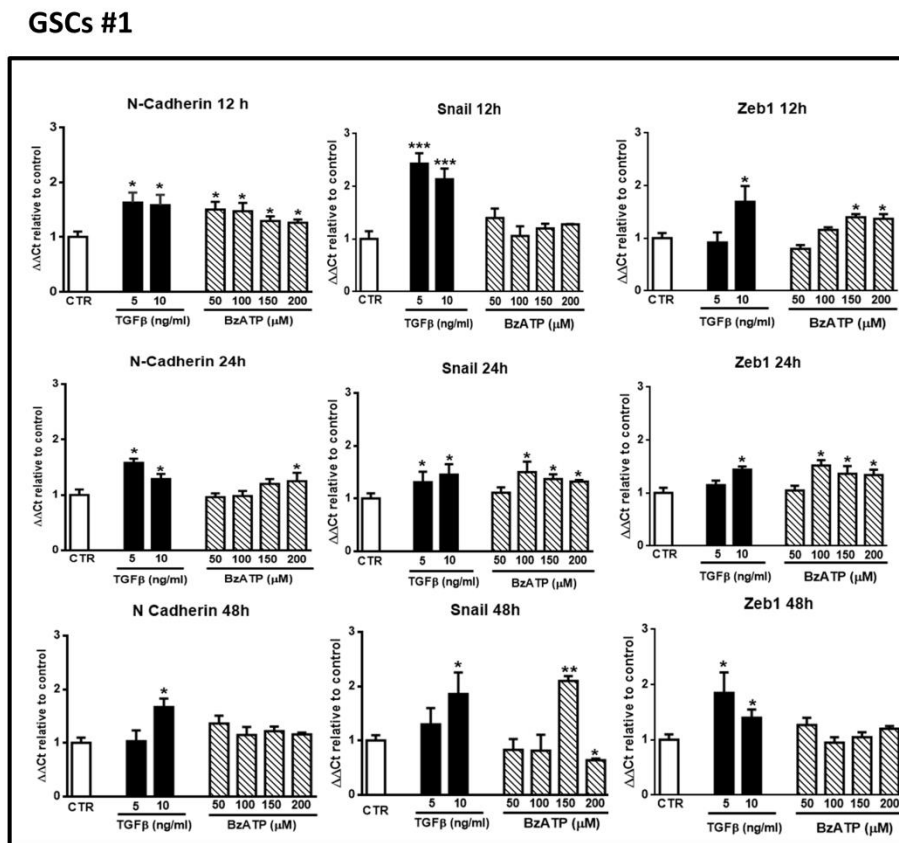


**Figure 2.** Effect of Transforming Growth Factor β1 (TGFβ1) or 2'-(3')-O-(4-benzoylbenzoyl)-ATP (BzATP) on EMT markers evaluated by qRT-PCR at different times after drug administration to cultured GSCs #1. GSCs, grown up to their confluence in vitro, were exposed to different concentrations of TGFβ1 or BzATP. At the indicated time points cells were collected to obtain their mRNA to analyze the gene expression of the indicated EMT markers. mRNA levels were normalized (ΔCt) by using the house keeping GAPDH as endogenous control and the results were analyzed for relative quantitation among groups using the comparative 2<sup>-ΔΔCt</sup> method. Values, calculated as fold of increase vs. untreated cells assumed as control (CTR) are the mean ± S.E.M. of three independent experiments, in which each sample was tested in duplicate. \**p* < 0.05, \*\**p* < 0.01, \*\*\**p* < 0.001: statistical significance vs. CTR (one-way ANOVA plus Dunnett's test).



## GSCs #3

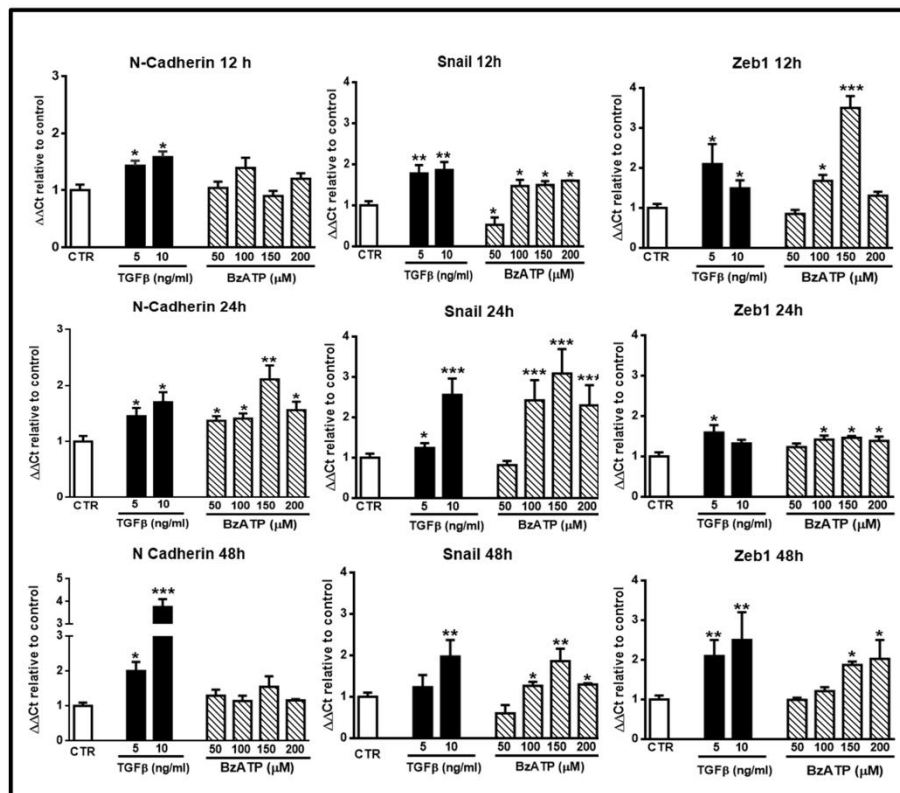
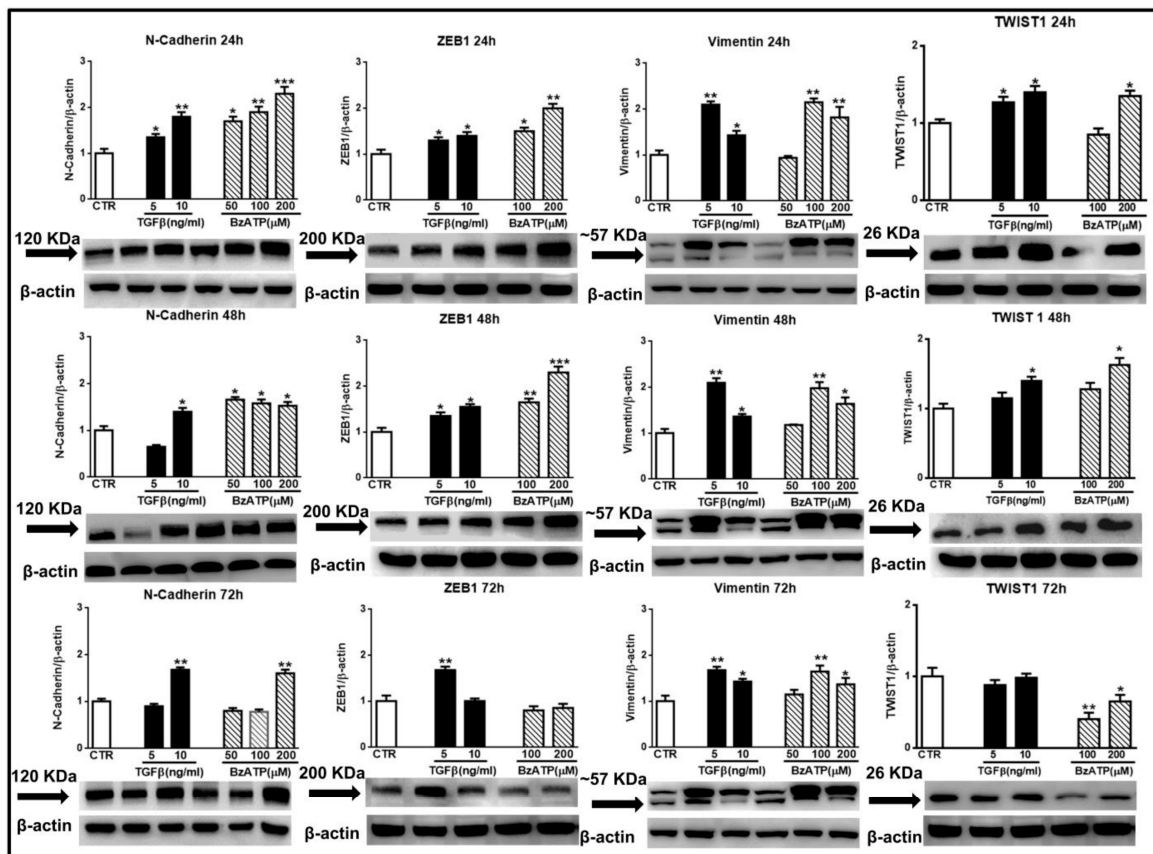


**Figure 3.** Effect of TGFβ1 or BzATP on EMT markers evaluated by qRT-PCR at different times after drug administration to cultured GSCs #3. Similar to what is reported in the legend of the Figure 2, confluent GSCs were exposed to TGFβ1 or BzATP for the indicated times, at the end of which cells were collected and their mRNA was analyzed for the gene expression of EMT markers. mRNA levels were normalized ( $\Delta C_t$ ) by using the house keeping GAPDH as endogenous control and the results were analyzed for relative quantitation among groups using the comparative  $2^{-\Delta\Delta C_t}$  method. Values, calculated as fold of increase vs. untreated cells assumed as control (CTR) are the mean  $\pm$  S.E.M. of three independent experiments in which each sample was tested in duplicate. \* $p < 0.05$ , \*\* $p < 0.01$ , \*\*\* $p < 0.001$ : statistical significance vs. CTR (one-way ANOVA plus Dunnett's test).

These findings were corroborated by those obtained performing western blot analysis to evaluate N-cadherin, ZEB1, vimentin and Twist1 expression at different time periods. As shown in the Figures 4 and 5, related to GSCs #1 and #2, both pharmacological agents were effective. In particular, in GSCs #1, BzATP caused a greater effect on N-cadherin and ZEB1 at 24 and 48 h after drug administration, thus reflecting the timeline of events observed by mRNA analysis. Moreover, the increase of vimentin was evident up to 72 h following cell exposure to TGFβ1 or BzATP whereas that of Twist was limited to the first 24 h. GSCs #2, like GSCs #3 (see data from real time PCR in Figure 3), showed a high responsiveness to BzATP, being the protein content of all EMT markers under investigation significantly increased throughout the 72 h observation period.



GSCs #1

**Figure 4.** Effect of TGFβ1 or BzATP on EMT markers evaluated by western blot analysis at different times after drug administration to cultured GSCs. GSCs #1 were exposed to different concentrations of TGFβ1 or BzATP and harvested at the indicated times. The protein levels of EMT markers were determined by western blot analysis. Over the arrows close to the immune-bands the molecular weight (MW) of each EMT marker is reported according to the MW indicated in the data sheet of the used antibody. To note that for vimentin, which showed a double immune-band, as also reported in literature [35], the molecular weight is equal to about (~) 57 KDa to indicate an average of the weights of the two bands. Immunoblots were re-probed with an antibody against β actin, quantified by densitometric analysis, normalized to β actin used as an internal control, and reported in the histograms assuming the value of control/β-actin = 1. Immunobands in the figure are representative of three independent experiments. Of note, β-actin bands are the same for some blots reported in the figure, since they were obtained by cutting the same membrane at different heights corresponding to the molecular weights of the selected markers. \**p* < 0.05, \*\**p* < 0.01, \*\*\**p* < 0.001: statistical significance vs. untreated GSCs assumed as control (CTR) (one-way ANOVA plus Dunnett’s test).

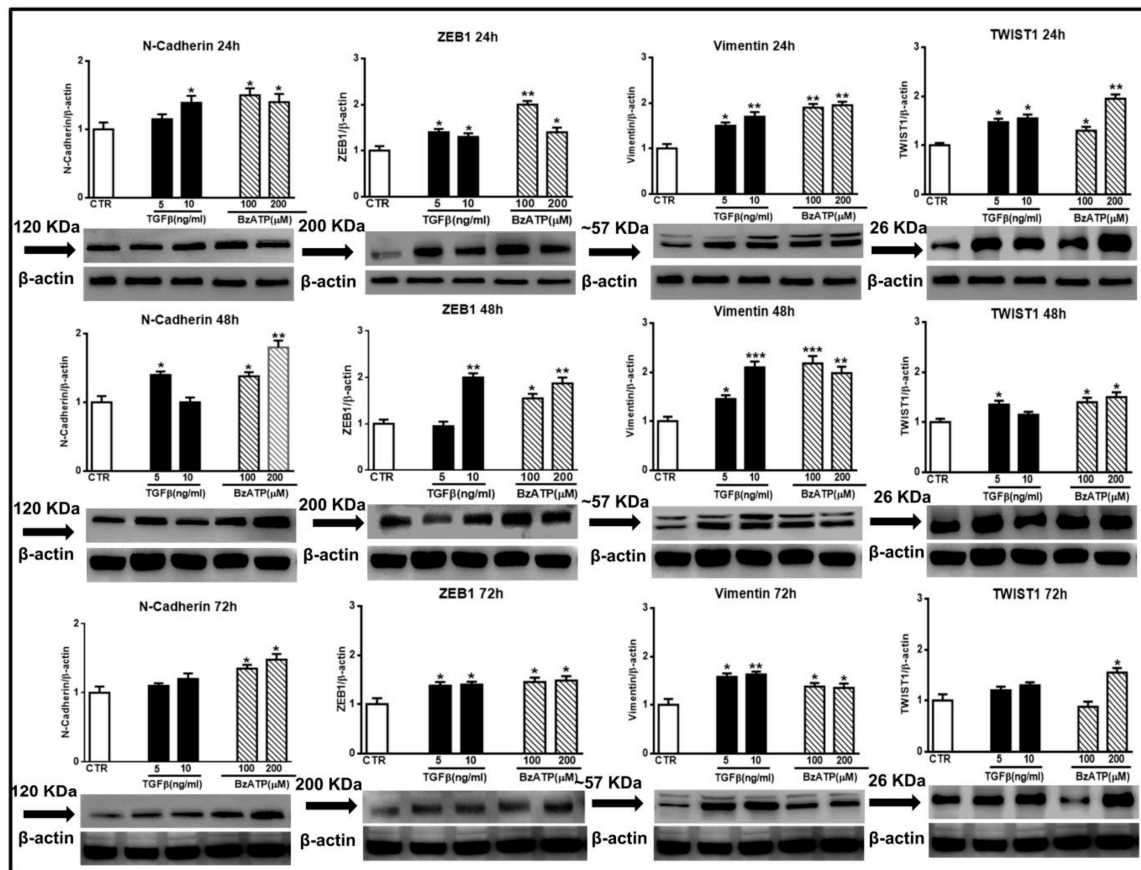


**Figure 5.** Effect of TGFβ1 or BzATP on EMT markers evaluated by western blot analysis at different times after drug administration to cultured GSCs #2. After exposure of the cells to different concentrations of TGFβ1 or BzATP, they were harvested at the indicated time periods. The protein levels of selected EMT markers were determined by western blot analysis. Immunoblots were obtained by exposing membranes to appropriate antibodies, recognizing proteins with different molecular weights (indicated close to the immunobands, over the arrows). Immunoblots were then re-probed with an antibody against β actin and quantified by densitometric analysis, the values of which, normalized to β actin used as an internal control, are reported in the histograms, assuming the value of control/β-actin=1. Immunobands reported in the figure are representative of three independent experiments using the same cells. Also in this case, the bands of β-actin are the same for the blots related to the same time point, as they were obtained by cutting the same membrane at different heights kDa corresponding to the molecular weights of the selected markers. \**p* < 0.05, \*\**p* < 0.01, \*\*\**p* < 0.001: statistical significance vs. untreated GSCs assumed as control (CTR) (one-way ANOVA plus Dunnett’s test).

Cell pre-treatment with the selective P2X7R antagonist A438079 substantially counteracted the effects of BzATP, mainly when this drug was administered at the concentration of 200 μM (Figure 6).

### 3.2. Effect of the Exposure of GSCs to the P2X 7R Agonist, BzATP, or TGFβ1 on Cell Migration and Invasion

We then evaluated the effect of the treatments with TGFβ1 or BzATP on GSC migration and invasion. The scratch assay showed that both TGFβ1 and BzATP shortened wound healing at 6 and 24 h of treatment (Figure 7).

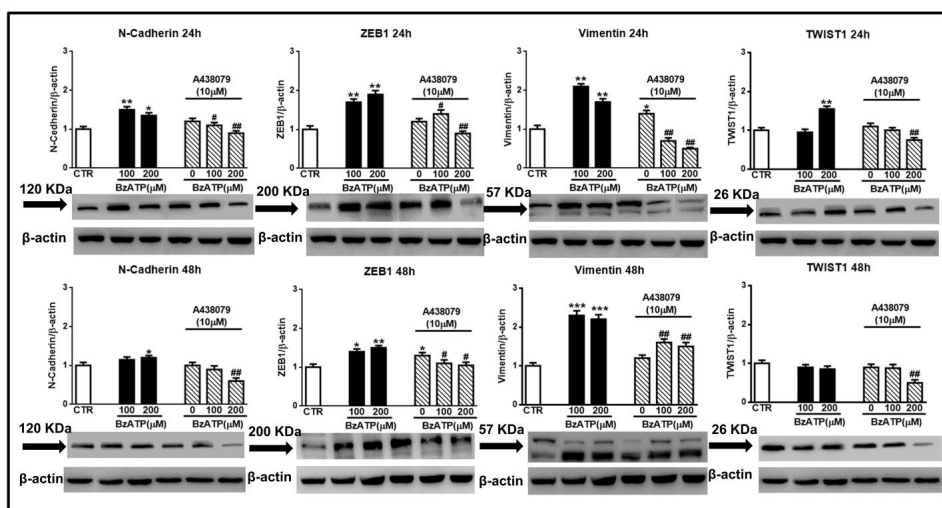


**Figure 6.** Blockade of the BzATP effect on EMT markers by the P2X7R selective antagonist A438079. Confluent GSCs were exposed to different concentrations of BzATP, alone or in the presence of the P2X7R antagonist, A438079 added 1 h before BzATP administration. Immunoblots were re-probed with an antibody against  $\beta$  actin, quantified by densitometric analysis, normalized to  $\beta$  actin used as an internal control, and reported in the histograms assuming the value of control/ $\beta$ -actin=1.  $\beta$ -actin bands are the same for some blots reported in the figure, since they were obtained by cutting the same membrane at different heights corresponding to the molecular weights of the selected markers. Immuno-bands reported in the figure are representative of three independent experiments carried out in GSCs #3. \* $p < 0.05$ , \*\* $p < 0.01$ , \*\*\* $p < 0.001$ : statistical significance vs. untreated GSCs assumed as control (CTR); # $p < 0.05$ , ## $p < 0.01$ , ### $p < 0.001$ : statistical significance vs. GSCs treated with BzATP (one-way ANOVA plus Dunnett’s test).

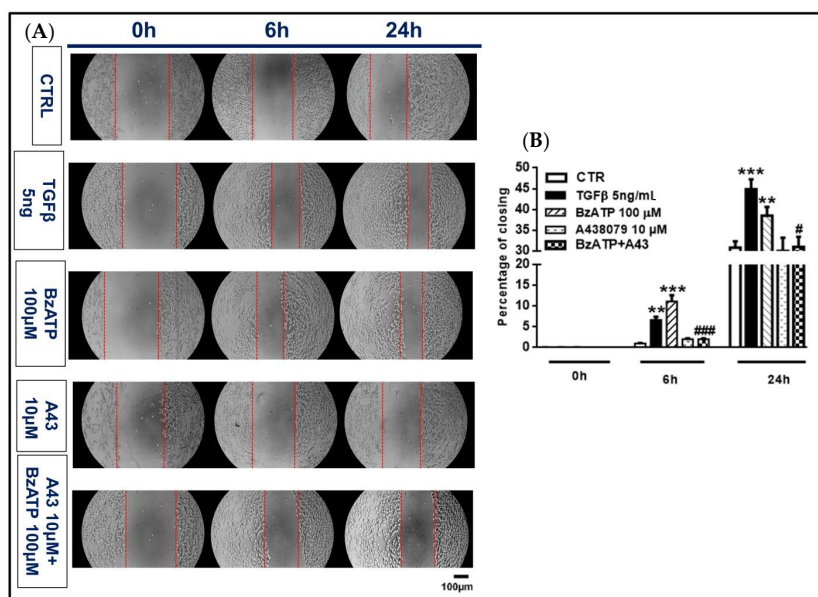


**Figure 7.** Effect of TGF $\beta$ 1 and BzATP on GSC migration evaluated by scratch assay. Nearly confluent GSCs (80%) were incubated in the presence or absence of TGF $\beta$ 1 or BzATP and when present, the P2X7R antagonist A438079 (A43), was added 1 h prior to the agonist. Cells were then scratch wounded and imaged at indicated times after injury. (A) Images of control and treated cells (GSCs #1) prior to (0 h) and 6 and 24 h after injury are representative of four independent experiments (scale bar = 100  $\mu$ m for all panels) carried out for each cell type, giving similar results. (B) Quantification of the wound size was performed using ImageJ and graphed as percentage of wound closure. The values in the histograms are given as means $\pm$  SEM and analyzed by one-way ANOVA and Dunnett’s post hoc test \*\* $p < 0.01$ ; \*\*\* $p < 0.001$  vs. control (CTR); # $p < 0.05$ , ### $p < 0.001$  vs. BzATP. Similar data were obtained using GSCs #2 and #3.

Also, the transwell migration assay used to assess tumor cell invasiveness, demonstrated that both drugs enhanced cell migration through the membranes (Figure 8).

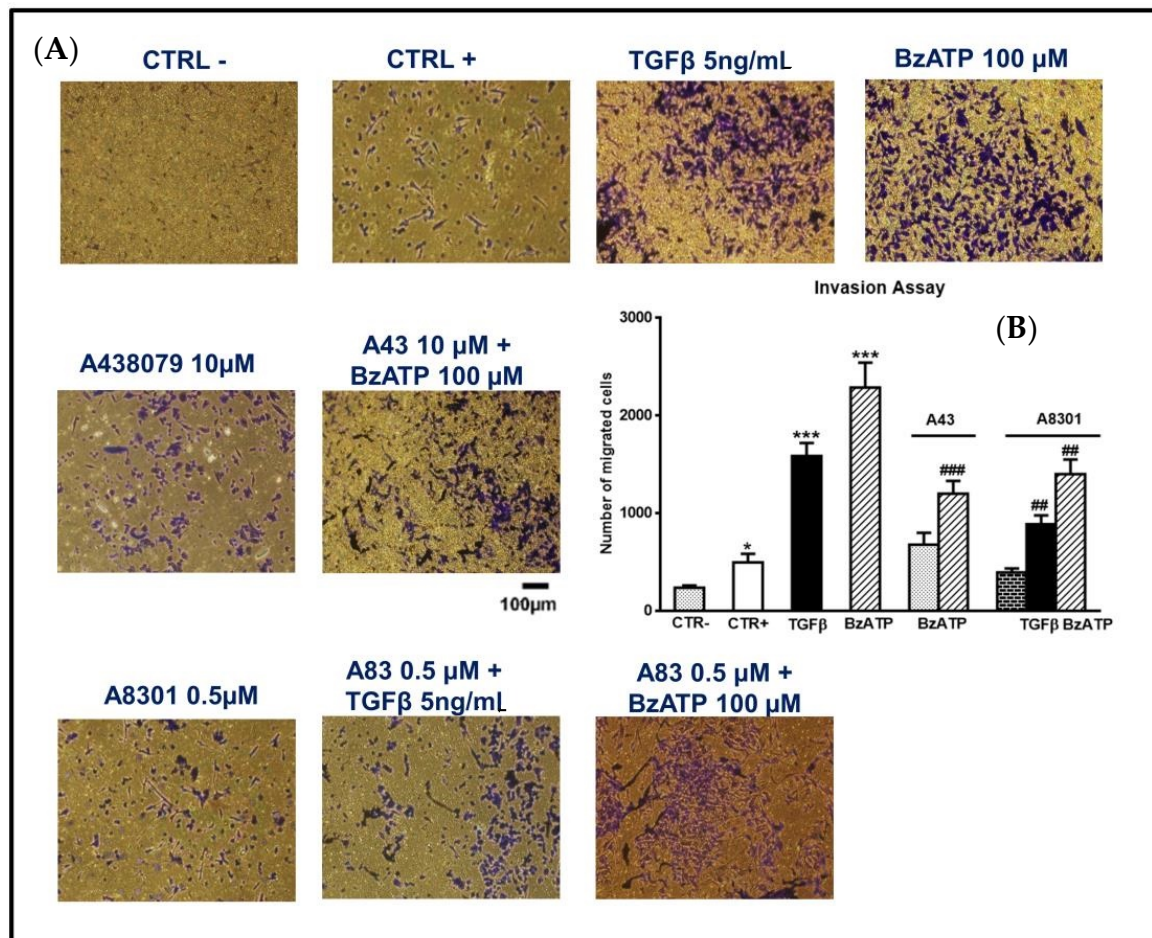


**Figure 8.** Effect of TGFβ1 and BzATP on GSC invasiveness evaluated by transwell migration assay. (A) GSCs, plated in the upper surface of a membrane inserted into a suitable plate, were incubated in the usual culture medium alone (CTR-) or in the presence of TGFβ1 or BzATP. In some experiments cells were pretreated with A438079 (A43), a P2X7R antagonist, or A8301 (A83), inhibitor of TGFβ type I receptors, which were added alone and 1 or 2 h, respectively, prior to the further pharmacological treatments. In another set of cells, a high percentage of serum (10%), usually acting as an attractant for cells, was added to the medium and cells were indicated as CTR+. The cells were allowed to migrate to the lower chamber for 24 h. The membranes were then removed and the cells, fixed and stained using crystal violet, were counted under a light microscope (at an average of five semirandom non-overlapping fields at 10x magnification). The images reported in the figure (scale bar = 100 μm) are related to GSCs #2 and are representative of three independent experiments carried out for each cell type, giving similar results. (B) Accordingly, values in the histograms are the mean ± SEM of these independent experiments and have been analyzed by one-way ANOVA and Dunnett’s post hoc test \**p* < 0.05, \*\*\**p* < 0.001 vs. control (CTR+); ##*p* < 0.01; ###*p* < 0.001 vs. cells treated with TGFβ1 or BzATP.

In both types of experiments, the P2X7R antagonist A438079 abolished the BzATP-induced effect (Figures 7 and 8).

### 3.3. The Activity of BzATP on EMT Markers and GSC Migration is Linked to the Phosphorylation of SMAD2, A Downstream Effector of TGFβ Signaling

As reported in glioma cell lines, TGFβ is an inducer of ZEB1-dependent mesenchymal trans-differentiation coupled to enhancement of their invasion capability. Interestingly, this effect

was mediated by phosphorylation of SMAD2 [36], a protein involved in direct signaling of TGF $\beta$  type I receptors [37]. Since in our GSCs derived from patients' tumor TGF $\beta$  had a behavior similar to that shown in GBM cell lines, i.e., as for ZEB1 and invasion increase, we wondered whether the effects caused by TGF $\beta$  and also by BzATP in our GSCs could be mediated by the same signal transduction pathway. Figure 9 shows that not only TGF $\beta$  but also BzATP, although to a lesser extent, increased SMAD2 phosphorylation. These effects were evident already after 24 h (data not shown), becoming maximal at 48 h. Accordingly, cell pretreatment with A8301, a potent blocker of the TGF $\beta$  type I receptors [36] was effective in inhibiting the TGF $\beta$ - and BzATP-induced increase in SMAD2 phosphorylation as well as the activity of both drugs on ZEB1 and vimentin expression (Figure 9) and GSC invasiveness (Figure 8).

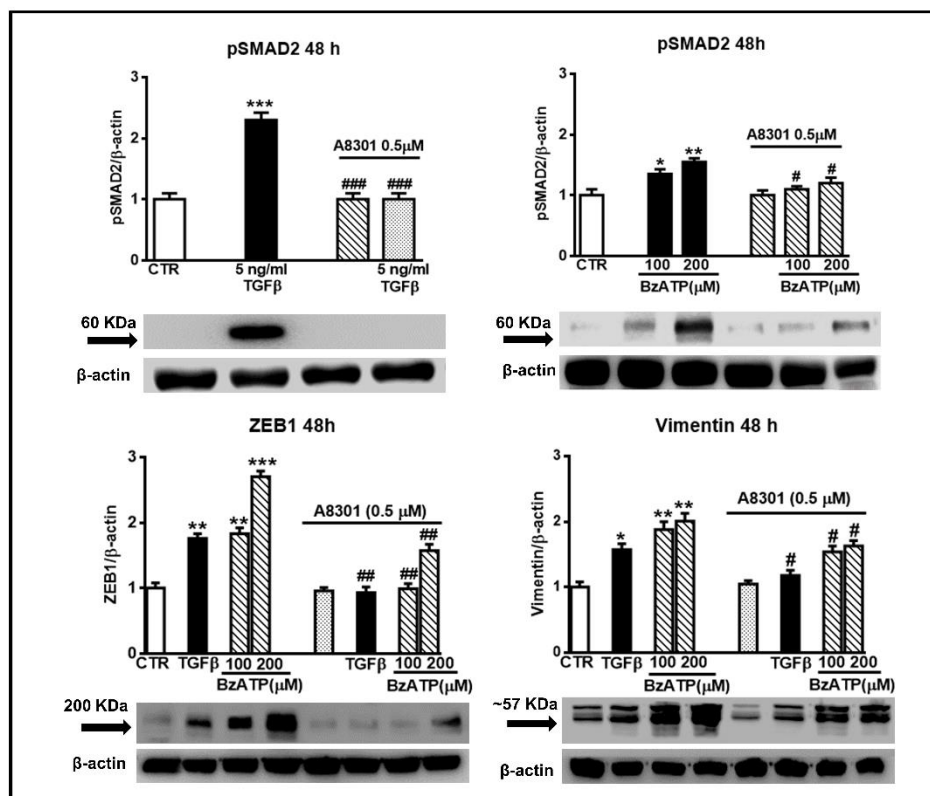


**Figure 9.** Increase in SMAD2 phosphorylation is involved in the effects promoted by either TGF $\beta$  or BzATP on EMT markers. GSCs were exposed to TGF $\beta$ 1 or BzATP at the indicated concentrations. In some experiments, cells were pretreated with A8301, inhibitor of TGF $\beta$  type I receptors, which was added alone or 2 h prior to the other two drugs. After 48 h, cells were harvested and the protein levels of phosphorylated SMAD2 (pSMAD2) and some EMT markers were determined by western blot analysis. As for pSMAD2, different aliquots of proteins, derived from TGF $\beta$  or BzATP treated cells (60 or 80  $\mu$ g, respectively), were used for the electrophoretic run, to make more evident the BzATP effect. Immunoblots were obtained by exposing membranes to the appropriate antibodies. Then, they were reprobbed with an antibody against  $\beta$  actin and quantified by densitometric analysis, the values of which, normalized to  $\beta$  actin used as an internal control, are reported in the histograms, assuming the value of control/ $\beta$ -actin = 1. Immunoblots in the figure are related to GSCs #2 and are representative of three independent experiments carried out for each cell type giving similar results. \* $p$  < 0.05, \*\* $p$  < 0.01, \*\*\* $p$  < 0.001: statistical significance vs. untreated GSCs assumed as control (CTR) (one-way ANOVA plus Dunnett's test); # $p$  < 0.05; ## $p$  < 0.01; ### $p$  < 0.001 vs. cells treated with TGF $\beta$ 1 or BzATP.

### 3.4. Influence of BzATP on GSC Viability

Finally, by MTS assay we found that cell exposure to BzATP at the chosen concentrations did not affect cell viability after 48 h, while modestly reducing it at 96 h, but only when used at 200  $\mu\text{M}$  (Figure 10A). However, the evaluation of LDH and caspase 3/7 activity in the GSC culture medium, assumed as signals of necrotic and apoptotic death, respectively, showed that BzATP reduced the activity of the caspases without influencing that of LDH (Figure 10B,C). The effect of BzATP was once again counteracted by cell pre-treatment with the P2X7R antagonist that, when administered alone, increased LDH and caspases activity 96 h after its addition to the cells.

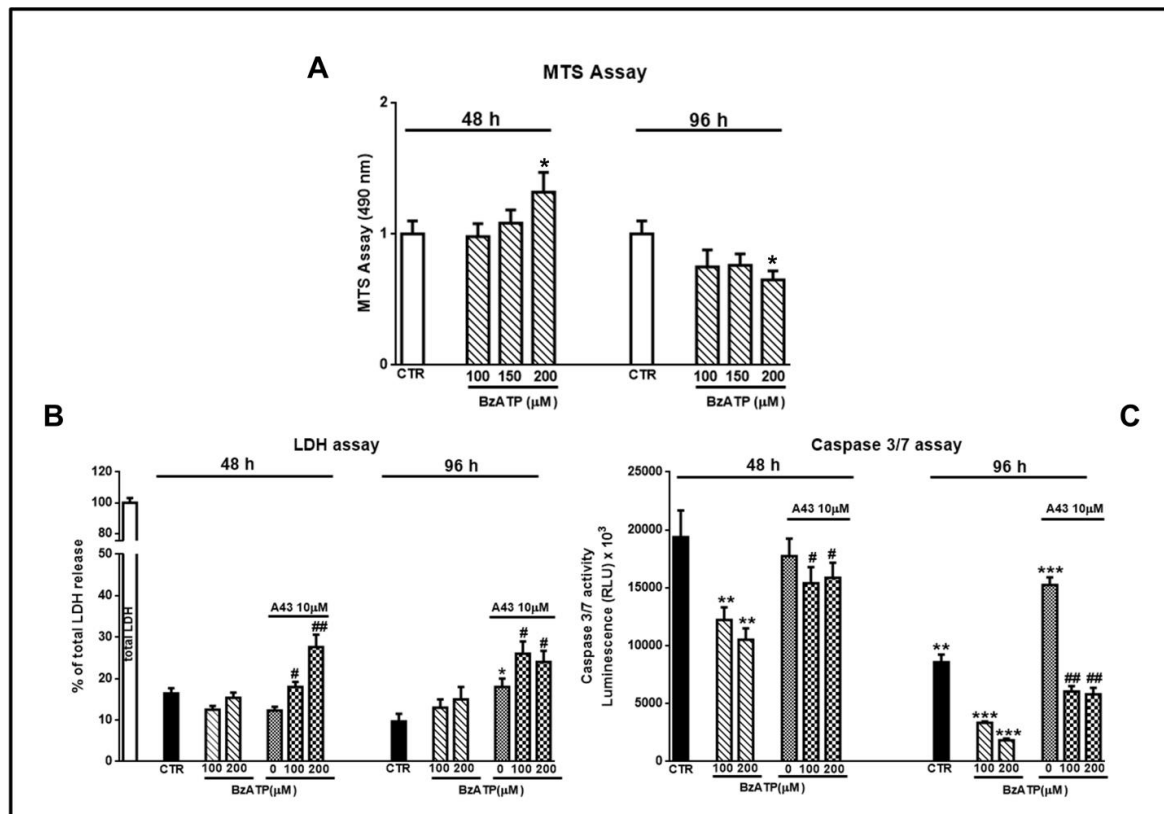


**Figure 10.** Evaluation of cell viability and of necrotic or apoptotic death induced by GSC exposure to BzATP. GSCs were treated with BzATP and in some experiments they were pretreated with the P2X7 receptor (P2X7R) antagonist A438079, administered 1 h prior to the agonist. After different times from the beginning of the pharmacological treatments cell viability (A), cell necrosis or apoptosis (B,C) respectively were assayed. (A) Cell medium was removed at the end of each time period and 3-[4,5-dimethylthiazol-2-yl]-5-[3-carboxymethoxy phenyl]-2-[4-sulfophenyl]-2H-tetrazolium (MTS) assay was performed. The values obtained by optical density at 490 nm for each sample are reported in the histograms, assuming the value of control = 1. (B) LDH release from cells, assumed as an index of necrotic death, was measured as reported in the Methods section. Values are expressed as the percentage of the total amount of the enzyme released in the medium from the cells after their lysis. (C) Apoptotic death was assessed by the evaluation of the release of caspase 3 and 7, the most involved in this process, by luminescence using a commercial kit and following the manufacturer’s instruction. All values in the histograms are related to GSCs #3, but similar findings were obtained using cells #1 or #2. They are expressed as the mean  $\pm$  S.E.M. of four independent experiments in which each sample was tested in triplicate. \* $p < 0.05$ , \*\* $p < 0.01$ , \*\*\* $p < 0.001$ : statistical significance vs. untreated cells; # $p < 0.05$ , ## $p < 0.01$ : statistical significance vs. cells treated with BzATP (one-way ANOVA plus Dunnett’s test).

3.5. Expression of the Splice Variants P2X7A and P2X7B in GSCs in Basal Conditions and after Exposure to BzATP

Based on the evidence previously reported about the high expression levels of P2X7R in GSCs [24], we wanted to better define the role played by this receptor in GSCs by examining the expression of the P2X7AR and P2X7BR splice variants, which could influence GSC aggressiveness in different ways. By real time PCR and western blot analysis, we observed that both P2X7R isoforms are present in GSCs (Figure 11) and that the expression of the subunits of the full length P2X7AR and of the shorter P2X7BR was nearly constant during 48 h (Figure 11A). Similar results were obtained by western blot analysis (Figure 11B).

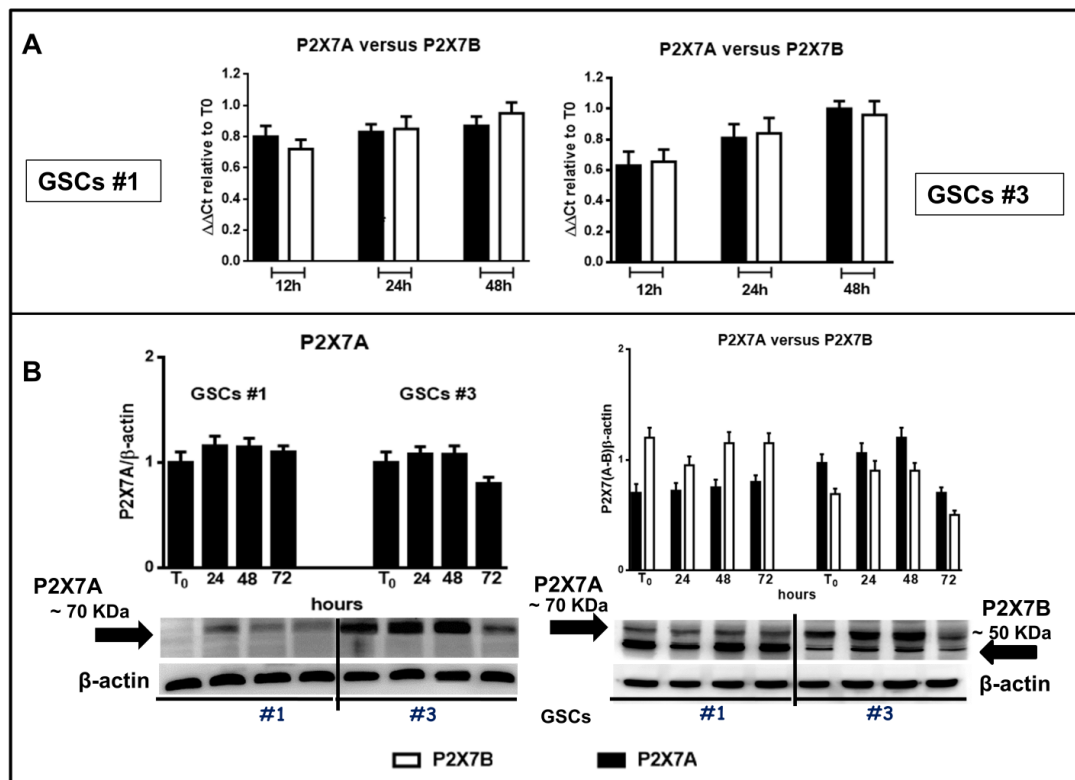


**Figure 11.** Expression of the two main human splice variants P2X7R A and B in GSCs. Confluent GSCs were harvested at different time periods to obtain their mRNA or proteins. (A) by qRT-PCR the evaluation of the mRNA levels was performed in relation to the principal P2X7R splice variants in humans that are the full-length form P2X7A and the truncated form (lacking the carboxy-terminal tail) P2X7B in GSCs #1 and #3 (panels on left or right, respectively). mRNA levels were normalized by using the house keeping  $\beta$ 2-microglobulin as endogenous control. Values, calculated as fold of increase vs. those measured in cells at the beginning of the experiments (time 0) are the mean  $\pm$  S.E.M. of 3 independent experiments performed using the cells above mentioned. Each sample was tested in duplicate. (B) protein levels of P2X7A and P2X7B monomers were determined by western blot analysis. Immunoblots were obtained by exposing membranes to two polyclonal antibodies, one recognizing among the others proteins at about 70 KDa and the second one recognizing proteins at about 70 and 50 KDa, respectively. Subsequently, immunoblots were re-probed with an antibody against  $\beta$  actin, to verify equal sample loading, and quantified by densitometric analysis. These values were then normalized to  $\beta$  actin and reported as such as for the histograms related to blots in which both P2X7R A and B subunits were recognized, whereas for the blots related to the only P2X7AR subunit the value were calculated assuming the ratio (cells at T<sub>0</sub>)/ $\beta$ -actin = 1. All values are the mean  $\pm$  SEM of three independent experiments for each cell type.



In order to assess this aspect, we used two different antibodies, one directed against an extracellular loop common to both subunits forming the splice variants P2X7AR or P2X7BR, and another one directed towards the C-terminal tail, present only in the P2X7AR variant. This second antibody, more specific towards the P2X7AR subunit, was used to confirm data obtained with the first one. However, both antibodies are polyclonal; therefore, they identified more than one immune-band. Among them, both antibodies recognized a band at about 70 KDa, likely corresponding to the calculated molecular weight of the P2X7AR subunit, whereas the antibody against the extracellular loop also recognized, among the others, a protein at about 50 KDa, compatible with the molecular weight of the shorter splice variant P2X7BR (Figure 11B). Thus, western blot analysis would confirm the presence of proteins related to the two splice variants A and B of the P2X7R in the examined cells.

Interestingly, cell exposure to BzATP induced an increased expression of mRNA for both splice variants, despite some differences. In GSCs #1, the expression of both isoforms was significantly increased even though that of the splice variant P2X7B was mainly evident at 24 h from drug treatment (Figure 12).

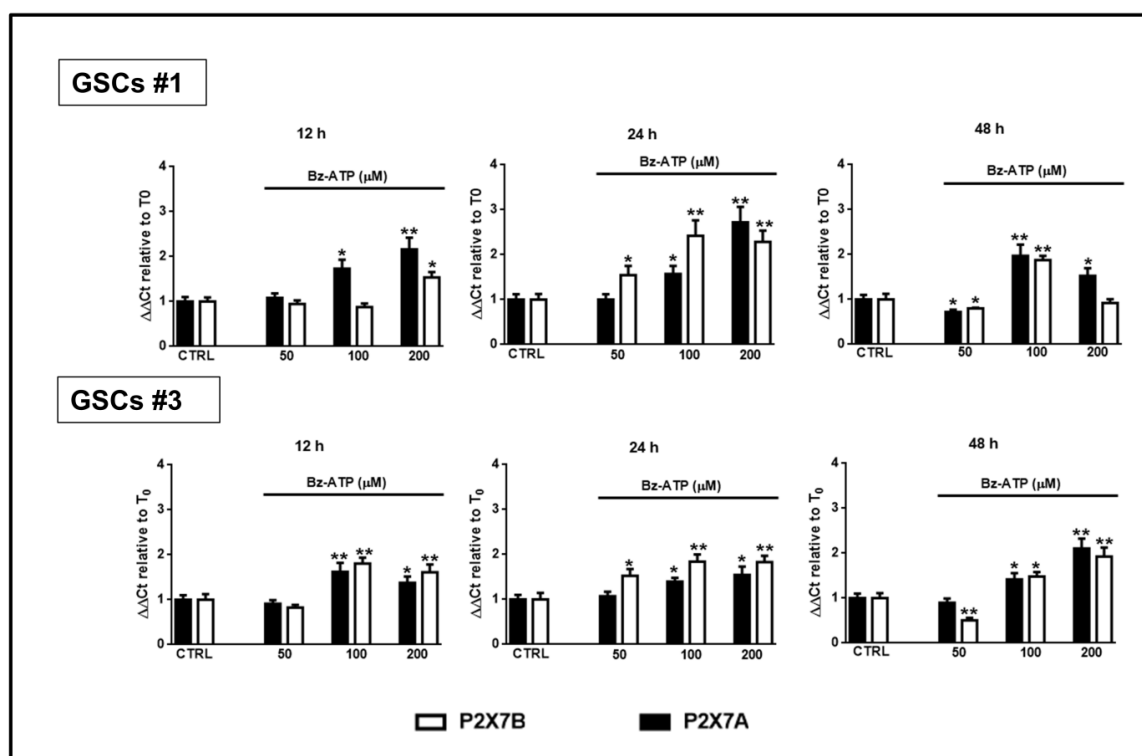


**Figure 12.** Modulation of the expression of the P2X7R splice variants A and B in GSCs exposed to BzATP. GSCs #1 and #3 were exposed to BzATP. At the indicated time points cells were collected to obtain their mRNA that was analyzed for the gene expression of the two splice variants P2X7R A and B. mRNA levels were normalized by using the house keeping  $\beta 2$ -microglobulin as endogenous control. Values, calculated as fold of increase vs. untreated cells (CTR assumed as = 1), are the mean  $\pm$  S.E.M. of three independent experiments in which each sample was tested in duplicate. \* $p < 0.05$ , \*\* $p < 0.01$ : statistical significance vs. untreated cells (one-way ANOVA plus Dunnett's test).

In GSCs #3, the BzATP-induced up-regulation was similar for both P2X7R subunits along the entire observation period. However, these differences were nullified when the expression of the two splice variants was evaluated in terms of protein content. Indeed, BzATP showed a similar effect in GSCs #1 and #3 up to 72 h (Figures 13 and 14).

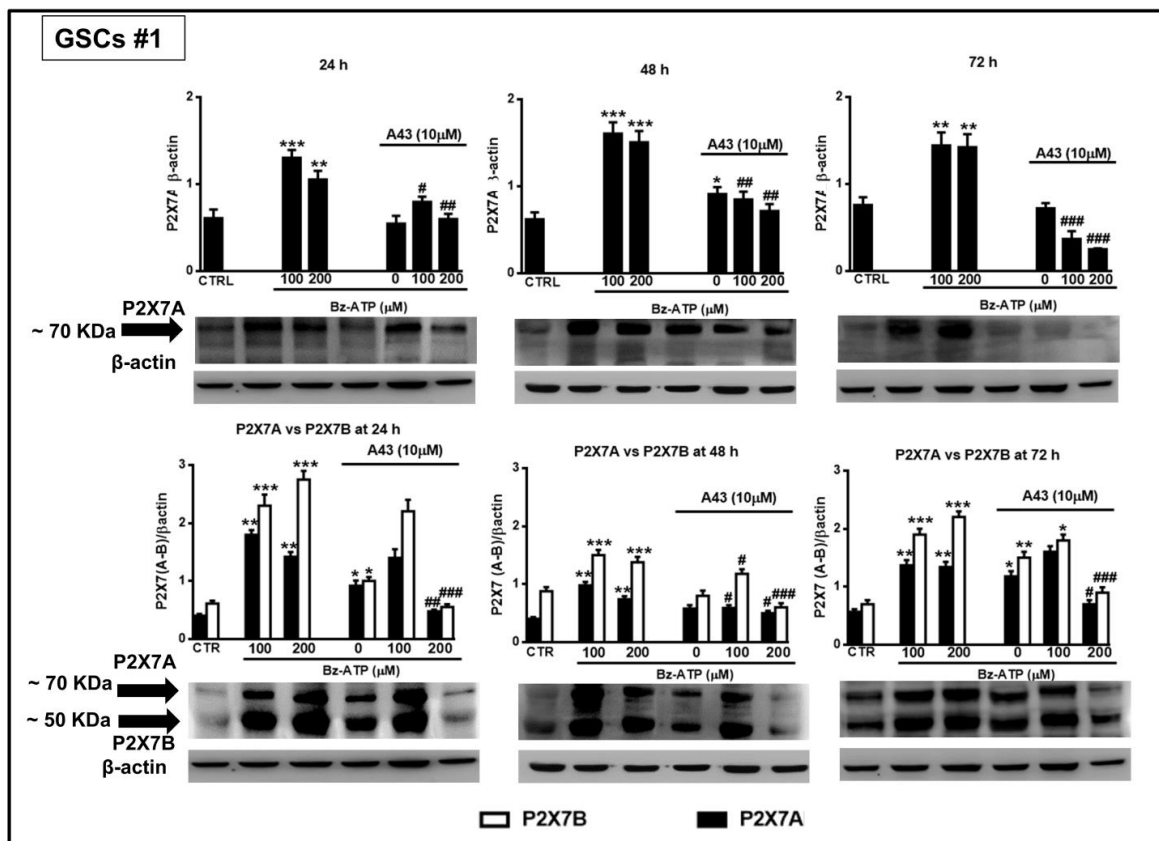


**Figure 13.** Modulation of the protein levels related to the P2X7R splice variants A and B in GSCs #1 exposed to BzATP. GSCs #1, cultured up to their confluence in vitro, were harvested at different time points after their exposure to BzATP and/or A438079. Protein levels of P2X7A and P2X7B isoforms were determined by western blot analysis. Immunoblots were obtained by exposing membranes to two antibodies, one recognizing only proteins at about 70 KDa and the second one recognizing proteins at about 70 and 50 KDa, respectively. Immunoblots were then re-probed with an antibody against β actin and quantified by densitometric analysis, the values of which, normalized to β actin used as an internal control, are reported in the histograms. The band of β-actin is the same for the blots at each time period, as the same membrane was first incubated with one antibody and then, after stripping, with the other antibody against the P2X7RA or B subunits. Densitometric values are the mean ± SEM of three independent experiments with very similar results. \**p* < 0.05, \*\**p* < 0.01, \*\*\**p* < 0.001: statistical significance vs. untreated cells (CTR); #*p* < 0.05, ##*p* < 0.01, ###*p* < 0.001: statistical significance vs. cells treated with BzATP (one-way ANOVA plus Dunnett’s test).

Cell pretreatment with the P2X7R antagonist, A438079, counteracted the effects induced by BzATP on the two receptor subunits, especially when it was administered at 200 μM (Figures 13 and 14).

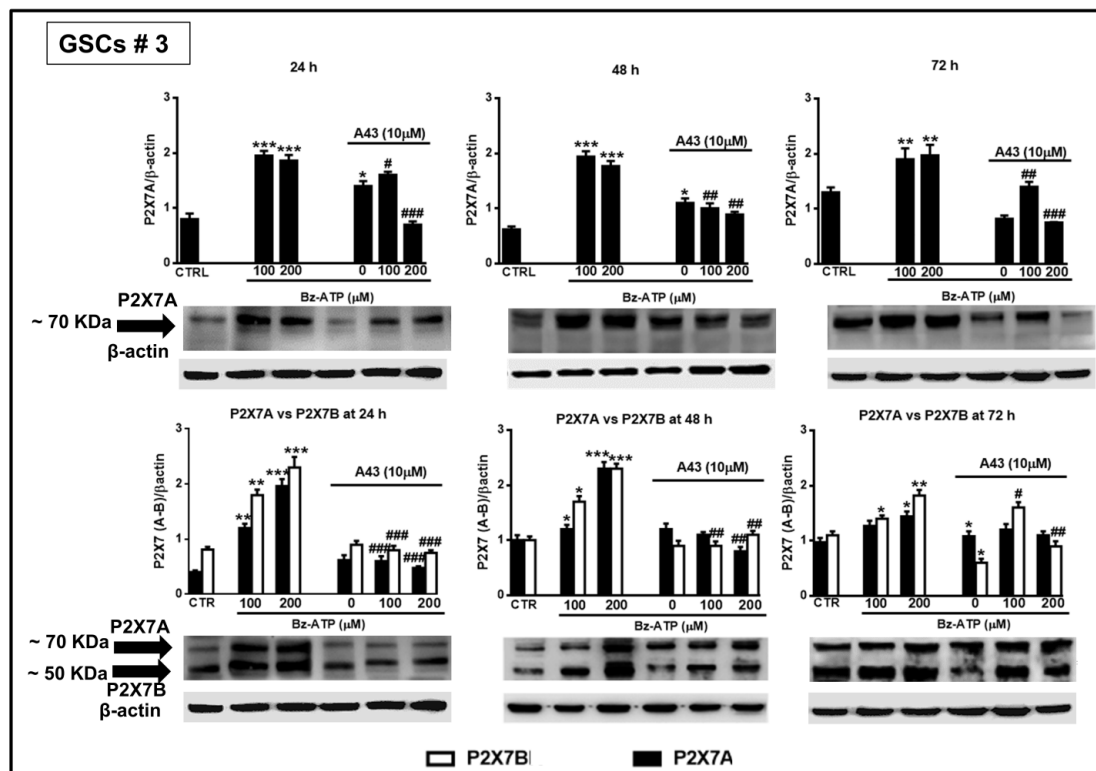


**Figure 14.** Modulation of the protein levels related to the P2X7R splice variants A and B in GSCs #3 exposed to BzATP. GSCs #3, cultured up to their confluence in vitro, were harvested at different time points following their exposure to BzATP and/or A438079. Protein levels of P2X7A and P2X7B splice variants were determined by western blot analysis as reported in the legend of the Figure 13. Immunoblots were re-probed with an antibody against β actin, quantified by densitometric analysis, normalized to β actin used as an internal control, and reported in the histograms. Densitometric values are the mean ± SEM of three independent experiments with very similar results. \**p* < 0.05, \*\**p* < 0.01, \*\*\**p* < 0.001: statistical significance vs. untreated cells (CTR); #*p* < 0.05, ##*p* < 0.01, ###*p* < 0.001: statistical significance vs. cells treated with BzATP (one-way ANOVA plus Dunnett’s test).

#### 4. Discussion

EMT is a complex process that, besides playing a crucial role during normal embryogenesis [38], has also been associated with the progression of many types of cancer [39]. As for GBM, it is also called epithelial-to-mesenchymal(-like) transition or glial-to-mesenchymal transition (GMT) [40,41], to underline that GBM is a non-epithelial derived tumor. However, a number of reports reported GMT as equivalent to EMT and showed its appearance as linked to GBM recurrence [7,42]. Since GSCs are regarded as cells triggering/supporting GBM malignancy, in this study we examined whether the modulation of EMT process in these cells might modify their aggressiveness. To note, we performed our experiments in the same cells used in a previous paper [24], derived from GBM of three different patients. Since these cells are not “cell lines”, we observed some differences in the onset and extent of drug effects, which, however, did not affect the overall validity of the results obtained, as discussed below.

EMT may be activated by different stimuli and, among them, we focused on purines, in particular ATP, being the environment around tumor cells, and in particular GBM, highly rich in ATP (few hundreds μmol/L) (reviewed by [23,24]). This is partially due to the low activity of enzymes metabolizing adenine nucleotides triphosphates in tumors compared to healthy tissues, as well as to the increased release of intracellular purines following cell death. Therefore, such high ATP concentration coupled to a longer permanence of the nucleotide at extracellular level is sufficient to activate P2X7R in glioma and, more in general, in brain tumors [43]. Thereby, it is not surprising that, using exogenous ATP at a relatively high

concentration (300  $\mu$ M) to stimulate GSC cultures, the expression levels of some key EMT markers related to GBM malignancy were enhanced, whereas cell pretreatment with a P2X7R antagonist reduced them.

Based on these findings, we better investigated the effect of the activation of these receptors on the same EMT markers. Indeed, their expression increased from 12–24 up to 48–72 h following GSCs exposure to the P2X7R agonist, BzATP, as well as to TGF $\beta$ 1, a well-known inducer of EMT in GBM [7,36]. However, mRNA analysis of the EMT markers showed some differences among the examined cells, which probably correlates with a different cell efficiency/rate of DNA transcription into mRNA in response to pharmacological stimulation. In contrast, the mRNA translation into the corresponding proteins resulted in a more constant response of the cells to the investigated drugs (TGF $\beta$ 1 and BzATP). Thus, our data confirm the need to look also to the proteins codified by the corresponding mRNAs, which may more reliably account for drug effects.

We also observed that both BzATP and TGF $\beta$ 1 increased the GSC migration and invasion ability *in vitro*, which were tested after 24 h upon drug administration. Since mRNA or protein levels for most EMT markers analyzed were increased by the two drugs starting from the first 12–24 h, it is conceivable that also cell migration and invasion were significantly enhanced during the same period, even though data here not reported (personal observation) showed that the effect of the two drugs on cells invasion was evident even after 48 h following their administration.

All these findings are consistent with literature, except data related to N-cadherin, which should not increase in GBM or, if increased, could restrain cell migration [17]. However, based on the controversy existing on the importance in the N-cadherin level change in GBM, the observed increase of this protein could be irrelevant for GSC invasiveness, which paralleled the general raise of other EMT markers induced by the pharmacological treatments reported here.

Collectively, our data demonstrate an involvement of P2X7R in directing GSCs towards EMT and enhancing/potentiating their aggressiveness, even though we cannot rule out the participation of other P2R. Indeed, GSC pre-treatment with A438079, a drug considered as one of the most selective P2X7R antagonists, completely counteracted or partially reduced the effect induced by 200 or 100  $\mu$ M BzATP, respectively. These findings may be explained by the “partial” selectivity of BzATP towards P2X7R, being this agent able to stimulate also other ATP P2R at lower concentrations than those stimulating P2X7R [44]. Consequently, we cannot exclude that other members of the P2R family could contribute to increase EMT markers expression and GSC invasiveness. Given the growing roles potentially played by P2X7R not only in tumor development/growth, but also in many other physiological and pathological conditions, we believe as extremely important that selective agonists for P2X7R have to be delivered in commerce as soon as possible.

We also explored a putative signaling pathway, which can be activated following P2X7R stimulation by BzATP. Based on the analogy of BzATP and TGF $\beta$  behavior in relation to EMT markers and GSC mobility/invasiveness, we checked whether they shared a common signal transduction pathway. Our results demonstrated that both agents, although to a different extent, increased the SMAD2 phosphorylation. Additionally, this effect was inhibited by cell pretreatment with an inhibitor of TGF $\beta$  type I receptors [36]. The same inhibitor also abrogated BzATP-induced increase in EMT markers and GSC invasion. Noteworthy, our results suggest that BzATP might favor the release of TGF $\beta$  from GSCs, which in turn would concur to increase their aggressiveness. Clearly, we cannot exclude the involvement of other molecular mechanisms more directly promoted by P2X7R activation, which need further investigation.

Here, we demonstrated that, in GSCs, high expression of P2X7R is coupled to the presence of the two main splice variants in humans, which are the full length P2X7AR and the truncated isoform named P2X7BR, lacking the C-terminal 249 amino acids but provided with 18 extra amino acids after the residue 346. More importantly, the expression of both splice variants was increased in GSCs following their treatment with BzATP. While the receptor assembled with P2X7A monomers shows both ion channel and pore activity, the one deriving from P2X7B monomer assembly lacks pore function [27]. However, this may represent an over-simplification of the P2X7R molecular structure. Indeed, it has also been reported that the co-expression of P2X7A with P2X7B splice variants may result in the

formation of a functional P2X7A-B heterotrimeric receptor that exhibits: i) An enhanced pore activity or ii) a higher affinity for ATP than a homotrimeric P2X7R and an increased support to cell energy and metabolism [25]. These conflicting results can be reconciled by a unifying explanation about the effects consequent to homo- or hetero-trimeric P2X7R activation, according to which the overstimulation of these receptors by high micromolar or millimolar ATP concentrations causes cell death, whereas tonic P2X7R stimulation at lower ATP concentrations favors cell survival/growth [21,23]. Consistently with this explanation, we previously found that ATP or BzATP administered at high concentrations and for two consecutive days caused GSC death. In contrast, in this paper we revealed that BzATP, administered only once at lower concentrations (100 and 200  $\mu\text{M}$ ), protected GSCs from apoptosis and did not induce necrosis. Thereby, it is not surprising that the P2X7R antagonist, when administered alone to the cells, increased LDH and caspase activity whereas, when co-administered with BzATP, reduced the protective effects of this agent against necrotic or apoptotic GSC death. On the other hand, the decrease in cell viability reported at 96 h after cell exposure to the highest BzATP concentration (200  $\mu\text{M}$ ) should not be due to cell death, but rather to an arrest in S phase of the cell cycle, as we previously demonstrated for the same cells following exposure with higher BzATP concentration (500  $\mu\text{M}$ ). Finally, the up-regulated expression of both P2X7R A and B variants induced by BzATP might also favor the increase in EMT marker expression and GSC invasiveness, provided that relatively low P2X7R agonist concentrations are used.

In conclusion, the effects induced in human GSCs by a “moderate” P2X7R stimulation could enhance GBM aggressiveness, even though the occurrence of these effects needs to be verified *in vivo*. If ascertained, it would follow that the GBM growth could be restrained by inhibiting P2X7R, as observed in other tumors [45]. Clearly, we are aware that GBM progression depends on multiple factors and that the expression of P2X7R might be different in tumor core or periphery, as observed for pancreatic tumor [46], or present also in peri-tumor cells, such as resident microglia or infiltrating macrophages, which may support tumor growth by releasing P2X7R-dependent factors [47]. Thus, further research needs to define this complex scenario and the role of P2X7R therein, in order to advantageously apply the pharmacological modulation of P2X7R expression/activity in GBM therapeutic management.

**Author Contributions:** S.Z., M.Z., M.C., and P.G. performed experiments. P.D.I. and F.C., contributed to data analyses. R.C. supervised the experiments and together with L.R.-V. and R.P. drafted the manuscript. All authors read and approved the final manuscript. All authors have read and agreed to the published version of the manuscript.

**Funding:** This research was in part funded by the University of Chieti-Pescara, grant number AT2018 to RC and PDI.

**Acknowledgments:** This work was supported by funds for research to RC and PDI from the University of Chieti-Pescara.

**Conflicts of Interest:** The authors declare no conflict of interest.

## Abbreviations

A438079, 3-[[5-[2,3-Dichlorophenyl]-1H-tetrazol-1-yl]methyl]pyridine hydrochloride;  
 A8301, 3-[6-methyl-2-pyridinyl]-N-phenyl-4-[4-quinolinyl]-1H-pyrazole-1-carbothioamide;  
 Bz-ATP, 2' [3']-O-[4-benzoylbenzoyl]-ATP;  
 EMT, epithelial-to-mesenchymal transition;  
 GBM, glioblastoma multiforme;  
 GMT, glial-to-mesenchymal transition;  
 GSCs, glioblastoma-derived stem cells;  
 MTS, 3-[4,5-dimethylthiazol-2-yl]-5-[3-carboxymethoxy phenyl]-2-[4-sulfophenyl]-2H-tetrazolium; P2R, P2 receptors;  
 P2X7R, P2X7 receptors;  
 P2X7AR and P2X7BR, P2X7A and P2X7B receptors;  
 qRT-PCR, quantitative real time polymerase chain reaction;  
 Snail1, snail family transcriptional repressor 1;  
 TGF $\beta$ 1, transforming growth factor  $\beta$ 1;  
 ZEB1, zinc finger E-box binding homeobox1.

## References

1. Szopa, W.; Burley, T.A.; Kramer-Marek, G.; Kaspera, W. Diagnostic and Therapeutic Biomarkers in Glioblastoma: Current Status and Future Perspectives. *BioMed Res. Int.* **2017**, *2017*, 8013575. [CrossRef] [PubMed]
2. Nakano, I. Stem cell signature in glioblastoma: Therapeutic development for a moving target. *J. Neurosurg.* **2015**, *122*, 324–330. [CrossRef] [PubMed]
3. Li, A.; Walling, J.; Kotliarov, Y.; Center, A.; Steed, M.E.; Ahn, S.J.; Rosenblum, M.; Mikkelsen, T.; Zenklusen, J.C.; Fine, H.A. Genomic changes and gene expression profiles reveal that established glioma cell lines are poorly representative of primary human gliomas. *Mol. Cancer Res.* **2008**, *6*, 21–30. [CrossRef] [PubMed]
4. Lee, J.; Kotliarova, S.; Kotliarov, Y.; Li, A.; Su, Q.; Donin, N.M.; Pastorino, S.; Purow, B.W.; Christopher, N.; Zhang, W.; et al. Tumor stem cells derived from glioblastomas cultured in bFGF and EGF more closely mirror the phenotype and genotype of primary tumors than do serum-cultured cell lines. *Cancer Cell* **2006**, *9*, 391–403. [CrossRef] [PubMed]
5. Wee, B.; Charles, N.; Holland, E.C. Animal models to study cancer-initiating cells from glioblastoma. *Front. Biosci.* **2011**, *16*, 2243–2258. [CrossRef]
6. Kalluri, R.; Weinberg, R.A. The basics of epithelial-mesenchymal transition. *J. Clin. Investig.* **2009**, *119*, 1420–1428. [CrossRef]
7. Iser, I.C.; Pereira, M.B.; Lenz, G.; Wink, M.R. The epithelial-to-mesenchymal transition-like process in glioblastoma: An update systematic review and in silico investigation. *Med. Res. Rev.* **2017**, *37*, 271–313. [CrossRef]
8. Prokop, J.W.; Liu, Y.; Milsted, A.; Peng, H.; Rauscher, F.J., 3rd. A method for in silico identification of SNAIL/SLUG DNA binding potentials to the E-box sequence using molecular dynamics and evolutionary conserved amino acids. *J. Mol. Model.* **2013**, *19*, 3463–3469. [CrossRef]
9. Liu, Y.; El-Naggar, S.; Darling, D.S.; Higashi, Y.; Dean, D.C. Zeb1 links epithelial-mesenchymal transition and cellular senescence. *Development* **2008**, *135*, 579–588. [CrossRef]
10. Sanchez-Tillo, E.; Siles, L.; de Barrios, O.; Cuatrecasas, M.; Vaquero, E.C.; Castells, A.; Postigo, A. Expanding roles of ZEB factors in tumorigenesis and tumor progression. *Am. J. Cancer Res.* **2011**, *1*, 897–912.
11. Sanchez-Tillo, E.; Liu, Y.; de Barrios, O.; Siles, L.; Fanlo, L.; Cuatrecasas, M.; Darling, D.S.; Dean, D.C.; Castells, A.; Postigo, A. EMT-activating transcription factors in cancer: Beyond EMT and tumor invasiveness. *Cell. Mol. Life Sci.* **2012**, *69*, 3429–3456. [CrossRef] [PubMed]
12. Danielsson, F.; Peterson, M.K.; Caldeira Araújo, H.; Lautenschläger, F.; Gad, A.K.B. Vimentin Diversity in Health and Disease. *Cells* **2018**, *7*, E147. [CrossRef] [PubMed]
13. Han, S.P.; Kim, J.H.; Han, M.E.; Sim, H.E.; Kim, K.S.; Yoon, S.; Baek, S.Y.; Kim, B.S.; Oh, S.O. SNAI1 is involved in the proliferation and migration of glioblastoma cells. *Cell. Mol. Neurobiol.* **2011**, *31*, 489–496. [CrossRef] [PubMed]
14. Myung, J.K.; Choi, S.A.; Kim, S.K.; Wang, K.C.; Park, S.H. Snail plays an oncogenic role in glioblastoma by promoting epithelial mesenchymal transition. *Int. J. Clin. Exp. Pathol.* **2014**, *7*, 1977–1987.
15. Siebzehnruhl, F.A.; Silver, D.J.; Tugertimur, B.; Deleyrolle, L.P.; Siebzehnruhl, D.; Sarkisian, M.R.; Devers, K.G.; Yachnis, A.T.; Kupper, M.D.; Neal, D.; et al. The ZEB1 pathway links glioblastoma initiation, invasion and chemoresistance. *EMBO Mol. Med.* **2013**, *5*, 1196–1212. [CrossRef]
16. Mikheeva, S.A.; Mikheev, A.M.; Petit, A.; Beyer, R.; Oxford, R.G.; Khorasani, L.; Maxwell, J.P.; Glackin, C.A.; Wakimoto, H.; Gonzalez-Herrero, I.; et al. TWIST1 promotes invasion through mesenchymal change in human glioblastoma. *Mol. Cancer* **2010**, *9*, 194. [CrossRef]
17. Asano, K.; Duntsch, C.D.; Zhou, Q.; Weimar, J.D.; Bordelon, D.; Robertson, J.H.; Pourmotabbed, T. Correlation of N-cadherin expression in high grade gliomas with tissue invasion. *J. Neuro-Oncol.* **2004**, *70*, 3–15. [CrossRef]
18. Satelli, A.; Li, S. Vimentin as a potential molecular target in cancer therapy Or Vimentin, an overview and its potential as a molecular target for cancer therapy. *Cell. Mol. Life Sci.* **2011**, *68*, 3033–3046. [CrossRef]
19. Giuliani, P.; Zuccarini, M.; Carluccio, M.; Ziberi, S.; Di Iorio, P.; Caciagli, F.; Ciccarelli, R. A New Investigational Perspective for Purines Against Glioblastoma Invasiveness. *Curr. Drug Targets* **2018**, *19*, 1871–1881. [CrossRef]
20. Burnstock, G. Physiology and pathophysiology of purinergic neurotransmission. *Physiol. Rev.* **2007**, *87*, 659–797. [CrossRef]

21. Di Virgilio, F.; Sarti, A.C.; Falzoni, S.; De Marchi, E.; Adinolfi, E. Extracellular ATP and P2 purinergic signalling in the tumour microenvironment. *Nat. Rev. Cancer* **2018**, *18*, 601–618. [CrossRef] [PubMed]
22. Uribe, D.; Torres, Á.; Rocha, J.D.; Niechi, I.; Oyarzún, C.; Sobrevia, L.; San Martín, R.; Quezada, C. Multidrug resistance in glioblastoma stem-like cells: Role of the hypoxic microenvironment and adenosine signaling. *Mol. Asp. Med.* **2017**, *55*, 140–151. [CrossRef] [PubMed]
23. Di Virgilio, F.; Adinolfi, E. Extracellular purines, purinergic receptors and tumor growth. *Oncogene* **2017**, *36*, 293–303. [CrossRef] [PubMed]
24. D’Alimonte, I.; Nargi, E.; Zuccarini, M.; Lanuti, P.; Di Iorio, P.; Giuliani, P.; Ricci-Vitiani, L.; Pallini, R.; Caciagli, F.; Ciccarelli, R. Potentiation of temozolomide antitumor effect by purine receptor ligands able to restrain the in vitro growth of human glioblastoma stem cells. *Purinergic Signal.* **2015**, *11*, 331–346. [CrossRef] [PubMed]
25. Di Virgilio, F.; Schmalzing, G.; Markwardt, F. The elusive P2X7 macropore. *Trends Cell Biol.* **2018**, *28*, 392–404. [CrossRef] [PubMed]
26. Ulrich, H.; Ratajczak, M.Z.; Schneider, G.; Adinolfi, E.; Orioli, E.; Ferrazoli, E.G.; Glaser, T.; Corrêa-Velloso, J.; Martins, P.C.M.; Coutinho, F.; et al. Kinin and Purine Signaling Contributes to Neuroblastoma Metastasis. *Front. Pharmacol.* **2018**, *9*, 500. [CrossRef] [PubMed]
27. Adinolfi, E.; Cirillo, M.; Woltersdorf, R.; Falzoni, S.; Chiozzi, P.; Pellegatti, P.; Callegari, M.G.; Sandonà, D.; Markwardt, F.; Schmalzing, G.; et al. Trophic activity of a naturally occurring truncated isoform of the P2X7 receptor. *FASEB J.* **2010**, *24*, 3393–3404. [CrossRef]
28. D’Alessandris, Q.G.; Biffoni, M.; Martini, M.; Runci, D.; Buccarelli, M.; Cenci, T.; Signore, M.; Stancato, L.; Olivi, A.; De Maria, R.; et al. The clinical value of patient-derived glioblastoma tumorspheres in predicting treatment response. *Neuro-Oncol.* **2017**, *19*, 1097–1108. [CrossRef]
29. Marziali, G.; Signore, M.; Buccarelli, M.; Grande, S.; Palma, A.; Biffoni, M.; Rosi, A.; D’Alessandris, Q.G.; Martini, M.; Larocca, L.M.; et al. Metabolic/Proteomic Signature Defines Two Glioblastoma Subtypes With Different Clinical Outcome. *Sci. Rep.* **2016**, *6*, 21557. [CrossRef]
30. Pallini, R.; Ricci-Vitiani, L.; Banna, G.L.; Signore, M.; Lombardi, D.; Todaro, M.; Stassi, G.; Martini, M.; Maira, G.; Larocca, L.M.; et al. Cancer stem cell analysis and clinical outcome in patients with glioblastoma multiforme. *Clin. Cancer Res.* **2008**, *14*, 8205–8212. [CrossRef]
31. Eramo, A.; Ricci-Vitiani, L.; Zeuner, A.; Pallini, R.; Lotti, F.; Sette, G.; Pillozzi, E.; Larocca, L.M.; Peschle, C.; De Maria, R. Chemotherapy resistance of glioblastoma stem cells. *Cell Death Differ.* **2006**, *13*, 1238–1241. [CrossRef] [PubMed]
32. Griffiero, F.; Daga, A.; Marubbi, D.; Capra, M.C.; Melotti, A.; Pattarozzi, A.; Gatti, M.; Bajetto, A.; Barbieri, F.; Favoni, R.E.; et al. Different response of human glioma tumor-initiating cells to Epidermal Growth Factor receptor kinase inhibitors. *J. Biol. Chem.* **2009**, *284*, 7138–7148. [CrossRef] [PubMed]
33. Giuliani, A.L.; Colognesi, D.; Ricco, T.; Roncato, C.; Capece, M.; Amoroso, F.; Wang, Q.G.; De Marchi, E.; Gartland, A.; Di Virgilio, F.; et al. Trophic activity of human P2X7 receptor isoforms A and B in osteosarcoma. *PLoS ONE* **2014**, *9*, e107224. [CrossRef] [PubMed]
34. Livak, K.J.; Schmittgen, T.D. Analysis of relative gene expression data using real-time quantitative PCR and the 2<sup>-11CT</sup> method. *Methods* **2001**, *25*, 402–408. [CrossRef] [PubMed]
35. Zelenko, Z.; Gallagher, E.J.; Tobin-Hess, A.; Belardi, V.; Rostoker, R.; Blank, J.; Dina, Y.; LeRoith, D. Silencing vimentin expression decreases pulmonary metastases in a pre-diabetic mouse model of mammary tumor progression. *Oncogene* **2017**, *36*, 1394–1403. [CrossRef]
36. Joseph, J.V.; Conroy, S.; Tomar, T.; Eggens-Meijer, E.; Bhat, K.; Copray, S.; Walenkamp, A.M.; Boddeke, E.; Balasubramanyian, V.; Wagemakers, M.; et al. TGF- $\beta$  is an inducer of ZEB1-dependent mesenchymal transdifferentiation in glioblastoma that is associated with tumor invasion. *Cell Death Dis.* **2014**, *5*, e1443. [CrossRef]
37. Massagué, J. TGF $\beta$  signaling in context. *Nat. Rev. Mol. Cell Biol.* **2012**, *13*, 616–630. [CrossRef]
38. Greenburg, G.; Hay, E.D. Epithelia suspended in collagen gels can lose polarity and express characteristics of migrating mesenchymal cells. *J. Cell Biol.* **1982**, *95*, 333–339. [CrossRef]
39. Thiery, J.P. Epithelial-mesenchymal transitions in tumor progression. *Nat. Rev. Cancer* **2002**, *2*, 442–454. [CrossRef]

40. Mahabir, R.; Tanino, M.; Elmansuri, A.; Wand, L.; Kimura, T.; Itoh, T.; Hoba, Y.; Nishihara, H.; Shirato, H.; Tsuda, M.; et al. Sustained elevation of Snail promotes glial-mesenchymal transition after irradiation in malignant glioma. *Neuro Oncol.* **2014**, *16*, 671–685. [CrossRef]
41. Kahlert, U.D.; Nikkhaha, G.; Maciaczyk, J. Epithelial-to-mesenchymal(-like) transition as a relevant molecular event in malignant gliomas. *Cancer Lett.* **2013**, *331*, 131–138. [CrossRef]
42. Tso, C.L.; Shintaku, P.; Chen, J.; Liu, Q.; Liu, J.; Chen, Z.; Yoshimoto, K.; Mischel, P.S.; Cloughesy, T.F.; Liao, L.M.; et al. Primary glioblastomas express mesenchymal stem-like properties. *Mol. Cancer Res.* **2006**, *4*, 607–619. [CrossRef]
43. Braganhol, E.; Wink, M.R.; Lenz, G.; Battastini, A.M. Purinergic Signaling in Glioma Progression. *Adv. Exp. Med.* **2013**, *986*, 81–102. [CrossRef]
44. Bianchi, B.R.; Lynch, K.J.; Touma, E.; Niforatos, W.; Burgard, E.C.; Alexander, K.M.H.; Park, S.; Yu, H.; Metzger, R.; Kowaluk, E.; et al. Pharmacological characterization of recombinant human and rat P2X receptor subtypes. *Eur. J. Pharmacol.* **1999**, *376*, 127–138. [CrossRef]
45. Roger, S.; Jelassi, B.; Couillin, I.; Pelegrin, P.; Besson, P.; Jiang, L.H. Understanding the roles of the P2X7 receptor in solid tumor progression and therapeutic perspectives. *Biochim. Biophys. Acta* **2015**, *1848*, 2584–2602. [CrossRef] [PubMed]
46. Giannuzzo, A.; Pedersen, S.F.; Novak, I. The P2X7 receptor regulates cell survival, migration and invasion of pancreatic ductal adenocarcinoma cells. *Mol. Cancer* **2015**, *14*, 203. [CrossRef] [PubMed]
47. McLarnon, J.G. Roles of purinergic P2X(7) receptor in glioma and microglia in brain tumors. *Cancer Lett.* **2017**, *402*, 93–99. [CrossRef]





© 2019 by the authors. Licensee MDPI, Basel, Switzerland. This article is an open access article distributed under the terms and conditions of the Creative Commons Attribution (CC BY) license (<http://creativecommons.org/licenses/by/4.0/>).



Article

# Identification of Astrocytoma Blood Serum Protein Profile

Paulina Vaitkiene <sup>1,\*</sup>, Ruta Urbanaviciute <sup>1</sup>, Povilas Grigas <sup>2</sup>, Giedrius Steponaitis <sup>1</sup>,  
Arimantas Tamasauskas <sup>1</sup> and Daina Skiriute <sup>1</sup>

<sup>1</sup> Laboratory of Molecular Neurooncology, Neuroscience Institute, Lithuanian University of Health Sciences, Eiveniu str. 4, LT50161 Kaunas, Lithuania; ruta.urbanaviciute@lsmuni.lt (R.U.); giedrius.steponaitis@lsmuni.lt (G.S.); arimantas.tamasauskas@lsmuni.lt (A.T.); dainski@gmail.com (D.S.)

<sup>2</sup> Laser Research Centre (VU LRC), Vilnius University, Sauletekio Ave 10, LT10223 Vilnius, Lithuania; pgrigas@gmail.com

\* Correspondence: paulina.vaitkiene@lsmuni.lt

Received: 22 November 2019; Accepted: 16 December 2019; Published: 19 December 2019



**Abstract:** High-grade astrocytomas are some of the most common and aggressive brain cancers, whose signs and symptoms are initially non-specific. Up to the present date, there are no diagnostic tools to observe the early onset of the disease. Here, we analyzed the combination of blood serum proteins, which may play key roles in the tumorigenesis and the progression of glial tumors. Fifty-nine astrocytoma patients and 43 control serums were analyzed using Custom Human Protein Antibody Arrays, including ten targets: ANGPT1, AREG, IGF1, IP10, MMP2, NCAM1, OPN, PAI1, TGF $\beta$ 1, and TIMP1. The decision tree analysis indicates that serums ANGPT1, TIMP1, IP10, and TGF $\beta$ 1 are promising combinations of targets for glioma diagnostic applications. The accuracy of the decision tree algorithm was 73.5% (75/102), which correctly classified 79.7% (47/59) astrocytomas and 65.1% (28/43) healthy controls. The analysis revealed that the relative value of osteopontin (OPN) protein level alone predicted the 12-month survival of glioblastoma (GBM) patients with the specificity of 84%, while the inclusion of the IP10 protein increased model predictability to 92.3%. In conclusion, the serum protein profiles of ANGPT1, TIMP1, IP10, and TGF $\beta$ 1 were associated with the presence of astrocytoma independent of its malignancy grade, while OPN and IP10 were associated with GBM patient survival.

**Keywords:** astrocytoma; glioblastoma; serum proteins; Protein Antibody Array; decision tree; survival

## 1. Introduction

High-grade astrocytomas, especially glioblastomas (GBMs), are one of the most aggressive brain tumors, with a poor prognosis. Generally, brain astrocytomas are diagnosed only after the occurrence of clinical symptoms, and a diagnosis is determined only after the histological examination of the tissue [1]. However, histological data and clinical symptoms fail to explain variation in astrocytoma progression and the response to treatment. There is an increasing interest in identifying molecular markers that better capture the status of a tumor to improve the existing predictions. Especially, there is a need of biomarkers that can indicate a change in protein expression which are related to the risk or progression of astrocytoma or with the response to a given treatment, survival, or recurrence [2,3]. Recently, gliomas could be subtyped based on several molecular markers like IDH1, 1p/19q co-deletion, EGFR amplification, loss of PTEN, MGMT methylation, etc., to predict patient prognosis while considering parameters like patient age and complete tumor histopathological profile [4]. Minimally invasive and early diagnostic techniques could play an important role in adapting the best treatment for astrocytoma patients [5]. A great effort is currently being made to achieve methods for early tumor detection,

especially including methods based on the detection of proteomic profiles in serum/plasma. A good alternative astrocytoma screening test should be as minimally invasive as possible, achieve excellent analytical outcomes regarding sensitivity and specificity, and still be fast and cost-effective. An optimal test could help to monitor if changes in the composition of serum proteins could indicate astrocytoma occurrence or recurrence and also help to optimize a treatment strategy. Therefore, the field of intensive research is moving toward extensive serum proteome profiling for tumor-specific markers [2]. Furthermore, the determination of a tumor-specific panel of markers could outperform the evaluation of individual markers regarding specificity and sensitivity. Moreover, multiple-protein profiling could provide a more detailed image of molecular networks and pathophysiological conditions of the disease. The determination of multiple proteins from a single sample could be done by using biochip array technology [6]. Biochip array technology is also practicable when volumes of clinical samples are limited.

Astrocytic glioma screening for the application of serological testing has not been established so far, even though very promising candidate markers have been reported based on proteomic [7–9] and individual target screenings [1–3]. Our study aimed to characterize preoperative protein levels in the blood serum of patients with different malignancy grade astrocytoma compared with healthy subjects. We focused on already-known cancer-related proteins based on a thorough literature review [1,3,6,10–22] and our earlier laboratory findings [23,24]. The ten proteins which were compatible to be analyzed in a protein multiplex array manner selected for the analysis were: ANGPT1 (angiopoietin-1), AREG (amphiregulin), IGF1 (insulin like growth factor I), IP10 (CXCL10, C-X-C motif chemokine 10), MMP2 (matrix metalloproteinase 2), NCAM1 (neural cell adhesion molecule 1), OPN (osteopontin), PAI1 (plasminogen activator inhibitor 1), TGF $\beta$ 1 (transforming growth factor beta 1), and TIMP1 (TIMP metalloproteinase inhibitor 1). The novelty of the study was the simultaneous assessment of ten serum proteins using a multiplex biochip array to identify a clinically applicable combination of serum markers for glioma screening. This study revealed the possibility of using a multiplex immunoassay to screen for novel and valuable blood-based protein biomarkers for malignant astrocytomas.

## 2. Materials and Methods

### 2.1. Study Group

This study was comprised of 102 serum samples that were collected at the Hospital of Lithuanian University of Health Sciences neurosurgery clinics (Kaunas, Lithuania) from 2015 to 2017. The study was carried out under the Ethical Principles for Medical Research Involving Human Subjects (Declaration of Helsinki) and the research methodologies were approved by the Kaunas Regional Biomedical Research Ethics Committee (No. P2-9/2003). All subjects gave their informed consent for inclusion before they participated in the study. We investigated 39 patients with histopathologically confirmed glioblastoma (grade IV), 3 patients with anaplastic astrocytoma (grade III), 17 patients with diffuse astrocytoma (grade II), and 43 healthy controls. The control group was age-adjusted to the case group (median/mean age for patient group 49.82/49.59 years; median/mean age for control group 44.21/45.01 years) (*t*-test, *p* > 0.05). For astrocytoma patients, blood was taken before the operation and any kind of treatment (e.g., chemotherapy or radiotherapy). Serum samples were prepared as follows: blood samples were allowed to clot for 30 min at room temperature before centrifuging for 15 min at 1000 $\times$  *g*. Serum was removed, aliquoted, and samples were stored at  $-70$  °C. Data on patient age at the time of the operation and gender were collected. None of the patients had received chemotherapy or radiation before surgery, while after surgery they had received the standard treatment. Patients' overall survival was computed from the date of the operation to the date of the death or the date of the survey database closure (censored). The database closure was in January 2018. The date and cause of death were obtained from The Lithuanian State Register of Death Cases.

## 2.2. Evaluation of Serum Proteins Level

For simultaneous quantitative detection of multiple proteins from a single patient sample we used Custom Human Antibody Array Membranes (ten targets) (Ab211921, Abcam, Cambridge, UK). The biochip comprised printed capture antibodies against ANGPT1, AREG, IGF1, IP10, MMP2, NCAM1, OPN, PAI1, TGF $\beta$ 1, and TIMP1. The protein array is an antibody-pair-based assay which performs analogously to ELISA but using a membrane as a substrate rather than a plate, as capture antibodies are spotted on a membrane. The assay was performed following the manufacturer's instructions with some modifications. A total of 1 mL of 5 $\times$  diluted blood serum was used for each reaction. After incubation, a Biotinylated 10 Antibody Cocktail (horseradish peroxidase (HRP)-labeled secondary antibodies) was added to the membranes. After following washes to remove unbound material, protein levels were quantified by chemiluminescence using the BioSpectrum Imaging System (UVP, Analytik Jena Company, Cambridge, UK). The signal intensity of each antigen-specific antibody spot represents a relative proportion of the antigen amount in the sample. Three control spots on every array were used: positive, negative, and blank control spots. The Positive Control (PC) spots (six spots per array), which contained biotin-conjugated IgG, were used for signal normalization. Negative Control (NC) (four spots per array) printed with buffer and blank spots (two spots per array) were used to determine nonspecific binding and for background subtraction. For the signal evaluation, the image processing program ImageJ was applied. After obtaining raw densitometry values, the intensity for every duplicated spot was averaged and normalized, subtracting mean intensity of the background (NC). Averaged PC spots were used for intra-array normalization. For inter-array normalization, all the membranes were adjusted to the reference array. The signal intensity of every spot representing different analyte was calculated as follows:  $X(Ny) = X(y) * P1/P(y)$ , where: P1—averaged signal density of PC spots on reference array; P(y)—averaged signal density of PC spots on membrane y; X(y)—averaged signal intensity of analyte X on membrane y; X(Ny)—normalized signal intensity for spot X on membrane y. For the reduction of technical variation and more accurate appreciation of biological differences, the relative protein level was calculated and used for further statistical analysis.

## 2.3. Statistical Analysis

For statistical analysis, the software package SPSS Statistics 19 (SPSS Inc., Chicago, IL, USA) and GraphPad Prism (GraphPad Software, La Jolla, CA, USA) were used. Chi-square test, linear regression analysis, Spearman's correlation coefficient, Kruskal–Wallis (comparison of >2 groups) and Mann–Whitney tests were used to analyze data. Decision tree classification was performed using R Software version 3.3.3, rpart package. The classification was carried out applying binary classification where RSS (ANOVA) selected as a split criterion. In total 100 random tree models were created at learning stage to ensemble method for classification. The random tree models test divided the dataset randomly into learning (approximately 60% of the data set) and test (approximately 40% of the data set) subsets. When we generated 100 tree models, the dominant model was chosen and used further. At the end of the process, the errors were counted from this dominant model. The Kaplan–Meier method was used to estimate survival functions. A significance level of 0.05 was selected to test the statistical hypothesis.

### 3. Results

#### 3.1. Serum Analysis of Single Candidate Proteins

The expressions of ten proteins in peripheral blood serum specimens were analyzed in our study using an ELISA-based multiplex protein array. Serum samples were collected prior to brain surgery from 59 patients with different-grade astrocytoma and 43 controls. The expression level of ten serum proteins was quantified and compared among groups (Figure 1). Comparisons of box-and-whiskers plots for every analyte measurement in the serum of astrocytoma patients and control samples revealed consistent distribution and median levels. No significant differences in the levels of single proteins were observed between the normal group and astrocytoma patients.

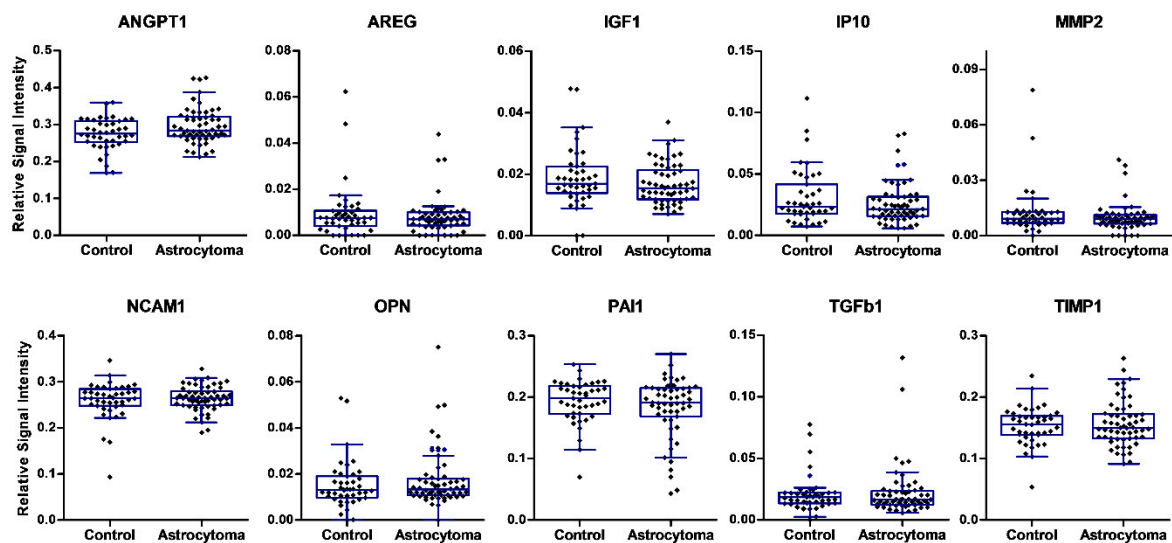


**Figure 1.** Proteomic analysis of ten proteins in preoperative blood serum in astrocytoma patients and controls. Box plots of relative expression measurements of proteins ANGPT1, AREG, IGF1, IP10, MMP2, NCAM1, OPN, PAI1, TGF $\beta$ 1, and TIMP1 obtained by protein array analysis of different malignancy grade astrocytoma patients' serum and normal controls. The line inside each box represents the median; the lower and upper edges of the boxes represent the 25th (first quartile) and 75th (third quartile) percentiles, respectively; the upper and lower edges of the boxes represent the Tukey's whiskers.

#### 3.2. Combined Analysis of Protein Levels in Astrocytoma Serum

The results of ten differentially expressed proteins on the array were used to construct a decision tree classification algorithm, in an attempt to identify potential serum biomarkers for astrocytoma.

In a decision tree analysis, relative expression level values of ten candidate proteins in 59 different grade astrocytoma patients' serum was compared with protein relative expression values in 43 healthy controls. Of ten analyzed proteins, statistically different values of four proteins were chosen as the predictor to build up the decision classification tree shown in Figure 2. The classification algorithm used values of four proteins, and five terminal nodes were determined with the relative cost of 0.27. ANGPT1, TIMP1, IP10, and TGF $\beta$ 1 together in the complex were identified as the most promising potentially diagnostic serum profile. The accuracy of the decision tree algorithm was 73.5% (75/102), which correctly classified 47 of 59 astrocytomas (79.7%) and 28 of 43 healthy controls (65.1%).

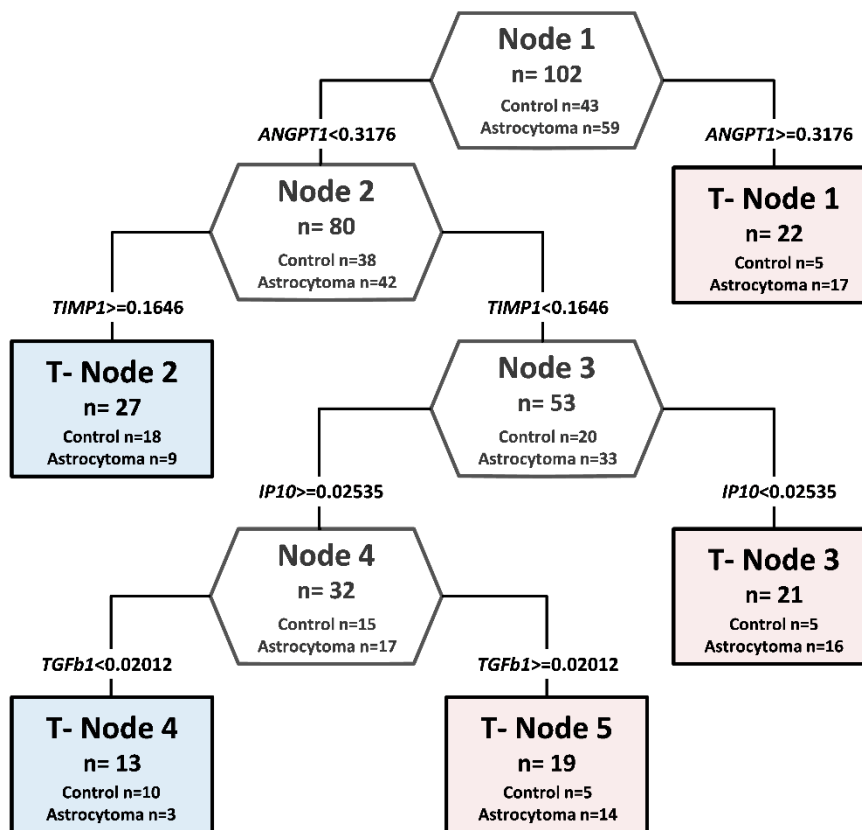


**Figure 2.** Decision tree classification diagram of protein relative values from astrocytoma patients and controls, using protein microarrays. Potential diagnostic serum protein profile composed of ANGPT1, TIMP1, IP10, and TGFβ1. The numbers in the root node (top), descendant nodes (hexagons), and terminal nodes (rectangles) represent the classes (astrocytoma patients and controls, *n* represents the sum of astrocytoma patients and controls). The number below the root and descendant nodes indicate the relative values of protein.

### 3.3. Survival Analysis

The GBM group was subdivided into two groups comprising patients who survived post surgery for more than one year (*n* = 26) and those who survived for less than one year (*n* = 13). For the clinical feature of post-surgery one-year survival, an association was achieved with serum profiles based on relative concentrations of OPN and IP10 (Figure 3A). Analysis of OPN protein relative value alone predicts the survival of more than one year with a specificity of 84% in GBM patients, while the inclusion of the other factor (IP10 protein relative value) increased specificity to 92.3%. The two survival groups were not distinguished by different treatment schemes because standard therapy, including surgery, radio, and chemotherapy, were used for both groups. The Kaplan–Meier analysis using the log-rank test showed an association between GBM patient overall survival and relative OPN expression groups (log-rank test,  $\chi^2 = 3.95$ , *df* = 1, *p* = 0.047) (see Figure 3C). Glioblastoma patients with low serum OPN expression had a significantly higher chance for longer survival when compared to patients having high serum OPN expression. Kaplan–Meier analysis showed that there was no significant difference in overall survival comparing all glioblastoma patients with relatively high or low IP10 expression (log-rank test,  $\chi^2 = 0.03$ , *df* = 1, *p* = 0.869) (see Figure 3D). Further, we aimed to identify the combination of protein expression values that could help to prognosticate patient survival after surgery.

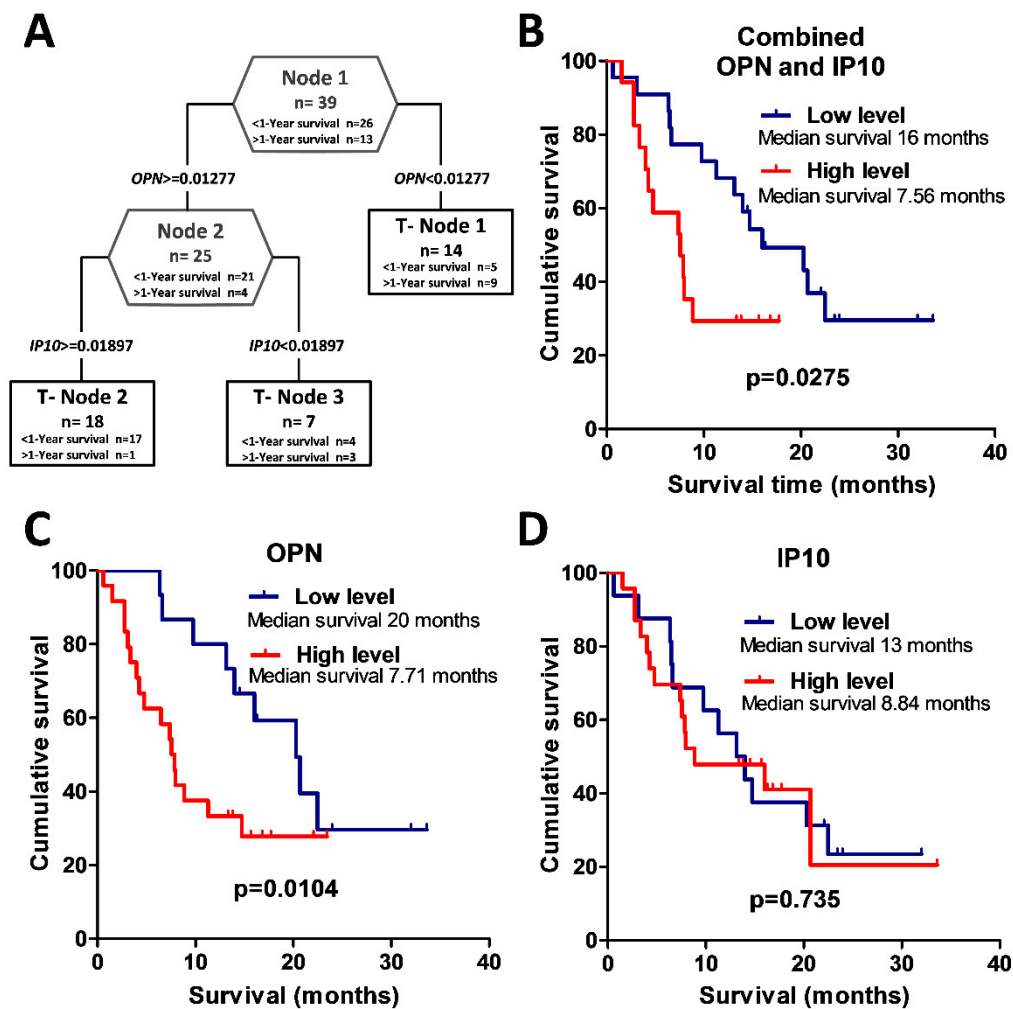


**Figure 3.** Potential prognostic serum protein profile for glioblastoma patients composed of OPN and IP10. **(A)** Glioblastoma patient decision tree with the clinical feature of one-year post-surgery survival. The numbers in the root node (top), descendant nodes (hexagons), and terminal nodes (rectangles) represent the classes (glioblastoma patients who survived less than one year after surgery and glioblastoma patients who survived more than one year after surgery);  $n$  = sum of glioblastoma patients in a class. The numbers below the root and descendant nodes indicate the relative values of protein. **(B–D)** Kaplan–Meier survival curves. **(B)** Kaplan–Meier analysis of glioblastoma patient overall survival differences between combined OPN and IP10 protein expression groups. Low- vs. high-level protein patient group median survival 16 months versus 7.56 months (log-rank test,  $p = 0.0275$ ). **(C)** Kaplan–Meier analysis of glioblastoma patient overall survival between OPN protein relative expression groups, where OPN low level means that relative OPN protein value is  $<0.01277$ , and OPN high level means that relative OPN protein value is  $\geq 0.01277$ . Low- vs. high-level protein patient group median survival 20 months versus 7.71 months (log-rank test,  $p = 0.0104$ ). **(D)** Kaplan–Meier analysis of glioblastoma patient overall survival in different IP10 protein relative expression groups, where IP10 low level means that relative IP10 protein value is  $<0.01897$ , and IP10 high level means the value is  $\geq 0.01897$ . Low- vs. high-level protein patient group median survival 13 months versus 8.84 months (log-rank test,  $p = 0.735$ ).

Therefore, to analyze glioblastoma patient survival, patients were divided into two groups. One group included glioblastoma patients who had the following relative expression value of protein OPN  $< 0.01277$  and OPN  $\geq 0.01277$ , but IP10  $< 0.01897$ . The other group consisted of glioblastoma patients with relative values of OPN  $\geq 0.01277$  and IP10  $\geq 0.01897$ . The Kaplan–Meier analysis using the log-rank test showed a significant association between glioblastoma patient overall survival and

combined OPN and IP10 protein expression groups (log-rank test,  $\chi^2 = 4.04$  df = 1,  $p = 0.044$ ) (see Figure 3B).

#### 4. Discussion

This study revealed the possibility of using multiplex immunoassays to screen for novel and valuable blood-based protein biomarkers for malignant astrocytoma. Both unique and prominent protein candidates associated with malignant astrocytoma were studied using multiplex protein immunoassays with serum samples.

In addition, protein biomarker candidates associated with malignant astrocytoma prognosis were included in this analysis. The aim was to characterize the preoperative levels of ten proteins in the blood serum of patients with different malignancy grades of astrocytoma and to compare them with healthy controls. The novelty of the study was the simultaneous assessment of ten serum proteins using multiplex biochip arrays to identify a clinically applicable combination of serum markers for glioma screening. Our decision was to focus on already-known cancer related proteins due to numerous published data. Based on a thorough literature review [1,3,6,10–22] and our laboratory findings [23,24], the ten proteins which were compatible to be analyzed in a protein multiplex array manner selected for the analysis were: ANGPT1, AREG, IGF1, IP10, MMP2, NCAM1, OPN, PAI1, TGF $\beta$ 1, and TIMP1. Many markers included in our multiplex biochip array have been thoroughly investigated individually in other researchers' previous studies. In our study, no significant differences in single protein levels between gliomas and healthy controls' serum were established. This could be related to the relatively small sample size in our study or the differences in the methodologies compared to other studies. Additionally, the variability in blood serum protein levels could be related to the size of the tumor and might prevent the establishment of precise protein level cutoff values for cancer diagnosis, considering large personal variations among patients—at least when using single protein biomarkers. Single protein markers in serum are mostly inadequate to follow the dynamics of glioma. This could be improved by using multiple marker profiles. In this study, we tried to search for a diagnostic serum profile in astrocytoma patients, using a multiplex protein array and target combination approach. When tested in serum, none of our chosen single proteins was sufficiently specific to serve as a diagnostic marker. Data showed that in contrast to single biomarkers, in a complex diagnostic profile of multiple proteins it may not be necessary for the concentrations of each protein to be significantly different between two groups [1]. Our results support these findings. Using the multiplex ten protein array and decision tree analysis, we found combinations of serum proteins with significant differences in protein levels between astrocytomas and healthy controls' serum. A profile with a relatively small number of proteins (ANGPT1, TIMP1, IP10, TGF $\beta$ 1) was sufficient to correctly assign 79.7% (47/59) of the astrocytoma and 65.1% (28/43) of the control subjects. Astrocytoma progression is related to rapid tumor growth and invasiveness. Astrocytomas express growth factors and receptors that are typically induced during angiogenesis; one of them is angiopoietin-1 (ANGPT1) [16]. During the development of the immature vasculature, ANGPT1 is critically involved in angiogenesis, and influences processes such as remodeling, maturation, and maintenance of the vascular plexus [16]. Depending on its function, ANGPT1 could be a molecular marker of glioma malignancy. Hands and colleagues, using a BioPlex immunoassay to provide cytokine and angiogenesis factor levels that differ between serum from glioma and non-cancer patients, found angiopoietin as the one important molecular marker [17]. In our study, ANGPT1 was one of the main serum proteins that helped to distinguish healthy subjects from glioma patients. TIMP1, a natural inhibitor of matrix metalloproteinase (MMP) enzymes, inhibits *in vitro* and *in vivo* tumor cell invasion and binds several members of the metalloproteinase family [18]. Crocker and colleagues' data suggest that, in glioblastoma patients, a higher serum TIMP1 level at tumor presentation predicted shorter survival and that TIMP1 levels in the glioblastoma patients are significantly higher than in normal controls [6]. We found TIMP1 as one of the proteins which help to distinguish healthy from gliomas, but in our study, its significance for survival was not confirmed. Schneider et al. analyzed plasma from 21 patients with glioblastoma before and after resection using

the ELISA method and found that concentrations of latent TGF $\beta$ 1 of patients with glioblastoma before surgery were significantly higher in comparison to healthy control probands [19]. They also found a weak relation between long survival and a low concentration of the latent form of TGF- $\beta$ 1 prior to surgery [19]. We identified that relative TGF $\beta$ 1 protein levels in astrocytoma patient serum samples before surgery may help in evaluating protein profiles. Our proposed algorithm includes IP10 protein values. It should be noted that these are in line with the data of Elstner and colleagues, where using conventional ELISA, reduced serum concentrations of IP10 were found in GBM patients compared to controls [1]. In our proposed algorithm, low IP10 protein values helped to identify astrocytoma patients. Sreekanthreddy et al. found that OPN expression in tissue was upregulated in GBM, and elevated serum OPN levels in GBM patients were also shown [13]. GBM patients with high serum OPN levels had poorer survival rates than those with low serum OPN levels [13]. Our study has shown that individually protein OPN was statistically and reliably associated with GBM survival, but after decision tree analysis, the specificity of the study could be improved by entering in the model protein IP10 relative value. On the other hand, single IP10 protein value was not significantly related to patient survival. This reaffirms the claim that in contrast to single biomarkers, in a complex prognostic protein profile it may not be necessary that each protein value be significantly different between two groups.

## 5. Conclusions

Our data suggest an algorithm for the indication of the presence of astrocytoma-specific serum profiles. Prospective and retrospective validation of the data on a larger sample would be necessary to evaluate the algorithm and perhaps adjust any other proteins, which would improve the accuracy of the method. Glioblastoma detection, applying the analysis of blood serum, could yield multiple benefits, including the early intervention of therapy, reduction in mortality and morbidity, as well as monitoring the effect of therapy.

**Author Contributions:** P.V., D.S., and G.S. originated the conception of the study; R.U., G.S., and A.T. acquainted protein microarray and patient data; G.S., P.V., P.G., and R.U. analyzed and interpreted protein microarray data; P.V. drafted the article. All authors have read and agreed to the published version of the manuscript.

**Funding:** This research was funded by a grant (No. MIP-052/2015) from the Research Council of Lithuania.

**Acknowledgments:** We appreciate Jūratė Žeglienė assistance in collecting blood serum samples and patient data.

**Conflicts of Interest:** The authors declare no conflict of interest.

## References

1. Elstner, A.; Stockhammer, F.; Nguyen-Dobinsky, T.N.; Nguyen, Q.L.; Pilgermann, I.; Gill, A.; Guhr, A.; Zhang, T.; Von Eckardstein, K.; Picht, T.; et al. Identification of diagnostic serum protein profiles of glioblastoma patients. *J. Neurooncol.* **2011**, *102*, 71–80. [CrossRef] [PubMed]
2. Kros, J.M.; Mustafa, D.M.; Dekker, L.J.M.; Sillevius Smitt, P.A.E.; Luider, T.M.; Zheng, P.-P. Circulating glioma biomarkers. *Neuro. Oncol.* **2014**, *17*, 343–360. [CrossRef] [PubMed]
3. Best, M.G.; Sol, N.; Zijl, S.; Reijneveld, J.C.; Wesseling, P.; Wurdinger, T. Liquid biopsies in patients with diffuse glioma. *Acta Neuropathol.* **2015**, *129*, 849–865. [CrossRef] [PubMed]
4. Boots-Sprenger, S.H.E.; Sijben, A.; Rijntjes, J.; Tops, B.B.J.; Idema, A.J.; Rivera, A.L.; Bleeker, F.E.; Gijtenbeek, A.M.; Diefes, K.; Heathcock, L.; et al. Significance of complete 1p/19q co-deletion, IDH1 mutation and MGMT promoter methylation in gliomas: Use with caution. *Mod. Pathol.* **2013**, *26*, 922–929. [CrossRef] [PubMed]
5. Ferrari, M. Cancer nanotechnology: Opportunities and challenges. *Nat. Rev. Cancer* **2005**, *5*, 161–171. [CrossRef] [PubMed]
6. Crocker, M.; Ashley, S.; Giddings, I.; Petrik, V.; Hardcastle, A.; Aherne, W.; Pearson, A.; Bell, B.A.; Zacharoulis, S.; Papadopoulos, M.C. Serum angiogenic profile of patients with glioblastoma identifies distinct tumor subtypes and shows that TIMP-1 is a prognostic factor. *Neuro. Oncol.* **2011**, *13*, 99–108. [CrossRef] [PubMed]




7. Zhang, H.; Wu, G.; Tu, H.; Huang, F. Discovery of serum biomarkers in astrocytoma by SELDI-TOF MS and proteinchip technology. *J. Neurooncol.* **2007**, *84*, 315–323. [CrossRef]
8. Petrik, V.; Saadoun, S.; Loosemore, A.; Hobbs, J.; Opstad, K.S.; Sheldon, J.; Tarelli, E.; Howe, F.A.; Bell, B.A.; Papadopoulos, M.C. Serum alpha 2-HS glycoprotein predicts survival in patients with glioblastoma. *Clin. Chem.* **2008**, *54*, 713–722. [CrossRef]
9. Kalinina, J.; Peng, J.; Ritchie, J.C.; Van Meir, E.G. Proteomics of gliomas: Initial biomarker discovery and evolution of technology. *Neuro. Oncol.* **2011**, *13*, 926–942. [CrossRef]
10. Chiorean, R.; Berindan-Neagoe, I.; Braicu, C.; Florian, I.S.; Leucuta, D.; Crisan, D.; Cernea, V. Quantitative expression of serum biomarkers involved in angiogenesis and inflammation, in patients with glioblastoma multiforme: Correlations with clinical data. *Cancer Biomark.* **2014**, *14*, 185–194. [CrossRef]
11. Iwadate, Y.; Hayama, M.; Adachi, A.; Matsutani, T.; Nagai, Y.; Hiwasa, T.; Saeki, N. High serum level of plasminogen activator inhibitor-1 predicts histological grade of intracerebral gliomas. *Anticancer Res.* **2008**, *28*, 415–418. [PubMed]
12. Lemos-González, Y.; Rodríguez-Berrocal, F.J.; Cordero, O.J.; Gómez, C.; Páez de la Cadena, M. Alteration of the serum levels of the epidermal growth factor receptor and its ligands in patients with non-small cell lung cancer and head and neck carcinoma. *Br. J. Cancer* **2007**, *96*, 1569–1578. [CrossRef] [PubMed]
13. Sreekanthreddy, P.; Srinivasan, H.; Kumar, D.M.; Nijaguna, M.B.; Sridevi, S.; Vrinda, M.; Arivazhagan, A.; Balasubramaniam, A.; Hegde, A.S.; Chandramouli, B.A.; et al. Identification of potential serum biomarkers of glioblastoma: Serum osteopontin levels correlate with poor prognosis. *Cancer Epidemiol. Biomarkers Prev.* **2010**, *19*, 1409–1422. [CrossRef] [PubMed]
14. Todaro, L.; Christiansen, S.; Varela, M.; Campodónico, P.; Pallotta, M.G.; Lastiri, J.; Sacerdote de Lustig, E.; Bal de Kier Joffé, E.; Puricelli, L. Alteration of serum and tumoral neural cell adhesion molecule (NCAM) isoforms in patients with brain tumors. *J. Neurooncol.* **2007**, *83*, 135–144. [CrossRef] [PubMed]
15. Tabouret, E.; Bertucci, F.; Pierga, J.-Y.; Petit, T.; Levy, C.; Ferrero, J.-M.; Campone, M.; Gligorov, J.; Lerebours, F.; Roché, H.; et al. MMP2 and MMP9 serum levels are associated with favorable outcome in patients with inflammatory breast cancer treated with bevacizumab-based neoadjuvant chemotherapy in the BEVERLY-2 study. *Oncotarget* **2016**, *7*, 18531–18540. [CrossRef] [PubMed]
16. Reiss, Y.; Machein, M.R.; Plate, K.H. The role of angiopoietins during angiogenesis in gliomas. *Brain Pathol.* **2005**, *15*, 311–317. [CrossRef] [PubMed]
17. Hands, J.R.; Abel, P.; Ashton, K.; Dawson, T.; Davis, C.; Lea, R.W.; McIntosh, A.J.S.; Baker, M.J. Investigating the rapid diagnosis of gliomas from serum samples using infrared spectroscopy and cytokine and angiogenesis factors. *Anal. Bioanal. Chem.* **2013**, *405*, 7347–7355. [CrossRef]
18. Fillmore, H.L.; VanMeter, T.E.; Broaddus, W.C. Membrane-type matrix metalloproteinases (MT-MMPs): Expression and function during glioma invasion. *J. Neurooncol.* **2001**, *53*, 187–202. [CrossRef]
19. Schneider, T.; Sailer, M.; Ansorge, S.; Firsching, R.; Reinhold, D. Increased concentrations of transforming growth factor beta1 and beta2 in the plasma of patients with glioblastoma. *J. Neurooncol.* **2006**, *79*, 61–65. [CrossRef]
20. Lin, Y.; Wang, J.F.; Gao, G.Z.; Zhang, G.Z.; Wang, F.L.; Wang, Y.J. Plasma levels of tissue inhibitor of matrix metalloproteinase-1 correlate with diagnosis and prognosis of glioma patients. *Chin. Med. J.* **2013**, *126*, 4295–4300.
21. Deighton, R.F.; McGregor, R.; Kemp, J.; McCulloch, J.; Whittle, I.R. Glioma pathophysiology: Insights emerging from proteomics. *Brain Pathol.* **2010**, *20*, 691–703. [CrossRef] [PubMed]
22. Güttler, A.; Giebler, M.; Cuno, P.; Wichmann, H.; Keßler, J.; Ostheimer, C.; Söling, A.; Strauss, C.; Illert, J.; Kappler, M.; et al. Osteopontin and splice variant expression level in human malignant glioma: Radiobiologic effects and prognosis after radiotherapy. *Radiother. Oncol.* **2013**, *108*, 535–540. [CrossRef] [PubMed]
23. Sincevičiūtė, R.; Vaitkienė, P.; Urbanavičiūtė, R.; Steponaitis, G.; Tamašauskas, A.; Skiriūtė, D. MMP2 is associated with glioma malignancy and patient outcome. *Int. J. Clin. Exp. Pathol.* **2018**, *11*, 3010–3018.
24. Steponaitis, G.; Kazlauskas, A.; Skiriute, D.; Vaitkiene, P.; Skauminas, K.; Tamasauskas, A. Significance of Amphiregulin (AREG) for the Outcome of Low and High Grade Astrocytoma Patients. *J. Cancer* **2019**, *10*, 1479–1488. [CrossRef]



Review

# Relevance of Translation Initiation in Diffuse Glioma Biology and its Therapeutic Potential

Digregorio Marina <sup>1</sup>, Lombard Arnaud <sup>1,2</sup>, Lumapat Paul Noel <sup>1</sup>, Scholtes Felix <sup>1,2</sup>, Rogister Bernard <sup>1,3</sup>  and Coppieters Natacha <sup>1,\*</sup>

<sup>1</sup> Laboratory of Nervous System Disorders and Therapy, GIGA-Neurosciences Research Centre, University of Liège, 4000 Liège, Belgium; marina.digregorio@uliege.be (D.M.); alombard@chuliege.be (L.A.); pnlumapat@uliege.be (L.P.N.); felix.scholtes@uliege.be (S.F.); bernard.rogister@uliege.be (R.B.)

<sup>2</sup> Department of Neurosurgery, CHU of Liège, 4000 Liège, Belgium

<sup>3</sup> Department of Neurology, CHU of Liège, 4000 Liège, Belgium

\* Correspondence: ncoppieters@uliege.be

Received: 18 October 2019; Accepted: 26 November 2019; Published: 29 November 2019



**Abstract:** Cancer cells are continually exposed to environmental stressors forcing them to adapt their protein production to survive. The translational machinery can be recruited by malignant cells to synthesize proteins required to promote their survival, even in times of high physiological and pathological stress. This phenomenon has been described in several cancers including in gliomas. Abnormal regulation of translation has encouraged the development of new therapeutics targeting the protein synthesis pathway. This approach could be meaningful for glioma given the fact that the median survival following diagnosis of the highest grade of glioma remains short despite current therapy. The identification of new targets for the development of novel therapeutics is therefore needed in order to improve this devastating overall survival rate. This review discusses current literature on translation in gliomas with a focus on the initiation step covering both the cap-dependent and cap-independent modes of initiation. The different translation initiation protagonists will be described in normal conditions and then in gliomas. In addition, their gene expression in gliomas will systematically be examined using two freely available datasets. Finally, we will discuss different pathways regulating translation initiation and current drugs targeting the translational machinery and their potential for the treatment of gliomas.

**Keywords:** gliomas; protein synthesis; translation; cap-dependent; IRES

## 1. Introduction

Gliomas are the most frequent tumors of the central nervous system and include diffuse and circumscribed gliomas [1]. Diffuse gliomas are the most frequent cancer of the central nervous system in adults and will therefore be the focus of this review. In the latest classification for diffuse gliomas, the World Health Organization (WHO) has taken molecular characteristics into account as it becomes evident that histology on its own is not sufficient to characterize these brain tumors. For example, the presence of mutations in the isocitrate dehydrogenase 1 and 2 (*IDH1* and *IDH2*) and the association of complete 1p/19q co-deletion is now included in the classification of diffuse gliomas [1]. Grade II gliomas are low grade gliomas and include diffuse astrocytomas and oligodendrogliomas. Grade III gliomas include anaplastic astrocytomas and anaplastic oligodendrogliomas. Grade IV is the highest grade and includes glioblastomas also known as glioblastoma multiforme (GBM). GBM is the most aggressive glioma subtype and accounts for 60% of total gliomas [2–4]. Based on single-cell gene expression, GBM tumor cells can be further sorted into four states: oligodendrocyte-precursor-like, neural-progenitor-like, astrocyte-like, or mesenchymal-like [5]. Interestingly, these four states

correspond to the four subtypes previously established by Verhaak et al. from The Cancer Genome Atlas Research (TCGA) whole-genome RNA sequencing study: Proneural, Neural, Classical, and Mesenchymal, respectively [6,7]. Unfortunately, so far, the Verhaak's classification remains unhelpful for the choice of a specific treatment for a particular GBM subtype. Indeed, the median survival following GBM diagnosis remains short (ranging from 9 to 14 months) independently of the genetic subtype and despite standard therapy which combines surgical resection of the tumor followed by radiotherapy and chemotherapy using temozolomide (TMZ), the most commonly used chemotherapeutic agent [8]. The identification of new targets for the development of novel therapeutics are therefore needed in order to improve this devastating overall survival rate.

Cancer cells are highly proliferative, migratory and invasive. In addition, they are continually exposed to stressors such as hypoxia and nutrient deprivation, forcing them to constantly and rapidly adapt their protein production to survive. To do so, cancer cells can exploit their translational machinery to maintain cellular activity even in times of high physiological stress and can continue to synthesize proteins promoting their survival and necessary for their biology [9]. This phenomenon has been described in several cancers including human lung, breast, and prostate cancers and has been recently reviewed [10]. Thus, targeting the protein synthesis pathway has been postulated as an interesting new therapeutic avenue for several types of cancer [10,11]. However, the specific oncogenic role of translation in gliomas and in GBM, in particular, remains to be clarified. Translation is composed of four main phases, namely initiation, elongation, termination, and ribosome recycling. In this review, we will focus on translation initiation in gliomas, as this is the most critical and rate-limiting step of protein synthesis [12]. The different translation initiation protagonists will be described then their expression and roles in gliomas will be discussed. In addition, their gene expression in gliomas will systematically be examined using two freely available datasets: the REpository for Molecular BRAin Neoplasia DaTa (REMBRANDT; Affymetrix HG U133 v2.0 Plus; Control:  $n = 21$ , oligodendroglioma:  $n = 66$ , astrocytomas:  $n = 145$ , and GBM:  $n = 214$ ) and data generated by The Cancer Genome Atlas Research Network (TCGA, <https://www.cancer.gov/tcga>, Affy Human Exon 1.0 ST; Control:  $n = 11$ , Classical:  $n = 54$ , Mesenchymal  $n = 58$ , Neural = 33, and Proneural  $n = 57$  based on Verhaak's classification) (Tables 1 and 2) [6,13]. These two datasets were obtained through the independent Betastasis genomics analysis and visualization platform, and GraphPad Prism (version 5.03 for Windows, GraphPad Software, San Diego California USA, [www.graphpad.com](http://www.graphpad.com)) was used for statistical analysis. Finally, we will discuss different pathways regulating translation initiation as well as current drugs targeting the translational machinery and their potential for the treatment of gliomas.

## 2. Overview on Translation Initiation

Two distinct initiation processes exist in eukaryotic cells: cap-dependent and cap-independent initiation [14]. Cap-dependent translation can be divided into two major steps (Figure 1). During the first step, the eukaryotic translation initiation factor (eIF) 4F (eIF4F) complex comprised of eIF4E, eIF4G, and eIF4A, assembles on the 7-methylguanosine 5'-triphosphate (m7GTP) cap structure present on the 5' end of the mRNA (Figure 1a). During the second step of cap-dependent translation, the small ribosomal subunit (40S) associated with eIF1, eIF1A, eIF3, and eIF5 interacts with the ternary complex constituted of eIF2, a switch-protein bound to GTP and the initiator methionyl-transfer RNA (Met-tRNA<sub>i</sub>). Together they form the 43S preinitiation complex (43S PIC) (Figure 1b). The 43S PIC then recognizes and binds the eIF4F complex near the cap to create the 48S PIC (Figure 1c). The 40S ribosomal subunit associated with eIFs uses ATP hydrolysis as energy supply to scan mRNA from the 5' untranslated region (UTR) until it reaches the initiation codon (AUG), allowing the localization of the Met-tRNA<sub>i</sub> in the future peptidyl site, or P site, of the ribosome. The 60S ribosomal subunit is then recruited and joins the 40S ribosomal subunit which triggers eIF2-GTP hydrolysis, leading to eIFs release and the formation of the 80S initiation complex (Figure 1d) [15]. At this stage, the initiation complex is fastened on the mRNA and the elongation begins by accepting a second tRNA with its amino acid in the aminoacyl site (A site) of the ribosome [16].

Whereas translation of most eukaryotic mRNAs depends on the presence of a m<sup>7</sup>GTP cap on the 5' UTR end, there is now evidence that it is not the only mode of initiation. Indeed, in the absence of cap-binding machinery or when cap-dependent initiation has been inhibited following cellular stress, alternative mechanisms can be initiated to ensure that proteins required for cell survival remain expressed. Several modes of translation have been proposed to explain cap-independent translation of mammalian mRNA with internal ribosomal entry site (IRES) being the most studied so far [17,18]. IRES-dependent initiation and current research in gliomas will be discussed hereafter.

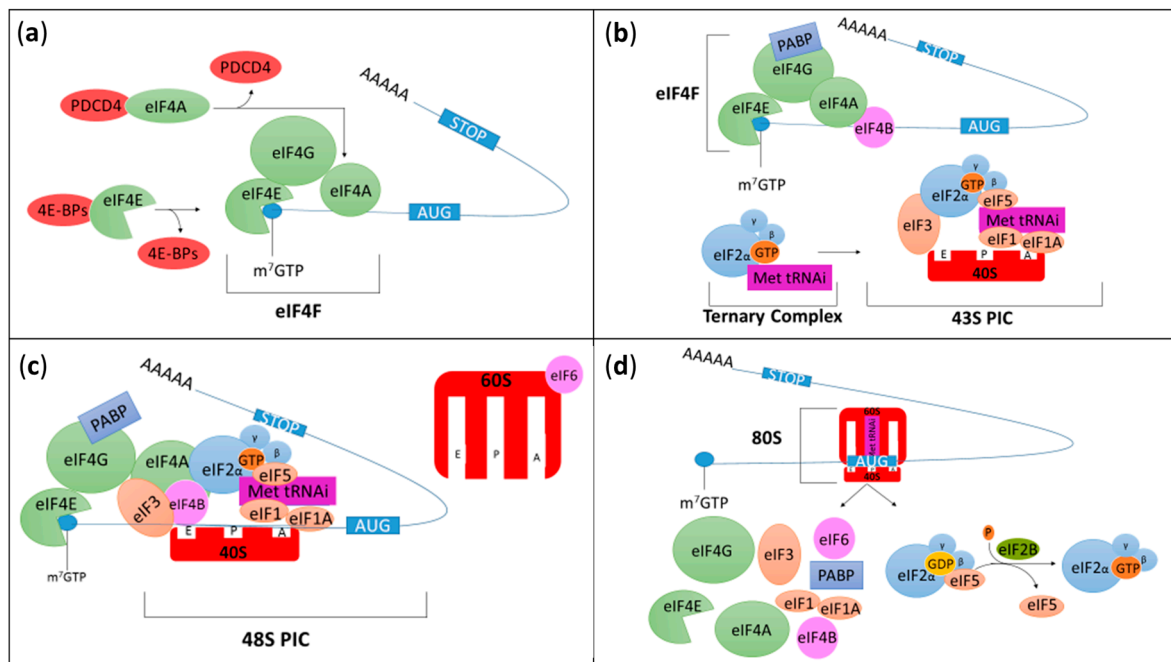


**Figure 1.** Schematic representation of cap-dependent translation initiation. **(a)** During the first step of translation, the eukaryotic translation initiation factor (eIF) 4F (eIF4F) complex is formed and associates with mRNAs. eIF4F is composed of three subunits (represented in green): eIF4E which binds the 7-methylguanosine 5'-triphosphate (m<sup>7</sup>GTP) cap structure present on the 5' end of the mRNA; eIF4G which is a scaffold protein and eIF4A which is an RNA helicase ATP-dependent protein unwinding mRNA during translation. The formation of eIF4F complex can be inhibited by programmed cell death 4 (PDCD4) and eIF4E-binding proteins (4E-BPs) which bind eIF4A and eIF4E, respectively. **(b)** During the second step of cap-dependent translation, the small ribosomal subunit (40S, red) associated with eIF1, eIF1A, eIF3 and eIF5 interacts with the ternary complex constituted of eIF2, a switch-protein bound to guanosine triphosphate (GTP) and the initiator methionyl-transfer RNA (Met-tRNA<sup>i</sup>). Together they form the 43S preinitiation complex (43S PIC). eIF2 is a heterotrimeric structure composed of three subunits (α, β and γ). At this stage, poly(A) binding protein (PABP, an RNA-binding protein) binds eIF4G and the 3' poly(A) tail to induce mRNA circularization. eIF4B also interacts with eIF4A to stabilize unwounded mRNA and stimulate eIF4A RNase and helicase activities. **(c)** The 43S PIC associates with the eIF4F complex to form the 48S PIC before scanning the mRNA until it reaches and recognizes the start codon (AUG), and Met-tRNA<sup>i</sup> binds the peptidyl (P) site of the ribosome. The 60S ribosomal subunit associated with eIF6 will then be recruited. **(d)** The 60S binds the 40S which triggers eIF2-GTP hydrolysis into guanosine diphosphate bound (GDP), leading to eIFs release and the formation of the 80S initiation complex. At this stage, the initiation complex is fastened on the mRNA and the elongation begins. The aminoacyl (A) and the exit (E) sites present in the ribosome correspond to the sites where a second tRNA with its amino acid enters the ribosome and the amino acid depleted tRNA exits the ribosome, respectively. Finally, once the ternary complex has been released, eIF2B frees up eIF5 and restores eIF2-GDP into eIF2-GTP.

### 3. Cap-Dependent Initiation

Translation initiation includes several steps and involves multiple players. We will attempt to facilitate the comprehension of this rather complex biological process by describing and discussing intermediary steps as depicted in Figure 1. We therefore encourage readers to use Figure 1 as a visual support.

#### 3.1. The eIF4F Initiation Complex

The eIF4F complex includes three subunits, each with their specific role in the initiation process: (i) eIF4E binds m<sup>7</sup>GTP at the 5' UTRs of mRNAs and is the less abundant eIF making it a limiting factor of translation, (ii) eIF4G is a scaffold protein whose role is to coordinate binding of ribosomal subunits with other eIFs and (iii) eIF4A is a RNA helicase ATP-dependent protein which unwinds mRNA during translation [10].

##### 3.1.1. eIF4E

eIF4E is a limiting factor and thus a key element during protein synthesis due to its low abundance and its regulation through phosphorylation and its interaction with other proteins [19–21]. The eIF4E family comprises three members; eIF4E1, eIF4E2 also called 4EHP, and eIF4E3, all of which have the capacity to bind mRNA caps but with different affinity [22]. eIF4E1 is considered as the canonical eIF4E and binds m<sup>7</sup>GTP with the highest affinity [22]. In the literature, eIF4E1 is the most studied. However, the distinction between these three members is often unclear. Hereby, we will clarify which member has been studied, when possible, or use eIF4E for investigations which did not specify which isoform was considered.

In 2005, Gu et al. reported that eIF4E protein was overexpressed in astrocytes, proliferative endothelial cells, and in vascular endothelial cells present in human GBM tissue samples [23]. This conclusion was based on immunohistochemistry performed on paraffin embedded tissue from five human GBM cases. Their protocol included a primary antibody incubation step of 25 minutes which is rather short to allow sufficient time for a typical antibody-antigen interaction. Furthermore, no co-labelling was performed and haematoxylin-eosin counterstaining alone does not permit clear conclusion on the cell types expressing eIF4E [23]. Nevertheless, higher expression of EIF4E in GBM was later confirmed by another team. They used a tissue microarray including cores of GBM ( $n = 25$ ) and control brains ( $n = 50$ ) combined with assisted quantitative scoring of the immunostaining [20]. Levels of eIF4E and its phosphorylated form (p-eIF4E) increase with glioma tumor grade and are predictive of poor survival [24]. Phosphorylation of eIF4E on Ser209 is regulated by mitogen-activated protein kinase (MAPK) interacting protein kinases (MNKs) and occurs once eIF4E is bound to the m<sup>7</sup>GTP cap structure and has been stabilized by eIF4G (Figure 2). Phosphorylation of eIF4E modifies the repertoire of translated mRNA with increased translation of mRNAs encoding pro-tumorigenic factors such as matrix metalloproteinases or vascular endothelial growth factor C [21]. Interestingly, expression of p-eIF4E is highly sensitive for the diagnosis of GBM (94.3%) and to a lesser extent for the differentiation between high-grade and low-grade astrocytomas (81.4%). Furthermore, the combination of elevated levels of p-eIF4E and eIF4E-binding protein 1 (4E-BP1, an inhibitor of eIF4E discussed below) has a positive predictive value of 100% for GBM diagnosis and was therefore suggested as a diagnostic tool for GBM in small biopsy materials [24]. In line with this finding, it was shown that lower levels of eIF4E phosphorylation, together with alteration of other proteins including p-Akt, could act as anti-angiogenic factors in glioma cells [25].

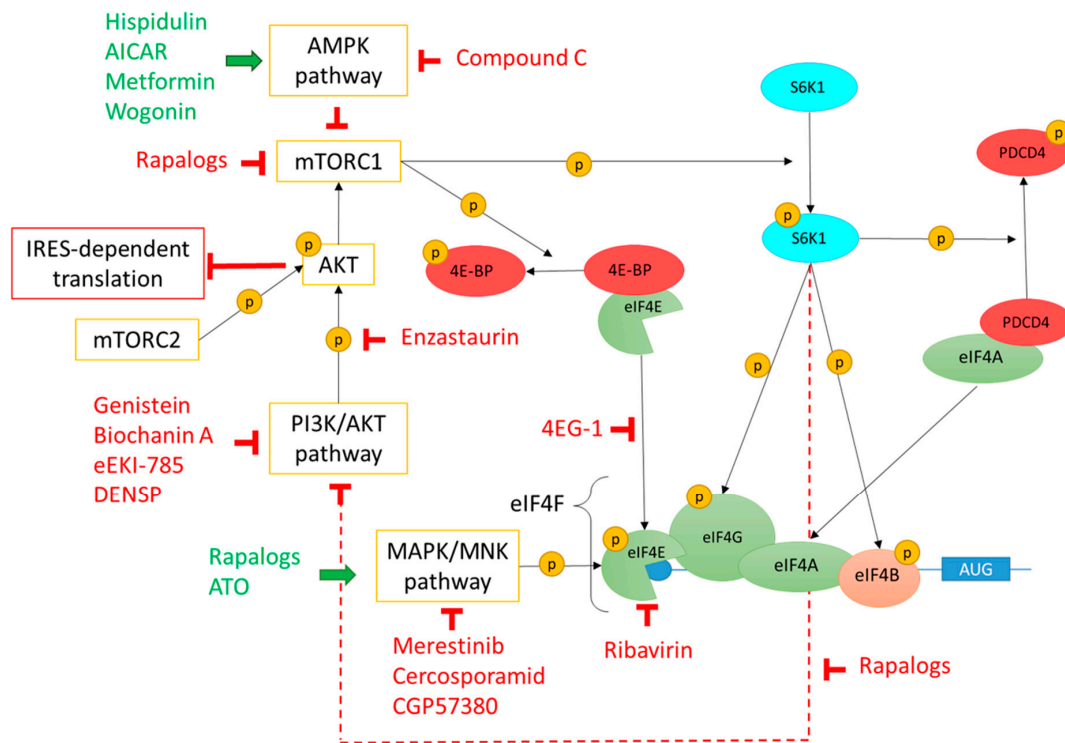


**Figure 2.** Regulation of eIF4F complex formation by PI3K/Akt/mTOR, MAPK/MNK, and AMPK pathways and drugs targeting these pathways. mTOR, a downstream effector of PI3K/Akt pathway, is a serine/threonine kinase which is the core of two protein complexes: mTORC1 and mTORC2. mTORC1 phosphorylates 4E-BP and the S6K1 kinase. 4E-BP phosphorylation leads to 4E-BP1/eIF4E dissociation and consequently formation of the eIF4F complex. S6K1 phosphorylation leads to its activation which in turn phosphorylates eIF4G, eIF4B, and PDCD4. Once phosphorylated, PDCD4 is degraded thus freeing eIF4A which can then join the eIF4F complex. Phosphorylated eIF4B stabilizes unwound mRNA and stimulates eIF4A RNase and helicase activities. Phosphorylated S6K1 also inhibits the PI3K/Akt pathway by a feedback loop (dotted red line). mTORC2 can phosphorylate and activate Akt which inhibits IRES-dependent translation. MNKs are downstream effectors of the MAPK/MNK pathway able to phosphorylate eIF4E which then promotes mRNA translation initiation. Finally, the AMPK pathway modulates protein synthesis by inhibiting mTORC1 and consequently blocking 4E-BP/eIF4E dissociation and eIF4F complex formation. Drugs acting as activators or inhibitors of these different pathways are represented in green or in red, respectively. mTOR—mechanistic target of rapamycin; PI3K—phosphoinositide 3-kinase; Akt—protein kinase B; mTORC—mechanistic target of rapamycin complex; 4E-BP—eukaryotic translation initiation factor 4E-binding protein; S6K1—S6 kinase 1; eIF—eukaryotic initiation factor; PDCD4—programmed cell death 4; IRES—internal ribosome entry site; MAPK—Mitogen-activated protein kinase (MAPK); MNK—MAPK interacting protein kinases; AMPK—AMP-activated protein kinase. Phosphorylation is represented by a yellow sphere containing the letter P.

Analysis of data available on REMBRANDT and TCGA databases revealed that *EIF4E1* and *EIF4E3* mRNA levels are downregulated whereas *EIF4E2* is overexpressed in gliomas (Table 1). Interestingly, contrary to eIF4E1, eIF4E2 has lower affinity for the m7GTP cap and more importantly, might be a repressor of translation [22]. Thus, decreased expression of eIF4E1 and eIF4E3 together with increased eIF4E2 expression suggests a global repression of cap-dependent translation in gliomas. Although data obtained from REMBRANDT and TCGA databases need to be validated at protein levels, this observation illustrates the importance of distinguishing members of the eIF4E protein family when studying them in gliomas.

**Table 1.** Expression of factors involved in the cap-dependent initiation step in gliomas. mRNA expression levels of eukaryotic initiation factors (eIFs) and other players of the cap-independent initiation detected in control brain tissues ( $n = 21$ ) were compared with their expression in the three glioma subtypes (oligodendroglioma,  $n = 66$ ; astrocytoma,  $n = 145$ ; glioblastoma multiform (GBM),  $n = 214$ ) using the REMBRANDT database. Levels of these mRNAs from control tissues ( $n = 11$ ) were then compared to expression found in the four GBM subtypes defined by the Verhaak’s classification (classical,  $n = 54$ ; menchymal,  $n = 58$ ; neural,  $n = 33$ ; proneural,  $n = 57$ ) using the TCGA dataset. These two datasets were obtained through the independent Betastasis genomics analysis and visualization platform. GraphPad Prism (version 5.03 for Windows, GraphPad Software, San Diego California USA, www.graphpad.com) was used for statistical analysis. D’Agostino & Pearson omnibus normality test was used to control for normal distribution. One-way analysis of variance (ANOVA) followed by Bonferroni’s Multiple Comparison Test was used for parametric analysis and if required Kruskal-Wallis test followed by Dunn’s Multiple Comparison Test was performed for non-parametric analysis. ns—not significant, +/-  $p < 0.05$ , +/+/-  $p < 0.01$ , and +++/+/-  $p < 0.001$  where “+” and “-” indicate an increase and a decrease in expression, respectively. REMBRANDT—REpository for Molecular BRAin Neoplasia DaTa; TCGA—The Cancer Genome Atlas.

eIFs and Modulators	Gene	REMBRANDT			TCGA			
		Oligodendroglioma	Astrocytoma	GBM	Classical	Mesenchymal	Neural	Proneural
eIF1	EIF1	ns	ns	ns	ns	ns	ns	ns
eIF1A	EIF1A	ns	ns	ns	ns	ns	ns	ns
eIF1AD	EIF1AD	++	ns	+++	ns	ns	ns	ns
eIF2 alpha	EIF2S1	ns	ns	ns	ns	ns	ns	ns
eIF2 beta	EIF2S2	++	+	+++	ns	ns	ns	ns
eIF2 gamma	EIF2S3	+++	++	+++	ns	+	ns	ns
HRI	EIF2AK1	++	+	++	ns	ns	ns	ns
PKR	EIF2AK2	+	++	+	ns	ns	ns	ns
PERK	EIF2AK3	ns	ns	+++	ns	ns	ns	ns
GCN2	EIF2AK4	ns	ns	++	ns	ns	ns	ns
eIF2B1	EIF2B1	+++	+++	+++	ns	ns	ns	++
eIF2B2	EIF2B2	+++	+++	+++	ns	ns	ns	ns
eIF2B3	EIF2B3	---	---	ns	-	ns	ns	ns
eIF2B4	EIF2B4	+++	+++	+++	ns	ns	+	ns
eIF2B5	EIF2B5	++	+	++	ns	ns	ns	ns
eIF3A	EIF3A	+++	+++	ns	ns	ns	ns	ns
eIF3B	EIF3B	+++	+++	+++	+++	+++	ns	++
eIF3D	EIF3D	+++	+++	+++	+	++	ns	++
eIF3E	EIF3E	+++	+++	+++	ns	ns	ns	ns
eIF3F	EIF3F	+++	+++	+++	ns	ns	ns	ns
eIF3G	EIF3G	+++	+++	+++	+++	++	++	++
eIF3H	EIF3H	+++	+++	+++	ns	ns	ns	ns
eIF3I	EIF3I	ns	ns	+++	+	+	+++	ns
eIF3J	EIF3J	+	ns	ns	ns	ns	ns	ns
eIF3K	EIF3K	ns	ns	ns	ns	ns	+	ns
eIF3L	EIF3L	+++	+++	ns	ns	ns	ns	ns
eIF3M	EIF3M	+++	++	+++	ns	ns	ns	ns
eIF4A1	EIF4A1	+++	+++	+++	++	+++	+	+++
eIF4A2	EIF4A2	---	---	---	---	---	ns	---
eIF4A3	EIF4A3	+++	+++	+++	+	++	+++	++
eIF4B	EIF4B	++	ns	ns	ns	ns	ns	ns
eIF4E1	EIF4E1	---	---	---	---	---	ns	---
eIF4E2	EIF4E2	++	++	+++	++	+++	+++	+
eIF4E3	EIF4E3	---	---	---	---	---	ns	---

Table 1. Cont.

eIFs and Modulators	Gene	REMBRANDT			TCGA			
		Oligodendroglioma	Astrocytoma	GBM	Classical	Mesenchymal	Neural	Proneural
4E-BP1	<i>EIF4EBP1</i>	+++	+++	+++	+	+++	++	+++
4E-BP2	<i>EIF4EBP2</i>	+++	+++	ns	+	+	+	ns
4E-BP3	<i>ANKHD1</i>	+++	+++	+++	ns	ns	ns	ns
4E-T	<i>EIF4ENIF1</i>	ns	-	---	---	---	---	--
eIF4G1	<i>EIF4G1</i>	+++	+++	+++	ns	ns	ns	ns
eIF4G2	<i>EIF4G2</i>	+++	ns	+++	ns	ns	ns	ns
eIF4G3	<i>EIF4G3</i>	---	---	---	---	---	---	--
eIF4H	<i>EIF4H</i>	ns	ns	ns	ns	ns	-	ns
PDCD4	<i>PDCD4</i>	ns	ns	ns	--	ns	ns	ns
eIF5	<i>EIF5</i>	ns	--	ns	ns	-	ns	--
eIF5B	<i>EIF5B</i>	+++	+++	+++	ns	ns	ns	ns
eIF6	<i>EIF6</i>	+++	++	+++	++	++	++	ns

The importance of making the distinction between eIF4E family members is also illustrated by a potential role for eIF4E2 in GBM. Indeed, eIF4E2 is required for tumor progression and controls 3' UTR hypoxia response element-containing mRNA translation. Inhibition of eIF4E2 under hypoxic condition decreases wound healing, cell migration, and sphere formation in the U87MG human glioma cell line [26]. These interesting findings should be confirmed in primary GBM cells. Additional in vitro and in vivo studies support a role for eIF4E in gliomas. For example, eIF4E is involved in the regulation of genes coding for proto-oncogene proteins like c-myc and cyclin D1 which are involved in cell proliferation and promote tumor growth [27–31]. This potential role of eIF4E proteins in tumor biology is also supported by studies confirming that eIF4E is involved in cell proliferation and tumor growth [32,33]. Ribavirin, an anti-viral drug that disrupts the interaction between eIF4E and the 5' UTR end of mRNA (Figure 2), inhibits GBM cell growth and migration, and increases radio-/chemo-therapy efficacy in vivo [33,34]. In agreement with this observation, the overexpression of eIF4E in U373 cells, a human GBM astrocytoma cell line, increases cell proliferation under normoxic conditions and overall tumor size in a xenograft model. Contrary to the study showing that inhibition of eIF4E increases radiosensitivity, Rouschop et al. showed that eIF4E overexpression induces a decrease in the number of hypoxic cells and increases radiosensitivity [32]. Furthermore, a research group investigated the effect of hypoxia and serum deprivation, two conditions often present in the tumor microenvironment [9], on the proteome of U87MG cells and found that eIF4E was overexpressed under these conditions [35]. Finally, eIF4E was suggested to play a role in the maintenance and self-renewal capacity of GBM initiating cells (GICs) through Sox2 regulation [36]. GICs infiltrate the parenchyma surrounding the tumor mass and consequently escape surgical resection. In addition, GICs are resistant to radio- and chemo-therapy, making them strong suspect in GBM recurrence and therefore, an ideal target to prevent those relapses [37,38].

As eIF4E expression is low under basal conditions and is a limiting factor of cap-dependent translation initiation, it is important to consider factors regulating its availability. One of the two known mechanisms involved in the regulation of eIF4E availability is the eukaryotic translation initiation factor 4E nuclear import factor 1 (*EIF4ENIF1* also known as 4E-T), which regulates eIF4E trafficking to the nucleus [39]. Depletion of eIF4E from the cytoplasm would ultimately result in the suppression of cap-dependent translation. The presence of eIF4E in the nucleus suggests additional functions beside its role in translation. One potential role for eIF4E in the nucleus is the regulation of mRNA trafficking outside the nucleus [39]. Interestingly, whereas eIF4E is present in the cytoplasm and in the nucleus in normal cells, the majority of eIF4E is nuclear in cancer cells [39]. In addition to its role in the processes responsible for the subcellular localization of eIF4E, 4E-T also participates in mRNA turnover through its direct interaction with eIF4E and components of the mRNA decay machinery [40]. According to our analysis shown in Table 1, the expression of *EIF4ENIF1* is significantly decreased in astrocytomas and all GBM subtypes suggesting a potential decrease in mRNA recycling in gliomas and/or an alteration in eIF4E subcellular localization. This, of course, requires further investigation and validation. Other



major inhibitors of eIF4E include 4E-BPs which are small proteins competing for eIF4G, the direct partner of eIF4E in the eIF4F initiation complex. Therefore, 4E-BPs will be discussed in the next section.

### 3.1.2. eIF4G

Among the eIF4G family members, only eIF4G1 and eIF4G3 (also known as eIF4GI and eIF4GII, respectively) are directly involved in the cap-dependent translation, while eIF4G2 (also known as Dap5) has been found to play a role in cap-independent translation and will be discussed in the corresponding section [41,42]. eIF4Gs are scaffold proteins which means that they interact with RNA as well as many other proteins including eIF4E, poly(A) binding proteins (PABPs), eIF3, eIF4A, and MNK1 (the kinase able to phosphorylate eIF4E, see above) [41,43]. Thus, they participate in the eIF4F complex formation during cap-dependent translation (Figure 1). PABP is an RNA-binding protein which links eIF4G with the 3' poly(A) tail of eukaryotic mRNAs, thus circularizing mRNAs. PABP contributes to translation initiation potentially by several mechanisms including enhancing eIF4F affinity for the cap structure, increasing eIF4F activity or promoting ribosome recycling [44]. The expression of eIF4G proteins is altered in different types of human cancer including in gliomas as shown in our REMBRANDT and TCGA data analysis (Table 1) [45]. These analyses reveal indeed that the expression of *EIF4G1* and *EIF4G2* is significantly increased in gliomas whereas *EIF4G3* is decreased in gliomas and all GBM subtypes.

Direct interaction between eIF4G and eIF4E seems to be a critical step in the initiation of protein synthesis. Members of the 4E-BP family, namely 4E-BP1, 4E-BP2, and 4E-BP3, bind and thus sequester eIF4E which prevents its interaction with eIF4G and in turn blocks translation (Figure 1a). Phosphorylation of 4E-BPs triggers eIF4E release and consequently permits eIF4E-eIF4G interaction and translation initiation [46]. Pathways involved in the regulation of 4E-BP phosphorylation will be discussed below in the corresponding section. Whereas *EIF4EBP1* and *EIF4EBP3* seem to be overexpressed in gliomas, this is less clear for *EIF4EBP2* as data from REMBRANDT show an increase in mRNA levels in oligodendrogliomas and astrocytomas, but not in GBM, whereas, according to the TCGA analysis, there is a decrease in *EIF4EBP2* in most GBM subtypes (Table 1). In agreement, Martínez-Sáez et al. used immunohistochemistry to investigate 4E-BP1 in 104 diffuse infiltrating astrocytomas including diffuse astrocytomas (grade II,  $n = 19$ ), anaplastic astrocytomas (grade III,  $n = 25$ ), and GBM (grade IV,  $n = 60$ ). They found that levels of 4E-BP1 and p-4E-BP1 correlate with tumor grades, with the highest level detected in GBM. However, no significant difference in survival was observed between the different groups [24]. Disruption of eIF4F complex using a 4E-BP mimetic molecule (4EG-1) triggers apoptosis in GBM cells and reduces tumor growth in a xenograft model (Figure 2) [47,48]. In line with this, Dubois et al. demonstrated that 4E-BP1 silencing accelerates the growth of xenografted U87MG cells in mice [49]. Results obtained from these studies are surprising since 4E-BP1 is increased in gliomas, which suggests that higher expression of 4E-BP1 facilitates the development of the disease [24].

### 3.1.3. eIF4A

The last subunit belonging to the eIF4F initiation complex is the RNA helicase eIF4A, which unwinds mRNA secondary structures and permits the recruitment of the 43S PIC (Figure 1). In addition, eIF4A is also required to untwist mRNA during scanning, leading to recognition of the initiation codon then assembly of the 60S subunit and the beginning of the elongation step. Three eIF4A isoforms, eIF4A1-A3, have been identified in mammals and their structures and functions have been reviewed [50,51]. eIF4A1 and eIF4A2 take part in the eIF4F complex while eIF4A3 is involved in the nonsense-mediated decay machinery, a mechanism used by eukaryotes to eliminate mRNA transcripts which contain premature stop codons or nonsense mutations. eIF4A1 is highly expressed in actively dividing cells and is upregulated in various cancers. Conversely, eIF4A2 is present at high levels in resting cells and low levels of eIF4A2 has been associated with poor outcome for patients with breast and non-small-cell lung cancers [52,53]. In agreement with this finding, our analysis shows that *EIF4A1*

and *EIF4A3* are significantly increased in gliomas including GBM for the four subtypes compared to non-cancerous brain tissue whereas *EIF4A2* expression is significantly downregulated (Table 1). To the best of our knowledge, eIF4A proteins have not yet been investigated in human GBM samples by other teams and further studies should thus aim at confirming these data.

The RNA helicase activity of eIF4A1 and eIF4A2 as well as their interaction with eIF4G can be inhibited by programmed cell death 4 (PDCD4). PDCD4 prevents eIF4F complex assembly and consequently inhibits cap-dependent translation by binding eIF4A (Figure 1a). PDCD4 phosphorylation triggers its degradation which frees up eIF4A thus allowing eIF4F complex formation [54]. PDCD4 acts as tumor suppressor and is often decreased in cancer [55,56]. In 2007, Gao et al. studied PDCD4 at mRNA and protein levels in 30 glioma samples from grade I-II to grade IV. Using RT-PCR, western blot and immunocytochemistry, they found that PDCD4 was decreased in gliomas [57]. These findings were confirmed by our analysis of TCGA dataset but only for the classical GBM subtype. PDCD4 expression can be regulated at various levels including by miRNAs [58], some of which have been reported to be upregulated in GBM [59,60]. Inhibition of PDCD4, and consequently release of eIF4A and activation of translation, decreases apoptosis, promotes cell cycle arrest at G0/G1, and stimulates glioma stem cell proliferation as well as GBM cell invasiveness. Furthermore, enhanced expression of PDCD4 decreases tumorigenic capacity of glioma stem cells in vivo as demonstrated in a GBM xenograft mouse model [60].

Natural compounds including pateamine have also been shown to interfere with eIF4G and eIF4A interaction leading to a lower number of mRNA-associated ribosomes and subsequently to inhibition of translation initiation. However, pateamine has not yet been investigated in glioma cells and subsequent biological impacts on gliomas as well as other cancer types remain to be studied [61,62].

### 3.2. The 43S Preinitiation Complex (PIC): eIF1, eIF1A, eIF3, and eIF5

Following eIF4F complex formation on the m<sup>7</sup>GTP cap structure at the 5' UTR end of an mRNA, the 43S PIC is put into place. During this second step of translation initiation, eIF3 together with eIF1, a key factor in the initiation codon recognition [63], eIF1A and eIF5 associate with the 40S ribosomal subunit and the ternary complex to form the 43S PIC (Figure 1b) [64–68].

#### 3.2.1. eIF3

eIF3 is composed of 13 subunits in human and among these, five of them have been shown to be overexpressed in different cancer types, namely eIF3A, B, C, D, and E [69–73]. According to our REMBRANDT data analysis, all EIF3 subunits, except subunit K, are upregulated in gliomas (however not always in all glioma subtypes) relative to non-tumoral brain tissue. When considering the different GBM subtypes separately using the TCGA dataset, it appears that specific eIF3 subunits are preferentially overexpressed in different genetic subtypes. For example, *EIF3B*, *D*, *G*, and *I* subunits are significantly overexpressed in classical and mesenchymal subtypes, the later having the worst prognosis. Unfortunately, REMBRANDT and TCGA databases on Betastasis do not encompass the expression of *EIF3C* (Table 1). Nevertheless, eIF3C together with other eIF3 subunits have been studied in glioma tissues, in vitro and in vivo by other research teams [74–78].

In 2012, Liang et al. were the first to find evidence that eIF3 subunits could play a role in glioma. They investigated *EIF3B* expression by RT-PCR in gliomas ( $n = 10$ ) ranging from grade I to grade IV and found no significant difference between tumor grades. However, they found that reduction of eIF3B expression decreases cell proliferation, induces cell cycle arrest and triggers apoptosis in U87MG cells [76]. In a later study, the same group found that eIF3D is increased in gliomas ( $n = 35$ ) and that its inhibition in U87MG cells induces similar effects as what they obtained for eIF3B [77]. Sesen et al. (2014) studied eIF3E in human GBM cell lines and demonstrated that blocking its expression decreases GBM cell proliferation, blocks cell cycle and increases apoptosis [78].

In addition, eIF3C (which expression data are lacking in REMBRANDT and TCGA as evoked above) was investigated by immunohistochemistry in glioma samples ( $n = 83$ ). This study showed a

significant increase in eIF3C staining in glioma samples compared to staining detected in brain tissues from traumatic brain injury patients used as control ( $n = 25$ ). Increased levels of eIF3C positively correlated with tumor grades. Furthermore, it was demonstrated that inhibition of eIF3C in vitro using siRNA reduces cell proliferation, decreases colony formation, increases apoptosis and promotes cell cycle arrest in U87MG cells. Finally, these authors showed that lower eIF3C expression reduces tumor growth in vivo using a glioma xenograft mouse model [75].

Altogether, these studies corroborate our REMBRANDT and TCGA analyses and all support a role for eIF3 subunits in major biological processes and their potential involvement in gliomas. A study published during the preparation of this manuscript investigated all *EIF3* subunits expression in glioma using the Chinese Glioma Genome Atlas (CGGA,  $n = 272$ ) together with data from TCGA ( $n = 595$ ). Contrary to our findings showing that only specific *EIF3* subunits were overexpressed in all glioma subtypes, Chai et al. reported a significant increase for all subunits in glioma. The reason for this discrepancy is unclear but might be explained by the type of analysis used or the higher number of cases they analyzed [74]. Nevertheless, it can be concluded that eIF3 subunits are altered in gliomas and are involved in GBM cell proliferation. This conclusion is not surprising since eIF3 directly binds mRNA coding for proteins involved in the regulation of cancer cell growth including cell cycle arrest and apoptosis [79].

### 3.2.2. eIF1, eIF1A, eIF5, and eIF5B

eIF1 and eIF1A are two small peptides which act synergistically to induce and maintain a conformational change in the 40S ribosomal subunit and promote an open conformation permitting efficient mRNA scanning. Once the 43S PIC scanning complex recognizes the start codon and the Met-tRNA<sub>i</sub> anticodon associates with it, eIF1 is released and eIF2-GTP is converted to eIF2-GDP with the help of eIF5, the eIF2 GTPase activating protein (Figure 1). Ejection of eIF1 from 40S induces a switch from an open to closed conformation thus probably ending the scanning step [80]. Finally, eIF5B together with eIF1A triggers the dissociation of most remaining eIFs and facilitates the assembly of the 60S ribosomal subunit to form the 80S complex [80,81].

The expression of eIF1 and eIF1A have not yet been studied in gliomas. Here, we found no change in mRNA levels between control brain tissue and any of the three gliomas subtypes (Table 1). However, as shown in the analysis of the REMBRANDT dataset, eIF1A domain-containing protein (*EIF1AD*) was significantly overexpressed in oligodendrogliomas and GBM. eIF1AD is an analogue of eIF1A. The role of eIF1AD is still unclear but its analogy with eIF1A suggests its involvement in ribosome biogenesis or protein synthesis [81]. The fact that *EIF1AD* but not eIF1 or eIF1A, is abnormally expressed in gliomas should encourage studies aiming at elucidating its function, in particular in gliomas.

Finally, we have analyzed *EIF5* and *EIF5B* expression in gliomas and found that *EIF5* is downregulated in astrocytomas and in GBM, only for the mesenchymal and proneural subtypes (Table 1). In addition to its role in the cap-dependent translation, eIF5B can act as ITAFs and is thus involved in the IRES-dependent initiation. So far, the involvement of eIF5B in gliomas has only been studied in the context of IRES-dependent translation and will therefore be discussed in the cap-independent section [82].

### 3.3. Additional eIFs: eIF4B, eIF4H, and eIF6

In addition to eIFs taking part in the eIF4F and 43S PIC complexes, crucial adjunct eIFs including eIF4B, eIF4H, and eIF6 also coordinate translation initiation.

#### 3.3.1. eIF4B/eIF4H

eIF4B and its paralogue eIF4H are chaperone proteins able to bind mRNA and eIF4A to stabilize unwound mRNA and stimulate eIF4A RNase and helicase activities [83,84]. Current literature on the role of eIF4B and eIF4H suggests a role in cell survival, cell proliferation, resistance to chemotherapy, and cell migration [85–87]. The expression and the role of eIF4B or eIF4H in gliomas have not yet

been studied in details; however, the REMBRANDT data analysis shows a significant increase in *EIF4B* expression in oligodendrogliomas whereas no alteration was observed for neither of the two paralogues in GBM and astrocytomas compared to non-tumoral tissues. Though when GBM subtypes are considered separately using the TCGA database, *EIF4H* is downregulated in GBM but only in the proneural subtype (Table 1). As eIF4B activity is regulated at least partially by phosphorylation including on Ser422 by the S6-kinase 1 (S6K1) (Figure 2) [87,88], phosphorylation state of eIF4B and eIF4H should also be considered when studying gliomas.

### 3.3.2. eIF6

Thanks to its double localization in the nucleus and in the cytoplasm, eIF6 takes part in ribosome biogenesis and maturation, respectively [89]. eIF6, also known as p27(BBP) or  $\beta$ 4 integrin interactor, binds the 60S ribosomal subunit in the nucleus and, once in the cytoplasm, dissociates from 60S which leads to formation of the 80S complex and subsequent protein synthesis (Figure 1c,d) [90]. Its implication in human cancers has recently been reviewed by Zhu W. and colleagues [89]; however, its function and expression in gliomas remain unknown, with a single study published in 2014 by Saito K. et al. which demonstrated an indirect role for eIF6 in ribosomal biogenesis using U87MG cells. In fact, impaired expression of elongation factor Tu-GTP binding domain containing protein 1 (*EFTUD1*) involved in ribosome biogenesis, delocalizes eIF6 from the nucleus to the cytoplasm in U87MG cells. *EFTUD1* being overexpressed in gliomas might alter eIF6 subcellular localization and consequently prevent eIF6 from performing its functions [91]. Supporting a role for eIF6 in gliomas, we found that *EIF6* is overexpressed in gliomas including in GBM for all subtypes except the proneural (Table 1).

### 3.4. Ternary Complex (eIF2-GTP and the Initiator Methionyl-Transfer RNA)

eIF2 is a switch protein that associates with GTP and Met-RNAi to form the Ternary complex. This complex then binds the 40S ribosomal subunit together with several eIFs to give rise to the 43S PIC which will first associate with the eIF4F complex then scan the 5' end of mRNA until it reaches the initiation codon (Figure 1b,c). Upon association of the 40S with the 60S ribosomal subunit, eIF2 latent GTPase enzymatic activity is released and eIF2-bound GTP is converted to GDP. This is the signal for eIFs to dissociate from the complex, ending the translation initiation step, and for protein synthesis to start with the elongation phase (Figure 1d) [15]. Once in its eIF2-GDP form, eIF2 is bound to eIF5 and is no longer active. eIF2B is then required to induce the dissociation of eIF2-GDP from eIF5 and for the catalytic exchange of GDP to GTP (Figure 1d) [92,93]. eIF2B comprises five subunits annotated  $\alpha$ - $\epsilon$  and coded by *EIF2B1-5* genes respectively. The  $\alpha$ ,  $\beta$ , and  $\delta$  subunits recognize phosphorylated eIF2 $\alpha$  and modulate eIF2B activity by regulating the catalytic subunits  $\gamma$  and  $\epsilon$  [94–96]. The catalytic subunit  $\epsilon$  is overexpressed in different human cancers and is involved in tumorigenicity [97]. The non-catalytic subunits have been less studied in cancers and none of the eIF2B subunits were investigated in gliomas. In our analysis of gene expression, all *EIF2B* subunits except *EIF2B3* (encoding the  $\gamma$  subunit) are overexpressed in gliomas compared to non-tumoral brain tissue. On the contrary, the *EIF2B3* subunit is down-regulated in gliomas including in GBM, but only in the classical subtype (Table 1).

eIF2 is a heterotrimeric structure composed of three subunits ( $\alpha$ ,  $\beta$ , and  $\gamma$ ) coded by three distinct genes *EIF2S1-3*, respectively [98]. *EIF2S1* is not significantly differentially expressed in gliomas compared to non-tumoral brain tissues nor in GBM when the different subtypes are considered individually. *EIF2S2* and *EIF2S3*, on the other hand, are both upregulated in gliomas with the  $\gamma$  isoform being the only subunit to be overexpressed in the mesenchymal GBM subtype compared to non-tumoral tissue (Table 1).

Phosphorylation of the eIF2 $\alpha$  subunit plays a major role in the regulation of mRNA translation as it blocks the catalytic exchange of GDP to GTP catalyzed by eIF2B and, as a result, triggers the arrest of translation initiation [99]. It is therefore crucial to also consider eIF2 $\alpha$  phosphorylation status. Accordingly, some of the pathways involved in the regulation of eIF2 $\alpha$  phosphorylation and known to be disturbed in gliomas will be discussed below.

Four kinases are able to phosphorylate eIF2 $\alpha$ : HRI, PKR, PERK, and GCN2 encoded by *EIF2AK1*, *EIF2AK2*, *EIF2AK3*, and *EIF2AK4*, respectively. During cellular stress, these kinases phosphorylate eIF2 $\alpha$  on Ser51 to decrease global mRNA translation and allow cell adaptation to environmental conditions. These kinases are not activated by the same stress. HRI is activated by heme deficiency, PKR by viral infection, PERK by endoplasmic reticulum (ER) stress and GCN2 by decreased essential amino acids [100]. According to the REMBRANDT database, *EIF2AK1* is significantly overexpressed in gliomas compared to non-tumoral brain tissues (Table 1) which is in agreement with a TCGA analysis from Haapa-Pananen S. et al. in 2013. However, the latter considered all GBM subtypes together and performed a student *t*-test. In our TCGA analysis, the four GBM subtypes were considered separately and analyzed by a one-way analysis of variance (ANOVA) test which revealed no significant change in *EIF2AK1* expression. Nevertheless, blocking *HRI* expression using miRNA decreased proliferation and increased apoptosis in GBM cells [101]. PKR, the second eIF2 $\alpha$  kinase, is generally activated by dsRNA from virus infecting cells. Once PKR is activated, it inhibits cell growth and protein synthesis to allow cell adaptation to environmental conditions [100]. This activation could therefore be used to inhibit protein synthesis and subsequently cell growth in glioma cells. Shir A. et al. have indeed demonstrated that, when complementary RNA specific to RNA from GBM cells is injected in these cells, dsRNA can be reconstituted to activate PKR. This activation induces GBM cell apoptosis in vitro and in vivo [102,103]. As activated PKR inhibits cell growth, it is surprising to note that *EIF2AK2* expression is significantly higher in gliomas compared to non-tumoral brain tissues (Table 1). However, as PKR activation is necessary for eIF2 $\alpha$  phosphorylation, it is possible that assessing the expression of its gene *EIF2AK2* is not sufficient to assess its function in gliomas. *EIF2AK3*, the gene coding for PERK, is overexpressed in GBM compared to non-tumoral brain tissue but not in the other two gliomas subtypes. Also, surprisingly, when GBM subtypes are considered separately using the TCGA dataset, this significance is lost (Table 1). The implication of PERK in glioma cell biology will be described in the ER stress section. Finally, decrease in levels of essential amino acids activates GCN2, leading to eIF2 $\alpha$  phosphorylation and activation of activating transcription factor 4 (ATF4). ATF4 is a transcription factor able to modulate amino acid response elements (AAREs)-containing genes [104]. In LN229 GBM cells, tryptophan (Trp) depletion activates the GCN2-p-eIF2 $\alpha$ -ATF4 pathway but does not decrease protein synthesis. This pathway activation leads to tryptophanyl-tRNA synthetase overexpression. This last enzyme increases Trp incorporation in cancer cell proteins despite a lack of this amino acid in the environment. GCN2-p-eIF2 $\alpha$ -ATF4 pathway could therefore maintain protein synthesis despite a decrease in essential amino acids in the environment [105]. Interestingly, we found that *EIF2AK4* (coding for GCN2) is increased only in GBM compared to non-tumoral brain tissues (Table 1). As for the other three kinases involved in eIF2 $\alpha$  phosphorylation, our analysis of the TCGA database shows that *EIF2AK4* is not differentially expressed in GBM when the four subtypes are considered separately (Table 1).

The ER stress response is a good illustration of the role of eIF2 $\alpha$  phosphorylation in the regulation of protein synthesis. Environmental stressors are prompt to trigger ER stress during which unfolded or misfolded proteins accumulate in the ER lumen thereby triggering an adaptive response called the “unfolded protein response” (UPR) [9,106]. During the UPR, cells under stress stop protein synthesis, attempt to refold proteins, and eventually trigger apoptosis if ER stress is too intense or persistent. Cancer cells, however, manage to survive in challenging environmental conditions particularly thanks to the UPR pathway in which eIF2 $\alpha$  is implicated. The role of the UPR in cancer and in GBM has recently been reviewed [9,106]. We encourage readers to refer to Figure 1 published in the review from Obacz et al. (2017) to obtain a good illustration of the players involved in the UPR pathway [9]. During the UPR, the glucose regulated protein 78KDa (GRP78 or BIP) expressed in the ER lumen, binds to misfolded or unfolded proteins and dissociates from transmembrane ER stress sensors such as activating transcriptional factor 6 (ATF6), inositol-requiring enzyme 1 (IRE1) and protein kinase-like ER kinase (PERK). Only the role of PERK will be described in this review as it is the only UPR actor controlling mRNA translation. After GRP78 dissociation from PERK and its activation upon

phosphorylation, eIF2 $\alpha$  gets phosphorylated on Ser51 leading to repression of protein synthesis [107]. PERK also controls translation of the transcription factor ATF4 in order to modulate the expression of foldase/chaperon and autophagy genes but also cytidine-cytidineadenosine-adenosine-thymidine (CCAAT)/enhancer binding homologous protein (CHOP) expression to control cell apoptosis [9,108].

In glioma cells, ER stress triggered by different drug treatments increases p-eIF2 $\alpha$  in conjunction with elevated expression of other ER stress transducers (i.e. p-ERK, ATF6, p-IRE-1, GRP78, CHOP, XBP-1) enhancing glioma cell death [109–111]. Interestingly, ER stress can also induce glioma cell autophagy through eIF2 $\alpha$  and decrease tumor cell survival [112–115]. However, inhibition of autophagy with various drug treatments decreases p-4E-BP1, p-70S6K1, and the ribosomal S6 protein and increases expression of CHOP and p-eIF2 $\alpha$  levels leading to glioma cell death. These last observations therefore suggest that autophagy could have a cytoprotective or cytotoxic effect in glioma cells through various ER stress transducers [112,116,117].

As already and briefly mentioned, another challenge in the therapeutic strategy for GBM is constitutively variable resistance to TMZ, which can develop after or during treatment. DNA alkylation damage induced by TMZ can be repaired by the DNA repair enzyme O6-methylguanine methyltransferase (MGMT) which can be overexpressed in GBM and cause TMZ resistance. MGMT inhibitors have therefore been studied in order to overcome TMZ chemoresistance. Bortezomib, a Food and Drug Administration (FDA), and European Medicines Agency (EMA) approved proteasome inhibitor used for the treatment of multiple myeloma, stabilizes poly-ubiquitinated proteins, and triggers cell cycle arrest and cell death [118]. Interestingly, Bortezomib decreases NF $\kappa$ B and MGMT mRNA amounts, but can also induce eIF2 $\alpha$  phosphorylation to decrease protein synthesis of MGMT and therefore acts as translational repressor of MGMT. These two effects of Bortezomib lead to inhibition of DNA repair in T98G GBM cells and is therefore expected to sensitize cells to TMZ [119]. However, through eIF2 $\alpha$  phosphorylation, Bortezomib also induces stress granules formation and increases GBM cell resistance to death signals [120]. Despite promising effects in cultured GBM cells, Bortezomib did not show sufficient efficacy in GBM patients during phase II clinical trials [121]. This was further supported by others using in vitro experiments showing that Bortezomib also increases Akt and 4E-BP1 phosphorylation in GBM cell lines leading to cell division [122]. TMZ also acts as an ER stress inducer leading to dissociation of PERK from prolyl 4-hydroxylase beta polypeptide (P4HB), a chaperone protein implicated in ER stress. PERK thereby phosphorylates eIF2 $\alpha$  and triggers GBM cell apoptosis due to protein synthesis arrest. One explanation for GBM cell resistance to TMZ is P4HB overexpression found in recurrent and TMZ-resistant GBM tumors. P4HB suppression with siRNA or bacitracin therefore bypasses TMZ resistance and sensitizes GBM cells to TMZ-induced ER stress [123]. Finally, TMZ resistance has also been linked with cap-independent translation and this will be discussed in the appropriate section below [28,124,125].

#### 3.4.1. PI3K/Akt/mTOR, MAPK/MNK, and AMPK Regulating Pathways

A number of studies have demonstrated that key pathways which regulate major metabolic functions, such as PI3K/Akt/mTOR, MAPK/MNK, and AMPK pathways, are deregulated in cancers including in gliomas. These pathways are also known to be involved in the regulation of protein synthesis [126–132]. The involvement of these pathways on the regulation of eIFs and their effect on translation in gliomas will successively be described in the following parts (Figure 2).

#### 3.4.2. PI3K/Akt/mTOR pathway

mTOR, a downstream effector of PI3K/Akt pathway, controls cell growth, survival, and motility through protein, lipid, and nucleotide synthesis regulation in response to environmental conditions. mTOR is a serine/threonine (Ser/Thr) protein kinase which is the core of two protein complexes: mTORC1 and mTORC2 [133–136]. mTORC1 and mTORC2 activities are high in different types of cancer including malignant gliomas. mTORC1 modulates the activity of 4E-BP1 and S6K to control protein synthesis and cell growth. 4E-BP1 phosphorylation through mTORC1 leads to 4E-BP1/eIF4E

dissociation. As previously described, free eIF4E can thereby bind the cap structure and eIF4G, and promote eIF4F complex formation leading to protein synthesis. mTORC1-mediated S6K activation modulates the phosphorylation status of several substrates involved in protein synthesis including eIF4G, eIF4B, and PDCD4 leading to protein synthesis activation. In contradiction with data obtained for p-70S6K1, levels of p-4E-BP1 correlate with glioma grade and with patient overall survival, making it a potential prognosis factor to select patients who might benefit from mTOR inhibitor therapies [137]. mTORC2 associates with ribosomes to regulate cell cytoskeleton reshuffle and metabolism [138]. In addition to its well-known function, mTORC2 activates Akt, a kinase also largely implicated in cancers and protein synthesis.

eIF4E/4E-BP1 association controlled by PI3K/Akt/mTOR pathway is a critical step in the translation initiation making this pathway an interesting target for gliomas treatment. For example, Enzastaurin blocks Akt phosphorylation and thus represses PI3K/Akt pathway, decreases 4E-BP1 phosphorylation, and consequently the formation of the eIF4F complex, leading to apoptosis in GBM cells [139]. In addition, N1,N11-diethylnorspermine (DENSP) which targets the polyamine pathway, has been shown to decrease the expression of mediators of mTOR pathway (i.e., Akt, p-Akt, mTOR, p-mTOR, p-70S6K1, p-p70S6K1, 4E-BP, and p-4E-BP) in GBM cells and to reduce mTOR dependent protein synthesis [140]. mTORC1 is the direct target of rapamycin, an antifungal, immunosuppressive, and antitumor agent. However, rapamycin treatment presumably also inhibits the negative feedback from S6K1 to insulin receptor substrate 1 (IRS1) leading to Akt activation [141]. mTORC1 inhibition with rapamycin analogues (i.e., rapalogs) monotherapy therefore increases Akt-eIF4E pathway and generates therapeutic resistance which has already been widely studied [129,142]. That is why scientists have combined rapamycin analogues with drugs targeting alternative pathways of protein synthesis. For example, Genistein and Biochanin A, two isoflavones used as chemopreventive drugs, block tyrosine kinase receptor (TKR)-Akt pathway and eIF4E phosphorylation in order to sensitize U87MG cells to rapamycin [142]. The association of eEKi-785, a TKR inhibitor, with rapamycin also increases eIF4E-4E-BP1 binding and therefore decreases growth capacity of GBM cells in vitro [143]. Drug combinations targeting the PI3K/Akt/mTOR pathway alter cell growth capacity in vitro and in vivo through eIF4E-4E-BP1 regulation. However, direct consequences of drug combinations on global protein synthesis remain to be demonstrated.

### 3.4.3. MAPK/MNK Pathway

MNKs (see above), downstream effectors of MAPK pathway, are Ser/Thr kinases able to phosphorylate eIF4E to promote mRNA translation initiation [22]. Interestingly, the two members of the MNK family, MNK1, and MNK2, are overexpressed in GBM [126,144]. MNK1 and 2 share a lot of similarities. They are both able to phosphorylate eIF4E even if they are not equally sensitive to the recruitment by the MAPK pathway [126,145]. Once activated, MNKs associate with the C-terminal domain of eIF4G in order to phosphorylate eIF4E on Ser209 [43,146]. This eIF4E phosphorylation increases its affinity for the m7GTP cap of mRNA. As a consequence, eIF4E deregulation by MNKs promotes cancer cell proliferation, malignant transformation and metastasis [19,41,147]. Interestingly, the constitutive activation of MAPK pathway in GBM induces the phosphorylation of MNK1 and its activation [146,148]. p-eIF4E and p-MNK1 overexpression was also associated with a decreased overall survival of patients with astrocytoma [19].

In line with these observations, MNKs could thus be relevant targets for glioma treatments. Recently developed selective MNKs inhibitors can now be used as potential anticancer therapy. For example, Merestinib inhibits several protein kinases including MNKs, leading to decreased p-eIF4E and increased overall survival of GBM xenograft mice [144]. Other inhibitors of MNKs activity, like CGP57380 and Cercosporamid, have also been correlated with decreased eIF4E phosphorylation, cell cycle arrest, and increased sensitivity of GBM cells to TMZ [149,150]. Silencing of MNK1 with shRNA in U87MG cells decreases their tumorigenicity in a glioma xenograft mouse model [126]. It has also been demonstrated that rapamycin, an mTORC1 inhibitor, can upregulate MNKs pathway and

confers resistance to this therapy [129]. The combination of MNKs and mTORC1 inhibitors further inhibits 4E-BP1 phosphorylation at Ser65, increases eIF4E/4E-BP1 association and inhibits glioma cell protein synthesis and proliferation [129]. To illustrate the importance of MNKs pathway in gliomas, a drug called Arsenic trioxide (ATO) (used and approved by the FDA for the treatment of acute promyelocytic leukaemia (APL) with t(15;17) translocation) demonstrated resistance in patient-derived xenograft model of GBM. ATO resistance correlates with higher MNK1 kinase activity and mRNA translation through the MNK/eIF4E pathway. GBM stem cells belonging to the mesenchymal subtype are resistant to ATO and the use of MNK1 inhibitor in combination with ATO could potentially sensitize them to the treatment [127].

#### 3.4.4. AMPK Pathway

AMP-activated protein kinase (AMPK), a highly conserved Ser/Thr kinase, is a sensor of cellular energy allosterically regulated by intracytoplasmic AMP concentration. In conditions of nutrient deprivation, intracellular AMP/ATP ratio increases and activated AMPK is then able to inhibit mTORC1. AMPK is implicated in tumor development and in the regulation of protein synthesis through modulation of mTOR pathway [130,151,152]. AMPK activation by flavones such as Hispidulin and Wogonin as well as other drugs already under clinical investigation like Metformin and 5-aminoimidazole-4-carboxamide ribonucleotide (AICAR) suppresses the mTOR pathway and decreases p-4E-BP1 causing apoptosis and cell cycle arrest in GBM cell lines [153–160]. Wogonin also induces GBM cell apoptosis by inducing ER stress during which protein synthesis is impaired and this implication will be discussed in the next section [109]. Regarding Metformin and AICAR, their modes of action are however not totally dependent on AMPK inhibition [160,161]. They can indeed block cell cycle through direct inhibition of mTOR and by increasing cdc25c phosphatase degradation, respectively [161]. The role of cdc25 phosphatase is to dephosphorylate various cyclin-dependent kinases during cell cycle, allowing its progression. GBM cell apoptosis mediated by AMPK activation is nevertheless in conflict with the observation of the constitutively active status of AMPK in GBM and with the anti-glioma effect of Compound C, also known as dorsomorphin, through its capacity to inhibit AMPK activity [162]. Inhibition of AMPK caused by Compound C is nonetheless not the only event responsible for GBM cell death [161,163]. This discrepancy in the effect of activation or inhibition of AMPK on GBM cells may be the consequence of multiple roles for AMPK in tumors. Indeed, active AMPK inhibits protein synthesis and lipogenesis thereby interfering with tumor growth [157]. AMPK also promotes metabolic reprogramming of cancer cells undergoing metabolic stresses, leading to cancer survival and progression despite an unfavorable environment [164].

#### 4. IRES-Dependent Initiation

In addition to the canonical cap-dependent mode of translation (reviewed above), the IRES-dependent mode of initiation has gained interest in the recent years, in the research field of cancer in particular. IRES, first discovered in viruses, consists of RNA secondary structures present in the 5' UTR end of mRNAs, upstream of the AUG start codon. IRES allows the association of the 40S small ribosomal subunit with mRNA through interaction with trans-activator factors (ITAFs), thus triggering the initiation of translation in a cap-independent manner [17]. ITAFs can be classified into three categories: class I includes ITAFs localized in the nucleus which are able to translocate to the cytoplasm, class II ITAFs are present only in the cytoplasm and class III are non-coding RNA (Table 2) [17]. IRES structures were later discovered in cellular mRNAs and have since been postulated to play a role in cancer development [14]. The first eukaryotic cellular IRES was discovered in the mRNA coding for GRP78 or BiP, a key player in the UPR pathway [165]. Additional cellular IRES have since been identified in mRNA encoding proteins involved in major biological processes such as c-myc, cyclin D1, EGFR, and c-jun [28,124,125,166,167]. Furthermore, a role for IRES in cancer development and resistance has been demonstrated and there is evidence that targeting the IRES machinery could be used as a therapeutic approach for the treatment of cancers, including gliomas [168].



**Table 2.** Expression of IRES trans-acting factors in gliomas. Internal ribosomal entry site (IRES) trans-acting factors (ITAFs) can act as activator (A) or inhibitor (I) of cap-independent translation. Class I ITAFs are localized in the nucleus and can translocate to the cytoplasm; class II ITAFs are only present in the cytoplasm [17]. The expression of ITAFs reviewed by Godet AC et al. (2019) was compared between control brain tissue ( $n = 21$ ) and gliomas (oligodendrogliomas,  $n = 66$ ; astrocytomas,  $n = 145$ ; glioblastoma multiform (GBM),  $n = 214$ ) using the REMBRANDT database. ITAF expression from control tissue ( $n = 11$ ) was then compared to expression found in the four GBM subtypes defined by the Verhaak’s classification (classical,  $n = 54$ ; menchymal,  $n = 58$ ; neural,  $n = 33$ ; proneural,  $n = 57$ ) using the TCGA dataset. These two datasets were obtained through the independent Betastasis genomics analysis and visualization platform. GraphPad Prism (version 5.03 for Windows, GraphPad Software, San Diego California USA, www.graphpad.com) was used for statistical analysis. D’Agostino & Pearson omnibus normality test was used to control for normal distribution. One-way analysis of variance (ANOVA) followed by Bonferroni’s Multiple Comparison Test was used for parametric analysis and if required, Kruskal-Wallis test followed by Dunn’s Multiple Comparison Test was performed for non-parametric analysis. ns: not significant, +/-  $p < 0.05$ , ++/-  $p < 0.01$ , and +++/-  $p < 0.001$  where “+” and “-” indicate an increase and a decrease in expression, respectively. # indicates ITAFs also acting as eIFs, REMBRANDT: REpository for Molecular BRAin Neoplasia DaTa; TCGA: The Cancer Genome Atlas.

ITAFs	Gene	REMBRANDT			TCGA				Activity
		Oligodendroglioma	Astrocytoma	GBM	Classical	Mesenchymal	Neural	Proneural	
<b>Class I</b>									
Annexin A2	<i>ANXA2</i>	ns	++	+++	+++	+++	+	ns	A
CUGBP1	<i>CUGBP1</i>	ns	ns	ns	ns	--	---	ns	A/I
DAP5 #	<i>EIF4G2</i>	+++	ns	+++	ns	ns	ns	ns	A
FBP3	<i>FUBP3</i>	+++	+++	+++	+++	+++	+	+++	A
FUS	<i>FUS</i>	+++	+++	+++	++	ns	ns	+++	A
GRSF1	<i>GRSF1</i>	---	---	---	--	---	ns	-	A
H-ferritin	<i>FTH1</i>	ns	ns	ns	ns	ns	ns	ns	A
HDMX	<i>MDM4</i>	+++	+++	+++	ns	ns	ns	++	A
hnRNPA1	<i>HNRNPA1</i>	+++	++	ns	++	ns	ns	+++	A/I
hnRNPC	<i>HNRNPC</i>	+++	+++	+++	ns	ns	ns	ns	A
hnRNPD	<i>HNRNPD</i>	+++	+++	+	ns	ns	ns	ns	A
hnRNPE1	<i>PCBP1</i>	ns	ns	++	ns	ns	ns	ns	A
hnRNPE2	<i>PCBP2</i>	+++	+++	+++	+	ns	ns	+++	A

Table 2. Cont.

ITAFs	Gene	REMBRANDT			TCGA				
		Oligodendroglioma	Astrocytoma	GBM	Classical	Mesenchymal	Neural	Proneural Activity	
hnRNPE3	PCBP3	ns	ns	---	---	---	--	--	A
hnRNPE4	PCBP4	++	ns	ns	ns	ns	ns	+++	A
hnRNPH2	HNRNPH2	ns	ns	---	---	---	--	--	A
hnRNPK	HNRNPK	+++	+++	+++	++	ns	ns	+++	A
hnRNPL	HNRNPL	ns	ns	ns	ns	ns	ns	+++	A
hnRNPM	HNRNPM	+++	+++	+++	++	ns	ns	ns	A
hnRNPO	SYNCRIP	+++	+++	+++	+	ns	ns	++	A
hnRNPR	HNRNPR	++	+++	+++	ns	ns	ns	+	A
HuR	ELAV1	+	+	+++	---	---	---	ns	A/I
La auto antigen	SSB	+	+	++	ns	ns	ns	ns	A/I
Mdm2	MDM2	+++	+++	+++	ns	+	+	ns	A
NF45	ILF2	+++	+++	+++	++	ns	+++	+++	A
nPTB	PTBP2	---	--	---	---	---	ns	ns	A
nucleolin	NCL	Not available			ns	ns	ns	ns	A/I
p54nrb	NONO	+++	+++	+++	+++	++	ns	+++	A
PDCD4 #	PDCD4	ns	ns	ns	--	ns	ns	ns	A/I
PSF	SFPQ	++	ns	ns	ns	ns	ns	+	A/I
PTB	PTBP1	+++	+++	+++	+++	+++	ns	+++	A/I
RHA	DHX9	+++	+++	+++	ns	ns	ns	+	A
SMAR 1	BANP	+++	+++	+++	+	++	+++	++	A/I
YB1	YBX1	+++	+++	+++	+++	++	+	+++	A
<b>Class II</b>									
4E-BP1 #	EIF4EBP1	+++	+++	+++	+	+++	++	+++	A
APP (AICD)	APP	---	---	---	---	---	---	---	A
eeF1A2	EEF1A2	---	---	---	---	---	-	-	A
eIF3A #	EIF3A	+++	+++	ns	ns	ns	ns	ns	A
eIF3B #	EIF3B	+++	+++	+++	+++	+++	ns	++	A
eIF3D #	EIF3D	+++	+++	+++	+	++	ns	++	A
eIF3E #	EIF3E	+++	+++	+++	ns	ns	ns	ns	A
eIF3F #	EIF3F	+++	+++	+++	ns	ns	ns	ns	A
eIF3G #	EIF3G	+++	+++	+++	+++	++	++	++	A
eIF3H #	EIF3H	+++	+++	+++	ns	ns	ns	ns	A
eIF3I #	EIF3I	ns	ns	+++	+	+	+++	ns	A
eIF3J #	EIF3J	+	ns	ns	ns	ns	ns	ns	A
eIF3K #	EIF3K	ns	ns	ns	ns	ns	+	ns	A
eIF3L #	EIF3L	+++	+++	ns	ns	ns	ns	ns	A
eIF3M #	EIF3M	+++	++	+++	ns	ns	ns	ns	A
eIF4A1 #	EIF4A1	+++	+++	+++	++	+++	+	+++	A
eIF4A2 #	EIF4A2	---	---	---	---	---	ns	---	A
eIF4A3 #	EIF4A3	+++	+++	+++	+	++	+++	++	A
eIF4G1 #	EIF4G1	+++	+++	+++	ns	ns	ns	ns	A
eIF5B #	EIF5B	+++	+++	+++	ns	ns	ns	ns	A
eL38	RPL38	+++	+++	++	-	ns	ns	ns	A

Table 2. Cont.

ITAFs	Gene	REMBRANDT			TCGA				
		Oligodendroglioma	Astrocytoma	GBM	Classical	Mesenchymal	Neural	Proneural Activity	
eS19	RPS19	+++	+++	+++	+++	+++	+++	++	A
eS25	RPS25	+++	+++	+++	ns	ns	++	ns	A
Gemin5	GEMIN5	+++	+++	+++	+	+	ns	++	A/I
Hepsin	HPN	---	---	-	ns	ns	ns	ns	I
PINK1	PINK1	---	---	---	---	---	---	---	A
Rack1	GNB2L1	+++	+++	+++	+++	+++	+	+++	A/I
TCP80	ILF3	+++	+++	+++	+++	ns	ns	+++	A
uL1	RPL10A	+++	+++	+++	ns	ns	++	ns	A
uL24	RPL26	Not available			ns	ns	ns	ns	A
uL5	RPL11	+++	+++	+++	ns	+++	+	+++	A
VASH1	VASH1	+	++	+	++	ns	ns	++	A

As already discussed above, the mTOR pathway is often altered in gliomas and has led to the development of mTOR inhibitors as a therapeutic approach. Resistance to mTOR inhibitors used as monotherapy is related to the degree of Akt activity. Cancer cells with high Akt activity are sensitive to the mTORC1 inhibitor rapamycin, whereas cancer cells with low Akt activity are resistant. Unfortunately, the majority of GBM cases have low Akt activity and are thus likely to be resistant

to mTORC1 inhibition [169]. One of the mechanisms used by GBM cells to resist mTOR inhibitors involves an increase in IRES-dependent translation and thus an upregulation of proteins coded by IRES-containing mRNAs such as c-myc and cyclin D1, two well-known proto-oncogenes [28,124,125]. The treatment of GBM cells presenting low Akt activity with rapamycin activates p38 which in turn triggers IRES mediated translation of c-myc and cyclin D1. Inhibition of p38 genetically, using siRNA, or chemically, prevents rapamycin induced c-myc and cyclin D1 expression. Furthermore, combining mTORC1 and p38 inhibitors significantly enhances G1 cell cycle arrest, increases apoptosis, decreases proliferation in GBM cells in vitro, and inhibits tumor growth in vivo [28]. In addition, Akt activation leads to phosphorylation of hnRNPA1, an ITAF belonging to Class I, which subsequently leads to the inhibition of IRES-dependent translation. Using immunohistochemical and western blot analyses on GBM samples ( $n = 22$ ), they found that elevated Akt activity correlated with increased hnRNPA1 phosphorylation levels [125]. Furthermore, they identified a novel compound able to block the association between hnRNPA1 and its IRES structure localized on c-myc and cyclin D1 which therefore blocks c-myc and cyclin D1 translation and consequently sensitizes GBM cells to mTOR inhibitors. Combining IRES and mTOR therapies significantly decreases GBM cell proliferation in vitro, reduces tumor size in vivo, and increases overall survival in mice grafted with GBM cells [124]. Together, these findings therefore suggest that combined therapy targeting mTORC1 and IRES dependent translation might be a suitable approach for the treatment of GBM [28,124]. Another example highlighting the importance of IRES-dependent translation in gliomas was published by Blau et al. in 2012. They found that c-Jun, a transcription factor often increased in cancer, was overexpressed in GBM at protein levels but not at the level of transcription. They excluded that higher levels of c-jun resulted from accumulation of the protein and more importantly, they demonstrated that this change in c-jun expression was due to an increase in translation in an IRES-dependent manner [166]. Furthermore, the epidermal growth factor receptor (EGFR) is often mutated and overexpressed in cancers including in GBM where increased wild type EGFR can often be observed. Hypoxia, present in GBM microenvironment, is an inhibitor of cap-dependent translation through phosphorylation of eIF2 $\alpha$  and an activator of IRES-dependent translation. EGFR protein expression is increased under hypoxic conditions without changes in mRNA levels. This can be explained by the presence of an IRES structure in the 5' UTR region of EGFR mRNA which allows its translation in the presence of eIF4A acting as an ITAF (see Table 2) [167].

In addition to hnRNPA1 studied by Holmes et al., other ITAFs have been identified in recent years and have been reviewed [17]. ITAFs have several roles aside from regulating IRES-dependent translation. Interestingly, some ITAFs are known to also act as eIFs (Table 2). Moreover, several ITAFs can act as RNA binding proteins (RBP) thereby modulating mRNA stability and translation of different transcripts depending on cell needs. This additional step in the control of mRNA translation will not be described in this review as our focus is the initiation step of translation. We therefore encourage readers to refer to review from Wurth L. and Gebauer F. (2015) for more information about the roles of RBPs in cancers [170]. As part of our work, we have investigated the expression of ITAFs reviewed by Godet et al. (2019) in gliomas using REMBRANDT and TCGA datasets and found that the expression of the majority of ITAFs are altered in gliomas with both increases and decreases being observed (Table 2). According to the REMBRANDT dataset, 78% of investigated ITAFs are overexpressed, 14% are downregulated, and 7.8% are unchanged in gliomas relative to controls. When focusing on GBM subtypes using TCGA database, we found that only 54.5% of ITAFs are increased in GBM tissue whereas 18.2% are significantly decreased and 27.3% of ITAFs are not altered. Altogether, these results suggest an overall overexpression of ITAFs in gliomas which is in agreement with current literature supporting a role for cap-independent translation in cancer including gliomas [168,171]. Additional ITAFs are likely to be identified in the future. In addition, most ITAFs discovered so far have been identified as activators of IRES-dependent translation; however, further work is still required to better understand the role of each ITAF and their potential interaction to unravel their possible implication in glioma development and progression. This is particularly true and important for ITAFs

which are also involved in the cap-dependent translation. For example, eIF5B, mostly studied for its role in assembling the small and large ribosomal subunits during cap-dependent translation, has been found to be necessary for the translation of IRES containing mRNAs during cellular stress [172]. eIF5B therefore plays an activating role in cap-dependent and IRES-dependent translation. eIF5B is often overexpressed in cancer which is in agreement with our REMBRANDT data analysis showing that *EIF5B* is overexpressed in gliomas (Table 2) [172]. Interestingly, silencing *EIF5B* in GBM cells stimulates the expression of XIAP, a protein involved in apoptosis which includes an IRES motif in its mRNA. Consequently, suppression of *EIF5B* in GBM cells increased their sensitivity to apoptosis through caspase activation [172]. Other examples of eIFs which have been found to be involved in IRES-dependent translation are eIF4G1 and eIF4G2 where the latter is also known as DAP5. During apoptosis, caspases cleave eIF4G1 into fragments which blocks cap-dependent translation. eIF4G1 cleavage releases a smaller fragment containing the eIF3-eIF4A-binding domain (m4G) which is able to drive IRES-dependent translation. The N-terminal extremity of DAP5 is similar to the m4G domain and can therefore also activate IRES-dependent translation [42]. Indeed, using a cell-free in vitro system, Hundsdoerfer et al. demonstrated that recombinant DAP5 could strongly induce the expression of proteins in an IRES-dependent manner [42]. Interestingly, our REMBRANDT analysis showed that both *EIF4G1* and *EIF4G2* are overexpressed in gliomas (Table 2).

IRES are also found in circular RNAs (circRNAs). CircRNAs were first thought to be evolutionary conserved non-coding RNAs; however, it has recently been proven that circRNAs have coding capacity in vitro and in vivo [173,174]. Interestingly, Zhang and colleagues have identified a new circRNA coding for SHPRH146aa, a shorter form of the tumor suppressor SHPRH (a SNF2, histone linker, PHD-finger, RING-finger, and helicase domain-containing protein), a protein containing domains characteristic of DNA repair proteins and transcription factors. Their findings support a role for SHPRH146aa in protecting full length SHPRH from degradation. Interestingly, SHPRH146aa was found to be downregulated in 81% of GBM cases studied [175]. This therefore suggests that expression of IRES-containing mRNA can also be downregulated in GBM. Consequently, developing specific inhibitors targeting particular ITAFs rather than developing global IRES inhibitors might be more suitable for the establishment of novel polytherapy for gliomas. Current strategies developed to target IRES include, among others, antisense oligonucleotides, short hairpin RNAs, small interfering RNAs, and small molecule inhibitors. Their therapeutic potential as well as their respective advantages and disadvantages have been previously reviewed [168].

## 5. Conclusions

This review describes translation initiation occurring in cap-dependent and IRES-dependent manners and assembles the current knowledge on these two initiation mechanisms in gliomas. While it is clear that key players involved in both types of translation initiation are abnormally regulated in gliomas, the majority of existing studies are performed in vitro and in vivo, with research in human glioma samples being limited. Using two freely available datasets, we investigated the gene expression of proteins involved in the regulation of cap-dependent and IRES-dependent machineries and identified new proteins altered in gliomas, indicating possible novel targets for the treatment of gliomas with the potential to ultimately improve survival of GBM patients. Future studies should aim at elucidating whether and how global protein synthesis is affected in human gliomas and at identifying which proteins are actively synthesized by cancerous cells. Indeed, mouse models developed to study translation in vivo permitted to identify mRNAs actively translated in transformed cells compared to non-tumoral surrounding cells [176,177]. This RiboTag technique highlighted genes specifically up-translated or down-translated in cancerous compared to non-tumoral cells. It also showed that changes in translation occurring in gliomas affect specific mRNA rather than being an on/off switch in translation. Drugs currently used to modulate protein synthesis target major indirect pathways instead of specific eIFs or ITAFs, thus increasing the risk of therapeutic escape via compensatory mechanisms. Moreover, current therapies have been shown to modulate translation. For example,

GIC irradiation induces an increase in eIF4G translation suggesting an induction of cap-dependent translation upon treatment [178]. As GICs are resistant to radio-therapy and are suspected to play a key role in GBM recurrences, targeting specific actors in protein synthesis could help overcome GBM relapses. Furthermore, targeting key players involved in both the cap-dependent and the cap-independent mechanisms of translation such as 4E-BP1 or members of the eIF3 family would therefore present the advantage of inhibiting both modes of translation.

**Author Contributions:** Writing—original draft preparation, D.M. and C.N.; Writing—review and editing, L.P.N., L.A., S.F., and R.B.; supervision, S.F. and R.B.

**Funding:** This research was funded by the Neurological Foundation of New Zealand, the National Fund for Scientific Research (F.N.R.S) and the Télévie sub-organization, the Special Funds of the University of Liège, the Anti-Cancer Centre Léon Frédéricq Foundation and the NanoFar (Erasmus Mundus, European doctorate in nanomedicine and pharmaceutical innovation).

**Acknowledgments:** The authors would like to thank the Neurological Foundation of New Zealand, the National Fund for Scientific Research (F.N.R.S) and the Télévie sub-organization, the Special Funds of the University of Liège, the Anti-Cancer Centre Léon Frédéricq Foundation and the NanoFar (Erasmus Mundus, European doctorate in nanomedicine and pharmaceutical innovation) for their financial support. The results presented here are in whole based upon data generated by the TCGA Research Network: <https://www.cancer.gov/tcga>.

**Conflicts of Interest:** The authors declare that they have no conflict of interest.

## References

1. Wesseling, P.; Capper, D. WHO 2016 Classification of gliomas. *Neuropathol. Appl. Neurobiol.* **2018**, *44*, 139–150. [CrossRef] [PubMed]
2. Capdevila, C.; Rodríguez Vázquez, L.; Martí, J. Glioblastoma Multiforme and Adult Neurogenesis in the Ventricular-Subventricular Zone: A Review. *J. Cell. Physiol.* **2017**, *232*, 1596–1601. [CrossRef] [PubMed]
3. Furnari, F.B.; Fenton, T.; Bachoo, R.M.; Mukasa, A.; Stommel, J.M.; Stegh, A.; Hahn, W.C.; Ligon, K.L.; Louis, D.N.; Brennan, C.; et al. Malignant astrocytic glioma: Genetics, biology, and paths to treatment. *Genes Dev.* **2007**, *21*, 2683–2710. [CrossRef] [PubMed]
4. Louis, D.N.; Perry, A.; Reifenberger, G.; von Deimling, A.; Figarella-Branger, D.; Cavenee, W.K.; Ohgaki, H.; Wiestler, O.D.; Kleihues, P.; Ellison, D.W. The 2016 World Health Organization Classification of Tumors of the Central Nervous System: A summary. *Acta Neuropathol.* **2016**, *131*, 803–820. [CrossRef] [PubMed]
5. Nefel, C.; Laffy, J.; Filbin, M.G.; Hara, T.; Shore, M.E.; Rahme, G.J.; Richman, A.R.; Silverbush, D.; Shaw, M.L.; Hebert, C.M.; et al. An Integrative Model of Cellular States, Plasticity, and Genetics for Glioblastoma. *Cell* **2019**, *178*, 835–849. [CrossRef] [PubMed]
6. Verhaak, R.G.W.; Hoadley, K.A.; Purdom, E.; Wang, V.; Qi, Y.; Wilkerson, M.D.; Miller, C.R.; Ding, L.; Golub, T.; Mesirov, J.P.; et al. Integrated Genomic Analysis Identifies Clinically Relevant Subtypes of Glioblastoma Characterized by Abnormalities in PDGFRA, IDH1, EGFR, and NF1. *Cancer Cell* **2010**, *17*, 98–110. [CrossRef]
7. McLendon, R.; Friedman, A.; Bigner, D.; Van Meir, E.G.; Brat, D.J.; Mastrogianakis, G.M.; Olson, J.J.; Mikkelsen, T.; Lehman, N.; Aldape, K.; et al. Comprehensive genomic characterization defines human glioblastoma genes and core pathways. *Nature* **2008**, *455*, 1061–1068.
8. Stupp, R.; Mason, W.P.; van den Bent, M.J.; Weller, M.; Fisher, B.; Taphoorn, M.J.B.; Belanger, K.; Brandes, A.A.; Marosi, C.; Bogdahn, U.; et al. Radiotherapy plus Concomitant and Adjuvant Temozolomide for Glioblastoma. *N. Engl. J. Med.* **2005**, *352*, 987–996. [CrossRef]
9. Obacz, J.; Avril, T.; Le Reste, P.-J.; Urrea, H.; Quillien, V.; Hetz, C.; Chevet, E. Endoplasmic reticulum proteostasis in glioblastoma—From molecular mechanisms to therapeutic perspectives. *Sci. Signal.* **2017**. [CrossRef]
10. Robichaud, N.; Sonenberg, N.; Ruggero, D.; Schneider, R.J. Translational Control in Cancer. *Cold Spring Harb. Perspect. Biol.* **2018**. [CrossRef]
11. Bhat, M.; Robichaud, N.; Hulea, L.; Sonenberg, N.; Pelletier, J.; Topisirovic, I. Targeting the translation machinery in cancer. *Nat. Rev. Drug Discov.* **2015**, *14*, 261–278. [CrossRef] [PubMed]
12. Shah, P.; Ding, Y.; Niemczyk, M.; Kudla, G.; Plotkin, J.B. Rate-limiting steps in yeast protein translation. *Cell* **2013**. [CrossRef] [PubMed]

13. Gusev, Y.; Bhuvaneshwar, K.; Song, L.; Zenklusen, J.-C.; Fine, H.; Madhavan, S. The REMBRANDT study, a large collection of genomic data from brain cancer patients. *Sci. Data* **2018**. [CrossRef] [PubMed]
14. Svitkin, Y.V.; Herdy, B.; Costa-Mattioli, M.; Gingras, A.-C.; Raught, B.; Sonenberg, N. Eukaryotic Translation Initiation Factor 4E Availability Controls the Switch between Cap-Dependent and Internal Ribosomal Entry Site-Mediated Translation. *Mol. Cell. Biol.* **2005**, *25*, 10556–10565. [CrossRef] [PubMed]
15. Jackson, R.J.; Hellen, C.U.T.; Pestova, T.V. The mechanism of eukaryotic translation initiation and principles of its regulation. *Nat. Rev. Mol. Cell Biol.* **2010**, *11*, 113–127. [CrossRef] [PubMed]
16. Dever, T.E.; Green, R. The Elongation, Termination, and Recycling Phases of Translation in Eukaryotes. *Cold Spring Harb. Perspect. Biol.* **2012**, *4*, 13706. [CrossRef]
17. Godet, A.-C.; David, F.; Hantelys, F.; Tatin, F.; Lacazette, E.; Garmy-Susini, B.; Prats, A.-C. IRES Trans-Acting Factors, Key Actors of the Stress Response. *Int. J. Mol. Sci.* **2019**, *20*, 924. [CrossRef]
18. Shatsky, I.N.; Terenin, I.M.; Smirnova, V.V.; Andreev, D.E. Cap-Independent Translation: What's in a Name? *Trends Biochem. Sci.* **2018**, *43*, 882–895. [CrossRef]
19. Fan, W.; Wang, W.; Mao, X.; Chu, S.; Feng, J.; Xiao, D.; Zhou, J.; Fan, S. Elevated levels of p-Mnk1, p-eIF4E and p-p70S6K proteins are associated with tumor recurrence and poor prognosis in astrocytomas. *J. Neurooncol.* **2017**, *131*, 485–493. [CrossRef]
20. Yang, S.X.; Hewitt, S.M.; Steinberg, S.M.; Liewehr, D.J.; Swain, S.M. Expression levels of eIF4E, VEGF, and cyclin D1, and correlation of eIF4E with VEGF and cyclin D1 in multi-tumor tissue microarray. *Oncol. Rep.* **2007**, *17*, 281–287. [CrossRef]
21. Furic, L.; Rong, L.; Larsson, O.; Koumakpayi, I.H.; Yoshida, K.; Brueschke, A.; Petroulakis, E.; Robichaud, N.; Pollak, M.; Gaboury, L.A.; et al. EIF4E phosphorylation promotes tumorigenesis and is associated with prostate cancer progression. *Proc. Natl. Acad. Sci. USA.* **2010**, *107*, 14134–14139. [CrossRef] [PubMed]
22. Joshi, B.; Cameron, A.; Jagus, R. Characterization of mammalian eIF4E-family members. *Eur. J. Biochem.* **2004**, *271*, 2189–2203. [CrossRef] [PubMed]
23. Gu, X.; Jones, L.; Lowery-Norberg, M.; Fowler, M. Expression of eukaryotic initiation factor 4E in astrocytic tumors. *Appl. Immunohistochem. Mol. Morphol. AIMM* **2005**, *13*, 178–183. [CrossRef] [PubMed]
24. Martínez-Sáez, E.; Peg, V.; Ortega-Aznar, A.; Martínez-Ricarte, F.; Camacho, J.; Hernández-Losa, J.; Ferreres Piñas, J.C.; Ramón y Cajal, S. pEIF4E as an independent prognostic factor and a potential therapeutic target in diffuse infiltrating astrocytomas. *Cancer Med.* **2016**, *5*, 2501–2512. [CrossRef] [PubMed]
25. Chang, Y.; Wu, Q.; Tian, T.; Li, L.; Guo, X.; Feng, Z.; Zhou, J.; Zhang, L.; Zhou, S.; Feng, G.; et al. The influence of SRPK1 on glioma apoptosis, metastasis, and angiogenesis through the PI3K/Akt signaling pathway under normoxia. *Tumor Biol.* **2015**, *36*, 6083–6093. [CrossRef]
26. Kelly, N.J.; Varga, J.F.A.; Specker, E.J.; Romeo, C.M.; Coomber, B.L.; Uniacke, J. Hypoxia activates cadherin-22 synthesis via eIF4E2 to drive cancer cell migration, invasion and adhesion. *Oncogene* **2018**, *37*, 651–662. [CrossRef]
27. Abdelfattah, N.; Rajamanickam, S.; Panneerdoss, S.; Timilsina, S.; Yadav, P.; Onyeagucha, B.C.; Garcia, M.; Vadlamudi, R.; Chen, Y.; Brenner, A.; et al. MiR-584-5p potentiates vincristine and radiation response by inducing spindle defects and DNA damage in medulloblastoma. *Nat. Commun.* **2018**. [CrossRef]
28. Cloninger, C.; Bernath, A.; Bashir, T.; Holmes, B.; Artinian, N.; Ruegg, T.; Anderson, L.; Masri, J.; Lichtenstein, A.; Gera, J. Inhibition of SAPK2/p38 Enhances Sensitivity to mTORC1 Inhibition by Blocking IRES-Mediated Translation Initiation in Glioblastoma. *Mol. Cancer Ther.* **2011**, *10*, 2244–2256. [CrossRef]
29. Culjkovic, B.; Topisirovic, I.; Borden, K.L.B. Controlling Gene Expression through RNA Regulons: The Role of the Eukaryotic Translation Initiation Factor eIF4E. *Cell Cycle* **2007**, *6*, 65–69. [CrossRef]
30. Hsieh, A.C.; Ruggero, D. Targeting eukaryotic translation initiation factor 4E (eIF4E) in cancer. *Clin. Cancer Res.* **2010**, *16*, 4914–4920. [CrossRef]
31. Sonenberg, N. Translation factors as effectors of cell growth and tumorigenesis. *Curr. Opin. Cell Biol.* **1993**, *5*, 955–960. [CrossRef]
32. Rouschop, K.M.A.; Dubois, L.; Schaaf, M.B.E.; van den Beucken, T.; Liewes, N.; Keulers, T.G.H.; Savelkoul, K.G.M.; Bussink, J.; van der Kogel, A.J.; Koritzinsky, M.; et al. Deregulation of cap-dependent mRNA translation increases tumour radiosensitivity through reduction of the hypoxic fraction. *Radiother. Oncol.* **2011**, *99*, 385–391. [CrossRef] [PubMed]

33. Volpin, F.; Casaos, J.; Sesen, J.; Mangraviti, A.; Choi, J.; Gorelick, N.; Frikeche, J.; Lott, T.; Felder, R.; Scotland, S.J.; et al. Use of an anti-viral drug, Ribavirin, as an anti-glioblastoma therapeutic. *Oncogene* **2017**, *36*, 3037–3047. [CrossRef] [PubMed]
34. Kentsis, A.; Topisirovic, I.; Culjkovic, B.; Shao, L.; Borden, K.L.B. Ribavirin suppresses eIF4E-mediated oncogenic transformation by physical mimicry of the 7-methyl guanosine mRNA cap. *Proc. Natl. Acad. Sci. USA* **2004**, *101*, 18105–18110. [CrossRef] [PubMed]
35. Khan, Z.; Shervington, A.; Munje, C.; Shervington, L. The Complexity of Identifying Cancer Stem Cell Biomarkers. *Cancer Invest.* **2013**, *31*, 404–411. [CrossRef]
36. Ge, Y.; Zhou, F.; Chen, H.; Cui, C.; Liu, D.; Li, Q.; Yang, Z.; Wu, G.; Sun, S.; Gu, J.; et al. Sox2 is translationally activated by eukaryotic initiation factor 4E in human glioma-initiating cells. *Biochem. Biophys. Res. Commun.* **2010**, *397*, 711–717. [CrossRef]
37. Goffart, N.; Lombard, A.; Lallemand, F.; Kroonen, J.; Nassen, J.; Di Valentin, E.; Berendsen, S.; Dedobbeleer, M.; Willems, E.; Robe, P.; et al. CXCL12 mediates glioblastoma resistance to radiotherapy in the subventricular zone. *Neuro. Oncol.* **2017**, *19*, 66–77. [CrossRef]
38. Kroonen, J.; Nassen, J.; Boulanger, Y.-G.; Provenzano, F.; Capraro, V.; Bours, V.; Martin, D.; Deprez, M.; Robe, P.; Rogister, B. Human glioblastoma-initiating cells invade specifically the subventricular zones and olfactory bulbs of mice after striatal injection. *Int. J. Cancer* **2011**, *129*, 574–585. [CrossRef]
39. Dostie, J.; Ferraiuolo, M.; Pause, A.; Adam, S.A.; Sonenberg, N. A novel shuttling protein, 4E-T, mediates the nuclear import of the mRNA 5' cap-binding protein, eIF4E. *EMBO J.* **2000**, *19*, 3142–3156. [CrossRef]
40. Nishimura, T.; Padamsi, Z.; Fakim, H.; Milette, S.; Dunham, W.H.; Gingras, A.-C.; Fabian, M.R. The eIF4E-Binding Protein 4E-T Is a Component of the mRNA Decay Machinery that Bridges the 5' and 3' Termini of Target mRNAs. *Cell Rep.* **2015**, *11*, 1425–1436. [CrossRef]
41. Dobrikov, M.; Dobrikova, E.; Shveygert, M.; Gromeier, M. Phosphorylation of Eukaryotic Translation Initiation Factor 4G1 (eIF4G1) by Protein Kinase C Regulates eIF4G1 Binding to Mnk1. *Mol. Cell. Biol.* **2011**, *31*, 2947–2959. [CrossRef] [PubMed]
42. Hundsdorfer, P.; Thoma, C.; Hentze, M.W. Eukaryotic translation initiation factor 4GI and p97 promote cellular internal ribosome entry sequence-driven translation. *Proc. Natl. Acad. Sci. USA* **2005**, *102*, 13421–13426. [CrossRef] [PubMed]
43. Pyronnet, S.; Imataka, H.; Gingras, A.C.; Fukunaga, R.; Hunter, T.; Sonenberg, N. Human eukaryotic translation initiation factor 4G (eIF4G) recruits Mnk1 to phosphorylate eIF4E. *EMBO J.* **1999**, *18*, 270–279. [CrossRef] [PubMed]
44. Kahvejian, A.; Svitkin, Y.V.; Sukarieh, R.; M'Boutchou, M.-N.; Sonenberg, N. Mammalian poly(A)-binding protein is a eukaryotic translation initiation factor, which acts via multiple mechanisms. *Genes Dev.* **2005**, *19*, 104–113. [CrossRef] [PubMed]
45. Chu, J.; Cargnello, M.; Topisirovic, I.; Pelletier, J. Translation Initiation Factors: Reprogramming Protein Synthesis in Cancer. *Trends Cell Biol.* **2016**, *26*, 918–933. [CrossRef]
46. Gingras, A.C.; Raught, B.; Sonenberg, N. Regulation of translation initiation by FRAP/mTOR. *Genes Dev.* **2001**, *15*, 807–826. [CrossRef]
47. Wu, M.; Zhang, C.; Li, X.-J.; Liu, Q.; Wanggou, S. Anti-Cancer Effect of Cap-Translation Inhibitor 4EGI-1 in Human Glioma U87 Cells: Involvement of Mitochondrial Dysfunction and ER Stress. *Cell. Physiol. Biochem.* **2016**, *40*, 1013–1028. [CrossRef]
48. Yang, X.; Dong, Q.-F.; Li, L.-W.; Huo, J.-L.; Li, P.-Q.; Fei, Z.; Zhen, H.-N. The cap-translation inhibitor 4EGI-1 induces mitochondrial dysfunction via regulation of mitochondrial dynamic proteins in human glioma U251 cells. *Neurochem. Int.* **2015**, *90*, 98–106. [CrossRef]
49. Dubois, L.; Magagnin, M.G.; Cleven, A.H.G.; Weppeler, S.A.; Grenacher, B.; Landuyt, W.; Lieuwes, N.; Lambin, P.; Gorr, T.A.; Koritzinsky, M.; et al. Inhibition of 4E-BP1 Sensitizes U87 Glioblastoma Xenograft Tumors to Irradiation by Decreasing Hypoxia Tolerance. *Int. J. Radiat. Oncol.* **2009**, *73*, 1219–1227. [CrossRef]
50. Raza, F.; Waldron, J.A.; Quesne, J.L. Translational dysregulation in cancer: eIF4A isoforms and sequence determinants of eIF4A dependence. *Biochem. Soc. Trans.* **2015**, *43*, 1227–1233. [CrossRef]
51. Parsyan, A.; Svitkin, Y.; Shahbazian, D.; Gkogkas, C.; Lasko, P.; Merrick, W.C.; Sonenberg, N. mRNA helicases: The tacticians of translational control. *Nat. Rev. Mol. Cell Biol.* **2011**, *12*, 235–245. [CrossRef] [PubMed]

52. Shaoyan, X.; Juanjuan, Y.; Yalan, T.; Ping, H.; Jianzhong, L.; Qinian, W. Downregulation of EIF4A2 in Non-Small-Cell Lung Cancer Associates with Poor Prognosis. *Clin. Lung Cancer* **2013**, *14*, 658–665. [CrossRef] [PubMed]
53. Yan, L.X.; Wu, Q.N.; Zhang, Y.; Li, Y.Y.; Liao, D.Z.; Hou, J.H.; Fu, J.; Zeng, M.S.; Yun, J.P.; Wu, Q.L.; et al. Knockdown of miR-21 in human breast cancer cell lines inhibits proliferation, in vitro migration and in vivotumor growth. *Breast Cancer Res.* **2011**. [CrossRef] [PubMed]
54. Schmid, T.; Jansen, A.P.; Baker, A.R.; Hegamy, G.; Hagan, J.P.; Colburn, N.H. Translation inhibitor Pdc4 is targeted for degradation during tumor promotion. *Cancer Res.* **2008**, *68*, 1254–1260. [CrossRef] [PubMed]
55. Hwang, S.-K.; Baker, A.R.; Young, M.R.; Colburn, N.H. Tumor suppressor PDCD4 inhibits NF- $\kappa$ B-dependent transcription in human glioblastoma cells by direct interaction with p65. *Carcinogenesis* **2014**, *35*, 1469–1480. [CrossRef] [PubMed]
56. Yang, H.-S.; Cho, M.-H.; Zakowicz, H.; Hegamy, G.; Sonenberg, N.; Colburn, N.H. A novel function of the MA-3 domains in transformation and translation suppressor Pdc4 is essential for its binding to eukaryotic translation initiation factor 4A. *Mol. Cell. Biol.* **2004**, *24*, 3894–3906. [CrossRef]
57. Gao, F.; Zhang, P.; Zhou, C.; Li, J.; Wang, Q.; Zhu, F.; Ma, C.; Sun, W.; Zhang, L. Frequent loss of PDCD4 expression in human glioma: Possible role in the tumorigenesis of glioma. *Oncol. Rep.* **2007**, *17*, 123–128. [CrossRef]
58. Wang, Q.; Yang, H.-S. The role of Pdc4 in tumour suppression and protein translation. *Biol. Cell* **2018**, *110*, 169–177. [CrossRef]
59. Chan, J.A.; Krichevsky, A.M.; Kosik, K.S. MicroRNA-21 Is an Antiapoptotic Factor in Human Glioblastoma Cells. *Cancer Res.* **2005**, *65*, 6029–6033. [CrossRef]
60. Ma, Q.; Huang, J.; Xiong, Y.; Yang, X.; Han, R.; Zhu, W. MicroRNA-96 Regulates Apoptosis by Targeting PDCD4 in Human Glioma Cells. *Technol. Cancer Res. Treat.* **2017**, *16*, 92–98. [CrossRef]
61. Bordeleau, M.E.; Matthews, J.; Wojnar, J.M.; Lindqvist, L.; Novac, O.; Jankowsky, E.; Sonenberg, N.; Northcote, P.; Teesdale-Spittle, P.; Pelletier, J. Stimulation of mammalian translation initiation factor eIF4A activity by a small molecule inhibitor of eukaryotic translation. *Proc. Natl. Acad. Sci. USA.* **2005**, *102*, 10460–10465. [CrossRef] [PubMed]
62. Low, W.K.; Dang, Y.; Schneider-Poetsch, T.; Shi, Z.; Choi, N.S.; Merrick, W.C.; Romo, D.; Liu, J.O. Inhibition of eukaryotic translation initiation by the marine natural product pateamine A. *Mol. Cell* **2005**, *20*, 709–722. [CrossRef] [PubMed]
63. Pestova, T.V.; Kolupaeva, V.G. The roles of individual eukaryotic translation initiation factors in ribosomal scanning and initiation codon selection. *Genes Dev.* **2002**, *16*, 2906–2922. [CrossRef] [PubMed]
64. des Georges, A.; Dhote, V.; Kuhn, L.; Hellen, C.U.T.; Pestova, T.V.; Frank, J.; Hashem, Y. Structure of mammalian eIF3 in the context of the 43S preinitiation complex. *Nature* **2015**, *525*, 491–495. [CrossRef] [PubMed]
65. Obayashi, E.; Luna, R.E.; Nagata, T.; Martin-Marcos, P.; Hiraishi, H.; Singh, C.R.; Erzberger, J.P.; Zhang, F.; Arthanari, H.; Morris, J.; et al. Molecular Landscape of the Ribosome Pre-initiation Complex during mRNA Scanning: Structural Role for eIF3c and Its Control by eIF5. *Cell Rep.* **2017**, *18*, 2651–2663. [CrossRef] [PubMed]
66. Sokabe, M.; Fraser, C.S.; Hershey, J.W.B. The human translation initiation multi-factor complex promotes methionyl-tRNA binding to the 40S ribosomal subunit. *Nucleic Acids Res.* **2012**, *40*, 905–913. [CrossRef] [PubMed]
67. Villa, N.; Do, A.; Hershey, J.W.B.; Fraser, C.S. Human eukaryotic initiation factor 4G (eIF4G) protein binds to eIF3c, -d, and -e to promote mRNA recruitment to the ribosome. *J. Biol. Chem.* **2013**, *288*, 32932–32940. [CrossRef]
68. Hershey, J.W.B. The role of eIF3 and its individual subunits in cancer. *Biochim. Biophys. Acta-Gene Regul. Mech.* **2015**, *1849*, 792–800. [CrossRef]
69. Emmanuel, R.; Weinstein, S.; Landesman-Milo, D.; Peer, D. eIF3c: A potential therapeutic target for cancer. *Cancer Lett.* **2013**, *336*, 158–166. [CrossRef]
70. Fan, Y.; Guo, Y. Knockdown of eIF3D inhibits breast cancer cell proliferation and invasion through suppressing the Wnt/ $\beta$ -catenin signaling pathway. *Int. J. Clin. Exp. Pathol.* **2015**, *8*, 10420–10427.
71. Li, Z.; Lin, S.; Jiang, T.; Wang, J.; Lu, H.; Tang, H.; Teng, M.; Fan, J. Overexpression of eIF3e is correlated with colon tumor development and poor prognosis. *Int. J. Clin. Exp. Pathol.* **2014**, *7*, 6462–6474. [PubMed]



72. Spilka, R.; Ernst, C.; Bergler, H.; Rainer, J.; Flechsig, S.; Vogetseder, A.; Lederer, E.; Benesch, M.; Brunner, A.; Geley, S.; et al. eIF3a is over-expressed in urinary bladder cancer and influences its phenotype independent of translation initiation. *Cell. Oncol.* **2014**, *37*, 253–267. [CrossRef] [PubMed]
73. Wang, H.; Ru, Y.; Sanchez-Carbayo, M.; Wang, X.; Kieft, J.S.; Theodorescu, D. Translation Initiation Factor eIF3b Expression in Human Cancer and Its Role in Tumor Growth and Lung Colonization. *Clin. Cancer Res.* **2013**, *19*, 2850–2860. [CrossRef] [PubMed]
74. Chai, R.-C.; Wang, N.; Chang, Y.-Z.; Zhang, K.-N.; Li, J.-J.; Niu, J.-J.; Wu, F.; Liu, Y.-Q.; Wang, Y.-Z. Systematically profiling the expression of eIF3 subunits in glioma reveals the expression of eIF3i has prognostic value in IDH-mutant lower grade glioma. *Cancer Cell Int.* **2019**. [CrossRef] [PubMed]
75. HAO, J.; LIANG, C.; JIAO, B. Eukaryotic translation initiation factor 3, subunit C is overexpressed and promotes cell proliferation in human glioma U-87 MG cells. *Oncol. Lett.* **2015**, *9*, 2525–2533. [CrossRef] [PubMed]
76. Liang, H.; Ding, X.; Zhou, C.; Zhang, Y.; Xu, M.; Zhang, C.; Xu, L. Knockdown of eukaryotic translation initiation factors 3B (EIF3B) inhibits proliferation and promotes apoptosis in glioblastoma cells. *Neurol. Sci.* **2012**, *33*, 1057–1062. [CrossRef] [PubMed]
77. Ren, M.; Zhou, C.; Liang, H.; Wang, X.; Xu, L. RNAi-Mediated Silencing of EIF3D Alleviates Proliferation and Migration of Glioma U251 and U87MG Cells. *Chem. Biol. Drug Des.* **2015**, *86*, 715–722. [CrossRef]
78. Sesen, J.; Cammas, A.; Scotland, S.; Elefterion, B.; Lemarié, A.; Millevoi, S.; Mathew, L.; Seva, C.; Toulas, C.; Moyal, E.; et al. Int6/eIF3e Is Essential for Proliferation and Survival of Human Glioblastoma Cells. *Int. J. Mol. Sci.* **2014**, *15*, 2172–2190. [CrossRef]
79. Lee, A.S.Y.; Kranzusch, P.J.; Cate, J.H.D. eIF3 targets cell-proliferation messenger RNAs for translational activation or repression. *Nature* **2015**, *522*, 111–114. [CrossRef]
80. Passmore, L.A.; Schmeing, T.M.; Maag, D.; Applefield, D.J.; Acker, M.G.; Algire, M.A.; Lorsch, J.R.; Ramakrishnan, V. The Eukaryotic Translation Initiation Factors eIF1 and eIF1A Induce an Open Conformation of the 40S Ribosome. *Mol. Cell* **2007**, *26*, 41–50. [CrossRef]
81. Yu, J.; Marintchev, A. Comparative sequence and structure analysis of eIF1A and eIF1AD. *BMC Struct. Biol.* **2018**. [CrossRef] [PubMed]
82. Ross, J.A.; Vanden Dungen, K.; Bressler, K.R.; Fredriksen, M.; Khandige Sharma, D.; Balasingam, N.; Thakor, N. Eukaryotic initiation factor 5B (eIF5B) provides a critical cell survival switch to glioblastoma cells via regulation of apoptosis. *Cell Death Dis.* **2019**. [CrossRef] [PubMed]
83. Andreou, A.Z.; Harms, U.; Klostermeier, D. eIF4B stimulates eIF4A ATPase and unwinding activities by direct interaction through its 7-repeats region. *RNA Biol.* **2017**, *14*, 113–123. [CrossRef] [PubMed]
84. Rozovsky, N.; Butterworth, A.C.; Moore, M.J. Interactions between eIF4AI and its accessory factors eIF4B and eIF4H. *RNA* **2008**, *14*, 2136–2148. [CrossRef]
85. Shahbazian, D.; Parsyan, A.; Petroulakis, E.; Hershey, J.W.B.; Sonenberg, N. eIF4B controls survival and proliferation and is regulated by proto-oncogenic signaling pathways. *Cell Cycle* **2010**, *9*, 4106–4109. [CrossRef]
86. Vaysse, C.; Philippe, C.; Martineau, Y.; Quelen, C.; Hieblot, C.; Renaud, C.; Nicaise, Y.; Desquesnes, A.; Pannese, M.; Filleron, T.; et al. Key contribution of eIF4H-mediated translational control in tumor promotion. *Oncotarget* **2015**, *6*, 39924–39940. [CrossRef]
87. Wang, Y.; Begley, M.; Li, Q.; Huang, H.-T.; Lako, A.; Eck, M.J.; Gray, N.S.; Mitchison, T.J.; Cantley, L.C.; Zhao, J.J. Mitotic MELK-eIF4B signaling controls protein synthesis and tumor cell survival. *Proc. Natl. Acad. Sci. USA* **2016**, *113*, 9810–9815. [CrossRef]
88. Kroczyńska, B.; Kaur, S.; Katsoulidis, E.; Majchrzak-Kita, B.; Sassano, A.; Kozma, S.C.; Fish, E.N.; Plataniias, L.C. Interferon-Dependent Engagement of Eukaryotic Initiation Factor 4B via S6 Kinase (S6K)- and Ribosomal Protein S6K-Mediated Signals. *Mol. Cell. Biol.* **2009**, *29*, 2865–2875. [CrossRef]
89. Zhu, W.; Li, G.X.; Chen, H.L.; Liu, X.Y. The role of eukaryotic translation initiation factor 6 in tumors. *Oncol. Lett.* **2017**, *14*, 3–9. [CrossRef]
90. Sanvito, F.; Piatti, S.; Villa, A.; Bossi, M.; Lucchini, G.; Marchisio, P.C.; Biffo, S. The  $\beta$ 4 Integrin Interactor p27<sup>BBP/eIF6</sup> Is an Essential Nuclear Matrix Protein Involved in 60S Ribosomal Subunit Assembly. *J. Cell Biol.* **1999**, *144*, 823–838. [CrossRef]

91. Saito, K.; Iizuka, Y.; Ohta, S.; Takahashi, S.; Nakamura, K.; Saya, H.; Yoshida, K.; Kawakami, Y.; Toda, M. Functional analysis of a novel glioma antigen, EFTUD1. *Neuro. Oncol.* **2014**, *16*, 1618–1629. [CrossRef] [PubMed]
92. Jennings, M.D.; Zhou, Y.; Mohammad-Qureshi, S.S.; Bennett, D.; Pavitt, G.D. eIF2B promotes eIF5 dissociation from eIF2\*GDP to facilitate guanine nucleotide exchange for translation initiation. *Genes Dev.* **2013**, *27*, 2696–2707. [CrossRef] [PubMed]
93. Yang, W.; Hinnebusch, A.G. Identification of a regulatory subcomplex in the guanine nucleotide exchange factor eIF2B that mediates inhibition by phosphorylated eIF2. *Mol. Cell. Biol.* **1996**, *16*, 6603–6616. [CrossRef] [PubMed]
94. Fabian, J.R.; Kimball, S.R.; Heinzinger, N.K.; Jefferson, L.S. Subunit Assembly and Guanine Nucleotide Exchange Activity of Eukaryotic Initiation Factor-2B Expressed in Sf9 Cells. *J. Biol. Chem.* **1997**, *272*, 12359–12365. [CrossRef] [PubMed]
95. Fabian, J.R.; Kimball, S.R.; Jefferson, L.S. Reconstitution and Purification of Eukaryotic Initiation Factor 2B (eIF2B) Expressed in Sf21 Insect Cells. *Protein Expr. Purif.* **1998**, *13*, 16–22. [CrossRef]
96. Gordiyenko, Y.; Schmidt, C.; Jennings, M.D.; Matak-Vinkovic, D.; Pavitt, G.D.; Robinson, C.V. eIF2B is a decameric guanine nucleotide exchange factor with a  $\gamma 2\epsilon 2$  tetrameric core. *Nat. Commun.* **2014**. [CrossRef]
97. Gallagher, J.W.; Kubica, N.; Kimball, S.R.; Jefferson, L.S. Reduced Eukaryotic Initiation Factor 2B $\epsilon$ -Subunit Expression Suppresses the Transformed Phenotype of Cells Overexpressing the Protein. *Cancer Res.* **2008**, *68*, 8752–8760. [CrossRef]
98. Yatime, L.; Mechulam, Y.; Blanquet, S.; Schmitt, E. Structure of an archaeal heterotrimeric initiation factor 2 reveals a nucleotide state between the GTP and the GDP states. *Proc. Natl. Acad. Sci. USA* **2007**, *104*, 18445–18450. [CrossRef]
99. Jiang, H.-Y.; Wek, R.C. Phosphorylation of the  $\alpha$ -Subunit of the Eukaryotic Initiation Factor-2 (eIF2 $\alpha$ ) Reduces Protein Synthesis and Enhances Apoptosis in Response to Proteasome Inhibition. *J. Biol. Chem.* **2005**, *280*, 14189–14202. [CrossRef]
100. Taniuchi, S.; Miyake, M.; Tsugawa, K.; Oyadomari, M.; Oyadomari, S. Integrated stress response of vertebrates is regulated by four eIF2 $\alpha$  kinases. *Sci. Rep.* **2016**. [CrossRef]
101. Haapa-Paananen, S.; Chen, P.; Hellström, K.; Kohonen, P.; Hautaniemi, S.; Kallioniemi, O.; Perälä, M. Functional Profiling of Precursor MicroRNAs Identifies MicroRNAs Essential for Glioma Proliferation. *PLoS ONE* **2013**. [CrossRef] [PubMed]
102. Friedrich, I.; Eizenbach, M.; Sajman, J.; Ben-Bassat, H.; Levitzki, A. A cellular screening assay to test the ability of PKR to induce cell death in mammalian cells. *Mol. Ther.* **2005**, *12*, 969–975. [CrossRef] [PubMed]
103. Shir, A.; Ogris, M.; Wagner, E.; Levitzki, A. EGF Receptor-Targeted Synthetic Double-Stranded RNA Eliminates Glioblastoma, Breast Cancer, and Adenocarcinoma Tumors in Mice. *PLoS Med.* **2005**. [CrossRef] [PubMed]
104. Chaveroux, C.; Bruhat, A.; Carraro, V.; Jousse, C.; Averous, J.; Maurin, A.-C.; Parry, L.; Mesclon, F.; Muranishi, Y.; Cordelier, P.; et al. Regulating the expression of therapeutic transgenes by controlled intake of dietary essential amino acids. *Nat. Biotechnol.* **2016**, *34*, 746–751. [CrossRef]
105. Adam, I.; Dewi, D.L.; Mooiweer, J.; Sadik, A.; Mohapatra, S.R.; Berdel, B.; Keil, M.; Sonner, J.K.; Thedieck, K.; Rose, A.J.; et al. Upregulation of tryptophanyl-tRNA synthetase adapts human cancer cells to nutritional stress caused by tryptophan degradation. *Oncoimmunology* **2018**, *7*. [CrossRef]
106. Harvey, R.F.; Willis, A.E. Post-transcriptional control of stress responses in cancer. *Curr. Opin. Genet. Dev.* **2018**, *48*, 30–35. [CrossRef]
107. Harding, H.P.; Zhang, Y.; Ron, D. Protein translation and folding are coupled by an endoplasmic-reticulum-resident kinase. *Nature* **1999**, *397*, 271–274. [CrossRef]
108. Peñaranda Fajardo, N.M.; Meijer, C.; Kruyt, F.A.E. The endoplasmic reticulum stress/unfolded protein response in gliomagenesis, tumor progression and as a therapeutic target in glioblastoma. *Biochem. Pharmacol.* **2016**, *118*, 1–8. [CrossRef]
109. Tsai, C.-F.; Yeh, W.-L.; Huang, S.M.; Tan, T.-W.; Lu, D.-Y. Wogonin Induces Reactive Oxygen Species Production and Cell Apoptosis in Human Glioma Cancer Cells. *Int. J. Mol. Sci.* **2012**, *13*, 9877–9892. [CrossRef]

110. Lu, D.-Y.; Chang, C.-S.; Yeh, W.-L.; Tang, C.-H.; Cheung, C.-W.; Leung, Y.-M.; Liu, J.-F.; Wong, K.-L. The novel phloroglucinol derivative BFP induces apoptosis of glioma cancer through reactive oxygen species and endoplasmic reticulum stress pathways. *Phytomedicine* **2012**, *19*, 1093–1100. [CrossRef]
111. Tungkum, W.; Jumnonprakon, P.; Tocharus, C.; Govitrapong, P.; Tocharus, J. Melatonin suppresses methamphetamine-triggered endoplasmic reticulum stress in C6 cells glioma cell lines. *J. Toxicol. Sci.* **2017**, *42*, 63–71. [CrossRef] [PubMed]
112. Ciechomska, I.A.; Gabrusiewicz, K.; Szczepankiewicz, A.A.; Kaminska, B. Endoplasmic reticulum stress triggers autophagy in malignant glioma cells undergoing cyclosporine A-induced cell death. *Oncogene* **2013**, *32*, 1518–1529. [CrossRef] [PubMed]
113. Fan, Q.-W.; Cheng, C.; Hackett, C.; Feldman, M.; Houseman, B.T.; Nicolaidis, T.; Haas-Kogan, D.; James, C.D.; Oakes, S.A.; Debnath, J.; et al. Akt and Autophagy Cooperate to Promote Survival of Drug-Resistant Glioma. *Sci. Signal.* **2010**, *3*, 81. [CrossRef] [PubMed]
114. Galavotti, S.; Bartesaghi, S.; Faccenda, D.; Shaked-Rabi, M.; Sanzone, S.; McEvoy, A.; Dinsdale, D.; Condorelli, F.; Brandner, S.; Campanella, M.; et al. The autophagy-associated factors DRAM1 and p62 regulate cell migration and invasion in glioblastoma stem cells. *Oncogene* **2013**, *32*, 699–712. [CrossRef] [PubMed]
115. Jia, W.; Loria, R.M.; Park, M.A.; Yacoub, A.; Dent, P.; Graf, M.R. The neuro-steroid, 5-androstene 3 $\beta$ ,17 $\alpha$  diol; induces endoplasmic reticulum stress and autophagy through PERK/eIF2 $\alpha$  signaling in malignant glioma cells and transformed fibroblasts. *Int. J. Biochem. Cell Biol.* **2010**, *42*, 2019–2029. [CrossRef] [PubMed]
116. Liu, W.-T.; Huang, C.-Y.; Lu, I.-C.; Gean, P.-W. Inhibition of glioma growth by minocycline is mediated through endoplasmic reticulum stress-induced apoptosis and autophagic cell death. *Neuro. Oncol.* **2013**, *15*, 1127–1141. [CrossRef]
117. Shen, S.; Zhang, Y.; Wang, Z.; Zhang, R.; Gong, X. Bufalin Induces the Interplay between Apoptosis and Autophagy in Glioma Cells through Endoplasmic Reticulum Stress. *Int. J. Biol. Sci.* **2014**, *10*, 212–224. [CrossRef]
118. Anderson, K.C. The 39th David, A. Karnofsky Lecture: Bench-to bedside translation of targeted therapies in multiple myeloma. *J. Clin. Oncol.* **2012**, *30*, 445–452. [CrossRef]
119. Vlachostergios, P.J.; Hatzidaki, E.; Stathakis, N.E.; Koukoulis, G.K.; Papandreou, C.N. Bortezomib Downregulates MGMT Expression in T98G Glioblastoma Cells. *Cell. Mol. Neurobiol.* **2013**, *33*, 313–318. [CrossRef]
120. Vilas-Boas, F.d.A.S.; da Silva, A.M.; de Sousa, L.P.; Lima, K.M.; Vago, J.P.; Bittencourt, L.F.F.; Dantas, A.E.; Gomes, D.A.; Vilela, M.C.; Teixeira, M.M.; et al. Impairment of stress granule assembly via inhibition of the eIF2 $\alpha$  phosphorylation sensitizes glioma cells to chemotherapeutic agents. *J. Neurooncol.* **2016**, *127*, 253–260.
121. Friday, B.B.; Anderson, S.K.; Buckner, J.; Yu, C.; Giannini, C.; Geoffroy, F.; Schwerkoske, J.; Mazurczak, M.; Gross, H.; Pajon, E.; et al. Phase II trial of vorinostat in combination with bortezomib in recurrent glioblastoma: A north central cancer treatment group study. *Neuro. Oncol.* **2012**, *14*, 215–221. [CrossRef] [PubMed]
122. Lin, L.; Gaut, D.; Hu, K.; Yan, H.; Yin, D.; Koeffler, H.P. Dual targeting of glioblastoma multiforme with a proteasome inhibitor (Velcade) and a phosphatidylinositol 3-kinase inhibitor (ZSTK474). *Int. J. Oncol.* **2014**, *44*, 557–562. [CrossRef] [PubMed]
123. Sun, S.; Lee, D.; Ho, A.S.W.; Pu, J.K.S.; Zhang, X.Q.; Lee, N.P.; Day, P.J.R.; Lui, W.M.; Fung, C.F.; Leung, G.K.K. Inhibition of prolyl 4-hydroxylase, beta polypeptide (P4HB) attenuates temozolomide resistance in malignant glioma via the endoplasmic reticulum stress response (ERSR) pathways. *Neuro. Oncol.* **2013**, *15*, 562–577. [CrossRef] [PubMed]
124. Holmes, B.; Lee, J.; Landon, K.A.; Benavides-Serrato, A.; Bashir, T.; Jung, M.E.; Lichtenstein, A.; Gera, J. Mechanistic Target of Rapamycin (mTOR) Inhibition Synergizes with Reduced Internal Ribosome Entry Site (IRES)-mediated Translation of Cyclin D1 and c-MYC mRNAs to Treat Glioblastoma. *J. Biol. Chem.* **2016**, *291*, 14146–14159. [CrossRef]
125. Martin, J.; Masri, J.; Cloninger, C.; Holmes, B.; Artinian, N.; Funk, A.; Ruegg, T.; Anderson, L.; Bashir, T.; Bernath, A.; et al. Phosphomimetic Substitution of Heterogeneous Nuclear Ribonucleoprotein A1 at Serine 199 Abolishes AKT-dependent Internal Ribosome Entry Site-transacting Factor (ITAF) Function via Effects on Strand Annealing and Results in Mammalian Target of Rapamycin Complex 1 (mTORC1) Inhibitor Sensitivity. *J. Biol. Chem.* **2011**, *286*, 16402–16413.

126. Ueda, T.; Sasaki, M.; Elia, A.J.; Chio, I.I.C.; Hamada, K.; Fukunaga, R.; Mak, T.W. Combined deficiency for MAP kinase-interacting kinase 1 and 2 (Mnk1 and Mnk2) delays tumor development. *Proc. Natl. Acad. Sci. USA* **2010**, *107*, 13984–13990. [CrossRef]
127. Bell, J.B.; Eckerdt, F.; Dhruv, H.D.; Finlay, D.; Peng, S.; Kim, S.; Kroczyńska, B.; Beauchamp, E.M.; Alley, K.; Clymer, J.; et al. Differential Response of Glioma Stem Cells to Arsenic Trioxide Therapy Is Regulated by MNK1 and mRNA Translation. *Mol. Cancer Res.* **2018**, *16*, 32–46. [CrossRef]
128. Ceccarelli, M.; Barthel, F.P.; Malta, T.M.; Sabedot, T.S.; Salama, S.R.; Murray, B.A.; Morozova, O.; Newton, Y.; Radenbaugh, A.; Pagnotta, S.M.; et al. Molecular Profiling Reveals Biologically Discrete Subsets and Pathways of Progression in Diffuse Glioma. *Cell* **2016**, *164*, 550–563. [CrossRef]
129. Grzmil, M.; Huber, R.M.; Hess, D.; Frank, S.; Hynx, D.; Moncayo, G.; Klein, D.; Merlo, A.; Hemmings, B.A. MNK1 pathway activity maintains protein synthesis in rapalog-treated gliomas. *J. Clin. Investig.* **2014**, *124*, 742–754. [CrossRef]
130. Laderoute, K.R.; Calaoagan, J.M.; Chao, W.; Dinh, D.; Denko, N.; Duellman, S.; Kalra, J.; Liu, X.; Papandreou, I.; Sambucetti, L.; et al. 5'-AMP-activated Protein Kinase (AMPK) Supports the Growth of Aggressive Experimental Human Breast Cancer Tumors. *J. Biol. Chem.* **2014**, *289*, 22850–22864. [CrossRef]
131. Masri, J.; Bernath, A.; Martin, J.; Jo, O.D.; Vartanian, R.; Funk, A.; Gera, J. mTORC2 Activity Is Elevated in Gliomas and Promotes Growth and Cell Motility via Overexpression of Rictor. *Cancer Res.* **2007**, *67*, 11712–11720. [CrossRef] [PubMed]
132. Saini, K.S.; Loi, S.; de Azambuja, E.; Metzger-Filho, O.; Saini, M.L.; Ignatiadis, M.; Dancey, J.E.; Piccart-Gebhart, M.J. Targeting the PI3K/AKT/mTOR and Raf/MEK/ERK pathways in the treatment of breast cancer. *Cancer Treat. Rev.* **2013**, *39*, 935–946. [CrossRef] [PubMed]
133. Boutouja, F.; Stiehm, C.M.; Platta, H.W. mTOR: A Cellular Regulator Interface in Health and Disease. *Cells* **2019**. [CrossRef] [PubMed]
134. Duzgun, Z.; Eroglu, Z.; Biray Avci, C. Role of mTOR in glioblastoma. *Gene* **2016**, *575*, 187–190. [CrossRef]
135. Gulati, N.; Karsy, M.; Albert, L.; Murali, R.; Jhanwar-Uniyal, M. Involvement of mTORC1 and mTORC2 in regulation of glioblastoma multiforme growth and motility. *Int. J. Oncol.* **2009**, *35*, 731–740.
136. Urbanska, M.; Gozdz, A.; Swiech, L.J.; Jaworski, J. Mammalian Target of Rapamycin Complex 1 (mTORC1) and 2 (mTORC2) Control the Dendritic Arbor Morphology of Hippocampal Neurons. *J. Biol. Chem.* **2012**, *287*, 30240–30256. [CrossRef]
137. Korkolopoulou, P.; Levidou, G.; El-Habr, E.A.; Piperi, C.; Adamopoulos, C.; Samaras, V.; Boviatsis, E.; Thymara, I.; Trigka, E.-A.; Sakellariou, S.; et al. Phosphorylated 4E-binding protein 1 (p-4E-BP1): A novel prognostic marker in human astrocytomas. *Histopathology* **2012**, *61*, 293–305. [CrossRef]
138. Jhanwar-Uniyal, M.; Amin, A.G.; Cooper, J.B.; Das, K.; Schmidt, M.H.; Murali, R. Discrete signaling mechanisms of mTORC1 and mTORC2: Connected yet apart in cellular and molecular aspects. *Adv. Biol. Regul.* **2017**, *64*, 39–48. [CrossRef]
139. Dumstorf, C.A.; Konicek, B.W.; McNulty, A.M.; Parsons, S.H.; Furic, L.; Sonenberg, N.; Graff, J.R. Modulation of 4E-BP1 Function as a Critical Determinant of Enzastaurin-Induced Apoptosis. *Mol. Cancer Ther.* **2010**, *9*, 3158–3163. [CrossRef]
140. Jiang, R.; Choi, W.; Hu, L.; Gerner, E.W.; Hamilton, S.R.; Zhang, W. Activation of polyamine catabolism by N1, N11-diethylnorspermine alters the cellular localization of mTOR and downregulates mTOR protein level in glioblastoma cells. *Cancer Biol. Ther.* **2007**, *6*, 1644–1648. [CrossRef]
141. Cloughesy, T.F.; Yoshimoto, K.; Nghiemphu, P.; Brown, K.; Dang, J.; Zhu, S.; Hsueh, T.; Chen, Y.; Wang, W.; Youngkin, D.; et al. Antitumor Activity of Rapamycin in a Phase I Trial for Patients with Recurrent PTEN-Deficient Glioblastoma. *PLoS Med.* **2008**. [CrossRef]
142. Puli, S.; Jain, A.; Lai, J.C.K.; Bhushan, A. Effect of Combination Treatment of Rapamycin and Isoflavones on mTOR Pathway in Human Glioblastoma (U87) Cells. *Neurochem. Res.* **2010**, *35*, 986–993. [CrossRef] [PubMed]
143. Rao, R.D.; Mladek, A.C.; Lamont, J.D.; Goble, J.M.; Erlichman, C.; James, C.D.; Sarkaria, J.N. Disruption of Parallel and Converging Signaling Pathways Contributes to the Synergistic Antitumor Effects of Simultaneous mTOR and EGFR Inhibition in GBM Cells. *Neoplasia* **2005**, *7*, 921–929. [CrossRef] [PubMed]
144. Bell, J.B.; Eckerdt, F.D.; Alley, K.; Magnusson, L.P.; Hussain, H.; Bi, Y.; Arslan, A.D.; Clymer, J.; Alvarez, A.A.; Goldman, S.; et al. MNK Inhibition Disrupts Mesenchymal Glioma Stem Cells and Prolongs Survival in a Mouse Model of Glioblastoma. *Mol. Cancer Res.* **2016**, *14*, 984–993. [CrossRef] [PubMed]

145. Waskiewicz, A.J.; Flynn, A.; Proud, C.G.; Cooper, J.A. Mitogen-activated protein kinases activate the serine/threonine kinases Mnk1 and Mnk2. *EMBO J.* **1997**, *16*, 1909–1920. [CrossRef]
146. Brown, M.C.; Dobrikov, M.I.; Gromeier, M. Mitogen-Activated Protein Kinase-Interacting Kinase Regulates mTOR/AKT Signaling and Controls the Serine/Arginine-Rich Protein Kinase-Responsive Type 1 Internal Ribosome Entry Site-Mediated Translation and Viral Oncolysis. *J. Virol.* **2014**, *88*, 13149–13160. [CrossRef]
147. Zheng, J.; Li, J.; Xu, L.; Xie, G.; Wen, Q.; Luo, J.; Li, D.; Huang, D.; Fan, S. Phosphorylated Mnk1 and eIF4E Are Associated with Lymph Node Metastasis and Poor Prognosis of Nasopharyngeal Carcinoma. *PLoS ONE* **2014**. [CrossRef]
148. Lineham, E.; Spencer, J.; Morley, S.J. Dual abrogation of MNK and mTOR: A novel therapeutic approach for the treatment of aggressive cancers. *Future Med. Chem.* **2017**, *9*, 1539–1555. [CrossRef]
149. Grzmil, M.; Morin, P.; Lino, M.M.; Merlo, A.; Frank, S.; Wang, Y.; Moncayo, G.; Hemmings, B.A. MAP Kinase-Interacting Kinase 1 Regulates SMAD2-Dependent TGF- Signaling Pathway in Human Glioblastoma. *Cancer Res.* **2011**, *71*, 2392–2402. [CrossRef]
150. Grzmil, M.; Seebacher, J.; Hess, D.; Behe, M.; Schibli, R.; Moncayo, G.; Frank, S.; Hemmings, B.A. Inhibition of MNK pathways enhances cancer cell response to chemotherapy with temozolomide and targeted radionuclide therapy. *Cell. Signal.* **2016**, *28*, 1412–1421. [CrossRef]
151. Ng, T.L.; Leprivier, G.; Robertson, M.D.; Chow, C.; Martin, M.J.; Laderoute, K.R.; Davicioni, E.; Triche, T.J.; Sorensen, P.H.B. The AMPK stress response pathway mediates anoikis resistance through inhibition of mTOR and suppression of protein synthesis. *Cell Death Differ.* **2012**, *19*, 501–510. [CrossRef] [PubMed]
152. Xiao, B.; Sanders, M.J.; Underwood, E.; Heath, R.; Mayer, F.V.; Carmena, D.; Jing, C.; Walker, P.A.; Eccleston, J.F.; Haire, L.F.; et al. Structure of mammalian AMPK and its regulation by ADP. *Nature* **2011**, *472*, 230–233. [CrossRef] [PubMed]
153. Chlebowski, R.T.; McTiernan, A.; Wactawski-Wende, J.; Manson, J.E.; Aragaki, A.K.; Rohan, T.; Ipp, E.; Kaklamani, V.G.; Vitolins, M.; Wallace, R.; et al. Diabetes, Metformin, and Breast Cancer in Postmenopausal Women. *J. Clin. Oncol.* **2012**, *30*, 2844–2852. [CrossRef] [PubMed]
154. Tai, M.C.; Tsang, S.Y.; Chang, L.Y.F.; Xue, H. Therapeutic potential of wogonin: A naturally occurring flavonoid. *CNS Drug Rev.* **2005**, *11*, 141–150. [CrossRef] [PubMed]
155. Van Den Neste, E.; Cazin, B.; Janssens, A.; González-Barca, E.; Terol, M.J.; Levy, V.; Pérez de Oteyza, J.; Zachee, P.; Saunders, A.; de Frias, M.; et al. Acadesine for patients with relapsed/refractory chronic lymphocytic leukemia (CLL): A multicenter phase I/II study. *Cancer Chemother. Pharmacol.* **2013**, *71*, 581–591. [CrossRef] [PubMed]
156. Zhang, Z.-J.; Zheng, Z.-J.; Kan, H.; Song, Y.; Cui, W.; Zhao, G.; Kip, K.E. Reduced Risk of Colorectal Cancer With Metformin Therapy in Patients With Type 2 Diabetes: A meta-analysis. *Diabetes Care* **2011**, *34*, 2323–2328. [CrossRef] [PubMed]
157. Guo, D.; Hildebrandt, I.J.; Prins, R.M.; Soto, H.; Mazzotta, M.M.; Dang, J.; Czernin, J.; Shyy, J.Y.-J.; Watson, A.D.; Phelps, M.; et al. The AMPK agonist AICAR inhibits the growth of EGFRvIII-expressing glioblastomas by inhibiting lipogenesis. *Proc. Natl. Acad. Sci. USA* **2009**, *106*, 12932–12937. [CrossRef]
158. Lee, D.-H.; Lee, T.H.; Jung, C.H.; Kim, Y.-H. Wogonin induces apoptosis by activating the AMPK and p53 signaling pathways in human glioblastoma cells. *Cell. Signal.* **2012**, *24*, 2216–2225. [CrossRef]
159. Lin, Y.-C.; Hung, C.-M.; Tsai, J.-C.; Lee, J.-C.; Chen, Y.-L.S.; Wei, C.-W.; Kao, J.-Y.; Way, T.-D. Hispidulin Potently Inhibits Human Glioblastoma Multiforme Cells through Activation of AMP-Activated Protein Kinase (AMPK). *J. Agric. Food Chem.* **2010**, *58*, 9511–9517. [CrossRef]
160. Sesen, J.; Dahan, P.; Scotland, S.J.; Saland, E.; Dang, V.-T.; Lemarié, A.; Tyler, B.M.; Brem, H.; Toulas, C.; Cohen-Jonathan Moyal, E.; et al. Metformin Inhibits Growth of Human Glioblastoma Cells and Enhances Therapeutic Response. *PLoS ONE* **2015**. [CrossRef]
161. Liu, X.; Chhipa, R.R.; Nakano, I.; Dasgupta, B. The AMPK Inhibitor Compound C Is a Potent AMPK-Independent Antiglioma Agent. *Mol. Cancer Ther.* **2014**, *13*, 596–605. [CrossRef] [PubMed]
162. Liu, X.; Chhipa, R.R.; Pooya, S.; Wortman, M.; Yachyshin, S.; Chow, L.M.L.; Kumar, A.; Zhou, X.; Sun, Y.; Quinn, B.; et al. Discrete mechanisms of mTOR and cell cycle regulation by AMPK agonists independent of AMPK. *Proc. Natl. Acad. Sci. USA* **2014**, *111*, 435–444. [CrossRef] [PubMed]
163. Vucicevic, L.; Misirkic, M.; Janjetovic, K.; Harhaji-Trajkovic, L.; Prica, M.; Stevanovic, D.; Isenovic, E.; Sudar, E.; Sumarac-Dumanovic, M.; Micic, D.; et al. AMP-activated protein kinase-dependent and -independent




- mechanisms underlying in vitro antiglioma action of compound C. *Biochem. Pharmacol.* **2009**, *77*, 1684–1693. [CrossRef] [PubMed]
164. Kato, K.; Ogura, T.; Kishimoto, A.; Minegishi, Y.; Nakajima, N.; Miyazaki, M.; Esumi, H. Critical roles of AMP-activated protein kinase in constitutive tolerance of cancer cells to nutrient deprivation and tumor formation. *Oncogene* **2002**, *21*, 6082–6090. [CrossRef]
  165. Yang, Q.; Sarnow, P. Location of the internal ribosome entry site in the 5′ non-coding region of the immunoglobulin heavy-chain binding protein (BiP) mRNA: Evidence for specific RNA-protein interactions. *Nucleic Acids Res.* **1997**, *25*, 2800–2807. [CrossRef]
  166. Blau, L.; Knirsh, R.; Ben-Dror, I.; Oren, S.; Kuphal, S.; Hau, P.; Proescholdt, M.; Bosserhoff, A.-K.; Vardimon, L. Aberrant expression of c-Jun in glioblastoma by internal ribosome entry site (IRES)-mediated translational activation. *Proc. Natl. Acad. Sci. USA* **2012**, *109*, 2875–2884. [CrossRef]
  167. Webb, T.E.; Hughes, A.; Smalley, D.S.; Spriggs, K.A. An internal ribosome entry site in the 5′ untranslated region of epidermal growth factor receptor allows hypoxic expression. *Oncogenesis* **2015**, *4*, 134. [CrossRef]
  168. Komar, A.A.; Hatzoglou, M. Exploring Internal Ribosome Entry Sites as Therapeutic Targets. *Front. Oncol.* **2015**. [CrossRef]
  169. SUZUKI, Y.; SHIRAI, K.; OKA, K.; MOBARAKI, A.; YOSHIDA, Y.; NODA, S.; OKAMOTO, M.; SUZUKI, Y.; ITOH, J.; ITOH, H.; et al. Higher pAkt Expression Predicts a Significant Worse Prognosis in Glioblastomas. *J. Radiat. Res.* **2010**, *51*, 343–348. [CrossRef]
  170. Wurth, L.; Gebauer, F. RNA-binding proteins, multifaceted translational regulators in cancer. *Biochim. Biophys. Acta-Gene Regul. Mech.* **2015**, *1849*, 881–886. [CrossRef]
  171. Walters, B.; Thompson, S.R. Cap-Independent Translational Control of Carcinogenesis. *Front. Oncol.* **2016**. [CrossRef] [PubMed]
  172. Ross, J.A.; Bressler, K.R.; Thakor, N. Eukaryotic Initiation Factor 5B (eIF5B) Cooperates with eIF1A and eIF5 to Facilitate uORF2-Mediated Repression of ATF4 Translation. *Int. J. Mol. Sci.* **2018**, *19*, 4032. [CrossRef] [PubMed]
  173. Legnini, I.; Di Timoteo, G.; Rossi, F.; Morlando, M.; Briganti, F.; Sthandier, O.; Fatica, A.; Santini, T.; Andronache, A.; Wade, M.; et al. Circ-ZNF609 Is a Circular RNA that Can Be Translated and Functions in Myogenesis. *Mol. Cell* **2017**, *66*, 22–37. [CrossRef] [PubMed]
  174. Pamudurti, N.R.; Bartok, O.; Jens, M.; Ashwal-Fluss, R.; Stottmeister, C.; Ruhe, L.; Hanan, M.; Wyler, E.; Perez-Hernandez, D.; Ramberger, E.; et al. Translation of CircRNAs. *Mol. Cell* **2017**, *66*, 9–21. [CrossRef]
  175. Zhang, M.; Huang, N.; Yang, X.; Luo, J.; Yan, S.; Xiao, F.; Chen, W.; Gao, X.; Zhao, K.; Zhou, H.; et al. A novel protein encoded by the circular form of the SHPRH gene suppresses glioma tumorigenesis. *Oncogene* **2018**, *37*, 1805–1814. [CrossRef] [PubMed]
  176. Gonzalez, C.; Sims, J.S.; Hornstein, N.; Mela, A.; Garcia, F.; Lei, L.; Gass, D.A.; Amendolara, B.; Bruce, J.N.; Canoll, P.; et al. Ribosome profiling reveals a cell-type-specific translational landscape in brain tumors. *J. Neurosci.* **2014**, *34*, 10924–10936. [CrossRef]
  177. Helmy, K.; Halliday, J.; Fomchenko, E.; Setty, M.; Pitter, K.; Hafemeister, C.; Holland, E.C. Identification of Global Alteration of Translational Regulation in Glioma In Vivo. *PLoS ONE* **2012**. [CrossRef]
  178. Wahba, A.; Rath, B.H.; Bisht, K.; Camphausen, K.; Tofilon, P.J. Polysome profiling links translational control to the radioresponse of glioblastoma stem-like cells. *Cancer Res.* **2016**, *76*, 3078–3087. [CrossRef]



© 2019 by the authors. Licensee MDPI, Basel, Switzerland. This article is an open access article distributed under the terms and conditions of the Creative Commons Attribution (CC BY) license (<http://creativecommons.org/licenses/by/4.0/>).

Article

# Intracellular Redox-Balance Involvement in Temozolomide Resistance-Related Molecular Mechanisms in Glioblastoma

Alessia Lo Dico <sup>1,†</sup>, Daniela Salvatore <sup>1,2,†</sup> , Cristina Martelli <sup>1</sup> , Dario Ronchi <sup>3</sup>, Cecilia Diceglie <sup>1</sup>, Giovanni Lucignani <sup>4</sup> and Luisa Ottobrini <sup>1,5,\*</sup> 

<sup>1</sup> Department of Pathophysiology and Transplantation, University of Milan, 20090 Segrate (MI), Italy; alessia.lodico@unimi.it (A.L.D.); daniela.salvatore@unimi.it (D.S.); cristina.martelli@unimi.it (C.M.); cecilia.diceglie@unimi.it (C.D.)

<sup>2</sup> Doctorate School of Molecular and Translational Medicine, University of Milan, 20122 Milan, Italy

<sup>3</sup> Neurology Unit, Neuroscience Section, Department of Pathophysiology and Transplantation, Dino Ferrari Centre, IRCCS Foundation Ca' Granda Ospedale Maggiore Policlinico, University of Milan, 20122 Milan, Italy; dario.ronchi@unimi.it

<sup>4</sup> Department of Health Sciences, University of Milan, 20146 Milan, Italy; giovanni.lucignani@unimi.it

<sup>5</sup> Molecular Bioimaging and Physiology (IBFM), CNR, 20090 Segrate (MI), Italy

\* Correspondence: luisa.ottobrini@unimi.it; Tel.: +39-02-503-30404

† These authors have contributed equally to this work.

Received: 27 September 2019; Accepted: 22 October 2019; Published: 24 October 2019



**Abstract:** Glioblastoma (GBM) is the most common astrocytic-derived brain tumor in adults, characterized by a poor prognosis mainly due to the resistance to the available therapy. The study of mitochondria-derived oxidative stress, and of the biological events that orbit around it, might help in the comprehension of the molecular mechanisms at the base of GBM responsiveness to Temozolomide (TMZ). Sensitive and resistant GBM cells were used to test the role of mitochondrial ROS release in TMZ-resistance. Chaperone-Mediated Autophagy (CMA) activation in relation to reactive oxygen species (ROS) release has been measured by monitoring the expression of specific genes. Treatments with H<sub>2</sub>O<sub>2</sub> were used to test their potential in reverting resistance. Fluctuations of cytoplasmic ROS levels were accountable for CMA induction and cytotoxic effects observed in TMZ sensitive cells after treatment. On the other hand, in resistant cells, TMZ failed in producing an increase in cytoplasmic ROS levels and CMA activation, preventing GBM cell toxicity. By increasing oxidative stress, CMA activation was recovered, as also cell cytotoxicity, especially in combination with TMZ treatment. Herein, for the first time, it is shown the relation between mitochondrial ROS release, CMA activation and TMZ-responsiveness in GBM.

**Keywords:** oxidative stress; chaperone mediated autophagy (CMA); mitochondrial scavenger; drug resistance; reactive oxygen species (ROS), cell motility

## 1. Introduction

Malignant Glioblastomas (GBMs) are the most common primary brain tumors and are characterized by a dismal prognosis mainly due to the resistance to conventional therapies. The current therapeutic regimen is based on chemotherapy with Temozolomide (TMZ) combined with radiotherapy [1]. The O<sup>6</sup>-methylguanine-DNA methyltransferase (MGMT) promoter methylation status is the main biomarker to foresee GBM responsiveness to TMZ, but its predictive value is limited and additional functions of TMZ unrelated to MGMT activity are likely to underlie a further distinction between responders and non-responders due to specific features. For example, TMZ might influence cell viability

by increasing reactive oxygen species (ROS) [2,3], or by modulating autophagy [4], apoptosis [5], hypoxia inducible factor (HIF)-1 $\alpha$  activity [6–8] and epithelial-mesenchymal transition (EMT) [9].

Autophagy plays a critical role in cellular homeostasis: in fact, it is involved both in pro-survival [10] and pro-apoptotic mechanisms [11]. Autophagy also affects the migration and invasion capabilities of tumor cells [12]. Taking into account all these evidences, there are several clues suggesting that autophagy could be involved in the onset and modulation of cell resistance or sensitivity to treatment [13]. Furthermore, different autophagic mechanisms have been described presenting specific drivers, effectors and functional consequences [14].

It is known that TMZ might induce autophagy and that the activation of this pathway is crucial for the susceptibility to the treatment [15,16]. In particular, it has been recently demonstrated that chaperone mediated autophagy (CMA) is the main mechanism by which TMZ treatment decreases HIF-1 $\alpha$  activity in sensitive cells, thus improving responsiveness by promoting cell apoptosis [7]. Moreover, the depletion of CMA related genes [17,18] is sufficient to annul the sensitivity to TMZ, demonstrating its important role in the response to this drug.

CMA activity is induced by a transitory release of ROS into the cytoplasm by mitochondria following the endoplasmic reticulum stress. ROS have been described to be regulators of multiple redox-dependent pathways related to growth, differentiation, survival and others [19–21]. However, since radicals can impair cell integrity, a redox-homeostasis system exists in cells to detoxify ROS. This enzymatic repertoire includes: Super Oxide Dismutase (SOD), Glutathione Reductase (GR), and Catalase [22]. Irreversible ROS mediated damage might enhance both proteasomal and lysosomal (autophagic) degradation of oxidized proteins. The impairment or overload of these compensatory mechanisms results in compromised cell viability [23]. Cancer cells usually show an elevated basal intracellular level of ROS without harmful consequences due to adaptation mechanisms sustaining tumorigenesis. Further oxidative stress could overcome these mechanisms restoring the vulnerability of cancer cells to ROS-mediated damage, improving therapeutic response [2,24,25].

In this study we investigate the possibility to use ROS-mediated damage to restore CMA inducibility and GBM cell sensitivity to TMZ.

## 2. Materials and Methods

### 2.1. Cell Lines and Reagents

U251 cell line was obtained from Dr. G. Melillo, and T98 cell line was obtained from Dr. V. Vaira and were routinely maintained as adherent cells in RPMI 1640 medium, supplemented with 10% heat-inactivated fetal bovine serum, penicillin and streptomycin (50 IU/mL), and 2 mM glutamine (all Euroclone, Pero, MI, Italy). Cells were maintained in a humidified atmosphere of 5% CO<sub>2</sub> at 37 °C in normoxia. Cells were plated at 15,000 cells/cm<sup>2</sup> and after 24 h, in vitro treatments were performed as follow: 100  $\mu$ M Temozolomide, TMZ, for 24 h (h); 200  $\mu$ M or 1 mM of Hydrogen Peroxide, H<sub>2</sub>O<sub>2</sub>, for 24 h; 25  $\mu$ M MitoTEMPO, MitoT, for 1 h of pre-treatment (all Sigma-Aldrich, St. Louis, MO, USA). After treatments samples were analyzed for cell viability through Trypan Blue exclusion test. Glioma cells were transfected for 24 h with 10 nM of *HSC70* or *PHLPP1* siRNA or a scrambled negative control (Eurofins, Italy) in presence of a T-Pro-P-Fect reagent (T-Pro Biotechnology, New Taipei, Taiwan), and then cells were treated with TMZ.

### 2.2. Biochemical Assays

The ROS content after different treatments was tested by using ROS-Glo™ H<sub>2</sub>O<sub>2</sub> Assay kit (Promega, Milan, Italy). HIF-1 $\alpha$  activity was measured on lysates through Luciferase Biochemical assay, using GloMax-Multi Detection System (Promega, Milan, Italy), and normalized for protein content [26]. The cytotoxicity of treatments was tested utilizing Cell Tox™ Green Cytotoxicity Assay kit (Promega, Milan, Italy) and Cell Titer-Glo® Luminescent Cell Viability Assay (Promega). Detection and quantification of Glutathione (GSH) was performed after treatment by the commercially



available GSH-Glo™ Glutathione Assay (Promega). Data were expressed as Glutathione concentration. All the assays performed by using commercially available kits were carried out according to the manufacturer's instructions.

### 2.3. RNA Extraction and Real-Time PCR

RNA was extracted by using a commercially available Illustra RNA spin Mini Isolation Kit (GE Healthcare, Milan, Italy) in accordance with the manufacturer's instructions. Total RNA was reverse-transcribed to cDNA by using a High-Capacity cDNA Reverse Transcription Kit (Applied Biosystems, Monza, Italy). The real-time PCRs were performed in triplicate for each data point by using the Sybr Green technique; the oligonucleotides used are shown in Table 1. Target mRNA content changes in relation to the  $\beta$ -ACTIN housekeeping gene were determined using the  $\Delta\Delta$ Ct Method (and represented as FOI, fold of induction, compared to control level).

**Table 1.** Primer sequences.

Gene	Forward	Reverse
BAX	ATGGACGGGTCCGGGGAG	ATCCAGCCCAACAGCCGC
BAD	CCCAGAGTTTGAGCCGAGTG	CCCATCCCTTCGTCGCCT
BCL-2	GATTGTGGCCTTCTTTGAG	CAAACCTGAGCAGAGTCTC
PHLPP1	CCTACCTTCTCCAGTGCCT	CCAGCAGTTCCAAGTTTCT
LAMP2A	TGCTGGCTACCATGGGGCTG	GCAGCTGCCTGTGGAGTGAGT
HSC70	ATTGATCTTGGCACCACCTA	GGGTGCAGGAGGTATGCCTGTGA
HIF-1 $\alpha$	TGATTGCATCTCCATCTCTAC	GACTCAAAGCGACAGATAACACG
VEGF	CGAGGGCCTGGAGTGTGT	CGCATAATCTGCATGGTGATG
SNAIL	GCGAGCTGCAGGACTCTAAT	CCCGAATGGTCCACAAAAC
SLUG	CATGCCTGTCATACCACAAC	GGTGTGAGATGGAGGAGG
E-CAD	GATCAAGTCAAGCGTGAGTCG	AGCCTCT CAATGGCGAACAC
SOD-2	TTAACGCGCAGATCATGCA	GGTGGCGTTGAGATTGTTCA
CATALASE	TAAGACTGACCAGGGCA	CAAACCTTGGTGAGATCGAA
GR	AACATCCCAACTGTGGTCTTCAGC	TTGGTAACTGCGTGATACATCGGG
GPX	CGCAACGATGTTGCCTGGAACCTT	AGGCTCGATGTCAATGGTCTGGAA
GSS	ATGCTGTGCAGATGGACTTCAACC	TGGATGTCAAACAGACGAGCGGTA
$\beta$ -ACTIN	TCAAGATCATTGCTCCTCCTG	CCAGAGGCGTACAGGGATAG

### 2.4. Wounding Assay

For the wound healing assay, at the end of the treatment, a wound was created by manually scraping the confluent glioma monolayer with a p200 pipette tip. Images at time zero ( $t = 0$  h) were acquired to record the initial area of the wounds, and the recovery of the wounded monolayers due to cell migration toward the free area was evaluated at 24 h ( $t = 24$  h). The area of wound was quantified by Java's Image J software (<http://rsb.info.nih.gov>) and the migration of cells toward the wounds was expressed as percentage of wound closure: % of wound closure =  $[(A_{(t=0\text{h})} - A_{(t=24\text{h})}) / A_{(t=0\text{h})}] \times 100$ , where,  $A_{(t=0\text{h})}$  is the area of wound measured immediately after scratching, and  $A_{(t=24\text{h})}$  is the area of wound measured 24 h after scratching.

### 2.5. Protein Studies

Samples were prepared in Novex Bolt LDS sample buffer and Novex Bolt Reducing Agent and were boiled for 3 min. Lowry method was used for protein quantification. Proteins (10–30  $\mu$ g) were loaded in Precast Bolt® Bis-Tris Plus Gels 4–12% and run for 30 min at 200 V in Novex Bolt 1X MES/SDS Running buffer. Transfer to nitrocellulose membrane was performed by a Trans-Blot® Turbo™ system (BioRad, Hercules, CA, USA). Membranes were blocked in Odyssey® Blocking Buffer (LICOR, Lincoln, NE, USA) and incubated with secondary fluorescent antibodies (IRDye®, LICOR, Lincoln, NE, USA). Protein bands were visualized by an Odyssey Fc device, model 2800 (LICOR Biosciences). Bands intensity was quantified by Image Studio Lite Ver 5.2 software. Subcellular fractions of cells were

obtained using Protein Fractionation Kit (ThermoScientific, Waltham, MA, USA) [27], according to manufacturer's instruction. Protein signals were normalized for the respective fraction marker: TUBULIN for cytosol and LAMP1 for lysosomes.

Samples were probed with the following antibodies: LAMP2A (51-2200 1:1000, Invitrogen, Carlsbad, CA, USA), HSC70 (MA1-26078 1:000, Invitrogen), GAPDH (sc4772 1:1200, Santa Cruz, Santa Cruz, CA, USA), NDUFB8 (ab110242 1:1000, Abcam, Cambridge, UK), SDHB (ab14714 1:1000, Abcam), UQCRC2 (ab14745 1:1000, Abcam), MTCO2 (ab110258 1:1000, Abcam), ATP5A (ab14748 1:1000, Abcam), SDHA (459200 1:10000, Invitrogen), COXIV (A21347 1:2000, Invitrogen), SOD1 and CATALASE (Abcam, ab179843 1:500), LAMP1 (ab25630 1:900, Abcam), ACTIN (A2066 1:200, Sigma-Aldrich, St. Louis, MO, USA),  $\alpha$ -TUBULIN (3873S 1:800, Cell signaling, Danvers, MA, USA).

### 2.6. Mitochondrial Complex Activity Studies

Protein extraction was performed by sonication (50 W for 10 s, 3 times) after suspending cell pellets in the proper buffer (pH 7.2). Lysates were centrifuged at 750 $\times$  g for 10 min and supernatant was recovered. Lowry method was used for protein quantification. A Lambda 2 spectrophotometer (Perkin Elmer, Waltham, MA, USA) was used to assess enzymatic activities. Analyses were performed at specific wavelengths for each enzymatic activity after preparing proper solutions as previously described [27] with minor changes. Experiments were performed at 30 °C. Analyses were performed through the Perkin Elmer software. Measurements were normalized for the activity level of citrate synthase, a stable matrix mitochondrial enzyme; this latter step was performed in order to normalize respiratory chain activity for mitochondrial mass.

### 2.7. Statistical Analyses

The *in vitro* experiments were repeated at least three times and led to reproducible results. The data are presented as the mean values  $\pm$  SD of the independent experiments and were statistically analyzed using a t-test or one- or two-way analysis of variance, followed by Dunnett's or Bonferroni's multiple comparison and Prism 4 software (GraphPad Software Inc., San Diego, CA, USA).

## 3. Results

### 3.1. Mitochondrial ROS are Crucial for TMZ Responsiveness in U251 Cells

Aiming to characterize ROS involvement in TMZ-sensitivity, first we measured ROS levels in TMZ-sensitive (U251) and TMZ-resistant (T98) GBM cell lines before and after exposure to TMZ. ROS basal levels were 8-fold higher in T98 compared to U251 cells. After 24 h of treatment, TMZ induced a significant increase in ROS levels in U251 sensitive cells but not in T98 resistant cells (Figure 1A).

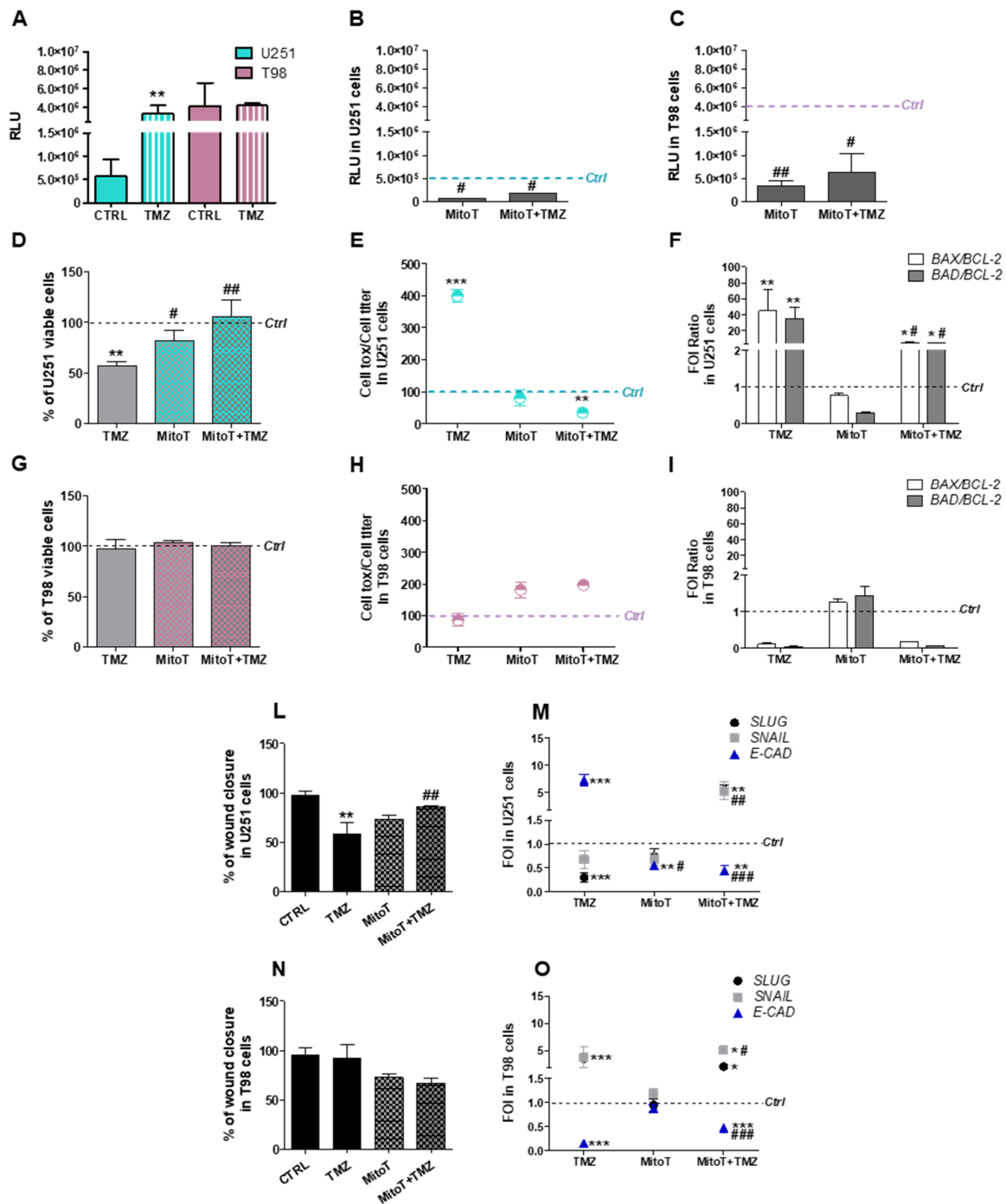


**Figure 1.** Crucial role of mitochondrial reactive oxygen species (ROS) in Temozolomide-responsiveness in U251 and T98 cells. (A) Luminescent assay applied to measure H<sub>2</sub>O<sub>2</sub> levels in cell culture medium of U251 and T98 cells in untreated cells and after 24 h treatment with 100 μM Temozolomide (TMZ). Data were expressed as relative luminescence units (RLU) obtained by luciferase counts normalized for the amount of proteins quantified by Bradford assay. \*\* *p* < 0.01 vs. control cells. (B) ROS levels measured in U251 and (C) T98 cells after 1h of treatment with MitoTempo (MitoT) 25 μM ± TMZ for 24 h. Data were expressed as RLU. # *p* < 0.05, ## *p* < 0.01 vs. TMZ-treated cells. (D) Viability of U251 and (G) T98 cells, assessed by means of Trypan blue exclusion test, and expressed as the percentage of viable cells after treatment with 100 μM TMZ ± 25 μM MitoT. \*\* *p* < 0.01 vs. control cells; # *p* < 0.05, ## *p* < 0.01 vs. TMZ-treated cells. (E) Cell toxicity in U251 and (H) T98 cells analyzed by Cell Tox Green normalized on Cell Titer Glo and expressed as percentage compared to control cells. \*\*\* *p* < 0.001 vs. control cells.

(F) Gene expression analysis for *BAX*, *BAD* and *BCL-2* analyzed by means of Real-time PCR in U251 and (I) T98 cells after treatment with 100  $\mu$ M TMZ  $\pm$  25  $\mu$ M MitoT. Data were normalized to  $\beta$ -*ACTIN*, and the  $\Delta\Delta$ Ct values were expressed as fold of induction (FOI) of the ratio between treated and control cells and then as the ratio *BAX/BCL-2* and *BAD/BCL-2*. \*  $p < 0.05$ ; \*\*  $p < 0.01$ ; \*\*\*  $p < 0.001$  treated vs. control cells. #  $p < 0.05$ , ##  $p < 0.01$ , ###  $p < 0.001$  vs. TMZ-treated cells. (L) Scratch test performed after treatments in U251 and (N) in T98 cells. Wound closure percentage compared to controls was analyzed with Image J software. \*\*  $p < 0.01$  treated vs. control cells. ##  $p < 0.01$  vs. TMZ-treated cells. (M) Gene expression analysis for EMT-related genes (*SLUG*, *SNAIL*, *E-CADHERIN* -*E-CAD*-) analyzed by means of Real-time PCR in U251 and (O) in T98 cells. Data were normalized and expressed as mentioned above. \*\*  $p < 0.01$ ; \*\*\*  $p < 0.001$  treated vs. control cells. ##  $p < 0.01$ , ###  $p < 0.001$  vs. TMZ-treated cells. Mean values  $\pm$  SD of three independent experiments.

We replicated the experiment by treating cells with the selective mitochondrial ROS scavenger Mitotempo (MitoT). MitoT was able to reduce ROS levels in both cell lines, confirming their mitochondrial origin, however, residual ROS levels were still higher in TMZ-resistant cells (Figure 1B,C). Interestingly, the inhibition of mitochondrial ROS release by MitoT impaired the cytotoxic effect of TMZ in U251 cells, as assessed by the count of viable cells (Figure 1D) and the evaluation of cellular toxicity (Figure 1E). Global U251 cellular viability was unaffected by MitoT in absence of TMZ. At molecular level, MitoT engaged a pro-survival response in TMZ-treated U251 cells and counteracted the pro-apoptotic gene expression signature induced by TMZ (Figure 1F).

A different behavior was observed in T98 cells: TMZ-resistance was unchanged after TMZ treatment and/or MitoT. Indeed, MitoT was ineffective in modifying cellular viability and toxicity in TMZ-treated T98 cells (Figure 1G,H). Similarly, the “resistant-like” gene expression signature observed in T98 cells after TMZ treatment was preserved after the combined administration of MitoT (Figure 1I).

The functional consequences of the combined TMZ and MitoT treatment were also investigated by monitoring GBM cell motility. The scratch test, performed in U251 TMZ-sensitive cells, suggested that MitoT favored the scratch closure, annulling the anti-proliferative effect of TMZ in these cells (Figure 1L). This conclusion was supported by gene expression profile analysis performed on EMT genes: the reduction of *SLUG* and the increase of *E-CADHERIN* (*E-CAD*) expression in TMZ-treated U251 sensitive cells was partially or almost totally counteracted by MitoT when administered alone or in combination with TMZ, respectively (Figure 1M). Once again, this effect was restricted to sensitive U251 cells (Figure 1N,O).

### 3.2. Involvement of Chaperone Mediated Autophagy in GBM Responsiveness to TMZ

We have previously associated the activation of the CMA and HIF-1 $\alpha$  activity reduction with GBM cell responsiveness to TMZ [6,7]. These findings prompted to investigate how MitoT could affect CMA, an intracellular pathway engaged by ROS release [28] and known to modulate HIF-1 $\alpha$ -activity [7].

To extend the evaluation of consequences of ROS scavenging on CMA activity and TMZ-responsiveness, we assessed CMA activity before and after MitoT delivery in our experimental conditions by checking the expression levels of three genes involved in the positive regulation of CMA: lysosome-associated membrane protein (*LAMP2A*), heat shock cognate 70 kDa protein (*HSC70*) and pleckstrin homology domain and leucine rich repeat protein phosphatase (*PHLPP1*). Transcript levels were found higher in TMZ-treated versus untreated U251 cells supporting the activation of CMA program in relation to TMZ-responsiveness. This effect was not observed with MitoT co-administration. Notably, CMA-related gene expression profile was significantly reduced by MitoT itself (Figure 2A).

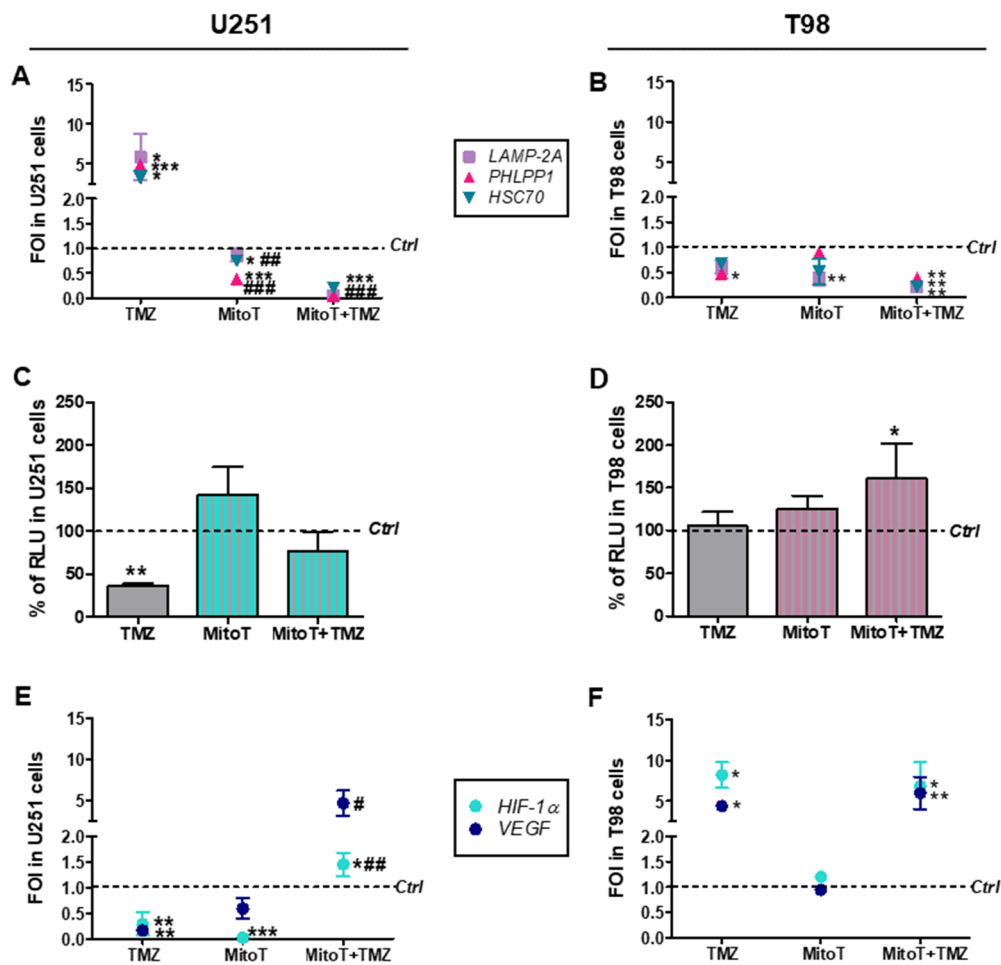


**Figure 2.** Involvement of chaperone-mediated-autophagy (CMA) after Temozolomide and MitoTempo (MitoT) treatment. (A) Gene expression analysis for CMA-related genes (*LAMP2A*, *HSC70*, *PHLPP1*) analyzed by means of Real-time PCR in U251 and (B) T98 cells after treatment with 100  $\mu$ M Temozolomide (TMZ)  $\pm$  25  $\mu$ M MitoT. Data were normalized for  $\beta$ -ACTIN, and the  $\Delta\Delta$ Ct values were expressed as FOI of the ratio between treated and control cells. \*  $p < 0.05$ ; \*\*  $p < 0.01$ ; \*\*\*  $p < 0.001$  treated vs. control cells. #  $p < 0.05$ , ##  $p < 0.01$ , ###  $p < 0.001$  vs. TMZ-treated cells. (C) Biochemical assay for HIF-1 $\alpha$  activity in U251 and (D) T98 cell lines. Data were expressed as RLU, obtained normalizing luciferase counts for the amount of proteins quantified by Bradford assay. \*\*  $p < 0.01$  vs. control cells. (E) Gene expression analysis for HIF-1 $\alpha$  and vascular endothelial growth factor (*VEGF*) expression in U251 and (F) T98 cells. \*  $p < 0.05$ ; \*\*  $p < 0.01$  vs. control cells; #  $p < 0.05$ , ##  $p < 0.01$  vs. TMZ-treated cells. Mean values  $\pm$  SD of three independent experiments.

In T98 resistant cells, with or without TMZ, gene expression levels were unaltered by MitoT with the only exception of *LAMP2A* expression, which was found decreased in MitoT-treated cells (Figure 2B).

As regards the reduction of HIF-1 $\alpha$  activity in relation to TMZ-responsiveness in sensitive cells [6,7], MitoT prevented this effect in TMZ-treated U251 sensitive cells. Conversely, MitoT produced no modification in cell responsiveness when administered to T98 resistant cells (Figure 2C,D). Quantitative RT-PCR studies, evaluating the expression levels of HIF-1 $\alpha$  gene (*HIF-1 $\alpha$* ) and its established target gene vascular endothelial growth factor (*VEGF*), supported this conclusion (Figure 2E,F), even showing an increase in *HIF-1 $\alpha$*  and *VEGF* transcripts in MitoT and TMZ-containing treatments in U251 cells.

### 3.3. Chaperone Mediated Autophagy Activity is Dependent Upon Different Proteins

To check LAMP2A and HSC-70 intracellular localization, we performed cell fractionation in U251 and T98 cells with or without TMZ (Figure 3A,B; Figure S1).

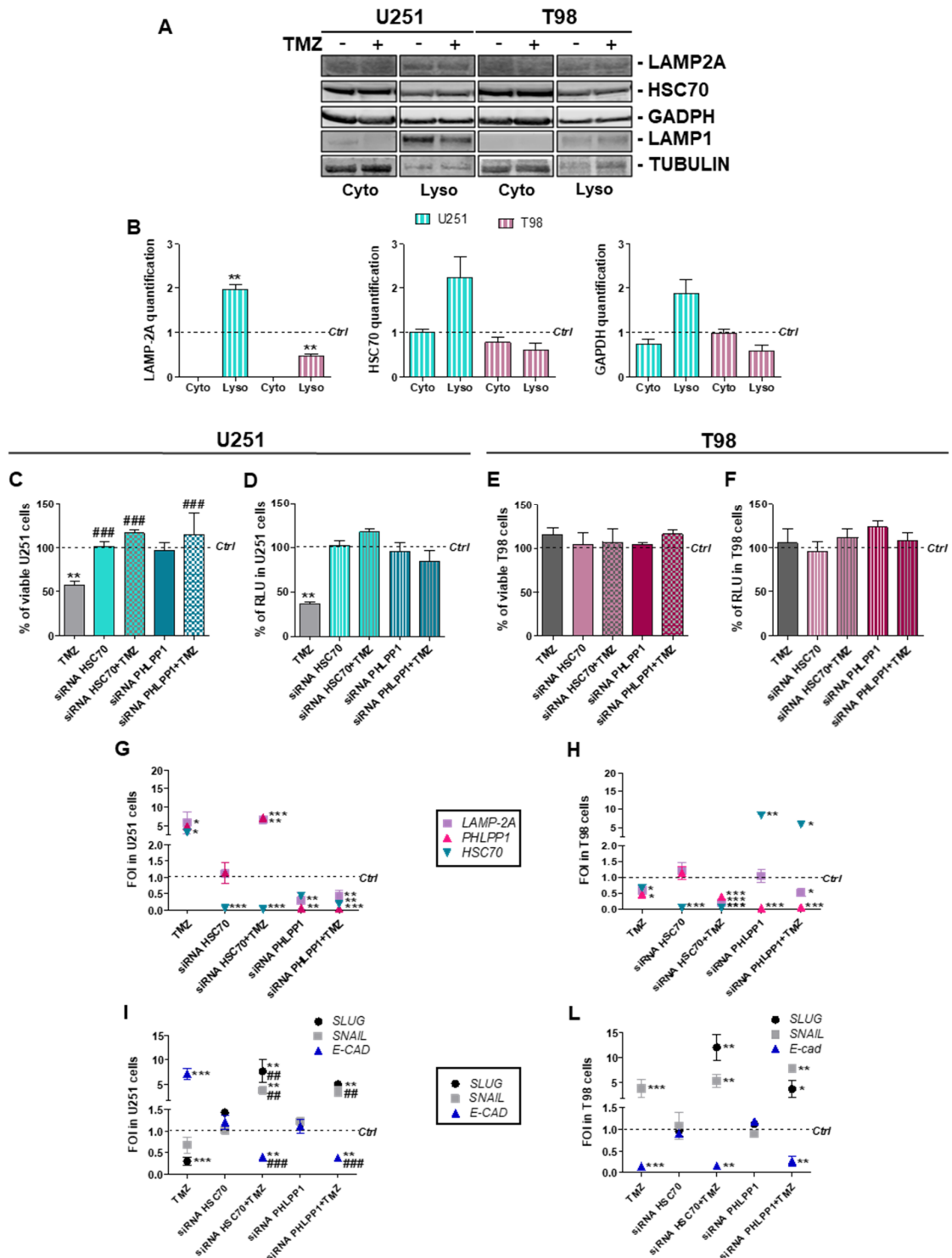


**Figure 3.** Essential chaperone-mediated-autophagy related gene involvement in Temozolomide response in U251 and T98 cells. **(A)** Western blot analysis of LAMP2A, HSC70 and GAPDH protein levels in subcellular fractions (Cyto = cytosolic fraction; Lyso = Lysosomal fraction) obtained from untreated (–) and Temozolomide (TMZ) treated (+) U251 and T98 cell lines. **(B)** Protein signals were

normalized for the respective fraction marker: TUBULIN (cytosol) and LAMP1 (lysosomes). Histograms show the distribution of target proteins in the fractions compared to untreated control levels. \*\*  $p < 0.01$  treated vs. control cells. Lysosomal content of the three considered proteins are significantly different in U251 compared to T98 cells (LAMP2A  $p = 0.003$ ; HSC70  $p = 0.04$ ; Glyceraldehyde 3-phosphate dehydrogenase (GAPDH)  $p = 0.03$ ). (C) Viability analysis and (D) assessment of HIF-1 $\alpha$  activity in U251 and in (E,F) T98 cells after *PHLPP1* or *HSC70* silencing  $\pm$  100  $\mu$ M TMZ treatment. Data were expressed as percentage of viable cells and as RLU, as previously described. \*\*  $p < 0.01$  treated vs. control cells; ###  $p < 0.001$  vs. TMZ-treated cells. (G) Gene expression profile for CMA-related genes (*LAMP2A*, *HSC70*, *PHLPP1*) in U251 and (H) T98 cells. (I) Gene expression profile for EMT-related genes (*SLUG*, *SNAIL*, *E-CAD*) in U251 and (L) T98 cells. Gene expression was analyzed by means of Real-time PCR. All data were normalized for  $\beta$ -ACTIN, and the  $\Delta\Delta$ Ct values were expressed as FOI of the ratio between treated and control cells. \*  $p < 0.05$ ; \*\*  $p < 0.01$ ; \*\*\*  $p < 0.001$  treated vs. control cells; ##  $p < 0.01$ , ###  $p < 0.001$ , vs. TMZ-treated cells. Mean values  $\pm$  SD of three independent experiments.

After the normalization for the relative fraction markers, we observed a statistically significant increase in lysosomal recruitment of the CMA receptor LAMP2A and an increase in cytosolic-to-lysosomal translocation of the CMA chaperone HSC70 in TMZ-treated U251 cells ( $p = 0.065$ ) but not in TMZ-treated T98 cells (compared to untreated control level). The lysosomal level of the CMA substrate Glyceraldehyde 3-phosphate dehydrogenase (GAPDH) was also increased in TMZ-treated U251 cells ( $p = 0.059$ ). Overall, these findings support the selective engagement of CMA pathway in TMZ-sensitive cells.

We have previously demonstrated that blocking CMA by *LAMP2A* silencing provoked TMZ-resistance in U251 cells [7]. To expand these observations to other key players of CMA, we evaluated TMZ-responsiveness after transient downregulation of *HSC70* and *PHLPP1* in both TMZ sensitive and resistant cells. In the sensitive U251 cells, siRNA against *HSC70* or *PHLPP1* abolished TMZ-dependent cell death and HIF-1 $\alpha$  activity reduction (Figure 3C,D). TMZ-responsiveness and HIF-1 $\alpha$  activity in T98 cells was not changed under the same experimental conditions (Figure 3E,F). Transcriptional changes underlining the acquisition of TMZ-resistance were observed in TMZ-treated U251 cells after *HSC70* or *PHLPP1* silencing (Figure 3G), paralleling previous achievements in *LAMP2A*-silenced cells [7]. T98 cells were not affected by CMA downregulation and maintained their resistant-like behavior for CMA-related (Figure 3H) and *HIF-1 $\alpha$ /VEGF* gene expression (Figure S2).

The investigation of EMT-related gene expression profile showed that, in U251 cells, *HSC70* and *PHLPP1* silencing *per se* did not produce any change in *SNAIL*, *SLUG* and *E-CAD* expression. However, TMZ treatment in silenced cells induced a mesenchymal-like expression profile, with an increase in *SNAIL* and *SLUG* expression and a downregulation of *E-CAD* mRNA level, typical of TMZ-resistant cells (Figure 3I). T98 cells did not show any difference in EMT modulation after TMZ treatment even after *HSC70* and *PHLPP1* silencing (Figure 3L).

#### 3.4. Deregulation of Redox-Homeostasis is Involved in GBM Responsiveness to TMZ

To better understand the mechanisms involved in cytoplasmic ROS increase after TMZ treatment in sensitive cells, mitochondrial and cytosolic detox mechanisms were assessed.

Since ROS production and thus redox-homeostasis is dependent by the induction of the respiratory chain, we measured the activities of mitochondrial respiratory chain complexes I, II, I+III and IV in U251 and T98 cells at basal levels and after 24 h treatment with TMZ. We observed that basal activities of complexes I, III and IV were consistently higher in T98 compared to U251 cells and this difference was maintained after treatment (Figure 4A,B).

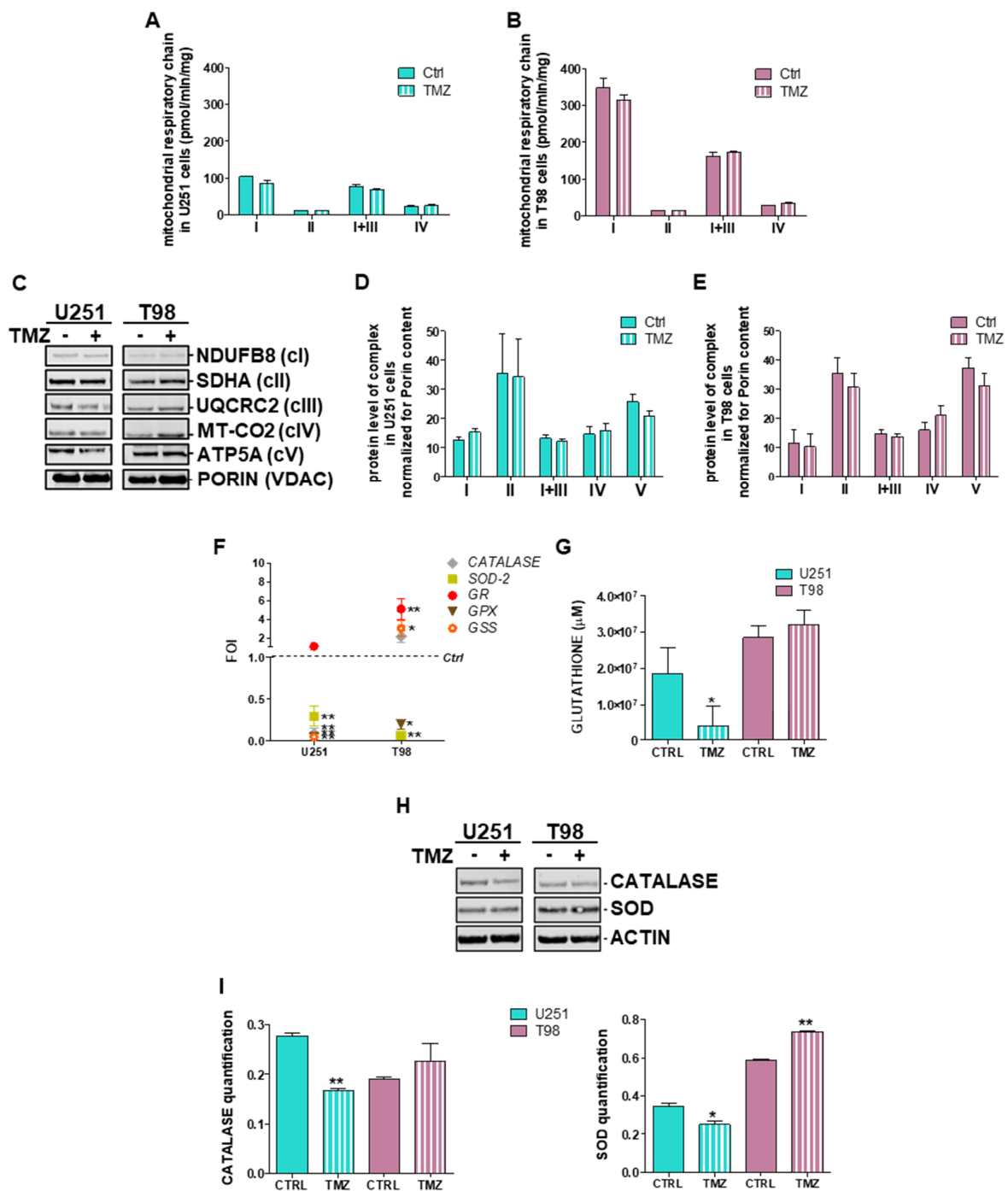


**Figure 4.** Deregulation of redox-homeostasis after Temozolomide treatment in U251 and T98 cells. (A) Spectrophotometric analysis of mitochondrial respiratory chain complex activities measured before and after 24 h of treatment with Temozolomide (TMZ) in U251 and (B) T98 cells. Values are expressed as mean values of complex I, II, I+III and IV normalized for citrate synthase activities (pmol/min/mg of proteins). (C) Descriptive image of Western Blot analysis of representative subunits of the mitochondrial respiratory chain assessed before and after 24 h of treatment with TMZ and their quantification in (D) U251 and (E) T98 cells. Values are expressed as mean values of protein content (arbitrary units) normalized for the signal of PORIN (VDAC). (F) Gene expression profile for detox enzymes (SOD-2, CATALASE, GLUTATHIONE PEROXIDASE -GPX-, GLUTATHIONE SYNTHETASE -GPS-, and REDUCTASE -GR-) after treatment with 100 μM TMZ in U251 and T98 cells. Data were normalized for



$\beta$ -ACTIN, and the  $\Delta\Delta$ Ct values were expressed as FOI of the ratio between treated and control cells. \*  $p < 0.05$ ; \*\*  $p < 0.01$  vs. control cells. (G) Glutathione concentration assessed after TMZ treatment in both cells by means of a commercially available kit. Data were expressed as glutathione concentration ( $\mu$ M). \*  $p < 0.05$  treated vs. control cells. (H) Western blot analysis of CATALASE and SOD in protein lysates from untreated (–) and TMZ-treated (+) U251 and T98 cell lines at 24 h of treatment, and (i) their quantification. Protein signals were normalized to ACTIN levels. \*  $p < 0.05$ ; \*\*  $p < 0.01$  treated vs. control. Mean values  $\pm$  SD of three independent experiments.

No differences were observed in citrate synthase levels, ruling out the chance of altered global mitochondrial content (data not shown). A slight reduction of Complex I activity was observed in TMZ-treated U251 cells after 24 h (18%). In T98 cells treatment with TMZ did not produce any reduction of complex activities (Figure 4B).

To check whether these differences are the consequence of altered stability of mitochondrial respiratory chain complexes, we performed SDS-PAGE analysis of representative oxidative phosphorylation system (OXPHOS) subunits in the same samples used for biochemical studies. Despite the detection of heterogeneous signals, we failed to disclose any difference between U251 and T98 cells in basal conditions as well as after TMZ treatment (Figure 4C–E). These findings suggest that increased OXPHOS activities observed in TMZ-resistant cells and the decrease observed after TMZ delivery might originate from deregulated OXPHOS homeostasis and/or altered ROS management while steady state levels of mitochondrial proteins are conserved.

To assess the role of the redox-homeostasis in TMZ-responsiveness, we assessed also the gene expression profile of the main modulators of the detox machinery. In detail we observed that, despite the different basal levels of SOD and CATALASE expression (Figure S3), in U251 TMZ-responsive cells glutathione peroxidase (GPX), glutathione synthetase (GSS), SOD-2 and CATALASE, were downregulated by TMZ treatment (Figure 4F). On the contrary, in T98 cells, with the exception of SOD-2 and GPX, all other genes resulted up-regulated by the treatment (Figure 4F). Moreover, GSH amount was analyzed in both cell lines, showing, in addition to the high levels measured in T98 TMZ-resistant cells, that TMZ treatment was able to reduce the GSH concentration only in U251 TMZ-sensitive cells (Figure 4G). Diminished residual levels of CATALASE and SOD-1 after TMZ treatment were also observed at protein level in U251, but not in T98 cells where SOD-1 was even statistically increased after 48h treatment with TMZ (Figure 4H,I).

### 3.5. Chemical-Induced Oxidative Stress Weakens the Resistance of T98 Cells to TMZ

Data so far presented suggest that mitochondrial ROS scavenging drives the transition from TMZ-sensitive to TMZ-resistant phenotype in U251 cells. In the last set of experiments, we aimed to verify whether chemically-induced ROS build-up might influence TMZ-responsiveness in U251 and, more importantly, in T98 cells. For this purpose, CMA-mediated GBM cytotoxicity was assessed in TMZ-sensitive and -resistant cells after treatment with both TMZ and H<sub>2</sub>O<sub>2</sub>. Oxidative stress promoted by low concentrations of H<sub>2</sub>O<sub>2</sub> (200  $\mu$ M, “mild” dose) was ineffective in reducing U251 viability while H<sub>2</sub>O<sub>2</sub> and TMZ co-treatment displayed the same effect observed for single TMZ delivery (Figure 5A).

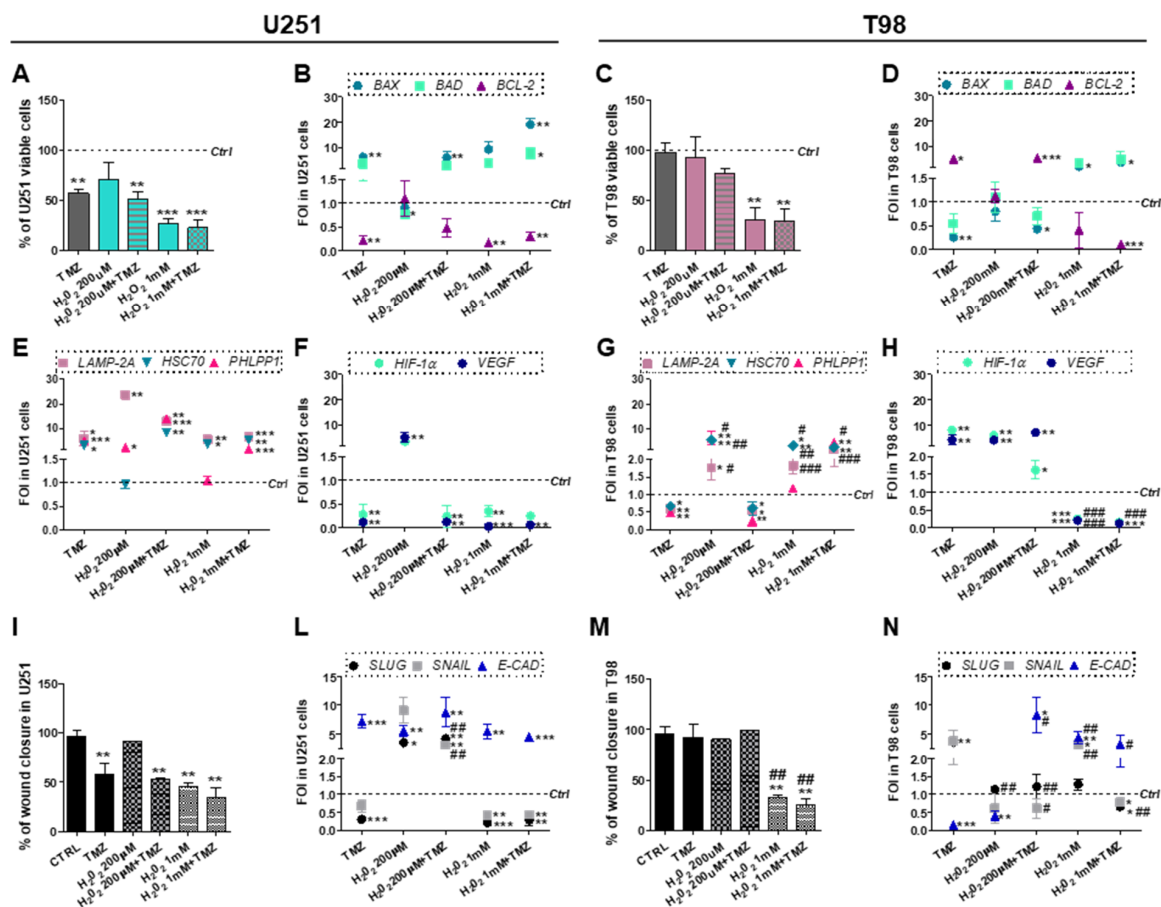


**Figure 5.** Role of oxidative stress in overcoming Temozolomide resistance. (A) Viability analysis and (B) gene expression profile for apoptotic-related genes (*BAX*, *BAD* and *BCL-2*) in U251 and (C,D) in T98 cells. Viability was assessed by means of Trypan blue exclusion test after treatment with 200µM or 1mM H<sub>2</sub>O<sub>2</sub> ± 100 µM Temozolomide (TMZ). Data of viability were expressed as percentage of viable cells; \*\* *p* < 0.01; \*\*\* *p* < 0.001 treated vs. control cells. (E) Gene expression profile for CMA-related genes (*LAMP2A*, *HSC70*, *PHLPP1*), and for (F) *HIF-1α* and *VEGF* in U251 and in (G,H) T98 cell after treatment with 200 µM or 1 mM H<sub>2</sub>O<sub>2</sub> ± 100 µM TMZ. \* *p* < 0.05; \*\* *p* < 0.01; \*\*\* *p* < 0.001 treated vs. control cells. All data of gene expression were normalized for β-ACTIN, and the ΔΔCt values were expressed as FOI of the ratio between treated and control cells. \* *p* < 0.05; \*\* *p* < 0.01; \*\*\* *p* < 0.001 treated vs. control cells. # *p* < 0.05, ## *p* < 0.01, ### *p* < 0.001 vs. TMZ-treated cells. (I) Scratch test and (L) gene expression for EMT-related genes (*SLUG*, *SNAIL*, *E-CAD*) performed after treatments in U251 and (M,N) T98 cells. Wound closure percentage compared to control was analyzed with Image J software. \*\* *p* < 0.01 treated vs. control cells. ## *p* < 0.01 vs. TMZ-treated cells. Data of gene expression were normalized and expressed as mentioned above. \* *p* < 0.05; \*\* *p* < 0.01; \*\*\* *p* < 0.001 treated vs. control cells. # *p* < 0.05, ## *p* < 0.01, ### *p* < 0.001 vs. TMZ-treated cells.

However, an increase of H<sub>2</sub>O<sub>2</sub> dose (1 mM, “high” dose) was sufficient to mimic the effect of single TMZ treatment although, even in this case, we did not observe synergy between H<sub>2</sub>O<sub>2</sub> and TMZ (Figure 5A). The induction of apoptotic gene expression pattern fitted with viability data (Figure 5B). In T98 cells, “mild” oxidative stress failed to perturb cellular survival. On the other hand, the “high” H<sub>2</sub>O<sub>2</sub> dose produced a significant decrease in cell viability, both alone and in combination with TMZ (Figure 5C). Gene expression studies showed that only the combination of the “high” H<sub>2</sub>O<sub>2</sub> dose and TMZ was able to redirect the molecular profile towards apoptosis (Figure 5D).

The cytotoxic effect induced by the “high” H<sub>2</sub>O<sub>2</sub> dose in U251 cells was matched by increased expression of *LAMP2A* and *HSC70* and reduced expression of *HIF-1α* and *VEGF*. Upregulation of all CMA-related genes was obtained only after concurrent TMZ treatment (Figure 5E,F). The same results

were described for TMZ-resistant T98 cells (Figure 5G,H), where only the “high” H<sub>2</sub>O<sub>2</sub> dose produced an upregulation of all CMA genes. These data confirm that induced oxidative stress exerts a cytotoxic effect through CMA activation. Importantly, oxidative stress seems to overcome TMZ-resistance in T98 cells.

Mild oxidative stress was not able to induce any delay in wound closure in absence of TMZ in U251 cells (Figure 5I). However, the “high” H<sub>2</sub>O<sub>2</sub> concentration promoted the acquisition of an epithelial expression profile overlapping the one obtained after TMZ treatment (Figure 5L). In T98 cells, the efficacy of the combined treatment with the “high” H<sub>2</sub>O<sub>2</sub> dose and TMZ was also demonstrated by scratch test (Figure 5M). Once again, at the molecular level, only the combined use of TMZ and H<sub>2</sub>O<sub>2</sub> allowed to achieve a sensitive-like profile as demonstrated by the upregulation of *E-CAD* and the downregulation of *SNAIL* and *SLUG* (Figure 5N).

#### 4. Discussion

Results shown herein give emphasis to the importance of ROS in inducing CMA and its fundamental role in determining responsiveness to TMZ. CMA has been described as a sensor of the oxidative stress, being involved in the removal of proteins altered by ROS intracellular activity and concurring in cell homeostasis regulation by selectively degrading specific proteins. It is known that oxidative stress allows the upregulation of CMA key players such as LAMP2A and HSC70 [28].

Despite their oxidizing action, ROS levels are important to maintain cellular homeostasis, also mediating some key transduction pathways [29,30] and promoting apoptotic switch [3] and CMA activation [28], also in hypoxic microenvironment [30].

Here, we described that different ROS levels detected in sensitive and resistant cells after treatment might play an essential role in cell responsivity to TMZ, and in modulating CMA activity.

Starting from ROS analysis, U251 TMZ-responsive cells are characterized by a lower basal level of cytoplasmic ROS compared to T98 TMZ-resistant ones, and only in sensitive cells, TMZ can induce an increase of cytoplasmic ROS. TMZ-induced ROS are fundamental for GBM cell responsiveness driving CMA activation, the expression of pro-apoptotic genes and the re-programming of an epithelial-like expression pattern. On the other hand, the lack in transitory increase of cytoplasmic ROS after TMZ treatment in T98 resistant cell line, avoid CMA activation, pro-apoptotic and pro-epithelial gene expression, confirming the crucial role played by the increase of ROS level in leading the onset of the cytotoxic effect driven by CMA. In this work, we showed that ROS increase is due to their mitochondrial release. Indeed, the use of MitoT, a mitochondrial ROS scavenger, highlighted that mitochondria play a fundamental role in response to TMZ. In fact, the combined use of TMZ with MitoT in U251 sensitive cells, impairs the cytotoxic effect mediated by TMZ treatment by inhibiting mitochondrial ROS release. Future studies will be aimed at elucidating the mechanisms underlying this phenomenon since mitochondria not only are the main ROS producer within the cell, but they are also key regulator of oxidative metabolism, involved also in the apoptotic switch [31].

Treatment with MitoT in U251 cells not only prevented TMZ-dependent decrease in cell viability, the induction of cytotoxicity, the expression of a pro-apoptotic and pro-epithelial gene expression pattern and the decrease in cell motility, but the abrogation of mitochondrial ROS reverted also the TMZ induced pattern of expression of CMA-related genes (*LAMP2A*, *HSC70*). The same effect was observed also for *PHLPP1* expression, which was altered even by MitoT treatment itself. *PHLPP1* has been proposed as a negative modulator of tumorigenesis, being associated to the promotion of apoptosis [32] and, in U251 cell line, it was demonstrated to be involved in the suppression of tumor malignancy and in the modulation of inflammatory cytokines [33]. *PHLPP1* activity is of great importance also for its role in the positive regulation of CMA activity and in the AKT dephosphorylation [34]. Results described herein propose an important role for *PHLPP1*, whose activity could be directly regulated by cytoplasmic ROS levels and switching on CMA.

Supporting the molecular data, CMA activity and inhibition is always in line with HIF-1 $\alpha$  expression and activity, and *VEGF* transcript level. HIF-1 $\alpha$  is in fact a CMA target and *VEGF* is one of

its main direct target genes. For this reason, here we reaffirm the use of HIF-1 $\alpha$  activity and *VEGF* expression as biomarkers for CMA activity assessment.

Classically speaking, HIF-1 $\alpha$  activity is strictly regulated by oxygen availability whose decrease is able to reduce HIF-1 $\alpha$  proteasome degradation by inhibiting Prolyl Hydroxylase (PHD) activity, and consequently, is able to induce an increase of the activity of this important transcription factor. However, many other mechanisms have been described to be able to modulate HIF-1 $\alpha$  activity independently from oxygen availability. This is the reason why to clarify the direct relation between GBM responsiveness to TMZ, CMA and HIF-1 $\alpha$  activity, we performed all the experiments in normoxia, to prevent a disguise of modulations due to hypoxia. We have previously analyzed the relation between GBM responsiveness to TMZ and hypoxia, reporting that low oxygen condition is able to increase resistance even in previously sensitive cells. Further analyses to elucidate the influence of an increase in HIF-1 $\alpha$  activity due to different causes including hypoxia upon resistance and in relation to CMA activity will be carried out as a future development of the project. Major aims will include trying to identify the molecular mechanisms mainly involved, but nowadays, they are beyond the aims of this paper. Indeed, independently from oxygen availability, the regulation played by CMA on HIF-1 $\alpha$  activity is a fundamental issue to be investigated in relation to the modulation of cell metabolism and of several processes involved in proliferation, stemness and invasiveness, as we have already demonstrated [7].

To clarify molecular results, it is important to note that CMA is a complex mechanism characterized by the synergic functions of different proteins. The whole CMA mechanism can be influenced at three different levels. A first control level is related to the expression and function of carrier proteins that bind a KFERQ-like motif in specific proteins (*HSC70*, *STUB/CHIP* and related proteins) and drive them to the lysosome. The second control level includes the expression and activity of the transporter *LAMP2A*, whose function is determined by post-translational modifications modulating its multimerization and function. Third level is the real check-point driving activation of CMA activity and is related to the activity of specific modulators such as *PHLPP1* and the expression of proteins acting as bridge between CMA players and the lysosome (*RAC-1*).

Now, it is easy to understand the complexity in CMA activity regulation and our results demonstrate the crucial role of each component of the machinery. As a matter of fact, the silencing of just one player results in the abrogation of the whole mechanism. We had already demonstrated that *LAMP2A* silencing is sufficient to block CMA activity, driving U251 cells toward a resistant profile [7]. Here we show that even the silencing of other CMA players such as *HSC70* or *PHLPP1* is sufficient to block CMA activation reverting TMZ-responsiveness in U251 cells to a resistant phenotype. What is most interesting is that while *HSC70* silencing impaired CMA activity without influencing other CMA-related genes, *PHLPP1* silencing, albeit inducing the same functional effects upon CMA activity, was also able to negatively modulate the other CMA related genes (*LAMP2A* and *HSC70*), after treatment with TMZ, exactly reproducing TMZ effects occurring in naturally resistant cells. All these data suggested an essential role for CMA and in particular for *PHLPP1*-regulated pathways in relation to TMZ responsiveness. In T98 cells, the silencing of CMA-related genes did not produce differences in responsiveness to TMZ but at the molecular level, *PHLPP1* silencing statistically induced the expression of *HSC70*. This phenomenon could be due to the modulation of a phosphorylation-dependent pathway involved in *HSC70* modulation, but the exact explanation of this mechanism is beyond the aim of this study and will be investigated in the future.

Another aim of this study was the elucidation of the mechanisms involved in the increase of cytoplasmic ROS after treatment with TMZ. ROS are mainly produced by mitochondria respiratory chain, but cells have developed several mechanisms to avoid their detrimental effect within the cells. Our results demonstrated that basal differences in ROS levels between sensitive and resistant cells are mainly due to a different activity of the respiratory chain, but that this mechanism is not involved in the transitory increase of ROS level measured after TMZ treatment in sensitive U251 cells.

Similarly, the stability of respiratory chain complexes is not modified by treatment and cannot account for ROS release after treatment. Resistance to therapy has recently been associated to the activation of anti-oxidant cell species, also in GBM [35]. For instance, the activation of GR [35], CATALASE [36] and SOD-2 [37] was higher in TMZ-resistant cells, providing evidences of their involvement in mediating resistance. Results described herein confirm these data showing differential expression and activity of genes involved in detoxification from ROS (*GSH*, *GSS*, *GPX*, *CATALASE*, *SOD-2*).

Several therapeutic approaches aimed at reducing cell detoxifying agents in tumor cells have already been described [38,39], as well as several treatments inducing an increase in oxidative stress (e.g., the Stupp protocol itself [1]). Here we have demonstrated that an exogenous increase in intracellular ROS level induces the same mechanisms activated by TMZ-dependent ROS release in sensitive cells and is able to overcome detox systems in resistant ones. In detail, 1 mM H<sub>2</sub>O<sub>2</sub> treatment in U251 cells was able to induce a pro-apoptotic pattern of expression, to activate CMA and to determine an epithelial-like expression profile, similarly to what happens after treatment with TMZ. On the other hand, in T98 TMZ-resistant cells, even if 1 mM H<sub>2</sub>O<sub>2</sub> treatment produced a reduction in cell viability and CMA activation, a completely responsive-like gene expression pattern for both apoptosis, CMA, and EMT was obtained only after concurrent TMZ treatment. These results highlight the importance of the coexistence of TMZ molecular effects with an increase in intracellular oxidative stress and the fundamental role played by CMA in mediating its cytotoxicity.

## 5. Conclusions

This work demonstrates that CMA activity is induced by a transitory increase in intracellular ROS level, and that GBM cell sensitivity to TMZ is strictly related to this ROS temporary increment. Sensitive and resistant cells show differences in detox system that could explain the phenotypic differences between TMZ-sensitive and -resistant cells. Starting from these considerations, two main conclusions can be drawn. First, TMZ drives the burst of mitochondrial ROS in sensitive cells leading to cell death and the presence of ROS is crucial for TMZ-responsiveness since ROS abrogation blocks its effects. Second, mitochondrial ROS release drives CMA activation and this phenomenon is essential for inducing cell toxicity by treatment. Overall these findings provide evidences for improving the design of innovative GBM therapies aimed at overcoming resistance by inducing CMA activity.

**Supplementary Materials:** The following are available online Figure S1. LAMP2A and HSC70 quantification; Figure S2. *HIF-1a* and *VEGF* expression after CMA-related gene silencing; Figure S3. *SOD* and *CATALASE* basal level.

**Author Contributions:** Conceptualization, A.L.D. and L.O.; data curation, A.L.D., D.S., C.M., D.R. and C.D.; formal analysis, A.L.D., D.S., C.M., D.R., C.D. and L.O.; funding acquisition, L.O.; supervision, L.O.; writing—original draft, A.L.D., D.S. and D.R.; writing—review and editing, D.R., G.L. and L.O.

**Funding:** This research was funded by FP7-INSERT project (HEALTH-2012-INNOVATION-1, GA305311).

**Acknowledgments:** The authors would like to thank G. Melillo for providing the U251-HRE cells.

**Conflicts of Interest:** The authors declare no conflict of interest.

## References

1. Stupp, R.; Mason, W.P.; Van Den Bent, M.J.; Weller, M.; Fisher, B.; Taphoorn, M.J.B.; Belanger, K.; Brandes, A.A.; Marosi, C.; Bogdahn, U.; et al. Radiotherapy plus Concomitant and Adjuvant Temozolomide for Glioblastoma. *New Engl. J. Nucl. Med.* **2005**, *352*, 987–996. [CrossRef] [PubMed]
2. Valtorta, S.; Dico, A.L.; Raccagni, I.; Gaglio, D.; Belloli, S.; Politi, L.S.; Martelli, C.; Diceglie, C.; Bonanomi, M.; Ercoli, G.; et al. Metformin and temozolomide, a synergic option to overcome resistance in glioblastoma multiforme models. *Oncotarget* **2017**, *8*, 113090–113104. [CrossRef] [PubMed]
3. Zhang, W.; Wang, Z.; Shu, F.; Jin, Y.; Liu, H.; Wang, Q.; Yang, Y. Activation of AMP-activated protein kinase by temozolomide contributes to apoptosis in glioblastoma cells via p53 activation and mTORC1 inhibition. *J. Biol. Chem.* **2010**, *285*, 40461–40471. [CrossRef]

4. Yan, Y.; Xu, Z.; Dai, S.; Qian, L.; Sun, L.; Gong, Z. Targeting autophagy to sensitive glioma to temozolomide treatment. *J. Exp. Clin. Cancer Res.* **2016**, *35*, 23. [CrossRef]
5. Roos, W.P.; Batista, L.F.Z.; Naumann, S.C.; Wick, W.; Weller, M.; Menck, C.F.M.; Kaina, B. Apoptosis in malignant glioma cells triggered by the temozolomide-induced DNA lesion O6-methylguanine. *Oncogene* **2007**, *26*, 186–197. [CrossRef]
6. Lo Dico, A.; Martelli, C.; Valtorta, S.; Raccagni, I.; Diceglie, C.; Belloli, S.; Gianelli, U.; Vaira, V.; Politi, L.S.; Bosari, S.; et al. Identification of imaging biomarkers for the assessment of tumour response to different treatments in a preclinical glioma model. *Eur. J. Nucl. Med. Mol. Imaging* **2015**, *42*, 1093–1105. [CrossRef]
7. Lo Dico, A.; Martelli, C.; Diceglie, C.; Lucignani, G.; Ottobrini, L. Hypoxia-Inducible Factor-1 $\alpha$  Activity as a Switch for Glioblastoma Responsiveness to Temozolomide. *Front. Oncol.* **2018**, *8*, 249–259. [CrossRef]
8. Lo Dico, A.; Valtorta, S.; Ottobrini, L.; Moresco, R.M. Role of Metformin and AKT Axis Modulation in the Reversion of Hypoxia Induced TMZ-Resistance in Glioma Cells. *Front. Oncol.* **2019**, *9*, 463. [CrossRef]
9. Kahlert, U.D.; Nikkiah, G.; Maciaczyk, J. Epithelial-to-mesenchymal(-like) transition as a relevant molecular event in malignant gliomas. *Cancer Lett.* **2013**, *331*, 131–138. [CrossRef]
10. Das, C.K.; Mandal, M.; Kögel, D. Pro-survival autophagy and cancer cell resistance to therapy. *Cancer Metastasis Rev.* **2018**, *37*, 749–766. [CrossRef]
11. Denton, D.; Kumar, S. Autophagy-dependent cell death. *Cell Death Differ.* **2019**, *26*, 605–616. [CrossRef]
12. Colella, B.; Faienza, F.; Di Bartolomeo, S.; Colella, B.; Faienza, F.; Di Bartolomeo, S. EMT Regulation by Autophagy: A New Perspective in Glioblastoma Biology. *Cancers (Basel)* **2019**, *11*, 312. [CrossRef] [PubMed]
13. Trejo-Solís, C.; Serrano-Garcia, N.; Escamilla-Ramírez, Á.; Castillo-Rodríguez, R.; Jimenez-Farfan, D.; Palencia, G.; Calvillo, M.; Alvarez-Lemus, M.; Flores-Nájera, A.; Cruz-Salgado, A.; et al. Autophagic and Apoptotic Pathways as Targets for Chemotherapy in Glioblastoma. *Int. J. Mol. Sci.* **2018**, *19*, 3773. [CrossRef] [PubMed]
14. Mizushima, N.; Levine, B.; Cuervo, A.M.; Klionsky, D.J. Autophagy fights disease through cellular self-digestion. *Nature* **2008**, *451*, 1069–1075. [CrossRef] [PubMed]
15. Buccarelli, M.; Marconi, M.; Pacioni, S.; De Pascalis, I.; Giorgio D’alessandris, Q.; Martini, M.; Ascione, B.; Malorni, W.; Larocca, L.M.; Pallini, R.; et al. Inhibition of autophagy increases susceptibility of glioblastoma stem cells to temozolomide by igniting ferroptosis. *Cell Death Dis.* **2018**, *9*, 841–857. [CrossRef]
16. Kriel, J.; Müller-Nedebock, K.; Maarman, G.; Mbizana, S.; Ojuka, E.; Klumperman, B.; Loos, B. Coordinated autophagy modulation overcomes glioblastoma chemoresistance through disruption of mitochondrial bioenergetics. *Scientific Reports* **2018**, *8*, 10348. [CrossRef]
17. Ding, Z.-B.; Fu, X.-T.; Shi, Y.-H.; Zhou, J.; Peng, Y.-F.; Liu, W.-R.; Shi, G.-M.; Gao, Q.; Wang, X.-Y.; Song, K.; et al. Lamp2a is required for tumor growth and promotes tumor recurrence of hepatocellular carcinoma. *Int. J. Oncol.* **2016**, *49*, 2367–2376. [CrossRef]
18. Saha, T. LAMP2A overexpression in breast tumors promotes cancer cell survival via chaperone-mediated autophagy. *Autophagy* **2012**, *8*, 1643–1656. [CrossRef]
19. Cabello, C.M.; Bair, W.B.; Wondrak, G.T. Experimental therapeutics: Targeting the redox Achilles heel of cancer. *Curr. Opin. Investig. Drugs* **2007**, *8*, 1022–1037.
20. Chiu, W.-T.; Shen, S.-C.; Chow, J.-M.; Lin, C.-W.; Shia, L.-T.; Chen, Y.-C. Contribution of reactive oxygen species to migration/invasion of human glioblastoma cells U87 via ERK-dependent COX-2/PGE2 activation. *Neurobiol. Dis.* **2010**, *37*, 118–129. [CrossRef]
21. D’Autréaux, B.; Toledano, M.B. ROS as signalling molecules: Mechanisms that generate specificity in ROS homeostasis. *Nat. Rev. Mol. Cell Biol.* **2007**, *8*, 813–824. [CrossRef] [PubMed]
22. Sies, H. Glutathione and its role in cellular functions. *Free Radic. Biol. Med.* **1999**, *27*, 916–921. [CrossRef]
23. Valko, M.; Leibfritz, D.; Moncol, J.; Cronin, M.T.D.; Mazur, M.; Telser, J. Free radicals and antioxidants in normal physiological functions and human disease. *Int. J. Biochem. Cell Biol.* **2007**, *39*, 44–84. [CrossRef]
24. Landriscina, M.; Maddalena, F.; Laudiero, G.; Esposito, F. Adaptation to Oxidative Stress, Chemoresistance, and Cell Survival. *Antioxid. Redox Signal.* **2009**, *11*, 2701–2716. [CrossRef]
25. Laurent, A.; Nicco, C.; Chéreau, C.; Goulvestre, C.; Alexandre, J.; Alves, A.; Lévy, E.; Goldwasser, F.; Panis, Y.; Soubrane, O.; et al. Controlling tumor growth by modulating endogenous production of reactive oxygen species. *Cancer Res.* **2005**, *65*, 948–956.

26. Lo Dico, A.; Valtorta, S.; Martelli, C.; Belloli, S.; Gianelli, U.; Tosi, D.; Bosari, S.; Degrassi, A.; Russo, M.; Raccagni, I.; et al. Validation of an engineered cell model for in vitro and in vivo hif-1 $\alpha$  evaluation by different imaging modalities. *Mol. Imaging Biol.* **2014**, *16*, 210–223. [CrossRef]
27. Monzio Compagnoni, G.; Kleiner, G.; Bordoni, A.; Fortunato, F.; Ronchi, D.; Salani, S.; Guida, M.; Corti, C.; Pichler, I.; Bergamini, C.; et al. Mitochondrial dysfunction in fibroblasts of Multiple System Atrophy. *Biochim. Biophys. Acta-Mol. Basis Dis.* **2018**, *1864*, 3588–3597. [CrossRef]
28. Kiffin, R.; Christian, C.; Knecht, E.; Cuervo, A.M. Activation of chaperone-mediated autophagy during oxidative stress. *Mol. Biol. Cell* **2004**, *15*, 4829–4840. [CrossRef]
29. Baas, A.S.; Berk, B.C. Differential Activation of Mitogen-Activated Protein Kinases by H<sub>2</sub>O<sub>2</sub> and O<sub>2</sub><sup>-</sup> in Vascular Smooth Muscle Cells. *Circ. Res.* **1995**, *77*, 29–36. [CrossRef]
30. Salazar-Ramiro, A.; Ramírez-Ortega, D.; Pérez de la Cruz, V.; Hernández-Pedro, N.Y.; González-Esquivel, D.F.; Sotelo, J.; Pineda, B. Role of Redox Status in Development of Glioblastoma. *Front. Immunol.* **2016**, *7*, 156. [CrossRef]
31. Chen, H.; Wang, J.; Liu, Z.; Yang, H.; Zhu, Y.; Zhao, M.; Liu, Y.; Yan, M. Mitochondrial DNA depletion causes decreased ROS production and resistance to apoptosis. *Int. J. Mol. Med.* **2016**, *38*, 1039–1046. [CrossRef] [PubMed]
32. Mei, Z.; He, Y.; Feng, J.; Shi, J.; Du, Y.; Qian, L.; Huang, Q.; Jie, Z. MicroRNA-141 promotes the proliferation of non-small cell lung cancer cells by regulating expression of PHLPP1 and PHLPP2. *FEBS Lett.* **2014**, *588*, 3055–3061. [CrossRef] [PubMed]
33. Teng, D.-C.; Sun, J.; An, Y.-Q.; Hu, Z.-H.; Liu, P.; Ma, Y.-C.; Han, B.; Shi, Y. Role of PHLPP1 in inflammation response: Its loss contributes to gliomas development and progression. *Int. Immunopharmacol.* **2016**, *34*, 229–234. [CrossRef] [PubMed]
34. Arias, E.; Koga, H.; Diaz, A.; Mocholi, E.; Patel, B.; Cuervo, A.M. Lysosomal mTORC2/PHLPP1/Akt Regulate Chaperone-Mediated Autophagy. *Mol. Cell* **2015**, *59*, 270–284. [CrossRef]
35. Zhu, Z.; Du, S.; Du, Y.; Ren, J.; Ying, G.; Yan, Z. Glutathione reductase mediates drug resistance in glioblastoma cells by regulating redox homeostasis. *J. Neurochem.* **2018**, *144*, 93–104. [CrossRef]
36. Smith, P.S.; Zhao, W.; Robbins, M. Knocking down catalase leads to increased ROS production and proliferation in glioma cells. *Cancer Res.* **2006**, *66*, 1037.
37. Chang, K.-Y.; Hsu, T.-I.; Hsu, C.-C.; Tsai, S.-Y.; Liu, J.-J.; Chou, S.-W.; Liu, M.-S.; Liou, J.-P.; Ko, C.-Y.; Chen, K.-Y.; et al. Specificity protein 1-modulated superoxide dismutase 2 enhances temozolomide resistance in glioblastoma, which is independent of O6-methylguanine-DNA methyltransferase. *Redox Biol.* **2017**, *13*, 655–664. [CrossRef]
38. Iida, M.; Sunaga, S.; Hirota, N.; Kuribayashi, N.; Sakagami, H.; Takeda, M.; Matsumoto, K. Effect of glutathione-modulating compounds on hydrogen-peroxide-induced cytotoxicity in human glioblastoma and glioma cell lines. *J. Cancer Res. Clin. Oncol.* **1997**, *123*, 619–622. [CrossRef]
39. Rocha, C.R.R.; Garcia, C.C.M.; Vieira, D.B.; Quinet, A.; de Andrade-Lima, L.C.; Munford, V.; Belizário, J.E.; Menck, C.F.M. Glutathione depletion sensitizes cisplatin- and temozolomide-resistant glioma cells in vitro and in vivo. *Cell Death Dis.* **2014**, *5*, e1505. [CrossRef]



© 2019 by the authors. Licensee MDPI, Basel, Switzerland. This article is an open access article distributed under the terms and conditions of the Creative Commons Attribution (CC BY) license (<http://creativecommons.org/licenses/by/4.0/>).

MDPI AG  
Grosspeteranlage 5  
4052 Basel  
Switzerland  
Tel.: +41 61 683 77 34

*Cells* Editorial Office  
E-mail: [cells@mdpi.com](mailto:cells@mdpi.com)  
[www.mdpi.com/journal/cells](http://www.mdpi.com/journal/cells)



Disclaimer/Publisher's Note: The title and front matter of this reprint are at the discretion of the Guest Editors. The publisher is not responsible for their content or any associated concerns. The statements, opinions and data contained in all individual articles are solely those of the individual Editors and contributors and not of MDPI. MDPI disclaims responsibility for any injury to people or property resulting from any ideas, methods, instructions or products referred to in the content.







Academic Open  
Access Publishing

[mdpi.com](http://mdpi.com)

ISBN 978-3-7258-2933-0